

Lecture Notes in Civil Engineering

Carlo Rainieri · Giovanni Fabbrocino ·
Nicola Caterino · Francesca Ceroni ·
Matilde A. Notarangelo *Editors*

Civil Structural Health Monitoring

Proceedings of CSHM-8 Workshop

 Springer

Lecture Notes in Civil Engineering

Volume 156

Series Editors

Marco di Prisco, Politecnico di Milano, Milano, Italy

Sheng-Hong Chen, School of Water Resources and Hydropower Engineering,
Wuhan University, Wuhan, China

Ioannis Vayas, Institute of Steel Structures, National Technical University of
Athens, Athens, Greece

Sanjay Kumar Shukla, School of Engineering, Edith Cowan University, Joondalup,
WA, Australia

Anuj Sharma, Iowa State University, Ames, IA, USA

Nagesh Kumar, Department of Civil Engineering, Indian Institute of Science
Bangalore, Bengaluru, Karnataka, India

Chien Ming Wang, School of Civil Engineering, The University of Queensland,
Brisbane, QLD, Australia

Lecture Notes in Civil Engineering (LNCE) publishes the latest developments in Civil Engineering—quickly, informally and in top quality. Though original research reported in proceedings and post-proceedings represents the core of LNCE, edited volumes of exceptionally high quality and interest may also be considered for publication. Volumes published in LNCE embrace all aspects and subfields of, as well as new challenges in, Civil Engineering. Topics in the series include:

- Construction and Structural Mechanics
- Building Materials
- Concrete, Steel and Timber Structures
- Geotechnical Engineering
- Earthquake Engineering
- Coastal Engineering
- Ocean and Offshore Engineering; Ships and Floating Structures
- Hydraulics, Hydrology and Water Resources Engineering
- Environmental Engineering and Sustainability
- Structural Health and Monitoring
- Surveying and Geographical Information Systems
- Indoor Environments
- Transportation and Traffic
- Risk Analysis
- Safety and Security

To submit a proposal or request further information, please contact the appropriate Springer Editor:

- Pierpaolo Riva at pierpaolo.riva@springer.com (Europe and Americas);
- Swati Meherishi at swati.meherishi@springer.com (Asia—except China, and Australia, New Zealand);
- Wayne Hu at wayne.hu@springer.com (China).

All books in the series now indexed by Scopus and EI Compendex database!

More information about this series at <http://www.springer.com/series/15087>

Carlo Rainieri · Giovanni Fabbrocino ·
Nicola Caterino · Francesca Ceroni ·
Matilde A. Notarangelo
Editors

Civil Structural Health Monitoring

Proceedings of CSHM-8 Workshop

 Springer

Editors

Carlo Rainieri
Construction Technologies Institute (ITC)
National Research Council of Italy (CNR)
Naples, Italy

Giovanni Fabbrocino
Department of Biosciences and Territory
University of Molise
Campobasso, Italy

Nicola Caterino
Parthenope University of Naples
Napoli, Italy

Francesca Ceroni
Parthenope University of Naples
Napoli, Italy

Matilde A. Notarangelo
S2X srl
Campobasso, Italy

ISSN 2366-2557

ISSN 2366-2565 (electronic)

Lecture Notes in Civil Engineering

ISBN 978-3-030-74257-7

ISBN 978-3-030-74258-4 (eBook)

<https://doi.org/10.1007/978-3-030-74258-4>

© The Editor(s) (if applicable) and The Author(s), under exclusive license to Springer Nature Switzerland AG 2021

This work is subject to copyright. All rights are solely and exclusively licensed by the Publisher, whether the whole or part of the material is concerned, specifically the rights of translation, reprinting, reuse of illustrations, recitation, broadcasting, reproduction on microfilms or in any other physical way, and transmission or information storage and retrieval, electronic adaptation, computer software, or by similar or dissimilar methodology now known or hereafter developed.

The use of general descriptive names, registered names, trademarks, service marks, etc. in this publication does not imply, even in the absence of a specific statement, that such names are exempt from the relevant protective laws and regulations and therefore free for general use.

The publisher, the authors and the editors are safe to assume that the advice and information in this book are believed to be true and accurate at the date of publication. Neither the publisher nor the authors or the editors give a warranty, expressed or implied, with respect to the material contained herein or for any errors or omissions that may have been made. The publisher remains neutral with regard to jurisdictional claims in published maps and institutional affiliations.

This Springer imprint is published by the registered company Springer Nature Switzerland AG
The registered company address is: Gewerbestrasse 11, 6330 Cham, Switzerland

Preface

This volume collects the papers submitted to the 8th Civil Structural Health Monitoring Workshop, which was held online on March 29–31, 2021. The workshop was jointly organized by the University of Molise, the University of Naples “Parthenope,” S2X s.r.l., and the ISHMII Association.

The workshop is part of an international conference series with a long tradition. Previous editions of the workshop were organized since 2004 in the USA, Italy, Canada, Germany, Japan, Northern Ireland, and Colombia. This edition was originally intended to be organized in Naples (Southern Italy), but it turned into a full online event in agreement with the social distancing norms due to the COVID-19 pandemic.

The main theme of the workshop was “Ageing structures and infrastructures in hazardous environment”; this is currently a very hot topic worldwide and particularly in Italy, after the collapses of several bridges and, above all, of the Morandi’s Bridge in Genoa.

Within the general theme of the Workshop, the following main topics have been addressed:

- Challenges in the practical application of structural health monitoring to civil structures, with particular attention to bridges and historical structures;
- Vibration-based structural assessment and monitoring, including SHM in earthquake-prone regions;
- Innovative sensing technologies;
- Advanced data processing methods;
- Geotechnical and geological monitoring.

The collected papers provide an extensive overview of the key themes, emerging trends, and current practices in the field of civil SHM. The international perspective contributed by participants coming from different countries in Europe, America, and Asia makes this volume a useful reference for the researchers as well as the practitioners involved in the development of civil SHM technologies. The papers collected in this volume, in particular, remark the following aspects concerning the current research in the field of civil SHM:

- Novel SHM approaches based on image processing, even in combination with robotic systems or drones, or SAR, including satellite applications, are becoming very attractive for SHM and nondestructive evaluation of civil structures and infrastructures because of the opportunity to overcome some typical limitations of contact-type approaches. Nevertheless, novel sensing technologies as well as new methods of installation and measurement strategies based on traditional sensors are being developed for civil SHM applications, with interesting results.
- Among the new sensing technologies, a special mention goes to the promising applications of smart materials, which show very interesting applicative perspectives in the field of civil SHM owing to their sensitivity to strain and damage.
- Vibration-based SHM systems, in combination with artificial intelligence, still play a significant role in civil SHM applications. They are under continuous development with the objectives of enhancing their robustness and accuracy in view of effective timely and automated structural health and performance assessment.

The editors would like to thank all the distinguished authors contributing to this volume for the high scientific quality and diversity of their papers, successfully addressing the main topics of the 8th Civil Structural Health Monitoring Workshop, and contributing to the development of the civil SHM discipline and the enhancement of its already promising applicative perspectives. The editors would also like to acknowledge the work made by all referees, who have professionally and timely completed the peer-reviewing tasks of the papers collected in this volume. Finally, the editors would like to thank the Institute for Construction Technologies (ITC) of the National Research Council of Italy (CNR) involved in the research project “GRISIS—Risks and Safety Management of Infrastructures at Regional Scale” (financed with European funds in the framework of the Regional Operational Program FESR Campania 2014-2020) for the contribution to the dissemination of the scientific studies and results collected in this volume.

Naples, Italy
Campobasso, Italy
Napoli, Italy
Napoli, Italy
Campobasso, Italy

Carlo Rainieri
Giovanni Fabbrocino
Francesca Ceroni
Nicola Caterino
Matilde A. Notarangelo



UNIVERSITÀ
DEGLI STUDI
DEL MOLISE



Funding Acknowledgment

The printed copy of this book and its delivery to the 8th Civil Structural Health Monitoring Workshop participants at their respective offices were financially supported by the Institute for Construction Technologies (ITC) of the National Research Council of Italy (CNR). This scientific dissemination initiative is part of a research project, of which ITC-CNR is part (GRISIS—Risks and Safety Management of Infrastructures at Regional Scale), financed with European funds in the framework of the Regional Operational Program FESR Campania 2014–2020, with the research consortium STRESS Scarl as implementing body (Cup: B63D18000280007, Surf:18033BP000000001, DD prot. 368 24/10/2018).

The GRISIS project aims at developing methods, techniques, and procedures for the risk assessment and the safety management of civil infrastructures at regional scale. The project is based on a multidisciplinary approach to achieve a holistic analysis of both natural and anthropic risks on civil infrastructures on the Campania region, in South Italy. In detail, the aim of GRISIS is not only to develop techniques and tools for the mitigation and the management of risks, but also to define safety measures for civil infrastructures. The research topics are organized into four implementation objectives:

- (1) Products and methodologies for the management and mitigation of seismic risk in the pre- and post-event for infrastructures and networks of strategic buildings;
- (2) Development of a hydrogeological risk assessment and mitigation model;
- (3) Development of methodologies and prototypes for the treatment and disposal of disaster and hazardous wastes generated by a natural or anthropogenic event and for the management of the risk of water, air and soil pollution;
- (4) Methodologies, techniques and systems for monitoring large-scale network infrastructures (Internet).

More details about the research project can be found here <http://www.progetto-grisis.it/>. The project will end at the end of the year 2021. Some results are reported in the following papers included in the present volume:

- Nuzzo et al.: “A technological platform for multi-risk management and mitigation in Campania region, Italy”;
- Santo et al.: “Slope stability assessment of the test site in Pagani (Campania, Southern Italy)”;
- Bilotta et al.: “Machine learning approach for damage detection of railway bridges: preliminary application”;
- Losanno et al.: “Structural monitoring of a railway bridge in Southern Italy for automatic warning strategy.”



Contents

Fiber Optic Monitoring and Forecasting of Reservoir Landslides	1
Hong-Hu Zhu, Bin Shi, Lei Zhang, and Xiao Ye	
Dynamic Testing and Continuous Dynamic Monitoring of Transportation, Stadia and Energy Infrastructures	15
Álvaro Cunha, Elsa Caetano, Filipe Magalhães, Carlos Moutinho, and Sérgio Pereira	
Operational Modal Analysis of a Historic GRP Structure	57
Zachariah Wynne, Tim Stratford, and Thomas P. S. Reynolds	
Mass and Temperature Changes in Operational Modal Analysis	69
Zachariah Wynne, Georgios Kanellopoulos, Vasileios Koutsomarkos, Angus Law, Tim Stratford, and Thomas P. S. Reynolds	
Characterizing Footbridge Response from Cyclist Crossings with Computer Vision-Based Monitoring	83
Rolands Kromanis	
Damage Detection Through Modal Flexibility-Based Deflections: Application to a Full-Scale RC Shear Wall Building	97
Giacomo Bernagozzi, Said Quqa, Luca Landi, and Pier Paolo Diotallevi	
Vision-Based Damage Detection Using Inclination Angles and Curvature	115
Chidiebere B. Obiechefu, Rolands Kromanis, Fouad Mohammad, and Zakwan Arab	
Consequences of Heuristic Distortions on SHM-Based Decision	129
Andrea Verzobio, Denise Bolognani, John Quigley, and Daniele Zonta	

Fatigue Life Prediction for a Concrete—Steel Composite Viaduct: A Process Based on Indirect Measurements 151
 A. Del Grosso, M. Cademartori, P. Basso, S. Osmani, F. Di Gennaro, and F. Federici

Estimation of Seismic Resilience of Road Infrastructures: An Integrated Approach 159
 A. Del Grosso, M. Cademartori, S. Osmani, and D. Pastorelli

Distributed Fiber-Optic Strain Sensing: Field Applications in Pile Foundations and Concrete Beams 167
 Nils Nöther and Massimo Facchini

Seismic Damage Quantification for the SHM of Existing RC Structures 177
 Alessandro Lubrano Lobianco, Marta Del Zoppo, and Marco Di Ludovico

Data-Driven Nonparametric Structural Nonlinearity Identification Under Unknown Excitation with Limited Data Fusion 197
 Ye Zhao, Bin Xu, Baichuan Deng, and Jia He

Out-of-Plane Ambient Vibration Tests of an Infill Wall in RC Frame Subjected to Previous In-Plane Damage 205
 Giuseppe Santarsiero, Alessandra De Angelis, Vincenzo Manfredi, Francesco Santamato, Angelo Masi, and Marisa Pecce

Assessment of an Historical Masonry Bell Tower by Modal Testing 219
 Alessandra De Angelis, Francesco Santamato, and Marisa Pecce

Data Processing Strategies for Monitoring an Offshore SPM System 233
 Paolo Castelli, Michele Rizzo, and Ostilio Spadaccini

Health Monitoring of Structures Using Integrated Unmanned Aerial Vehicles (UAVs) 243
 Efstathios Polydorou, Des Robinson, Su Taylor, and Patrick McGetrick

Infrastructure Health Monitoring Using SAR Tomography 257
 Alessandra Budillon, Giampaolo Ferraioli, Angel Caroline Johnsy, Vito Pascazio, and Gilda Schirinzi

Monitoring and Evaluation of a Highway Bridge During Major Rehabilitation 271
 Juan A. Quintana, Francisco J. Carrión, Miguel Anaya, Germán M. Guzmán, Jorge A. Hernández, Luis A. Martínez, José M. Machorro, and Héctor M. Gasca

Vibration Monitoring of a Railway Bridge Using Distributed Macro-strain Data Obtained with Fiber Bragg Gratings 289
 Edwin Reynders, Dimitrios Anastasopoulos, and Guido De Roeck

Monitoring of Base Isolated Building Subjected to Far Fault Earthquake 311
 Antonello Salvatori, Antonio Di Cicco, and Paolo Clemente

Non-parametric Optimization Using Subspace-Based Objective Functions 339
 Angelo Aloisio, Riccardo Cirella, Massimo Fragiaco, and Rocco Alaggio

Slope Stability Assessment of the Test Site in Pagani (Campania, Southern Italy) 359
 Antonio Santo, Marianna Pirone, Giovanni Forte, Melania De Falco, and Gianfranco Urciuoli

Use of a Roving Vision Sensor Setup to Train an Autoencoder for Damage Detection of Bridge Structures 367
 Darragh Lydon, Myra Lydon, Juliana Early, and Su Taylor

An Advanced Approach to the Long Term SHM of Structures and Transport Infrastructures 373
 Felice Carlo Ponzio, Chiara Iacovino, Rocco Ditommaso, Gianluca Auletta, Francesco Soldovieri, Manuela Bonano, and Vincenzo Cuomo

Acoustic Emission Monitoring of Prestressed Concrete Bridges: Differences Before and After the First-Crack Opening 389
 Daniel Tonelli, Francesco Rossi, Michele Luchetta, Daniele Zonta, Placido Migliorino, Alberto Selleri, Enrico Valeri, Alessandra Marchiondelli, and Gianluca Ascari

Weight-in-Motion System for Traffic Overload Detection: Development and Experimental Testing 403
 D. Di Giacinto, V. Musone, G. Laudante, L. Grassia, and E. Ruocco

Bayesian-Based Damage Assessment of Historical Structures Using Vibration Monitoring Data 415
 Laura Ierimonti, Nicola Cavalagli, Enrique García-Macías, Ilaria Venanzi, and Filippo Ubertini

Analytic Wavelet Selection for Time–Frequency Analysis of Big Data Form Civil Structure Monitoring 431
 Ahmed Silik, Mohammad Noori, Wael A. Altabay, Ramin Ghiasi, and Zhishen Wu

Influence of Operational Conditions on the Modal Based Damage Analysis of Pedestrian Bridges 457
Mareike Kohm and Lothar Stempniewski

Advanced Monitoring of Structures and Infrastructures Through Smart Composite Sensors and Systems 485
Antonella D’Alessandro, Hasan Borke Birgin, and Filippo Ubertini

Monitoring System of an Industrial Steel Tower Structure 499
João Zeferino, Eduardo Gonçalves, Paulo Carapito, and Filipe Santos

Two-Dimensional Deflection Maps by Using Fiber Bragg Grating Sensors 507
Pasquale Di Palma, Massimo Della Pietra, Vincenzo Canale, Mariagrazia Alviggi, Agostino Iadicicco, and Stefania Campopiano

Bayesian Model Updating and Parameter Uncertainty Analysis of a Damaged Fortress Through Dynamic Experimental Data 515
Federico Ponsi, Elisa Bassoli, and Loris Vincenzi

Dynamic Identification and Model Updating of a Masonry Chimney 535
Valentino Santoro, Elisa Bassoli, and Loris Vincenzi

Evolution of Modal Parameters of a Reinforced Concrete Building Subjected to Moderate Earthquakes 557
Davide Arezzo, Vanni Nicoletti, Sandro Carbonari, and Fabrizio Gara

Innovative Non-destructive Technique for the Structural Survey of Historical Structures 569
Alessio Cascardi, Andrea Armonico, Francesco Micelli, and Maria Antonietta Aiello

Structural Monitoring of a Railway Bridge in Southern Italy for Automatic Warning Strategy 585
Daniele Losanno, Nicola Caterino, Eugenio Chioccarelli, Carlo Rainieri, and Carolina Aiello

Dynamic Identification and Monitoring of a New Highway Bridge 603
Laura Marcheggiani, Francesco Clementi, and Antonio Formisano

SS#1 Investigation in Structural Performances of High-Power Horizontal Axis Wind Turbines by OMA-Based SHM 619
Luca Sbaraglia

Digital Tools for the Knowledge and Safeguard of Historical Heritage 645
Adriana Marra, Ilaria Trizio, and Giovanni Fabbrocino

A Technological Platform for Multi-risk Management and Mitigation in Campania Region, Italy 663
 I. Nuzzo, N. Caterino, A. Novellino, M. Esposito, A. Occhiuzzi, and E. Rubino

Machine Learning Approach for Damage Detection of Railway Bridges: Preliminary Application 677
 A. Bilotta, G. Testa, C. Capuano, and E. Chioccarelli

Assessment of the Applicability of DInSAR Techniques for Structural Monitoring of Cultural Heritage and Archaeological Sites 691
 Luisa Berto, Andrea Doria, Anna Saetta, Alberto Stella, and Diego Talledo

On the Dynamic Performance of the Santa Maria Maddalena Church, Ischia Island (Italy): Numerical and Experimental Comparative Analysis 699
 Claudia Casapulla, Thomas Celano, Carlo Rainieri, Giovanni Fabbrocino, and Francesca Ceroni

Monitoring of Bridges by Using Static and Dynamic Data from MEMS Accelerometers 725
 Mathieu Desbazeille, Nathalie Saguin Sprynski, Viviane Cattin, Malvina Billères, Laurent Jouanet, and Audrey Vidal

Realization and Testing of Textile Reinforced Concrete Panels Sensorized with Distributed Fiber Optic Sensors 747
 Paolo Corvaglia, Eriselda Lirza, Michael Brancato, Marco Nucci, and Vincent Lanticq

Increasing the Resilience of European Transport Infrastructure 761
 Kostas Bouklas, Angelos Amditis, Rafael Weilharter, Visvanathan Ramesh, Miguel Ángel Trujillo Soto, Guillermo Heredia, Luca Belsito, Stephanos Camarinopoulos, and Friedrich Fraundorfer

Possibilities of Composite Distributed Fibre Optic 3DSensor on the Example of Footing Pulled Out from the Ground: A Case Study 775
 Rafał Sieńko, Łukasz Bednarski, Tomasz Howiacki, Katarzyna Zuziak, and Sławomir Labocha

Multidisciplinary Investigations of a Steel–Concrete Composite Bridge 793
 Lorenzo Benedetti, Paolo Borlenghi, Manuel D’Angelo, Alessandro Menghini, Giacomo Zonno, Francesco Ballio, Marco Belloli, and Carmelo Gentile

Data Management in Structural Health Monitoring	809
Elia Favarelli, Enrico Testi, and Andrea Giorgetti	
Distributed Fibre Optic Sensing for Long-Term Monitoring of Tunnel Inner Linings in Anhydrite	825
Fabian Buchmayer, Christoph M. Monsberger, and Werner Lienhart	
Long-Term Monitoring Using GNSS: Lessons Learned and Experiences from 20 years of Operation	839
Caroline Schönberger and Werner Lienhart	
Assessment of Similar Reinforced Concrete Arch Bridges by Operational Modal Analysis and Model Updating	853
Giacomo Zonno and Carmelo Gentile	
Digital Environment for Remote Visual Inspection and Condition Assessment of Architectural Heritage	869
Ilaria Trizio, Francesca Savini, Andrea Ruggieri, and Giovanni Fabbrocino	
Stange Overpass: Finite Element Model Updating of an Unconventional Railway Bridge	889
Emrah Erduran, Kltigin Demirlioglu, Albert Lau, Kameran Aziz, Ian Willoughby, Endre Hyldmo, Tomislav Arsenovic, and Enzo Martinelli	
OMA: From Research to Engineering Applications	903
Salvatore Russotto, Alberto Di Matteo, Chiara Masnata, and Antonina Pirrotta	
Time-Domain Damage Detection of Structures with Complex Modes Under Variable Environmental Conditions Using Bayesian Virtual Sensors	921
Jyrki Kullaa	
Use of Sar Satellite Data in Bridge Monitoring with Application to Urban Areas	935
Luca Sartorelli, Mattia Previtali, Pier Francesco Giordano, Maria Pina Limongelli, Francesco Ballio, and Andrea Uttini	
Expeditious Dynamic Tests for the Estimation of Infill Masonry Wall Stiffness	957
Vanni Nicoletti, Davide Arezzo, Sandro Carbonari, and Fabrizio Gara	
Field Evaluation of Sensing Sheet Prototype Exposed to Cracking	967
Vivek Kumar, Levent E. Aygun, Mattew Gerber, Campbell Weaver, Sigurd Wagner, Naveen Verma, James C. Sturm, and Branko Glisic	
Long-Term Vibration Monitoring of the Sultan Ahmet Mosque in Istanbul	977
Eser Çaktı and Kökcan Dönmez	

**Experimental Evidence for Structural Damage During
the 30.10.2020 Samos-Sığacik Earthquake by Laser Vibrometry** 991
Eser Çakti and Sefer Ömercan Ertürk

**Structural Monitoring and Dynamic Characterization
of the Main Fire Station Building in Naples** 997
M. Spizzuoco, D. Losanno, I. Nuzzo, V. Schiavone, and G. Serino

**A Structural Engineering Perspective on the Use of Remote
Sensing Measurements for Civil SHM** 1015
Giovanni Fabbrocino, Emanuele Petracca, and Carlo Rainieri

Author Index 1035

Fiber Optic Monitoring and Forecasting of Reservoir Landslides



Hong-Hu Zhu, Bin Shi, Lei Zhang, and Xiao Ye

Abstract Landslide hazards triggered by atmospheric precipitation and periodic water level fluctuations frequently occur in reservoir areas all over the world, resulting in severe fatalities and loss of properties. For the purpose of detecting geological disasters ahead of time, a series of advance monitoring techniques have been developed and applied to engineering practices. Among them, the Distributed Fiber Optic Sensing (DFOS) technologies have shown their great potential for monitoring the tempo-spatial distribution of multi-fields (displacement, stress, temperature, seepage, etc.) of reservoir landslides. In this paper, the working principles, characteristics and applicability and these technologies are briefly introduced. In particular, several representative DFOS-based monitoring instruments and equipment are elaborated, which have been successfully used in several landslides in Three Gorges Reservoir (TGR) area in China for long-term in situ observation and comprehensive evaluation of relevant geohazards. The monitoring results of Majiagou landslide show that the sliding surfaces, deformation pattern, and groundwater evolution can be sensitively captured based on the DFOS measurements. Seasonal rainfall and water level fluctuations are found to be the two main triggering factors of the landslide. Meanwhile, long time-series monitoring data shed a bright light on real-time deformation prediction and stability analyses of reservoir landslides. Finally, the challenges and future trends of applying the DFOS systems to landslide monitoring are summarized.

Keywords Distributed fiber optic sensing (DFOS) · Field monitoring · Reservoir landslides · Three gorges reservoir (TGR)

1 Introduction

In the past few decades, natural and anthropogenic geohazards have frequently occurred all over the world, causing heavy loss of life and properties. Different from other types of landslides, reservoir landslide is a typical geological disaster

H.-H. Zhu (✉) · B. Shi · L. Zhang · X. Ye
School of Earth Sciences and Engineering, Nanjing University, Nanjing 210023, China
e-mail: zhh@nju.edu.cn

related to the construction and operation of hydropower stations, which poses a great threat to bank infrastructures and human lives in the reservoir regions [1]. In the history of reservoir landslides, the 1963 Vajont landslide is the most famous one. The main triggering factors include the fluctuation of the water level, heavy rainfall, and strong earthquake. It should be noted that huge surge waves will be induced by these landslides, leading to other disastrous consequences.

To mitigate these geo-risks, field monitoring is of great importance as an effective means of capturing the changes of geotechnical parameters and identifying their causes and trends. However, if a landslide risk identification system solely depends on displacement measurements, there will be considerable errors. Thus it is necessary to obtain real-time multi-field information to improve the level of early detection and warning of reservoir landslides.

In the past few decades, the Distributed Fiber Optic Sensing (DFOS) technologies have shown their great potential for monitoring a variety of geotechnical infrastructures [2]. One special feature of these technologies is that the distribution of strain, temperature, displacement, stress can be captured using optical fibers with high accuracy. On the other hand, a variety of data-driven models have been developed and employed for reservoir-induced landslide prediction, such as the updated grey model [3], logistic regression model [4], and the newly developed machine learning models [5–10].

In this paper, the recent advancement in fiber optic monitoring systems for monitoring reservoir landslides is introduced, together with newly established forecasting models. A case study in the Three Gorges Reservoir (TGR) region of China is presented in details. Finally, the challenges in DFOS-based landslide monitoring are summarized.

2 Distributed Fiber Optic Sensing (DFOS) System

2.1 Quasi-Distributed Fiber Optic Sensors

Fiber Bragg Grating (FBG) is a popular quasi-distributed strain and temperature measuring technology. That means all the FBG sensors can be collected along a series and the optical fiber cable serves as both the sensing elements and the data transmission channels. Through physical or thermal elongation of the sensing segment and through the change in the refractive index of the fiber due to photo-elastic and thermo-optic effects, the Bragg wavelength λ_B of an FBG will change linearly with applied strain $\Delta\varepsilon$ or temperature ΔT , as described by [11]

$$\frac{\Delta\lambda_B}{\lambda_B} = (1 - p^{eff})\Delta\varepsilon + (\alpha + \xi)\Delta T \quad (1)$$

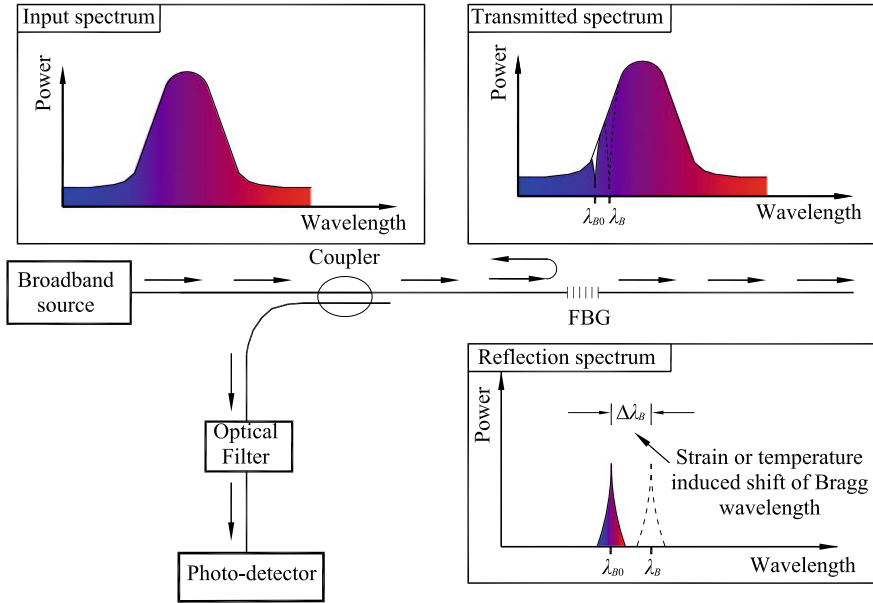


Fig. 1 Genetic concept of the FBG sensor

where $\Delta\lambda_B$ is the change in the Bragg wavelength due to applied strain and temperature changes; λ_B is the original Bragg wavelength under strain free and 0°C condition; p^{eff} is the photo-elastic parameter; α and ξ are the thermal expansion and thermo-optic coefficients, respectively (Fig. 1).

Using this technology, strain and temperature sensors can be easily made by simply packaging the FBG. More importantly, some special geotechnical sensors can be designed based on strain and temperature measurements, such as displacement sensors, soil moisture sensors, load cells, accelerometers, earth pressure cells, and pore water pressure cells. Figure 2 shows the working principle of a newly developed FBG in-place inclinometer, which makes full use of the linear relationship between strains and inclination angles of uniform strength beams [8]. After laboratory calibration, the displacement profile of a borehole can be calculated. As shown in Fig. 3, an FBG temperature sensor with regularly active heating function is successfully developed to measure moisture content in ground soils [12].

2.2 Distributed Temperature Sensing (DTS)

Different from the quasi-distributed FBG technology, the fully distributed sensing technologies normally utilize the scattering light phenomena in an optical fiber, as shown in Fig. 4. Raman Optical Time-Domain Reflectometry (ROTDR) is a mature

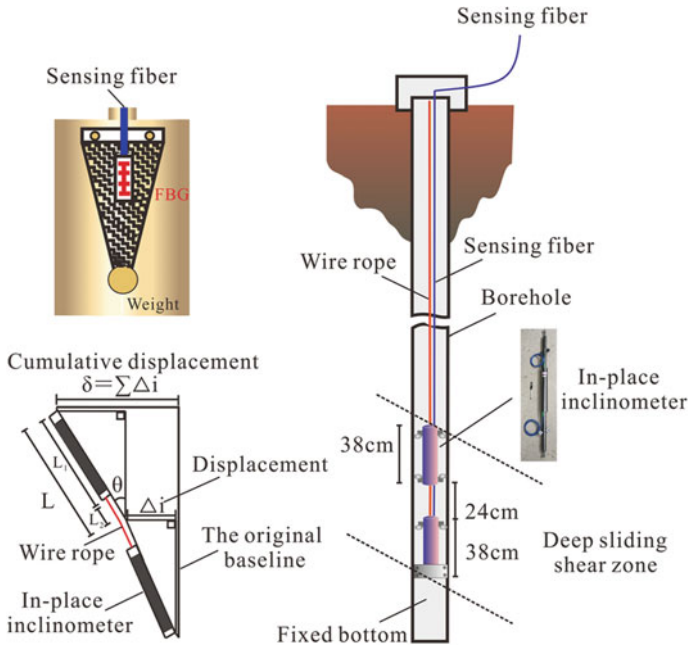


Fig. 2 FBG in-place inclinometers [8]

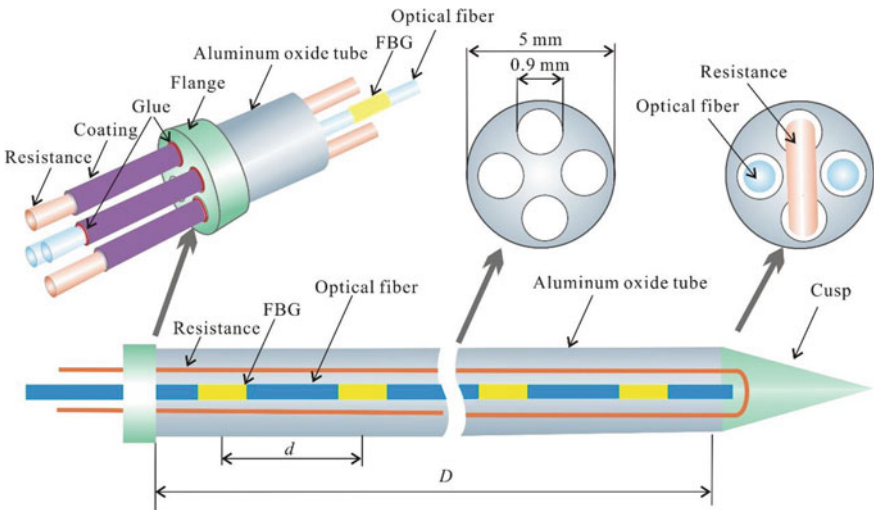


Fig. 3 FBG soil moisture sensor [12]

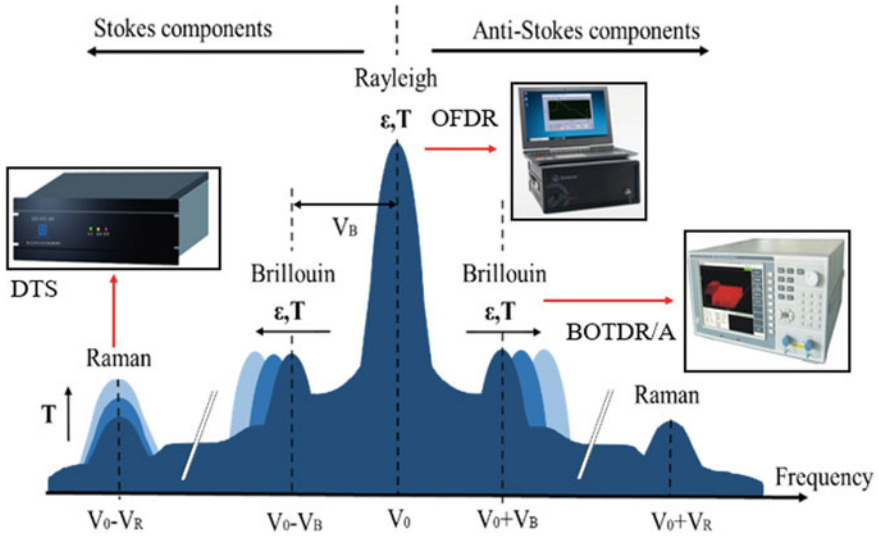


Fig. 4 Spectrum of backscattered lights in an optical fiber

distributed temperature sensing (DTS) technology, which employs the Raman scattering effect. It is generated inside the optical fiber when a pulse light is launched into an optical fiber. By measuring the Raman scattered light, it becomes possible to measure the temperature as a distribution in the longitudinal direction of an optical fiber.

To apply this technology in monitoring temperatures, soil moistures, or even seepage rates in landslides, special optical fiber cables have to be developed [13, 14], which should have adequate packaging and protection measures while maintaining good sensitivity. Figure 5 shows several DTS cables widely used in field monitoring. All of them have a loose optical fiber packaged in a plastic or metal tube.

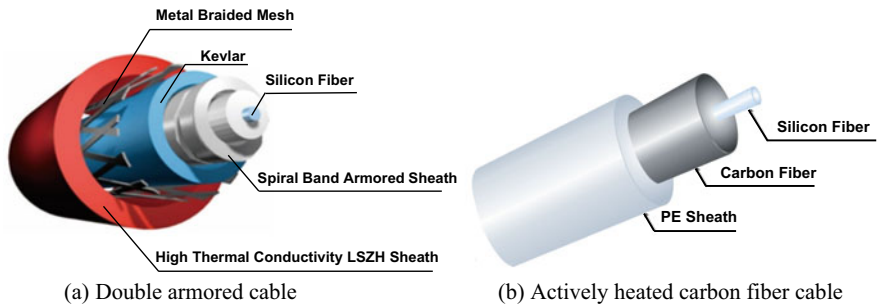


Fig. 5 Typical distributed temperature sensing cables. a Double armored cable. b Actively heated carbon fiber cable

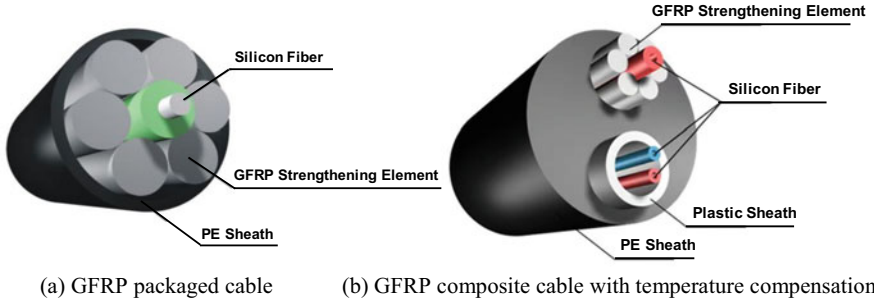


Fig. 6 Typical distributed strain sensing cables. **a** GFRP packaged cable. **b** GFRP composite cable with temperature compensation

2.3 Distributed Strain Sensing (DSS)

There are a variety of distributed strain sensing technologies, such as BOTDR (Brillouin Optical Time-Domain Reflectometry), BOTDA (Brillouin Optical Time-Domain Analysis), and BOFDA (Brillouin Optical Frequency-Domain Analysis). These technologies utilize Brillouin scattering and can provide distributed measurements of temperature and strain over tens of kilometers at the spatial resolution of 1 m or less. As a super-high sensitivity and spatial resolution technology, OFDR (Optical Frequency Domain Reflectometry) is based on Rayleigh scattering. To apply these technologies to geotechnical monitoring, robust and high strength optical fiber cables should be properly installed in the field with care. Figure 6 shows some typical distributed strain sensing cables. As the fiber optic measurements are related to both strain and temperature, temperature compensation is necessary in most cases. This can be achieved by adding a loose fiber in the same cable. One important issue to perform deformation monitoring of landslides using soil embedded or borehole installed cables is how to ensure the deformation compatibility between the cables and the in situ soil/rock. A recent work has demonstrated the feasibility of distributed strain sensing in monitoring shear displacements in landslides [15, 16].

3 Case Study in the TGR Area

As shown in Fig. 7, the Three Gorges of the Yangtze River in China is characterized by complex geological structures, deep valleys, and steep terrains [17]. The TGR is a super large artificial lake formed after the Three Gorges Dam started to dam water. The fluctuation of water levels (145 ~ 175 m) along with abundant rainfalls in this region have induced reactivation of many ancient landslide since the first impoundment of TGR in 2003 [18]. Till now, more than 5000 landslides have occurred, which has posed a great threat to the local residents and properties. Figure 8 shows some

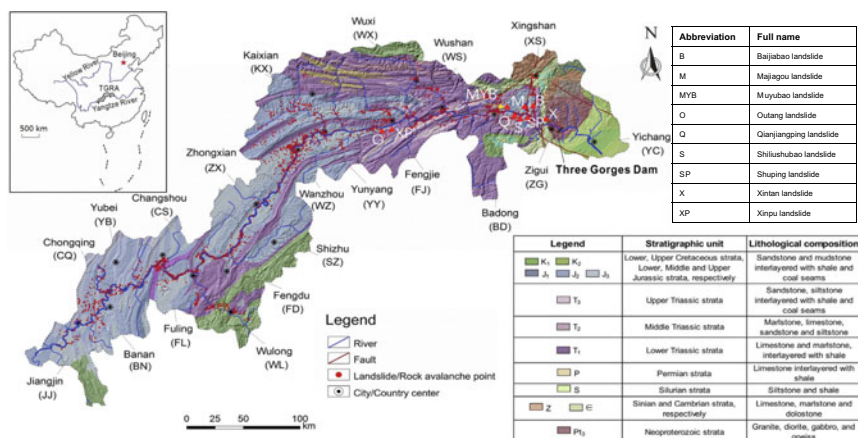


Fig. 7 Geological map of the TGR region showing the locations of landslides and rockfalls (red dots). (adapted from [18])

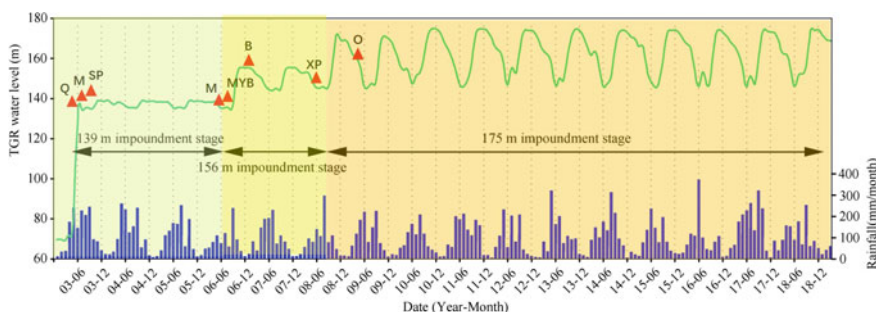


Fig. 8 Typical landslide events in the TGR region and their relationship with water level fluctuations and rainfall (B, Baijiabao landslide; M, Majiagou landslide; MYB, Muyubao landslide; O, Outang landslide; Q, Qianjiangping landslide; SP, Shuping landslide; X, Xintan landslide; XP, Xinpu landslide)

critical landslide events triggered by the water level fluctuation and rainfall. To reduce such risks, deformation forecasting and stability evaluation of potential landslides based on field monitoring data become very important [19].

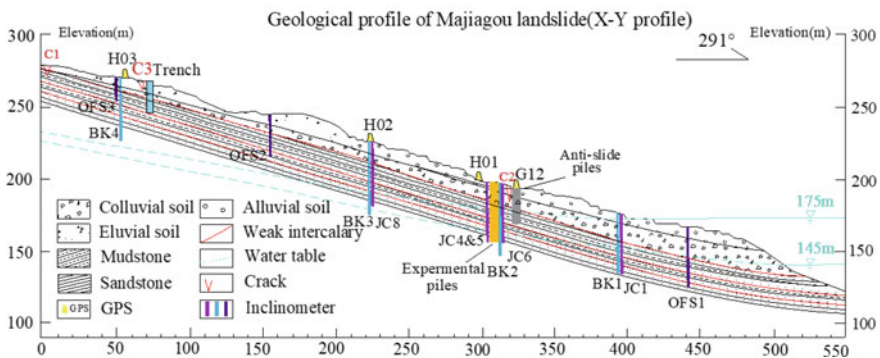
Numerous field monitoring systems have been installed in the TGR region and have played an important role in prediction and early warning of potential landslides. These systems can be categorized into two groups, namely, remote sensing and ground-based monitoring. The former can only detect large deformation on the ground surface since the landslides are generally covered by dense vegetation. For the latter, different geotechnical instruments have been developed in the past few decades, such as crackmeters, borehole inclinometers, extensometers, and pore water pressure cells. However, most of them are point (discrete) sensors and therefore their

measurements can hardly represent the deformation pattern and overall stability of the landslides under investigation. In addition, their long-term stability is quite poor due to the limitation of waterproof measures and electric noise. As the distributed fiber optic sensing technologies can monitor the distribution of strain, temperature and other physical parameters along the optical fiber cables, the spatial and temporal variations of multi-fields (strain field, temperature field, displacement field, etc.) can be captured. This has great potential for investigating multiphysics problems such as reservoir landslides.

The Majiagou landslide is located on the left bank of a tributary of the Yangtze River in Zigui County, Hubei Province, China. Figure 9 shows a geomorphologic map of the landslide site. The landslide forms and develops at the front of a giant paleo-landslide deposits ($\sim 2 \times 10^8 \text{ m}^3$ in volume). It is tongue shaped, with a length of 537.9 m, a width of 150 m, and an average depth of 32 m. The overall volume



(a) Plan view of the study area



(b) Geomorphology and field monitoring deployment.

Fig. 9 Location and monitoring arrangement of Majiagou landslide

Table 1 List of field monitoring layout

No.	DFOS technologies	Monitoring parameters
P1, P2	FBG, BOTDR, ROTDR	Strain and temperature of the piles, earth pressure at the pile-soil interface
OFS1, OFS2, OFS3	FBG, BOTDR, ROTDR	Inclinometer, soil strain, soil temperature, pore water pressure, groundwater level
JC1, JC3, JC8	FBG, BOTDR, ROTDR	Inclinometer, soil strain
S1, S2	BOTDR, ROTDR	Soil strain and temperature of shallow layers

is $3.1 \times 10^6 \text{ m}^3$ and the average slope of the landslide is 15° . The toe of the front slope is submerged in reservoir water. Therefore the change of the water level causes significant erosion phenomena and periodically disturbs the original critical balanced state.

Field investigation and observations indicate that there are two main slip surfaces. A shallow slip surface is located at the contact between Quaternary deposits and the underlying rock stratum, and the sliding zone is composed of 0.5–0.8 m-thickness silty clay with silty mudstones. A deep slip surface is found along a weak mudstone interlayer within the bedrock [20]. Anti-sliding piles and drainage channels have been constructed and they effectively mitigated the landslide.

To demonstrate the performance of the distributed fiber optic sensing in landslide monitoring, an integrated, in situ multi-parameter fiber optic monitoring system was established by Nanjing University with the aid of China University of Geosciences (Wuhan) at the landslide site. Long-term monitoring of the landslide initiated in 2012 [3, 8, 9, 21, 22]. The monitoring system aims at monitoring ground surface displacement, borehole displacement, pile loading conditions, ground water level and so on. Distributed strain sensing cables were deployed along anti-sliding piles (P1 and P2) and inclinometers (OFS 1 ~ 3), and were directly embedded in boreholes (JC 1 ~ 6) and shallow surface trenches (S1 and S2). The field instrumentation scheme is listed in Table 1 and Fig. 10 shows some typical monitoring results. The monitoring results clearly show that water level fluctuation and seasonal rainfall are found to be the two main triggering factors while the former is the dominant one. The time series data from the monitoring boreholes show that the landslide deformation continued to develop and the sliding surfaces, deformation pattern, and groundwater evolution were sensitively captured based on the DFOS measurements. It can be concluded that this landslide is currently in the creep deformation stage.

4 Forecasting of the Reservoir Landslide

Both physical and data-driven models have been employed to predict the performance of reservoir landslides. The physical models attempt to establish the mechanical relationship between the load and deformation of landslides [21–23], which is a

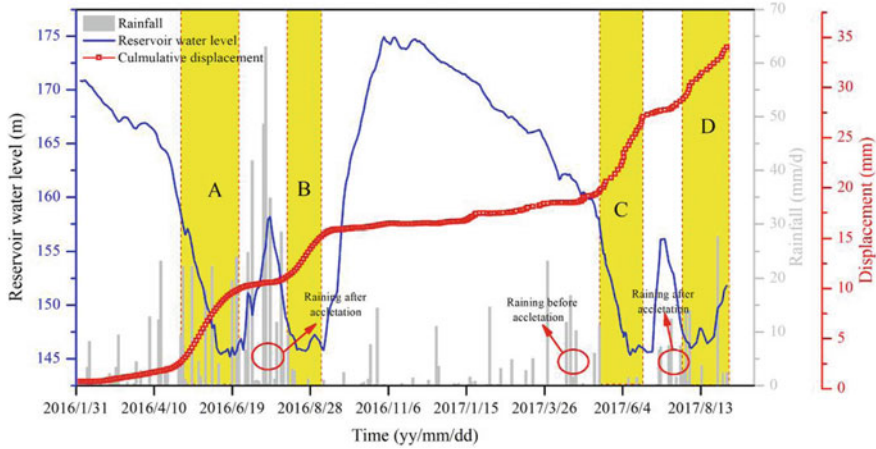
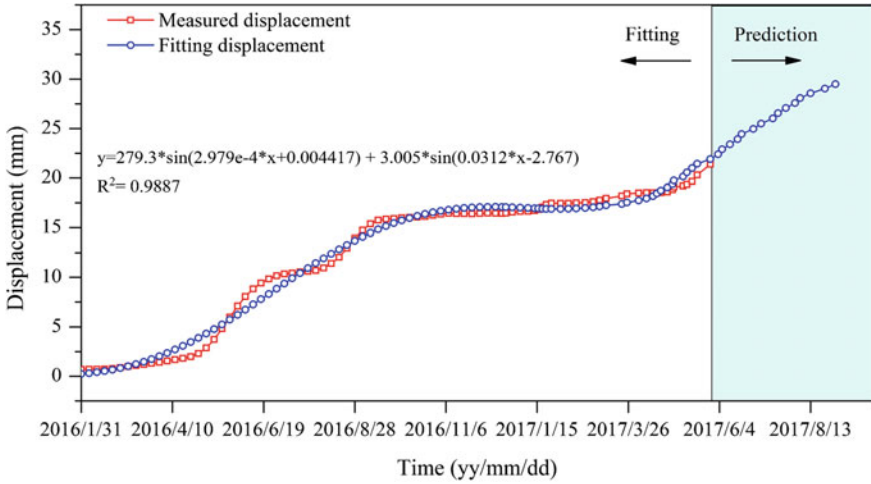


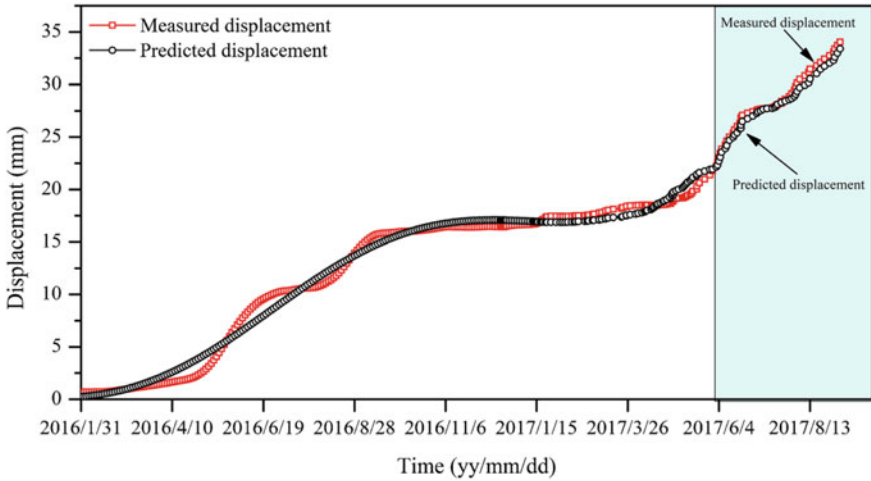
Fig. 10 Time-dependent variation of internal displacement measurements with rainfall and reservoir water level [9]

challenge due to the complexity involved in the triggering mechanism and geological properties [24]. On the contrary, the data-driven models, including the updated grey model, logistic regression model and other nonlinear models, have been successfully employed for early warning of reservoir-induced landslide. They input observed measurements into mathematical models to output variables as landslide predictors [9]. As the DFOS technologies enable the collection of huge amounts of monitoring data, it has become possible to use advanced machine learning and artificial intelligence methods as effective tools to provide accurate and fast forecasting of landslides. A series of innovative models, including support vector machines, extreme learning machines, random forest and artificial neural networks, as well as their hybrids, have been applied to forecast deformation of reservoir landslides.

To predict the internal displacements of Majiagou landslide, the set pair analysis (SPA) method combined with particle swarm optimization (PSO) and support vector machine (SVM) is used. Considering the deformation hysteresis effect, the set pair analysis (SPA) method is utilized to determine the deformation lag time based on the long-term monitoring results, which is found to be 18 days. Then, the time series method was adopted to decompose the cumulative displacement into the trend part and the periodic part. The trend part is dependent mostly on the geological conditions and can be fitted by mathematical functions, while the periodic part is governed by external factors such as rainfall and fluctuation of reservoir water level. As the dominant landslide-triggering factor, the water level fluctuations were input into the PSO-SVM model to forecast the periodic displacement. Afterward, the cumulative displacements are determined by adding up the trend displacements and the periodic displacements. Figure 11 shows the fitted results of the displacement-time curve using the conventional triangular function and the predictions of SPA-PSO-SVM model, respectively. It is demonstrated that the proposed SPA-PSO-SVM model is



(a) Fitted results using the triangular function



(b) Predicted results using the SPA-PSO-SVM model

Fig. 11 Comparison of the variations of internal displacement of the landslide [9]

reliable and effective in predicting landslide displacements, taking into account the deformation hysteresis effect.

5 Conclusion Remarks

In this paper, the recent development and application of DFOS technologies to monitor reservoir landslides are introduced, as well as the related forecasting method. The field instrumentation of the Majiagou landslides is presented in details. The following conclusions can be drawn in this study:

1. The FBG sensing technology enables quasi-distributed and real-time monitoring of multiple parameters such as strain and temperature, while the distributed strain and temperature sensing technologies can be used to monitor displacements and moisture contents profiles over tens of kilometers.
2. In the Majiagou landslide, the long-term monitoring data provides useful information on the landslide stability during the reservoir operation. It is confirmed that this landslide is in the creep stage and the main influencing factor of landslide displacement is the fluctuation of the reservoir water level.
3. Long time-series monitoring data shed a bright light on real-time deformation prediction and stability analyses of reservoir landslides. The comparison between the predicted and measured displacements show that the prediction accuracy of the proposed SPA-PSO-SVM model is satisfactory.

It is noted that despite the verified feasibility and reliability of DFOS systems for landslide monitoring, these systems are still new to most geotechnical practitioners. There are many challenges to be solved, such as protection of the cables and temperature compensation of the measurements. Therefore, prior to field instrumentation, systematic and professional training is of great importance. Secondly, the costs of the fiber optic monitoring systems are still higher than conventional ones. It is important for manufacturers to develop instruments and sensors of low prices or high performance cost ratios. Finally, establishment of guidelines and standards for system deployment and maintenance is crucial to promote DFOS applications to landslides. These challenges, in turn, provide abundant opportunities for geotechnical practitioners to explore the great potential of DFOS technologies in mitigating geohazard problems. Advanced fiber optic monitoring systems have been successfully installed in Xinpu, Outang and Canlian landslides to demonstrate their great potential in early warning of reservoir landslides. Laboratory 1-g and centrifuge model tests are been conducted as well [25].

References

1. Paronuzzi P, Bolla A (2012) The prehistoric vajont rockslide: an updated geological model. *Geomorphology* 169–170:165–191
2. Shi B, Zhang D, Zhu HH (2019) Distributed fiber optic sensing for geoenvironmental monitoring (in Chinese). Science Press, Beijing
3. Zhang W, Xiao R, Shi B, Zhu HH, Sun YJ (2019) Forecasting slope deformation field using correlated grey model updated with time correction factor and back-ground value optimization. *Eng Geol* 260:

4. Dong JJ, Tung YH, Chen CC, Liao JJ, Pan YW (2011) Logistic regression model for predicting the failure probability of a landslide dam. *Eng Geol* 117(1–2):52–61
5. Liu ZB, Shao JF, Xu WY, Chen HJ, Shi C (2014) Comparison on landslide nonlinear displacement analysis and prediction with computational intelligence approaches. *Landslides* 11(5):889–896
6. Lian C, Zeng ZG, Yao W, Tang HM (2015) Multiple neural networks switched prediction for landslide displacement. *Eng Geol* 186:91–99
7. Zhou C, Yin KL, Cao Y, Ahmed B (2016) Application of time series analysis and PSO–SVM model in predicting the Bazimen landslide in the Three Gorges Reservoir, China. *Eng Geol* 204:108–120
8. Zhang L, Shi B, Zhu H, Yu X, Wei G (2020) A machine learning method for inclinometer lateral deflection calculation based on distributed strain sensing technology. *B Eng Geol Environ* 79:3383–3401
9. Zhang L, Shi B, Zhu H, Yu X, Han H, Fan X (2021) PSO-SVM-based deep displacement prediction of Majiagou landslide considering the deformation hysteresis effect. *Landslides* 18:179–193
10. Li CD, Tang HM, Ge YF, Hu XL, Wang LQ (2014) Application of backpropagation neural network on bank destruction forecasting for accumulative landslides in the three Gorges Reservoir Region. *China Stoch Env Res Risk A* 28(6):1465–1477
11. Zhu HH, Shi B, Zhang CC (2017) FBG-based monitoring of geohazards: current status and trends. *Sensors* 17:452
12. Cao D, Fang H, Wang F, Zhu H, Sun M (2018) A fiber Bragg-grating-based miniature sensor for the fast detection of soil moisture profiles in highway slopes and subgrades. *Sensors* 18(12):4431
13. Sayde C, Gregory C, Gil-Rodriguez M et al (2010) Feasibility of soil moisture monitoring with heated fiber optics. *Water Resour Res* 46(6):W06201–W06208
14. Yan JF, Shi B, Zhu HH, Wang BJ, Wei GQ, Cao DF (2015) A quantitative monitoring technology for seepage in slopes using DTS. *Eng Geol* 186:100–104
15. Wu H, Zhu HH, Zhang CC, Zhou GY, Zhu B, Zhang W, Azarafza M (2020) Strain integration-based soil shear displacement measurement using high-resolution strain sensing technology. *Measurement* 166:108210
16. Zhang CC, Zhu HH, Liu SP, Shi B, Zhang D (2018) A kinematic framework for calculating shear displacement of landslides using distributed fiber optic strain measurements. *Eng Geol* 234:83–96
17. Chen DJ (1999) Engineering geological problems in the Three Gorges Project on the Yangtze. *China Eng Geol* 51(3):183–193
18. Tang HM, Wasowski J, Jung CH (2019) Geohazards in the three Gorges Reservoir Area, China-Lessons learned from decades of research. *Eng Geol* 261:105267
19. Sassa K, Canuti P (eds) (2009) *Landslides-disaster risk reduction*. Springer-Verlag, Berlin Heidelberg
20. Ma J, Tang H, Hu X, Bobet A, Zhang M, Zhu T, Song Y, Ez Eldin MAM (2017) Identification of causal factors for the Majiagou landslide using modern data mining methods. *Landslides* 14:311–322
21. Sun YJ, Zhang D, Shi B, Tong HJ, Wei GQ, Wang X (2014) Distributed acquisition, characterization and process analysis of multi-field information in slopes. *Eng Geol* 182:49–62
22. Hu X, Tan F, Tang H, Zhang G, Su A, Xu C et al (2017) In-situ monitoring platform and preliminary analysis of monitoring data of Majiagou landslide with stabilizing piles. *Eng Geol* 228:323–336
23. Chen HR, Qin SQ, Xue L, Yang BC, Zhang K (2018) A physical model predicting instability of rock slopes with locked segments along a potential slip surface. *Eng Geol* 242:34–43
24. Zhang J, Huang HW, Zhang LM, Zhu HH, Shi B (2014) Probabilistic prediction of rainfall-induced slope failure using a mechanics-based model. *Eng Geol* 168:129–140
25. Zhu HH, Shi B, Yan JF, Zhang J, Zhang CC, Wang BJ (2014) Fiber Bragg grating-based performance monitoring of a slope model subjected to seepage. *Smart Mater Struct* 23:095027

Dynamic Testing and Continuous Dynamic Monitoring of Transportation, Stadia and Energy Infrastructures



Álvaro Cunha, Elsa Caetano, Filipe Magalhães, Carlos Moutinho, and Sérgio Pereira

Abstract The Laboratory of Vibrations and Structural Monitoring (ViBest, www.fe.up.pt/vibest) of CONSTRUCT/FEUP has been implementing, since 2007, a significant set of long-term dynamic monitoring systems in large Civil structures with different typologies (e.g. roadway, railway and pedestrian bridges, stadia suspension roofs, wind turbines, concrete dams or high voltage transmission lines). This paper briefly describes some of these applications, showing the interest and potential of the developed technology, as well as of the huge high quality database created, which can be used for joint collaborative research at European level.

Keywords Continuous dynamic monitoring · Footbridges · Railway bridges · Roadway bridges · Stadia suspension roof · Wind turbines · Concrete dams

1 Introduction

The Laboratory of Vibrations and Structural Monitoring (ViBest, www.fe.up.pt/vibest) of CONSTRUCT/FEUP has been implementing, since 2007, a significant set of long-term dynamic monitoring systems in large Civil structures with different typologies (e.g. roadway, railway and pedestrian bridges, stadia suspension roofs, wind turbines, concrete dams or high voltage transmission lines).

This paper briefly describes some of these applications, showing the interest and potential of the developed technology, as well as of the huge high quality database created, which can be used for joint collaborative research at European level.

The representative set of monitoring applications presented shows the efficiency of the developed tools and the usefulness of the testing and monitoring programs implemented, enabling the achievement of different objectives, such as: (i) the development of finite element model correlations and updating; (ii) the vibration serviceability safety checking, particularly in case of lively bridges involving the inclusion of vibration control devices; (iii) the implementation of automated versions of the

Á. Cunha (✉) · E. Caetano · F. Magalhães · C. Moutinho · S. Pereira
CONSTRUCT-ViBest, Faculty of Engineering (FEUP), University of Porto, Porto, Portugal
e-mail: acunha@fe.up.pt

most powerful methods of Operational Modal Analysis, and their application for tracking the time evolution of modal parameters in long-term dynamic monitoring applications; (iv) the application of statistical methods to remove the influence of environmental and operational factors (e.g. temperature, intensity of traffic, wind) on the modal variability, supporting the development of reliable techniques for vibration based damage detection; (v) the experimental assessment of fatigue, based on the measurement of effects of real traffic loads; (vi) the experimental assessment of aerodynamic problems in bridges based on in situ measurements; (vii) the tracking of modal parameters in wind turbines, enabling damage detection and fatigue assessment and (viii) the characterization of the influence of the water level in the reservoir on the dynamic properties of concrete arch dams.

2 From Dynamic Testing to Continuous Dynamic Monitoring

The experimental identification of modal parameters in Civil structures was initially performed using input-output modal analysis techniques developed and applied in Mechanical and Aeronautical Engineering [1–4]. This required the use of appropriate equipment for structural excitation (e.g. impulse hammer devices, large electrodynamic shakers, eccentric mass vibrators or servo-hydraulic shakers), data acquisition and data processing, involving normally the evaluation of frequency response functions (FRFs) as basis for the application of single or multi-degree of freedom modal identification algorithms [5, 6].

However, when dealing with large structures, it becomes hard and expensive to excite the most significant modes of vibration in a low frequency range with sufficient energy and in a controlled manner.

Therefore, the use of modern transducers and digitizers, enabling to accurately measure very low levels of dynamic response induced by ambient excitations, motivated the development of modern and powerful techniques for output-only modal identification of civil engineering structures, at construction, commissioning or rehabilitation stages without interruption of normal operation [7].

Although some pioneering studies have been developed with this perspective still in the era of the analogue equipment [8–14], it was the recent use of sensors specially suitable for ambient vibration measurements in large structures, conjugated with high level digitizers with local storage and time synchronization capabilities that enabled the accurate modal testing of large structures in a short time and in a rather comfortable way, as happened at the Vasco da Gama Bridge [15], at the Millau Viaduct [16] or at the Humber Bridge [17].

In the reception tests of some large and slender structures, the concern with the accurate identification of modal damping ratios led frequently also to the performance of free vibration tests, as happened at several outstanding cable-stayed bridges (e.g.

Normandy, Vasco da Gama or Millau bridges), inducing a sudden rupture of tensioned cable connected from the ground [16] or a suspended barge to the deck [15].

The results from these modal identification tests have been used over a number of decades, normally at the commissioning stage, to establish correlations with numerical predictions, or in some cases to develop finite element model updating studies [10, 15, 16].

It was then assumed that such tests would characterize the baseline condition of the structural behavior, allowing subsequent detection of structural changes, which made ambient vibration tests gradually more common before and after rehabilitation works [18, 19], and several research attempts have been developed to detect early damage based on variations of modal parameters estimates, despite the disturbing influence of environmental and operational factors [20, 21].

However, the remarkable progress achieved in the last years in the areas of data acquisition and online information made it feasible, however, the permanent dynamic monitoring of the structural behavior [22, 23], which may complement other components of structural monitoring, such as the monitoring of loads, static behavior and durability [24]. These systems can nowadays play a major role in the observation and understanding of the structural behavior either during the bridge construction, or during the service lifetime [25], as will be shown with the examples presented in this paper, concerning several continuous dynamic monitoring programs implemented by ViBest/FEUP on large Civil structures with different typologies.

3 Continuous Dynamic Monitoring of Transportation Infrastructures

3.1 Footbridges

Modern footbridges are often light structures characterized by very high slenderness and low damping, which makes them easily susceptible to vertical vibrations for spans longer than 50 m or to horizontal vibrations and lock-in for spans usually in the range 80–120 m.

Therefore their design normally requires a reliable numerical prediction of the levels of vibration and degree of human comfort associated to normal walking (of groups or flows of pedestrians) or jogging, which can be in general obtained on the basis of simplified load models and analysis procedures established in recent guidelines and recommendations [26, 27].

In case of occurrence of excessive lateral and/or vertical human induced vibrations, the design and implementation of vibration control devices (normally tuned-mass or viscous dampers) may be required, and though the efficiency of such devices can be preliminary assessed on the basis of forced vibration tests [28], the most reliable verification of their efficiency is based on temporary or long-term dynamic monitoring.

Moreover, continuous dynamic monitoring duly conjugated with the application of robust software tools to develop an online output-only modal identification of the collected data and the statistical removal of the influence of environmental and operational factors on the modal variability can be also used to detect early damage by construction of suitable control charts [29, 30].

In this context, this section presents three different case studies of continuous dynamic monitoring of Portuguese lively footbridges, aiming at the verification of vibration serviceability limits defined by recent footbridge guidelines, as well as the demonstration of the feasibility of vibration based damage detection.

3.1.1 Continuous Dynamic Monitoring for Vibration Serviceability Assessment

(a) Excessive vertical vibrations: the case of Santo Tirso footbridge

Santo Tirso footbridge (Fig. 1) is formed by a steel arch with 60 m chord and 6 m rise, supporting a 5 m wide deck with total length of 84 m, divided by spans of 12 m. The deck cross-section, formed by a light concrete slab 0.15 m thick supported by three longitudinal hot-rolled profiles, is slightly asymmetric due the inclusion of a timber path on one edge.

The design of this arch footbridge pointed to a lively behavior, marked essentially by vertical vibrations induced by crowd walking and jogging of pedestrian groups. The dynamic behavior of the footbridge was therefore investigated upon construction by means of ambient, free vibration and pedestrian tests [31]. From these tests it was concluded that the foot-bridge reached a medium comfort level with the excitation by groups of 20 pedestrians walking in resonance with the first and second footbridge modes (Fig. 2), at 1.64 Hz and 2.04 Hz, respectively. For the jogging scenarios, at about 2.71 Hz (mode 3), it was observed that a very small number of pedestrians



Fig. 1 Santo Tirso footbridge: lateral view (left), installation of a TMD (right)

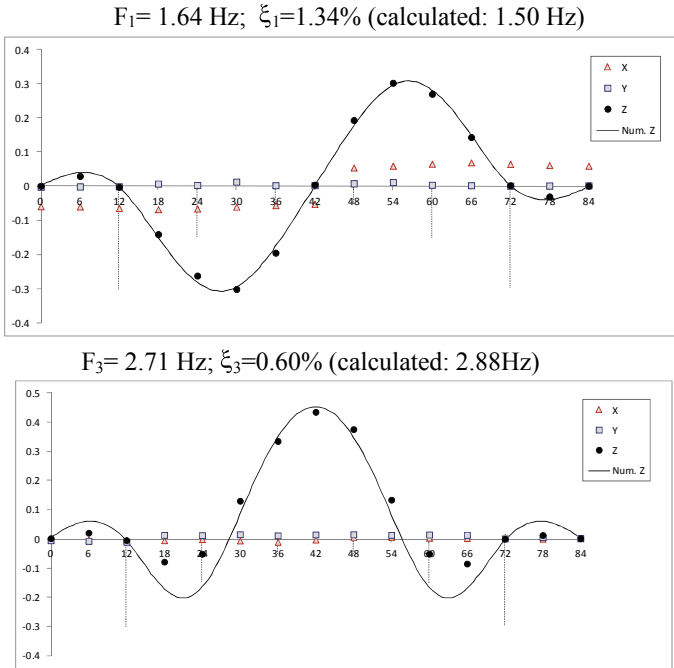


Fig. 2 Critical vibration modes, comparison between numerical and experimental estimates

(2, 3) could generate extremely high amplitudes of vibration, 5 jogging pedestrians generating intolerable vertical vibrations [32].

Considering these aspects, a final decision was taken together by the Structural Engineer and the Owner of the bridge to implement two vertical TMDs, one for slow walk of crowds (at the antinode of mode 1) and a second one for jogging and running of small groups of pedestrians (at the antinode of mode 3, mid-span). The limited space underneath the bridge deck to accommodate the TMDs motivated the splitting of each device into two units, which were installed symmetrically with respect to the bridge axis.

According to the calculations conducted with a calibrated numerical model, the installation of TMDs with a total mass of 2100 kg would provide an added damping ratio of about 4%, largely contributing to the attenuation of resonance effects on the footbridge.

In order to evaluate the degree of efficiency of the installed TMDs, a new series of dynamic tests was conducted on the footbridge after their installation [33]. These tests involved the measurement of the dynamic response induced by a group of 10 pedestrians walking in resonance with the first vibration mode (1.64 Hz), or else by jogging pedestrians in resonance with the third vibration mode (2.7 Hz).

Inspection of their results shows the important attenuation of the response achieved with the installation of the TMDs. It could be observed, for example, that the acceleration of 3.2 m/s^2 caused by 5 pedestrians jogging reduced by 3 times upon installation of the TMDs, causing the evolution of the footbridge classification from “intolerable comfort”, prior to installation of TMDs, to “medium comfort” level upon installation of TMDs, in the situation of excitation by groups of joggers.

As for the identification of the level of damping introduced by the TMDs, free vibration tests were conducted. During these tests, one pedestrian jumped in resonance at the antinodes of the controlled modes and suddenly interrupted its motion. The envelopes of the free vibration records of accelerations are formed by two branches, the first being characterized by a higher slope and corresponding to the phase of activation of the TMD, during the higher vibrations, while the second branch reflects the vibration of the footbridge when the TMD de-activates due to a reduction of the response. For the third vibration mode, a damping ratio of 2.5% was measured in the first branch, reducing to 0.7% in the second part of the record.

In order to check the good performance of the implemented TMDs in service, a dynamic monitoring system was installed in the bridge and a one-year continuous monitoring program was established in agreement with the footbridge Owner [34]. This system comprises 7 accelerometers and 4 thermal sensors connected to an acquisition system. Three accelerometers are located on the bridge deck close to the TMDs (two of them measuring vertical and lateral accelerations at mid-span and a third one measuring vertical accelerations near the other TMD), whereas the other four accelerometers are installed on the masses of the four TMD units to accurately observe their behavior.

The analysis of the acceleration records collected over a period of one year has permitted to conclude that the maximum vertical and lateral acceleration has reached values of 1.0 m/s^2 and 0.15 m/s^2 , respectively. These values would allow the classification of the foot-bridge as providing a medium comfort level. It is noted however that these values are sporadic, as evidenced by one of the monthly plots of the maximum daily vertical and lateral acceleration represented in Fig. 3. It is further observed that the maximum daily amplitudes of acceleration at mid-span are generally greater than 0.5 m/s^2 , indicating a frequent activation of the TMD used to control vibrations induced by jogging activities. The same may not occur for the other TMD, which was designed for slow walking crowds.

(b) Excessive lateral vibrations and lock-in: the case of Coimbra footbridge

The Pedro e Inês footbridge in Coimbra is formed by a central parabolic arch with 110 m chord and 9 m rise, and two lateral half arches in steel, supporting with total continuity a composite steel-concrete deck (Fig. 4).

A specific characteristic of this structure is the anti-symmetrical development of both the arch and deck cross sections along the longitudinal axis of the bridge. In the central part, two L-shaped box-sections and the arch “meet”, to form a rectangular box cross-section $8 \text{ m} \times 0.90 \text{ m}$, while at the ends of the lateral spans the “meeting”

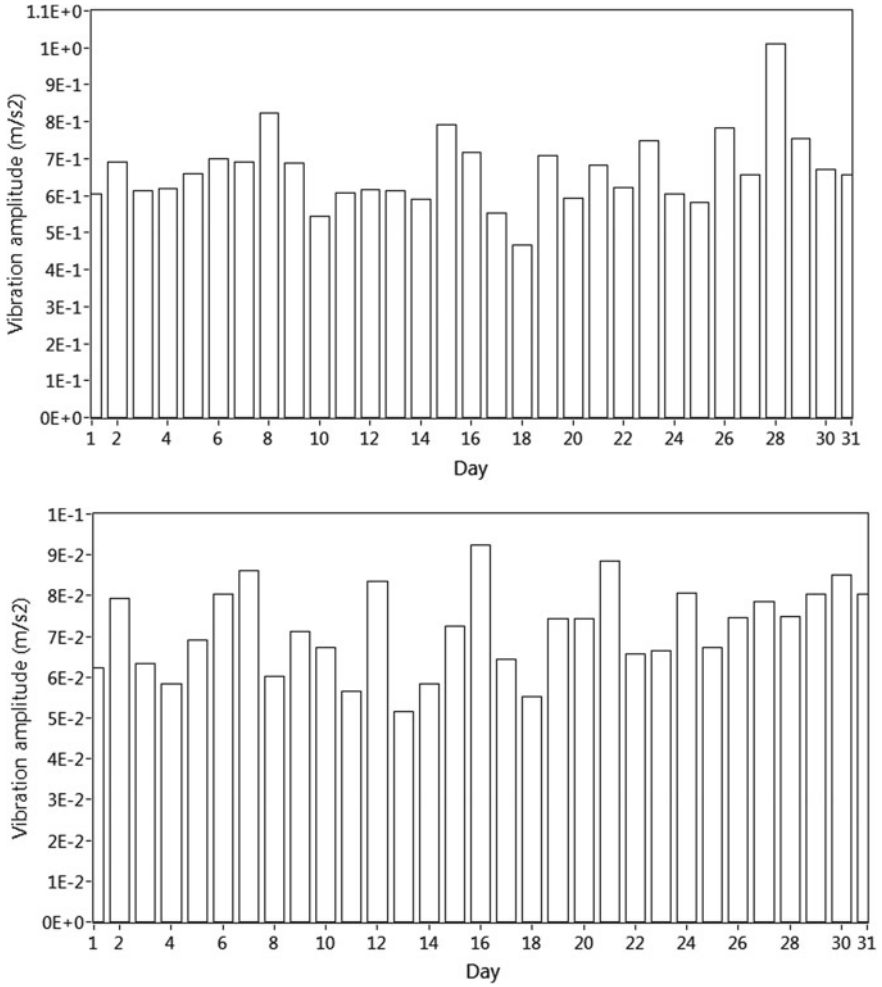


Fig. 3 Santo Tirso footbridge: maximum daily vertical (top) and lateral (bottom) acceleration during the month of August 2013



Fig. 4 Coimbra footbridge: lateral view

of the arch and deck generate a rectangular box cross-section $4\text{ m} \times 0.90\text{ m}$. These characteristics result in a complex torsional behavior under vertical loads.

Due to the poor characteristics of the soil, the arch is founded on long piles, reaching 35 m in length. The flexibility of these piles in the horizontal directions compromises the behavior as arch of this structure, resulting instead in an intermediate behavior between an arch and a girder.

Following an initial evaluation by the Structural Engineer, who identified a potential for lateral and vertical pedestrian induced vibrations, the Coimbra footbridge was extensively investigated. It was concluded in particular that the footbridge was prone to lateral synchronization (lock-in) in the first lateral mode, at about 0.9 Hz, and this behavior was actually observed by test as soon as the number of persons crossing the bridge reached about 70 [28]. It was therefore an option of the Structural Engineer to install a TMD for lateral vibrations at mid-span whose characteristics were determined on the basis of the modal parameters identified upon construction of the footbridge.

The mass of the implemented TMD was about 15 t, representing 7.3% of the modal mass of the footbridge loaded with a pedestrian density of 0.5 person/m^2 . This TMD was split into 6 units with a mass of 2465 kg each that were accommodated inside the box section at the mid-span (see Fig. 5). The observation that the various identical units forming the TMD behaved differently under vibration of the footbridge motivated a thorough characterization of these units and of the actual damping provided by the installed TMDs. A forced vibration test was therefore conducted consisting of the application of a sinusoidal load at frequencies varying in the range 0.58–0.98 Hz, containing the footbridge fundamental lateral frequency. Figure 6 represents the amplitudes of acceleration recorded at the deck mid-span for a sine sweep with amplitude 200 and 1300 N, as well as the amplitudes of acceleration measured in correspondence at each TMD unit. The theoretical deck and TMD acceleration amplitudes are also represented in this figure for comparison.

The analysis of Fig. 6 evidences different deck behavior for different force amplitudes, and shows also different amplitudes of vibration of the various TMD units.

Fig. 5 Lateral TMD of Coimbra footbridge



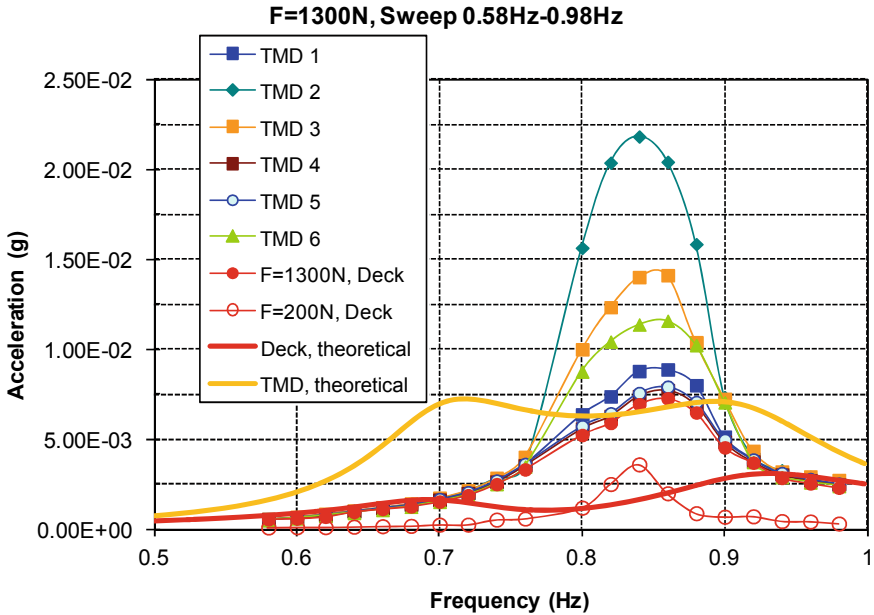


Fig. 6 Coimbra footbridge: comparison between theoretical and measured response of deck and TMD units during a sine sweep

Generally, the TMD vibration amplitudes diverge from those of the deck when the deck acceleration is greater than 0.03 m/s^2 . Furthermore, three of the six TMD units have always amplitudes of vibration close to those of the deck, meaning that their activation is very slight. Comparing the observed deck and TMD vibration amplitudes with the corresponding expected values, also represented in Fig. 6, it can be concluded that the attenuation of the response achieved with the TMDs is significantly lower than predicted, and that the TMD masses exhibit vibration amplitudes that more than double the expected values. The identification of modal parameters from the deck frequency response curves and their comparison with the ones expected from a numerical formulation of the two-degree-of-freedom system enable the conclusion that the implemented TMDs are much less efficient than expected, the achieved damping being of the order of 50% the expected. The combination of the splitting of the TMD into various units with the difficult activation of some of the TMD units are the reasons for this behavior and have motivated the continuous dynamic monitoring of the footbridge with a six-channel system for five years, with conclusion of the observation in 2012.

It was therefore relevant to analyze how in practice the footbridge behaved during this period. For this purpose, the maximum daily lateral acceleration recorded at the mid-span between June 2007 and January 2012 by a 6-channel PCB continuous dynamic monitoring system is represented in Fig. 7. The red line marking the amplitude of 0.03 m/s^2 is exceeded for most of the days, meaning the TMD is activated

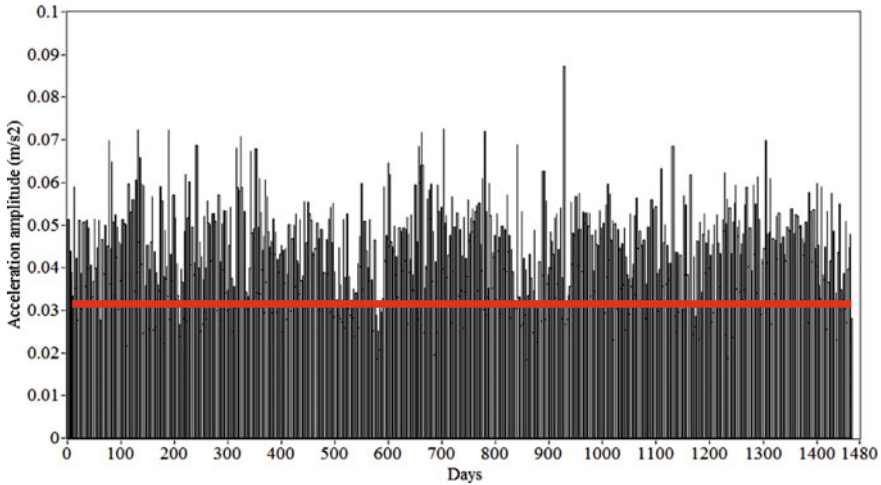
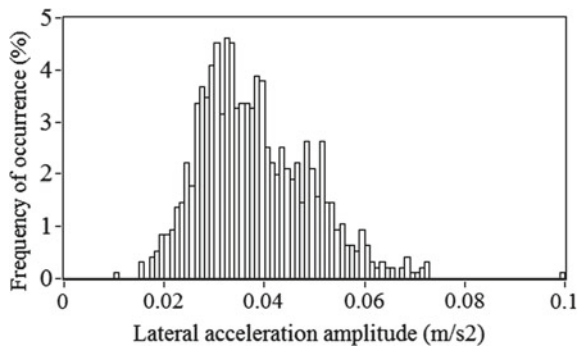


Fig. 7 Coimbra footbridge: maximum daily acceleration at mid-span between June 2007 and January 2012

almost every day. At the same time, the maximum daily lateral acceleration rarely attains amplitudes of 0.07 m/s^2 , with a maximum close to 0.09 m/s^2 , therefore never reaching the threshold for lock-in specified as 0.1 m/s^2 in [27, 28] and leading to a classification of “maximum comfort” for lateral vibrations according to the same guideline. In this respect, it is relevant to note that the maximum recorded response of the footbridge was 0.094 m/s^2 and occurred at the inauguration, which took place in November 2006.

In order to better characterize the activation of the TMD, a histogram is presented in Fig. 8 showing the frequency of occurrences of the maximum lateral acceleration over the period between June 2007 and May 2010. The analysis of this figure shows that the frequency of observation of the highest amplitudes of vibration is extremely low, meaning that the occurrence of vibrations is sporadic.

Fig. 8 Coimbra footbridge: histogram of maximum daily lateral acceleration between June 2007 and May 2010



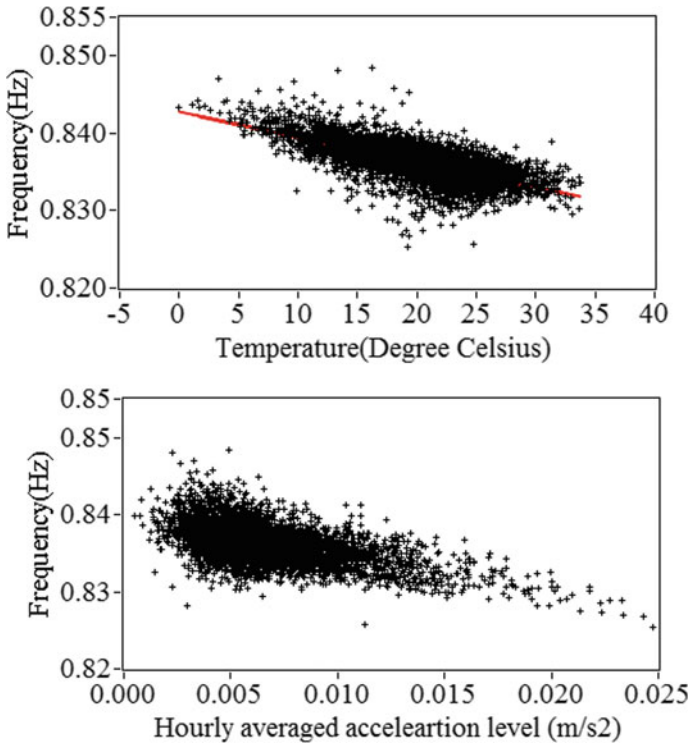


Fig. 9 Coimbra footbridge: variation of lateral frequency with temperature and with amplitude of vibration between June 2007 and May 2010

This is further evident in Fig. 9, showing the variation of identified natural frequency as a function of both temperature and amplitude of acceleration [29]. The identified natural frequency of the lateral mode varies in the interval 0.824–0.848 Hz, and the standard deviation of the estimates is 0.003 Hz. This narrow interval of variation is useful to understand that the TMD does not get severely detuned, the expected damping reduction due to this effect not exceeding 5%, and that the corresponding activation is so sporadic that globally the characteristics of the footbridge are hardly changed with time. So, to conclude, it can be said that the lateral TMD at Coimbra footbridge is generally very slightly activated and, even though the actual efficiency is about 50% of expected, the footbridge generally fulfils the serviceability criteria for lateral vibrations.

(c) Vibration-based SHM: the case of FEUP stress-ribbon footbridge

This stress-ribbon footbridge links the main buildings of FEUP with the students’ canteen (Fig. 10). The bridge is formed by two continuous spans 28 and 30 m long, rising 2 m from the abutments to the intermediate pier. A continuous concrete cast-in situ slab embedding four pre-stressing cables takes a catenary shape over the two

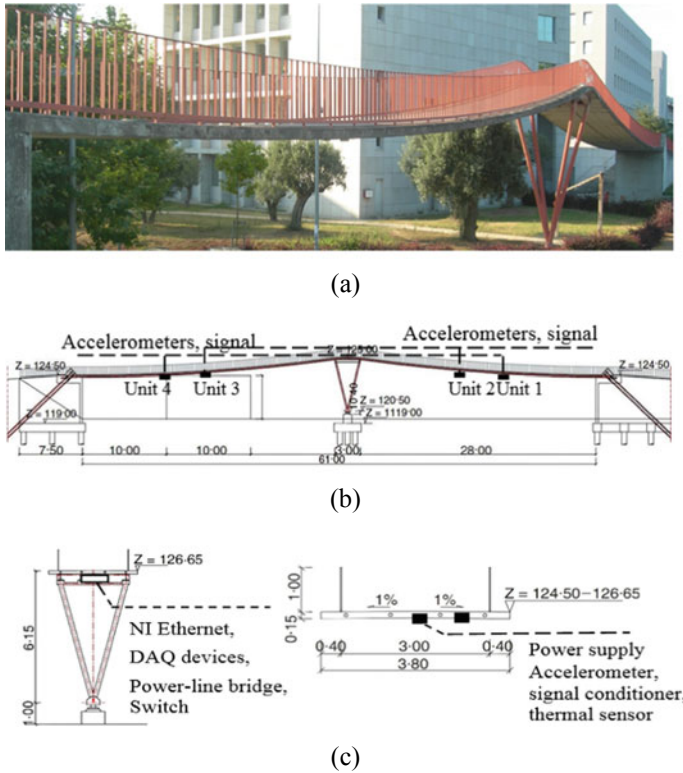


Fig. 10 FEUP footbridge: **a** General view; **b** elevation with instrumentation layout; **c** section over column and instrumented cross-section

spans, with a circular transition over the intermediate support, which is made of four steel pipes and forms an inverted pyramid hinged at the base.

The constant cross-section of the deck is approximately rectangular with external design dimensions of 3.80 m \times 0.15 m.

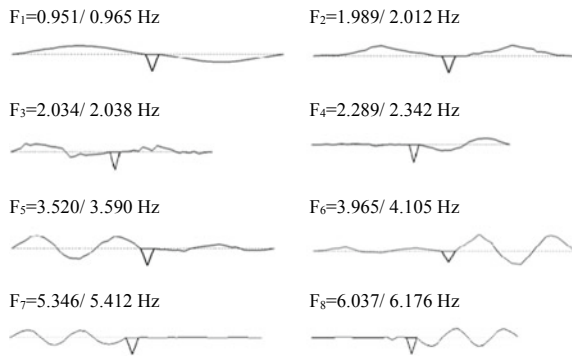
The high flexibility of the footbridge and the significant vibration levels observed during the crossing by pedestrians motivated the development of a numerical study of the dynamic behavior which was calibrated on the basis of experimental tests [35, 36]. Table 1 and Fig. 11 summarize the resulting natural frequencies and modal shapes in vertical direction, and pre-sent a comparison with the corresponding values identified on the basis of two ambient vibration tests conducted with a five-year time lag.

With the purpose of investigating vibration-based SHM techniques using real data, a continuous dynamic monitoring system based on four sensor units and National Instruments data acquisition devices was installed in this footbridge [37]. Each unit comprises a vertical accelerometer PCB-393C, a signal conditioner PCB-488A03 and a thermal sensor PT100. These sensors are mounted separately on the lower

Table 1 Comparison of identified and calculated modal parameters

Mode no.	FE freq. (Hz)	Identified modal parameters			
		3/10/2009		5/10/2004	
		Freq. (Hz)	Damp. (%)	Freq. (Hz)	Damp. (%)
1	0.940	0.951	1.03	0.965	1.14
2	2.152	1.989	1.09	2.012	1.45
3	2.101	2.034	1.16	2.038	1.48
4	2.344	2.289	2.05	2.342	1.59
5	3.736	3.520	1.87	3.590	2.08
6	4.188	3.965	1.71	4.105	1.87
7	5.761	5.346	1.80	5.412	1.70
8	6.820	6.037	2.03	6.176	2.12

Fig. 11 Identified mode shapes using the SSI-COV method



surface of the bridge deck at both 1/2 and 1/3 of each span (Fig. 10b, c), a nearly real-time zipped acceleration signal file being generated and transmitted via Internet every 10 min and a temperature file every 30 min continuously.

In order to track the variation of modal properties, a Continuous Structural Modal Identification (CSMI) toolkit has been developed and implemented in LabVIEW environment, which runs automatically without any manual interaction [37, 38].

The application of the automated Covariance driven Stochastic Subspace Identification (SSI-COV) method to 1 h acceleration records permitted the identification of frequency estimates of 12 modes in the range of 0–20 Hz from June 2009 to May 2011. These are shown in Fig. 12. It is noticed that the automated identification of the vibration modes with natural frequency close to 2 Hz was not possible, due to perturbation introduced by the harmonics in close frequencies associated with the pedestrians’ movement. For the remaining frequencies, a clear time variation is perceptible, especially for those associated with higher order modes. The tendency of

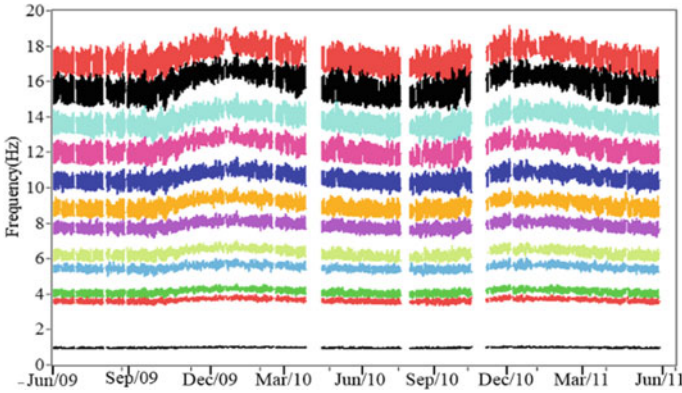


Fig. 12 Variation of identified modal frequencies from 1st June 2009 to 31st May 2011

increasing in winter time and decreasing in summer time reflects the seasonal environmental effects. It is worth noting that the maximum relative variation of modal frequency estimates is of the order of 20%.

The development of correlation analyses could show that the variability of modal frequency estimates depends on temperature and intensity of human traffic, with special emphasis to the first factor. Temperature, in particular, has a non-linear effect on those modal estimates for temperatures above 30 °C. Despite this non-linear behavior, strong linear relations between frequency estimates of the different modes were noticed. This fact allowed the use of an output-only approach for the statistical removal of the effects of environmental and operational factors on the modal properties based on the Principal Component Analysis (PCA) [30].

Subsequently, Novelty analysis on the residual errors of PCA builds a statistical damage indicator for long term structural health monitoring. To check the feasibility and potential of this approach, possible damage scenarios were simulated using a duly calibrated 3D finite element model. In order to represent different levels of damage, the clamped boundary conditions at the abutments were replaced by spring elements, with the stiffness constants de-fined as $K_1 = 1E13$ kN m/rad, $K_2 = 1E10$ kN m/rad and $K_3 = 1E7$ kN m/rad. The continuous monitoring results during the 1st year (from June 2009 to May 2010) were selected as reference and the frequency estimates in the second year (from June 2010 to May 2011) were affected by the relative change of calculated frequencies caused by simulated damage.

Figure 13 shows the Novelty index NI (grey points) and center line CL of reference state (in red) and three different damage scenarios (in blue, purple and black, respectively). Obvious deviation of CL comparing with the reference state is noted when releasing the rotation with decreasing stiffness constants of spring elements at both abutments. It means that such damage can be clearly detected.

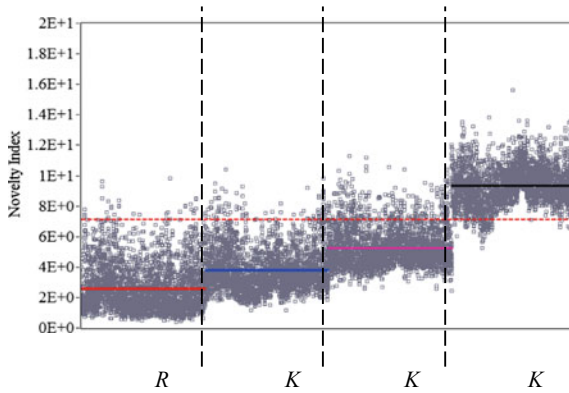


Fig. 13 Detection of simulated damage by decreasing the stiffness of spring element at the abutments (Ref, K1, K2, K3)

3.2 Railway Bridges

Another interesting case study regards the experimental evaluation of the dynamic effects induced by traffic loads on the Trezói railway bridge (Fig. 14) for fatigue assessment. This bridge is a single track metallic riveted structure with three spans of 39, 48 and 39 m, supported by two intermediate trapezoidal metallic piers and two masonry abutments at the extremities.

A temporary monitoring campaign (Fig. 15) was also developed at this bridge by ViBest/FEUP so as to characterize the global and local structural behavior, enabling the calibration and validation of numerical models used in numerical simulations for the analysis of stress distributions in critical elements and connections, the construction of histograms of stress cycles suitable for fatigue assessment, and collecting reliable information regarding the characteristics of real traffic crossing the bridge in terms of velocity, axle loads, number of axles and axles distances [39, 40].



Fig. 14 Trezói bridge: **a** lateral view; **b** view inside the deck

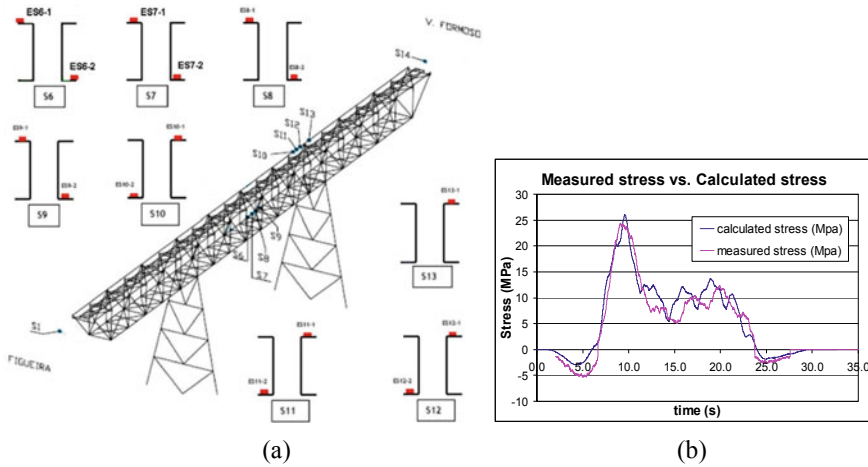


Fig. 15 a Instrumentation with strain gages; b measured versus calculated stresses

In a first instance, measurements were performed during two days of higher level of traffic. During that period, the bridge was crossed by 8 freight trains and 16 passenger trains. Figure 15b shows the very good agreement between measured and calculated stresses at an inferior chord of the truss at mid-span, which is the element subjected to higher traction stresses. These results provided a higher confidence on the developed numerical simulations, as well as on the trains' characteristics obtained. The fatigue damage was then evaluated for the 14 instrumented sections and for each train.

This investigation was subsequently extended to all structural elements of the bridge, which led to the conclusion that the most susceptible elements to fatigue damage are the transversal stringers (Fig. 16), which are affected by local vibrations. This aspect motivated a new research component specifically focused on these local effects, which involved also the development of more sophisticated numerical models (Fig. 16b) and the continuous dynamic monitoring of two transversal stringers [41].

3.3 Roadway Bridges

(a) Vibration-based SHM: the case of Infante D. Henrique bridge

With the purpose of assessing the structure health condition, a demonstrator system was installed by ViBest/FEUP at Infante D. Henrique bridge.

The Infante D. Henrique Bridge (Fig. 17), over river Douro at Porto, Portugal, is composed of two mutually interacting fundamental elements: a very rigid pre-stressed reinforced concrete box beam, 4.50 m height, supported by a very flexible reinforced concrete arch 1.50 m thick. The arch spans 280 m between abutments and

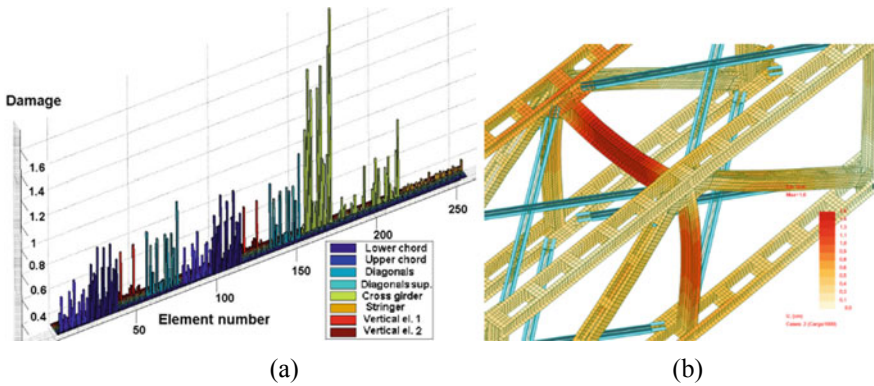


Fig. 16 a Evaluation of fatigue damage for real traffic; b shell finite element modelling



Fig. 17 Aerial view of Maria Pia, Infante D. Henrique and Luiz I bridges (from bottom to top) over Douro river at Porto

rises 25 m until the crown, thus exhibiting a shallowness ratio greater than 11/1. In the 70 m central segment, arch and deck join and define a box-beam 6 m height. The arch has constant thickness and the width in-creases linearly from 10 m in the central span up to 20 m at the abutments.

The dynamic monitoring system of the Infante D. Henrique Bridge, in operation since September 2007, is composed by two digitizers that receive the signals collected by 12 force balance accelerometers installed inside the deck box girder according to the scheme of Fig. 18. Three sensors equip each of four sections, one to measure the lateral acceleration and two for the vertical acceleration at the downstream and upstream sides. The data produced by the digitizers is continuously transferred to

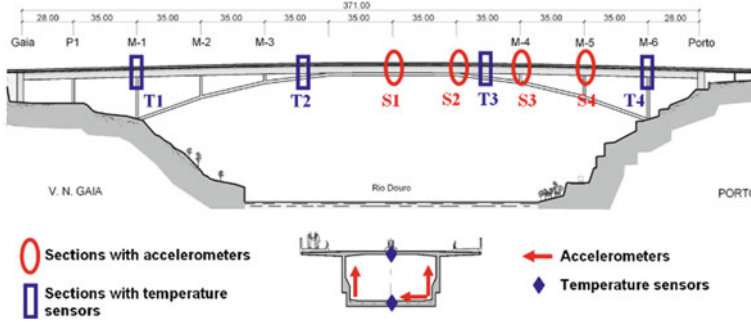


Fig. 18 Position of accelerometers and temperature sensors

FEUP in the form of ASCII files with as many columns as the number of sensors, containing acceleration time series with a length of 30 min sampled at a rate of 50 Hz.

This dynamic monitoring system is complemented by an independent static monitoring system (performing six acquisitions per hour) that was installed in the bridge during construction, comprising strain gages, clinometers and temperature sensors. In particular, the temperature sensors embedded in the concrete (Fig. 18) were crucial to eliminate the influence of temperature in the modal parameters.

The Dynamic Monitoring system produces two files with acceleration time series per hour, which are then handled by the monitoring software package, DynaMo [42], which performs the following tasks:

- Downloading and archiving in a database of the original data file, for later testing of alternative processing methodologies;
- Pre-processing of the data to eliminate the offset and reduce the sampling frequency to 12.5 Hz (the first 12 modes are below 5 Hz);
- Automatic identification of modal parameters using three different identification algorithms: FDD, SSI-COV and p-LSCF;
- Removal of environmental and operational effects from the identified natural frequencies;
- Updating of the control chart for the identification of abnormal values;
- Updating of the database with the results of the processing.

All the collected data and results can then be consulted using a graphical user interface (DynaMo Viewer) that comprehends tools to create several types of plots for a given time interval.

To exemplify, Fig. 19 presents the time evolution, from September 2007 to May 2010, of the bridge first four natural frequencies associated with vertical bending modes. The influence of the annual temperature fluctuations on the values of the natural frequencies is evident. The additional observation of the influence of the amplitude of vibration on those frequencies led to the construction of an optimised regression model that can minimize the effects of these variables on the modal parameters. Figure 20 shows the narrow range of variation of the natural frequency estimates

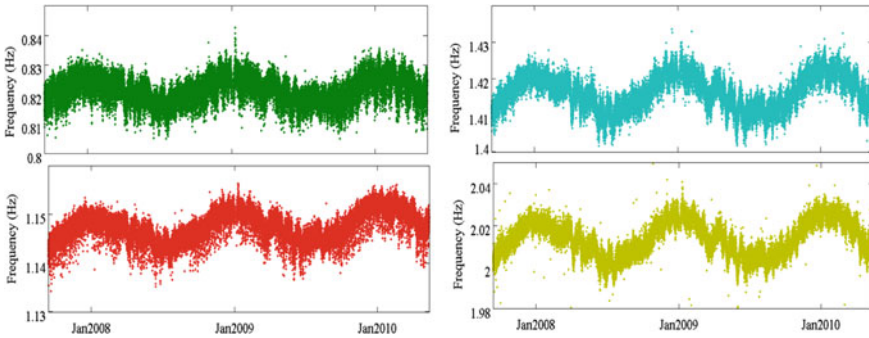


Fig. 19 Time evolution of the natural frequencies of the first 4 vertical bending modes

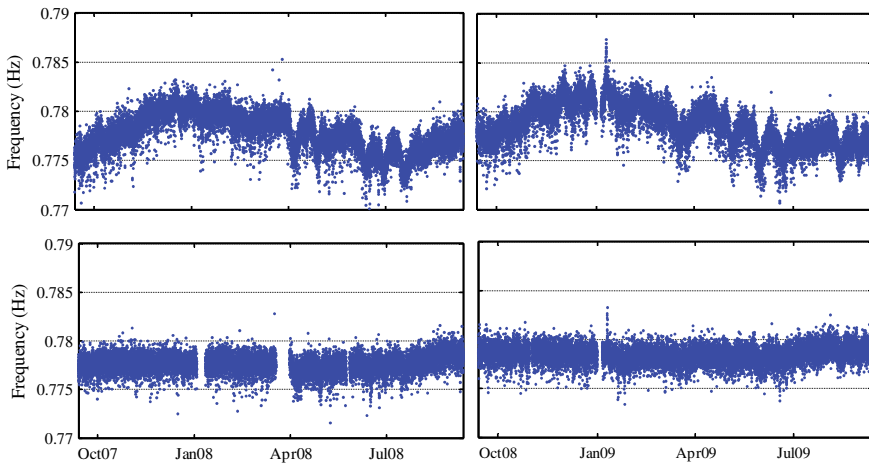


Fig. 20 Time evolution of the first natural frequency before and after minimization of environmental/operational effects

associated with the first lateral mode upon removal of the referred effects, using a multiple linear regression model [43].

Despite the good results obtained with the regression model, a complementary study with PCA was conducted to eliminate the influence of unmeasured factors on the natural frequencies. The first 12 natural frequencies of the bridge corrected by the two statistical tools are then used in the construction of a multivariable control chart. In the chart presented in Fig. 21a, one point refers to a group of 48 observations, as the performance of averages over 48 observation periods permitted to increase the accuracy in the detection of small frequency changes. It can be seen that the majority of the values are below the control line, defined taking into account observations associated with a reference period during which the structure is assumed undamaged.

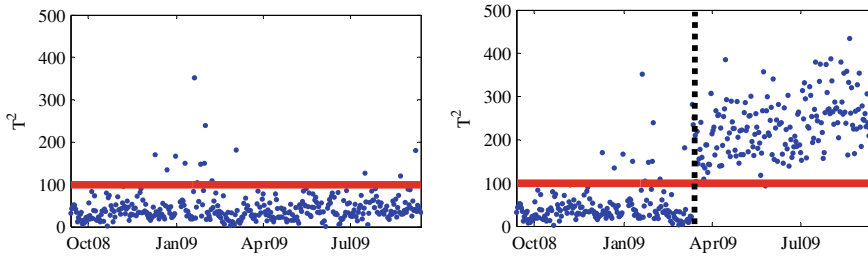


Fig. 21 Control charts without (left) and with (right) the numerical simulation of damages

In order to test the ability of control charts to detect damage, several damage scenarios were simulated with a numerical model of the bridge previously tuned. These were simulated in simplified form as bending stiffness reduction of 10% over lengths of 5 m at selected regions along the bridge [42]. The damage scenario that is analysed here is a stiffness reduction of the deck at mid-span. This led to frequency variations in some modes of the order of 0.15%. These variations, quantified with the tuned numerical model, were applied to the experimental data collected after March 2009. The control chart in Fig. 21b, designated Shewhart or T2, demonstrates that after introduction of the frequency shifts due to the simulated damage the points of the control chart are outside the control area. Therefore, it is concluded that it would be possible to automatically detect such a small damage in the bridge with the installed monitoring system.

(b) **Dynamic monitoring of wind effects: the case of Grande Ravine bridge**

Continuous dynamic monitoring can also play an interesting role in Wind Engineering studies developed on prototypes, especially in the case bridges located in zones with high susceptibility to the occurrence of extreme events, such as cyclones or typhoons, demanding an adequate characterisation of loads and an accurate assessment of the corresponding response.

Such type of research has been carried out by ViBest/FEUP on the Grande Ravine viaduct (Fig. 22), which is a slender girder bridge crossing a volcanic breach of 320 m width and 170 m depth, at the Reunion Island. This viaduct is located in an area frequently affected by tropical cyclones and has a particular structural configuration that, although stiff when compared to cable-stayed and suspended bridges, is slender in comparison to ordinary girder bridges.

These aspects led the Designer SETEC tpi [44] to idealise a continuous monitoring system with aerodynamic character, grouping a set of anemometers, pressure cells, temperature sensors and accelerometers (Fig. 23). Collaboration between the Designer, ViBest/FEUP and CSTB was established for the processing and analysis of recorded data, in order to validate the wind studies carried out during the design stage. Several other experimental tests were also conducted. In particular, ambient vibration tests were performed to characterise the bridge structure after construction, and



Fig. 22 Grande Ravine viaduct, Reunion Island

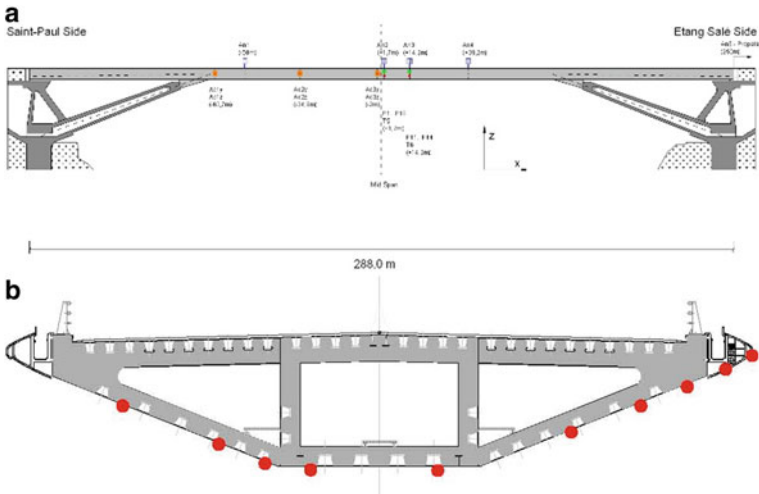


Fig. 23 Monitoring of Grande Ravine viaduct: location of **a** anemometers and accelerometers; **b** pressure cells

detailed wind tunnel tests were developed, using simultaneous measurement of aerodynamic forces with balance and through pressures on the surface of cross section of the deck model, in order to characterise the aerodynamic forces acting on the viaduct model.

This research [45] used 2 years of monitoring data in order to analyse and validate the design studies of Grande Ravine viaduct and also to explore recent numerical methodologies of analysis through the development/implementation of numerical tools for the assessment of structural response calibrated with results from full-scale measurements.

In this context, a wind model for the Grande Ravine implantation site was proposed based on the results of the analysis of the full-scale data recorded by the anemometers. These include the identification of predominant wind directions, incidence and design mean wind velocity, as well as local wind turbulence intensities, length scales and coherence.

Force coefficients were assessed based on the full-scale measurement of pressures, and compared with values established for structural design based on detailed wind tunnel studies. Correlations between wind and pressures were also established for the dominant wind directions and aerodynamic admittance was estimated from full-scale measurements and compared with experimental and theoretical formulations. Coherence between aerodynamic forces was also estimated and compared with the coherence of incident wind.

These results were compared with those from wind tunnel detailed study and from CFD simulations of flow around the deck cross section using stationary and unstationary turbulence models.

The structural response was studied based on the treatment of acceleration records from the continuous monitoring system installed at the viaduct. Modal identification under natural excitation was performed and the variation of structural dynamic properties was studied after removal of operational effects.

The structural response was analysed aiming at separating the effect of wind and characterising the effect of aerodynamic excitation, particularly the development of aerodynamic damping. A case of vortex induced vibrations was also identified and described.

4 Continuous Dynamic Monitoring of Stadia Suspension Roof

The Braga Municipal Stadium (Fig. 24) was built for the 2004 European Football Championship that took place in Portugal, and a particular aspect of this structure is the suspension roof structure, formed by 34 pairs of cables spanning 202 m and supporting two composite slabs 0.245 m thick over the stands, in extensions of 57 m from the anchorages.



Fig. 24 Braga Municipal Sports Stadium: view of roof from the west side. Cross section

This very slender structure was object of various design studies, which comprehended numerical studies for dynamic assessment and wind tunnel tests on rigid and flexible physical models, to determine pressure coefficients, identify potential aeroelastic instabilities and assess the response to turbulent wind. These studies pointed in general to a risk of high vibrations due to resonant effects and of high local vortex shedding stresses.

These factors motivated extensive tests conducted on the constructed structure to assess damping, and the installation of a monitoring system in order to monitor the roof response under wind excitation.

In this context, complementary monitoring systems were installed by ViBest/FEUP, including two sonic anemometers and various accelerometers, aiming at providing a characterization of the wind loads on the roof and establishing correlations with the response.

The roof structure has been monitored by two different systems (Fig. 25): one to monitor the dynamic response and the other to collect wind measurements. In operation since March, 2009, the continuous dynamic monitoring system is set to acquire the vertical acceleration by means of 6 force-balance accelerometers. The wind monitoring system was installed in the beginning of December, 2011, and is composed by two ultrasonic anemometers that are suitable to measure the ambient temperatures, velocity and direction of the wind at high sampling frequencies. This new independent and complementary wind measurement system was installed on the west slab of the stadium in order to characterize the wind model and analyze correlations between the structure's dynamic response and the wind load.

The installation of both monitoring systems comprised several elements as described in Fig. 25. The correlation between the data provided by both systems has

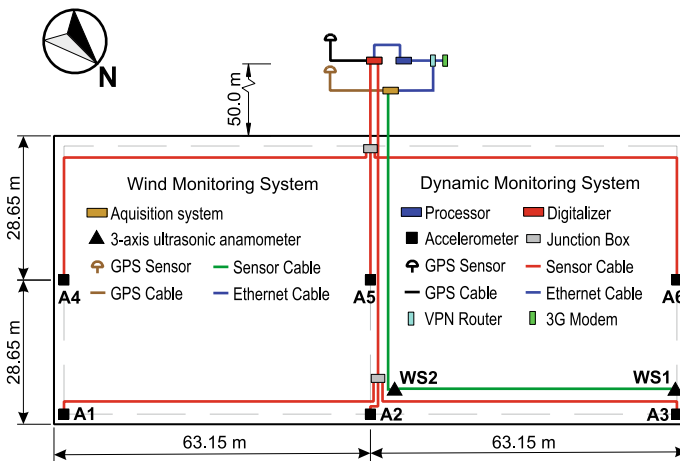


Fig. 25 Location of components of the two monitoring systems installed for wind measurements and acquisition of vertical accelerations on the Braga stadium suspension roof (top view of the west slab)

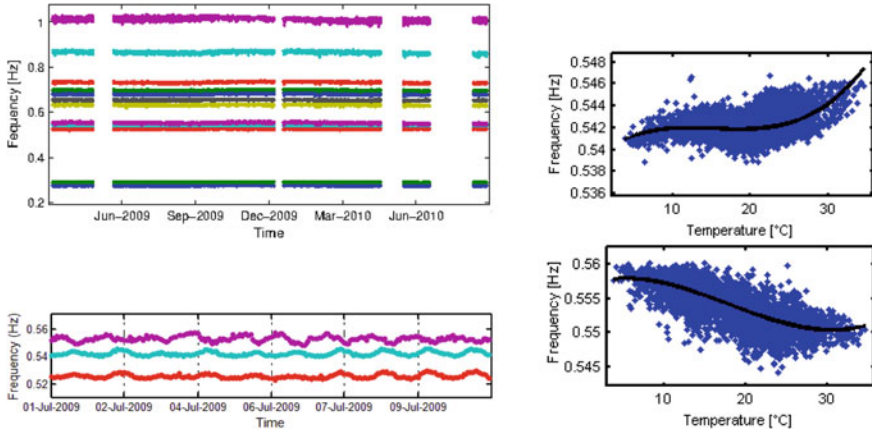


Fig. 26 (Left) Time evolution of natural frequencies: (top) from 2009/03/25 to 2010/09/27 in the range of 0–1.1 Hz; (bottom) from 2009/07/1 to 2009/07/10 of the modes 3, 4 and 5; (Right) correlation of estimated frequencies and measured temperatures from 2009/07/01 to 2009/12/31

allowed the assessment of the complex non-linear interactions between the monitored structure and the environmental effects.

Careful inspection of the monitoring results [46], as well as of temperature data available since the construction phase reveals that temperature plays also a major role in the variations of natural frequency estimates, as shown in Fig. 26 (left). However, it's interesting to note that, probably due to the peculiar geometrically non-linear behavior of the roof, the in-crease of temperature does not induce always a decrease of frequency estimates. Moreover, these variations have some non-linear nature, as shown in Fig. 26 (right). The variations of the natural frequency estimates obtained along almost two years of permanent monitoring of the roof structure are summarized in Table 2 and show relative variations no larger than 4.9%.

On the other hand, the wind monitoring system enabled an accurate characterization of mean wind speed, direction and elevation angles, turbulence intensity, wind speed power spectra, turbulence integral length scales and influence of wind on the structural response (Fig. 27), as explained in detail in [47].

5 Continuous Dynamic Monitoring of Energy Infrastructures

5.1 Wind Turbines

The technology previously developed for continuous dynamic monitoring of bridges and stadia roofs can be also applied with success in the field of energy infrastructures.

Table 2 Variations of frequency estimates

Average frequency (Hz)	Frequency range (Hz)	Max. relative variation (%)
0.275	0.272–0.277	1.8
0.290	0.287–0.293	2.1
0.525	0.519–0.532	2.5
0.542	0.538–0.547	1.7
0.553	0.543–0.560	3.1
0.632	0.619–0.639	3.2
0.654	0.647–0.658	1.7
0.681	0.670–0.691	3.1
0.698	0.688–0.703	2.1
0.732	0.724–0.740	2.2
0.866	0.843–0.877	3.9
1.013	0.981–1.031	4.9

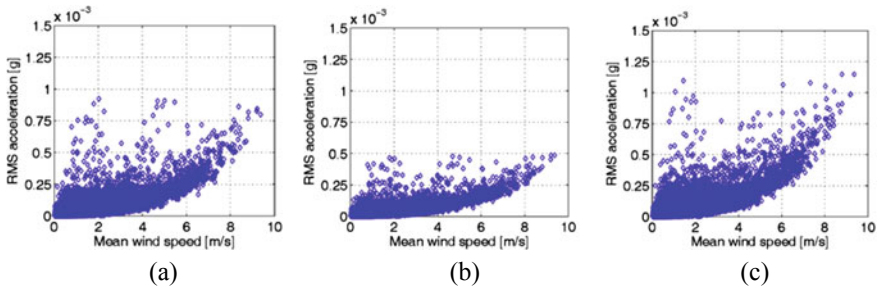


Fig. 27 Relationship between the 10-min mean wind speeds measured by wind sensor WS1 and the RMS of the vertical acceleration responses for: **a** accelerometer A1; **b** accelerometer A2; **c** accelerometer A3

With this purpose, a vibration-based monitoring system was also installed by ViBest/FEUP in a 2.0 MW onshore wind turbine, aiming at identifying abnormal structural changes at the support structure. This element, composed by the tower (76 m height) and foundation, is a crucial component of the wind turbine, representing an important share of the capital costs [48]. The main components of the developed monitoring system are introduced in Fig. 28. This aims not only the OMA based early detection of structural changes (damages), but also the evaluation of fatigue life.

The wind turbine is equipped with a SCADA system recording the mean, maximum and minimum values of several operational and environmental parameters from 10 min periods (e.g. wind speed and direction, rotor speed, yaw angle, blades pitch angle, outdoor temperature).

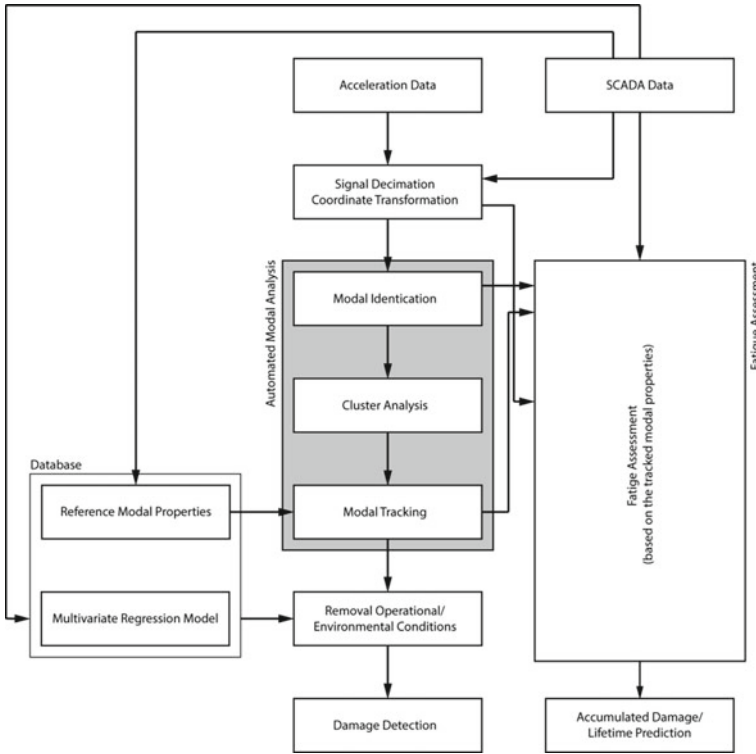


Fig. 28 Main steps of the vibration-based monitoring system (the grey box identifies the module related to automated modal analysis)

The installed vibration-based monitoring system is based on a GeoSIG CR-5P central acquisition system connected to 9 Guralp uniaxial force balance accelerometers distributed along the tower height and at the foundation level (Fig. 29).

Due to the frequent change of the nacelle orientation, a coordinate transformation was applied to the decimated acceleration signals so as to obtain the signal associated to the fore-aft (FA) and side-side (SS) directions of the turbine. Subsequently, automated operational modal analysis procedures were applied using the SSI-COV and p-LSCF methods and a hierarchical clustering algorithm of the stabilization diagram poles [49].

Since wind turbines are time-varying structures, with slightly different structural configurations according to the various regions of operation, different operating regimes have to be considered when defining the reference properties of the vibration modes. In that sense, six different operating regimes are defined, reflecting the major variations of structural configuration of the wind turbine. These regimes are described in Table 3.

Figure 30 shows the selected clusters in a Campbell diagram (frequency vs rotor rotation velocity), considering datasets collected during one year. In this figure, the

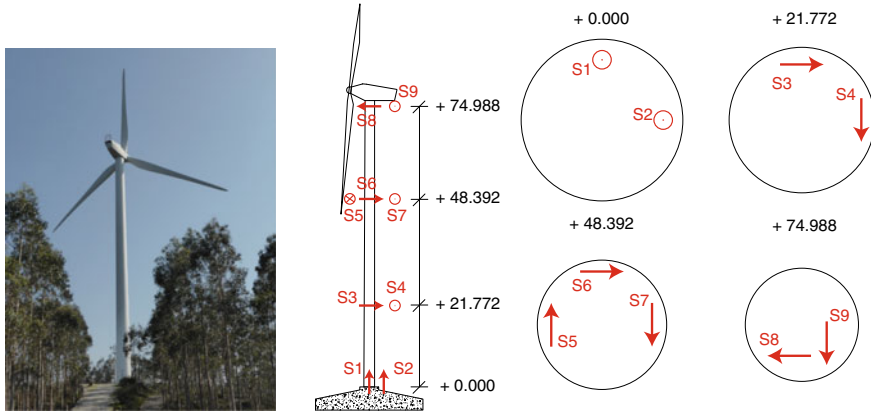


Fig. 29 Distribution of the sensors along the wind turbine

Table 3 Regimes considered for reference modal properties of the vibration modes

Operating regime	Wind turbine condition
1	Parked or idling (with high pitch angle values higher than 72°)
2	Parked or idling (with pitch angle value lower than 72°)
3	Transition regime from non-operation to operation (rotor speed between 0 and 8.7 rpm)
4	Operating regime, defined by the lowest operating rotor speed and the point where the pitch angle starts to increase to avoid excessive rotor torque values (around mean wind speed of 10 m/s)
5	Operating regime, between regime 4 and the highest operating rotor speed
6	Wind speed higher than cut-out speed

clusters are represented according to the main direction of vibration of the mode (FA or SS). Several alignments of clusters are clearly identified, corresponding to vibration modes. However, it also shows some clusters located around the inclined dashed lines (corresponding to the harmonics associated with the rotor rotation). These clusters, are only present when the turbine is in operation (rotor speed higher than 8.7 rpm), corresponding to poles motivated by the harmonic excitation.

Once the most important vibration modes of the wind turbine were identified, and their reference properties defined, a suitable tracking procedure could be implemented [49]. With this step, the alignments of points associated with the modes were selected and the influence of the harmonics was eliminated (Fig. 31).

Figure 31 exposes the quality of the modal identification obtained with the monitoring system along the whole operating regime of the turbine. Even for closely spaced modes (as is the case of the pairs of bending modes), the adopted processing strategy is capable of accurately distinguish them.

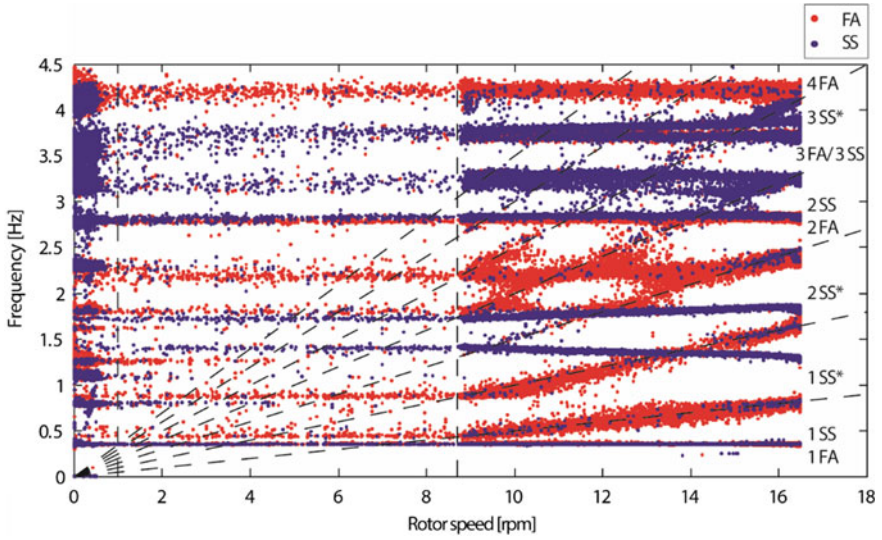


Fig. 30 Campbell diagram of considered clusters of stable poles. The vertical dashed lines separate the non-production situation, a transition state and the operating regimes of the wind turbine

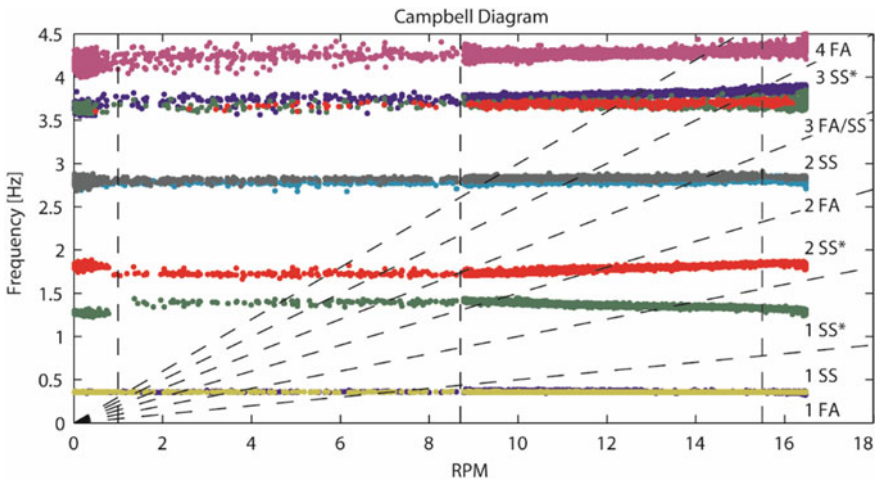


Fig. 31 Campbell diagram with tracked vibration modes (p-LSCF algorithm)

The evolution of the 1SS* and 2SS* modes with the rotor speed is illustrated, with greater detail, in Fig. 32. This figure resembles the typical behavior of rotor whirling modes [50].

Once the monitoring system is tuned to continuously track the vibration modes, the system is capable of operate in an automated way.

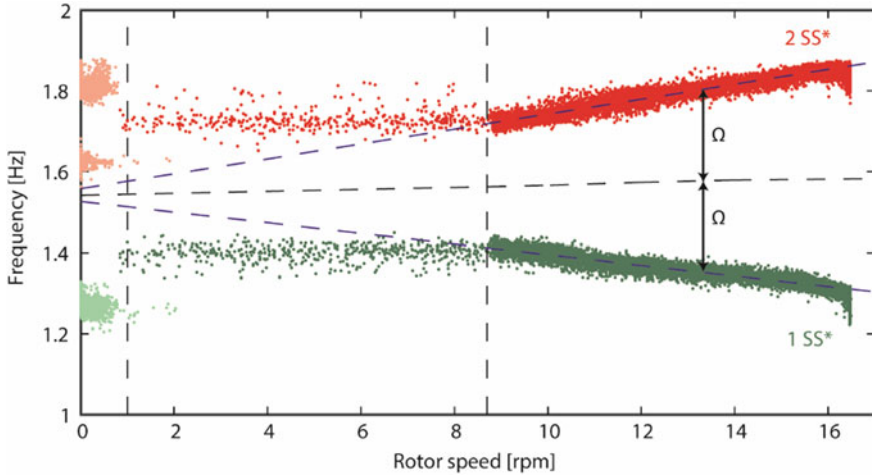


Fig. 32 Zoom of the Campbell diagram with the tracked vibration modes (p-LSCF algorithm)

The analysis of the damping results allows extracting very interesting conclusions regarding this modal property. Damping is a crucial characteristic in the design of wind turbines, directly affecting the fatigue analysis of the support structure and, consequently, its estimated lifetime. The quantification of the damping is especially complex due to (non-linear) phenomena, such as the aeroelastic interaction between the wind turbine and the wind flow. This phenomenon affords an additional portion of damping to the structural system, usually named as aerodynamic damping.

Globally, the damping ratio of the FA modes is expected to increase with the increase of the wind speed (which usually implies a higher operating regime). This is mostly due to the contribution of the aerodynamic component of damping. As expected, this increase of the damping values is not expected to be significant in the SS modes since the aerodynamic damping affects more modes vibrating on the direction of the wind.

A detailed analysis of the damping values of the first pair of tower bending modes is shown in Fig. 33. Figure 33a illustrates the evolution of the damping ratio of the 1 FA mode with the wind speed. The shape of the adjusted line (connecting the median values of each wind speed interval) clearly shows an increase of the damping with the wind speed, followed by a drop for wind speeds around 15–17 m/s. This situation is consequence of the increase of the pitch angle in the operating regime 5 which reduces the thrust force at the tower top and, consequently, reduces the opposition of the rotor blades to the wind flow in the FA direction.

On the other hand, the adjusted line for the damping values of the 1SS mode (Fig. 33b) only shows small variations over the different operating conditions, with a reduction when the turbine starts operating and an increase until reaching its rated speed.

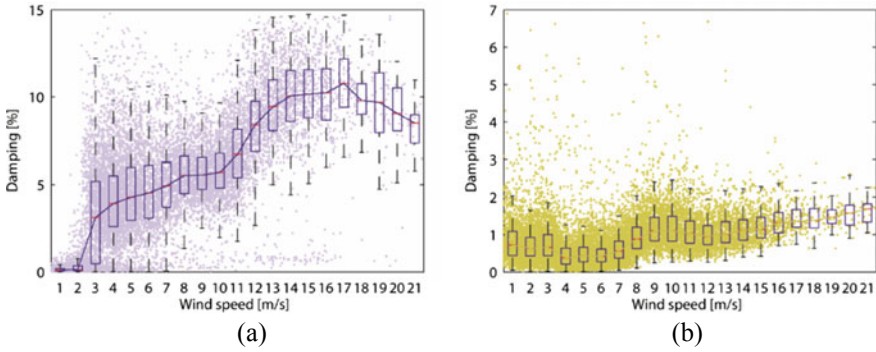


Fig. 33 Modal damping ratios of the 1 FA mode (a) and 1 SS mode (b) versus wind speed. In this figure, the median values (and box plots) are shown to characterize the damping variability in each wind speed interval

5.2 Concrete Dams

The implementation of vibration based SHM systems in concrete dams has been the most challenging application of ViBest/FEUP, owing to the extremely low signal to noise ratios.

This has been done, for instance, at the Baixo Sabor dam (Fig. 34), which is a concrete double-curvature arch dam, 123 m high, located in the north-east of Portugal, which is being monitored by a dynamic system comprising 20 uniaxial accelerometers implementation.

When monitoring large and massive civil structures, it is advantageous to have digitizers distributed along the monitored structure in order to reduce cable length and thus electrical interferences that can corrupt the signals [52]. Therefore, the dynamic monitoring system installed in Baixo Sabor arch dam is divided in three



Fig. 34 Baixo Sabor arch dam, aerial view of dam and reservoir and detail of the spillway from downstream [51]

subsystems connected by optical fiber. Subsystem 1 and subsystem 2 are composed by 6 uniaxial force balance accelerometers and a digitizer each, and both subsystems are connected to a field processor which is, in turn, linked to a computer (NUC). The two groups of accelerometers are radially installed along the upper gallery, disposed on each side of the spillway. Subsystem 3 is composed by 8 uniaxial force balance accelerometers, radially installed along the second and third upper galleries, and two digitizers that are connected to the computer, which is responsible for running the acquisition.

To perform modal analysis a good synchronization of the data recorded by all digitizers must be assured, which required the installation of GPS antennas. In addition, the field computer is connected to the optical fiber network between the dam and the plant allowing remote access. A scheme representing the monitoring system main elements is presented in Fig. 35, while the position of the total 20 accelerometers is characterized in Fig. 36 by red marks.

The force balance accelerometers used (FBA ES-U and FBA ES-U2 from Kinematics) have a dynamic range of 140 dB and 155 dB, respectively, and a frequency bandwidth that goes from DC to 200 Hz. These accelerometers can measure up to 4 g, but in this application they were configured to measure in the range 0.25 g/+0.25 g, in order to allow the accurate characterization of very low acceleration signals.

The dynamic monitoring system is configured to continuously record acceleration time series with a sampling rate of 50 Hz and a duration of 30 min at all instrumented points, thus producing 48 groups of time series per day. These data are automatically

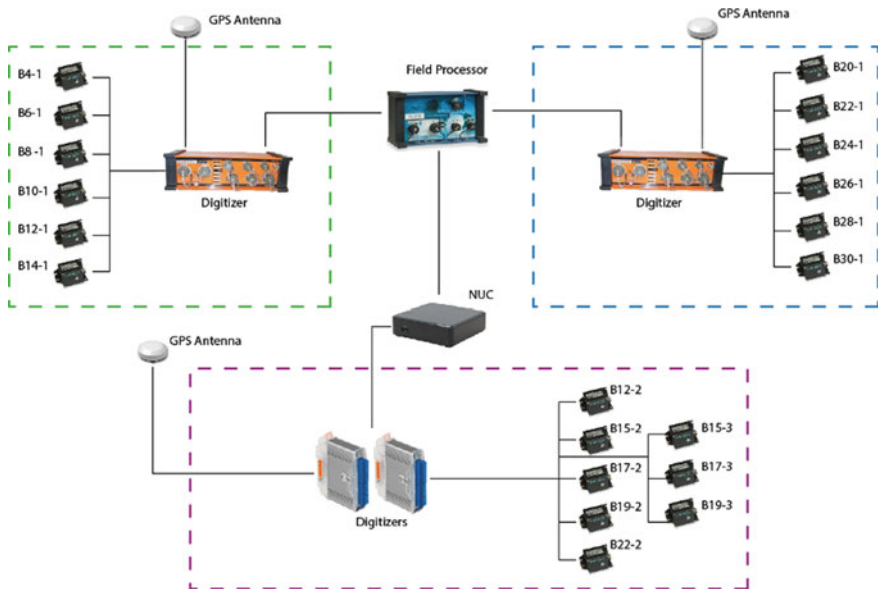


Fig. 35 Scheme of the monitoring system [24]

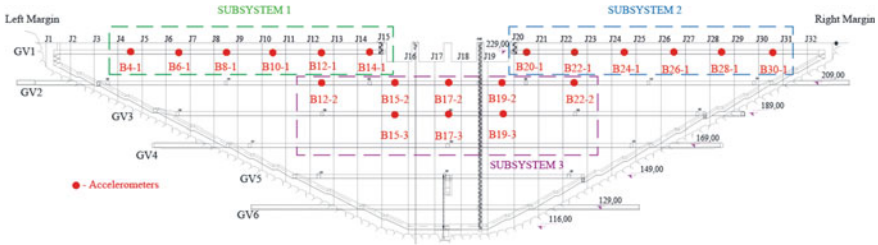


Fig. 36 Position of measuring points and subsystem components of Baixo Sabor dynamic monitoring system

stored in the field computer and then transferred remotely both to FEUP and LNEC, with a FTP connection, where they are stored and processed.

The data processing is accomplished with the software DynaMo, which was initially developed at ViBest/FEUP for continuous dynamic monitoring of bridges and was now adapted for the monitoring of dams [53].

For the most important and challenging task, the continuous automated identification of the modal parameters, alternative output only algorithms [54] were tested, and it was concluded that good results could be achieved through the combination of the Covariance Driven Stochastic Subspace Identification (SSI-Cov) with a routine for automated interpretation of the obtained results based on clusters analysis.

Figure 37 presents the stabilization diagram that stemmed from application of the SSI-Cov method to a set of time series collected in the instrumented dam. The six vertical alignments of stable poles presented in the diagram represent the first six vibration modes of the dam.

When monitoring dams integrated in a hydroelectric power plant, the turbine rotation frequency and its harmonics may be associated with mode shapes that are similar to the physical mode shapes of the dam with close natural frequencies. This may lead to the incorrect classification of a harmonic as a dam vibration mode. Since these

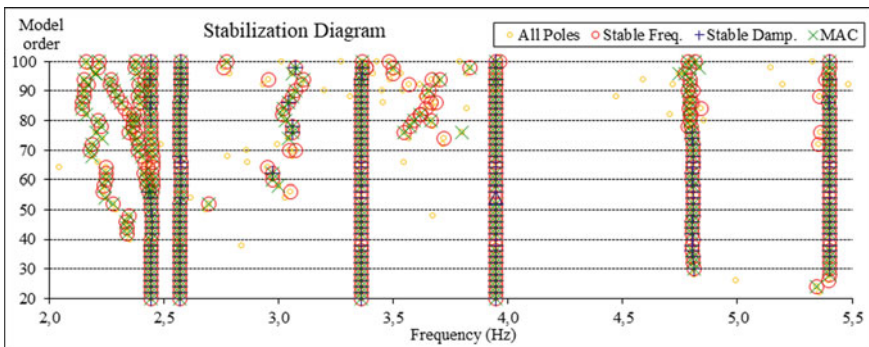


Fig. 37 Stabilization diagram obtained for the analysis of the time series collected at 2016/05/08 13:00

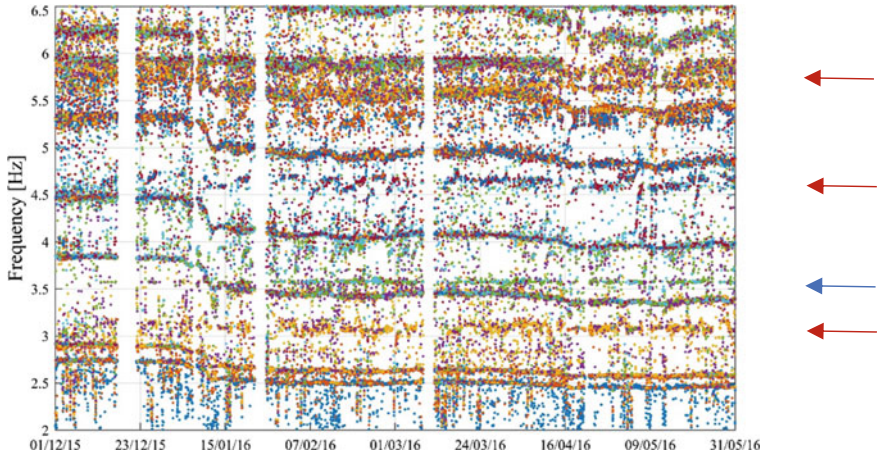


Fig. 38 Natural frequencies identified with SSI-Cov method; blue arrow—turbine rotation frequency; red arrows—harmonics and spurious modes

harmonics are associated with low damping values, to prevent this, before comparing the entire set of estimates with the references, the estimates with frequencies close to those of the harmonics and whose damping values are lower than 0.75% are eliminated. This is possible because a preliminary analysis of the data showed that all the tracked vibration modes present damping values higher than 1%.

The efficiency of the implemented tracking and harmonic removal procedures [55] is shown by comparing Fig. 38 with Fig. 39, which respectively present the identified natural frequencies obtained before and after their application. The algorithm searches between the entire set of estimates to find the ones that correspond to true vibration modes. In Fig. 38, besides the natural frequencies evolution over time, one can also identify horizontal distributions of estimates that are associated with the referred harmonics and spurious modes (which were pointed out with red arrows). While the natural frequencies of the structure vary over time due to operational and environmental factors, the frequencies associated with the turbines operation are almost constant over time.

Automated operational modal analysis was applied to the first six months of data recorded by the dynamic monitoring system, in order to track the evolution of the modal parameters of the first six modes (Fig. 40).

Natural frequencies and modal damping ratios were obtained for each setup of 30 min, from December 2015 to May 2016, and then 12 h averages were calculated. Thus, the evolution of the first six natural frequencies over time is characterized in Fig. 41. Sudden frequency variations are still well defined, as it can be seen by the fast value decline that all the six frequencies suffered in early January.

The sudden fall of natural frequencies values in January is explained with the temporal evolution of the reservoir water level. Comparing Figs. 41 with 42, it is

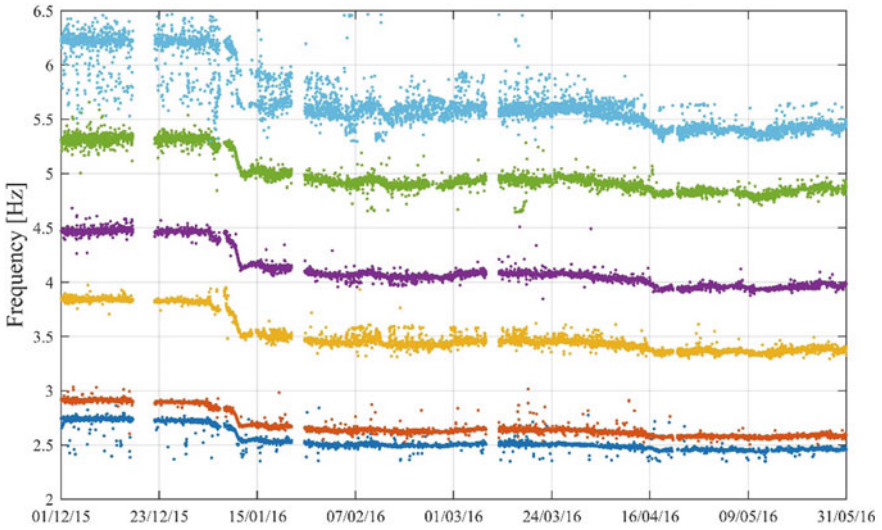


Fig. 39 Natural frequencies identified with the SSI-Cov method after using reference modal parameters

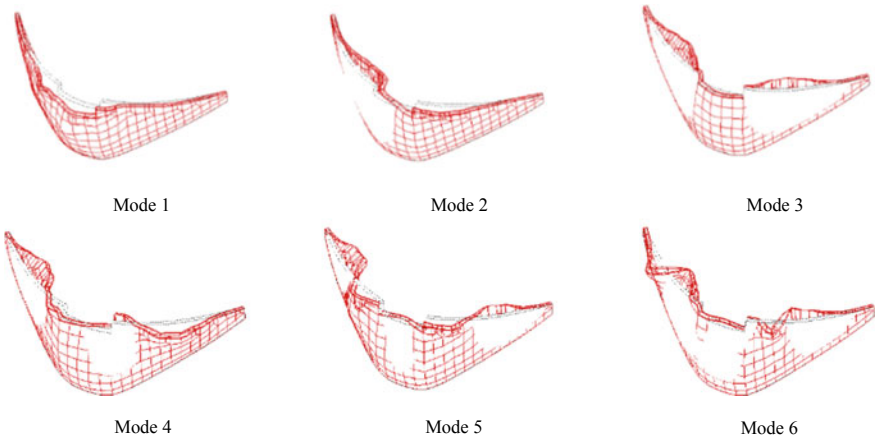


Fig. 40 Modal configuration of the first six modes of Baixo Sabor arch dam

possible to notice that an inverse proportionality occurs between natural frequency values and reservoir water level.

Statistical relationships between the vibration frequencies of the structure and the water level in the reservoir were developed with the aim of minimizing these effects (Fig. 43).

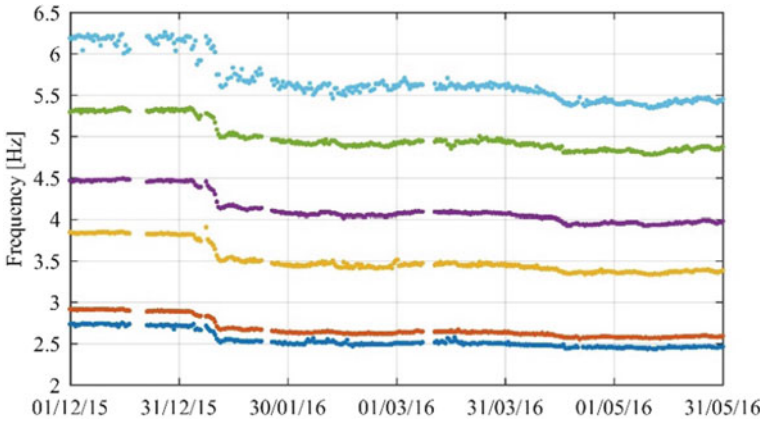


Fig. 41 Time evolution of natural frequencies' 12 h averages

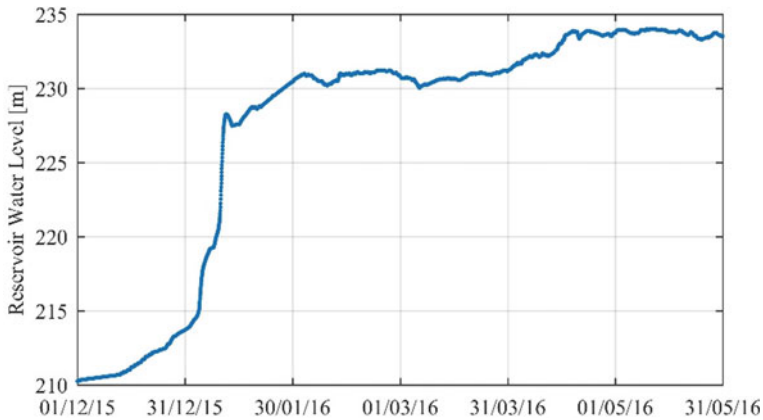


Fig. 42 Time evolution of reservoir water level

The obtained regressions were very important to validate and update numerical models, and to improve the understanding about the dam-foundation-reservoir system and thus enhance the quality of future models.

The effect of water level was then mitigated. For each vibration mode, individual frequency estimates were subtracted by the frequency value obtained with the regression model taking into account the water level associated with that particular estimate. Afterwards, the frequency averages of each mode were added to the obtained residues, resulting in the evolution of corrected frequencies over time.

The temporal evolution of frequencies after correction is much more stable. These stable frequencies may now be used as a starting point for the implementation of tools for damage detection [56].

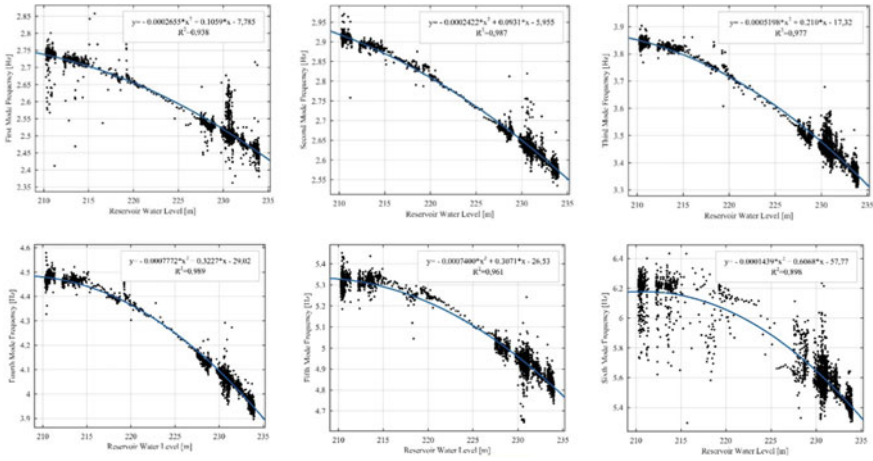


Fig. 43 Correlation between the reservoir water level and the first six natural frequencies

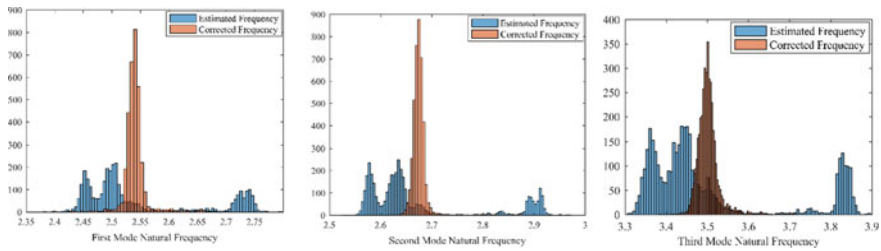


Fig. 44 Histograms with the first 3 natural frequencies before and after correction of the water level effect

The effect of this correction is clearly shown by the histograms of frequencies presented in Fig. 44, for the first three vibration modes. The distribution of frequencies was completely asymmetric before the correction of the water level effect (in blue) and acquired a well-defined symmetric shape after this correction (in orange), as it was expected.

The future collection of additional data will certainly permit to enrich these models with the incorporation of other factors with a lower influence on the natural frequencies of this type of structures, as for instance temperature and levels of vibration. Moreover, long-term effects such as the variation of the dam-rock-reservoir system deformation modulus, the state of the dam’s contraction joints and concrete hardening must also be taken into account when performing long-term evaluations.

Parallel to the continuous monitoring, a forced vibration test [57] was performed on Baixo Sabor arch dam in early May 2016, when the water reservoir was full, at a level of 234 m. For this purpose, the vibrator of eccentric masses presented in Fig. 45 was used. During the test, the vibrator imposed on the structure harmonic horizontal

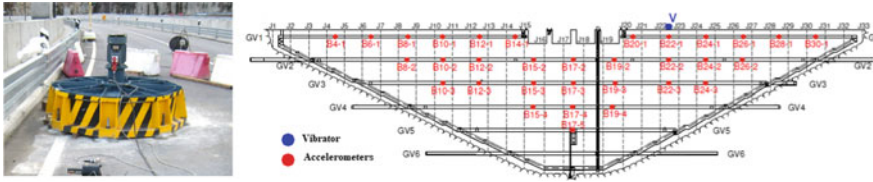


Fig. 45 LNEC eccentric mass vibrator used in Baixo Sabor arch dam and accelerometer position [57]

forces with different amplitudes and frequencies, and the dynamic response of the structure was measured with accelerometers and velocity transducers disposed over the dam’s five upper galleries, as represented in Fig. 45. The recorded time series allowed the identification of natural frequencies, modal damping ratios and mode shapes for the structure’s first 12 modes.

The results obtained from this forced vibration test were later confronted with results obtained from a numerical model developed by LNEC. This model, based on discrete and finite elements, takes into account the dam’s contraction joints, the deformability of the foundation and the reservoir [58]. To model the dam, 32 vertical blocks were discretized in isoparametric 20-node brick finite elements. This model has a simplified representation of the reservoir and the foundation, and it is intended to allow a preliminary comparison with the experimental data. The dynamic dam-reservoir interaction was simulated with Westergaard’s added mass technique, for the nodal points of the model located in the upstream face below the reservoir level.

The natural frequencies obtained both through the forced vibration test and through the numerical model, when the reservoir water level was stable at 234 m are presented in Table 4 together with the results of the monitoring system for the same water level. The results from the forced vibration test and the average frequencies obtained with the monitoring system during the test are almost identical. In turn, the numerical model, in spite of its simplifications, also produces results very close to those of the vibration test.

Table 4 Natural frequencies of the first 6 vibration modes, obtained with ambient vibration, forced vibration and numerical modelling

Mode	Natural Frequency (Hz)		
	Continuous monitoring	Forced vibration test	Numerical model
1	2.45	2.44	2.44
2	2.57	2.57	2.67
3	3.34	3.34	3.56
4	3.93	3.93	4.03
5	4.78	4.78	4.81
6	5.35	5.37	5.49

6 Conclusions

The set of long-term dynamic monitoring programs gradually implemented by the Laboratory of Vibrations and Structural Monitoring (ViBest, www.fe.up.pt/vibest) of CONSTRUCT/FEUP in large transportation and energy infrastructures with different typologies has enabled to better understand the potential of Continuous Dynamic Monitoring in different perspectives, such as:

- The interest of continuous dynamic monitoring of human induced vibrations to support the verification of safety with regard to vibration serviceability limit states in lively structures and of the efficiency of vibration control devices in pedestrian bridges with excessive vertical or lateral oscillations;
- The interest of continuous monitoring of dynamic effects in roadway and railway bridges enabling an accurate fatigue assessment under real traffic loads, including local fatigue effects;
- The feasibility of application of vibration based Structural Health Monitoring techniques in bridges and special structures, enabling the early detection of slight structural modifications induced by damage by tracking the time variation of modal estimates, statistically removing the influence of environmental and operational factors on the modal variability and building appropriate control charts where the variation of a suitable novelty index can flag the occurrence of abnormal changes;
- The interesting role of continuous dynamic monitoring in Wind Engineering studies developed on prototypes, especially in the case bridges located in zones with high susceptibility to the occurrence of extreme events, such as cyclones or typhoons, demanding an adequate characterization of loads and an accurate assessment of the corresponding response;
- The feasibility of application of the vibration based SHM technology previously developed and implemented in bridges and stadia roofs to energy structures, like wind turbines and concrete dams, enabling their accurate modal tracking and damage detection, after suitable statistical removal of effects of environmental factors.

Acknowledgements This work was financially supported by: UID/ECI/04708/2019—CONSTRUCT—Instituto de I&D em Estruturas e Construções funded by national funds through the FCT/MCTES (PIDDAC), PTDC/ECM-EST/0805/2014/16761 and PTDC/ECM-EST/2110/2014/16877, funded by FEDER funds through COMPETE2020—Programa Operacional Competitividade e Internacionalização (POCI)—and by national funds through FCT—Fundação para a Ciência e a Tecnologia.

References

1. Cantieni R, Deger Y, Pietrzko S (1994) Large structure investigation with dynamic methods: the bridge on the river Aare at Aarburg. In: Prestressed concrete in Switzerland, Report of the Swiss FIP Group to the 12th FIP congress, Washington D.C.
2. Pietrzko S, Cantieni R, Deger Y (1996) Modal testing of a steel/concrete composite bridge with a servo-hydraulic shaker. In: Proceedings of the 14th International Modal Analysis Conference (IMAC), Dearborn, Michigan, pp 91–98
3. Keightley W, Housner G, Hudson D (1961) Vibration tests of the Encino Dam intake tower. California Institute of Technology, Pasadena
4. Cantieni R (2001) Assessing a dam's structural properties using forced vibration testing. In: Proceedings of the IABSE international conference on safety, risk and reliability—trends in engineering, Malta
5. Caetano E (1992) Identificação Experimental de Parâmetros Dinâmicos em Sistemas Estruturais, Tese de Mestrado, FEUP
6. Maia N et al (1997) Theoretical and experimental modal analysis. Research Studies Press, UK
7. Cunha A, Caetano E, Magalhães F (2007) Output-only dynamic testing of bridges and special structures. *Struct Concr J FIB* 8(2):67–85
8. Carder D (1936) Observed vibrations of buildings. *Bull Seismol Soc Am* 26(4):245–277
9. Vincent G (1958) Golden gate bridge vibration study. *ASCE J Struct Div* 4:ST6
10. McLamore V, Hart G, Stubbs J (1971) Ambient vibration of two suspension bridges. *ASCE J Struct Div* 97(ST10):2567–2582
11. Trifunac M (1972) Comparisons between ambient and forced vibration experiments. *Earth Eng Struct Dyn* 1:133–150
12. Brownjohn JM, Dumanoglu AA, Severn RT, Blakeborough A (1989) Ambient vibration survey of the Bosphorus suspension bridge. *Earthq Eng Struct Dyn* 18:263–283
13. Brownjohn JMW, Dumanoglu AA, Severn RT (1992) Ambient vibration survey of the Fatih Sultan Mehmet (Second Bosphorus) suspension bridge. *Earthq Eng Struct Dyn* 21:907–924
14. James GH, Carne TG, Lauffer JP, Nord AR (1992) Modal testing using natural excitation. In: Proceedings of the 10th international modal analysis conference, San Diego, California, USA, pp 1209–1216
15. Cunha A, Caetano E, Delgado R (2001) Dynamic tests on a large cable-stayed bridge. *Efficient Approach J Bridge Eng ASCE* 6(1):54–62
16. Flamand O, Grillaud G (2006) Dynamic testing of the Millau Viaduct. In: Proceedings of the third international conference on bridge maintenance, safety and management, Porto, Portugal
17. Brownjohn JMW, Magalhães F, Caetano E, Cunha A (2010) Ambient vibration re-testing and operational modal analysis of the Humber Bridge. *Eng Struct* 32(8):2003–2018
18. Catbas FN, Grimmelman KA, Aktan AE (2000) Structural identification of the Commodore Barry Bridge. In: Proceedings of the SPIE, 3995, pp 84–97
19. Brownjohn JMW, Moyo P, Omenzetter P, Lu Y (2003) Assessment of highway bridge upgrading by dynamic testing and finite element model updating. *ASCE J Bridge Eng* 8:162–172
20. Alampalli S (1998) Influence of in-service environment on modal parameters. In: Proceedings of 16th international modal analysis conference, Santa Barbara, USA
21. Kramer C, de Smet CAM, De Roeck G (1999) Z24 Bridge damage detection tests. In: Proceedings of IMAC XVII, Kissimmee, Florida, pp 1023–1029
22. Wong KY (2004) Instrumentation and health monitoring of cable-supported bridges. *Struct Control Health Monit* 11:91–124
23. Ko JM, Ni YQ (2005) Technology developments in structural health monitoring of large-scale bridges. *Eng Struct* 27(12):1715–1725
24. FIB, FIB Bulletin 22 (2003) Monitoring and safety evaluation of existing concrete structures
25. Cunha A, Caetano E, Magalhães F, Moutinho C (2013) Recent perspectives in dynamic testing and monitoring of bridges. *J Struct Control Health Monit* 20(6):853–877
26. SÉTRA/AFGC, Footbridges (2006) Assessment of vibrational behaviour of footbridges under pedestrian loads

27. HIVOSS (2007) Human induced vibration of steel structures guidelines. RFCS European Project. 2007. See <http://www.stb.rwth-aachen.de/projekte/2007/HIVOSS/download.php>
28. Caetano E, Cunha A, Moutinho C, Magalhães F (2010) Studies for controlling human-induced vibration of the Pedro e Inês footbridge, Portugal. Part 2: implementation of tuned mass dampers. *Eng Struct* 32:1082–1091
29. Hu W-H, Moutinho C, Caetano E, Magalhães F, Cunha A (2012) Continuous dynamic monitoring of a lively footbridge for serviceability assessment and damage detection. *Mech Syst Signal Process* 33:38–55
30. Hu W-H, Caetano E, Cunha A (2013) Structural health monitoring of a stress-ribbon footbridge. *Eng Struct* 57:578–593
31. Caetano E, Cunha A (2013) Implementation of a control system in a lively footbridge. IABSE conference, Rotterdam, Netherlands
32. Caetano E, Cunha A (2014) Vibration mitigation of footbridges: case studies. International conference FOOTBRIDGE 2014, London, UK
33. Caetano E, Cunha A (2012) Dynamic characterisation of the new footbridge over the rio Ave at Parque da Rabada after installation of TMDs, ViBest/FEUP Report (in Portuguese)
34. Moutinho C, Hu W-H, Caetano E, Cunha A (2013) Dynamic monitoring of the new footbridge over the rio Ave at Parque da Rabada: one year monitoring, ViBest/ FEUP Report (in Portuguese)
35. Caetano E, Cunha A (2004) Experimental and numerical assessment of the dynamic behaviour of a stress-ribbon footbridge. *Struct Concr* 5(1):29–38
36. Caetano E, Cunha A (2005) Study of the potential of collapse of a footbridge under vandal loads. IABSE Symposium on structures and extreme events, Lisbon, Portugal
37. Hu W-H (2010) Operational modal analysis and continuous dynamic monitoring of footbridges. Ph. D. Thesis, Faculty of Engineering, University of Porto, Portugal
38. Hu W-H, Cunha A, Caetano E, Magalhães F, Moutinho C (2010) LabVIEW toolkits for output-only modal identification and long-term dynamic structural monitoring. *Struct Infrastruct Eng* 6(5):557–574
39. Marques F, Hu W-H, Moutinho C, Magalhães F, Cunha A (2011) Evaluation of dynamic effects and fatigue assessment of a railway bridge supported by temporary monitoring. In: Proceedings of the EUROLYN'2011, Leuven, Belgium
40. Marques F, Moutinho C, Hu W-H, Cunha A, Caetano E (2016) Weigh-in-motion implementation in an old metallic railway bridge. *Eng Struct* 123:15–29
41. Marques F, Cunha A, Caetano E, Moutinho C, Magalhães F (2014) Analysis of dynamic and fatigue effects in a old metallic riveted bridge. *J Constr Steel Res* 99C:85–101
42. Magalhães F (2010) Operational modal analysis for testing and monitoring of bridges and special structures. PhD Thesis, Faculty of Engineering of the University of Porto
43. Magalhães F, Cunha A, Caetano E (2012) Vibration based structural health monitoring of an arch bridge: from automated OMA to damage detection. *Mech Syst Sig Process* 28:212–228
44. Croiset JE, Ryckaert J, Spielmann A, Viel G (2005) Viaduc de la Grande Ravine, Travaux n°823, 01/10/05, pp 110–116
45. Bastos F (2015) Aerodynamic behaviour of long span structures. numerical analysis and experimental validation based on full-scale measurements, PhD Thesis (in English), FEUP
46. Amador S, Magalhães F, Cunha A, Caetano E, Martins N (2017) Automated modal tracking in a football stadium suspension roof for detection of structural changes. *Struct Control Health Monit* 24(11)
47. Martins N, Caetano E, Diord S, Magalhães F, Cunha A (2014) Dynamic monitoring of a stadium suspension roof: wind and temperature influence on modal parameters and structural response. *Eng Struct* 59C:80–94
48. Blanco M (2009) The economics of wind energy. *Renew Sustain Energy Rev* 13(6–7):1372–82
49. Oliveira G, Magalhães F, Cunha A, Caetano E (2018) Continuous dynamic monitoring of an onshore wind turbine. *Eng Struct* 164:22–39
50. Hansen MH (2007) Aeroelastic instability problems for wind turbines. *Wind Energy* 2007(10):551–77

51. EDP. Energias de Portugal. [cited 2018 06/04/2018]; Available from: http://www.a-nossa-energia.edp.pt/centros_produtores/
52. Magalhães F, Cunha Á, Caetano E (2008) Dynamic monitoring of a long span arch bridge. *Eng Struct* 30(11):3034–3044
53. Magalhães F, Amador S, Cunha Á, Caetano E (2012) DynaMo—software for vibration based structural health monitoring. In: *Bridge maintenance, safety, management, resilience and sustainability—proceedings of the sixth international conference on bridge maintenance, safety and management*
54. Magalhães F, Cunha A (2011) Explaining operational modal analysis with data from an arch bridge. *Mech Syst Signal Process* 25(5):1431–1450
55. Oliveira G, Magalhães F, Cunha A, Caetano E (2018) Vibration based damage detection in a wind turbine using one year of data. *Struct Control Health Monit* (in press). <https://doi.org/10.1002/stc.2238>
56. Magalhães F, Cunha A, Caetano E (2012) Vibration based structural health monitoring of an arch bridge: from automated OMA to damage detection. *Mech Syst Signal Process* 28:212–228
57. LNEC (2017) Barragem do Baixo Sabor. Caracterização do comportamento dinâmico através da realização de ensaios de vibração forçada em maio de 2016 com a albufeira à cota 234,0 m. (In Portuguese)
58. Gomes J, Lemos JV (2016) Characterization of the dynamic behavior of an arch dam by means of forced vibration tests. In *1st meeting of EWG dams and earthquakes*. Balkema: Saint Malo, France

Operational Modal Analysis of a Historic GRP Structure



Zachariah Wynne , Tim Stratford , and Thomas P. S. Reynolds 

Abstract The Aberfeldy Footbridge was the world's first major advanced composite footbridge. Constructed from glass-fibre reinforced plastic (GFRP) in 1991, the lightweight cable-stayed footbridge provided the client with a low-cost access route which needed minimal site equipment for erection. Since opening to the public, the resin used within the structure has degraded exposing the glass fibres and there have been issues with the connections between various components of the bridge. Following damage to the structure in 1997 by the crossing of a light vehicle, the bridge deck was strengthened with bonded GFRP panels. It has been reported that there has been a gradual change in dynamic properties. Between 1995 and 2000 the damping of the first vertical mode is reported to have reduced by 52% with a reduction in natural frequency of 2%. Additional testing carried out in 2011 suggests that the natural frequency of the first vertical mode had reduced by a further 5%. This paper presents a new analysis of data from previous dynamic tests carried out by other researchers in 2011 and 2013, alongside data from tests carried out by the authors in 2019. A variety of time and frequency domain operational modal analysis techniques are used to quantify the uncertainty within the results. The reported changes in dynamic properties over the past 14 years are compared to the known degradation and repair work carried out on the structure. These results indicate that the previously reported changes in dynamic properties may be due to weakly non-linear behaviour of the structure, close modes and non-damage induced changes in dynamic behaviour. This illuminates the information which can be gained from in-depth dynamic analysis of civil structures, the challenges of damage detection and the need to quantify the range of dynamic behaviour a structure may exhibit.

Keywords GRP footbridge · Non-linear dynamic behaviour · Structural health monitoring

Z. Wynne (✉) · T. Stratford · T. P. S. Reynolds
Institute for Infrastructure and Environment, School of Engineering,
University of Edinburgh, Edinburgh, UK
e-mail: Z.Wynne@sms.ed.ac.uk

© The Author(s), under exclusive license to Springer Nature Switzerland AG 2021
C. Rainieri et al. (eds.), *Civil Structural Health Monitoring*, Lecture Notes in Civil
Engineering 156, https://doi.org/10.1007/978-3-030-74258-4_3

1 Introduction

The Aberfeldy footbridge is a pedestrian cable-stayed bridge spanning the River Tay in Scotland. The primary structure is glass-fibre reinforced polymer (GFRP), a lightweight and flexible composite material. The bridge is easily excited by footfall loading due to its low mass. Within this document Operational Modal Analysis (OMA), where the dynamic characteristics of a structure (natural frequencies, damping ratios and mode shapes) are estimated from an unknown input loading, is applied to data collected from the bridge under footfall excitation in 2011 [1], 2013 and 2019. These results are compared to the results of ambient testing of the structure in 1995 [2] and forced excitation testing of the structure carried out in 2000 [3]. The results show the challenges of analysing data from lightweight and degraded structures due to weak non-linearity introduced by changes in the dynamic behaviour caused by human-structure interaction, damage to the structure and loose connections.

2 Description and Condition of the Bridge

Opened in 1992, the bridge's primary structure is formed of pultruded glass-fibre reinforced polymer (GFRP) sections and aramid suspension cables. With a main span of 63 m, symmetric approach spans of 25 m and a deck width of 2.12 m, the bridge was the largest advanced composite bridge at the time of construction. At a total weight per metre span of less than 200 kg [3], the bridge was assembled on site with minimal heavy equipment, reducing disruption and cost for the bridge owner, the Aberfeldy Golf Club [4]. An overview of the materials used within the structure and their masses is shown in Fig. 1.

To reduce uplift against wind, improve footfall behaviour and reduce flutter instability, the central cells of the deck at mid-span are filled with concrete. Despite this additional mass the structure experiences large amplitudes of oscillation under light footfall loading.

Considerable degradation of the GFRP has occurred since construction, most notably in the parapets of the structure where glass fibres have been exposed in numerous places. Debonding of the GFRP is visible on the edge and cross beams and has been exacerbated by the growth of moss and algae on the structure. Separation of the components and loosening of joints is visible in numerous places including both parapets and the aluminium columns which act to tie down and support the approach-spans. Friction joints were used to connect the handrails to the upright to stiffen the parapet. However due to a lack of rigidity between the upright and the deck, these frictional joints have loosened leading to separation of the components [5]. This results in audible rattles as the bridge oscillates. The parapets have suffered extensive damage, likely due to vandalism, with numerous railings broken or missing on the northern approach span. Apart from surface degradation caused by moss and algae, the pylons do not exhibit signs of damage.

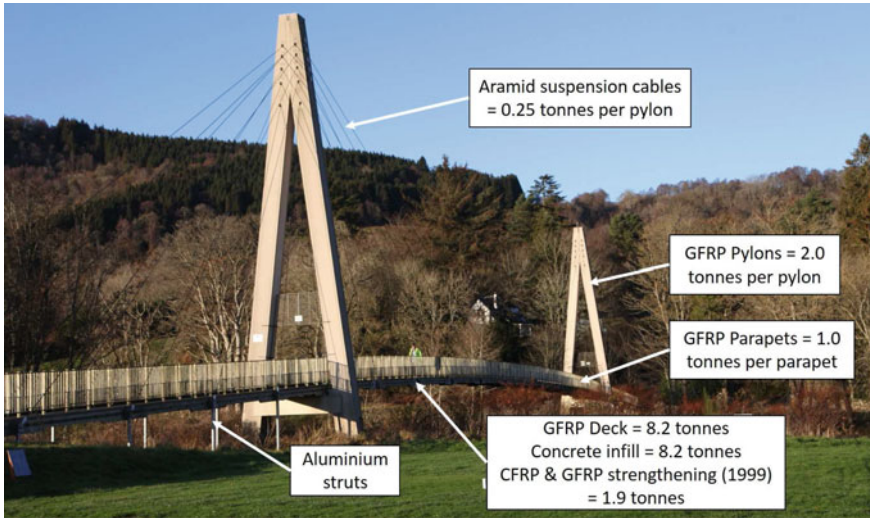


Fig. 1 Material use within the Aberfeldy Footbridge [1]

The bridge deck was damaged in 1999 by the passage of a small vehicle towing a trailer of sand. Following this damage, the deck was reinforced with pultruded GFRP plates, adhesively bonded to the top of the deck, and strengthening of the deck edge beams through the addition of Carbon Fibre Reinforced Polymer (CFRP) sheets. The strengthening increased the weight of the structure by 0.17 kN/m span [4].

There is visible sagging of the bridge deck between the edge beams at mid-span of the structure. This sagging has not been referred to in previous reports on the condition of the structure and was anecdotally reported by local residents to have worsened in the past decade. There is extensive mould and algae growth on the deck structure but few signs of wear or erosion of the GFRP plates or CFRP.

Presented in Table 1 are the Natural Frequencies and damping ratios for two sets of ambient excitation measurements collected in 1995 and 2011 [1, 2], and a single set of forced excitation measurements collected in 2000 [3]. Frequency results are based on inspection of the power spectral density and frequency response functions (FRFs) for the ambient and forced excitation respectively. The damping results for 1995 are based on the free decay following a jumping test by a single pedestrian. The damping results for 2000 are based upon direct-curve fitting of a FRF.

A new analysis of the 2011 data sets; tri-axial data collected from a mobile phone accelerometer at 50 Hz, alongside data collected in 2013 using a mobile phone accelerometer at a variable sample rate between 20 Hz and 100 Hz, is included in later sections. The 2013 data has been resampled through linear interpolation to achieve a constant sample rate of 20 Hz. The loading on the structure over the course of these data sets includes jumping, heel drops and jogging of a single pedestrian.

Alongside this, 95 min of data were collected in December 2019 at a sample rate of 1024 Hz from 3 triaxial accelerometers, located at mid-span and 10.5 m either side

Table 1 Natural frequency and damping values for 1995 [2], 2000 [3] and 2011 [1]. H = Horizontal mode, V = Vertical mode, T = Torsional mode

Mode	Frequency (Hz)			Damping (%)	
	1995	2000	2011	1995	2000
H1	1.00	0.98	0.93	–	1.0
V1	1.59	1.52	1.49	0.84	0.4
V2	1.92	1.86	1.77	0.94	0.7
V3	2.59	2.49	2.41	1.20	0.7
H2	2.81	2.73	2.58	–	1.2
V4	3.14	3.01	–	–	0.8
T1	3.44	3.48	3.39	–	5.5
V5	3.63	3.50	–	–	0.6
V6	4.00	3.91	–	–	0.9
T2	4.31	4.29	–	–	3.2
V7	4.60	4.40	–	–	0.8
V8	5.10	4.93	5.13	–	1.8

of midspan on the west side of the bridge deck, and 2 bi-axial accelerometers, located 10.5 m either side of midspan on the east side of the bridge deck. The accelerometers used had a sensitivity of 1067 mv/g. This data constitutes both light wind and footfall excitation of the structure by individuals and groups of pedestrians.

Where possible the data from 2011 and 2013 has been analysed in Sect. 4. However due to the low-quality of these data sets, much of the analysis has been focused on the use of the high-quality data collected in 2019.

3 Analysis Methods

As the input force to the structure is unmeasured, assumptions about both the force and the structure must be made to allow the application of Operational Modal Analysis (OMA). The structure is assumed to behave linearly; for a given input force the bridges behaviour is constant. The loading is assumed to be a gaussian, broadband stochastic force; it has no dominant frequency component which falls within the same range as the natural frequencies of the structure and the force is uncorrelated with previous forces applied to the structure. By collecting a large data set under a range of operational conditions we can increase the likelihood that the loading approximates this assumption due to the variability in footfall and wind loading. The challenge with light-weight structures under footfall excitation is that the changes in dynamic properties with the number of people interacting with different parts of the structure is significant, violating the assumption of linear dynamic behaviour.

Within this document four OMA methods are used to identify the dynamic properties of the structure; Welch's method [6], Covariance-driven Stochastic Subspace Identification (SSI-Cov) [7], the Random Decrement Technique (RDT) [8] and a novel variant of RDT developed by the authors, the short-time Random Decrement Technique (ST-RDT).

The ST-RDT is similar to conventional RDT except that Random Decrement Signatures (RDSs) are formed for short overlapping windows of data and correlation between data segments is allowed. This has the advantage that the behaviour of the structure is assumed to be linear only over the length of the window, not over the full data set. This allows weakly non-linear behaviour; where a structure has identifiable modes of vibration but the response of a mode exhibits variations in behaviour [9], to be observed and quantified.

4 Results & Discussion

4.1 Frequency Domain Analyses

In Fig. 2 the Welch PSDs for the 2011, 2013, and 2019 data are plotted based on a Hanning window, a weighted tapered cosine, of length 3 min with 1.5 min overlap. Modification of the type of window and the window length was found to have little impact on the peaks of the frequency spectra. The 2019 PSDs are noisy, despite the strength of the measured acceleration signal, preventing accurate natural frequency and damping estimates. These noisy peaks are believed to be due to both the loose joints and connection of the bridge, leading to step changes in vibration behaviour, and the human-structure interaction leading to changes in the frequency and damping behaviour of the structure over the length of the data set. The 2011 data set shows peaks at lower frequencies than the 2013 or 2019 data set, the reason for this is unknown. The 2013 data set, collected using a mobile phone accelerometer, shows numerous windowing artefacts, believed to be induced by the re-sampling of the data. These results indicate that whilst the sensitivity of mobile phone accelerometers may be sufficient to monitor civil structures, the lower sample rates and inconsistent sample rates introduces significant artefacts into modal estimates.

4.2 Time Domain Analyses

4.2.1 Covariance-Driven Stochastic Subspace Identification (SSI-Cov)

SSI-Cov was applied to the data using a maximum Toeplitz block length of 1.6s with a maximum model order of 100. All channels of acceleration data were used, with the data down sampled 1024Hz to 102.4Hz prior to application of SSI-Cov. The

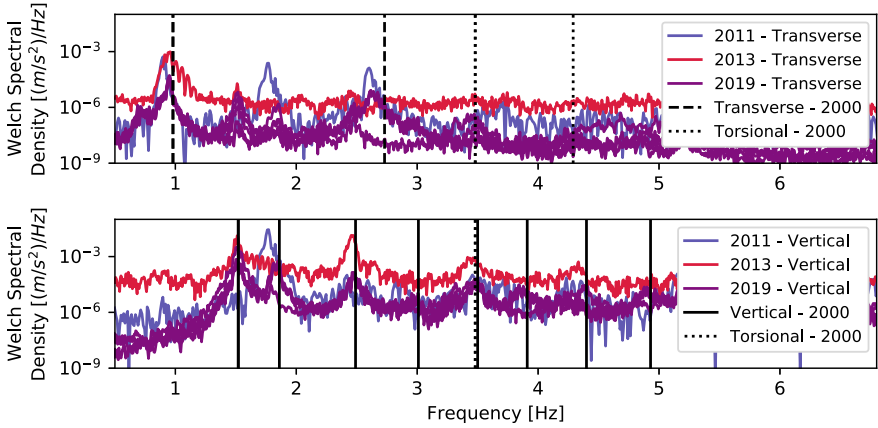


Fig. 2 Welch Power Spectral Density of 2011, 2013 and 2019 acceleration data. Top plot: Transverse acceleration. Lower plot: Vertical acceleration. Modes identified by Pavic et al. [3] shown for comparison

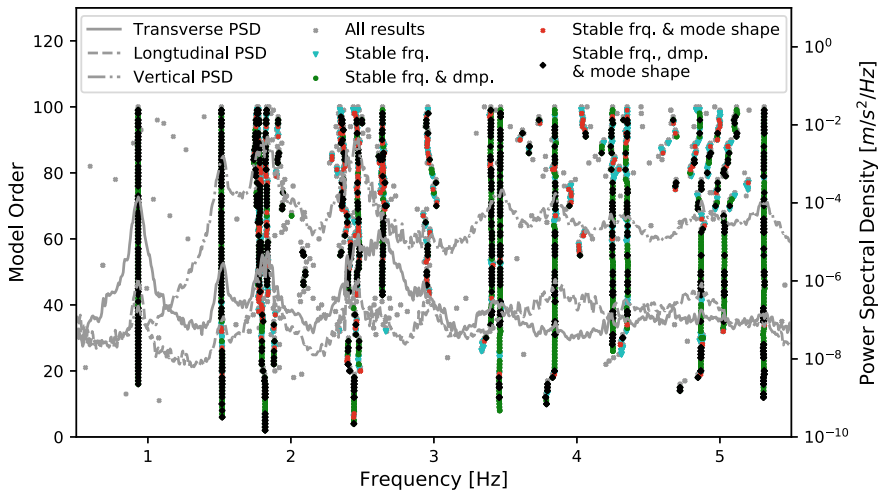


Fig. 3 SSI-Cov results (Toeplitz block length of 1.6s) and Welch Power Spectral Density (PSD) for 2019 data

results of the SSI-Cov analysis are shown as a stability diagram in Fig. 3. The natural frequency (frq.) and damping (dmp.) are deemed to be stable if they have varied by less than 0.5% and 5% respectively from the previous model order. The Modal Assurance Criteria (MAC) is used to identify stable modes. A mode is identified as stable if the MAC value is greater than 98%. For reference, the average of the 2019 Welch PSD results presented previously in Fig. 2 are plotted on the second y-axis.

4.2.2 Random Decrement Technique (RDT)

Each of the 2019 vertical and transverse acceleration data sets were analysed individually using the RDT with a range-crossing trigger level with upper and lower bounds of 1 and 1.1 multiples the standard deviation of the data set. An equivalent negative trigger level was applied simultaneously and all segments meeting it multiplied by -1. The segments were averaged together to form a random decrement signature (RDS) of 1.5 s length.

Each RDS was fitted individually on the assumption that they were the free response of a system with N degrees of freedom:

$$RDS = \sum_{i=0}^N X_i e^{-\xi_i \omega_i t} \cos(\omega_{d,i} t) \quad (1)$$

where N is the number of modes, X_i is the initial amplitude of the free-decay, ξ_i is the damping of the mode as a percentage of critical damping, ω_i is the natural frequency of the mode, $\omega_{d,i}$ is the damped natural frequency and t is a time array corresponding to the length of the RDS. Fitting of the RDSs was carried out using the Levenberg-Marquardt algorithm non-linear least-squares curve fitting [10] of Eq. (1) with the value of N varying from 1 to 20.

Each RDS contained between 8726 and 12,030 segments of data. The RDSs for all transverse acceleration data sets are well described by 2 modes of vibration, an example is shown in Fig. 4, with average natural frequencies of 0.94 Hz and 2.63 Hz, and damping ratios of 1.05% and 2.00% respectively. The vertical RDSs are poorly fitted, as shown in Fig. 5. This poor fitting is believed to be caused primarily by the human-structure interaction. As pedestrians cross the bridge, the mass concentrated within each mode changes, changing its natural frequency. In tandem to this, the damping of each mode changes due to the additional energy dissipation introduced by the pedestrians. This results in the distinctive sharp peaks and troughs of the RDS in Fig. 5 due to the presence of multiple close and overlapping modes of vibrations within the different segments.

4.2.3 Short-Time Random Decrement Technique (ST-RDT)

The ST-RDT was applied to the 2019 vertical and horizontal acceleration data using an all points triggering condition, with a window length of 60s and an overlap between neighbouring windows of 59s. Data was down sampled 1024 to 102.4 Hz prior to analysis. The results for the first vertical and horizontal modes are presented in Figs. 6 and 7 respectively.

There is a clear variation in the behaviour of the structure with relation to the amplitude of the oscillation due to the human-structure interaction, with this behaviour remaining consistent across all accelerometers. This is characterised for each mode by the reduction in the frequency as a pedestrian approaches the anti-node of the

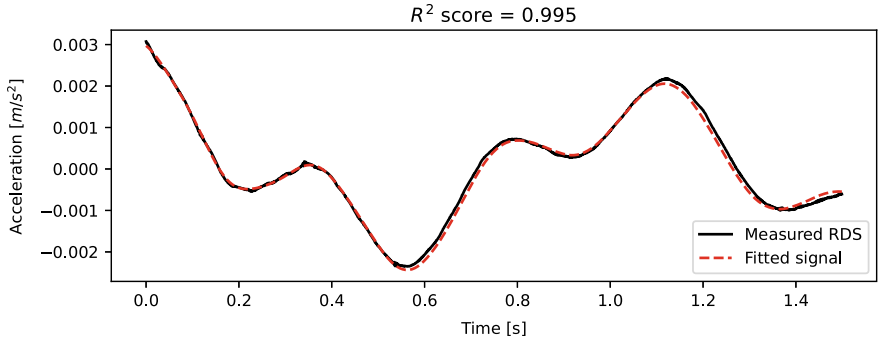


Fig. 4 Transverse RDS for accelerometer at mid-span. Fitted signal based on 5 modes of vibration

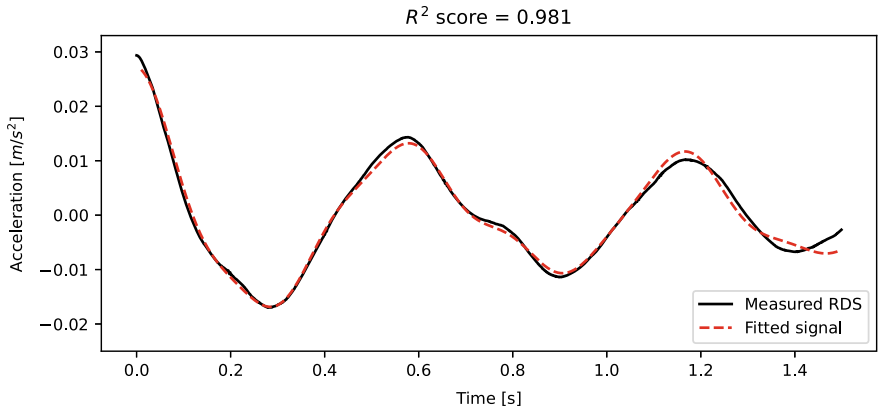


Fig. 5 Vertical RDS for accelerometer at mid-span. Fitted signal based on 5 modes of vibration

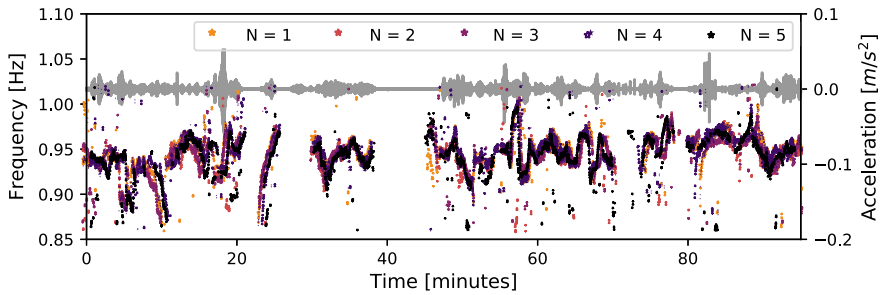


Fig. 6 ST-RDT frequency estimates for 1st horizontal mode assuming an N degree of freedom system. Results limited to where fitting of RDS achieves R^2 score > 0.99

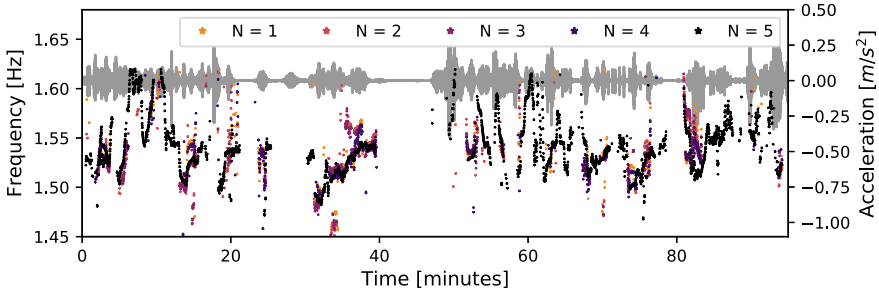


Fig. 7 ST-RDT frequency estimates for 1st vertical mode assuming an N degree of freedom system. Results limited to where fitting of RDS achieves R^2 score > 0.99

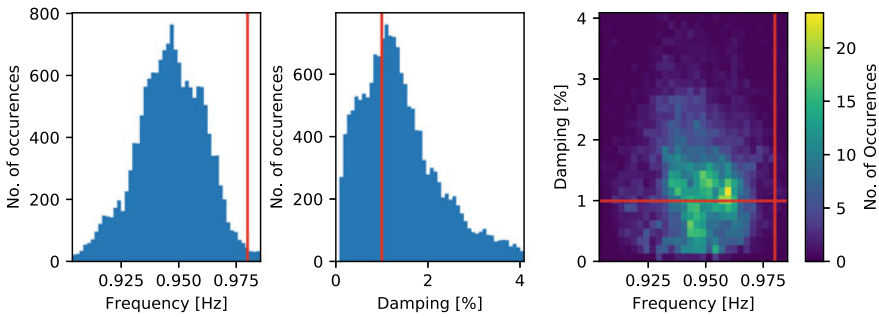


Fig. 8 Histograms of frequency and damping values for 1st horizontal mode. Histograms plotted to show 95% of estimated values. Values shown only where $R^2 > 0.99$. Red lines indicate results of 2000 testing of bridge [3]

mode. The damping behaviour exhibits much larger ranges of weak non-linearity but remains consistent between separate sections of data. This weak non-linearity may be due to the changes in the number of people on the structure and their relationship to one another as well as the anti-nodes of the mode shapes. Despite the weak non-linearities across the data sets, the results for each mode of vibration may be pooled to create distributions of likely values based on the data collected, as shown in Figs. 8 and 9 for the 1st horizontal and vertical modes respectively.

5 Comparison and Discussion

The results of analysing the data en-masse, either through Welch’s method, SSI-Cov or conventional RDT do not identify clear linear modes. The analysis using the ST-RDT suggests that this is because the properties of those modes vary with time, likely because of the additional mass from people crossing the bridge.

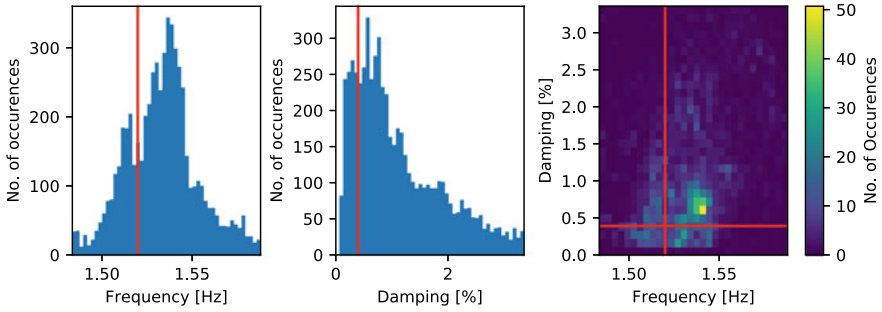


Fig. 9 Histograms of frequency and damping values for 1st vertical mode. Histograms plotted to show 95% of estimated values. Values shown only where $R^2 > 0.99$. Red lines indicate results of 2000 testing of bridge [3]

Modes of vibration which could be clearly identified from the ST-RDT are summarised in Table 2. These results are based on the bootstrapped mean values of the distributions of frequency and damping, examples of which were given in Figs. 8 and 9. Frequency and damping values are treated as pairs of values; a given bootstrap sample contains a fixed pair of frequency and damping values which must be re-sampled as a set.

The damping results show a clear increase for the values obtained from the analysis of the 2019 ambient data. Part of this is likely due to the increased damping imparted by pedestrians, however an over estimation of damping values may occur due to the rapid shifts in natural frequency which exist over the 60s window length.

The bootstrapped mean natural frequency is lower for most modes. However, this lower mean value is likely due to the reduction in natural frequencies due to additional mass from pedestrians. Examining the ST-RDT results for the lowest horizontal mode in the time domain, as shown in Fig. 6, it can be seen that the measured natural frequency, with a bootstrapped mean of 0.945 Hz, returns to a value of around 0.98 or 1.00 Hz as the amplitude of the signal dies away. This could indicate that once a pedestrian moves off the bridge, its unloaded natural frequency remains close to the values recorded in 1995 and 2000. This behaviour is repeated across the majority of modes of the structure.

The exception to this behaviour is the 1st vertical mode. This appears to revert to a baseline natural frequency of between 1.6 and 1.65 Hz, higher than the value recorded in 2000. As noted earlier, there is some non-linear behaviour induced by rattling of connections and tie-downs, which may lead to the recorded increase in natural frequency. Alternatively, it may be that the sagging of the bridge at mid-span has led to a change in the natural frequency. There is the possibility that differing temperatures between the 2000 and 2019 data collection regimes could result in the variation in results, however it would be expected that this would have a blanket effect on all natural frequencies, something which the results for other modes of vibration provide no evidence to support.

Table 2 Natural frequency and damping values obtained from ST-RDT analysis. Values shown in brackets represent the 95% confidence intervals of mean values obtained from bootstrapping of distributions. n value represents the number of occurrences of the mode in ST-RDT results

Mode	Frequency (Hz)			Damping (%)			n
	1995	2000	2019	1995	2000	2019	
H1	1.00	0.98	0.945 (0.0003)	–	1.0	1.56 (0.019)	11,241
V1	1.59	1.52	1.53 (0.0009)	0.84	0.4	1.83 (0.047)	7465
V2	1.92	1.86	1.84 (0.0013)	0.94	0.7	2.33 (0.043)	9145
V3	2.59	2.49	2.48 (0.0009)	1.20	0.7	1.50 (0.035)	8025
H2	2.81	2.73	2.63 (0.0010)	–	1.2	2.14 (0.025)	13,177
V4	3.14	3.01	–	–	0.8	–	–
T1	3.44	3.48	–	–	5.5	–	–
V5	3.63	3.50	3.46 (0.0012)	–	0.6	2.37 (0.037)	9722
V6	4.00	3.91	3.84 (0.0023)	–	0.9	4.63 (0.089)	3591
T2	4.31	4.29	–	–	3.2	–	–
V7	4.60	4.40	–	–	0.8	–	–
V8	5.10	4.93	4.91 (0.0016)	–	1.8	2.40 (0.061)	3425

6 Conclusions

The analyses have shown that the natural frequencies of the Aberfeldy footbridge are lower for the 2019 dataset than previous measurements but there is evidence that this is due to the differences in pedestrian loading of the structure between the different data sets. Little evidence has been found that any significant change in dynamic properties of the Aberfeldy footbridge has occurred in the past twenty years, despite continued degradation and damage to the structure.

Understanding the weak non-linear behaviour of structures in-service could allow damage induced changes in the dynamic behaviour to be identified. However, dynamics based structural health monitoring is limited to types of degradation and damage which affect the global dynamic properties. Some of the damage to the Aberfeldy footbridge, such as the sagging of the bridge deck, is likely to fall outside of this scope. The lack of significant changes in the dynamic behaviour of the bridge would suggest limited damage of the primary load resisting systems.

A key challenge for long-term monitoring of structures, particularly lightweight structures like the Aberfeldy footbridge, is separating changes in dynamic behaviour

due to damage from those induced by changes in external factors such as loading and temperature. Short-time operational modal analysis methods, such as the short-time random decrement technique, provide a simple method through which changes in structural behaviour may be visually identified and assessed.

Acknowledgements Support for Z. Wynne was provided by an EPSRC Doctoral Training Partnership Studentship (EP/R513209/1).

References

1. Stratford T (2012) The condition of the Aberfeldy Footbridge after 20 years of service
2. Pimentel RL, Waldron P, Harvey WJ (1995) Assessment of the dynamic behaviour of Aberfeldy GRP plastic cable-stayed footbridge. In: Analysis and testing of bridges. SETO LTD, London, pp 38–40
3. Pavic A, Reynolds P, Cooper P, Harvey WJ (2000) Dynamic testing and analysis of Aberfeldy Footbridge. Final Report - Ref, CCC/00/79A, Sheffield
4. Cadei J, Stratford T (2002) The design, construction and in-service performance of the all-composite Aberfeldy footbridge, *Adv Polym Compos Struct Appl Constr*, 445–455
5. Skinner JM (2009) A critical analysis of the Aberfeldy Footbridge, Scotland. In: Proceedings of Bridge Engineering 2 Conference 2009, Bath
6. Welch PD (1967) The use of Fast Fourier Transform for the estimation of power spectra: a method based on time averaging over short. Modified periodograms. *IEEE Trans Audio Electroacoust* 15(2):70–73
7. Rainieri C, Fabbrocino G (2014) Operational modal analysis of civil engineering structures, 1st edn. Springer, New York City
8. Asmussen JC, Brincker R (1997) Modal analysis based on the random decrement technique—application to civil engineering structures, 1st edn. Aalborg University, Aalborg
9. Ewins DJ (2000) Modal testing: theory and practice. Research Studies Press, Boston
10. Morè JJ (1978) The Levenberg-Marquardt algorithm: implementation and theory. In: Watson GA (eds) Numerical analysis. Springer, Heidelberg, pp 105–116

Mass and Temperature Changes in Operational Modal Analysis



Zachariah Wynne , Georgios Kanellopoulos, Vasileios Koutsomarkos , Angus Law , Tim Stratford , and Thomas P. S. Reynolds 

Abstract A challenge in identifying the dynamic properties of large structures through operational modal analysis (OMA), whereby the response of a structure is measured under ambient excitation, is the changes in added mass and temperature which may occur during data collection. The effect of these changes may mask any damage to the structure or lead the investigator to incorrectly conclude damage has occurred. Quantification of such effects requires the use of short-time OMA methods, where the structure's response is assumed to be linear across short periods of time. Two experiments were carried out to identify methods through which such variations can be accurately identified and quantified. The first experiment consisted of a simple I-beam with spring supports to which a small mass was added at a variety of locations. This simulated changes in mass similar to that which may be induced by pedestrian or vehicle loading of civil structures. The changes in the dynamic properties were quantified through the short-time Fourier transform and a variant on the random decrement technique to test their ability to detect small changes in mass. An inversion of the mass change method is used to estimate both the quantity and location of the added mass. The second experiment investigated the efficacy of the same short-time OMA methods in the presence of temperature variation. A flat plate was heated in laboratory conditions using radiant panels. The changes in dynamic properties were measured during heating, steady temperature and cooling of the plate. The results were correlated to the changes in temperature using variations on established relationships between elastic modulus and temperature. The results presented within this paper provide an experimental basis for the viability of short-time OMA methods for quantifying temperature and added mass induced variation in dynamic parameters which may be used to guide future structural monitoring.

Keywords Non-linear dynamics · Temperature change · Mass change

Z. Wynne (✉) · G. Kanellopoulos · V. Koutsomarkos · A. Law · T. Stratford · T. P. S. Reynolds
Institute for Infrastructure and Environment, School of Engineering, University of Edinburgh,
Edinburgh, UK
e-mail: Z.Wynne@sms.ed.ac.uk

© The Author(s), under exclusive license to Springer Nature Switzerland AG 2021
C. Rainieri et al. (eds.), *Civil Structural Health Monitoring*, Lecture Notes in Civil
Engineering 156, https://doi.org/10.1007/978-3-030-74258-4_4

1 Introduction

Operational modal analysis (OMA), where the natural frequencies, damping ratios and mode shapes of structures are estimated under ambient excitation [1], makes two key sets of assumptions about the dynamical system. The first, that the excitation is a broadband stochastic process, has been extensively studied, with techniques put forward for both strongly harmonic or cyclic loading and mitigating the impact of non-stochastic loading (e.g. [2–5]). The second, that the systems behaviour is linear; for a given input force the response of the system is constant, has seen growing interest in recent years due to increased adoption of long-term monitoring of structures. With long-term monitoring of civil structures variations in behaviour due to external factors are often prominent in the systems response. Most notable are the impact of temperature and additional mass, such as pedestrians or vehicle traffic, on the systems behaviour.

The key challenge to be overcome to allow quantification of such non-linear behaviour is that it requires a short-time approach whereby the systems behaviour is assumed to be linear over a short-time interval. This can limit the effectiveness of many OMA techniques which rely on large quantities of data to account for the stochastic forcing on the system.

Within this paper two experiments are used to simulate changes in dynamic loading and temperature for simple dynamic systems. These are referred to as the mass-change and temperature-change experiments. Two short-time OMA methods; the short-time Fourier transform (STFT) and the short-time Random Decrement Technique (ST-RDT), developed by the authors and described for the first time in this paper, are used to analyse the experimental results.

STFT is a frequency-domain analysis technique whereby the Fourier transform is calculated for short overlapping windows of data [6]. A peak picking method may be used to track the natural frequencies of the system over time. Due to the short window lengths of data used in STFT, damping and mode-shape estimation is challenging due to the high levels of noise often present in the results.

ST-RDT is a time-domain OMA method developed by the authors to allow for easier identification of dynamic parameters for non-linear systems. Application of ST-RDT is similar to conventional random decrement analysis whereby segments of data are averaged together wherever a user-defined triggering condition is met [7]. The average of the segments, referred to as the Random Decrement Signature (RDS), is an estimate of the systems behaviour for a known initial condition. For the range-crossing triggering level, where segments of data are collected starting from each time the amplitude of the data falls within a given amplitude range, the RDS is an estimate of the systems behaviour to an initial amplitude of response with zero initial velocity. The components of the segments associated with their initial velocity have randomly distributed directions and approach zero as segments are averaged together. Similarly, the impact of forcing on the segments is uncorrelated with the triggering condition and approaches zero as the number of segments in the

RDS increases. The initial amplitude of the segments is correlated with the triggering condition and will approach its mean value as the number of segments in the RDS increases [8].

For application of ST-RDT the data is divided into overlapping windows of data and an RDS formed for each window. Segments of data are no longer assumed to be independent, as they are for conventional RDT, which may lead to an oscillation in estimated dynamic parameters due to corruption of the RDS by non-zero velocities and correlated forcing. For a small ratio (<0.5) between the length of data windows and the length of overlap between windows the impact of this effect on the estimated dynamic parameters is minimal. The amplitude of this oscillation is related to the window length and triggering condition selected as well as the dynamic parameters themselves. By increased overlapping of windows, real variations and numerical variations in parameters may be visually distinguished.

2 Experimental Setup

2.1 Mass Change

A 3 m length of IPE 80 steel beam, steel grade S235, was suspended from spring supports to give an approximation of free-free support conditions. Two accelerometers were fixed to the beam at 1 m and 1.3 m from the end of the left-hand-side (LHS) of the span. A 0.2 kg mass, equal to approximately 1% of the total mass of the beam, was fixed to the beam. The locations at which the mass was fixed were 0.8, 1.15 and 1.6 m from the LHS of the span. Separate 10-min data sets were collected at each fixing location alongside a 10-minute data set prior to addition of the mass, referred to as the unloaded data set. The beam was excited with random unmeasured impulse excitation from multiple sources (Fig. 1).

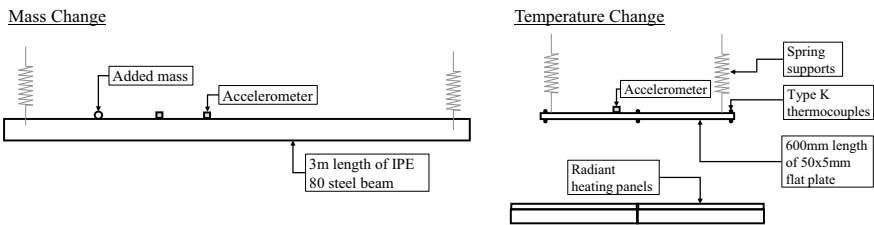


Fig. 1 Experimental setup for mass change and temperature change experiments

2.2 *Temperature Change*

A 600 mm length of 50×5 mm flat plate, steel grade S235, was suspended 0.59 m above two 400 mm by 300 mm radiant heating panels. Suspended supports, located 25 mm from either end of the plate, were shaped to minimize the contact area and provide an approximation of a free-free support condition. The plate was excited through random impulse excitation, with the acceleration response measured using a high-temperature accelerometer bolted to the plate at 80 mm from mid-span. The thickness of the plate was chosen with the intent of minimising the temperature gradients both along the length of the plate and through the cross section (i.e. to ensure that the imposed heat flux was relatively uniform over the exposed surface, and to ensure that the Biot number was much less than 1.0). To verify (and quantify) this, the temperature of the plate was measured using six type K thermocouples welded directly to the plate at equal intervals along the top and bottom face of the plate. Once the radiant panels were ignited, the plate heated to a maximum temperature of 290°C in approximately 13 min before the radiant panels were shut-off and the plate allowed to cool to ambient temperature.

The intent of this experiment is to investigate the application of OMA techniques to the fire condition, rather than the typical temperature ranges associated with common building operation. However, the increased temperature can inform the use of OMA at normal operating temperatures by allowing the limits of short-time OMA methods to be examined, both with respect to temperature variations across a structure and across the length of an individual analysis window.

3 Analysis

3.1 *Mass Change*

3.1.1 **Mass Change Identification—Concatenated Data Sets**

The four mass-change data sets (1 unloaded plus 3 mass locations) were concatenated to form a single continuous data set. The STFT and ST-RDT analysis were applied with a window length of 30 s and a window overlap of 15 s. The ST-RDT was triggered where the absolute amplitude of the acceleration exceeds 2 standard deviations of the concatenated data set. Segments were multiplied by the sign (+ve/–ve) of the acceleration at the start of the segment to maintain correlation of the initial amplitude. An RDS length of 0.05 s was used, approximately 3 times the period of the lowest vertical mode of vibration. Natural frequencies and damping ratios were estimated using non-linear least squares curve fitting of the RDS to the equation of motion of a 6 degree-of-freedom dynamic system with an unknown initial amplitude and zero initial velocity in each mode of oscillation. Natural frequencies were extracted from the STFT results using peak-picking.

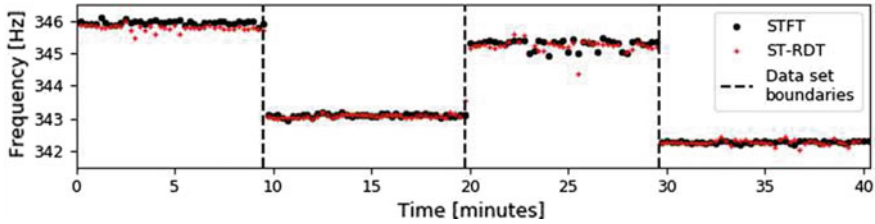


Fig. 2 ST-RDT and STFT results for 3rd vertical mode of vibration

The results of the analysis for the 3rd vertical mode of vibration are presented in Fig. 2. Both the STFT and ST-RDT allow changes in mass to be easily distinguished across all 6 measured vertical modes of vibration.

3.1.2 Mass Change Quantification—Independent Data Sets

To relate the change in mass to the change in natural frequencies, the mode shape scale factors must be estimated.

The mass-change method [9] has been demonstrated as a useful tool for estimating mode shape scale factors for unmeasured forcing via changes in natural frequency induced by small changes in mass of the structure. Two sets of parameters are measured, one for the unloaded structure, denoted with subscript 0, and one for the structure following the introduction of a small additional mass (Δm), denoted with subscript 1. By formulating the classical eigenvalue equation for proportional damping and assuming the scaled mode shape is unchanged by Δm ($\phi_0 \approx \phi_1$) we can establish a relationship between the scaled (ϕ) and unscaled (ψ) mode shapes such that $\phi = \alpha\psi$. The value of α , the mode shape scaling factor, is calculated using the change in natural frequencies ω_0 and ω_1 due to addition of the mass [9]:

$$M\phi_0\omega_0^2 = K\phi_0 \tag{1}$$

$$(M + \Delta M)\phi_1\omega_1^2 = K\phi_1 \tag{2}$$

$$\alpha = \sqrt{\frac{\omega_0^2 - \omega_1^2}{\omega_1^2 \cdot \psi^T \cdot \Delta M \cdot \psi}} \tag{3}$$

where ΔM is the mass matrix for the added mass. For the addition of a single point mass located at point x on the span, Eq. 3 reduces to:

$$\alpha = \sqrt{\frac{\omega_0^2 - \omega_1^2}{\omega_1^2 \cdot \Delta m \cdot \psi_x^2}} \tag{4}$$

where Δm is the added mass (kg) and ψ_x is the amplitude of the unity scaled mode shape at the location at which the mass is introduced.

Using the same derivation, an equation may be formulated to calculate the change in natural frequency by the addition of a small point mass at a given location:

$$\Delta m \cdot \psi_x^2 = \frac{\omega_0^2 - \omega_1^2}{\omega_1^2 \alpha^2} \quad (5)$$

By minimizing the difference between the left and right hand sides of Eq. 5 across multiple modes of vibration simultaneously, the likely location and mass of a point mass may be estimated. This minimization is quantified for each i -th mode of vibration in terms of an error term, ε_i , with the total error, ε , expressed as the sum of the errors across all measured modes of vibration:

$$\varepsilon_i = \frac{\omega_{0,i}^2 - \omega_{1,i}^2}{\omega_{1,i}^2 \alpha_i^2} - \Delta m \cdot \psi_{x,i}^2 \quad (6)$$

$$\varepsilon = \sum_{i=0}^N \varepsilon_i \quad (7)$$

Each of the three additional mass data sets, referred to by the mass location as $\Delta m_{0.8m}$, $\Delta m_{1.15m}$ and $\Delta m_{1.6m}$, were used to generate a set of α values for the 6 first vertical modes of vibration. Estimates of the natural frequency of each mode were obtained by peak picking of the Welch frequency spectra with a Hanning window with length 150s and window overlap of 75s.

The beam was assumed to act as a free-free beam with symmetric behaviour. The ε term was found by iterating through values of mass change between 0kg and 1kg (0% and 5% of the total mass of the beam) acting as a point load at discrete locations along the span across the 6 vertical modes of vibration. The results of this analysis are presented in Fig. 3 in terms of the total error term ε scaled to the maximum error recorded in the plotted data. Columns of Fig. 3 correspond to the three sets of mode shape scale factors (α) obtained using $\Delta m_{0.8m}$, $\Delta m_{1.15m}$ and $\Delta m_{1.6m}$. Rows of Fig. 3 correspond to the $\Delta m_{0.8m}$, $\Delta m_{1.15m}$ and $\Delta m_{1.6m}$, whose added mass and mass location are to be estimated.

On the diagonal of Fig. 3 there is perfect identification of both the mass change and the mass location as these results correspond to where the shape factors were generated using the given data set. On the off-diagonal results the identified minima of ε are close to the true locations and Δm values, demonstrating the potential for such a method to estimate and identify mass locations.

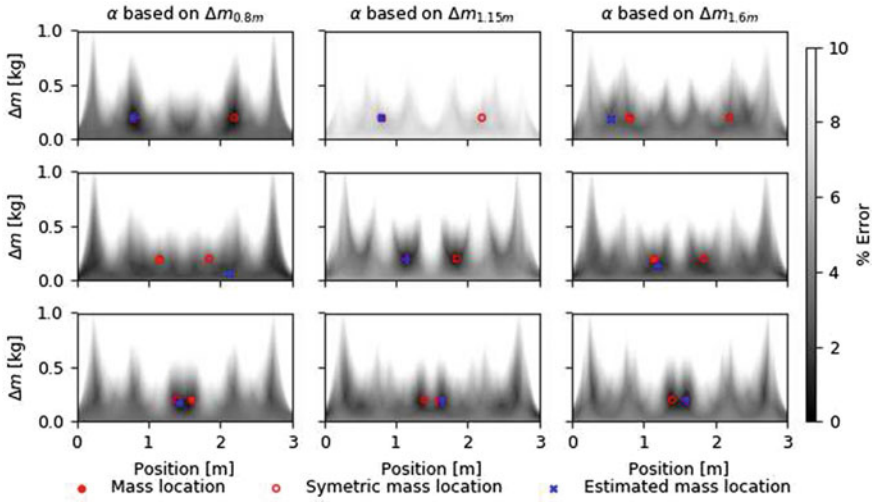


Fig. 3 Identification of mass change locations and quantity based on minimization of the error term for the inverse mass-change method for the 6 dominant vertical modes. Natural frequencies based on peak picking Welch frequency spectra of separate mass-change data sets

3.1.3 Mass Change Quantification—Concatenated Data Sets

Using the shape factors and unloaded natural frequency (ω_0) estimated from the independent data sets, presented in the previous section, the mass and mass location have been estimated using the STFT and ST-RDT results, as shown in Fig. 4. Results are based on the minimized error term ε across the 6 measured vertical modes of vibration. As the beam is symmetric, the mass location is estimated for one half of the span.

3.1.4 Mass Change Experiment—Discussion

The results presented in Fig. 4 show the potential for short-time quantification and locating of mass changes. The STFT leads to more consistent results than the ST-RDT, however it is expected that ST-RDT will achieve lower errors for noisy data and structures under continuous excitation. The difference between the true and estimated masses/mass locations can be attributed to two sets of factors. The first are those associated with errors in the natural frequency estimation using short-time OMA methods. These errors are stochastic and result in the small variations in the estimated parameters. The more pressing set of factors are those which result in continuous misidentification of mass and mass location.

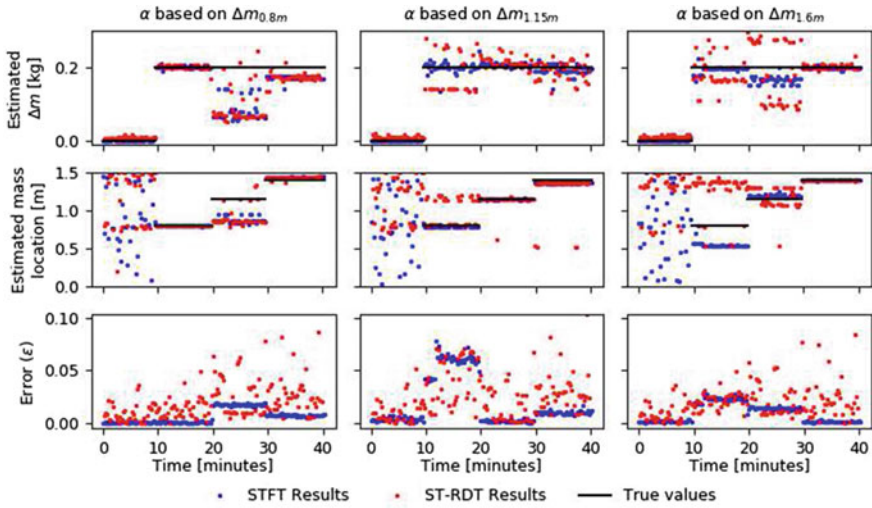


Fig. 4 Mass quantity and location estimated using the inverse mass-change method applied to STFT and ST-RDT estimated natural frequencies of the 6 dominant vertical modes

Through comparison of the columns of results in Fig. 4 and examination of the results for each mode of vibration it was found that the shape factors for the higher modes showed far larger variations across the three mass change data sets. This results in the higher modes of vibration having consistent errors. Evidence for this can be seen in the lowest row of Fig. 4, where the error does not reach zero and exhibits consistent values across all time steps. This results in the consistent misidentification of the mass location and quantity, an effect which is reinforced by the large changes in frequency exhibited by the higher order modes for small changes in mass. The variations in the shape factors suggest that the assumption that the mode shapes are free-free mode shapes and that the impact of the mass of the accelerometers (0.5% of the mass of the beam) is minimal may not be true and highlights the importance of accurate mode shape scale factors. By limiting the analysis to the first three modes of vibration a higher average accuracy of mass quantity and location could be achieved, however the individual results displayed great stochasticity, likely due to lower levels of error cancellation between modes.

Only the results for vertical modes have been used within the mass quantification and locating. By including the lateral and torsional modes of oscillation it is expected that the accuracy of the method could be further improved and may allow the use of shorter time windows.

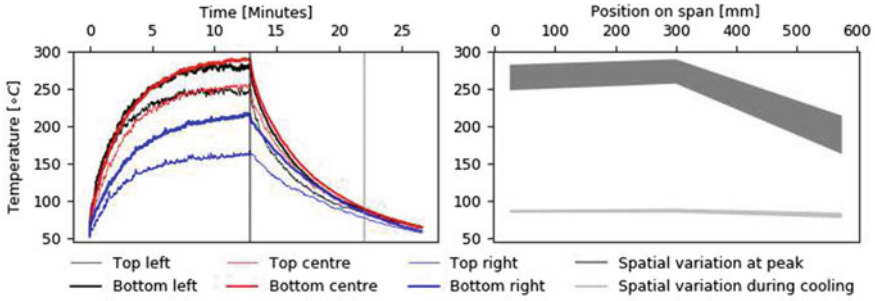


Fig. 5 Left plot: Measured temperature at thermocouples. Right plot: Variation in temperature across length of plate, interpolated at times shown on left plot

3.2 Temperature Change

3.2.1 Temperature Change—Temperature Variation

As shown in Fig. 5, the temperature differential across the depth of the plate reaches a maximum value of 37 °C, with an average difference in temperature between the bottom and top of the plate of +23.8 °C during heating and +11.3 °C during cooling of the plate.

There is a significant temperature differential between the right-hand side (RHS) and the centre/left-hand side (LHS) of plate, illustrated in the right plot of Fig. 5. This temperature differential is supported by preliminary data from an infrared camera recorder. The discrepancy can be attributed to both a slight increased elevation of the RHS and an asymmetry of the heated air plume due to the location of extraction fans and draughts during the experiment. These factors result in a lower incident heat flux, and therefore a decreased temperature, on the RHS which is most pronounced during heating of the plate.

As the change in dynamic response of the plate is expected to be dominated by the higher temperatures, due to larger decreases in elastic modulus at these areas, the temperature used for fitting of the natural frequencies is based on an average of the top and bottom thermocouple data recorded at the centre and LHS of the plate.

3.2.2 Temperature Change—Identification

The STFT and ST-RDT results for the second vertical mode of vibration are presented in Fig. 6 alongside the average temperature. Both analyses used a window length of 10s with an overlap between windows of 9 s. The maximum value of the STFT at each time-step in a user-defined range is taken as the natural frequency of the plate at that instant. ST-RDT results are based on an RDS length of 0.05 s, approximately 3 times the period of the lowest mode of vibration, with segments of data collected

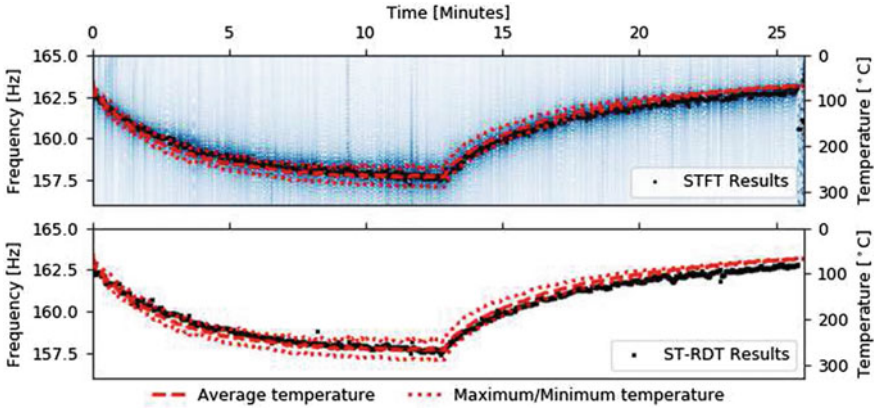


Fig. 6 STFT and ST-RDT results for second vertical mode of vibration for heating and cooling of a flat plate

where the absolute acceleration was greater than 0.5 times the standard deviation of the data set. Segments of data were multiplied by the sign (+ve/−ve) of the amplitude prior to averaging within the RDS to maintain amplitude correlation. The RDSs are fitted using non-linear least squares curve fitting to the equation of motion of a 6 degree-of-freedom dynamic system with an unknown initial amplitude and zero initial velocity in each mode of oscillation. All ST-RDT results where the coefficient of determination (R^2 score) for the fitting of the RDS is less than 0.99 are excluded from further analysis.

The variation in natural frequency is clearly identifiable in both sets of results and closely follows the variation in temperature.

3.2.3 Temperature Change—Comparison

To allow comparison of the results from STFT and ST-RDT each has been fitted with an equation adapted from Eurocode 3 Part 1–2 [10], defined as follows:

$$f_T = \begin{cases} f_0, & \text{if } 20\text{ }^\circ\text{C} \leq T < 100\text{ }^\circ\text{C} \\ f_0 + \beta \left(1 - \frac{T-100}{1000}\right), & \text{if } T \geq 100\text{ }^\circ\text{C} \end{cases} \quad (8)$$

where f_0 is the natural frequency of the system at 20 °C, f_T is the natural frequency at a given average temperature T , and β is a constant factor relating the elastic modulus to the modal stiffness of the mode f_0 . This relationship is used as the modal scale factors, which relate the elastic modulus to the modal stiffness, are unknown. Based on visual inspection of the results, the fitting was separated into the heating phase, whilst the radiant panels were ignited, and the cooling phase, after the radiant panels were switched off. It was found that more rapid changes in natural frequency

were observed for some modes during the heating phase, perhaps due to the larger temperature differentials between the top & bottom and/or LHS & RHS of the plate during heating.

Alongside this, and in recognition that the Eurocode equations provide an approximation of material behaviour, an equation adapted from direct fitting of experimental results by Wang et al. [11] was also used:

$$f_T = \gamma + \delta(1.02 - 0.0035e^{T/280}) \text{ if } 20^\circ\text{C} \leq T \leq 800^\circ\text{C} \quad (9)$$

where γ and δ are factors proportional to the initial modal stiffness and the change in modal stiffness respectively (Fig. 7).

Equation 9 well describes all data sets for the 2nd vertical mode of vibration, with the coefficient of determination (R^2 score), a measure of fit of the results, in excess of 0.98 for STFT & ST-RDT for both heating and cooling periods. The other modes of vibration are less clearly identified within both the STFT and ST-RDT results, resulting in a larger deviation of frequency estimates and poorer fitting of Eq. 9, as illustrated in Fig. 8.

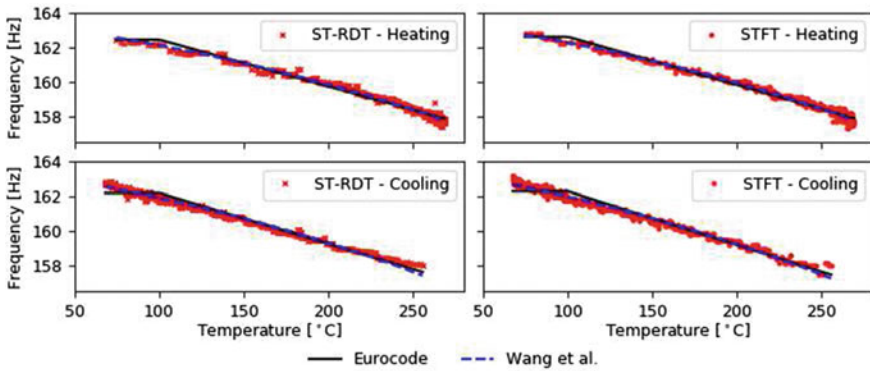


Fig. 7 Change in natural frequency of 2nd vertical mode with change in average temperature

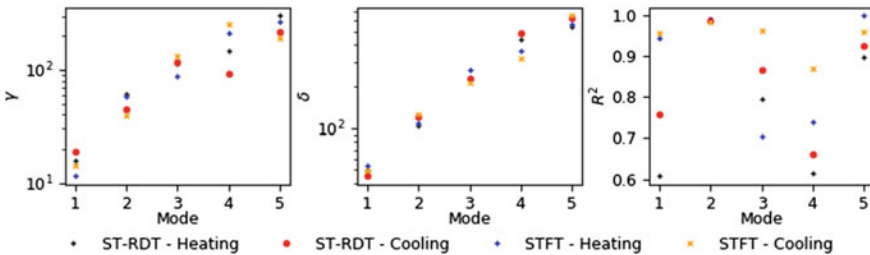


Fig. 8 Coefficients of Eq. 9 and R^2 score for fitting of 5 first vertical modes of vibration

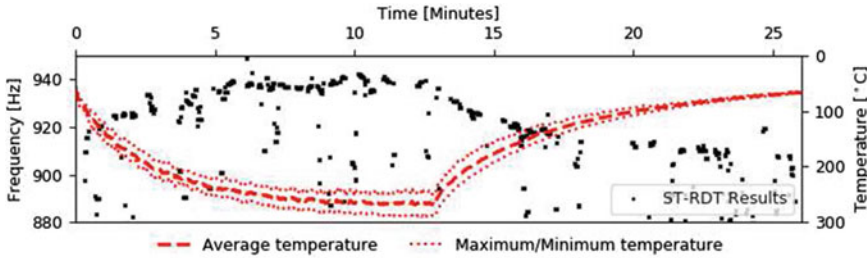


Fig. 9 High frequency mode exhibiting increase in natural frequency with temperature

3.2.4 Temperature Change—Discussion

Figure 8 shows the expected variation in natural frequency with temperature due to the changes in modal stiffness. This results in larger fitted coefficients for the higher order modes due to the increased ratio of modal stiffness to modal mass. The results obtained from the ST-RDT also illustrated a significant increase ($\approx 50\%$) in damping across the temperature range suggesting a decrease in the critical damping but a consistent actual damping. However, these results show a high degree of stochasticity making accurate quantification of the effect challenging.

The STFT and ST-RDT both lead to excellent natural frequency identification across the 5 dominant vertical modes of the structure, with ST-RDT showing higher levels of variations between neighbouring windows. The results offer good agreement with those derived through conventional stiffness measurements made by Wang et al. [11]. A key reason for the lower R^2 for some modes were the presence of close modes, believed to be induced primarily by the unequal mass distribution caused by the off-centre location of the accelerometer. This is to be addressed in further experimental work.

The ST-RDT results suggest a higher mode of vibration that exhibited an increase in natural frequency with temperature, as shown in Fig. 9. The cause of this behaviour is unknown but may be induced by the temperature differential across the plate, changes in support conditions or stiffening of the accelerometer fixing at elevated temperatures.

4 Conclusions

This paper has presented analyses of simple structures under varying additional mass or temperature and demonstrated the challenges of extracting dynamic properties from non-linear data. The short-time Fourier transform and the short-time random decrement technique have been demonstrated as methods of extracting data from time-varying systems with a high degree of accuracy. This allows changes in mass to be quantified and located, and temperature induced changes in stiffness to be quantified.

Acknowledgements Support for Z. Wynne was provided by an EPSRC Doctoral Training Partnership Studentship (EP/R513209/1).

References

1. Rainieri C, Fabbrocino G (2014) *Operational modal analysis of civil engineering structures*, 1st edn. Springer, New York City
2. Guillaume P, Hermans L, Van der Auwerer H (1999) Maximum likelihood identification of modal parameters from operational data. In: *Proceedings of 17th Int Modal Anal Conf, The International Society for Optical Engineering, Kissimmee, Florida*, pp 1887–1893
3. Asayesh M, Khodabandeloo B, Siami A (2009) A random decrement technique for operational modal analysis in the presence of periodic excitations. *Proc Inst Mech Eng Part C J Mech Eng Sci* 223(7):1525–34
4. Peeters B, Cornelis B, Janssens K, van der Auweraer H (2007) Removing disturbing harmonics in operational modal analysis. *Int Oper Modal Anal Conf IOMAC (Copenhagen)*
5. Yuen KV, Beck JL, Katafygiotis LS (2002) Probabilistic approach for modal identification using non-stationary noisy response measurements only. *Earthq Eng Struct Dyn* 31(4):1007–23
6. Welch PD (1967) The use of Fast Fourier Transform for the estimation of power spectra: a method based on time averaging over short. Modified periodograms. *IEEE Trans Audio Electroacoust* 15(2):70–73
7. Cole HA (1971) Failure detection of a space shuttle wing flutter model by random decrement, vol TM X-62,04, NASA Technical Memorandum
8. Asmussen JC, Brincker R (1997) *Modal analysis based on the Random Decrement technique—application to civil engineering structures*, 1st edn. Aalborg University, Aalborg
9. Aenlle ML, Fernandez PF, Brincker R, Canteli AF (2007) Scaling factor estimation using an optimized mass change strategy. Part 1: Theory. In: *Proceedings of the 2nd International Operational Modal Analysis Conference IOMAC 2007, Copenhagen*
10. British Standards Institution (2005) BS EN 1993-1-2:2005. Eurocode 3. Design of steel structures. General rules. Structural fire design. BSI, London
11. Wang WY, Liu B, Kodur V (2013) Effect of temperature on strength and elastic modulus of high-strength steel. *J Mater Civ Eng* 25(2):174–82

Characterizing Footbridge Response from Cyclist Crossings with Computer Vision-Based Monitoring



Rolands Kromanis 

Abstract Computer vision applications are frequently selected for short-term monitoring of bridges. The availability of high resolution and frame rate consumer-grade cameras such as action cameras makes the computer vision-based monitoring an attractive and affordable option. This paper presents findings from monitoring deformations of a steel girder footbridge subjected to cyclist loads captured with an action camera. A modified GoPro action camera with a zoom lens was located 35 m from the centre of the bridge. High resolution (720×1080 pixel) and high frame rate (240 fps) videos were recorded during cyclist crossings. Image processing, measurement denoising, vertical deflection interpretation and influence line (bridge signature) derivations are presented and discussed. Both static and dynamic responses are identifiable (discernible in vision measurements) and even tiny (a fraction of a millimetre) vertical deflections can be accurately computed from videos collected with the action camera.

Keywords Computer vision-based monitoring · Deformation monitoring · Measurement pre-processing · Signal interpretation · Vertical deflections · Structural dynamics

1 Introduction

The knowledge of bridge's load and response mechanisms is the key for understanding its behaviour. Such knowledge can be used to identify early signs of fatigue, onset of damage or anomalous structural behaviour. A dense sensor network is usually desirable to capture as much information on applied loads and bridge response as possible. A rich profusion of sensors is a costly luxury, which is associated with challenging sensor installation and tedious maintenance works, and management of the sensor network itself. Measurements for a deluge of sensors may also result in data redundancy and create unnecessary challenges when dealing with big data. Besides

R. Kromanis (✉)

University of Twente, Drienerlolaan 5, 7522 NB Enschede, The Netherlands

e-mail: r.kromanis@utwente.nl

the era of technology offers a wide variety of hardware (sensing technologies) and software (algorithms, measurement analysis packages) that ‘promise’ easy solutions to system identification challenges. Yet, it is still a challenge to choose (i) the most suitable structural response parameter to measure, (ii) type of sensors, their number and locations on the structure, (iii) and measurement interpretation techniques.

Bridge response is driven by environmental loads (temperature, wind) and effects (humidity), and traffic loads. Temperature is known to govern bridge response in long-term [1]. Distributed temperatures are needed to characterize bridge thermal response [2]. The location and weight of applied loads are needed to characterize traffic induced response. The load and response information can then be used to, firstly, establish baseline bridge performance and, secondly, assess bridge conditions during follow-up monitoring events, unless the bridge is monitored continuously. The information of all applied loads and dense bridge response is desirable, however a sensing system that provides such information is expensive and also impractical. Instead, a mobile sensing system, which is used periodically can be a good alternative. Vision-based technologies (i.e., cameras) can measure surface temperature, traffic and movements of targets (e.g., bolts) on structure’s surface [2–5]. A ubiquitous sensing system, which could collect all desirable parameters, could be composed by a multi-camera robotic system.

In the past decades the computer vision-based measurement has broadened the scope of the structural health monitoring. The availability of cost-effective solutions for measurement collection (e.g., smartphones) creates opportunities for researchers and civil engineers to expand their research or practice and explore new methodologies/approaches for the condition assessment of bridges. Many studies have evaluated the performance of action cameras and smartphone cameras to produce comparable results with professional cameras and contact sensors, when appropriate image processing algorithms, frequently open source algorithms, are used [4, 6–8]. Cost-effective off-the-shelf cameras, have been employed to measure response of footbridge induced by pedestrians and crowds [8–11]. Load application events such as by a person crossing the bridge can provide statistical bridge signatures [12], which can be in a form of influence lines. Bridge signatures can be characterized using statistical tools or machine learning. The characterized signature can be compared with the obtained signature in the following measurement collection events for the bridge condition assessment.

This paper drafts a vision-based measurement approach for footbridge condition assessment utilizing the load and response relationship. The premise is that datasets of footbridge response to known loads (i.e., pedestrians and cyclists) and their locations can be used to derive the bridge signature, from which bridge conditions can be assessed in upcoming measurement collections. The manuscript introduces the first steps towards a methodology for such data-driven bridge response characterization approach from moving loads, which in this study are cyclists crossing the bridge. The paper demonstrates the initial effort to lay the foundation for the future research, which is envisioned to analyse much larger data sets, employ machine learning and Bayesian approaches to characterize the bridge response.

2 Characterizing Bridge Response

The focus of the paper is on footbridges, therefore, traffic relates to people (i.e., people, cyclists) crossing the bridge. Figure 1 explains the processes involved in the proposed computer vision-based measurement approach for the condition assessment of footbridges. The structural system (a footbridge) is subjected to environmental (e.g., temperature, wind) and traffic (e.g., pedestrians, cyclists) loads. The magnitude of the load, its location and bridge response are needed to characterize the structural system, i.e., the bridge. For this reason the monitoring system consists of a number of cameras capturing deformations, traffic and temperature. The datasets are passed to data analysis packages such as image processing and signal interpretation for the condition assessment of bridge.

The focus of this study is on developing processes for the condition assessment of footbridges rather performing it, which is the task for future studies. The next sections describe computer vision-based measurement and bridge response characterization (or signature) methods.

2.1 Vision-Based Measurement

Vision measurement has been studied extensively for bridge monitoring. The fundamental steps in image processing for bridge response computation have some common traits. Figure 2 shows three image processing stages that are commonly found in the literature for computer vision-based measurement for an easy, fast and accurate generation of structural response [8, 11, 13]. The three stages are described below:

1. **Image processing initiation stage** starts with selecting a reference frame, in which desired regions of interest (ROIs) are drawn. A target(s) is then specified

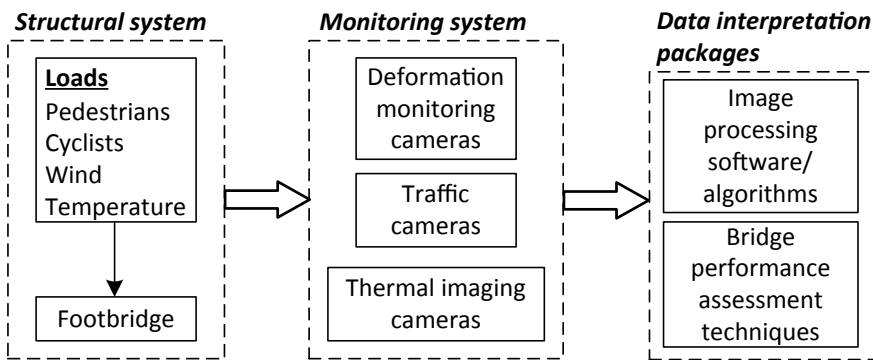


Fig. 1 Footbridge condition assessment flow using vision measurement

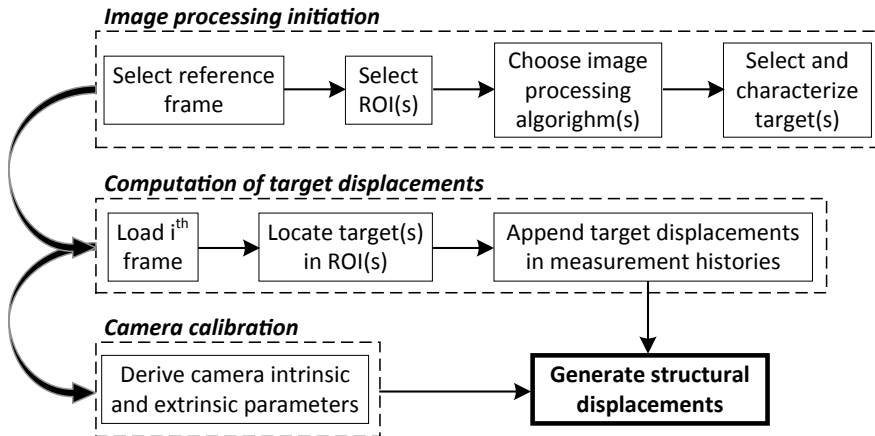


Fig. 2 Image processing steps for generating structural displacements

in each ROI. When measuring bridge response, target movements are relatively small (a few pixels) therefore it is more practical to search for the target in the specified ROI than searching the entire image frame. Different techniques such as template matching and feature matching [8, 11] can be selected to detect features characterizing a target. These features are then matched in ROIs of consecutive image frames.

2. **Computation of target displacements stage** locates the target in the ROI of i^{th} frame. The template or features characterizing the target are sought in the ROI. The x and y coordinates of the target on the image plane for each frame compose measurement histories. Each new measurement is appended to the measurement histories.
3. **Camera calibration stage** is compulsory to obtain accurate target movements in real-world coordinate system, which is the bridge surface plane. This stage may consist of two processes: derivation of camera intrinsic (related to the camera, its lens) and/or extrinsic (camera position to the bridge) parameters. Camera intrinsic parameters can be derived using a standard checkerboard method [14]. Camera extrinsic parameters can be set using a scale factor [7] or using image homography method, in which two-dimensional (2D) points in the image plane are matched with 2D points in the structural system [15, 16].

The product of the target displacements and camera calibration is structural displacements of targets. Displacements are primary response, from which any secondary derivatives such as strain, tilt angle and curvature can be computed. Displacements are collected at known time intervals, therefore bridge dynamic response (e.g., vibration frequencies) can be derived.

When employing computer vision for identification of the type of load and its position on a specified 2D surface plane on the structure, a multitude of image processing techniques such as background removal [4], heat source detection [2]

and skeletonizing people [17] are available. Thermal imaging cameras can have a dual purpose: capture distributed bridge temperature and locate traffic load (i.e., pedestrians) [2, 18].

2.2 Characterizing Bridge Response

Displacement measurements may be noisy and need pre-processing before they can be used for meaningful derivation of the bridge signature. The source of the noise usually is camera movements, which could result from wind or even a slight ground vibration. Camera drifts are also observed. If the image frame contains an object, which is not related to the structure and which does not move, in the foreground/background, then its displacement can be subtracted from bridge displacements, therefore removing camera movements. Other techniques, which can remove camera movements, may apply large moving average windows on pixel motion history to estimate camera movement, which is then removed from displacements, leaving the structural response. The next step is to analyse time histories with fast Fourier transform (FFT) to obtain power spectral density (PSD). The PSD plot reveals frequency range of the first few vibration modes of the bridge and short-term load events with similar length such as cyclists crossing the bridge. High-pass and moving average filters can then be applied to remove the remaining measurement noise and camera drifts. After the application of the required measurement processing filters, in an ideal situation, the response histories should be free of camera drifts and noise, and ready to be characterized (derive the bridge signature).

The bridge response from cyclist crossings consists of static and dynamic components. Figure 3 illustrates vertical displacements of a target at the mid-span of the bridge for three cyclist crossings. The response for static and dynamic components can be identified from the PSD plot. The aim is then to extract static component, which quantifies bridge response to applied load (providing that the load and its path are known). Influence lines, which are bridge response at selected location over time of the load application i.e., cyclist crossing the bridge, for different load application scenarios need to be compiled and characterized to establish bridge signature. Ideally many loading scenarios (i.e., bridge temperatures, load locations, loads) should be provided to derive an accurate bridge signature. Computation of the signature from

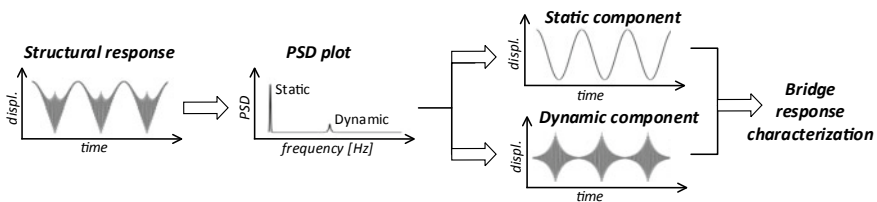


Fig. 3 Preparation of structural response for its characterization

load and response information can be an intensive regression model generation or machine learning task, which is not covered in this study.

3 Case Study

The University of Twente (UT), the Netherlands, campus bridge serves as the test bed in this study. The bridge is 2 m wide and spans 27 m across a pond. The wooden deck is supported on three steel girders with diagonal bracings. Balusters are connected to the outer girder with two M12 bolts. The bridge crosses the pond in the northeast (NE) to southwest (SW) direction. The vision measurement system (wide angle camera and zoom camera) is set at NE side. The camera frames are synchronized manually at the data postprocessing stage. The wide angle camera (Samsung S8 smartphone), which is very close to the bridge, monitors traffic on the bridge at 30 fps with a frame size of 720×1280 px. In this study, the exact location of the moving load (i.e., pedestrian) on the bridge is not computed. Its purpose is of informative nature only. The zoom camera (GoPro Hero 5 with a 25–135 mm varifocal lens) is set approximately 35 m away from the mid-span of the bridge where a bolt is chosen as a target. The zoom camera records 240 fps videos with a frame size of 720×1280 px. The bridge and its location on the map, and locations of cameras are shown in Fig. 4. In this study the researcher himself was the subject crossing the bridge on the bicycle and only crossings performed by the subject are considered, therefore avoiding any data privacy issues related to filming people using the bridge. Table 1 lists the selected load application cases. In all cases the crossings are initiated at



Fig. 4 UT campus bridge on the map (left) and looking from SW (right)

Table 1 Bridge load cases

Case #	Duration (sec)	Description
1	168	Cycling over the bridge on its <i>close side</i> and back five times
2	153	Cycling over the bridge at its <i>centre</i> and back five times
3	209	Cycling over the bridge on its <i>far side</i> and back five times; and crossing the bridge on foot at the close side

NE end of the bridge. The size of 530 s videos recorded with wide angle and zoom cameras are 0.45 and 2.34 GB.

3.1 Image Processing and Measurement Pre-processing

Many studies on vision measurement have been devoted to compare multiple methods and promote advantages of one method over another one. Also measurement accuracy and reliability from computer vision are compared to contact sensor such as linear variable differential transformer measurement. Usually, the difference between methods is very small or even negligible after measurements are pre-processed. In this study two image processing techniques are selected to derive target displacements: feature matching technique and template matching technique. Figure 5a shows the reference frame (as captured with the zoom camera), in which a ROI is drawn. In the ROI a target is selected for the two vision measurement techniques. The ROI contains a rectangular washer, holding the baluster to the steel girder (horizontal timber boards behind fill the space between the baluster and ‘I’ beam), M12 steel bolt and a nut. The target is located exactly at the mid-span of the bridge. Figure 5b shows features characterizing the target for the feature matching technique. The target is set as the left side of the nut, including the tip of the bolt, and edges of grooves (above and



Fig. 5 Image processing: **a** reference frame with a selected ROI, **b** features for the feature matching technique, and **c** template for template matching technique

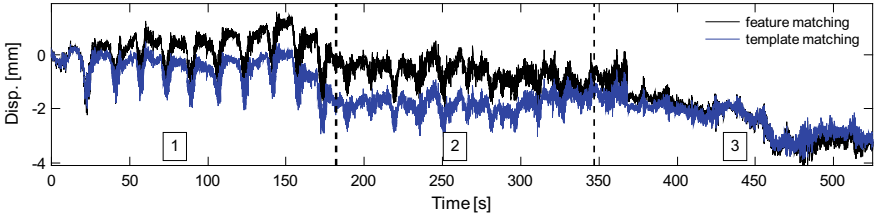


Fig. 6 Displacement histories. The number in boxes correspond to the load cases in Table 1

below the washer) in the timber baluster. Template matching techniques can be more resource intensive than feature matching technique. For this reason only a part of the nut and bolt (see Fig. 5c) are set as the target. Matching the target in a new frame takes 0.01 s and 1 s with the feature and template matching techniques, respectively.

The camera lens is narrow angle with no or very little image distortion. The scale factor for converting pixel values to corresponding engineering units (e.g., millimetres) can be obtained using the corners of the square plate (in Fig. 5b it appears as a diamond). At such conditions camera intrinsic parameters are not required for the camera calibration [11]. Figure 6 shows vertical displacement time histories computed from both image processing techniques. Although the vertical histories mismatch between 25 and 400, and 420–530 s, the displacement patterns remain similar. The measurement history might appear stochastic, however, there are patterns induced by bridge crossings. These can be found when performing further analysis, for which the displacement history from the template matching technique is chosen.

A logarithmic PSD plot is generated from FFT (see Fig. 7). Signal spikes are discernible at low frequencies and around 3–4 Hz. No clear peaks are discernible at frequencies above 8 Hz, therefore, the plot is terminated at 8 Hz. The static component corresponds to the cyclist crossings at 0.13 Hz, which is 7.7 s, i.e., for the 27 m long bridge the average speed of the cyclist is 12.5 km/h. The other peak (at 0.066 Hz, corresponding to 15.2 s cycle) corresponds to the subject crossing the bridge on foot. Dynamic components corresponding to the bridge vibrations start after 2 Hz.

The information from the FFT analysis serves as an input to the measurement pre-processing. The measurement noise (and maybe higher frequencies) is removed

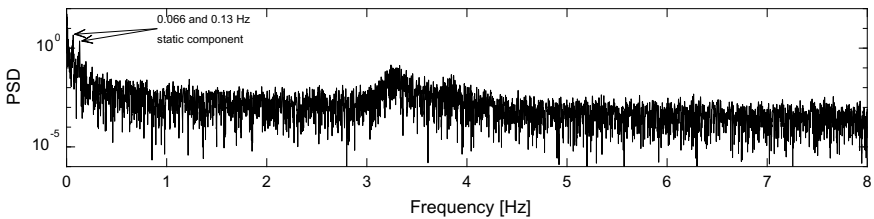


Fig. 7 PSD plot from displacements generated with the template matching technique

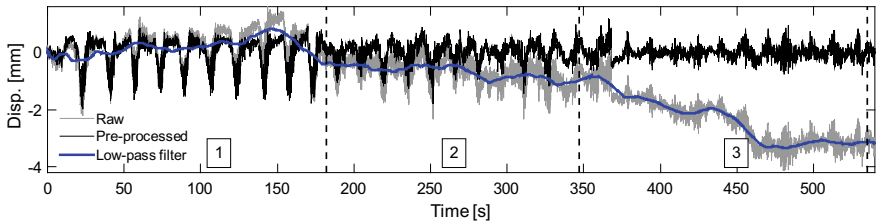


Fig. 8 Measurement histories of displacements. The number in boxes correspond to the load cases in Table 1

using 8 Hz low pass filter. Camera movements are removed using 20 s moving average filter. Raw and pre-processed vertical displacements are shown in Fig. 8.

3.2 Bridge Response

Bridge static response for load case #1 are clearly discernible in Fig. 8. This, however, is not the case for the other two load cases. The static component is extracted from measurements by leaving low-pass signal trends. In this study the low pass filter is set to 0.5 Hz. The filter reveals static components and remaining measurement fluctuations resulting from camera movements (see Fig. 9).

Representative influence lines (or bridge signatures) for all load cases are manually selected and plotted in Fig. 10. The selected signature for case #1 is clearly discernible in vertical response histories in Fig. 9, which is not the case for the other two load cases. The signature that most accurately describes the bridge response for case #2 and #3 is selected from time histories by accurately assessing them. For case #1 the mid-span of the bridge moves vertically downwards and twist at the same time. Therefore the vertical deflection for case #1 is larger than for case #2 when the load is applied at the centre of the deck. In case #3 the load is applied at the far side of the bridge, but the bridge response is the same as for case #1. However, the target remains the same and therefore it lifts up when the bridge twists. This happens when

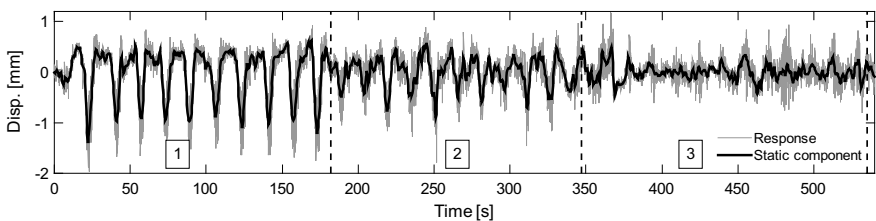


Fig. 9 Raw displacements and static component. The number in boxes correspond to the load cases in Table 1

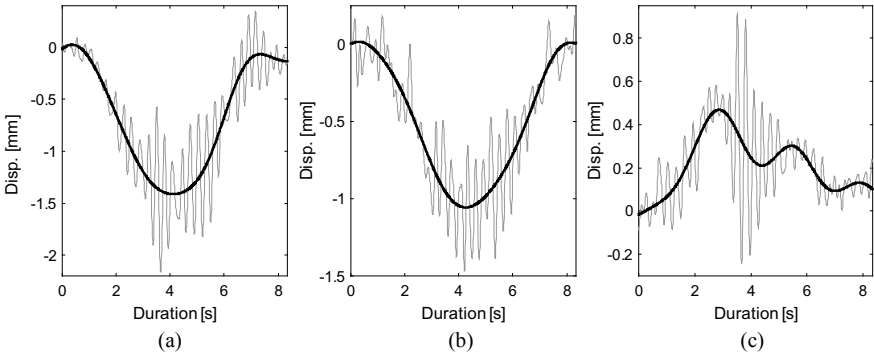


Fig. 10 Response (grey line) and static component (thick black line) of a representative crossing from case #1, #2 and #3, in (a), (b) and (c), respectively

the cyclist crosses the bridge. The slight downwards movement takes place when the cyclist reaches the mid-span of the bridge.

As discussed above, only for case #1 static components are clearly discernible in response histories, therefore influence lines for case #1 are shown and analysed in Fig. 11. The maximum and minimum vertical deflections are 1.87 and 1.32 mm. The difference is 0.55 mm, which is 42% of the minimum deflection. The vertical deflection is larger than 1.52 mm only for two crossing. The variation of vertical deflections could be related to measurement error and location of the load, which was not accurately tracked and integrated in the measurement analysis (task for future studies). The mean deflection (μ) is 1.51 mm and standard deviation (σ) 0.195 mm.

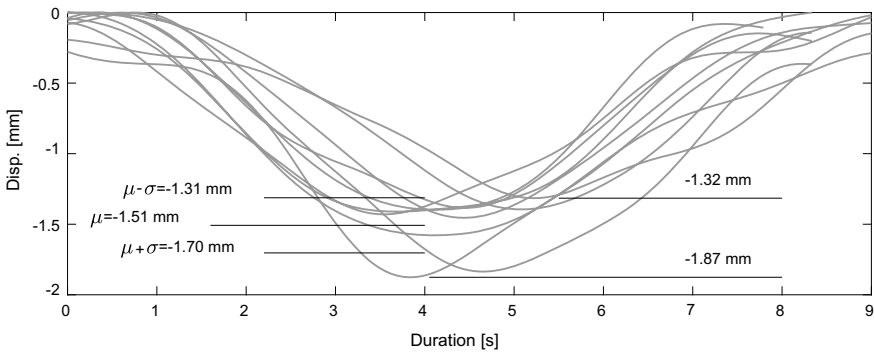


Fig. 11 Influence lines from all crossings for case 1

3.3 Discussion

When collecting visual data of people (e.g., pedestrians, cyclists), it is important to comply with general data protection regulations, which are becoming very strict. Therefore the application of the traffic camera and data analysis may need ethical approval and diligent use. In this study, the researcher himself was the subject crossing the bridge, however, when collecting such information continuously, bridge users have to be informed of their data being collected, data has to be stored securely and bridge users should be anonymized [19].

In this study the purpose of the traffic camera was to capture activities on the bridge not an exact location of cyclists crossing the bridge. Results show that, although bridge response can be measured accurately, traffic and deformation monitoring cameras need to be synchronized and much more data (many more cyclist crossing) obtained to generate an accurate bridge signature and implement the proposed bridge response characterization approach. Alternatively a roving camera technique, in which one camera is set as a reference camera while locations of other cameras are changed, can be considered [20]. This technique also required the load and its application to be kept consistent.

4 Conclusions

This manuscript laid the foundation for a data-driven approach for interpreting bridge response for condition assessment using computer vision-based measurements. The steps involved in the approach are introduced. A footbridge served as a demonstrator. A single cyclist (i.e., the same load) performed multiple bridge crossings, which were captured with two cameras: (1) traffic camera and (2) deformation monitoring camera. The following conclusions are drawn:

- Although many image processing algorithms coexist, it is recommended to analyse data with a few techniques/algorithms to decide which algorithm is more appropriate for the specific case. In this study, a template matching digital image correlation approach provided better results than the keypoint matching approach.
- Static and dynamic components can be separated when determining their dominant frequencies. The components can then be characterized based on the load cases, which should be captured with the traffic camera.
- Datasets of many scenarios with known loads and response are needed in order to perform accurate structural response characterization. In this study, only ten bridge crossings were considered for each case. Only for case #1 (cyclist crossing the bridge at it close side to the camera) static and dynamic components had clear characteristics—vertical deflection trend (influence line) and vibration frequencies, respectively.

References

1. Catbas FN, Ciloglu SK, Hasancebi O et al (2007) Limitations in structural identification of large constructed structures. *J Struct Eng* 133:1051–1066. [https://doi.org/10.1061/\(ASCE\)0733-9445\(2007\)133:8\(1051\)](https://doi.org/10.1061/(ASCE)0733-9445(2007)133:8(1051))
2. Kromanis R, Kripakaran P (2017) Data-driven approaches for measurement interpretation: analysing integrated thermal and vehicular response in bridge structural health monitoring. *Adv Eng Informatics* 34:46–59. <https://doi.org/10.1016/j.aei.2017.09.002>
3. Dong C-Z, Catbas FN (2020) A review of computer vision-based structural health monitoring at local and global levels. *Struct Heal Monit* 1. <https://doi.org/10.1177/1475921720935585>
4. Zaurin R, Necati Catbas F (2010) Structural health monitoring using video stream, influence lines, and statistical analysis. *Struct Heal Monit* 10:309–332. <https://doi.org/10.1177/1475921710373290>
5. Feng D, Feng MQ (2017) Experimental validation of cost-effective vision-based structural health monitoring. *Mech Syst Signal Process* 88:199–211. <https://doi.org/10.1016/j.ymsp.2016.11.021>
6. Feng D, Feng MQ, Ozer E, Fukuda Y (2015) A vision-based sensor for noncontact structural displacement measurement. *Sensors (Switzerland)* 15:16557–16575. <https://doi.org/10.3390/s150716557>
7. Kromanis R, Xu Y, Lydon D et al (2019) Measuring structural deformations in the laboratory environment using smartphones. *Front Built Environ* 5. <https://doi.org/10.3389/fbuil.2019.00044>
8. Lydon D, Lydon M, Taylor S et al (2019) Development and field testing of a vision-based displacement system using a low cost wireless action camera. *Mech Syst Signal Process* 121:343–358. <https://doi.org/10.1016/j.ymsp.2018.11.015>
9. Kromanis R, Al-Habaibeh A (2017) Low cost vision-based systems using smartphones for measuring deformation in structures for condition monitoring and asset management. In: SHMII 2017—8th International conference on structural health monitoring of intelligent infrastructure, proceedings. International Society for Structural Health Monitoring of Intelligent Infrastructure, ISHMII, pp 430–440
10. Kromanis R, Forbes C (2019) Multi-angle measurement collection and analysis approach of bridge dynamic response using smartphones. In: SHMII 2019—9th international conference on structural health monitoring of intelligent infrastructure, proceedings. ISHMII, St. Louis, USA, pp 1–6
11. Xu Y, Brownjohn JMW, Huseynov F (2019) Accurate deformation monitoring on bridge structures using a cost-effective sensing system combined with a camera and accelerometers: case study. *J Bridge Eng* 24:1–14. [https://doi.org/10.1061/\(ASCE\)BE.1943-5592.0001330](https://doi.org/10.1061/(ASCE)BE.1943-5592.0001330)
12. Follen C, Sanayei M, Brenner B, Vogel R (2014) Statistical bridge signatures. *J Bridge Eng* 1–11. [https://doi.org/10.1061/\(ASCE\)BE.1943-5592.0000596](https://doi.org/10.1061/(ASCE)BE.1943-5592.0000596)
13. Busca G, Cigada A, Mazzoleni P, Zappa E (2014) Vibration monitoring of multiple bridge points by means of a unique vision-based measuring system. *Exp Mech* 54:255–271. <https://doi.org/10.1007/s11340-013-9784-8>
14. Khuc T, Catbas FN (2017) Computer vision-based displacement and vibration monitoring without using physical target on structures. *Struct Infrastruct Eng* 13:505–516. <https://doi.org/10.1080/15732479.2016.1164729>
15. Kromanis R, Liang H (2018) Condition assessment of structures using smartphones: a position independent multi-epoch imaging approach. In: 9th European Workshop on Structural Health Monitoring Series (EWSHM). Manchester, UK
16. Xu Y, Brownjohn JMW, Hester D (2019) Enhanced sparse component analysis for operational modal identification of real-life bridge structures. *Mech Syst Signal Process* 116:585–605. <https://doi.org/10.1016/j.ymsp.2018.07.026>
17. Lee B, Lee M, Zhang P et al (2019) Demo: semantic human activity annotation tool using skeletonized surveillance videos. In: UbiComp/ISWC '19 adjunct: adjunct proceedings of

- the 2019 ACM international joint conference on pervasive and ubiquitous computing and proceedings of the 2019 ACM international symposium on wearable computers, pp 312–315. <https://doi.org/10.1145/3341162.3343807>
18. Yarnold MT (2013) Temperature-based structural identification and health monitoring for long-span bridges. Drexel University
 19. Cammers-Goodwin S, Nagenborg M (2020) From footsteps to data to art: seeing (through) a bridge. *Contemp Aesthet* 8:1–18
 20. Lydon D, Lydon M, Kromanis R et al (2021) Bridge damage detection approach using a roving camera technique. *Sensors (Basel)* 21(4):1246

Damage Detection Through Modal Flexibility-Based Deflections: Application to a Full-Scale RC Shear Wall Building



Giacomo Bernagozzi , Said Quqa , Luca Landi ,
and Pier Paolo Diotallevi 

Abstract In civil engineering structures it is highly desirable to detect the presence of damage and changes in the global structural behavior at the earliest possible stage, and, among the many existing strategies for vibration-based damage detection, modal flexibility (MF)-based approaches are promising tools. However, in most of the existing studies, the experimental validation of such approaches has been performed on small-scale laboratory structures, where damage has been artificially imposed as stiffness reductions, for example by substituting some structural elements. It is thus important to continue to test the effectiveness of such MF-based approaches on full-scale structures characterized by more realistic damaged conditions. This paper focuses on the methods for output-only damage detection and localization that are based on the estimation of structural deflections from modal flexibility, and the objective of this paper is to test the applicability of such methods for locating damage in a full-scale reinforced concrete (RC) structure that has experienced earthquake-induced damage. The considered structure is a shear wall building that can be modeled as a bending moment-deflecting cantilever structure, and was tested on the large-scale University of California, San Diego—Network for Earthquake Engineering Simulation (UCSD-NEES) shaking table. Two approaches, which are based, respectively, on the estimation of the curvature and the damage-induced rotation from the deflections, have been applied and compared on the data of the considered case study. These approaches have been applied in different scenarios characterized by different data sets and by a different number of degrees-of-freedom measured on the considered structure.

Keywords Structural health monitoring · Damage detection · Modal flexibility · Shear wall building · Output-only modal identification

G. Bernagozzi (✉) · S. Quqa · L. Landi · P. P. Diotallevi
Department DICAM, University of Bologna, Viale Del Risorgimento 2, 40136 Bologna, Italy
e-mail: giacomo.bernagozzi2@unibo.it

1 Introduction

Structural health monitoring (SHM) strategies are becoming essential parts of the management process of civil structures and infrastructures [1]. These strategies aim to detect the presence of potential damage and changes in the structural behavior at the earliest possible stage. Such strategies also aim to support decision making in maintenance and retrofitting operations. For civil structures and infrastructures, a convenient monitoring strategy is to implement a vibration-based monitoring system and acquire the responses of the structure under ambient vibrations. Then, the acquired data can be used for identification and damage detection purposes. Referring to these two mentioned purposes, applying output-only modal identification techniques [2, 3] and modal-based damage detection techniques [1] is probably one of the most common and used approaches. These techniques are closely related since the outcomes of the former represent the starting point for the application of the latter. Moreover, the development in recent years of automated modal identification procedures [4] has contributed to close the gap between the discipline of output-only modal identification and the application of modal-based damage detection and monitoring strategies.

Among the vast class of the existing modal-based methods for damage detection, the methods based on modal flexibility and its derivatives [5–19] are promising tools. According to these approaches, the modal parameters, in terms of natural frequencies and mode shapes, are used to obtain an estimate of the static flexibility matrix of the structure. Such matrix can be considered as an experimentally-derived model of the structure, to be used for damage detection purposes. Some methods in this class are also based on an additional main step: such modal flexibility-based models are loaded by virtual loads, called inspection loads, to estimate structural deflections. Information contained in the modal flexibility matrix is thus condensed in a deflection vector, which is then used to track eventual variations that can be associated to a damaged state. Such approaches, developed in the late '90s [10], have been progressively improved and refined over the last two decades [11–19]. Some approaches based on similar damage locating concepts have been also developed to be applied from static deflections [20].

All the damage detection methods based on the estimation of modal flexibility-based deflections have some inherent common characteristics. However, each method has other specific features that depend on the type of structures for which the method has been developed. For example, such methods can be grouped into two main classes: methods developed for shear-type structures (e.g., [11–13]) and methods developed for flexure-type structures (e.g., [14–17]). Such approaches are briefly reviewed herein. In [11] an approach has been proposed for detecting and localizing damage in buildings that can be modeled as planar shear-type structures. Based on the theory presented in [11], an extension of such method has been presented in [12], where the considered structures are plan-symmetric shear-type buildings with asymmetric damage. The problem of detecting damage in shear-type buildings using modal flexibility-based deflections is also addressed in [13], where different

strategies have been proposed for performing the calculations with minimal or no a priori information about the structural masses, even in the case in which the masses are varied before and after damage. In [14] the displacements and the curvatures of modal flexibility-based deflections have been analyzed for damage localization on a steel grid laboratory model. In [15] the concept of the Positive Bending Inspection Load (PBIL) has been introduced, and a method has been presented for damage localization in simply supported and continuous beams. In [16] the damage localization for beam-like structures is carried out using the normalized curvature of the uniform load surface evaluated from modal flexibility. This approach has been verified through numerical simulations performed for a cantilever beam and for a simply supported beam, by considering measured degrees-of-freedom (DOFs) at the same spacing. In [17] a method is presented for damage localization in cantilever beam-type structures. The experimental verification of this approach has been performed using a laboratory 10-story frame model with constant interstory heights and by measuring the structural responses at all stories.

It is important to underline that in most of the existing studies related to the application of methods based on modal flexibility-based deflections, the experimental validation has been performed on small-scale laboratory structures. Studies where these approaches have been validated using full-scale structures exist, but the number of such studies with full-scale validations is quite small compared to the studies that considered small-scale laboratory structures. For example, in [18] modal flexibility and modal flexibility-based deflections have been used for condition assessment in real-life bridges. As another example, in [19] the approach presented in [11] has been validated on a full-scale shear building, where damage has been imposed by replacing a spring member with other members having reduced stiffness. Based on these premises, it is thus evident that is important and of interest to continue to test the effectiveness of the methods based on modal flexibility-based deflections on full-scale structures.

The objective of this paper is to test the applicability of the damage localization methods based on the estimation of modal flexibility-based deflections on a full-scale reinforced concrete (RC) structure that has experienced earthquake-induced damage. The considered structure is a shear wall building that can be modeled as a bending moment-deflecting cantilever structure. In particular, two approaches for damage localization have been applied and compared on the data of the considered case study. These approaches have been applied by considering different scenarios characterized by different data sets and by a different number of degrees-of-freedom measured on the considered structure.

2 Damage Detection Through Modal Flexibility-Based Deflections in Bending Moment-Deflecting Cantilever Structures

The modal flexibility matrix of a generic structure can be defined as an estimate of the static flexibility matrix of the considered structure obtained from a vibration test, and specifically from the extracted modal parameters. When dealing with input-output tests, such matrix can be directly extracted from the data if for at least one degree-of-freedom both the input force and the output response are measured. This requirement guarantees that mass-normalized mode shapes can be estimated. When dealing with output-only tests, the modal flexibility matrix is not readily available from the data [8]. However, solutions exist to circumvent the problem and to obtain the mass-normalizing constants required to estimate the modal flexibility from output-only data. One can use mode shape scaling techniques, which generally need the execution of additional tests with some imposed structural modifications [3]. As a second option, one can use an a priori estimate of the system mass matrix [11, 12] or can use the mass matrix of the structure derived from a FEM model [3]. As a third option, one can try to extract from the output-only data unscaled matrices that are proportional to the mass and flexibility matrices of the structure [6, 8, 9, 13, 21], indicated, respectively, as proportional mass matrices (PMMs) and proportional flexibility matrices (PFMs). When considering this last case and using the estimated proportional flexibility matrices for damage detection purposes, it is important to consider PFMs in the baseline and in the potentially damaged states that are properly scaled. Usually, this condition is guaranteed if the masses are unchanged in the different considered states of the structure and if the same PMM is used to normalize the mode shapes in the baseline and in the potentially damaged states [6, 13]. Estimating modal flexibility matrices from vibration data is in general an operation that can be performed also in the case in which not all the DOFs of the structure are measured, as shown in [7] for the input-output case or in [6, 9] for the output-only case.

The modal flexibility matrix of a generic MDOF classically-damped structure can be obtained using the following equation [7–9]:

$$\mathbf{F}_{r \ n \times \ n} = \sum_{i=1}^r \frac{1}{(s_i \omega_i)^2} \boldsymbol{\psi}_i \boldsymbol{\psi}_i^T \quad (1)$$

where n is the number of the DOFs measured on the structure, r is the number of the modes included in the calculations, $\boldsymbol{\psi}_i$ is the i th real arbitrarily-scaled mode shape vector (with dimensions $n \times 1$), ω_i is the i th natural circular frequency, and s_i is the mass normalization factor for the i th mode.

After having estimated the modal flexibility matrices, a convenient approach to tackle the damage detection problem is to calculate the modal flexibility-based deflections. Such deflections can be determined by applying some inspection loads to the

flexibility-based experimentally-identified model of the structure, as follows

$$\mathbf{v} = \mathbf{F}_r \mathbf{p} \quad (2)$$

where $\mathbf{v}_{n \times 1}$ is the modal flexibility-based deflection and $\mathbf{p}_{n \times 1}$ is the inspection load. When considering bending moment-deflecting beam-like structures, a Positive Bending Inspection Load (PBIL) is usually selected as the inspection load. The PBIL is a load that generates positive bending moments in the inspection region of the structure and no inflection points in the deflection within that region [15].

After having estimated the modal flexibility-based deflections, different features computed from these deflections can be used for damage detection. Some examples of existing approaches are mentioned: in [14] the displacement and the curvature are used; in [15] the additional deflection measured from the chord that connects two DOFs is evaluated; in [16] the normalized curvature of a uniform load surface is used; in [17] the interstory deflection is evaluated. The works [15–17] also show the relationship that exists between damage in beam-like structures (e.g., a localized stiffness reduction) and the damage-induced deflection, i.e., the difference between the deflections in the damaged and undamaged states. These mentioned approaches represented the starting point for the development of the damage detection approaches that in this paper are applied to the data of the considered case study, which, as already mentioned, is a full-scale reinforced concrete structure that has experienced earthquake-induced damage. This structure, described in Sect. 3, can be modeled as a bending moment-deflecting cantilever structure, and thus the analytical formulation presented in the remaining part of this section was developed by considering these types of structures. It is also important to mention that the approaches and analyses presented in this paper focus on planar structures, whose structural behavior is analyzed in one direction (Fig. 1).

For a cantilever structure, a convenient inspection load to be adopted for evaluating the modal flexibility-based deflections is a uniform load with unitary values at all the DOFs—i.e., $\mathbf{p} = \{1 \ 1 \ \dots \ 1\}^T$. This load is a PBIL load for a cantilever structure, as shown in [15]. Starting from the displacements of the calculated deflection, the rotations and the curvatures can be estimated using the finite difference method, as a numerical derivation technique.

The rotation of a portion of the structure located between two measured DOFs—i.e., the $(j + 1)$ th and the j th DOFs—can be estimated as follows:

$$\varphi_{(j+1,j)} = \frac{v_{j+1} - v_j}{h_{j+1} - h_j} \quad (3)$$

where h_j is the height of the j th DOF evaluated with respect to the base of the cantilever structure. If the measured DOFs are located at a constant spacing equal to Δh , Eq. (3) is simplified as follows:

$$\varphi_{(j+1,j)} = \frac{v_{j+1} - v_j}{\Delta h} \quad (4)$$

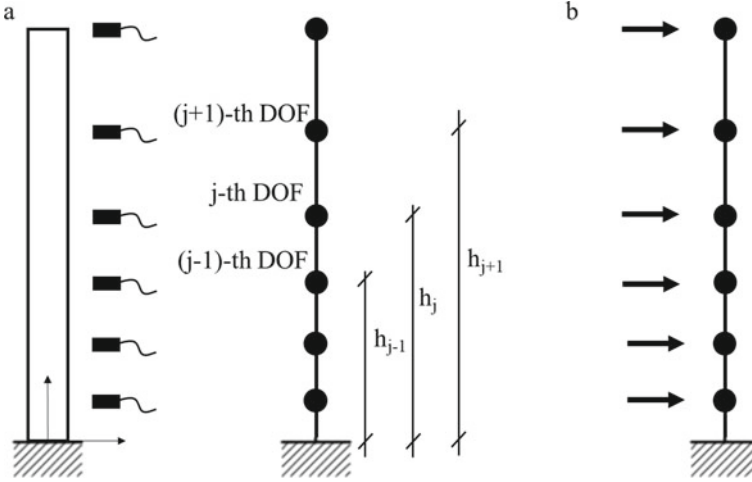


Fig. 1 Bending moment-deflecting cantilever structure: **a** structural model with a generic sensor layout; **b** applied inspection load

The curvature at the j th measured DOF of the modal flexibility-based deflections can be estimated as follows:

$$\chi_j = \frac{\frac{v_{j+1}-v_j}{h_{j+1}-h_j} - \frac{v_j-v_{j-1}}{h_j-h_{j-1}}}{\frac{h_{j+1}-h_{j-1}}{2}} \quad (5)$$

Equation (5) is valid for measured DOFs that are unevenly distributed along the height of the structure. Such equation was obtained by adapting the formulation presented in [22], for evaluating the curvature of mode shapes and operational deflection shapes, to the case of the modal flexibility-based deflections. If the measured DOFs are located at a constant spacing equal to Δh , Eq. (5) is simplified as follows:

$$\chi_j = \frac{v_{j+1} - 2v_j + v_{j-1}}{\Delta h^2} \quad (6)$$

In this paper, the quantities presented in Eqs. (3) and (5) are used for damage localization purposes. Of course, uncertainties are always present on quantities extracted from real noisy vibration data. Thus, statistical approaches based on outlier analysis [1] are introduced in the damage localization process. To implement these statistical approaches, it is required that the calculations related to the baseline structure are repeated using different portions of the training data set. This is done to estimate the degree of variability that affects the quantities related to the baseline structure.

Two different damage localization strategies were developed and then applied to the data of the considered case study.

According to the first strategy, the values of the curvature are monitored, and it is of interest to see if the values of the curvature in the potentially damaged state deviate from the values of the curvature related to the baseline structure. This strategy is implemented through the calculation of the following index, which is herein defined as z-index based on curvature

$$z_{\chi,j} = \frac{\chi_{I,j} - \bar{\chi}_{B,j}}{s(\chi_{B,j})} \tag{7}$$

Equation (7) can be evaluated for each *j*th measured DOF with $j = 1 \dots n - 1$, where $j = 1$ is the first measured DOF at the bottom of the structure. In Eq. (7) $\chi_{I,j}$ is the curvature related to the structure in the inspection stage, and $\bar{\chi}_{B,j}$ and $s(\chi_{B,j})$ are the sample mean and the sample standard deviation of the curvature $\chi_{B,j,i}$ evaluated from the training data set (for $i = 1 \dots q$ where q is the total number of damage-sensitive features extracted from the training data set).

In the second strategy for damage localization, the concept of the damage-induced rotation is introduced, which is the difference between the rotation in the inspection stage and the rotation related to the baseline state. In particular, the second strategy is based on tracking eventual variations in the damage-induced rotation along the height of the cantilever structure. This strategy is implemented through the calculation of the following index, which is herein defined as z-index based on a damage-induced rotation

$$z_{\varphi,j} = \frac{\Delta\bar{\varphi}_{(j+1,j)} - \Delta\bar{\varphi}_{(j,j-1)}}{s(\Delta\varphi_{(j,j-1)})} \tag{8}$$

Equation (8) can be evaluated for each *j*th measured DOF with $j = 1 \dots n - 1$, and in Eq. (8) the damage-induced rotations of adjacent portions of the structure are considered. The terms $\Delta\bar{\varphi}_{(j+1,j)}$ and $\Delta\bar{\varphi}_{(j,j-1)}$ are defined as follows:

$$\Delta\bar{\varphi}_{(j+1,j)} = \varphi_{I,(j+1,j)} - \bar{\varphi}_{B,(j+1,j)} \tag{9}$$

$$\Delta\bar{\varphi}_{(j,j-1)} = \varphi_{I,(j,j-1)} - \bar{\varphi}_{B,(j,j-1)} \tag{10}$$

where the symbol Δ indicates that, for the considered quantity, the difference between the inspection stage and the baseline state is performed. As already shown for Eq. (7), the operators $\bar{\cdot}$ and $s(\cdot)$ present in Eqs. (8), (9) and (10) calculate the sample mean and the sample standard deviation, respectively, and are applied on quantities related to the baseline state.

Both in the first and in the second strategy, the z index has to be compared to a threshold value z^{TH} in order to understand if the structure has undergone structural modifications which can be associated with a damaged state and to identify the locations of the damage. For the *j*th measured DOF, the structure in the inspection stage is considered as unaltered with respect to the baseline structure if $z_{\chi,j} \leq z^{TH}$

(first strategy) and $z_{\varphi,j} \leq z^{TH}$ (second strategy). For the j th measured DOF, it is recognized that the structure in the inspection stage deviates from the baseline state if $z_{\chi,j} > z^{TH}$ (first strategy) and $z_{\varphi,j} > z^{TH}$ (second strategy). Assuming that the features extracted from the training data set have a normal distribution, as it is also done in [12, 13] where similar statistical tests have been performed, the value of the threshold is assumed as equal to $z^{TH} = 3$.

As shown in Eqs. (7) and (8), the quantities considered in the two indices for the damage localization statistical tests are different, and thus different outcomes are in general obtained using the two strategies. However, it is also important to underline that the two strategies have an inherent similarity, which is shown using the following analytical formulation.

The numerator in the expression of the z index based on damage-induced rotation—i.e., the numerator of the second term in Eq. (8)—is considered, and such term is divided by the term $\frac{h_{j+1}-h_{j-1}}{2}$, as shown in Eq. (11a). Then, Eqs. (9) and (10) are substituted into Eq. (11a), and the terms of the derived Eq. (11b) are rearranged as shown in Eqs. (11c) and (11d). Through the definitions of the rotation and the curvature expressed by Eqs. (3) and (5), it can be recognized that Eq. (11d) can be finally reformulated as the difference between the curvature in the inspection stage and the sample mean of the curvature related to the baseline structure. This difference is the numerator in the expression of the z index based on curvature—i.e., the numerator of the second term in Eq. (7).

$$\frac{\Delta\bar{\varphi}_{(j+1,j)} - \Delta\bar{\varphi}_{(j,j-1)}}{\frac{h_{j+1}-h_{j-1}}{2}} = \quad (11a)$$

$$= \frac{\varphi_{I,(j+1,j)} - \bar{\varphi}_{B,(j+1,j)} - (\varphi_{I,(j,j-1)} - \bar{\varphi}_{B,(j,j-1)})}{\frac{h_{j+1}-h_{j-1}}{2}} = \quad (11b)$$

$$= \frac{\varphi_{I,(j+1,j)} - \varphi_{I,(j,j-1)} - (\bar{\varphi}_{B,(j+1,j)} - \bar{\varphi}_{B,(j,j-1)})}{\frac{h_{j+1}-h_{j-1}}{2}} = \quad (11c)$$

$$= \frac{\varphi_{I,(j+1,j)} - \varphi_{I,(j,j-1)}}{\frac{h_{j+1}-h_{j-1}}{2}} - \frac{\bar{\varphi}_{B,(j+1,j)} - \bar{\varphi}_{B,(j,j-1)}}{\frac{h_{j+1}-h_{j-1}}{2}} = \chi_{I,j} - \bar{\chi}_{B,j} \quad (11d)$$

3 Application to a Full-Scale RC Shear Wall Building

The damage localization approaches described in the previous section were applied on the data of experimental tests that were performed on a full-scale reinforced concrete structure that has experienced earthquake-induced damage. These experimental tests were performed between September 2005 and May 2006 at the Englekirk Structural Research Center, using the University of California–San Diego Network

for Earthquake Engineering Simulation (UCSD-NEES) large outdoor unidirectional shake table. The data of this experimental program were retrieved from [23]. The tested structure is 63 ft (i.e., 19.2 m) high and is formed by shear walls. Such structure can be considered as a portion of a 7-story residential building that has structural walls as the lateral force-resisting system (Fig. 2). The structure has one main longitudinal web wall, which is 12 ft (i.e., 3.66 m) long, and two transverse walls, which provided lateral and torsional stability during the tests. A 12 ft by 26 ft–8 in. (i.e., 3.66 m by 8.13 m) slab is present at each floor level, and such slab is supported by the walls and by some gravity columns. The structure was positioned on the shake table with the main longitudinal wall aligned to the direction of the base excitation (i.e., east–west direction) and was instrumented with a dense array of sensors, including accelerometers for measuring the vibration responses. During the experimental program, some historical earthquake records were applied at the base of the structure, which induced progressively increasing levels of damage. After each strong motion test, low-amplitude white noise base excitation tests and ambient vibration tests were performed for damage characterization purposes. More detailed information about the structure and the performed vibration tests can be found in [24–26].

For the analyses of the present paper, only a subset of the vibration tests, sensor data, and structural configurations of the whole experimental program performed on the UCSD-NEES shake table has been considered. Referring to the structural

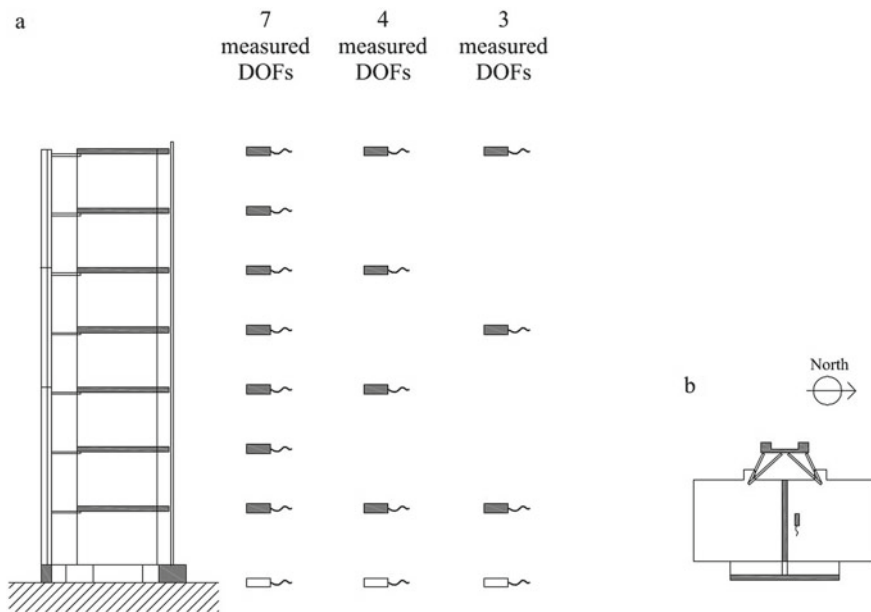


Fig. 2 Schematic drawing of the geometry of the structure with indications of the measured DOFs (geometry retrieved from [23, 24]): **a** elevation—south face; **b** floor plan view

configurations, in this paper the following configurations (tested progressively) and damaged states were considered: S0 which is the baseline configuration; S1 which is the damaged state that resulted from the application of the longitudinal component of the San Fernando earthquake measured in 1971 at the Van Nuys station (EQ1); S2 which is the damaged state obtained by subsequently subjecting the structure to the transversal component of the above-mentioned San Fernando earthquake (EQ2); S3.1 which is the damaged state generated by subsequently applying at the base of the structure the longitudinal component of the Northridge earthquake measured in 1994 at the Oxnard Boulevard station in Woodland Hill (EQ3) [25, 26]. The other damaged states shown in [25, 26] (i.e., S3.2 and S4) were not considered in the analyses of the present paper. As observed in [25, 26], after state S3.1 some braces present in the structure were strengthened and stiffened. Thus, for the analyses of the present paper it was considered appropriate to start focusing on the configurations tested before the strengthening intervention, and the states S3.2 and S4 may be considered in future developments of the work.

Referring to the type of vibration tests, the analyses of the present paper focus on the data of the tests performed, for each configuration and damaged state, by applying at the base of the structure a 0.03 g root mean square (RMS) white noise excitation with a duration of 8 min. Referring to the sensor data, this paper focuses on the analysis of the data collected using the accelerometers that were positioned at the different floor levels near the main longitudinal wall and oriented in the direction of the base excitation (Fig. 2b). These data were used to perform a planar analysis of the considered structure. In particular, three different scenarios characterized by different data sets and by a different number of degrees-of-freedom measured on the structure were considered in the analyses. As shown in Fig. 2a, a first analysis was done by considering the data collected at 7 DOFs—i.e., the data measured at each floor level from 1 to 7. In a second analysis, 4 measured DOFs were considered—i.e., the DOFs located at floor levels 1,3,5,7. Finally, a third analysis was performed by considering the data measured at 3 DOFs—i.e., the data measured at floor levels 1,4,7. In all three different considered scenarios, the accelerations at the base of the structure (i.e., floor level 0) were also included in the calculations, as discussed later in this section. All the measurements used for the analyses have a sampling frequency (f_s) equal to 240 Hz.

Before proceeding with the presentation of the performed analyses and related results, it is important to describe the damage that was observed in the structure during the experimental tests. This in fact represents the expected outcome of the applied damage localization approaches. As described in detail in [25], damage in the structure was observed visually (through pictures and video recordings), and it was also deduced from strain sensors. As stated in [25], the actual damage observed in the structure is characterized by a concentration of damage at the bottom two stories of the longitudinal web wall. This damage scenario matches the outcome of the vibration-based strategy for damage detection, localization, and quantification that was applied in [25] starting from the acceleration measurements—i.e., a sensitivity-based finite element (FE) model updating strategy. Through the analysis of the strain data and using the FE model updating damage detection method, in [25] it was also

observed that the extent of damage increases as the structure is exposed to stronger earthquake excitations.

As a first step in the analyses, the absolute accelerations related to each measured DOF were converted into relative accelerations, by subtracting from the absolute accelerations the accelerations measured at the base of the structure. Then, an output-only modal identification algorithm—i.e., the Natural Excitation technique (NExT) [27] combined with the Eigensystem Realization Algorithm (ERA) [28]—was used to estimate the modal parameters of the structure. In particular, the training data set was divided into 8 different portions (with a duration of 1 min each), and each different portion was used to estimate the modal parameters. This was done for estimating the degree of variability that affects the quantities related to the baseline state, which is a fundamental step required for applying the subsequent statistical approaches for damage localization. It is important to point out that considering only 8 portions of the signals is not the optimal number of samples for the assumed model of having baseline DSFs with a normal distribution. However, given the duration of the training data set related to the 0.03 g RMS white noise base excitation tests, this choice was done to manage the trade off between the considered number of the measurement portions and the time length of such signals. It is worth noting that an attempt was also made to perform similar operations for the training data set by considering the ambient vibration tests, which have a duration of 3 min. In such case, however, due to a shorter measurement duration, it was much harder to estimate adequately the degree of variability on the quantities related to the baseline state. The data of such ambient vibration tests were thus not considered in the analyses of the present paper, and they may be considered in future developments of the work focused on performing the calculations with small training data sets.

The NExT-ERA identification algorithm was also applied for the other considered states of the structure. In general, starting from the data of the considered measured DOFs (Fig. 2) it was possible, for each structural state, to identify the first three longitudinal modes of the structure in the direction of the applied white noise base excitation. These first three longitudinal modes were then used for the damage detection analyses of the present paper, which is the same number of modes that was considered for detecting damage in the analyses presented in [25]. The natural frequencies identified for the different states of the structure are provided in Table 1, which also shows the percent variations evaluated with respect to the frequencies

Table 1 Identified natural frequencies of the structure in the different states

State	Natural frequency f_i (Hz) (% variation w.r.t. baseline state S_0)		
	1st mode	2nd mode	3rd mode
S_0^a	1.69	11.53	24.81
S1	1.53 (−9.8)	11.32 (−1.9)	24.67 (−0.6)
S2	1.23 (−27.3)	10.56 (−8.4)	23.41 (−5.6)
S3.1	1.11 (−34.4)	7.88 (−31.6)	19.72 (−20.5)

^aMean values of natural frequencies

of the baseline state S_0 . From Table 1, it can be observed, as expected, that the frequencies related to the damaged states are lower than the frequencies of the baseline structure. Moreover, the frequencies progressively decrease when considering structural states characterized by more severe damage.

The identified modal parameters were used to assemble the modal flexibility matrices of the structure in the different states using Eq. (1). In particular, the mass matrix of the structure was estimated a priori using the available information about the structure and used for obtaining the mass normalization factors for the different modes. When evaluating the mass matrix of the considered beam-like cantilever structure, the following two simplified assumptions were made: it was assumed to neglect the rotational inertia of the considered DOFs, and it was assumed that the mass is uniformly distributed along the height of the structure. Moreover, it was not of interest to estimate the true scaled values of the masses, but only values that are proportional to the corresponding true scaled values. This resulted in estimating diagonal mass matrices whose components are proportional to the structural masses that refer to the measured DOFs, considered in the different scenarios. The use of proportional mass matrices led to the estimation of proportional flexibility matrices, which were then used to estimate the modal flexibility-based deflections. This was done according to Eq. (2), and a uniform load with unitary values at all the measured DOFs was considered as the inspection load. As an example, the modal flexibility-based deflections of the structure in the different states evaluated for the scenario with 7 measured DOFs are reported in Fig. 3. In particular, the displacements, the rotations, and the curvatures of the deflections are reported in Fig. 3a, b, and c, respectively.

By analyzing Fig. 3, it can be observed that the experimentally-derived deflections are in general in agreement with the deflections that one expects to have from a theoretical model of a bending moment-deflecting cantilever structure. There are, however, some discrepancies between the former and the latter, especially referring to the curvatures. The values of the curvature shown in Fig. 3c tend to increase from the upper to the lower DOFs, as expected. However, it can be observed that there is an inversion in the curvature at DOF number 6, while the curvature goes to zero at DOF number 3, creating an irregular trend. On one side, these effects and observed trends could be due to inevitable uncertainties related to the process of estimating the curvature of experimental deflections using the approximated finite difference method. On the other side, it is evident that idealizing and modeling the considered structure as a bending moment-deflecting cantilever structure (Fig. 1) is probably one of the simplest approaches, which leads to inevitable approximations. Using more complex numerical FE models for damage detection purposes is, however, beyond the scope of the present research, which has been developed based on the following general idea that is behind all modal flexibility-based approaches for damage detection—i.e., it is attempted to extract an experimental model of the structure directly from the measured data, without the actual need of assembling a numerical FE model.

From Fig. 3a, it can also be observed that the values of the displacements increase when considering, in the order, the baseline state and the states S_1 , S_2 , and $S_{3.1}$. This is a clear indication that structural modifications have occurred between the

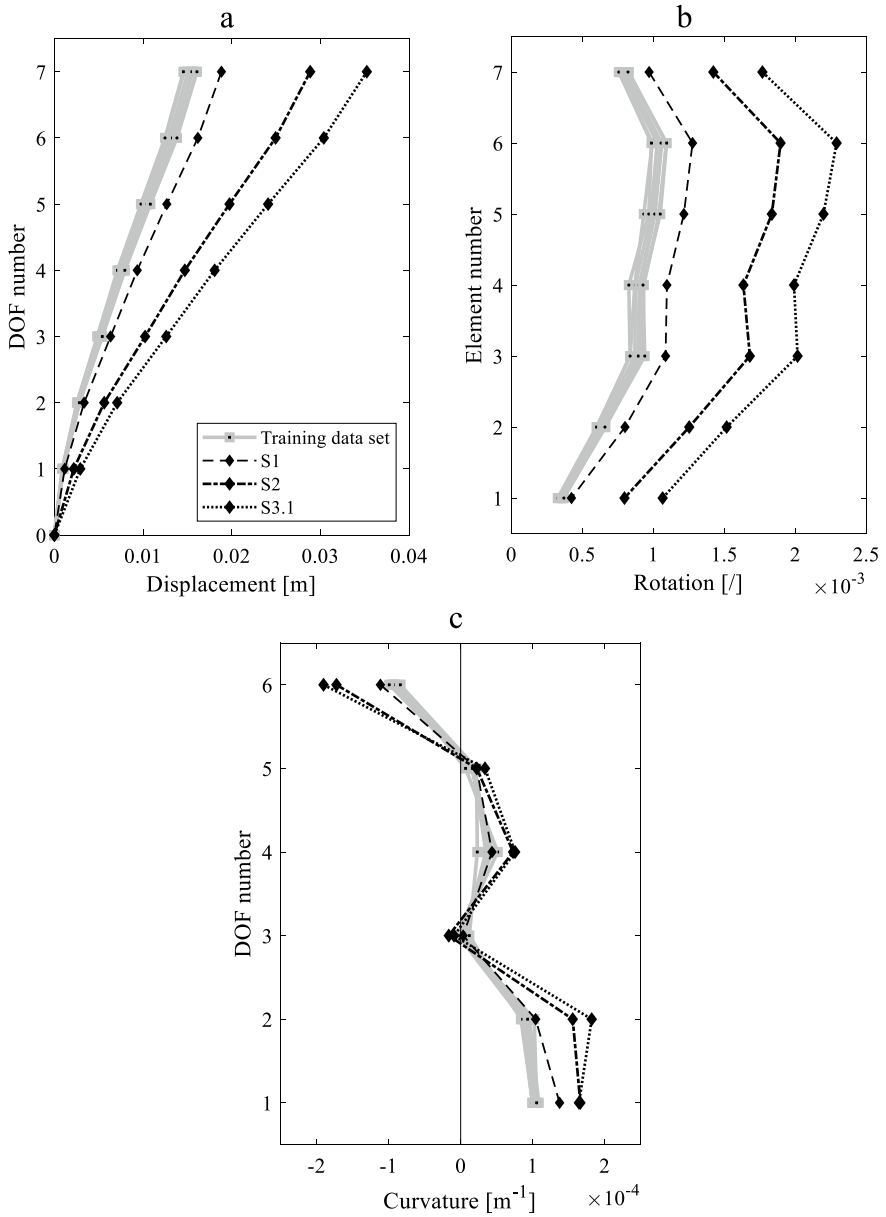


Fig. 3 Modal flexibility-based deflections of the structure in the different states obtained for the scenario with 7 measured DOFs: **a** displacements; **b** rotations; **c** curvatures

different states. These deflections in fact have been evaluated for the same load, and the observed increases in the values of the displacements show evidence that the considered structural states are characterized by increasing values of the flexibility (i.e., decreasing values of the stiffness).

The results of the damage localization are reported in Fig. 4, where Fig. 4a, c, and e show the results obtained using the z index based on curvature (Eq. 7), while Fig. 4b, d, and f present the results obtained through the z index based on damage-induced rotation (Eq. 8). In this figure, the application of the approaches based on the z index is presented for the three considered scenarios: Fig. 4a, b refer to the scenario with 7 measured DOFs; Fig. 4c, d show the results obtained in the scenario with 4 measured DOFs; Fig. 4e, f refer to the scenario with 3 measured DOFs. As shown in the figure, both two z indices were evaluated for $j = 1 \dots n - 1$, where n is the number of the measured DOFs.

As evident in Fig. 4a, b for the scenario with 7 measured DOFs, both two z indices provide localization of the damage that is consistent with the actual damage observed in the structure, which, as mentioned in [25], is concentrated at the bottom two stories of the structure. In particular, through the adopted z indices it is possible to detect the DOFs of the structure that have been affected by the damage. It can be observed from Fig. 4b that the values of the z index based on damage-induced rotation at the upper DOFs are lower than the corresponding values at the bottom of the structure, with values of z index at the DOF number 3, 4, 5 and 6 that are all below the threshold. This is in general true also for Fig. 4a (z index based on curvature), where, however, it can be observed that for some upper DOFs the z index is slightly higher than the threshold (such cases shown in Fig. 4a can be considered as false positives). The results obtained for the scenarios with 4 measured DOFs and 3 measured DOFs also show a concentration of damage for the DOFs at the bottom of the structure, and if one compares the results obtained using the two z indices, this effect is more evident in the results obtained using the z index based on damage-induced rotation (Fig. 4d, f).

The considered z indices were developed for performing statistical tests for damage detection and localization, and they were not explicitly derived for damage quantification purposes. However, the results presented in Fig. 4 clearly show that the values of both two z indices tend to increase for states that have undergone a higher number of earthquake excitations (i.e., considering in the order the states S1, S2, and S3.1), and this is consistent with what has been observed in [25]. In this perspective of considering the z indices also for obtaining an indication of the extent of damage, some important differences can be observed in the results obtained using the two z indices. Using the z index based on curvature in the scenario with 4 measured DOFs (Fig. 4c) the maximum value of the z index is at the DOF number 3, and this is especially evident for state S3.1. This observed trend with a maximum for an intermediate DOF of the structure seems to be not consistent with the results obtained in this paper using the same z index in the other scenarios (Fig. 4a, e) and not consistent with the concentration of damage at the bottom of the structure observed in the experimental tests [25]. This inconsistency found in the results obtained using the z index based on curvature, is, on the contrary, not present in the results obtained using the z index

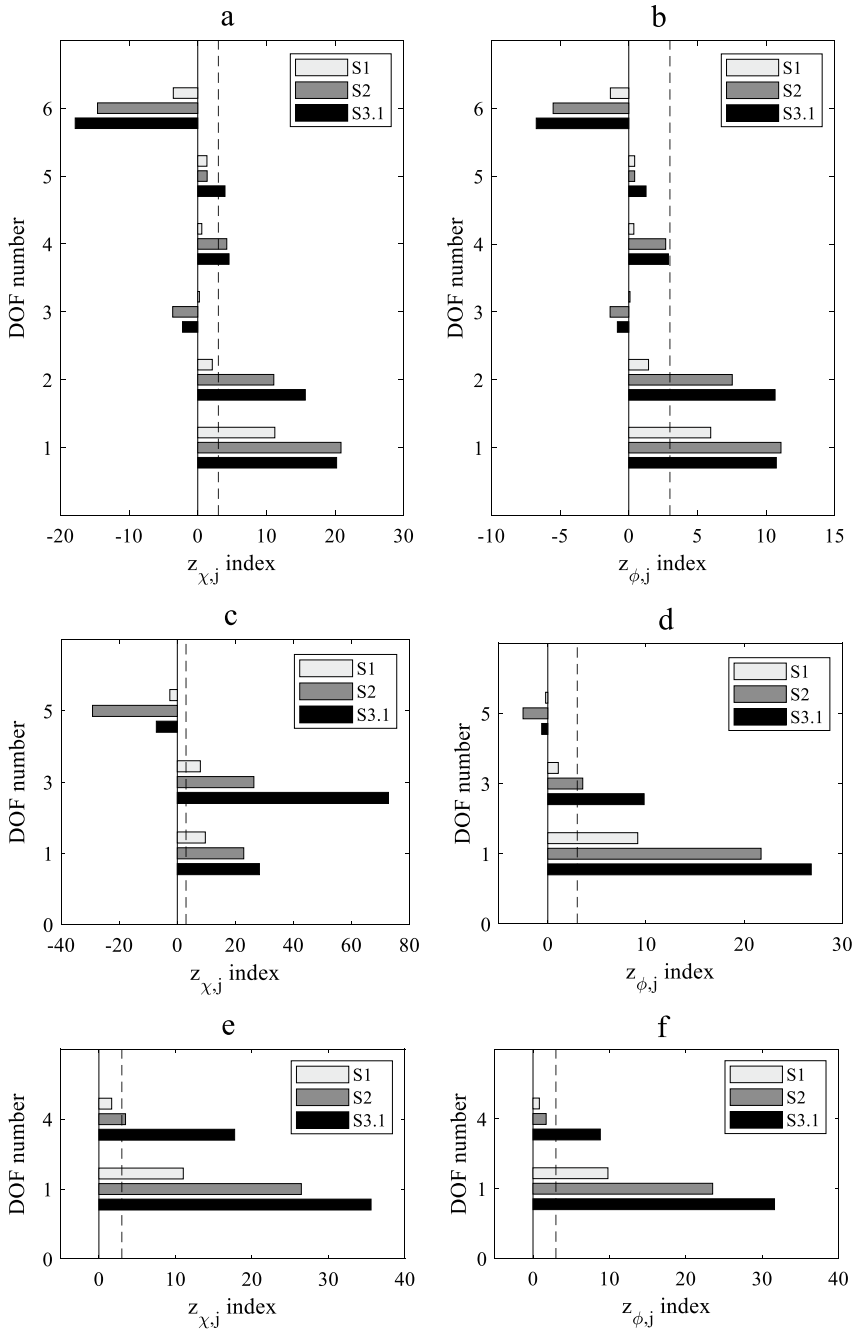


Fig. 4 Damage detection and localization for the structure in the different states. Approaches: **a**, **c**, **e** z index based on curvature; **b**, **d**, **f** z index based on damage-induced rotation. Scenarios: **a**, **b** 7 measured DOFs; **c**, **d** 4 measured DOFs; **e**, **f** 3 measured DOFs

based on damage-induced rotation. As shown in Fig. 4b, d and f for all three considered scenarios with a different number of measured DOFs, the values of the z index tend to decrease from the upper to the lower DOFs and the maximum value of the z index is at the DOF number 1. This trend is consistent with the concentration of damage at the bottom of the structure observed in the experimental tests [25].

4 Conclusions

In this paper, two approaches for output-only damage detection and localization that are based on the estimation of structural deflections from modal flexibility have been considered and applied. One approach is based on monitoring the curvature of the modal flexibility-based deflections. The other approach is based on tracking eventual variations in the damage-induced rotation along the height of the structure. Such approaches have been applied to the data of a benchmark reinforced concrete shear wall building that was tested on the University of California, San Diego—Network for Earthquake Engineering Simulation (UCSD-NEES) large outdoor unidirectional shake table. In particular, different scenarios characterized by different data sets and by a different number of degrees-of-freedom measured on the structure have been considered in the analyses (i.e., three scenarios with 7, 4, and 3 measured DOFs, respectively). The analyses performed in the different scenarios have demonstrated the applicability of the considered methods on a full-scale structure that has experienced earthquake-induced damage, by providing damage identification results that are consistent with the actual damage observed in the structure, especially for the analyses performed using the second approach based on the estimation of the damage-induced rotations from the modal flexibility-based deflections. This is the main conclusion that can be derived from the analyses performed for the considered case study, and, as potential future developments of the work, it is planned to carry out further investigations and analyses on similar benchmark structures.

Acknowledgements The use of the data of the experimental tests performed on the shear wall building using the UCSD-NEES shake table (Englekirk Structural Research Center, San Diego, USA) is gratefully acknowledged.

References

1. Farrar CR, Worden K (2013) Structural health monitoring: a machine learning perspective, 1st edn. Wiley, Chichester, UK
2. Rainieri C, Fabbrocino G (2014) Operational modal analysis of civil engineering structures. Springer-Verlag, New York
3. Brincker R, Ventura CE (2015) Introduction to operational modal analysis, 1st edn. Wiley, Chichester, UK

4. Rainieri C, Fabbrocino G (2010) Automated output-only dynamic identification of civil engineering structures. *Mech Syst Signal Process* 24(3):678–695
5. Pandey AK, Biswas M (1994) Damage detection in structures using changes in flexibility. *J Sound Vib* 169(1):3–17
6. Bernal D (2001) A subspace approach for the localization of damage in stochastic systems. In: Chang FK (ed) *Structural health monitoring: the demand and challenges*, proceedings of the 3rd international workshop in structural health monitoring, pp 899–908. CRC Press, Boca Raton, FL, USA
7. Gao Y, Spencer BF Jr, Bernal D (2007) Experimental verification of the flexibility-based damage locating vector method. *J Eng Mech* 133(10):1043–1049
8. Duan Z, Yan G, Ou J, Spencer BF (2005) Damage localization in ambient vibration by constructing proportional flexibility matrix. *J Sound Vib* 284:455–466
9. Duan Z, Yan G, Ou J, Spencer BF (2007) Damage detection in ambient vibration using proportional flexibility matrix with incomplete measured DOFs. *Struct Control Health Monit* 14(2):186–196
10. Zhang Z, Aktan AE (1998) Application of modal flexibility and its derivatives in structural identification. *Res Nondestr Eval* 10(1):43–61
11. Koo KY, Sung SH, Park JW, Jung HJ (2010) Damage detection of shear buildings using deflections obtained by modal flexibility. *Smart Mater Struct* 19(11):115026
12. Bernagozzi G, Ventura CE, Allahdadian S, Kaya Y, Landi L, Diotallevi PP (2020) Output-only damage diagnosis for plan-symmetric buildings with asymmetric damage using modal flexibility-based deflections. *Eng Struct* 207:110015
13. Bernagozzi G, Mukhopadhyay S, Betti R, Landi L, Diotallevi PP (2018) Output-only damage detection in buildings using proportional modal flexibility-based deflections in unknown mass scenarios. *Eng Struct* 167:549–566
14. Catbas FN, Gul M, Burkett JL (2008) Damage assessment using flexibility and flexibility-based curvature for structural health monitoring. *Smart Mater Struct* 17(1):015024
15. Koo KY, Lee JJ, Yun CB, Kim JT (2008) Damage detection in beam-like structures using deflections obtained by modal flexibility matrices. *Smart Struct Syst* 4(5):605–628
16. Sung SH, Jung HJ, Jung HY (2013) Damage detection for beam-like structures using the normalized curvature of a uniform load surface. *J Sound Vib* 332(6):1501–1519
17. Sung SH, Koo KY, Jung HJ (2014) Modal flexibility-based damage detection of cantilever beam-type structures using baseline modification. *J Sound Vib* 333(18):4123–4138
18. Catbas FN, Brown DL, Aktan AE (2006) Use of modal flexibility for damage detection and condition assessment: case studies and demonstrations on large structures. *J Struct Eng* 132(11):1699–1712
19. Sung SH, Koo KY, Jung HY, Jung HJ (2012) Damage-induced deflection approach for damage localization and quantification of shear buildings: validation on a full-scale shear building. *Smart Mater Struct* 21(11):115013
20. Le NT, Thambiratnam DP, Nguyen A, Chan THT (2019) A new method for locating and quantifying damage in beams from static deflection changes. *Eng Struct* 180:779–792
21. Quqa S, Landi L, Diotallevi PP (2018) On the use of singular vectors for the flexibility-based damage detection under the assumption of unknown structural masses. *Shock Vibr* 9837694
22. Giordano PF, Limongelli MP (2020) Response-based time-invariant methods for damage localization on a concrete bridge. *Struct Concr* 21(4):1254–1271
23. Restrepo J (2017) Shake table response of full scale reinforced concrete wall building slice (NEES-2006-0203). <https://datacenterhub.org/resources/14548>
24. Panagiotou M, Restrepo JI, Conte JP (2007) Shake table test of a 7 story full scale reinforced concrete structural wall building slice—phase I: rectangular wall section. Report No SSRP-07/07, University of California, San Diego
25. Moaveni B, He X, Conte JP, Restrepo JI (2010) Damage identification study of a seven-story full-scale building slice tested on the UCSD-NEES shake table. *Struct Saf* 32(5):347–356
26. Moaveni B, He X, Conte JP, Restrepo JI, Panagiotou M (2011) System identification study of a 7-story full-scale building slice tested on the UCSD-NEES shake table. *J Struct Eng (ASCE)* 137(6):705–717

27. James GH III, Carne TG, Lauffer JP (1995) The natural excitation technique (NExT) for modal parameter extraction from operating structures. *Int J Anal Exp Modal Anal* 10(4):260–277
28. Juang JN, Pappa RS (1985) An eigensystem realization algorithm for modal parameter identification and model reduction. *J Guid Control Dyn* 8(5):620–627

Vision-Based Damage Detection Using Inclination Angles and Curvature



Chidiebere B. Obiechefu, Rolands Kromanis, Fouad Mohammad, and Zakwan Arab

Abstract This paper presents damage detection techniques for structural health monitoring of horizontal structures using computer vision. A technique based on the derivation of curvature from the second order polynomial equations of the deflection curve is introduced. The technique, as well as inclination angles, and the primary deflection data are applied for damage detection on a simply supported laboratory beam subjected to a point load at its midspan. The beam is loaded and unloaded at intact and damaged states. Measurements are obtained with a smartphone. The measurement resolution is 1 mm/px—a relatively low value. Measurements are pre-processed for measurement noise. Results show that damage can be detected using all three responses analysis techniques. The curvature and inclination angle techniques outperform the deflection technique, especially for damage identification.

Keywords Computer vision · Damage detection · Curvature · Inclination angle · Static response

1 Introduction

Ensuring the safety of bridges is paramount for their continuous operation. This creates opportunities for the development of easy-to-use and affordable structural health monitoring (SHM) and measurement interpretation methods. Computer vision-based SHM (CV-SHM) is gaining much popularity and has a vast potential to become ubiquitous due to its low cost, easy use and accurate measurements [22, 25]. Deformation monitoring is perhaps one of the most popular applications of CV measurement. The first application of CV measurements on full scale bridges dates back to the early 90s [23, 26]. Since then CV measurement systems have been deployed for monitoring both short to medium span [4, 12, 15], and long span

C. B. Obiechefu (✉) · F. Mohammad · Z. Arab
Nottingham Trent University, Nottingham, UK
e-mail: brendan.obiechefu@ntu.ac.uk

R. Kromanis
University of Twente, Enschede, The Netherlands

bridges [27, 29]. An extensive review of all major aspects in CV systems and their applications, and CV-SHM can be found in Refs. [7, 28].

CV-SHM systems must have effective response interpretation techniques compatible with the type of collected response. For example, interpretation techniques for dynamic response seek to find relevant structural dynamic parameters (e.g., vibration frequencies and corresponding mode shapes), while a global static response interpretation technique may seek displacements derived parameters. The parameters are obtained from motions of structural targets, which are either attached to the structure (i.e., artificial targets with known dimensions and patterns) or found on the structure (i.e., natural targets such as bolts in steel bridges). Dynamic testing is the most developed method for vibration-based damage identification in bridges [6]. But the collection of useful vibration parameters may be costly and challenging. For example, (i) high measurement accuracy is needed to capture higher order vibration modes, and (ii) temperature affects dynamic properties, thus also bridge distributed temperature needs to be measured. Static testing maintains the advantage of requiring only stiffness properties of structures, which can be obtained from bridge deflections and yield reliable results for damage detection [2].

In static testing, displacements, tilts, curvatures and strains can form the basis for damage detection [1, 5, 13, 18, 19, 24]. Curvatures, and tilts, for example, are derivatives of deflection curve, and thus directly related to the structure's bending moment and flexural rigidity. This relationship can be explored for damage detection. A change in stiffness affects structural response, hence indicating a change in structure's conditions. An example applications of such relationship for damage detection in horizontal structures is presented in a numerical study [1], where Grey relation analysis was used to detect deviations in the displacement curvatures. Lee and Eun [20] validated an analytical method on a one meter long cantilever beam with severe damages, i.e., 67% stiffness loss at several tested locations also using displacement curvatures. These however were not tested for compatibility with CV measurement systems. Erdenebat et al. [9] proposed a deformation area difference (DAD) based method on the deflection curve from which inclination angles and curvatures are derived. The DAD method uses numerical or theoretical models as a reference system and is able to detect local stiffness reductions of as little as 1% in theoretical models, and 23.8% in laboratory models, with CV measurement [9, 10]. The method has also shown to be suitable for measurement collection on real structures with stationary loads only [8].

The use of derivatives of the deflection curve in the afore-mentioned applications may require information on material properties, boundary conditions, geometry, and load properties (e.g., location, amount, distribution). A measurement approach of similar applicability and accuracy, requiring as little information about the structure as possible, is therefore of interest to researchers and asset owners. In this paper, a curvature technique, where a curvature is computed from second-degree polynomial equations from displacements of reference points (i.e., targets) on the structure, is demonstrated as a part of CV-SHM. The technique has been shown applicable for damage detection on a bridge girder using CV derived parameters using a numerical model [24]. In this study, the application of the technique is demonstrated to

the measurement set obtained from a laboratory beam. At relatively low measurement resolution and low-cost camera sensor the detection of damage was still made possible. The requirements of measurement resolution for in situ applications are discussed, and conclusions from the study are drawn.

2 Method

2.1 Computer Vision-Based SHM

The assumption is that consumer-grade cameras, focused either on an entire bridge or parts of it, are used during measurement collection events to capture deformations of the structure subjected to known loads. Structural displacements along the length of the bridge are computed using image processing from each image frame of a video. Absolute maximum response values at each target location are extracted forming the profile of bridge response along its length. Response at a first measurement collection event is assumed to represent baseline conditions of the bridge. In each new event, bridge response is obtained and compared to baseline response for condition assessment. The CV-SHM process proposed in this study has the following stages:

1. Image acquisition and processing
2. Structural response computation
3. Damage detection.

Image acquisition and processing

The image acquisition stage generally begins with setting up tripod with image acquisition device (with attached lens if required) mounted on a remote, stable ground, and within clear view of the structure. Images/videos are recorded of the required loading event and saved.

Image processing serves to extract structural information from image frames. This is done using available image processing algorithms. These can be either proprietary software (e.g., Video Gauge™ [14]), open source software (e.g., QUBDIsp [22] and DeforMonit [16]), or other appropriate algorithms that can detect and track targets in image frames. An in-depth review of image processing algorithms used in CV-SHM can be found in Ref. [3]. The general steps for most feature or template matching techniques is summarized below and presented in Fig. 1. The reader can seek detailed descriptions in Refs. [17, 18, 28].



Fig. 1 Image processing steps with feature point matching or shape-based tracking

- (i) select a reference image;
- (ii) define a region of interest (ROI) containing pre-selected targets. ROI is usually set such that anticipated target movement is contained within;
- (iii) detect targets using any keypoint or shape-based detector computing a set of their pixel motions;
- (iv) scale pixel displacements to engineering units such as millimetres using either a scale factor or image homography method.

Structural response computation

Vertical displacement

The output of the image processing phase is a set of measurements for each target. Vertical displacement (δ) is the change of a target position in vertical axis (Δy_i), calculated from the target location in the reference and i th image frames (y_0 and y_i respectively). δ at an i th time step can be given by Eq. (1).

$$\delta_i = \Delta y_i = y_i - y_0 \tag{1}$$

These time series are transformed into a displacement response profile (r_δ) for the structure by extracting maximum response (δ_{max}) for each target’s time history (see Fig. 2).

Curvature

For any specified length of a horizontal structure, a second degree polynomial curve can be fit using three equidistant points. A univariate quadratic function that best approximates this fit in a two-dimensional Euclidean plane can then be generated as shown in Eq. (2):

$$f(x) = ax^2 + bx + d \tag{2}$$

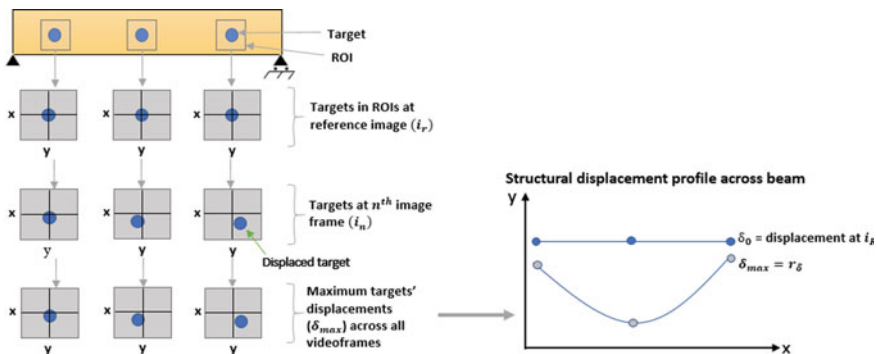


Fig. 2 Obtention of structural response profile

The quadratic coefficient (a), linear coefficient (b) and constant (d) are obtained from Eq. (2). The three equidistant points are targets on a structure [forming a target set (T)]. a determines the degree of curvature of the resultant fit, and therefore becomes the damage-sensitive feature. A larger a value denotes a reduced curvature, a smaller a indicates the opposite. Any target combinations is possible. The curvature response (c_i) for any i th time step is the residual of quadratic coefficients at the first (baseline) and i th time steps given by:

$$c_i = a_0 - a_i \tag{3}$$

In a no-damage condition, and assuming that no noise is added to the measurements, c_i should be 0. The procedure for obtaining a along any specified length of a bridge is described diagrammatically in Fig. 3, also summarized below:

1. Select three targets (t). Targets should be equally spaced. The lesser the space between targets, the better the localization.
2. Specify a target set (T) to contain the three selected targets for which curvature is to be calculated. If a curvature profile for the entire beam is required, then a moving window can be used to derive curvature at each target set (T) across the beam. For example, if target set $T_1 = \{t_1, t_2, t_3\}$, then a moving window can slide from T_1 along the bridge, moving one target each time until the far end is reached, e.g., $T_1 = \{t_1, t_2, t_3\}$, $T_2 = \{t_2, t_3, t_4\}$, $T_3 = \{t_3, t_4, t_5\}$, and so on.

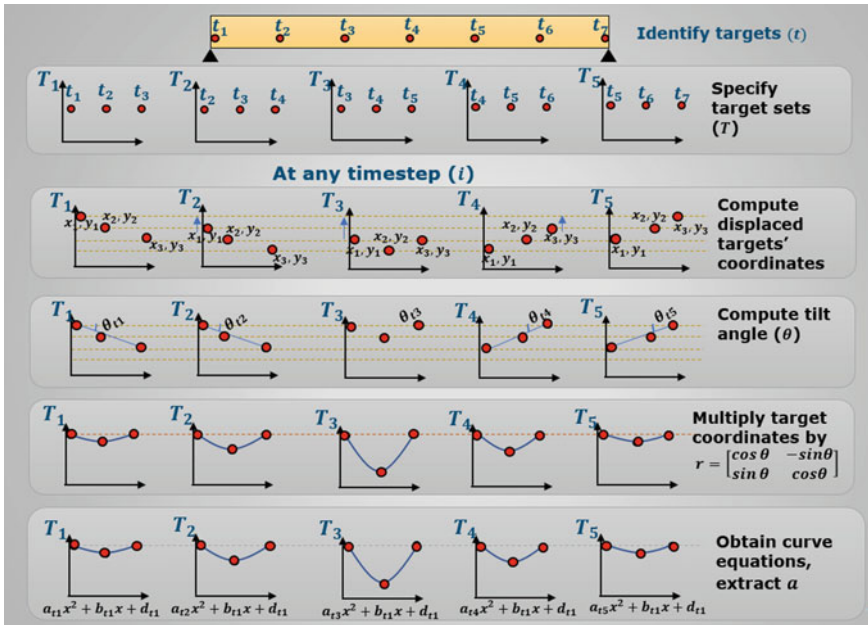


Fig. 3 Curvature calculation

3. Obtain a at T for any image frame using the following procedure:
 - (a) Record target coordinates in each set T .
 - (b) Subtract the three target coordinates in each set T from either the first or last coordinate, whichever is smaller.
 - (c) Obtain inclination angle (θ) of the three coordinate points.
 - (d) Multiply all target coordinates in each set by a rotation matrix.
 - (e) Fit a quadratic curve on each target set and generate quadratic function.
 - (f) Extract quadratic coefficient (a).

Inclination angles

The angle (tangent relationship) (α) between two targets t_k and t_m is computed using Eq. 4. θ_i is the residual between α in the first and i th time steps (see Eq. 5). Inclination angles can be calculated for any two targets on the structure.

$$\alpha = \tan^{-1} \left(\frac{y_{Tk} - y_{Tm}}{x_{Tk} - x_{Tm}} \right) \quad (4)$$

$$\theta_i = \alpha_0 - \alpha_i \quad (5)$$

Damage detection

Structural conditions are evaluated from differences in response, which are due to changes in structural properties, which can be due to the presence of some damage. A response difference curve (Δr) is the difference between a new response and baseline response. This difference is further expressed as a ratio ($e_{r,j}$). The subscripts differentiate between types of response, for example, $e_{\delta,j}$ is the damage feature derived from deflection (δ) at the j th measurement collection event or loading cycle. $e \gg 0$ indicates that the structure is damaged. Damage indicating threshold(s) (γ) can be case-specific. In this study, it is set to 10%. Damage is located where e values spike.

$$e_{r,j} = \frac{\Delta r_j}{r_0} = \frac{r_j - r_0}{r_0} \quad (6)$$

A derivation of e_θ (as proposed in Ref. [24]) is given in Eq. (7) to obtain $e_{\theta,g}$ at the g th response measurement location along the length of a beam. e_θ is computed as the ratio of the range of Δr_θ (q_n) to the mean of r_θ (\bar{r}_θ) for n number of consecutive response measurements. To compute e_θ at the g th response location, values to its left and right are selected so that the g th response location is in the middle. Therefore n needs to be an odd integer, larger or equal to 3. Large n values round q_n and \bar{r}_θ hindering damage locations, thus damages close to supports may not be revealed. However small n values can be sensitive to small, local changes to the response. The selection of n depends on the number of distributed targets (f) on the structure and distance between them. In this study n is set to 3.

$$e_{\theta,g} = \frac{q_{n,g}}{\bar{r}_{\theta,n,g}}, \begin{cases} \frac{(n-1)}{2} < g < f - \frac{(n-1)}{2} \\ n \geq 3 \\ n = \{2k + 1 : k \in \mathbb{Z}\} \end{cases} \quad (7)$$

$$q_{\theta,n,g} = \max_{l,m=1,\dots,n} (\Delta r_{\theta,g-l-1} - \Delta r_{\theta,g-m-1}) \quad (8)$$

$$\bar{r}_{\theta,n,g} = \frac{1}{n} \sum_{l=1}^n |r_{\theta,g-l-1}| \quad (9)$$

3 Laboratory Experiment

3.1 Set up and Loading Scenarios

The data from a test rig used in the study by Kromanis and Kripakaran [18] is selected in this study to demonstrate the curvature and tilt techniques. It is a simply supported, 1080 mm by 25 mm by 45 mm (length by width by depth) timber beam subjected to static, cyclic (loading and unloading phases) point loads at its midpoint (see Figs. 4 and 5). Targets are artificially drawn circles numbered from top left to bottom right as shown. Three 45 mm long section cuts are made at the top of the beam. They are tight fit wooden blocks to simulate an intact condition; removal of a block simulate a damaged condition. Manually, with a 100 N weight, the beam is loaded, and unloaded, for both undamaged and damaged states. Only measurements

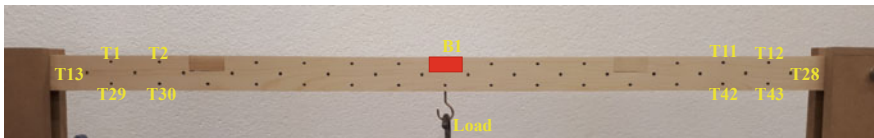


Fig. 4 Laboratory beam set-up

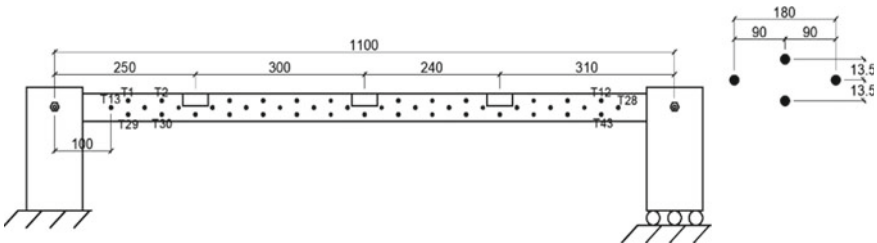


Fig. 5 Laboratory set-up schematic

with the middle block (B1) removed are used in this paper for brevity. The reader is referred to Kromanis and Kripakaran [18] for other damage scenarios. The entire sequence of events involves loading of the undamaged beam, unloading, introduction of damage, and loading again. A Samsung A5 phone camera is positioned to the left of the beam and used for measurement collection. Its field of view covers the entire beam which delivers a measurement resolution of less than 1 mm/px. The adoption of this more affordable but with relatively slightly lower resolution (compared to the very latest iPhones for example) enables us to test the limits of CV-SHM and evaluate that damage detectability at low resolution.

Image processing

The image processing phase is briefly outlined. The three stages in the image processing phase are:

1. **Generation of the geometric projection matrix:** Using four known target coordinates, a geometric projection matrix is generated for use in projective transformation.
2. **Computation of target locations:** The Circular Hough Transform (CHT) method was used for the target detection and location as it is suited for finding circles [30]. The aim of the CHT is to find circular formations of a specified radius R , in an image.
3. **Computation of target motions:** The modified DeforMonit technique is used.
4. **Transformation of target locations to engineering units** using computed geometric transformation matrix.

Response generation

Displacements

Vertical target displacements (δ) are derived from transformed target locations from the projective transformation phase. Figure 6 shows displacement measurement series from target at beam midpoint. Measurements of each target consists of two loading cycles—undamaged, and damaged. The increase in deflection at the second loading cycle as damage is introduced is visible in displacement measurements in

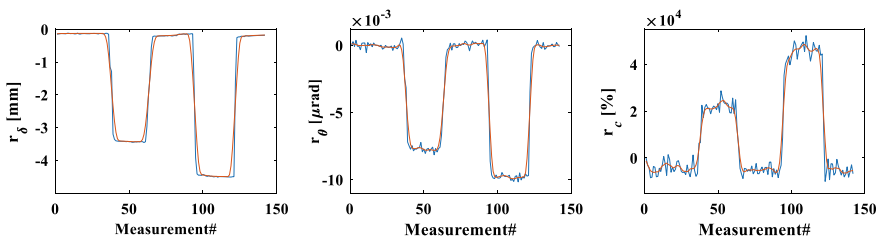


Fig. 6 L–R: displacement series at t_{29} ; tilt series at T_1 (i.e., between t_{29} and t_{30}); curvature series at T_7 (i.e., at beam midpoint). Pre-processed data is represented with amber lines

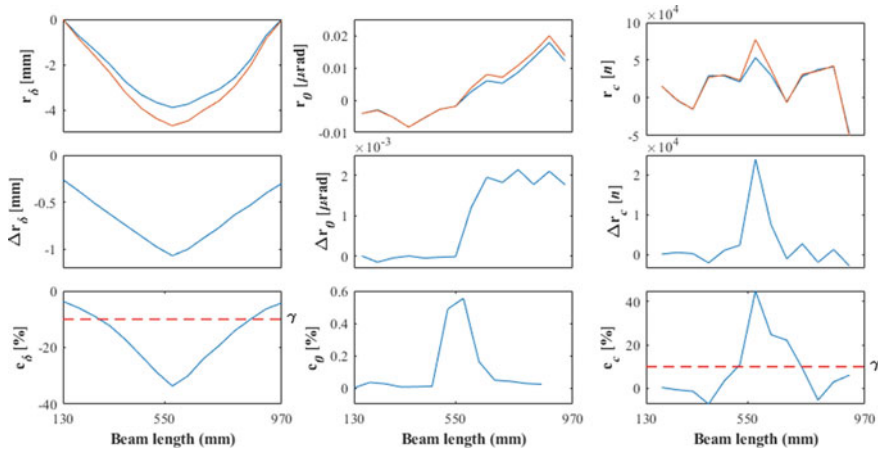


Fig. 7 From left to right: deflection, inclination angle and curvature profiles. From top to bottom: response (r), change in response (Δr) and damage sensitive feature (e). Blue and amber lines in the first row are response at no damage and damage states. Red dashed lines indicate damage threshold

Fig. 6. The response profile is shown in Fig. 7 (left column) for both damaged and undamaged scenarios. The values represent the maximum response of a target.

Tilts

An inclination angle is composed of two targets. To obtain a profile, tilts have to be calculated from successive target sets from one end of the beam to the other. A total of 14 target sets are formed (T_1 to T_{14}). An example of tilt measurements for T_1 and near the left end of the beam is given in Fig. 6 (middle). Maximum inclination angles are then extracted to give the curvature profile of the beam as shown in Fig. 7 (middle).

Curvatures

A target set (T) consist of three successive targets. Bottom targets are used. The first set (T_1) consists of t_{29} , t_{30} , and t_{31} ; T_2 consists of t_{30} , t_{31} , and t_{32} ; and so on until the other end of the beam is reached. There are 13 target sets (T_1 to T_{13}) on the beam. Curvature is calculated for all target sets, at all measurement steps. An example using T_7 near the middle of the beam (where curvature is expected to be the largest) is given in Fig. 6 (left). Maximum curvature is then extracted to give the beam’s curvature profile as shown in Fig. 7 (right column).

Response pre-processing

Since collated structural displacement data can be expected to be noisy, an appropriate technique may be used for its de-noising or smoothening. The choice of smoothing method depends on the signal characteristics. A linear regression over a window of 10 elements for each step worked best with measurements obtained. Pre-processed data is represented with amber lines in Fig. 6. De-noised displacement data is used

for obtention of secondary response. A second de-noising phase may be necessary if secondary data still appears noisy, but this is not the case in this test.

Damage detection

Δr , j and $e_{r,j}$ are obtained for $r = \{\delta, c, \theta\}$ respectively. j th measurements are those taken at the second load cycle where damage was introduced. Figure 7 displays structural performance and damage detection results from the experiment.

From Fig. 7: The first row shows response profile of the beam for all response types. From here response distribution across the beam can be observed. Δr plots (second row) show differences between intact and damaged response. Δr_c but also with Δr_δ values are gradually increasing/decreasing towards the midspan of the beam. e_r plots quantify response deviations hence revealing damage locations where they spike. Damage location is clearly discernible from e_θ and e_c plots, the challenge however is to set a suitable damage indicating threshold. For this study however, spikes in e_r plots indicate damage locations. Damage features from all response types are robust to noise, showing clear spikes that accurately pinpoint damage location. However, e_θ values do not reach the set threshold, therefore the spikes alone will suffice for damage localization at this stage.

Discussions

This paper applies a damage detection technique using beam curvatures from target displacements collected with an affordable camera. Curvature, displacements and inclination angles are measured on a simply supported beam. Structural response computed directly from target displacements (i.e. deflections) are less sensitive to damage; it changes very slowly (see Δr_δ and e_δ plots), hence cannot be relied upon for damage localisation. This is supported by similar studies using the deflection curve of horizontal structures, for example in Erdenebat et al [9]. Tilts and curvatures have sharp spike at damage locations. Damaged locations are clearly discernible when observing e_r plots despite the initially noisy measurements. Damage threshold should be selected based on the level of measurement noise. If measurements are less noisy, it can be set to 5% [24, 21]. If we use 5% here, a lot more areas will be captured, which makes damage localization a bit more difficult. This may, in addition to noise, be partly due to the nature of loading, i.e., moving loads were used in cited studies against point loads in this paper. Developing a more robust damage thresholding system would be a focal point for future studies.

Camera specifications and challenges in field applications

The measurement accuracy of a CV-SHM system is of a vital importance for both monitoring and damage detection purposes. This is largely determined by camera resolution, image processing algorithm, and field of view. The Samsung Galaxy A5 has a resolution of 1080×1920 px, with aspect ratio of 16:9. The field of view covers the entire beam which provides a camera measurement accuracy of about 1 mm/px—a relatively low value, which is insufficient for strain measurement, especially considering the measurement noise. A higher grade camera with sub-pixel image processing could improve the measurement accuracy.

The major challenge of CV-SHM field applications rely on measurement accuracy. Affordable cameras and open source image processing tools makes vision measurement an attractive option for short term measurement collection [7, 11]. But consumer-grade cameras are limited in measurement resolution which limits achievable accuracy, which is further diminished as field of view increases. The CV-SHM approach used in this paper is applicable for short span bridges. Multiple cameras may have to be used if larger areas are to be captured, perhaps with the help of a robotic camera system [17]. The techniques proposed in this paper do not require time synchronisation of vision measurement since maximum response is used. Also, cameras do not need being placed in the same positions at each measurement event since a position-independent approach can be used [18].

Summary and conclusions

This paper describes a damage detection technique using beam curvature, which is obtained from target displacements. By means of an affordable CV measurement collection, the suitability of the technique is validated. The following conclusions are drawn:

- Damage can be detected and located with as low measurement resolution as 1 mm/px and maximum beam midspan deflection of about 5 mm using displacements, curvatures and tilts.
- Pre-processing target displacements may help deriving more accurate structural response, from which bridge response and damage sensitive features are calculated.
- The proposed damage detection techniques do not require a synchronized measurement collection, when multiple cameras are employed. Only the absolute maximum response values, which are extracted from influence lines, are need to derive bridge response.

Future research will evaluate the proposed damage detection techniques on CV measurements from a laboratory setup using a moving load to simulate a bridge-traffic system.

References

1. Abdo MAB (2012) Parametric study of using only static response in structural damage detection. *Eng Struct* 34:124–131. <https://doi.org/10.1016/j.engstruct.2011.09.027>
2. Bakhtiari-Nejad F, Rahai A, Esfandiari A (2005) A structural damage detection method using static noisy data. *Eng Struct* 27:1784–1793. <https://doi.org/10.1016/J.ENGSTRUCT.2005.04.019>
3. Brownjohn JMW, Xu Y, Hester D (2017) Vision-based bridge deformation monitoring. *Front Built Environ* 3. <https://doi.org/10.3389/fbuil.2017.00023>
4. Busca G, Cigada A, Mazzoleni P, Zappa E (2014) Vibration monitoring of multiple bridge points by means of a unique vision-based measuring system. *Exp Mech* 54:255–271. <https://doi.org/10.1007/s11340-013-9784-8>

5. Chen X, Hong-ping Z, Chuan-yao C (2005) Structural damage identification using test static data based on grey system theory. *J Zhejiang University-science A* 6:790–796. <https://doi.org/10.1631/jzus.2005.A0790>
6. Doebling SW, Farrar CR, Prime MB (1998) A summary review of vibration-based damage identification methods. *Shock Vibr Dig* 30:91–105. <https://doi.org/10.1177/058310249803000201>
7. Dong C-Z, Catbas FN (2020) A review of computer vision-based structural health monitoring at local and global levels. *Struct Health Monit* 1. <https://doi.org/10.1177/1475921720935585>
8. Erdenebat D, Waldmann D (2020) Application of the DAD method for damage localisation on an existing bridge structure using close-range UAV photogrammetry. *Eng Struct* 218:110727. <https://doi.org/10.1016/j.engstruct.2020.110727>
9. Erdenebat D, Waldmann D, Scherbaum F, Teferle N (2018) The Deformation Area Difference (DAD) method for condition assessment of reinforced structures. *Eng Struct* 155:315–329. <https://doi.org/10.1016/j.engstruct.2017.11.034>
10. Erdenebat D, Waldmann D, Teferle N (2019) Curvature based DAD-method for damage localisation under consideration of measurement noise minimisation. *Eng Struct* 181:293–309. <https://doi.org/10.1016/j.engstruct.2018.12.017>
11. Feng D, Feng MQ (2016) Output-only damage detection using vehicle-induced displacement response and mode shape curvature index. *Struct Control Health Monit* 23:1088–1107. <https://doi.org/10.1002/stc.1829>
12. Feng D, Feng MQ, Ozer E, Fukuda Y (2015) A vision-based sensor for noncontact structural displacement measurement. *Sensors* 15:16557–16575. <https://doi.org/10.3390/s150716557>
13. Gauthier JF, Whalen TM, Liu J (2008) Experimental validation of the higher-order derivative discontinuity method for damage identification. *Struct Control Health Monit* 15:143–161. <https://doi.org/10.1002/stc.210>
14. Imetrum (2020) Digital image correlation
15. Kim SW, Kim NS (2011) Multi-point displacement response measurement of civil infrastructures using digital image processing. *Procedia Eng.* <https://doi.org/10.1016/j.proeng.2011.07.023>
16. Kromanis R, Al-Habaibeh A (2017) Low cost vision-based systems using smartphones for measuring deformation in structures for condition monitoring and asset management. In: The 8th international conference on structural health monitoring of intelligent infrastructure. Available at: <https://www.researchgate.net/publication/323028607>. Accessed 23 July 2019
17. Kromanis R, Forbes C (2019) A low-cost robotic camera system for accurate collection of structural response. *Inventions* 4(47). <https://doi.org/10.3390/inventions4030047>
18. Kromanis R, Kripakaran P (2021) A multiple camera position approach for accurate displacement measurement using computer vision. *J Civ Struct Health Monit* 1–18. <https://doi.org/10.1007/s13349-021-00473-0>
19. Kromanis R, Liang H (2018) Condition assessment of structures using smartphones : a position independent multi-epoch imaging approach. In: 9th European workshop on structural health monitoring, 10–13 July 2018, Manchester, UK, pp 1–10. Available at: <http://www.ndt.net/?id=23271>
20. Lee E-T, Eun H-C (2008) Damage detection of damaged beam by constrained displacement curvature. *J Mech Sci Technol* 22:1111–1120. <https://doi.org/10.1007/s12206-008-0310-3>
21. Lydon D, Lydon M, Kromanis R, Dong C-Z, Catbas N, Taylor S (2021) Bridge damage detection approach using a roving camera technique. *Sensors* 21:1246. <https://doi.org/10.3390/s21041246>
22. Lydon D, Lydon M, Taylor S, Del Rincon JM, Hester D, Brownjohn J (2019) Development and field testing of a vision-based displacement system using a low cost wireless action camera. *Mech Syst Signal Process* 121:343–358. <https://doi.org/10.1016/j.ymsp.2018.11.015>
23. Macdonald JHG, Dagless EL, Thomas BT, Taylor CA (1997) Dynamic measurements of the second severn crossing. *Proc Inst Civ Eng Transp* 123:241–248. <https://doi.org/10.1680/itrans.1997.29978>

24. Obiechefu CB, Kromanis R (2021) Damage detection techniques for structural health monitoring of bridges from computer vision derived parameters. *Struct Monit Maintenance* 8:91–110. <https://doi.org/10.12989/smm.2021.8.1.091>
25. Shao S, Zhou Z, Deng G, Du P, Jian C, Yu Z (2020) Experiment of structural geometric morphology monitoring for bridges using holographic visual sensor. *Sensors* 20:1–25. <https://doi.org/10.3390/s20041187>
26. Stephen GA, Brownjohn JMW, Taylor CA (1993) Measurements of static and dynamic displacement from visual monitoring of the Humber Bridge. [https://doi.org/10.1016/0141-0296\(93\)90054-8](https://doi.org/10.1016/0141-0296(93)90054-8)
27. Xu Y, Brownjohn J, Hester D, Koo KY (2016) Dynamic displacement measurement of a long span bridge using vision-based system. In: 8th European Workshop On Structural Health Monitoring (EWSHM 2016), July 5–8 2016, Spain, Bilbao
28. Xu Y, Brownjohn JMW (2018) Review of machine-vision based methodologies for displacement measurement in civil structures. *J Civ Struct Health Monit* 8:91–110. <https://doi.org/10.1007/s13349-017-0261-4>
29. Ye XW, Ni YQ, Wai TT, Wong KY, Zhang XM, Xu F (2013) A vision-based system for dynamic displacement measurement of long-span bridges: algorithm and verification. *Smart Struct Syst.* <https://doi.org/10.12989/sss.2013.12.3-4.363>
30. Yuen HK, Princen J, Dlingworth J, Kittler J (2013) A comparative study of hough transform methods for circle finding pp 29.1–29.6. <https://doi.org/10.5244/c.3.29>

Consequences of Heuristic Distortions on SHM-Based Decision



Andrea Verzobio, Denise Bolognani, John Quigley, and Daniele Zonta

Abstract The main purpose of structural health monitoring (SHM) is to provide accurate and real-time information about the state of a structure, which can be used as objective inputs for decision-making regarding its management. However, SHM and decision-making occur at various stages. SHM assesses the state of a structure based on the acquisition and interpretation of data, which is usually provided by sensors. Conversely, decision-making helps us to identify the optimal management action to undertake. Generally, the research community recognizes people tend to use irrational methods for their interpretation of monitoring data, instead of rational algorithms such as Bayesian inference. People use heuristics as efficient rules to simplify complex problems and overcome the limits in rationality and computation of the human brain. Even though the results are typically satisfactory, they can differ from those derived from a rational process. Many heuristic behaviors have been studied and demonstrated, with applications in various fields such as psychology, cognitive science, economics, and finance, but not yet in SHM-based decision. SHM-based decision-making is particularly susceptible to the representativeness heuristic, where simplified rules for updating probabilities can distort the decision maker's perception of risk. In this paper, we examine how representativeness affects the interpretation of data, providing a deeper understanding of the differences between a heuristic method affected by cognitive biases and the classical approach. Our study is conducted both theoretically through comparison with formal Bayesian methods

A. Verzobio (✉) · D. Bolognani · D. Zonta
Department of Civil, Environmental and Mechanical Engineering, University of Trento, Via
Mesiano 77, 38123 Trento, Italy
e-mail: andrea.verzobio@unitn.it

D. Bolognani
e-mail: denise.bolognani@unitn.it

D. Zonta
e-mail: daniele.zonta@unitn.it

J. Quigley
Department of Management Science, University of Strathclyde, SBS Duncan Wing, Glasgow,
Scotland G1 1XQ, UK
e-mail: j.quigley@strath.ac.uk

as well as empirically through the application to a real-life case study about the evaluation of a bridge safety.

Keywords Heuristics · Representativeness · Bayesian inference · Decision-making · Reliability · Bridge management

1 Introduction

Structural health monitoring (SHM) is commonly recognized as a powerful tool that allows bridge managers to make decisions on maintenance, reconstruction, and repair of their assets [4]. The logic of making decisions based on SHM is formally stated in Cappello et al. [8], under the assumption that the decision maker is an ideal rational agent, who judges using Bayes' theorem [6] and decides consistently with Neumann-Morgenstern's Expected Utility Theory (EUT) [22]. Not that surprisingly, it is often observed that real-life decision makers depart from this ideal model of rationality, judging and deciding using common sense and preferring fast and frugal heuristics to rational analytic thinking. Hence, if we wish to describe mathematically and to predict the choices of real-world bridge managers, we have to accept that their behaviour may not necessarily be fully rational. Biased judgement and decision-making have been widely reported and systematically investigated since the 1970s in the fields of cognitive sciences, social sciences, and behavioral economics: key papers include the fundamental works by Kahneman and Tversky [18–20, 31, 32]; Kahneman's famous textbook [13] is an extensive reference for those approaching the topic for the first time.

As regards SHM-based bridge management, apparent irrational behaviors are reported in Zonta et al. [36, 5], Tonelli et al. [29], Verzobio et al. [33, 34], and suggested in Cappello et al. [8]. A typical example of cognitive bias frequently observed in bridge management is the confusion between condition state and safety of a bridge, as reported for instance in Zonta et al. [37]. Safety is about the capacity of a bridge to withstand the traffic loads and the other external actions without collapsing, while the condition state expresses the degree of deterioration of a bridge, or bridge element, with respect to its design state. The condition state is usually appraised through a combination of routing visual inspections, non-destructive evaluation and SHM. It is expressed in the form of a condition index that depends on the specific management system. For example, bridge management systems based on AASHTO [1] Commonly Recognized (CoRe) Standard Element System, such as PONTIS, BRIDGIT and the APT-BMS reported in Zonta et al. [37], classify the state of an element on a scale from 1 to 5, where 1 means 'as per design' and 5 corresponds to the most severe observable deterioration state. On the contrary, the safety of a bridge is typically encoded in its probability of failure P_F , reliability index β , or safety factor γ , evaluated through formal structural analysis.

Condition state and safety are obviously correlated (logically, the load-carrying capacity of a deteriorated bridge is equal or lower than that of the same bridge

in undamaged condition) but are not the same. For example, an old bridge can be unsafe, regardless of its preservation state, simply because it was designed to an old code, which does not comply with the current load demand. As a counterexample, we may have the case of a bridge, severely deteriorated, but still with enough capacity to safely withstand all the external loads, either because of overdesign or simply because its deterioration does not affect its load-carrying capacity. In principle, rational bridge management should target the safety of the bridge stock, and therefore prioritize retrofit of unsafe bridges, regardless of their degree of deterioration. In practice, it is frequently observed that bridge managers tend to delay retrofit of substandard bridges which do not show sign of deterioration, while repair promptly deteriorated bridges as soon as the damage is observed, regardless of the actual residual load-carrying capacity. The biased rationale behind this apparent behaviour is that undamaged bridges ‘look’ safe, while damaged bridges ‘look’ unsafe, simply because it is acknowledged that deterioration negatively affects safety.

The aim of this paper is to describe mathematically this observed biased judgement, a condition that we will show, is broadly described by Kahneman and Tversky’s representativeness heuristic [17]. We clarify that it is not an objective of this paper to suggest that it is correct to use representativeness to judge the state of a bridge: we presume it is evident to any reader that we shall always judge using rational logic, rather than a heuristic method. Indeed, our goal here is to verify whether the irrational judgment sometimes observed in bridge managers could be described and possibly predicted using Kahneman and Tversky’s representativeness heuristic model. Being able to predict the behavior of an irrational manager is necessary when we set a general policy for bridge maintenance and we know, or suspect, that someone else who is going to enact the policy may behave irrationally. As an example, [14] discuss a case where modelling the irrational behavior of a manager is instrumental to an optimization process in bridge maintenance: they use Kahneman and Tversky’s Prospect theory [20] to simulate the biased decision of bridge managers. The authors conclude that the optimal maintenance policy should change if we properly account for the heuristic behavior of the decision makers.

To address our goal, we begin, in Sect. 2, with a review of the formal framework of rational decision based on SHM information. Section 3 discusses various classical judgmental heuristics and the consequential biases, while, in Sect. 4, various mathematical models of representativeness are analyzed and formulated to appropriately reproduce the heuristic behaviour. Finally, Sect. 5 presents an engineering application where the model is used to reproduce the biased evaluation about the safety of a bridge, based on the condition state appraised through visual inspections. Some concluding remarks are presented at the end of the paper.

2 SHM-Based Decision-Making

We refer to the problem of optimal decision-making based on data provided by SHM. As shown in Fig. 1, SHM-based decision-making is properly a two-step process,

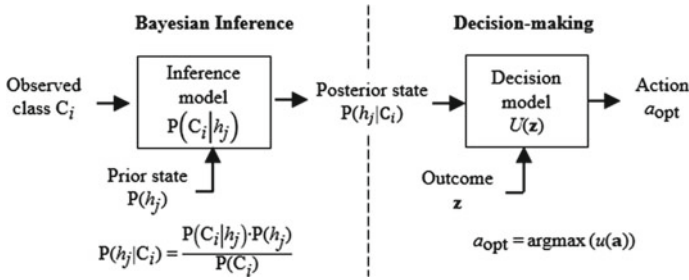


Fig. 1 The rational process of SHM-based decision-making

which includes the judgement of the state of the structure h based on the observations y , and the decision of the optimal action a_{opt} based on the uncertain knowledge of the state. Within the scope of this paper, we define observation to be any information acquired on site which is suitable to infer the state of the structure. Sources of observation, in the broad sense, could be visual inspections, site tests, sensors temporarily or permanently installed on the structure.

Assume that the safety state of the bridge is described by one of n mutually exclusive and exhaustive state hypothesis $\mathcal{H} = \{h_1, h_2, \dots, h_j, \dots, h_n\}$ (e.g.: $h_1 =$ ‘safe’, $\dots, h_n =$ ‘failure’). Further assume that observing the bridge, or bridge element, either through visual inspection or SHM, ultimately consists of assessing its condition out of a number of m possible classes $C_1, C_2, \dots, C_i, \dots, C_m$ which express its degree of damage or deterioration (e.g.: $C_1 =$ ‘not damaged’, $C_2 =$ ‘moderately damaged’, $C_3 =$ ‘severely damaged’, \dots). Therefore, the value of an observation y_i is one of the possible condition classes: $y_i \in \{C_1, C_2, C_3, C_4, C_5\}$. Multiple independent observations on the same bridge may occur because of repeated inspections by different inspectors, or redundant independent measurements by the monitoring system. We indicate with vector \mathbf{y} the full set of observations $\mathbf{y} = \{y_1, y_2, \dots, y_k, \dots, y_N\}$. The likelihood of condition C_i for a bridge, or bridge element, in state h_j is then encoded in the probabilistic distribution $P(C_i|h_j)$.

If we restrict the problem to a single-observation case, the first step of the process consists of judging the state of a structure h_j based on the i th class observed C_i . In the presence of uncertainty, the state of the structure after observing the class C_i is probabilistically described by the posterior probability $P(h_j|C_i)$, and the inference process followed by a rational agent is mathematically developed in Bayes’ rule [6, 26]:

$$P(h_j|C_i) = \frac{P(C_i|h_j)P(h_j)}{P(C_i)}, \quad (1)$$

where $P(h_j|C_i)$ is the posterior knowledge of the structural state and represents the best estimation after the acquisition of SHM observation. It depends on the likelihood $P(C_i|h_j)$ and the prior knowledge $P(h_j)$, which is our estimate of the structural state h_j before the acquisition of the observation. $P(C_i)$ is simply a normalization constant,

referred to as evidence, calculated as:

$$P(C_i) = \sum_{j=1}^n P(C_i|h_j)P(h_j). \quad (2)$$

The second step of the process starts after the assessment of the posterior probability of the structure, and concerns choosing the ‘best’ action. The decision maker can choose between a set of M alternative actions a_1, a_2, \dots, a_M (e.g.: $a_1 =$ ‘do nothing’, $a_2 =$ ‘limit traffic’, $a_3 =$ ‘close the bridge to traffic’, ...). Taking an action produces measurable consequences (e.g.: a monetary gain or loss, a temporary downtime of the structure, in some case causalities) and the consequences of an action can be mathematically described by several parameters (e.g.: the amount of money lost, the number of days of downtime, the number of casualties), encoded in an outcome vector \mathbf{z} . The outcome \mathbf{z} of an action depends on the state of the structure; thus, it is a function of both action a and state h_j , i.e. $\mathbf{z}(a, h_j)$. When the state is certain the consequence of an action is deterministically known; therefore, the only uncertainty in the decision process is the state of the structure h_j . The rational decision-maker ranks actions based on the consequences \mathbf{z} through a utility function $U(\mathbf{z})$, which can vary among different individuals with different behaviors. According to the different risk appetite of the decision-maker, the utility function can be risk neutral, risk adverse or risk seeking. Expected utility theory (EUT) describes the analysis of decision-making under risk and is considered as a normative model of rational choice [23]. EUT was introduced by von Neumann and Morgenstern [22] and later developed in the form that we currently know by Raiffa and Schlaifer [24]. Its axioms state that the decision-maker ranks their preferences based on the expected utility u , defined as:

$$u(a) = E_{h_j}[U(\mathbf{z}(a, h_j))], \quad (3)$$

where E_{h_j} is the expected value operator of the random variable h_j , while U indicates the utility function. The latter is very important and represents the evaluation of a decision-maker’s beliefs about the outcome \mathbf{z} . The decision-maker then chooses the action that maximizes the expected utility.

In summary, the rational way to decide based on observation in the presence of uncertainties goes through a judgment based on Bayes’ theorem and a proper decision based on EUT.

3 Heuristics and Biases

While an ideal rational decision maker judges and decides using Bayes’ theorem and EUT, it is frequently observed that most people in everyday life favor heuristic approaches [13, 20] to this rational framework in order to judge or make decisions.

The concept of heuristic has been defined in different ways in the scientific literature, depending on the discipline and the scope of application, see for instance [10, 12, 25, 30]. For the purpose of this paper, we define a heuristic, together with [10], as any approach to judgement or decision based on rules of thumb, logical simplifications or shortcuts rather than the proper rational process, as described in Sect. 2. Possibly, the most important contribution to the formal characterization of the heuristic behavior is the work that Kahneman and Tversky carried out in the early 1970s [17–19, 31], which had a significant impact to the understanding and description of the human behavior and represents the basis of a discipline we currently refer to as behavioral economics. They developed the so-called heuristics and biases approach, challenging the dominance of strictly rational models. The main innovation lays in the analysis of the descriptive adequacy of ideal models of judgment and in the proposal of a cognitive alternative that explained human error without invoking motivated irrationality. Evidence displays that people's assessments of likelihood and risk do not conform to the laws of probability. They offer a list of frequently observed heuristics [31], which include:

- i. **Representativeness.** Events are ranked according to their representativeness; people consistently judge the more representative event to be the more likely, whether it is or not [17]. Representativeness is not affected by several factors that affect rational judgments instead and this leads to relevant biases, such as: insensitivity to prior probability, insensitivity to sample size, misconceptions of chance, insensitivity to predictability, illusion of validity and misconceptions of regression [31].
- ii. **Availability.** An individual evaluates the frequency of classes or the probability of events by availability, i.e. by the ease with which relevant instances come to mind [18, 19, 31]. Thus, a person could estimate the numerosity of a class, the likelihood of an event or the frequency of co-occurrences by assessing the ease with which the relevant mental operation of retrieval, construction or association can be conducted. It leads to predictable biases, e.g.: biases due to the retrievability of instances, biases due to the effectiveness of a search set, biases of imaginability and biases in the judgment of the frequency with which two events co-occur, i.e. illusory correlation.
- iii. **Adjustment or anchoring.** People make estimates by starting from an initial value (which may be suggested by the formulation of the problem, or it may be the results of a partial computation), that is adjusted to yield the definitive answer. However, adjustments are typically insufficient, that is, different starting points yield different estimates, which are biased toward the initial values, and this phenomenon is called anchoring [31].

Depending on their nature, a heuristic can affect the process outlined in Sect. 2 in the inference step, in the decision step, or in both cases. The rest of the paper will focus on the representativeness, as the heuristic that better reproduces the irrational behaviour introduced in the Introduction. This specific heuristic affects the inference step of the process, i.e. the judgment.

4 The Representativeness Heuristic

Representativeness is commonly intended as the level of how well or how accurately something reflects upon a sample. A judgment is biased by the representativeness heuristic when the ordering of hypotheses h_j by subjective perceived probabilities coincides with their ordering by representativeness, rather than by Bayes' posterior probability [17]. In other words, a hypothesis, or event A, is judged more probable than a hypothesis, or event B, whenever A appears more representative than B. Citing [17], an individual who follows the representativeness heuristic "evaluates the probability of an uncertain event, or a sample, by the degree to which it is: (i) similar in essential properties to its parent population; and (ii) reflects the salient features of the process by which it is generated". This criterion for assessment does not coincide with the Bayesian posterior assessment and so results in a bias.

The literature illustrates numerous cases of behavioral experiments where representativeness bias is observed. For example, in a classic experiment reported in Tversky and Kahneman [31], the interviewee is asked to assess the probability of Steve's employment from a list of possibilities (e.g. farmer, salesman, airline pilot, librarian or physician), simply based on this description: "Steve is very shy and withdrawn, invariably helpful, but with little interest in people, or in the world of reality. A meek and tidy soul, he has a need for order and structure, and a passion for detail." It is observed that most interviewees tend to judge highly likely that Steve is a librarian, simply because the description provided is representative of the stereotype of a librarian, and with complete disregard for the proportion of the population that are librarians compared with the other employments. This example also clarifies that to be representative an uncertain event should not only be similar to its parent population, but it should also reflect the properties of the uncertain process by which it is generated. This agreement on the representativeness formulation is in line with the definition in Tversky and Kahneman [32]; they write that: "an attribute is representative of a class if it is very diagnostic; that is, the relative frequency of this attribute is much higher in that class than in the relevant reference class."

While representativeness heuristic has been widely analyzed from a descriptive point of view, in the literature there are only few models attempting to describe this heuristic from a mathematical perspective, see for instance [3, 7, 9, 11, 15, 16, 27]. While introducing these models, we have two key research questions to explore the definition of representativeness and its application, which are:

- i. What is the mathematical formulation of representativeness proposed by different authors?
- ii. To what extent and how does representativeness bias the final judgment in comparison to Bayes' rule?

4.1 Formulation of Representativeness

In the literature mentioned above there is a general agreement whereby the degree of representativeness of an observable class C_i for a reference hypothesis h_j is in some way related to the odds of observable C_i , which is the ratio between its likelihood $P(C_i|h_j)$ and the likelihood of its negation $P(C_i|-h_j)$, where $-h_j$ denotes the set of alternative hypotheses.

Edward [9], Gigerenzer [11] and Bordalo et al. [7] all define the quantity representativeness $R(C_i, h_j)$ of a class C_i for the reference hypothesis h_j , exactly as the odds of class C_i :

$$R(C_i, h_j) = \frac{P(C_i|h_j)}{P(C_i|-h_j)}. \quad (4)$$

Therefore, they assume that a class C_i is representative for a hypothesis h_j , relative to an alternative hypothesis $-h_j$, if it scores high on the likelihood ratio described by Eq. (4).

Similarly, Tenenbaum and Griffiths [27] define representativeness with the likelihood ratio described by Eq. (4), but using a logarithm scale, apparently to provide a more natural measure of how good a class C_i is in representing a hypothesis h_j :

$$R(C_i, h_j) = \log \frac{P(C_i|h_j)}{P(C_i|-h_j)}. \quad (5)$$

Grether [15, 16] agrees on Eq. (5) for a problem with two possible hypotheses. In the case of more alternative hypotheses, Tenenbaum and Griffiths [27] suggest the following expression:

$$R(C_i, h_j) = \log \frac{P(C_i|h_j)}{\sum_{h_k, k \neq j} P(C_i|h_k)P(h_k|-h_j)}, \quad (6)$$

where $P(h_k|-h_j)$ is the prior probability of the k th hypothesis, given that the reference hypothesis h_j is not the true explanation of C_i : 0 when $j = k$ and $P(h_k)/(1 - P(h_j))$ when $j \neq k$. Equation (6) effectively says that C_i is representative of h_j to the extent that its likelihood under h_j exceeds its average likelihood under alternative hypotheses.

4.2 Representativeness in Judgment

Before revising the mathematical models proposed to reproduce the representativeness bias in judgment, recall that the rational way to judge the probability of a hypothesis h_j based on an observation class C_i is to calculate its posterior probability $P(h_j|C_i)$ in Bayesian sense, using Eq. (1). When judging using the representativeness

heuristic, an individual ranks the hypothesis h_j by a subjective perceived probability which departs from standard Bayesian posterior. In analogy with [7], we define this subjective perceived probability as distorted posterior $P(h_j|C_i)^{st}$. While all authors agree on that representativeness distorts judgment, there is not a general agreement on the cognitive mechanism whereby representativeness affects the distorted posterior probability, i.e. how the standard Bayes' rule, which reflects the judgment of a rational thinker, must be adjusted to consider representativeness instead. Most authors do not provide an explicit expression for the distorted posterior, but understand the vanilla statement that ordering hypotheses by perceived probability follows representativeness rather than Bayesian posterior. From a strict mathematical standpoint, it is possible to define different models of distorted posterior that satisfy this statement. A simple approach would be through assuming that (i) representativeness is used instead of likelihood and (ii) the prior information is neglected. In this case, judgment by representativeness should be consistent with the following expression:

$$P(h_j|C_i)^{st} = \frac{R(C_i, h_j)}{R(C_i, h_j) + R(C_i, -h_j)}. \quad (7)$$

Some of the authors introduced above provide more refined models. Bordalo et al. [7] suggest that representativeness $R(C_i, h_j)$ distorts Bayesian likelihood $P(C_i, h_j)$ as follows:

$$P(C_i|h_j)^{st} = P(C_i|h_j) \cdot (R(C_i, h_j))^\theta \quad (8)$$

where $\theta \geq 0$ is a subjective parameter that describes how heavily representativeness biases the likelihood. According to the same authors, this parameter should be calibrated with cognitive tests and could vary considerably among different people. A biased posterior is therefore inferred, using this distorted likelihood into Bayes' theorem:

$$P(h_j|C_i)^{st} = \frac{P(C_i|h_j)^{st} P(h_j)}{P(C_i)^{st}}, \quad (9)$$

where $P(C_i)^{st}$ is the distorted evidence, calculated as:

$$P(C_i)^{st} = \sum_{j=1}^n P(C_i|h_j)^{st} P(h_j). \quad (10)$$

It is easily noticed that Eq. (9) is exactly Bayes' theorem when $\theta = 0$.

A different approach is provided by Grether [15, 16]. The author suggests a model that provides the final judgment of h_j , by considering the representativeness heuristic:

$$\log O(h_j|C_i) = \alpha + \beta_1 \cdot R(C_i, h_j) + \beta_2 \cdot \log O(h_j), \quad (11)$$

where $O(h_j|C_i)$ is the posterior odds, $R(C_i, h_j)$ is the representativeness calculated as in Eq. (5), $O(h_j)$ is the prior odds, while α , β_1 and β_2 are subjective parameters that

must be calibrated. Thus, the interpretation of Kahneman and Tversky's representativeness heuristic suggested by the author is that individuals place greater weight on the likelihood ratio than on the prior odds. Consequently, the author proposed $\beta_1 > \beta_2 \geq 0$ for this inference model, in contrast with $\alpha = 0, \beta_1 = \beta_2 > 0$ of Bayes' rule.

With the aim to compare these last two judgement models, we express Bordalo et al.'s model, stated in Eq. (8), in its logarithmic posterior odds:

$$\log O(h_j|C_i) = (2\theta + 1) \cdot R(C_i, h_j) + \log O(h_j), \quad (12)$$

where $R(C_i, h_j)$ is, in the same way as in Eq. (11), the representativeness calculated as in Eq. (5). It is possible to notice that this final equation agrees with the one proposed by Grether, i.e. Equation (11), if it is assumed that $\alpha = 0, \beta_1 = (2\theta + 1)$ and $\beta_2 = 1$. This means that the two models are based on the same mathematical formulation, they only differ in the representation of the subjective parameters.

In summary, while there is a general agreement on the definition and the mathematical formulation of the representativeness, different inference models are proposed or understood to describe the biased judgment. Moreover, some of these models account for a number of subjective parameters that have to be properly calibrated on the individual who judges.

5 Case Study

In this section we wish to verify whether the judgment models introduced in Sect. 4 are suitable to describe the typical confusion between condition state and safety of a bridge frequently observed in bridge management. As described in the Introduction, bridge managers often tend to delay retrofit of substandard bridges which do not show sign of deterioration, while repair promptly deteriorated bridges as soon as the damage is observed, regardless of their actual residual load-carrying capacity. We have already observed that the biased rationale behind this apparent behaviour is that undamaged bridges 'look' safe, while damaged bridges 'look' unsafe, simply because, generally speaking, we know that deterioration negatively affects safety.

We discuss this bias with reference to one of the case studies reported in Zonta et al. [37], i.e. the SP65 bridge on the Maso River, which is operated by the Autonomous Province of Trento (APT). The bridge, shown in Fig. 2a, is a common type of bridge in the APT stock. The structure has two simple spans of 19.0 m and 22.0 m, and a total length of 43.0 m. Each span has four girders spaced at 2.1 m, 2.4 m and 2.1 m respectively. The cross-section of the girders is shown in Fig. 2b. The deck slab consists of 22–27 cm of reinforced concrete and a 15 cm surface layer of asphalt. The roadway width is 7 m with 0.70 m pedestrian pavements and hand railing on each side.

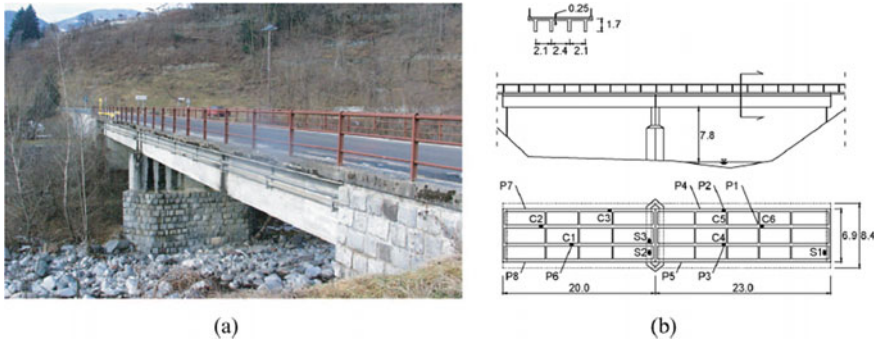


Fig. 2 SP65 bridge on Maso River: **a** overview; **b** plan view, elevation and cross section of the deck [37]

Managing its bridges, APT uses an inventory model and condition state appraisal system consistent with the AASHTO [1] Commonly Recognized (CoRe) Standard Element System. The CoRe element standard has been adopted since 1995 by FHWA and AASHTO as broadly accepted way to represent bridges condition on a uniform scale. The CoRe element standard inventories a bridge into a set of Standard Elements (SE), each specified in term of quantity (surface, length or number). For example, the bridge deck of the SP65 bridge includes the following SE: slab, beam, pavement, sidewalk, guard rail and railing.

The state of deterioration of each element is appraised through routine visual inspections. The inspector classifies the state of deterioration of an element choosing among five possible deterioration levels, called Condition States (CS), specified, for each element type, in the inspector manual. Table 1 reports, as an example, the definition of the five CS of a concrete slab, or CoRe standard element #12, as reported in APT inspection manual available from the website of the APT [2]. As a general rule, Condition State 1 (CS1) always means ‘as per design’, or ‘no deterioration’, while CS5 corresponds to the most severe observable deterioration state.

Table 1 SE #12 concrete slab: state description for each condition state (CS)

CS	State description of the slab surface
1	No delamination, spalling or water infiltration
2	Possible delamination, spalling or water infiltration. Possible segregation and consequently reinforcement exposure
3	Previously repaired or subjected to delamination or spalling. Segregation and consequently reinforcement exposure. Limited water infiltration
4	Extended parts previously repaired or subject to delamination or spalling; deep segregation phenomena with extended exposure of reinforcement. Extended water infiltration
5	Deep deterioration or anomalies. Reinforcement corrosion and cross-section loss require a deep analysis to verify the structural safety of the element

While the deterioration condition is appraised through visual inspection, its safety level is evaluated separately, through a five-step formal assessment procedure [37], whose ultimate objective is to calculate the bridge reliability index β . We have already observed in the Introduction that condition state and safety are obviously correlated, but not the same thing, and that we can well have a severely deteriorated bridge which is perfectly safe or an intact bridge which is not safe. We have also noticed that a rational bridge manager should address safety above all, while in practice the intervention priority is often biased by the apparent state of deterioration of the bridges, regardless their actual residual load-carrying capacity.

In this section, we want to numerically analyze and describe the following case:

- As far as its safety is considered, the bridge could be in two possible states: SAFE (h_S) or FAIL (h_F). SAFE means that, following to a formal safety assessment carried out by an expert structural engineer, the bridge load-carrying capacity is judged sufficient for the bridge to operate without restrictions. On the other hand, FAIL means that the bridge is not found to have sufficient load-carrying capacity and should be closed to traffic.
- Based on a frequentist analysis of the load-carrying capacity formally assessed for similar bridges of the same type and age, it is estimated that only one bridge out of one thousand is found to be in the FAIL state. We formalize this information assuming prior base rates $P(h_F) = 0.001$ for the state hypothesis FAIL, and therefore $P(h_S) = 0.999$ for the state hypothesis SAFE.
- Based on the last visual inspection, the bridge exhibits no or minimal deterioration, except for the concrete slab, which is classified in the most severe condition state, or CS5.
- Based on the condition state assessed via visual inspection, the bridge manager judges the bridge in FAIL state.

This case study effectively describes a prototypical situation where the bridge manager judges the state of safety of the bridge based on the condition state of one of its elements and disregarding any information on its actual residual load-carrying capacity. The manager implicitly assumes that a severe deterioration of an element automatically implies that the bridge load-carrying capacity is insufficient, simply because deterioration is representative for a reduced capacity. We hypothesize this situation could be described as a case of the representativeness bias, where the safety is improperly judged based on how much deterioration is representative of loss in capacity.

In order to verify this conjecture, we will answer quantitatively the following questions:

- (i) What is the likelihood $P(\text{CS}_5|h_F)$ of an unsafe bridge to be in CS5?
- (ii) How much CS5 is representative of a bridge in FAIL state?
- (iii) What is the proper posterior probability of this bridge to be in FAIL state?
- (iv) How does representativeness bias distort the manager judgment as to the bridge safety?

5.1 Likelihood and Representativeness

To start, we have to define a proper likelihood distribution for each hypothesis, i.e. $P(CS_i|h_F)$ and $P(CS_i|h_S)$. In the following, the procedure used for the definition of the likelihood is the same as in Zonta et al. [37].

According to [21], we employ II level probabilistic methods, which allows to calculate the reliability index $\beta = -\Phi^{-1}(P_{h_F})$, where Φ is the cumulative normal distribution function. Two stochastic variables are considered: the loads effect S and the starting resistance R_0 of the bridge, both supposed to be Normal distributions (Norm), with their mean μ and coefficient of variation V . In formula:

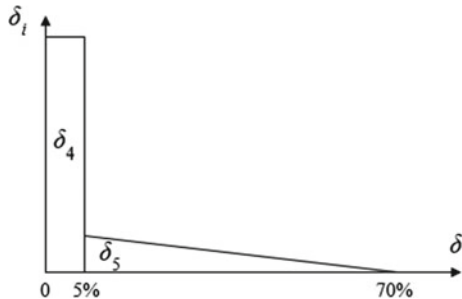
$$f_{R_0}(r) = \text{Norm}(r, \mu_{R_0}, V_{R_0}), \quad f_S(s) = \text{Norm}(s, \mu_S, V_S). \tag{13a,b}$$

Because of the prioritization approach, we assume that the structure will not maintain its mechanical characteristics in the years, i.e. we have to take into account the deterioration of construction material through the following probabilistic degradation model [37]:

$$R = R_0(1 - \delta(CS_i)) \tag{14}$$

where $\delta(CS_i)$ is a probabilistic capacity degradation function, depending only on the CS_i of the SE that controls the capacity of the structural unit at the limit state. Its density function δ_i is the probability density function of the loss in capacity when the element is in the i th CS. Recall that the elements are rated based on visual inspections, δ_i represents the likelihood of a certain loss in capacity when the element has been rated into the i th reference state. Typically, low values of CS, i.e. CS_1 CS_2 and CS_3 , are not associated with any loss of capacity: in this case δ_i coincides with a Dirac delta function and therefore $R = R_0$. On the other hand, higher CS_i are associated with distributions that reflect the uncertainty of the system in correlating the actual loss in capacity, with the verbal description of the reference state proposed by the inspection manual. CS_4 is associated with a uniform distribution δ_4 of loss in capacity, for values of δ included in $[0, 5\%]$. In the same way, the system associates the reference state 5 with a triangular distribution, for values of δ included in $[5\%, 70\%]$, as Fig. 3 shows.

Fig. 3 Capacity degradation function



Because most of the information required to define the distribution of capacity R and actions S are not explicitly contained in the system database, a simplified approach must be adopted. It is convenient to define a normalized capacity $r = R/\mu_S$, with mean value $\mu_r = \mu_{R_0}/\mu_S$, equal to the central safety factor γ_0 , associated with the limit state Z , and a normalized demand $s = S/\mu_S$ with mean value $\mu_s = 1$. The coefficients of variations of the normalized variables γ and s are equal to those of R and S . The Normal distribution of the capacity and actions become:

$$f_{\gamma_0}(r) = \text{Norm}(r, \gamma_0, V_R), \quad f_S(s) = \text{Norm}(s, 1, V_S), \quad (15a,b)$$

where the reliability index is related to the central safety factor γ_0 through the expression:

$$\beta = \frac{\gamma_0 - 1}{\sqrt{V_R^2 \cdot \gamma_0^2 + V_S^2}} \quad (16)$$

Finally, the normalized limit state function is $z = r - s$, and the probability of failure P_{h_F} associated with the limit state Z coincides with that of z :

$$P_{h_F}(\text{CS}_i) = P(Z < 0) = P(z < 0). \quad (17)$$

According to Eurocode 0, if we employ II level probabilistic methods, the target reliability index β for Class RC2 structural member in the Ultimate Limit State and with a reference time of 1 year is equal to $\beta = 4.75$. Assuming $V_R = 0.05$ and $V_S = 0.10$, from Eq. (16) we can obtain $\gamma_0 = 1.96$. Once we know γ_0 , the probability of failure $P_{h_F}(\text{CS}_i)$ is then calculated through Monte Carlo methods by computing the cumulative-time failure probability of the normalized limit state z , by using a normalized Gaussian distribution for the demand $f_S(r)$ and a normalized non-Gaussian distribution for the reduced capacity $r = \gamma_0(1 - f_\delta)$, which depends on CS_i :

$$f_r(r, \text{CS}_i) = f_{\gamma_0}(r)(1 - f_\delta). \quad (18)$$

Consequently, assuming $P_{h_F}(\text{CS}_1) = P_{h_F}(\text{CS}_2) = P_{h_F}(\text{CS}_3)$, we obtain the following failure probability for each CS_i :

$$\begin{aligned} & [P_{h_F}(\text{CS}_1); P_{h_F}(\text{CS}_2); P_{h_F}(\text{CS}_3); P_{h_F}(\text{CS}_4); P_{h_F}(\text{CS}_5)] \\ &= [2.35 \cdot 10^{-5}; 2.35 \cdot 10^{-5}; 2.35 \cdot 10^{-5}; 6.61 \cdot 10^{-4}; 2.04 \cdot 10^{-1}]. \end{aligned} \quad (19)$$

Assuming the following a priori distributions for CS , i.e. $P(\text{CS}) = [50\%, 20\%, 15\%, 10\%, 5\%]$, we can calculate the probability for each hypothesis, i.e. “FAIL = h_F ” and “SAFE = h_S ” respectively:

$$P_{h_F} = \sum_{i=1}^{\text{CSmax}=5} P_{h_F}(\text{CS}_i) \cdot P(\text{CS}_i) = 0.0102, \quad (20)$$

$$P_{h_S} = 1 - P_{h_F} = 0.9898. \tag{21}$$

It is important to explain why these values are different from the assumed prior base rates (i.e. $P(h_F) = 0.001$ and $P(h_S) = 0.999$): APT, as most of the transportation agencies, calculates the nominal probability of collapse using a mechanical model, which is based on conservative assumptions and an estimate of the loss in capacity due to degradation, which is also based on conservative assumptions. In theory, if the model used by APT was unconditionally correct, then P_{h_F} and the prior $P(h_F)$ should be identical. However, in practice the model is clearly conservative and predicts a number of fail cases greater than 1% (i.e. $P_{h_F} = 0.0102$), that is much higher than the actual number frequentistically observed (i.e. $P(h_F) = 0.001$). This is a very typical situation for transportation agencies because prediction models are deliberately conservative. In order to cope with this apparent contradiction, we assume that, although the model is overconservative in the prediction of the probability of collapse, the ratio between two different probability of collapse is reasonably correct. In other words, the mechanical model is not suitable to predict the actual absolute probability of collapse given the CS, but is reliable enough to predict that the probability of collapse of a structure in CS_5 is about 300 times bigger than the probability of collapse in CS_4 .

Then, according to Bayes’ rule, for both hypothesis “S = SAFE” and “F = FAIL” we can evaluate the relative likelihood distributions for each Condition State CS_i , as follows:

$$P(CS_i|h_F) = \frac{P_{h_F}(CS_i) \cdot P(CS_i)}{P_{h_F}}, \quad P(CS_i|h_S) = \frac{(1 - P_{h_F}(CS_i)) \cdot P(CS_i)}{P_{h_S}}. \tag{22a,b}$$

Figure 4 shows the results for each CS_i , which numerically correspond to the following likelihood distributions:

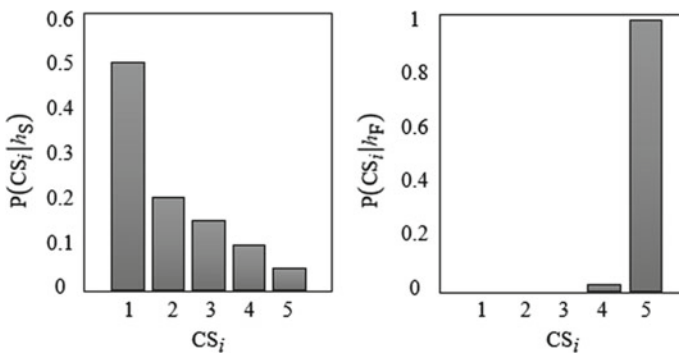


Fig. 4 Likelihood distributions for each state hypothesis

$$\begin{aligned} P(\text{CS}_i|h_S) &= [50\%, 20\%, 15\%, 10\%, 5\%], \\ P(\text{CS}_i|h_F) &= [0, 0, 0, 2\%, 98\%]. \end{aligned} \quad (23a,b)$$

After the evaluation of the likelihoods, we are interested in understanding how much CS_5 is representative of the bridge in FAIL state. We can calculate it according to Eq. (4):

$$R(\text{CS}_5|h_F) = 19.6, \quad R(\text{CS}_5|h_S) = 0.05. \quad (24a,b)$$

These outcomes show that, as expected, CS_5 is very representative of the failure state of the bridge, with an enormous difference in comparison to the safe state of the bridge, i.e. $R(\text{CS}_5|h_F) \gg R(\text{CS}_5|h_S)$: this is very important because we have learnt that this can be the reason for a distorted final judgment.

5.2 Posterior Judgment

We evaluate the posterior judgment of the manager, in the case that the bridge is classified in CS_5 . The proper posterior probabilities, computed using the rational framework provided by Bayes' theorem, results:

$$P(h_F|\text{CS}_5) = 1.92\% < P(h_S|\text{CS}_5) = 98.08\%. \quad (25)$$

This means that rational managers, in line with Bayes' rule and after observing CS_5 , would judge the possibility that the bridge could be in the FAIL state as very unlikely.

However, we have introduced before that, based on the condition state assessed via visual inspection, the bridge manager has judged the bridge in FAIL state. It is possible to explain this judgment by evaluating the distorted posterior probability. Using the vanilla inference model of Eq. (7), we achieve:

$$P(h_F|\text{CS}_5)^{st} = 99.75\% > P(h_S|\text{CS}_5)^{st} = 0.25\%. \quad (26)$$

Similarly, accepting the inference model of Bordalo et al., the distorted posterior probability is:

$$P(h_F|\text{CS}_5)^{st} = 69.97\% > P(h_S|\text{CS}_5)^{st} = 30.03\%. \quad (27)$$

In both cases the failure state turns out to be the most likely, and this outcome allows to explain the judgment of the manager, which is biased since CS_5 is very representative of a fault bridge.

Table 2 reports all the achieved results; the last row of the table presents again the results that come from the inference model of Grether, which agree with those

Table 2 Achieved results for each model

Model	Likelihood $P(C_i h_j)$ or representativeness $R(C_i h_j)$	Posterior probability $P(h_j C_i)$	Posterior odds $P(h_j C_i)/P(-h_j C_i)$
Bayes	$P(CS_5 h_F) = 0.98$ $P(CS_5 h_S) = 0.05$	$P(h_F CS_5) = 1.92\%$ $P(h_S CS_5) = 98.08\%$	$\frac{P(h_F CS_5)}{P(h_S CS_5)} = 0.02$
Vanilla model (Eqs. 4 and 7)	$R(CS_5 h_F) = 19.6$ $R(CS_5 h_S) = 0.05$	$P(h_F CS_5)^{st} = 99.75\%$ $P(h_S CS_5)^{st} = 0.25\%$	$\frac{P(h_F CS_5)^{st}}{P(h_S CS_5)^{st}} = 399$
Bordalo et al. ($\theta = 0.8$)	$R(CS_5 h_F) = 19.6$ $R(CS_5 h_S) = 0.05$	$P(h_F CS_5)^{st} = 69.97\%$ $P(h_S CS_5)^{st} = 30.03\%$	$\frac{P(h_F CS_5)^{st}}{P(h_S CS_5)^{st}} = 2.33$
Grether ($\alpha = 0; \beta_1 = 0.8; \beta_2 = 0.2$)	$R(CS_5 h_F) = 2.98$ $R(CS_5 h_S) = -2.98$	$P(h_F CS_5)^{st} = 73.19\%$ $P(h_S CS_5)^{st} = 26.81\%$	$\frac{P(h_F CS_5)^{st}}{P(h_S CS_5)^{st}} = 2.73$

obtained with the other biased models, i.e. the FAIL state is the most likely, in contrast to the rational conclusion inferred through Bayes’ theorem.

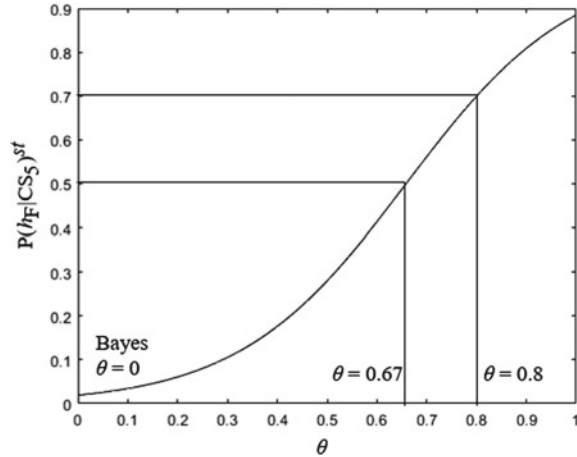
In summary, we have demonstrated that when an inspector judges the safety state of a bridge by only accounting for the observed condition state CS, they are biased by representativeness: in their posterior judgments they tend to neglect the prior probability of the failure condition, which is typically very low, $P(h_F) = 0.001$ in this specific case study, and to weight too much the ratio between the likelihood of the observations, which is the representativeness itself. Therefore, their final judgment results distorted in comparison to the one achieved by a manager who stick to rational thinking.

5.3 Discussion About Inference Models

To develop the numerical calculations in the previous sections, we had to assume specific values for the subjective parameters of the inference models introduced in Sect. 4.2, i.e. $\theta = 0.8, \alpha = 0, \beta_1 = 0.8, \beta_2 = 0.2$: these values correspond to a high level of the representativeness heuristic since they maximize the importance of R and minimize the contribute of the prior information. Since these parameters depend on different behaviour of people and could vary considerably, it is interesting to develop a sensitivity analysis in order to understand how they affect the model and then the conclusive results.

Let’s take for instance the model of Bordalo et al.: as we can see from Eq. (8), it depends only on one subjective parameter, i.e. $\theta \geq 0$. Figure 5 shows how the posterior failure probability of the bridge, after observing CS_5 , varies according to θ : even if θ can be also larger than 1, we study just the interval $0 \leq \theta \leq 1$ since this is sufficient to understand how the results change. The previous assumption of $\theta = 0.8$ resulted

Fig. 5 How the distorted posterior probability $P(h_F|CS_5)$ st varies according to the subjective parameter θ



in $P(h_F|CS_5) = 69.97\%$, but we notice that the outcome is highly sensitive to the choice of θ : it changes from $P(h_F|CS_5) = 1.92\%$ if $\theta = 0$, i.e. in line with a rational manager who follows Bayes' rule, to $P(h_F|CS_5) = 88.49\%$ if $\theta = 1$, i.e. in line with an irrational manager biased with a high level of the representativeness heuristic. Furthermore, we observe that the posterior failure probability $P(h_F|CS_5)$ is larger than the posterior safe probability $P(h_S|CS_5)$ when $\theta > 0.67$. These results demonstrate the importance of calibrating properly the subjective parameters according to the specific inspector. The same generic conclusions can be extended to the model of Grether, since we have demonstrated that it is based on the same mathematical formulation.

Conversely, the vanilla model introduced in Eq. (7) is less sophisticated because it does not depend on a subjective parameter. Even if this may seem like a shortcoming, the results obtained in Sect. 5.2 demonstrate the correctness of the vanilla model in reproducing the distorted judgment based on the representativeness bias. In detail, it is evident that its outcomes are similar to those that can be obtained assuming the maximum level of representativeness in the subjective parameters of the other inference models. As such, the vanilla model reproduces the behaviour of an inspector completely biased by this heuristic. This conclusion is consistent with the mathematical formulation of the model itself, since it overlooks the contribution of the prior and it completely replaces the likelihood with the representativeness.

6 Conclusions

Judging the state of a bridge based on SHM observations is an inference process which should be rationally carried out using a logical approach. However, we often observe that real-life decision makers depart from this ideal model of rationality, judge and decide using common sense, and privilege fast and frugal heuristics to

rational analytic thinking. For instance, confusion between condition state and safety of a bridge is one of the most frequently observed examples in bridge management. In this contribution, we have demonstrated that this bias can be described by Kahneman and Tversky's representativeness heuristic.

A review of the technical literature shows that representativeness heuristic has been widely analyzed from a descriptive point of view, while only few models have been proposed to describe this bias from a mathematical perspective. In the literature there is a general agreement that the degree of representativeness of an observable class for a reference hypothesis is in some way related to odds of observable quantities. However, there is not a general agreement on how the standard Bayes' rule, which is typically taken as the baseline model to reproduce the judgment of a rational thinker, should be distorted to consider representativeness. Most authors do not provide an explicit expression for the distorted posterior, but understand the statement that ordering hypotheses by perceived probabilities follows representativeness rather than Bayesian posterior. This is consistent with a distorted judgement model, here referred to as 'vanilla', whereby (i) representativeness is used instead of likelihood and (ii) the prior information is neglected. Bordalo et al. and Grether provide more refined models for reproducing the subjective distorted judgement, which allow to blend more flexibly likelihood, representativeness and prior information, through a number of subjective parameters, in order to better reproduce the distorted perception of a particular subject.

We have applied the mathematical models to the case of a transportation manager who wrongly judges a particular bridge unsafe simply because deteriorated, regardless its actual residual load-carrying capacity. Their judgment is biased due to the apparent behaviour that damaged bridges 'look' unsafe, in contrast with undamaged bridges which 'look' safe. In the particular case study, we have demonstrated that Bayes' theorem correctly identifies the bridge as safe, while application of the three judgment models analysed (vanilla, Bordalo et al.'s and Grether's) all predict the manager will mistakenly judge the bridge as unsafe based on the observed condition state. Given the simplicity of the case study, which is essentially a two hypotheses inference problem where the individual distorted behaviour is characterized by the ordering of the two hypotheses by subjective probabilities, the three models are equivalent in this particular instance, as they reproduce equally well the observed distorted perception. The main difference between these three inference models is that 'vanilla' model reproduces the behaviour of an individual whose judgement is blatantly driven by representativeness, while the other two models describe more subtle forms of distorted judgment, whose limit cases are rational Bayesian inference on one side and the vanilla representativeness bias on the other. The three models may not be equivalent in a more complex setting, where the vanilla inference model may fail to reproduce the observed representativeness bias. Bordalo et al.'s and Grether's model are clearly more flexible, but at the same time very sensitive to a number of subjective parameters, which have to be accurately calibrated, typically with cognitive tests, on the particular individual whose distorted judgment is to be described. While it is not the objective of this paper, we suggest that there may be applications which require to precisely identify the best representativeness model, and then the

subjective parameters, for example if we need to predict the rational behaviour of the manager in a future instance: in this case we would need additional observations of the manager behaviour, in order to identify the proper model. This can be done either by further unelicited observations or through proper cognitive tests in an elicitation process: see Verzobio et al. [35] for an example of elicitation process applied to an engineering real-life case study.

To conclude, we reiterate once again that we are not suggesting in any way that representativeness should be used instead of rational logic. At the same time, predicting the actual behavior of managers is required when setting a general policy for bridge maintenance, acknowledging that the managers who are going to enact the policy may behave irrationally.

References

1. American Ass. State Highway and Transportation Off. (1997). AASHTO guide for commonly recognized (CoRe) structural elements. AASHTO, Washington D.C.
2. Autonomous Province of Trento (2018) www.bms.provincia.tn.it/bms
3. Barberis N, Shleifer A, Vishny R (1998) A model of investor sentiment. *J Financ Econ* 49(3):307–343
4. Bolognani D, Verzobio A, Tonelli D, Cappello C, Glisic B, Zonta D, Quigley J (2018) Quantifying the benefit of structural health monitoring: what if the manager is not the owner? *Struct Health Monit* 17(6):1393–1409
5. Bolognani D, Verzobio A, Tonelli D, Cappello C, Zonta D, Glisic B (2017) An application of prospect theory to a SHM-based decision problem. In: *Proceedings of SPIE, Portland*
6. Bolstad WM (2010) *Understanding computational Bayesian statistics*. Wiley, NJ, USA
7. Bordalo P, Coffman K, Gennaioli N, Shleifer A (2016) Stereotypes. *Quart J Econ* 131(4):1753–1794
8. Cappello C, Zonta D, Glisic B (2016) Expected utility theory for monitoring-based decision-making. *Proc IEEE* 104(8):1647–1661
9. Edward W (1968) Conservatism in Human information processing. In: Kleinmuntz B (ed) *Formal representation of human judgment*. Wiley, New York, pp 17–52
10. Feigenbaum EA, Feldman J (1963) *Computers and thought*. McGraw-Hill Inc, New York
11. Gigerenzer G (1995) How to improve Bayesian reasoning without instruction: frequency formats. *Psychol Rev* 102(4):684–704
12. Gigerenzer G, Gaissmaier W (2011) Heuristic decision making. *Annu Rev Psychol* 62:451–482
13. Gilovich T, Griffin DW, Kahneman D (2002) *Heuristics and biases: the psychology of intuitive judgment*. Cambridge University Press
14. Gong C, Frangopol DM (2020) Condition-based multiobjective maintenance decision making for highway bridges considering risk perceptions. *J Struct Eng* 146(5)
15. Grether DM (1980) Bayes rule as a descriptive model: the representativeness heuristic. *Quart J Econ* 95(3):537–557
16. Grether DM (1992) Testing Bayes rule and the representativeness heuristic: some experimental evidence. *J Econ Behav Organ* 17(1):31–57
17. Kahneman D, Tversky A (1972) Subjective probability: a judgment of representativeness. *Cogn Psychol* 3:430–454
18. Kahneman D, Tversky A (1973) Availability: a heuristic for judging frequency and probability. *Cogn Psychol* 5(2):207–232
19. Kahneman D, Tversky A (1973) On the psychology of prediction. *Psychol Rev* 80(4):237–251

20. Kahneman D, Tversky A (1979) Prospect theory: an analysis of decision under risk. *Econometrica* 47(2):263–292
21. Melchers RE (1999) Structural reliability: analysis and prediction, 2nd edn. Wiley, Chichester
22. Neumann JV, Morgenstern O (1944) Theory of games and economic behavior. Princeton University Press, New Jersey
23. Parmigiani G, Inoue L (2009) Decision theory: principles and approaches. Wiley, Chichester
24. Raiffa H, Schlaifer R (1961) Applied statistical decision theory. Clinton Press, Boston
25. Romanycia MH, Pelletier FJ (1985) What is a heuristic? *Comput Intell* 1(1):47–58
26. Sivia D, Skilling J (2006) Data analysis: a Bayesian tutorial. Oxford University Press, Oxford
27. Tenenbaum JB, Griffiths T (2001) The rational basis of representativeness. In: Proceedings of the annual meeting of the cognitive science society. 23. Edinburgh: Proceedings of the 23rd annual conference of the cognitive science society
28. Tonelli D, Verzobio A, Cappello C, Bolognani D, Zonta D, Bursi SO & Costa C (2017) Expected utility theory for monitoring-based decision support system. Stanford, USA, Proceedings of the 11th International Workshop on Structural Health Monitoring
29. Tonelli D, Verzobio A, Bolognani D, Cappello C, Glisic B, Zonta D, & Quigley J (2018) The conditional value of information of SHM: what if the manager is not the owner?. Proceedings of SPIE, Denver (USA)
30. Tonge FM (1960) Summary of a heuristic line balancing procedure. *Manage Sci* 7(1):21–42
31. Tversky A, Kahneman D (1974) Judgment under uncertainty: heuristics and biases. *Sci New Ser* 185:1124–1131
32. Tversky A, Kahneman D (1983) Extensional versus intuitive reasoning: the conjunction fallacy in probability judgment. *Psychol Rev* 90(4):293–315
33. Verzobio A, Bolognani D, Quigley J & Zonta D (2018) The consequences of Heuristic distortions on SHM-based decision problems. Manchester, UK, Proceedings of the 9th European Workshop of Structural Health Monitoring
34. Verzobio A, Bolognani, D, Zonta D & Quigley J (2019) Quantifying the benefit of structural health monitoring: can the value of information be negative?. Proceedings of the 12th International Workshop on Structural Health Monitoring, Stanford (USA)
35. Verzobio A, El-Awady A, Ponnambalam K, Quigley J & Zonta D (2020, in press): An elicitation process to quantify Bayesian networks for dam failure analysis. *Can J Civ Eng. Advance online publication*. <https://doi.org/10.1139/cjce-2020-0089>
36. Zonta D, Glisic B, Adriaenssens S (2014) Value of information: impact of monitoring on decision-making. *Struct Control Health Monit* 21:1043–1056
37. Zonta D, Zandonini R, Bortot F (2007) A reliability-based bridge management concept. *Struct Infrastruct Eng* 3(3):215–235

Fatigue Life Prediction for a Concrete—Steel Composite Viaduct: A Process Based on Indirect Measurements



A. Del Grosso, M. Cademartori, P. Basso, S. Osmani, F. Di Gennaro,
and F. Federici

Abstract Traffic fatigue cycles generated in steel bridge components is one of the major issues that can affect these types of structures. This paper introduces a strategy aimed at the fatigue damage assessment and remaining fatigue life prediction of concrete—steel composite bridges under traffic loads using monitoring data. The novelty of the proposed approach consists in the possibility of performing the assessment by means of indirect measurements, i.e. predicting damage at structural sections different from sensors positions. The proposed predictive model can work with real monitoring data collected, providing information on the fatigue life of selected hotspots, thus contributing to plan lifetime maintenance. To support real-time life-cycle management of infrastructures, the acquired data and the corresponding fatigue predictions are visualized in the BIM model. The strategy has been developed in the context of the European Project RAGTIME European Commission Research and Innovation Action, Horizon 2020 [1] and has been applied on a real viaduct in the northern Italy, the Mondalavia viaduct.

Keywords BIM · Fatigue damage · Predictive maintenance · SHM · Multiple linear regression · Machine learning

1 Introduction

The paper deals with the assessment of fatigue damages on concrete—steel composite bridges originated by traffic loads. Specifically, a predictive model that makes possible such an assessment based on indirect measurements, i.e. measures taken

A. Del Grosso
University of Genova, Genoa, GE, Italy

M. Cademartori · P. Basso · S. Osmani (✉)
Rina Consulting S.p.A, via Cecchi, Genoa, GE, Italy
e-mail: Saimir.osmani@rina.org

F. Di Gennaro · F. Federici
Aiscat Servizi S.R.L, Rome, Italy

at locations or structural components other than those where fatigue needs to be quantified (hotspots), is introduced.

In order to be applicable, the proposed model requires the preliminary development of a virtual representation of the structure, e.g. a Finite Element (FE) model or a surrogate model. Then, via the virtual model, it is possible to perform a set of simulations to build the correlations among the measurements at sensor positions and fatigue at hotspots.

Simulations of pseudo—random traffic flows over the bridge are performed as Direct Integration Time Histories (DITH) analyses for which loads of realistic vehicles are considered. For the evaluation of the fatigue damage, the Palmgren-Miner rule is applied, while for the count of the stress cycles, the Rainflow method is adopted.

Once tested, the predictive model can be used for the evaluation of fatigue life of selected hotspots starting from a generic set of monitoring data.

2 Predictive Model for Concrete—Steel Composite Bridges Fatigue Assessment

The main steps of the proposed model are reported in the next sections. The first step consists in the implementation of the BIM model of the Bridge. Then, an analytical model is associated to the BIM model in order to perform FE analyses. Once the FE model is defined, realistic traffic flows are represented as combinations of moving loads and dynamic analyses can be performed. From each analysis, i.e. simulation of traffic flow on the bridge, the strains at sensor locations originated from each traffic load scenario and the corresponding stresses at hotspots, required for the determination of the damage accumulation, are recorded. Based on these two sets of data, the machine learning training process for the predictive model generation is finally undertaken.

2.1 BIM and FE Models Validation

The initial development of a virtual representation of the bridge structure is required. Such a representation can be made through different kind of models; typical representations are made through surrogate/mathematical models or FE models [2]. More recently, some authors [3] have introduced the advantages in using BIM as the primary representation of the structure (Building Information Model), still coupling it with the analytical model, i.e. FE model, but keeping input and output data available in the BIM environment.

Following this last approach, the BIM of the bridge is developed, thus characterizing each principal component of the bridge, principal steel girders, diaphragms,

studs and deck. Within the BIM, the position of the fiber optic sensors for the local strain measurement is placed with the aim of getting a significant deformed configuration of the bridge deck during the traffic loads. In the same way, fatigue hotspots are identified, in order to correlate the BIM to the FE model. In principle, any selection in terms of number and location of hotspots, as well as sensors, is possible. Anyway, this selection should consider some criteria, e.g. number and distribution proportional to the bridge dimension and heterogeneity of structural components. For the purpose of the selected case study, the selected hotspots were the girder beams joints, as they represent the most critical points for the type of bridge against fatigue phenomenon.

From the BIM the FE model of the structure can be easily obtained. However, for the sake of analyses performance, a simplification of the BIM representation is carried out within the transformation process.

Once the link between the BIM and the FE model is set, it is then possible to store, visualize and manage in unique place all the inputs and outputs coming from the analytical model, from the Predictive Model that will be generated on top of it, and from the Structural Health Monitoring (SHM). In this manner, for instance, it is trivial for the infrastructure manager to control and interpret the fatigue damage accumulation over years. The BIM can be additionally used to manage and visualize the implementation of any intervention or mitigation action developed during the infrastructure life, thus becoming a fully integrated part of the decision support process.

2.2 Traffic Simulations Through Dynamic Analysis

In order to build a correlation between the strains at sensor locations and the fatigue damage generated at critical locations of the bridge structure (hotspots), a set of dynamic analyses is conducted in the FE model considering typical vehicle loads.

To generate pseudo-random realistic traffic flows over the bridge, a list of typical vehicles classes is assumed (Fig. 1) and, for each class, a range of possible values for axis loads, axes spacing, vehicle speed, distance between vehicles, etc. is set up.

Then the traffic flows simulations are developed as Monte Carlo simulations, by varying the previously mentioned parameters, e.g. the speed and distance between vehicles in the longitudinal direction and the vehicle distribution in the other direction. The output of the dynamic analyses is reported in terms of strains at sensors locations and stress cycles at hotspots.

2.3 Machine Learning Training

The simulations data are processed through a machine learning algorithm developed in Python Language which consider the two matrices of data derived from the previous analyses, the first one containing the list of strain values at sensor locations

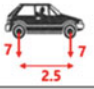
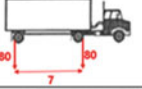
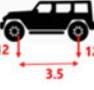
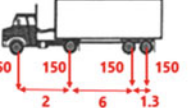
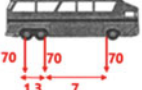
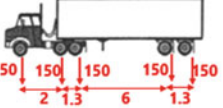
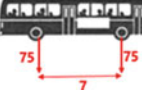
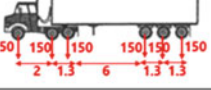
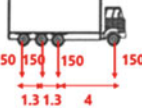
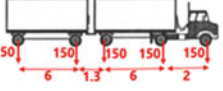
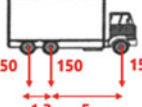
Vehicle classes	Distance between axes [m] and loads for each axis [kN]	Vehicle classes	Distance between axes [m] and loads for each axis [kN]
Passenger Car Category 1		Single Trailer Truck Category 1	
Passenger Car Category 2		Single Trailer Truck Category 2	
Bus Category 1		Single Trailer Truck Category 3	
Bus Category 2		Single Trailer Truck Category 4	
Single Unit Trucks Category 1		Trailers Truck Category	
Single Unit Trucks Category 2			

Fig. 1 Typical vehicle classes considered in the dynamic analyses

(Matrix A) and the second one the matrix of stresses at hotspots for each simulated traffic scenario. The matrix A is used as the Input, necessary for the identification of the deck deformation during each simulation, and the Matrix B is the correspondent Output. The matrix B contains the hotspots' stresses useful for the evaluation of the fatigue damage through the Palmgren-Miner rule [4] and the cycles are counted by the use of the Rainflow Approach [5, 6].

These two matrices are the input and output matrices of the process that is considered for the training phase of the machine learning through a Multiple Linear Regression method (Fig. 2).

The aim of the machine learning algorithm is to interpret the existing correlation between sensor strains and hotspot fatigue damage accumulated. Once established the correlation between these two matrices, is possible to use the Predictive model for the evaluation of fatigue damage over years starting from the monitoring data derived from the sensors installed over the bridge. These outputs are directly connected and stored inside the BIM model of the bridge [3]. In the BIM model is also possible to store and visualize the sensors' strains (from SHM) trend and stories (Fig. 3).

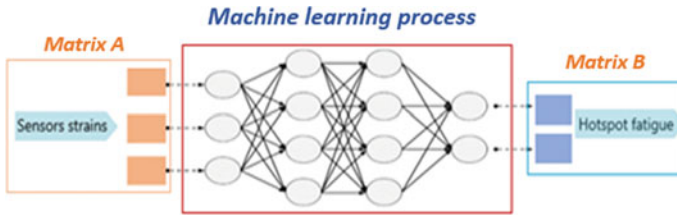


Fig. 2 Machine learning training phase—input and output

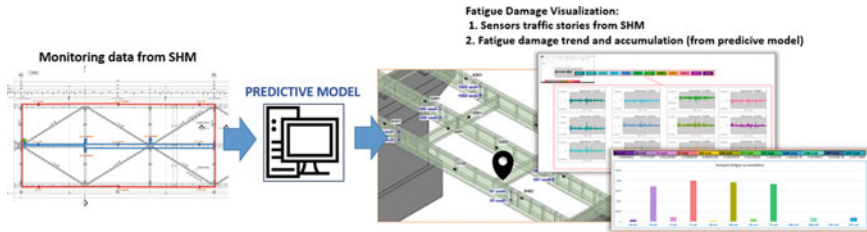


Fig. 3 Application of the predictive model

3 Predictive Model Validation

For the validation phase of the Predictive Model a big number of simulations was run at first in order:

- to guarantee a realistic correlation between strain values at sensor locations and the correspondent induced fatigue damage at hotspots, and
- to cover as much as possible different combinations of traffic loads.

As a first validation test to prove the effectiveness of the proposed model, a comparison of the cumulated fatigue damage after N simulations, determined using the FE model results and the Palmgren-Miner rule with the predicted fatigue accumulation obtained using the Predictive Model was performed. The results are reported in Fig. 4 and demonstrate that the corresponding calculated and predicted values are close to match.

A second validation test was then performed where the predicted cumulated fatigue damage is compared this time with an assumed constant cumulated damage, i.e. assuming a constant value of damage equal to the mean damage derived from all the simulations (blind assumption).

As it can be interpreted from Fig. 5, the blind assumption overestimates the real cumulated damage by far.

And at the end, a validation considering how much differ the predicted values and the blind assumption values from the real one. The results show that the predicted values differ only 6% from the real values of fatigue damage. Meanwhile, the blind assumption values differ almost 94% from the real values.

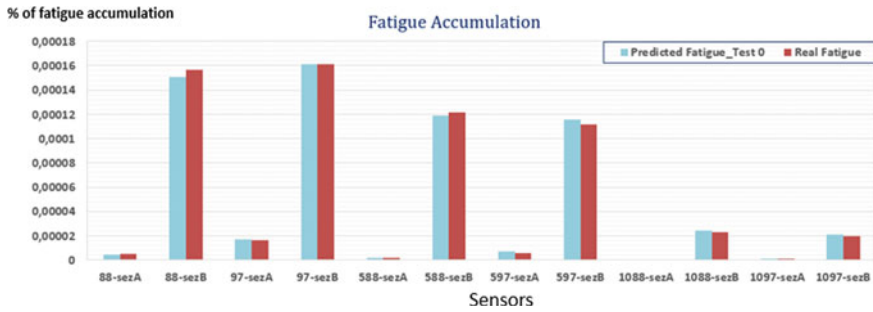


Fig. 4 Fatigue accumulation comparison

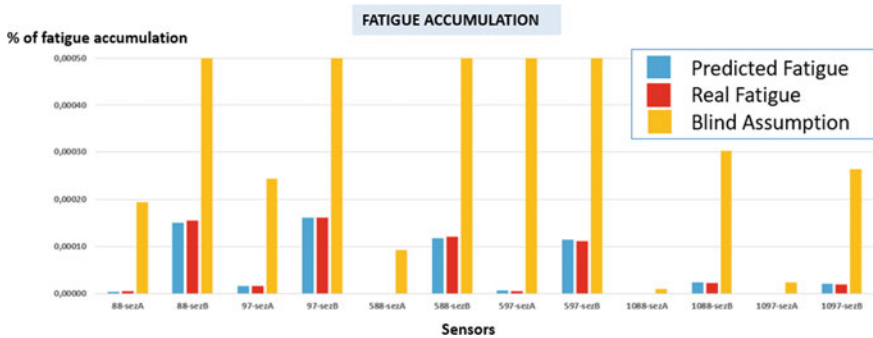


Fig. 5 Fatigue accumulation comparison for the three methods

4 Achievements and Conclusion

The proposed approach can provide some benefits compared to a more traditional evaluation of fatigue damage based on monitoring data. Indeed, by building a predictive model to correlate strains and stresses, from N sensors it is possible to predict fatigue cumulation at infinite hotspots, thus:

- drastically reducing the number of required sensors;
- saving installation time;
- providing a way to inspect structural locations which are hardly accessible.

Moreover, achievable information are not limited anymore to the ones obtained from the n sensors types installed on the bridge, because it is possible to create correlations between the sensors data and potentially many other sources of data (e.g. IoT), via the different bridge phenomena that can be simulated inside the implemented FE model.

More in general, the predictable trend of fatigue damage cumulation at the different hotspots can be used to define residual lifetime of bridge components, to plan maintenance, specially the extraordinary one, and to have a constant control

of the inspections (that can be intensified or reduced at the varying of the fatigue trend).

References

1. European Commission Research and Innovation Action, Horizon 2020, RAGTIME
2. Icke P, Margheriti C The benefits and use of FE modelling in bridge assessment and design, ResearchGate
3. Del Grosso A, Basso P, Ruffini L, Figini F, Cademartori M (2017) Infrastructure management integrating SHM and BIM procedures. SMAR
4. Gardner L, Nethercot DA (2005) Designer's guide to EN 1993-1-1—Eurocode 3: design of steel structures, general rules and rules for buildings. ISBN: 97807277 31630
5. Schijve J (2009) Fatigue of structures and materials. Springer Science and Business Media
6. Hendy CR, Johnson R (2006) Designers' guide to EN 1994-2 Eurocode 4: design of composite steel and concrete structures Part 2. General rules and rules for bridges

Estimation of Seismic Resilience of Road Infrastructures: An Integrated Approach



A. Del Grosso, M. Cademartori, S. Osmani, and D. Pastorelli

Abstract The asset management of road infrastructures in zones prone to seismic hazard requires the estimation of the seismic resilience of the network. This involves implications of both structural and transport engineering methods in order to correlate the possible damage of a given structure to the consequence on the entire network. The paper aims at developing a simplified, but still reliable method, for the estimation of the seismic resilience of a road network considering different structures and including a transport module. First, the seismic vulnerability of the structures is defined by means of fragility curves developed with different methods depending on the level of knowledge of the structures. Second, the consequence of the structural damage on the road capacity has been estimated. The different scenarios of road capacity after the seismic event are then included in the traffic module in order to estimate the post earthquake response of the road network.

Keywords Seismic vulnerability · Seismic resilience · Road infrastructures

1 Introduction

Nowadays, the resilience concept of a network has become primary in the infrastructure management environment, to evaluate losses suffered by the community.

This paper aims at connecting the structural and seismic fields to transport engineering as these disciplines are strongly correlated within the management of a road network.

This approach has been developed within the FORESEE Project [1] in order to link structural and transport engineering parameters.

A. Del Grosso (✉)
University of Genova, Genoa, GE, Italy
e-mail: andrea.delgrosso@rina.org

M. Cademartori · S. Osmani · D. Pastorelli
RINA Consulting SPA, Via A. Cecchi, Genoa, GE, Italy

In road networks, bridges and tunnels are vulnerable elements when a disruptive event occurs. A key element for road managers is the best allocation of budgets in order to improve network resilience through corrective actions.

The main objective of this study is to define an integrated and practical procedure, able to link seismic vulnerability of bridges and tunnels within the network, to the overall system behavior in terms of transport parameters for different hazard scenarios.

The resilience assessment requires the evaluation of the difference between the Level of Service provided by the network in a baseline scenario (i.e., in the absence of seismic events) and the same in case of hazard scenarios. Moreover, it requires knowledge about service restoration time and service restoration path.

In order to define losses and resilience of a network, several steps are necessary:

- Definition of suitable methodologies for seismic fragility and vulnerability analysis and risk evaluation about assets located in the network
- Multiple traffic analysis, in order to link structural characteristics to transport quantities
- Traffic analysis outputs interpretation in order to evaluate Resilience Key Performance Indicators.

2 Fragility and Vulnerability Analysis

The Fragility and Vulnerability Analysis tool, which is under development as part of FORESEE project [1], is the starting step for the Infrastructures resilience assessment: it contains the main inputs of the entire process and the knowledge level affects the analysis detail level.

Whatever the knowledge level is, full or simplified knowledge, it is important to describe the Transport System, including assets and components.

The fragility and vulnerability of an asset against a specific hazard requires the knowledge about the hazard characteristics and the asset's structural capacity.

In the following, a description of the main analyses carried out is shown.

2.1 Fragility Analysis

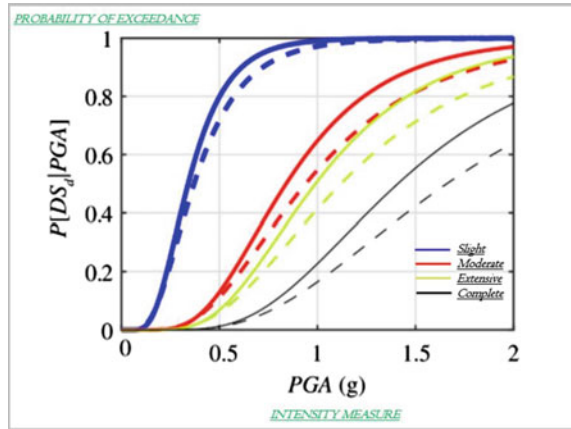
The fragility of an asset is defined through fragility functions.

A fragility function is a curve as a log-normal cumulative probability distribution that defines the probability of exceedance of a certain limit state or level of damage, for a given or a smaller hazard intensity measure (IM) (Fig. 1).

The fragility functions can be derived from several kinds of analysis:

- Literature or databases sources;
- Simplified Displacement-Based Assessment [2, 3];

Fig. 1 Example of seismic fragility curves for a given asset



- Non-Linear Static Analysis [4];
- Non-Linear Dynamic Analysis or Incremental Dynamic Analysis (IDA);

The literature method consists of a collection of fragility curves based on the study of different authors and guidelines. The user will select the most applicable fragility curve set for the different bridges or tunnels within a road segment. This method is applicable for a first step analysis in case of a large portfolio of structures and when the level of knowledge does not permit a more refined method. For this method, fragility functions parameters from different approaches have been implemented (e.g. Hazus method [5], fragility functions parameters contained in the Syner-G Project [6]).

The simplified Displacement Based Assessment and the Non-linear static method are approaches useful when an accurate level of knowledge is achieved and when the structures, in particular bridges can be included in regular typologies.

The IDA method is the most accurate, it requires a significant computational effort and a high level of knowledge of the structures. This method is applicable for specific and strategic structures of high importance.

2.2 Vulnerability Analysis

Once the fragility functions are selected, the vulnerability analysis should be performed, in order to evaluate the operativity losses for different levels of damage in the assets.

The first step of the procedure is the definition of the percentage of operativity loss for different limit states. This is achieved through discretized or detailed restoration functions, which are the tool able to provide the operativity loss for a limit state occurred in an asset, related to the elapsed time after a disruptive event.

An example of discretized restoration function for the bridge, from Hazus method [5], is shown in Table 1.

Table 1 Discretized restoration functions for bridges

Restoration period	Functional percentage for damage levels			
	Slight	Moderate	Extensive	Complete
1 day	70	30	2	0
3 days	100	60	5	2
7 days	100	95	6	2
30 days	100	100	15	4
90 days	100	100	65	10

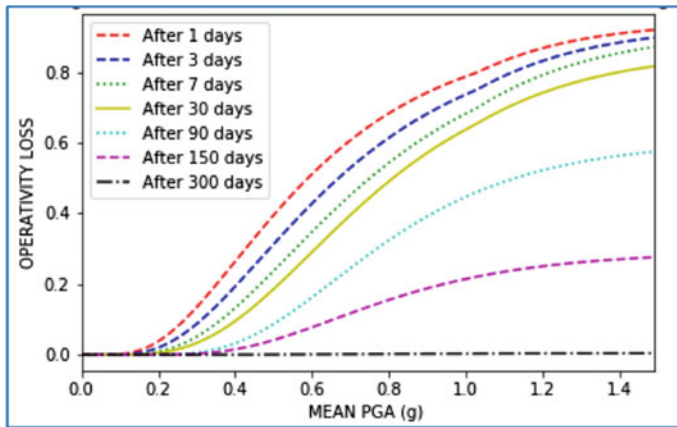


Fig. 2 Example of seismic vulnerability curves for a given asset

Thus, it is possible to have a knowledge of the recovery time for the assets.

Combining fragility and restoration functions, it is possible to obtain a set of curves able to link the values of intensity measure to the respective expected operational losses: the vulnerability curves. Each curve expresses the relation between losses and intensity measure for an asset and for a specific elapsed time starting from an event (Fig. 2).

3 Traffic Module

Fragility and vulnerability analysis and the definition of the resilience of a system, performed by the Decision Support Module are correlated through the Traffic Module.

This tool is used to perform traffic analysis in the initial situation and repeat them in the operativity loss scenarios in order to evaluate the Resilience Indicators. The idea is to investigate the change in the behavior of the system during the recovery

phase and to evaluate the Level of Service (LoS) in different scenarios. It leads to the evaluation of the Transport System recovery time and path, then the Resilience of the system. The main inputs for the transportation model are the capacity of the lanes for each arc of the road (i.e. the number of vehicles that cross the arc per unit of time) and the maximum allowed speed for the vehicles in each arc. These quantities shall be provided for the baseline scenario for the first simulation. In order to assess the change in transport parameters due to a disruptive event, it is important to correlate the loss of operability, derived from vulnerability analysis, for each asset to the modified values of capacity and speed for the arcs in the different selected scenarios after the event.

4 Decision Support Module (DSM)

The main objective of the DSM is to guarantee an instrument able to help Infrastructure Managers through the connection between of structural vulnerability and the corresponding transport flows modifications. The Traffic Module outputs (e.g. travel times, flow speeds, flow rates, flow densities, etc.) should be interpreted, in order to make an efficient decision-making process.

Starting from these outputs, it is possible to evaluate the variation of LoS in different scenarios.

Moreover, from the Traffic Module outputs, it is possible to evaluate Resilience Indicators about the infrastructure seen as a system.

Considering the recovery phase and the operativity losses of the assets, for different time intervals after an event, the description of the Resilience curves at either asset or system level is performed. At the system level, these analyses may be developed in deterministic or probabilistic terms (Fig. 3).

As consequence of the application of this framework, some Resilience Indicator are obtained.

These are associated to the “4 R” (i.e. Rapidity, Robustness, Redundancy, Resources).

The main Key Performance Indicators (KPIs) are:

- *Risk Quantification* (not necessary connected to one of the 4 “R” but affecting all of them being the probability to have an event. Especially the robustness determining the hazard input to be absorbed by the system);
- *Direct Losses* (directly connected to the robustness of the resilience);
- *Indirect Losses* (mainly connected to the redundancy and resources);
- *Resilience Assessment at the asset Level* (connected mainly to the rapidity and robustness of the infrastructure’s assets);
- *Resilience Assessment at the system Level* (connected to all the contributions).

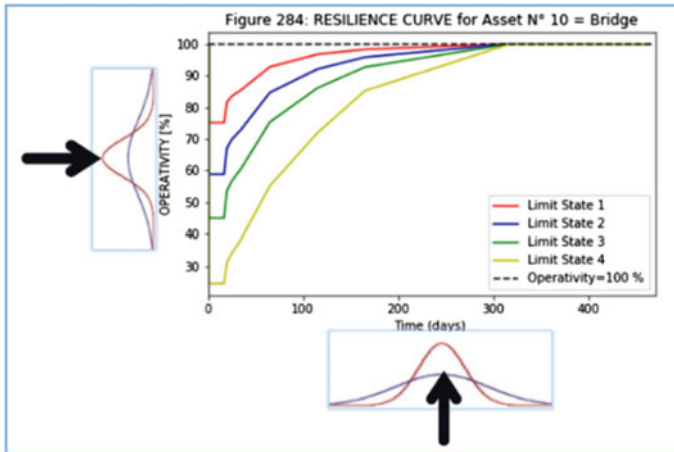


Fig. 3 Probabilistic resilience indicators at the system level

5 Conclusions

Because of the importance of transport infrastructures (i.e. typically facilities and networks that enable mobility of persons, goods and services), the need of decision support processes and methods to help managers and owners in the decision making are essential.

The approach presented in this paper tries to generate an integrated and flexible instrument that gives an overview of the infrastructure condition in terms of risk, possible losses and resilience assessment. It is still being applicate to several case studies as part of the FORESEE Project [1] and the result will soon be available.

Acknowledgements The work developed in this paper received funding from the European Union's Horizon 2020 research and innovation program under grant agreement No. 769373 FORESEE.

References

1. European Union: FORESEE Project, Horizon 2020
2. Cademartori M, Sullivan TJ, Osmani S (2020) Displacement-based assessment of typical Italian RC bridges. *Bull Earthq Eng* 18:4299–4329
3. Del Grosso A, Cademartori M, Basso P, Osmani S (2018) A simplified displacement based seismic Loss Assessment method for reinforced concrete bridges. In: IABSE conference, engineering the past, to meet the needs of the future, Copenhagen, Denmark
4. Fajfar P (2000) A nonlinear analysis method for performance—based seismic design. *Earthquake Spectra* 16(3):573–592

5. HAZUS MR4 (2003) Multi-hazard loss estimation methodology. Earthquake model. Department of Homeland Security Emergency Preparedness and response Directorate. FEMA, Mitigation Division. Washington D.C.
6. Syner-G: D3.6 Systemic seismic vulnerability and risk analysis for building, lifeline networks and infrastructures safety gain

Distributed Fiber-Optic Strain Sensing: Field Applications in Pile Foundations and Concrete Beams



Nils Nöther and Massimo Facchini

Abstract This paper gives an overview over industrial applications of distributed fiber-optic strain sensing in structural health monitoring, outlining both the benefits of the technology and its challenges regarding installation of the fiber-optic sensing cables and limitations of the measurement technology itself.

Keywords Distributed fiber-optic sensing · Brillouin sensing · Geotechnical monitoring · Structural health monitoring · DTSS · DSTS

1 Distributed Fiber-Optic Strain Sensing Techniques

The family of fiber-optic sensing techniques has become wide during the past two decades, spreading into numerous applications not only in geotechnical and structural monitoring [1], but even into chemical industries, medical and health-care applications and many more. Means for categorizing the numerous members of this family include distinguishing by physical (or chemical quantity) such as strain, temperature, pressure, vibration frequency, refractive index or alike; by the specific optical effect being the provider of the desired information such as linear and nonlinear scattering, frequency-selective reflectivity of a grating, interferometry or other; or by the configuration of the physical or virtual sensing points along the fiber. This latter categorization is used here to set the focus on the group of distributed sensing techniques as opposed to discrete or point-wise sensors as well as quasi-distributed sensors, as shown in Fig. 1.

The advantageous nature of truly distributed measurements becomes apparent from the perspective of conventional measuring methods: Classic deformation monitoring (performed by strain gauges etc.) and temperature monitoring (Pt100 and alike) deliver data from fixed, single spots of a structure; quasi-distributed measurements (fiber Bragg gratings) provide a chain of discrete measurement points.

N. Nöther (✉) · M. Facchini
fibrisTerre Systems GmbH, Berlin, Germany
e-mail: nils.noether@fibristerre.de

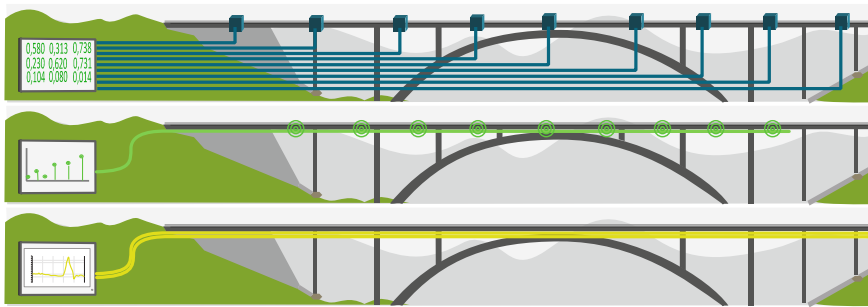


Fig. 1 Categories of fiber-optic sensing techniques—top: discrete sensor elements; center: quasi-distributed sensing elements along an optical fiber; bottom: truly distributed fiber-optic sensing

In contrast, an optical fiber connected to a device for distributed sensing will provide a continuous profile of the desired measurand—spatially resolved and over long lengths.

Table 1 gives an overview over the most common distributed fiber-optic sensing

Table 1 Overview of common distributed fiber-optic sensing techniques

Common name	Measurands	Optical effect	Fiber length	Spatial resolution
DTS	Temperature	Raman scattering	>50 km	<1 m
c-OFDR	Static and dynamic strain and temperature	Rayleigh scattering [2]	>100 m	<1 mm
BOTDA/BOFDA (DTSS)	Static strain and temperature	Brillouin scattering [3]	>100 km	<0.5 m
DAS/DVS	Vibrations; acoustic signals; dynamic strain; temperature gradients	Rayleigh scattering	>50 km	<1 m

techniques categorized with respect to the optical phenomenon on which they base their sensing capabilities.

In the context of structural health monitoring systems, these techniques can be considered as valuable sources of sensing data that can be not only used to stream strain and temperature data upon which threshold alarms can be triggered, but also to contribute to complex modelling and structural assessment methods. By merging distributed sensing data with other technologies like geodetic measurements, structural health monitoring systems can be created with comprehensive, high resolution deformation data beyond the accuracy of the single component technologies [4].

In the following, we will put the specific focus on distributed strain sensing techniques, based mainly on Distributed Brillouin Sensing, commonly referred to as

DTSS (Distributed Temperature and Strain Sensing), or BOTDA/BOFDA (Brillouin Optical Time / Frequency Domain Analysis).

2 Brillouin Sensing and the Nature of Distributed Data

The common basic concept of all distributed fiber-optic sensing technologies is to measure the response of an optical fiber to the excitation by an injected optical pulse. The optical pulse travels along the fiber under test (e.g. the strain sensing fiber attached to the structure) and is subject to various backscattering effects along the way. From every location the signal passes by, portions of light are being thrown back and travel to the injection end, where they are recorded over time. From the time of flight, the origin of the received backscattering at every instance in time can be reallocated. Thus, a distributed profile of optical backscattering can be recorded for the entire length of the fiber under test (Fig. 2).

In the specific case of Distributed Brillouin Sensing, the backscattering carries the information of the fiber’s local density, and thus on its strain and temperature condition at every position. This briefly outlines the principle of BOTDA measurements. An advancement of this concept, the BOFDA technology, substitutes the pulses with a series of harmonic signals, but remains equivalent regarding the result in terms of distributed strain and temperature data, retrieved from the optical fiber and resolved spatially along its length.

From this conceptual view, it is clear that the nature of sensing data from distributed measurements will differ substantially from that of conventional discrete sensors. Figure 3 shows a typical example of a distributed strain measurement from a structural health monitoring installation (embedding in concrete).

From this data example, it becomes clear that distributed sensing techniques are not to be considered a one-to-one replacement of discrete, point-wise sensors. In the above installation, discrete sensors such as extensometers or strain gauges would correspond to specific spatial sampling points of the distributed data curve. Whether point sensors would detect local mechanical events (cracks, localized deformation) depends on the selected positioning and the pre-defined gauge length, both parameters

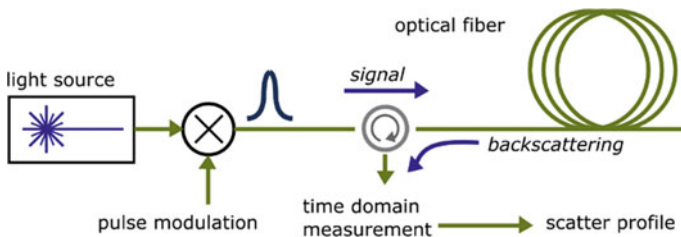


Fig. 2 Basic principle of distributed sensing techniques based on optical backscattering reflectometry

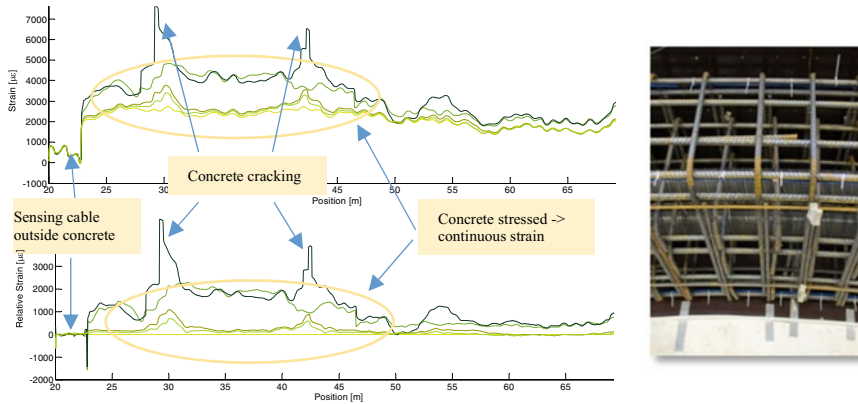


Fig. 3 Typical data set from distributed fiber-optic strain measurements using the BOFDA technology. Top: Direct strain reading, 5 data sets with increased load on structure. Bottom: Relative strain reading, first data set used as a baseline. Right: Installation with fiber-optic strain sensing cable (blue) fixed to the reinforcement before concrete pouring

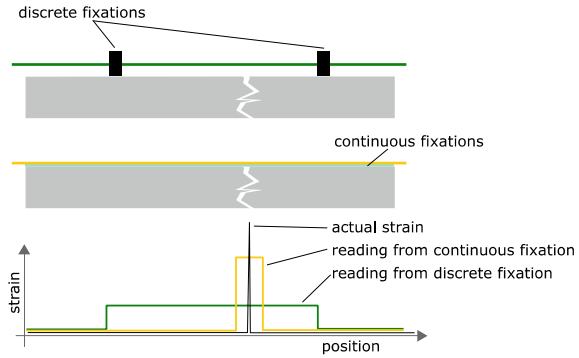
being subject to arbitrary decisions in the typical case of a priori unknown behavior of a structure during loading.

Table 2 summarizes the considerations of data handling for discrete and distributed sensors for the case of a fiber-optic sensing cable embedded into concrete, distinguishing between continuous and discrete strain events (as highlighted in Fig. 3).

Table 2 Comparison between discrete and distributed fiber-optic sensing techniques

	Continuous strain event: Stress, deformation	Discrete strain event: cracking
Discrete sensor (strain gauge); also: Quasi-distributed (FBG)	Returns elongation of the structure over a previously defined gauge length (as a supporting point of the actual, continuous strain distribution)	Returns opening width of the crack Requires previous knowledge of the crack position; otherwise, no information is obtained
Distributed sensor (DTSS)	Returns full strain profile as a representation of the strain distribution in the structure	Returns crack detection as a localized event (with instrument spatial accuracy), but no quantified width of crack opening (no gauge length defined) Requires event width in range of instrument spatial resolution; otherwise, no information is obtained

Fig. 4 Discrete and continuous fixations of sensing fibers to surfaces for crack measurements



When focusing on crack detection and monitoring in concrete installation, the shortcomings of the DTSS configuration in Table 2 can be addressed by discretizing the sensor configuration of the fiber-optic strain sensing cable, which is specifically feasible in surface application on concrete, as illustrated in Fig. 4.

In effect, the discretization of distributed fiber-optic sensing configurations introduces a defined gauge length that even allows to quantify crack opening widths, while maintaining the advantage to provide information when no knowledge of the likely positions of crack appearance is available.

A comparison of both continuous and discretized surface application of optical sensing fibers has been performed on a concrete beam that was loaded after sensor installation applying defined load steps in order to induce stress resulting in cracking along the bending line. The discretization was achieved by fixing the sensing fiber at defined points with a distance of 0.25 m on the concrete surface. As a reference, a third sensing fiber was continuously applied in parallel and was interrogated using the c-OFDR technique at millimeter resolution [5]. The fixation is shown in the photographs in Fig. 5.

The strain curve acquired with the c-OFDR measurement technique (Fig. 6, top) stands out due to several peak values in strain.

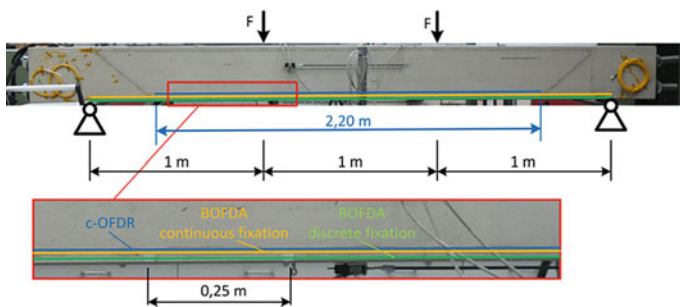


Fig. 5 Four-point-bending-test on a prestressed concrete beam and measurement setup

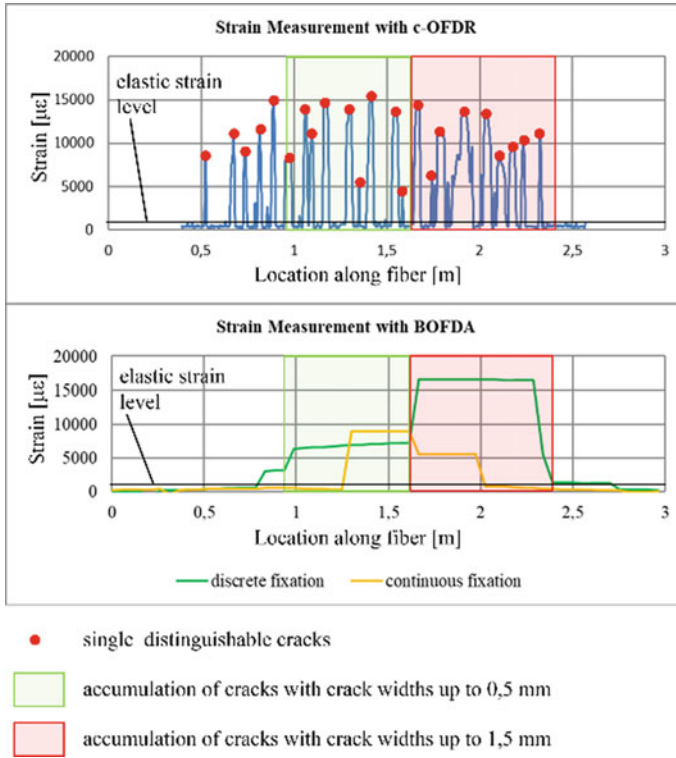


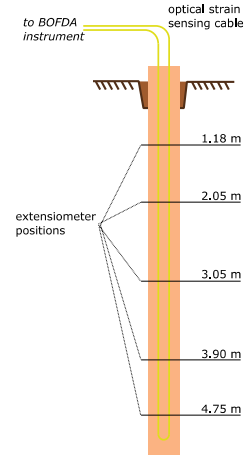
Fig. 6 Continuous strain measurement sample; (top) c-OFDR; (bottom) BOFDA

Since these peak values clearly exceed the elastic strain level of concrete, they correspond to crack openings. Because of the high spatial resolution of c-OFDR it is possible to distinguish single cracks from each other, to determine their corresponding crack width, and to locate the position of the cracks along the fiber. This digitally captured information about the cracks is in good agreement to the results which were determined by conventional, visual crack observations.

As expected, the BOFDA measurement using continuously fixed sensing fibers does not provide information on the crack opening, because every single crack is smaller in dimension than the instrument's spatial resolution of 20 cm.

The strain curve of the BOFDA measurement in combination with the discrete fixation, on the other hand, exceeds the elastic strain limit in a larger portion of the sensor-fiber. Due to the discrete fixation, the local strain event caused by a single crack is distributed along the fixation distance of 0.25 m. Since this length is larger than the spatial resolution of the BOFDA method, the distributed strain enhancement due to the crack can be recognized. The resulting strain curve is in good agreement to the c-OFDR measurement and to the visual inspection. Although, single cracks and their width are not determinable, an accumulation of cracks can clearly be identified.

Fig. 7 Measurement set-up for static pile load testing



3 Field Experience Showing Distributed Sensing Data

An example of distributed strain measurements in loaded concrete structures, with a direct reference to discrete strain sensors, is given with the following installation in bored piles (Fig. 7).

Such measurements, using Brillouin DTSS systems for static load testing of concrete piles, have been reported for various sensing configurations [6].

The present application comprises a concrete-poured pile of 5 m depth; reinforced, steel-armored fiber-optic sensing cables were fixed to the reinforcement cage before entering the cage into the ground.

During the tests, an increasing vertical load from 150 to 900 kN was induced onto the pile, while subsequently extensometer data as point-wise references, temperature data at the extensometer positions and distributed Brillouin strain data were recorded.

With the exemption of the lowest extensometer, all the measurement points show good agreement between the classical data and the fiber-optic sensing data [7].

The following figures shows the evolution of strain for both the extensometers and the distributed Brillouin sensors (at the exact extensometer positions, compensated for the base line reading at 0 kN load) over time (Fig. 8) and spatial distribution (Fig. 9).

4 Conclusion

The distributed nature of fiber-optic strain measurements using the Brillouin sensing technology has been discussed and compared to the discrete configuration of conventional strain gauges. The advantages and limitations of distributed sensing techniques was shown with hands-on measurement examples.

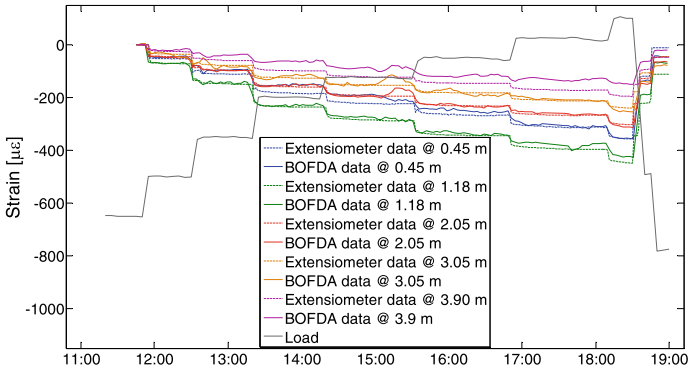
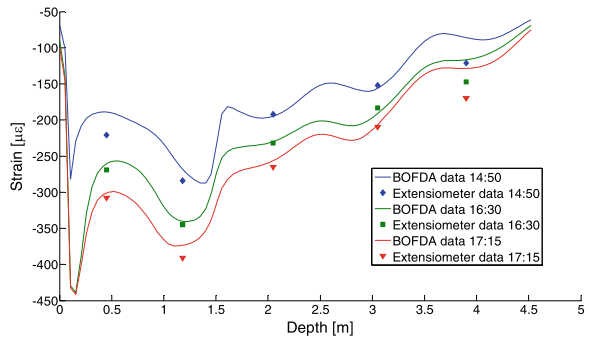


Fig. 8 Strain evolution: Extensometer and Brillouin DTSS data

Fig. 9 Spatial strain in extensometer and Brillouin DTSS data



From the presented examples, it becomes clear that distributed fiber-optic measurement techniques play their economic advantages specifically in large installations, where the cost of the sensing elements—which is considerably low for DFOS technologies using standard telecommunication fibers—is dominating the installation cost over the cost of the equipment. However, even in monitoring assignments of limited size, as in the examples described in here, the ability of distributed fiber-optic sensors to be daisy-chained, as well as installed in parallel and interrogated subsequently, introduces a strong cost advantage against classic single-point (discrete) sensors.

References

1. Glisic B, Inaudi D (2008) Fibre optic methods for structural health monitoring
2. Palmieri L, Schenato L (2013) Distributed optical fiber sensing based on Rayleigh scattering. *Open Opt J* 7(1)
3. Nikles M, Thévenaz L, Robert PA (1996) Simple distributed fiber sensor based on Brillouin gain spectrum analysis. *Opt Lett* 21(10):758–760

4. Monsberger CM, Lienhart W (2021) Distributed fiber optic shape sensing along shotcrete tunnel linings: Methodology, field applications, and monitoring results. *J Civ Struct Health Monitor* 1–14
5. Nöther N, Künzel A, Vogdt F (2019) Surface-applied distributed fiber-optic monitoring for crack detection in concrete structures. In: *Proceedings of SMAR*
6. Schwamb T, Elshafie M, Ouyang Y et al (2011) A monitoring of a secant piled wall using fibre optics sensors. In: *Proceedings of 8th FMGM, Berlin, Germany*
7. Nöther N, von der Mark S (2019) Distributed Brillouin sensing for geotechnical infrastructure: capabilities and challenges. *Geotech Eng J SEAGS & AGSSEA* 50(1)

Seismic Damage Quantification for the SHM of Existing RC Structures



Alessandro Lubrano Lobianco, Marta Del Zoppo, and Marco Di Ludovico

Abstract One of the main issues in civil engineering is to estimate the level of damage for existing buildings subjected both to decay due to natural ageing and to additional loads that could affect their serviceability during lifetime. This paper looks at the process of Structural Health Monitoring (SHM) in the context of seismic damage detection and quantification. The aim of the paper is to define ranges of variation for parameters commonly monitored as structural damage indicators, like fundamental periods, residual drift ratios and lateral stiffness, in relation with seismic damage levels. For this purpose, a methodology is proposed for simulating the seismic damage of existing reinforced concrete (RC) columns and assessing the correlation between the variation of such parameters with increasing damage levels. Seismic damage levels are defined based on the Park and Ang damage index, and preliminary ranges of variation of damage indicators are derived for the seismic damage quantification in existing RC columns.

Keywords Structural health monitoring · Damage quantification · Period elongation · Stiffness degradation

1 Introduction

Safety, durability and serviceability are requirements that a structure should meet during its lifetime. Damage in civil structures and infrastructure may occur from a plenty of causes. Structural damage can be associated with the deterioration of materials (i.e., aging problems), fatigue, or extraordinary events such as fires, earthquakes, hurricanes, impact loads, among many others.

A. Lubrano Lobianco (✉) · M. Del Zoppo · M. Di Ludovico
University of Naples “Federico II”, Naples, Italy
e-mail: alessandro.lubranolobianco@unina.it

M. Del Zoppo
e-mail: marta.delzoppo@unina.it

M. Di Ludovico
e-mail: diludovi@unina.it

The process of implementing a damage identification strategy is referred to as Structural Health Monitoring (SHM). SHM has become an important research discipline in several areas including civil engineering, with the goal of assessing the health condition of structures by monitoring their characteristics during the lifetime. The goal of SHM is to detect the structural damage, assessing the presence of damage, the location of damage, the damage severity, and estimating the remaining service life of a structure [1]. A proper implementation of a SHM system can help in detecting the structural performance deterioration at an early stage, increasing the safety level, and bringing efficiency and effectiveness in maintenance operations. A current challenge in SHM is to correctly identify when variations obtained from monitoring data can be associated to a structural damage rather than to environmental noise, and to correlate such variations with a damage level associated to the serviceability of the structure.

In vibration-based SHM, the dynamic properties of a structure (i.e., mode shapes, natural periods) are monitored for the structural damage identification, localization and quantification. A widespread damage detection technique consists in processing the acceleration acquired through operational modal analysis (OMA) [2] in the frequency domain (i.e., Fourier analysis). Indeed, dynamic properties are extremely sensitive to changes in the lateral stiffness of structures, and are commonly used as predictors for damage detection systems.

In the context of vibration-based seismic damage quantification, the elongation of fundamental period is a widely adopted damage indicator to estimate the overall inelastic structural performance after earthquakes [3]. In reinforced concrete (RC) structures, the period elongation is a function of the ground motion parameters [4] as well as the geometry of the structure and the presence of infill walls [5]. Some studies experimentally assessed the changes in dynamic properties on a few structures affected by seismic damage using OMA data, and proposed period elongation ranges as a function of the level of damage experienced by such structures during a specific earthquake [5–7]. However, a detailed framework for assessing the changes in dynamic properties as a function of the experienced damage level is currently missing, due to epistemic and aleatory uncertainties in the structural geometry and ground motion characteristics [8].

In this work, a framework for the seismic damage quantification is proposed for existing RC columns. Changes in lateral stiffness and fundamental period of RC columns are assessed through extensive numerical analyses on experimentally validated FEM models. Residual drift ratios, commonly used as seismic damage indicator during visual inspections [9], are also monitored during the analyses. Damage levels are defined, based on the damage index proposed by Park and Ang, which combines accumulated damage due to lateral deformations and hysteretic energy dissipation during the seismic excitation [10]. Preliminary ranges of variation of the selected damage indicators are finally proposed in relation to the defined damage levels for a dataset of 90 RC columns. Comparison of numerical results with damage models and thresholds from relevant literature are finally reported. The framework herein proposed can represent a sound technique to define reliable thresholds of damage indicators to be used for triggering alerts in long-term SHM of civil structures and infrastructures.

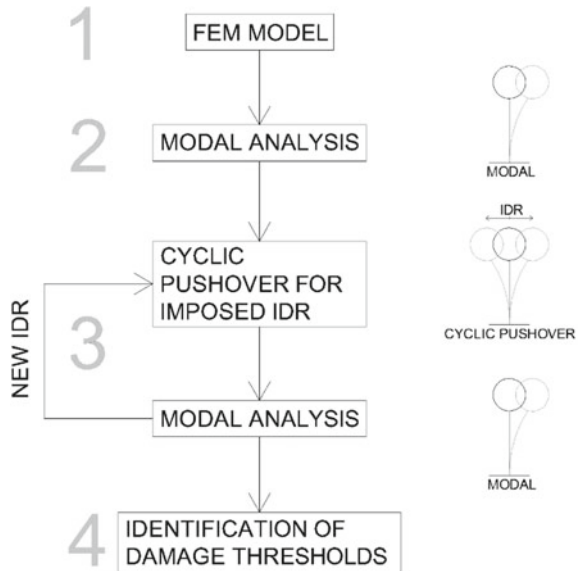
2 Methodology

In the context of seismic damage quantification from SHM data, a methodology is herein proposed for estimating the variation of selected damage indicators (termed in the next as damage measures, DM) as a function of the damage level experienced by a structure through numerical simulations. Selecting suitable seismic DMs depends on the type of monitoring system adopted and on the structure itself. Possible DMs could be maximum base shear, modal periods, maximum interstorey drift ratios, residual drift ratios, modal shape and lateral stiffness degradation [11].

In this work, the methodology is presented for SDOF systems and the analysis is carried out on cantilever RC columns typical of existing frames in the Mediterranean region. However, the proposed framework is suitable for applications on more complex MDOF systems. The DMs selected for the cantilever column subject to seismic damage are fundamental period (T), residual drift ratio (d_r) and lateral stiffness (k). The seismic excitation is simulated through nonlinear static analysis (i.e., pushover analysis) and the interstorey drift ratio (IDR) is assumed as the seismic demand parameter. Thus, the DMs are computed as a function of the imposed IDR (i.e., $DM(IDR)$) to correlate the changes in those parameters with the seismic damage level. Uncertainties related to the ground motion selection are herein neglected.

The methodological framework consists in four steps, as shown in Fig. 1. The first step consists in the development of a refined FEM model for the structure of interest. In the second step, the modal periods of the structure in the undamaged condition are preliminary assessed through modal analysis. In the third step, a cyclic pushover analysis is carried out to simulate the seismic damage on the structure for an

Fig. 1 Methodological framework for seismic damage quantification



imposed *IDR*. Lateral stiffness and residual drift for the imposed *IDR* are estimated from the pushover curve. A new modal analysis is then carried out for evaluating the modified modal periods of the damaged structure. The sequential cyclic pushover-modal analyses are repeated for increasing *IDRs* up to the structural collapse. Structural damage levels are defined and ranges of variation of the selected DMs are derived from analyses results for each damage level. Threshold values associated to each damage level can be also defined for the structural system under investigation.

The level of seismic damage and its reparability is herein classified adopting the Park and Ang damage index (DI) [10], which is defined as the linear combination of ductility and dissipated energy as follows:

$$DI = \frac{\delta_M}{\delta_u} + \frac{\beta}{Q_y \delta_u} \int dE \quad (1)$$

in which δ_M is the maximum deformation experienced during the seismic event, δ_u is the ultimate deformation capacity under monotonic loading, Q_y is theoretical yield strength and dE is incremental absorbed hysteretic energy. The constant parameter β is taken equal to 0.25 for slightly reinforced structures [12].

The classification of damage level and structural reparability as a function of the Park and Ang DI is reported in Table 1 [13]. The DI for the structure is computed from pushover analysis for each imposed *IDR*.

The residual drift ratio is computed as the permanent deformation that the structure exhibits when the applied loads go to zero during the last cycle of the analysis. The initial lateral stiffness, k_0 , is computed as the secant stiffness at 70% of maximum lateral force on the envelope curve, as shown in Fig. 2. The lateral stiffness at a generic imposed *IDR* (k_i) is computed as the ratio between peak force at that *IDR* and related displacement in the positive load direction. This coincides with the peak-to-peak stiffness on the FEM curve.

Table 1 Damage scale and DI thresholds from Park et al. [13]

Damage index threshold	Damage level	Reparability
$DI < 0.10$	No or slight damage	Repairable damage
$0.10 \leq DI \leq 0.25$	Minor damage (DS1)	Repairable damage
$0.25 < DI \leq 0.40$	Moderate damage (DS2)	Repairable damage
$0.40 < DI < 0.80$	Severe damage (DS3)	Irreparable damage
$DI \geq 0.80$	Collapse (DS4)	Irreparable damage

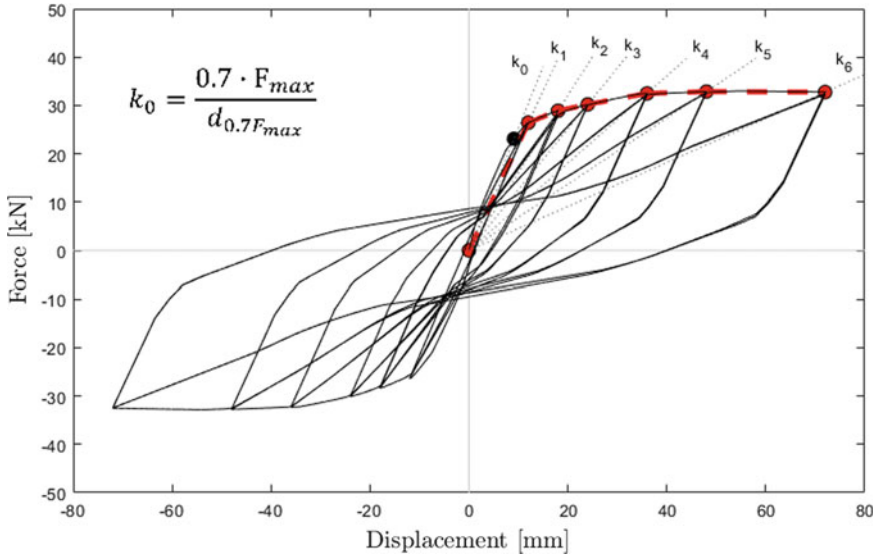


Fig. 2 Assessment of the lateral stiffness for each imposed IDR

3 Development of the FEM Model

A refined FEM model for simulating the performance of a cantilever RC column subject to seismic damage is developed. The software OpenSees [14] is adopted to model the nonlinear behaviour of columns through a distributed plasticity model. In distributed plasticity models, the interaction of moments and axial forces is considered simultaneously, and the plasticity is spread along the entire element length. The *BeamWithHinges* command is used to build a *forceBeamColumn* element. The element formulation allows to use a hinge integration approach but also to spread plasticity beyond the plastic hinge region, if needed [15]. For the cantilever column, a single plastic hinge is defined at the base of the element. Four Gauss-Radau integration points are adopted, two located in the plastic hinge region and two in the element interior. The plastic hinge length is computed as follows [16]:

$$L_{pl} = 0.08L_s + 0.022f_{ym}d_b \tag{2}$$

where L_s is the shear length, f_{ym} is the steel yield strength and d_b the longitudinal bars diameter.

The cross section of the beam-column element is uniformly discretised into thirty fibres to represent closely small stress-strain variations. The concrete nonlinear behaviour is simulated with the *Concrete01* material, which implements the Kent-Scott-Park stress-strain model [17], while the longitudinal steel reinforcement is modelled with the uniaxial *Hysteretic* material [14]. The parameters adopted for

both stress-strain models are calibrated against experimental data, as discussed in detail in the next paragraph.

The member's end rotation due to bond slip resulting from strain penetration effects is modelled using a zero-length section element at the end of the beam-column element, as shown in Fig. 3.

The *Bond_SP01* material is assigned to the steel fibres of the zero-length section element for taking into account the cyclic bond slip law proposed by Zhao and Sritharan [18]. For the material parameters definition, the yield slip s_y is determined as follows:

$$s_y(\text{mm}) = 2.54 \left(\frac{d_b(\text{mm})}{8437} \frac{f_{ym}(\text{MPa})}{\sqrt{f_c(\text{MPa})}} (2\alpha + 1) \right)^{1/\alpha} + 0.34 \quad (3)$$

where f_c is the concrete compressive strength and α is taken as 0.4 in accordance with the CEB-FIB Model Code 90 [19]. The ultimate slip s_u is taken as $40s_y$, the initial hardening ratio is assumed equal to 0.4 and the pinching factor is 0.6 [18].

A fixed restraint is adopted at the base node. Geometric nonlinearities effects are taken into account in the model by means of the geometric transformation *PDelta*.

A constant compressive axial load and the lateral cyclic displacements are applied at the top of the column element, following the load protocol adopted in experimental tests discussed in Di Ludovico et al. [20], see Table 2. For each imposed *IDR*, three cycle repetitions are adopted to simulate the seismic shaking. The Newton–Raphson solution algorithm is adopted to solve the model nonlinear equations.

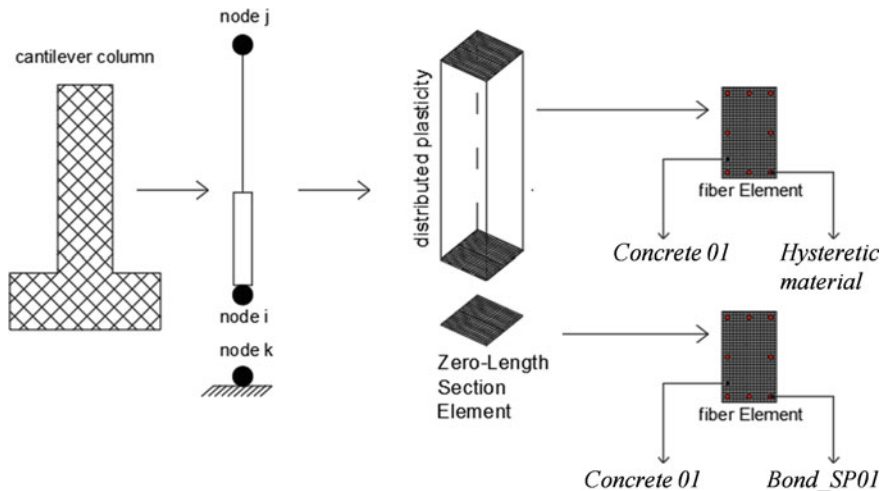


Fig. 3 RC column modelling using distributed plasticity element

Table 2 Load protocol for the cyclic pushover

Pushover cycle	IDR (%)	Imposed displacement (mm)	Number of repetitions for each cycle
I	0.40	6.0	3
II	0.80	12.0	3
III	1.20	18.0	3
IV	1.60	24.0	3
V	2.40	36.0	3
VI	3.20	48.0	3
VII	4.80	72.0	3

4 Validation of FEM Model

The refined FEM model is validated on seven experimental tests on full-scale cantilever columns subject to cyclic quasi-static loads. One test, named R500P-c-bis, is original while the other tests were presented in Di Ludovico et al. [20]. All columns were tested following the cyclic load protocol reported in Table 2 (in terms of peak interstorey drift ratio, *IDR*, and imposed displacements) with a constant axial load ratio of 0.1, and the failure mode was controlled in each case by flexure. The experimental setup is shown in Fig. 4, and further details about the instrumentation adopted can be found in Di Ludovico et al. [20]. The experimental tests were carried out on square and rectangular columns with plain rebars and deformed rebars. The columns

**Fig. 4** Experimental setup for the cyclic pushover tests

Table 3 Geometric and mechanical parameters for selected tests on RC columns for model validation (*tests from Di Ludovico et al. [20])

Reference Specimen	*R300P-c	*R500P-c	R500P-c-bis	*S300P-c	*R300D-c	*R500D-c	*S300D-c
b (mm)	500	300	300	300	500	300	300
h (mm)	300	500	500	300	300	500	300
f_{cm} (MPa)	18.8	18.8	28.8	18.8	18.8	18.8	18.8
f_{ym} (MPa)	330	330	330	330	520	520	520
Type of bars	plain	plain	plain	plain	deformed	deformed	deformed

were designed according to gravity loads criteria widely adopted between before 1980s and do not meet the current seismic provisions and detailing requirements.

The specimens consisted of a foundation block and a column with shear length of 1500 mm. Columns with three different cross section are herein considered: (1) square 300×300 mm; (2) rectangular 300×500 mm; and (3) rectangular 500×300 mm. Bars with 12 mm diameter were used as longitudinal reinforcement, and 8 mm diameter ties spaced at 150 mm were adopted as transverse reinforcement.

Information on specimens' geometry and mechanical properties of steel and concrete are reported in Table 3. In details, Table 3 reports: the cross-section base, b ; the cross-section height, h ; the compressive strength of concrete, f_{cm} ; the yielding strength of steel reinforcement, f_{ym} ; the type of rebars (plain or deformed). The original notation of specimen is XNY-z, where X refers to the columns cross section (S for square and R for rectangular), N denotes the cross-section depth, Y identifies the type of reinforcement (D for deformed bars and P for plain rebars), and z identifies the type horizontal action applied to the column (c for cyclic test).

Parameters for the steel stress–strain relationship adopted in the FEM are generalised from mean experimental values of mechanical properties reported in [20]. The peak hardening strength is taken as $1.3 f_{ym}$, the elastic modulus is assumed equal to 200 GPa, the strain at peak strength is taken as $11 \epsilon_y$, and the post-hardening strain corresponding to a strength degradation of 20% is taken as 6 times the strain at peak strength (i.e., $66 \epsilon_y$). For the concrete, the strain at peak strength is assumed as 0.004 while the ultimate strain is set to 0.03. These values are set to provide a good accuracy of the FEM model predictions in terms of lateral stiffness against the experimental data for the first cycle ($IDR = 0.40\%$). The comparison between experimental and numerical lateral stiffness is shown in Fig. 5 for the seven specimens used for validation. The FEM model is able to provide on average a good estimate of the initial lateral stiffness of the columns. This is fundamental for computing the undamaged fundamental period. The effect of confinement is neglected in the FEM model, due to the lack of detailing of transverse reinforcement in typical existing RC columns considered for the study.

The comparison between numerical and experimental results in terms of base shear vs. imposed displacement for specimens with plain reinforcement and for those with

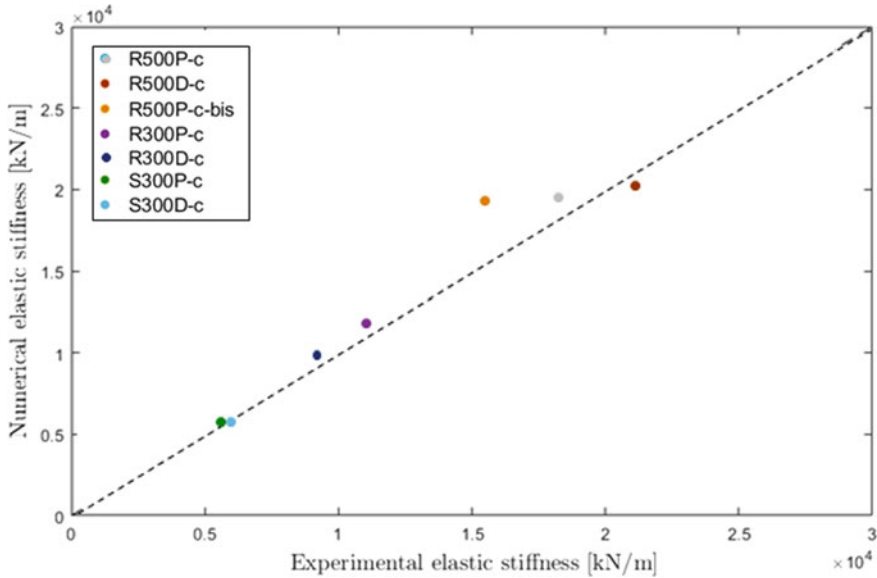


Fig. 5 Comparison between lateral stiffness from FEM model and experimental curves at *IDR* = 0.40%

deformed reinforcement are depicted in Figs. 6 and 7, respectively. The numerical curves fit quite well with the experimental ones, providing a reliable simulation of the cyclic performance of RC columns. To further investigate on the accuracy of the FEM model with respect to the experimental results, statistics of the error in the estimated most critical parameters (i.e., peak force, lateral stiffness, energy dissipation, residual drift) have been analysed. Indeed, numerical models provide an approximate representation of real word phenomena and, thus, simulations invariably suffer from a certain level of inaccuracy. In terms of peak force evaluated for each cycle of the pushover, the error between numerical and experimental test has a mean value of 9% with a covariance (*CoV*) of 3.6%. The comparison of numerical and experimental lateral stiffness (taken as the peak-to-peak stiffness at each cycle of the pushover) gives an average error of 19% (*CoV* 15%). The average error associated to the residual drift ratios is 40% with a *CoV* of 26%. Finally, the average error on the hysteretic energy is 29% with a *CoV* of 18%.

5 Application to a Case Study

The methodology presented in Fig. 1 is adopted to derive ranges of variation of DMs for a dataset of RC columns through the experimentally validated FEM tool previously presented. The dataset consists of RC columns with cross-section dimensions

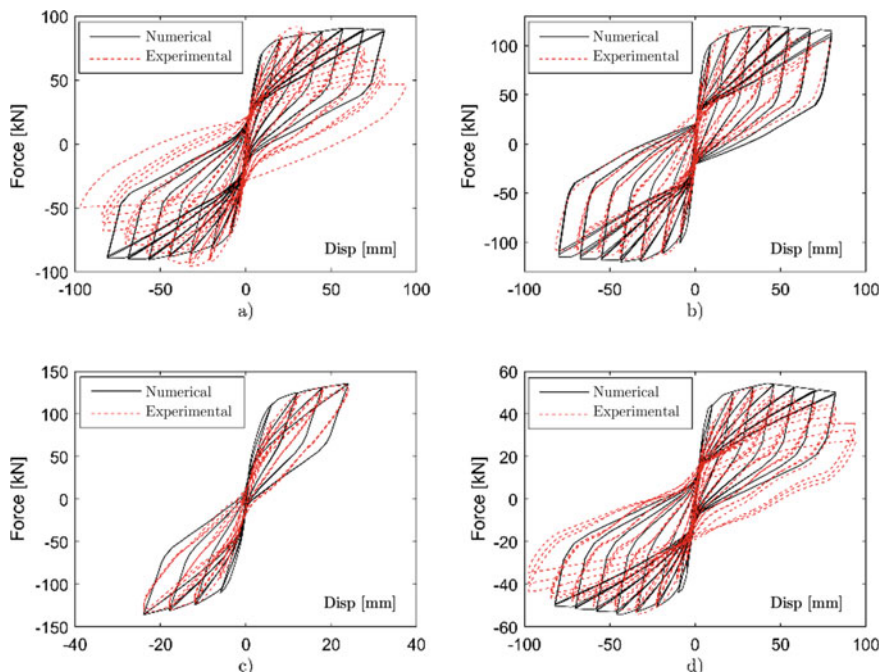


Fig. 6 Comparison between numerical simulation and experimental test for RC columns with plain rebars: **a** R300P-c, **b** R500P-c, **c** R500P-c-bis, **d** S300P-c

of 300×300 mm and a height of 1500 mm. Five different values of concrete compressive strength (f_{cm}), three values of steel yielding strength (f_{ym}), and six layouts of longitudinal rebars (comprising both number of rebars in the cross-section and their diameter (ϕ)) are considered, as reported in Table 4. All possible combinations of the selected parameters are analysed, resulting in 90 column configurations. The longitudinal reinforcement ratio ρ is also reported for each geometric configuration. All combinations of random variables have been considered for populating the dataset. For this preliminary application, variations of DMs for the dataset are considered for a constant axial load ratio of 0.1.

According to the methodological framework herein proposed, a FEM model is generated for each column of the dataset. Modal analysis is carried out to identify the modal periods in the undamaged configuration. Then, a first cyclic pushover is performed for the first imposed *IDR* according to the load protocol in Table 3 (i.e., *IDR* = 0.4%). At the end of the pushover, a new modal analysis is carried out to assess the fundamental period (i.e., $T(\text{IDR})$). Furthermore, the residual drift ratio and the lateral stiffness are also estimated (i.e., $d_r(\text{IDR})$ and $k(\text{IDR})$). The dissipated hysteretic energy is also computed to define the Park and Ang DI associated with each imposed *IDR*. Then, a new cyclic pushover is performed up to the second *IDR* (i.e., *IDR* = 0.8%), following the load protocol in Table 3, and the variation of DMs associated with the imposed *IDR* is again evaluated. The sequence of analysis is

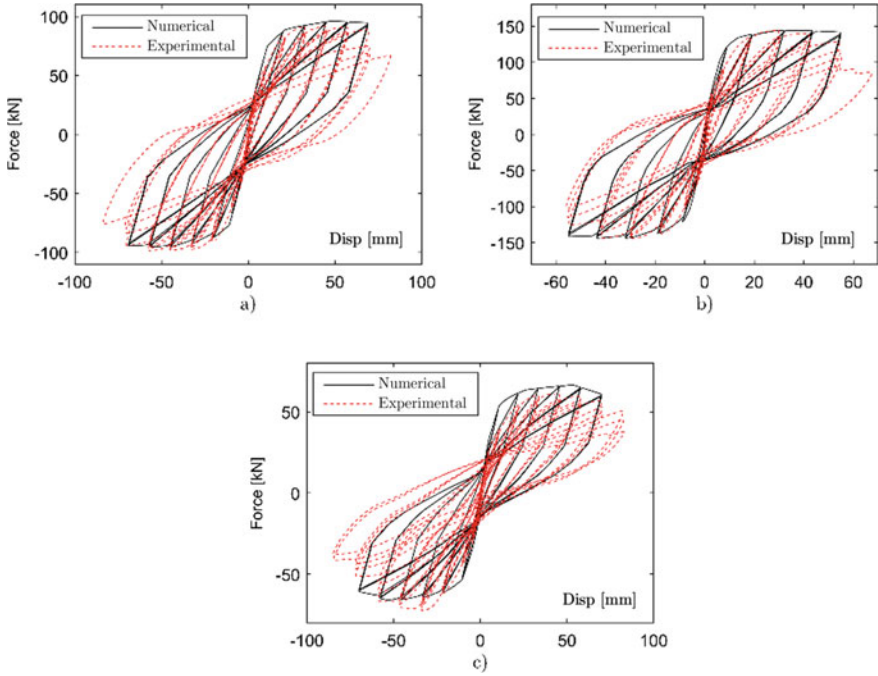


Fig. 7 Comparison between numerical simulation and experimental test for RC columns with deformed rebars: **a** R300D-c, **b** R500D-c, **c** S300D-c

Table 4 Variability of geometrical and mechanical properties in the dataset

Geometry (mm × mm)	n. bars (-)	φ (mm)	ρ (%)
300 × 300	4	12	0.5
	6 + 2	12	1.0
	6 + 2	14	1.4
	6 + 2	16	1.8
	6 + 2	18	2.3
	6 + 2	20	2.8
f_{cm} (MPa)	10 – 15 – 20 – 25 – 30		
f_{ym} (MPa)	315 – 375 – 430		

repeated up to an imposed drift ratio of 4.8%, which is herein assumed as an *IDR* threshold for the structural collapse.

6 Discussion of Numerical Results

The variation of the selected DMs as a function of the imposed IDR and the damage level is investigated and discussed for the dataset of 90 RC columns. Figure 8 reports the computed Park and Ang DI for all columns in the dataset as a function of the imposed *IDR* (e.g., Minor Damage = DS1, Moderate Damage = DS2, Severe Damage = DS3, Collapse = DS4). The figure shows that the Park & Ang DI is similar for all numerical simulation at the same imposed *IDR*, and it is not significantly affected by variations in section geometry or mechanical properties of materials. For interstorey drift ratios smaller than 0.8% the columns experience a slight or minor damage and is repairable. When the interstorey drift is greater than 1.2%, the damage level is moderate but still repairable, whereas drift ratios exceeding 2.4%, the structural damage is severe and not repairable.

In terms of fundamental period elongation (ΔT) derived from natural periods, the numerical data collected for each damage level can be well approximated with a right skewed lognormal distribution for DS1 and DS2, as shown in Fig. 9. Conversely, this approximation is less effective for DS3 and DS4. Mean and lognormal standard deviations for the distributions associated with the period elongation are reported in Table 5. The period elongation is computed as the percentage of variation of the fundamental period in the damaged condition for a certain *IDR* with respect to the undamaged (i.e., elastic) fundamental period.

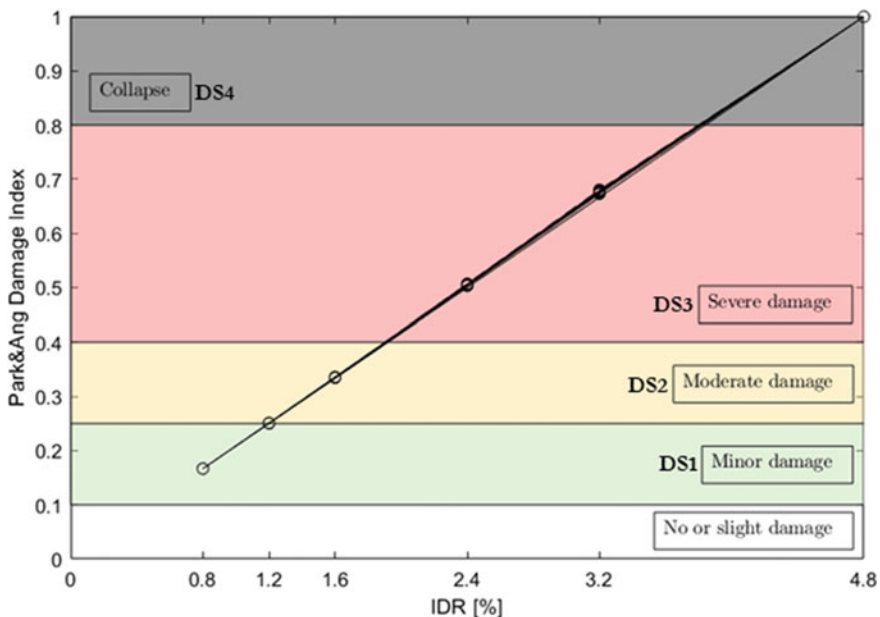


Fig. 8 Correlation between imposed *IDR* and Park and Ang damage index for the case-study columns (90 elements)

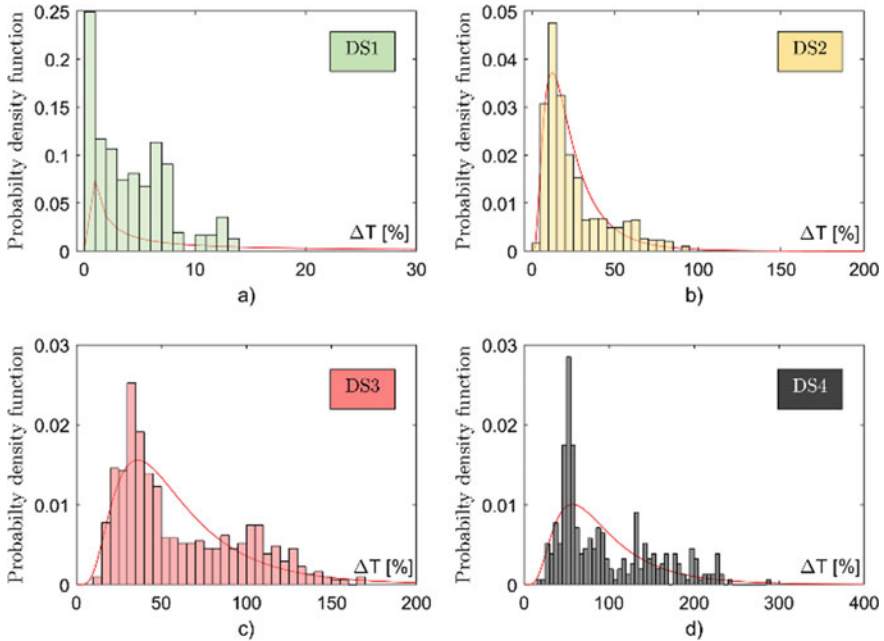


Fig. 9 Distribution of period elongation for each damage level: **a** DS1; **b** DS2; **c** DS3; **d** DS4

Table 5 Parameters of lognormal distributions associated with the period elongation for DS

Damage state	Probability distribution	Variable	Value of fitting parameters	
DS1	Lognormal	ΔT	$\mu = 1\%$	$\sigma = 5.30$
DS2	Lognormal	ΔT	$\mu = 11\%$	$\sigma = 0.69$
DS3	Lognormal	ΔT	$\mu = 30\%$	$\sigma = 0.59$
DS4	Lognormal	ΔT	$\mu = 49\%$	$\sigma = 0.58$

Ranges of variation of period elongation derived for the dataset are depicted in Fig. 10 for each damage level. In detail, the range of variation defined as the 16th–84th percentiles is reported in the plot along with the mean value. The plot indicates that a period elongation less than 13% with respect to the elastic period can be associated to a minor damage for RC columns. Conversely, period elongation up to 40% can represent a moderate to severe structural damage. Period elongation greater than 40% can be associated to severe damage or collapse. However, a significant overlap among ranges of variation of the period elongation for different damage levels is generally observed for the dataset of columns herein investigated. This, along with the large scatter of results, can prevent the correct identification of the damage level based on the monitoring of such DM.

The range of variation of residual drift ratios has been also analysed and plotted in Fig. 11 for each defined damage level. It is observed that the ranges of variation for

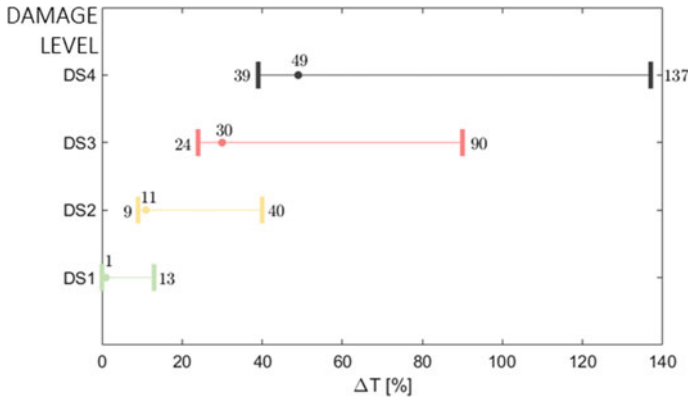


Fig. 10 Ranges of variation of period elongation for each damage level

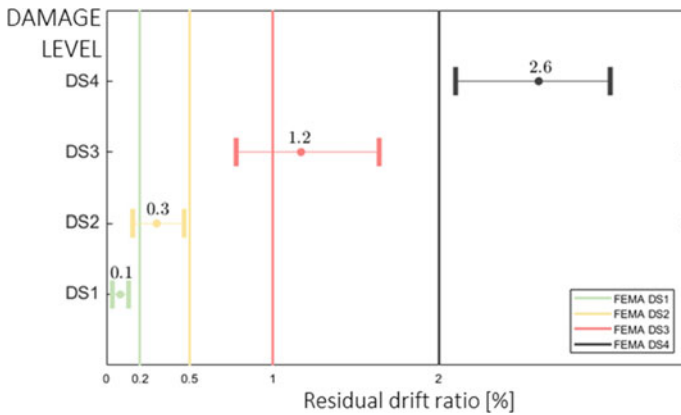


Fig. 11 Ranges of variation of residual drift ratios for each damage level and comparison with FEMA 356 thresholds

each damage level are not overlapped for the case of residual drift ratios, allowing for an unbiased damage quantification. Figure 11 also reports thresholds for the classification of damage states identified by the FEMA 356 [21]. The standard identifies four damage states associated with the residual drift, as reported in Table 6. DS1 corresponds to a residual drift of 0.2%, DS2 corresponds to a residual drift of 0.5%, DS3 is achieved for a residual drift of 1% and, finally, for DS4 the range of residual drift is between 1 and 4% depending on the inelastic capacity of the system.

For DS4, the threshold on residual drift is assumed equal to 2%, assuming a moderate ductility for the selected non-conforming columns adopted as case-study. The lower bounds (16th percentile) of the range of variation of residual drift from the numerical analysis is also reported in Table 6. The comparison between numerical results and FEMA thresholds shows that the numerical model generally

Table 6 Damage States classification based on the residual story drift ratio according to FEMA 356 [21] and comparison with lower bound values from numerical results

Damage state	Residual drift ratio (FEMA)	Lower bounds of residual drift ratios (numerical analysis)
DS1	0.20%	0.08%
DS2	0.50%	0.20%
DS3	1.00%	0.80%
DS4	High ductility systems 4.00%	—
	Moderate ductility systems 2.00%	2.10%
	Limited ductility systems 1.00%	—

provides a safe estimation of residual drifts associated to each damage level. Only for the collapse damage level, the FEMA threshold is slightly lower than the 16th percentile of the numerical data distribution. It should be noted that the definition of damage classification is different between FEMA and Park and Ang, as the latter refers to structural damage only. However, a quite good agreement between the two damage level classifications is recognised, attesting the soundness of the proposed methodological framework.

The columns' lateral stiffness degradation is computed as $\Delta k = 1 - k_i/k_0$, where k_0 is the initial lateral stiffness and k_i the lateral stiffness at the i -cycle (i.e., $k(IDR)$), as shown in Fig. 2. Ranges of variation of stiffness degradation for each damage level are plotted in Fig. 12. As previously observed for residual drift ratios, no overlap among ranges of variation of the stiffness degradation at different damage levels is found. Based on numerical results, a stiffness degradation ranging between 22–30%

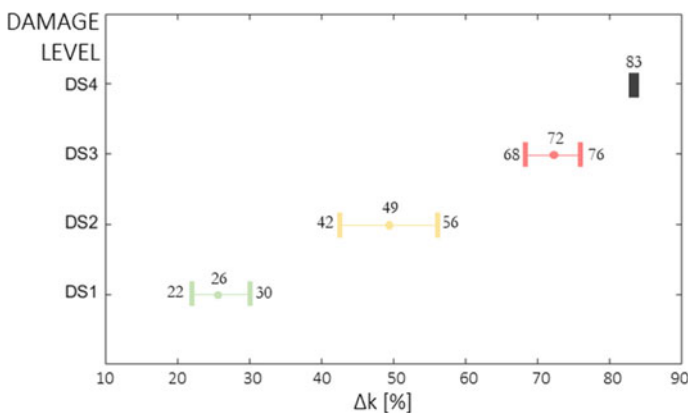


Fig. 12 Ranges of variation of stiffness degradation for each damage level

can be associated to a minor structural damage, while a stiffness degradation from 42 to 56% indicates a moderate damage level. A stiffness reduction in the range between 68%-76% means a severe damage, and degradation greater than 83% is associated with the structural collapse for the dataset of RC columns.

The trend of lateral stiffness degradation herein derived is compared with the stiffness degradation model proposed in Di Ludovico et al. [22]. Di Ludovico et al. proposed an empirical model that relates the stiffness degradation factor, $\lambda_k = k_i/k_0$, with the ductility experienced by RC columns, as follows:

$$\lambda_k = 1.0 \text{ for } \frac{\theta}{\theta_y} \leq 1.1 \quad (4)$$

$$\lambda_k = 1 - \left[1.07 - 1.15 \cdot \left(\frac{\theta}{\theta_y} \right)^{-0.92} \right] \text{ for } 1.1 < \frac{\theta}{\theta_y} \leq \theta_u/\theta_y$$

where θ is the columns chord rotation θ_y is the chord rotation at yielding; θ_u is ultimate chord rotation.

The model proposed by Di Ludovico et al. is compared with the stiffness degradation ranges derived from numerical analyses in Fig. 13 as a function of the ratio θ/θ_y . The comparison shows a perfect agreement between the empirical model and the results derived from numerical analyses on the dataset of RC columns herein considered, confirming the goodness of the numerical simulation for assessing the changes in DMs associated with the increasing seismic damage.

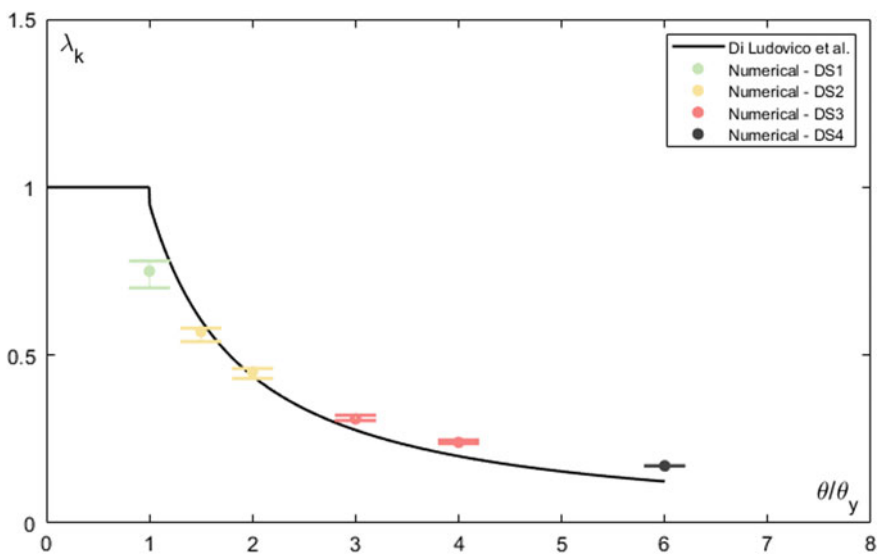


Fig. 13 Stiffness degradation from numerical analyses on the dataset and comparison with Di Ludovico et al. [22] model for the stiffness modification factor

7 Conclusions

In this paper, a methodological framework for the definition of ranges of variation of damage indicators commonly monitored with SHM systems is presented to detect and quantify the seismic damage in civil structures and infrastructures. The general framework is first illustrated, and an application is then presented for a dataset of 90 RC columns typical of existing frames with poor seismic detailing. A refined FEM model has been developed and validated on seven experimental cyclic quasi-static tests on full-scale RC columns with plain and deformed bars. The model has been used to simulate the seismic damage, considering the *IDR* as seismic demand parameter, and the variation of Damage Measures (DM) as a function of the experienced damage has been monitored. Fundamental period, residual drift ratio and lateral stiffness have been selected as DMs for the study. Damage levels have been defined, based on the Park and Ang damage index, and ranges of variation of selected DMs have been preliminary derived within the proposed framework. Based on the results of this preliminary study, the following conclusions can be derived:

- The methodological framework herein presented appears a sound technique to correlate the changes in dynamic properties and stiffness of structures in relation with an occurred damage. This system, combined with refined model updating techniques, represents a reliable tool for the damage detection, localization and quantification during long-term SHM;
- The fundamental period elongation can be simulated through sequential pushover-modal analysis on refined FEM model, providing ranges of variation of such DM as a function of the imposed *IDR* or the damage level. From preliminary results on the investigated dataset of RC columns, the ranges of variation of period elongation showed a large scatter of results and a significant overlap among damage levels, making difficult the clear identification of the level of damage if period elongation is used as DM during SHM. For the dataset of RC columns herein investigated, period elongation less than 13% is associated to a minor damage, period elongation up to 40% represent a moderate to severe structural damage. Period elongation greater than 40% is associated to severe damage or collapse;
- The ranges of variation of residual drift ratios derived on the dataset for each defined damage levels showed a good agreement with the thresholds and damage levels classification provided by the FEMA 356, confirming the goodness of the damage simulation and of the damage classification adopted for the study. For the dataset under investigation, residual drift greater than 0.2% is associated to a moderate damage. Residual drift greater than 0.8% is associated to severe damage, whereas values of residual drift higher than 2.1% are associated to structural collapse;
- A correlation between seismic damage level, *IDRs* and lateral stiffness degradation has been derived. This can be useful for seismic damage modelling in sequential analysis (i.e., mainshock-aftershock, earthquake followed by tsunami). For the dataset of RC columns a stiffness degradation greater than 22% is associated to a minor damage, while a stiffness degradation greater than 42% indicates a

moderate damage level. A stiffness reduction higher than 68% means a severe damage, and degradation greater than 83% is associated with the collapse;

- A good match between the numerical results on lateral stiffness degradation and the empirical model from Di Ludovico et al. [22] is found, attesting the reliability of the methodology in simulating the structural performance and damage under load reversal.

Future studies will look at extending the application of the proposed methodology to a wider dataset of RC columns and to more complex structural systems, like RC frames with masonry infill walls. Furthermore, the FEM model validation on real (or simulated) SHM processes will be performed to assess the variation of models' dynamic properties as a function of the experienced damage. Based on the preliminary results of the study related to the fundamental period elongation, other DMs related to the structural dynamic properties (e.g., modal shapes, other modal periods) will be also monitored in the analysis, to point out their sensitivity to structural damage for a reliable damage detection and quantification.

Acknowledgements This research is performed in the framework of the Research Project of National Relevance PRIN 2017 "Life-long optimized structural assessment and proactive maintenance with pervasive sensing techniques", Prot. 20172LHSEA.

References

1. Farrar CR, Worden K (2007) An introduction to structural health monitoring. *Philosoph Trans Royal Soc A: Math Phys Eng Sci* 365(1851):303–315
2. Zhang L, Brincker R (2005) An overview of operational modal analysis: major development and issues. In: 1st international operational modal analysis conference, pp 179–190
3. Trevelopoulos K, Guéguen P (2016) Period elongation-based framework for operative assessment of the variation of seismic vulnerability of reinforced concrete buildings during aftershock sequences. *Soil Dyn Earthq Eng* 84:224–237
4. Katsanos EI, Sextos AG (2015) Inelastic spectra of predict period elongation of structures under earthquake loading. *Earthq Eng Struct Dynam* 44(11):1765–1782
5. Masi A, Vona M (2010) Experimental and numerical evaluation of the fundamental period of undamaged and damaged RC framed buildings. *Bull Earthq Eng* 8:643–656
6. Vidal F, Navarro M, Aranda C, Enomoto T (2014) Changes in dynamic characteristics of Lorca RC buildings from pre-and post-earthquake ambient vibration data. *Bull Earthq Eng* 12(5):2095–2110
7. Mucciarelli M, Masi A, Gallipoli MR, Harabaglia P, Vona M, Ponzio F, Dolce M (2004) Analysis of RC building dynamic response and soil-building resonance based on data recorded during a damaging earthquake (Molise, Italy, 2002) *Bull Seismol Soc Am* 94(5):1943–1953
8. Di Sarno L, Amiri S (2019) Period elongation of deteriorating structures under mainshock-aftershock sequences. *Eng Struct* 196:109341
9. Dai K, Wang J, Li B, Hong HP (2017) Use of residual drift for post-earthquake damage assessment of RC buildings. *Eng Struct* 147:242–255
10. Park Y, Ang AH-S (1985) Mechanistic seismic damage model for reinforced concrete. *J Struct Eng* 111(4):722–739
11. Vamvatsikos D, Cornell Allin C (2002) Incremental dynamic analysis. *Earthq Eng Struct Dynam* 31:491–514

12. Del Zoppo M, Di Ludovico M, Balsamo A, Prota A (2018) Comparative analysis of existing RC columns jacketed with CFRP or FRCC. *Polymers* 10(4):361
13. Park YJ, Ang AH-S, Wen YK (1985) Seismic damage analysis of reinforced concrete buildings. *J Struct Eng* 111(4):740–757
14. Mazzoni S, McKenna F, Scott MH, Fenves GL (2006) OpenSees command language manual, from <https://opensees.berkeley.edu/>
15. Scott MH, Ryan KL (2013) Moment-rotation behavior of force-based plastic hinge elements. *Earthq Spectra* 29(2):597–607
16. Scott BD, Park R, Priestley MJN (1982) Stress–strain behavior of concrete confined by overlapping hoops at low and high strain rates. *ACI J* 79(1):13–27
17. Paulay T, Priestley MJN (1992) *Seismic design of reinforced concrete and masonry buildings*. Wiley
18. Zhao J, Sritharan S (2007) Modeling of strain penetration effects in fiber-based analysis of reinforced concrete structures. *ACI Struct J* 104
19. FIB Task Group on Bond Models (2000) *Bond of reinforcement in Concrete*, Bulletin 10, Lausanne, Switzerland
20. Di Ludovico M, Verderame GM, Prota A, Manfredi G, Cosenza E (2014) Cyclic behavior of nonconforming full-scale RC columns. *J Struct Eng* 140(5):04013107
21. Federal Emergency Management Agency (FEMA) (2000) n. 356: *Prestandard and Commentary for the seismic rehabilitation of building*
22. Di Ludovico M, Polese M, D'Aragnona MG, Prota A, Manfredi G (2013) A proposal for plastic hinges modification factors for damaged RC columns. *Eng Struct* 51:99–112

Data-Driven Nonparametric Structural Nonlinearity Identification Under Unknown Excitation with Limited Data Fusion



Ye Zhao, Bin Xu, Baichuan Deng, and Jia He

Abstract In this paper, a nonparametric data-driven NRF identification approach for multi-degree-of-freedom (MDOF) structures under unknown input measurements using limited fused dynamic response measurements is proposed, where a double Chebyshev polynomial combined with an updated Extended Kalman filter (UEKF) approach is employed. The proposed approach is validated numerically with MDOF structures equipped with various nonlinear members, including MR damper (damping-dominant) and SMA damper (stiffness-dominant) at first. An experimental study on a four-story steel frame model structure equipped with a MR damper on its fourth story is carried out and the test measurement is employed to validate the proposed method by comparing the identified excitation, unknown acceleration response and MR damping force with test measurements. Results show that the proposed approach is capable of identifying the NRF provided by different dampers and unknown excitation nonparametrically, which is very helpful for post-event condition evaluation of engineering structures where structural nonlinearity should be considered but input is usually unknown.

Keywords Nonlinear restoring force · Updated extended kalman filter (UEKF) · Double chebyshev polynomial model · SMA dampers · MR dampers · Nonparametric identification

Y. Zhao · B. Xu (✉)
College of Civil Engineering, Huaqiao University, Xiamen 361021, China
e-mail: binxu@hqu.edu.cn

B. Xu
Key Laboratory for Intelligent Infrastructure and Monitoring of Fujian Province (Huaqiao University), Xiamen 361021, China

B. Deng · J. He
College of Civil Engineering, Hunan University, Changsha 410082, China

1 Introduction

Structural identification (SI) plays key roles in structural health monitoring (SHM). Different from the structural stiffness, structural nonlinearity and excitations identification results can be used to estimate the structural energy consumption, the remaining service life and remaining load-carrying capacity of structures after the excitation of dynamic loadings [1].

In the early days, the Least Square Estimation-based algorithm was proposed to identify structural parameters with all the structural responses [2]. In practice, it could be difficult to obtain all the measurements. Therefore, various methods based on the minimum variance estimation and Bayesian principle, such as the particle filter (PF) and Kalman filter (KF), have been proposed. But the SI with unknown excitation is still a challenging task. Yang et al. proposed an extended Kalman filter with unknown input (EKF-UI) algorithm for SI with limited acceleration measurements and unknown inputs [3]. Lei et al. extend Yang's method with data fusion to solve the drift problem of the SI under unknown excitations [4]. Pan et al. proposed a general unknown input extended Kalman filter to solve the coupling problem of acceleration and excitations [5]. Aiming at the strong nonlinear structural identification, Song proposed an unscented minimum variance unbiased (UMVU) estimation scheme to realize the SI via unscented transform [6]. The proposed method mainly validates via numerical model and the structural nonlinearity model is always known.

In practice, the structural nonlinear properties are very complex and cannot be accumulated accurately in prior. Identification nonlinear structures using nonparametric model has received great attentions. Xu et al. proposed a method to describe the the structural nonlinearity with a nonparametric model and validated this method with a four-degree-of-freedom steel framework model experiment [7]. After that, He et al. presented a model-free nonlinear restoring force (NRF) identification method with a modified observation equation based on EKF and the NRF was identified by means of least squares estimation (LSE) at each time step [8]. In these methods, the structural external excitations are always set to be known.

This paper proposed a nonparametric nonlinear structural identification approach with limited measurements and unknown inputs. The double Chebyshev polynomial combined with an updated Extended Kalman filter approach is combined. The data fusion technique is used to avoid the drift problem in structural response forecasting. The proposed approach was numerically validated with MDOF structures equipped with different dampers mimicking different nonlinear behavior and experimentally with a four-story steel frame model equipped with a MR damper.

2 Nonparametric Polynomial Model and the EKF with Unknown Input

In physical science and mathematics, the Chebyshev polynomial is composed of a system of complete and orthogonal polynomials, with obvious advantages and applications. In this study, without using any parametric models for structural nonlinear behavior, the NRF could be described in the form of the double Chebyshev polynomial of structural relative velocity, relative displacement as shown in the Eq. (1),

$$\mathbf{R}_{i,i-1}[\dot{\mathbf{x}}(t), \mathbf{x}(t), \boldsymbol{\theta}] \approx \sum_{i=0}^k \sum_{j=0}^q c_{i,i-1,h,j}^{non} T_h(v'_{i,i-1}) T_j(s'_{i,i-1}) \quad (1)$$

where $\mathbf{R}_{i,i-1}[\dot{\mathbf{x}}(t), \mathbf{x}(t), \boldsymbol{\theta}]$ is the NRF between the i th DOF and $i - 1$ th DOF, $v_{i,i-1}$ and $s_{i,i-1}$ are relative velocity and relative displacement vectors, $c_{i,i-1,h,j}^{non}$ is the coefficient of the polynomial, k and q are integers which depend on the nature and extent of the nonlinearity. $T_h(v'_{i,i-1})$ and $T_j(s'_{i,i-1})$ are Chebyshev polynomial.

The advantage of the proposed method over the conventional Kalman filter is the estimation of the unknown excitation and identification of nonparametric NRF, in which unknown excitation is obtained by minimizing the observation error vector. In this paper, the Chebyshev polynomial coefficients are introduced into the extended state vector, which is the key to the nonparametric structural nonlinearity identification method. The detail steps of the proposed identification algorithm are shown in Ref. [9]. The main flow of the algorithm is as follows,

1. Setting the initial values of the extended state vector, the error covariance matrix and the unknown excitation.
2. Calculating priori state estimate: Using the extended state vector estimate from the k step to predict the extended state vector from the $k + 1$ step.
3. Calculating estimate error covariance matrix: Using the estimated value of the error covariance matrix at step k to obtain the predicted value of the error covariance matrix at step $k + 1$.
4. Calculating Kalman gain matrix.
5. Calculating posteriori state estimate: Computing the extended vector estimated value for step $k + 1$ using the extended state vector predicted value from step $k + 1$.
6. Estimating the unknown external excitation: Based on the least-squares estimation, the unknown external excitation can be estimated by minimizing the observation error vector.

3 Numerical Simulation Validation

A seven-story shear frame model is used to validate the proposed method. In the numerical model, the linear structural parameters are $m_i = 300 \text{ kg}$, $c_i = 0.2 \text{ kN}\cdot\text{s}/\text{m}$, and $k_i = 250 \text{ kN}/\text{m}$ ($i = 1, \dots, 7$). An SMA damper and an MR damper are installed on the second floor and the seventh floor of the structure to mimic the different kinds of structural nonlinearities. In the identification algorithm, the accelerations on the sixth floor and the fourth floor are measured, and the displacement responses on the first and third floors are used as data fusion. The acceleration response measurements are all polluted with white noise with a 2% noise-to-signal ratio in terms of root-mean-square (RMS). A wide-band random excitation with frequencies ranging from 0.1 to 30 Hz is applied on the third floor of the structure. The initial values of stiffness and damping coefficients are assumed to be 80% of the real value.

The Dahl model is used to model the NRF of the used MR damper [10]. The parameters in the model take the following values: $\sigma = 500 \text{ s}/\text{m}$, $K_0 = 20 \text{ N}/\text{m}$, $C_0 = 400 \text{ N}\cdot\text{s}/\text{m}$ and $f_0 = 0$.

In this study, the corresponding mathematical expression of the used SMA damper is shown in Ref. [11]. In this section, the following values are taken for the parameters, $S_a = 0.005 \text{ m}$, $S_b = 0.012 \text{ m}$, $k_1^{SMA} = 100 \text{ kN}/\text{m}$, $k_2^{SMA} = 50 \text{ kN}/\text{m}$.

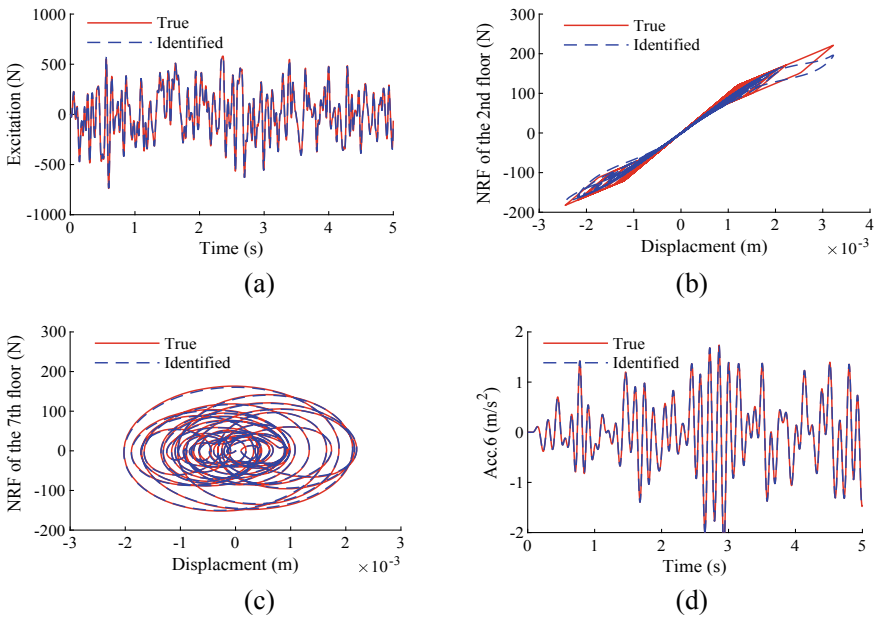


Fig. 1 The comparison of identified results: **a** unknown external excitation, **b** the hysteretic of SMA damper on the second floor **c** the hysteretic of MR damper on the seventh floor, **d** the acceleration on the sixth floor

Fig. 2 A four-story steel experimental model

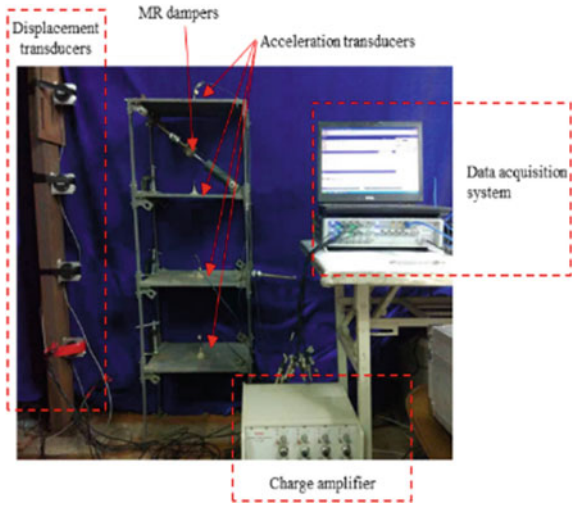


Figure 1 shows the comparison of the identified unknown external excitation, the hysteretic force of SMA damper on the second floor and that of MR damper on the seventh floor with their simulated results. It can be seen from Fig. 1 that the identified results are close to their true values with acceptable accuracy. The normal root-mean-square errors (NRMSE) for the excitation, SMA damper, MR damper and unmeasured acceleration on the sixth floor are 0.012, 0.025, 0.0035 and 0.0083, respectively.

4 Experimental Validation

A four-story steel frame structure model is established in the laboratory as shown in Fig. 2. Information on the parameters of the structural model is given in Ref. [12]. An MR damper is installed on the 4th floor of the model to mimic the nonlinear behavior during the vibration test. A random excitation is applied on the 2nd floor.

In the experimental validation of the proposed method, the initial structural parameters, including stiffness and damping coefficients, are assumed as 80% of the reference values. The acceleration responses at the first, second and third floors are measured, and at the same time, displacement measurements at the first and third floors are used for data fusion. Figure 3 shows the comparison between the acceleration on the fourth floor, excitation on the second floor. The comparison between the NRF on the fourth floor and the test measurement is shown in Fig. 4 in the form of the hysteretic curve and the time domain history, respectively.

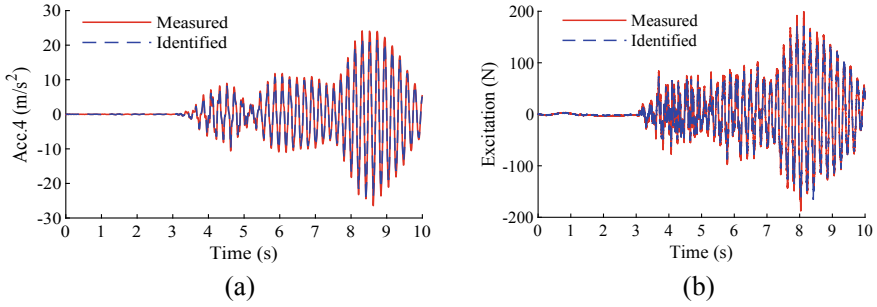


Fig. 3 The comparison of identified results: **a** unknown acceleration on the fourth, **b** the unknown excitation on the second floor

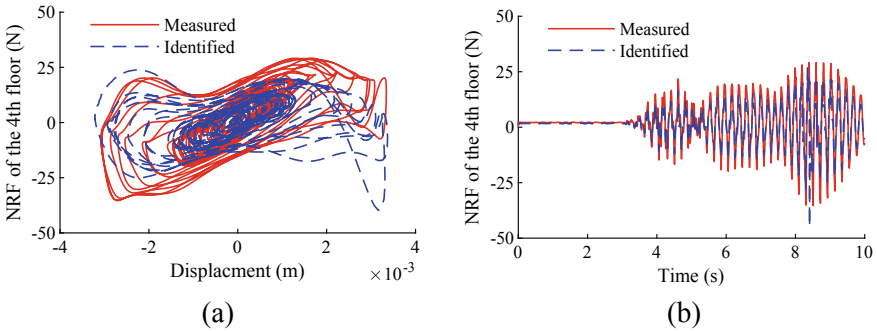


Fig. 4 The identified results of NRF: **a** the hysteretic of NRF on the fourth floor, **b** the time history of the identified NRF

5 Concluding Remarks

In this paper, a NRF, unknown excitation and acceleration response identification method combining the double Chebyshev polynomial and an updated extended Kalman filter with data fusion with limited acceleration and displacement measurements is proposed. The approach is firstly validated numerically with a seven-story shear model equipped with two kinds of dampers. Results show the unknown inputs, structural responses and NRF are identified with good accuracy. Dynamic test on a four-story steel frame model is carried out and limited acceleration response fused with displacements are used to validate the proposed approach. Results show that even model error and measurement noises exist the proposed approach can identify the damping force by the MR damper and the unknown excitation and response with acceptable accuracy using very limited information. Identified NRF and dynamic loading are helpful for the evaluation of the remaining service life and remaining load-carrying capacity evaluation of structures, which are the major tasks of damage prognosis (DP).

Acknowledgements The authors gratefully acknowledge the Scientific Research Funds of Huaqiao University (605-50Y18016) and the International Science and Technology Cooperation and Exchange Fund Projects (2014DFE70230) of Ministry of Science and Technology of China.

References

1. Olivier A, Smyth AW (2017) Review of nonlinear filtering for SHM with an exploration of novel higher-order kalman filtering algorithms for uncertainty quantification. *J Eng Mech* 143(11):04017128
2. Yang JN, Pan S, Lin S (2007) Least-squares estimation with unknown excitations for damage identification of structures. *Struct Control Health Monit* 14(3):497–521
3. Yang JN, Pan S, Huang H (2007) An adaptive extended Kalman filter for structural damage identifications II: unknown inputs. *J Eng Mech* 133(1):12–21
4. Lei Y, Luo S, Su Y (2016) Data fusion based improved Kalman filter with unknown inputs and without collocated acceleration measurements. *Smart Struct Syst* 18(3):375–387
5. Pan S, Xiao D, Xing S, Law SS, Du P, Li Y (2017) A general extended Kalman filter for simultaneous estimation of system and unknown inputs. *Eng Struct* 109:85–98
6. Song W (2018) Generalized minimum variance unbiased joint input-state estimation and its unscented scheme for dynamic systems with direct feedthrough. *Mech Syst Signal Process* 99:886–920
7. Xu B, He J, Masri SF (2015) Data-based model-free hysteretic restoring force and mass identification for dynamic systems. *Comput-Aided Civ Infrastruct Eng* 30(1):2–18
8. He J, Zhang X, Qi M, Xu B (2019) Model-free identification of nonlinear restoring force with modified observation equation. *Appl Sci* 306(9):9020306
9. Liu L, Su Y, Zhu J, Lei Y (2016) Data fusion based EKF-UI for real-time simultaneous identification of structural systems and unknown external inputs. *Measurement* 88:456–467
10. Zhou Q, Qu WL (2002) Two mechanic models for magneto-rheological damper and corresponding test verification. *Earthq Eng Eng Vib* 22(4):144–150
11. Li H, Mao C (2001) Seismic response of buildings with SMA passive energy dissipation devices: analysis and design. *Earthq Eng Eng Vib* 21(4):133–139
12. Xu B, Li J, Dyke SJ, Deng BC, He J (2020) Nonparametric identification for hysteretic behavior modeled with a power series polynomial using EKF-WGI approach under limited acceleration and unknown mass. *Int J Non-Linear Mech* 119:103324

Out-of-Plane Ambient Vibration Tests of an Infill Wall in RC Frame Subjected to Previous In-Plane Damage



Giuseppe Santarsiero , Alessandra De Angelis, Vincenzo Manfredi ,
Francesco Santamato, Angelo Masi , and Marisa Pecce 

Abstract Masonry infill walls are widely used as enclosure elements in reinforced concrete (RC) buildings to provide thermal and acoustic insulation. Past earthquakes have identified the masonry infill walls' out-of-plane collapse as one of the predominant modes of failure. Out-of-plane failure is characterized by brittle behavior and it is, therefore, a threat to human safety. Moreover, the out-of-plane capacity is significantly affected by the presence of cracks due to the in-plane damage related to the interstorey drift. In order to identify the out-of-plane behavior of infill walls depending on the in-plane damage, an experimental campaign based on cyclic quasi-static tests has been initiated on a full-scale infilled RC portal frame at the Laboratory of Structures of the University of Basilicata. The one-bay (4.5 m span), one story (3 m height) frame infilled with two layers of hollow clay brick walls 8 and 12 cm thick, has been subjected to in-plane loading by means of three reversed cycles for each increasing amplitude, until the story drift was equal to 2% and extensive damage occurred to both the infills and the RC members. After each set of three in-plane cycles, a dynamic identification of the infills' layers has been carried out based on ambient vibrations in order to detect changes in its dynamic behavior. This latter, using nine accelerometers placed on the infills' surface. The identification tests provided valuable information regarding the out-of-plane (OOP) frequencies during the test as a function of the in-plane drift. The paper describes the results of in-plane tests in correlation with the results of the ambient vibration tests.

Keywords Infill walls · Dynamic identification · Out-of-plane frequency · In-plane damage

G. Santarsiero · V. Manfredi · A. Masi
School of Engineering, University of Basilicata, Potenza, Italy

A. De Angelis (✉) · F. Santamato · M. Pecce
Department of Engineering, University of Sannio, Benevento, Italy
e-mail: alessandra.deangelis@unisannio.it

1 Introduction

Masonry infill walls are widely used as enclosure elements in reinforced concrete (RC) buildings to provide thermal and acoustic insulation.

Recently, the interest in the out-of-plane (OOP) response of infills has been growing because it was found as the main cause of extensive damage on exterior infill walls and interior partitions in RC framed buildings during recent earthquakes in Italy and Europe (e.g., [1, 2]). Many buildings displayed a complete loss of the masonry infill walls also at lower stories, furthermore OOP failure of a single layer of the infill or tilting of infills were observed [3].

Various experimental tests [4–6] and theoretical studies [7, 8] were carried out on this subject, highlighting how the OOP response of infill walls is noticeably affected by the slenderness and the boundary conditions of the panel, the mechanical characteristics of the masonry, the stiffness of the surrounding frame elements, and the presence of cracks due to prior in-plane damage.

Some ambient vibration tests on damaged and undamaged infill masonry walls with the aim of characterizing their OOP dynamic properties and understanding the influence of the damage and opening on their OOP frequencies were carried out in Nepal [9].

In situ tests were recently carried out also by Furtado et al. [10] on infill masonry walls with the main goal of characterizing the dynamic properties such as the in-plane and OOP frequencies of the panel with different characteristics.

Other ambient vibration tests including the calibration of the numerical model and the discussion related to the influence of the interaction between infill and surrounding RC frame on the out-of-plane response of the infill wall are described in [11, 12].

Moreover, in the last decades, the measuring of the variation in the dynamic parameters for the detection of structural damage has appeared to be a promising technique [13]. The dynamic behavior of structures is described by their dynamic characteristics such as natural frequencies, mode shapes, and modal damping ratios. The natural frequency is the most common damage feature because it is very easy to determine with a high level of accuracy by using few sensors.

In the field of RC structures, several authors conducted shaking table tests on frames and measured the variation in the dynamic properties due to progressive damage [14] or numerically simulated the response of RC frames [15], also taking into account the influence of the infill walls [16].

The paper presents the first results of an experimental campaign based on cyclic quasi-static tests, started on a full-scale infilled RC portal frame at the Laboratory of Structures of the University of Basilicata, with the aim to identify the out-of-plane behavior of infill walls depending on the in-plane damage. The one-bay (4.5 m span), one story (3 m height) frame infilled with two layers of hollow clay brick walls 8 and 12 cm thick, has been subjected to in-plane loading by means of three reversed cycles for each increasing amplitude until the story drift was equal to 2% and extensive damage occurred to both the infills and the RC members. After each set

of three in-plane cycles, dynamic identification of the infills' layers has been carried out based on ambient vibrations in order to detect changes in its dynamic behavior.

2 Experimental Tests

2.1 Specimen Description

The experimental campaign on full-scale reinforced concrete portal frames, designed for vertical loads only according to the technical rules of the '70s and equipped with different infill systems here reported, has the primary purpose of developing integrated techniques for the seismic and energy upgrading of buildings.

The whole program comprises totally four portals structurally identical. The first is a bare frame used as a benchmark in terms of seismic performance, the second portal (the one here studied) is equipped with a traditional infill solution consisting of a double layer of hollow clay bricks (12 + 8 cm thickness) with void cavity in between, as reported in Fig. 1. Brick units shown in Fig. 1c, d have 60% of voids and are also usually adopted in partitions. A third portal derives from the second with the replacement of the external infill layer (12 cm thickness) with a 20 cm infill layer devoted to reducing thermal transmittance and increasing seismic response of the

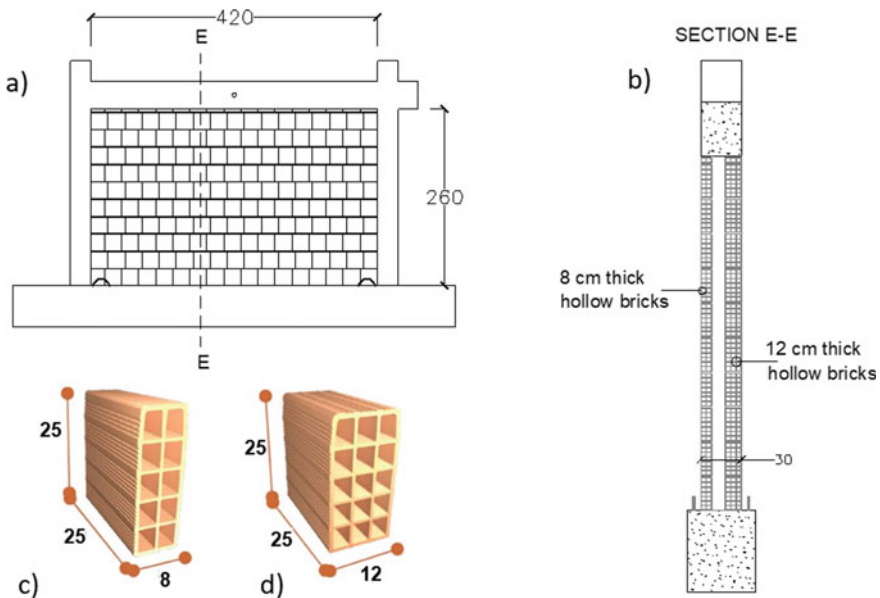


Fig. 1 Full-scale portal frame (a), section view (b) of the double layer infill made of 8 cm (c) and 12 cm (d) thick brick units (dimensions in cm)

frame. The latest portal will be equipped with an innovative infill system still under development. It is worth noting that all the infilled portals were equipped with also a 1 cm plaster layer on the external sides of infills.

The RC structure is made of columns with a 30×30 cm cross-section, while the beam has a 30×40 cm cross-section. Only one of the beam-column joints is partially confined, as can be seen from Fig. 1.

Concrete with a mean cylinder strength equal to $f_c = 20$ MPa and reinforcing steel of class B450C (characteristic yield strength 450 MPa) were used. Regarding steel, the choice is related to the scarce availability of the typical steel used in the '70s that is FeB32 having a characteristic yielding strength of 320 MPa. Therefore, the amount of steel reinforcement has been reduced to allow the use of B450C steel.

The beam is provided with 12 mm diameter bars, four on the top and two on the bottom (for the full length), while columns are equipped with four 14 mm diameter bars placed at corners. Moreover, the beam-column joints are not provided with any kind of hoops according to the design related to only vertical loads.

Finally, stirrups and hoops in beams and columns are equipped with 90° bents, and due to this, they cannot be assumed as able to provide a confining effect to the concrete section. The foundation beam has been designed to provide large stiffness and strength compared to the column members and it is consequently reinforced.

During the concrete grouting of RC members and construction of infills, several material specimens were collected to determine the material properties. In particular, concrete cubes for evaluating the concrete compressive strength, cylinder concrete specimens for tensile tests, rebar specimens for determining the yielding and ultimate stress of the reinforcing steel. Test results showed that concrete cubic compressive strength is 17.6 MPa (significantly lower than the expected one) while the mean steel yielding stress is 490 MPa according to the adopted steel grade.

Moreover, bricks were collected, and wallets were also constructed using the different types of brick units, depending on the adopted infill solutions, to be subjected to subsequent characterization tests. Details about the type and number of specimens collected is reported in [17].

2.2 *In-Plane Test and Damage Pattern*

In order to apply in-plane loading to the infilled frame, a test apparatus was purposely designed and constructed to make it work with the loading system of the Laboratory of Structures at the University of Basilicata.

As can be seen from Fig. 2a, the test apparatus was conceived to apply the horizontal load through a hydraulic actuator connected to a reaction wall and to the midpoint of the beam. Columns were subjected to a constant axial load exerted by hydraulic jacks monitored during the tests. They were contrasted by steel ties rods connected to the reaction floor. This latter was also used to restraint the foundation beam (see Fig. 2b). Instrumentation to measure the frame displacements and deformations was made-up of: (i) LVDT transducers to measure deformations of column

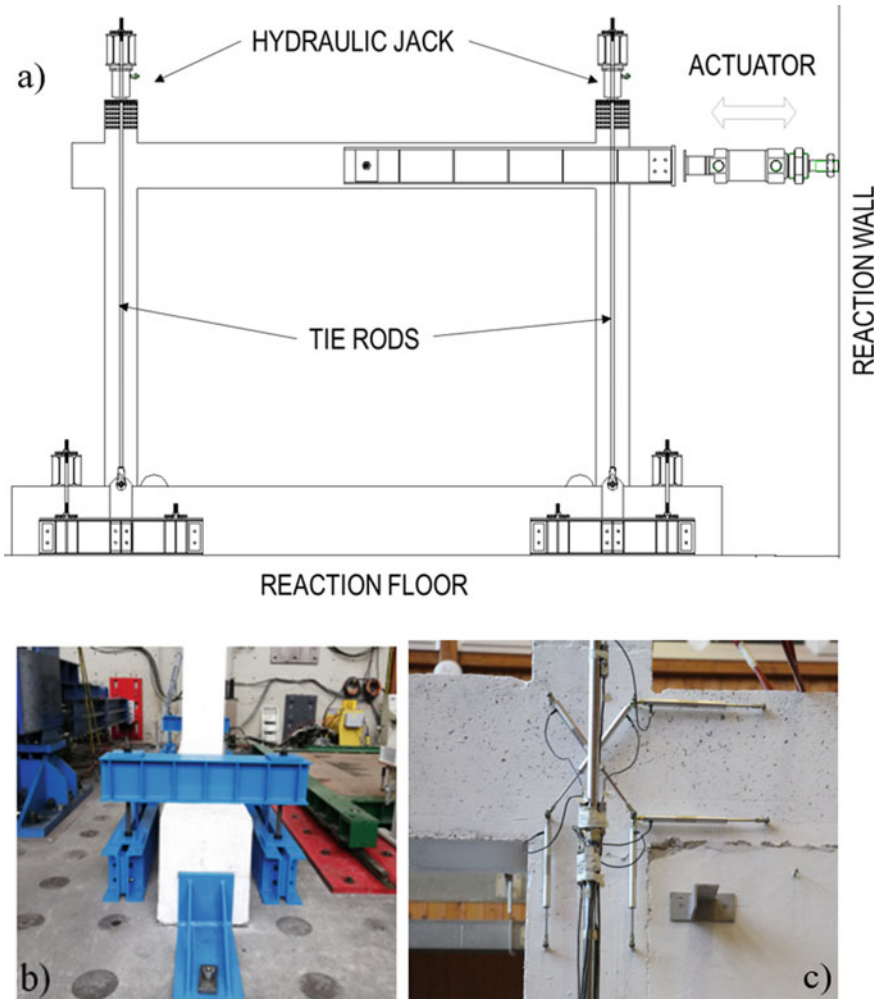


Fig. 2 a) Whole test apparatus, b) restraint system of the foundation beam and c) LVDT sensors applied to a beam-column joint, beam and column ends

ends and beam-column joints distortions, (ii) wire transducers to measure the global story displacement and the diagonal deformation of infill panels. Load cells were used to measure axial load exerted by jacks on the columns and the horizontal actuator's force needed to reproduce the loading history.

The experimental program (Table 1) was set in order to perform in-plane tests with a certain level of drift applied to the beam and immediately after carrying out an ambient vibration test allowing the modal identification of infill panels to detect changes in their dynamic properties due to the in-plane damage.

Table 1 Experimental program

Test n	Type	Drift (%)	Test n	Type	Drift (%)
0	Identification	–	12	Identification	–
1	Cyclic	0.01	13	Cyclic	0.75
2	Identification	–	14	Identification	–
3	Cyclic	0.02	15	Cyclic	1.00
4	Identification	–	16	Identification	–
5	Cyclic	0.05	17	Cyclic	1.25
6	Identification	–	18	Identification	–
7	Cyclic	0.10	19	Cyclic	1.50
8	Identification	–	20	Identification	–
9	Cyclic	0.20	21	Cyclic	2.00
10	Identification	–	22	Identification	–
11	Cyclic	0.50			

The in-plane cyclic loading has been made through a displacement-controlled procedure increasing drift values in the range 0.01–2.0% and related story displacements between 0.3 and 60 mm. The maximum drift value (2.0%) was chosen in order to lead the structure to a near-collapse condition at the end of the test. This evaluation was based on preliminary numerical analyses carried out before the test.

According to previous experimental studies (e.g. [18]), three complete loading cycles were performed at each drift amplitude, using a loading velocity equal to 4 mm/s.

The specimen's response under cyclic in-plane loading is reported in Fig. 3 through the envelope of load–displacement curves. The positive peak load is equal to 234 kN at 1.0% drift, while the max negative load is 248 kN at 0.5% drift.

Peak loads are about three times the values obtained from test results on the benchmark frame (bare), which showed peak values near 80 kN [17].

First damage was observed as a detachment between frame and infill (0.5% drift) along with diagonal cracks at the top end of the column and beam on the left (see Fig. 4a). These cracks progressively widened involving the joint panel.

Masonry crushing started at 1.00% drift on the internal infill's leaf (see Fig. 4b).

Figures 4c, d show the main damage patterns on the thicker (12 cm) infill layer's side for the max applied drift (2%). Damage on the right side of the frame is represented by the column top end's shear failure, with a significant residual displacement. Localized crushing of the masonry infills has been observed at both sides of the infill panel, caused by the interaction between masonry and RC frame, while the substantial absence of cracks in the central part of infill walls was observed.

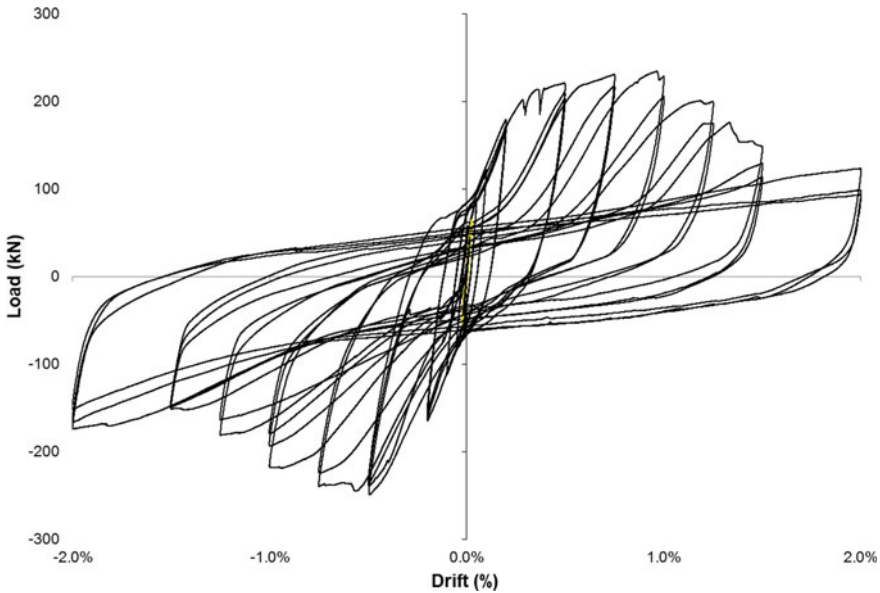


Fig. 3 Load-drift envelope of in-plane loading

3 Out-of-Plane Ambient Vibration Investigations

3.1 Test Setup of the Ambient Vibration Tests

There are basically two different experimental measurement methods: the ambient vibration test (AVT) and the forced vibration test (FVT). In the FVT, the structure is vibrated by a known input force, such as impulse hammers, drop weights, and electro-dynamics shakers. In the AVT, only the response is measured using environmental excitation, such as wind, human walking, or traffic.

The main advantages of the AVT are (a) testing is cheap and fast; (b) testing does not interfere with the operation of the structure; (c) the measured response represents the real operating conditions of the structure.

In this paper, according to the symmetry of the out-of-plane dynamic response, the ambient vibration tests were carried out using 9 accelerometers distributed as following: 7 accelerometers on the infill wall and 2 accelerometers on the RC frame as reported in Fig. 5. The adopted sensors are uniaxial servo-accelerometers with the following characteristics: 10 V/g sensitivity, ± 0.5 g measurement range and frequency range from 0.15 to 1000 Hz. The equipment used for the tests also includes signal cables, a 16-channel data acquisition system, a signal amplifier and a portable computer.

As already said, two ambient vibration tests, named test_0, were conducted separately, first on the internal leaf and then on the external one according to the test setup



Fig. 4 Final damage state: **a** left side and **b** right side of the frame

in Fig. 5, to investigate the out-of-plane dynamic response of the tested frame with the infill wall in a healthy state.

The frequencies obtained from these tests have been considered as a reference for the subsequent correlation analysis, described in the following section, between the first out-of-plane frequencies (of the entire system (frame + infill wall) and the internal and external leaves) and the in-plane damage.

During the in-plane test, instead, the test setup adopted for the ambient vibration tests after each cycle of in-plane loading, is reported in Fig. 6, since it was not possible to move the accelerometers from one leaf to another one during the in-plane tests.

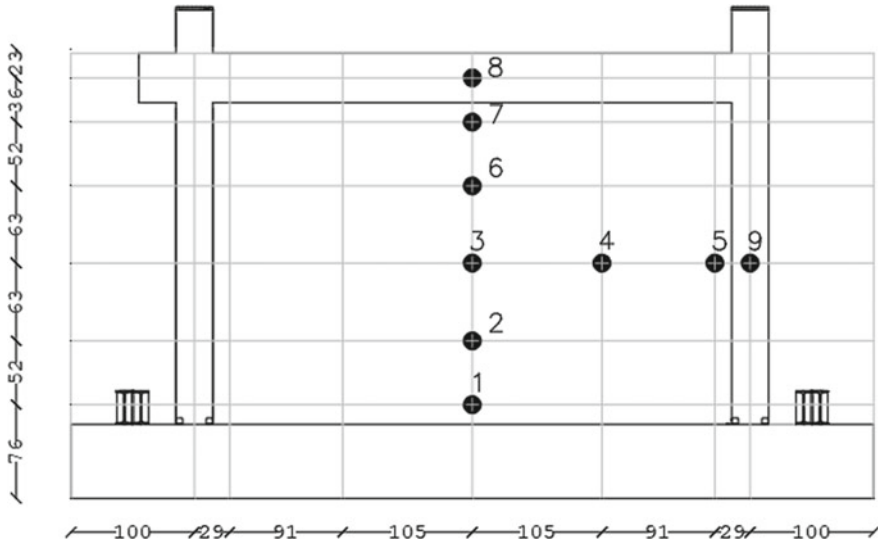


Fig. 5 Layout of the ambient vibration Test_0

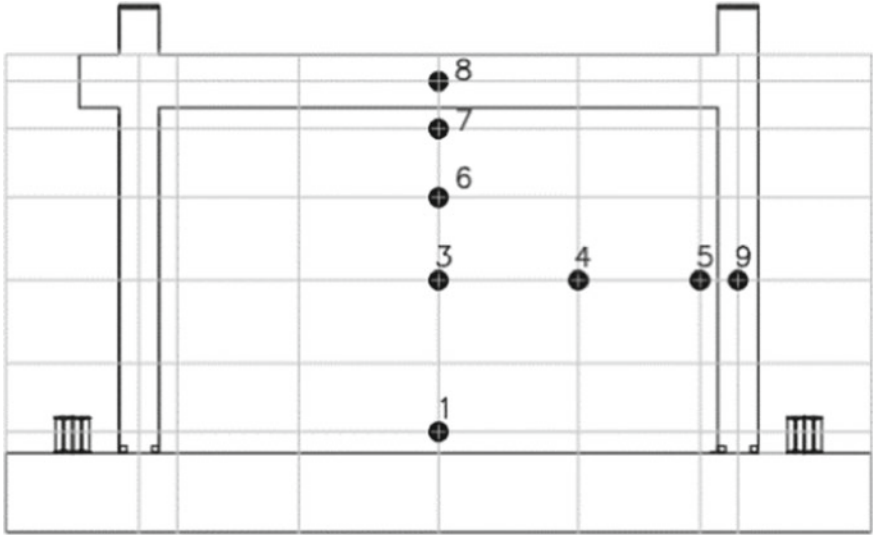
3.2 Modal Identification Results and Correlation with the In-Plane Damage.

System identification techniques obtained through ambient vibration measurements have become very attractive due to the main advantages of the AVT. Moreover, system identification results based on ambient vibration tests can provide an accurate and reliable description of dynamic characteristics for a structure. In OMA (Operational Modal Analysis), the structure is excited by unknown input force, and the structure’s responses are measured.

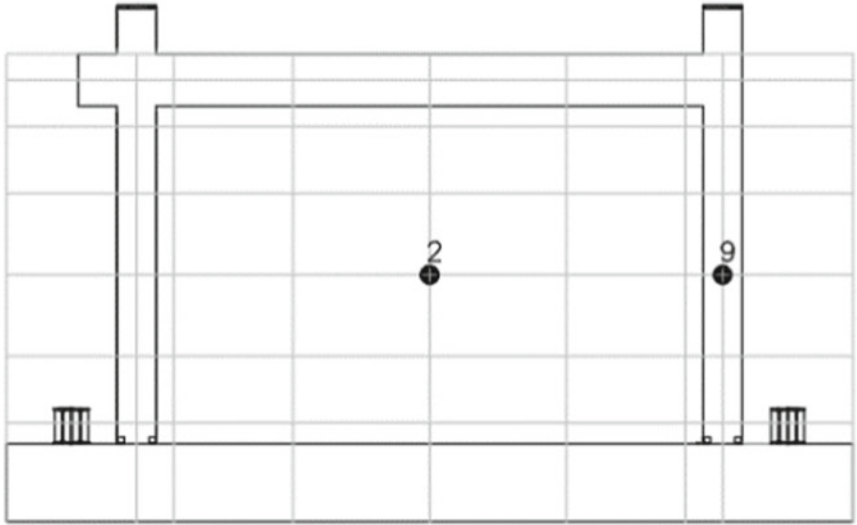
In this case, the ambient vibration response of the specimens was acquired for 900 s at a sampling frequency of 200 Hz. Before the data elaboration, i.e., extracting the modal properties, the time series have been deeply inspected. It was found that accelerometers indicated with 6, 7 and 8 in Fig. 6 were out of order due to damage of the specimen during the in-plane tests; as a consequence, the data recorded from these sensors have been neglected in the analysis, i.e. these accelerometers are not be considered in the present work.

The OMA technique named Frequency Domain Decomposition (FDD) has been applied. FDD is a nonparametric frequency domain technique meaning that modal parameters are estimated directly from curves. The frequencies are obtained by the simple Peak Picking technique applied in the first singular value line of the singular value decomposition (SVD) plot. The theoretical background of FDD is published in many references, including [19–21].

In this case, three clear modes were identified for the tested structure in the healthy state as reported in Table 2.



a)



b)

Fig. 6 Layout of the ambient vibration Test_2-22: **a** external leaf; **b** internal leaf

Table 2 Modal identification results (Test_0)

Mode	Frequency (Hz)
1st mode of the frame-infill system	6.25
1st out-of-plane mode of the internal leaf	30.08
1st out-of-plane mode of the external leaf	39.99

The same processing was carried out for all ambient vibration tests at the end of each in-plane cycle load. The results obtained are summarized in Table 3, which shows the experimental frequencies for each step of the test and its variation with respect to the corresponding frequencies of Test_0 representative of the health specimen’s status.

Moreover, the evolution of the frequencies during the test is reported in Fig. 7.

As shown in Table 3, it can be assumed that there is not a significant variation of the out-of-plane frequencies up to test 10 since values less than 1% have been registered. This result is consistent with the damage pattern found during the in-plane tests; in fact, up to test 9, no cracks appeared on the frame or on the infill walls.

At the end of test 9 (in-plane cyclic test), slight signs of detachment were found, which mainly affect the plaster; the subsequent ambient vibration test (Test_10) revealed a slight variation of the out-of-plane frequency with a maximum value of about 3% for the first mode of the whole system (frame + infills) while values of frequency variation lower than 1% are detected for the out-of-plane frequencies related to the internal leaf (−1%) and external one (−0.2%).

However, significant variation (higher than 5%) of the out-of-plane frequencies have been detected at Test_12. This is probably related to the extended detachment

Table 3 Modal identification results (all tests)

Test	Drift (%)	1st mode frame-infill wall		1st out-of-plane mode internal leaf		1st out-of-plane mode external leaf	
		f ₁ (Hz)	Δf ₁ (%)	f ₂ (Hz)	Δf ₂ (%)	f ₃ (Hz)	Δf ₃ (%)
0	–	6.25		30.08		39.99	
2	0.01	6.25	0.0	30.08	0.0	39.99	0.0
4	0.02	6.25	0.0	30.24	0.5	39.88	−0.3
6	0.05	6.25	0.0	30.02	−0.2	39.98	0.0
8	0.10	6.19	−1.0	29.86	−0.7	39.93	−0.1
10	0.20	6.04	−3.4	29.79	−1.0	39.90	−0.2
12	0.50	5.90	−5.6	24.84	−17.4	37.22	−6.9
14	0.75	5.58	−10.7	24.94	−17.1	36.69	−8.3
16	1.00	5.50	−12.1	22.47	−25.3	33.30	−16.7
18	1.25	5.32	−15.0	22.44	−25.4	32.90	−17.7
20	1.50	4.91	−21.4	22.22	−26.1	32.57	−18.6
22	2.00	4.16	−33.4	18.67	−37.9	29.93	−25.2

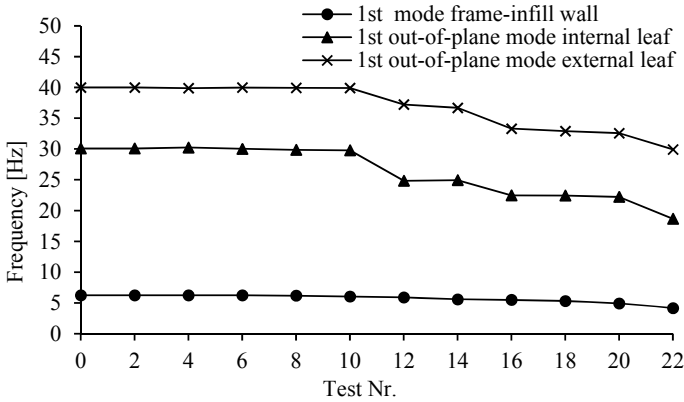


Fig. 7 Evolution of the frequencies during the test

along the perimeter of the infill wall and due to the cracks at the upper beam of the RC frame found in the previous in-plane cyclic test (Test 11) already described and shown in Fig. 4a. At this stage, the maximum value of about 17% of frequency decrease was obtained for the infill wall's internal leaf.

Starting from Test 12, according to the increase of in-plane damage, there is a significant decrease in the out-of-plane frequency. It is worth noting that the higher value of frequency reduction is related to the internal leaf (8 cm thick). This result agrees with the progressive damage detected during the in-plane cyclic tests; in fact, as shown in Fig. 4b, the masonry crushing started at 1.00% drift on the internal infill's leaf.

At the last test conducted (Test_22), the extracted frequencies for the first three out-of-plane modes considered are respectively 4.16 Hz, 18.67 Hz and 29.93 Hz. Therefore, values of the out-of-plane frequency variations up to 25%- 38% are detected for all the identified modes. At the previous in-plane cyclic stage (Test_21) localized crushing of the masonry infills have been observed at both sides of the infill panel caused by the interaction between masonry and RC frame.

Therefore, it can be stated that the first remarkable stiffness reduction of infills is observed for a drift of 0.5%, corresponding to the damage limitation state (SLD) prescribed by the Italian seismic code (17% and 8% frequency reduction for the internal and the external infill layers respectively). For higher drift values, which could be referred to a life safety condition (e.g. 1.0% drift or more), the frequency reduction ranges between 16 and 25%.

Thus, the variations of the out-of-plane frequencies, here detected, are strongly related to the type and amount of damage observed during the in-plane cyclic tests.

As highlighted by recent studies [22–24], the masonry infill walls damaged by in-plane actions are characterized by an out-of-plane response with reduced strength and stiffness with respect to an undamaged infill. Obviously, the reduction of the OOP response (the stiffness in this case) depends on the IP damage level, and it can be evaluated by empirical formulation recently proposed in the literature [25].

These results lead the authors to believe that it could be a promising technique for the detection of structural damage even using a limited number of sensors. Surely, other tests are needed to validate the obtained results and compare them with the expected out-of-plane stiffness reduction from existing literature formulations.

4 Conclusions

In this paper, the first results of an experimental campaign based on cyclic quasi-static tests started on a full-scale infilled RC portal frame at the Laboratory of Structures of the University of Basilicata are reported.

The main objective is identifying the out-of-plane behavior of infill walls depending on the in-plane damage.

The one-bay (4.5 m span), one story (3 m height) frame infilled with two layers of hollow clay brick walls 8 and 12 cm thick, has been subjected to in-plane loading by means of three reversed cycles for each increasing amplitude until the story drift was equal to 2% and extensive damage occurred to both the infills and the RC members. After each set of three in-plane cycles, dynamic identification of the infills' layers has been carried out based on ambient vibrations to detect changes in its dynamic behavior.

Results show that the external layer (12 cm thick) is subjected to lower damage with respect to the internal one (8 cm thick), as shown by a lower frequency reduction.

It is shown as the identification of the out-of-plane frequencies and their variations could be a promising technique for the detection of structural damage even using a limited number of sensors.

Acknowledgements The work reported in this paper was partly carried out within the framework of the DPC-ReLUIIS 2019-21 Project, WP5 "Rapid, low impacting and integrated upgrading interventions and WP17 "Code Contributions for non-structural components".

References

1. Masi A, Chiauzzi L, Santarsiero G, Manfredi V, Biondi S, Spacone E, Del Gaudio C, Ricci P, Manfredi G, Verderame GM (2019) Seismic response of RC buildings during the Mw 6.0 August 24, 2016 Central Italy earthquake: the Amatrice case study. *Bullet Earthq Eng* 17(10):5631–5654
2. Vicente RS, Rodrigues H, Varum H et al (2012) Performance of masonry enclosure walls: lessons learned from recent earthquakes. *Earthq Eng Vib* 11:23–34
3. Braga F, Manfredi V, Masi A, Salvatori A, Vona M (2011) Performance of non-structural elements in RC buildings during the L'Aquila, 2009 earthquake. *Bull Earthq Eng* 9:307–324
4. Hak S, Morandi P, Magenes G (2014) Out-of-plane experimental response of strong masonry infills. In: Presented at the second European conference on earthquake engineering and seismology, Istanbul.

5. Pereira PMF, Pereira NMF, Ferreira DJE, Lourenço PB (2011) Behavior of masonry infill panels in RC frames subjected to in plane and out of plane load. In: 7th Amcm international conference, Krakow, Poland
6. Ricci P, Di Domenico M, Verderame GM (2018) Experimental investigation of the influence of slenderness ratio and of the in-plane/out-of-plane interaction on the out-of-plane strength of URM infill walls. *Constr Build Mater* 191:505–522
7. Abrams DP, Angel R, Uzarski J (1996) Out of plane strength of unreinforced masonry infill panels. *Earthq Spectra* 12(4):825–844
8. Manfredi V, Masi A (2014) Combining in-plane and out-of-plane behaviour of masonry infills in the seismic analysis of RC buildings. *Earthq Struct* 6(5):515–537
9. Varum H, Furtado A, Rodrigues H, Oliveira J, Vila-Pouca N, Arêde A (2017) Seismic performance of the infill masonry walls and ambient vibration tests after the Ghoroka 2015. Nepal earthquake. *Bull Earthq Eng* 15(3):1185–1212
10. Furtado A, Rodrigues H, Arede A, Varum H (2017) Modal identification of infill masonry walls with different characteristics. *Eng Struct* 145:118–134
11. De Angelis A, Pecce MR (2018) Out-of-plane structural identification of a masonry infill wall inside beam-column RC frames. *Eng Struct* 173:546–558
12. Rainieri C, Di Domenico M, De Risi MT, Ricci P (2019) Output-only modal testing and model validation of unreinforced masonry infill walls in reinforced concrete frames. In: 8th international operational modal analysis conference, Copenhagen
13. Doebling S, Farrar C, Prime M (1998) A summary review of vibration-based damage identification methods. *Shock and Vibration Digest* 30:91–105
14. Li S, Zuo Z, Zhai C, Xu S, Xie L (2016) Shaking table test on the collapse process of a three-story reinforced concrete frame structure. *Eng Struct* 118:156–166
15. Paultre P, Weber B, Mousseau S, Proulx J (2016) Detection and prediction of seismic damage to a high-strength concrete moment resisting frame structure. *Eng Struct* 114:209–225
16. Pepe V, De Angelis A, Pecce MR (2019) Damage assessment of an existing RC infilled structure by numerical simulation of the dynamic response. *J Civ Struct Heal Monit* 9:385–395
17. Ventura G, Masi A, Santarsiero G, Manfredi V, Digriolo A, Nigro D (2019) Sviluppo di tecniche integrate di miglioramento delle prestazioni sismiche ed energetiche: descrizione e risultati preliminari del programma sperimentale su portali in c.a.. Convegno ANIDIS L'ingegneria Sismica in Italia – Ascoli Piceno, Italy, 15–19 September 2019
18. Masi A, Santarsiero G (2013) Seismic tests on RC building exterior joints with wide beams. *Adv Mater Res* 787:771–777
19. Brincker R, Zhang L, Andersen P (2001) Modal identification of output-only systems using frequency domain decomposition. *Inst Phys Publ Smart Mater Struct* 10:441–445
20. Gade S, Moller N, Herlufsen H (2006) Identification techniques for operational modal analysis—an overview and practical experiences. In: 24th conference and exposition on structural dynamics (IMAC–XXIV), Missouri
21. Brincker R, Ventura C, Anderson P (2003) Why output-only modal testing is a desirable tool for a wide range of practical applications. In: 21st international modal analysis conference IMAC, Kissimmee, Florida
22. Kadysiewski S, Mosalam KM (2009) Modelling of unreinforced masonry infill walls considering in-plane and out-of-plane interaction. Pacific Earthquake Engineering Research Center
23. Agnihotri P, Singhal V, Rai DC (2013) Effect of in-plane damage on out-of-plane strength of unreinforced masonry walls. *Eng Struct* 57:1–11
24. Ricci P, Di Domenico M, Verderame GM (2018) Experimental assessment of the in-plane/out-of-plane interaction in unreinforced masonry infill walls. *Eng Struct* 173:960–978
25. Di Domenico M, De Risi MT, Ricci P, Verderame GM, Manfredi G (2021) Empirical prediction of the in-plane/out-of-plane interaction effects in clay brick unreinforced masonry infill walls. *Eng Struct* 227:111438

Assessment of an Historical Masonry Bell Tower by Modal Testing



Alessandra De Angelis , Francesco Santamato, and Marisa Pecce 

Abstract Masonry heritage structures are among the most vulnerable typologies during earthquake. Their safety assessment requires a higher degree of accuracy due to the lack of knowledge on the original design and the construction procedures. The collection of information about the hidden geometry and the material properties should be performed by non-destructive techniques to avoid any damage to the artistic value. Moreover, for the assessment of the structural behavior a reliable method is the structural identification by on-site dynamic test. In this paper the results of the ambient vibration test and operational modal analysis are reported to calibrate a FE model of the historical masonry bell-tower of S. Sofia. The bell tower of S. Sofia is part of the monumental complex of S. Sofia, in Benevento together with the S. Sofia church, the monastery and the fountain. In 2011, this monumental complex was added in the World Heritage List of UNESCO. The bell tower is about 26 m high and it is characterized by a shaft which extends for a height of about 12 m, it has the shape of a hollow parallelepiped with a square base. The belfry is characterized by regular and equal openings on all four faces and it is surmounted by an octagonal lantern with a dome with eight segments. The calibrated model of the tower underlines the collaboration of a heavy external stone coating in the structural response.

Keywords Structural identification · Bell tower · Ambient vibration test · FE model

1 Introduction

Ancient masonry towers constituting the main part of the Italian architectural heritage are the most vulnerable typology among traditional and monumental structures as shown by the last seismic events in Italy such as the Emilia earthquake (2012) and the Amatrice earthquake (2016).

A. De Angelis (✉) · F. Santamato · M. Pecce
Department of Engineering, University of Sannio, 82100 Benevento, Italy
e-mail: adeangelis@unisannio.it

The structural safety assessment of a masonry tower requires both analytical and experimental analyses with a higher degree of accuracy due to the lack of knowledge of the original design and the construction procedures. Therefore, field survey of the structure and its crack pattern, including non-destructive or slightly destructive tests for the mechanical characterization of the materials is the starting point for the finite element modelling of the structure. However, always there are several uncertainties in geometry and material properties but also in boundary conditions. For this reason, dynamic testing and experimental modal analysis have received great attention since they are useful to have a complete description of the dynamic behavior of the structures. In particular, Ambient Vibration Tests (AVT) are practical and economical dynamic tests that permit an accurate identification of modal parameters of structures without disturbing their current functionality [1]. This procedure has been widely applied to bell-towers [2–6] and historical masonry structures [7].

It is also worth to underline that, the use of finite element (FE) model updating techniques allows obtaining useful information on the boundary conditions and mechanical properties of the constituent materials as shown by many researchers [8–12].

In the paper, the dynamic behavior of an important historical structure, the S. Sophia bell-tower, in Benevento, Italy, is investigated by ambient vibration test and operational modal analysis. AVT has been carried out on the bell-tower in a particularly windy days (24th January 2020) in order to determine its dynamic behavior and develop a subsequently model updating. The extraction of the modal parameters (frequencies and modal shapes) from ambient vibration data has been carried out by using the ARTeMIS software [13] both in the frequency and time domain. Two different well-known identification techniques—the Enhanced Frequency Domain Decomposition (EFDD) [14] and -the Stochastic Subspace Identification (SSI) [15] were applied yielding to very similar results for all identified modes.

The investigation was completed developing a 3D finite element model of the bell-tower and the correlation between measured and predicted modal parameter is presented and discussed showing the importance of modelling the external stone façade.

After that calibration the model allows to study the seismic risk of the structure.

2 The Case Study of S. Sophia Bell-Tower

2.1 Description of the Structure

The bell-tower of S. Sophia in Benevento, Italy (Fig. 1), is part of the monumental complex of S. Sofia, including the S. Sofia church, the monastery and the fountain. In 2011, this monumental complex was added in the World Heritage List of UNESCO and actually it is the most important symbol of the city itself.

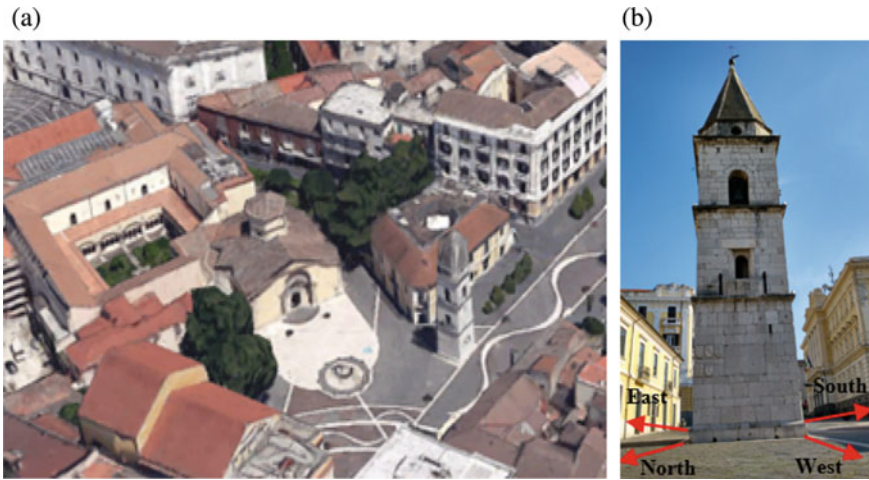


Fig. 1 a The S. Sophia complex in Benevento and b a view of the bell-tower with analysis directions reference labels

The construction of the bell-tower started at the bidding of Gregory II, abbot of Saint Sophia, between 1038 and 1056 as reported by the stone epigraph embedded in the façade of the bell tower.

In 1688, Benevento was struck by a severe earthquake during which the church was partially destroyed by the collapse of the dome and the bell tower, standing on the left of the church's façade. The bell tower, under reconstruction, collapsed again in 1702 due to another earthquake; therefore, it was decided to rebuilt it away from the church itself.

The present bell-tower (about 26 m high), with the principal façade exposed to the North-West direction, consists of the main body, belfry and pinnacle. The main body has got a square plan with a side of about 5.2 m from the base to the level of the belfry where it reaches 4.8 m. The pinnacle is constituted by an octagonal cell (about 1.5 m high) and pyramidal cusp. Inside there is a stone stairway that gives access to the belfry (12.70 m) and a wooden stairway up to the floor at 7.0 m. There is a door at the base level of the tower on North-East facade. Some small quadrangular openings exist on the different levels of the main body. There is also a large arch type opening on each facade of the belfry.

2.2 *In-Situ Investigations*

An accurate investigation on the structure to reach an in-depth knowledge of its geometry as well as of the adopted materials was performed. A topographic and photographic survey with a drone together with a direct in situ inspections were conducted on the bell tower to generate a graphical representation with planar and

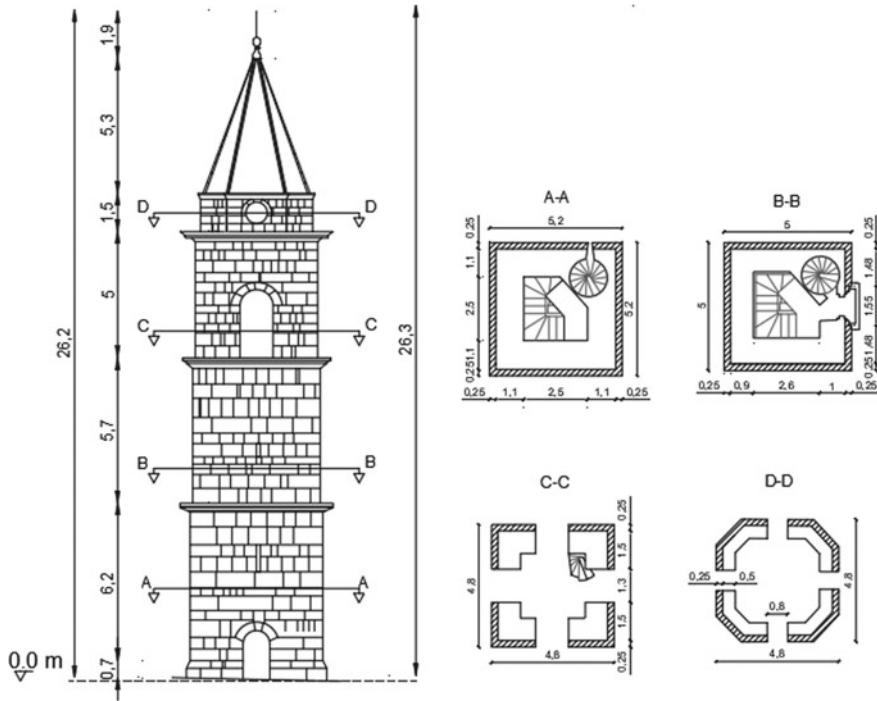


Fig. 2 Front prospect and planar views of the bell-tower

vertical views as well as cross-sections. In particular, the survey helped to determine wall thickness at the different levels (which varied from 0.5 to 1.1 m), the thickness and configuration of the masonry vaults and reinforced concrete (RC) slabs, the horizontal and vertical layout of the stairs and the location of the openings. Figure 2 shows the front prospect and four plant views along the height of the tower.

The materials survey was made by a preliminary visual analysis to define the variability of materials and texture. Surface plaster was removed at various internal points to identify masonry texture (frame with dimensions about 50×50 cm). Visual scanning was also accomplished with a video camera through the holes (diameter 40 mm) realized in the walls. It was found that the tower comprises faced masonry with an external covering and an internal texture characterized by roughly squared stones with a regular shape (Fig. 3a) for the main body (up to 12.70 m) while the internal texture is made by heterogeneous masonry with red clay bricks, natural stone conglomerate and medium-sized pebbles for the walls of the upper levels (Fig. 3b). A similar texture was found for the circular wall at the staircase (Fig. 3c).

The external covering was constructed by well-squared and aligned prismatic-shaped stones approximately 25 cm thick and with thin mortar joints of 1.5 cm.

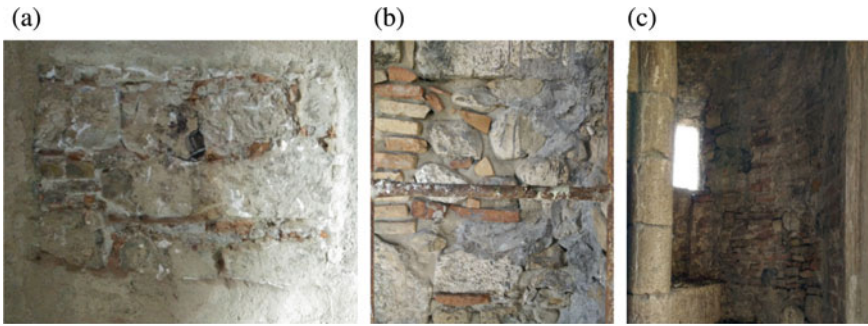


Fig. 3 Internal texture of the main body walls (a), belfry walls (b) and circular wall at staircase (c)

To evaluate the mechanical properties of the masonry of the main body a double flat-jack was performed obtaining a compressive strength equal to 6.64 MPa and a modulus of elasticity of 3728 MPa.

3 The Ambient Vibration Test

3.1 The Test Setups

The AVT was conducted on the tower to measure the dynamic response in 11 different points, with the excitation being associated only to environmental loads. It should be noted that these measurements were executed on a particularly windy day and that the structure was not subjected to any other action.

The tests were conducted using a 16-channel data acquisition system with tri-axial MEMS piezoelectric accelerometers with a nominal sensitivity of about 1 V/g; the accelerometers were installed by means of special metal bases fixed directly on the walls with expansion anchors (Fig. 4) and connected to a centralized data acquisition board by means of long transducer cables.

Figure 5 shows a schematic representation of the sensor's layout; since only 5 sensors were available for the testing three set-ups were used to cover the 11 measurement points of Fig. 5 leaving one sensor (placed at point P3 in Fig. 5) at the same position for reference measurements. It is worth to note that the layout has been established according to the preliminary results of a modal analysis carried out on a simplified model of the structure.

For each setup, time series of 30 min were collected with a sampling frequency of 1000 Hz.

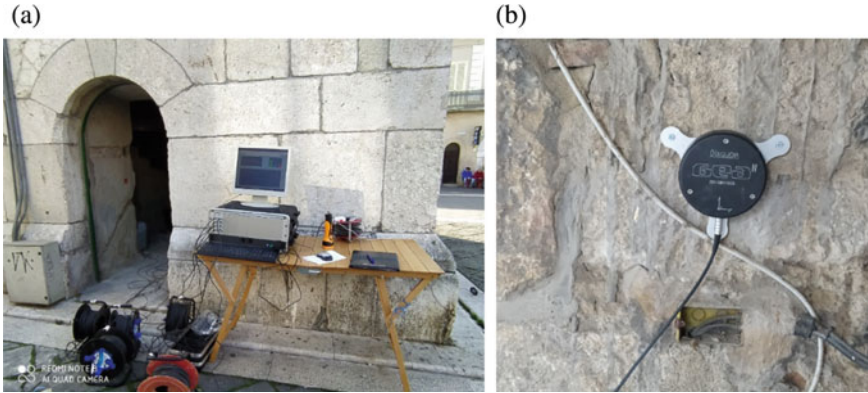


Fig. 4 Accelerometers and acquisition board used for the tests

3.2 Data Processing and OMA

The data recorded from sensors belonging to setup 1 were not used for the analysis presented in the following because their measurements resulted very noisy.

The signals measured were treated; in particular a cut-off frequency of 25 Hz has been adopted for the low-pass filter while the frequency sampling was decimated to 50 Hz. The goal of the measurements consisted in identifying the first 5 natural frequencies and corresponding mode shapes, with the purpose of calibrating the finite element model.

The extraction of the modal parameters from ambient vibration data was carried out according to the Operational Modal Analysis (OMA) by using, in particular, the EFDD-Enhanced Frequency Domain Decomposition [14] and the SSI-Stochastic Subspace Identification [15] methods. The SSI method, computationally more consuming, has been applied in order to validate the results obtained by using the EFDD technique and also to have a more accurate identification in case of closely-spaced modes as it is expected in this case.

After a deep analysis of the Singular Value Decomposition diagrams (SVD) only eight channels were selected for the identification analysis.

The first 5 frequencies identified for each method are shown in Table 1. As expected, the identified modes can be classified as bending and torsional modes. They have been compared through the frequency discrepancy using Eq. (1) and MAC values.

$$D_f = (f_{SSI} - f_{EFDD})/f_{SSI} \quad (1)$$

The results in Table 1 demonstrate the consistency of the two methods in terms of natural frequencies with the D_f being generally less than 2%. A good agreement is also found for most mode shapes, with the MAC values ranging between 0.93 and 0.98 for the bending modes while for the torsional mode the MAC value is 0.86.

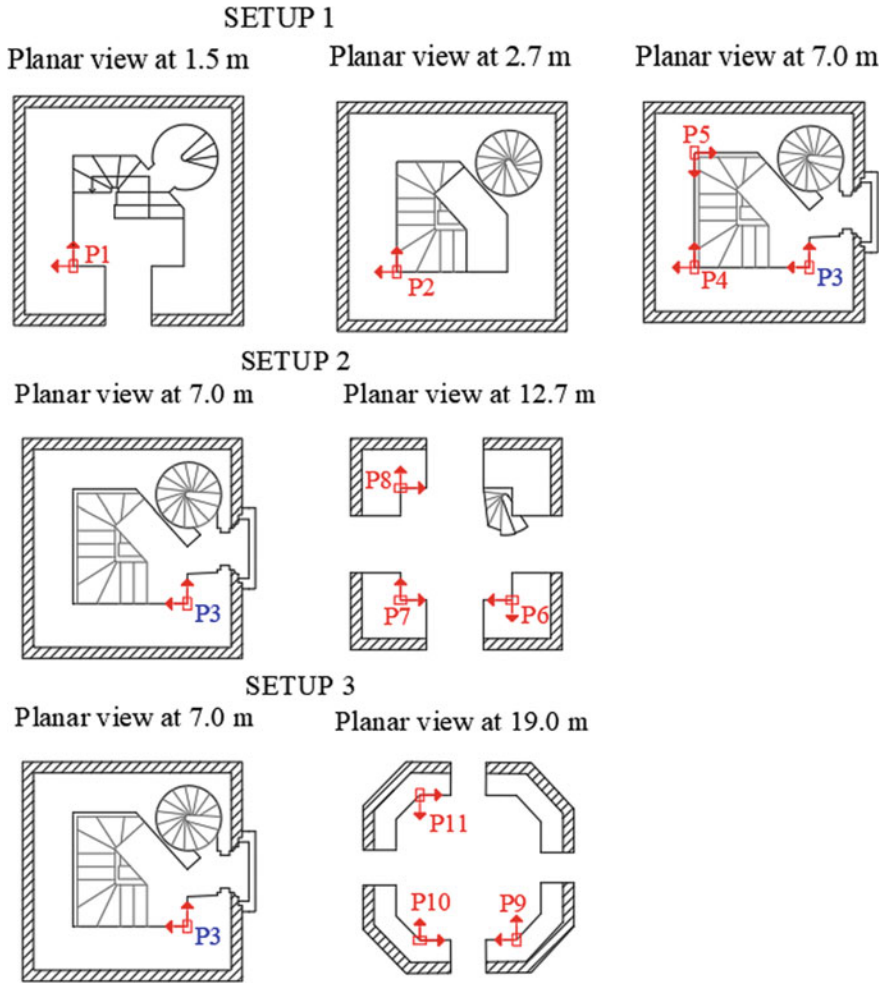


Fig. 5 Lay-out of the accelerometers on the bell-tower

Table 1 First five natural frequencies identified from ambient vibration measurements

Mode N	Mode type	f_{EFDD} (Hz)	f_{SSI} (Hz)	Df (%)	MAC
1	1 st Bending E-W	3.17	3.18	0.31	0.95
2	1 st Bending S-N	3.22	3.23	0.31	0.97
3	Torsion	11.86	12.03	1.41	0.86
4	2 nd Bending ES-NW	12.38	12.42	0.32	0.98
5	2 nd Bending EN-SW	12.86	12.91	0.39	0.93

3.3 Modes Identification

The mode shapes identification has been carried out by introducing some note relations between the measured and unmeasured degrees of freedom of the structure as shown in Fig. 6. It is evident that from the identification procedure it is possible to classify mode 1 (East–West direction), mode 2 (North–South direction), mode 4 (East–West direction) and mode 5 (North–South direction) as bending modes, and mode 3 as torsional mode.

4 Numerical Modelling

In order to better interpret the dynamic behavior of the masonry bell tower and increase the confidence on the collected experimental data, a numerical 3D finite element model of the tower was built by using the FE code MIDAS FEA NX [16] using the macro-modelling approach, i.e. the masonry was modelled as an isotropic continuum. A three-dimensional view of the model is shown in Fig. 7. Masonry walls were modelled by means of Solid elements (8 node brick elements) paying attention

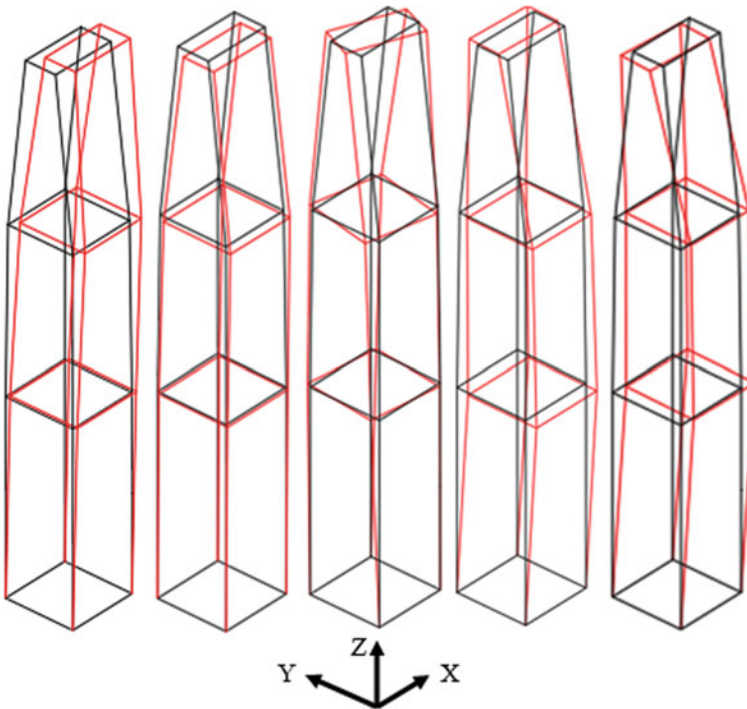


Fig. 6 Vibration modes identified from the AVT

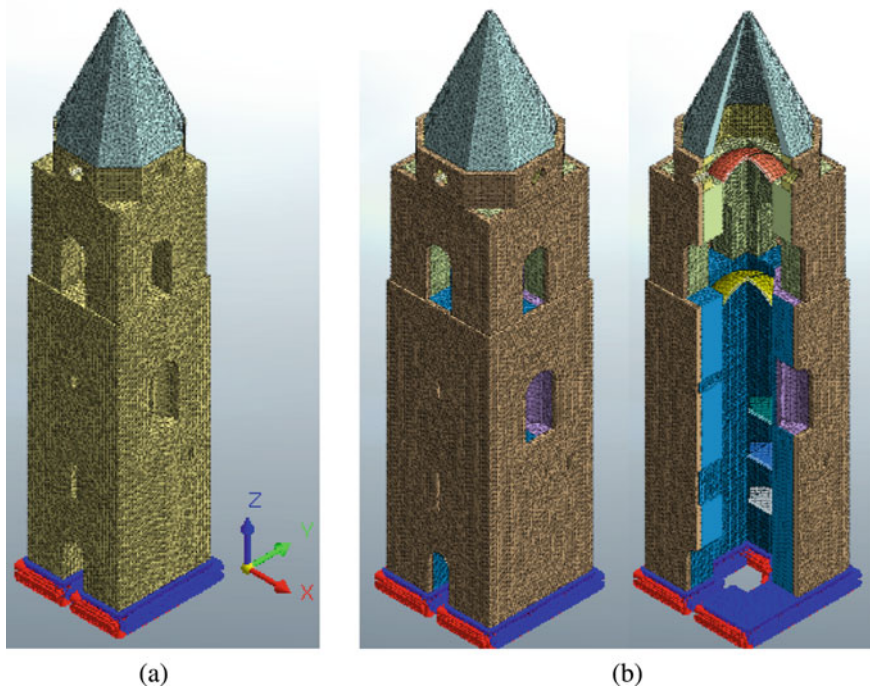


Fig. 7 Finite element model without (a) and with (b) the external stone covering layer

to reproduce the main geometrical irregularities in the wall thickness. The major openings in the tower were reproduced together with the vaults. Only structural elements were included in the model whereas non-structural elements (i.e., bells, ledge stone, stairs) are considered as extra masses. As support conditions, it is decided to assume all displacements of the base nodes fixed. Moreover, in order to understand the role of the external stone covering, two models were developed: (i) Model A in which the stone covering is considered only as mass and (ii) Model B in which the external stone covering is modelled as another layer of masonry with its thickness, as estimated by in situ inspections and shown in Fig. 7b. The elastic properties for the materials reported in Table 2 were adopted for the preliminary model according to the survey and the technical literature.

The numerical frequencies obtained according to the Model A in which the external stone covering is considered only as a mass are reported at the third column of Table 3. The correlation between the dynamic characteristics of the model and the experimental results (both EFDD and SSI estimates) is also shown in Table 3 via the frequency discrepancy. The results show a not good correlation with frequency discrepancy ranging from -42 to -52% . Such differences are surely related to the fact that for small vibrations the external stone covering is collaborative; therefore a new model, called Model B, where the external stone covering is modelled as a layer with its thickness, was developed.

Table 2 Material elastic properties

Element	Elastic modulus E (MPa)	Poisson's ratio	Specific weight γ (kN/m ³)
External stone covering	11,000	0.25	24
Masonry of the main body	2760	0.25	22
Masonry of the belfry	1420	0.25	20
Vaults	1770	0.25	19
Concrete slab	30,000	0.20	25

Table 3 Comparison between the numerical frequencies (Model A) and the experimental ones

Mode N	Mode type	$f_{FEA (Model A)}$ (Hz)	EFDD		SSI	
			f_{exp} (Hz)	Df (%)	f_{exp} (Hz)	Df (%)
1	First bending E-W	1.78	3.17	-43.85	3.18	-44.03
2	First bending N-S	1.98	3.22	-38.51	3.23	-38.70
3	Torsional	5.72	11.86	-51.77	12.03	-52.45
4	Second bending ES-NW	6.96	12.38	-43.78	12.42	-43.96
5	Second bending EN-S	7.37	12.86	-42.69	12.91	-42.91

The natural frequencies and corresponding mode shapes obtained from the finite element analysis by the Model B are presented in Fig. 8. It can be clearly seen that the first one is a bending mode in East–West direction ($f = 3.47$ Hz), the second is a bending mode in South-North direction ($f = 3.54$ Hz), and the third one is a torsional mode ($f = 11.37$ Hz), respectively. Because of the nearly symmetric shape of the tower, the first two bending modes of the tower have close frequency values. The frequencies of 13.17 Hz and 13.69 Hz are related to the second bending modes in ES-NW and EN-SW direction, respectively.

In the following for the process of structural identification the numerical frequencies obtained from Model B and the estimates from SSI method as experimental frequencies are adopted.

4.1 Structural Identification Procedure

The modal analysis results indicate that the initial theoretical frequencies are lower than the experimental frequencies, while mode shapes have a good agreement. Taking into account the uncertainty related to some parameters with major influence in the

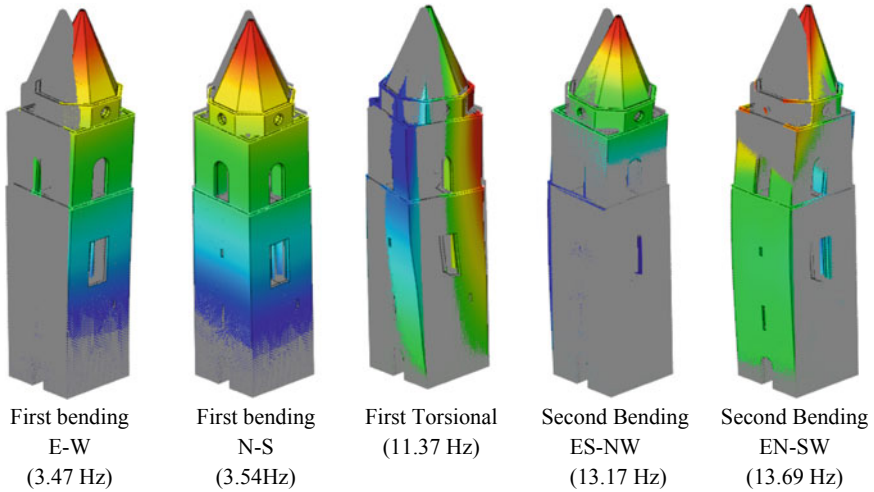


Fig. 8 The numerical natural frequencies and corresponding mode shapes

dynamic behavior of the tower, such as the Young’s modulus and shear modulus of the walls, it was decided to update the finite element model by trial-and-error, until a suitable coincidence with the experimental results for the first five natural frequencies was registered.

The calibrated elastic properties were defined minimizing the total frequency discrepancy (2):

$$D_f = (f_{FEM} - f_{SSI})/f_{SSI} \tag{2}$$

The manual tuning provided the optimal values reported in Table 4.

The comparison between the natural frequencies from dynamic identification (estimates obtained from SSI method) and those from numerical model is reported in Table 5. A good correlation between measured and calculated frequencies was obtained, especially for the first and second couple of bending modes being D_f less than 5%. A higher value of frequency discrepancy equal to 13% was found for the torsional mode. In terms of modal shape (MAC values) a good correlation

Table 4 Optimized material properties

Element	Elastic modulus E (MPa)	Specific weight γ (kN/m ³)
External stone covering	7500	24
Masonry of the main body	3750	22
Masonry of the belfry	1440	19
Vaults	1800	18
Concrete slab	30,000	25

Table 5 The correlation between the numerical and experimental frequencies

Mode	f_{SSI} (Hz)	f_{FEM} (Hz)	D_f (%)	MAC (%)
First bending E-W	3.18	3.19	0.25	89
First bending N-S	3.23	3.32	2.84	89
Torsional	12.03	10.38	-13.72	79
Second bending ES-NW	12.42	12.24	-1.50	76
Second bending EN-S	12.91	12.72	-1.44	71

was found only for the first three modes. However, the correlation between theoretical and experimental modes seems to provide a sufficient verification of the model assumptions, being a one-to-one correspondence between the mode shapes, even if further investigations on the stone covering could contribute to the efficiency of the procedure.

5 Remarks and Future Perspectives

In this paper the investigations carried out to assess the model of the S. Sophia bell-tower, in Benevento, Italy, are described. In particular the calibration of the model using the AVT results by the OMA procedure was developed, extracting the modal parameters (frequencies and modal shapes) both in the frequency and time domain. The following conclusions can be drawn from this study:

1. The fundamental mode of the tower, with a natural frequency of about 3.18 Hz, involves bending in E/W direction. The coupled motion (3.23 Hz) is referred to N/S direction.
2. The second couple of bending modes are around 12.4–12.9 Hz and between these two couples of modes there is a torsional mode at a value of about 12 Hz.
3. A very good agreement, with a frequency discrepancy less than 2%, was found for the modal estimates obtained from the two classical OMA methods, EFDD and SSI.
4. The modelling of the external stone covering with squared stone blocks played an important role in the updating of the model; a good correlation between measured and calculated frequencies was obtained for the first and second couple of bending modes being the frequency discrepancy less than 5%
5. A lack correlation was found for the torsional mode as well as for the mode shapes of the higher modes since the MAC values are less than 80%.

The study demonstrated the importance of the stone covering in the procedure of structural identification underlying that in monumental constructions the heavy stone coverings have a not negligible role in the dynamic response and it is necessary to investigate their characteristics. Finally the low efficiency of the model respect to

the higher modes highlights the probable influence of the soil structure interaction, that will be the next step of this research.

Acknowledgements The work was carried out within the framework of the PON Research and Innovation 2014-2020, Axis I-Investments in Human Capital, MIUR notice AIM- “International Attraction and Mobility”-Line 1, Project: AIM 1823125-3—Cultural Heritage.

References

1. Sepe V, Speranza E, Viskovic A (2008) A method for large-scale vulnerability assessment of historic towers. *Struct Control Health Monit* 15(3):389–415
2. Ivorra S, Pallarés FJ (2006) Dynamic investigations on a masonry bell tower. *Eng Struct* 28(5):660–667
3. Gentile C, Saisi A (2007) Ambient vibration testing of historic masonry towers for structural identification and damage assessment. *Constr Build Mater* 21(6):1311–1321
4. Julio ENBS, da Silva Rebelo CAS, Dias da Costa DASG (2008) Structural assessment of the tower of the University of Coimbra by modal identification. *Eng Struct* 30:3648–3677
5. Diaferio M, Foti D, Mongelli M, Giannoccaro NI (2010) Dynamic behavior of a historic tower in Bari. In: *Proceeding of 14th European conference on earthquake engineering*, 30 August-3 September 2010, Ohrid, Republic of Macedonia
6. Rainieri C, Fabbrocino G (2011) Il periodo elastico delle torri in muratura: correlazioni empiriche per la previsione. In: *XIV Convegno ANIDIS “L’Ingegneria Sismica in Italia”*, Bari
7. Ramos LF, Marques L, Lourenco PB, de Roeck G, Campo-Costa A, Roque J (2010) Monitoring historical masonry structures with operational modal analysis: two case studies. *Mech Syst Signal Process* 24:1291–1305
8. D’Ambrisi A, Mariani V, Mezzi M (2012) Seismic assessment of a historical masonry tower with nonlinear static and dynamic analyses tuned on ambient vibration tests. *Eng Struct* 36:210–219
9. Bartoli G, Betti M, Giordano S (2013) In situ static and dynamic investigations on the “Torre Grossa” masonry tower. *Eng Struct* 52:718–733
10. Sabia D, Aoki T, Cosentini RM, Lancellotta R (2015) Model updating to forecast the dynamic behavior of the Ghirlandina Tower in Modena Italy. *J Earthq Eng* 19(1):1–24
11. Ferraioli M, Miccoli L, Abruzzese D, Mandara A (2017) Dynamic characterisation and seismic assessment of medieval masonry towers. *Nat Hazards* 86(2):489–515
12. de Silva F, Ptilakis D, Ceroni F, Sica S, Silvestri F (2018) Experimental and numerical dynamic identification of a historic masonry bell tower accounting for different types of interaction. *Soil Dyn Earthq Eng* 109:235–250
13. ARTEMIS Modal Pro 6.1 software. Issued by Structural Vibration Solutions ApS. NOVI Science Park, Niels Jernes Vej 10, DK 9220 Aalborg East, Denmark 2019
14. Brincker R, Zhang L, Andersen P (2001) Modal identification of output-only systems using frequency domain decomposition. *Smart Mater Struct* 10:441–445
15. Peeters B, De Roeck G (2001) Stochastic system identification for operational modal analysis: a review. *J Dyn Syst Meas Contr* 123(4):659–667
16. Midas FEA NX- Midas Engineering Software - Manual

Data Processing Strategies for Monitoring an Offshore SPM System



Paolo Castelli, Michele Rizzo, and Ostilio Spadaccini

Abstract Near the offshore production platform Vega A, the tanker FSO Leonis is moored to a steel column with circular section, 130 m high and 10 m in diameter, installed in 1988 in the Sicilian Channel, the connection is via a bridge structure (yoke) with welded steel box sections that make up the system SPM (Single Point Mooring). The structural system, steel yoke and column with its cylindrical hinges, is calls-to the actions of the sea that induce cyclic stresses and fatigue. The document presents the improvement strategies of the monitoring system of the structure that connects the ship to the column, originally installed in October 2009. The original monitoring system is composed of strain gauges sensors, in fiber optic, and inclinometers biaxial that detect rotations of the column and the bridge. New gyro on the tanker FSO and optical thermal sensors on yoke are installed, and a new control unit will allow, together with the inclination data, to verify the ship's pull on the column. The new control unit will have a high acquisition frequency that will allow us to investigate the structural modes shape of the system and yoke. The results allowed to evaluate the critical conditions of the structural system and to define a program of monitoring and maintenance of structures.

Keywords Offshore · Single point mooring · Dynamic identification · Operational modal analysis

1 Introduction

The tanker ship Leonis is located in the VEGA field that is approximately 12 miles south of the southern coast of Sicily, off the coast of Pozzallo. The field includes the platform called VEGA-A for the exploitation of the oil field and a 110,000 ton floating deposit obtained from the transformation of the former oil tanker Leonis

P. Castelli
Energean Italy, Siracusa, Italy

M. Rizzo (✉) · O. Spadaccini
DICEA, University of Florence, Florence, Italy
e-mail: mrizzo@dicea.unifi.it

in FSO (Floating—Storage—Offloading). The float is moored at SPM (single point mooring) located about 1.5 miles from the platform and connected to it via pipelines. In Fig. 1 the ship Leonis and the SPM (column and yoke) are shown.

Single Point Mooring Systems (SPM) are designed to accommodate high draft tankers as they transfer crude oil and fuel oil to and from shore. The study configuration of this paper is shown in Fig. 1. The characteristics of the system is column with the rotating head and its anchoring by means of a spherical hinge to the seabed. This articulated system allows, through the connection system with the ship (Yoke), a series of articulated rigid body movements. The frequency of these movements are characterized by several hundredths of seconds, as shown in the section below.

The current SPM monitoring is constituted by a series of optical strain gauges and installed on the ship (# 25 strain gauge sensors, Fiber Bragg Gratings (FBG)) and on the Yoke (# 12 strain gauge sensors, Fiber Bragg Gratings (FBG)). Two biaxial inclinometers were also installed on SPM (# 2×2 inclinometer sensors).

Therefore both the monitoring systems installed are able to reconstruct the actions of the sea states and the wind e the correlations with the strain in the element.

In Fig. 2 the location of sensors on the Yoke are shown. The time data acquisition for stress is 60 min with a sampling frequency $f_c = 0.5$ Hz, while tilt angles are recorded with a sampling frequency $f_c = 1$ Hz. The direction of the ship is recorded by hand by the Captain of Leonis. The conditions of sea and wind conditions are available by the monitoring system on the platform. FBG sensors are a multiplexed strain and temperature monitoring system based on Fiber Bragg Gratings. The multiplexed acquisition system of the optical strain gauges is composed of a control unit that



Fig. 1 VEGA field, SPM, the ship Leonis and the mooring system

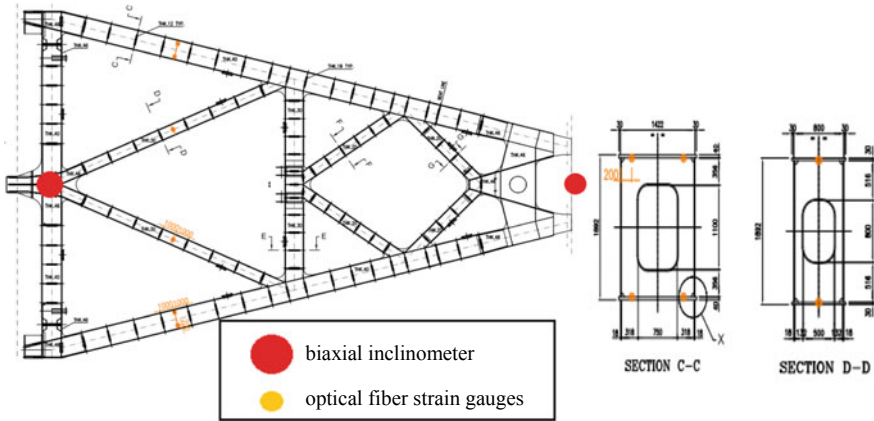


Fig. 2 VEGA field, The SPM monitoring system

acquires through 16 channels the signals from the sensors; the sensors are installed both on the ship that yoke (63 sensors, strain and temperature).

In the next sections we will be analyzed the data made available by the monitoring system. In particular we can see how it is possible to perform a dynamic identification system; in addition, through the analysis of these, through the use of only the data of inclinometers and strain gauges we can perform a structural health analysis.

2 The Output-Only Monitoring

The SHM relies on the repetitive observation of damage-sensitive features such as natural frequencies. The difficult is that changes in temperature, relative humidity, operational loading, and so on also influence those features. This influence is in general nonlinear and also nonlinear is the system SPM-Yoke-Vessel. In this work, the technique based on kernel principal component analysis, improved by Reynders, Wursten and De Roeck [1], is developed for eliminating environmental and operational influences. It enables the estimation of a general nonlinear system model in a computationally very efficient way. The technique is output-only, which implies that only the damage-sensitive features need to be measured, not the environmental parameters. In this method the nonlinear output-only model is identified by fitting it to the damage-sensitive features during the undamaged state. Afterwards, the structure is monitored by comparing the model predictions with the observed features. The method is modified by using a Gaussian RBF (radial base function) more powerful than the original method, as described in the job of Rizzo, Spadaccini and Castelli [2, 3] and Rizzo and Spadaccini [4].

The method used for the identification of frequencies is the Stochastic Subspace Identification algorithm (SSI), which compute state space models from given output

data. The following are the basic steps of the method as shown in Peeters and De Roeck [5], in the covariance-driven version of the algorithm. The output $y_k \in \mathfrak{R}^l$ is supposed to be generated by the unknown stochastic system of order n :

$$\begin{aligned} x_{k+1}^S &= Ax_{k+1}^S + w_k \\ y_k &= Cx_{k+1}^S + v_k \end{aligned} \tag{1}$$

$$E \left[\begin{pmatrix} w_p \\ v_p \end{pmatrix} \begin{pmatrix} w_q^t & v_q^t \end{pmatrix} \right] = \begin{pmatrix} Q & S \\ S^t & P \end{pmatrix} \delta_{pq} \tag{2}$$

with w_k and v_k zero mean, white vector sequences with covariance matrices given by (2). The order n of the system is unknown. The system matrices have to be determined $A \in \mathfrak{R}^{n \times n}$, $C \in \mathfrak{R}^{l \times n}$ up to a similarity transformation as well as $Q \in \mathfrak{R}^{n \times n}$, $S \in \mathfrak{R}^{n \times l}$, $R \in \mathfrak{R}^{l \times l}$ so that the second order statistics of the output of the model and of the given output are equal.

The key step of stochastic subspace identification problem is the projection of the row space of the future outputs into the row space of the past outputs, as shown in Van Overschee and De Moor [6].

The eigen-frequencies estimated can be used to evaluate the corresponding modal shapes by means of the Singular Value Decomposition (SVD). The Probability Density Function (PDF) could be built by means of a Gaussian base according to Eq. 3 where O_{\min} and O_{\max} represent the minimum and maximum order of the SSI model and N_f is the number of identified main frequencies. In Fig. 3 is shown also the stabilization diagram of structural resonance. In Fig. 4 the first three modal forms

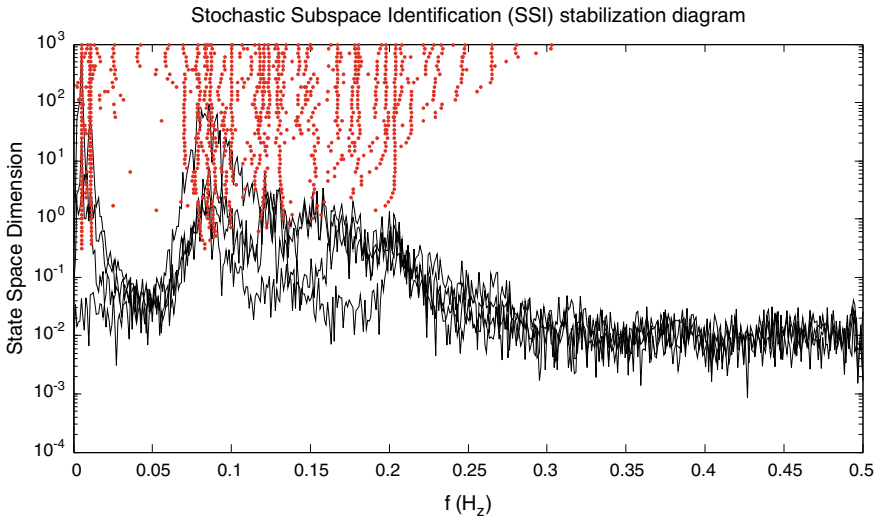


Fig. 3 Stochastic subspace identification analysis: stabilization diagram

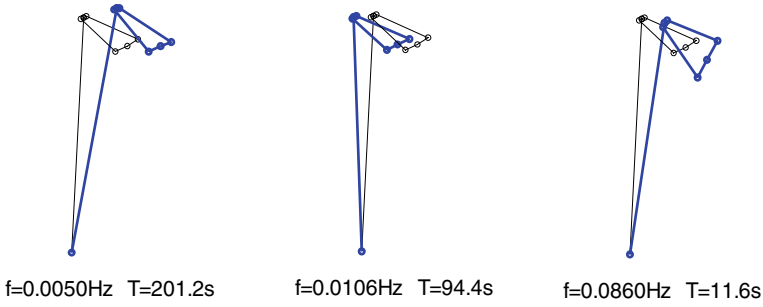


Fig. 4 Identified mode shapes of mooring system, $f_1 = 0.0050$ Hz, $f_2 = 0.0106$ Hz, $f_3 = 0.0860$ Hz

of rigid body of the structure are shown. The first two are purely translational while the third is rolling around the yoke-ship longitudinal axis.

Therefore the damage survey should take into account the structural behavior as well as being able to remove all the environmental effects on frequencies of oscillation. A method for SHM in changing environmental conditions is kernel PCA (principal component analysis). This is a nonlinear version of PCA for which the type of nonlinearity does not need to be explicitly defined. In this work, an improved output-only technique for eliminating nonlinear environmental and operational influences on the monitored features is developed and validated on real-life monitoring data. It is based on Gaussian kernel PCA, where the two parameters of the global system model are automatically determined.

$$\begin{aligned}
 p(f) &= K \sum_{h=0}^{O \max} \sum_{k=1}^{Nf} \exp\left(-\frac{(f - f_{hk})^2}{2\sigma_h^2}\right) \\
 K &= \left[\int_{-\infty}^{+\infty} \sum_{h=0}^{O \max} \sum_{k=1}^{Nf} \exp\left(-\frac{(f - f_{hk})^2}{2\sigma_h^2}\right) df \right]^{-1}
 \end{aligned}
 \tag{3}$$

The first parameter, which represents the standard deviation of the Gaussian (or radial basis function (RBF)) kernel, is chosen in such a way that the matrix of mapped output correlations is maximally informative; in particular, unlike that in the work of Reynders et al. [1], we use a matrix of standard deviations to improve the RBF. If the output of the model is identified as a sequence of vectors $\mathbf{y}_k \in R^{ny}$, $k = 1, \dots, n_s$, the elements of which are damage-sensitive quantities, the RBF kernel is defined as

$$\begin{aligned}
 k(y_i, y_j) &= \exp\left(-\delta_{ij}^t C \delta_{ij}\right); \\
 \delta_{ij} &= |y_i| - |y_j|;
 \end{aligned}
 \tag{4}$$

$$y_k = \begin{Bmatrix} y_{k,1} \\ \dots \\ y_{k,m} \end{Bmatrix} \quad (5)$$

In the vector y_k are present in the modal displacements ranked in column, each normalized with the respect of the unity norm, $y_{k,m}$ is the m -th modal form obtained in the k -th identification (k -th sample).

$$C = \begin{pmatrix} 1/2\sigma_1^2 & 0 & 0 \\ 0 & \dots & 0 \\ 0 & 0 & 1/2\sigma_m^2 \end{pmatrix}; \quad (6)$$

$$F \leq \frac{\sum_{k=1}^{nu} \Sigma_{kk}}{\sum_{k=1}^{nt} \Sigma_{kk}}; \quad (7)$$

In this case we use m values of σ , one for each frequency. The number of principal components to retain, n_u , is then determined by inequality (5); Σ_{kk} denotes the k^{th} diagonal element of Σ , matrix of eigenvalues. It can be seen that K is more informative when σ approach the optimal value which corresponds to the maximum entropy. The parameter σ controls the bandwidth of the inner product matrix K . When σ is very small, this matrix is approximately diagonal. In this case, K provides no information on the correlation among the data points and PCA becomes meaningless. When σ is very large, all elements of the matrix are approximately equal, which makes it again uninformative. As noted in Widjaja et al. [7], an optimal value of σ can be found by requiring that the corresponding inner product matrix is maximally informative as measured by Shannon's information entropy. In particular, σ is determined by maximizing the information entropy of the inner product matrix K . The performance of this kernel PCA-modified in resolving the monitoring problem is investigated for the SPM case-study.

The records available from the monitoring system are the inclinometers and strain gauges data's. Therefore, these two sets of data's can be used for the dynamic identification of the system. Below are the trends of the first two frequencies of the system both with by the use of inclinometric data.

A first analysis of the frequencies of the system shows, in Fig. 5, that they are very variable in function, as well as the environmental effects and non-linearity of the system due to large displacements, also by the variability of the mass of the system itself.

In fact, approximately, 330 tons of blends are loaded daily from the platform to the ship, while 70 tons of diluent are sent from the vessel to the platform. The diluent is loaded onto the ship once a year for about 25,000 tons. The ship is discharged from the blend about 5 times a year with a load of 30,000–35,000 tons. This extreme mass variability means that there is a sudden jump on the frequency trend, in particular a sudden increase in fundamental frequencies. A inspection of the time evolution of the first natural frequencies identified in the frequency on the basis of the SSI

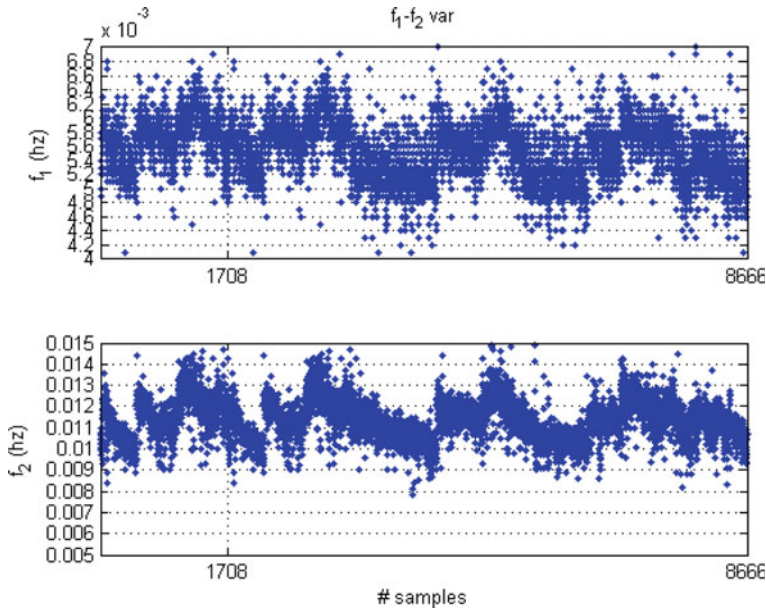


Fig. 5 Trend frequencies extracted from inclinometer data; January 2014 to December 2016

method may suggest that it is not possible to understand exactly, from the study of the frequency trend, if there was a structural damage in the SPM system. For this reason it is necessary to apply a method of the kernel-PCA family.

3 Revamping of Monitoring System

The problem of thermal data compensation in this system is a very delicate issue, in Fig. 5 two compensation analyzes are shown. For the revamping of the system, a new control unit will be installed which will provide compensated data as well as provide a sampling frequency of 20 Hz. Furthermore, the monitoring system will be improved through the introduction of new thermal sensors (one for each strain measurement). All data acquired by the new monitoring system, strain gauges, inclinometers and gyrocompass data will be synchronized on a single PC server which will also be used to view the data processed in real time (Figs. 6 and 7).

The replacement of the current monitoring system will also allow the modal identification of the structural modes of the system and not only those of rigid body through the introduction of a system with an acquisition frequency at 50 Hz. The following figure shows the main structural frequencies of the yoke that can be identified.

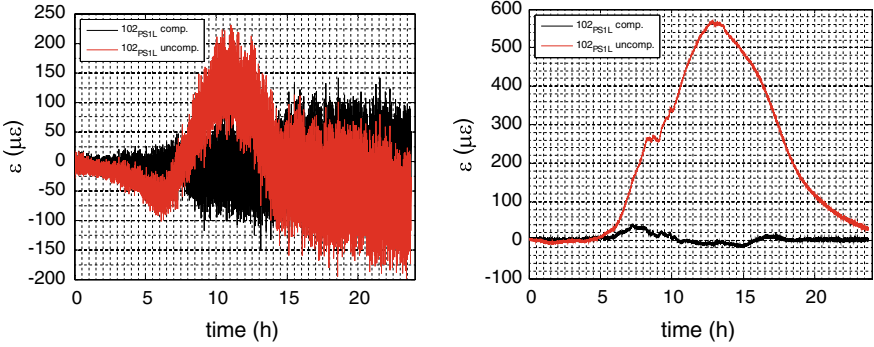


Fig. 6 Example of temperature compensation for two raw data set (red line uncompensated data, black line compensated data)

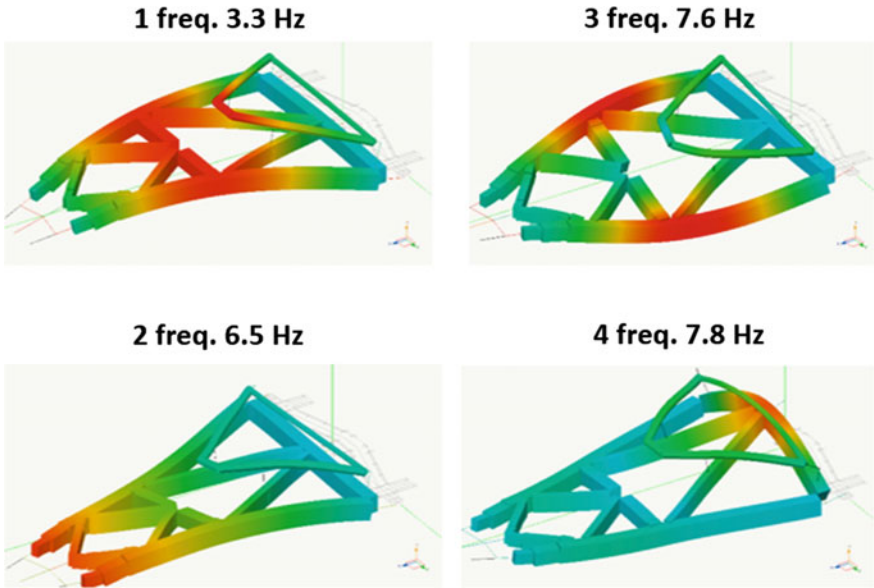


Fig. 7 Main modal forms by Commercial FEM software

4 Conclusion

A monitoring approach has been adopted for the control of SHM of a SPM system. This method consists of three stages: a data reduction by identification of damage-sensitive features such as frequency characteristics, an identification of a nonlinear environmental model using the damage-sensitive features from the previous stage as outputs, and a monitoring of the prediction error of the global model. For estimating the nonlinear environmental model, a technique was used based on kernel PCA,

where an optimal value of the Gaussian kernel parameters (improved method with more than one σ) and the number of retained principal components are automatically determined.

The revamping of the strain gauges and control unit with a new control unit is currently under installation and data analysis will be updated. The gyrocompass present on the ship, to detect the ship direction (true heading), will be acquired continuously by the control unit. At the end the data acquired by strain gauges, inclinometers, gyrocompass will be synchronized on a single PC server which will also serve to display the data processed. The new control unit for the acquisition of strain signals will allow to manage the optical strain gauges with high frequency acquisition. The high acquisition frequency will allow to elaborate the dynamic structural behavior of the yoke and better to estimate the fatigue life of the SPM system.

References

1. Reynders E, Wursten G, De Roeck G (2014) Output-only structural health monitoring in changing environmental conditions by means of nonlinear system identification. *Struct Health Monit* 13(1):82–93
2. Rizzo M, Spadaccini O, Castelli P (2015) Fatigue and monitoring of SPM, ISOPE 2015, the twenty-sixth international offshore and polar engineering conference, Rodos, Greece, June 26–July 2, 2016.
3. Rizzo M, Spadaccini O, Vignoli A (2018) Fatigue and monitoring of SPM, ISOPE 2018, the 28th international ocean and polar engineering conference sapporo, Japan, June 10–15, 2018
4. Rizzo M, Spadaccini O, Castelli P (2017) Improvement of structural monitoring of jacket platform, ISOPE 2017, the twenty-seven international offshore and polar engineering conference, San Francisco, USA, June 25–30, 2017
5. Rizzo M, Spadaccini O (2016) Wave-structure dynamic interaction of vega platform. In: *Proceedings of insights and innovations in structural engineering, mechanics and computation—SEMC2016, 1935–1940*, Cape Town, South Africa, 5–7 September 2016
6. Peeters B, De Roeck G (1999) Reference-based stochastic subspace identification for output-only modal analysis. *Mech Syst Signal Process* 13(6):855–878
7. Van Overschee P, De Moor B (1996) *Subspace identification for linear systems: theory-implementation-applications*. Kluwer Academic Publishers, Dordrecht, Netherlands

Health Monitoring of Structures Using Integrated Unmanned Aerial Vehicles (UAVs)



Efstathios Polydorou, Des Robinson, Su Taylor, and Patrick McGetrick

Abstract Unmanned aerial vehicles (UAVs), known as drones, is an advanced remote sensing technology gaining much interest in the field of civil engineering in the last few years. According to the Association of Unmanned Vehicle Systems International, it is estimated that drones have the potential of reaching an economic benefit of US \$82 billion by 2025. This paper investigates novel strategies for the visual inspection assessment and damage detection of bridge condition by maximizing the full potential of UAVs remote technology combined with advanced camera vision methods. The investigation starts by assessing the functionality of modern UAVs and matching the capabilities to the requirements of bridge monitoring. This is important as the driving force behind the technology development of drones has not come from bridge maintenance, but it is important that we exploit the new technologies and the same argument is also true for image processing. The paper explores how these assessment techniques can be transferred on to a UAV platform. The paper not only looks at the important technical issues such as camera stabilization both from flight control and image processing but also the use of UAVs as an inspection and measuring device. The investigation makes use of both laboratory experiments and field trials to assess the effectiveness of the proposed schemes.

Keywords Unmanned aerial vehicles · Structural health monitoring · Bridge engineering · Dynamic displacements · Computer vision

1 Introduction

More efficient bridge maintenance and inspection techniques are essential to assure bridge safety, ensure safe service life, potential reduce unnecessary maintenance costs, improve the reliability of the transportation system and the safe operation [1, 2].

E. Polydorou (✉) · D. Robinson · S. Taylor
Queen's University Belfast, Northern Ireland, UK
e-mail: s.polydorou@qub.ac.uk

P. McGetrick
National University of Ireland, Galway, Ireland

Most of the bridges across the world are primarily inspected and monitored using traditional techniques such as visual observations by engineers and occasionally by inspecting the conditions of bridge elements using various non-destructive methods. Most often the major visual inspections take place at + 5 year intervals with little or no information about the time and/or rate of deterioration. In many cases, time consuming visual inspection of structural elements is required for condition assessment of in-service bridges where human access is potentially hazardous for inspectors involving specialised equipment like elevating platforms [3]. The inspections are also prone to variation depending on the experience of the inspector which can have an impact on the accuracy due to differences in surface types causing high inconsistency in the results and increasing the inspection time, maintenance cost and staff time. A promising solution to these inspection concerns is increased digitisation and in this research the development and implementation of remote non-contact technologies such as unmanned aerial vehicles.

Unmanned aerial vehicles (UAVs), also known as drones, are an advanced remote sensing technology gaining much interest in the field of Civil Engineering in the last few years. According to the International Association of Unmanned Vehicle Systems, it is estimated that drones have the potential of reaching an economic benefit of US \$82 billion by 2025. The market investments in UAV technology systems and more particularly in drones has reached record levels of US \$172 M in 2015 compared to US \$165 M cumulative funding since 2012. By equipping the drone with high resolution cameras, visual inspection methods can be simplified providing unrestricted accessibility for bridge condition and monitoring. However, the implementation of such systems for bridge inspection present challenges associated with UAVs (payload, control stabilisation, flight duration, battery life of the drone, electronic speed controllers, inbuilt accelerometers to assess natural frequency etc.) and suitable imaging and sensing devices. The paper presents research into the development of a novel strategy for visual inspection assessment which can be used to assess damage detection of bridge condition and give accurate information about true loading levels using UAVs remote technology combined with advanced camera vision methods. The capabilities of the proposed system are demonstrated in laboratory measurements by tracking dynamic displacements and identifying control stabilisation of the motion of the mounting camera. In addition, vehicle tracking movement is investigated using UAV technology.

2 Classification of Functional Available Unmanned Aerial vehicles (UAVs)

2.1 Aircraft Frame Types

Depending on the operating system and the frame configuration, drones are commonly classified into two main types known as fixed-wing aircrafts and multi-motor aircrafts [4]. Fixed-wing aircrafts consist of fixed, rigid wings which take off and fly because of the aircraft's forward airspeed using the wings to generate the lift. The airspeed of the aircraft is achieved by forward thrust typically using a jet engine or a propeller. Examples of fixed-wing aircrafts include traditional airplanes and kites. On the other hand, multi-motor aircrafts use a set of rotary blades or propeller systems to generate lift, hover and maneuver in the air [5]. Compared to fixed-wing aircrafts, multi-motor aircrafts are equipped with small rotors that provide constant rotation to the rotor blades for flight [6]. Configurations of multi-motor aircrafts include four, six or eight rotor blades. This type of drones has the ability to take off, land vertically and fly in all directions allowing entrance and landing in narrow areas. One of the important merits of multi-motor aircrafts is the ability to hover in a fixed altitude maintaining stability which makes them suitable for hard to reach

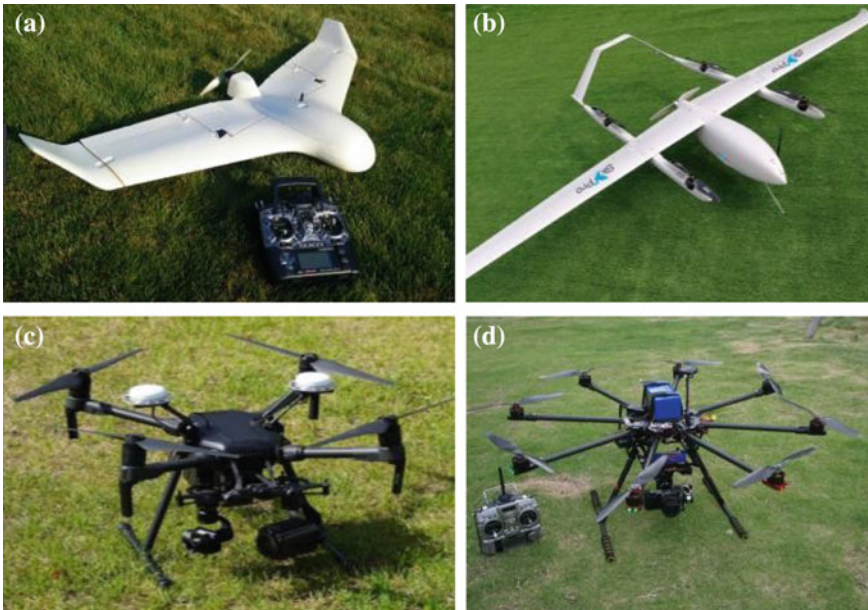


Fig. 1 a Fixed-wing aircraft, b Fixed-wing Hybrid vertical take-off and landing drone (VTOL), c Multi-rotor aircraft (4 rotor blades), d Multi-rotor aircraft (8 rotor blades)

places such as powerline and bridge inspections. Figure 1 shows commonly used fixed-wing and multi-motor aircrafts.

2.2 *Payload*

One of the main reasons behind the rapid growth in the market for UAV technology systems is the drone's ability to carry high lifting capacities maintaining a stable position and altitude while hovering in the air. The term 'payload' is used to describe the additional weight that a drone can carry which is usually independent to the weight of the drone. Typical payload types used in UAVs include visual cameras, thermal sensors, infrared sensors etc. to collect and store information on-board for post-processing analysis to a base station. These sensors enable high resolution footage, night vision and heat sensing and are used in a variety of applications including search and rescue, public safety, military, agriculture, construction and infrastructure inspections etc.[7].

Commonly, drones are capable of carrying a limited payload such as a small camera with the use of a 3-axis mechanical gimbal. For higher weight capacities, heavy lift drones are preferred to perform thermal inspections or light detection and ranging (LiDAR) surveys. The payload capacity a drone can lift is directly related to the power-to-weight ratio of the drone design. For example, a higher power-to-weight ratio can carry higher payload capacities whereas the flight time reduces when extra weight is added to the drone. Furthermore, drones with higher payload capacities are dependent on a number of factors including the design of the motor and its corresponding power, size and number of propellers, self weight of the drone and the type and number of batteries to provide power to the drone [7]. In general, the efficiency of the drone to carry higher payload increases using larger propellers. However, the dynamic thrust produced by the combination between the motors and propellers needs to be twice the flying weight of the UAV. Other payload sensors may include drones equipped with wireless mesh nodes for deploying communication networks under emergency and disaster recovery scenarios and UAV-based wireless power transfer systems [8–10].

2.3 *Legislations and Regulations for Drones*

In the UK, laws and regulations relating to UAV systems are described in two categories: 'Recreational drone flights' and 'Commercial drone flights'. The term 'recreational drone flights' is used to describe the operation of a drone for personal interest or non-business purposes whereas commercial drone flights involve a contract between a drone operator and a customer for undertaking commercial work. Each category contains guidelines and requirements that drone operators must comply with. All aviation laws in the UK are regulated by the Civil Aviation Authority

(CAA) and guidelines and regulations are accessible through the CAA website for any drone operator in regard to commercial or recreational flights. All relevant legislations and regulations concerning drones are described in detail in the 'Air Navigation Order 2016' which is the document that outlines aviation regulations within the UK. The CAA outline simplified guidelines for recreational operators highlighting the statement that "aircraft pilots are responsible for flying aircrafts in a safe manner, must not endanger any person or property with the aircrafts". Further to this, it is outside the regulations to fly any aircraft recreationally outside of the direct line of site in order to avoid collisions with objects or other aircrafts. Article 241 of the Air Navigation Order (ANO) 2016 states that all aircraft pilots must not recklessly or negligently cause or permit an aircraft to endanger any persons or properties. In addition to that, certain hazard factors are heavily mitigated if the aircraft is flying in an enclosed environment and access to the venue is controllable. In this study, laboratory experiments were carried out indoors and therefore a safety net was used as recommended by the CAA.

The CAA attempts to establish regulations exclusively for drones as oppose to other aviation equipment. To date, this has been managed by establishing regulations for different aircraft weight classes. According to the CAA statement in the Air Navigation Order 2016, a set of specific, simpler, regulations apply to aircraft having a weight of 20 kg or less (which are termed 'small unmanned aircraft' within the ANO) in order to keep the regulations at an appropriate level for small drones. Based on articles 166 and 167 of the Air Navigation Order, prohibitions will be applied to aircraft pilots flying the aircraft in certain airspace areas without explicit permission from CAA. In addition, drone altitude restriction of 120 m above the ground surface must not be exceeded for safety. For drones within the 7 kg weight limit, permission is not required to fly by the CAA unless partaking in commercial activity. The UAV that was used in this study weighs less than 7 kg and therefore it can be flown within the current guidelines and regulations.

In the UK, Air Navigation Order provides restrictions to all aircraft operators that must be considered for establishing available areas for these devices to be used. Drone operators must keep drones within their line of sight and below an altitude of 120 m. Drones must not be flown within 50 m of people and property, or within 150 m of crowds and built-up areas. An important regulation is that drones are not flown near aircraft, airports and airfields. According to the CAA law, pilots who endanger the safety of an aircraft through the use of drones could face serious consequences as this can be considered as an offence. CAA permission is required for undertaking commercial work using drones or flying the drones within certain areas such as private lands or closer than the minimum distances stated in the regulations for drone operators. Completion of a training course and registration with the CAA is required for commercial drone operators as well as full insurance of the aircraft in case of an accident.

3 Preliminary Laboratory Tests

3.1 Equipment and Setup Details

In this study, a simply supported foam beam with dimensions of $100 \times 100 \text{ mm}^2$ in cross section and 2000 mm in length was used to allow sufficient vertical movement for tracking the midspan displacement using a drone. The beam was loaded in the middle twice and then allowed to return back to its rest position. All of the UAV based investigations throughout this study were performed using a commercially available multi-rotor UAV namely, DJI Mavic Pro. This UAV is a compact, powerful quadcopter with dimensions 83 mm in high, 83 wide and 198 mm long and weight of 743 g. The body shell frame of the drone is made of carbon fibre and uses four doubled-bladed folding propellers to reduce the noise and increase its aerodynamic performance and stability. An intelligent flight battery capacity of 3830 mAh and voltage indication of 11.4 V was used to provide power to the drone allowing for maximum flight time of 24 min under low wind conditions. Furthermore, the Mavic Pro utilizes smart forward and downward vision positioning sensors and satellites from the global positioning system (GPS) for precise hover and positioning. The transmission system range of 7 km allows the drone to inspect long bridges and provide easy access to places that are difficult to reach. For the purpose of this study, a Samsung Galaxy S7 was used to control the drone using the DJI Go 4 app. Table 1 provides the specifications of the multi-rotor Mavic Pro used in this study.

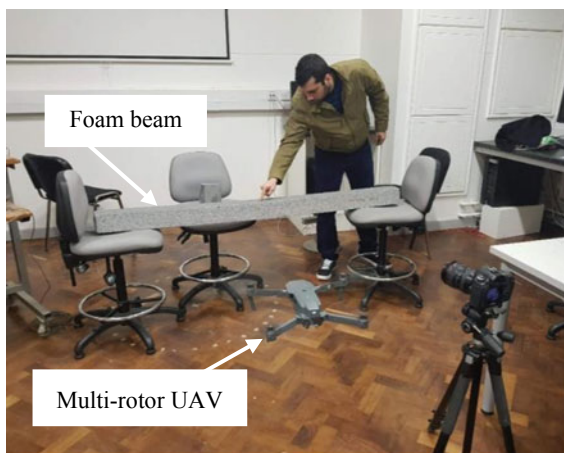
The camera embedded to the front system of the drone provides a stable 4 K video recording at 30 frames per second (fps) and full 1080 p high definition at up to 96 fps. The stabilization of the camera is achieved through an optimised 3-axis mechanical gimbal with a pitch controllable range between -90° and $+30^\circ$ and controllable roll range between 0° and $+90^\circ$ horizontally and vertically. This particular camera is a CMOS sensor (6.17 mm wide by 4.55 mm high) with a total effective pixel count of 12.34 M recording photos at 4000×3000 pixels. The camera focus to an area of interest is achieved using the ‘auto’ focus function that features a minimum focusing distance of 0.5 m. In this study, 4 K video resolution was used at 30 fps despite the fact that the UAV can reach a maximum frame speed of 120 fps at a lower resolution. Table 2 provides the camera specifications of the multi-rotor Mavic Pro. In addition to the camera, Mavic Pro incorporates a ‘flight autonomous’ system which means that the internal system contains a complex network of hardware and software with five cameras, GPS and GLONASS navigation system, a pair of ultrasonic range finders, redundant sensors and 23 powerful computing cores. Flight autonomy can

Table 1 Mavic Pro specifications

Max. take-off weight (kg)	Max. speed (m/s)	Max. altitude (m)	Temperature range ($^\circ\text{C}$)	Transmission distance (km)	Transmission power (GHz)
743	17.88	5000	0–40	7	2.4

Table 2 Camera specifications for Mavic Pro

Sensor	Lens (m)	Field of view (°)	Shutter speed (s)	Image size (pixels)	Video resolution (pixels)	Video format
CMOS	28	5.6	8-1/8000	4000 × 3000	4096 × 2160	MP4

Fig. 2 Deflection of a beam and video recording using DJI Mavic Pro in flight and Canon static camera

position, navigate and plan routes for the Mavic Pro enabling the drone to avoid obstacles in various environments, with or without the help of satellite signals. This feature will be used for bridge investigations that will be performed by the Structural Health Monitoring (SHM) team at Queen's University Belfast (QUB). Additionally, significant to this study both the forward and downward facing cameras have an obstacle sensory range with precision measurements in the range between 0.7 m and 15 m. These figures do however depend on the quality of lighting in the environment. The suggested operating environment for the downward stabilization cameras is that of a clear pattern with adequate lighting (>15 lm) (Fig. 2).

4 Experimental Results

4.1 Deflection Measurements

The SHM team at QUB have been working on the use of digital cameras to measure deflection of bridges [11]. In previous studies, tracking based-techniques were used to analyse video footage for deflection measurements of the Governor's bridge located in Belfast, Northern Ireland. The validation and accuracy of this technique

was compared using linear variable differential transducers (LVDTs) and fibre optic displacement gauge sensors which indicated high accuracy showing displacements less than 0.05 mm. In this study, the same approach was used with the use of the drone to track the displacement of a beam. The method adopted was a modification of face detection and tracking algorithm within the MatLab Computer Vision toolbox software. The tracking analysis method is described below based on a three state operation:

1. A small region was identified as the target point of interest for the deflection measurement. This region of interest was used as input to the feature detection algorithm which returned a collection of points deemed to represent features within the area. The minimum eigenvalue algorithm was used to undertake this task, although alternative methods can be substituted instead [12].
2. The set of points within the area of interest were tracked and analysed frame by frame throughout the video sequence. The Kanade-Lucas-Tomasi (KLT) algorithm was used to execute this procedure [13, 14].
3. An estimate of the geometric transformation was performed between the deformed and undeformed frames. The algorithm best fits an affine transformation between the two sets which provides estimates of the translation scale and skew of the two sets of points. The translation output was then extracted for the calculations.

Figure 3 shows the image quality resolution comparison between the camera mounted to the drone with a static Nikon camera. As aforementioned in the test description, Mavic Pro incorporates a high resolution 4 K camera which provides higher resolution for detection features on the bridge surface compared to the Nikon

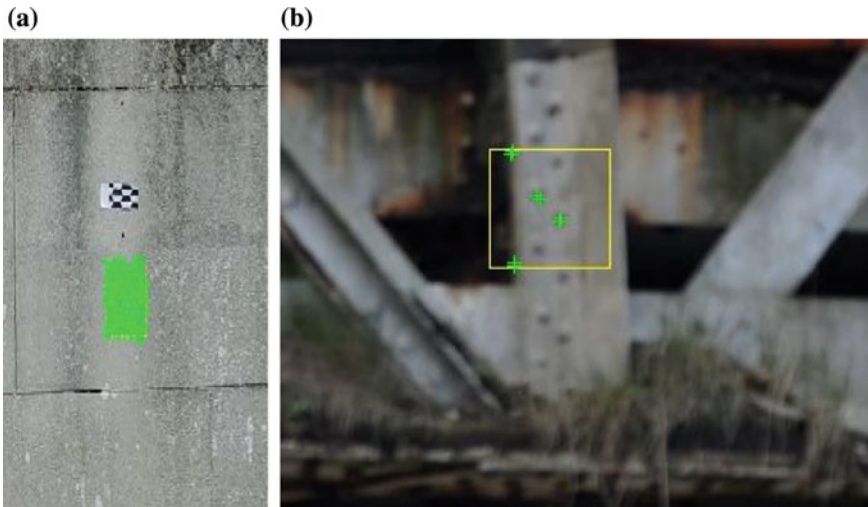


Fig. 3 **a** Region of interest detection using the drone, **b** Region of interest detection using a high resolution static camera (default resolution)

camera. Within the subset area, the drone camera detects multiple number of points compared to the static camera which is important in allowing the tracking of points from frame to frame. Despite the fact that many commercially available cameras provide relatively low default resolution, Fig. 3 shows the advantages of using a 4 K resolution camera for tracking the deformation points.

Figures 4 and 5 present the experimental results using the drone to measure the mid-span deflection of a simply supported beam. Figure 4 show the deflection profile of the beam pushed down twice and then allowed to return to its original position. The deflection starts at zero while the beam rests to its original position followed by a downward movement twice without the beam being able to return to zero position after the load was removed. This is explained by the movement of the drone, despite the tripod mode use of the drone which is a feature that allows a better degree of stability. To mitigate against the movement of the drone, a solid concrete block was located behind the beam with the aim of subtracting the drone movement from the calculations. Figure 5 shows the drone deflection profile obtained using the same video recording by tracking a region of interest of the solid block which in this case remained stationary. Figure 6 shows the adjusted deflection profile of the simply

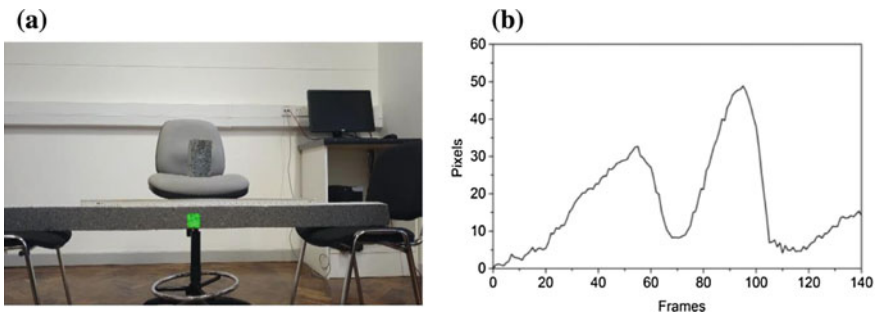


Fig. 4 a Measuring the deflection of the beam using the drone, b Unadjusted deflection profile obtained by the drone

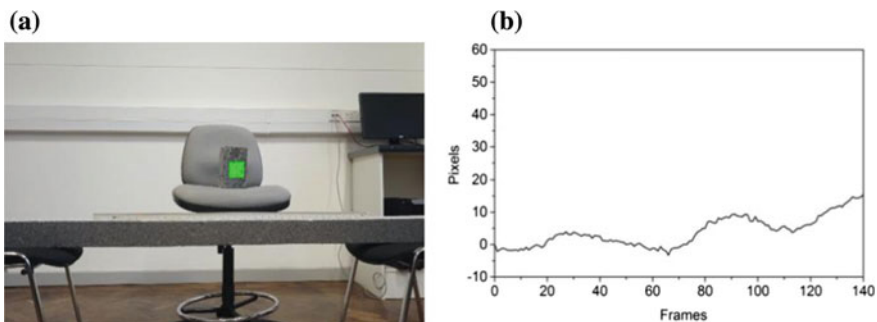


Fig. 5 a Measuring the movement of the drone by tracking a stationary object, b Deflection profile of the drone

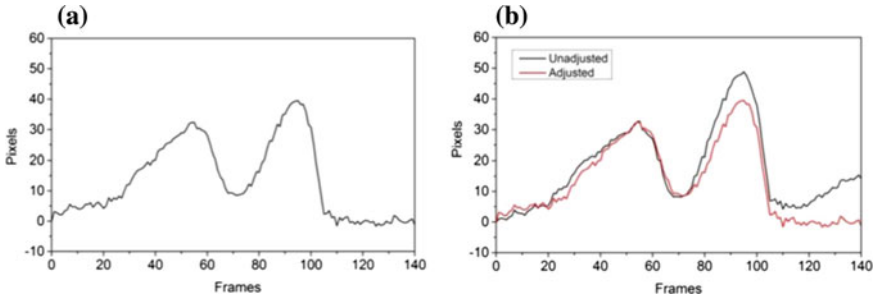


Fig. 6 **a** Adjusted movement of beam member, **b** Comparison between unadjusted and adjusted movement profiles of beam member

supported beam obtained by subtracting the movement of the drone from the beam downward movement. It is also evident that the deflection of the beam returned to zero once the drone movement was taken into account in the calculations.

4.2 Tracking Measurements

Traditional methods used for vehicle monitoring and management include the use of strain gauges and accelerometers to provide useful data such as weight and effect of vehicles on the structure [15]. The advances in computer vision methods make possible the use of this technique for tracking vehicles and other essential information. In this study, the visual capabilities of the multi-rotor Mavic Pro were implemented for performing vehicle detection and tracking which are extremely useful in structural health monitoring. Figure 7 shows a car being tracked from footage recorded using the drone. The ability of the drone to accommodate the tracking object feature is achieved using a deep learning approach. Tracking analysis was performed using foreground detection with Gaussian mixture models where the algorithm uses a box around the car for detection and tracking [16]. Preliminary results showed that the algorithm highlighted tracked objects over the surrounding area such as road markings and door frames. This is explained by the movement of the drone making these objects appear to be moving. Despite the many challenges presented with drones for tracking objects due to real-time constraints and view angles, footage recorded by the drone can be improved though stabilisation of the video footage [17]. The SHM team at QUB are currently developing a deep learning approach specifically for vehicles which will allow drones to undertake reliable vehicle tracking.



Fig. 7 Tracking of vehicle movement

4.3 Visual Inspection

One of the most important applications drone can be used for is the visual inspection of structures and mainly visual inspection of bridges for structural safety and maintenance. While an equivalent picture could have been recorded using a static camera (Fig. 8a), capturing a closer picture of the bridge and reaching hard to reach spaces is not easily achievable using a static camera. This indication highlights the benefit for the implementation of an effective UAV system that would increase the inspection efficiently and accuracy. Figure 8b shows a picture of the King’s bridge located 0.6 miles away from Queen’s University Belfast recorded using the drone. Existence of cracks was noted in concrete on both the upper and lower parapets of the bridge. A closer analysis of the images revealed excessive spalling in concrete

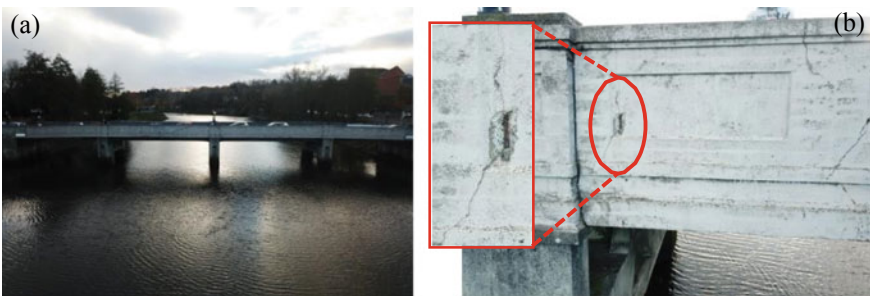


Fig. 8 a King’s bridge located in Belfast, Northern Ireland, b Closer detection of cracks using the multi-rotor Mavic Pro

with exposed reinforcement. Such deterioration condition, especially developed on the bridge deck, will result in poor condition rating and reduction in the capacity of the bridge.

5 Conclusions

The present study assessed the applicability of a drone to measure beam deflections, perform vehicle tracking and visual inspections of deterioration mechanisms in a bridge. An innovative tracking method for measuring displacements of a beam member under laboratory conditions and tracking the movement of a vehicle was also studied. The results of the practical investigations in this study demonstrated the potential use of UAVs for critical safety bridge inspections, vehicle tracking management. It was also shown that the accuracy of the beam deflection is dependent on the accuracy of the UAV movement. Generating the acceleration profile of the drone through the API onboard SDK (Standard Developer Kit) will allow a reliable, accurate and cost-effective measurement of the bridge deflections and vehicle tracking which are important aspects in structural health monitoring of bridges and transportation structures.

References

1. Lydon D, Taylor SE, Robinson D, Lydon M, Hester D (2017) Development of a vision based SHM for bridge damage identification. In: Proceedings of the 8th international conference on structural health monitoring of intelligent infrastructure. SHMII-8, Brisbane, Australia, pp 5–8
2. Hallermann N, Morgenthal G (2014) Visual inspection strategies for large bridges using unmanned aerial vehicles (UAV). In: 7th international conference on bridge maintenance, safety and management, IABMAS. IJCAI'81, Shanghai, China, pp 661–667
3. Spencer BF, Ruiz-Sandoval M, Kurata N (2004) Smart sensing technology for structural health monitoring. In: Proceedings of the 13th world conference on earthquake engineering. Vancouver, Canada, pp 1791–1803
4. Kim J-W, Kim S-B, Park J-C, Nam J-W (2015) Development of crack detection system with unmanned aerial vehicles and digital image processing. In: Proceedings of the world congress on advances in structural engineering and mechanics. ASEM15, Incheon, Korea, pp 25–29
5. Schauwecker K, Ke NR, Scherer SA, Zell A (2012) Markerless visual control of a quadrotor micro aerial vehicle by means of on-board stereo processing autonomous mobile systems. In: Proceedings of the autonomous mobile systems Conference. Berlin, Germany, pp 11–20
6. Hassanalilian M, Abdelkefi A (2017) Classifications, applications and design challenges of drones: a review. *Prog Aerosp Sci* 91:99–131
7. Vergouw B, Nagel H, Bondt G, Custers B (2016) Drone technology: types, payloads, applications, frequency spectrum issues and future developments. In: Custers B (eds) *The future of drone use. information technology and law series*, vol 27. T.M.C. Asser Press, The Hague
8. Mittleider A, Griffin B, Detweiler C (2015) Experimental analysis of a UAV-based wireless power transfer localization system. *Exp Robot* 109:357–371

9. Polydorou E, Robinson D, Treanor G, Taylor S, McGetrick P (2019) A new method for vibration-based damage detection in structural health monitoring using autonomous UAVs. In: Proceedings of the bridge engineering institute conference. BEI, Honolulu, Hawaii
10. Polydorou E, Robinson D, Treanor G, Taylor S, McGetrick P (2018) Vision-based deformation and free vibration measurements of beams using unmanned aerial vehicles (UAVs). In: Proceedings of the civil engineering research in Ireland, Dublin, Ireland
11. Lydon M, Robinson D, Taylor SE, Amato G, Brien EJO (2017) Improved axle detection for bridge weight-in-motion systems using fiber optic sensors. *J Civ Struct Heal Monit* 7:325–332
12. Martinez J, Orrite C, Herrero JE (2007) An efficient particle filter for color-based tracking in complex scenes. In: Proceedings of the international conference on advanced video and signal-based surveillance, AVSS, IEEE. IEEE conference, London, U.K., pp 317–332
13. Tomasi C, Kanade T (1991) Detection and tracking of point features. Carnegie Mellon University Technical Report, pp 91–132
14. Bruce DL, Kanade T (1981) An iterative image registration technique with an application to stereo vision. In: Proceedings of the 7th international joint conference on artificial intelligence. IJCAI'81, Vancouver, Canada, pp 674–679
15. Ye Z, Wang L, Xu W, Gao Z, Yan G (2017) Monitoring traffic information with a developed acceleration sensing node. *Sensors* 17(12):1–16
16. Stauffer C, Grimson WEL (1999) Adaptive background mixture models for real-time tracking. In: Proceedings of the computer society conference on computer vision and pattern recognition. USA, pp 2246–2252
17. Girshick R, Donahue J, Darrell T, Malik J (2004) Rich feature hierarchies for accurate object detection and semantic segmentation. In: Proceedings of the conference on computer vision and pattern recognition, IEEE. IJCAI'81, Vancouver, Canada, pp 580–587

Infrastructure Health Monitoring Using SAR Tomography



Alessandra Budillon, Giampaolo Ferraioli, Angel Caroline Johnsy, Vito Pascazio, and Gilda Schirinzi

Abstract Static structures, such as bridges and dams, are in need of continuous structural health monitoring due to the risk of collapse or destabilization, which leads to casualties and material loss. From economical point of view, the frequent inspection of these structures is cost-ineffective and time consuming. This shortage is overcome by using remote sensing systems such as synthetic aperture radar (SAR) systems, that do not require the in situ positioning of sensors and observe the Earth on a very large spatial scale and at regular time intervals. In particular, Tomographic Synthetic Aperture Radar (TomoSAR) has proved to be an effective tool for structure health monitoring. It is a multi-dimensional imaging technique that exploits stacks of interferometric SAR images acquired with slightly different view angles and at different times. TomoSAR is able to analyze the temporal deformations and the millimeter displacements on buildings. The small movements that occur due to thermal sensitivity of the structure can be also captured, so that the coefficient of thermal expansion, which is a fundamental parameter in health structure monitoring, can be computed. The widespread deterioration and some recent collapses of infrastructures have highlighted the importance of developing early warning monitoring strategies, devoted to identify structural problems before they become critical. A problem to be considered is that effective monitoring techniques have to rely on approaches capable of identifying few representative points, which describe well the dynamical behavior of the structure. A TomoSAR technique recently developed,

A. Budillon (✉) · A. C. Johnsy · V. Pascazio · G. Schirinzi
Dipartimento di Ingegneria, Università di Napoli Parthenope, Naples, Italy
e-mail: alessandra.budillon@uniparthenope.it

A. C. Johnsy
e-mail: angel.johnsy@uniparthenope.it

V. Pascazio
e-mail: vito.pascazio@uniparthenope.it

G. Schirinzi
e-mail: gilda.schirinzi@uniparthenope.it

G. Ferraioli
Dipartimento di Scienze e Tecnologie, Università di Napoli Parthenope, Naples, Italy
e-mail: giampaolo.ferraioli@uniparthenope.it

based on a multi-step binary hypothesis GLRT test, has shown a good capability of selecting reliable control points on the structure for estimating its deformations. In order to demonstrate the potentialities of this technique for structure health monitoring, two tall structures will be considered. The results obtained using different SAR sensors, such as COSMO-SkyMed, Sentinel-1A and TerraSAR-X, are presented.

Keywords Infrastructure health monitoring · Remote sensing · SAR · Tomography · Generalized likelihood ratio

1 Introduction

All man-made structures, such as buildings and bridges, suffer from the phenomenon of aging that can deteriorate them up to the point of causing their collapse. Moreover, a structural breakdown can be caused by natural disasters, such as earthquakes, hurricanes, fires, and subsidence. While natural disasters cannot usually be predicted, general deterioration can be detected by means of structure health monitoring (SHM) [1], which is intended to detect anomalies in the static and dynamic behavior of structures so that appropriate measures can be put in place to make structures more resilient to adverse events and structural problems can be prevented before they occur.

Generally, SHM involves the placement of sensors on the monitored structure. These sensors can monitor the forces acting on potential stress points in structures, detecting factors that may be symptoms of poor structural health, such as anomalous displacements. Many methods are also based on understanding the relationship between the temperature of the structure and the resultant strain and displacement, that can provide in depth knowledge of the structural condition (Temperature Driven-Structural Health Monitoring or TD-SHM) [2, 3]. These methods consider temperature as the driving force in structural behavior and compare an input temperature to an output strain and displacement to form three-dimensional signatures that describe the behavior for the structure. Changes in these signatures indicate unusual behavior or damage in the structure. A fundamental parameter for this form of analysis is the Coefficient of Thermal Expansion (CTE), which is the amount of expansion or contraction a material undergoes per degree change in temperature.

From economical point of view, a problem that has to be faced is that the frequent inspection of structures, by means of sensors positioning on it, is cost-ineffective and time consuming. This shortage can be overcome by using satellite-borne remote sensing systems such as synthetic aperture radar (SAR) systems, that do not require the positioning of sensors on the structure to be monitored. SAR systems are nowadays established tools for Earth observation. Thanks to their all day/all weather imaging capabilities and thanks to the increasing available resolutions of the latest sensors, they offer the possibility to effectively monitor natural scenes and/or man-made structures [4] based on different applications. Among them, Differential Interferometric SAR (DInSAR) [5] aims at measuring surface deformation, based on the exploitation of at least one pair of complex SAR images (interferogram).

Among the different proposed methods for surface deformation measurement in the DInSAR framework, the Permanent Scatterers (PS) technique has showed to be effective and largely applied. It makes use of several SAR images of the same scene, acquired during time (i.e. stacks). It is essentially phase model-based and it assumes the presence of one dominant scatterer within a resolution cell [6–11]: the deformation is measured only over the available coherent pixels.

Recently the introduction of new sensors in X-Band such as TerraSAR-X and the Italian COSMO-SkyMed constellation have stimulated this research field. The very small wavelength (~ 3.1 cm) allows to measure small surface displacements, even those caused by thermal dilation of the imaged targets. In fact, the total observed deformation contains both the thermal expansion and the deformation signal of interest. In order to derive proper deformation estimates, the two components have to be separated [9, 10]. An extended PS model has been proposed in [10], which allows separating the thermal expansion from the total observed deformation thus generating the map of the thermal expansion parameter.

The limitation of PS approaches is the assumption of only single scatterer in the resolution cell, that does not allow to properly treat the layover problem that severely affect urban areas. In case of layover multiples scatterers interfere in the same resolution, impairing the performance method: misdetection of persistent scatterers and inaccuracies of height velocity and time series measurements can be present.

This limitation can be overcome using SAR tomography (TomoSAR) [12, 13] where scatterers interfering within the same range-azimuth resolution cell are separated by synthesizing apertures along the elevation direction. This allows to provide the full 3-D scene reflectivity profile along azimuth, range, elevation. A 4D map can also be generated, by adding the velocity deformation [14]. TomoSAR mainly consists in resolving an inversion problem: different spectral estimators, such Singular Value Decomposition (SVD) [15], and Compressive Sensing (CS) [16–18], have been proposed.

One of the main issues that TomoSAR techniques have to face is to correctly detect true scatters in presence of outliers. This detection problem has been addressed in [19] by discriminating between single and double scatterers, on the base of a sequential Generalized Likelihood Ratio Test (GLRT). The latter does not exhibit good performance when trying to resolve close scatterers.

In [20] a GLRT approach that achieves super resolution has been proposed. It is based on the exploitation of the sparsity assumption and on the search of the best signal support (i.e. the positions of the significant samples in the unknown vector) matching the data (Sup-GLRT). This statistical test exploits a non-linear maximization for detecting at most K_{\max} different scatterers in the same range-azimuth resolution cell and for estimating their elevation. It allows evaluating detection performance in terms of probability of detection achievable with a given number of measurements and signal to noise ratio and with an assigned probability of false alarm. Moreover, since it is based on non-linear processing, in principle, it allows improved spatial and radiometric resolution. A drawback of this method is that numerical complexity increases very rapidly with the size of the reflectivity unknown vector. In [21] an

approximated estimation of the signal support of cardinality K , denoted Fast-Sup-GLRT, has been proposed. It is performed by means of the sequential estimation of K supports of cardinality one has been proposed, achieving a numerical complexity that is linear with the size of the unknown vector.

Extended phase models [22–26] can be additionally employed to allow simultaneous retrieval of scatterer elevation and of deformation parameters, showing effectiveness also in estimating the thermal dilation contribution (5D maps), useful for analyzing the infrastructure structural behavior.

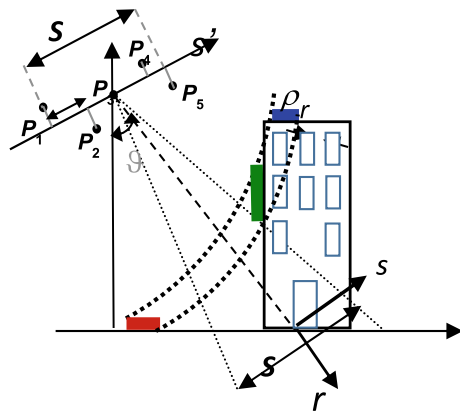
In this paper, an extended phase model and a detection test [21] in order to retrieve the 5-D reconstruction of buildings in urban areas has been used. Results on real SAR data, TerraSAR-X (TSX), COSMO-SkyMed (CSK) and Sentinel-1A (S1A) data, are presented in order to show how remote sensing can be used for structure monitoring by means of 5D maps.

2 Signal Model and Method

Let us assume to have a stack of M SAR interferometric images of the same scene, acquired at different times t_m and with different orthogonal baselines s'_m respect to a reference acquisition (see Fig. 1).

The images are properly registered, with a sub-pixel accuracy, and preprocessed in such a way to remove flat Earth interferometric phase and to deperate the focused images from the atmospheric and nonlinear deformation contributions on small scale (low resolution) [19]. Then, in any azimuth-range pixel, the m -th acquired image u_m is given by the superposition of the signal backscattered by the targets located in the given azimuth-range resolution cell at different elevation values. Then, the image signal, in the case of slow moving scatterers can be expressed by [22, 25]:

Fig. 1 Multi-baseline SAR geometry



$$u(s'_m, t_m) = \int_{S_1} \gamma(s) e^{-j \left[\frac{4\pi}{\lambda R_0} s'_m s + \frac{4\pi}{\lambda} d(s, t_m) \right]} ds \quad (1)$$

where λ is the operating wavelength, R_0 the distance between the image pixel and the reference antenna, S_1 the extension of the observed scene along elevation, and $d(s, t_m)$ is the deformation of the scatterer at the elevation s and at the time t_m , which is typically related to land subsidence phenomena. With the advent of the last generation SAR sensors, working at higher frequency, such as CSK and TSX working at X-Band, the model of the deformation signal $d(s, t_m)$ has been extended by including minute deformation components, such as thermal dilation. This is a direct consequence of the reduction of the wavelength, that allows a higher phase sensitivity to range variations. Than the model adopted for the deformation signal is typically assumed to be composed of linear and a nonlinear contribution [22, 25]:

$$d(s, t_m, T_m) = v_0(s)t_m + k_0(s)T_m + d_{NL}(s, t_m, T_m), \quad (2)$$

where T_m is the temperature of the scene at the time t_m , $v_0(s)$ is the velocity of the slow linear deformation, having the dimension of (m/s), and $k_0(s)$ is the coefficient of thermal dilation, having the dimension of (m/°C), of the scatterer at elevation s , representing the phase-to-temperature sensitivity and depending upon material and/or physical structure.

The coefficient of thermal dilation k_0 in Eq. (2) is given by $k_0 = \Delta L / \Delta T$, where ΔL is the change in length of the solid structure due to a change in temperature ΔT . It is related to the Coefficient of linear Thermal Expansion (CTE) of the solid structure α , having the dimension of (1/°C), by the relation $k_0 = \alpha L_0$, where L_0 is the initial length of the given solid [27].

Substituting Eq. (2) in (1) and applying some manipulations [2], it is obtained:

$$u(s'_m, t_m, T_m) = \int_{S_1} \int_{V_1} \int_{K_1} \gamma(s, v, k) e^{-j2\pi \left(\frac{2s'_m}{\lambda R_0} s + \frac{2t_m}{\lambda} v + \frac{2T_m}{\lambda} k \right)} ds dv dk \quad (3)$$

where V_1 and K_1 are the range of values of v and k .

Equation (3) can be discretized and written in matrix form, introducing the $N \times 1$ column vector γ , whose elements are the samples computed in all the triplets (i, l, n) , with $i = 1, \dots, N_s, l = 1, \dots, N_v, n = 1, \dots, N_k$, and $N = N_s N_v N_k$, and the $M \times 1$ data vector \mathbf{u} collecting the measurements $u(s'_m, t_m, T_m)$, with $m = 1, \dots, M$, so that:

$$\mathbf{u} = \Phi \gamma + \mathbf{w} \quad (4)$$

where \mathbf{w} is an $M \times 1$ vector representing noise and the returns from incoherent scatterers (clutter), and Φ is an $M \times N$ measurement matrix, whose m -th row ϕ_m

is given by $\text{vect}(\Phi_{m3})$, where vect is the operator transforming a three-dimensional matrix of size $N_s \times N_v \times N_k$ in a row vector of size $N = N_s N_v N_k$, by loading in the vector all the elements of the matrix scanned in a preassigned order, and Φ_{m3} is the three-dimensional matrix of size $N_s \times N_v \times N_k$, whose element of entries (i, l, n) is given by:

$$\{\Phi_{m3}\}_{i l n} = \frac{1}{\sqrt{N}} e^{j \left(\frac{4\pi}{\lambda R_0} s_i s'_m + \frac{4\pi}{\lambda} v_l t_m + \frac{4\pi}{\lambda} k_n T_m \right)} \quad (5)$$

In the case of urban areas, most of the elevation profiles are sparse, i.e. they consist only of a few discrete scatterers, typically corresponding to scatterers located on the ground, facade and roof. With the assumption of sparseness in the elevation direction, the presence of one or more scatterers can be verified by performing a statistical test. In Eq. (4), the noise vector \mathbf{w} can be assumed as circularly symmetric complex (or proper complex) Gaussian vector, with uncorrelated samples and mutually uncorrelated real and imaginary parts, with zero-mean and same variance. Fixing a number of K_{\max} scatterers present in the range-azimuth resolution cell, the problem of detection is formulated for $K_{\max} + 1$ statistical hypotheses as follows:

$$H_i: \text{presence of } i \text{ scatterers, with } i = 0, \dots, K_{\max}$$

The two hypotheses are identified applying the Fast-Sup-GLRT detector, which is a multi-step detector [21], that at each step i applies the following binary test:

$$\Lambda_i(\mathbf{u}) = \begin{cases} \frac{[\mathbf{u}^H \Pi_{\hat{\Omega}_{i-1}}^\perp \mathbf{u}]}{[\mathbf{u}^H \Pi_{\hat{\Omega}_{K_{\max}}}^\perp \mathbf{u}]} < \eta_i & H_{i-1} \\ > \eta_i & H_{K_{\max} \geq i} \end{cases} \quad (6)$$

where $\hat{\Omega}_{i-1}$, with $i = 1, \dots, K_{\max} + 1$, is the support of cardinality $i - 1$ (i.e. the positions of the $i - 1$ elements different from zero in the vector $\boldsymbol{\gamma}$) obtained minimizing the term $[\mathbf{u}^H \Pi_{\hat{\Omega}_{i-1}}^\perp \mathbf{u}]$ and $\Pi_{\hat{\Omega}_i}^\perp = \mathbf{I} - \Phi_{\hat{\Omega}_i} (\Phi_{\hat{\Omega}_i}^H \Phi_{\hat{\Omega}_i})^{-1} \Phi_{\hat{\Omega}_i}^H$. All the thresholds η_i can be numerically evaluated by means of Monte Carlo simulations. Assuming $K_{\max} = 2$ the two thresholds will be evaluated in such a way to obtain an assigned probabilities of false alarm and false detection, respectively, $P_{FA} = P(H_1|H_0)$ and $P_{FD} = P(H_2|H_1)$.

The following consideration can be done:

- (1) The number K of the scatterers lying in the same azimuth-range resolution cell and providing a reliable estimate of elevation, deformation velocity and thermal expansion coefficient, is automatically estimated through the sequential application of the statistical test (6);
- (2) the estimate of elevation, deformation velocity and thermal expansion coefficient of each reliable scatterer is provided by the estimation of the best support

- matching the data (i.e. the positions of the K non zero elements tin the unknown vector γ), obtained assuring a given probability of false detection;
- (3) the accuracy of the parameters estimates is related to the scatterers intensity and to their coherence over time: higher the scatterer intensity and the temporal coherence, more accurate the parameter estimation.

3 Experimental Results

In this Section some results obtained on real multi-pass satellite data are shown, with the purpose of investigating the possibility of structure monitoring. In particular, the CTE estimation is considered.

The method described in the previous Section is applied to three different data sets acquired by means of different SAR sensors. Refer to Table 1 for the three system configuration parameters.

The first experiment is carried out on StripMap TSX data. A stack of $M = 21$ azimuth-range focused TSX interferometric images is considered, whose spatial and temporal baselines and temperature are reported in Fig. 2.

The proposed detector is applied to the urban area of Barcelona, Spain, where one of the tallest buildings of Barcelona, the Agbar tower, with a height of 144 m, is present. In Fig. 3 the optical and the intensity SAR image of the tower are shown. A tall building has been chosen since in this case it is visible the effect of the layover, as it can be seen in the SAR image, the building is folded onto the ground toward the sensor; hence, different scatterers are expected interfering in each pixel. The thresholds η_i

Table 1 SAR sensor parameters

Sensor	Pass	Wavelength (cm)	Spatial resolution (m × m)	Angle (°)
TSX	Descending	3.1	3 × 3	35
S1A	Descending	5.5	22 × 3	33.83
CSK	Ascending	3.1	3 × 3	33.98

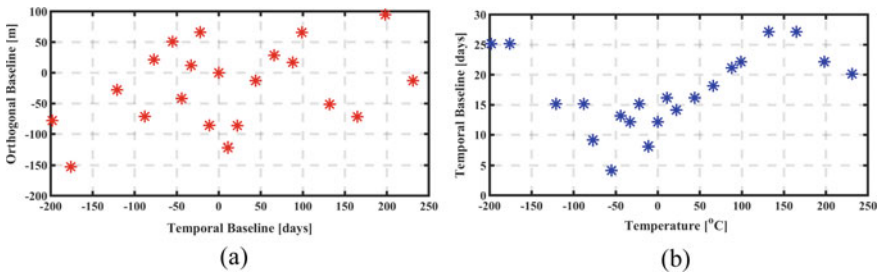
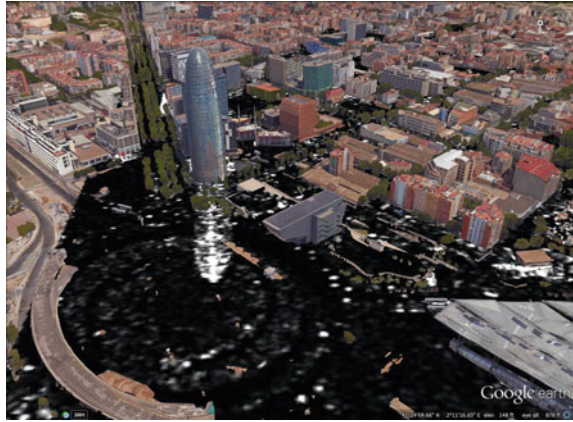


Fig. 2 Distribution of orthogonal versus temporal baselines for TSX (a). Distribution of temperature versus temporal baselines TSX (b)

Fig. 3 Optical image of Agbar Tower, Barcelona, Spain, with the TSX image superimposed on it



have been computed by Monte Carlo simulation for the considered system parameters and acquisition configuration and fixing $P_{FD} = P_{FA} = 10^{-3}$. The search is limited to two targets per resolution cell, so that $K_{\max} = 2$. The results obtained with Fast-Sup-GLRT are shown in two cases: when no surface deformation and thermal dilation are considered and when they are taken into account. The estimation revealed that there is no surface deformation. In Fig. 4a, b are shown, respectively, the scatterers detected by Fast-Sup-GLRT reported on the optical image with a coloring based on the height are shown, and the scatterers detected considering the thermal dilation contribution. It can be noted that the estimation of the thermal dilation contribution helps in recovering the top of the building. In Fig. 5a, b are shown, respectively, a detected point and the corresponding thermal deformation effect. In particular, with the solid line, the estimated linear trend is reported, and with blue asterisks the residual phases of the pixel, for each SAR image after topographic phase compensation. The linear trend seems to well describe the detected point behavior with the different



Fig. 4 Detected scatterers relocated on optical image without (a) and with considering the effect of thermal dilation (b)

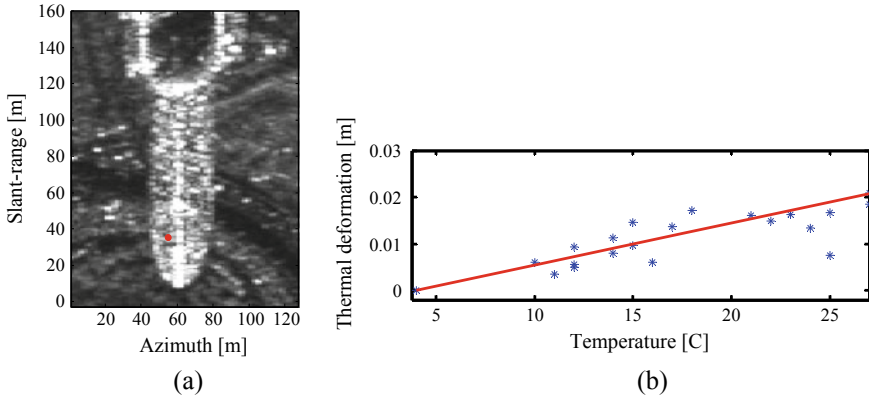


Fig. 5 A scatterer detected on the top of the building (a) the thermal deformation in the observed time period (b)

temperature. The coefficient of thermal expansion estimated is $0.07 \text{ mm}/^\circ\text{C}$. This value is compatible with a coefficient of linear thermal expansion of a 144 m structure whose module perimeter is concrete ($9.8 \times 10^{-6}/^\circ\text{C}$ linear thermal coefficient) and coated with a first skin created by modules lacquered and tinted aluminum ($20 \times 10^{-6}/^\circ\text{C}$ linear thermal coefficient).

The second experiment is carried out on S1A and CSK data. The S1A data set consists of $M = 93$ acquisitions, whose spatial baselines and temperatures vs temporal baselines are reported in Fig. 6a, c, respectively. The CSK data set consists of $M = 42$ acquisitions, whose spatial baselines and temperatures vs temporal baselines are reported in Fig. 6b, d, respectively. The overall time intervals of acquisition for the two datasets are the same, in order to validate the common behaviors and to complement the results.

In this case the proposed detector is applied to the urban area of Genoa, Italy, where a tower with a height of 100 m, is present.

The thresholds η_i have been computed by Monte Carlo simulation for the considered system parameters and acquisition configuration and fixing $P_{FD} = P_{FA} = 10^{-3}$. The search is limited to two targets per resolution cell, so that $K_{\max} = 2$. Results obtained with Fast-Sup-GLRT considering the two sensors are compared.

In Fig. 7a the mean intensity SAR image for the S1A data set is shown. It can be noted that the tower appearing in the upper right part of the image is characterized by high reflectivity values (corresponding to very bright pixels). Then several reliable points on the tower are expected. In Fig. 7b the scatterers detected by Fast-Sup-GLRT are reported on the three dimensional optical image with a coloring based on the height value. As reported in Table 1, the S1A sensor exhibit low spatial resolution which results in a lower density of detected points compared to the density found using the TSX data set (see Fig. 4), since their spacing along the horizontal directions is related to the azimuth and range resolution, whereas the point density along the vertical (elevation) direction is high, as expected. In Fig. 7c, d, respectively,

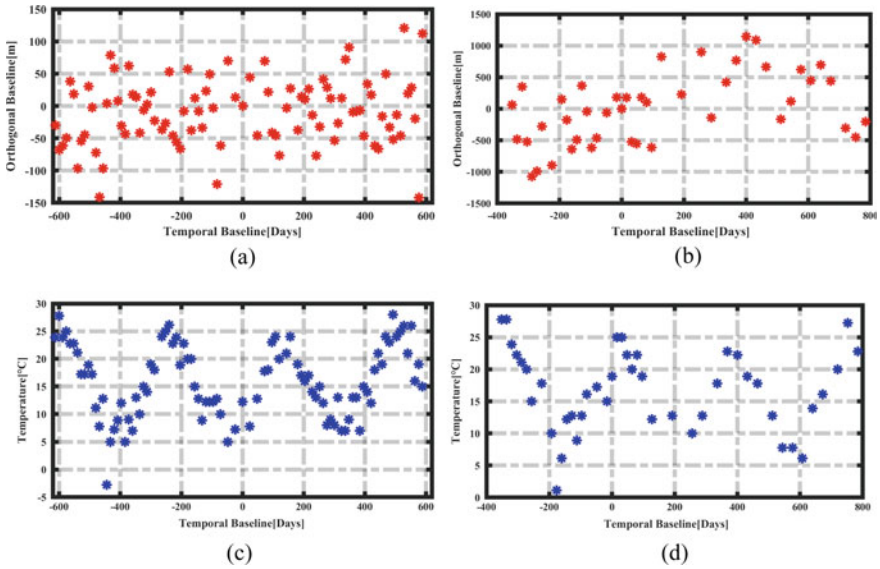


Fig. 6 Distribution of orthogonal versus temporal baselines for S1A (a) and CSK (b) datasets. Distribution of temperature versus temporal baselines for S1A (c) and CSK (d) datasets

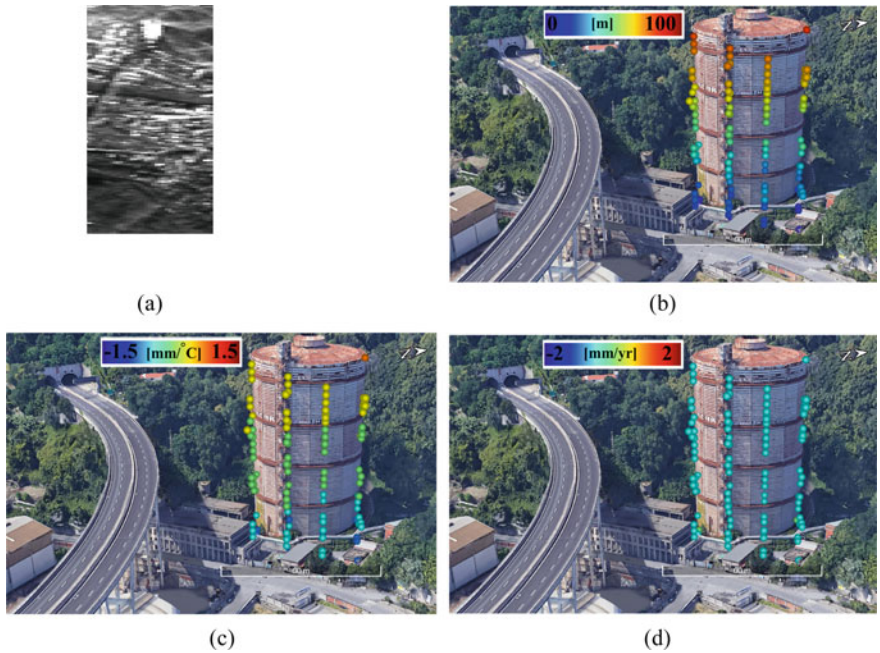


Fig. 7 Tower, Genoa, Italy: mean intensity of S1A SAR image (a), height map (b), thermal dilation map (c), deformation map (d)

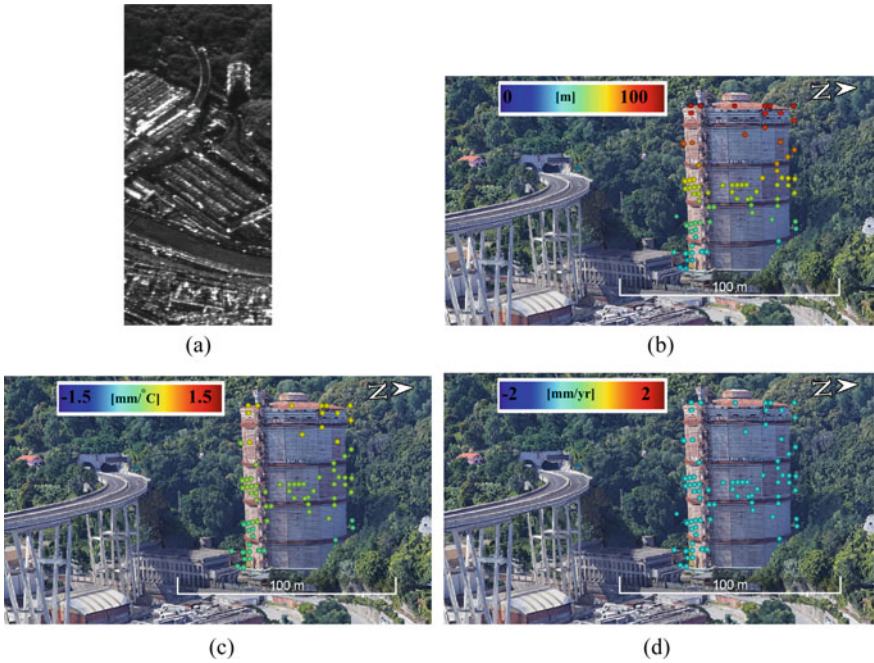


Fig. 8 Tower Genoa, Italy: mean intensity of CSK SAR image (a), height map (b), thermal dilation map (c), deformation (d)

thermal dilation and deformation maps are reported. It can be noted that there is no deformation, while the coefficient of thermal dilation map roughly ranging from 0 to 1.5 mm/°C, is compatible with a coefficient of linear thermal expansion of $9.8 \times 10^{-6}/^{\circ}\text{C}$ for a concrete structure of 100 m.

In Fig. 8a the mean intensity SAR image for the CSK data set is shown. In Fig. 8b the scatterers detected by Fast-Sup-GLRT are reported on the three dimensional optical image with a coloring based on the height values, while in Fig. 8c, d, respectively, thermal dilation and deformation maps are reported. It can be noted that in this case the point density is higher in the tower regions characterized by a high reflectivity (corresponding to bright pixels in the SAR image in Fig. 8a), since the sensors has a higher spatial resolution (see Table 1). Anyway, in the tower regions characterized by low reflectivity (corresponding to dark pixels in the SAR image in Fig. 8a) few scatterers are detected. This is due to the fact that low reflectivity scatterers in general provide not sufficiently reliable results. In Fig. 9a a zoom of the mean intensity SAR image of the tower for the CSK data set with the indication of a scatterer in red, detected in both data sets, is shown. In Fig. 9b, c the residual phase (red line), given by the interferometric phase compensated for the topographic phase term, and the sum of the estimated temporal and thermal deformation phases (blue) for the selected point, respectively for CSK data set and S1A data set are shown. It can be noted that the seasonal behaviour is very evident and in accordance with

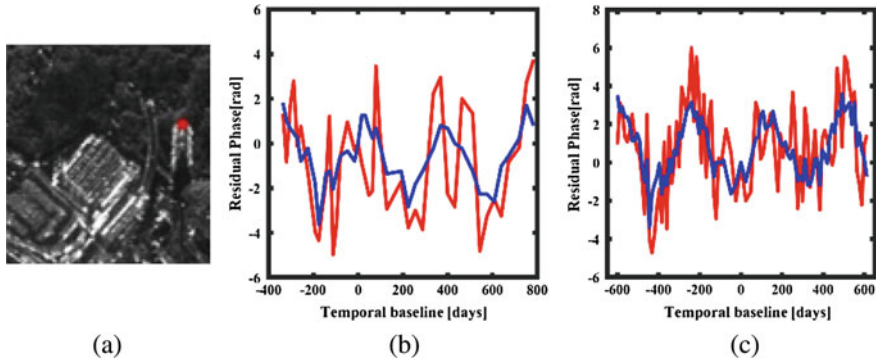


Fig. 9 **a** Mean intensity SAR image of the tower with the indication of the point (in red) analyzed; residual phase (red line) and sum of the estimated temporal and thermal deformation phases (blue) for the selected point and for **b** CSK data, **c** S1A data

the distribution of temperature versus temporal baselines shown in Fig. 6c, d. It is also worth noting the correspondence between the estimated trends based on the two sensors data sets.

4 Conclusions

In this paper the estimation of temporal displacements of buildings by using multi-baseline and multi-temporal interferometric SAR images has been investigated. By using a GLRT based SAR tomographic technique, reliable reference points on the observed structures can be selected and two components of their temporal displacements at a millimeter scale can be estimated: a deformation component linear with time, which is usually related to presence of subsidence and structural damages, and a displacement component linear with the temperature, which is related to the thermal dilation effect of solid structures. The estimates displacements can be, then, usefully employed for the structure health monitoring.

Some numerical experiments have been carried out on TSX, CSK and S1A data, which are SAR sensors differing each other for the operating wavelength and for the spatial image resolution. Obtained results show the effectiveness of the proposed tomographic approach in detecting scatterers on urban structures and in providing displacement estimations which comply with the expected values. Position, deformation velocity and thermal dilation coefficient for the selected scatterers have been estimated for two different buildings, and linear deformation and thermal dilation contributions have been recovered and separated. The presented approach has proven to be able to estimate coefficients of thermal expansion with an absolute value ranging from 0 to 1.5 mm/°C, compatible with a coefficient of linear thermal expansion of $9.8 \times 10^{-6}/^{\circ}\text{C}$ for a concrete structure. The linear trend has been verified and it has

been found a good correspondence between the estimated trends based on the two sensors data sets.

Presented results show that SAR tomography represents a promising technique for structure health monitoring, since it provides sufficient accurate estimates of temporal deformation velocity and of the CTE, without requiring on site placement of sensors. Moreover, the very large spatial scale of satellite SAR sensors, together with the short revisiting time and the high spatial resolution assured by recent systems, allows a very wide variety of monitoring applications at low economical costs. Anyway, many issues have still to be addressed. For instance, the study of an effective criterion for the selection of the structure reference points to be monitored, which should behave both as structure stress points and as strong and temporally coherent scatterers, in such a way to assure highly reliable results. The development of appropriate structure models to be included in the signal processing technique is then of great interest and can lead to important achievements in SHM from space.

References

1. Kralovec C, Schagerl M (2020) Review of structural health monitoring methods regarding a multi-sensor approach for damage assessment of metal and composite structures. *Sensors (Basel)* 20(3):826
2. Yarnold MT, Moon F (2015) Temperature-based structural identification of long-span bridges. *J Struct Eng* 141(11)
3. Reilly J, Glisic B (2018) Identifying time periods of minimal thermal gradient for temperature-driven structural health monitoring. *Sensors (Basel)* 18(3):734
4. Fornaro G, Pascazio V (2013) SAR interferometry and tomography: theory and applications. In: Academic Press Library in signal processing, communications and radar signal processing, vol 2. Elsevier Ltd., pp 1043–1117
5. Gabriel AK, Goldstein RM, Zebker HA (1989) Mapping small elevation changes over large areas: Differential radar interferometry. *J Geophys Res*:9183–9191
6. Ferretti A, Prati C, Rocca F (2000) Nonlinear subsidence rate estimation using permanent scatterers in differential SAR interferometry. *IEEE Trans Geosci Remote Sens* 38:2202–2212
7. Gernhardt S, Adam N, Eineder M, Bamler R (2000) Potential of very high resolution SAR for persistent scatterer interferometry in urban areas. *Ann GIS* 16:103–111
8. Crosetto M, Monserrat O, Iglesias R, Crippa B (2010) Persistent scatterer interferometry: potential, limits and initial C- and X-band comparison. *Photogramm Eng Remote Sens* 76:1061–1069
9. Crosetto M, Monserrat O, Cuevas-Gonzalez M, Devanthery N, Luzi G, Crippa B (2015) Measuring thermal expansion using X-band persistent scatterer interferometry. *ISPRS J Photogramm Remote Sens* 100:84–91
10. Monserrat O, Crosetto M, Cuevas M, Crippa B (2011) The thermal expansion component of persistent scatterer interferometry observations. *IEEE Geosci Remote Sens Lett* 8:864–868
11. Ferretti A, Fumagalli A, Novati F, Prati C, Rocca F, Rucci A (2011) A new algorithm for processing interferometric data-stacks: SqueeSAR. *IEEE Trans Geosci Remote Sens* 49:3460–3470
12. Reigber A, Moreira A (2000) First demonstration of airborne SAR tomography using multibaseline L-band data. *IEEE Trans Geosci Remote Sens* 38:2142–2152
13. Budillon A, Crosetto M, Johnsy AC, Monserrat O, Krishnakumar V, Schirinzi G (2018) Comparison of persistent scatterer interferometry and SAR tomography using sentinel-1 in urban environment. *Remote Sens* 10:1–14

14. Lombardini F (2005) Differential tomography: A new framework for SAR interferometry. *IEEE Trans Geosci Remote Sens* 43:37–44
15. Fornaro G, Lombardini F, Serafino F (2005) Three-dimensional multipass SAR focusing: experiments with long-term spaceborne data. *IEEE Trans Geosci Remote Sens* 40:702–714
16. Budillon A, Evangelista A, Schirinzi G (2011) Three-dimensional SAR focusing from multipass signals using compressive sampling. *IEEE Trans Geosci Remote Sens* 49:488–499
17. Zhu XX, Bamler R (2012) Super-resolution power and robustness of compressive sensing for spectral estimation with application to spaceborne tomographic SAR. *IEEE Trans Geosci Remote Sens* 50:247–258
18. Budillon A, Ferraioli G, Schirinzi G (2014) Localization performance of multiple scatterers in compressive sampling SAR tomography: results on COSMO-SkyMed data. *IEEE J Sel Topics Appl Earth Observ Remote Sens* 7:2902–2910
19. Pauciullo A, Reale D, De Maio A, Fornaro G (2012) Detection of double scatterers in SAR tomography. *IEEE Trans Geosci Remote Sens* 50:3567–3586
20. Budillon A, Schirinzi G (2016) GLRT based on support estimation for multiple scatterers detection in SAR tomography. *IEEE J Sel Top Appl Earth Observ Remote Sens* 9:1086–1094
21. Budillon A, Johnsy A, Schirinzi G (2017) A fast support detector for superresolution localization of multiple scatterers in SAR tomography. *IEEE J Sel Topics Appl Earth Obs Remote Sens* 10(6):2768–2779
22. Fornaro G, Serafino F, Reale D (2009) 4D SAR imaging for height estimation and monitoring of single and double scatterers. *IEEE Trans Geosci Remote Sens* 47:224–237
23. Fornaro G, Reale D, Verde S (2013) Bridge thermal dilation monitoring with millimeter sensitivity via multidimensional SAR imaging. *IEEE Geosci Remote Sens Lett* 10:677–681
24. Reale D, Fornaro G, Pauciullo A (2013) Extension of 4-D SAR imaging to the monitoring of thermally dilating scatterers. *IEEE Trans Geosci Remote Sens* 51:5296–5306
25. Budillon A, Johnsy A, Schirinzi G (2017) Extension of a fast GLRT algorithm to 5D SAR tomography of urban area. *Remote Sens* 9(8), 844:1–21
26. Rambour C, Budillon A, Johnsy AC, Denis L, Tupin F, Schirinzi G (2020) From interferometric to tomographic SAR: a review of synthetic aperture radar tomography-processing techniques for scatterer unmixing in urban areas. *IEEE Geosci Remote Sens Mag* 8(2):6–29
27. Ho CY, Taylor RE (1998) Thermal expansion of solids. ASM International, Materials Park, OH

Monitoring and Evaluation of a Highway Bridge During Major Rehabilitation



Juan A. Quintana, Francisco J. Carrión, Miguel Anaya,
Germán M. Guzmán, Jorge A. Hernández, Luis A. Martínez,
José M. Machorro, and Héctor M. Gasca

Abstract After a severe accident, El Carrizo Bridge reported extensive damage and was closed to traffic. This bridge is on the Mazatlán-Durango highway, which is an important route for tourism and commerce in the northwest region of Mexico; for that reason, it was a priority to open traffic and reduce the economic impact estimated at more than USD 250,000 per day. To address the emergency and recover the traffic on the highway, even partially, the authorities proposed a two-stage rehabilitation strategy; the first stage, to build two provisional lanes to allow traffic under restricted conditions and, the second, to rehabilitate the bridge with the provisional lanes in operation. The previous strategy put forward several safety challenges and required the installation of a SHM system with a permanent evaluation to assure structural and operational conditions. This work describes the way that specialists designed the monitoring system and the evaluation strategy, based on the conditions of the rehabilitation works and processes.

Keywords SHM · Bridge rating · Structural evaluation · Load testing and monitoring

1 Introduction

The El Carrizo Bridge is the second most important bridge on the Mazatlán-Durango highway (see Fig. 1). This highway is located in the northwestern region of Mexico and is particularly important because it connects the port of Mazatlán on the Pacific Coast with the northcentral part of México, the US Border and the Altamira and Tampico ports on the Gulf of Mexico. In addition to the commercial importance that the port of Mazatlán has with the Asian market, it is also one of the most important

J. A. Quintana · F. J. Carrión (✉) · M. Anaya · J. A. Hernández · L. A. Martínez ·
J. M. Machorro · H. M. Gasca
Instituto Mexicano del Transporte, 76703 Sanfandila, QRO, Mexico
e-mail: carrion@imt.mx

G. M. Guzmán
Universidad Autónoma de Sinaloa, 80040 Culiacán, SIN, Mexico



Fig. 1 El Carrizo Bridge

touristic centers in the country. By the end of 2017, the Mazatlán-Durango highway reported an annual average daily traffic of almost 3500 vehicles with significant increases during Christmas and Easter Holydays.

The construction of the El Carrizo Bridge started in 2011 and concluded in 2013. It is a complex bridge with a total length of 487 m and with three different types of structures. The main section is a 364 m cable-stayed segment that continues with another 70.6 m double cantilever structure and ends with 38 m simple supported post-tensioned Nebraska NU type girders. The stayed structure has four semi-harps with 14 cables, each, and a steel deck. The double cantilever structure has two widely spaced post-tensioned box girders with steel cross girders to support the reinforced concrete deck. The main span of the El Carrizo Bridge has a total length of 217.3 m, which goes from the cable-stayed pylon to the double cantilever pillar. An important feature of this bridge is that the cantilever supports one end of the stayed section with a counterweight of 100,000 kg on each box girder to keep it fix [1].

2 The Accident that Damaged the Bridge

On the night of January 12, 2018, a heavy truck double semi-trailer tanker carrying diesel fuel, traveling in the direction of Mazatlán to Durango, lost control due to speeding just outside the tunnel and the second trailer came off and flipped over to the double cantilever section of the bridge. Consequently, the fuel spilled over the

entire section and caused a fire that lasted for about 6 h with temperatures reaching 900 °C (see Fig. 2).

As shown in Figs. 3 and 4, the accident caused severe structural damage to the section of the double cantilever, especially in the half that supports the cable-stayed section.

A post-accident analysis reported the total loss of the bridge deck of the lanes heading Durango (side A) and severe damage to the two lanes heading Mazatlán (side B). The steel crossbeams supporting the deck were completely deformed and



Fig. 2 Fire on the El Carrizo Bridge, view from the tunnel



Fig. 3 View of the El Carrizo Bridge the day after the accident



Fig. 4 Some details of the damage caused to the bridge deck

damaged. The inside walls of both box girders were damaged and it was estimated that 8 post-tensioning cables (out of 38) were practically lost. As a result, the bridge was determined to be unsafe and closed to traffic with daily economic losses estimated at 250,000 USD.

Considering the economic and social effects that the accident produced in the region, the rehabilitation strategy proposed a two-phase process. The first, the rehabilitation of the box girders and the construction of temporary bypass lanes over these rehabilitated girders for limited traffic, so it could be open by March 23, just before Easter's Holyday. The box girders' repair considered the recovery and reinforcement of the damaged walls and additional post-tensioning cables to recover those damaged by the accident. The second phase considered the installation of new crossbeams, without removing the damaged ones, and the construction of the new deck; these rehabilitation works being carried out 24/7, with temporary bypasses operating all time.

Considering the uncertainty about the condition of the bridge and the effects of the structural rehabilitation, CAPUFE, the government agency in charge of the highway, requested The Mexican Institute of Transport to install a monitoring system and evaluate the process to guarantee the structural condition of the bridge and safety of workers and highway users [2–4]. Complementary, they required load tests at the end of each phase, according to the AASHTO Manual for Bridge Evaluation [5, 6].

3 Rehabilitation Stages and Load Tests

For the second rehabilitation phase, the process was divided into seven stages. The first stage corresponds to the completion of the first phase and its evaluation from the first load test. For the following, the progress of the project defined each stages until full rehabilitation, which was evaluated from the second load test.

Additionally, for reference, two other stages were considered: initial stage, corresponding to the condition of the bridge before the accident, according to the available

design and inspection data prior to the event; and the damaged condition, corresponding to an estimated state from the damage survey, the post-accident diagnosis, and the initial stage condition.

The Rating Factor, as defined in the Manual for the Evaluation of Bridges of the AASTHO [5, 6], served as a reference to evaluate the structural condition of the double cantilever section of the bridge at each stage. The calculation of these factors was through a finite element model calibrated, at each stage, from the load test or monitoring data. In the absence experimental data for the initial and damaged stages, the analysis group estimated the Rating Factors from a finite element model using design and post-accident information.

According to the above and considering the rehabilitation process, the defined stages were as follows:

Stage 1: Two temporary bypass lanes in operation with the box girder already repaired with four additional post-tensioning cables each. None rehabilitation on the bridge deck, 0% completed and 100% damaged.

Stage 2: Two temporary bypass lanes in operation, bridge deck with 40% in the process of rehabilitation and 60% still damaged.

Stage 3: Two temporary bypass lanes in operation and bridge deck with 10% repaired, 40% in the repair process and the remaining 50% damaged. At this point, 40% of the new steel crossbeam girders were installed.

Stage 4: Two temporary bypass lanes in operation, 95% of the bridge deck already repaired, and 5% damaged. All new steel crossbeam girders installed 100%.

Stage 5: One temporary bypass lane in operation, alternating traffic flow in both directions (B side), deck with 95% repaired and 5% damaged. Temporary bypass lane on A side removed.

Stage 6: One lane in service with alternating traffic flow in both directions of the rehabilitated deck on side A, deck with 97.5% repaired and 2.5% damaged. Temporary bypass on B side removed.

Stage 7: Conclusion of maintenance works, bridge 100% rehabilitated. Structural condition of the bridge rated from the second load test to authorize its normal operation.

It is important to mention that the two load tests provided information to approve the partial and total bridge operation, but especially, the first load served as an important reference to infer retrospectively the structural state of the bridge before and immediately after the accident and, from that, to develop the simulation FE model to calculate their corresponding Rating Factors. The structural Rating Factor calculated for each stage and for each load test, considered only the maximum service load at each moment, which were not the same due to the imposed traffic restrictions or limitations due to repair works. The rating factors for the initial condition and after the accident assumed that four lanes of the bridge were operating with the maximum service load (four double trailer trucks with 75.5 tons each on each lane), although the traffic was canceled after the accident. To rate the condition of the bridge in stages 1 to 4, the maximum load on both temporary bypasses assumed two trailers with 54 tons on each side; and for stages 5 and 6, the maximum load condition assumed two trailers with 54 tons each, one after the other on the only lane in service. At the end,

for the last load test with fully rehabilitated bridge, the loads were the same as those used before the accident.

During all the maintenance process, the structural parameters served as reference for permanent real time monitoring of the bridge. Among these parameters, the most important were the vibration frequencies and modes, the box girder centroid, and the statistical stress–strain responses due to live loads from traffic and absolute stress–strain responses due to changes of dead loads. In the latter case, dead load changes were due to the post-tensioning of additional cables, removal of damaged bridge deck and temporary bypass lanes, or placement of new cross girders and new bridge deck sections. At each stage, simulations of the calibrated FE model for the particular rehabilitation state, defined the alarm limits for all parameters, considering normal, extreme loading and design limit conditions.

4 Evaluation of Maintenance Stages and Load Tests

4.1 Monitoring System

Three fundamental aspects were considered for the design of the monitoring system:

Post-tensioning effect. To monitor the structural responses of the bridge during the post-tensioning of the additional cables in the box girders, at the end of phase one.

Real time. To evaluate the rehabilitation process continuously with real time monitoring 24/7.

Structural behavior. To measure static and dynamic structural responses of the bridge to calibrate the FE simulation model and to calculate the Rating Factor for each stage.

As mentioned previously, the El Carrizo Bridge is a complex structure with three different types of structural sections. Considering that damage was practically limited to the section of the double cantilever and that it can be assumed that the structural interaction of this with the others is known, it was decided to have instrumentation only in the double cantilever section (see Fig. 5). The continuous monitoring instrumentation was made of strain gages and tiltmeters fiber optic sensors (FOS), all of them temperature FO sensors to compensate for thermal changes. In addition, for the load tests and cable post-tensioning process, monitoring was complemented with temporary electric strain gages and LVDT sensors.

The FOS system included 16 strain gages located inside both box girders on the upper and lower sides (8 on each box girder), 4 tiltmeters and 4 independent temperature sensors, two of each on each side, as indicated in Fig. 6.

The electric sensor system involved 20 strain gages, placed inside both box girders on the left and right sides, and two LVDT sensors at the end of the cantilever section that connects to the cable-stayed structure (see Fig. 7).

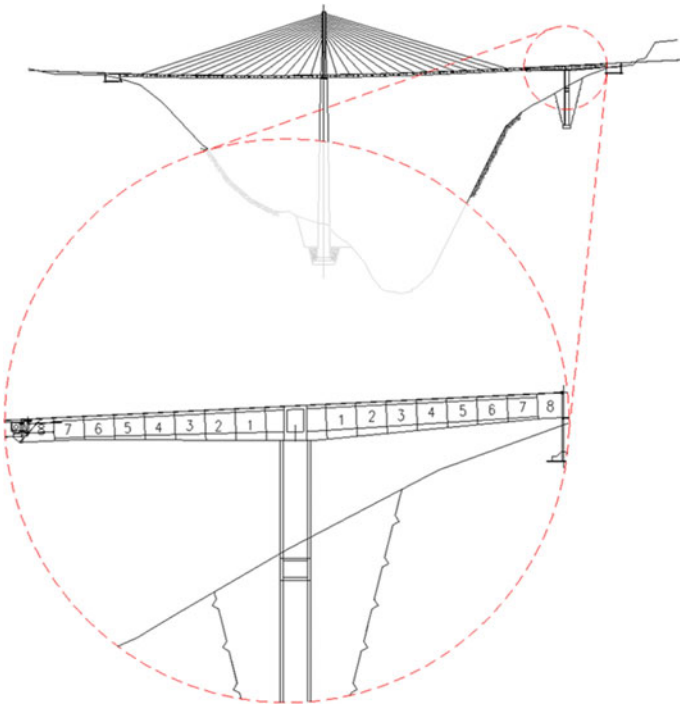


Fig. 5 Damaged and instrumented section of the bridge

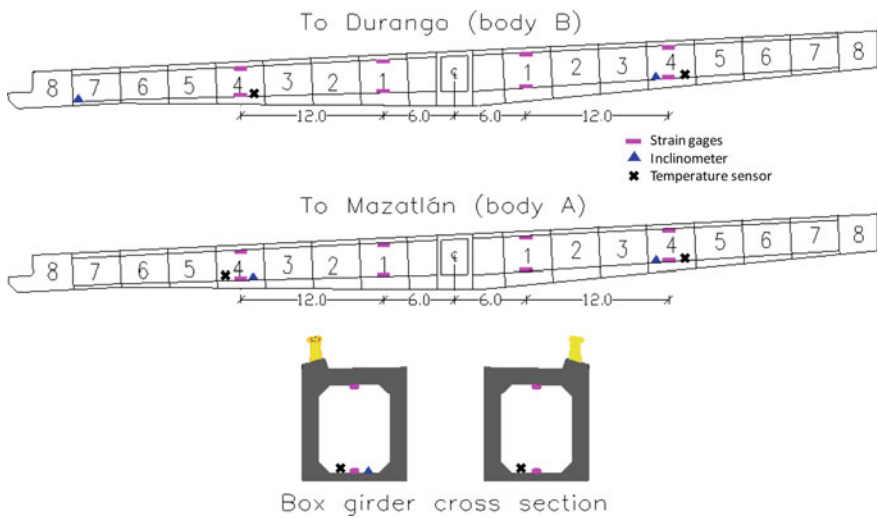


Fig. 6 Fiber optics instrumentation for permanent monitoring

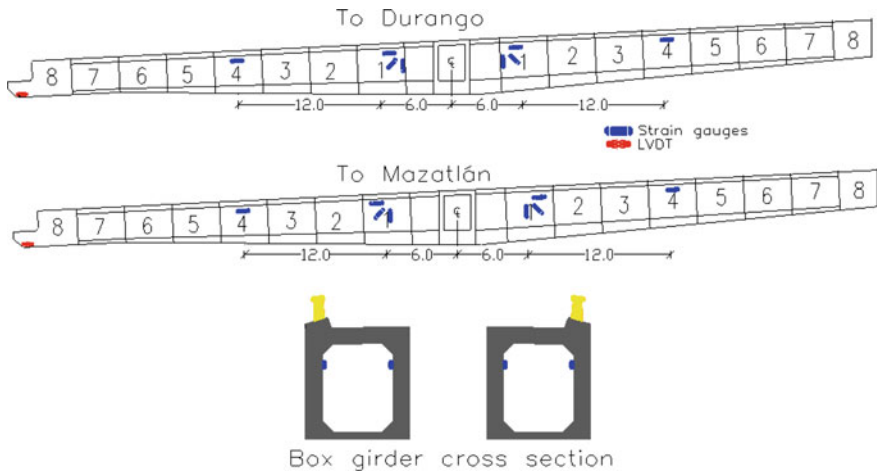


Fig. 7 Complementary electric strain gauges and LVDT sensors for temporary monitoring and load tests

4.2 Modal and Frequency Analysis

Dynamic responses from the eight horizontally oriented FO strain gauges (see Fig. 7.) were used for modal analysis. In this case, the two first frequency modes were monitored by selecting vibration data immediately after passing a heavy vehicle. For initial identification, researchers used dynamic responses from a controlled test with a three-axle truck with 21,860 kg gross weight and travelling at a speed of 50 km/h (see Fig. 8).

For modal identification, signals recorded at a 32 Hz sampling rate, were filtered, correlated and transformed in the range in-between 0.2 and 5 Hz (see Figs. 9 and 10).

Fig. 8 Dynamic response of a strain gage during dynamic controlled test with test vehicle

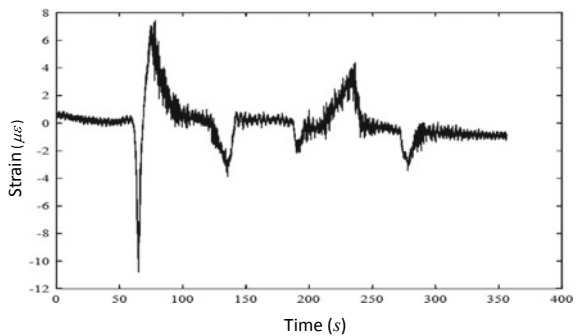


Fig. 9 Filtered strain response under controlled conditions

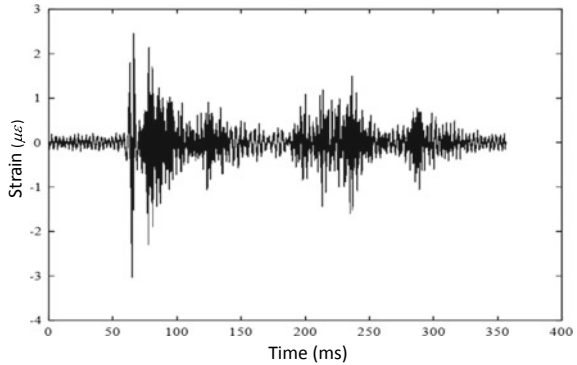
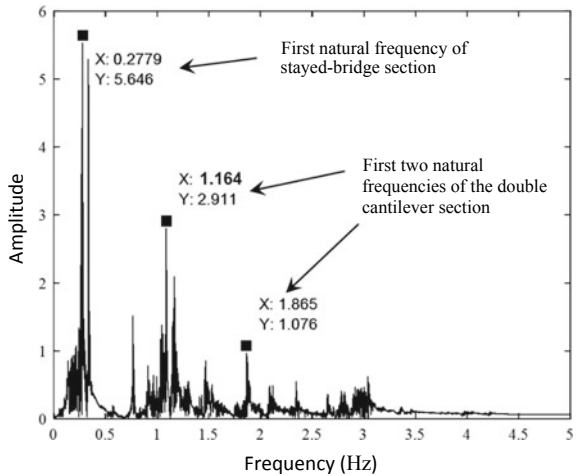


Fig. 10 FFT of strain response under controlled conditions



First load test data and modal data were used to calibrate the FEM, and from this, vibration modes identified. Figure 11a, b show the first two vibration modes of the double cantilever section.

During the monitoring period, the system operator evaluated the vibration frequency by selecting strain gages data obtained under conditions as close to those existing in the controlled test and without interference from the rehabilitation works. Analysis was following the same process for the initial frequency evaluation, except that in this case, analysis was focused to specific frequency ranges associated to the first and second modes of the double cantilever bridge section.



(a) First vibration mode.



(b) Second vibration mode.

Fig. 11 Double cantilever vibration modes

4.3 Finite Element Model Calibration

Experimental data from dynamic and static tests served as a reference to calibrate the FEM of the El Carrizo Bridge. Static strains and tilt angles from a given loading condition (weights and positions of the trucks on the bridge) set up a data group that was used directly, without additional processing, to calibrate the bridge model. On the other hand, as previously described, dynamic strain data was processed to identify the first two vibration frequencies and modes of the double cantilever section. Model calibration was done with engineering judgement and an iterative optimization process where structural parameters of the constitutive materials and geometric dimensions were changed within a priori defined ranges [7, 8]. Table 1 reports a comparison of the two first experimental vibration frequencies of the double cantilever section with

Table 1 Experimental and model frequencies

Mode	Frequency (Hz)		Error (%)
	Experimental	MEF	
1	1.191	1.168	1.93
2	2.455	2.448	- 0.32

Table 2 Updated structural parameters

Structural parameter	Calibrated value	Units
Equivalent elasticity module of post-tensioned segments	3.10×10^9	kg/m ²
Segment equivalent density	2.65×10^3	kg/m ³
Equivalent density of provisional lanes	3.00×10^3	kg/m ³
Deck equivalent density	2.65×10^3	kg/m ³
Steel elasticity module (damaged elements)	1.26×10^{10}	kg/m ²
Steel elasticity module (new elements)	2.10×10^{10}	kg/m ²
Deck asphalt layer thickness	1.40×10^{-1}	m

those from the calibrated model. Table 2 presents the parameter values associated with the best fit of the model.

Load tests used two different types of heavy vehicles: the single 3-axle truck (identified as C3) with 27,500 kg of gross weight and a single trailer (T3-S3) with 6-axle configuration and a gross vehicle weight of 50,000 kg. Static tests considered different positions on the bridge and dynamic test were under controlled conditions with the bridge closed to traffic and with the test vehicles traveling on the bridge at different speeds and, alternatively, on different lanes. These tests involved a total of four C3 trucks and two T3-S3 heavy vehicles.

The SAP 2000 FE software was the main platform for the structural analysis of the double cantilever section of the El Carrizo Bridge (see Fig. 12). The overall model has 1,088 frame elements, 3360 shell elements and 3958 nodes. The box girders, crossbeam girders and pylon FE models used frame elements, while the bridge deck was modelled with shell elements. The FE model of the temporary bypass lanes was built with frame elements fixed to the box girder with body constrains. Boundary conditions on one side were simply supported and on the cantilever side connected to the cable-stayed section was only restricted for lateral displacements and 100,000 kg of dead load counterweight on each box girder.

The comparison of static experimental data with numerical simulations under the same conditions, allowed corroborating and validating the calibration of the FEM [8]. In general, the overall accuracy of the model was within 5% error, with a maximum difference of 10%, with respect to the experimental data.

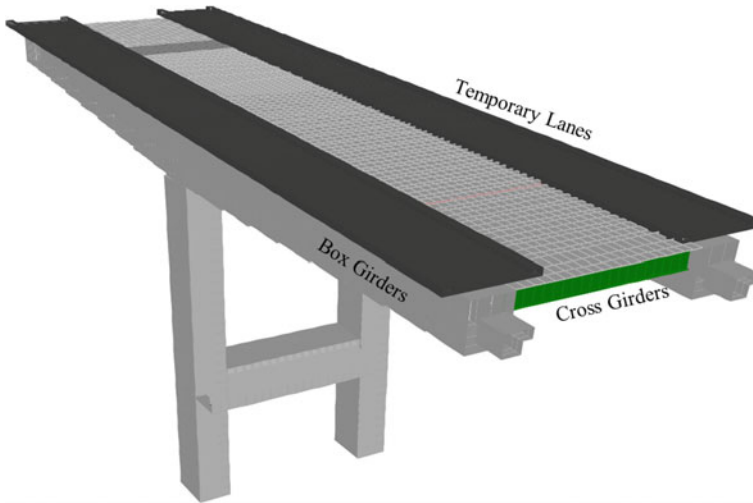


Fig. 12 General view of the FE model with provisional lanes on main girders

4.4 Bridge Rating Factor

The Rating Factor calculation for the bending moments and shear forces, according to The Manual for Bridge Evaluation of the American Association of State Highway and Transportation Officials (AASHTO) [5, 6], used the FE model already calibrated as previously described. For the analysis, the live loads due to traffic, considered the maximum service load for each one of the rehabilitation stages, including the initial and after accident conditions. Equation 1 defines the Rating Factor according to the AASHTO Manual for resistance state limits.

$$RF = \frac{C - (\gamma_{DC})(DC) - (\gamma_{DW})(DW) \pm (\gamma_P)(P)}{(\gamma_{LL})(LL + IM)} \quad (1)$$

where

- RF* Rating factor.
- C* Member capacity.
- R_n* Nominal member resistance (as inspected).
- DC* Dead load effect due to structural components and attachments.
- DW* Dead load effect due to wearing surface and utilities.
- P* Permanent loads other than dead loads (secondary prestressing effects, etc.)
- LL* Live load effect of the rating vehicle.
- IM* Dynamic load allowance.
- γ_{DC} LRFD load factor for structural components and attachments.
- γ_{DW} LRFD load factor for wearing surfaces and utilities.
- γ_P LRFD load factor for permanent loads other than dead loads.

- γ_{LL} LRFD live load factor for the chosen limit state and rating vehicles.
- φ_c Condition Factor.
- φ_s System Factor.
- φ LRFD Resistance Factor.

Table 3 shows the values of the parameters used to estimate the Rating Factors.

According to the monitoring system data and the progress status in each of the different maintenance stages already described, the calibration of the finite element model was updated for each of them. Table 4 shows the values and variation of the first two natural frequencies obtained from the calibrated model of finite elements, with respect to those experimentally measured with the monitoring system in each of the maintenance stages considered.

Figures 13 and 14 show the calculated rating factors for the bending moments and shear forces of the different maintenance stages, considering the maximum possible load for each stage condition and their corresponding operating conditions.

Table 3 Parameter values used to calculate the rating factor

Factor	Description	Value
Load factor	γ_{DC} —load factor for structural components and attachments	1.25
	γ_{LL} —live load factor for the chosen limit state and rating vehicles	1.75
	γ_{LL} —live load—operating condition	1.35
	γ_w —load factor for wearing surfaces and utilities	1.50
	IM —dynamic load allowance	20%
Resistance factor, φ	Reinforced concrete structure under flexural/tension loads (deck)	0.90
	Concrete prestressed structure under flexural/tension loads (girder)	1.00
	Reinforced concrete structure under shear loads	0.90
Condition factor, φ_c	Reinforced concrete structure (new deck)	0.85
	Prestressed concrete structure (new girder)	1.00
System factor, φ_s	Prestressed concrete girder	1.00

Table 4 Frequencies used to calibrate the model to estimate rating factors

Stage	First vibration mode frequency			Second vibration mode frequency		
	Monitoring data (Hz)	FEM data (Hz)	% variation	Monitoring data	FEM Data	% variation
E1	1.191	1.168	1.93	2.455	2.448	0.28
E2	1.139	1.130	0.79	1.850	1.850	0.00
E3	1.170	1.143	2.30	1.878	1.920	2.23
E4	1.171	1.200	2.47	2.397	2.100	12.39
E5	1.193	1.217	2.01	2.470	2.150	12.95
E6	1.194	1.256	5.19	2.478	2.220	10.41
E7	1.191	1.230	3.27	2.466	2.200	10.78

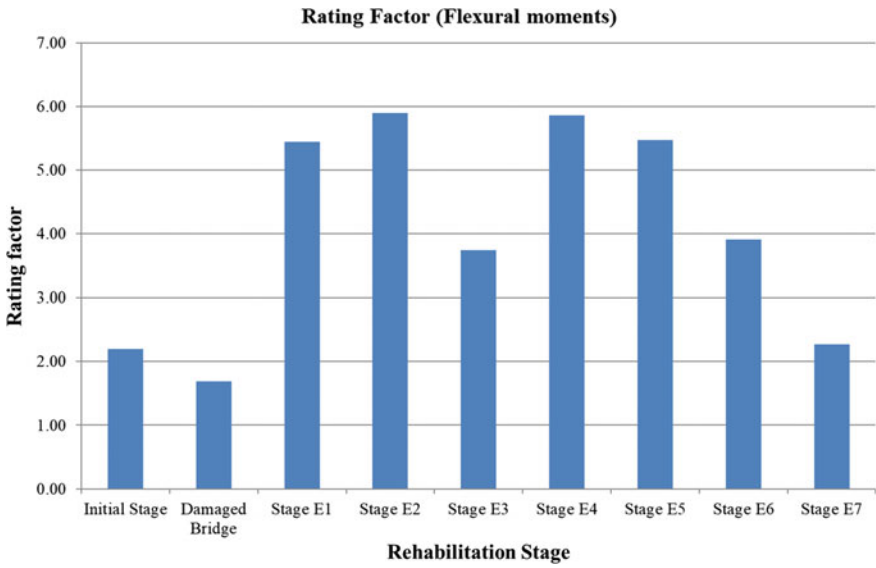


Fig. 13 Rating factor for flexural moments

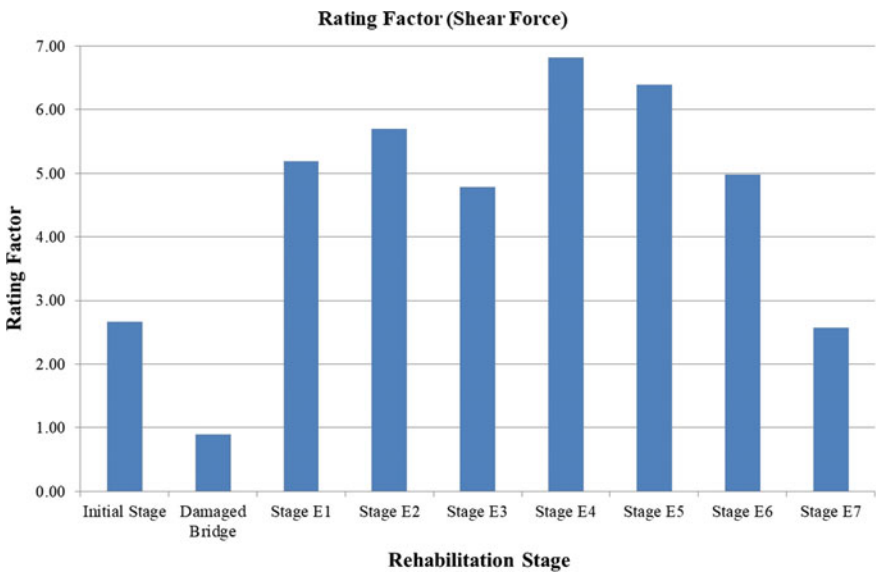


Fig. 14 Rating factors for shear forces

As described before and due to the lack of experimental data before (initial stage) and after the accident (damaged bridge), the structural condition in those cases was inferred with the best possible engineering judgment and information available. With this approach, it was found that the rating factors of the initial stage were 2.20 for the bending moments and 2.66 for shear forces.

In the same way, the evaluation of the damaged condition of the bridge resulted from a retrospective analysis, which included mechanical property changes due to damage to the structural elements. In this case, the rating factors for the box girder were 1.69 for bending moments and 0.89 for shear forces. Considering the level of damage on the bridge deck and crossbeam girders, the estimation of the rating factors made no sense and was not necessary. In this case, shear forces cause the most critical condition in box girders due to the loss of effective cross section area. After conclusion of this first stage, the rating factors increased significantly 3 times for bending moments and 5 times for shear forces, which was a clear indication of the effectiveness of the repairs made to the box girders.

As rehabilitation continued, the monitoring system recorded the responses of the sensors to structural changes and from those, the FE model was updated and rating factors calculated. For instance, the rating factors for stage 2 increased because of the demolition of the damaged bridge deck and therefore the dead load was reduced. Contrary to the latter, during stage 3 the rating factor decreased due to the construction of the new diaphragms in the box girders, the placement of the new cross girders, and the construction of the new bridge deck, with a net increase in the dead load.

For stage 4, the rating factor increased again because both box girders, with the cross girders and bridge deck, started to work structurally together with an effective increase on the bridge stiffness. In stage 5, a small decrease was present mainly because of the removal of the temporary bypass on side A, and, although the dead load decreased, the stress distribution changed on the cross section of the box girder. This change was due to the forces from the post-tension cables and, therefore, the compression stress distribution changed for the entire the cross section area of the box girder and the neutral axis also changed. Again, during stage 6 the rating factors decreased because of the removal of the temporary bypass lane on side B, with similar effect like the one that occurred in stage 5, but on the other box girder.

Finally, stage 7, which corresponds to the second load test, represents the rehabilitated structure and the end of the maintenance work. With respect to stage 6, the rating factors decrease in almost 50%, mainly because the bridge was at 100% of its structural condition and the service loads considered in the analysis were significantly higher and the same as those used for the initial condition before the accident. In this last analysis, the loads considered four lanes in service with four double trailers with 75.5 tons each, according to the Mexican standard (NOM-012-SCT-2-2017), which states the maximum loads and dimensions of heavy trucks on the Mexican highways. Comparing the the initial stage with final stage, results reveal that the rating factor for flexural moments changed from 2.20 to 2.28, slightly larger but practically the same. On the other hand, the rating factor for shear forces changed from 2.66 to 2.57. These results show that the repair project was sufficient to recover the structural condition of the bridge to which it had before the accident.

It is important to notice that, during stages 4–7, the second natural frequency of the calibrated FE model reported errors within 10–13%, which was due to the many uncertainties in stiffness of the bridge deck and steel crossbeams, which have a strong effect on the torsional mode. As a result, the calculated rating factors had also higher uncertainties with respect to those in the initial stages. Despite this, the general trend of the rating factors can be explained from the analysis and simulation of the monitoring data and final load results and it was concluded that the overall error was within 5%.

5 Conclusions

One of the benefits of monitoring systems is to confirm the integrity of the structures during rehabilitation works, especially in cases where this is still in operation. In addition, it guarantees the safety of the users.

The evaluation of the maintenance stages was carried out through the timely monitoring of the bridge through structural parameters and simulating the different scenarios with a FEM, calibrated to each condition. At the same time, this evaluation permitted the establishment of safe conditions for the structural parameters.

For this particular study, the structural rating factors, according to the AASTHO Manual for Bridge Evaluation, were the main criteria to evaluate each maintenance stage. The advantage of this criterion is the direct relationship between the experimental measurement data and the safety level of the structure, which in this case, was estimated for each stage of maintenance.

The use of the rating factors to evaluate the maintenance process of a bridge, allowed establishing criteria to maintain the safety of the bridge and avoid conditions that could put it at risk.

The most important conclusion of the study is that, once the bridge rehabilitation was completed, the bridge's safety and service levels recovered practically to the same levels as before the accident.

Acknowledgements The authors would like to thank Mr. Hector Hernandez of CAPUFE, Mr Ignacio E. Hernandez Quinto of the DGST-SCT and Mr. Luis Rojas and Mr. Adalberto Lara Castro of Freyssinet de México, S. A. de C. V., for their support and trust for this project. Appreciation and recognition to Jose Manuel Alvarez for their enthusiastic participation for the instrumentation. Thanks to Catedras Program of the National Science and Technology Council of Mexico (CONACYT), Project No. 34/2018.

References

1. Sánchez J (2018) Puente el Carrizo Carretera Durango-Mazatlán Km 162 +720. Vías Terrestres 9(53):12–16

2. Quintana J, Carrión F, Crespo S, Martínez A, Gasca H, Hernández J, Martínez M (2017) Impact of SHM system during bridge rehabilitation. In: CSHM-7 proceedings. Universidad EAFIT, Medellín, Colombia, pp 86–97
3. Crespo S, Carrión F, Quintana J (2013) Monitoring the aqueduct of Queretaro during the expansions Works to increase the traffic capacity. In: The 6th international conference on structural health monitoring of intelligent infrastructure. The Hong Kong Polytechnic Institute, Hong Kong, China
4. Quintana J, Carrión F, Crespo S (2013) Strategies for assessing the Rio Papaloapan Bridge structural integrity. In: The 6th international conference on structural health monitoring of intelligent infrastructure. The Hong Kong Polytechnic Institute, Hong Kong, China
5. AASHTO (2011) The manual for bridge evaluation, 2nd edn. American Association of State Highway and Transportation Officials, Washington, D.C.
6. AASHTO (2013) Interim revision to the manual for bridge evaluation. American Association of State Highway and Transportation Officials, Washington, D.C.
7. Friswell MI, Mottershead JE (1995) Finite element model updating in structural dynamics, vol 38. Springer Science
8. Zong Z, Lin X, Niu J (2015) Finite element model validation of bridge based on structural health monitoring—Part I: response surface-based finite element model updating. *J Traffic Transp Eng (English Edn)* 2–4:258–278

Vibration Monitoring of a Railway Bridge Using Distributed Macro-strain Data Obtained with Fiber Bragg Gratings



Edwin Reynders, Dimitrios Anastasopoulos, and Guido De Roeck

Abstract Recent advances in optical sensing and signal processing technologies have resulted in strain sensing systems that can accurately capture the very small dynamic strain levels occurring in civil structures during ambient excitation. In particular, it has been demonstrated in a laboratory environment that the combination of fiber Bragg grating (FBG) sensors with an acquisition system that interrogates those sensors with a swept monochromatic signal, can accurately capture RMS strain values with an order of magnitude of 0.01 microstrain. In the present work, the potential of this novel sensing technology for civil structural health monitoring is explored for a steel bow-string railway bridge that has been monitored for over one year. Both sides of the bridge deck have been instrumented with chains of multiplexed FBG sensors that are fixed to the bridge at discrete points. In this way, dynamic macro-strains are measured in a continuous way along the entire length of the bridge. During the monitoring period, the bridge underwent a retrofitting operation, in which all connections between the hangers and the bridge's deck and arch were altered. The influence of this retrofit on the monitored eigenfrequencies and strain mode shapes has been investigated and compared with their regular environmental variation. As the retrofitting resulted in global mass and stiffness changes of the structure, it is found to have an influence mainly on the eigenfrequencies, except when it induces an interaction between previously well-separated modes: in that case the strain mode shapes are also affected.

Keywords Optic strain sensing · Modal testing · Bridge engineering

The financial support of this research by the Research Foundation—Flanders, Belgium (project G099014N) and by Flanders Innovation and Entrepreneurship (Vlaio), Belgium (project Cook HBC.2019.2505) is gratefully acknowledged.

E. Reynders (✉) · D. Anastasopoulos · G. De Roeck
Department of Civil Engineering, University of Leuven (KU Leuven), Kasteelpark Arenberg 40,
3001 Leuven, Belgium
e-mail: edwin.reynders@kuleuven.be
URL: https://perswww.kuleuven.be/edwin_reynders

© The Author(s), under exclusive license to Springer Nature Switzerland AG 2021
C. Rainieri et al. (eds.), *Civil Structural Health Monitoring*, Lecture Notes in Civil Engineering 156, https://doi.org/10.1007/978-3-030-74258-4_20

289

1 Introduction

Vibration-Based structural health monitoring (SHM) relies the fact that the modal characteristics of a structure (eigenfrequencies, damping ratios and mode shapes) depend entirely on its stiffness, mass and energy dissipation. Structural damage results in a stiffness change, so it can therefore be detected, in principle, by monitoring modal characteristics [7, 10, 11].

Eigenfrequencies can be obtained from only one or a few sensors, e.g. accelerometers, placed at proper locations [20]. As a result, they are very often used for SHM [8, 11, 15]. Eigenfrequencies are mainly sensitive to global stiffness modifications. Local damage of small or moderate severity therefore has a small influence on eigenfrequencies [11, 25], while the global stiffness is often influenced by variations in environmental factors such as temperature [19]. That influence can be high enough to completely mask the presence of even severe damage, necessitating data normalization [7, 24]. Displacement mode shapes can also be used for SHM. They are attractive in the sense that they are more sensitive to local stiffness changes than eigenfrequencies, and less sensitive to temperature variations [29, 30]. The main disadvantage is that a dense sensor grid is required for good damage localization capabilities [8], which is generally costly when conventional sensors, such as accelerometers, are employed.

Strain mode shapes are an attractive alternative for the more conventional displacement mode shapes [6, 26], because modal strains are much more sensitive to local damage than modal displacements [17], and dense sensor grids can be achieved at relatively low cost thanks to the multiplexing capacity of some sensor types such as fiber Bragg gratings (FBG) [16]. The main challenge has been that the dynamic strains that occur in large civil structures in operational conditions are very small, typically in the sub-microstrain range. However, recent experiments involving FBG sensors have demonstrated that with improved sensor interrogation [6] or signal processing techniques [5], the required sensing accuracy can be attained. Laboratory experiments on concrete [3, 5, 27] and steel beams [9] or pipes [28] have illustrated that modal strains are highly sensitive to local damage of low or moderate severity, while they are insensitive to global temperature changes [3].

The present work takes the step of monitoring the detailed strain mode shapes of a full-scale civil structure in operational conditions. To this end, the deck of a steel bow-string railway bridge was instrumented with a dense grid of multiplexed FBG macro-strain sensors as a proof of concept. For a time period of more than a year, the eigenfrequencies and strain mode shapes were automatically identified every hour from the low-amplitude operational and free vibration strain data. The results demonstrate the feasibility and accuracy of the strain monitoring methodology of [5] in field conditions.

Next, the present work also investigates the temperature influence on the eigenfrequencies and modal strains on this full-sized civil structure with complex boundary conditions and temperature fluctuations. Small but clear influences are found for the eigenfrequencies, while the strain mode shapes are insensitive to temperature. The

investigation therefore confirms the finding of an earlier study involving uniform temperature changes on a free-free prestressed concrete beam tested in controlled laboratory conditions [3].

Finally, during the monitoring period, the investigated bridge underwent a retrofit: all connections of the hangers between the arches and the bridge deck were strengthened in order to resolve a design error that was detected during inspection. The influence of this retrofit on the eigenfrequencies and strain mode shapes is investigated and compared with the temperature influence. The present conference paper is an abbreviated version of a more detailed analysis to be found in Ref. [4].

2 The KW51 Bridge

The KW51 bridge (Fig. 1) is a 117 m long steel bowstring bridge that crosses the Leuven-Mechelen canal close to the city of Leuven, Belgium. The bridge carries two tracks that are part of railway Line 36 that runs from Brussels to Liège. The bridge deck consists of a steel orthotropic (i.e., rib-stiffened) steel plate that is supported by two longitudinal steel girders and thirty-three steel transverse beams. The bridge deck is suspended from the arch with thirty-two inclined braces. The ends of the main girders rest on neoprene bearings, which directly sit on two concrete abutments.

From 16 May 2019 until 15 September 2019, the bridge was retrofitted so that a design error, related to the bolted connections of the braces with the deck and the arch, could be resolved. All bolted connections between the braces and the arch, and the braces and the deck of the bridge were strengthened with welded steel plates, as displayed in Fig. 2. The influence of the strengthening on the modal characteristics will be investigated in this paper, as it resembles the case of a slightly damaged structure (before retrofitting), which has been restored to a healthy structural condition (after retrofitting). Monitoring data from during the retrofitting period itself will be excluded from the study as during this period, scaffolding was installed on the bridge and this modified the overall mass and stiffness very significantly.



Fig. 1 The KW51 bridge, (left) as seen from the north side, after retrofitting, and (right) view on the bridge deck from below

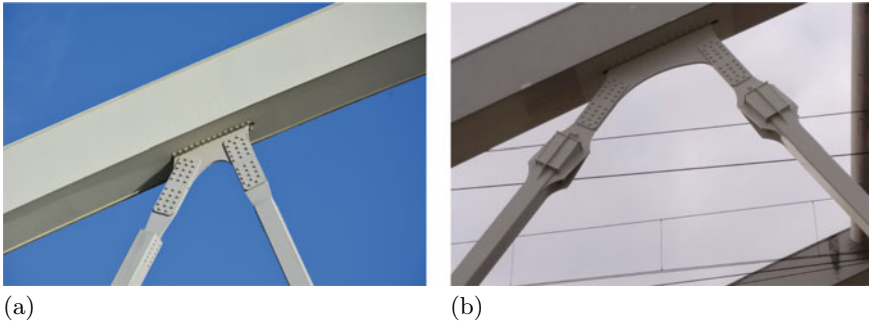


Fig. 2 Typical bolted connection between two braces and the arch of the KW51 bridge. **a** Before retrofitting and **b** after retrofitting

3 Strain Monitoring

Dynamic macrostrains of the bridge have been monitored with four chains of FBG sensors, inscribed in optical fibers with a glass fiber reinforced polymer coating. The fibers are located at the top surface of the bottom flange of the main girders of the bridge. Each fiber contains 20 FBG sensors, except from the northwest one that contains 19 FBG sensors (Fig. 3). The fibers are prestressed to ensure that they remain in tension when the corresponding bridge part is under compression. They are attached to the flanges using custom-made small clamping blocks [5]. There is one clamping block in between two FBG sensors, such that each FBG sensor measures the average strain, also termed macrostrain or long-gauge strain, in between to clamping blocks. The corresponding measurement distance is about 2.5 m except at locations NW9, NE9, SW9 and SE9 (see Fig. 3), where the gauge length was limited to 1 m for practical reasons. Since FBGs are sensitive to both strain and temperature, the fibers are covered with thermal insulation to ensure that fast temperature fluctuations would not affect the dynamic measurements.

The strain acquisition is conducted with an interrogator that offers the required high accuracy and precision for dynamic sub-microstrain measurements [5, 6], the FAZ Technologies FAZT-I4. The sampling frequency is $f_s = 1000$ Hz. The acquisition system and the laptop that is required to operate the acquisition system, and to store the data, are placed inside a cabinet that is located close to one end of the bridge and is attached on a transverse beam via magnets. The FBG fibers are connected to the acquisition system through a telecom fiber that spans the distance (≈ 60 m) between the cabinet and the midspan of the bridge, where all four fibers are connected to the telecom fiber in a wall mount box.

Throughout the monitoring period, the temperature of the bridge has also been measured with a thermocouple. It is attached on the same transverse beam as the cabinet that contains the acquisition system (Fig. 3).

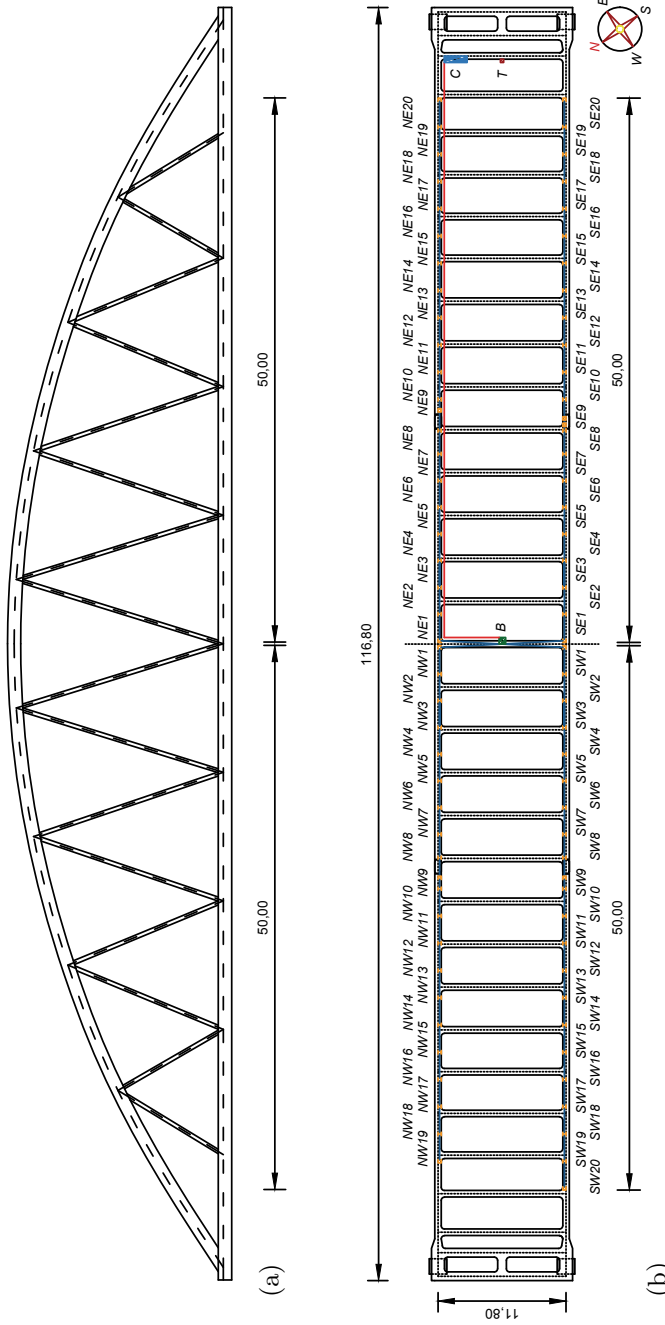


Fig. 3 **a** South view of the KW51. **b** Schematic representation of the attachment of the optical fibers. The small cubes represent the clamping blocks and the rectangles the FBGs in between the clamping blocks. All FBGs are labeled. B: connection box. C: acquisition cabinet. T: thermocouple. The telecom fiber is represented with a line connecting B and C (dimensions in m)

4 Strain-Based Operational Modal Analysis

Every hour, the fiber optic strain monitoring system that was presented in the previous section captures 900 s of dynamic strain data under ambient excitation from all FBGs installed on the bridge at a sampling rate of 1000 Hz. Each set of ambient strain data is used for Operational Modal Analyses (OMA), to identify the modal characteristics that represent the state of the bridge. In total, 8022 operational excitation tests were conducted during the first year of the monitoring that is being reported here.

4.1 Automatic Identification of Modal Characteristics

The data processing and the system identification is conducted with the Matlab toolbox MACEC [23]. First, the static offset is removed from all measured strain signals. Second, the data are low-pass filtered with an eighth-order Chebyshev Type I filter with a cut-off frequency 16 Hz and then re-sampled 40 Hz. A fourth-order Butterworth filter with a high-pass frequency of 0.35 Hz is subsequently applied to all channels, in order to remove the influence of the temperature fluctuations on the FBG measurements. The position-averaged root-mean-square (RMS) strain value is around 0.01 microstrain ($\mu\epsilon$). Then, the output-only, data-driven stochastic subspace identification (SSI-data) method [18] is employed for identifying a range of state-space models from the strain data. The half number of Hankel block rows is set to 40 and the model order ranges from 30 to 120 in steps of 2. When the time signals include one or more train passages, the data Hankel matrix [18] is modified to exclude them from the identification process, i.e. the columns of the Hankel matrix that contain data from times when a train is on the bridge, are removed. The train passages are automatically detected via peaks in the strain data with amplitude larger than $1 \mu\epsilon$, which are caused by train boggies. The computed modal characteristics are used for constructing stabilization diagrams [21]. The modes are automatically selected from each stabilization diagram by means of hierarchical agglomerative clustering, has proved to be a suitable automatization approach if the diagram is sufficiently clear [14].

Hierarchical clustering requires a measure for the *similarity* between every pair of objects. In the present work, the similarity is measured by a distance d between two modes that incorporates both the relative natural frequency difference and the correlation between the mode shapes:

$$d_{i-j} = \frac{|f_i - f_j|}{\sqrt{f_i f_j}} + (1 - \text{MAC}_{i,j}) \quad (1)$$

where f_i and f_j are the eigenfrequencies of the mode estimates i and j and $\text{MAC}_{i,j}$ is the modal assurance criterion [1] between the strain mode shape estimates i and j . If the distance between two mode estimates is short, then the two modes have similar

Table 1 Mode types and eigenfrequencies (f_j^{ssi}) of the modes of the KW51 bridge, as identified from strain-based OMA using SSI-data identification and data from a test that was conducted at 16:52 on 14/2/19

Mode	Type	$f_j^{ssi,s}$ (Hz)	$\mu[f_j^{ssi,s}]$ (Hz)
1	1st lateral mode of the arch	0.51	0.51
2	2nd lateral mode of the arch	1.24	1.24
3	1st lateral mode of the deck	1.89	1.90
4	3rd lateral mode of the arch	2.45	2.45
5	1st bending mode of the deck	2.54	2.55
6	2nd bending mode of the deck	2.92	2.92
7	Lateral mode of the arch	3.67	–
8	Lateral mode of the arch	3.72	–
9	1st torsion mode of the deck	4.10	4.10
10	3rd bending mode of the deck	4.27	4.31
11	Torsion mode of the deck [?]	4.36	–
12	4th bending mode of the deck	5.30	5.32
13	5th bending mode of the deck	6.25	6.32
14	Bending mode of the deck (?)	7.00	–
15	Bending mode of the deck (?)	7.65	–
16	Torsion mode of the deck (?)	7.90	–
17	Torsion mode of the deck (?)	8.97	–
18	Torsion mode of the deck (?)	11.13	–

The mean natural frequency ($\mu[f_j^{ssi}]$) of the systematically identified modes during February 2019 (Fig. 6b) is also provided. The modes whose type cannot be confirmed by [13] are denoted with [?]

eigenfrequencies and strain mode shapes and consequently, they should belong to the same cluster. Once the distance between any two modes in the stabilization diagram has been determined, the hierarchical tree can be constructed in an agglomerative way. The single-linkage method is employed for this, as it can detect a wide range of clustering patterns [12] and it has shown its efficacy in earlier studies [14].

After formation of the hierarchical tree, it needs to be cut at a certain level, such that all mode estimates that are attached to a branch are grouped into the same cluster, representing a single physical mode. The cut-off level of the tree was determined by setting the maximum allowable distance between the different clusters to $d_{i-j} \leq 0.03$.

The automatic identification of modal characteristics is now illustrated with the ambient strain data that were obtained on 14/2/19 at 16:52. Twenty one modes are automatically identified from this modal test in the frequency range (0–15) Hz. The character of the first eighteen modes is described in Table 1, and some identified strain mode shapes are displayed in Fig. 4. In order to facilitate the physical interpretation of the identified modes, the results of an acceleration-based OMA that was performed by colleagues of the Structural Mechanics Section of KU Leuven [13] are displayed in Fig. 5. There are minor differences between the eigenfrequencies of

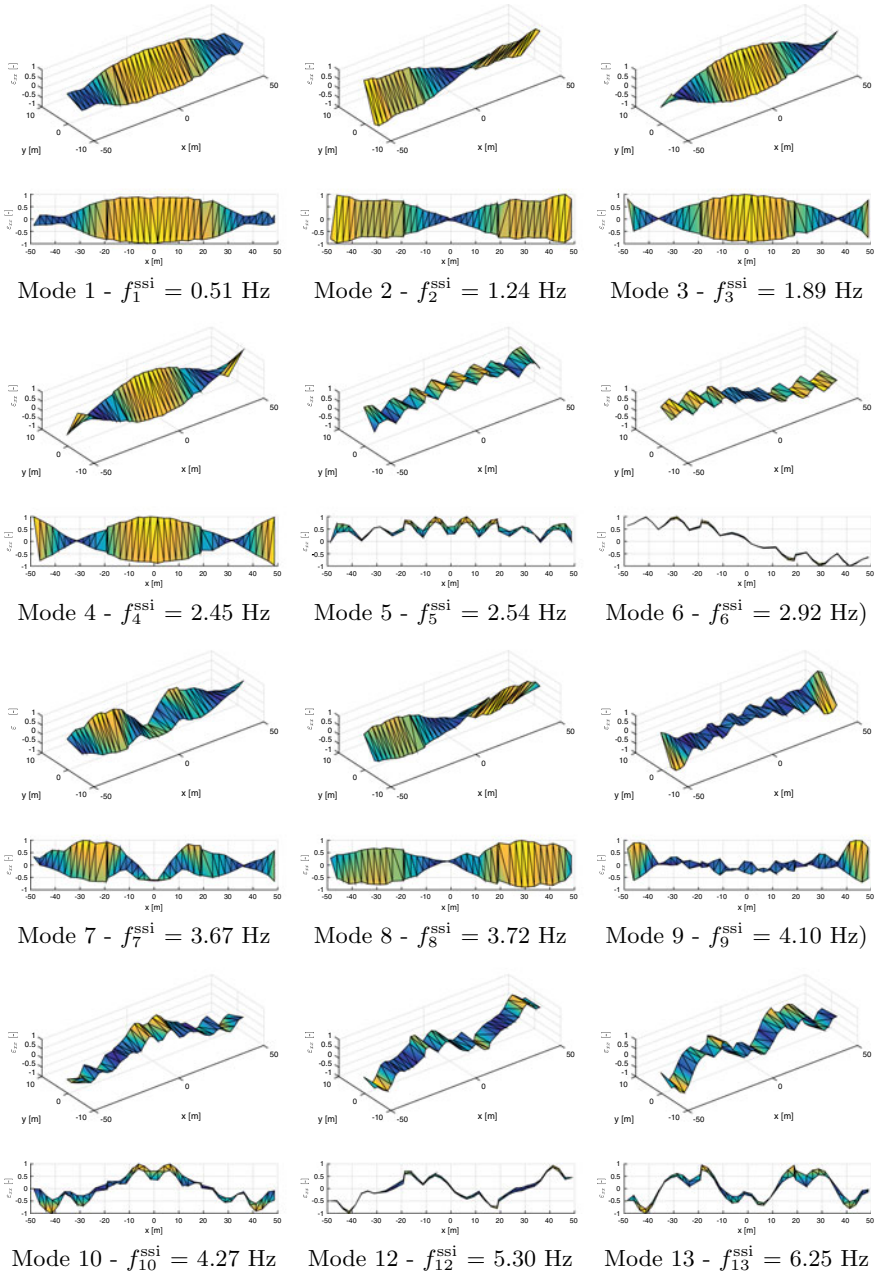


Fig. 4 Strain mode shape and natural frequency of some modes of the KW51 bridge, as identified from strain-based OMA using SSI-data identification and data from a test that was conducted at 16:52 on 14/2/19

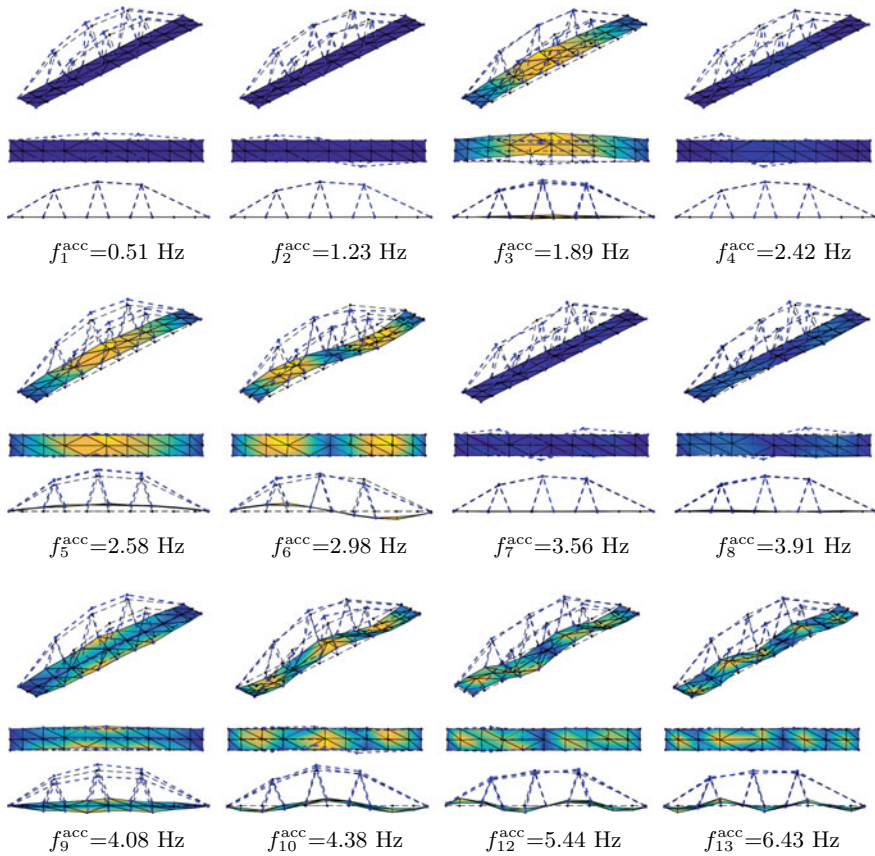


Fig. 5 Displacement mode shape and natural frequency of modes 1–10 and 12–13 of the KW51 bridge, as identified from an acceleration-based OMA [13]

Figs. 4 and 5 because they result from different identifications, using data obtained with different sensors and on a different date and time. The first thirteen modes that were identified from the acceleration-based OMA correspond to the ones identified from the strain-based OMA, with the exception of mode 11, which is not identified by the acceleration-based OMA. The modes of the bridge can be classified as deck or arch modes, depending on which part of the bridge is predominantly deformed.

The same automated procedure is followed for all dynamic strain tests. The eigenfrequencies of all the modes that have been identified during the period 14/2/2019 to 28/2/2019 are displayed in Fig. 6a. The gap that is observed around February 26 is due to a temporary power cut that kept the monitoring system off for a few hours. Some of the modes that are contained in Fig. 6a are only identified from a few data records, possibly because they are rarely excited. In order to remove these modes and to track the well-excited modes over time, the same hierarchical clustering procedure

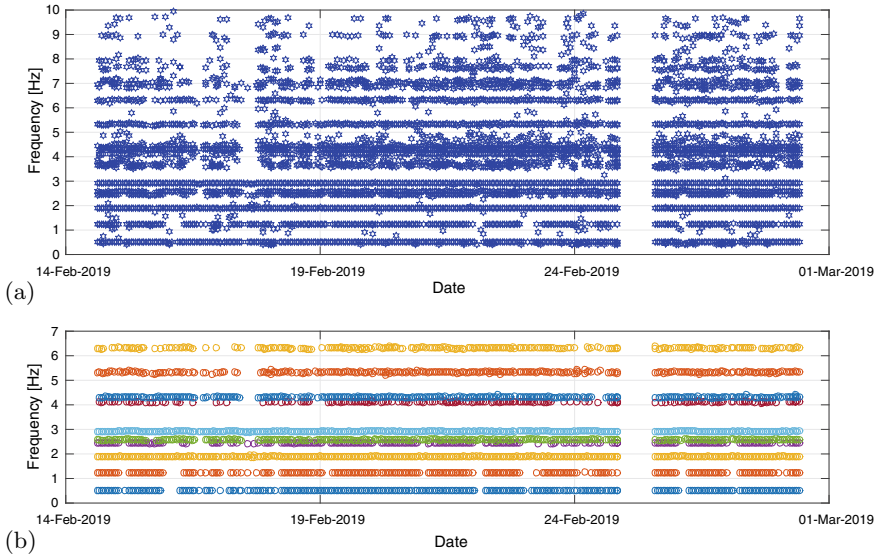


Fig. 6 Eigenfrequencies of the modes of KW51 bridge as they are automatically identified during February 2019, **a** before and **b** after removing the modes that are not systematically identified from strain-based OMA

that was used to automate the mode selection process from a stabilization diagram is applied again, but this time on the time history of automatically identified physical modes of all modal tests that were conducted within a month. In Fig. 6b, the final time history of physical modes is displayed for the period 14/2/2019 to 28/2/2019. Ten modes are consistently identified during the considered period. Their mean natural frequency is also listed in Table 1.

4.2 Influence of temperature on modal characteristics before retrofitting

The influence of temperature on the modal characteristics of the bridge is investigated for the period before retrofitting, from 14/2/2019 to 15/5/2019, with a temperature range of 24°C.

The eigenfrequencies of the first six modes are plotted as a function of temperature in Fig. 7; the vertical axis limits span $\pm 3\%$ of the mean natural frequency value so as to have a common relative scaling for all modes. The linear regression and the coefficient of determination (R^2) between temperature T and natural frequency f is also computed for each mode separately and displayed in Fig. 7. The linear regression is given by:

$$f(T) = \alpha T + f_0 \tag{2}$$

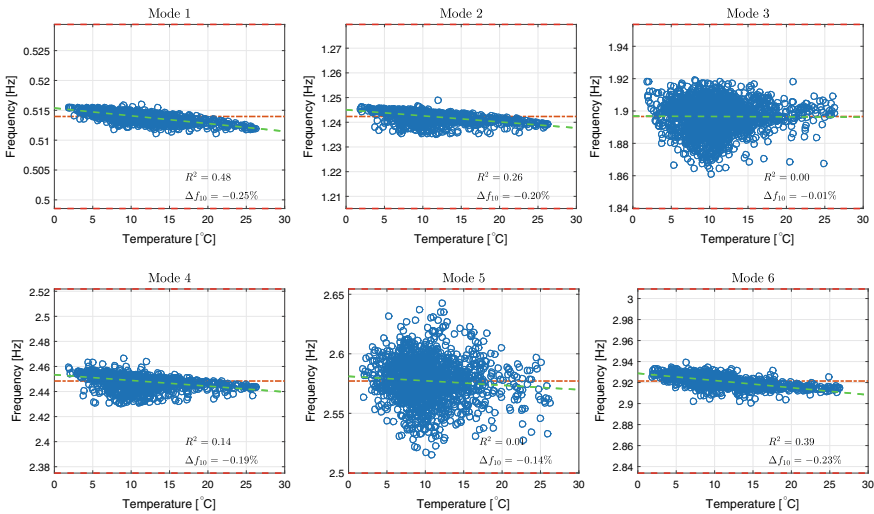


Fig. 7 Eigenfrequencies of modes 1–6 of the KW51 bridge as a function of temperature, as identified from SSI-data (f_j^{SSI}) and during the period before the retrofiting. The dash-dotted line denotes the mean natural frequency $\mu[f_j^{SSI}]$, while the dashed line denotes the linear regression of the data $f(T)$. The y-axis limits of the plots, which correspond to $\pm 3\%$ of $\mu[f_j^{SSI}]$, are also denoted with dashed lines

where α is the slope of the linear regression and f_0 the natural frequency that corresponds to temperature $T = 0^\circ\text{C}$. Based on Eq. (2), the relative change of the natural frequency of each mode $\Delta f[\%]$, for a temperature change of $\Delta T = +10^\circ\text{C}$ is given by:

$$\Delta f_{10}[\%] = \frac{f(10) - f_0}{f_0} = \frac{\alpha 10}{f_0} 100\% \tag{3}$$

It can be observed in Fig. 7 that the measured temperature correlates better with the modes of the arch (modes 1, 2 and 4) and the second bending mode of the deck (mode 6) than with the other deck modes (modes 3 and 5). An increase of $\Delta T = 10^\circ\text{C}$ in temperature results in a relative decrease of about $\Delta f_{10} = 0.2 - 0.25\%$ for the eigenfrequencies of the arch modes and deck mode 6. The low correlation between the measured temperature value and the natural frequency of deck modes 3 and 5, together with the relatively large scatter of the natural frequency values, indicate that these eigenfrequencies can be influenced by other factors, such as solar radiation), wind intensity, thermal inertia of the structure and identification errors. Similar conclusions are drawn for the other identified arch and deck modes [2] and therefore additional plots are not reproduced here.

The strain mode shapes that have been determined from the ambient vibration tests that are conducted every hour, have been normalized such that the strain mode

shape vector has unit norm and that its largest component is purely real. This normalization scheme, that was proposed in [22], facilitates the comparison between strain mode shapes that have been determined from different ambient vibration tests [3]. After normalization, the strain mode shapes are clustered into groups based on the temperature that was recorded during the corresponding ambient vibration test. Each temperature group has a range of 2 °C and the groups are not overlapping. For each temperature group k , the sample mean $\mu[\psi_j^{\text{ssi},(k)}]$ of all strain mode shapes in the group is then computed, as well as the sample standard deviation $\sigma[\psi_j^{\text{ssi},(k)}]$ and the related $\pm 2\sigma$ confidence interval $\text{CI}[\psi_j^{\text{ssi},(k)}]$, which boils down to a 95% confidence interval when the samples are normally distributed, as is usually the case in operational modal analysis [22].

As an example, Fig. 8b displays the mean strain mode shape of the second bending mode of the deck (mode 6) with the 95% confidence interval for all temperature groups. The confidence intervals for the different temperature groups overlap completely, and they all have nearly the same width. The same observation holds for all other identified strain mode shapes [2], and therefore these results are not reproduced here. It can be concluded that, in the present experiment, there is no statistically significant influence of the temperature on the strain mode shapes, for the given temperature range of 24 °C.

Since temperature does not influence the strain mode shapes, the statistical uncertainty must relate to other causes of variability in the strain mode shapes at a given temperature group, such as identification errors. The corresponding variance error can be reduced by averaging the identified strain mode shapes that belong to the same temperature group. Indeed, the standard deviation of the *sample mean* of the entire set of N_k independent samples (i.e. identified strain mode shapes) obtained at a given temperature group k is related to the standard deviation of the set as:

$$\sigma[\mu[\psi_j^{\text{ssi},(k)}]] = \frac{\sigma[\psi_j^{\text{ssi},(k)}]}{\sqrt{N_k}} \quad (4)$$

and the related 95% confidence interval reads:

$$\text{CI}[\mu[\psi_j^{\text{ssi},(k)}]] = [-2\sigma[\mu[\psi_j^{\text{ssi},(k)}]], 2\sigma[\mu[\psi_j^{\text{ssi},(k)}]]] \quad (5)$$

$$= \left[-\frac{2}{\sqrt{N_k}}\sigma[\psi_j^{\text{ssi},(k)}], \frac{2}{\sqrt{N_k}}\sigma[\psi_j^{\text{ssi},(k)}] \right] \quad (6)$$

Figure 8c displays, for mode 6, the sample mean of the complete set of all the repeatedly identified strain mode shapes $\mu[\psi_j^{\text{ssi},(k)}]$ that are obtained at a given temperature group k , together with the 95% confidence interval of the *sample mean* of each set. Note that the sample mean values of Figs. 8b and 8c are identical, but that the width of the confidence intervals in Fig. 8c is a factor $1/\sqrt{N_k}$ narrower than in Fig. 8b, because in Fig. 8c the uncertainty of the averaged, sample mean values is considered. The narrow confidence intervals of the *sample mean* of the different temperature groups

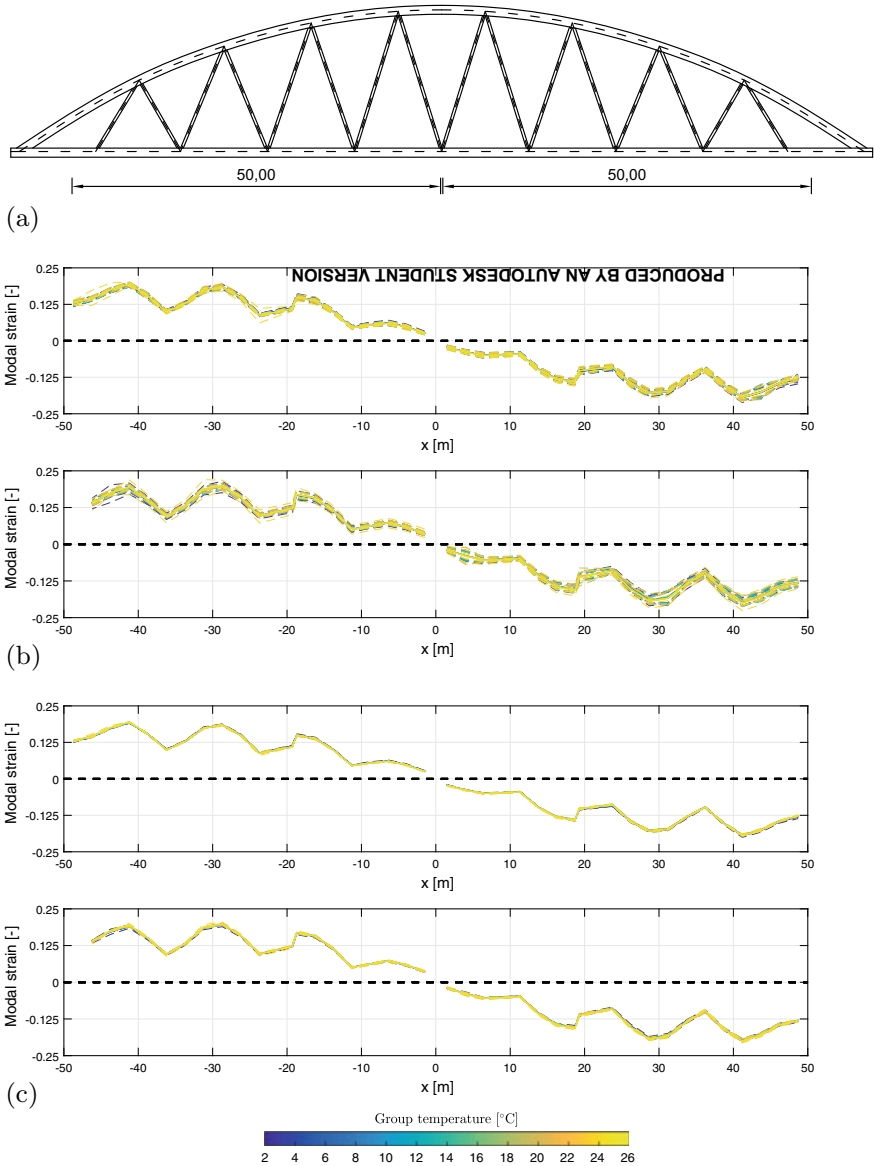


Fig. 8 a South view of the KW51. b Sample mean $\mu[\psi_j^{ssi,(k)}]$ and 95% CI $[\psi_j^{ssi,(k)}]$ of the strain mode shapes that have been identified in each temperature group k for mode 6, for the period before the retrofiting. c Sample mean $\mu[\psi_j^{ssi,(k)}]$ and 95% CI $[\mu[\psi_j^{ssi,(k)}]]$ of the sample mean, of the strain mode shapes that have been identified in each temperature group k for mode 6, for the period before the retrofiting. The top and bottom subplots contain the strain mode shapes at the north and south sides of the bridge, respectively

overlap completely, and they all have nearly the same width, which strengthens the conclusion that there is no statistically significant influence of the temperature on the strain mode shapes, for the temperature range of 24°C. The same observation holds for all other identified strain mode shapes, so the corresponding plots are not reproduced here.

4.3 Influence of Temperature on Modal Characteristics After Retrofitting

The influence of temperature on the modal characteristics of the bridge is now investigated for the period after retrofitting, i.e. from 15/9/2019 to 24/02/2020, with a temperature range of 26°C.

The eigenfrequencies of the first six modes are plotted as a function of temperature in Fig. 9; the vertical axis limits span $\pm 3\%$ of the mean natural frequency value so as to have a common relative scaling for all modes, similar to Fig. 7 before the retrofitting. The linear regression between temperature and natural frequency is also computed. The measured temperature correlates better with the the modes of the arch (modes 1, 2 and 4) and the second bending mode of the deck (mode 6) than with the other deck modes (modes 3 and 5). An increase of $\Delta T = 10^\circ\text{C}$ in temperature results in a relative decrease of about $\Delta f_{10} = 0.2 - 0.23\%$ for the eigenfrequencies of the arch modes and deck mode 6. A similar observation was made before retrofitting.

The strain mode shapes have been normalized and clustered into temperature groups in the same way as before retrofitting. As an example, Fig. 10b displays the mean strain mode shape of the second bending mode of the deck (mode 6) with the 95% confidence interval for all temperature groups after retrofitting. It should be noted that the NE fiber went out of service in August 2019 and for practical reasons it could only be repaired at the beginning of November 2019. Therefore, Fig. 10 does not contain results for this fiber for the period from 1/9/2019 to 31/10/2019.

The confidence intervals for the different temperature groups overlap completely, and they all have nearly the same width. The same observation holds for all other identified strain mode shapes [2], and therefore these results are not reproduced here. It can be concluded that, in the present experiment, there is no statistically significant influence of the temperature on the strain mode shapes, for the given temperature range of 26°C.

The variance error on the identified strain mode shapes can be further reduced by averaging, similarly to the period before the retrofitting. The standard deviation and the related 95% confidence interval of the sample mean of the entire set of N_k identified strain mode shapes obtained at a given temperature group k is calculated by Eqs. (4) and (6). Figure 10c displays, for mode 6, the sample mean of the complete set of all the repeatedly identified strain mode shapes $\mu[\psi_j^{\text{ssi},(k)}]$ that are obtained at a given temperature group k , together with the 95% confidence interval of the sample mean of each set. The narrow confidence intervals of the sample mean of the

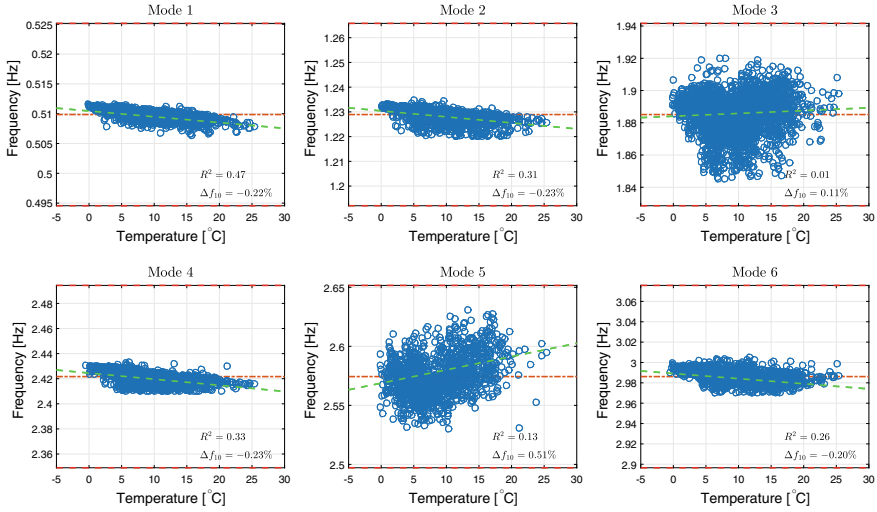


Fig. 9 Evolution of the eigenfrequencies of modes 1–6 of the KW51 bridge as a function of temperature, as identified from SSI-data (f_j^{SSI}) and during the period after the retrofiting. The dash-dotted line denotes the mean natural frequency $\mu[f_j^{SSI}]$, while the dashed line denotes the linear regression of the data $f(T)$. The y-axis limits of the plots, which correspond to $\pm 3\%$ of $\mu[f_j^{SSI}]$, are also denoted with dashed lines

different temperature groups overlap completely, and they all have nearly the same width. The same observation holds for all other identified strain mode shapes, so the corresponding plots are not reproduced here. These observations strengthen the conclusion that there is no statistically significant influence of the temperature on the strain mode shapes, for the investigated temperature range of 26 °C.

4.4 Influence of Retrofitting on Modal Characteristics

During the retrofitting, all of the bolted connections between the diagonal braces and the deck and arch were strengthened (see Sect. 2 and Fig. 2). The weaker situation before retrofitting thus resembles a damage case, and the strengthened situation can then represent the healthy condition. In the present section, the influence of this quasi-distributed damage on the monitored eigenfrequencies and strain mode shapes is investigated.

The eigenfrequencies of the first six systematically identified modes are plotted as a function of temperature in Fig. 11 for the time periods before and after the retrofitting. The vertical axis limits span $\pm 5\%$ of the average natural frequency value before retrofitting so as to have a common relative scaling for all modes. The relative change of the mean value of natural frequency of each mode before and after the retrofitting, $\Delta\mu[f]$, is also provided. There is a small but clear influence of the

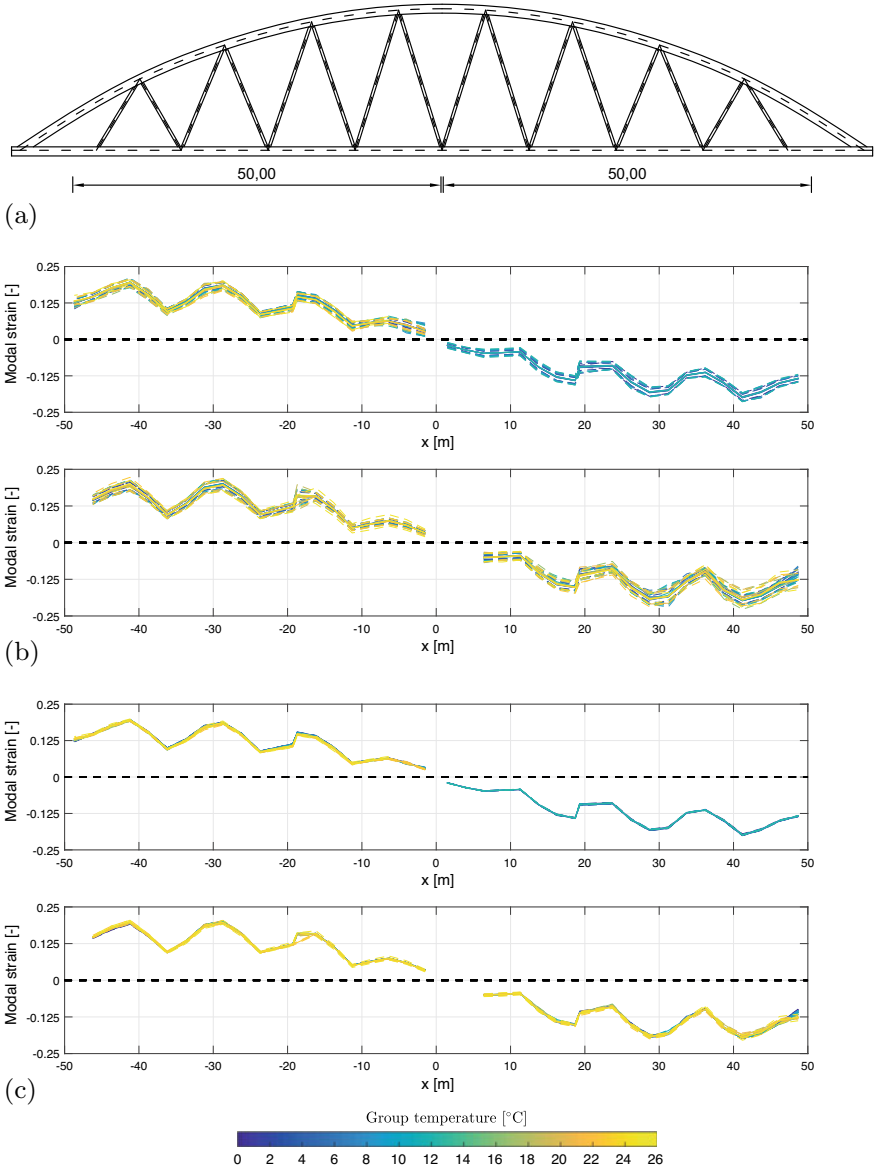


Fig. 10 a South view of the KW51. b Sample mean $\mu[\psi_j^{ssi,(k)}]$ and 95% CI of the strain mode shapes that have been identified in each temperature group k for mode 6, for the period after the retrofitting. c Sample mean $\mu[\psi_j^{ssi,(k)}]$ and 95% CI of the sample mean, of the strain mode shapes that have been identified in each temperature group k for mode 6, for the period after the retrofitting. The top and bottom subplots contain the strain mode shapes at the north and south sides of the bridge, respectively

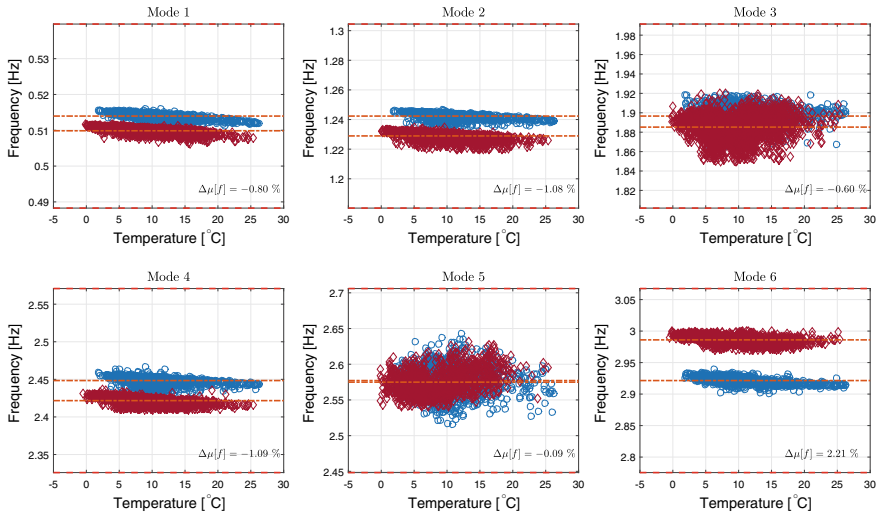


Fig. 11 Evolution of the eigenfrequencies of modes 1–6 of the KW51 bridge as a function of temperature, as identified from SSI-data (f_j^{SSI}) and during the periods before (circles) and after (diamonds) the retrofitting. The dash-dotted lines denote the mean natural frequency $\mu[f_j^{SSI}]$ of each period, while the dashed lines the $\pm 5\%$ of $\mu[f_j^{SSI}]$ (before retrofitting) y-axis limits of the plot

retrofitting on the eigenfrequencies of most modes. The changes that are induced by the retrofitting are different for the different types of mode.

For the modes of the arch, i.e., modes 1, 2 and 4, a reduction of the eigenfrequencies of about 1% is observed. For these modes, the mass increase due to the welded steel plates that strengthen the connections of the braces (Fig. 2b) is important while the additional stiffness is relatively unimportant. For the bending modes of the deck, i.e., such as mode 6, the opposite influence is observed: the retrofitting results in an increase of their eigenfrequencies of about 1.8–2.6%. For these modes, the increased stiffness that is offered by the steel plates that are welded at the brace connections as a larger effect than the added mass. For modes 3, 5 and 9, the influence is less clear due to the larger scatter of the natural frequency values. It can be concluded that the influence of the retrofitting is larger than the influence of temperature, for the given temperature ranges of about 24 and 26°C that were achieved before and after the retrofitting respectively, and for the modes that correlated well with temperature [2].

In order to investigate the influence of retrofitting on the strain mode shapes, combined graphs are constructed, where the strain mode shapes before and after the retrofitting are plotted on top of each other. Previously, it was concluded that temperature does not affect the strain mode shapes before nor after retrofitting. Therefore, all the identified strain mode shapes of a mode (i.e. for all temperatures) are clustered in two groups, one containing the strain mode shapes before retrofitting and one after. The sample mean $\mu[\psi_j^{SSI}]$ of the complete set of strain mode shapes of each group is

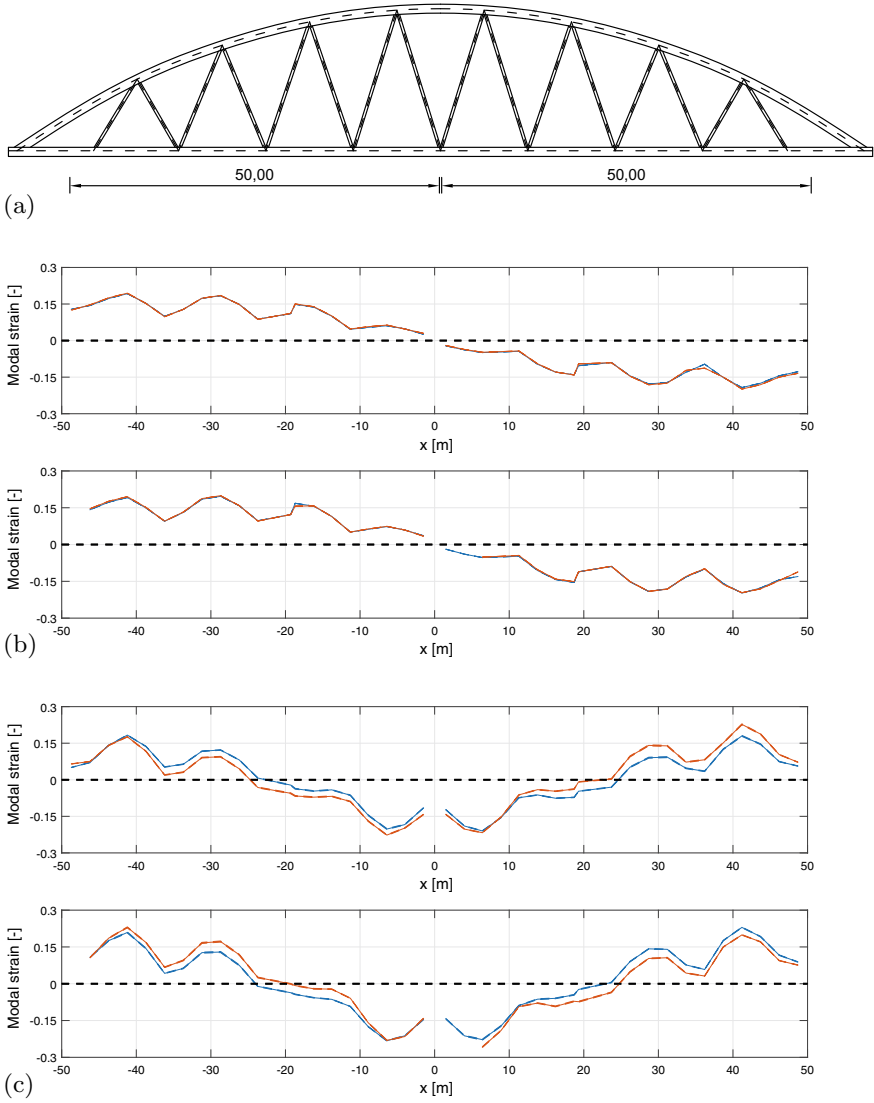


Fig. 12 a South view of the KW51. b and c Sample mean $\mu[\psi_j^{ssi}]$ (solid lines) and 95% CI $[\mu[\psi_j^{ssi}]]$ of the sample mean (dashed lines), of the strain mode shapes that have been identified during the periods before (blue) and after (orange) the retrofitting for b mode 6 and c mode 10. The top and bottom subplots contain the strain mode shapes at the north and south sides of the bridge, respectively

plotted, together with the 95% confidence interval of *the sample mean* of that group $CI[\mu[\psi_j^{ssi}]]$ in Fig. 12, for modes 6 and 10.

It can be clearly observed, due to the very narrow confidence intervals of *the sample mean of* the two groups that the retrofitting has an insignificant influence on the strain mode shapes of mode 6, while for mode 10, where an influence can be observed. For all other modes, the retrofitting has an insignificant influence on the strain mode shape, just as for mode 6, and therefore they are not reproduced here. This is due to the fact that the retrofitting results in a quasi-uniform modification of mass and stiffness along the bridge, and the strain mode shapes are sensitive to local changes, as experimentally demonstrated in e.g. [3, 5]. Global changes do not affect the strain mode shapes, unless they are scaled in an absolute way, e.g. through mass normalization.

The fact that the retrofitting does have an influence on the strain mode shape of mode 10, can be explained as follows. Before retrofitting, modes 10 and 11 have well separated eigenfrequencies and they can be characterized as a bending and torsion mode of the deck, respectively (see Table 1). Due to the stiffening effect of the retrofitting, the natural frequency of mode 10 has increased such that it almost coincides with that of mode 11. As a result, both modes interact after retrofitting such that mode 10 is not a purely bending mode anymore but it has gained also a torsion component.

5 Conclusions

The KW51 railway bridge was monitored with four chains of multiplexed FBGs for a period of one year, during which it underwent retrofitting. Every hour, the dynamic strain data under ambient excitation as well as the free response after train passages were used in an operational modal analysis. The modal characteristics of the bridge were automatically identified with a hierarchical agglomerative clustering algorithm. Despite the very low dynamic strain levels, the eigenfrequencies and detailed strain mode shapes of ten modes could be accurately and continuously identified throughout the entire monitoring period. This provides an experimental proof of concept for ambient dynamic strain monitoring of large civil structures with a dense sensor grid.

Furthermore, the influence of temperature on the monitored eigenfrequencies and strain mode shapes was investigated. The eigenfrequencies of the arch modes and some of the deck modes were seen to correlate well with the measured temperature, which implies that the temperature is a dominant factor in the regular environmental variation of those modes. The strain mode shapes of all identified modes were found to be insensitive to temperature variations, so they can be directly used for damage identification, without requiring data normalization.

The retrofitting increased both the overall mass and stiffness of the bridge. As eigenfrequencies are sensitive to overall mass and stiffness changes, a clear influence of the retrofitting on the monitored eigenfrequencies was observed. The eigenfrequencies of the arch modes decreased, as the mass effect is more important for

those modes, while the eigenfrequencies of the deck modes increased, as the stiffness effect is more important for those modes. Since the retrofitting did not result in local changes in the bridge deck, the monitored strain mode shapes were not influenced, except when the retrofitting induces an interaction between previously well-separated modes. Dynamic monitoring in a dense grid of fiber optic strain sensors enables to accurately capture both eigenfrequencies and strain mode shapes, which complement each other very well in a structural health monitoring context as they are sensitive to global and local stiffness changes, respectively.

References

1. Allemang RJ (2003) The modal assurance criterion—twenty years of use and abuse. *Sound Vibrat Magaz*, 14–21
2. Anastasopoulos D (2020) Structural health monitoring based on operational modal analysis from long-gauge dynamic strain measurements. Ph.D. thesis, Department of Civil Engineering, KU Leuven
3. Anastasopoulos D, De Roeck G, Reynders EPB (2019) Influence of damage versus temperature on modal strains and neutral axis positions of beam-like structures. *Mech Syst Sig Proc* 134
4. Anastasopoulos D, De Roeck G, Reynders EPB (2021) One-year operational modal analysis of a steel bridge from high-resolution macrostrain monitoring: influence of temperature vs. retrofitting. *Mech Syst Sig Process* 161:107951
5. Anastasopoulos D, De Smedt M, Vandewalle L, De Roeck G, Reynders E (2018) Damage identification using modal strains identified from operational fiber-optic Bragg grating data. *Struct Health Monit* 17(6):1441–1459
6. Anastasopoulos D, Moretti P, Geernaert T, De Pauw B, Nawrot U, De Roeck G, Berghmans F, Reynders E (2017) Identification of modal strains using sub-microstrain FBG data and a novel wavelength-shift detection algorithm. *Mech Syst Sig Proc* 86A:58–74
7. Brownjohn J, De Stefano A, Xu YL, Wenzel H, Aktan A (2011) Vibration-based monitoring of civil infrastructure: challenges and successes. *J Civil Struct Health Monit* 1(3–4):79–95
8. Carden EP, Fanning PJ (2004) Vibration based condition monitoring: a review. *Struct Health Monit* 3(4):355–377
9. Cheng L, Busca G, Cigada A (2017) Experimental strain modal analysis for beam-like structure by using distributed fiber optics and its damage detection. *Measur Sci Technol* 28
10. Doebling SW, Farrar CR, Prime MB (1998) A summary review of vibration-based damage identification methods. *Shock Vib Dig* 30(2):91–105
11. Fan W, Qiao P (2010) Vibration-based damage identification methods: a review and comparative study. *Struct Health Monit* 10(1):83–111
12. Hair JF, Black WC, Babin BJ (2014) *Multivariate data analysis*, 7th edn. Pearson Education Limited, Essex, UK
13. Maes K, Lombaert G (2021) Monitoring railway bridge KW51 before, during, and after retrofitting. *ASCE J Brid Eng* 36(3):
14. Magalhães F, Cunha A, Caetano E (2009) Online automatic identification of the modal parameters of a long span arch bridge. *Mech Syst Sig Proc* 23(2):316–329
15. Magalhães F, Cunha A, Caetano E (2012) Vibration based structural health monitoring of an arch bridge: from automated OMA to damage detection. *Mech Syst Sig Proc* 28:212–228
16. Meltz G, Morey WW, Glenn WH (1989) Formation of Bragg gratings in optical fibers by a transverse holographic method. *Opt Lett* 14(15):823–825
17. Pandey A, Biswas M, Samman M (1991) Damage detection from changes in curvature mode shapes. *J Sound Vibr* 145(2):321–332

18. Peeters B, De Roeck G (1999) Reference-based stochastic subspace identification for output-only modal analysis. *Mech Syst Sig Proc* 13(6):855–878
19. Peeters B, De Roeck G (2001) One-year monitoring of the Z24-bridge: environmental effects versus damage events. *Earthq Eng Struct Dynam* 30(2):149–171
20. Reynders E (2012) System identification methods for (operational) modal analysis: review and comparison. *Arch Comput Methods Eng* 19(1):51–124
21. Reynders E, Houbrechts J, De Roeck G (2012) Fully automated (operational) modal analysis. *Mech Syst Sig Proc* 29:228–250
22. Reynders E, Maes K, Lombaert G, De Roeck G (2016) Uncertainty quantification in operational modal analysis with stochastic subspace identification: validation and applications. *Mech Syst Sig Proc* 66–67:13–30
23. Reynders E, Schevenels M, De Roeck G (2014) MACEC 3.3: a Matlab toolbox for experimental and operational modal analysis. Report BWM-2014-06, Department of Civil Engineering, KU Leuven (2014)
24. Reynders E, Wursten G, De Roeck G (2014) Output-only structural health monitoring in changing environmental conditions by means of nonlinear system identification. *Struct Health Monit* 13(1):82–93
25. Salawu O (1997) Detection of structural damage through changes in frequency: a review. *Eng Struct* 19(9):718–723
26. dos Santos FLM, Peeters B (2017) Strain modal analysis. In: Doerffer P, Barakos G, Luczak M (eds) Recent progress in flow control for practical flows. Springer, Cham, Switzerland, pp 405–428
27. Unger J, Teughels A, De Roeck G (2005) Damage detection of a prestressed concrete beam using modal strains. *ASCE J Struct Eng* 131(9):1456–1463
28. Wang ZC, Liu MY, Qu YZ, Wei Q, Zhou ZD, Tan YG, Hong L, Song H (2019) The detection of the pipe crack utilizing the operational modal strain identified from fiber Bragg grating. *Sensors* 19(11):2556
29. Xia Y, Chen B, Weng S, Ni YQ, Xu YL (2012) Temperature effect on vibration properties of civil structures: a literature review and case studies. *J Civil Struct Health Monit* 2(1):29–46
30. Xia Y, Hao H, Zanardo G, Deeks A (2006) Long term vibration monitoring of an RC slab: temperature and humidity effect. *Eng Struct* 28(3):441–452

Monitoring of Base Isolated Building Subjected to Far Fault Earthquake



Antonello Salvatori, Antonio Di Cicco, and Paolo Clemente

Abstract Dynamic monitoring of base isolated buildings is analyzed to evaluate structural behavior during earthquakes and gain experience on the specific behavior of rubber isolators. Some structures with seismic base isolation have been monitored during recent strong earthquakes in Italy, namely Amatrice earthquake (2016/08/24, $M_w = 6.0$) and Norcia earthquake (2016/10/30, $M_w = 6.5$) and aftershocks. For these structures, amplification phenomena have been observed up to about twice the accelerations on the superstructure, for very low energy value inputs. In these cases, however, monitoring revealed amplified accelerations extremely small, and very far from being able to damage the structure. Records from the ENEA permanent accelerometric network, installed on these structures, and the tests carried out on the same isolators during qualification tests of the same rubber isolators positioned below the analyzed structure, describe the behavior of the isolators in terms both of force and displacement defining two non-linear laws, for small and large displacement, derived from experimental data.

Keywords Seismic isolation · Rubber isolator · Monitoring · Earthquake

1 Introduction

It's well known that seismic isolation of a structure, decoupling ground motion from super-structure motion represents still now the better solution to prevent both collapse condition (especially if the structure is designed according to capacity design) and any level of damage to building structure, infills and plants [11, 14, 23, 24].

Its realization usually is done by a physical disconnection in the structure which is then divided into two parts: the substructure, rigidly connected to the ground and which must have noticeable high stiffness properties, and the superstructure,

A. Salvatori (✉) · A. Di Cicco
University of L'Aquila, L'Aquila, Italy
e-mail: antonello.salvatori@univaq.it

P. Clemente
ENEA, Rome, Casaccia, Italy

which, according to recent studies, must conceive capacity design for its elements (beams, pillars, walls) [27]. Seismic isolation, instead of increasing the capacity of the structure, use RID's strategy, drastically reducing the energy transmitted from the ground to the building [20–22, 28].

The substructure, which normally has to be realized with high shear stiffness, to decrease significant relative displacements and deformations, and to minimize the main modal period of vibration relevant to substructure itself, has roughly the same acceleration of the ground and must be designed in elastic field (like a rigid body), while the superstructure takes advantage from the increased deformability deriving from the introduction of the isolation system, obviously with respect of capacity design concepts in order to avoid nonlinear behaviour in case of an exceptional seismic event [7, 13].

Typically, response spectra in terms of accelerations of most earthquakes reveal large amplification in the range $0.1 \div 0.8$ s, where generally is located the main vibration period of many traditional buildings (in particular, concrete cast building) [1, 5, 29]).

Assuming, for simplicity's sake, a linear elastic or comparable behaviour of the rubber isolators, (in particular when considering collapse prevention or life safety) the increase of global deformability must correctly be evaluated by considering the effects of all structural components (Substructure—isolating system—superstructure), which can influence the modal dynamic behaviour of the isolated structure also in the case of small displacement.

As a result, the earthquake-generated accelerations on the isolated structure are drastically lower than those relevant to the fixed-base configuration, so it's well known that the structure can be easily designed to withstand extreme earthquakes without damage both in structural and in non-structural components, in particular infills and plants [19, 25, 32].

Of course, an increase in fundamental period means also an increase in displacement, but the large component of displacement is localized in the isolating devices, independently from typology and technology, and most of the energy of the earthquake is low-pass filtered and also, in part, dissipated (by elastic cycles in the case of elastomeric isolators, or by friction in the case of pendulum devices) [15].

From analysis of experimental data on isolated structures, performed in the present work in many buildings, however, it has been noticed that for low acceleration values (like those in areas sufficiently far from earthquake epicenters) the whole system reveals vibration periods not suited to those of an isolated structure, due to different displacements and excitation frequency, according to greater stiffness of elastomeric devices (well known phenomenon in rubber or to static friction in pendulum devices), but almost closer to the ones of a fixed base traditional structure, as can be observed from recordings of low energy seismic events carried out by the authors in the structure under examination [2, 4].

Corresponding to low input energies at the base of the structure, the equivalent stiffness of the structure itself leads to frequency values different from those for which it was designed (<0.5 Hz). The reduction of the modal vibration period typically increases the seismic acceleration more than the case of higher periods [1].

These accelerations are higher than those evaluated in the design with possible low damage to nonstructural component (infills). Thus, a noticeable role is played by structural monitoring both for high and low earthquake intensities [6, 8, 16–18].

2 The Monitored Building: Foligno Regional Civil Protection Center

A monitoring system has been setup in some buildings in the Regional Civil Protection Centre in Umbria Region (Figs. 1 and 2).

The Regional Civil Protection Centre of the Umbria region is located in Foligno [3, 30, 31].

The Regional Centre is composed by a building (operative room, analyzed in detail in the present work), a regional building (emergency and training) where the Special Office for Reconstruction (Umbria Region 2016 Earthquake) is currently located and a third building (Amphitheatre – Plants building) [12].

The first two buildings are seismically isolated (and monitored by ENEA) and the third is a traditional one [2, 3].

The main structure (Operation room building), analyzed in the present work, has three floors above ground and a basement for a total area of about 1532.25 m² above ground, and a volume equal to 8630.00 m³.



Fig. 1 Monitored operation room building

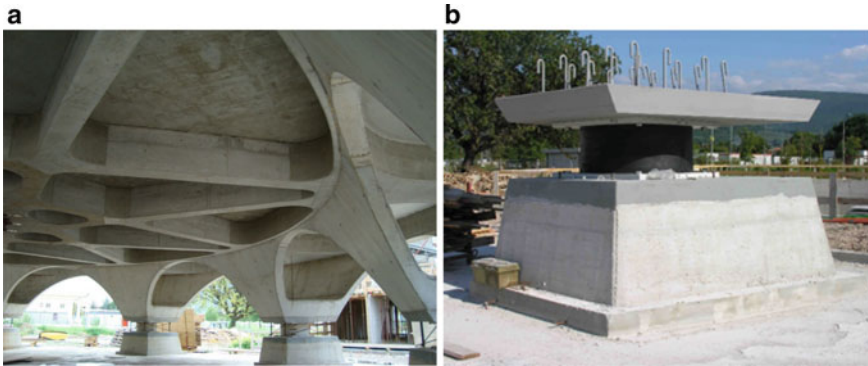


Fig. 2 a Isolators below the dome structure b Elastomeric isolator basement

The structure is in reinforced concrete, with a dome space composed by ten main concrete arches, and it is seismically isolated by ten high damping elastomeric isolators, located externally on the ground floor.

The size of the dome is 22 m in height and 31 m in diameter base.

The isolated superstructure has a dome supported by ten half arches with cross Section 40×120 cm, converging towards a single ring from which two concentric cylinders of 16 cm thickness are suspended, with a prestressed reinforced concrete.

The two concentric cylinders have inside a spiral staircase and an elevator placed inside the innermost cylinder. The inner most cylinder and the outermost one are suspended, with a sufficient interface towards the soil so that they can freely move during earthquake.

The outermost cylinder stops at the height of the first floor while the innermost cylinder continues to the basement, at a height of -4.00 m.

The external cylinder is formed, as the elevator core, by a reinforced concrete wall with 16 cm thickness but, unlike the latter part, from the height of the first deck.

The two cylinders end at the top with a reinforced concrete closure ring where the two cylinders connect to the semi-arches; above the latter there is an additional ring beam with a transverse Section 75×150 cm connected both to the closure ring and to the semi-arches.

The inner cylinder ends with a 30 cm thick slab inside the basement, at -3.74 m below the ground level, and it is isolated from the surrounding underground structure, then “suspended” and anchored to the isolated superstructure.

The foundation system is formed by plinths based on four piles each, linked together by a reinforced concrete beam with cross Section 80×80 cm, and by radial beams converging in a ring beam with cross Section 50×140 cm and diameter, measured on the longitudinal axis, equal to 7.20 m.

There is no connection between the elevator core and the ring beam above.

Above the beams connecting the plinths there is a 20 cm thick slab which is also the base of the dome.

The pedestrian access to the structure is possible by means of a slab (18 cm thickness) that extends as a cantilever from the core elevator suspended on the base of the dome. There is no connection between the slab for pedestrian access and the base of the structure.

Above the foundation plinths, there are 10 concrete supports on which the elastomeric isolation devices are positioned (Fig. 2).

The floors, with a radial dimension descending from the bottom towards the top of the structure, are supported by circular and radial beams that connect the half arches to the outer vertical cylinder.

The two upper floors are used as offices for the Civil protection operative room and more precisely:

- The first floor consists of 14 offices, in addition to the services and organized through furniture-equipped walls.
- The second floor is divided into a meeting room of about 145.50 m², a direction hall of about 60.00 m², a meeting hall of about 136.60 m² and services.
- The third floor contains other offices and a room for air conditioning systems.

3 Elastomeric Isolators Properties

The isolators are elastomeric one with soft-rubber, with circular steel plates between the rubber layers, identified by the code SI-S 1000/240. Their mechanical characteristics are shown in Table 1.

Before production, trial test was performed to determine isolator characteristics.

The experimental test evidenced an increasing cyclical stress at constant frequency and a corresponding increasing capacity of the isolator. The results reported the following values for the shear resistance module and damping (Table 1).

Table 1 Mechanical properties of the seismic isolators

External diameter	D _g	1000	mm
Total high without anchorage plates	H	392	mm
Total high with anchorage plate	H _t	472	mm
Volume of the nucleus	Vol	307.88	dm ³
Total weight without anchorage	W	1834	kg
Maximum horizontal force with maximum seismic displacement	F _{xy}	497	kN
Maximum seismic uniform pression = V/A'	σ _{vs,max}	3.98	Mpa
Minimum seismic uniform pressure = V _{min} /A'	σ _{vs,min}	0.00	Mpa
Vertical stiffness = E _c · A' / t _c	K _v	2310	kN/mm
Horizontal equivalent stiffness = G _{din} · A · t _e	K _e	1.31	kN/mm
Stiffness ratio	K _v /K _e	1764	

The devices have an increase in the damping and in the shear stiffness modulus with the decrease in the deformation.

Trial tests have been executed to determine:

- the vertical stiffness values of the elastomeric isolators,
- the static G modulus values,
- the rubber—steel adhesion values related to maximum shear deformation.

These tests have been performed by scaling test isolators by a 1/2 factor (type SI-S 500/120), applying cyclic stresses with fixed frequency, measuring the reaction force of each isolator. All the results have been scaled to the original isolator dimension.

It can be noticed that for a deformation values from 30 to 5%, the rubber isolators show a sharp increase in stiffness and damping values (Figs. 3 and 4).

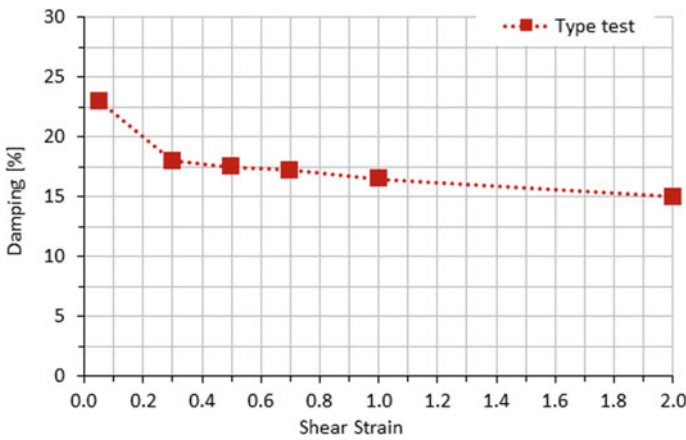


Fig. 3 Variation damping versus shear strain

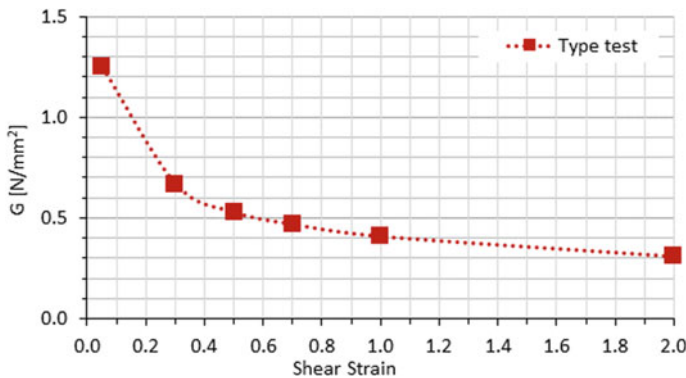


Fig. 4 Variation dynamic shear modulus versus shear strain

This characteristic in dynamic behavior of the rubber isolators can clearly affect the global response of the structure subjected to different earthquakes, both of low and of high intensity.

4 Monitoring Setup and Installation in the Isolated Structure

The following control equipment was installed, in 2014, to monitor the structure:

- Data acquirer Kinematics K2, absolute timing using GPS, equipped with 24-bit A/D converter (digital analogue), 12 acquisition channels, 3 of which are connected to the sensor triad in-side the acquirer and 9 connected to the external sensors;
- 12 Sensors Kinematics Force Balance model with dynamic >120 DB and full scale 2G, three of which, orthogonal each other, are contained in the acquirer; the remaining 9 are arranged at the level of the first deck, below the floating floor (also used for cable passage).

The instrumentation is arranged on the structure in elevation (Fig. 5) and in plan (Fig. 6), where the arrows indicate direction and positive sensors and the point corresponds to the arrowhead, so the sensors for the channels A02, A04, A05 and A06 are vertical.

The sensor group inside the acquirer, A01, A02 and A03, is positioned below the isolating plane, in the lowest attainable position, near the terminal part of the Elevator Core, so they are measuring soil input under earthquake condition [9].

This position permits to observe the direct energy input at the base of the building foundation, thus permitting to evaluate various seismic intensity of the aftershock after 2016 earthquakes.

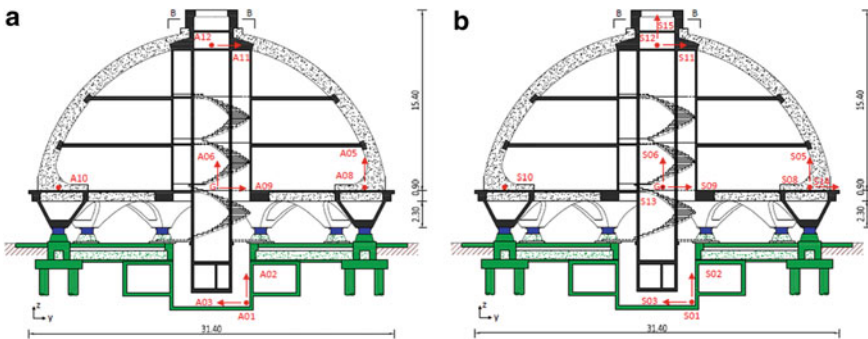


Fig. 5 a Elevation positioning of accelerometers b Elevation positioning of velocimeters

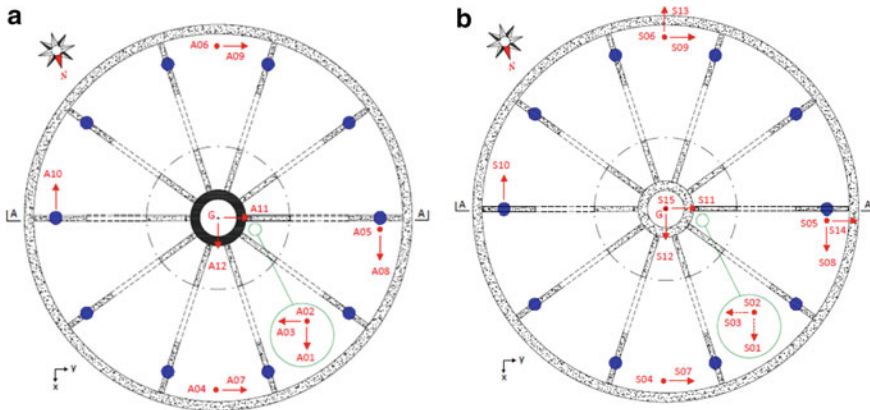


Fig. 6 **a** Plan positioning of accelerometers **b** Plan positioning of velocimeters

To verify the correct functioning of the fixed accelerometric network, a campaign of environmental noise measurements was carried out with a temporary network made with velocimeters.

The 12 fixed accelerometers were flanked by 12 velocimetric sensors, and, in addition, three other velocimetric sensors (S13, S14, S15) were added to this configuration to have a more complete configuration.

In the points where the S13, S14 and S15 sensors were installed there were only two accelerometers. The triplet at the base (A01, A02, A03) was placed below the isolating system, joint to the foundations and the ground. The velocimeters are placed directly on the ground.

The seven sensors from S04 to S10 were positioned on the first level above the isolators, precisely in contact with the reinforced concrete structure below the floating floor, and the velocimetric sensors were placed on the same floor adjacent to the accelerometers.

The positioning of sensors on the structure, i.e. the accelerometers relative to the channels from A04 to A10, is located to the share of the first floor, immediately above the isolating plane, (Fig. 5), while the sensors related to channels A11 and A12 are positioned at the top of the inner core (Fig. 6).

In these positions they can show properly global behaviour of the building.

All the instruments are connected to a single acquirer to contemporaneously acquire the recordings, this requirement is fundamental to obtain the modal forms associated with the recorded structural frequencies.

The recognition of seismic events is carried out in STA/LTA logic (Short Term Average/Long Term average), i.e. by comparing the mean signal measured by each sensor, filtered pass 0.1–10 Hz band, in a short time interval, in this case 0.6 s, (STA) and the mean signal rate detected by the same sensor, band pass filtered 0.1–10 Hz, in a long time interval, in this case 60 s, (LTA). If the STA/LTA value exceeds a

preset value, in this case equal to 4, the signal from the channel generates a trigger command.

To reduce the amount of recorded spurious signals, the trigger condition for a single channel is not sufficient to initiate the recording. To start the recording a determined number of sensors must exceed simultaneously trigger conditions, by activating the sensors at the base and the two sensors at the top, clearly less affected by local noise.

If two sensors exceed at the same time the trigger condition, then it begins the recording of the acquirer. The expected trigger value of acceleration is not fixed, it can be variable because depending on the LST/LTA values, and on the noise condition.

To record the entire signal the acquirer adds to the head of the recording the portion of the signal prior to the trigger for a preset duration, in this case 30 s.

The detected event is considered terminated when the selected sensors check the condition of dettrigger, i.e. the signal amplitudes fall below a preset value, in this case the 40% of the trigger conditions. Starting from the time of dettrigger, the acquirer continues the recording for a preset time, post event, in this case 30 s.

The accelerometer network recorded all the events that struck Central Italy since August 24th, 2016. A detailed analysis of the behaviour of the seismic isolation system under different energy earthquakes was carried out [31].

By additional sensors (velocimeters) arranged on the structure, it was possible to recognize some experimental dynamic characteristics of the structure, i.e. natural frequencies and associated modal forms.

Velocimetric sensors are particularly suitable for low intensity vibrational phenomena; these instruments are simply placed on the measuring points and record the speed of the point where they are placed.

The stress used was the simple environmental noise which, having energy content on the entire spectrum of interest (like a straight line on the spectrum), allows to enhance the natural frequencies of the structure.

Some of the eigenspectra of the 15 velocimetric sensors are shown, deriving from the analysis of broadband noise signal (Figs. 7, 8 and 9).

The results show an amplification at 2.67 Hz in the vertical sensor, while in the horizontal sensors the amplification reveals at 1.94 Hz (Fig. 10).

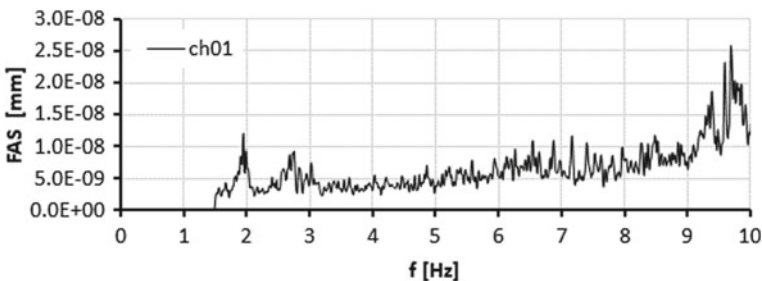


Fig. 7 Eigenspectrum of velocimeter CH 01

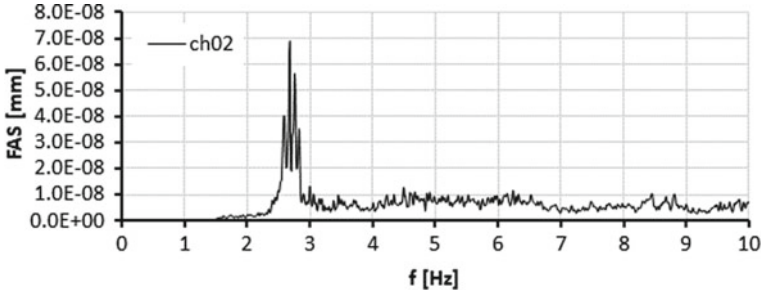


Fig. 8 Eigenspectrum of velocimeter CH 02

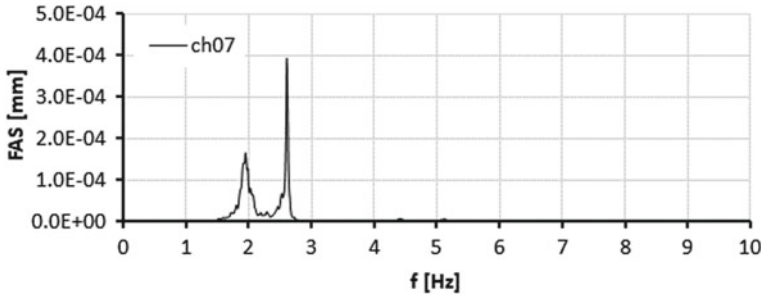


Fig. 9 Eigenspectrum of velocimeter CH 07

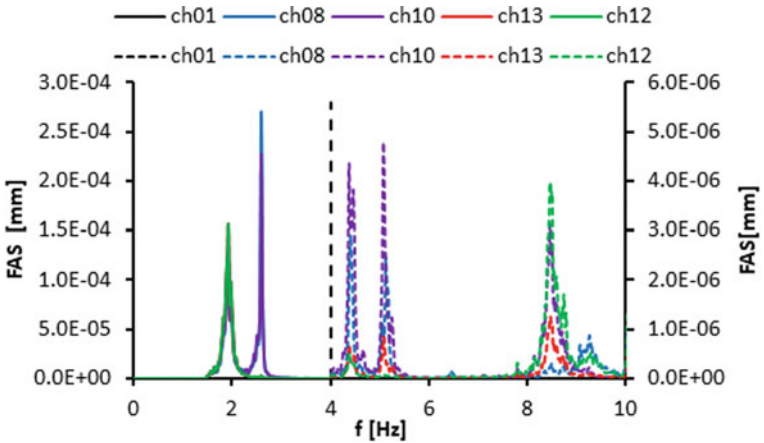


Fig. 10 Amplification factor in horizontal (solid line dir. 1) and vertical sensor (dashed line dir. 3)

In the foundation plate the three vertical sensors, S04, S05, S06, exhibit an amplification factor at about 8.80; 8.80 Hz can reasonably be thought to be a structural frequency in the vertical direction.

Observing the horizontal sensors, it can be noticed that, regardless of the level in which they are positioned, the radial sensors (S13 and S14 at the base, and S11 and S12 at the top) show a single evident peak at 1.94 Hz, a probable signal of a translational frequency with components prevalent in the direction of sensors S12 and S13.

The tangential sensors, obviously arranged only on the base level, in addition to the aforementioned frequency 1.94 Hz, have a further frequency at 2.60, decidedly higher and extremely defined; this second frequency could have origin by a torsional dynamic behaviour; this is confirmed because it is present only in tangential sensors and the subsequent analysis of the cross-spectra confirm this hypothesis. Finally, the vertical S15 sensor at the top still shows the 8.80 Hz frequency.

The graphs of the spectral and cross spectral analysis confirm the frequency behaviour observed (Fig. 11). The torsional nature of the frequency 2.60 Hz is clearly confirmed, while also the frequencies at 4.40 Hz and 5.20 Hz seem to be of a torsional nature even if their amplitude is much lower. The correlation between velocimetric analysis and accelerometric one validates the modal frequency results-.

This analysis has been performed for all the input channels, evidencing the directional behaviour and the relevant frequencies. A low intensity rocking behaviour

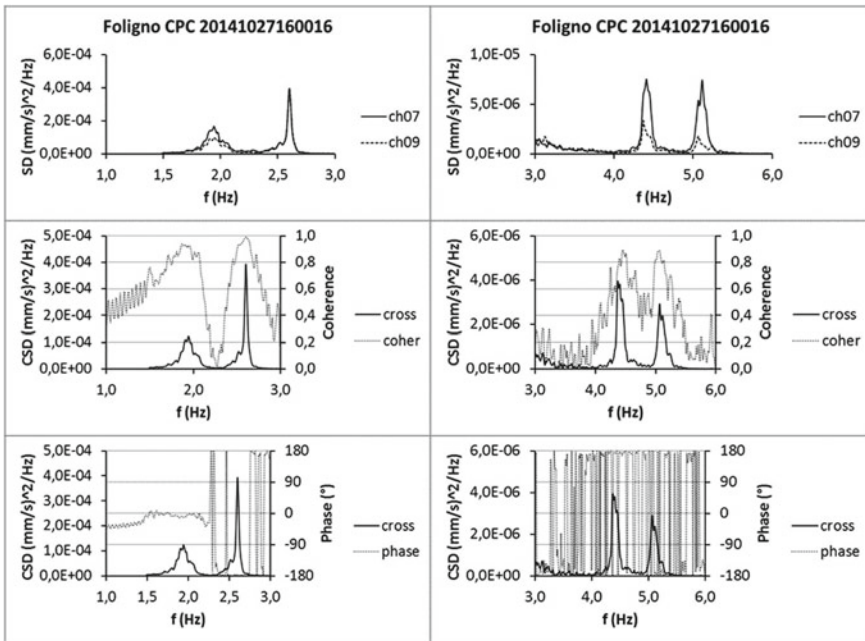


Fig. 11 Results from spectral and cross spectral analysis for CH07 and CH09

has been evidenced by cross spectral analysis for channels S04–S06, and S06–S12 (vertical component).

5 The in Situ Seismic Behaviour of the Isolation System

The design fundamental frequency of the isolated building was equal to 0.38 Hz. Different values were found during the earthquakes recorded. A fundamental frequency of about 1.9 Hz was estimated during ambient vibration tests and low energy earthquakes, while a first resonance frequency of about 1.0 Hz was found under the strongest event recorded. Anyway, the effectiveness of the seismic isolation system under all the events of the sequence was verified and discussed in a previous paper [12, 30].

Corresponding to low input energies at the base of the structure the frequency of the structure itself leads to frequency values different from those for which it was designed (<0.5 Hz). The reduction of the vibration period increases the acceleration more than the case of higher period, depending also from the earthquake properties [26]. These accelerations are higher than those evaluated in the design with consequent possible damage to the superstructure.

The change of the first resonance frequency was verified also during the single events.

In the following sections, the earthquake that caused the maximum effects at the site is considered. It occurred on October 30th, 2016 ($M_w = 6.5$), 36 km far from the building location.

This was also the earthquake of the seismic sequence with the maximum magnitude value.

The change of the resonance frequencies was pointed out by means of a time frequency analysis based on the wavelet transforms, obtained with appropriate time and frequency resolutions and whose amplitudes are a measure of the relative energy content at each time–frequency point.

In Table 2 are reported all the seismic event recordings with M_w or $M_L \geq 4.5$ relative to the seismic sequence started on August 24, 2016 (with an event of magnitude $M_w = 6.0$) until 31 December 2017. The table lists the events defined from time source, localization (latitude, longitude, depth), the source of the data (Seismic Bulletin INGV), the name of the registration (ENEA internal code for the archiving of events), the epicentral distance and eventual notes.

The procedure of the recorded data requires that the following processing be carried out for each registration:

- Transformation of data from acquirer units, Volt, into cm/s/s units.
- Calculation and graphical representation of Fourier transforms to select the filtering frequencies.
- Instrumental correction for the characteristics of each sensor, natural frequency and damping.

Table 2 Recorded seismic events

Source time (Utc)	Latit	Longit	Depth (km)	Magnitude	Source	Name record	D_{Epi} (Miles)
24/08/2016 01:36:32	42,698	13,234	8.1	6.0-Mw	BULLETIN	TN015	53
24/08/2016 02:33:29	42,792	13,151	8.0	5.4-Mw	BULLETIN	TN032	41
24/08/2016 11:50:31	42.82	13.16	9.8	4.5-Mw	BULLETIN	TN066	41
26/08/2016 04:28:26	42,605	13,292	8.7	4.8-Mw	BULLETIN	TN086	63
26/10/2016 17:10:36	42.88	13,128	8.7	5.4-Mw	BULLETIN	TP021	36
26/10/2016 19:18:06	42,909	13,129	7.5	5.9-Mw	BULLETIN	TP026	35
26/10/2016 21:42:02	42,863	13,121	9.9	4.5-Mw	BULLETIN	TP053	36
30/10/2016 06:40:17	42,832	13,111	9.2	6.5-Mw	BULLETIN	TP151	36
30/10/2016 12:07:00	42,845	13,078	9.7	4.5-Mw	Survey	TP237	33
01/11/2016 07:56:40	43	13,158	9.9	4.8-Mw	Survey	TP354	37
03/11/2016 00:35:01	43,029	13,049	8.4	4.7-Mw	Survey	N.R	29

- change of direction for sensors related to ACH03 and ACH10,
- frequency filtering and dual integration to obtain the corrected temporal histories in terms of acceleration, speed and displacement.
- For magnitude ≥ 5.0 , the calculation of the Accelerometric Group response spectra at the base was also carried out.
- For all recordings, the maximum, in acceleration and displacement, for each channel was calculated, the maximum for each recording and the channel on which that value was obtained.

The event which gave the major values had magnitude $M_w = 6.5$, registered under the name **TP151** (Norcia earthquake PG of 30/10/2016). This event is discussed in more detail in the following chapter.

The experimental results obtained by in situ recording were compared to original calculation design results, by applying linear and nonlinear analyses to a finite element structural model.

To test the finite element model implemented and the isolator characteristics, the event recordings were also used with the name TN015, relative to the effects of the event of 24/08/2016 with magnitude $M_w = 6.0$ with epicentral zone near Amatrice [10]. The numerical results have been compared with the recorded ones.

5.1 Recording Analysis TP151 (Norcia Earthquake, M_w 6,5)

The comparison between the temporal histories of the accelerations at the three monitored levels and for the two directions, shown below, shows that seismic actions are different in both directions.

Moving from the ground motion to the motion above the isolator plane, there is a decrease in the amplitude of the accelerations and a noticeable lowering of the frequency content. Moving from the level above the isolator plane there is an increase in accelerations, which are still lower than those of the ground.

The dominant frequency appears to be still the same, but it is evident, more in the direction of CH11, the presence of higher frequencies (Figs. 12, 13, 14, 15 and 16).

The analogous comparison between the Fourier spectra shows that the frequency content in the two points above the isolator plane, ACH08 and ACH12 in one direction and ACH07 and ACH11 in the other direction, is substantially identical, for each direction.

In the direction of ACH07 and ACH11 a significant frequency content is manifested between 7 and 9 Hz, even dominant for ACH11 (Fig. 17).

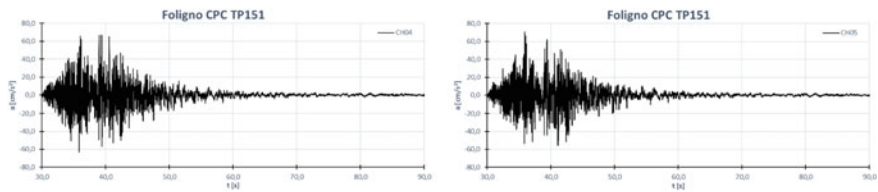


Fig. 12 Acceleration time history sequence TP151 at ACH04, ACH05

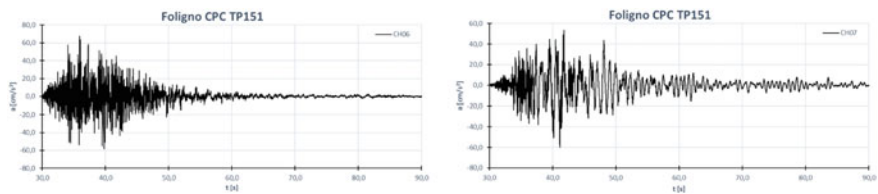


Fig. 13 Acceleration time history sequence TP151 at ACH06, ACH07

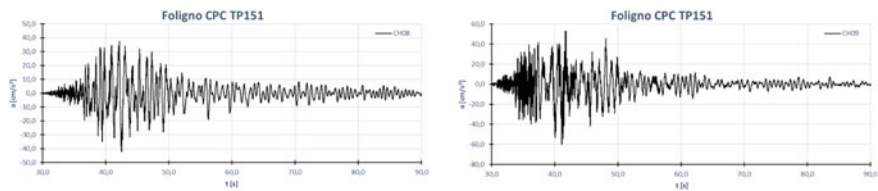


Fig. 14 Acceleration time history sequence TP151 at ACH08, ACH09

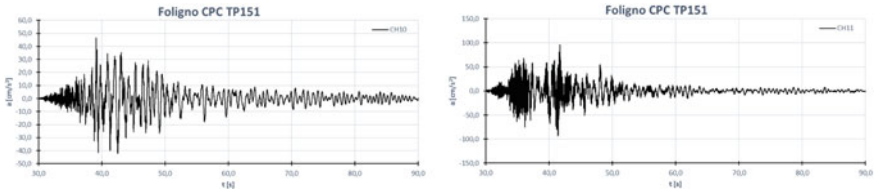


Fig. 15 Acceleration time history sequence TP151 at ACH10, ACH11

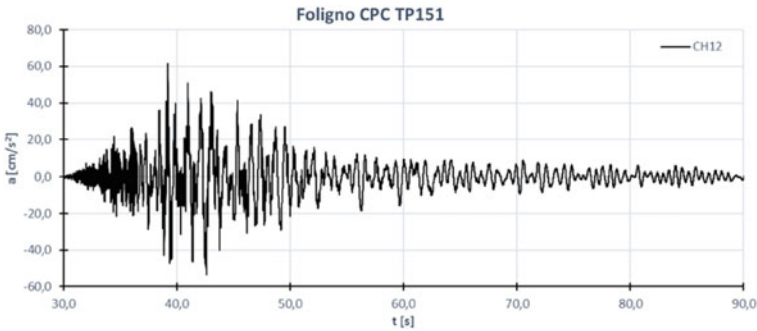


Fig. 16 Acceleration time history sequence TP151 at ACH12

Such frequency content is not justified in a structure with seismic isolation at the base.

In the following this behaviour will be explained by analyzing the Fem model both in linear and nonlinear characterization for the rubber isolators.

Cross-spectral analysis, ACH08 ACH12 and ACH07 ACH11, (Fig. 18), stresses that the motion of the structure above the isolator plane increases very little by proceeding upwards in the range in frequency less than 2 Hz, and it is also consistent and in phase.

This frequency range can be considered representative of the motion of the isolated structure.

The frequency content between 7 and 9 Hz has much greater amplitudes on the top of the structure and in the direction of ACH11, which decrease by going downwards. Consistency is high and the motion of the two points of measurement is in opposition to phase. It can be stressed that the motion at these frequencies is originated within the isolated superstructure.

There is a small frequency shift for amplitude peaks respect to velocimeter spectra, in particular for the horizontal component. Acceleration spectra revealed amplitude peaks at light small frequency values. This could depend on different amplitude level respect to velocimetric analysis, due to nonlinearity of material.

To explain the presence of several frequency peaks in the recordings examined, a time–frequency analysis was carried out for the ACH11 and ACH12 channels. From

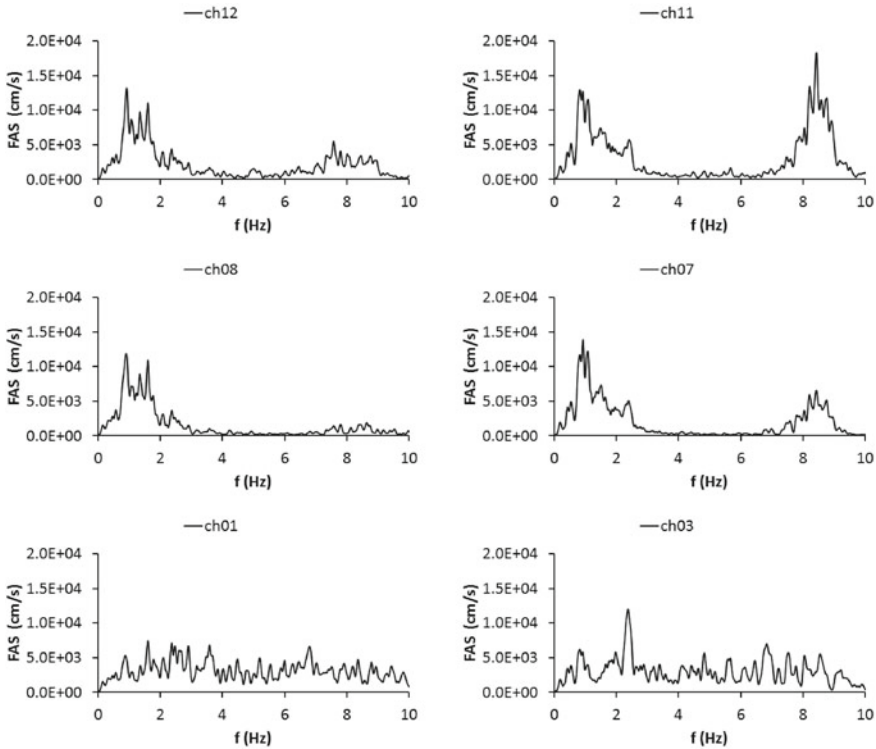


Fig. 17 TP151 comparison of the acceleration Fourier spectra. Channel id is referred to acceleration channels ACH_i

these it is evident that the dominant frequency varies during the seismic action as it is expected for a structure with seismic isolation at the base [3].

6 The Experimental Test on Seismic Isolation System and Comparison with FEM Model

To evaluate the actual characteristics of the isolator for deformations less than 5%, a test was performed on the same isolators used for the trial test using as input data the relative displacements between the isolated structure and the ground, deriving from the double integration of the accelerations recorded by the ACH03 accelerometer located at the base of structure under examination, integral to the ground, and the barycentric displacement of the structure, calculated by mediating the displacement deriving from the recordings of the accelerometers ACH07 and ACH09, placed in correspondence of the first scaffold, in diametrically position opposite, just above the elastomeric isolators.

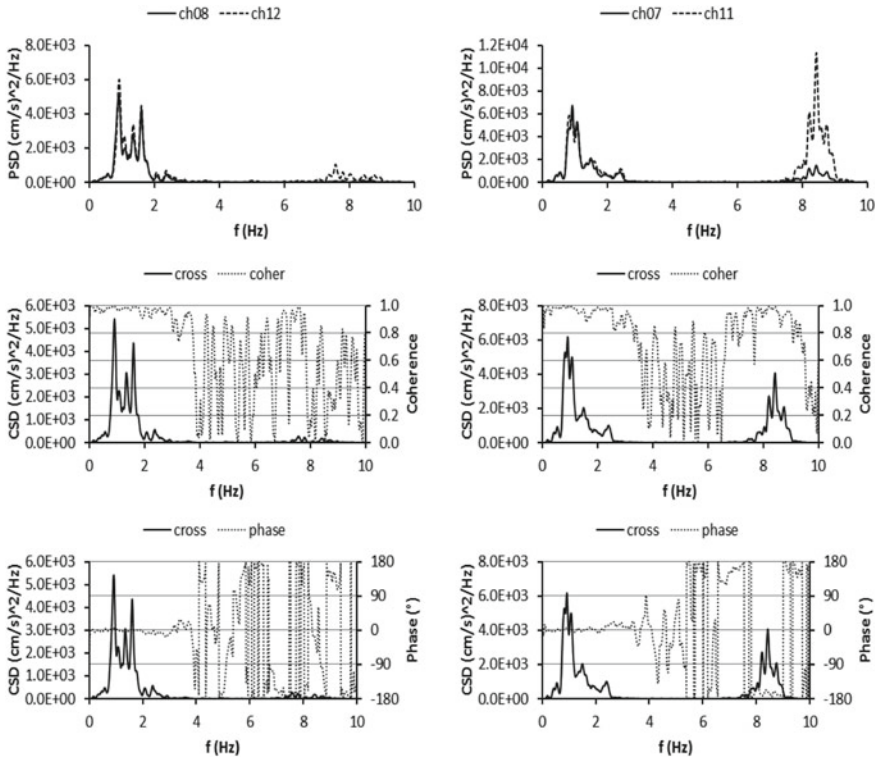


Fig. 18 TP151 cross spectral analysis. Channel id is referred to acceleration channels ACH_i

The registrations for the TP151 event were used for the test. The event TP151 is the recording, of the accelerometers installed on the structure, of the event of the day 30/10/2016 06:40:17 of magnitude Moment (M_w) of 6.5, with an epicenter at a distance of about 36 km, near Norcia (PG) (Table 2).

The deformation of the test is below 5% deformation of the isolator, the height of the isolator being equal to 240 mm. The trial tests were performed on SI-S 500/120 type insulators, i.e. on a 2: 1 scale, subject to increasing cyclic stresses at a constant frequency measuring the corresponding shear force (Fig. 3, 4). Some test results are shown in the displacement-force graph (Fig. 19).

The curves relating to the time history test obtained from the TP151 event data are shown in blue while the red line curves derive from a trial test with deformation of 5% performed at a constant frequency.

Amplitude variations determine, in the two cases, the differences between the two hysteretic responses, due to nonlinear rubber behavior which is displacement dependent.

To verify the validity of the law and analyze the structure’s behaviour, a finite element model of the structure was analyzed.

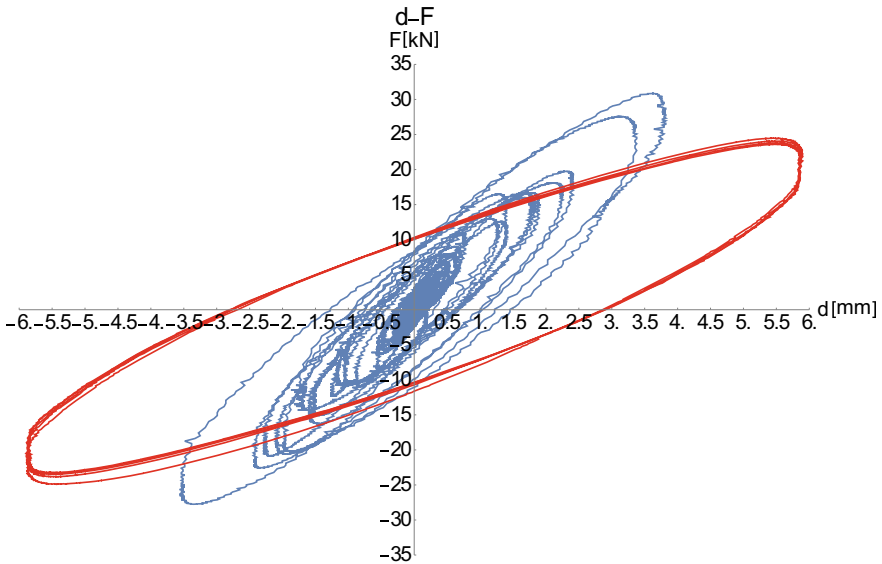


Fig. 19 Curves related to the test with the time history obtained from the data of the event TP151

The definition of a model that is correct and adherent to that which is the real situation is a very delicate operation, also through the model you have to recreate, in the most likely way possible, the condition of load on the structure at the time of recorded events. A nonlinear dynamic modal analysis has been performed, (considering the first 50 modes of vibration of the structure), with recorded acceleration time histories.

The model has been optimized by inserting the nonlinear behavior of the elastomeric isolator, using the laws obtained from the results of the trial test, performed on the isolator based on the displacement recordings of the TP151 event (Fig. 20). The model of the rubber isolator has been applied starting from the displacement—force time dependent behaviour, obtained with the trial test. By this analysis, two interpolation functions are developed, time—displacement and time—force. A proper range has been chosen (with values above a threshold value for each curve), between 40.5 and 65 s. The time interval between two values where the time-force function has zero value will define a cycle in terms of force, therefore with the same logic, extrapolating data from the time-displacement interpolation function for the same time interval, all pairs of force—displacement values defining the cycle are obtained. The same operation has been repeated for each time value for which the time-force function has zero value. 78 different cycles were found, but only 15 had acceptable characteristics, with symmetry in force—displacement properties.

An example of the nonlinear model of the rubber isolator is shown (Fig. 21).

Calculating the equivalent stiffness of the isolator as:

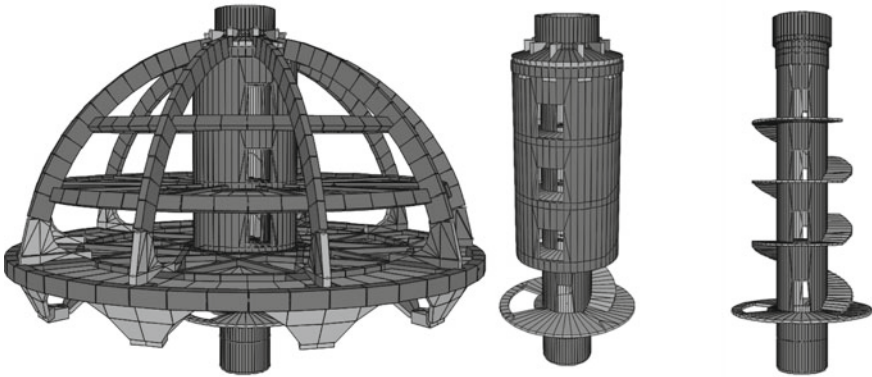


Fig. 20 The FEM model

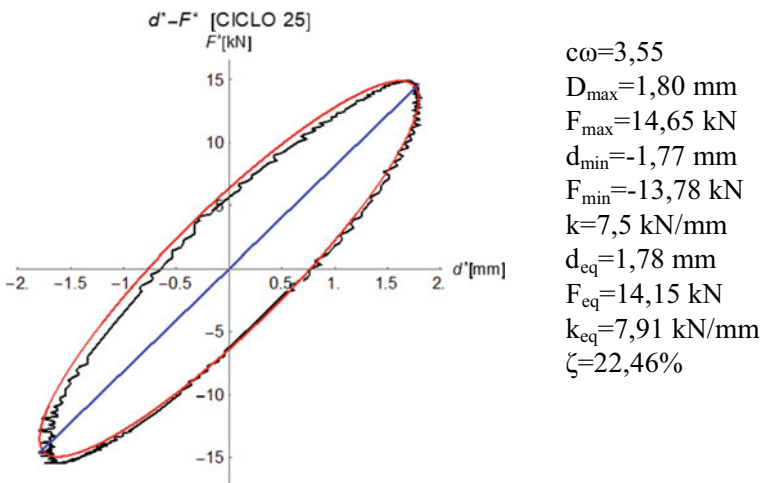


Fig. 21 Example of one of the various nonlinear rubber isolator cycles—Cycle 25

$$k_{i\ eq\ TT} = \frac{f_{i\ eq\ TT}}{d_{i\ eq\ TT}} \text{ [kN/mm]} \tag{1}$$

Is possible to evaluate, for each analyzed cycle,

$$f_{i\ eq\ R} = k_{i\ eq\ R} \cdot d_{i\ R} \tag{2}$$

in order so plot displacement – force data for the isolator SI-S 1000/240, resulting in the graph where force—displacement law is plotted for each cycle.

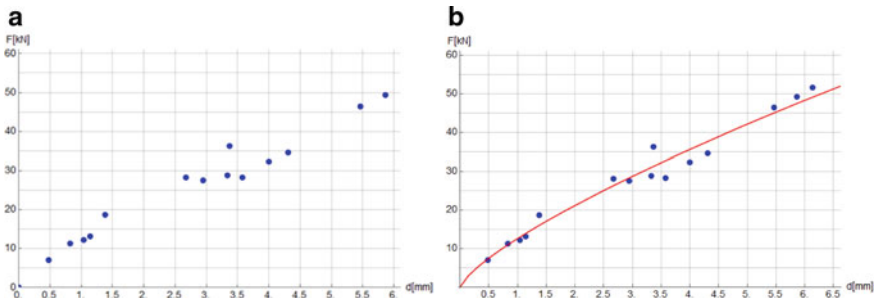


Fig. 22 **a** Data points for each analyzed cycle. **b** Nonlinear resultant force—displacement

The local law (small displacement) can be formulated as $F_L(d) = 12.6 \bullet d^{0.75}$. The graph fits very well to the real behavior of the isolator for shear deformation values $\gamma_i < 5\%$ (Fig. 22).

The data reported from the trial test are also added to the displacement—force graph, obtaining the resisting force of the isolator for shear deformation values from 0 to 200%, obtaining the global law (large displacement): $F_G(d) = 14.2 \bullet d^{0.57}$.

For small displacements ($\gamma_i < 5\%$) the isolator stiffness is slightly underestimated (Fig. 23).

The choice of a function like $f(x) = a \bullet xb$ is acceptable, well approximating the values, and, for a null displacement, with null value.

The results are shown both for displacement and acceleration, in the same position where the accelerometers are in the monitoring, and they are compared with the actual recordings of accelerations and displacement recorded during the analyzed events.

It is known that the orientation of the accelerometers with respect to the structure is the same even within the model and in particular:

- The ACH03 is oriented in the model according to the X-axis
- The ACH01 is oriented in the model according to the Y-axis
- The ACH02 is oriented in the model according to the Z-axis.

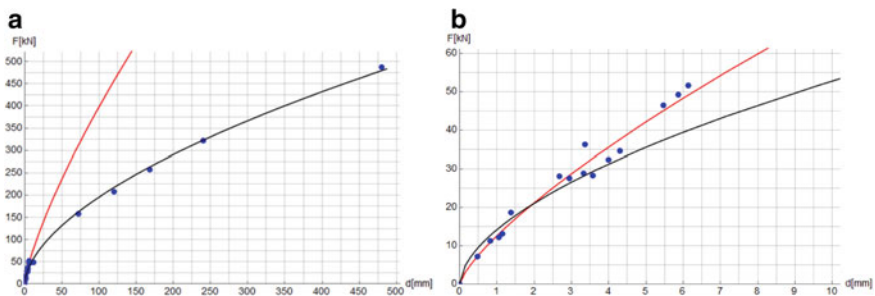


Fig. 23 **a** Nonlinear isolator global rule. **b** Nonlinear global rule for $\gamma_i < 5\%$

The results of the various analyses carried out below are shown below. It was inserted into the finite element model, as input data, the time history of the recording at the base, in terms of acceleration, of the event named TP151.

The input acceleration time histories are shown in (Fig. 24).

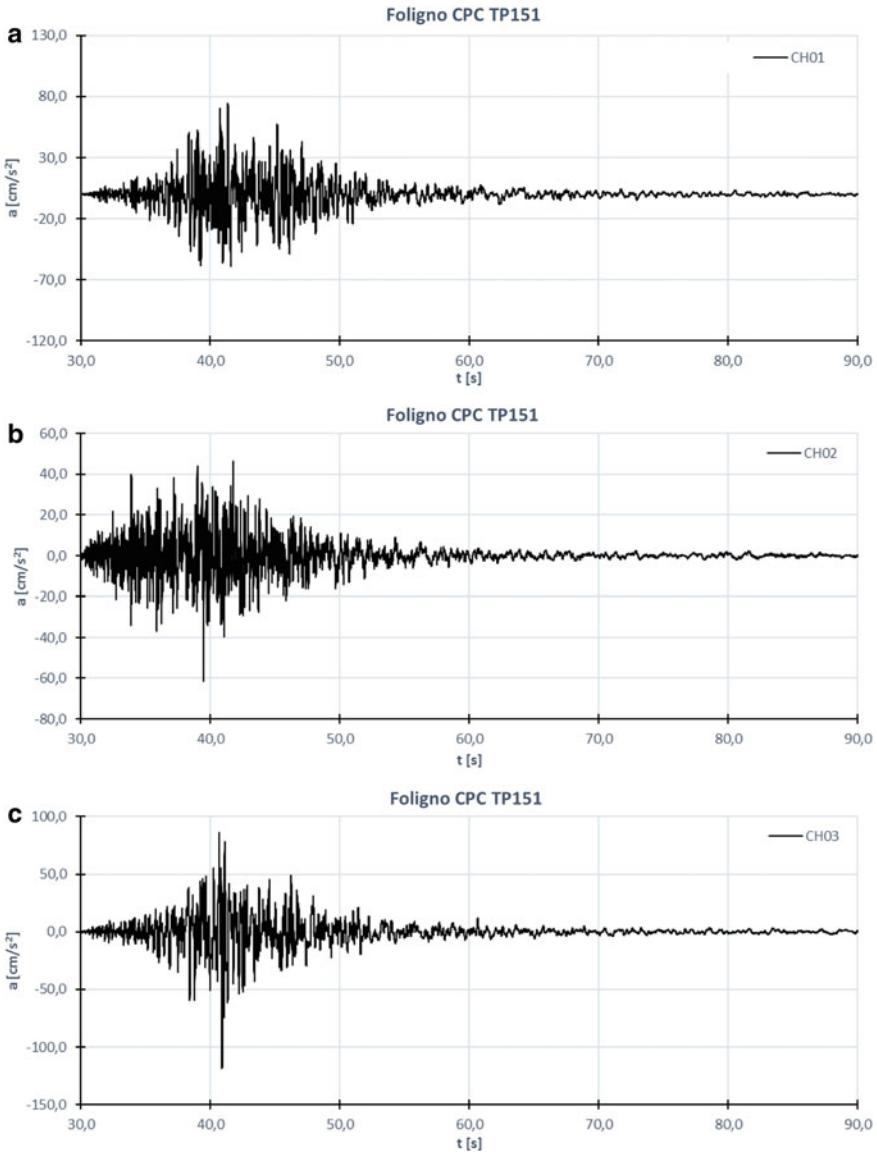


Fig. 24 Nonlinear input acceleration TP151 a ACH01, b ACH02, c ACH03

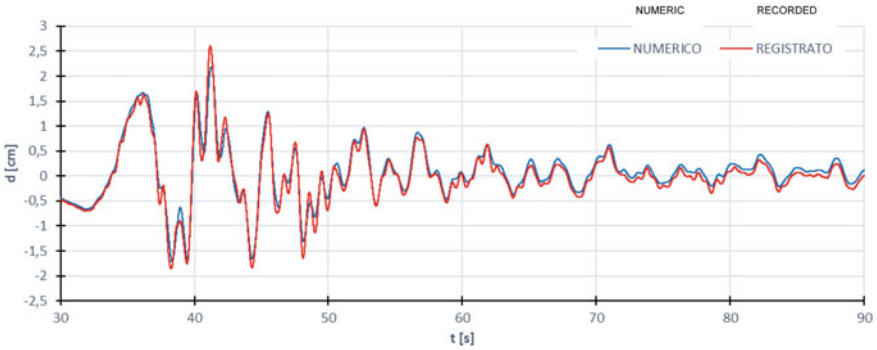


Fig. 25 Comparison of recorded displacement with numeric ones TP151 ACH07

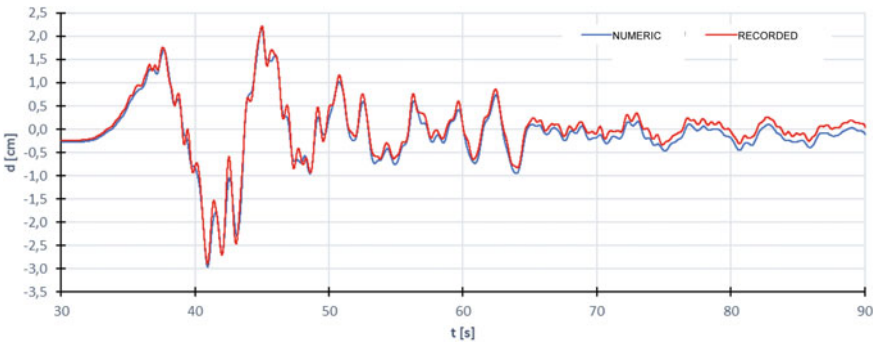


Fig. 26 Comparison of recorded displacement with numeric ones TP151 ACH08

Some of the displacement results are compared with the monitoring recordings (Figs. 25, and 26).

Then a comparison sample between recorded and numerical data is shown (Figs. 27 and 28).

It can be easily observed that the model with the non-linear law has a good correspondence with the recorded data, with some exception in for low amplitudes at higher frequencies in ACH07 (Fig. 27), probably due to the interaction with a little slab at the ground floor, connected to the cylindrical staircase.

As regards to acceleration, it reveals a frequency, in most cases, almost equal to the recorded one, but with slightly lower values.

As in the previous case, even the model implemented with the global law turns out to have a good correspondence with the recordings.

It is worthwhile to point out the effectiveness of the model and the implementation of the latter with the non-linear characteristics of the isolator to perform a linear analysis using the equivalent horizontal stiffness of isolators $K_e = 1.31 \text{ KN/mm}$, also using acceleration recordings of the TP151 event in the three main directions as input data.

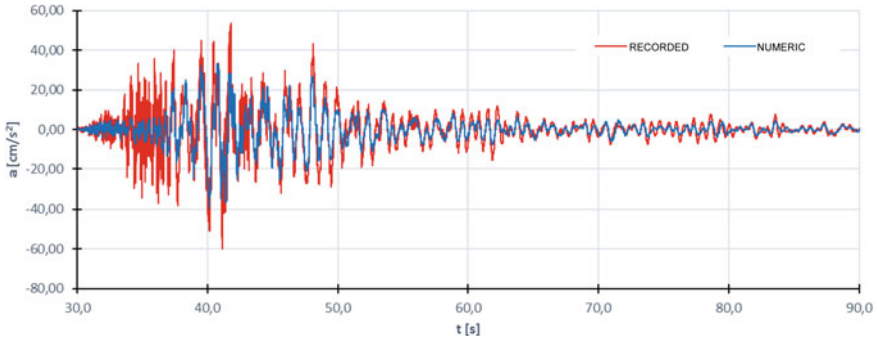


Fig. 27 Comparison of recorded acceleration with numeric ones TP151 ACH07

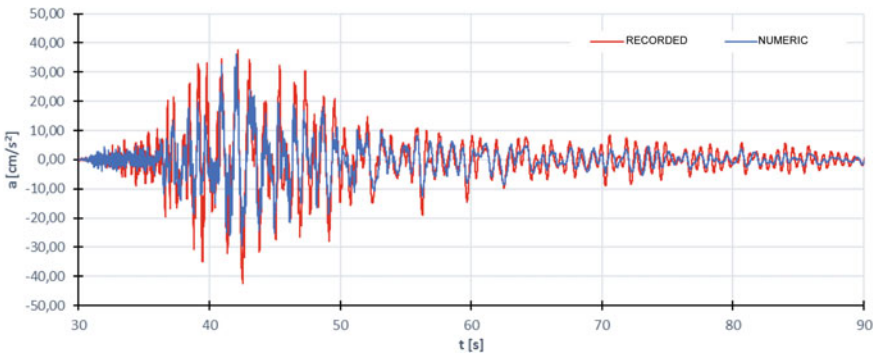


Fig. 28 Comparison of recorded acceleration with numeric ones TP151 ACH08

The results on two channels at the level of the first floor, one in the X-direction (ACH09) and another in the Y-direction (ACH08) are shown (Figs. 29 and 30), both for displacement and for acceleration.

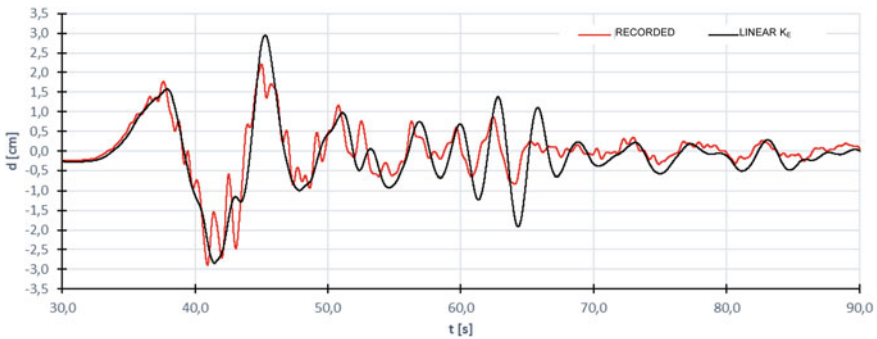


Fig. 29 Comparison of displacement: linear analysis and recorded data TP151 ACH08

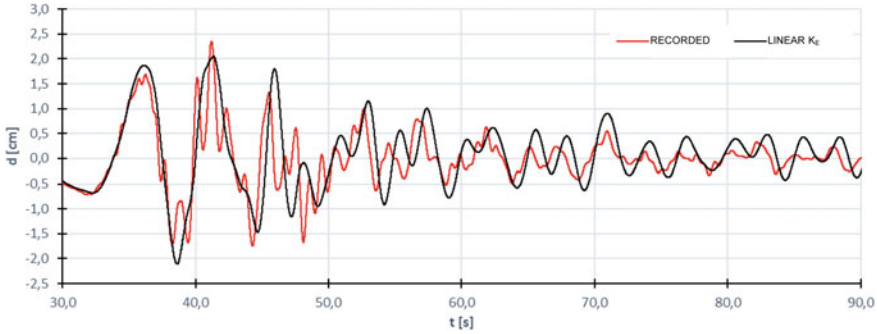


Fig. 30 Comparison of displacement: linear analysis and recorded data TP151 ACH09

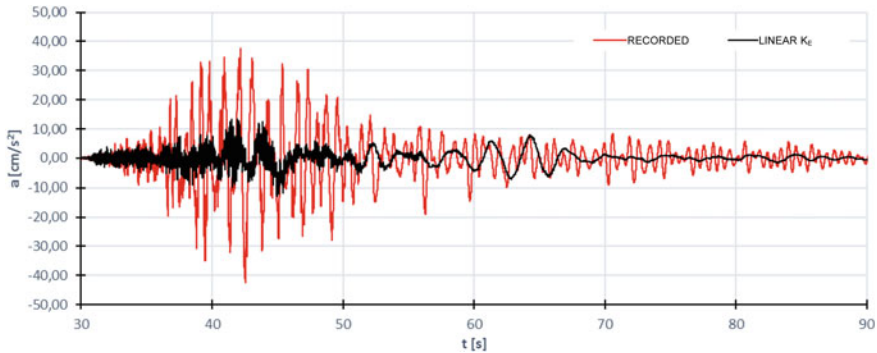


Fig. 31 Comparison of acceleration: linear analysis and recorded data TP151 ACH08

The differences between linear analysis with K_e and the analysis with the non-linear characteristics of the isolator are very pronounced. As for displacement, the highest recorded peak almost fits, but the relevant response time history does not fit the recorded one.

Considering acceleration time histories, however, it can be observed that that the numerical solution obtained by linear analysis doesn't fit, and heavily underestimates the acceleration in the structure, and the acceleration time sequence does not fit the recorded law (Figs. 31 and 32).

There is also a dominant frequency in the acceleration spectra of the model, different from that recorded on the actual structure.

7 Conclusion

In the structure under examination, amplification phenomena have been noticed, up to about twice the acceleration on the superstructure, for very low input energy

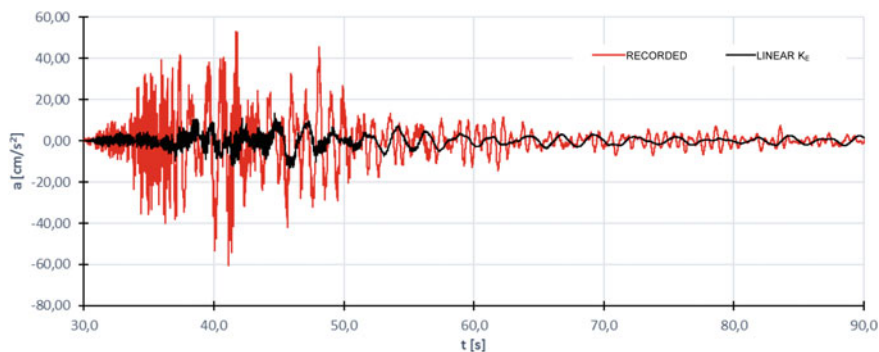


Fig. 32 Comparison of acceleration: linear analysis and recorded data TP151 ACH09

values. In these cases, however, it has been observed that the amplified accelerations are extremely small one, and very far from the damage level of the structure. This is because, as seen, isolation systems with high-damping elastomeric isolators have a nonlinear stiffness that increases as the deformation decreases (as required to avoid noise vibrations even under weak horizontal loads such as wind, etc.), with nonlinear performance; in the case of low-energy seismic input, the isolation system is more rigid even than the equivalent horizontal stiffness K_e .

However, the isolation devices correctly operate also in low stress conditions, with frequencies higher than the design ones, but still carrying out a filter function less than in extremely low acceleration condition. It can be observed, from the recordings, the presence of a frequency spectrum different from that of the fixed-base structure. At the same time, it has been verified that the stresses on the structure were less than the design ones.

By the recordings of ENEA permanent accelerometric network, installed on the test structure, and to the tests carried out on the same isolators used for the trial, it has been described the behavior of isolators both by shear force and displacement, defining two non-linear formulations, (for small displacement and for large displacement of the isolator) derived from experimental data. Obviously, while the first local formulation seems to be more appropriate to describe the behavior of the isolator for deformations below 5%, the global law is also suitable for large displacement and deformation of the isolators.

The FEM model fits very well the actual behavior of the structure and, using the nonlinear rules of the isolator, shows a very good feedback with the experimental measurements during the seismic events. However, the results of the numerical model cannot match exactly the recording ones, because of many other variables to consider in the FEM model.

In the linear analyses, with the equivalent horizontal stiffness modulus, the comparison of the results with the recordings of low energy seismic events, shows major differences, especially considering the acceleration values, which result considerably undervalued (75% less than about).

References

1. Bongiovanni G, Buffarini G, Clemente P, Saitta F, De Sortis A, Nicoletti M, Rossi G (2015) Behaviour of the base isolated Jovine School in San Giuliano di Puglia, Italy, under the December 20th 2013 earthquake. In: Proceedings 14th world conference on seismic isolation, energy dissipation and active vibration control of structures, University of California San Diego, CA USA
2. Bongiovanni G, Buffarini G, Clemente P, Saitta F, Serafini S, Felici P (2016) Ambient vibration analysis of a strategic base isolated building. In: Proceedings 6th International civil structures. Health Monitoring Workshop CSHM-6, Queen's University Belfast
3. Bongiovanni G, Buffarini G, Clemente P, Saitta F, Salvatori A, Scafati F (2019) Experimental seismic behaviour of base isolation systems in Italy during the 2016–2017 seismic sequence in central Italy. In: Proceedings of XVIII Convegno Nazionale ANIDIS L'Ingegneria Sismica in Italia, SS01–125 – SSS01–133, Ascoli Piceno, Italy, ISBN 978–88- 3339–256–1, ISSN 2532-120X
4. Buffarini G, Clemente P, Serafini S, De Stefan OA, Olivieri R, Salvatori A (2015) Experimental dynamic analysis and seismic rehabilitation of Palazzo Margherita in L'Aquila. EAI Knowledge, Diagnostics and Preservation of Cultural Heritage, spec. II, ISBN E185775 - ISSN: 1124-0016
5. Çelebi M, Bazzurro P, Chiaraluze L, Clemente P, Decanini L, De Sortis A, Ellsworth W, Gorini A, Kalkan E, Marcucci S, Milana G, Mollaioli F, Olivieri M, Paolucci R, Rinaldis D, Rovelli A, Sabetta F, Stephens C (2010) Recorded Motions of the M_w 6.3 Apr. 6, 2009 L'Aquila (Italy) Earth. and implications for building structural damage: a review. *Earth Spectra* 26(3):651–684 EERI
6. Clemente P (2002) L'analisi dinamica sperimentale nella salvaguardia dei beni culturali. EAI, ENEA, ISBN 88-8286-012-4
7. Clemente P (ed) (2015) Avezzano 1915 – 2015: Cento anni di ingegneria sismica". *Energia, Ambiente e Innovazione*, No. 5, ENEA
8. Clemente P (2017) Seismic isolation: past, present and the importance of SHM for the future. *J Civil Struct Health Monit* 7(2):217–231. <https://doi.org/10.1007/s13349-017-0219-6>
9. Clemente P, Bongiovanni G, Buffarini G, Saitta F (2015) Seismic input in the structural design: considerations and application to the Italian territory. *Int J Safety Secur Eng WIT Pres* 5(2):101–112. ISSN 2041-9031 (paper format), ISSN 2041-904X (on-line). <https://doi.org/10.2495/SAFE-V5-N2-101-112>
10. Clemente P, Bongiovanni G, Benzoni G (2017) Monitoring of seismic isolated buildings: state of the art and results under high and low energy inputs. *Proceeding New Zealand society for earthquake annual conference and 15th world conference on seismic Isolation, Energy Dissipation and Active Vibration Control of Structures, NZSEE2017 and 15WCSI, Wellington*, pp 27–29
11. Clemente P, Bontempi F, Boccamazzo A (2016) Seismic Isolation in masonry buildings: technological and economic issues. In: Modena C, da Porto F, Valluzzi MR (eds) *Brick and block masonry: trends, innovation and challenges (Proceeding 6th International Conference IB²MAC, 26-Padua)*, 2207–2215, Taylor & Francis Group, London, UK, ISBN 978-1-138-02999-6
12. Clemente P, Bongiovanni G, Buffarini G, Saitta F (2016) Experimental analysis of base isolated buildings under low magnitude vibration. *Int J Earthq Impact Eng* 1(1–2):199–223. <https://doi.org/10.1504/IJEIE.2016.10000961>
13. Clemente P, Buffarini G (2010) Base isolation: design and optimization criteria. *J Seism Isolat Protect Syst* 1–1:17–40. <https://doi.org/10.2140.siaps.2010.1.17>
14. Clemente P, Martelli A (2017) Anti-seismic systems: worldwide application and conditions for their correct use. In: *Proceedings 16th world conference on earth engineering (16WCEE, Santiago, Chile)*, IAEE & ACHISINA

15. De Stefano A, Matta E, Clemente P (2016) Structural health monitoring of historical heritage in Italy: some relevant experiences. *J Civil Struct Health Monit* 6(1):83–106. <https://doi.org/10.1007/s13349-016-0154-y>
16. Losanno D, Londono JM, Spizzuoco M (2013) Structural monitoring for the management of emergency due to natural events. In: IEEE workshop on environmental, energy and structural monitoring systems, EESMS 2013, Proceedings. <https://doi.org/10.1109/EESMS.2013.6661703>
17. Losanno D, Spizzuoco M, Serino G (2013) An application of SHMS to a passively controlled structure. In: IEEE workshop on environmental, energy and structural monitoring systems, EESMS 2014, Proceedings. <https://doi.org/10.1109/EESMS.2014.6923273>
18. Martelli A, Clemente P (2015) Need for an adequate seismic monitoring of seismically isolated buildings to ensure safety during their life. In: De Stefano A (ed) Proceeding 7th international conference on structural health monitoring of intelligent infrastructure (SHMII-7, Turin), RS2, ISHMII & Politecnico di Torino
19. Martelli A, Clemente P, Benzoni G (2017) State-of-the-art of development and application of anti-seismic systems in Italy. In: Proceeding New Zealand society for earthquake annual conference and 15th world conference on seismic isolation, energy dissipation and active vibration control of structures (NZSEE2017 and 15WCSI, Wellington)
20. Martelli A, Clemente P, De Stefano A, Forni M, Salvatori A (2013) Development and application of seismic isolation, energy dissipation and other vibration control techniques in Italy for the protection of civil structures, cultural heritage and industrial plants. In: Seismic isolation, energy dissipation and active vibration control of structures; Proceeding of the ASSISi 13th world conference (13WCSI) & JSSI 20th anniversary international symposium, JSSI XIII world conference on seismic isolation, energy dissipation and active vibration control of structures, Commemorating JSSI 20th anniversary, Sendai, Japan
21. Martelli A, Clemente P, De Stefano A, Forni M, Salvatori A (2014) Recent development and application of seismic isolation and energy dissipation and conditions for their correct use. In: *Geotechnical, geological and earthquake engineering*, 34:449–488. ISSN 1573-6059, ISSN 1872-4671 (electronic), ISBN 978-3-319-07117-6, ISBN 978-3-319-07118-3 (eBook). https://doi.org/10.1007/978-3-319-07118-3_14, Kluwer Academic Publisher, Springer Cham Heidelberg New York Dordrecht London, Library of Congress Control Number: 2014946618, (2014)
22. Martelli A, Clemente P, Forni M (2015) Worldwide state-of-the-art of development and application of anti-seismic systems based on the information provided at the ASSISi Sendai Conference in 2013 and later and conditions for their correct use. In: Proceeding 14th world conference on seismic isolation, energy dissipation and active vibration control of structures, Univ. of California San Diego, CA USA
23. Martelli A, Clemente P, Forni M, Panza GF, Salvatori A (2011) Recent development and application of seismic isolation and energy dissipation systems, in particular in Italy, conditions for their correct use and recommendations for code improvements. In: 12th world conference on seismic isolation, energy dissipation and active vibration control of structures, Sochi (Russia)
24. Martelli A, Clemente P, Saitta F, Forni M (2012) Recent worldwide application of seismic isolation and energy dissipation to steel and other materials structures and conditions for their correct use. In: Mazzolani FM, Herrera R (eds) *STESSA 2012* (Proceeding, seventh international conference structures in seismic areas, Santiago del Chile.), Taylor & Francis Group, London, ISBN 978-0-415-62105-2
25. Martelli A, Clemente P, Forni M, Salvatori A (2011) Ricostruire L'Aquila in sicurezza con l'isolamento ed altri sistemi antisismici, *21mo Secolo*, 22(2):14–28. ISSN: 1570-761X
26. Rinaldis D, Clemente P (2013) Seismic input characterization for some Italian sites. In: Brebbia CA, Hernández S (eds) *Earth resistant engineering structures IX* (Proc. ERES 2013, A Coruña, Jul 8–10), vol 79, pp 13–21, WIT Press, Southampton, UK, ISSN 1743-3509. <https://doi.org/10.2495.ERES130021>
27. Salvatori A (2009) Edifici con isolamento sismico alla base: la nuova facoltà di lettere, filosofia e scienze della formazione dell'università dell'Aquila. In: Proceeding of XIII national conference ANIDIS L'Ingegneria Sismica in Italia, Bologna

28. Salvatori A (2014) Structural faults and innovative repair techniques in the buildings damaged in the L'Aquila 2009 earthquake. In: Forde MC (ed) Proceedings of structural faults & repair 2014, London (UK), ISBN No: 0-947664-76-8
29. Salvatori A (2018) Seismic base isolation: retrofitting application in structures damaged by earthquake. In: Proceedings of 16th European conference on earthquake engineering ECEE, Thessaloniki, Greece
30. Salvatori A, Di Cicco A, Clemente P (2019) Seismic monitoring of buildings with base isolation. In Papadrakakis M, Fragiadakis M (eds) proceedings of 7th ECCOMAS thematic conference on computational methods in structural dynamics and earthquake engineering, COMPDYN 19, Hersonissos, Crete, Greece, 5254 - 5275, ISBN 978-618-82844-5-6, id. SCOPUS 2-s2.0-85079091857. <https://doi.org/10.7712/120119>, ISSN: 2623-3347
31. Salvatori A, Di Cicco A, Clemente P (2019) Seismic monitoring of base isolated buildings under low intensity earthquakes., In Proceedings of XVIII National Conference ANIDIS L'Ingegneria Sismica in Italia, SG13-2-SG13-14, Ascoli Piceno, Italy, ISBN 978-88-3339-256-1, ISSN 2532-120X
32. Salvatori A, Martelli A (2015) Safety evaluation of school located in historical buildings and correct application of seismic isolation. In: Proceedings of XVI National Conference ANIDIS L'Ingegneria Sismica in Italia, L'Aquila, Italy

Non-parametric Optimization Using Subspace-Based Objective Functions



Angelo Aloisio , Riccardo Cirella, Massimo Fragiacomò, and Rocco Alaggio

Abstract The tuning of structural models to the experimental dynamic response entails the choice of a proper objective function. The goal of the so-called model updating process is the optimization of the chosen objective function, which measures the discrepancy between the experimental and simulated dynamic responses. This research focuses on the application of a non-parametric subspace-based objective function to the estimation of the modelling parameters of a beam-like structure. Differently from parametric optimization, non-parametric objective functions do not require the assessment of the modal parameters and descend from direct manipulation of the experimental and simulated data. The use of parametric optimization may lead to the discard of important information, which could be lost when extracting the modal parameters. Conversely, non-parametric optimization may store valuable information, which may lead to the estimation of both the stiffness and mass matrices even in the case of operational response, characterized by unknown excitation. In a second step, the research focuses on the quantification of the uncertainty of the parameters following an elementary Bayesian approach. The authors attempt to estimate the probability density function of the parameters by isolating and quantifying two sources of uncertainties: the uncertainty of the structural model and that of the optimization method.

Keywords System Identification · Operational Modal Analysis · Uncertainty quantification · Discrete optimization · Finite Element model

1 Introduction

The optimization of structural models is a challenging task in structural engineering [6, 16, 20, 31]. However, the outcomes of the optimization may depend on the chosen objective function. Classical parametric optimization is based on the com-

A. Aloisio (✉) · R. Cirella · M. Fragiacomò · R. Alaggio
Università degli studi dell'Aquila, Via Giovanni Gronchi 18, 67100 L'Aquila, Italy
e-mail: angelo.aloisio1@graduate.univaq.it

parison between the experimental and simulated modal parameters [2, 4, 5, 10]. However, the extraction of the modal parameters may be associated with the discard of valuable information stored in the simulated or experimental dynamic response. The main drawback of parametric optimization is the indeterminacy of the estimation when assessing both the stiffness and mass matrix in so-called operational conditions. The operational modal analysis returns unscaled mode shapes, which cannot yield the estimate of both the elastic and inertial features of a structural model. The optimization problem would be ill-posed and would require the selection of either the inertia or elasticity as an unknown parameter. On the contrary, non-parametric objective functions, derived from the direct manipulation of the structural response to unknown excitation, but distinguished by known statistical properties (white noise excitation), may be used to determine the so-called complete modal model. In non-parametric optimization in operational conditions, the knowledge or assumption of the statistical properties of the exciting signal is the piece of information, lost in parametric optimization, which may help the scholar in estimating both the inertial and elastic features from the sole operational response of a structure.

There is substantial correspondence between the concept of damage detection and that of structural optimization [17, 19]. Damage detection is a process of identifying the presence of damage based on the use of a possibly scalar indicator, which synthetically compares the data corresponding to the reference or un-damaged state with those measured in the damaged state [25, 33]. However, the notion of structural damage may be viewed from a different perspective. A damage indicator measures the discrepancy between two sets of data: this is the same goal of an objective function, which maximizes the difference between the experimental and simulated structural response. Therefore, this paper presents the application of a scalar function, developed for damage detection purposes, in the field of structural optimization. A damage indicator has the quality to be susceptible to any discrepancy between two sets of data. The same property should be required for an objective function. Precisely, the authors chose a subspace-based function originated from a so-called robust metric [7, 8, 32]. The indicator, initially presented by Yan et al. [35], is the maximum singular value of the residual matrix, obtained by multiplying two matrices representative of the reference and damage state, respectively. Besides, the use of subspace-based metrics is growing popular in the field of structural health monitoring [12, 34, 36].

Any structural optimization should lead to an estimate of the reliability of the parameters [3, 8, 18, 23, 29]. There are diverse and numerous sources of uncertainties which may compromise the reliability of the optimization [30]. The authors attempt to determine the bias of the estimates due to the structural model and the optimization method. Accurately, the uncertainty of the model may encompass most of the limits of a structural optimization: the model may be inadequate or oversimplified. The modelling choices affect the final estimates and should be isolated and quantified [3, 9]. Additionally, the selection of the objective function may contribute to the reliability of the forecast. A basin-like shape of the objective function can be associated with higher reliability, compared to an almost flat shape function with several local minima.

The current paper has two primary purposes. The first is the testing of a subspace-based objective function in non-parametric optimization for the estimate of the inertial and elasticity parameters of beam-like structures in operational conditions. The second is the assessment of the uncertainties of the model and the optimization process, by estimating the probability density function of the parameters using an elementary application of the Bayes' theorem.

The first part of the paper presents the mathematical details of the optimization and the evaluation of the uncertainties. The second part details the application of the method to an experimental suspended beam. Specifically, as a first task, the authors investigate the performance of the chosen objective function in a numerical case. Then, they detail the experimental application and discuss some concluding remarks.

2 Optimization Problem: A Subspace-Based Formulation of the Objective Function

State-space representation of output-only measured vibration data corresponds to the following discrete time model [28]

$$\begin{aligned} x_{k+1} &= Ax_k + v_k \\ y_k &= Cx_k + w_k \end{aligned} \quad (1)$$

with the states $x_k \in R^n$, the outputs $y_k \in R^r$, the state transition matrix $A \in R^{n \times n}$ and the observation matrix $C \in R^{r \times n}$, where r is the number of sensors and n is the system order. The excitation v_k is an unmeasured Gaussian white noise sequence with zero mean and constant covariance matrix $Q = E(v_k v_k^T) Q \delta(k - k')$, where $E(\cdot)$ denotes the expectation operator and w_k is the measurement noise. Several scholars [13, 14] proposed a residual function to detect changes in the dynamic response of a structural system using the measurements y_k . The considered residual originates from the covariance-driven output-only subspace identification algorithm. Let $G = E(x_{k+1} y_k^T)$ be the cross-covariance between the states and the outputs, $\Lambda_i = E(y_k y_{k-i}^T) = CA^{i-1}G$ be the theoretical output covariances, and

$$H_{p+1,q} \begin{bmatrix} \Lambda_1 & \Lambda_2 & \dots & \Lambda_q \\ \Lambda_2 & \Lambda_3 & \dots & \Lambda_{q+1} \\ \vdots & \vdots & \ddots & \vdots \\ \Lambda_{p+1} & \Lambda_{p+2} & \dots & \Lambda_{p+q} \end{bmatrix} = Hank(\Lambda_i) \quad (2)$$

the theoretic block Hankel matrix. Using measured data $(y_k)_{k=1,\dots,n}$, a consistent estimate $\hat{H}_{p+1,q}$ is obtained from the empirical output covariances

$$\hat{\Lambda}_i = \frac{1}{N} \sum_{k=1}^n y_k y_{k-i}^T \quad (3)$$

$$\hat{H}_{p+1,q} = \text{Hank}(\hat{\Lambda}_i) \quad (4)$$

The residual function, originally proposed by [13, 14], compares the system undamaged or reference state with the damaged or current one. Let U_1 be the matrix of the left singular vectors obtained from an SVD of $H_{p+1,q}$. U_1 is a matrix with orthonormal columns and can be used to build a residual function that is robust to changes in the excitation covariance. The robust residual matrix can be written as

$$R_r = \hat{S}_0^T U_1^T \quad (5)$$

where \hat{S}_0^T is the left null space of the block Hankel matrix $\hat{H}_{p+1,q}$ in the reference state.

Following [35], a subspace-based objective function may be defined as an arbitrary scalar function of the residual matrix.

$$I_{y,r} = \text{norm}(R_r) \quad (6)$$

where *norm* picks the maximum singular value of a matrix. The nomenclature of $I_{y,r}$ descends from the initial of the scholar name and the robustness property of the metric.

In structural dynamics, the optimization of a structural model entails the definition of an objective function (\mathcal{C}), which compares the simulated (\mathbf{D}_s) and experimental data (\mathbf{D}_e).

$$\mathcal{C}(\boldsymbol{\theta}) = f(\mathbf{D}_s, \mathbf{D}_e) : \boldsymbol{\theta} \subset \mathbb{R}^{N_\theta} \rightarrow \mathbb{R} \quad (7)$$

where $\boldsymbol{\theta}$ is the set of the estimand parameters. In this paper, the objective function is the subspace-based indicator:

$$\mathcal{C} = I_{y,r} \quad (8)$$

3 Estimation of the Bayesian Uncertainty of the Model

The proposed procedure leads to the estimation of two sources of uncertainties. The first aims at quantifying the reliability of the model. The second quantifies the confidence in the outcomes of the optimization problem, by assuming the predictive capacity of the numerical model.

The first gives information about the model reliability, the second about the quality of the optimization, given the numerical model. As the last task, the authors combine the two uncertainties by estimating the posterior probability density function of the

parameters, scaled by the reliability of the model. The entire estimation process descends from an elementary application of the Bayesian theorem [11].

3.1 Mathematical Formulation

The general formulation of the Bayes theorem is:

$$p(\hat{C}|\hat{\theta}) = \frac{p(\hat{\theta}|\hat{C})p(\hat{C})}{p(\hat{\theta})} \tag{9}$$

where $\hat{\theta}$ represents the values of the optimum parameters, \hat{C} is the optimum value of the cost function. Three main terms can be identified in the Bayes theorem the prior probability density function (PDF) of the cost function can be written as:

$$p(\hat{C}) = \text{Half-normal}(\mu = 0, \sigma^2 = \sigma_C^2) \tag{10}$$

where \hat{C} is the optimum value of the cost function, μ and σ are the expected value and the standard deviation of the Half-normal distribution, and σ_C^2 is the variance of the cost function estimated from the sampled values of C in the chosen domain of the unknown parameters.

The likelihood PDF is:

$$p(\hat{\theta}|\hat{C}) = \text{Half-normal}(\mu = \hat{C}, \sigma^2 = \sigma_C^2) \tag{11}$$

where $\hat{\theta}$ is the vector of optimum parameters corresponding to the minimum value of the cost function \hat{C} , while σ_C^2 is the variance of the cost function. The normalization factor, ensuring that the posterior PDF integrates to 1, may have the following definition:

$$p(\hat{\theta}) = \int_{-\infty}^{+\infty} p(\hat{\theta}|\hat{C})p(\hat{C})dC \tag{12}$$

The reliability $\beta_{\mathcal{M}}$ of the model \mathcal{M} may be the integral of the posterior PDF:

$$\beta_{\mathcal{M}} = \int_{-\infty}^{+\infty} p(\hat{C}|\hat{\theta})dC \tag{13}$$

3.2 Discussion

The estimation of the uncertainty stems from an essential consideration. The optimum/minimum value of the objective function is intrinsically a measure of the reliability of the model. If $\hat{C} \rightarrow 0$, the discrepancy between the experimental and simulated data tends to vanish: in that case, the structural model almost mirrors the experimental data. If the minimum value increases, a sort of bias, related to the structural model, affects the agreement between the two sets of data: \hat{C} can be an indirect estimate of the bias of the model. Accurately, the reliability can be a scalar indicator, possibly derived from the probability distribution of the \hat{C} given the values of the parameters θ . According to the Bayesian inference, the prior probability can be the PDF of \mathcal{C} with maximum value in 0 and dispersion obtained from the standard deviation of the sampled values of the objective function. It represents the PDF of \hat{C} associated with the best matching between the model and the experiment. Whereas, the likelihood function is the PDF of the sampled objective function: the PDF derives from a suitable fitting of the data with maximum value in \hat{C} and the same variance of the prior. The normalization factor is the crucial term: it is estimated by ensuring that the likelihood and the prior integrates to one when both their maximum value is 0. It means that the reliability of the model $\beta_{\mathcal{M}}$, which is the integral of the posterior, is one when the maximum value of the likelihood is null. Otherwise, it decreases as \hat{C} grows.

In the mathematical formulation, the authors used a half-normal distribution. This choice depends on the pieces of evidence described in the following sections, where this PDF exhibits a satisfactory fitting capability.

4 Uncertainty of the Parameters from the Optimization

The results of model updating may depend on the choice of the objective function. It follows that the selection of the objective function is associated with a specific source of uncertainty.

In this section, the authors attempt to describe the uncertainty of the parameters due to the choice of the objective function in term of a PDF using the Bayes theorem.

In several cases, the parameters to optimize may be described by Gaussian PDFs. Theoretically, the use of Gaussian distributions can be inaccurate due to definition of the PDF in the negative range, where several parameters have no physical meaning: negative elastic moduli, or negative mass per unit of volume.

Still, Gaussian distributions are commonly used from the Standards to the research papers [26]: in many applications, the variance of the distribution is never so large to have significant values of the PDF in the negative axis. The elastic modulus of concrete, for instance, which has a higher scatter to that of steel, yields nearly zero values of the PDF approximating the origin of the axis. This simple example aims at endorsing the choice of the Gaussian distribution as a possible and first-attempt

candidate PDF to represent the distribution of some mechanical parameters (elastic modulus, e.g.).

The following mathematical derivations refer to Gaussian distributions, but the procedure is valid for any PDF, which seizes the statistical scattering of the unknown parameters.

4.1 Mathematical Formulation

The general formulation of the Bayes theorem is:

$$p(\boldsymbol{\theta}|\mathcal{C}, \mathcal{M}) = \frac{p(\mathcal{C}|\boldsymbol{\theta}, \mathcal{M})p(\boldsymbol{\theta}|\mathcal{M})}{p(\mathcal{C}|\mathcal{M})} \quad (14)$$

where $\boldsymbol{\theta}$ represents the hypotheses to be tested, e.g., the values of the model parameters, \mathcal{C} collects the sampled values of the objective function, and \mathcal{M} represents structural model. Three main terms can be identified in the Bayes theorem: $p(\boldsymbol{\theta}|\mathcal{M})$ is the prior probability density function (PDF) of the parameters, $p(\boldsymbol{\theta}|\mathcal{C}, \mathcal{M})$ is the posterior PDF, $p(\mathcal{C}|\boldsymbol{\theta}, \mathcal{M})$ is the likelihood function of the \mathcal{C} . Finally, the term $p(\mathcal{C}|\mathcal{M})$ at the denominator is a normalization factor ensuring that the posterior PDF integrates to 1.

4.1.1 Prior Probability

The prior PDF for the model parameters $\boldsymbol{\theta}$ were assumed to be independent Gaussian PDFs with mean $\boldsymbol{\theta}_n \in \mathbb{R}^{N_\theta}$ and covariance matrix $\boldsymbol{\Sigma}_{\theta_n} \in \mathbb{R}^{N_\theta \times N_\theta}$:

$$p(\boldsymbol{\theta}|\mathcal{M}) = \frac{1}{\sqrt{(2\pi)^{N_\theta} |\boldsymbol{\Sigma}_{\theta_n}|}} \exp \left[-\frac{1}{2} (\boldsymbol{\theta} - \boldsymbol{\theta}_n)^T \boldsymbol{\Sigma}_{\theta_n}^{-1} (\boldsymbol{\theta} - \boldsymbol{\theta}_n) \right] \quad (15)$$

The mean values and variances of the parameters can derive from acknowledged formulations (National Standards, e.g.) given the initial pieces of information about the structure.

4.1.2 Likelihood Probability

The likelihood function of the \mathcal{C} expresses the error of the estimates. It mirrors the agreement between experimental data and the outputs of a structural model: hence, according to standard formulations of the error function, the authors chose a Gaussian

probability model:

$$p(\mathcal{C}|\boldsymbol{\theta}, \mathcal{M}) = \frac{1}{\sqrt{(2\pi)^{N_\theta} |\boldsymbol{\Sigma}_{\hat{\boldsymbol{\theta}}}|}} \exp \left[-\frac{1}{2} (\boldsymbol{\theta} - \hat{\boldsymbol{\theta}})^T \boldsymbol{\Sigma}_{\hat{\boldsymbol{\theta}}}^{-1} (\boldsymbol{\theta} - \hat{\boldsymbol{\theta}}) \right] \quad (16)$$

where $\hat{\boldsymbol{\theta}} \in \mathbb{R}^{N_\theta}$ is the vector of the optimum parameters, and $\boldsymbol{\Sigma}_{\hat{\boldsymbol{\theta}}} \in \mathbb{R}^{N_\theta \times N_\theta}$ is the corresponding covariance matrix of the estimates.

The covariance matrix of the parameters $\boldsymbol{\Sigma}_{\hat{\boldsymbol{\theta}}}$ descends from the variance of the objective function. An estimate of the variance of $\hat{\boldsymbol{\theta}}$, $\boldsymbol{\Sigma}_{\hat{\boldsymbol{\theta}}}$, can be obtained by approximating the objective function to a first-order Taylor expansion:

$$\mathcal{C}(\boldsymbol{\theta}) \approx \mathcal{C}(\hat{\boldsymbol{\theta}}) + \mathbf{J}\boldsymbol{\theta} \quad (17)$$

where \mathbf{J} is the Jacobian matrix, collecting the approximations of the 1st order partial derivatives of $\mathcal{C}(\boldsymbol{\theta})$ with respect to $\boldsymbol{\theta}$ evaluated at $\hat{\boldsymbol{\theta}}$. Thus, the variance propagation of Eq.(17) can be written as

$$\sigma_c^2 = \mathbf{J}\boldsymbol{\Sigma}_{\hat{\boldsymbol{\theta}}}\mathbf{J}^T \quad (18)$$

where σ_c is the variance of the objective function evaluated at $\hat{\boldsymbol{\theta}}$. The inverse problem of estimating $\boldsymbol{\Sigma}_{\hat{\boldsymbol{\theta}}}$ given σ_c can be solved by computing the Moore–Penrose inverse of \mathbf{J} :

$$\boldsymbol{\Sigma}_{\hat{\boldsymbol{\theta}}} = \mathbf{J}^\dagger \sigma_c^2 (\mathbf{J}^\dagger)^T \quad (19)$$

4.1.3 Posterior Probability

The posterior probability distribution is proportional to:

$$p(\boldsymbol{\theta}|\mathcal{C}, \mathcal{M}) \propto \frac{1}{(2\pi)^{N_\theta} \sqrt{|\boldsymbol{\Sigma}_{\hat{\boldsymbol{\theta}}}| |\boldsymbol{\Sigma}_{\boldsymbol{\theta}_n}|}} \times \exp \left[-\frac{1}{2} \left((\boldsymbol{\theta} - \hat{\boldsymbol{\theta}})^T \boldsymbol{\Sigma}_{\hat{\boldsymbol{\theta}}}^{-1} (\boldsymbol{\theta} - \hat{\boldsymbol{\theta}}) - (\boldsymbol{\theta} - \boldsymbol{\theta}_n)^T \boldsymbol{\Sigma}_{\boldsymbol{\theta}_n}^{-1} (\boldsymbol{\theta} - \boldsymbol{\theta}_n) \right) \right] \quad (20)$$

The posterior distribution must integrate to one. By rearranging the expression, the posterior distribution can be written as a multivariate normal distribution:

$$p(\boldsymbol{\theta}|\mathcal{C}, \mathcal{M}) = \frac{1}{\sqrt{(2\pi)^{N_\theta} |\boldsymbol{\Sigma}_{\boldsymbol{\theta}}|}} \exp \left[-\frac{1}{2} (\boldsymbol{\theta} - \boldsymbol{\theta}^*)^T \boldsymbol{\Sigma}_{\boldsymbol{\theta}}^{-1} (\boldsymbol{\theta} - \boldsymbol{\theta}^*) \right] \quad (21)$$

where the mean is $\boldsymbol{\theta}^* = (\boldsymbol{\Sigma}_{\hat{\boldsymbol{\theta}}}^{-1} - \boldsymbol{\Sigma}_{\boldsymbol{\theta}_n}^{-1})^{-1} (\boldsymbol{\Sigma}_{\hat{\boldsymbol{\theta}}}^{-1} \hat{\boldsymbol{\theta}} - \boldsymbol{\Sigma}_{\boldsymbol{\theta}_n}^{-1} \boldsymbol{\theta}_n)$ and the covariance matrix $\boldsymbol{\Sigma}_{\boldsymbol{\theta}}^{-1} = (\boldsymbol{\Sigma}_{\hat{\boldsymbol{\theta}}}^{-1} - \boldsymbol{\Sigma}_{\boldsymbol{\theta}_n}^{-1})$.

4.2 Discussion

Equation(21) is the posterior PDF of the parameters based on the outcomes of the analyses \mathcal{C} and the chosen structural model \mathcal{M} . The assumption of the structural model is explicit in all terms of the Bayes' theorem: it means that the formulation does not express any judgment of confidence about the model, the model is always given. Accordingly, Eq.(21) determines the PDF of the parameters obtained from the sampled values of the cost function.

The sampled values of the objective functions may carry other sources of uncertainties, like aleatory uncertainties from the experimental data, not just the uncertainties due to the choice of the objective function. Nevertheless, the sampled values of the objective function may be representatives of all uncertainties related to the optimization process, excluded the uncertainty of the model. That is the reason why the authors named this section: "uncertainty of the parameters from optimization". The sampled values of the objective function comprise the uncertainties of the whole optimization process, from the experimental uncertainty to that of the objective function.

A significant aspect of the Bayesian updating is the choice of the prior PDF [21]. In many cases, the scholar roughly knows the values of the updating parameters and wants to estimate them with accuracy from the experimental data. The choice of an informative PDF depends on the eventuality that the scholar approximately knows the ranging values of the unknown parameters.

However, in the case of continuous dynamic monitoring, the information from experimental data should dominate that from the prior, based on personal expertise, scientific literature or Standards. The presented Bayesian formulation can be replicated in a sequence of updating steps, where the posterior PDF becomes a prior PDF in the subsequent step. As the number of updating rounds grows, the initial information of the first prior PDF vanishes, overwhelmed by the new data streaming from the monitoring system.

In this monitoring outlook [1, 24], the choice between an informative or noninformative prior may be in influent. Still, in isolated dynamic identification campaigns, where the experimental data may refer to a few hours of acquisitions, the choice of a suitable prior PDF may be decisive.

Further, the objective function is linearized in the proximity of the optimum value to propagate the uncertainty to the parameters. The use of a first-order Taylor series expansion is a simplification. The scholar can choose diverse and more accurate methods for variance propagation. The presentation focuses on the discussion of a method, and the approach followed for variance propagation can be considered secondary for the paper.

5 Uncertainty of the Parameters

The ultimate product of the propagation of uncertainty is the PDF of the parameters inclusive of the uncertainty of the model: $p(\boldsymbol{\theta}|\mathcal{C}, \mathcal{M}) \rightarrow p(\boldsymbol{\theta}|\mathcal{C})$. The confidence in the model is interpreted by a sort of reliability index.

Following a standard approach in structural engineering, safety factors divide the values of the mechanical parameters and multiply the effects of the load. Safety factors descend from the selection of reliability targets and have a direct effect on design inequality.

By analogy, the reliability of the model $\beta_{\mathcal{M}}$ scales the PDF of the parameters from the optimization process. $\beta_{\mathcal{M}}$ reduces confidence in the parameters.

$$p(\boldsymbol{\theta}|\mathcal{C}) = \beta_{\mathcal{M}} \frac{1}{\sqrt{(2\pi)^{N_{\theta}} |\boldsymbol{\Sigma}_{\theta}|}} \exp \left[-\frac{1}{2} (\boldsymbol{\theta} - \boldsymbol{\theta}^*)^T \boldsymbol{\Sigma}_{\theta}^{-1} (\boldsymbol{\theta} - \boldsymbol{\theta}^*) \right] \quad (22)$$

As a consequence the following integral would be:

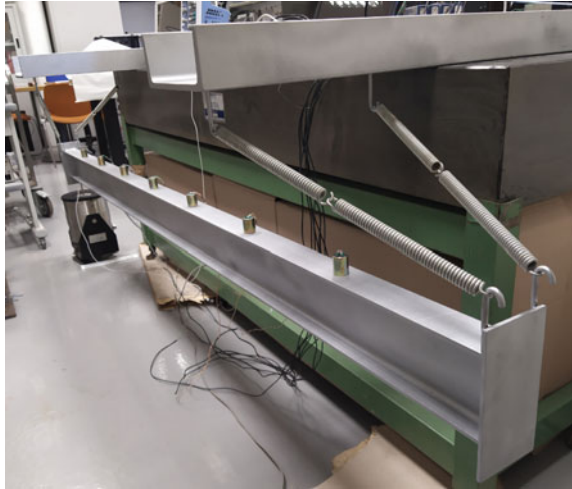
$$\int_{-\infty}^{+\infty} p(\boldsymbol{\theta}|\mathcal{C}) d\boldsymbol{\theta} = \beta_{\mathcal{M}} \quad (23)$$

It means that the cumulative density function of $\boldsymbol{\theta}$ would never converge to 1, due to the intrinsic, systematic bias of the structural model. The scholar can never have full confidence in the results due to the limits of the structural model.

6 Introduction to Tests and Preliminary Numerical Analyses

The authors apply the non-parametric subspace-based objective function to the identification of the elastic modulus and mass density of a suspended steel beam. Accurately, the objective function descends from the comparison between the experimental and simulated data. The experimental data are fixed and act as reference data—The numerical data change in each iteration by sampling a different couple of elastic modulus and mass density for the simulation of the time-history.

In the first step, a fully numerical analysis proves the validity of the approach. In the second step, the reference data are experimental. This section details the numerical analysis. However, the next paragraph describes the experimental setup, which gives essential information about the modelled structure and the experimental validation.

Fig. 1 Experimental setup

6.1 Experimental Setup

The structure considered in the numerical and experimental tests is a steel IPE120 beam, 2.5m long, with welded rectangular endplates 200mm \times 100mm \times 5mm. Two springs per side suspend the beam (Fig. 1).

The data acquisition system consists of seven vertical velocimeters, equidistant on the beam and aligned along its longitudinal axis. The input signal is white noise in the frequency band 0–1000 Hz applied by an electrodynamic shaker in correspondence of the left corner of the beam.

7 Numerical Analyses

A plane finite element model attempts to describe the dynamic response of the experimental beam. The model consists of eight frame-like shear-deformable finite elements [15], identified by the positions of the sensors on the real structure.

A white noise vertical displacement is the input signal applied to node 1. The output signals obtained from the model are the seven vertical velocities of the nodes corresponding to the positions of the seven velocimeters placed over the experimental beam. The authors chose a 1% damping ratio for all the modes involved in the analysis based on the results of the experimental dynamic identification.

Figures 2-3 depict the values of the objective function in the following ranges of the parameters $E \in \{100,000 - 350,000\}$ and $\rho \in \{10,000 - 200,000\}$ with the sampling intervals $dE = 1000$ $d\rho = 10$. The calculations of the objective function have been repeated a two thousand times in each couple E - ρ , and Fig. 3 depicts the

Fig. 2 Variation of the objective function in the chosen domain of the parameters. The white cross marks the couple of absolute minimum in \hat{C}

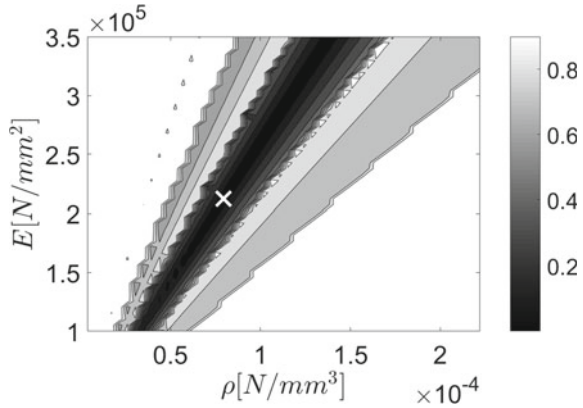
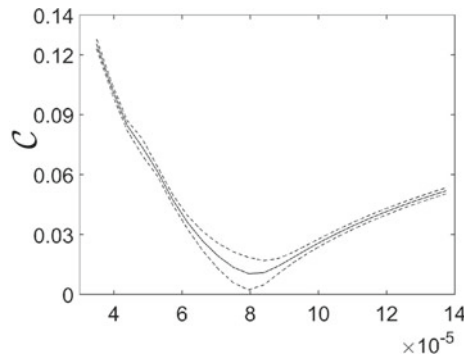


Fig. 3 Section along the direction with lower values of the objective function



averaged surface. The white cross marks the position of the optimum point, which corresponds precisely to the values adopted for the simulation of the reference data: $\hat{E} = 210,000$ and $\hat{\rho} = 78,500$.

The objective function has a peculiar V-like shape, with an area of lower values in the E - ρ plane substantially aligned. The alignment depends on the growing indeterminacy of the optimization problem when the dynamic system is characterized by the same ratio between the elastic modulus and the mass density, which is associated with the same set of possible natural frequencies. Still, the optimum point, as evidenced by the figure beside, is global—the figure shows the cross-section of the contour plot in the E - ρ plane. Additionally, the two dotted lines represent the upper and lower bounds of the averaged values corresponding to $\pm\sigma_C$, which is the variance of the sampled values of C . The variance originates from the use of different white noise inputs, generated in Matlab. In this example, the averaged optimum value and variance of \hat{C} are 0.00103 and 0.0041, respectively.

The objective function exhibited a global minimum, where expected, due to the additional information stored in the residual matrix and lost when extracting the modal parameters: the time-history carries the information about the statistical property of the input signal, a white noise.

This evidence could be understood from the following qualitative explanation. Let us consider the infinite couples of parameters characterized by the same E to ρ ratios and lower values of the objective function. This set of parameters comprises the optimum one, \hat{E} and $\hat{\rho}$. The dynamic systems described by these parameters have the same modal parameters, in term of natural frequencies and mode shapes. Still, the geometry of the Finite Element beam is the same in all the tested cases. The propagation of the excitation from one side of the beam, where the excitation source is independent on the E to ρ ratio in the Euler-Bernoulli theory.

The main restrictions of the Euler-Bernoulli theory are: plane cross-sections, initially perpendicular to the axis of the beam, remain plane and perpendicular to the neutral axis during bending, the neglect of the effects of the rotational inertia. The Timoshenko and Rayleigh theories extend the Euler-Bernoulli theory to the effects of shear deformation and rotational inertia, respectively. While the dispersion curve of the Euler-Bernoulli theory is dependent on the E to ρ ratios, the exact, Rayleigh and Timoshenko theories exhibit an explicit dependence of the phase velocity on E [22].

Therefore, the pulse propagation in a beam depends explicitly on E , according to the Timoshenko theory used in the FE simulation. The recorded signals have a memory of the time needed for a specific random impulse to propagate and bounce inside the beam. The residual matrix carries this information, and the minimum of the objective function stands where there is the optimum cause-effect correspondence. In the experimental and numerical beams, the phase velocity depends explicitly on E , thus making determinate the optimization problem. Essentially, the same beams with all possible and identical E to ρ ratios have a determinate dispersion law for wave propagation which characterize their dynamic response.

The authors are giving a qualitative illustration of a phenomenon, which should deserve a rigorous mathematical formulation. Still, they hope that these results represent a step forward in the estimation of complete modal models from the operational modal analysis.

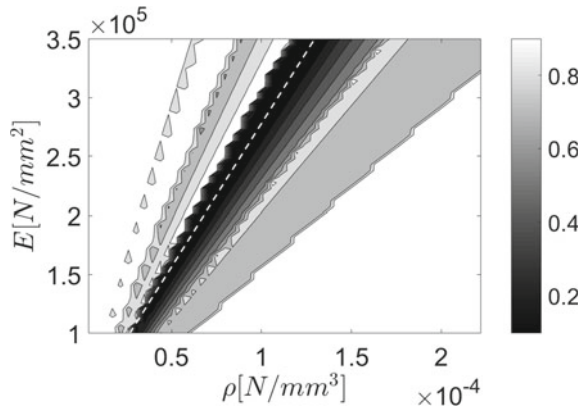
8 Experimental Validation

This section details the experimental validation: the objective function compares two sets of data, the experimental ones from the suspended beam and the simulated ones obtained from the FE model. The experimental modal parameters represent valuable data for the further validation of the dynamic system corresponding to the optimum point. The authors detail the experimental modal parameters, which are then compared to the numerical ones.

Table 1 Beam parameters, frequencies and damping ratios of the first three flexural modes from modal identification, with their 2σ uncertainty bounds

$E_{\text{exp}} \cdot 10^5$ (MPa)	$\rho_{\text{exp}} \cdot 10^{-5}$ (N/mm ³)	$f_{\text{exp},1}$ (Hz)	$f_{\text{exp},2}$ (Hz)	$f_{\text{exp},3}$ (Hz)	$\xi_{\text{exp},1}$ (%)	$\xi_{\text{exp},2}$	$\xi_{\text{exp},3}$ (%)
2.10	7.95	127.3±0.005	337.6±0.010	625.7±0.007	1.28±0.37	1.08±0.49	0.126±0.11

Fig. 4 Variation of the objective function over the selected range of values for parameters E and ρ in the experimental tests



8.1 Modal Identification Results

The SSI-cov algorithm [27] is used to estimate the natural frequencies, the damping ratios, and the mode shapes of the steel beam from the acquired signals. In the frequency range 0–1000 Hz, there are three rigid modes, followed by the three deformational modes described in Table 1. Accurately, Tab. 1 details the elastic modulus declared from the producer and the mass density obtained by simple weighing. The following columns report the experimental natural frequencies and damping ratios with their confidence bounds estimated according to [30].

The deformational mode shapes correspond to the first three mode shapes of a suspended beam-like structure.

8.2 Parametric Identification Results

The contour plot in Fig. 5 is quite similar to that obtained from fully numerical simulations. There is a region of lower values characterized by the same E to ρ ratios. Still, the method finds a minimum point close to the expected values of the estimand parameters. However, the section curve of the contour plot (Fig. 4) in Fig. 5 is not as determinate as in the numerical simulations in Fig. 3. The slope of the curve, after the optimum point, is lower, compared to that in the numerical case.

Fig. 5 Mean values of the objective function along the section of lower values

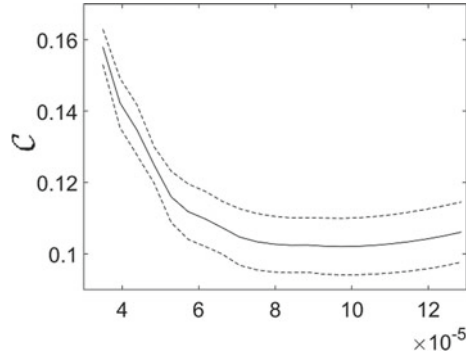


Table 2 Experimental case: identified parameters and discrepancies with measured values

\hat{E} (MPa)	$\hat{\rho}$ (N/mm^3)	\hat{C} (MPa)	$E_{exp} \cdot 10^5$ (MPa)	$\rho_{exp} \cdot 10^{-5}$ (N/mm^3)	ΔE (%)	$\Delta \rho$ (%)
$2.19 \cdot 10^5 \pm 379.60$	$7.62 \cdot 10^{-5} \pm 3.80 \cdot 10^{-17}$	0.109	2.10	7.925	4.19	-3.81

Table 3 Numerical frequencies obtained after the identification procedure and comparison with the experimental ones

f_1 (Hz)	$f_{exp,1}$ (Hz)	Δf_1 (%)	f_2 (Hz)	$f_{exp,2}$ (Hz)	Δf_2 (%)	f_3 (Hz)	$f_{exp,3}$ (Hz)	Δf_3 (%)
126.6	127.3	-0.55	336.1	337.6	-0.44	625.4	625.7	$-4.8 \cdot 10^{-6}$

A remarkable aspect regards the value of the minimum point of the objective function (0.1090), which is higher than that obtained from the entirely numerical simulations (0.0103). The variance is higher too, as manifested in the respective pictures Figs. 3b and 5b. The minimum value of the objective function quantifies the discrepancy between the responses of the real and simulated systems.

Indirectly, the \hat{C} value reveals the limits of the mathematical model.

Table 2, which reports the values of the optimum couple $(\hat{E}, \hat{\rho})$, makes a comparison with the experimental parameters and prove the substantial accordance with the expected values.

Additionally, Tables 3 and 4 compares the optimum numerical model with the experimental one in term of natural frequencies and mode shapes, respectively.

The main difference between the experimental and numerical sections stand in the limits of the numerical model, which may carry the most considerable amount of uncertainty in the optimization method. The next section evaluates the uncertainty of the parameters by estimating the PDF of θ scaled by the reliability factor of the model $\beta_{\mathcal{M}}$.

Table 4 MAC matrix, calculated between numerical and experimental modes

MAC	I_{num}	II_{num}	III_{num}
I_{exp}	0.9969	4.048e-04	0.2889
II_{exp}	3.014e-04	0.9980	8.896e-08
III_{exp}	0.2509	4.384e-04	0.9945

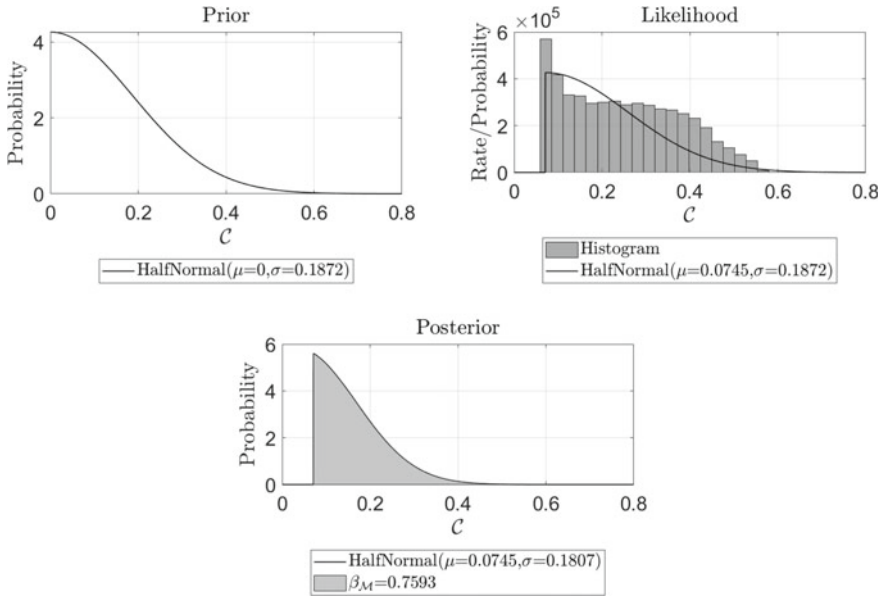


Fig. 6 Prior, likelihood and posterior PDF of C according to the formulations in Eqs.(9)-(13), respectively

9 Uncertainty Quantification

The reliability index of the model originates from the evaluation of the integral of the posterior PDF of C . Figure 6 depicts the prior, likelihood and posterior PDF of C . Namely, the prior PDF has the maximum value in 0 and identifies the best correspondence between the experimental and numerical data. The variance of the prior is the same as the experiment: the prior PDF mirrors the occurrence of an optimum correspondence between the experimental and numerical data by the optimum point. The likelihood PDF follows the scatter of the experimental data: the authors chose a half-normal distribution to achieve good accordance with the shape of the histogram plot of the sampled values of C .

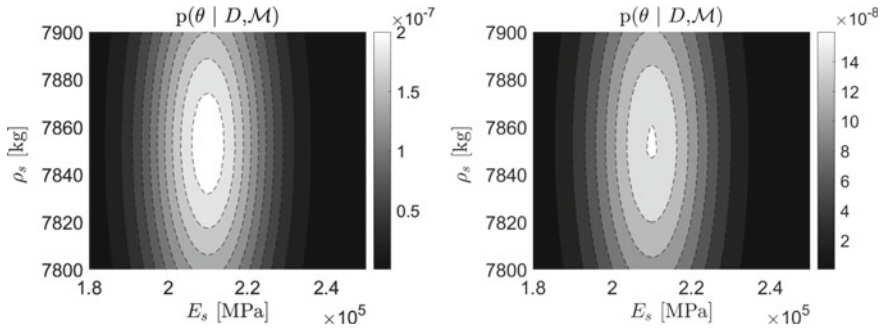


Fig. 7 Posterior PDF of the estimand parameters exclusive of the uncertainty of the model; Posterior PDF of the estimand parameters inclusive of the uncertainty of the model

The maximum point of the likelihood corresponds to the optimum value of the objective function. The distribution of the sampled values of \mathcal{C} determines a concentration of values by the optimum point, where the function has a lower slope. The rate of incidence of the parameters decreases when attaining higher values due to the increasing slope of the interpolating function of the sampled \mathcal{C} . The posterior, obtained by multiplying the prior and the likelihood does not integrate to one. The normalization factor makes the posterior integrates to one only when the likelihood has a maximum in 0, i.e. there is a perfect agreement between the physical and mathematical model. The integral of the posterior yields 0.793: it likely measures the reliability of the chosen FE model. The reliability index scales the PDF of the parameters, as illustrated in Fig. 7, where the left picture represents the posterior PDF exclusive of the model uncertainties. In contrast, the right picture comprises the confidence of the scholar in the chosen mathematical model.

10 Conclusions

The paper presents an application of a subspace-based objective function for the parametric identification of structural models. Differently from classical optimization driven by mode shapes and natural frequencies, the choice of a nonparametric objective function may yield determinate optimization problem even when estimating the inertial and elastic parameters in operational conditions. The selected objective function successfully estimated the elastic modulus and mass density of a suspended beam. Additionally, the paper focuses on the estimation of the uncertainty of the estimates, significantly affected by the bias on the numerical model. The Bayes' theorem yields the model reliability and the uncertainty of the parameters due to the optimization process. Future researches will aim at the mathematical formulation of the optimization of both the inertial and elastic parameters in operational conditions, by revealing the role of the objective function in obtaining a determinate

problem. Furthermore, the authors aim at integrating the estimation of the uncertainty inside the optimization process, thus obtaining a so-called Bayesian updating method, which seeks the optimum value of a posterior probability distribution, rather than the minimum of an objective function.

References

1. Alaggio R, Aloisio A, Antonacci E, Cirella R (2020) Two-years static and dynamic monitoring of the santa maria di collemaggio basilica. *Constr Build Mater* 121069
2. Aloisio A, Alaggio R, Fragiaco M. Bending stiffness identification of simply supported girders using an instrumented vehicle: full scale tests, sensitivity analysis, and discussion. *J Bridge Eng* 26(1): 04020115
3. Aloisio A, Alaggio R, Fragiaco M (2019) Dynamic identification of a masonry façade from seismic response data based on an elementary ordinary least squares approach. *Eng Struct* 197
4. Aloisio A, Alaggio R, Fragiaco M (2020) Dynamic identification and model updating of full-scale concrete box girders based on the experimental torsional response. *Constr Build Mater* 264
5. Aloisio A, Alaggio R, Fragiaco M (2020) Time-domain identification of the elastic modulus of simply supported box girders under moving loads: method and full-scale validation. *Eng Struct* 215
6. Aloisio A, Capanna I, Cirella R, Alaggio R, Di Fabio F, Fragiaco M (2020) Identification and model update of the dynamic properties of the san silvestro belfry in l'aquila and estimation of bell's dynamic actions. *Appl Sci* 10(12):4289
7. Aloisio A, Di Battista L, Alaggio R, Fragiaco M (2020) Sensitivity analysis of subspace-based damage indicators under changes in ambient excitation covariance, severity and location of damage. *Eng Struct* 208
8. Aloisio A, Di Pasquale A, Alaggio R, Fragiaco M (2020) Assessment of seismic retrofitting interventions of a masonry palace using operational modal analysis. *Int J Archit Heritage* 1–13
9. Aloisio A, Fragiaco M (2021) Reliability-based overstrength factors of cross-laminated timber shear walls for seismic design. *Eng Struct* 228
10. Aloisio A, Pasca D, Tomasi R, Fragiaco M (2020) Dynamic identification and model updating of an eight-storey clt building. *Eng Struct* 213
11. Aloisio A, Pasca DP, Alaggio R, Fragiaco M (2020) Bayesian estimate of the elastic modulus of concrete box girders from dynamic identification: a statistical framework for the a24 motorway in italy. In: *Structure and infrastructure engineering*, pp 1–13
12. Balmes E, Basseville M, Mevel L, Nasser H, Zhou W (2008) Statistical model-based damage localization: a combined subspace-based and substructuring approach. *Struct Control Health Monit: Official J Int Associ Struct Control Monit Eur Assoc Control Struct* 15(6):857–875
13. Basseville M, Abdelghani M, Benveniste A (2000) Subspace-based fault detection algorithms for vibration monitoring. *Automatica* 36(1):101–109
14. Basseville M, Mevel L, Goursat M (2004) Statistical model-based damage detection and localization: subspace-based residuals and damage-to-noise sensitivity ratios. *J Sound Vibration* 275(3–5):769–794
15. Bathe KJ, Wilson EL (1976) *Numerical methods in finite element analysis*. Prentice-Hall, No. BOOK
16. Cheung SH, Beck JL (2009) Bayesian model updating using hybrid monte carlo simulation with application to structural dynamic models with many uncertain parameters. *J Eng Mech* 135(4):243–255
17. De Cock K, De Moor B (2002) Subspace angles between arma models. *Syst Control Lett* 46(4):265–270

18. Der Kiureghian A, Ditlevsen O (2009) Aleatory or epistemic? does it matter? *Struct Safety* 31(2):105–112
19. Döhler M, Mevel L, Hille F (2014) Subspace-based damage detection under changes in the ambient excitation statistics. *Mech Syst Signal Process* 45(1):207–224
20. Friswell M, Mottershead JE (2013) *Finite element model updating in structural dynamics*, vol 38. Springer Science & Business Media
21. Gelman A, Carlin JB, Stern HS, Dunson DB, Vehtari A, Rubin DB (2013) *Bayesian data analysis*. CRC Press, Boca Raton
22. Graff KF (2012) *Wave motion in elastic solids*. Courier Corporation
23. Hofer E, Kloos M, Krzykacz-Hausmann B, Peschke J, Woltereck M (2002) An approximate epistemic uncertainty analysis approach in the presence of epistemic and aleatory uncertainties. *Reliab Eng Syst Safety* 77(3):229–238
24. Kita A, Cavalagli N, Ubertini F (2019) Temperature effects on static and dynamic behavior of Consoli palace in Gubbio, Italy. *Mech Syst Signal Process* 120:180–202
25. Long L, Döhler M, Thöns S (2020) Determination of structural and damage detection system influencing parameters on the value of information. In: *Structural health monitoring*, p 1475921719900918
26. Mustafa S, Matsumoto Y (2017) Bayesian model updating and its limitations for detecting local damage of an existing truss bridge. *J Bridge Eng* 22(7):04017019
27. Peeters B, De Roeck G (2000) Reference based stochastic subspace identification in civil engineering. *Inverse Prob Eng* 8(1):47–74
28. Rainieri C, Fabbrocino G (2014) *Operational modal analysis of civil engineering structures*. Springer, New York, pp 142–143
29. Rao KD, Kushwaha H, Verma AK, Srividya A (2007) Quantification of epistemic and aleatory uncertainties in level-1 probabilistic safety assessment studies. *Reliab Eng Syst Safety* 92(7):947–956
30. Reynders E, Pintelon R, De Roeck G (2008) Uncertainty bounds on modal parameters obtained from stochastic subspace identification. *Mech Syst Signal Process* 22(4):948–969
31. Sehgal S, Kumar H (2016) Structural dynamic model updating techniques: a state of the art review. *Arch Comput Methods Eng* 23(3):515–533
32. Shokravi H, Shokravi H, Bakhary N, Heidarrezaei M, Rahimian Koloor SS, Petru M (2020) Application of the subspace-based methods in health monitoring of civil structures: a systematic review and meta-analysis. *Appl Sci* 10(10):3607
33. Thöns S, Döhler M, Long L (2018) On damage detection system information for structural systems. *Struct Eng Int* 28(3):255–268
34. Wu WH, Wang SW, Chen CC, Lai G (2016) Application of stochastic subspace identification for stay cables with an alternative stabilization diagram and hierarchical sifting process. *Struct Control Health Monit* 23(9):1194–1213
35. Yan AM, Golinval JC (2006) Null subspace-based damage detection of structures using vibration measurements. *Mech Syst Signal Process* 20(3):611–626
36. Yang XM, Yi TH, Qu CX, Li HN, Liu H (2020) Continuous tracking of bridge modal parameters based on subspace correlations. *Struct Control Health Monit* 27(10)

Slope Stability Assessment of the Test Site in Pagani (Campania, Southern Italy)



Antonio Santo, Marianna Pirone, Giovanni Forte, Melania De Falco, and Gianfranco Urciuoli

Abstract Flowslides are rainfall-induced events initiating with the shear failure at a depth of few meters or less, which downslope increase in volume for avalanche effect and velocity. Unfortunately, Campania Region (Southern Italy) has been historically affected by such events. They represent a relevant hazard for the structures and the infrastructures located at foothills. Predisposing conditions for flowslide initiation are related to the current values of soil water content and matric suction into the subsoil. These parameters, if correctly monitored, can represent a valuable tool for the definition of early warning strategies against these phenomena. This paper reports preliminary results on the test site set up in Pagani (SA). Its position is strategic, as it is upslope of the highway connecting Naples to Salerno in an area affected by historical events respectively occurred in 1960, 1972 and 1997; the latter reached the highway and killed two people. Topographic survey of the area has been performed with a UAV, while stratigraphic and geotechnical characterization in both field and laboratory were carried out. Here the stratigraphic setting of the site and the preliminary geotechnical soil properties are reported. Finally, soil stability has been assessed through the infinite slope model; here, the variation in the safety factor (SF) as a function of the slope angle and of different suction scenarios is shown. These results permit to identify the most critical conditions and the most dangerous areas, where flowslide triggering could occur and, thus, affect the highway downslope.

Keywords Flowslides · Unsaturated soils · Slope stability · Campania region

1 Introduction

In Campania Region (Southern Italy), flowslides are recurrent phenomena; they involve the failure of unsaturated cohesionless soils, consisting of sand or volcanic ashes laying on a carbonate, volcanic or flysch bedrock [1, 2]. They represent a relevant hazard for the structures and the infrastructures located at foothills due to the

A. Santo · M. Pirone · G. Forte (✉) · M. De Falco · G. Urciuoli
DICEA, Dipartimento d'Ingegneria Civile, Edile e Ambientale, Università Degli Studi di Napoli Federico II, Napoli, Italy
e-mail: giovanni.forte@unina.it

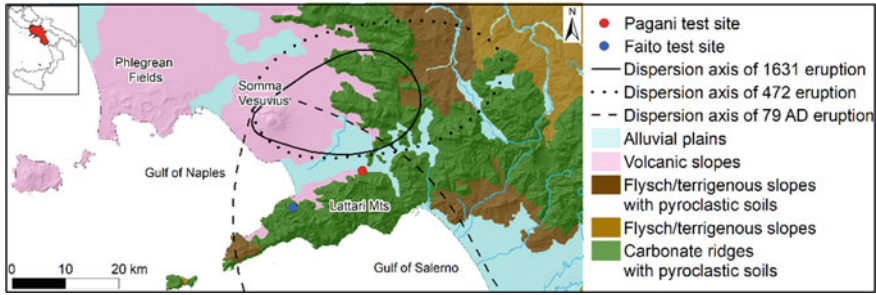


Fig. 1 Geological setting of the Lattari Mts. with ashfall dispersion axes

downslope increase in volume, due to avalanche effect, and velocity. Pyroclastic soils in Campania have been mainly deposited by the explosive eruptions of Phlaegrean Fields and Somma-Vesuvius. The latter had dispersion axis of almost all fall deposits oriented eastward, but those ejected during the famous 79 A.D. Pompei eruption were conveyed to South mantling the Lattari Mts., as shown in Fig. 1. Observations on past flowslide events in Campania have clearly shown that the trigger is influenced by local predisposing slope conditions, which can vary within a wide range, resulting in several unfavorable combinations [3–5]. In particular, the onset can be influenced by (i) local geomorphological and topographical factors, whether natural or anthropogenic, such as fault scarps and road cuts, (ii) stratigraphic features, such as the presence of finer soil layers at the bottom, (iii) hydrogeological features, such as groundwater flow and presence of springs. Several researches on this topic have also shown that these soils are partially saturated even in the winter period and the failure occurs in correspondence of critical rainfall events that increases the saturation degree, thus decreasing matric suction and shear strength. Therefore in situ monitoring of rainfall, suction and water content in the subsoil may be used to investigate seasonal effects in the groundwater regime, thus, the Safety Factor of the slope [6–11]. In this framework, an experimental site in Pagani (SA) has been chosen to study the effect of variations of matric suction and volumetric water content in the pyroclastic cover on the slope stability. The site chosen will be instrumented by tensiometers, soil moisture probes and weather station to monitor hourly matric suction, hourly soil water content and meteorological data. In this paper, stratigraphy and preliminary geotechnical characterization of the experimental site of Pagani (SA) will be described together with results of stability analyses of the test site, modelled as infinite slope.

2 The Test Site in Pagani (SA)

This study is part of the GRISIS project, which represents a multidisciplinary research aimed at assessing structures and infrastructures safety against natural hazards. The

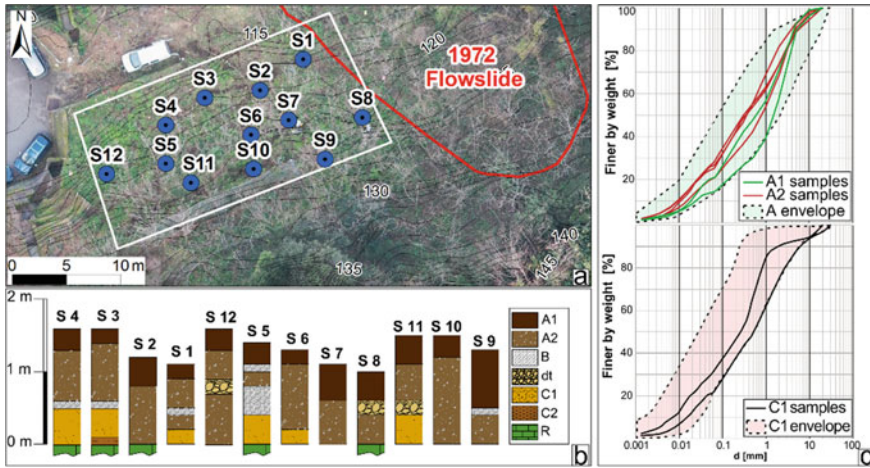


Fig. 2 a Location of the boreholes in the test site (white boundary) and perimeter of a historical flowslide crown (red line). b Stratigraphic logs. c. Grain-size curves for soils A1, A2 and C1 with the envelopes of the other samples collected on Lattari Mts

setup of an experimental field is a relevant asset for the Project that is devoted to define mitigation strategies useful for unstable slope that may affect regional infrastructures. The site chosen is in Pagani municipality (SA) as reported in Fig. 1. It is located on the northern-eastern edge of the slope of Lattari Mts. Its position is strategic, as it is upslope of a relevant highway and close to historical flowslides respectively occurred in 1960, 1972 and 1997; the latter reached the highway and killed two people. Site characterization was preceded by a detailed topographical survey carried out by UAV, which permitted to reconstruct high resolution DTM and orthophoto (Fig. 2a). Stratigraphic characterization of the soil cover was carried out with 12 hand-made boreholes less than 2 m depth, which corresponds to the depth of carbonate bedrock. At the same time, 8 undisturbed soil samples for geotechnical laboratory testing were collected. The stratigraphic and geotechnical characterization is discussed in next session (Sect. 2.1). All these data have been adopted to reconstruct the geological subsoil model necessary to carry out slope stability analyses with the infinite slope approach. The variation of the safety factor (SF) as a function of the slope angle and the suction scenario is reported in the last part (Sect. 3).

2.1 Stratigraphic and Geotechnical Characterization

The test site occupies an area of 350 m² (Fig. 2a), several stratigraphic logs were bored (Fig. 2b) and some grain-size curves were obtained (Fig. 2c). The soil cover is made of a pyroclastic succession of several fall deposits, laying on a carbonate bedrock. Bottom upward, the succession is made of a thin (20 cm) reddish-brown ash (C2

Table 1 Summary of the geotechnical parameters of the investigated soils for Lattari Mts (after [4])

Soil	γ (kN/m ³)	C' (kPa)	ϕ' (°)	e (–)	n (–)
A1	16.2	0.0	38.4	1.57	0.61
A2	14.8	0.0	38.4	2.65	0.73
B	10.0	0.0	41.0	–	0.80
C1	15.5	0.0	35.4	1.94	0.66
C2	18.8	5.0	35.0	0.87	0.47

silty-sand) with a clayey fraction of an ancient Phlaegrean eruption (pre-79 A.D.). Its upper part is made of an ash layer made of yellowish silty sands (C1) 20–50 cm thick. These horizons are unevenly overlaid by carbonate debris (Dt) or by a layer of coarse (2–4 cm in diameter) ungraded white pumices, in a thin sandy pyroclastic matrix (B). The latter is the basal fallout of the 79 A.D. eruption. The succession continues with an ash layer made of brown silty sands rich in pumices (A2), whose thickness is around 30–130 cm. The pumices belong to the volcanic eruptions of the 79 A.D. and to those occurred in 472 and 1631. However, these latter layers are 10 cm thick and discontinuous, hence they were not sampled. The uppermost layer is made of an ash affected by the action of microorganisms and vegetation (A1). Its thickness spans from 20 to 80 cm, with a mean value around 35 cm. Figure 2c shows the grain-size curves obtained from soils sampled in Pagani; the results are contained in the envelopes of the pyroclastic soils of the whole Lattari Mts. reported by [4] and those of Faito Mt. test site. The geotechnical characterization of the undisturbed soil samples collected at the test site is currently ongoing. However, it is worth noting that the soils sampled in Mt. Faito are similar to those recognized at Pagani in terms of both geological (eruption and stratigraphy) and geotechnical features (grain size distribution). Hence, the same mechanical properties can be assumed, and they are summarized in Table 1.

3 Slope Stability Analyses

The stratigraphy of Pagani test site along with the geotechnical characterization available for the pyroclastic cover of Lattari Mts. (Table 1), permitted to calculate the safety factor (SF) according to the infinite slope modelling. In particular, the analyses were carried out considering the increase in strength due to fixed values of matric suction, assuming the slope as infinite and the hypothetical shear surfaces located at the bottom of each soil horizon. The S3 log reported in Fig. 2b, which crossed the whole stratigraphic sequence, was adopted as representative of the whole test site. Adopting the Mohr–Coulomb failure criterion and applying the limit equilibrium method, the safety factor (SF) for the Bishop effective stress criterion for infinite slope is given as:

$$SF = \frac{\tau_{lim}}{\tau} = \frac{c' + (S_r * s + \gamma * z * (\cos \alpha)^2) * \tan \phi'}{\gamma * z * \sin \alpha * \cos \alpha} \tag{1}$$

where c', ϕ' , and γ are reported in Table 1, s is the soil matric suction, z is the depth from soil surface of each horizon reported in the log S3 of Fig. 2b, α is the slope of the site taken from the DTM obtained from UAV survey. The degree of saturation, S_r ; is determined from mean soil porosity, n , and water content is read on Soil Water Retention curves available for the soils of Mt. Faito test site [8] (Fig. 1). Figure 3 shows the profile of the safety factor (SF) calculated for three typical values of slope observed at site, i.e. 32°, 36°, 42° and for typical values of matric suction occurring in the wet season [6, 11], in order to detect the failure conditions. All the three modelled scenarios identify the base of C1 as the depth of the critical failure surface (SF = 1). In the case of 32° slope, the failure can only occur with positive pore water pressure. Increasing the slope at 36°, at the same value of soil friction angle of C1 soil, the failure is verified for null suction. In fact, assuming both suction and effective cohesion as null, Eq. (1) reduces to:

$$SF = \frac{\tau_{lim}}{\tau} = \frac{\cos \alpha * \tan \phi'}{\sin \alpha} = \frac{\tan \phi'}{\tan \alpha} \tag{2}$$

and at slope, α , equal to the soil friction angle, ϕ' , SF is 1. Then, with the highest slope value (42°), the failure occurs even in unsaturated soil conditions with a critical suction value identified at 3.2 kPa. Therefore, assuming the same geotechnical characterization, the values of suction that trigger flowslides in the infinite slope are affected by the soil slope angle. In the study area, the slope hit by past flowslides was higher than 36°, thus the failure occurred in partially saturated conditions or at null suction [11].

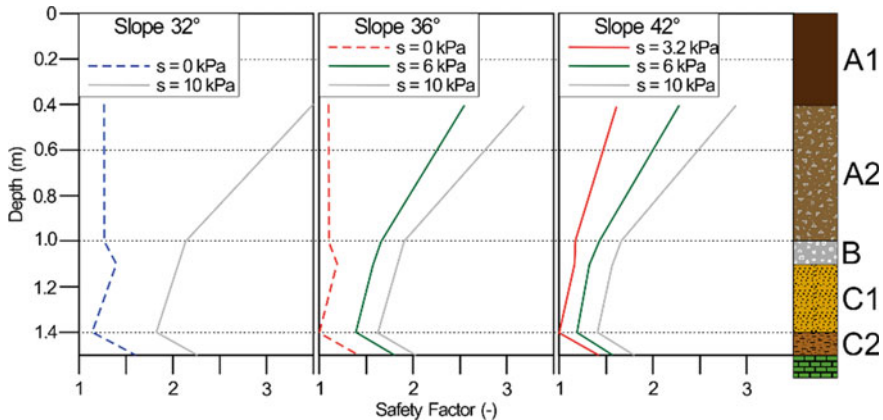
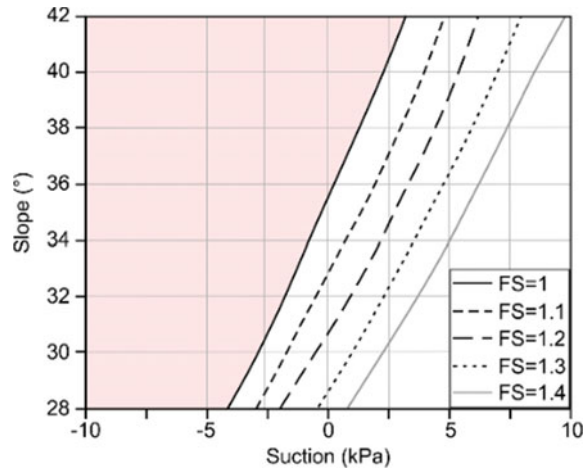


Fig. 3 Infinite slope stability analyses carried out for critical slope values and suction scenarios

Fig. 4 Safety Factor calculated at 1.40 m from the ground surface as function of suction on the sliding surface and slope angle (soil C1)



These results agree to those found out in other unsaturated pyroclastic slopes of Campania region [11, 12]. In Fig. 4 it is reported a chart containing the suction at 1.40 m (depth of layer C1) from the ground surface as a function of the slope angle of the infinite slope monitored at Pagani for fixed SFs (1.0–1.1–1.2–1.3–1.4). This chart proves that the condition $SF = 1$ occurs in correspondence of positive pore pressures for slope angles lower than 36° . Conversely, in steeper slopes, the instability can occur even in unsaturated conditions.

4 Conclusions

In this work, stability analyses assuming the infinite slope model point out that failure mechanisms in unsaturated shallow pyroclastic cover can be due to the drop of suction on slopes of 36° and 42° , while for lower slope angle (32°), the failure occurs with positive pore water pressure. These findings agree with those obtained at other unsaturated pyroclastic slopes in Campania region. Results highlight the relevant role of suction and soil water content in flowslide triggering because of rainfalls and infiltration. Hence, the automatic and continuous monitoring of these parameters represents an asset to forecast slope failure for developing early warning strategies against these phenomena.

Acknowledgements This work is supported by the GRISIS project (Cup:B63D18000280007, Surf:18033BP000000001, DD prot. 368 24/10/2018), implemented by STRESS scarl in the framework of FESR Campania 2014-2020. Società Autostrade Meridionali Spa is also acknowledged for the realization of the test site.

References

1. Santo A, Di Crescenzo G, Forte G, Papa R, Pirone M, Urciuoli G (2018) Flow-type landslides in pyroclastic soils on flysch bedrock in southern Italy: the Bosco de' Preti case study. *Landslides* 15:63–82. <https://doi.org/10.1007/s10346-017-0854-3>
2. Picarelli L, Olivares L, Damiano E, Darban R, Santo A (2020) The effects of extreme precipitations on landslide hazard in the pyroclastic deposits of Campania region: a review. *Landslides* 17:2343–2358
3. Di Crescenzo G, Santo A (2005) Debris slides—rapid earth flows in the carbonate massifs of the Campania region (Southern Italy): morphological and morphometric data for evaluating triggering susceptibility. *Geomorphology* 66(1–4):255–276
4. Forte G, Pirone M, Santo A, Nicotera MV, Urciuoli G (2019) Triggering and predisposing factors for flow-like landslides in pyroclastic soils: the case study of the Lattari Mts. (Southern Italy). *Eng Geol* 257: 105137
5. Guadagno FM, Martino S, Scarascia Mugnozza G (2003) Influence of man-made cuts on the stability of pyroclastic covers (Campania, Southern Italy): a numerical modelling approach. *Environ Geol* 43:371–384
6. Damiano E, Olivares L, Picarelli L (2012) Steep-slope monitoring in unsaturated pyroclastic soils. *Eng Geol* 1–12:137–138
7. Pirone M, Papa R, Nicotera MV, Urciuoli G (2015) Soil water balance in an unsaturated pyroclastic slope for evaluation of soil hydraulic behaviour and boundary conditions. *J Hydrol* 528:63–83. <https://doi.org/10.1016/j.jhydrol.2015.06.005>
8. Balzano B, Tarantino A, Nicotera MV, Forte G, De Falco M, Santo A (2018) Building physically-based model for rainfall-induced shallow landslide from geological survey and geotechnical investigation: the case study of the Sorrento Peninsula (Italy). *Can Geotech J* 56(9):1291–1303. <https://doi.org/10.1139/cgj-2017-0611>
9. Di Maio R, De Paola C, Forte G, Piegari E, Pirone M, Santo A, Urciuoli G (2020) An integrated geological, geotechnical and geophysical approach to identify predisposing factors for flowslide occurrence. *Eng Geol* 267: 105473
10. Pirone M, Papa R, Nicotera MV, Urciuoli G (2016) Hydraulic behaviour of unsaturated pyroclastic soil observed at different scales. *Proc Eng* 158:182–187
11. Pirone M, Papa R, Nicotera MV, Urciuoli G (2016) Analysis of Safety Factor in unsaturated pyroclastic slope. *Landslides and engineered slopes. Experience Theor Pract* 3: 1647–1654
12. Olivares L, Picarelli L (2003) Shallow flowslides triggered by intense rainfalls on natural slopes covered by loose unsaturated pyroclastic soils. *Geotechnique* 53(2):283–287

Use of a Roving Vision Sensor Setup to Train an Autoencoder for Damage Detection of Bridge Structures



Darragh Lydon, Myra Lydon, Juliana Early, and Su Taylor

Abstract This paper will demonstrate a solution for detecting damage to a bridge structure from measured displacements gathered using a roving vision sensor based approach. The measurement of displacement was accomplished using a synchronised multi-camera vision-based displacement measurement system. Displacement measurements can provide a valuable insight into the structural condition and service behaviour of bridges under live loading. Computer Vision systems have been validated as a means of displacement calculation, the research developed here is intended to form the basis of a real time damage detection system. This is done through the use of unsupervised deep learning methods for anomaly detection which could form the basis of a low cost durable alternative. The performance of the system was evaluated in a series of controlled laboratory tests. This research provides a means of detecting changes to a bridge structure through use of minimal sensor installation, reducing potential sources of error and allowing for potential live rating of bridge structures.

Keywords Computer Vision · Structural Health Monitoring · Anomaly Detection · Deep Learning

1 Introduction

The progressive deterioration of civil infrastructure is now of paramount concern to asset owners and users alike. Structural damage results in a change in the geometric or material properties of bridges which manifests through a change in stiffness or stability of the structure. Traditional bridge inspections are sensitive to human error and bias and can often result in over conservative assumptions on reduced load carrying capacity [1]. Structural Health Monitoring (SHM) systems provide a means of objectively capturing and quantifying this change under operational

D. Lydon (✉) · J. Early

School of Mechanical and Aeronautical Engineering, Queen's University Belfast, Belfast, UK
e-mail: D.Lydon@qub.ac.uk

M. Lydon · S. Taylor

School of Natural and Built Environment, Queen's University Belfast, Belfast, UK

conditions. The application of such systems has significant cost saving potential across the lifespan of bridge structures and can ensure the safe operation of our road and rail transport networks. With over one million bridges across Europe the task of assessing each structure often surpasses the available resources. This shortfall dramatically reduces the resilience of transport networks particularly considering 35% of Europe's rail bridges are over 100 years old [2]. The understanding of the true capacity of this aging infrastructure is now more critical than ever as in recent years the UK witnessed an increasing number of failure events in clusters of bridges such as those witnessed in Northern Ireland in 2017 and Yorkshire in 2019 [3, 4]. In response to this during the last two decades a significant amount of research has been dedicated to the development and enhancement of SHM systems for bridge monitoring. The challenge of accurately detecting and quantifying damage in civil infrastructure still exists globally and few systems have been deployed and verified on real bridges. Displacement measurements provide a valuable insight into the structural condition and service behaviour of structures under live loading. Displacement has been used as a metric for bridge condition rating in numerous studies outlined in the following section. Analysis of monitored displacement values over time can provide an insight in possible excessive loading or changes to structural behaviour, since displacement can be directly linked to structural stiffness and external loading. In a long term analysis (multiple years), the displacement responses can be used to create a pattern of structural response to temperature or vehicle loading, if measured responses display extreme variance from this pattern it could be surmised that there has been a change to the structural properties of the monitoring subject.

In [5], a displacement curve was used to detect damage to a cantilever beam structure. In [6], Zhang et al. used the displacement caused by a vehicle passing over a bridge structure as a modelling scenario for simulated damage detection.

This type of experiment, where the changes to the displacement curvature based on repeated passes by a vehicle established the methodology of the laboratory work described in this paper. A test setup by Catbas et al., where a bridge model is fully instrumented to determine displacement from a passing vehicle is laid out in [7]. This was developed upon in [8] where a series of Linear Variable Differential Transducers (LVDT) were used to detect damage under a roving sensor approach. The research presented below will further enhance the development of roving sensor systems for damage detection by replacing the cumbersome setup of the LVDT series with a system of time synchronised cameras for displacement measurement that was demonstrated by the authors in [9].

These studies all demonstrate the use of displacement measurements as a powerful means of assessing bridge condition through performance. The displacement measurements will be used as means for training an autoencoder [10], which is an unsupervised neural network frequently used for anomaly detection [11, 12]. An autoencoder consists of two parts, an encoder and a decoder. The encoder maps the input to a lower-dimensional space, and the decoder maps the encoded data back to the input. If an autoencoder is trained to recognize a certain type of input, in this case our baseline scenarios, any deviation from this output would have a high reconstruction error. This will be demonstrated in the following sections.

2 Methodology

A laboratory model study of a two-span bridge was developed in the Experimental Design and Monitoring (EDM) laboratory of Civil Infrastructure Technologies for Resilience and Safety (CITRS) at University of Central Florida (UCF). The bridge has two 300 cm main continuous spans supported by three steel frame sections as shown in Fig. 2. The bridge deck is 120 cm wide and 600 cm long of steel plate construction with the thickness of 3.18 mm. The steel deck is supported by two $25 \times 25 \times 3.2$ mm steel girders with the space of 0.61 m. The girders are denoted as A and B as illustrated in Fig. 1. The connection sets with four M6 bolts and 3.18-mm-thick plates are used to connect the girders and the deck. A small-scale toy truck is employed as the moving load on the bridge in this study.

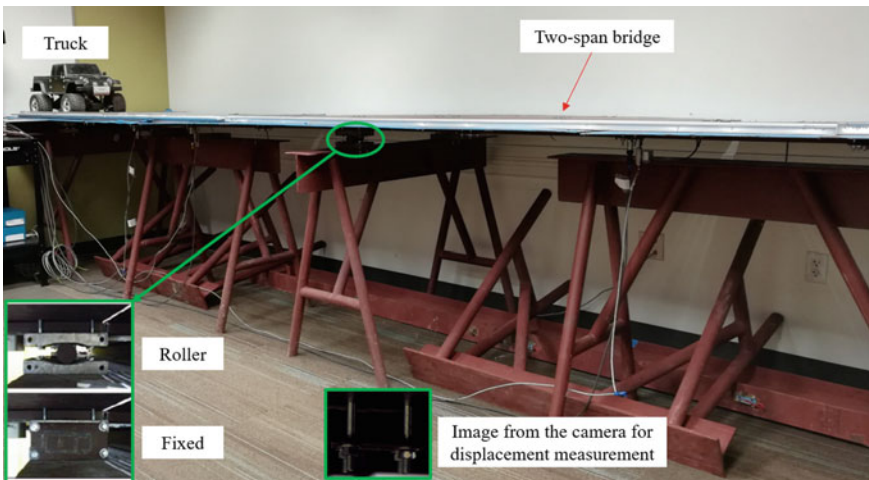


Fig. 1 Two span model bridge

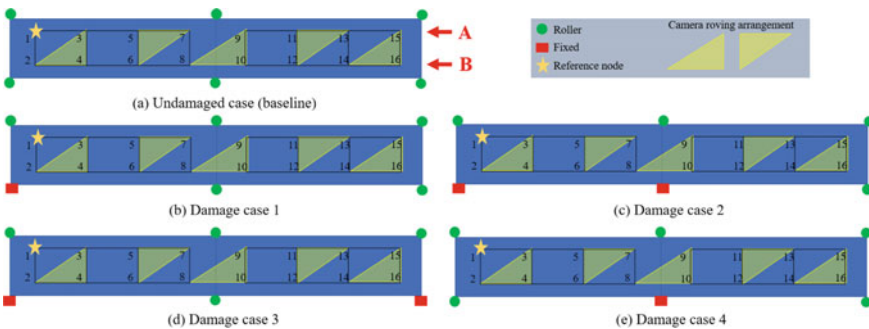


Fig. 2 Experimental cases and configurations

The supports of the bridge are varied during the experiment to simulate the change of boundary condition, replicating common real-life bridge conditions. The undamaged case, i.e., baseline, in this experiment is the case that all the supports are rollers. Four damage cases are designated by changing the supports of the Girder B. Two lanes were predefined on the deck: one was close to Girder A (lane 1) and the other was close to Girder B (lane 2). The truck ran on the lane 2 travelling longitudinally from left to right to simulate the moving load. Four cameras were employed to measure the displacements of the predefined measurement nodes on the girders, from 1 to 16, as shown in Fig. 2.

Each camera was set up using a fixed tripod to measure one node in each run, as such the measurement of all the nodes cannot be captured in one run. In the study, the cameras were roved to accommodate all the measurement nodes. As shown in Fig. 2, Node 1 was set as the reference node (Ref. Node) and it is measured in each run. The triangles in Fig. 2 represent the cameras used in each run in addition to the reference camera that remained fixed at Node 1. For Test 1, this indicates Nodes 2–4, Test 2 consists of Nodes 5–7 and so on until all nodes have been monitored. Vertical displacements of the Ref Node for the first crossing at no damage condition is shown in Fig. 3a.

The response pattern is similar to other nodes located on the left span. Vertical displacement histories of the nodes on the right span are opposite to the ones on the left support. When the vehicle is on the left span the right span lifts up, and vice versa. The raw response measurements contain both static component (bridge deflection) and dynamic component (bridge vibration induced by the vehicle). The static response can be isolated by processing the raw response with an adequate high-pass filter. The conversion of the response measurement from time domain to frequency domain reveals fundamental frequencies. The power spectrum density (PSD) plot is used to set a suitable high-pass filter. The lowest frequency component, which is 0.098 Hz, presents duration of the vehicle crossing. The crossing lasts approximately 10 s. The frequency range of the dynamic response is above 4 Hz (see Fig. 3b). Thus

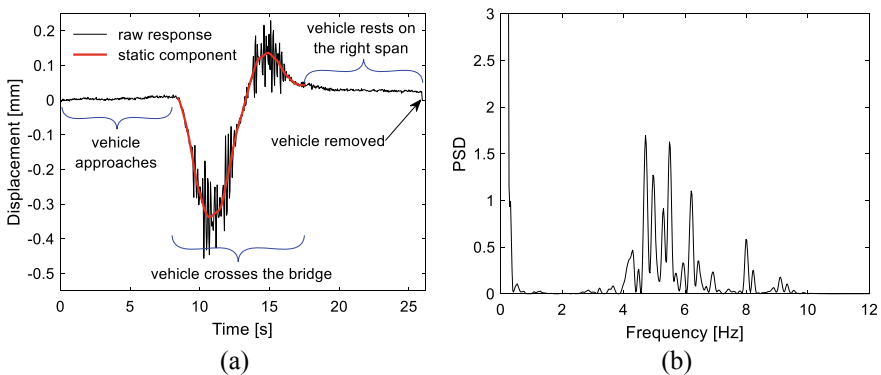


Fig. 3 Node 1 displacement time history (a) and its PSD plot (b)

Table 1 Results from Autoencoder predictions on Test Dataset

Scenario type	Predicted	Actual
Baseline	6401	6400
Damage	1499	1500

the high pass frequency is set to 1 Hz. The resulting signal is subtracted from the raw measurements leaving only the component of the static response. During the trials, it was not possible to ensure that all runs start and end at the same time. They also vary slightly in their duration. For these reasons, selecting the range of vertical displacements of each node as the damage factor (DF) is the best choice.

3 Results

The filtered displacement ranges were used as a basis for a 1-dimensional CNN autoencoder training dataset. This was done by using the variance between displacement ranges between runs 1–5 in the undamaged scenario as boundary conditions to generate displacement scenarios for all nodes on the bridge. This was repeated 50,000 times to make a dataset that encompassed “normal” behavior of the bridge. This was split into 45,000 training examples and 5000 validation examples. The 4 damage scenarios were also used as candidates for scenario generation in the test dataset, with 6500 “normal” scenarios and 1500 damaged scenarios generated. The autoencoder was then trained for 100 epochs with early stopping, the optimal loss was found after 63 epochs. A threshold for classification of undamaged vs damaged scenarios was then calculated by comparing the RMSE for the predictions on the test set and determining the optimal decision boundary. If the DF generated by the autoencoder from the supplied displacements was outside the boundary conditions determined in the training phase, the scenario was labeled as damaged. This method was successful at identifying damage was present, but was incapable of localizing where damage occurred on the structure. The results for the predictions from the trained autoencoder are shown in Table 1.

4 Conclusions and Future Work

As can be seen from the results, it is possible to use a roving sensor setup to establish a baseline scenario in which to detect changes to a bridge structure. This has shown that the sensor roving technique is viable as a means of data collection for vision based monitoring, which can lead to a reduction in monitoring costs for real life scenarios. The automated nature of the results analysis means that, if paired with an accurate method for load evaluation, real time damage detection can be implemented. The accuracy of the proposed system could also be improved by feeding in live data

in a continuous training methodology similar to the work in [13]. The next steps in this work are:

- Perform additional laboratory trials to obtain more undamaged scenario readings to validate that the boundary conditions set out in the initial runs are feasible. There are other scenarios which could also be explored, i.e. multiple vehicles, differing weights etc.
- Create less severe damage scenarios to determine the accuracy of the proposed system when damage is not at critical levels.
- Plan and execute field trials of the system to determine the accuracy of scenario measurement outside a controlled laboratory environment.

References

1. Phares BM, Washer GA, Rolander DD, Graybeal BA, Moore M (2004) Routine highway bridge inspection condition documentation accuracy and reliability. *J Bridg Eng* 9(4):403–413
2. Mainline (2013) Maintenance, renewal and improvement of rail transport infrastructure to reduce economic and environmental impacts. In: Deliverable D1.1: Benchmark of New Technologies to Extend the Life of Elderly Rail Infrastructure European Project, Luleå, Sweden, 7th, Sweden
3. BBC. Northern Ireland floods: More than 100 people rescued—BBC News
4. Telegraph. UK weather: Bridge collapses and roads washed away as flood warnings continue to midnight
5. Dworakowski Z, Kohut P, Gallina A, Holak K, Uhl T (2016) Vision-based algorithms for damage detection and localization in structural health monitoring. *Struct Control Heal Monit* 23(1):35–50
6. Zhang Y, Lie ST, Xiang Z (2013) Damage detection method based on operating deflection shape curvature extracted from dynamic response of a passing vehicle. *Mech Syst Signal Process* 35(1–2):238–254
7. Khuc T, Catbas FN (2018) Structural identification using computer vision-based bridge health monitoring. *J Struct Eng (United States)* 144(2):04017202
8. Celik O, Terrell T, Gul M, Necati Catbas F (2018) Sensor clustering technique for practical structural monitoring and maintenance. *Struct Monit Maint* 5(2): 273–295
9. Lydon D et al (2018) Development and field testing of a time-synchronized system for multi-point displacement calculation using low-cost wireless vision-based sensors. *IEEE Sens J* 18(23):9744–9754
10. Hinton GE, Salakhutdinov RR (2006) Reducing the dimensionality of data with neural networks. *Science (80-)* 313(5786): 504–507
11. Sakurada M, Yairi T (2014) Anomaly detection using autoencoders with nonlinear dimensionality reduction. In: *ACM international conference proceeding series*, vol 02, Dec 2014, pp 4–11
12. Zhou C, Paffenroth RC (2017) Anomaly detection with robust deep autoencoders. In: *Proceedings of the ACM SIGKDD international conference on knowledge discovery and data mining*, vol Part F129685, pp 665–674
13. Tonioni A, Tosi F, Poggi M, Mattoccia S, Di Stefano L (2019) Real-time self-adaptive deep stereo. In: *Proceedings of the IEEE computer society conference on computer vision and pattern recognition*, June 2019

An Advanced Approach to the Long Term SHM of Structures and Transport Infrastructures



Felice Carlo Ponzo, Chiara Iacovino, Rocco Ditommaso, Gianluca Auletta, Francesco Soldovieri, Manuela Bonano, and Vincenzo Cuomo

Abstract This work shows the preliminary monitoring results by applying in situ and remote sensing systems to a school building located in Ariccia (Rome), within the WP6 “Structural Health Monitoring and Satellite Data” 2019–21 Reluis Project. In particular, the use of the remote sensing Differential Interferometry Synthetic Aperture Radar (DInSAR) has provided a spatial map of the displacement of the investigated structure and the corresponding time-series with the aim of monitoring deformation phenomena, focusing on the local scale analysis, which produces suitable results for urban monitoring and damage assessment. The DInSAR results have been integrated with the identification of the dynamic characteristics of the structure. In-situ data was provided by the Seismic Observatory of Structures (OSS), a network of permanent seismic monitoring systems managed by the Italian Department of Civil Protection (DPC). Modal parameters were identified from the accelerometric responses recorded at several floors of the buildings. The integrated use of the two techniques has allowed to confirm the healthiness of the investigated structure, even in presence of several seismic events occurred in the area during the monitoring period. This case represents a good example about how the integration of in-situ sensors with remotely sensed data is a key factor for a sustainable structural and infrastructural monitoring and can support the planning of both maintenance and safety management.

F. C. Ponzo (✉) · C. Iacovino · R. Ditommaso · G. Auletta
School of Engineering, University of Basilicata, Viale dell’Ateneo Lucano 10, 85100 Potenza,
Italy

e-mail: felice.ponzo@unibas.it

R. Ditommaso

e-mail: r.ditommaso@unibas.it

F. Soldovieri · M. Bonano

Institute for Electromagnetic Sensing of the Environment (IREA), National Council of Research (CNR), Napoli, Italy

e-mail: soldovieri.f@irea.cnr.it

V. Cuomo

Institute of Methodologies for Environmental Analysis (IMAA), National Council of Research (CNR), Tito Scalo, Italy

Keywords Remote sensing · Synthetic aperture radar · Interferometry · Structural health monitoring · Transport infrastructures

1 Introduction

In the last years, the development of integrated systems for early warning, monitoring and quick damage assessment of the built environment and critical infrastructures, are gaining large interest [1, 2]. In fact, the integration is the key factor for achieving several aims such as:

-The development of a platform able to integrate different kind of sensing/diagnostics technologies (including new concept of operation, such as the citizen as a sensor and sensors no sensors) with Spatial Data infrastructure and ICT architectures;

- The capability to assimilate monitoring data and indicators coming from the sensing into civil engineering to assess the loss of performance of the structures. This is crucial to identify actions and strategies for an effective and economically sustainable management of the infrastructure;
- The possibility to couple current monitoring with early warning and quick damage assessment capabilities, driving and planning remedial solutions in crisis situations;
- The use of AI and Big Data for the monitoring and behavior prediction of the urban areas and embedding territory for the present status and future risk scenarios (climatic, pandemic, hydrogeological, seismic...).

Several examples of the exploitation of this approach are in [3, 4], where the focus was mainly of its suitability for the long-term monitoring of the transport infrastructure.

Anyway, in order to allow for the sustainability of such an integrated approach, it is crucial to design smart observational chains, which activate more sophisticated surveys, but only when necessary. An example of this chain is reported in [2, 3], where the first level of diagnostics has a low logistics impact and is able to provide outcomes over large scale and in a fast way. The results of the use of this level are used to decide if to activate more complex diagnostics stages focused on the detailed diagnostics of the structure (or of the single elements of it), by means of in-situ technologies, such as ground penetrating radar, infrared cameras, etc.

In this paper, we focus on the first stage of the observational chain, which combines the Interferometric Synthetic Aperture Radar (InSAR) and accelerometer based analysis for the monitoring of a strategic structure in Ariccia (Rome); this activity falls within the WP6 “Structural Health Monitoring and Satellite Data” 2019–21 Reluis Project.

About this first stage of observation, it provides information about: the long-term deformation status of the structure and of the surrounding soil; the frequencies of structural vibration and on their possible variation over time. Several studies

demonstrate the possibility to use changing in modal characteristics of a monitored structure to detect damages and criticalities on both structural and non-structural components (more information in [5–16]).

SAR data have been analyzed in partnership with “Consiglio Nazionale delle Ricerche, Istituto per il Rilevamento Elettromagnetico dell’Ambiente (IREA-CNR)”. In situ data have been provided by the Italian Civil Protection Department (DPC), through the Seismic Observatory of Structures (OSS) [17], a network of permanent seismic monitoring systems installed on public buildings, bridges and dams [18].

Moreover, this stage has been completed with a visual survey of the building and several ambient vibration measurements, which have been performed on October 2020, with the aim to evaluate the condition of the structure, assess any present or potential defects and identify possible anomalies.

2 Synthetic Aperture Radar

Remote sensing can provide valuable pieces of information thanks to its synoptic capability, in particular when the seismic event is located in remote regions, or the main communication systems are damaged [19]. The Synthetic Aperture Radar (SAR) is widely used for analyzing the surface displacements, uplifts and subsidence caused by earthquakes [20–23].

Research has been published regarding post-seismic building damage assessment performed by combining pre- and post-seismic images [24–26], using SAR simulations or combining radar and optical remote-sensing data [19, 27]. Satellite Differential SAR Interferometry (DInSAR) is one of the most innovative systems for ground and structures displacement monitoring in urban areas.

DInSAR is based on the exploitation of the phase difference (interferogram) between two temporally separated SAR images, thus retrieving information on the sensor Line of Sight (LOS) projection of the detected displacements occurred between the two acquisition times. Furthermore, the use of advanced DInSAR approaches [28–31], based on the exploitation of SAR acquisition sequences collected over large time spans, allows providing useful information on both the spatial and the temporal patterns of the detected displacements through the generation of time series, with centimeter to millimeter accuracy [32, 33]. The deformation time series are easily computed by searching for a least squares solution with a minimum norm energy constraint (the SVD technique is applied in presence of different data subsets separated by large baselines) [34].

The Differential SAR Interferometry technology allows to map and measure deformation phenomena due to both natural and man-made causes [35–37] with limited monitoring costs compared to the traditional in situ surveys [38]. Furthermore, this technique is a non-invasive tool to remotely detect, map and monitor deformation phenomena affecting urban areas by providing velocity maps and displacements time-series, for a large number of measurement points and long observation periods [39]. Remote sensing techniques have also demonstrated the capability to provide

valuable information on the displacements affecting single buildings [29]. Thanks to the ability to extend backwards the DInSAR investigations by exploiting the SAR data archives available since the early ERS-1 ESA mission in 1992, it can be possible to compare pre- with post-event conditions and contribute to the implementation of damage assessment analyses and to the evaluation of risk scenarios [40–42].

The multi-temporal SBAS-DInSAR technique allows investigating and mapping ground movements through the generation of mean deformation velocity maps and corresponding displacement time series [29, 34]. It relies on a proper selection of a large number of SAR image pairs characterized by short spatial and temporal separations (baseline) between the acquisition orbits, in order to mitigate decorrelation phenomena and to maximize the number of reliable SAR measure points [38]. Differently from other advanced multitemporal DInSAR techniques, the SBAS approach does not need any a-priori information on the investigated ground deformation phenomena, thus representing a valuable method to detect and measure non-linear LOS displacements over time. The SBAS-DInSAR technique is able to produce deformation maps of wide areas ($100 \text{ km} \times 100 \text{ km}$) with a ground spatial resolution ranging from about 30 to 100 m at regional scale [17]. At the local (full resolution) scale, the SBAS approach exploits single-look interferograms, generated at the full sensor spatial resolution (down to a few meters), to study local deformation that may affect buildings and man-made features [18, 32, 39]. The SBAS approach allows generating LOS displacement maps and associated time series spanning very long periods (decades), thus guaranteeing the continuity in the monitoring of the Earth's surface deformation phenomena, as well as providing unprecedented information for studying long-term ground movements at different spatial scales. At local scale, these measurements can contribute to the evaluation of the structural conditions of the constructions.

3 Description of the Test Case

The strategic building selected as a case study is the Elementary School “Bernini” (Fig. 1), located in Ariccia (Rome). This choice was also motivated by the fact that was monitored thanks to the Seismic Observatory of Structures (OSS) of the Italian Civil Protection Department.

The building, built in the 1950s, is a reinforced concrete framed structure with four floors and a flat roof. Adjacent to the structure there is a single-story building used as a library (Fig. 2).

The case study is included in the investigation area, covered by the COSMO-SkyMed satellite images provided by the Italian Space Agency (ASI) and processed by IREA-CNR through the SBAS-DInSAR technique. The municipality of Ariccia is included only in the dataset relating to the ascending orbit.

The monitoring system installed in the building consists of:



Fig. 1 The position of the elementary school “Bernini” in Ariccia (Rome)

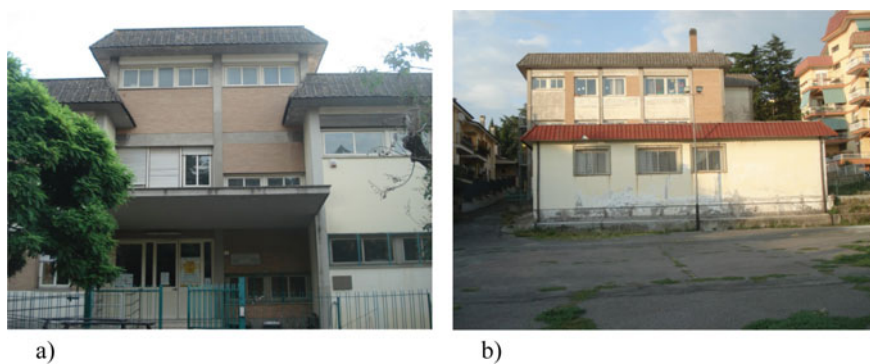


Fig. 2 **a** Front elevation and **b** rear elevation of the building

- n. 1 triaxial accelerometer;
- n. 6 biaxial accelerometer;
- n. 6 mono-axial accelerometers;
- n. 1 GPS receiver.

Figures 3, 4 and 5 show the sensors position and the measurements direction of the different recorders installed on the monitored structure.

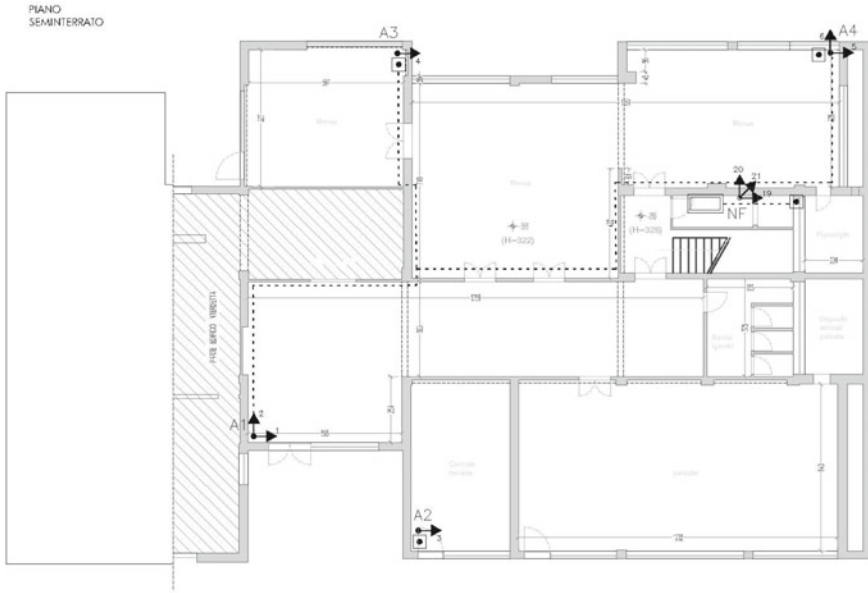


Fig. 3 Position of accelerometers placed at the basement floor



Fig. 4 Position of accelerometers placed at ground level

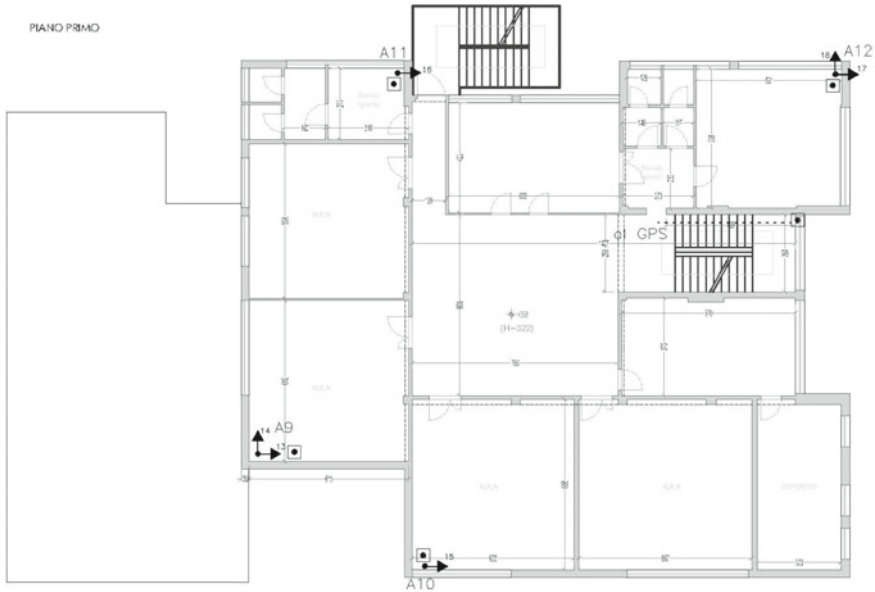


Fig. 5 Position of accelerometers placed at the first floor

4 Results

4.1 Remote Sensing Data

The multi-temporal SBAS-DInSAR technique [29, 34] allows investigating and mapping ground movements through the generation of mean deformation velocity maps and related displacement time series. It relies on a proper selection of a large number of SAR image pairs characterized by short spatial and temporal separations (baseline) between the acquisition orbits, in order to mitigate decorrelation phenomena [43], and to maximize the number of reliable SAR measure points.

IREA-CNR provided datasheets including several unique pixel identifiers for which several parameters are defined, namely: latitude; longitude; topography; mean deformation velocity; interferometric temporal coherence (a value between 0 and 1); components of Line of Sight (LOS) unit vector along the North, East, Vertical directions; LOS displacement Time Series (TS).

The available data were analyzed in a GIS software and categorized according to mean deformation velocity. After, several measurement points were selected on the investigated structure and their displacement time series have been analyzed.

Figures 6 and 7 show the deformation mean velocity map of the area under investigation embedding the structure and the single structure, i.e., the elementary school “Bernini”, respectively.

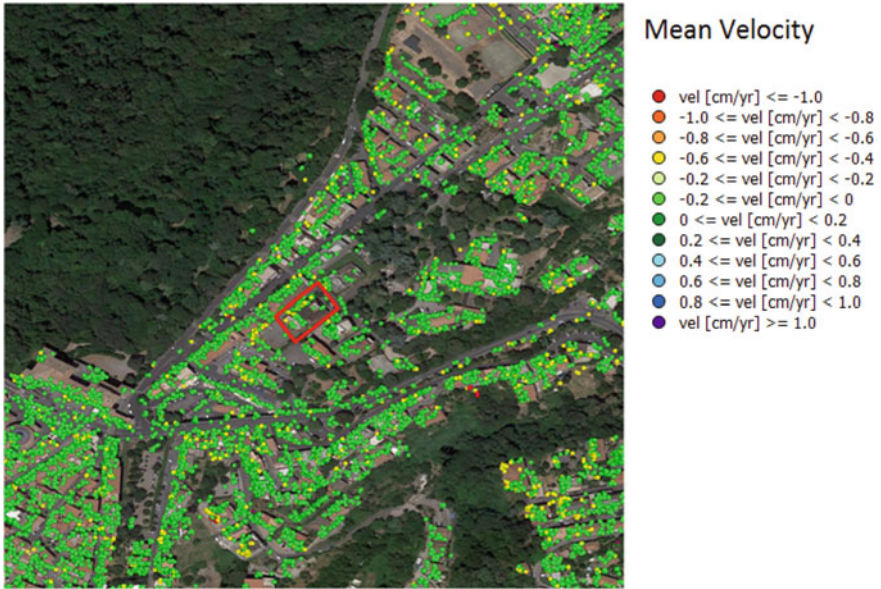


Fig. 6 Deformation velocity map of the study area



Fig. 7 Deformation velocity map of the study building

The following figures show the displacement time-series relevant to several measure points located on the elementary school and highlighted in Fig. 8.

Preliminary analyses of the interferometric data show low values of displacements on the line of sight except with a maximum displacement value equal to 1.00 cm. Figures 9, 10, 11, 12 and 13 also report the dates of the main seismic events occurred in the period 2011–2019 in Central Italy. For completeness, Tables 1 and 2 report the main characteristics of the seismic events recorded by two accelerometric stations selected within the National Accelerometric Network (RAN) managed by the Italian



Fig. 8 Selected measurement points

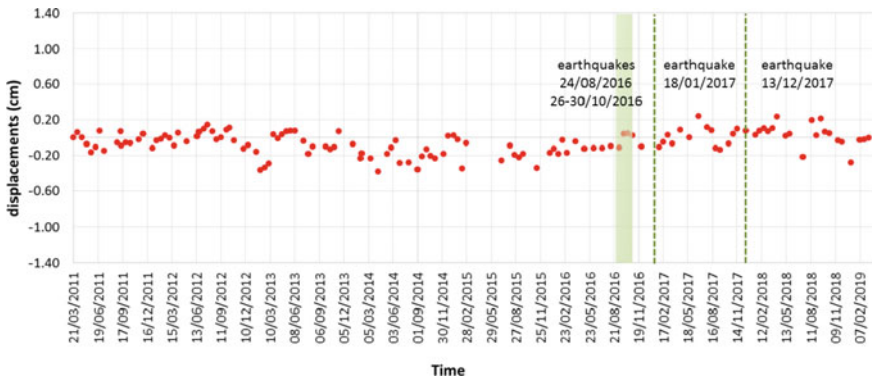


Fig. 9 Displacement time-series of the measure point ID 70168

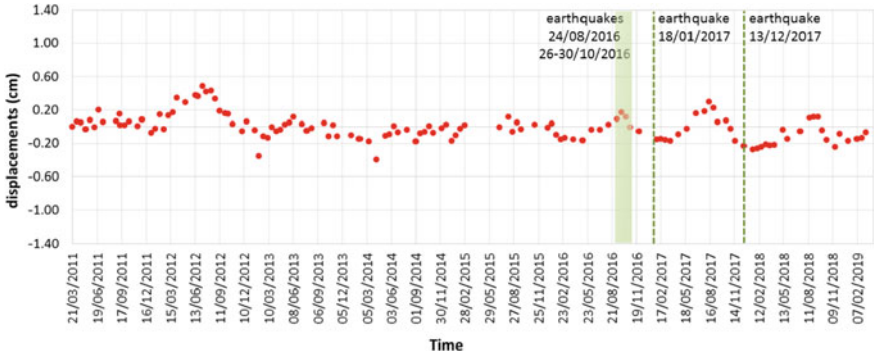


Fig. 10 Displacement time-series of the measure point ID 70412

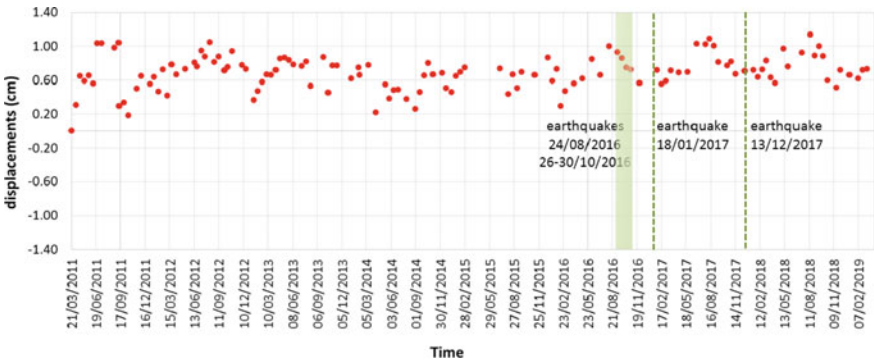


Fig. 11 Displacement time-series of the measure point ID 70085

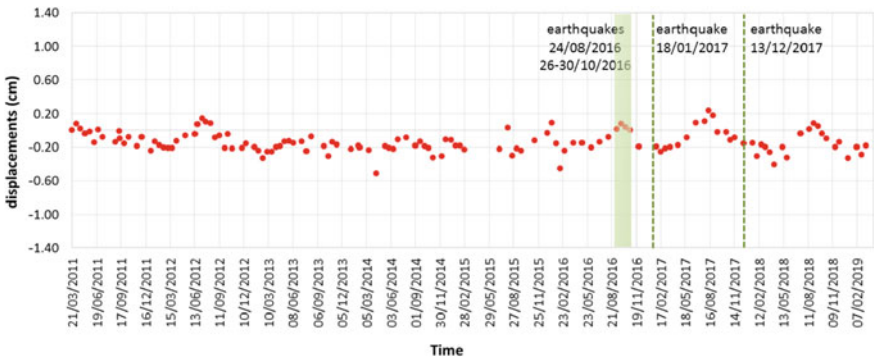


Fig. 12 Displacement time-series of the measure point ID 70895

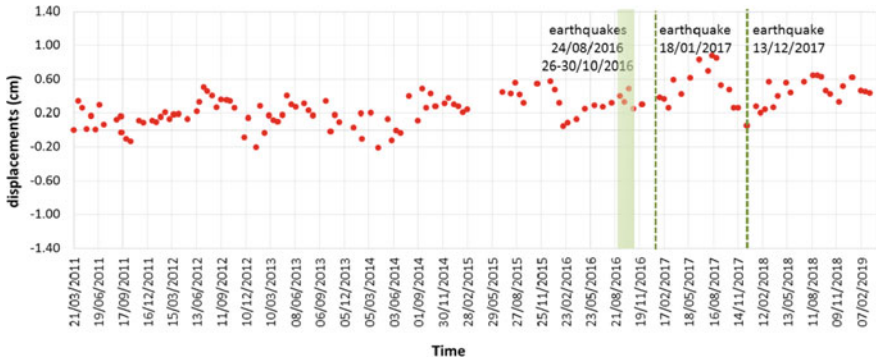


Fig. 13 Displacement time-series of the measure point ID 70542

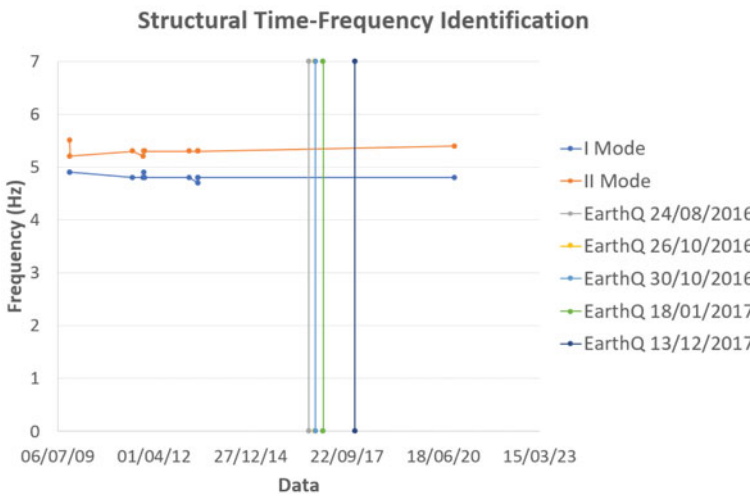


Fig. 14 Time–Frequency plot referred to the main modes of vibration of the monitored structure

Table 1 Accelerometric stations with site coordinates and EC8 soil type classification

Station code	Name RAN station	Latitude	Longitude	EC8 soil type
LAV9	LANUVIO	41.6775	12.6986	B
VLL	VELLETRI	41.6705	12.7727	B

Department of Civil Protection. LAV9 and VLL stations are distant around 5.5 km and 9.5 km respectively from Ariccia.

By observing the results in Figs. 9, 10, 11, 12 and 13, we can see that the displacement time-series does not change their behavior in correspondence of the earthquakes. In addition, the displacement has similar temporal behavior for all the

Table 2 Seismic events recorded by accelerometric stations, epicentral distance (R_{EP}) and magnitude

Date (YYYY-MM-DD)	Station	R_{EP} (km)	M_W	M_L
2016-08-24	VLL	120.3	6.0	6.0
2016-10-26	VLL	140.6	5.9	5.9
2016-10-30	LAV9	132.7	6.5	6.1
2017-01-18	LAV9	100.4	4.3	4.3
2017-12-03	VLL	115.4	5.0	5.1

selected locations, which is an indication of lack of differential displacement of the building.

4.2 *In Situ Testing*

The DInSAR observations were integrated by the experimental vibrational data provided by the OSS of the Italian Civil Protection Department. Between 2009 and 2013, the monitoring system installed on the building recorded a sequence of ambient vibrations and seismic events. Figure 14 illustrates the fundamental frequencies of the school, achieved by the analysis of accelerometric data.

In October 2020, an experimental campaign of ambient vibration measurements has been carried out (see Fig. 15) to evaluate the fundamental frequencies of the

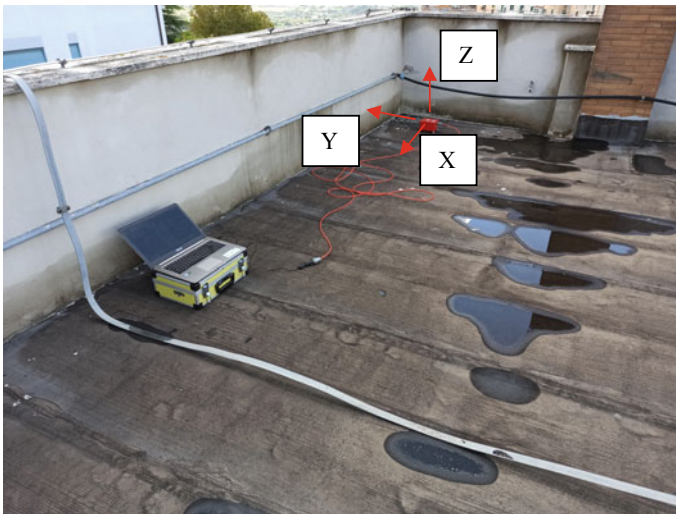


Fig. 15 Ambient vibration recording on the TOP of the building in October 2020

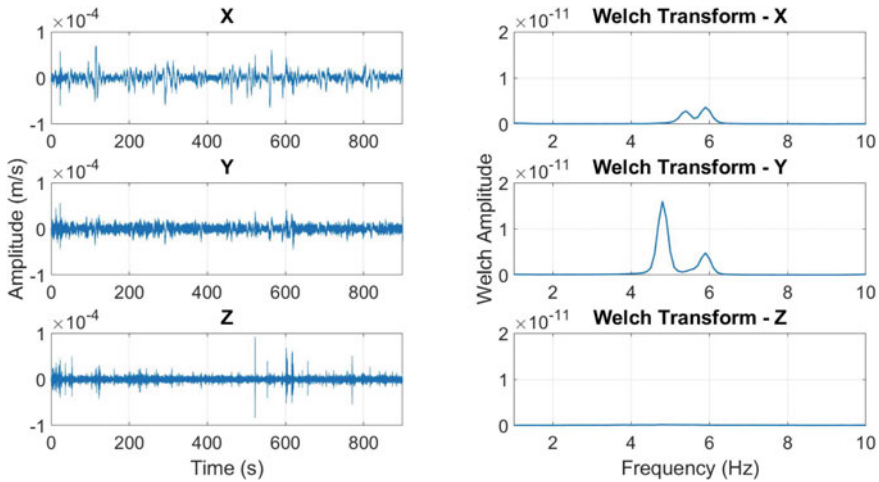


Fig. 16 Velocimetric data acquired on the top of the building and related spectra

structure and analyze possible variations from the data related to the period 2009–2013; the velocimetric data collected on the top of the building are shown in Fig. 16.

By examining Fig. 14, no change of the fundamental frequency was observed in 2020 with respect to the 2013, which is an indication of the fact that the occurred seismic events have not damaged the structure. An accurate visual survey has been performed to assess the present condition state of the structure and confirmed that no relevant damages were present.

As represented in Fig. 14. Time–Frequency plot referred to the main modes of vibration of the monitored structure. Figure 14 and confirmed by results depicted in Fig. 16, the first two modes of vibration of the monitored structure are respectively equal to 4.8 and 5.3 Hz.

5 Conclusions

In this work, in situ and remote sensing systems have been applied to a real case study located in Ariccia (Rome) in order to integrate the technologies and assess structural damages.

The ground settlements have been obtained by using displacement measurements retrieved from a satellite SBAS-DInSAR analysis. Data were provided by IREA-CNR and analyzed in a GIS software and categorized according to mean deformation velocity. SAR results showed values of LOS displacements below 1 cm and a similar behavior was observed for the points affected by larger displacements. Also, no significant changes of the displacement time-series were observed after several

seismic events affecting the area. Therefore, SAR results are indicative of absence of the change of the structural status of the building.

The experimental vibrational data provided by the Italian Civil Protection Department, recorded between 2009 and 2013, have been analyzed to evaluate the fundamental frequencies of the monitored structure. The ambient vibration measurements performed in October 2020 are in agreement with the previous recorded data, showing no significant variations in frequency values that could be associated with possible damages. This was also confirmed by the visual survey carried out on site which did not highlight any particular defects or anomalies on the building.

Therefore, we can conclude that the integration of results of SAR and the vibrational data can provide information about the healthiness status of a structure thanks to observations characterized by a global scale with in-situ data collected with a very low logistic effort. This result has a significant application impact as it allows, after an earthquake, to determine, quickly and economically, the buildings that have not suffered significant damage.

A next step of the research will be a series of parametric analyzes to be performed on non-linear numerical models of the study structure. These analyzes will aim to study the possible effects induced by assigned settlements, both on structural and non-structural elements. All information will be used to define the best strategies aimed at integrating in situ and satellite data for assessing the state of health of strategic structures.

Acknowledgements This research was partially funded by the Italian Civil Protection Department within the project RELUIS 2019–2022 WP6 “Structural Health Monitoring and Satellite Data”. Project carried out using CSK® Products, © of the Italian Space Agency (ASI), delivered under a license to use by ASI.

References

1. Cuomo V, Soldovieri F, Bourquin F, El Faouzi NE, Dumoulin J (2020) The necessities and the perspectives of the monitoring/surveillance systems for multi-risk scenarios of urban areas including COVID-19 pandemic. In: Proceedings of 2020 TIEMS Conference, “Citizens and Cities Facing New Hazards and Threats, Nov 2020
2. Cuomo V, Soldovieri F, Ponzo FC, Ditommaso R (2018) A holistic approach to long term SHM of transport infrastructures. In: The International Emergency Management Society (TIEMS) Newsletter 33, pp 67–84
3. Soldovieri F, Dumoulin J, Ponzo FC, Crinière A, Bourquin F, Cuomo V (2014) Association of sensing techniques with a designed ICT architecture in the ISTIMES project: application example with the monitoring of the Musmeci bridge. In: EWSHM 2014, 7th European workshop on structural health monitoring, Nantes, France, 8–11 July 2014
4. Proto M et al (2010) Transport Infrastructure surveillance and Monitoring by Electromagnetic Sensing: the ISTIMES project. *Sensors* 10(12):10620–10639
5. Rytter A (1993) Vibrational based inspection of civil engineering structures. Ph.D. Thesis, University of Aalborg, Denmark
6. Doebling SW, Farrar CR, Prime MB (1998) A summary review of vibration-based damage identification methods. *Shock Vib Dig* 30(2):91–105

7. Stubbs N, Perk S, Sikorsky C, Choi S (2000) A global non-destructive damage assessment methodology for civil engineering structures. *Int J Syst Sci* 31(11):1361–1373
8. Ponzo FC, Ditommaso R, Auletta G, Mossuca A (2010) A fast method for structural health monitoring of Italian reinforced concrete strategic buildings. *Bull Earthquake Eng* 2010(8):1421–1434. <https://doi.org/10.1007/s10518-010-9194-6>
9. Devin A, Fanning PJ (2012) The evolving dynamic response of a four storey reinforced concrete structure during construction. *Shock Vib* 19(2012):1051–1059. <https://doi.org/10.3233/SAV-2012-0711>
10. Devin A, Fanning PJ (2012) Effect of Non-structural elements on the dynamic response of floors. In: Conference: topics on the dynamics of civil structures. https://doi.org/10.1007/978-1-4614-2413-0_41
11. Ditommaso R, Mucciarelli M, Ponzo FC (2012) Analysis of non-stationary structural systems by using a band-variable filter. *Bull Earthquake Eng* 2012(10):895–911. <https://doi.org/10.1007/s10518-012-9338-y>
12. Ditommaso R, Vona M, Gallipoli MR, Mucciarelli M (2013) Evaluation and considerations about fundamental periods of damaged reinforced concrete buildings. *Nat Hazards Earth Syst Sci* 13(1903–1912):2013. <https://doi.org/10.5194/nhess-13-1903-2013>
13. Ditommaso R, Ponzo FC (2015) Automatic evaluation of the fundamental frequency variations and related damping factor of reinforced concrete framed structures using the Short Time Impulse Response Function (STIRF). *Eng Struct* 82(2015):104–112
14. Iacovino C, Ditommaso R, Ponzo FC, Limongelli MP (2018) The Interpolation Evolution Method for damage localization in structures under seismic excitation. *Earthquake Eng Struct Dyn* 2018:1–20. <https://doi.org/10.1002/eqe.3062>
15. Gerardi V, Ditommaso R, Auletta G, Ponzo FC (2018). Reinforced concrete framed structures: numerical validation of two physical models capable to consider the stiffness contribution of infill panels on framed structures in operative conditions. *Int J Earthquake Engineering*, Anno XXXV, num 3
16. Serlenga V, Gallipoli MR, Ditommaso R, Ponzo FC, Tragni N, Perrone A, Stabile TA, Calamita G, Vignola L, Carso RF, Pietrapertosa D, Lapenna V. An integrated approach for structural behavior characterization of the Gravina Bridge (Matera, Southern Italy), *Structural Health Monitoring* 1–22. <https://doi.org/10.1177/1475921720987544>
17. Lamonaca BG, Nicoletti M, Spina D (2001) Permanent monitoring of the seismic response of civil structures in Italy: the Seismic Observatory of Structure Project (in Italian). *Ingegneria Sismica* 1
18. Dolce M, Nicoletti M, De Sortis A, Marchesini S, Spina D, Talanas F (2017) Osservatorio sismico delle strutture: the Italian structural seismic monitoring network. *Bull Earthquake Eng* 15:621–641
19. Stramondo S, Bignami C, Chini M, Pierdicca N, Tertulliani A (2006) Satellite radar and optical remote sensing for earthquake damage detection: results from different case studies. *Int J Remote Sens* 27:4433–4447
20. Ardizzone F, Bonano M, Giocoli A, Lanari R, Marsella M, Pepe A, Solaro G (2012) Analysis of ground deformation using SBAS-DInSAR technique applied to CosmoSkymed images, the test case of Roma urban area. In: Proceedings of SPIE8536, SAR Image Analysis, Modeling, and Techniques XII, 85360D
21. Mroueh H, Shahrouh I (2003) A full3-Dfinite element analysis of tunnelling adjacent structures interaction. *Comput Geotech* 30:245–253
22. Chini M, Bignami C, Stramondo S, Pierdicca N (2008) Uplift and subsidence due to the 26 December 2004 Indonesian earthquake detected by SAR data. *Int J Remote Sens* 29:3891–3910
23. Massonnet D, Rossi M, Carmona C, Adragna F, Peltzer G, Feigl K, Rabaute T (1993) The displacement field of the Landers earthquake mapped by radar interferometry. *Nature* 364:138–142
24. Gamba P, Dell’acqua F, Trianni G (2007) Rapid damage detection in the Bam area using multitemporal SAR and exploiting ancillary Data. *IEEE Trans Geosci Remote Sens* 45: 1582–1589

25. Matsuoka M, Yamazaki F, Ohkura H (2007) Damage mapping of the 2004 Niigataken Chuetsu earthquake using Radarsat images. In: Urban Remote Sensing Joint Event, 11–13 April 2007, Paris, France
26. Yonezawa HA, Takeuchi S (2001) Decorrelation of SAR data by urban damage caused by the 1995 Hoyooken-Nanbu earthquake. *Int J Remote Sens* 22:1585–1600
27. Chini M, Pierdicca N, Emery WJ (2009) Exploiting SAR and VHR optical images to quantify damage caused by the 2003 Bam Earthquake. *IEEE Trans Geosci Remote Sens* 47:145–152
28. Ferretti A, Fumagalli A, Novali F, Prati C, Rocca F, Rucci A (2011) A new algorithm for processing interferometric data-stacks: SqueeSAR. *IEEE Trans Geosci Remote Sens* 49:3460–3470
29. Lanari R, Mora O, Manunta M, Mallorquí JJ, Berardino P, Sansosti E (2004) A small baseline approach for investigating deformations on full resolution differential SAR interferograms. *IEEE Trans Geosci Remote Sens* 42:1377–1386
30. Werner C, Wegmüller U, Strozzi T, Wiesmann A (2003) Interferometric point target analysis for deformation mapping. In: Proceeding of IEEE Geoscience and Remote Sensing Symposium. IGARSS, 7. Toulouse, France, pp 4362–4364
31. Mora O, Mallorquí JJ, Broquetas A (2003) Linear and nonlinear terrain deformation maps from a reduced set of interferometric SAR images. *IEEE Trans Geosci Remote Sens* 41:2243–2253
32. Bonano M, Manunta M, Pepe A, Paglia L, Lanari R (2013) From previous C-band to new X-band SAR systems: assessment of the DInSAR mapping improvement for deformation time-series retrieval in urban areas. *IEEE Trans Geosci Remote Sens* 51:1973–1984
33. Lanari R, Casu F, Manzo M, Lundgren P (2007) Application of the SBAS-DInSAR technique to fault creep: a case study of the Hayward fault, California. *Remote Sens Environ* 109:20–28
34. Berardino P, Fornaro G, Lanari R, Sansosti E (2002) A new algorithm for surface deformation monitoring based on small baseline differential SAR interferograms. *IEEE Trans Geosci Remote Sens* 40:2375–2383
35. Burgmann R, Rosen PA, Fielding EJ (2000) Synthetic aperture radar interferometry to measure Earth's surface topography and its deformation. *Ann Rev Earth Planetary Sci* 28:169–209
36. Gabriel K, Goldstein RM, Zebker HA (1989) Mapping small elevation changes over large areas: differential interferometry. *J Geophys Res* 94:9183–9191
37. Tesauro M, Berardino P, Lanari R, Sansosti E, Fornaro G, Franceschetti G (2000) Urban subsidence inside the city of Napoli (Italy) observed by satellite radar interferometry. *Geophys Res Lett* 27:1961–1964
38. Scifoni S, Bonano M, Marsella M, Sonnessa A, Tagliaferro V, Manunta M, Lanari R, Ojha C, Sciotti M (2016) On the joint exploitation of long-term DInSAR time series and geological information for the investigation of ground settlements in the town of Roma (Italy). *Remote Sens Environ* 182:113–127
39. Arangio S, Calò F, Di Mauro M, Bonano M, Marsella M, Manunta M (2013) An application of the SBAS-DInSAR technique for the assessment of structural damage in the city of Rome. *Struct Infrastructure Eng Maintenance Manage Life-Cycle Design Performance* 10:1469–1483
40. Sanabria MP, Guardiola-Albert C, Tomás R, Herrera G, Prieto A, Sánchez H, Tessitore S (2014) Subsidence activity maps derived from DInSAR data: Orihuela case study. *Natural Hazards Earth Sci Syst* 14:1341–1360
41. Sansosti E, Berardino P, Bonano M, Calò F, Castaldo R, Casu F, Manunta M, Manzo M, Pepe A, Pepe S, Solaro G, Tizzani P, Zeni G, Lanari R (2014) How second generation SAR systems are impacting the analysis of ground deformation. *Int J Appl Earth Obs Geoinf* 28:1–11
42. Cascini L, Ferlisi S, Peduto D, Fornaro G, Manunta M (2007) Analysis of a subsidence phenomenon via DInSAR data and geotechnical criteria. *Ital Geotech J* 41:50–67
43. Zebker HA, Villasenor J (1992) Decorrelation in interferometric radar echoes. *IEEE Trans Geosci Remote Sens* 30:950–959

Acoustic Emission Monitoring of Prestressed Concrete Bridges: Differences Before and After the First-Crack Opening



Daniel Tonelli, Francesco Rossi, Michele Luchetta, Daniele Zonta, Placido Migliorino, Alberto Selleri, Enrico Valeri, Alessandra Marchiondelli, and Gianluca Ascari

Abstract A great amount of highway bridges is reaching the lifespan for which they were designed, and most of them need frequent inspections and maintenance to guarantee the safety of users. Structural health monitoring can help infrastructure operators to estimate promptly and accurately the structures' health condition. The progress of technology has encouraged the development of modern non-destructive monitoring techniques, such as the acoustic emission (AE) method. Recent experiences testify its potential, especially applied to the detection of cracks' initiation and propagation in structures where it is difficult to perform visual inspection or direct measurements. In this paper, we analyze and correlate the results of AE techniques with the initiation and propagation of the damage in a full-size prestressed concrete highway bridge subjected to a load test up to its failure: the Alveo Vecchio Viaduct. The bridge was built in 1968 and regularly maintained over the years. It is representative, by type, age, and deterioration state, of similar bridges in operation on the Italian highway network. We aim to identify the differences in AE recorded on a real-life structure before and after the first-crack opening, and more in general, the effectiveness of AE techniques in permanent or short-term monitoring.

Keywords Acoustic emission · Damage detection · Crack initiation · Crack propagation · Prestressed concrete bridge · Load test · Structural health monitoring

D. Tonelli (✉) · M. Luchetta · D. Zonta
University of Trento, Trento, Italy
e-mail: daniel.tonelli@unitn.it

F. Rossi
University of Strathclyde, Strathclyde, UK

P. Migliorino
Ministry of Infrastructures and Transport, Rome, Italy

A. Selleri · E. Valeri · A. Marchiondelli
Autostrade per l'Italia SpA, Rome, Italy

G. Ascari
Akron Srl, Rome, Italy

1 Introduction

When civil infrastructures approach their design life, the effort required to identify their health conditions increases. Structural health monitoring (SHM) can support engineers to promptly detect structural damages resulting from natural deterioration or unexpected events [1, 2], providing remarkable benefits in infrastructure management [3–5]. As far as prestressed concrete bridges are concerned, one of the main signs of structural deterioration are concrete cracks in structural elements. They may be a symptom of the tension loss or failure of steel wires [6]; therefore, the monitoring of such damage is particularly recommended in prestressed concrete bridges.

In this contribution, we focus on the acoustic emission (AE) technique, a passive monitoring approach based on the detection of elastic waves in structural components generated by damages, such as the initiation and propagation of cracks, the failure of steel wires, and the failure of bonds [7]. The interest in AE has increased tremendously over the past decade because elastic waves generated by damage propagate throughout the structure, allowing remote detection of damage located in areas that are not easily accessible to visual inspections and direct measurements [8, 9].

The usage of AE in bridge monitoring started in the 1970s when Pollock and Smith monitored a portable military bridge subjected to proof testing [10]. After them, the AE technique has been used in numerous field bridge testing applications [11], concerning the detection of concrete cracks initiation and propagation [12, 13], the development of fatigue cracks in steel members [14], the failure of prestressed tendons in prestressed reinforced concrete elements [15]. A comprehensive review of AE monitoring applications on bridges from 1970 to 2010 can be found in [11].

Not that surprisingly, experimental works on AE are typically concerned with damage states that do not jeopardize the safety of bridges. Moreover, they do not verify directly how well an AE technique performs when the bridge is close to collapse. Indeed, we are not aware of any experiment on a full-scale bridge that verifies the capacity of AE to provide an early warning when the bridge is approaching its ultimate state.

In this paper, we wish to fill this gap by analyzing and discussing the AE recorded during a load test on a full-size prestressed concrete bridge span, carried out up to its failure. The bridge, the Alveo Vecchio viaduct, is a 1968 structure currently decommissioned but perfectly representative, by type, age, and deterioration state of similar bridges currently in operation on the Italian highway network. Our goal is to discuss how AE change while the load progressively increases and compare the results before and after the first-crack opening. Based on the outcomes of this experimentation, we aim to answer the following questions: (i) Can AE discriminate whether a viaduct has pre-existent damage, such as concrete cracks? (ii) Can AE identify the opening of the first crack? (iii) Can AE single out the maximum load withstood by the viaduct? (iv) Can AE recognize different types of damages?

In Sect. 2, we summarize the physical principle, the technology, and the most typical signal analysis techniques on which the AE technique is based. In Sect. 3, we introduce the Alveo Vecchio case study, the monitoring system, and of the load test.

In Sects. 4 and 5 we report the results from the monitoring system and in Sect. 6 we discuss them. Finally, in Sect. 7, we draw conclusions about the application of the AE technique to real-life prestressed concrete bridges.

2 Physical Principle and Observable Quantities

The AE is a phenomenon in which transient elastic waves are generated by the rapid release of strain energy from a localized source due to microstructural changes in the material [16]. They travel into the material and move to the surface of the structural element, where sensors can detect them and transduce them into an electrical signal. The electrical signal is recorded, amplified, and typically represented in the time domain. Since the background and the environmental noises, such as wind, passers-by, usually affect the signal, a band-pass filter is typically required to eliminate them [17]. Typically, AE sensors are piezoelectric or PZT devices [18] and capacitive MEMS acoustic emission transducers [19].

An AE, also called *hit* [20], is identified in the acoustic signal when: (i) the signal crosses a certain threshold, expressed in volts (V) or similarly in decibels (dB), which discriminate an AE from the noise [21]; (ii) the signal crosses that threshold at least three times consecutively. An AE can be described by characteristic parameters [21] both in the time domain (amplitude duration, count, and signal strength) and in the frequency domain (peak-frequency) (Fig. 1). To discriminate one AE from another, we must define three time-parameters: peak definition time (PDT), hit definition time (HDT), and hit lockout time (HLT) [22–24]. The first is the time after the peak amplitude in which a new greater peak amplitude can replace the original one. The

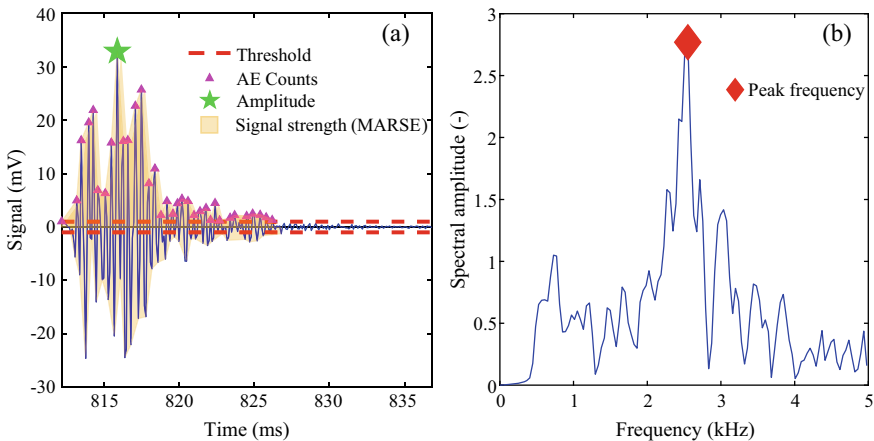


Fig. 1 **a** AE signal and parameters expressed in the time-domain; **b** AE signal and parameters expressed in the frequency-domain

second is the time after the last threshold-crossing that defines the end of the hit. The third is the time after the HDT during which a threshold-crossing will no longer trigger a new hit. Among the many, we recommend Grosse and Ohtsu [25] to the Reader who is approaching AE for the first time.

In theory, during loading and unloading cycles like those experienced by in-service bridges to the passage of vehicles a structural element with no pre-existent damage can experience damage and emit acoustic waves only when its maximum withstood load is exceeded [11]: that is known as Kaiser effect [7] and it is characteristic of an elastic structural response. In contrast, if the structural element has pre-existent damages, it produces AE during all the loading phase: that is called Felicity Effect [7].

In practice, we aim to verify to what extent this difference is appreciable in AE monitoring of full-size bridges. To do so, we analyze the AE acquired during a load test of a decommissioned highway viaduct consisting of a sequence of loading and unloading cycles up to three times the design load and compare the results before and after the first-crack opening.

3 AE Monitoring of a Prestressed Concrete Bridge Tested to Failure

The Alveo Vecchio viaduct is part of the old track of the A16 Napoli-Canosa Italian highway. It was built in 1968 and decommissioned in 2005, after a landslide hit and displaced one of its piers. It is representative of 70% of the Italian highway bridges in terms of the structural scheme, construction technology, maintenance state, age, and deterioration [26]. Figure 2 shows a top view, a lateral view, and a cross-section of the viaduct.

The viaduct consists of two structurally independent decks, one for each carriageway, each of them made of three 32.5 m long prestressed concrete simply supported spans. Each span consists of four prestressed concrete girders of depth 2 m that support a 20 cm-thick concrete deck slab. The prestressing was applied through 14 post-tensioned cables per girder, with initial jacking tension of 1250 MPa. Additional information on the structure is in [27].

During the load test, the viaduct was monitored by 119 sensors divided into 8 types: wire displacement sensors (WD), deformation sensors (strain gauges), crack-opening sensors (CO), electronic level, temperature sensors (RTD), inclinometers, accelerometers, and acoustic emission sensors (AE). Details about the structural health monitoring system installed on the viaduct and its design process are in [28] (in Italian) and [29].

We focus on wire displacement sensors, crack-opening sensors, and AE sensors. Figure 3 shows the layout of these sensors on the viaduct, while Table 1 shows their technical features. Crack-opening sensors are Gefran PZ12, wire displacement

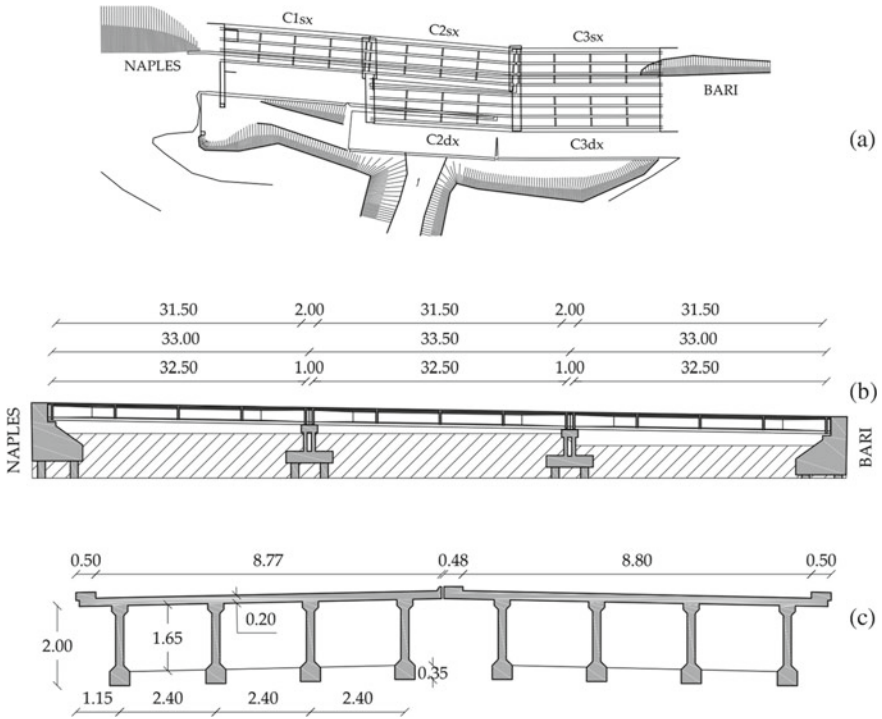


Fig. 2 a Top view; b lateral view; and c cross section of the Alveo Vecchio viaduct (Italy)

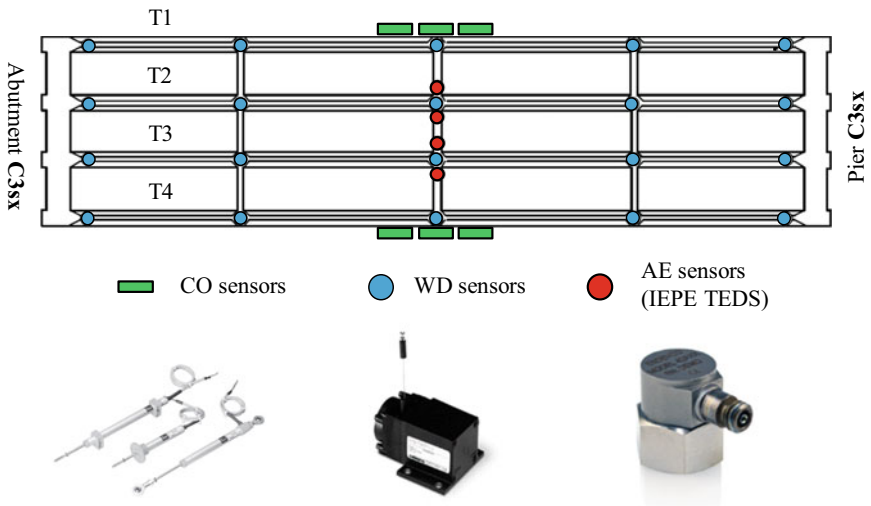


Fig. 3 Monitoring system layout (only the sensors relevant in our analysis)

Table 1 Technical features of sensors installed on the viaduct (only sensors relevant in our analysis)

Type	Full-scale (FS)/Range	Accuracy	Sampling frequency	Number
WD sensors (deflection)	50–100 mm	1.5‰ FS	1 Hz	20
WD sensors (deflection)	500 mm	5‰ FS	1 Hz	12
CO sensors (crack-opening)	10 mm	1‰ FS	1 Hz	22
AE sensors (acoustic emission)	50–10 kHz	500 mV/g	10 kHz	4

sensors are PT1DC from Celesco Transducer Products, Inc., and the AE sensors are Isotron® accelerometer Model 42a.

AE sensors measure accelerations with a sampling frequency of 10 kHz and record a 2100 ms-long sample every time the acceleration exceeds 10 mg (time t_0 of the sample): the sample starts 100 ms before t_0 and ends 2000 ms after that. We set the threshold at 60 dB and the high-pass filter frequency at 500 Hz to reject all the signals identified as noise in the first part of the loading phase P3. Moreover, we set the three time-parameters to recognize correctly at least 95% of the hits from a sample of 500 AE randomly extracted from those recorded in the loading phases P3 and P4: PDT = 20 ms, HDT = 10 ms, and HLT = 10 ms. Parameters investigated include amplitude, signal strength, and peak frequency.

The load-test protocol consists of five loading and unloading phases with a progressive number of steel ballast weights with a size of $2.35 \times 1.84 \times 0.45$ m and a weight of 100 kN each. They are placed in the middle of the span C3sx in layers of 12 ballast each. The load unit is 2400 kN (two layers of ballasts), which produces a bending moment in the girders' middle cross-section of 4200 kN m, corresponding to the load effect resulting from the design traffic load [26]. Figure 4 illustrates the five loading phases: P1 (1200 kN), P2 (2400 kN), P3 (4800 kN), P4 (7200 kN), and P5 (bridge's ultimate capacity). Details about the load-test protocol are in [28] (in Italian).

4 Results from Deflection and Crack-Opening Sensors

The girder T1 experienced the greatest deflection and deformation. Figure 5a shows the vertical displacements recorded by wire displacement sensors during the five phases of the load test. Figure 5b shows the load–deflection curve of its midspan, along with the trilinear idealized flexural response: the first-crack load is 3700 kN and the ultimate capacity is 8700 kN. Figure 5c, d show the longitudinal strain recorded by CO sensors at the bottom of the middle cross-section of the girder T1. During the loading phase P3 (Fig. 5c), there is a significant change in the curve slope for a load of 3300 kN, which marks the opening of the first crack and a change of the girder's

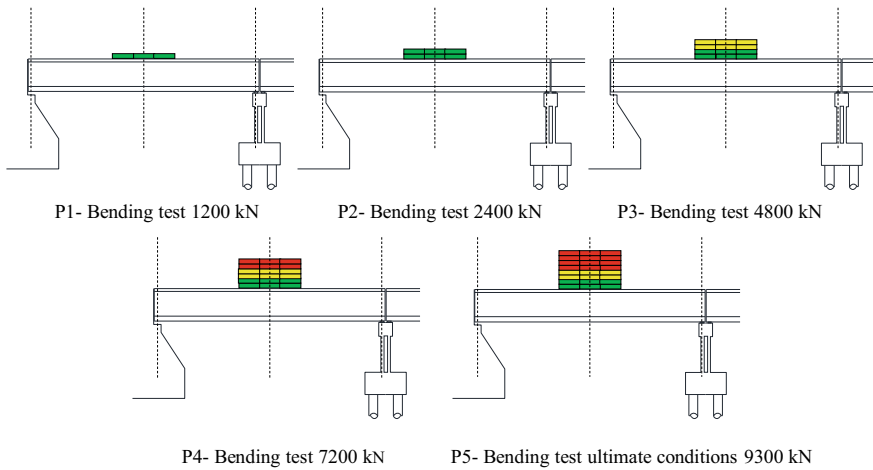


Fig. 4 Load-test protocol: five loading phases with an increasing number of ballast weights

structural response from stage I (elastic) and state II (cracked). In contrast, during the loading phase P4 (Fig. 5d), the girder's structural response is non-linear from the beginning, which confirms that the girder had pre-existent cracks before P4. To sum up, the girder T1 had no pre-existent cracks before P3, while it had pre-existent cracks before P3. The same happened for the other girders: T2, T3, and T4.

Colors green, yellow, and red in the graphs' background represent the layers of ballast on the viaduct: two green layers for 2400 kN, two yellow layers for 4800 kN, and two red layers for 7200 kN (see Fig. 4 for the load-test protocol).

5 Results from AE Sensors

The most significant results have been observed during test phases P3 (maximum load of 4800 kN, corresponding to two times the design load) and P4 (maximum load of 7200 kN, corresponding to three times the design load). In this section, we report the results from sensors T2AE1 and T2AE2 installed on the girder T2 during the loading phases P3 and P4. The No AE sensors have been installed on the girder T1.

Regarding the loading phase P3, Fig. 6 shows four graphs with the load from 0 to 4800 kN on the horizontal axis and the amplitude (Fig. 6a), the cumulative number of hits (Fig. 6b), the signal strength—MARSE (Fig. 6c), and the cumulative MARSE (Fig. 6d) on the vertical axis. The blue dashed lines at 4300 kN represent the value of the load corresponding to the AE generated by the opening of the first crack in the girder T2; after that, AE increase considerably. In contrast, the red dashed lines represent the first-crack load (3300 kN) identified by crack-opening sensors (CO).

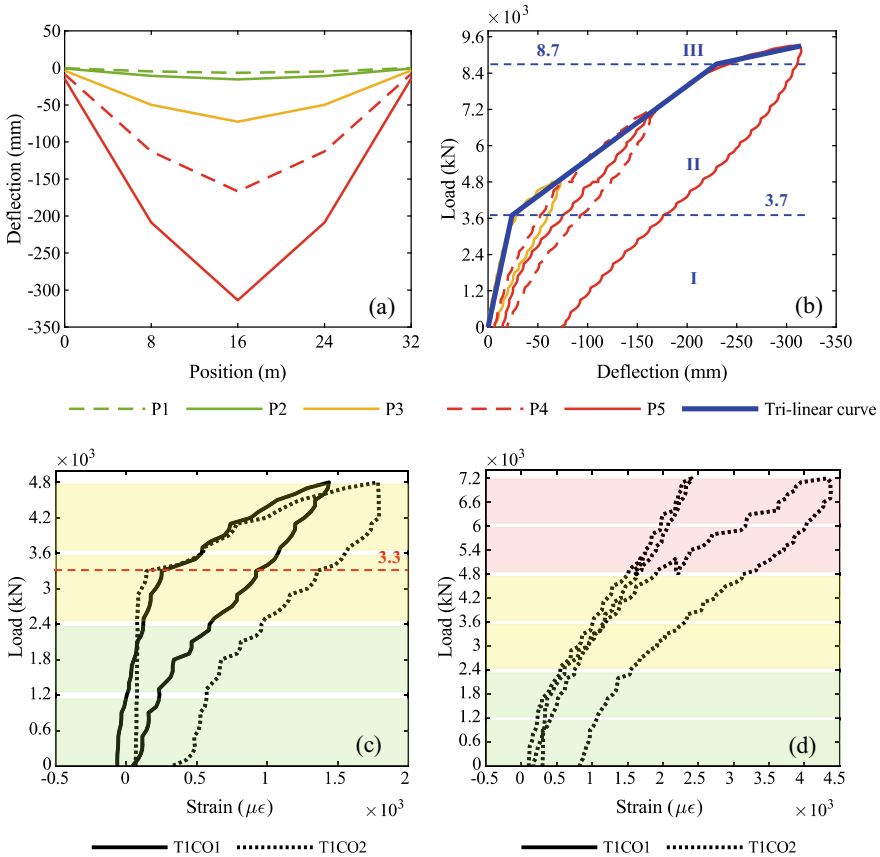


Fig. 5 **a** Vertical displacements of girder T1 in the five loading phases; **b** load–deflection curve of girder T1 and trilinear idealized flexural response. Longitudinal strain at the bottom of the middle cross section of girder T1: **c** at the loading phase P3; **d** at the loading phase P4. Blue dashed lines represent changes in the girder’s structural response based on deflection sensors. The red dashed line represents the first-crack load identified by crack-opening sensors

We analyzed AE also in the frequency domain (Fig. 7a) to verify whether it is possible to discriminate different types of damage, such as concrete cracks and steel wire failures. We identified two clusters in the amplitude–peak-frequency graph and load-peak-frequency graph from sensor T2AE1. They may represent a different source of the elastic waves [21]. In contrast, peak-frequencies are more scattered in data from sensor T2AE2. Figure 7b shows a histogram of the peak-frequency distribution of the AE recorded by both sensors.

Figures 8 and 9 represent the results for the loading phase P4 of the same analyses carried out for the loading phase P4 and reported in Figs. 6 and 7. Additional analyses and results on AE recorded during the load test can be found in [30, 32].

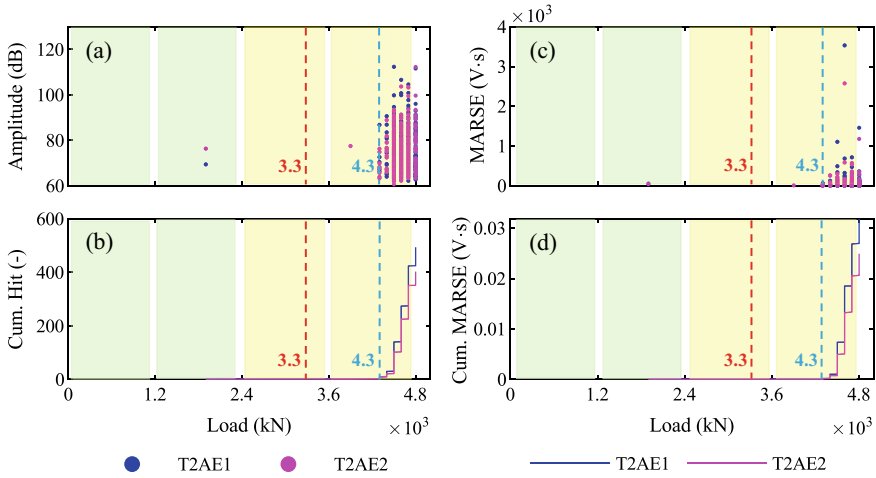


Fig. 6 Results in the time-domain from the loading phase P3 4800 kN: **a** amplitude; **b** cumulative number of hits; **c** signal strength; and **d** cumulative signal strength

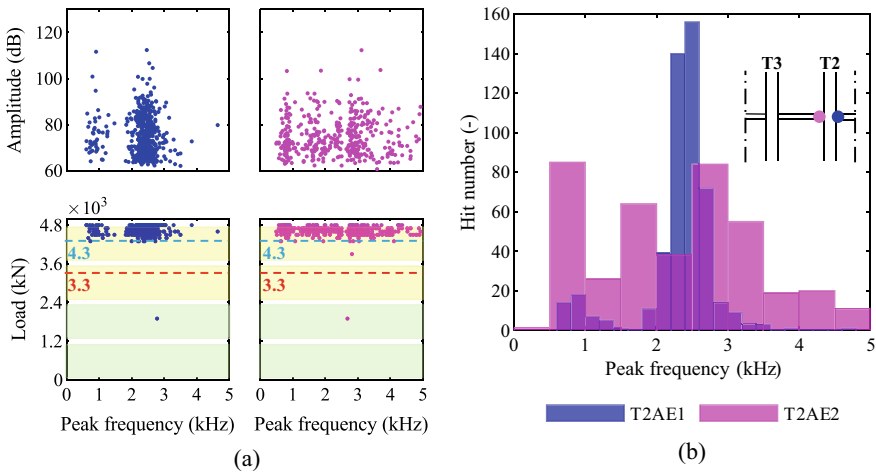


Fig. 7 Results in the frequency-domain from the loading phase P3 4800 kN; **a** amplitude and load-peak-frequency; **b** peak frequency distribution among hits

6 Discussion of Results

In this section, we answer the questions introduced in Sect. 1 based on the results reported in Sects. 4 and 5.

(i) *Can an AE monitoring system discriminate whether a viaduct has pre-existent damage, such as concrete cracks?* AE from the loading phase P3 are representative of

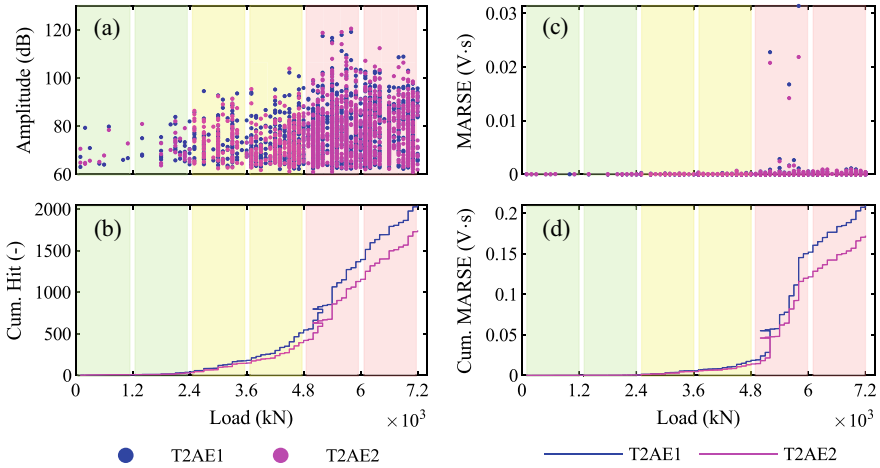


Fig. 8 Results in the time-domain from the loading phase P4 7200 kN: **a** amplitude; **b** cumulative number of hits; **c** signal strength; and **d** cumulative signal strength

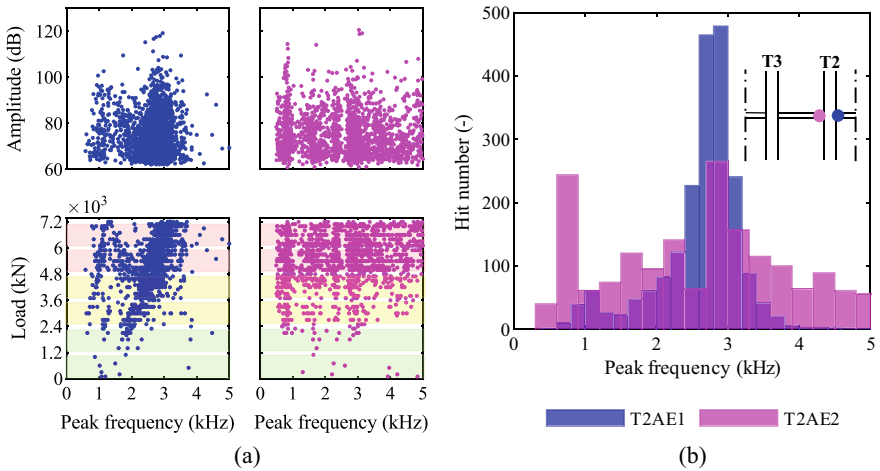


Fig. 9 Results in the frequency-domain from the loading phase P4 7200 kN: **a** amplitude and load–peak-frequency; **b** peak frequency distribution among hits

a structure without pre-existent cracks, whose response is elastic until the first crack occurs at 4300 kN; in contrast, AE from the loading phase P4 are representative of a structure with pre-existent cracks. Their difference is visible even for low values of the load: the amplitude–load graph shows that the girder with pre-existent cracks (phase P4—Fig. 8a) emits a higher number of AE than the girder without pre-existent cracks (phase P3—Fig. 6a). The cumulative number of hits–load graphs (Figs. 6b and Fig. 8b) and the cumulative MARSE–load graphs (Figs. 6d and 8d) show this

difference even more clearly: they are almost constant to zero for low values of the load during phase P3 (Fig. 6b, d), with a sharp change in the slope for 4300 kN; while they have a positive slope from the beginning to the end of the loading phase P4 (Fig. 8b, d).

(ii) *Can an AE monitoring system identify the opening of the first crack?* The graph of the amplitude plotted against the load for the loading phase P3 (Fig. 6a) shows almost no cracks for low values of the load, which suggests that the girder T2 had no cracks before the beginning of P3 [7]. In contrast, the number of AE increases significantly after 4300 kN. We can identify the opening of the first crack as the threshold between these two different behaviors resulting from AE records, graphically represented by a blue dashed line. We can identify it also in the graph of the cumulative MARSE plotted against the load (Fig. 6d) as the point at which the curve has a sharp change of slope. Figure 6a shows some AE even for loads lower than 4300 kN; since they are characterized by low energy (Fig. 6c), and they do not change the slope in the cumulative MARSE (Fig. 6d), they are probably just noise [13, 31]. In Sect. 4, crack-opening sensors (CO) at the bottom of the girder T1 suggested that the first crack opened for a load of 3300 kN (Fig. 5c). The difference between the first-crack load resulting from CO and AE sensors is mainly due to the difference in the girders monitored by the two technologies: girder T1 by COs and girder T2 by AE sensors. Indeed, during the load test, the girder T1 experienced the greatest deflection and deformation; therefore, it is reasonable to assume that cracks have opened first on the girder T1 and then on the girder T2.

(iii) *Can an AE monitoring system single out the maximum load withstood by the viaduct?* Based on our analysis, we can identify the maximum load withstood by the structure only when it has pre-existent cracks (loading phase P4). Indeed, both the cumulative-hits and cumulative-MARSE—load graph of phase P4 (Fig. 8b, d) shows a change in the curve slope around 4800 kN. This confirms that the maximum load withstood by this viaduct is 4800 kN (at the end of P3) and that the damage propagation starts only after that the maximum load withstood has been exceeded.

(iv) *Can an AE monitoring system recognize different types of damage?* Fig. 7a shows two clusters in data acquired during P3 by the sensor T2AE1 and analyzed in the frequency-domain (blue dots): around 1 and 2.5 kHz. They may represent different sources of elastic waves, such as different types of damage. In contrast, data from the sensor T2EA2 (magenta dots) are more scattered. The reason for this difference is not clear since the two sensors were placed on opposite sides of the same girder's middle cross-section. Results in the frequency-domain from the loading phase P4 (Fig. 9) are similar. The outcomes of our experiment are not enough to univocally establish which types of damage correspond to those clusters. That would require multiple load tests carried on until different loads followed by autopsies of the monitored girders, to correlate damages that occurred with the AE acquired in each test.

7 Conclusions

In this contribution, we presented results of the AE monitoring of a prestressed concrete highway viaduct, the Alveo Vecchio viaduct. It underwent a sequence of five loading and unloading cycles with progressively increasing loads up to three times the design load. We analyzed the AE signals recorded during the load test and extracted the following parameters: amplitude, signal strength (MARSE), and peak frequency. Our goals were to study the difference in the AE acquired before and after the first-crack opening and to analyze to what extent AE can provide useful information on the prestressed-concrete viaducts' health condition.

Results from deflection and crack-opening sensors suggested that the first crack opened at the end the loading phase P3 (maximum load of 4800 kN, corresponding to two times the design load). Therefore, AE acquired during P3 were representative of a viaduct without pre-existent damages; in contrast, AE acquired after P3 (during P4—maximum load of 7200 kN, corresponding to three times the design load) were representative of a viaduct with pre-existent damage.

The main outcomes of this research are:

(i) AE monitoring can discriminate whether a prestressed concrete bridge is cracked or not: a bridge with pre-existent cracks produces several AE under service load, whereas virtually no hit is recorded on a bridge with no cracks. The different behavior is evident by plotting the amplitude, the cumulative number of hits, or the cumulative MARSE against the load.

(ii) AE monitoring results allow clear identification of the first-crack opening, as this is typically accompanied by the first-time emission of a high-intensity signal, followed by several more as the cracks propagate. The opening of the first crack is easily detectable by plotting the amplitude or the cumulative number of hits against the load. Also, it corresponds to the first of a series of AE with a high MARSE in the MARSE graph and to a sharp change in the slope in the cumulative MARSE graph.

(iii) We can identify the maximum load withstood by the bridge based on AE only if the bridge has pre-existent cracks. It corresponds to a sharp change in the slope of the cumulative MARSE graph.

(iv) In principle, it is possible to classify damage by type by analyzing the AE in the frequency domain; therefore, it would be possible to identify the first crack-opening, the first steel-wire failure, etc. based on the frequency of the AE acquired. The outcomes of our experiment are not enough to univocally establish a correlation between clusters of data in the frequency-domain and types of damage (cracking, deboning, failure of steel wires, etc.).

Acknowledgements The work presented in this paper is part of a research collaboration among the University of Trento, the Italian Ministry of Infrastructures and Transport and Autostrade per l'Italia SpA, the largest Italian highway concessionary. The project aims to develop inspection and monitoring protocols for the assessment of the safety and reliability of in-service highway bridges. The Alveo Vecchio viaduct is part of the open-air Laboratory for Infrastructure Safety of the Italian Ministry of Infrastructures and Transport, a large-scale testing facility which aims to directly validate monitoring and non-destructive testing methods in a real-life setting. The financial

contribution from the Italian Ministry of Infrastructures and Transport and Autostrade per l'Italia SpA is acknowledged.

References

1. Tonelli D, Verzobio A, Cappello C, Bolognani D, Zonta D, Bursi OS, Costa C (2017) Expected utility theory for monitoring-based decision support system. In: Proceedings of the 11th international workshop on structural health monitoring, Stanford, CA, USA
2. Bolognani D, Verzobio A, Tonelli D, Cappello C, Glisic B, Zonta D, Quigley J (2018) Quantifying the benefit of structural health monitoring: what if the manager is not the owner? *Struct Health Monit* 17(6):1393–1409
3. Tonelli D, Verzobio A, Bolognani D, Cappello C, Glisic B, Zonta D, Quigley J (2018) The conditional Value of Information of SHM: what if the manager is not the owner? In: Proceedings of SPIE 10600-87, Denver, CO, USA
4. Bolognani D, Verzobio A, Tonelli D, Cappello C, Glisic B, Zonta D (2017) Quantifying the benefit of SHM: what if the manager is not the owner? In: Proceedings of the 11th IWSHM, Stanford, CA, USA
5. Bolognani D, Verzobio A, Tonelli D, Cappello C, Glisic B, Zonta D (2017) An application of prospect theory to a SHM-based decision problem. In: Proceedings of SPIE 10170-84, Portland, USA
6. Leonhardt F (1964) *Prestressed concrete: design and construction*. Ernst & Sohn, Berlin
7. Nazarchuk Z, Skalskyi V, Serhiyenko O (2017) *Acoustic emission—methodology and application*, I a cura di, Springer, Berlin
8. Meo M (2014) Acoustic emission sensors for assessing and monitoring civil infrastructures. In: *Sensor technologies for civil infrastructures*, vol 1. Woodhead Publishing, pp 159–178
9. Zandonini R, Baldassino N, Freddi F, Roverso G (2019) Steel-concrete frames under the column loss scenario: an experimental study. *J Constr Steel Res* 162
10. Pollock AA, Smith B (1972) Stress-wave-emission monitoring of a military bridge. *Non-Destructive Testing* 5(6): 348–353
11. Nair A, Cai C (2010) Acoustic emission monitoring of bridges: review and case studies. *Eng Struct* 32(6): 1704–1714
12. Chataigner S, Gaillet L, Falaise Y, David J-F, Michel R, Aubagnac C, Houel A, Germain D, Maherault J-P (2018) Acoustic monitoring of a prestressed concrete beam reinforced by adhesively bonded composite, Cape Town, South Africa
13. Anay R, Lane A, Jáuregui DV, Weldon BD, Soltangharaei V, Ziehl P (2020) On-site acoustic-emission monitoring for a prestressed concrete BT-54 AASHTO Girder Bridge. *J Performance Constr Facilities* 34(3)
14. Shigeishi M (2008) Superstructures. In: *Acoustic emission testing*. Springer, Berlin, pp 323–339
15. Yuyama S, Yokoyama K, Niitani K, Ohtsu M, Uomoto T (2007) Detection and evaluation of failures in high-strength tendon of prestressed concrete bridges by acoustic emission. *Constr Build Mater* 21(3): 491–500
16. Holford KM, Lark RJ (2005) Acoustic emission testing of bridges. In: *Inspection and monitoring techniques for bridges and structures*. Woodhead Publishing, Cambridge (UK), pp 183–215
17. Ohtsu M (2008) History and fundamentals. In: *Acoustic emission testing*. Springer, Berlin, pp 11–18
18. Ohtsu M (2008) Sensors and instruments. In: *Acoustic emission testing*. Springer, Berlin, pp 19–40

19. Jin X, Ladabaum I, Khuri-Yakub PT (1998) The microfabrication of capacitive ultrasonic transducers. *J Microelectromechanical Syst* 7(3): 295–302
20. ISO (2001) ISO 12716:2001 Non-destructive testing—acoustic emission inspection—Vocabulary. International Organization for Standardization
21. Shiotani T (2008) Parameter analysis. In: *Acoustic emission testing*. Springer, Berlin, pp 41–51
22. Beattie AG (2013) Acoustic emission non-destructive testing of structures using source location techniques. SAND2013–7779. Sandia National Laboratories, Albuquerque, NM
23. Tillmann AS, Schultz AE, Campos JE (2015) Protocols and criteria for acoustic emission monitoring of fracture-critical steel bridges. Minnesota Department of Transportation Research Services & Library, St. Paul, Minnesota
24. Moradian OZ, Li BQ (2015) Hit based acoustic emission monitoring of rock fractures: challenges and solutions. Honolulu, Hawaii
25. Ohtsu M, Grosse CU (2008) *Acoustic emission testing*. Springer, Berlin
26. Zonta D, Migliorino P, Selleri A, Valeri E, Marchiondelli A, Tonelli D, Bolognani D, Debiassi E, Bonelli A, Rossi F (2020) L'esperienza del campo prove Sicurezza Infrastrutture MIT. EDI-CEM Srl – Strade & Autostrade, vol 142
27. SPEA (1966) Relazione di Calcolo Viadotto Alveo Vecchio alla progr. 39 + 364.21, Opera N°14
28. D. Università degli Studi di Trento (2019) Campo Prove Sicurezza Infrastrutture MIT - Protocollo di Prova e Strumentazione Campata C3sx, Trento
29. Tonelli D, Cappello C, Zonta D (2021) Performance-based design of structural health monitoring systems. In: *EWSHM 2020, LNCE 128 Proceedings*, Palermo, Italy
30. Tonelli D, Luchetta M, Rossi F, Migliorino P, Zonta D (2020) Structural health monitoring based on acoustic emissions: validation on a prestressed concrete bridge tested to failure. *Sensors* 20(24): 1–20
31. El Batanouny MK, Larosche A, Ziehl PK, Yu L (2012) Wireless monitoring of in situ decommissioning of nuclear structures using acoustic emission. In: *8th international conference on nuclear plant instrumentation, control, and human-machine interface technologies*, La Grange Park, IL, USA
32. Tonelli D, Rossi F, Luchetta M, Caspani V, Zonta D, Migliorino P, Selleri A, Valeri E, Marchiondelli A, Ascari G (2021) Effectiveness of acoustic emission monitoring for in-service prestressed concrete bridges. *Proc. SPIE* 11591, *Sensors and Smart Structures Technologies for Civil, Mechanical, and Aerospace Systems 2021*, 115910V (22 March 2021). <https://doi.org/10.1117/12.2585527>

Weight-in-Motion System for Traffic Overload Detection: Development and Experimental Testing



D. Di Giacinto, V. Musone, G. Laudante, L. Grassia, and E. Ruocco

Abstract A new load cell-based Weight-in-Motion (WIM) equipment for detecting traffic overload conditions on the roadway structure is proposed. The system consists of two load detection sensors, a supporting and stiffening steel structure, a reinforced concrete (RC) basement, and a steel covering plate. Embedded within the road pavement at grade with the top asphalt surface, the sensors are offset to avoid missing values while gathering the data from the passing vehicle. This strategy ensures the passage of both the axle's wheels through the measuring area, which is the top surface of a steel beam supported by four load cells. Being the beam width smaller than the wheel's contact surface, a tailored algorithm has been implemented to process the gathered data and return the Gross Vehicle Weight (GVW). More than 500 experimental tests have been performed to assess the system's performance. A relatively rigid basement reduces the noise related to the vibrations generated by the system itself, which might affect the data analysis. Nonlinear dynamical FE analyses have been performed to support the structural design. A reduction in operating costs is allowed by the streamlined low-maintenance configuration of the system, along with its robustness.

Keywords Weight-in-motion · Data analysis · Traffic overload detection · Infrastructure monitoring

1 Introduction

Road infrastructures' durability is heavily impacted by traffic overload conditions [1], which can be detected by implementing a passing-vehicle axial weighing strategy. In particular, bridges [2] and viaducts [3] may undergo significant structural issue during their in-service life due to increasing traffic loads [4, 5]. Although remarkably

D. Di Giacinto (✉) · L. Grassia · E. Ruocco
Department of Engineering, University of Campania Luigi Vanvitelli, 81031 Aversa, Italy
e-mail: daniilo.digiacinto@unicampania.it

V. Musone · G. Laudante
Department of R&D, SMA Road Safety, 81025 Marcianise, Italy

accurate, static scale-based weighing techniques can be time-consuming and associated with high costs, both for the road system and the vehicle operators. Indeed, to reach the in-service station—often after waiting in a queue—it requires the deviation of the vehicle from the traffic stream for being weighed when stationary.

Weigh-in-motion systems have been developed for measuring the weight of a moving vehicle, both in low-speed (LS-WIM) and high-speed (HS-WIM) conditions. A Weigh-in-Motion system consists of a complexity of hardware (e.g. sensors and cameras) and software capable to detect moving vehicles' weight and speed in real-time. Typically placed at toll-booths or motorway entries, LS-WIM operations rely on load-cell or bending plates and require the vehicle to travel at a speed range between 5 and 15 km/h [6]. Instead, HS-WIM systems are intended to weigh dynamically a vehicle traveling at any speed—within the legal limits—with no need to specify a low-speed induced point along the road infrastructure. Most of the HS-WIM systems are based on capacitive, fiber-optic, and piezo-quartz sensor technologies. Although relatively cheap to install and maintain [7, 8], due to their tendency to lost accuracy or even stop functioning, they may involve high long-term costs associated with partial or full replacement [9]. Caprez et al. [10] investigated the reliability and maintenance cost of commercially available WIM systems installed in Zurich from 1991 to 1993, highlighting that piezo-quartz strip sensors accuracy is more susceptible to sensing and software issues.

A WIM system installed within the road pavement is known as a P-WIM system. In contrast, the B-WIM system—introduced by Moses in 1979 [11]—consists of equipping a bridge structure to evaluate the traffic loads through the measurement of the deck's deformation. Yu et al. [12] and Lydon et al. [13] presented comprehensive reviews of B-WIM systems and relative algorithms.

The present research goal is to develop a load-cell-based P-WIM system, which benefits from the accuracy and reliability of the load-cell technology while widening its working speed range. To this end, the design has taken into account the effects of the system structural characteristics on the measuring equipment performances—e.g. noise propagation and dynamic amplification—and the influence of the vehicle speed and the sensing device configuration on the estimation algorithm.

2 System Description

The proposed P-WIM system consists of an assembly of two sensing devices, a stiffening steel frame, a fiber-reinforced concrete foundation pit, and a covering plate (see Fig. 1). In a simplistic description, each sensing device resembles the structural scheme of simply-supported beams, where a relatively rigid joist transfers the wheel load to load-cells. The upper side of the presser, which is at grade with the top road surface, represents the *sensitive area*. To prevent vehicle slippage, specific surface treatment has been applied to the top surfaces of the closing plate and the pressers.

Fig. 1 The P-WIM system as it appears once installed



The offset configuration of the sensitive areas along the direction of travel allows computing the vehicle's speed at the post-processing stage. As depicted in the functional scheme (Fig. 2), both vehicle's entry and exit conditions are detected through inductive loops, which trigger the WIM station measurement.

The P-WIM system development seeks the following accomplishments:

- (I) OIML R134 [14] accuracy class for vehicle mass: 10. That means both a maximum $\pm 5\%$ -deviation to the conventional value of the vehicle mass (Ref. [14], Table 1).
- (II) ASTM E1318 [15] Type I classification that is $\pm 10\%$ -tolerance for 95% compliance, meaning that 95% of the estimated values must be within the tolerance (Ref. [15], Table 1).

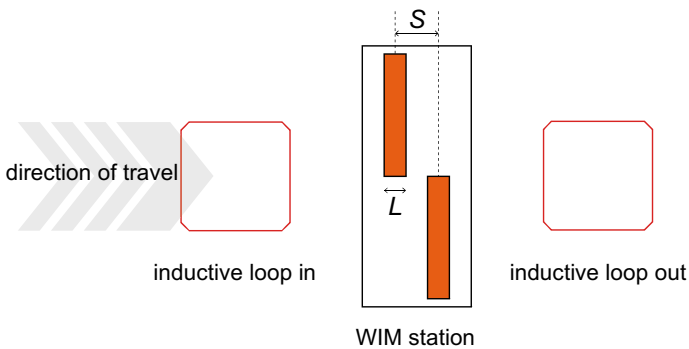


Fig. 2 Functional scheme of the proposed P-WIM system

Table 1 Vehicle involved in the experimental test campaign

Label	Category (COST 323)	Description	Weight (t)	Speed range (km/h)
Loaded truck	5	Iveco Eurostar	27.60	10 ÷ 25
Unloaded truck	5	Iveco Eurostar	17.52	10 ÷ 30
VAN	1	Fiat Ducato	2.85	10 ÷ 50
Compact car	1	Fiat Punto	1.74	10 ÷ 30

2.1 Measurement Principles

As depicted in the workflow chart reported in Fig. 3, a vehicle passing through the WIM station generates a signal, representing the raw datum for speed and weight calculation. As the strain gauge inside the load-cell deforms, the resulting change in terms of resistance can be measured as voltage directly related to the applied force (see Fig. 4a). An amplifier/digitizer receives and amplifies the low-voltage signal

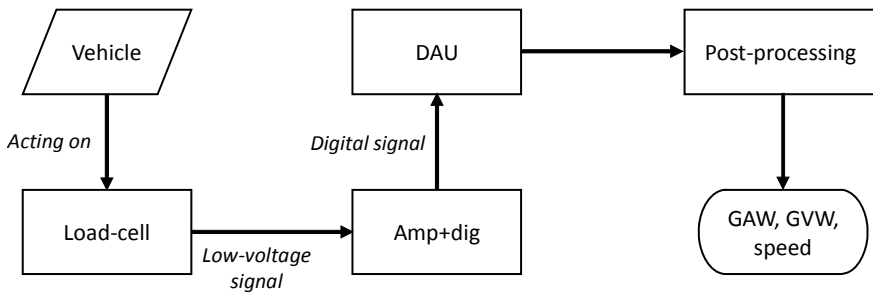


Fig. 3 Workflow chart of the proposed P-WIM system

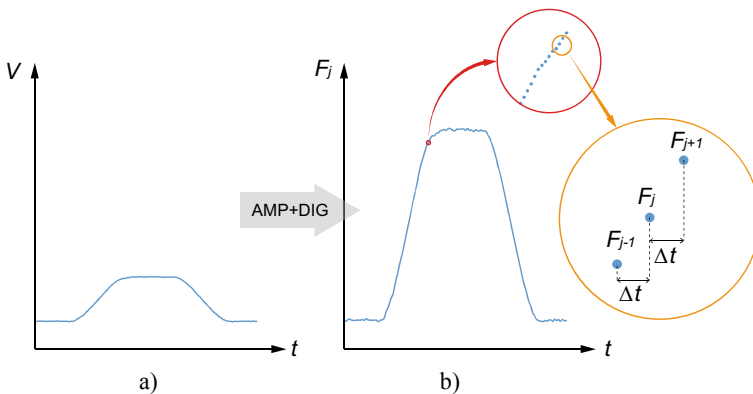


Fig. 4 The typical signal generated by a passing vehicle’s axle over the system: **a** voltage variation at the load-cell, and **b** conversion, amplification, and digitalization of the low-voltage signal

from the load-cell without applying any filter. After converting the signal in terms of voltage into applied force, it digitalizes the values over time according to a predefined sampling frequency f_c (see Fig. 4b), the choices of which depends on the required signal fidelity, that is data gathering without information leak and noise propagation. In the present study, a selected $f_c = 9600$ Hz as sampling frequency has been adopted. The digital data are then gathered and stored using a Data Acquisition Unit for the following post-processing stage which returns the three required output quantities: Gross Axle Weight (*GAW*), Gross Vehicle Weight (*GVW*), and vehicle's speed (v).

2.2 Post-Processing Algorithm

An estimation algorithm processes the digital signal acquired by the DAU returning the three output quantities *GAW*, *GVW*, and v .

The vehicle's speed v is the ratio between the sensor's center distance S along the direction of travel and the relative crossing time t_{xing} :

$$v = S/t_{xing} \quad (1)$$

The Gross Vehicle Weight (*GVW*) is defined as the sum of the Gross Axle Weights (*GAW*):

$$GVW = \sum_i GAW_i \quad (2)$$

with i raging from 1 to n , where n is the number of axles.

As shown in Fig. 4b, the digital signal consists of a series of instantaneous time-step values ($\Delta t = 1/f_c$) of the applied force F_j at the j th time step $t_j = t_{j-1} + \Delta t$. Thus, the i th GAW_i value coming from the integral of the applied force $F(t)$ function with respect to time becomes the sum of the product $F_j \cdot \Delta t$:

$$GAW_i = v_i/L \int F(t)dt = v_i/L \sum_j F_j \Delta t \quad (3)$$

The introduction term v_i/L allows the dimensional correctness of the GAW_i value, as well as to normalize the digital signal. In fact, for a known and constant L -value of the presser's width, the higher the vehicle axle's speed v_i the narrower the signal shape (see Fig. 5).

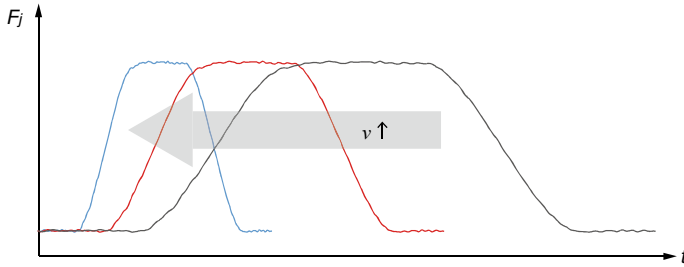


Fig. 5 Speed's influence on the signal-shape

3 Experimental Test Campaign and Results Discussion

More than 500 tests have been performed to assess the system's performance and evaluate whether it meets the EU (OIML R134) and US codes (ASTM E1318). The following vehicles (see Fig. 6), traveling at different speed levels (from 10 to 50 km/h), have been involved:

The weight of the testing vehicles has been previously measured statically through a high-precision industrial truck in-floor scale having 0.1% accuracy. This value is herein indicated as static-Gross Vehicle Weight (GVW_{st}).

For the sake of readability, only the sample of 93 estimated GVWs over more than 500 have been plotted in Fig. 7. The results show that, within the considered speed range, the system performances fulfill the OIML R134 $\pm 5\%$ acceptability requirements. Figure 8 shows the estimated GVWs with respect to the relative estimated speed.

Although the fulfillment of the OIML R134 requirements automatically accomplishes the ASTM E1318 ones for the given target WIM type (I), for the sake of completeness Fig. 9 shows that the errors relative to all the estimated values lie under the prescribed limit ($\pm 10\%$). Figure 10 reports the Gross Vehicle Weight estimation error:



Fig. 6 Vehicles involved in the testing campaign: **a** truck, **b** VAN, and **c** compact car

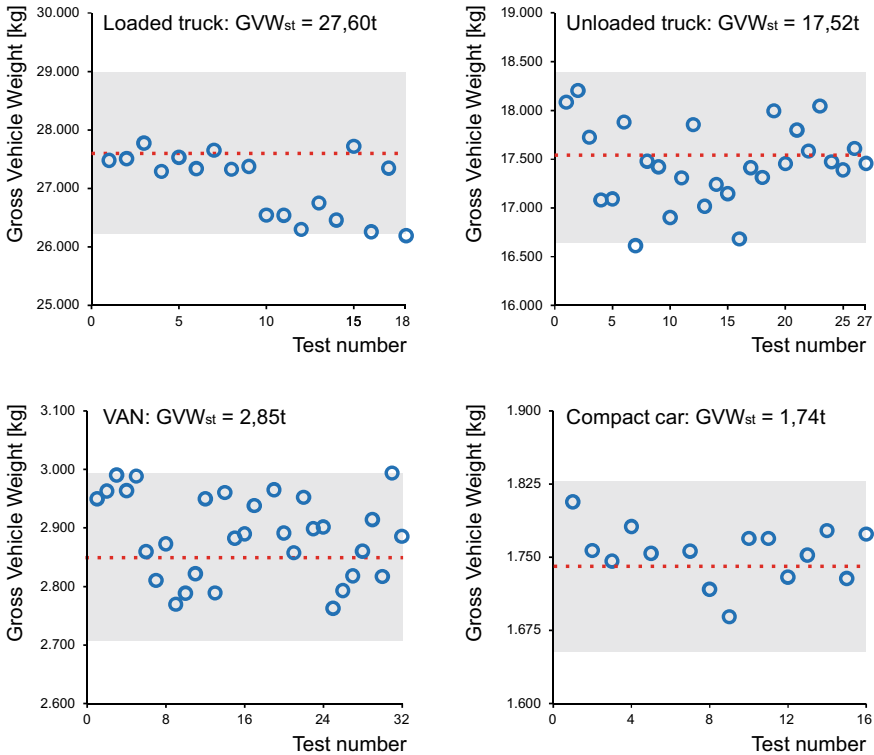


Fig. 7 Experimental test campaign results in terms of GVW. The red dotted line represents the statically measured gross vehicle weight (GVW_{st}) while the light-grey band indicates the OIML R134 ± 5% GVW acceptability range

$$GVW_{error, \%} = [(GVW_{estimated} - GVW_{static}) / GVW_{static}] \cdot 100 \quad (4)$$

to the relative estimated speed.

4 Conclusions and Future Developments

The development of a load-cell based in-Pavement Weigh-in-Motion system (P-WIM) is herein presented. Although being among the most accurate load-detecting sensors, the application of this type of WIM systems is limited to 15 km/h (Low-Speed WIM). This study aims to widen the operating speed range by investigating the parameters and conditions affecting the accuracy. The design of the system also takes into account the influence of the fundamental frequency of the system's structure, estimated through a modal FE analysis. An experimental testing campaign, involving three types of vehicles for a total of four different configurations (loaded truck,

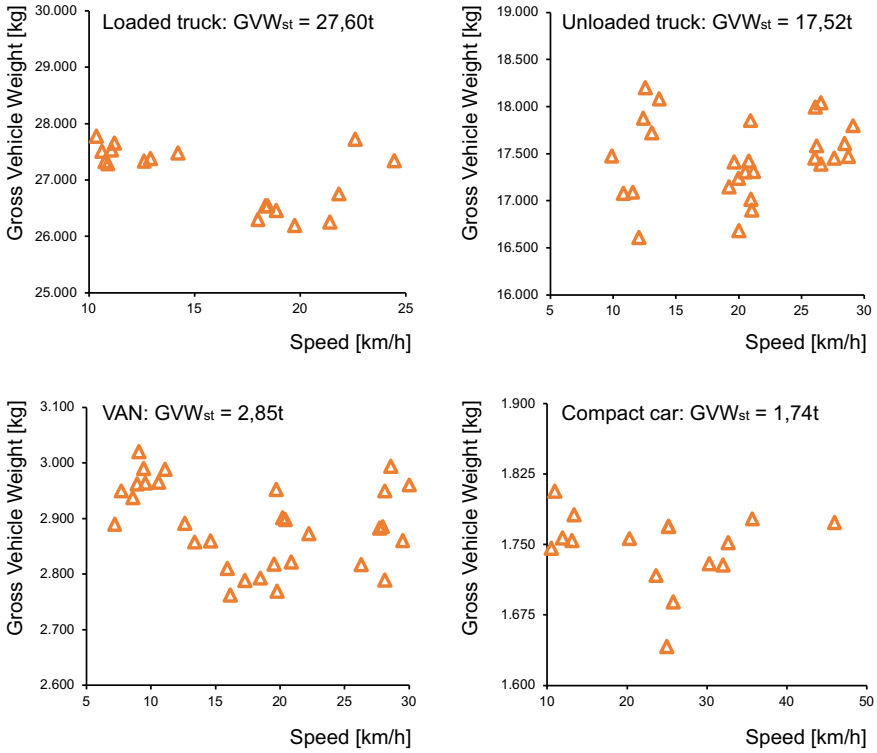


Fig. 8 Experimental test campaign results in terms of estimated GVW and relative estimated speed v

unloaded truck, VAN, and compact car) has been carried out to assess the performance of the system within a speed range of 10–50 km/h. Both the estimated Gross Vehicle Weight (GVW) values and the relative errors accomplish the EU (OIML R134) and the US (ASTM E1318) regulations.

Further investigation is needed with particular regard to the vehicle’s speed and entry-angle. Assuming that each GAW estimation error is stochastically independent, the percentage error is equal to the single axle error over the square root of the number of axles. Thus, the higher the number of axles the smaller the GVW estimation error, i.e. two-axles vehicles return the highest estimation error (scaling factor equal to $\sqrt{2} \approx 1.41$). Being the sensitive area width smaller than the footprint of the tires, a signal-time integral is need to compute the GAW during each passage:

$$GAW_i = v_i/L \int F(t)dt \tag{5}$$

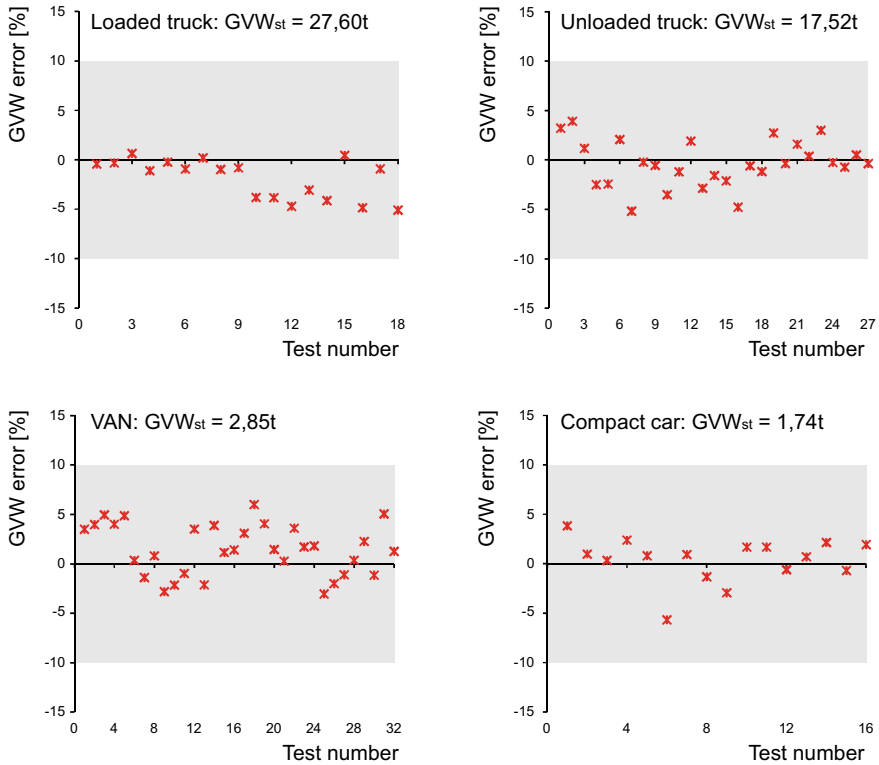


Fig. 9 Experimental test campaign results in terms of GVW estimation error. The light-grey band indicates the ASTM E1318 ± 10% GVW estimation error acceptability range. Items that exceed these limits must be limited to 5-percentile

where v is the vehicle’s speed and L the sensitive area width. Since the system is industrially manufactured by high-precision CNC machining, it is legitimate to neglect the measurement error of L . As a consequence, the GAW estimation error is the root sum squared of the load-cell measuring error and the speed estimation error:

$$\delta GAW_i / GAW_i = \sqrt{(\delta F / F)^2 + (\delta v / v)^2} \tag{6}$$

The load-cell manufacturer provides the measuring error in the datasheet. Because the estimation of the velocity (vehicle speed and direction) depends on the entry-angle and crossing time, the error is the following root sum squared:

$$\delta v / v = \sqrt{(\delta t / t)^2 + (\delta S / S)^2} S^\perp \tag{7}$$

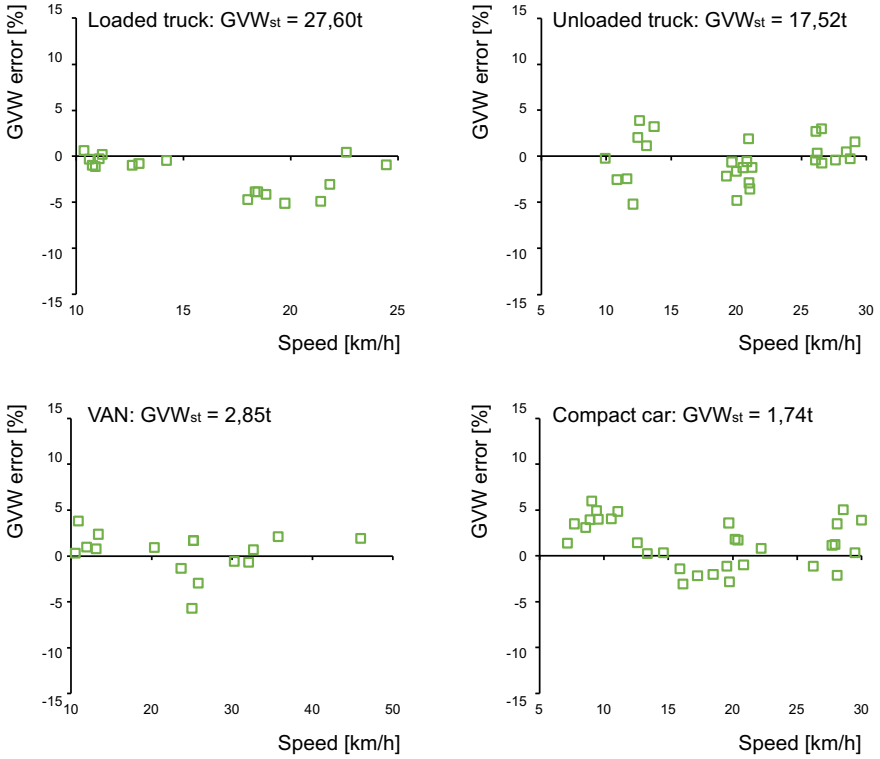
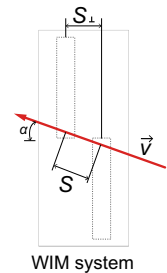


Fig. 10 Experimental test campaign results in terms of GVW estimation error and relative estimated speed v

where $\delta t/t$ is the crossing time estimation error and $\delta S/S$ is the sensor-to-sensor traveling distance which may be different from the one measured with respect to the longitudinal axis (S_{\parallel}) of the sensors. In fact, S is affected by the vehicle entry-angle α as shown in Fig. 11.

Currently, the authors' research is addressing those issues.

Fig. 11 Vehicle's velocity influence on the sensor-to-sensor traveling distance S



Acknowledgements The authors gratefully acknowledge the infrastructure and support of Industry AMS.

References

1. Pais JC, Amorim SIR, Minhoto MJC (2013) Impact of traffic overload on road pavement performance. *J Transp Eng* 139(9):873–879
2. Aggarwal V, Parameswaran L (2015) Effect of overweight trucks on fatigue damage of a bridge. In: *Advances in structural engineering*, pp 2483–2491
3. Malomo D, Scattarreggia N, Orgnoni A, Pinho R, Moratti M, Calvi GM (2020) Numerical study on the collapse of the Morandi Bridge. *J Perform Constr Facil* 34(4):04020044
4. Leahy C, O'Brien E, O'Connor A (2016) The effect of traffic growth on characteristic bridge load effects. *Transp Res Proc* 14:3990–3999
5. Righiniotis T (2006) Effects of increasing traffic loads on the fatigue reliability of a typical welded bridge detail. *Int J Fatigue* 28(8):873–880
6. Richardson J, Jones S, Brown A, O'Brien E, Hajializadeh D (2014) On the use of bridge weigh-in-motion for overweight truck enforcement. *Int J Heavy Veh Syst* 21(2):83
7. Bushman R, Pratt AJ (1998) Weigh in motion technology—economics and performance. International Road Dynamics, Inc.
8. Ryguła A, Brzozowski K, Maczyński A (2020) Limitations of the effectiveness of weigh in motion systems. *Open Eng* 10(1):183–196
9. Szary PJ, Maher A (2009) Implementation of weigh-in-motion (WIM) systems. New Jersey Department of Transportation (NJDOT), Report no. FHWA-NJ-2009-001
10. Caprez M, Doupal E, Jacob B, O'Connor AJ, O'Brien EJ (2000) Test of WIM sensors and systems on an urban road. *Int J Heavy Veh Syst* 7(2/3):169
11. Moses F (1979) Weigh-in-motion system using instrumented bridges. *Transp Eng J ASCE* 105(3):233–249
12. Yu Y, Cai C, Deng L (2016) State-of-the-art review on bridge weigh-in-motion technology. *Adv Struct Eng* 19(9):1514–1530
13. Lydon M, Taylor SE, Robinson D, Mufti A, Brien EJO (2015) Recent developments in bridge weigh in motion (B-WIM). *J Civ Struct Heal Monit* 6(1):69–81
14. OIML Automatic instruments for weighing road vehicles in motion and axle-load measuring. Part 1: metrological and technical requirements—tests, R134
15. ASTM (2017) Stan standard specification for highway weigh-in-motion (WIM) systems with user requirements and test method. ASTM Standard E1318

Bayesian-Based Damage Assessment of Historical Structures Using Vibration Monitoring Data



Laura Ierimonti , Nicola Cavalagli , Enrique García-Macías ,
Iliaria Venanzi , and Filippo Ubertini 

Abstract The high level of damage suffered by historical structures due to the interaction between materials' aging and seismic events that occurred during the last decade has revealed the need for developing reliable and long-lasting prevention techniques. In this context, long-term structural health monitoring (SHM) is a practice that has been spreading in recent years. A monitoring system is composed by an optimized network of sensors placed in strategic positions within the building. The data recorded by the sensors enable to track the structural behavior over time. In this study an automated Bayesian-based procedure, i.e., an inverse problem able to detect in real-time the occurrence of damage, is proposed. In particular, hourly data are periodically divided into subgroups and used for the automatic Bayesian update. The methodology can be summarized as follows: (i) preliminary calibration of a Finite Element (FE) model able to reproduce the structural dynamic behavior identified by the experimental vibration data; (ii) identification of damage-sensitive portions of the structure by performing non-linear static analyses (NLSA) on the FE model; (iii) calibration of a digital twin of the structure by surrogate modeling and definition of the sensitivity damage chart; (iv) real time Bayesian model updating of the selected uncertain parameters in order to continuously identify possible changes in the structural behavior that can be associated with a certain level of damage.

L. Ierimonti (✉) · N. Cavalagli · E. García-Macías · I. Venanzi · F. Ubertini
Department of Civil and Environmental Engineering, University of Perugia, Via G. Duranti,
06125 Perugia, Italy
e-mail: laura.ierimonti@unipg.it

N. Cavalagli
e-mail: nicola.cavalagli@unipg.it

E. García-Macías
e-mail: enrique.garciamacias@unipg.it

I. Venanzi
e-mail: ilaria.venanzi@unipg.it

F. Ubertini
e-mail: filippo.ubertini@unipg.it

Keywords Bayesian approach · Damage detection · Structural Health Monitoring · Architectural heritage

1 Introduction

A key step for decision-making in historical buildings located in regions characterized by high seismic hazard concerns the capability of damage estimation with immediate impact, since such structures are particularly prone to damage and degradation. In this context, SHM-based techniques can be notably suitable for tracking over time the structural modal parameters, which are diffusely considered to be connected with material's damage and deterioration [1–4]. SHM is largely exploited in literature for different structural applications: for the investigation of the dynamic behavior of masonry bell towers [5, 6]; for the evaluation of the environmental effects (temperature and humidity) [7, 8]; for the SHM of masonry buildings [9, 10] and bridges [11–13]. A brief review on SHM for data-driven damage identification problems is given in [14].

Within the complex task of damage-identification, a mathematical representation of the structures is mandatory given that purely data-driven techniques are lacking at damage localization and quantification. However, numerical models need to be calibrated on the basis of the measured data in order to minimize the discrepancy between predictions and experimental results. Such adjustments are classified as model updating. Model updating techniques can be affected by errors and uncertainties related to both models and measurements [15, 16]. The use of surrogate models for handling uncertainties in SHM was explored in [17, 18].

Recently, Bayesian-based methodologies are emerging in the SHM field in order to provide a statistical characterization of the uncertain parameters to be calibrated by exploiting the well known Bayes' theorem on conditional probability. The most widespread application of Bayesian Model Updating concerns the use of ambient vibration data for structures [19, 20] and bridges [21, 22].

Only a few recent contributions extend the use of the Bayesian model updating in the context of continuous SHM. In Behmanesh et al. [23, 24] hierarchical Bayesian model updating was proposed by accounting for different grouping of measured data, while in [25] the hierarchical Bayesian framework was used for updating a FE model. An iterative procedure for damage detection and localization was proposed in [26], where the Bayesian process was applied through the Transitional Markov Chain Monte Carlo (TMCMC). In [27] a Bayesian model-updating methodology of an isolated school building was proposed.

As confirmed by the literature review, the most common procedure in continuous civil SHM involves the two following steps: (i) data acquisition, (ii) feature extraction (frequencies and the mode shapes) [28, 29]. This procedure can be framed in the unsupervised learning field, where a modification in the structural behavior can be classified as novelty detection. During the last decades, the concepts of machine learning are approaching the SHM [30, 31], but a complete damage identification

process (detection, localization, classification, assessment, prediction) [28] is still a challenging goal to be reached. Hence, semi-supervised learning methodologies are particularly attractive in the SHM context [32], since one of the biggest limitations is the lack of representative data.

The idea behind this work is that one can learn relationships from data. In the context of SHM, this means that it is possible to assign a damage state or class by using a training numerical model in order to detect damage at the earliest possible time and in an automatic manner. Since model-based approaches are typically ill-conditioned, some priorities need to be made to cleverly label the data. The process of prioritising monitored data by using the numerical model allows to contextualize the proposed methodology into the semi-supervised learning approach where the learning algorithm is allowed to build a labeled training set autonomously [28].

This paper presents a Bayesian-based methodology aimed at evaluating the damage of monumental structures by making use of long-term monitoring data. The adopted approach is based on the training of a digital twin of the structure in order to use it as a formal prior belief of the possible damaged scenarios with a reduced number of damage-sensitive parameters (semi-supervised learning). The case study is the Consoli palace located in Gubbio, near Perugia, in Italy, that has been monitored by the Authors since 2015 with an updating of the monitoring system in 2020. The palace is an historical complex masonry building, developed on three levels. The monitoring system consists of: 12 high sensitivity accelerometers; 2 temperature sensors; 2 LVDT devices (see Sect. 3.1). Continuous monitoring data are automatically extracted through the MOSS software [33] and used for the Bayesian model updating of specific building properties. Nonlinear static analyses (NLSA) are performed on the FE model in order to identify the damage-sensitive regions. The posterior distribution of the uncertain parameters is computed through the well known Bayes' theorem. The prior knowledge of the uncertain parameters is sequentially updated on the basis of the trained digital twin. The effectiveness of the proposed methodology is demonstrated by the numerical simulation of a feasible damage scenario.

The rest of the paper is organized as follows. Section 2 presents the Bayesian-based proposed methodology. Section 3 describes the monumental building selected as case study, the continuous monitoring system and the FE model. Section 4 illustrates the results and, finally, Sect. 5 concludes the paper.

2 The Proposed Methodology

The main advantage of the proposed methodology, schematically represented in Fig. 1, is the possibility to evaluate in a timely and continuous manner any variation in the structure which is commonly considered as a sign of possible damage [2] and use this information in order to detect and localize damage by means of a digital twin. The different consequential steps can be summarized as follows:

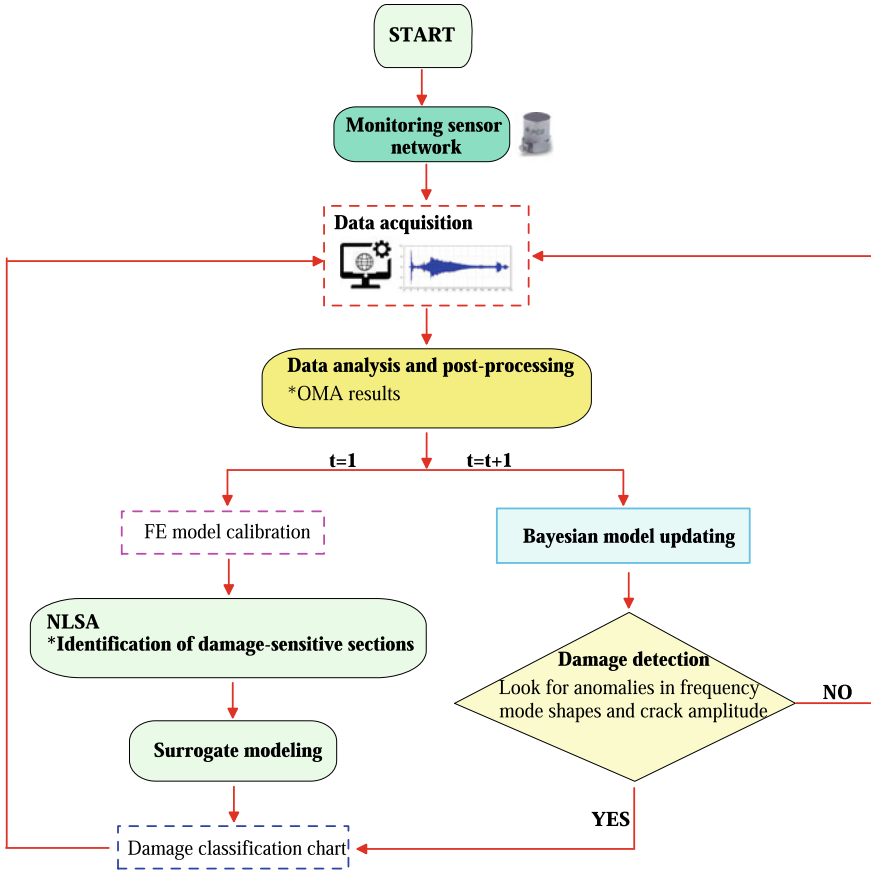


Fig. 1 The proposed methodology

1. Start the data acquisition from the dynamic monitoring system, i.e. acceleration data, and from the static environmental monitoring system, i.e. crack amplitudes and temperature information.
2. OMA analysis. This phase allows to estimate natural frequencies f_i^{exp} , mode shapes Φ_i^{exp} and damping coefficients ζ_i^{exp} associated to the i -th natural vibration mode from operational vibration measurements, continuously over time. Environmental effects should be removed from original signals on the basis of a selected training period. Different statistical models can be adopted for this purpose which allow to distinguish variations due to environmental conditions or possible damages. For the proposed methodology the principal component analysis (PCA) technique is used.
3. If $t=1$: Model training.

- Perform FE model construction and calibration of selected parameters in order to achieve the minimum deviation between the FEM results and the experimental measured data. The calibration process can be formulated as an optimization problem as follows:

$$\mathbf{Y}^{\text{opt}} = \arg \min_{\mathbf{Y}} \sum_{i=1}^M p_1 \eta_{f,i}(\mathbf{Y}) + p_2 \eta_{\Phi,i}(\mathbf{Y}) \quad (1)$$

where M is the number of vibration modes; $\mathbf{Y} = \{\mathbf{Y}_1, \dots, \mathbf{Y}_n, \dots, \mathbf{Y}_N\}$ is the vector collecting the n -th parameter to be calibrated (for instance \mathbf{Y}_n is the vector collecting Young's modulus E , shear modulus G , Poisson's ratio ν and mass density) with N total number of uncertain parameters; p_1 and p_2 represent the weight of the objective function; $\eta_{f,i}(\mathbf{Y}) = |f_i^{\text{exp}} - f_i^{\text{FEM}}|/f_i^{\text{exp}}$ is the residual frequency function; $\eta_{\Phi,i}(\mathbf{Y}) = 1 - \text{MAC}_i(\mathbf{Y})$ is the residual mode shape function where the term MAC_i denotes the Modal Assurance Criterion (MAC) between the i -th experimental Φ_i^{exp} and numerical Φ_i^{FEM} mode shape.

- Definition of damage-sensitive areas. Perform NLSA which, in conjunction with engineering judgment, allows to identify the damage-sensitive areas within the FE model, i.e. definition of j -th damage-sensitive sets of element $S = S_1, \dots, S_L$ and definition of the vector $\mathbf{X}(S) = \{\mathbf{X}_1(S_1), \dots, \mathbf{X}_N(S_L)\}$ collecting the mechanical characteristics of each set S to be updated, with L total number of damage-sensitive sets. For the sake of simplicity, the dependence on S in the term $\mathbf{X}(S)$ is dropped hereafter.
- Surrogate modeling. Define a sampling population for the j -th \mathbf{X}_j and numerically reconstruct the surrogate model in order to use it as a digital twin of the investigated structure. For the present paper, the Kriging model is used. The effectiveness of such a model in spatial interpolation was demonstrated in previous works by the Authors [17]. According to the Kriging method, the process that originated the data $y(\mathbf{X})$ can be divided into a regression model \mathcal{F} , i.e., the deterministic component, and an approximation error α , i.e., the stochastic component [34]:

$$y(\mathbf{X}) = \mathcal{F}(\beta, \mathbf{X}) + \alpha(\mathbf{X}) \quad (2)$$

where β are the regression parameters of \mathcal{F} . The approximation error α is assumed as a random process with zero mean and covariance $\text{cov}(X_i, X_j) = \sigma^2 \mathcal{R}(\theta, X_i, X_j)$, with σ^2 variance of $\mathcal{F}(\beta, \mathbf{X})$ and \mathcal{R} the matrix of stochastic-process correlations with components $r(\theta, X_i, X_j)$, where θ are the correlation parameters.

- Sensitivity damage chart through surrogate modeling. The sensitivity damage chart is elaborated from the surrogate model and represents the correlation between the uncertain parameters \mathbf{X} and the dynamic behavior of the structure in terms of frequency decay and MAC reduction.

4. if $t > 1$, Bayesian model updating of the mean value of the uncertain parameters and damage detection. At this level, the daily posterior probability density function (PDF) can be evaluated as follows:

$$p(\mathbf{X}|\hat{\mathbf{d}}, t) = \frac{p(\hat{\mathbf{d}}|\mathbf{X}, t)p(\mathbf{X}|\mu(t-1))}{c} \quad (3)$$

In the previous equation $\hat{\mathbf{d}}$ is the vector collecting the daily measured data, t is the variable selected to measure days, $c = \int p(\hat{\mathbf{d}}|\mathbf{X}, t)p(\mathbf{X}|\mu(t-1))dx$ is a normalizing factor called the evidence of the model, which ensure that the posterior distribution integrates to one; $p(\hat{\mathbf{d}}|\mathbf{X}, t)$ is the likelihood function which gives a measure of the agreement between the measured data $\hat{\mathbf{d}}$ and the predicted data (surrogate-based data) at time t ; $p(\mathbf{X}|\mu(t-1))$ is the prior PDF of \mathbf{X} depending on the mean value μ of \mathbf{X} updated at time $t-1$. It is worth noticing that, theoretically, the prior distribution has the main role of regulator for the Bayesian model updating before some evidence is taken into account (measured data $\hat{\mathbf{d}}$). Hence, the prior PDF becomes more informative as the number of data increases, getting barely persuaded by new data. In order to avoid the overwhelming of new data, especially in the case of damage occurrence, the co-variance of the prior distribution is assumed as known, while the mean value μ is updated step by step. In such a way, the posterior distribution at time t can inform us what values of damage-sensitive parameters are more plausible or believable, given the evidence of new data $\hat{\mathbf{d}}(t)$ and prior knowledge $p(\mathbf{X}|\mu(t-1))$.

Assuming that the identified modal parameters are statistically independent [21, 23], the likelihood function is modeled as a Gaussian distribution with zero mean and an unknown variance:

$$p(\hat{\mathbf{d}}|\mathbf{X}, t) = \frac{1}{\left[2\pi \prod_{i=1}^M (\sigma_{f_i} \sigma_{\Phi_i})^2\right]^{(MD)/2}} \exp\left(-\frac{1}{2} \sum_{k=1}^D \sum_{i=1}^M J_i^{\text{err}}(\mathbf{X}, \hat{d}_k, t)\right) \quad (4)$$

where index $i = 1, \dots, M$ refers to the reference parameter associated to the i -th vibration mode; index $k = 1, \dots, D$ represents the number of measured data collected in the vector $\hat{\mathbf{d}}$; $J_i^{\text{err}} = (\sigma_{f_i})^{-2} e_{f_i}^2(\mathbf{X}, \mathbf{d}) + (\sigma_{\Phi_i})^{-2} e_{\Phi_i}(\mathbf{X}, \mathbf{d})$ is the measure of fit function (error function) which quantifies the discrepancy between the experimental data and the FE model results with $\sigma_{f_i}, \sigma_{\Phi_i}$ standard deviations associated to the i -th natural frequency and vibration mode, $e_{f_i} = f_i^{\text{exp}} - \hat{f}_i(\mathbf{X})$ and $e_{\Phi_i} = 1 - MAC_i$.

3 The Case Study

The Consoli Palace is a medieval building built in the 14th century in Gubbio, Umbria, central Italy. The complex building has a rectangular plan and it is composed by a series of floors above (about 60 m) and under (about 10 m) the square level. Each façade overlooks the city with round arched windows and merlons in the rooftop. The Palace is built in calcareous stone masonry with regular and homogeneous texture. The load-bearing walls have a thickness of about 1.2 m and they are connected through horizontal masonry vaults. A loggia is connected to the main structure along the south wall.

3.1 The Monitoring System

The monitoring system (Fig. 2) was installed by the Department of Civil and Environmental Engineering of University of Perugia in July 2020 and it is characterized by:

- a data acquisition system model NI CompactDAQ-9132;
- n. 12 unidirectional accelerometers (A1-A12), model PCB393B12 (Table 1) installed on different levels of the structures . More in depth: accelerometers A1, A2, A3, A10, A11, A12 are installed on the rooftop; accelerometers A4, A5, A6 are installed on level 5; accelerometers A7, A8, A9 are installed on level 3.
- a wiring system connecting the sensors and the data acquisition system installed on level 6;
- 6 temperature sensors T1-T4;
- 4 LVDT sensors C1-C4;

The monitoring system was activated on July 17-th 2020. Data are stored with an hourly basis with a sampling frequency 100 Hz.

Fig. 3 shows the tracking of the natural frequencies identified from July 18-th 2020 to November 25-th 2020, highlighting the selected training period (July 18-th 2020 to November 4-th 2020). Environmental effects are removed by using PCA.

It is worth noticing that a training period of 1 year would be more appropriate in order to effectively remove environmental effects.

3.2 FE Model

A 3D FE model of the structure has been built and calibrated within the Abaqus environment [35] in order to reproduce local and global modes of vibration identified through Ambient Vibration Tests (AVT), as reported in [8]. Masonry is considered as an assemblage of solid hexahedral and tetrahedral elements with isotropic materials. The non-linear behavior is represented by the well known concrete damage

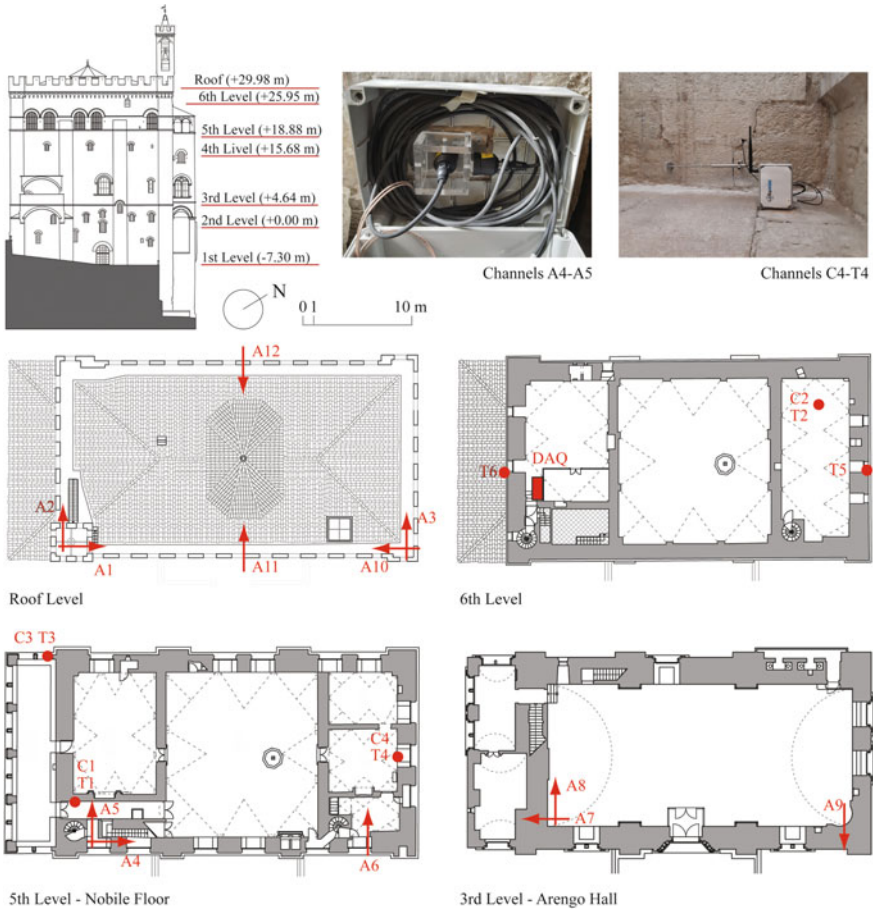


Fig. 2 Continuous monitoring configuration

Table 1 Technical characteristics of the PCB393B12 accelerometers

Characteristic	Numerical value
Sensitivity (mV/g)	10,000
Measurement range (g)	± 0.5
Frequency range (Hz)	0.15–1000
Broadband resolution (μ g)	8
Resonant frequency (Hz)	≥ 10 kHz

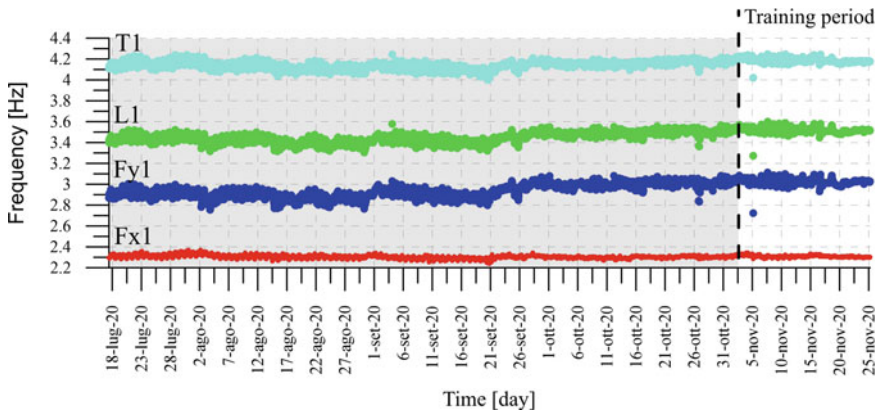


Fig. 3 Frequency tracking during the time period July 18-th 2020–November 25-th 2020

plasticity (CDP) model. The non-linear constitutive model takes into consideration the degradation of the elastic stiffness induced by plastic straining both in tension and compression. The analysis is performed by assuming a plane stress state.

NLSA in the two main directions of the building are carried out in order to determine the damage-sensitive portions of the building which can exhibit possible differences in material properties over time due to damage occurrence. In particular, the following areas are selected (Fig. 4): (D1) the loggia; (D2) the crack pattern resulting from NLDA along x direction; (D3) the crack pattern resulting from NLDA along y direction; (D4) the bell tower ; (D5) the principal staircase; (D6) the superficial texture of the main façade of the building, which is particularly prone to degradation. In such areas, the Young’s modulus is assumed as uncertain parameter. The vector collecting the uncertain parameters \mathbf{X} to be updated can be written as $\mathbf{X} = \{k_1, \dots, k_j, \dots, k_L\}$ with $L = 6$.

Figure 5 illustrates the selected FE model mode shapes of the Consoli Palace: Fx1 which is a global flexural mode along the East-West direction (MAC = 0.98); Fy1 a global flexural mode along the North-South direction direction (MAC = 0.76); L1 a local mode which pertains to the bell tower (MAC = 0.64); T1 a global torsional mode (MAC = 0.97). The relatively low quality of model calibration has been already discussed in [8, 36].

4 Numerical Results

In this section some preliminary results are presented. In order to calibrate the surrogate model, a total number of 64 samples are randomly simulated for the uncertain parameters contained in vector \mathbf{X} .

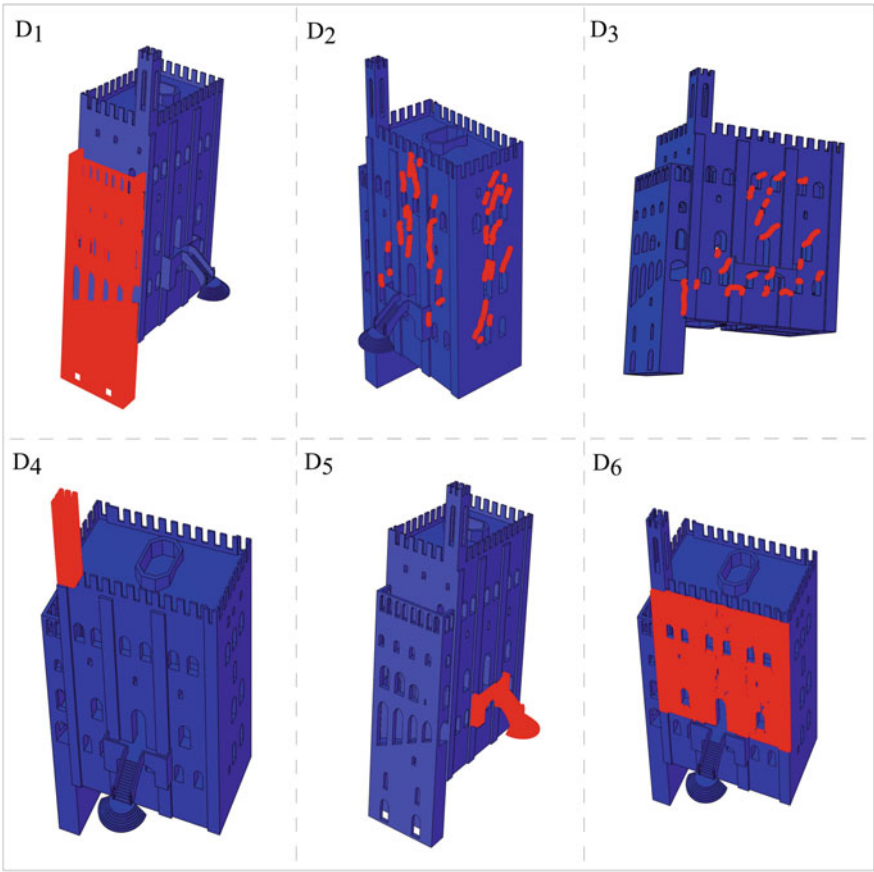


Fig. 4 Selected damage sensitive areas: D1; D2; D3; D4; D5; D6

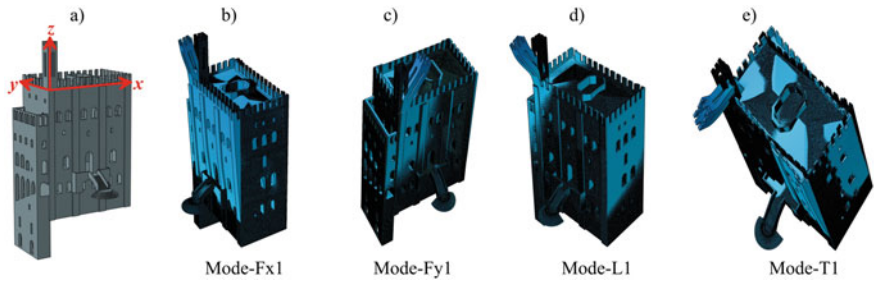


Fig. 5 Principal vibration modes: a) Fx1; b) Fy1; c) L1; d) T1

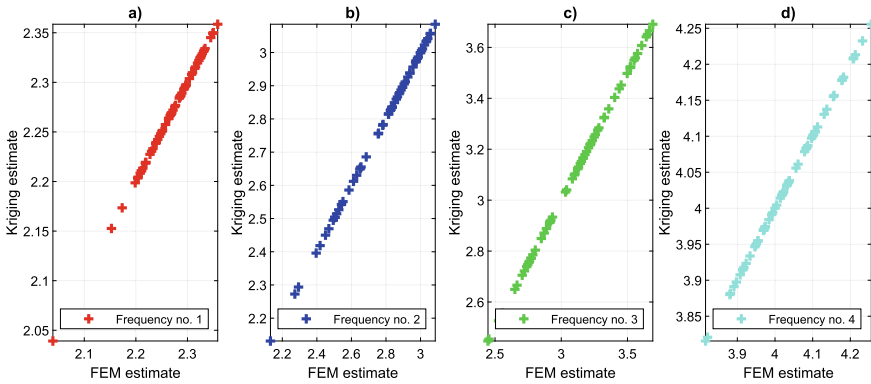


Fig. 6 FEM estimate vs Kriging estimate for the selected principal vibration modes: **a** Fx1; **b** Fy1; **c** L1; **d** T1

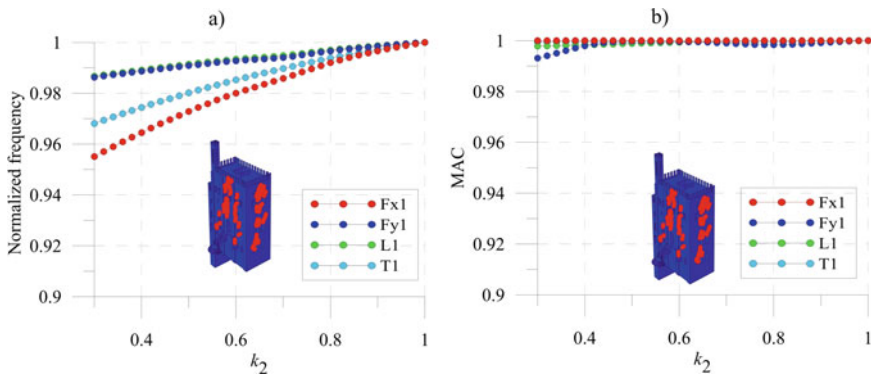


Fig. 7 Sensitivity damage chart as a function of k_2 : **a** Frequency decay; **b** MAC modification

Figure 6 shows that, for each sample of \mathbf{X} , the surrogate predicted frequencies and mode shapes (Kriging estimate) well fit the corresponding FEM values.

As a preliminary result, only the damage scenario D2 is included in the analysis. Hence, the sensitivity damage chart as a function of k_2 can be depicted from Fig. 7, which enables to associate the expected value of k_2 to a defined frequency decay and to a variation in terms of MAC value. From the Figure it can be noted that MAC values are not significantly affected by k_2 changes.

On the contrary, due to the observed frequency decay, Fx1 (flexural mode along the x direction) and T1 (torsional) appear as the most damage-sensitive vibration modes. Moreover, considering the fact that small variations can daily occur in the frequency tracking, even if environmental effects are removed, a frequency decay smaller than 1% can be considered as insignificant. Hence, the updated mean value of k_2 is expected to fluctuate between about 0.7 and 1.

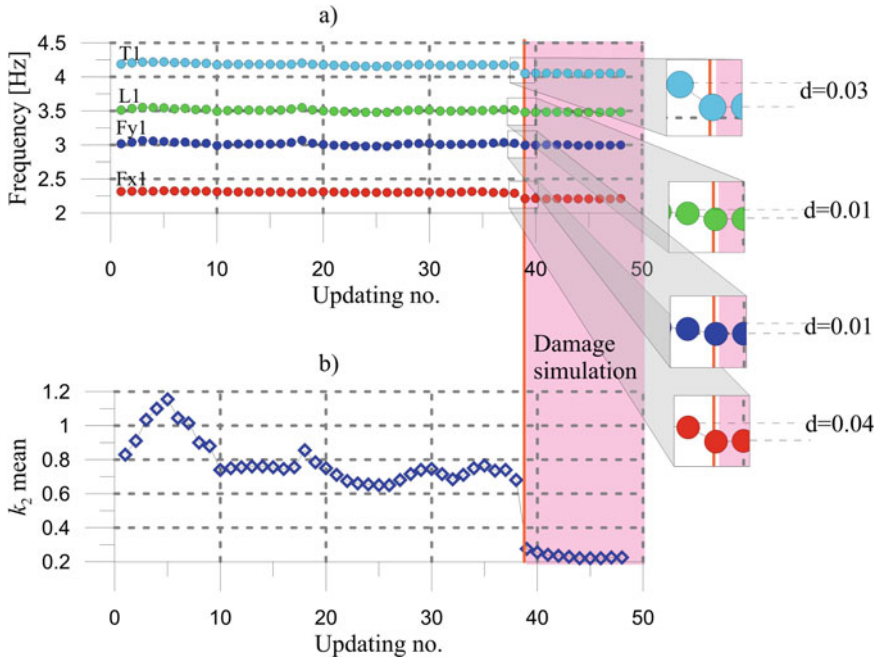


Fig. 8 Bayesian Model Updating: **a** mean value of natural frequencies for each update with the indication of the damage simulation and frequency decays d ; **b** Updated mean value of k_2 corresponding to each update

The results of the Bayesian model updating are depicted in Fig. 8. In detail, the uncertain parameter is updated once the model is trained, i.e., starting from November 5-th 2020. From that moment on, the monitored data are gathered together in subgroups of daily components (t) in order to perform the Bayesian model updating continuously over time. A damage scenario is simulated by adding the frequency decays evaluated from the sensitivity damage chart (Fig. 7a at $k_2 = 0.3$): (i) $d = 0.04$ for Fx1; (ii) $d = 0.01$ for Fy1; (iii) $d = 0.01$ for L1; (iv) $d = 0.03$ for T1.

The mean values of the principal natural frequencies are illustrated in Fig. 8a and the mean values of the updated k_2 are plotted in Fig. 8b. From the results, it can be observed that the Bayesian-based procedure is able to correctly account for the frequency decays by tracing back to the simulated damage scenario, i.e., $k_2 \approx 0.3$. Moreover, before the occurrence of damage (damage simulation), a fluctuation of k_2 between about 0.7 and 1 can be observed. This result is due to the fact that the reference sensitivity damage chart is sensitive to the slight variations (smaller than 1%) which can daily occur in the frequency tracking and to the initial FE modeling errors.

Figure 9 highlights the evolution of the posterior distribution in comparison with the prior distributions of k_2 for each Bayesian-based update. Consistently with the sensitivity damage chart (Fig. 7), in the healthy structural condition the updated

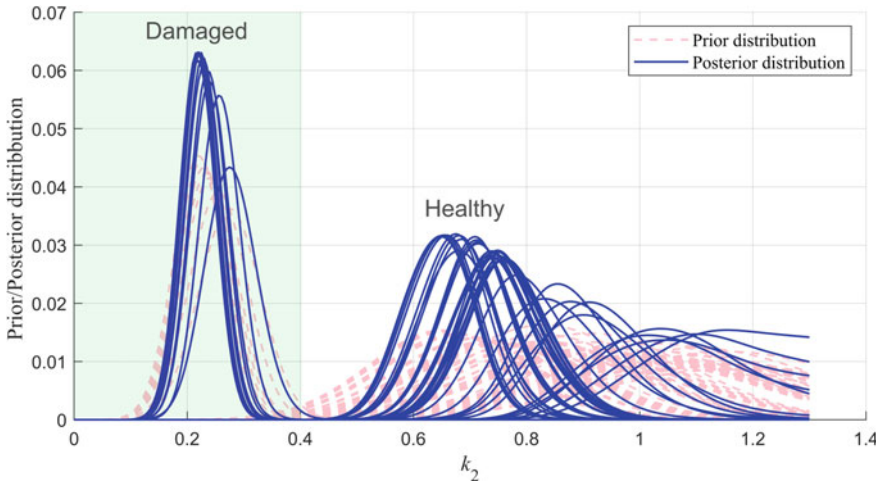


Fig. 9 Results of the Bayesian-based model updating: Prior distributions versus posterior distributions

distributions are grouped around higher values of k_2 while, the occurrence of the damage is clearly highlighted by a translation of the posterior curves towards reduced values of the selected uncertain parameter. It is worth mentioning that the sensitivity to changing environmental conditions can be considerably reduced by considering an appropriate training period, i.e. 1 year.

5 Conclusions

The present paper has discussed some preliminary results on the use of Bayesian-based updating technique for the damage detection in a monumental building. The case study is the Consoli Palace, located in Umbria (Italy), which has been monitored since 2015. The data stored between July 18-th 2020 and November 25-th 2020 are used for the numerical simulation. A FE model able to reproduce the identified structural dynamic behavior has been built and a series of NLSA, in conjunction with engineering judgment, enabled to select damage-sensitive portions of the structure. A digital twin of the structure has been calibrated by surrogate modeling in order to define a sensitivity damage chart as a prior knowledge of possible damage. Then, a real time Bayesian model updating of the selected uncertain parameters has been performed in order to continuously identify possible changes in the dynamic structural behavior. For the purpose, a damage scenario is artificially simulated by selecting an appropriate frequency decay from the sensitivity damage chart. As confirmed by the preliminary numerical results, the proposed approach is able to consistently check any variation of the structural condition by appropriately considering long term monitoring data.

Acknowledgements The Authors would like to acknowledge the support of the PRIN 2017 project, “DETECT-AGING” (Prot. 201747y73L).

References

1. Kaya Y, Safak E (2015) Real-time analysis and interpretation of continuous data from structural health monitoring (shm) systems. *Bull Earthquake Eng* 13(3):917–934
2. Cavalagli N, Comanducci G, Ubertini F (2018) Earthquake-induced damage detection in a monumental masonry bell-tower using long-term dynamic monitoring data. *J Earthquake Eng* 22(supl): 96–119
3. Downey A, D’Alessandro A, Laflamme S, Ubertini F (2018) Smart bricks for strain sensing and crack detection in masonry structures. *Smart Mater Struct* 27(1)
4. Venanzi I, Kita A, Cavalagli N, Ierimonti L, Ubertini F (2020) Earthquake-induced damage localization in an historic masonry tower through long-term dynamic monitoring and fe model calibration. *Bull Earthquake Eng* 18(5):224–2274
5. Gentile C, Saisi A, Cabboi A (2015) Structural identification of a masonry tower based on operational modal analysis. *Int J Archit Heritage* 9(2):98–110
6. Ubertini F, Cavalagli N, Kita A, Comanducci G (2018) Assessment of a monumental masonry bell-tower after 2016 central italy seismic sequence by long-term shm. *Bull Earthquake Eng* 16:775–801
7. Ubertini F, Comanducci G, Cavalagli N, Pisello A, Materazzi A, Cotana F (2017) Environmental effects on natural frequencies of the san pietro bell tower in Perugia, Italy, and their removal for structural performance assessment. *Mech Syst Signal Process* 82:307–322
8. Kita A, Cavalagli N, Ubertini F (2019) Temperature effects on static and dynamic behavior of Consoli palace in Gubbio, Italy. *Mech Syst Signal Process* 120:180–202
9. Kita A, Cavalagli N, Masciotta M, Loureno P, Ubertini F (2020) Rapid post-earthquake damage localization and quantification in masonry structures through multidimensional non-linear seismic ida. *Eng Struct* 219
10. Makoond N, Pel L, Molins C, Roca P, Alarcn D (2020) Automated data analysis for static structural health monitoring of masonry heritage structures. *Struct Control Health Monit* 27(10)
11. Cury A, Cremona C (2012) Assignment of structural behaviours in long-term monitoring: application to a strengthened railway bridge. *Struct Health Monit* 11:422–441
12. Ubertini F, Carmelo G, Materazzi A (2013) Automated modal identification in operational conditions and its application to bridges. *Eng Struct* 46:264–278
13. Cancelli A, Laflamme S, Alipour A, Sritharan S, Ubertini F (2020) Vibration-based damage localization and quantification in a pretensioned concrete girder using stochastic subspace identification and particle swarm model updating. *Struct Health Monit* 19(2):587–605
14. Tibaduiza Burgos D, Gomez Vargas R, Pedraza C, Agis D, Pozo F (2020) Damage identification in structural health monitoring: a brief review from its implementation to the use of data-driven applications. *Sensors (Switzerland)* 20(3)
15. Simoen E, De Roeck G, Lombaert G (2015) Dealing with uncertainty in model updating for damage assessment: a review. *Mech Syst Signal Process* 56–57:123–149
16. Venanzi I, Materazzi A, Ierimonti L (2015) Robust and reliable optimization of wind-excited cable-stayed masts. *J Wind Eng Industrial Aerodyn* 147:368–379
17. García-Macías E, Ierimonti L, Venanzi I, Ubertini F (2019) An innovative methodology for online surrogate-based model updating of historic buildings using monitoring data. *Int J Archit Heritage*
18. García-Macías E, Ierimonti L, Venanzi I, Ubertini F (2020) Comparison of surrogate models for handling uncertainties in shm of historic buildings. *Lecture Notes in Mechanical Engineering*, pp 1645–1657

19. Zhang FL, Ni YC, Au SK, Lam HF (2016) Fast Bayesian approach for modal identification using free vibration data, Part i—most probable value. *Mech Syst Signal Process* 70–71:209–220
20. Bartoli G, Betti M, Marra A, Monchetti S (2019) A Bayesian model updating framework for robust seismic fragility analysis of non-isolated historic masonry towers. *Philos Trans R Soc A Math Phys Eng Sci* 377(2155)
21. Jang J, Smyth A (2017) Bayesian model updating of a full-scale finite element model with sensitivity-based clustering. *Struct Control Health Monit* 24(11)
22. Pepi C, Gioffre' M, Grigoriu MD (2019) Parameters identification of cable stayed footbridges using Bayesian inference. *Meccanica* 54(9):1403–1419
23. Behmanesh I, Moaveni B, Lombaert G, Papadimitriou C (2015) Hierarchical Bayesian model updating for structural identification. *Mech Syst Signal Process* 64–65:360–376
24. Behmanesh I, Moaveni B (2016) Accounting for environmental variability, modeling errors, and parameter estimation uncertainties in structural identification. *J Sound Vib* 374:92–110
25. Sun H, Mordret A, Prieto G, Toksz M, Bykztrk O (2017) Bayesian characterization of buildings using seismic interferometry on ambient vibrations. *Mech Syst Signal Process* 85:468–486
26. Rocchetta R, Broggi M, Huchet Q, Patelli E (2018) On-line Bayesian model updating for structural health monitoring. *Mech Syst Signal Process* 103:174–195
27. Ierimonti L, Venanzi I, Cavalagli N, Comodini F, Ubertini F (2020) An innovative continuous bayesian model updating method for base-isolated rc buildings using vibration monitoring data. *Mech Syst Signal Process* 139
28. Farrar C, Worden K (2012) *Structural health monitoring: a machine learning perspective*. Wiley, Hoboken
29. Rosafalco L, Manzoni A, Mariani S, Corigliano A (2020) Fully convolutional networks for structural health monitoring through multivariate time series classification. *Adv Modeling Simulation Eng Sci* 7(1)
30. Neves A, González I, Leander J, Karoumi R (2018) A new approach to damage detection in bridges using machine learning. *Lect Notes Civil Eng* 5:73–84
31. Sun L, Shang Z, Xia Y, Bhowmick S, Nagarajaiah S (2020) Review of bridge structural health monitoring aided by big data and artificial intelligence: From condition assessment to damage detection. *J Struct Eng (United States)* 146(5)
32. Bull L, Worden K, Dervilis N (2020) Towards semi-supervised and probabilistic classification in structural health monitoring. *Mech Syst Signal Process* 140
33. García-Macías E, Ubertini F (2020) Mova/moss: two integrated software solutions for comprehensive structural health monitoring of structures. *Mech Syst Signal Process* 143
34. Lophaven S, Nielsen H, Søndergaard J (2002) *A matlab kriging toolbox, version 2.0*. Tech Rep IMM-TR-2002-12, Kongens Lyngby, Copenhagen, Denmark: Informatics and mathematical modelling, Technical University of Denmark, DTU
35. Simulia C (2010) *Abaqus analysis user's manual, vol III: Materials*. Dessault Systèmes, USA
36. Cavalagli N, Kita A, Castaldo V, Pisello A, Ubertini F (2019) Hierarchical environmental risk mapping of material degradation in historic masonry buildings: an integrated approach considering climate change and structural damage. *Constr Build Mater* 215:998–1014

Analytic Wavelet Selection for Time–Frequency Analysis of Big Data Form Civil Structure Monitoring



Ahmed Silik, Mohammad Noori, Wael A. Altabey, Ramin Ghiasi,
and Zhishen Wu

Abstract Structural health monitoring (SHM) of civil infrastructures has become one of the fastest-growing research areas over the past two decades. SHM has evolved into measuring, processing, collecting, and storing massive amounts of data to provide valuable information for owners and managers to control and manage their structure's integrity. One of the challenges in SHM is how to draw inferences and useful features about structural conditions from measurements collected by sensors. The structural dynamic response is often a complex time-varying process and is disposed to dynamic changes in time–frequency contents. To extract the signal components and capture the useful features associated with damage to infer structural conditions from collected data, a technique that combines the time and frequency analysis and shows the signal evolution in both time and frequency is required. Wavelet transform (WT) has proven to be an effective tool in this regard. It can decompose the signal into different signal components and then compare each component's characteristics with a resolution matched to its scale. However, the challenge is how to select a proper wavelet. This paper is aimed to choose appropriate wavelets for time–frequency analysis of structural dynamic response to detecting informative regions and transient events due to damage. Towards this purpose, various analytic wavelet and nonanalytic wavelets are used. For validation, quantitative measures based on novel correlation measures, Maximal information coefficient, energy distribution, sharing information, and Instantaneous Mean Frequency are investigated. The results

A. Silik · W. A. Altabey · R. Ghiasi · Z. Wu

International Institute for Urban Systems Engineering (IIUSE), Southeast University, Nanjing 210096, Jiangsu, China

M. Noori (✉)

Department of Mechanical Engineering, California Polytechnic State University, San Luis Obispo, CA 93405, USA

W. A. Altabey

Department of Mechanical Engineering, Faculty of Engineering, Alexandria University, Alexandria 21544, Egypt

A. Silik

Department of Civil Engineering, Nyala University, Nyala, Sudan

reveal that the analytic wavelets show promising results, especially the Bump wavelet shows the best results than the others.

Keywords Dynamic measurement · Analytic wavelet · Continuous wavelet transform · Time frequency analysis · Civil structure

1 Introduction

Civil structures may suffer overstated loading conditions during their service life due to destructive human-made or natural hazards and events. Even if the structure system can manage to resist these extreme events and survive, it is fateful to inspect its condition to ensure no substantial damages have occurred. Besides, even if a structure has not been exposed to extreme events or loads, the aging structure condition must be monitored to detect damage that could lead to failure. Thus, a continuous evaluation of the structural integrity is indispensable to diagnose a structure's health. A critical stage in any structural integrity evaluation is to process the measured data [40] to extract specific characteristics, such as modal parameters, or to directly create a model that matches the data, as in system identification. As a result, in the past years, extensive works related to research has been reported, and a number of damage detection algorithms have been developed, from basic frequency change based methods to advanced signal processing [15] and machine learning-based approaches [15, 19, 44].

The collected data sets obtained from SHM systems mounted in the structure are surely of the big data type owing to their sheer volume, diversity, and complexity, and carrying out relevant analyses of their content can help for identifying damage or failure during operation through the relationships between the measurements taken by several sensors. Most SHM strategies in civil engineering depend mainly on acceleration, strain, and displacement [4, 24], besides environmental conditions such as temperature and humidities [5, 19] through signal processing tools. Thus, signal processing is a critical component in SHM toward an integrated intelligent system design [2, 45]. Among various researched approaches, time–frequency/scale analysis techniques based on wavelet have proven to be a robust technique for non-stationary signal analysis due to its ability to localize in time and frequency and a successful method for assessing structural health conditions [27, 32–34]. For more details about wavelet applications, please see [21, 36].

Various works have used different wavelet functions to analyze different real-world signals to detect structural damage [45], and a wide range of wavelet functions have been reported in the literature. However, despite wavelet-based analyses do better for non-stationary data; its success depends on its chosen right wavelet mother, which are not always obvious. A suitable mother wavelet shows the wavelet's ability in signal retaining, feature extraction and enhances the de-noised signal's frequency spectrum [37, 39]. However, a critical issue to ensuring the wavelet transform effectiveness in civil structures monitoring is selecting the most appropriate

mother wavelet for a specific task. Still, there are no well-developed general rules, or no enough guide can be followed to describe how to select a base wavelet for a particular task in civil applications. Most previous wavelet selection works depend on subjective criteria accompanied by the users' knowledge and trial and error, which is tedious and challenging in finding an optimum wavelet. Thus, choosing the right wavelet is essential, and the selection should be considered various aspects combined with the signal and wavelet characteristics to achieve the study's intended purpose.

The research's main goal is to evaluate the effectiveness of analytic and nonanalytic wavelet basis for time–frequency analysis of dynamic structural measurements to discover informative time–frequency regions and show how the signal frequency content changes over time, besides to track the signal frequency components evolution to detect the transient events due to damage. The strategy is based on examining the wavelet type, wavelet characteristics, nature of data and its characteristics, application type, and quantitative measures. Both continuous wavelets transforms (CWT), and discrete wavelet transform (DWT) are investigated to show the direct links between them and demonstrate their ability in time–frequency analysis and select the proper one by comparing each other. The wavelet-based strategy selection's performance is tested and validated based on time–frequency energy representation, wavelet power spectrum, instantaneous mean frequency, mutual information, variance, and maximal information coefficient. To extract and visualize data from the wavelet, the wavelet scalograms were explored. The acceleration responses from the shaking table test and El-Centro earthquake are used.

This paper is organized as follows. Section 2 shows the methodology of the study and data source. Section 3 describes Continuous versus discrete wavelet transform. Section 4 shows the wavelet selection guide and choice procedures. In Sect. 5, discussion and results analysis through some experimental examples. Finally, Sect. 6 presents the conclusions.

2 The Methodology of the Study

Though there are various studies to determine optimal wavelets for DWT application, there is no research suggesting which wavelet is appropriate for CWT analysis, particularly in civil engineering applications. In this study, we attempt to choose optimal wavelet for CWT based time–frequency analysis according to the following procedures:

1. Describe the continuous and discrete wavelet transform and compare them to demonstrate their abilities in representing informative time–frequency regions to support the identification of wavelet type to be used in this analysis.
2. Investigate and understand the wavelet and signal characteristics to reduce the computation cost, and preselect candidate wavelets from the wavelet families.
3. Select novel quantitative measures based on time–frequency energy, wavelet power spectrum, instantaneous mean frequency, mutual information, variance, and maximal information coefficient.

4. Decompose the signals using various wavelet function and explore the wavelet scalograms to extract and visualize the data from the wavelet to highlight the salient features in the data.

5. The quantitative measures are examined from two varied aspects: (i) representing their corresponding wavelet coefficients in the time–frequency/scale plane and (ii) the relationship between the wavelets and the analyzed signal.

6. Compare several different wavelets used to analyze the structural dynamic measurement to realize the most reliable wavelet function for the time–frequency analysis.

2.1 Data Source

Two categories of time series have been used for the verification of the proposed wavelet selection strategy. First is California's 1940 EL-Centro earthquake as a single field data sampled at 50 Hz, which is publicly available at <http://vibrationdata.com>. Second is: the experimental accelerations sampled at 200 Hz, collected from a shaking table testing of a six-story steel frame building during the 7th Asia Pacific Summer School on Smart Structures Technology in the National Center for Research on Earthquake Engineering (NCREEE), NAR Labs, Taiwan.

3 Continuous Versus Discrete Wavelet Transform

As a rule, wavelet analysis is subdivided into DWT and CWT [26]. So, it is crucial to recognize the differences between them for successful wavelet analysis. CWT is an analog filtering function similar to DWT, with low and high pass filtering at various scales. However, the filtering functions are performed parallel at the input in a filter bank, with the high and low pass functions combined into a single bandpass function. The various scales in CWT are recognized as neighboring bands in the frequency domain, increasing the bandwidth corresponding to the band's center frequency.

Consequently, the CWT is characterized as a constant Q filter bank, and it splits the signal into a set of logarithmic frequency bands by passing it through a sequence of constant-Q bandpass filters. DWT filters are well-formulated mathematical models whose transfer functions are recursive. They provide an equivalent result by starting with a block of discrete data and performing sequential high and low pass filtering. The filtering process is repeated at the low-frequency component level as in conventional DWT. It is repeated at both high-frequency and low-frequency component levels as in discrete packet transform (PWT) to transfer the signal in a sequence of steps called scaling. Each scaling divides the current bin's frequency space in half, doubling the time interval, thereby keeping the time–frequency product constant. Both DWT and CWT are filter banks, although CWT takes a more intuitive form of a physical filter with a transfer function in the time and frequency domains. Also, both

are decimated and non-decimated versions. Due to the limitations of the DWT specification, all DWT filters are compactly supported. It is limited in time and frequency and has been proven not to be applied through physical filters in a continuous-time domain.

The CWT and DWT’s main difference is that the CWT loses the compact support concept, so it can not provide ideal compact support. Instead, similar to how elliptical filters such as Chebyshev and Butterworth filters are created, CWT functions are created to be as compact as possible according to specific criteria. Besides, the difference between them is how the scale is discretized. The scale values define to which degree the wavelet can be stretched or compressed. The low-scale values compress the wavelet and correlate better with the high-frequency content of the signal. High scale values extend the wavelet function and better correlate with the low-frequency components. In CWT, the low-scale components characterize the analyzed signal’s precise fine-scale characteristics, whereas high-scale components characterize the analyzed signal’s rough coarse-scale characteristics. Readers can refer to more details about different types of wavelet applications in the civil engineering field [20].

3.1 Wavelet Discretization

This section outlines the direct links between continuous and discrete wavelet analysis and defines the differences between them. The CWT discretizes finer scales than DWT and exponential scales are commonly employed with a base smaller than 2 to obtain different scales; for instance, $2^{j/v}$ where v is an integer > 1 , where v is voice per octave number, and $j = 1, 2, 3, \dots$. For a function $\psi(t) \in L^2(\mathbb{R})$ called the mother wavelet, the family of functions can be obtained by shifting and scaling this $\psi(t)$ as:

$$\psi_{j,k}(t) = \frac{1}{2^{j/v}} \psi\left(\frac{t - k}{2^{j/v}}\right) \tag{1}$$

where $2^{j/v} = s$, $sk = \tau$. The larger the v , the more precise the scale discretization will be; but, this increases the computation cost since the computation is done for each scale. The scaled-shifted version of wavelet $\psi(t)$ is defined as

$$\psi_{s,\tau}(t) = \frac{1}{\sqrt{s}} \psi\left(\frac{t - \tau}{s}\right) \tag{2}$$

Shifting a wavelet means delaying (or advancing) its onset. Mathematically, delaying a function $\psi(t)$ by τ is represented by $\psi(t - \tau)$. The signal is decomposed into various basic wavelets and presented as an integral of scaled and biased wavelets.

$$W_{s,\tau} = \frac{1}{\sqrt{s}} \int_{-\infty}^{\infty} x(t) \cdot \psi^* \left(\frac{t - \tau}{s} \right) dt \quad (3)$$

From Eq. (3), it is noted that the wavelet ψ is contracted and dilated by changing the scale s . The variation in scale s leads to a change in the central wavelet frequency F_c and the window length. So the scale s is used instead of the frequency for representing the wavelet analysis results. The shift parameter τ specifies the wavelet location in time, by varying τ , the wavelet can be shifted over the signal. For constant scale s and varying translation τ , the rows of the time-scale plane are filled, varying the scale s and keeping the translation τ constant fills the time-scale plane columns. The elements in $W_{s,\tau}$ are called wavelet coefficients; each one is associated with a scale (frequency) and a point in the time domain. These coefficients show how close the signal is to a given basis function. Since the CWT behaves as an orthonormal basis decomposition, it can reveal that it is isometric [17], i.e., it conserves energy. So, the signal $x(t)$ can be reconstructed from its transform. By changing the dilation factor s , we can see how the wavelet corresponds to the signal from one scale to the next, whereas changing the shifting from $\psi(t)$ shows how the nature of the signal changes with time. It is worth mentioning that the scales set for each wavelet's CWT is selected such that it gives a smooth graphical representation of the wavelet power spectrum.

Standard DWT is a kind of wavelets derived from CWT that restrict the scale and translation values based on a dyadic sampling. The the scale is a power of 2 ($a = 1, 2, 4, 8, \dots$) and position a subset is the integer ($b = 1, 2, 3, 4, \dots$). The scale s is related to level j by $s = 2^j$; and supposing the translation $b = 2^j \cdot k$ at a given scale, where j is the scale level, and k is an integer. If the resolution is defined as $1/s$, then the resolution increases as the scale decreases. The greater the resolution, the smaller and finer are the details that can be accessed. The scale s is gradually changed to approximate the signal in varied resolutions and localizes the wavelet in the frequency domain, while the shift b localizes the wavelet in the time domain. The discrete scale s is analogous to frequency. It is a number associated with the wavelet coefficients number, so it is regarded as a detailed amount in the signal. The scale selection relies on the wavelet itself, so its number is selected based on the overall energy displayed at each scale. For a certain scaling s , the wavelet function translates across the signal in time. In non-decimated DWT, the scale s is restricted to powers of two, but the translation m is an integer as in the CWT. The discretized wavelet for the DWT is defined as:

$$\psi_{j,m}(t) = \frac{1}{\sqrt{2^j}} \psi \left(\frac{1}{2^j} (n - 2^j m) \right) \quad (4)$$

The discretized wavelet for the non-decimated DWT is defined as:

$$\psi_{j,m}(t) = \frac{1}{\sqrt{2^j}} \Psi \left(\frac{n - m}{2^j} \right) \quad (5)$$

It should be noted that the decimated and non-decimated DWT vary in how they discretize the shift parameter. The decimated DWT is shifted by $2^j m$ while non-decimated DWT by integer shifts m . The DWT is defined as:

$$W_{j,k} = 2^{(-j/2)} \sum_n x(t) \psi(2^{-j}t - k) \quad (6)$$

where j indicates how much the wavelet is dilated, k represents the time index where the wavelet is localized after translation. DWT provides a sparse representation, and its coefficient number is the same as the original signal, but most coefficients can be close to zero. So, often these coefficients can be removed by de-noising the signal. The CWT produces M by N coefficients matrix, where M is the scale number and N length of the signal, and it is redundant but has the same time resolution as the original data in each frequency band; and there is an overlap between wavelets at each scale and others. The computing resources and time for analysis and store the coefficients are more extensive than DWT. Non-decimated DWT offers a redundant representation, but not similar to CWT and much lower because the scale parameter is not discretized so finely. The DWT discretization ensures orthonormal transform, which is useful in multi-resolution analysis and de-noising beside others, and it is not shift-invariant due to downsampling, whereas non-decimated DWT and CWT are not orthonormal transforms but shift-invariant. In DWT, the wavelet expression is not required because the filters are sufficient, while in CWT, those expressions are needed. The non-redundant representation is associated with an orthonormal basis, whereas the redundant representation uses much more scale and position values than a basis. For a classical fractal signal, the redundant methods are quite accurate. Thus, the application is influenced by the type of wavelet to be used.

4 Wavelet Selection Guidelines

In wavelet analysis, there are types of wavelets with various characteristics for various applications, and all of them do not work well for all signals [31]. Some may work well for a particular signal and may not work for another signal. Wavelets are characterized by diversity in their properties and their application. Thus their quality varies according to their applications and characteristics that are used to describe their actions and cover their behavior because various wavelet bases used to analyze the same data will induce various results [15]. From this, it's clear that the wavelet analysis type depends on what the user wants to do with the data and the nature of data needed to be analyzed. So, the issues are: First, how to select the proper type of wavelet, wavelet for our data? In terms of wavelet applications, the best-suited type of wavelet and its related analysis algorithm is data-dependent, either to be DWT or CWT, and second, how we find the best mother wavelet. Using a redundant representation close to the so-called continuous analysis, instead of a non-redundant discrete time-scale representation, can be useful for analysis purposes.

The non-redundant representation is associated with an orthonormal basis, whereas the redundant representation uses much more scale and position values than a basis.

For wavelet application, CWT is the ideal type for time–frequency analysis [16], so it is commonly used in most tasks associated with signal processing, such as localizing transients and detecting discontinuities in higher derivatives [38]. DWT has good sparse representation and energy compactification. The orthogonal DWT results in a perfect reconstructed signal. The CWT often does not give a good reconstructed signal because its numerical operation is somewhat unstable, so DWT is suited for on-line SHM [9]. The CWT’s plots are easier to interpret than the DWT’s plots [1]. Besides, DWT is suited for de-noising, feature extraction, and compression, and multi-resolution analysis, whereas CWT is suitable for detailed time–frequency representation, characterizing oscillatory behavior, spectral analysis, and localizing transients in non-stationary data and pattern recognition [11, 26].

Both DWT and CWT are used to analyze dynamic structural measurements to compare their abilities in time–frequency representation. Wavelet db3 is used for analyzing acceleration signal response and El-Centro earthquake. Figure 1 shows the comparison between CWT and DWT absolute coefficients. It is clear that CWT shows the most informative time–frequency regions than DWT due to finer scales, which result in higher-fidelity signal analysis. Thus, CWT is the ideal candidate for damage detection based signal analysis due to its finer resolution [18] and is usually chosen in most tasks (e.g., abrupt changes and singularity detection). While DWT is chiefly suited for removing noise and compressing the data, higher scales are required in the damage location determination. DWT’s applicability for damage detection is limited and has two weaknesses. One is the wavelet coefficient vector size decreases

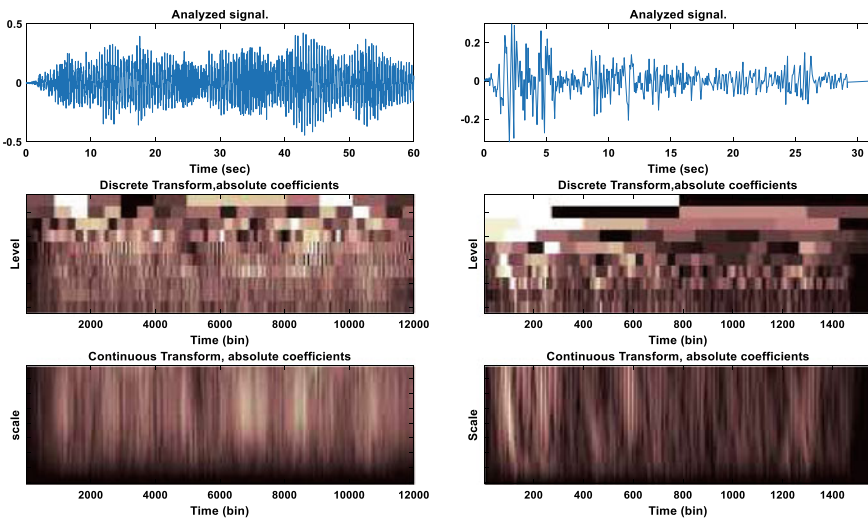


Fig. 1 Comparison between CWT and DWT absolute coefficients to show their abilities in representing informative time–frequency regions. (left) acceleration response of shaking table test of steel frame building of six stories. (right) El-Centro earthquake records

by half of its initial size at each scale level j , and the second is the scale limitation to dyadic sequence ($s = 2^j$). Therefore, if comparing scale 128 and scale 256, there will be a big gap in the wavelet resolution, and consequently, useful information can be lost. This gap can be described as detecting cracks on a wall at night using only a low-intensity light source, like a flashlight. If the light is directed at one part of the wall, then turned off, and subsequently moved to another position, some of the cracks may disappear or not be detected, but at least if the light constantly moves along the wall, damages can be detected. Thus, the calculation time, in this case, cannot be limited, and the use of continuous scales is recommended [12]. It is shown that CWT can capture the signal frequency content with finer accuracy and much more details than DWT.

Moreover, it also has the same time resolution as the data being analyzed in each frequency band. It allows for accurate scale plane decomposition, but the scaled translated versions of the base wavelet do not have orthogonality characteristics. To understand the exact feature of structural vibrational signals, it is crucial to study their time–frequency characteristics. For interpretative purposes, the CWT and DWT absolute coefficients are represented in the time–scale plane. Figure 1 shows the comparison between CWT and DWT to demonstrate their abilities in representing informative time–frequency regions. It is shown that CWT is more suitable for the time–frequency representation of non-stationary signals and is excellent for investigating the local signal features than DWT because DWT does not use all scales that compress and expand the mother wavelet. Suppose all scales in the range related to the signal bandwidth are not used. In that case, some information will be lost, leading to difficulties in extracting characteristics of the original signal [10]. The CWT is excellent for examining the local features of a signal [14].

As a summary, according to the above discussion and to the intended purpose of our study that associated with detailed time–frequency representation and accurate transient localization for the structure condition monitoring, the CWT is seemed to be a suitable choice for our objective and is a candidate for further analysis in this study (Fig. 2).

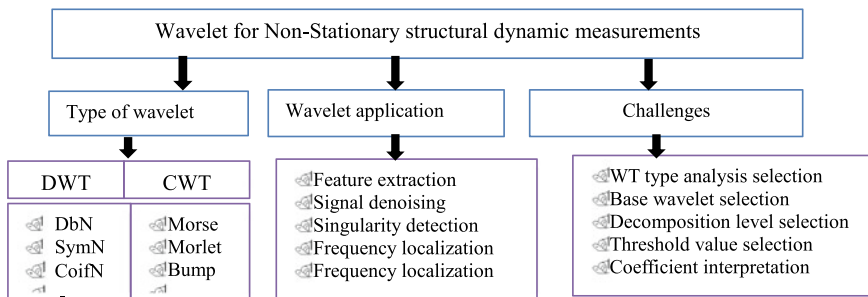


Fig. 2 Types of wavelet, wavelet application, and challenges in using wavelet analysis for non-stationary structural dynamic measurements

4.1 Wavelet Characteristics

Generally, wavelet transform can be classified into biorthogonal and orthogonal wavelets or real and complex values wavelet according to their characteristics. The orthogonal function is entirely introduced through the scale filter, and its associated wavelet transform is orthogonal, and its reconstruction filters are defined as an inverse time of its decomposition filters. In biorthogonal wavelets, the decomposition and reconstruction filters are defined as separate filters. The orthogonal wavelets are more popular than biorthogonal wavelets because of their simpler representation and signal recovery and have scaling functions to diagnose damage [28, 31, 34] It also performed slightly better overall than the other filters employed for non-stationary signals. Besides, the wavelet function is characterized by a number of properties that define its application in wavelet-based signal analysis, such as orthogonality, symmetry, vanishing moment, and compact support. Understanding these characteristics is necessary to reduce the computation process and preselect candidate wavelets from the wavelet families that limit the wavelet basis choice in a range of wavelet bases that have prosperities that match with signal characteristics according to the situation before the quantitative criteria are used to find an optimal wavelet for specific wavelet-based structural dynamic measurements analysis. These properties are shortly discussed below.

- (1) Orthogonality: indicates an inner product of the base wavelet with itself is equal to one, and between the base wavelet and scaled- shifted wavelet versions are equal to zero. As a result, an orthogonal wavelet base is efficient for signal decomposition into non-overlapping sub frequency bands.
- (2) Symmetry ensures that a base wavelet can serve as a linear phase filter. This is an important aspect of wavelet-based filtering operation, as the absence of this property can lead to phase distortion. This property is required when the signal shape is needed to be maintained and avoids signal distortion during decomposing and synthesizing the analyzed signal.
- (3) Compact support: It means the wavelet is non-zero only on a finite interval. This allows the wavelet to represent well signals which have localized features. Wavelets with short support have a constraint on their regularity and can show the local characteristic; however, long support increases arbitrary degrees of smoothness and numbers of zero moments.
- (4) Vanishing moment: it is associated with the decay rate, function order, and wavelet smoothness. It is closely related to the Lipchitz index and symbolizes the wavelet regularity and its ability to get localized information. A high number requires more extended support because a wavelet with n vanishing moments should have at least $2n - 1$ support width length.

4.2 Wavelet Family Selection

Despite the lack of rules, various real and complex wavelets have been used for damage detection, and their efficiency has been evaluated [18–46]. These wavelets can be explored for the wavelet transform implementation for signal analysis, but only a given wavelet can fit best with the features we are looking for in our data because each type has a different shape, compactness, and smoothness and is useful for various purposes. In civil structures, the dynamic measurements are mostly due to disturbances of operational and environmental variations and quite often are contaminated. Thus, wavelet analysis based time-frequency analysis is required to analyze and show how the frequency content changes over time. From the practical view, several analytic and nonanalytic wavelets are dominantly used in CWT and have been especially useful for time-frequency analysis. During the literature review and our ground study, we have observed that Daubechies, Symlet and Coiflets, were as real-valued wavelets and exhibited superior performance [36], and Morel, Morse, and Bump wavelets as complex wavelets exhibit superior performance for non-stationary signals analysis [34]. In the light of the above discussion, in this study, Daubechies, Symmet, Coiflet, Morel, Morse and Bump, Bior2.4, Meyer, and Mexican hat wavelets are selected as continuous wavelet functions for further analysis.

Daubechies Wavelet: is orthogonal, however, asymmetric. An asymmetric property introduces large phase distortion. It is compactly supported with a given support width $2N - 1$, in which N is the wavelet order. It does not have explicit expression except for $N = 1$, which is the Haar wavelet. As support width increases, it becomes more smooth, leading to better frequency localization, and consequently, their magnitude spectra decay quickly.

Coiflet Wavelet: is orthogonal and semi symmetric and is designed to produce the highest number of vanishing moments ($2N$) for both the base wavelet at order N and the scaling function for a given width a support width of $6N - 1$. The semi-symmetry property leads to the near-linear phase characteristics.

Symlet Wavelet: is orthogonal and near symmetric. The near symmetric property ensures minimal phase distortion. A Symlet wavelet of order N a given support width of $2N - 1$. They are similar to the Daubechies wavelet except for better symmetry.

Biorthogonal Wavelets: is biorthogonal and symmetry. The symmetry property ensures that they have linear phase characteristics. This type of base wavelet can be constructed by the spline method.

Morse wavelet: is parametrized by an oscillation control parameter $\beta > 0$, a shape parameter $\gamma > 0$, to change time and frequency spread and gives a broad range of forms and characteristics. It is useful for analyzing modulated signals and localized discontinuities [29]. For more details, see [23]. It is defined in the frequency domain as:

$$\psi_{\beta\gamma}(\omega) = \int_{-\infty}^{\infty} \psi_{\beta\gamma}(t) \exp(-i\omega t) dt = U(\omega) a_{\beta\gamma} \omega^\beta \exp(-\omega^\gamma) \tag{7}$$

Morlet wavelet: is designed to be a zero-mean function. It represents a sinusoidal function modulated by a Gaussian function [7, 8, 33]. It is infinite duration, but its energy is limited to a finite interval [7]. It is successfully used for vibrational signals analysis [33]. It has no scaling function and does not satisfy admissibility condition, except approximately. It is defined as:

$$\psi(t) = \frac{1}{\sqrt{\pi f_b}} e^{i2\pi f_c t} e^{-t^2/f_b} \tag{8}$$

where f_b is a bandwidth parameter, and f_c is the central wavelet frequency and must be $f_c > 5$. For engineering applications usually $f_c = 6$ [41, 43].

Bump wavelet: is bandlimited defined in the frequency domain with factors μ and σ and window w [22]. Values of μ are range in (3, 6) and σ are range in (0.1, 1.2). Smaller values of σ lead to superior-frequency localization but poorer time localization, whereas larger values produce better time localization and poorer frequency localization. It can be expressed as:

$$\hat{\psi}(s\omega) = e^{\left(1 - \frac{1}{1 - \frac{(s\omega - \mu)^2}{\rho^2}}\right)} \cdot I_{\left[\frac{\mu - \sigma}{s}, \frac{\mu + \sigma}{s}\right]} \tag{9}$$

where I is the indicator function for the interval. $(\mu - \sigma)/s \leq \omega \leq (\mu + \sigma)/s$. $(\mu - \sigma)/s \leq \omega \leq (\mu + \sigma)/s$

Meyer wavelet: is orthogonal, symmetric, and differentiable with unlimited support but decays quicker than the sine wavelet. It is defined in the frequency domain [42] as:

$$\hat{\psi}(\omega) = \begin{cases} (2\pi)^{-\frac{1}{2}} e^{\frac{i\omega}{2}} \cdot \sin\left(\frac{\pi}{2} v\left(\frac{3}{2\pi} |\omega| - 1\right)\right) & \text{if } \frac{2\pi}{3} \leq |\omega| \leq \frac{4\pi}{3} \\ (2\pi)^{-\frac{1}{2}} e^{\frac{i\omega}{2}} \cdot \cos\left(\frac{\pi}{2} v\left(\frac{3}{2\pi} |\omega| - 1\right)\right) & \text{if } \frac{4\pi}{3} \leq |\omega| \leq \frac{8\pi}{3} \\ 0 & \text{otherwise} \end{cases} \tag{10}$$

$$v(x) := \begin{cases} 0 & \text{if } x < 0 \\ x & \text{if } 0 < x < 1 \\ 1 & \text{if } x > a. \end{cases} \tag{11}$$

Mexican hat wavelet: is symmetric, nonorthogonal, and relative to Gaussian function negative value. Most of its energy is within the interval $(-5, 5)$ but, adequate support is $(-8, 8)$ [25]. It has no scaling function and defined in term of the standard deviation σ that controls the width, and an independent variable t as:

Table 1 Wavelet properties

No	Mother wavelet	Center frequency	Period	Vanishing moment
1	db3	0.800	1.25	3
2	db40	0.671	1.49	40
3	sym3	0.800	1.25	3
4	sym40	0.671	1.49	40
5	bior2.4	0.889	1.12	2.4
6	mexh	0.250	4.00	-
7	Meyer	0.690	1.45	-

$$\psi(t) = \frac{2}{\sqrt{3\sigma\pi^{1/4}}} \left(1 - \left(\frac{t}{\sigma} \right)^2 \right) e^{-\frac{t^2}{2\sigma^2}} \tag{12}$$

For orthogonal functions, the wavelet and scaling function is the basic parameters in CWT. Despite the fact that it may seem confusing that there are so many choices for the analyzing wavelet, it is actually a strength of wavelet analysis. Depending on what signal features are needed to be detected or what task is needed to be solved, you can choose a wavelet that facilitates your task. For instance, if you want to detect abrupt discontinuities in the signal, you may select one wavelet, whereas if you are interested in finding oscillations with smooth onsets and offsets, you can choose a wavelet that more closely matches that behavior. A vibration signals analyses require a narrow bandwidth to achieve better frequency resolution [12]. Each wavelet function is associated with a varied center frequency and bandwidth defined by period [10]. The center frequency F_c and the bandwidth parameter F_b of the wavelet is the tuning parameters [14]. To have a narrow bandwidth, a wavelet with a high period value and a low center frequency is required. ‘db40’ and ‘sym40’ base wavelets are selected from the ‘Daubechies’ wavelet family and its derivative Symmel family based on their high period value and low center frequency, as shown in Table 1. For a comparative study, wavelets ‘db3’ and ‘sym3’ with low period value and high center frequency are also taken, and Meyer and Mexican hat wavelet. Besides, the number of vanishing moments. The number of vanishing moments limits the wavelet’s ability to extract information from a signal.

4.3 Wavelet Selection Quantitative Criteria

Various studies in different fields have been conducted using various quantitative measures. Many techniques have been reported to select optimal wavelet based on correlation index, variance, maximum energy, and entropy [13, 14], and others. However, most works reported in the literature have focused on the similarity, although the similarity is not the proper measure for all wavelet-based signal

processing applications. In this study, we use novel quantitative measures related to wavelet energy distribution and sharing information.

Time–Frequency energy estimation: Time–Frequency energy distributions are very important in analyzing and processing non-stationary signals like dynamic structural measurements. An energy time–frequency representation (TFR) combines the concepts of a signal’s instantaneous power and spectral energy density. The energy of time–frequency representation satisfies the following marginal properties [40]:

$$\int T_x(t, f)df = P_x(t) = |x(t)|^2 \tag{13}$$

$$\int T_x(t, f)dt = P_x(f) = |X(f)|^2 \tag{14}$$

Equation (13) and (14) indicate that if the time–frequency (TF) energy density is integrated along with one variable, the energy corresponding to the other variable can be obtained.

$$E_x = \iint T_x(t, f)dt df = \int |x(t)|^2 dt = \int |X(f)|^2 df \tag{15}$$

The total signal energy in Eq. (15) is derived by integrating the TFR over the entire TF plane.

$$E = \int_{-\infty}^{\infty} |x(t)|^2 dt = x(t)^2 \tag{16}$$

For Eq. (16) to be useful, the signal must contain finite energy. The relative contribution of the signal energy at a specific scale s and location b is given by the two-dimensional wavelet energy density function:

$$E(s, b) = |T(s, b)|^2 \tag{17}$$

A plot of $E(a,b)$ is known as a scalogram, and it can be integrated across s and b to recover the total energy in the signal using the admissibility constant, C_g , as follows:

$$E = \frac{1}{C_g} \int_{-\infty}^{\infty} \int_0^{\infty} |T(s, b)|^2 \frac{ds}{s^2 db} \tag{18}$$

Wavelet power spectrum: From the standpoint of wavelet energy, the WT can be considered as the Fourier transform generalization, and by analogy with spectral approaches, at fixed scale and time shift, one can compute the local wavelet power spectrum as feature vectors measures

$$Eg(s) = \sum_{b=b_1}^{b_N} |C(s, b)|^2 \tag{19}$$

$$Eg(b) = \sum_{s=s_1}^{b_M} |C(s, b)|^2 \tag{20}$$

where scale vector $\vec{s} = (s_1, s_2, \dots, s_M)T$ time shift vector $\vec{b} = (b_1, b_2, \dots, b_N)T$.

Instantaneous Mean Frequency: As it is known, the non-stationary structural dynamic measurements, in particular, do not lend themselves well to decomposition into sinusoidal components. For such measurements, the frequency notion loses its effectiveness and needs to use a parameter that considers the process’s time-varying nature [6]. Since the time-varying frequency is a natural occurrence, its idea can be explored in this study to choose the appropriate wavelets for time–frequency analysis. The instantaneous mean frequency of the power spectral density is defined for the TFR, based on the CWT. The instantaneous mean frequency of the time-dependent power spectral density is defined as:

$$IMNF(t) = \frac{\int_0^F \omega P(t, \omega) d\omega}{\int_0^F P(t, \omega) d\omega} \tag{21}$$

where F is the Nyquist frequency, and P(t, ω) is the time-dependent power spectral density.

Wavelet Mutual information: Mutual information (MI) is the uncertainty reduction measures between two variables. It also measures the information amount that one variable x contains about the other. The MI is relative entropy between joint probability $P_{x,y}(x_i, y_j)$ and marginal probability densities $P_x(x_i), P_y(y_j)$ which is evaluated at (x, y). MI can be expressed in bits as [30]:

$$MI_{x,y}(Y; X) = \sum_{i,j} P_{x,y}(x_i, y_j) \log_2 \left[\frac{P_{x,y}(x_i, y_j)}{P_x(x_i)P_y(y_j)} \right] \tag{22}$$

Maximal information coefficient (MIC): Maximal information coefficient is a novel correlation measurement proposed by Reshef et al. [35]. It is an information theory-based linear or non-linear association measure that can capture functional and non-functional relationships between variables and takes values between 0 and 1, where 0 means statistical independence and 1 means a completely noiseless relationship [3]. The MIC of original signal x, and the reconstructed signal y, is defined as the mutual information between random variables normalized by their minimum joint entropy.

$$MIC = \max\{MI_{x,y}(x, y) / \log_2 \min\{n_x, n_y\}\}, n_x.n_y < B(n), B(n) = n^{0.6} \tag{23}$$

where nx, ny is the number of bins of the partition of the x- and y-axis.

5 Discussion and Results Analysis

Time-scale representation is a fundamental tool in various areas of signal analysis, especially in the damage detection process. To verify the effectiveness of various wavelets-based TFR and find out the best wavelet function for an accurate TFR, a comparative study of Morel, Morse, Bump, Mesh, Db3.Sym3, Coif3, Bior2.4, Db4, and Sym40 was conducted on El-Centro earthquake signal. Figure 3 shows the signal scale-time representations for various wavelets, which show the signal evolution in both time and scale. It is shown that the frequency components seem to be smeared across the entire duration of the signal as indicated by bright color. The blue bands result from the correlation integral evaluation to a small value due to overlap of the wavelet with positive and negative values. Although the wavelet produces similar representations, these representations differ from each other. Figure 3a, b, c and d are more different than Fig. 3e, f, g, h, I, j, k, and l. The results characterize that all analytic wavelets show the best time–frequency resolution than nonanalytic wavelets. It is noted that the coefficients are large in absolute value around scales 20 to 60, and this offers a limited frequency bandwidth between 20 and 60 Hz. The figures are plotted with a different wavelet transform components scale to highlight the frequency components changes over time. Regarding the real wavelets, each wavelet is associated with a different center frequency and bandwidth determined by period, so it's clear that the wavelet with small vanishes moments such as Db3.Sym3, Coif3 provides resolution better than wavelets with high vanishes moments such as Db4 and Sym40. Also, it is noted that the complex wavelet is more robust to noise as compared with another real wavelet. Based on these results, we can conclude that the Morel, Morse, Bump are more effective in time–frequency representation than the real wavelets Mexh, Db3.Sym3, Coif3, Bior2.4, Db4, and Sym40. Regarding analytic wavelets, it is seen that the Morse wavelet result is approximately identical to the Morlet; but, the bump wavelet shows it is more effective in noise separation and makes the results more amenable to interpretation. As a result, the Morel, Morse, Bump are used for further analysis.

Figure 4 shows the time–frequency–amplitude representations of the wavelet coefficients of complex Morel, Morse, and Bump wavelets for acceleration data of shaking table test and El-Centro earthquake. These figures demonstrate how rapidly the wavelet coefficient magnitude grows and show the component's range. The color brightness represents power. It shows that energy dominates in the lower scales in both signals. All wavelet shows promising result in separation of the signal frequency components, but Bump wavelet is more robust to noise than another wavelet. It is also shown that there are some nearly steady-state fluctuations above 10 Hz, and the transient events and the Morse wavelet result is almost identical to the Morlet wavelet (Fig. 5).

Figure 6 visualize the underlying processes associated with the wavelet transform and wavelet power spectrum computation. Figure 6a, b shows how spectral features evolve over time, whereas Fig. 6c, d show how spectral features evolve

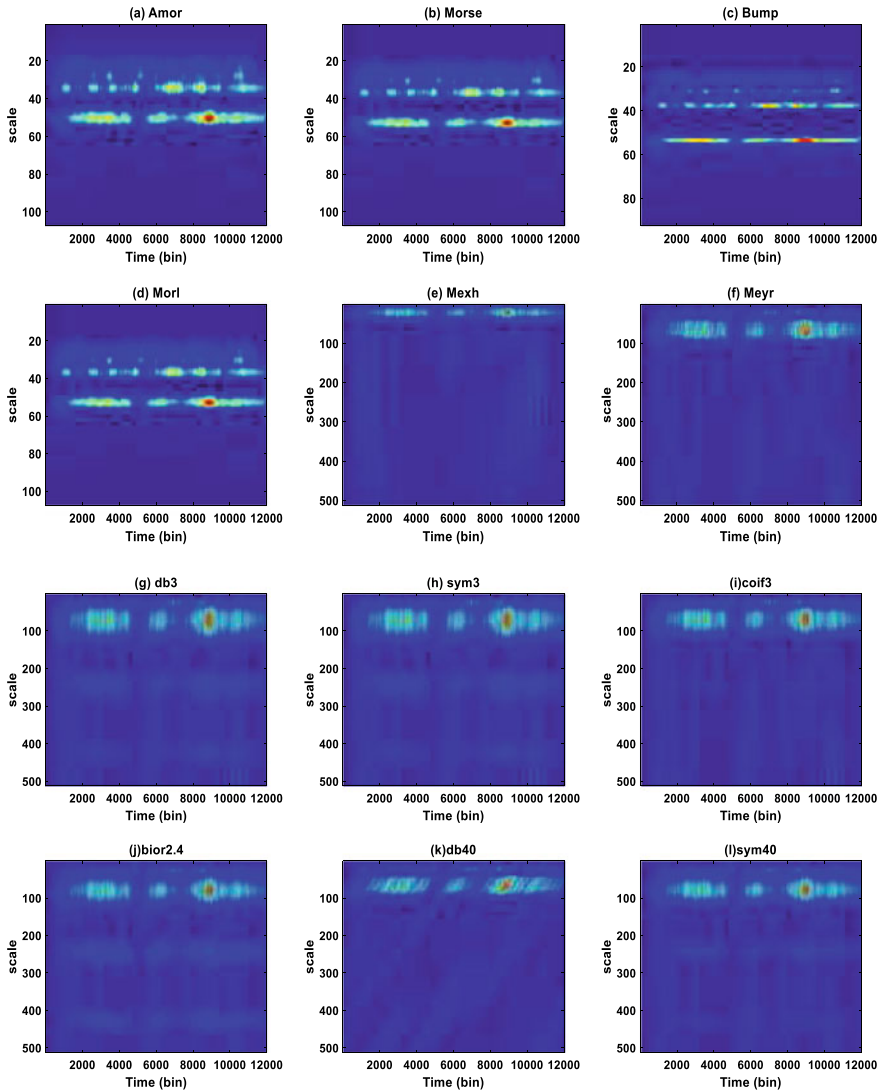


Fig. 3 Illustrates the time-scale representations of CWT coefficient of El-Centro earthquake using various complex and real wavelets. **a** Complex morel wavelet, **b** Morse wavelet, **c** Bump wavelet, **d** real morel wavelet, **e** Mexh wavelet, **f** Meyer wavelet, **g** db3 wavelet, **h** Sys3 wavelet, **i** Coif3 wavelet, **j** bior2.4 wavelet, **k** db40 wavelet, **l** sym40 wavelet

over frequency. Although these presentations’ general structures are similar, it can be seen that the frequency components magnitudes are different. According to the presentation, the Morse wavelet shows higher energy in both signals than Morel and Bump. This indicates that the Morse wavelet is robust in detecting the abrupt changes in the data, producing quite large absolute wavelet coefficients centered around the

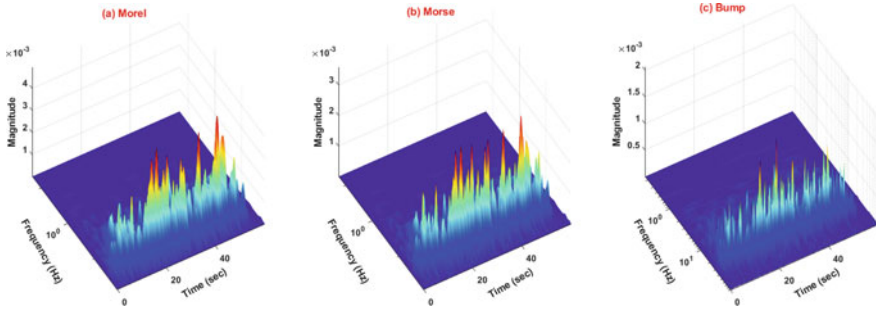


Fig. 4 Illustrates the Time–Frequency -Amplitude representations of Accerlation data from shaking table test. **a** complex morel wavelet, **b** Morse wavelet, **c** Bump wavelet

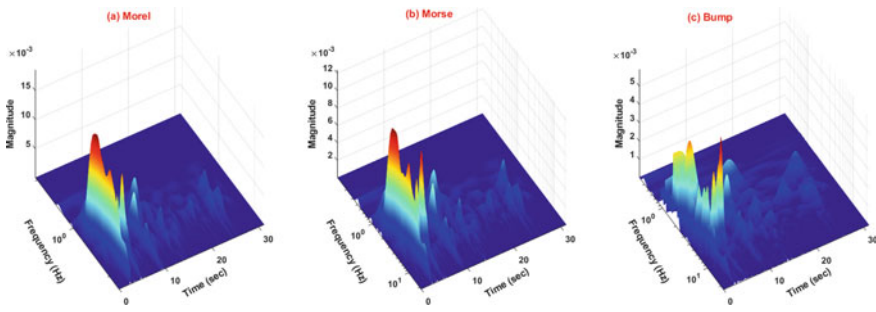


Fig. 5 Illustrates the Time–Frequency-Amplitude Representations are pertaining to the El-Centro earthquake acceleration. **a** complex morel wavelet, **b** Morse wavelet, **c** Bump wavelet

discontinuity at all scales. The Morse wavelet result is nearly identical to the Morlet in shape in both signals. Based on these results, we can conclude that the Morse function is the best candidate for detecting the abrupt changes in the data and more appropriate for oscillatory behavior.

The most accurate of the discontinuity localization based on the CWT coefficients can be obtained at the finest scales. Figure 7 demonstrates the smallest -scale coefficients combined with the analyzed acceleration waveform on the same figures. It's shown that the wavelet coefficient magnitudes capture the impulsive events at the exact times they take place in the signal being analyzed. All the functions show promising results, and the Morse wavelet is identical with the real morel wavelet, and the Bump wavelet is more de-noised the signal.

Figure 8 shows time–frequency representations for the El-Centro earthquake using Morlet, Bump, and Morse wavelet. It is shown that the modulus of the wavelet coefficients shows that energy is spread over a wide range of scales but dominate in the lower frequencies; there is a bright band for peaks. The blue bands result from the correlation integral evaluation to a small value due to overlap of the wavelet with positive and negative values. It is also shown that there are some nearly steady-state

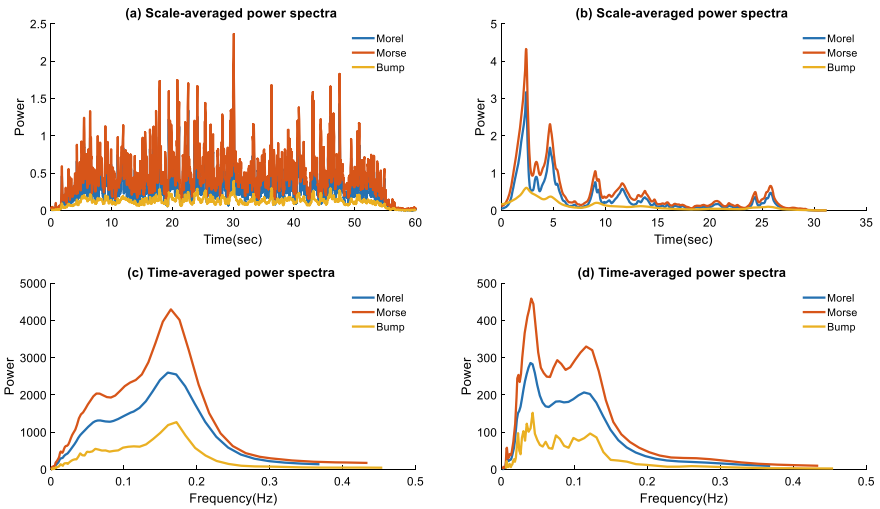


Fig. 6 Shows spectral features evolve over time and scale for both El-Centro earthquake and acceleration data, **a** scale-averaged power spectra of acceleration data, **b** scale-averaged power spectra of El-Centro earthquake data, **c** time-averaged power spectra of acceleration data (**a**) scale-averaged power spectra El-Centro earthquake data

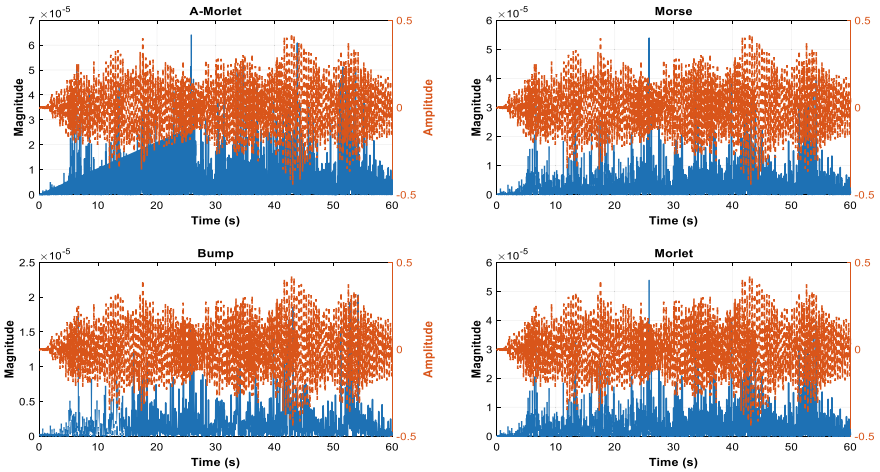


Fig. 7 Shows the finest-scale coefficients combined with the analyzed acceleration waveform on the same figure showing an overall roughly linear trend with some impulsive events

fluctuations above 8–20 Hz and transient events. The narrow bands represent the spikes in the signal, whereas thick bright bands represent the signal component.

Figure 9 shows the contour representations of acceleration waveform observed in the shaking table test using Morel, Morse, and Bump wavelets. Obviously, the

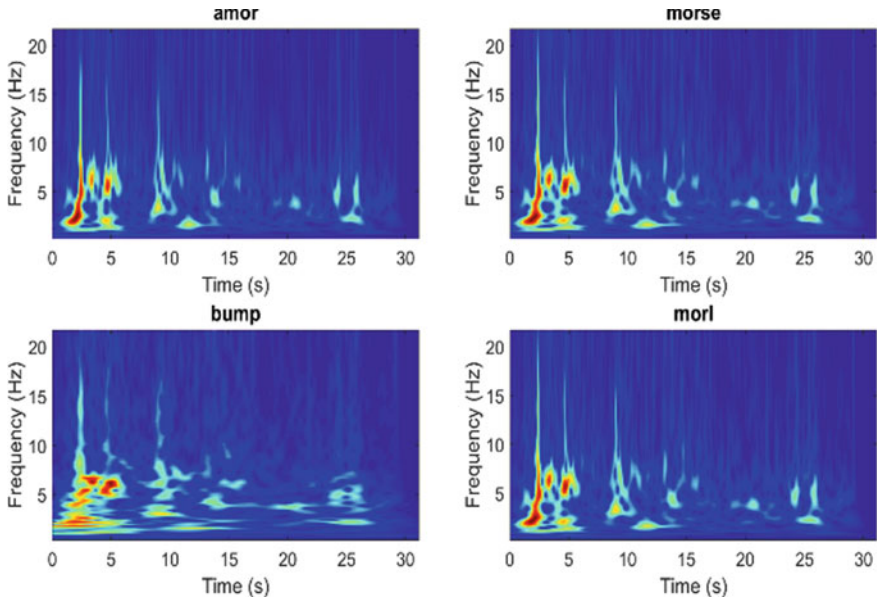


Fig. 8 Shows the time–frequency representations of the El-Centro earthquake’s continuous wavelet transform coefficient using complex and morel wavelet, Morse wavelet, Bump wavelet

frequencies are spread out, high about 18 Hz and low about 2 Hz in the analyzed signal. Yellow and blue indicate a power increase or decrease, respectively. Also, around two seconds, there is a small local disturbance. Also, it is noted that bump wavelet has good frequency localization than Mores and Morlet wavelets. The Morse wavelet is semi identical to the Morel wavelet. The bump wavelet is the most appropriate to describe the signals’ frequency content compared to the other wavelets. based on the above result, its difficulties

Figure 10 show three wavelet functions (Morel, Morse, and Bump) for comparing frequency attributes at each signal point of the El-Centro earthquake. Instantaneous mean frequency is shown in Fig. 10a, b show many variations and appear noisy to contain detailed information. The instantaneous frequency (Fig. 10c) shows many variations and appears less noisy, and contain detailed information. Based on the results, the Morse wavelet is nearly identical to the Morel wavelet. The bump wavelet seems the most appropriate to track the signals’ instantaneous mean frequency compared to the other wavelets.

Figure 11 show three wavelet function (Morel, Morse and Bump) for comparing energy percentage attributes per scale of the El-Centro earthquake. It is clear that the different information which the signal contains led to different signal energy distribution at scales (various frequency bands). The energy percentage shown in Fig. 11a, b, and c show the signal’s energy distribution at different scales. It is shown that the energy released due to seismic activities is mainly distributed in the frequency bands or scales. The energy percentage rises up to the maximum at scale

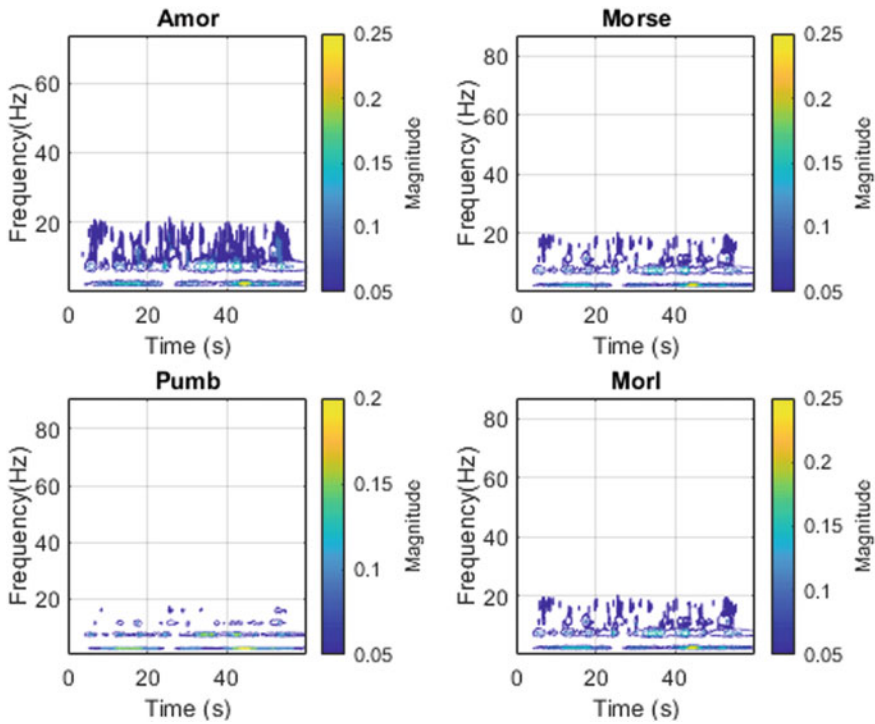


Fig. 9 Illustrates the contour representations of the El-Centro earthquake’s continuous wavelet transform coefficient using complex and real morel wavelet, Morse wavelet, Bump wavelet

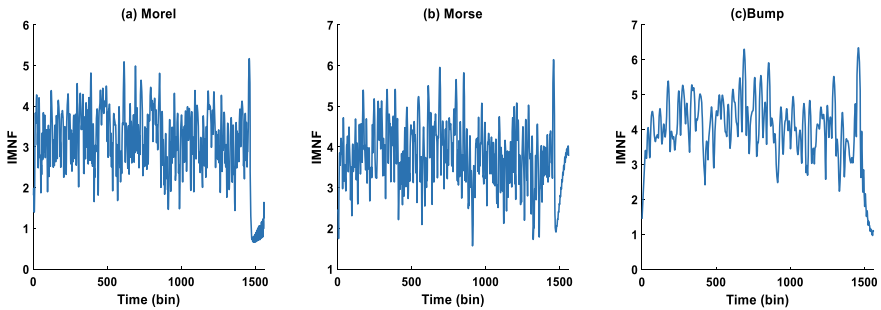


Fig. 10 Distribution of the El-Centro instantaneous mean frequency over the time domain after the continuous wavelet transform. **a** Instantaneous mean frequency using Morel wavelet. **b** Instantaneous mean frequency using Morse wavelet. **c** Instantaneous mean frequency using Bump wavelet

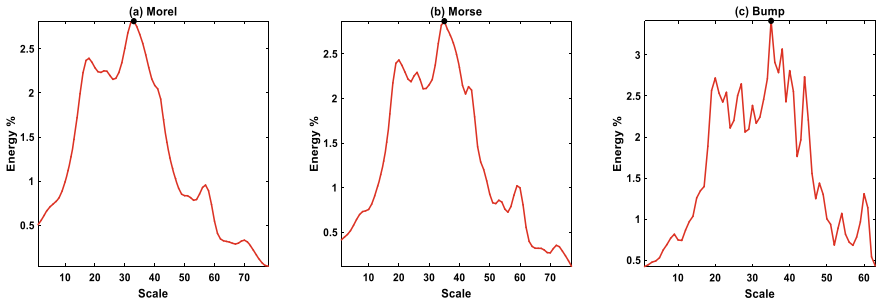


Fig. 11 Distribution of the El-Centro energy in the time domain at each scale after the CWT. **a** Energy Percentage using Morel wavelet. **b** Energy Percentage using Morse wavelet. **c** Energy Percentage using Bump wavelet

Table 2 Result of Different Criteria (Max. information coefficient, Max. Energy/ Shannon Entropy, Variance and Mutual information)

Mother wavelet	Max. information coefficient	Max.Energy/Shannon entropy	Variance	Mutual information
Morel	0.653	-1.043	0.756	7.2697e-06
Morse	0.650	-0.939	0.586	7.2697e-06
Bump	0.645	-0.508	0.863	7.2697e-06

35 for Bump and Morse wavelet, whereas at scale 33 for Morel wavelet and then decay down. There is amplitude variation between various wavelets, and the wavelet energy can be used to differentiate between active and silent regions in the structural dynamic signal.

Table 2 shows the quantitative measure analysis results, which include maximum information coefficient, maximum energy to Shannon entropy, variance, and Mutual information. All the three wavelets give nearly identical results except results of maximum energy to Shannon entropy and variance. The bump wavelet provides maximum energy to Shannon entropy and variance than the other wavelet.

As a summary, based on the above discussion, all three wavelets give acceptable results, but the Bump wavelet shows promising results.

6 Conclusion

This study’s objective was to evaluate the effectiveness of analytic and nonanalytic wavelet basis for time–frequency analysis of dynamic structural measurements to show informative time–frequency regions through tracking the signal frequency components evolution over time to detect the transient events due to damage. This paper reviewed and used various statistical procedures that have been extensively

utilized for data analysis issues in different engineering and other fields. In this study, a time-scale/frequency expansion based signal representation is used.

Time–Frequency analysis identifies the time at which various signal frequencies are present, usually by computing scalogram and a spectrum at regular time intervals. In this paper, a comparative analysis for choosing the type of wavelet and best-suited base wavelet for structural dynamic response analysis based on time–frequency is conducted. The El-Centro earthquake and acceleration measurement and both DWT and CWT are used for this study. The process was carried out in Matlab® environment using 107 to 512 different scaled versions of the wavelets. The comparison based time–frequency representation between CWT and DWT shows that CWT provides the most informative time–frequency regions than DWT due to finer scales. This confirms that CWT has considerable potential in digital signal processing and shows that the time–frequency. The wavelet scalograms using the various real values wavelets and no real wavelets of both signals are examined. It is seen that there is a significant difference between analytic and real values wavelets and shows that the time–frequency representation based analytic wavelets accurately captures the instantaneous frequencies of the signal and its evolution with time. Besides, the analytic wavelets among their selves are compared based on time–frequency-amplitude representation, time–frequency representation, a counter representation, wavelet spectrums, and the localization of the finest-scale components. Although these presentations’ general structures are analogous and some are semi identical, it can be shown that the locations and magnitudes of the frequency components are different. It can be concluded that the analytic wavelet is capable of revealing the informative regions in time–frequency representation, especially Morel, Morse, Bump wavelets. Of course, such a conclusion cannot be generalized for all types of data processing since the base wavelet best suited for specific work depends on the data form that is used, the application type, and the final objectives of the data analysis. From results, its clear that Morse wavelet results are semi identical to Morel wavelet, and all Morel, Morse, Bump wavelets are almost identical with respect to localized in time and frequency; however, it is shown that bump wavelet is more robust in de-noised and let the results to be more amenable for interpretation. From our previous studies, we found that by varying the Morse parameters, one can create Morse wavelets with properties similar to the Morel wavelet, which has one variable parameter. In other words, the generalized Morse wavelet can be identical to Morel and solved the disadvantage of the Morel wavelet. Thus, the Bump wavelet and Morse wavelet are recommended to implement time–frequency analysis for structural dynamic measurement successfully.

Finally, we can conclude that the proposed show promising results, and the analytic wavelets are well suited for studying how the frequency content in real-world non-stationary signals evolves as a function of time. The appropriate one needs to be chosen depending on the application’s goals and the mother wavelet parameters. This work’s significant contribution is comparing different analytic and nonanalytic wavelets to show their effectiveness in tracking the signal frequency components’ evolution over time to detect the transient events due to damage. For future work, the

authors recommend an in-depth investigation of Morse and Morel wavelets' optimal parameters.

Declaration of Conflicting Interests: The author(s) declare no potential conflicts of interest with respect to the research, authorship, and/or publication of this article.

References

1. Aguiar-Conraria L, Soares MJ (2014) The continuous wavelet transform: moving beyond uni- and bivariate analysis. *J Econ Surv*
2. Aguirre DA, Gaviria CA, Montejo LA (2013) Wavelet-based damage detection in reinforced concrete structures subjected to seismic excitations. *J Earthq Eng*
3. Albanese D, Riccadonna S, Donati C, Franceschi P (2018) A practical tool for maximal information coefficient analysis. *Gigascience*
4. Amezquita-Sanchez JP, Adeli H (2016) Signal processing techniques for vibration-based health monitoring of smart structures. *Arch Comput Methods Eng*
5. Beskhyroun S, Oshima T, Mikami S (2010) Wavelet-based technique for structural damage detection. *Struct Control Heal Monit*
6. Boashash B (1992) Estimating and interpreting the instantaneous frequency of a signal—Part 1: fundamentals. In: *Proceedings of IEEE*
7. Büssow R (2007) An algorithm for the continuous Morlet wavelet transform. *Mech Syst Signal Process*
8. Cohen MX (2019) A better way to define and describe Morlet wavelets for time-frequency analysis. *Neuroimage*
9. Ding YL, Li AQ, Yao XZ (2006) Combined application of dynamic loading testing and wavelet analysis on damage assessment of bridge structures. *Zhendong Gongcheng Xuebao/J Vib Eng*
10. Ergen B, Tatar Y (2001) The analysis of heart sounds based on linear and high order statistical methods. In: *Annual Reports of the Research Reactor Institute, Kyoto University*
11. Ben EY, Lembrikov BI, Schwartz M, Zarkovsky S (2018) Applications of Wavelet transforms to the analysis of superoscillations. *Wavelet Theor Appl*
12. Ferrante M, Brunone B, Meniconi S (2007) Wavelets for the analysis of transient pressure signals for leak detection. *J Hydraul Eng*
13. Fu J, Xu X, Chen Y (2017) Feature selection and optimization method based on CWT. In: *2017 IEEE Int. Conf. Signal Process. Commun. Comput. ICSPCC 2017. 2017-Janua 1–4*
14. Gaviria CA, Montejo LA (2018) Optimal wavelet parameters for system identification of civil engineering structures. *Earthq Spectra* 34(1):197–216
15. Ghiasi R, Ghasemi MR, Noori M, Altabey W (2019) A non-parametric approach toward structural health monitoring for processing big data collected from the sensor network. In: *Structural Health Monitoring 2019: Enabling Intelligent Life-Cycle Health Management for Industry Internet of Things (IIOT)—Proceedings of the 12th International Workshop on Structural Health Monitoring*
16. Gholizad A, Safari H (2017) Damage identification of structures using experimental modal analysis and continuous wavelet transform. *Numer Methods Civ Eng* 2(1):61–71
17. Grossmann A, Morlet J (2009) Decomposition of hardy functions into square integrable wavelets of constant shape. In: *Fundamental papers in wavelet theory*
18. Hera A, Hou Z (2004) Application of Wavelet approach for ASCE structural health monitoring benchmark studies. *J Eng Mech*
19. Hou Z, Noori M, Amand RS (2000) Wavelet-based approach for structural damage detection. *J Eng Mech*
20. Kim B, Jeong H, Kim H, Han B (2017) Exploring wavelet applications in civil engineering. *KSCE J Civ Eng*

21. Lei J, Meyer Y, Ryan RD (1994) Wavelets: algorithms & applications. Math Comput
22. Li L, Cai H, Jiang Q (2020) Adaptive synchrosqueezing transform with a time-varying parameter for non-stationary signal separation. Appl Comput Harmon Anal
23. Lilly JM, Olhede SC (2012) Generalized morse wavelets as a superfamily of analytic wavelets. IEEE Trans Signal Process
24. McNeill DK (2009) Data management and signal processing for structural health monitoring of civil infrastructure systems. Woodhead Publishing Limited
25. Mi X, Ren H, Ouyang Z, Wei W, Ma K (2005) The use of the Mexican Hat and the Morlet wavelets for detection of ecological patterns. Plant Ecol
26. Mukai M, Okano T, Nishimoto S, Kitani I, Arai K (1995) Study on degradation diagnosis of partial discharge in a void by wavelet analysis. In: Proceedings of the symposium on electrical insulating materials
27. No I (2016) Commerce mathematics comparative analysis of Wavelet Transform and Fourier Transform Amandeep Kaur Department of Mathematics. Guru Nanak Dev Univ Amritsar 1:106–108
28. Ogaja C, Wang J, Rizos C (2002) Principal component analysis of Wavelet transformed GPS data for deformation monitoring
29. Olhede SC, Walden AT (2002) Generalized Morse wavelets. IEEE Trans Signal Process
30. De Oliveira HM, De Souza DF (2006) Wavelet analysis as an information processing technique. In: 2006 International Telecommunication Symposium ITS. October, 7–12
31. Ovanesova AV, Suárez LE (2004) Applications of wavelet transforms to damage detection in frame structures. Eng Struct
32. Qiao L, Esmaeily A, Melhem HG (2009) Structural damage detection using signal pattern-recognition. Key Eng Mater
33. Quiñones MM, Montejo LA, Jang S (2015) Experimental and numerical evaluation of wavelet based damage detection methodologies. Int J Adv Struct Eng
34. Reda Taha MM, Noureldin A, Lucero JL, Baca TJ (2006) Wavelet transform for structural health monitoring: a compendium of uses and features
35. Reshef DN, Reshef YA, Finucane HK, Grossman SR, McVean G, Turnbaugh PJ, Lander ES, Mitzenmacher M, Sabeti PC (2011) Detecting novel associations in large data sets. Science (80-)
36. Rhif M, Abbes A, Ben, Farah IR, Martínez B, Sang Y (2019) Wavelet transform application for/in non-stationary time-series analysis: a review. Appl Sci 9(7): 1–22
37. Rodrigues AP, Mello GD, Pai PS (2016) Selection of mother wavelet for wavelet analysis of vibration signals in machining. J Mech Eng Autom 6(5A):81–85
38. Rucka M, Wilde K (2006) Application of wavelet analysis in damage detection and localization. J Sound Vib
39. Shao Y, Nezu K (2003) Extracting the symptoms of bearing faults in the wavelet domain. In: International Conference on Mechatronics, ICOM 2003
40. Sun H, He Z, Zi Y, Yuan J, Wang X, Chen J, He S (2014) Multiwavelet transform and its applications in mechanical fault diagnosis—a review
41. Torrence C, Compo GP (1998) A practical guide to wavelet analysis. Bull Am Meteorol Soc
42. Valenzuela V, Oliveira H (2015) Close expressions for Meyer Wavelet and scale function
43. Wachowiak MP, Wachowiak-Smolíková R, Johnson MJ, Hay DC, Power KE, Williams-Bell FM (2018) Quantitative feature analysis of continuous analytic wavelet transforms of electrocardiography and electromyography. Philos Trans R Soc A Math Phys Eng Sci
44. Wang T, Altabay WA, Noori M, Ghiasi R (2020) A Deep learning based approach for response prediction of beam-like structures. SDHM Struct Durab Heal Monit 14(4):283–301
45. Yan R, Chen X, Mukhopadhyay SC (2017) Structural health monitoring: an advanced signal processing perspective
46. Zhao Y, Noori M, Altabay WA, Beheshti-Aval SB (2018) Mode shape-based damage identification for a reinforced concrete beam using wavelet coefficient differences and multi-resolution analysis. Struct Control Heal Monit

Influence of Operational Conditions on the Modal Based Damage Analysis of Pedestrian Bridges



Mareike Kohm  and Lothar Stempniewski

Abstract Modal based monitoring systems for civil engineering structures, especially for bridge constructions, receive more attention in recent years. The goal of those systems is to detect damage processes at an early stage. This enables quick reaction to damages and ultimately extends the life of existing bridges while also minimizing maintenance costs. The modal parameters, namely natural frequencies and mode shapes are dependent on the stiffness and mass distribution of the structure. Since the traffic loads represent temporally and spatially variable stiffness and mass distributions of the bridge structure, the question arises how reliably the modal parameters can be estimated, and if structural stiffness changes can be distinguished from the variable stiffness and mass distributions of traffic load. In this paper, the influence of pedestrian traffic on the estimation of the modal parameters is investigated. Spring-Mass-Damper systems represent the pedestrians to be able to take human mass, damping and stiffness effects into account. The vertical acceleration responses are considered for single pedestrians and a crowd of pedestrians using probabilistic approaches. The influence of the operating loads is first numerically investigated using an Euler-Bernoulli beam model and then compared with the results of vibration measurements on a pedestrian bridge. We can substantiate, that pedestrian volume, the ratio of the natural frequencies of the bridge superstructure to the step frequency of the pedestrians as well as the measurement length are the decisive criteria for successful damage identification. A clear distinction between the amplitude scatter of the mode shapes due to traffic loads and a structural stiffness change is possible by appropriate selection of the damage identification methods. The contribution of this paper consists in the investigation of the influence of operational loads on the estimated mode shapes and the establishment of the relationship to the modal based damage analysis.

Keywords Modal based bridge monitoring · Operating conditions · Pedestrian bridge

M. Kohm (✉) · L. Stempniewski
Institute of Reinforced Concrete Structures and Building Materials, Karlsruhe Institute of Technology, 76131 Karlsruhe, Germany
e-mail: mareike.kohm@kit.edu
URL: <https://www.imb.kit.edu>

© The Author(s), under exclusive license to Springer Nature Switzerland AG 2021
C. Rainieri et al. (eds.), *Civil Structural Health Monitoring*, Lecture Notes in Civil Engineering 156, https://doi.org/10.1007/978-3-030-74258-4_30

1 Introduction

In recent years, *Operational Modal Analysis* (OMA) has gained increasing attention. Thanks to rapidly developing sensor and computer technology, it is now possible to record the vibration behaviour of structures with high resolution. While in some areas, such as mechanical engineering, it has been obvious for some years to permanently monitor machines using suitable monitoring systems, the application of such systems in the construction industry has not yet become a standard. Unlike large volume series production in mechanical engineering, bridge construction has project character making each bridge unique. This hinders the standardization due to low volume. However, bridge structures in particular are essential for the infrastructure network of a country. Furthermore, they represent a large asset of the country. Therefore, there is a great interest in global, effective, practicable and economic structural health monitoring systems that can help to minimise maintenance costs and extend the useful life of the bridges. Modal based monitoring systems are very promising in this context, since modal parameters are global parameters of a structure and depend on the physical properties (stiffness and mass) of the structure. Figure 1 shows the numerous parameters influencing the vibrational behaviour of a structure, which inevitably affect the modal parameters to different extents [20]. Furthermore, the recording of the vibration behaviour is significantly determined by the measurement chain used, which in turn is significantly influenced by numerous influencing factors. The aim is to detect and localise variations due to changes in the supports and structural stiffness changes. The basic prerequisite for a reliable monitoring system is to know the different characteristic effects of the individual influencing parameters on the modal parameters and to be able to distinguish these from the changes caused by damage. In the context of this paper the main focus is on the investigation of the light green deposited influencing factors (Fig. 1). The emphasis is the investigation of the influence of the temporally and spatially variable stiffness and mass distributions of the operational loads on the estimation of the modal parameters. Furthermore, the influence of the signal length on the estimated modal parameters is examined. Finally, the quality of the estimated modal parameters is measured on the basis of whether structural changes in stiffness and damage to the supports can still be detected and localized independently of the operating loads.

1.1 Literature Review: Human-Structure-Interaction

Due to increasing architectural requirements and more efficient materials, there is a growing interest in slim and lightweight constructions. Pedestrian bridge constructions in particular are becoming more susceptible to vibrations thanks to their modern design. In the last decades some problematic constructions have been created due to insufficient consideration of walking pedestrian loads. This can lead to considerable financial losses and costly refurbishment work, such as in the case of the Millennium

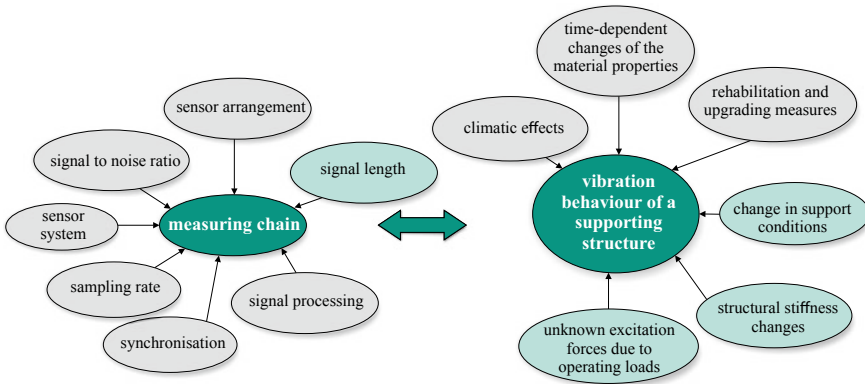


Fig. 1 Influencing parameters on the modal based structural health monitoring

Bridge in 2000 [11]. Therefore, there are numerous studies [10, 12, 14, 22] to investigate the influence of walking pedestrians on the serviceability limit state. In this context, the maximum acceleration amplitude as well as the ratio of the pedestrian's step frequency to the natural frequencies of the bridge structure play an essential role. Shahabpoor et al. [24] gives an overview of the work done to investigate the interaction between walking pedestrians and a structure oscillating in a vertical direction. In connection with the vibration-related serviceability of structures, human-structure-interaction (HSI) is defined as the continuous reciprocal dynamic action of human and structure on each other which acts in a feedback loop as long as the structure and the human on it are in contact. The main influencing factors are the human body (body weight, posture etc.) and the type of activity (standing, walking, running). The investigations show that humans can influence the structural response in different directions through different mechanisms. Usually, the effects of the human body on the dynamic properties of the structure (mass, stiffness and damping) are investigated, but without considering the influence of the structural vibrations on the human body and its movement behaviour. The literature review of [24] substantiates that all studies show that standing people lead to an increase in the damping of the structure and/or changes in the natural frequencies of the structure. Shahabpoor et al. [23] showed that if the human step frequency is below the natural frequency of the structure, the natural frequency of the structure under walking pedestrians is higher than the empty structure. If the step frequency is higher than the natural frequency of the empty structure, the natural frequency decreases due to the walking pedestrians. In this study, however, the time-varying position of the pedestrians was not considered. In addition, no studies could be found which investigate, the influence on the associated mode shapes. Therefore, the probabilistic modeling approach of [9] is adopted. The influence of pedestrians on the vibration behaviour of the structure is not evaluated from the point of view of serviceability limit state but is examined

with regard to the effects on a modal based damage analysis. In this context, it is interesting to what extent the changes in the modal parameters due to pedestrian traffic can mask possible changes in those parameters due to damage processes.

2 Modal Based Damage Identification Methods

The modal based damage identification is based on the comparison of a reference state (RS) and a later possibly damaged comparative state (CS). If there are changes between RS and CS , a change in the system can be concluded. The modal parameters, natural frequencies, mode shapes and modal damping, are global parameters and functions of the stiffness and mass of a structure. In the context of the modal based damage identification presented in this paper, the term *damage* describes any structural stiffness changes that occur. The basic idea of the modal based damage analysis is that damage processes are primarily associated with stiffness changes and stiffness reductions. Thus, the modal parameters change accordingly in dependence of the stiffness changes. According to Rytter [1], four different stages of damage identification are distinguished, whereby only the first two stages (identification and localisation) are dealt with in this paper. In the context of this paper, only damage identification methods based on natural frequencies and mode shapes are considered. The reason for this is, that modal damping has no clear connection to progressive damage processes [7]. Furthermore, modal damping is strongly dependent on the calculation method used, so that it cannot be considered as a reliable damage identification parameter. Other work [6, 26] describe numerous modal based damage identification methods with different advantages and disadvantages. Experts agree, that a suitable combination of several methods is promising, but there are different views on which combination provides the most reliable results and is globally applicable to different systems. Own investigations have shown that a combined consideration of the change in natural frequencies, mode shapes, curvatures of the mode shapes [13] and the Continuous Wavelet Transformation (CWT) of the difference of the mode shapes ΔMS_{RS-CS} [25] can reliably detect and localize a wide variety of damage types and damage intensities independent of the static system. The curvatures of the mode shapes are calculated in this paper using the Mixed Approach (v2) [16].

3 Introduction of the Pedestrian Bridge

The pedestrian bridge on Richard-Willstätter-Allee (Fig. 2) in Karlsruhe (Germany) was built in 1972 as one of three almost identical pedestrian bridges crossing the street *Adenauerring*. It is a three-span prestressed concrete bridge (27 m–35 m–27 m) with a total length of 96.90 m and a width of 4 m. The middle section has the constructive peculiarity that a 19.20 m long section was designed as a suspension plate (Fig. 3),



Fig. 2 Pedestrian bridge on Richard-Willstätter-Allee in Karlsruhe (Germany)

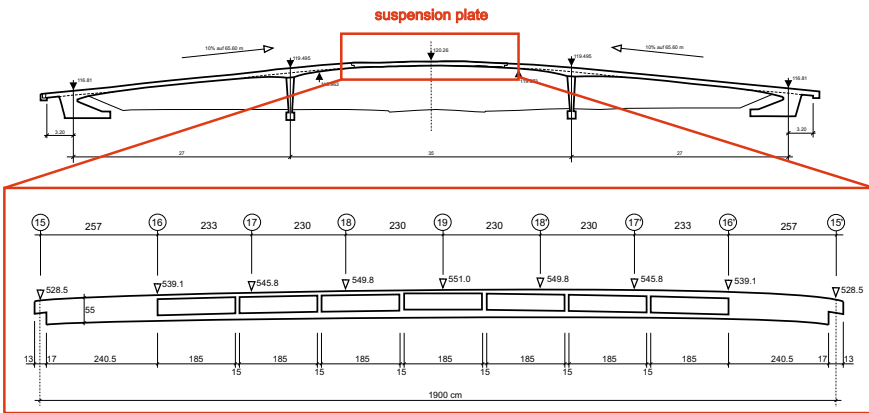


Fig. 3 top: View of the bridge; bottom: Longitudinal section of the suspension plate

which is supported by consoles on the cantilevers of the adjoining bridge spans. The main focus was on the metrological investigation of this suspension plate. The view of the bridge and the longitudinal section of the suspension plate is shown in Fig. 3. It shows that the mass distribution of the suspension plate is not constant. Over a length of ≈ 13.60 m the suspension plate is not designed as a full cross section but has hollow bodies in order to reduce the dead weight of the plate.

3.1 Vibration Measurements

Within the scope of the vibration measurements, the main focus was on the analysis of this suspension plate, since the support consoles showed corrosion-related damages. Figure 4 shows the corrosion damage on the eastern support console, the corrosion plumes in the support area as well as corrosion plumes on the expansion joint.



Fig. 4 *left*: Corrosion damage on the eastern support console; *center*: Corrosion plums in the support area; *right*: Corrosion plums on the expansion joint

Since 2018, four measuring campaigns have been carried out on this pedestrian bridge. The first measurement took place on 05.04.2018. The developed measuring system **DiaBriS**—**Diagnostic Bridge System** was to be tested. *DiaBriS* consists of individual measurement boxes called *Menhir* from *SEMEX EngCon GmbH* [21] containing the respective sensor (MEMS or geophone), the power supply as well as the necessary communication technology for wireless data transmission. The data is transferred from the *Menhir* directly to a cloud and then stored and saved in a relational database. A total of eleven capacitive MEMS accelerometers (measuring range of ± 2.0 g, sensitivity 0.625 V/g and 4.5 kg of weight of the complete *Menhir* system) were used. The *Menhir* systems were positioned on one side along the longitudinal axis of the suspension plate. They are aligned using a tripod system and have a secure stand thanks to their dead weight. Pedestrians were able to pass the bridge unhindered during the measurements, as the width of the footpath was only restricted by about 0.5 m. For data protection reasons, only pictures without passing pedestrians are shown. Before estimating the modal parameters, data processing was carried out. First a detrend correction was performed and high- and low-pass butterworth filters (4th order) with cut-off frequencies of 0.5 Hz and 20 Hz were applied. The measurement campaigns lasted between 3 h and 24 h, whereby the evaluation was executed for time windows between 1 min and 15 min. Initially, the *Menhir* systems were synchronized via real time clocks. However, during subsequent measurements [13] it was determined that GPS synchronization was required, so that each measurement box is now equipped with a GPS antenna (Fig. 5).

In summer 2019, the bridge was renovated. The renovation included the repair of the support consoles of the suspension plate and a strengthening in the support area by near surface mounted (NSM) carbon fibre reinforced polymer (CFRP) strips. This paper focuses on the metrological investigations prior to the rehabilitation of the bridge, so that the results of the measurement campaign of 05.04.2018 (sampling rate: 1000 Hz) will be presented in the following, despite the missing GPS synchronization. Due to the low natural frequencies of the suspension plate, the synchronization with the real-time clocks was sufficient. The modal parameters are estimated using the FDD method [5]. The estimated mode shapes and natural frequencies of the measurements on 05.04.2018 are shown in Fig. 6. The first natural frequency $f_1 = 1.46$ Hz of the suspension plate is in the range of the step frequency of pedestrians (1.4 Hz - 3.3 Hz) [18]. Since the suspension plate is supported on the cantilevers



Fig. 5 *left*: Sensor positioning before the renovation; *center*: Sensor positioning after the renovation; *right*: *Menhir* with GPS antenna

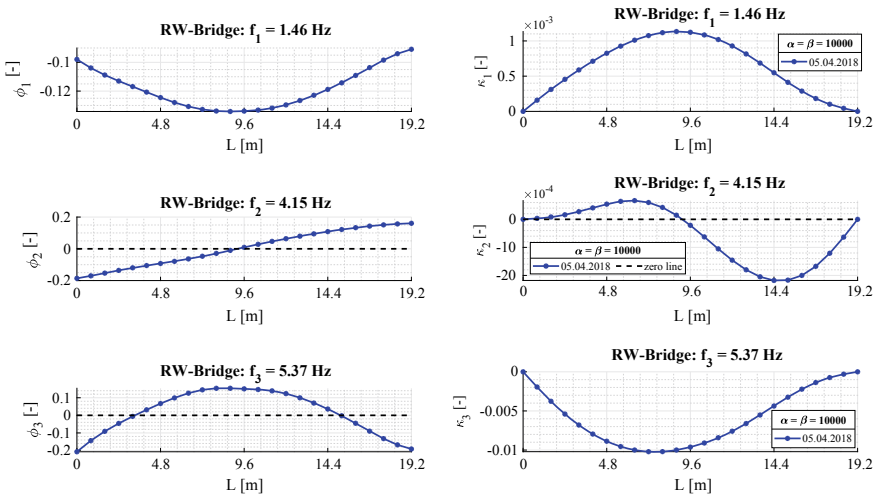


Fig. 6 *left*: Modal parameters of the suspension plate (05.04.2018); *right*: Curvature of the zero-line adjusted mode shapes (05.04.2018)

of the adjacent bridge spans, the suspension plate can be modelled in a simplified way as a spring-supported single-span beam (Fig. 7). Due to the spring support of the suspension plate, the amplitudes at the support points are not equal to zero. This requires a zero-line adjustment of the mode shapes for the following reasons:

- (1) Damage localization using CWT requires an asymmetrical expansion of the mode shapes to avoid the edge effect [25]. Therefore it is necessary that the amplitudes at the support points are zero.
- (2) The curvatures of the mode shapes are used as a further damage localization method. These are calculated using the Mixed Approach (v2) [16]. Since the spring stiffnesses of the support consoles are unknown, this model approach involves unknown boundary conditions which cannot be taken into account in

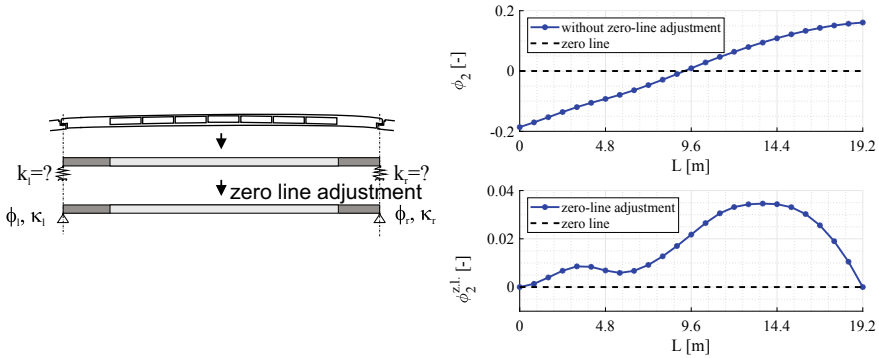


Fig. 7 *left*: Numerical model of the suspension plate: transformation of the boundary conditions due to the zero line adjustment; *right*: Comparison of the 2. mode shape with and without zero-line adjustment (05.04.2018)

the Mixed Approach (v2). The zero line adjustment of the mode shapes allows the transformation of the unknown spring support into a known simply supported beam (Fig. 7) so that the curvatures of the mode shapes can be calculated using the Mixed Approach (v2).

- (3) Due to the amplitude relationships between the support and the loops of the second mode shape, changes in the amplitude curve are not apparent without a zero line adjustment (Fig. 7 *right*).

The support points are connected with a straight line that represents the new zero-line. The new amplitude values are determined by the distance of the mode shape amplitude from the new zero-line. Figure 7 on the left illustrates the numerical model of the suspension plate including the transformation of the boundary conditions due to the zero line adjustment. On the right the comparison of the second mode shape with the zero-line adjusted mode shape is represented. The significantly asymmetrical course of the mode shape becomes apparent through the fitting. This should not occur with an undamaged symmetrical system. Together with the lower amplitude of the first mode shape (Fig. 6) at the left support (eastern support) a damage can be concluded, although no comparison measurement is available. The curvatures of the mode shapes show a clear asymmetry, too (Fig. 6 on the right). In particular, the curvature of the second mode shape shows that the loop adjacent to the damage cannot develop completely, so that the vibration node is shifted in the direction of the damage. The penalty factors α and β were chosen to 10, 000 (Fig. 6) for the calculation of the curvatures of the mode shapes using the Mixed Approach (v2) [16].

4 Numerical Investigations

The objective of the numerical investigations is the elaboration of characteristic behaviours of the modal parameters in dependence of selected influencing factors. Hereby, it is explicitly pointed out that the numerical calculations do not claim to represent experimental investigations as accurately as possible in a quantitative matter. It is not a matter of a finite element updating but of assigning characteristic changes that could be made in the context of the experimental investigations to the respective influencing factors. The aim is to develop mechanical models which reflect the real characteristic behaviour with sufficient accuracy and which are generally applicable to bridge structures depending on their respective static system. For the numerical parameter study a finite element model named **NumDiaBriS (Numerical Diagnostic Bridge System)** was implemented in MATLAB® (R2019b). The goal is to be able to investigate different static systems, different excitation modes and the relevant metrological parameters such as sampling rate, signal length and synchronisation accuracy. In this paper, the procedure and the parameter study will be demonstrated on the static system of the suspension plate of the pedestrian bridge in Sect. 3 and the results will be compared with the observations from the in-situ measurements in Sect. 5. In order to investigate the interaction between pedestrians and the bridge superstructure and the associated effects on the estimation of the modal parameters, the bridge superstructure, the walking pedestrians and other unknown sources of excitation, e.g. due to the running traffic under the bridge, must be considered. Since the damage identification methods are based on the bending natural frequencies and mode shapes, only the vibrations in vertical direction are considered.

The bridge structure is modeled as a finite element beam. Since only the vertical bending mode shapes are of interest, the Euler-Bernoulli beam theory was chosen instead of the Timoshenko beam theory, which takes into account the shear deformation of the cross-sectional plane. Therefore, the displacement field is approximated using 1-dimensional elements with cubic Hermitian interpolation shape functions and two degrees of freedom per node. The selected parameters of the model are shown in Fig. 8. Furthermore, Fig. 8 shows the simplified consideration of the variable cross-section of the suspension plate. In the areas close to the supports, the full cross-section A and the moment of inertia I_y is applied and in the middle region of the beam (suspension plate), the hollow spaces are considered over the reduced cross-sectional area A_h as well as the reduced moment of inertia $I_{y,h}$. The damping ratio of the structure alone was taken to be 1% and 2% for the first two modes, with Rayleigh damping assumed thereafter.

The pedestrian modelling approach presented in this paper is based on the modelling method introduced in Caprani et al. [9]. Since the modal parameters depend on the mass and stiffness distribution of a structure, it is necessary to model each pedestrian as a moving spring-mass-damper (SMD) system (Fig. 8). A continuous contact between the SMD systems (pedestrians) and the beam (suspension plate structure) is assumed. Furthermore, human walking implies a periodic time-dependent force with components in vertical, horizontal-lateral and horizontal-longitudinal direction.

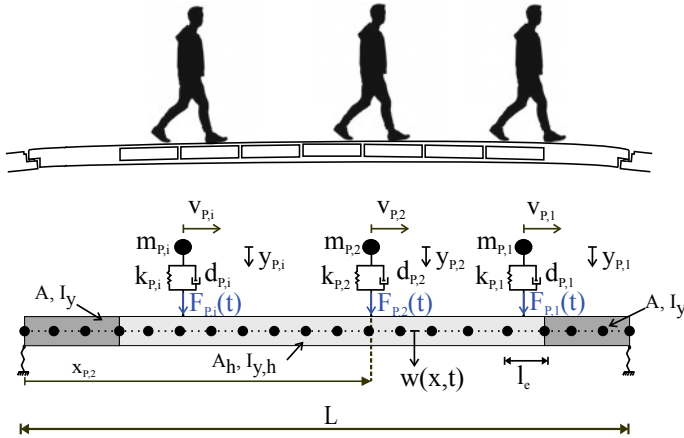


Fig. 8 NumDiaBriS: Bridge model of the suspension plate including the pedestrians

Since only the bending modal parameters are considered in the damage identification procedures and the vertical component of the applied step force has the highest amplitude, only this component is considered and evaluated in the following investigations. Based on the assumption that healthy people in whom the induced forces of the left and right leg are equal, the periodic time-dependent force can be combined into a continuous vertical walking force $F(t)$ (Eq. 1) [4, 18].

$$F(t) = m_p \cdot g \cdot (1 + \sum \alpha_j \cdot \sin(2 \cdot \pi \cdot j \cdot f_{st} t + \phi_j)) \tag{1}$$

m_p is the body weight of the pedestrian, g the acceleration due to gravity, α_j the dynamic load factor of the j th harmonic [18], f_{st} the step frequency and ϕ_j the phase shift of the j th harmonic [18].

In order to use a SMD system to study the interaction between pedestrian and bridge superstructure, it is necessary to select reasonable values for human stiffness and damping ratio. Numerous investigations have been carried out by biomechanics, so that a large number of publications can be found. For example, Caprani et al. [2] offers a comprehensive overview of the biomechanical literature. To reflect the diversity of the population, a probabilistic approach is selected, which uses statistical distributions to determine the characteristic properties of pedestrians (Table 1).

In the context of the investigations with *NumDiaBriS* synchronisation effects (bridge \leftrightarrow human and human \leftrightarrow human) were not explicitly considered, since these are not limit value considerations of the serviceability or load-bearing capacity but the simulation of average pedestrian flows. Furthermore, synchronisation effects could not be observed on this example bridge so far. In this paper only traffic flows from one direction are considered. Overtaking by individual pedestrians due to different walking speeds is possible. As long as a pedestrian (SMD model) is on the bridge (beam model), the two systems interact according to the following equation:

Table 1 Main pedestrian properties

Body weight [19]	m_P	Logarithmic normal distribution	$\bar{x} = 73.85 \text{ kg}$ $\sigma = 15.68 \text{ kg}$
Damping ratio [2]	ξ_P	Uniformly random distribution	[0.2 0.6]
Walking velocity	v_P		$l_s \cdot f_{st}$
Step frequency [3]	f_{st}	Uniformly random distribution	[1.4 Hz 2.4 Hz]
Step length [4]	l_s	Normal distribution	$\bar{x} = 0.66 \text{ m}$ $\sigma = 0.066 \text{ m}$
Arrival gap [17]	–	Exponential distribution (Poisson Process)	$\bar{x} = 3 \text{ m}$ or $\bar{x} = 10 \text{ m}$
Phase angle of the pedestrian's vertical harmonic force $F(t)$ [8]	ϕ_P	Uniformly random distribution	[0 2π]

$$f_{P,i}(x, t) = F_{P,i}(t) + d_{P,i}[\dot{y}_{P,i} - \dot{w}(x, t)] + k_{P,i}[y_{P,i} - w(x, t)] \quad (2)$$

$F_{P,i}(t)$ ist the walking force according to equation (1), $d_{P,i}$ is the damping coefficient, $k_{P,i}$ is the spring stiffness of the i^{th} pedestrian, $y_{P,i}$ is the displacement of the pedestrian mass $m_{P,i}$ from equilibrium position and $w(x, t)$ is the deflection of the beam. These are calculated according to equation (3) and (4):

$$d_{P,i} = 2 \cdot m_{P,i} \cdot 2 \cdot \pi \cdot f_{st,P,i} \cdot \xi_{P,i} \quad (3)$$

$$k_{P,i} = \frac{2 \cdot d_{P,i}^2}{4 \cdot m_{P,i} \cdot \xi_{P,i}^2} \quad (4)$$

First, the physical properties of the passing pedestrians are calculated taking into account the probabilistic approaches in Table 1. Then the corresponding vertical walking force $F_{P,i}(t)$ (Eq. 1) per pedestrian P_i can be determined. Depending on the arrival gap of each pedestrian and the walking speed $v_{P,i}$, the time at which each pedestrian reaches the bridge and leaves it again can be calculated. While crossing the bridge, the pedestrian interacts with the bridge according to the equation (2). Furthermore, the position of the pedestrians $\sum P_i$ walking on the bridge at time t_c can be determined per time step and the interaction with the respective beam element can be calculated via the shape function $N_{P,i}(x)$:

$$N_{P,i}(x) = \begin{pmatrix} 1 - 3\xi^2 + 2\xi^3 \\ (\xi - 2\xi^2 + \xi^3)l_e \\ 3\xi^2 - 2\xi^3 \\ (-\xi^2 + \xi^3)l_e \end{pmatrix}^T \quad (5)$$

l_e is the element length, $\xi = x_l/l_e$ is the non-dimensional distance along the element and x_l is the local position coordinate of the respective pedestrian. x_l takes values between 0 and the element length l_e . The superposition of all pedestrians on the bridge results in the overall system with $N_b + \sum n_{P,i}$ degrees of freedom. N_b are the degrees of freedom of the pure beam model and $n_{P,i}$ is one additional degree of freedom per pedestrian walking on the beam at time t_c . The calculation of the $N_b + \sum n_{P,i}$ coupled linear differential equations of motion with time-dependent coefficients is performed using the Newmark- β method. The Newmark's parameters are chosen to be $\beta = 0.25$ and $\delta = 0.5$. The complete derivation of the overall system consisting of an SMD crowd model of the pedestrian crowd and FE model of the beam can be found in Caprani et al. [9]. In addition to walking pedestrians, the bridge is also excited by the wind, flowing traffic below the bridge and micro earthquakes. Therefore, the additional unknown external excitation F_R is simplified and considered as white noise with a mean value of $\bar{x} = 0$ and a standard deviation of $\sigma = 1$. Figure 8 shows the overall system with the relevant parameters.

4.1 Operating Loads

The aim is to determine the influence of pedestrian traffic on the estimated modal parameters. However, before entire pedestrian flows were studied, the influence of a single pedestrian crossing the bridge at a constant speed v and step frequency f_{st} was examined. Three different walking speeds with the corresponding step frequencies were investigated:

- (1) slow walking: $f_{st} = f_1^{Bridge}$
- (2) moderate walking: $f_{st} > f_1^{Bridge}$
- (3) fast walking: $f_{st} \gg f_1^{Bridge}$

The influence of body weight was also investigated. It was shown that the mass input of the pedestrian leads to a decrease of the natural frequencies as long as the signal length maximum corresponds to the crossing time of the pedestrian. If the signal length is longer (i.e. the swing-out behaviour is taken into account or the pure noise excitation) the natural frequencies correspond to those of the pure bridge construction. But, the step frequency of the pedestrian is still included in the frequency spectrum. Thus, it can be stated that with sufficient signal length the mass and stiffness influences of the pedestrian on the estimation of the natural frequencies can be eliminated. In case the step frequency is in the range of the natural frequency of the bridge, special attention must be paid to the distinction of these two frequencies. However, by looking at different measurement records, this is easily possible,

because the natural frequency of the bridge occurs in all frequency spectra, whereas the pedestrian's step frequency varies from one pedestrian to the other. On the other hand, the mode shapes do not show any scattering of the amplitude independent of the pedestrian properties. The basic prerequisite for this is, that the signal length was chosen sufficiently long so that the mode shapes could be formed.

Using these findings as a basis, two different pedestrian flows were investigated. Based on the probabilistic approaches for the characteristics of the pedestrians, the results of 50 calculations per configuration are evaluated. The first configuration *F60s2010m* considers a low traffic density (mean arrival gap = 10 m). The second *F60s203m* considers a heavy traffic density (mean arrival gap = 3 m). In both configurations a signal length of 60 s with a sampling rate of 1000 Hz was simulated and the maximum number of pedestrians during the signal period of 60 s was limited to 20. In order to investigate the influence of the traffic volume as well as the signal length, the modal parameters were determined after 20 %, 40 %, 60 %, 80 % and 100 % of the signal length.

Validation The model is validated on the one hand by means of comparative calculations of the deflection curve under pedestrian load at the five aforementioned points in time. Figure 9 shows the deflection curves after 20 %, 60 % and 100 % of the maximum signal length of 60 s. A good agreement can be seen between the results from *NumDiaBriS* (solid line) and the comparison calculations with the program *Stab2D* [15] (dotted line). The vertical dashed lines indicate the position of the respective pedestrian at the considered time. Due to the probabilistic model approach, the dynamic maintenance of the model cannot be validated by means of comparative calculations. If, however, the acceleration time curves of the individual pedestrians on the bridge during the 60 s measurement length are considered and compared with the response oscillation of the suspension plate in the middle of the beam, the superposition of the pedestrian-induced excitation and the applied noise excitation is evident. Figure 10 compares the acceleration amplitudes during the measurements on 24.03.2020 (sampling rate = 1000 Hz) and the numerical calculations using the example of two simulations per pedestrian density (3 m and 10 m). It can be seen that the amplitudes of the simulation with *NumDiaBriS* are significantly higher than those recorded in reality. Furthermore, it is clear that the pedestrian density on the bridge tends to be lower in reality than in the model. Thus, the excitation forces induced by the pedestrians are overestimated. A further cause could be deviating stiffness properties of the bridge structure, since the material properties of the bridge are not clearly known. Consequently, the numerical investigations provide conservative results. If, however, the RMS value of the acceleration time histories of the measurements are compared with the RMS values of the simulations (Fig. 10), it becomes clear that the average RMS value of the simulation (red line) is in the range of the RMS values of the measurements, provided that pedestrians pass the bridge.

Parameter Study: Operating Loads In the following, the standard deviation is regarded as a measure for the scatter of the natural frequencies. Figure 11 shows the natural frequencies of the suspension plate for *F60s203m* determined after 20 % and after 100 % of the signal length.

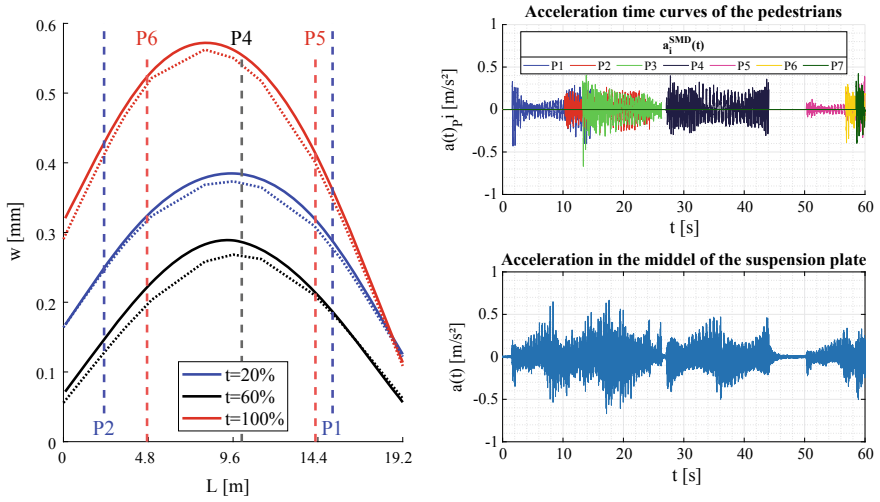


Fig. 9 *left* Deflection curve of the suspension plate; *right* Acceleration time curves of pedestrian and in the middle of the suspension plate

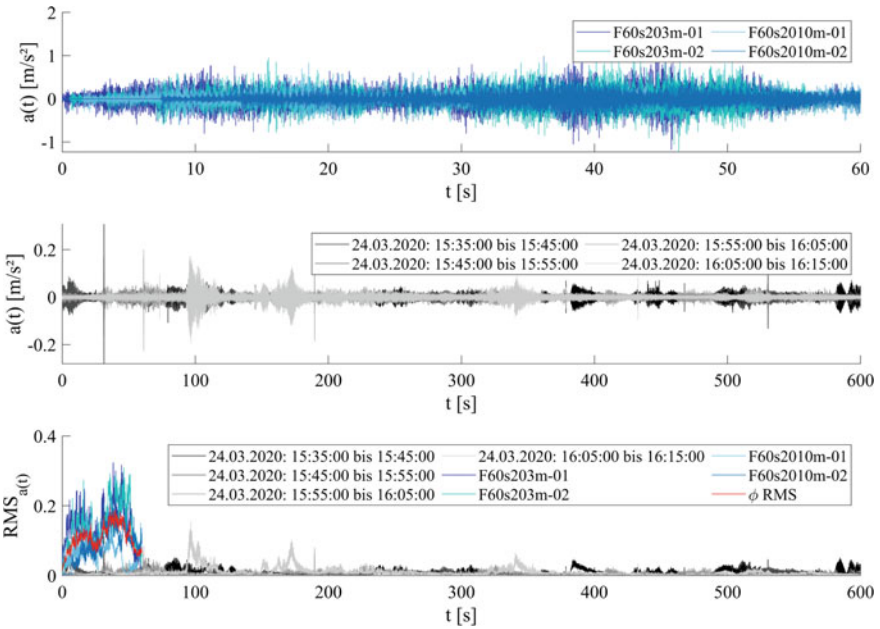


Fig. 10 Comparison of the acceleration amplitudes: measurement 24.03.2020—*NumDiaBriS*

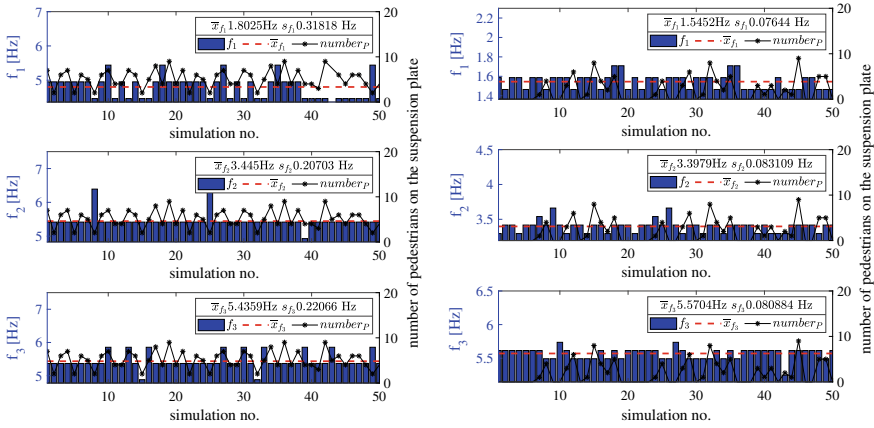


Fig. 11 left: Natural frequencies $t = 20\%$ *F60s203m*; right: Natural frequencies $t = 100\%$ *F60s203m*

After 20% of the signal length, the standard deviations of the natural frequencies are more than twice as large as after 100% of the signal length. Especially the standard deviation of the first natural frequency is significantly higher than the other two, because the first natural frequency of the bridge is in the range of the pedestrians step frequencies. Basically this observation is also valid for the second configuration *F60s2010m*. However, if one compares the two configurations each after 100% of the signal length (Fig. 12), the scattering is greater at low pedestrian density than at high density. The reason for this is probably that the step frequencies overlap to a kind of “broadband noise” at high traffic density, which is advantageous because this corresponds to the white noise and thus to the basic assumption for the excitation on which the OMA procedures are based. However, this broadband excitation is not given with lower traffic volume.

The mode shapes show the same dependencies. Figure 13 shows the mean values of the mode shapes and the corresponding scatter range per configuration for $t=100\%$. The lower traffic density also leads to a significantly higher scatter range. The natural frequencies deviate from each other by up to 1.5%.

Finally, it can be stated that the signal length is decisive for the quality of the estimated modal parameters. In addition, the scattering of the modal parameters decreases with increasing traffic density due to the increasing broadband excitation. However, the consideration of the mean values from a certain number of time windows allows to deal with the scatter due to the temporally and spatially variable stiffness and mass ratios within the considered period.

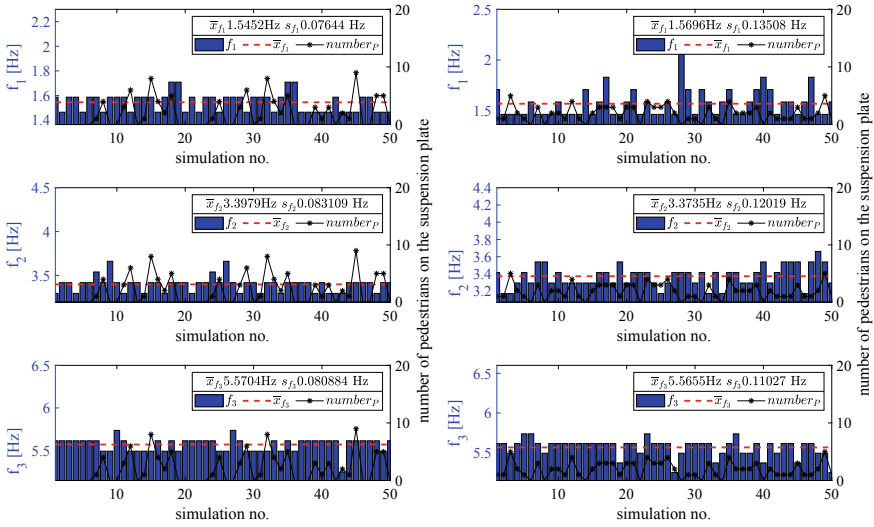


Fig. 12 *left*: Natural frequencies $t = 100\%$ F60s203m; *right*: Natural frequencies $t = 100\%$ F60s2010m

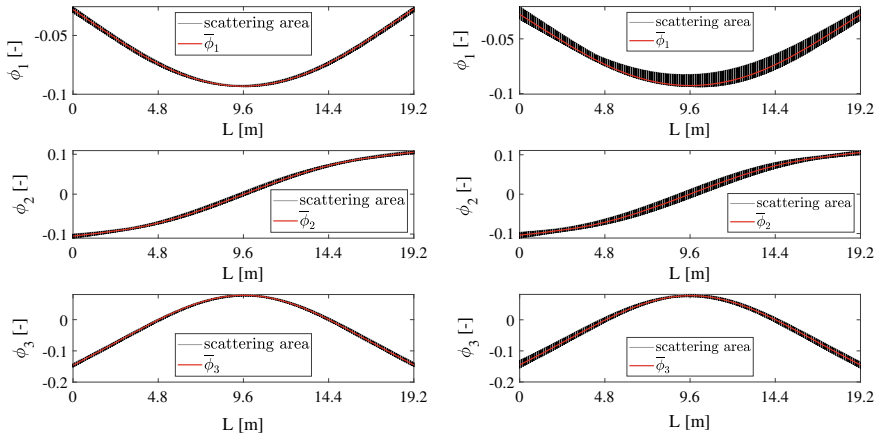


Fig. 13 *left*: Mode shapes $t = 100\%$ (F60s203m) ; *right*: Mode shapes $t = 100\%$ (F60s2010m)

4.2 Operating Loads and Structural Damage Detection

In the context of modal based damage analysis, it is of interest to detect and localize structural stiffness changes. Of particular interest is the extent to which the scatter of the modal parameters due to pedestrian traffic may overlap the changes of the modal parameters due to damage processes. Here, a structural stiffness change is taken into account by reducing the Young's modulus in the FE model of the bridge.

For this purpose the damage function according to Maeck [16] is extended so that asymmetrical damage patterns can also be displayed (Fig. 14). α indicates the maximum reduced Young's modulus with respect to the origin Young's modulus $E_{i,100\%}$, γ indicates the position of the maximum damage along the beam axis, β_1, β_2 are the number of elements of the beam that have a reduced Young's modulus and n_1, n_2 influence the shape of the damaged area. The parameters of the damage function make it possible to map any type of damage pattern. In [13] it could be shown that, in addition to the maximum stiffness reduction, the spatial propagation and the location of the structural stiffness change are decisive for the success of modal based damage localization. The previously presented traffic density configurations *F60s203m* and *F60s2010m* were also considered. Studies on the required sample size have shown that 20 simulations per configuration provide equivalent results. Therefore, 20 simulations per configuration and damage scenario were calculated for the parameter studies of damage identification. Table 2 gives an overview of the damage scenarios examined. Here, any structural stiffness reductions are considered as damage regardless of the strength. *RS* presents the undamaged reference condition. The spring stiffnesses of the suspension plate k_{left} and k_{right} were chosen so that the first natural frequency of the modeled suspension plate corresponds approximately to the measured first natural frequency of the Richard-Willstätter-Allee bridge. The damage patterns *D1* and *D2* represent a symmetrical loss of stiffness starting from the centre of the beam. The damage *D3* represents an asymmetric reduction of the Young's modulus over a total length of 12 m. The damage *D4* and *Dx D4* simulate the corrosion damage to the eastern support console observed on Richard-Willstätter-Allee by reducing the spring stiffness of the left support. The damage pattern *Dx D4* additionally considers a symmetrical damage over a total length of 6 m. In Sect. 4.1 it was shown that the consideration of the mean values of the modal parameters from a certain number of measurement records "filters out" the scatter due to the operational loads. Therefore, the mean values of the modal parameters calculated from the 20 simulations per damage scenario are compared and are the input data for the four damage identification methods. The results of the damage *D1* as well as *D4* of *F60s2010m* are now presented in more detail. Only the results after 100 % are shown. However, it should be noted that even after 20 % of the signal length, any damage could be successfully detected and localized thanks to the combination of the four identification methods. This applies to both traffic density models *F60s203m* and *F60s2010m*. However, since the low traffic density leads to a significantly higher dispersion of the modal parameters, the results for *F60s2010m* are presented.

Influence on the Natural Frequencies Table 3 shows the development of the averaged first three natural frequencies per scenario. The numbers in black are the results of the model with consideration of the pedestrian flows, the numbers in grey show the results of the pure bridge model. These were calculated by solving the eigenvalue problem of the equation of motion of the pure beam without any pedestrian or other excitation forces. When considering the results of the pure bridge model (grey), the percentage frequency changes are as expected: the natural frequencies show the largest percentage decreases, whereas the second natural frequency is almost unaffected, since the damage is located in the vibration node of the second mode

Fig. 14 Extended damage function according to [16].

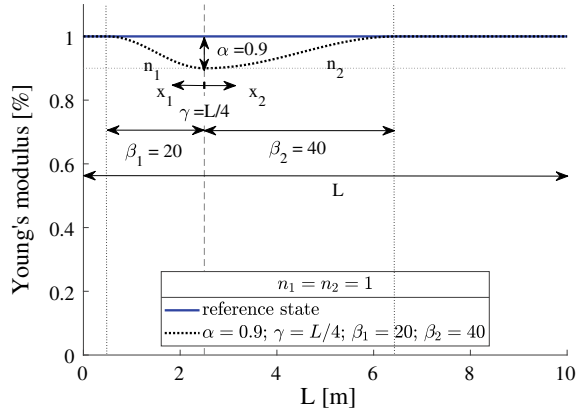


Table 2 Overview of the examined damage scenarios

Damage scenario	α	β_1	β_2	n_1	n_2	γ	k_l [kN/m]	k_r [kN/m]
RS	1.0	—	—	—	—	—	6000	6000
D1	0.8	20	20	1	1	$0.5 \cdot L$	6000	6000
D2	0.9	80	80	2	2	$0.5 \cdot L$	6000	6000
D3	0.9	40	80	2	2	$0.25 \cdot L$	6000	6000
D4	1.0	—	—	—	—	—	5000	6000
$Dx D4$	0.8	30	30	1	1	$0.5 \cdot L$	5000	6000

shape. The results of damage scenario *D4* are also as expected. However, in contrast to *D1*, all three mode shapes are affected, with the second mode shape showing the largest decrease, since the damage at the support has a significant influence on the amplitude of the second mode shape. When considering the results with regard to pedestrian flows, it is noticeable that the first natural frequency shows only minimal frequency changes in both damage scenarios. With damage scenario *D4* there is even an increase in frequency. This is due to the scattering of the first natural frequency evoked by the pedestrian flows (Sect. 4.1). The influence of the step frequencies is thus greater than the effects of the two damage scenarios. Furthermore, it should be noted that the second natural frequency shows a significant frequency increase in damage scenario *D1*, although it should be almost unaffected by the damage at the vibration node. The remaining frequency decreases are as expected.

Influence on the Mode Shapes Fig. 15 shows the mode shapes for the two damage scenarios. Due to the spring support, the mode shapes as well as the zero-line adjusted mode shapes for the damage assessment are considered. For *D1* almost no amplitude changes are visible. The reduced spring stiffness for *D4*, on the other hand, leads to a visible amplitude decrease at the left support of the first mode shape. If, on the other hand, the zero-line adjusted mode shapes (Fig. 16) are considered, a minimal

Table 3 *F60s2010m*: Development of natural frequencies depending on the damage scenarios

Scenario	f_1 [Hz]	f_2 [Hz]	f_3 [Hz]	Δf_1 [%]	Δf_2 [%]	Δf_3 [%]
<i>RS</i>	1.5696 1.4649	3.3735 3.3756	5.5655 5.5581	—	—	—
<i>D1</i>	1.5622 1.4434	3.4235 3.3752	5.4679 5.4778	-0.47 -1.47	+1.48 -0.01	-1.75 -1.44
<i>D4</i>	1.5806 1.4372	3.2404 3.2412	5.4251 5.4249	+0.70 -1.89	-3.95 -3.98	-2.52 -2.40

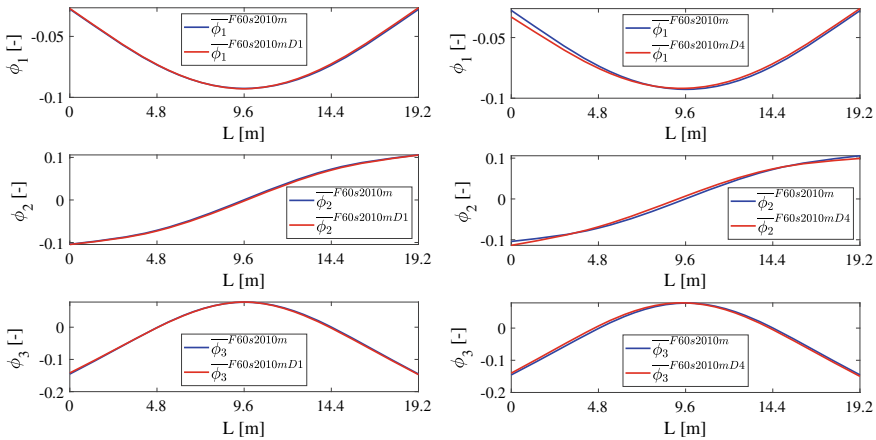


Fig. 15 *left: D1—Mode shapes ; right: D4—Mode shapes*

amplitude increase in the area of the damage is evident at *D1*. However, much more remarkable for the second mode shape is the amplitude decrease of the right antinode and the associated displacement of the vibration node. This also explains the increase of the second natural frequency in Tabel 3. The zero-line adjusted mode shapes of the pure bridge model do not show this change in the second mode shape, so that, as expected, there was no change in frequency. These changes are thus solely due to pedestrian flows. The consideration of the zero-line adjusted mode shapes of the damage scenario *D4* illustrates the decisive effects on the second mode shape. Due to the reduced spring stiffness at the left support, the adjacent loop can no longer be formed completely, so that an asymmetrical course and thus a displacement of the oscillation node in the direction of the damage occurs. The third mode shape shows only minimal changes in both damage scenarios.

Influence on the Curvatur of the zero-line adjusted Mode Shapes: If the smoothed curvatures of the mode shapes (Fig. 17) are considered, which are fitted to the zero-line, the two damage scenarios can be clearly recognized and distinguished from each other. *D1* leads to a significant curvature increase in the area of reduced stiffness for the first and third mode shapes. In contrast, the curvature of the second mode shape shows hardly any amplitude differences, as expected. On the other hand,

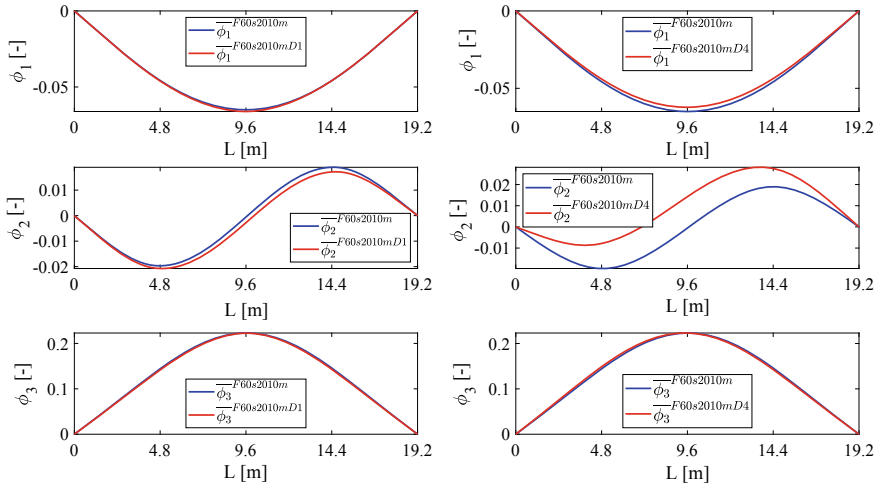


Fig. 16 *left: D1—Zero-line adjusted mode shapes; right: D4—Zero-line adjusted mode shapes.*

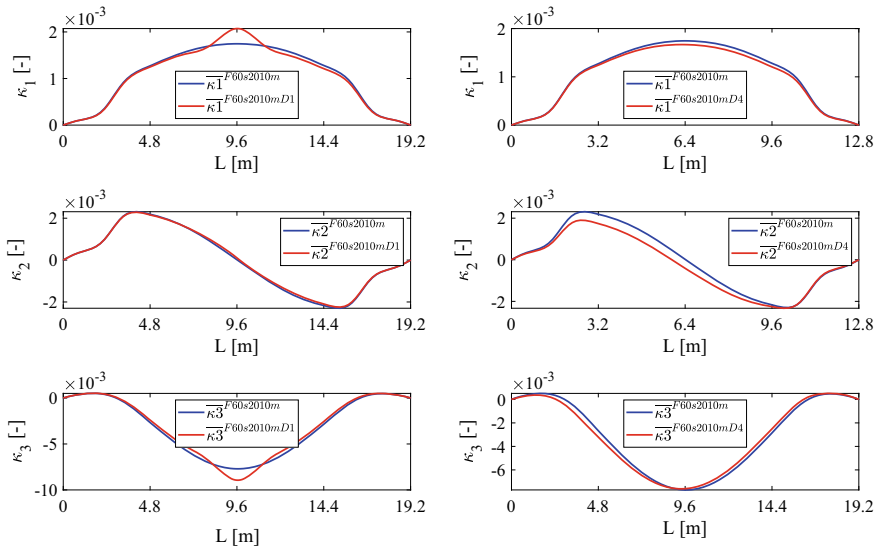


Fig. 17 *left: D1—curvature of zero-line adjusted mode shapes ; right: D4—curvature of zero-line adjusted mode shapes*

damage scenario *D4* does not lead to local changes in the curvature but affects the curvature of the whole structure. In particular, the curvature of the second and third mode shapes develop asymmetries and thus shifts of the antinodes in the direction of the damage occur.

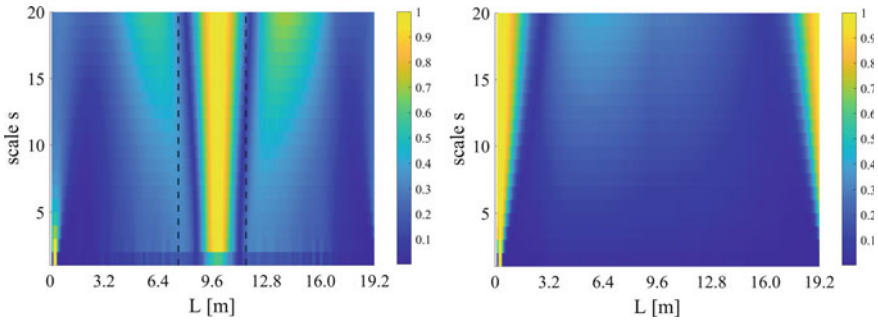


Fig. 18 *left: D1—wavelet analysis; right: D4—wavelet analysis*

Wavelet analysis of the zero-line adjusted mode shapes: Figure 18 shows the weighted and normalized wavelet coefficients for the two damage scenarios. The symmetrical damage $D1$ in the center of the field is clearly detectable and localizable by means of the increased coefficient values. On the other hand, the reduced spring stiffness at the left support ($D4$) cannot be clearly determined by means of the CWT. Although increased coefficient values are visible on the left support across all scales, increased coefficient values also occur on the right support from scale values greater than 4. However, it clearly shows that there is no other damage in the structure.

Interim Conclusion In conclusion, it can be stated that both damage scenarios were successfully identified and localised independently of pedestrian flows. However, a prerequisite for this is a sufficient signal length and the averaging of several recorded time windows. In the FE model, a measurement length of 60 s and a consideration of 5 to 10 time windows would have been sufficient. In reality it can be expected that significantly longer time windows (approx. 10 min) should be considered. Furthermore, it has been confirmed that a combined consideration of all damage identification procedures is purposeful, since different procedures are suitable depending on the damage characteristic. The results of the CWT (Fig. 18) of the two damage scenarios $D1$ and $D4$ illustrate this particularly well. If all the damage scenarios listed in Table 2 are evaluated, a kind of action instruction in the form of a matrix (Table 4 and 5) can be created for the evaluation of the results. This can be done for any type of static system. In this way, the characteristic changes in the modal parameters can be unambiguously assigned to the different types of damage. Here the decisive description criteria for the respective damage pattern are: symmetry, spatial extension and system damage at supports. However, special caution is required when investigating the natural frequencies, since these are particularly strongly influenced by pedestrian traffic, provided that the natural frequency is in the range of the step frequencies. If only the changes of the natural frequencies are available, this should not necessarily be considered as an indication of damage but rather as a possible false alarm. Conversely, changes in the mode shapes, their curvature and high coefficient values of the CWT are reliable indications of a structural stiffness change independent of the development of the natural frequencies.

Table 4 Action instruction for the damage identification evaluation of linear spring supported systems

	<i>D1</i> : symmetric, local	<i>D2</i> : symmetric, global	<i>D3</i> : asymmetric, global
Natural frequencies	f_1, f_3	f_1, f_2, f_3	f_1, f_2, f_3
Mode shapes	–	–	–
Zero-line adjusted mode shapes	–	–	Asymmetric change of the 1. and especially the 2. mode shape
Curvature of zero-line adjusted mode shapes	Formation of turning points at the transition undamaged ↔ damaged; local increase of curvature amplitude	Spatially extended amplitude difference between RS and CS	Asymmetric change of the 1. and especially the 2. curvature of the mode shape
CWT	CWT coefficients ≈ 1 across all scales in the area of the damage	CWT coefficients ≈ 1 across all scales in the area of the damage	Asymmetric damage is detectable but an exact localization of the damaged area is difficult because the CWT coefficients are also ≈ 1 to the left and right of the damage area. This is due to the global amplitude changes of the mode shapes.

5 Comparison of Numerical Investigations and Ambient Vibration Tests

In this section, the characteristic changes in the modal parameters recorded within the framework of the numerical parameter study as a result of damage to the support are compared with the results of vibration measurements on the Richard-Willstätter-Allee bridge. The measurement results before the rehabilitation (05.04.2018) are used to investigate the influence of damage to the eastern support. To investigate the influence of pedestrian traffic on the modal parameters, the measurement results from 17.07.2019 are used. It is emphasized again, that it is not the goal to quantitatively recalculate the results of the bridge measurements but rather to qualitatively compare the characteristic changes of the modal parameters. Figure 19 shows the comparison of the mode shapes. The amplitude decrease at the damaged eastern support (left support) is clearly visible. Also the characteristic change of the vibration amplitudes of the second mode shape in dependence of the damage of the support is shown in Fig. 20 on the basis of the mode shapes adjusted to the zero-line. The loop facing the damage cannot develop completely. The second measured zero-line adjusted mode

Table 5 Action instruction for the damage identification evaluation of linear spring supported systems

	<i>D4</i> : support	<i>Dx D4</i> : support, symmetric, local
Natural frequencies	f_1, f_2, f_3	f_1, f_2, f_3
Mode shapes	Reduction of the amplitude at the damaged support	Reduction of the amplitude at the damaged support
Zero-line adjusted mode shapes	Asymmetrical 2. mode shape, oscillation loop adjacent to damage has a significantly lower amplitude	Asymmetrical 2. mode shape, oscillation loop adjacent to damage has a significantly lower amplitude
Curvature of zero-line adjusted mode shapes	Curvature of the 2. mode shape: oscillation loop adjacent to damage has a significantly lower amplitude	Combination of <i>D1</i> and <i>D4</i>
CWT	CWT is not suitable for locating damage to edge supports due to the method used. However, it clearly shows that there is no other damage in the structure	Combination of <i>D1</i> and <i>D4</i>

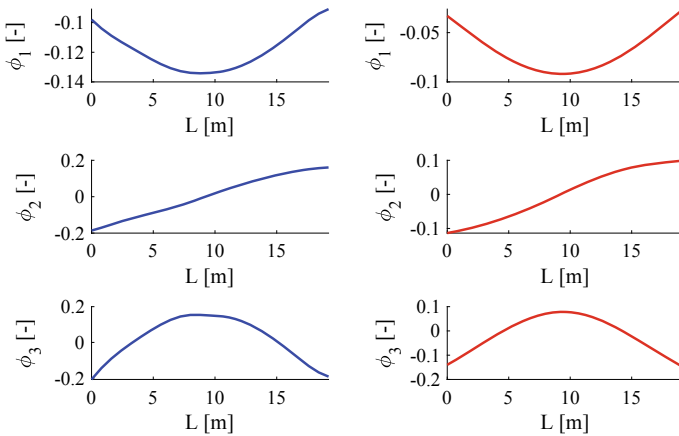


Fig. 19 left RWA Bridge 05.04.2018: mode shapes; right NumDiaBriS: mode shapes (*D4*)

shape even shows a contrary formation of the antinode, so that it can be assumed that the damage is larger in reality and that there may be further damages (Fig. 4). However, this cannot be assessed due to the lack of comparative measurements before the rehabilitation.

However, if one compares the first mode shape before (05.04.2018) and after (17.07.2019) the rehabilitation measures with each other (Fig. 21 top left), one can

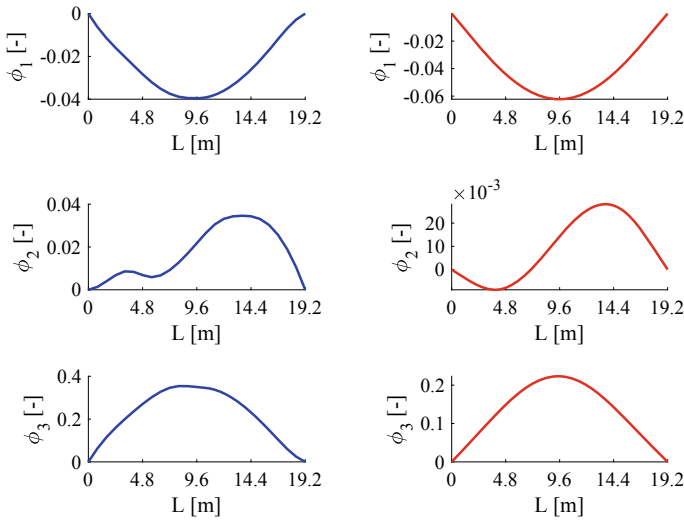


Fig. 20 *left* RWA Bridge 05.04.2018: zero-line adjusted mode shapes; *right* NumDiaBriS: zero-line adjusted mode shapes (*D4*)

see a decrease in the amplitudes at the support consoles. Additionally, the comparison of the zero-line adjusted mode shapes (Fig. 21 *top right*) illustrate that after the rehabilitation of the bridge both loops of the second mode shape can be formed again. Considering the measurement of July 17, 2019 as the new *RS* and the measurement of April 5, 2018 as a *CS*, the CWT coefficients at the eastern support show significantly increased coefficients across all scales (Fig. 21 *bottom*). Furthermore, no other stiffness changes are visible along the bridge axis. This confirms the conclusions from *NumDiaBriS* according to the Table 5 for the damage type *D4*. Figure 22 compares the results of the ambient vibration measurements of 17.07.2019 (*left*) with the numerical results (*right*). A sampling rate of 400Hz was chosen and signal lengths between 60 s and 300 s were investigated. The black hatched area shows the scattering range of the mode shapes at 60 s signal length. The blue line shows the averaged mode shapes from the 60 s measurements. Comparing the scattering range of the ambient measurements with the scattering range of the numerical calculations, it can be seen that the first mode shape with 60 s signal length has significantly higher scattering ranges. The scatter ranges of the second and third mode shapes are similar. However, if one compares the averaged mode shape from 60 s (blue line) with those of 300 s (red line), they are almost congruent. This confirms the assumption that in reality larger signal lengths are required. Nevertheless, the averaged mode shape curves reflect the essential characteristics and can be used for damage identification. It should also be noted, that even after the rehabilitation measures, a lower amplitude can be seen at the eastern support (Fig. 21 *left*), but this is smaller than before the rehabilitation. Consequently, an improvement could be identified, but a completely symmetrical system could not be restored.

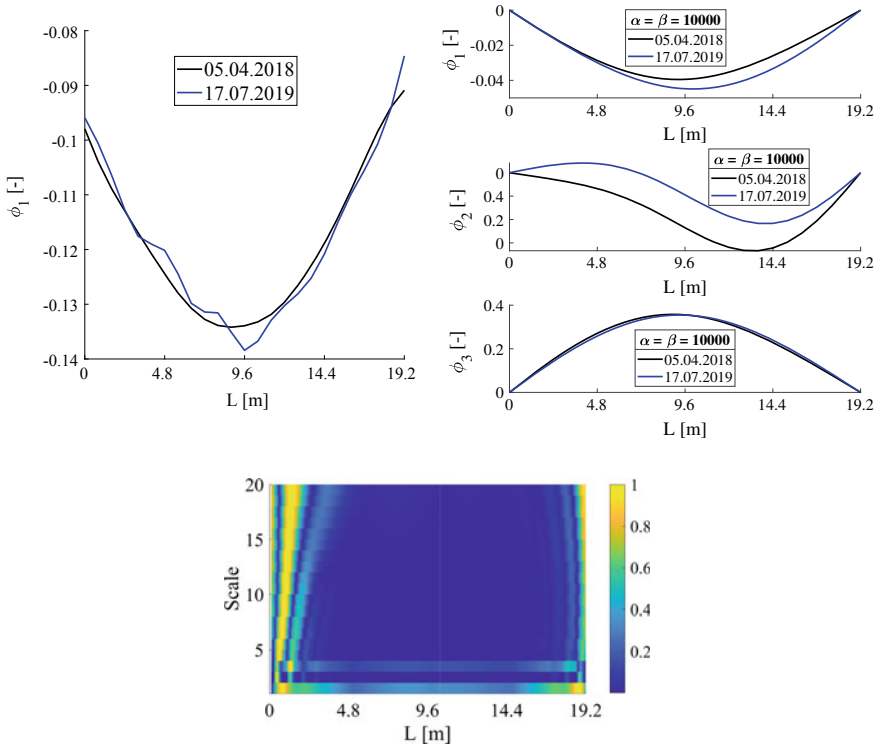


Fig. 21 top left: Comparison of the first mode shape 05.04.2018 ↔ 17.07.2019; top right: Comparison of the zero-line adjusted mode shapes 05.04.2018 ↔ 17.07.2019; bottom: D4—CWT (Daubechies Wavelet) 05.04.2018 ↔ 17.07.2019

6 Conclusions

This paper presents numerical and experimental investigations on the suspension plate of a pedestrian bridge. The aim was to examine the influence of pedestrian traffic on the estimation of the modal parameters. Special attention was paid to the consideration of the temporally and spatially variable stiffness and mass distributions due to different traffic densities. Furthermore, the influence of the signal length on the estimation of the modal parameters was evaluated. The numerical investigations with *NumDiaBriS* could shown that the modal parameters scatter due to pedestrian traffic, especially if the natural frequency of the bridge is in the range of the pedestrians' step frequency. Furthermore, it could be shown that by choosing a sufficient signal length and averaging several time intervals, the characteristic changes of the modal parameters due to damage can still be detected and localized. However, the basic prerequisite for this is a combined consideration of the results of several damage identification methods. It should be noted that the natural frequencies show the greatest dependence on the operating loads. Therefore their changes are not necessar-

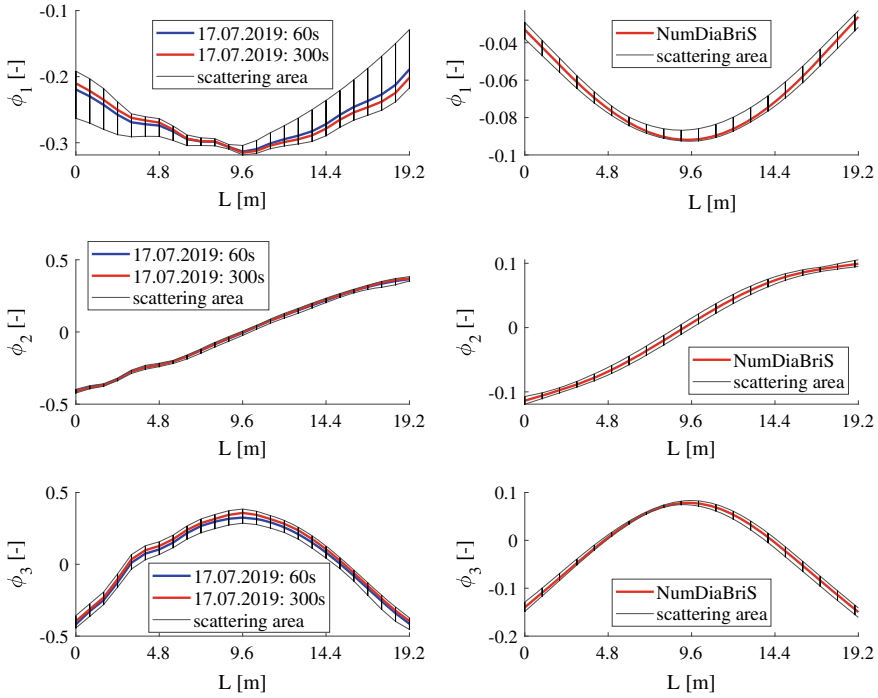


Fig. 22 *left* RWA Bridge 17.07.2019: scattering area of the mode shapes; *right* NumDiaBriS: scattering area of the mode shapes ($D4$)

ily reliable indicators. In contrast, the averaged mode shapes, curvatures of the mode shapes as well as the CWT could be applied successfully. The comparison with the ambient vibration measurements at the Richard-Willstätter-Allee bridge confirm the characteristic changes of the mode shapes due to damage at the support. Moreover, it can be shown that a sufficient measurement length is crucial for the reduction of the scatter of the modal parameters. Even when averaging the 60s measurements, the characteristic properties of the mode shapes could be successfully reflected. Furthermore, the effects of the repair and strengthening measures on the pedestrian bridge by means of NMS CFRP strips could be reconstructed using the modal parameters. In the future, the influence of road traffic on the modal parameters will be investigated. Due to the lower mass ratio between traffic and bridge construction and the different movement characteristics, the results of pedestrian bridges cannot be directly transferred to road bridges. In conclusion it can be summarized that the results suggest that under high demands on the measurement chain and with appropriate choice of the damage identification methods a modal based condition assessment of pedestrian bridges under ambient conditions can be successfully performed. This paper discusses the importance of mode shapes for a reliable modal based monitoring system and points out and substantiates the suitability of modal parameters especially of

the mode shapes as damage localisation parameters even under significant influence of operating loads.

References

1. Anders Rytter: Vibrational Based Inspection of Civil Engineering Structures. Fracture and Dynamics, Ph.D.-Thesis defended publicly at the University of Aalborg, April 20, 1993 PDF for print. 206pp, Denmark
2. Archbold P, Caprani CC, Fanning P, Keogh J (2011) Characteristic vertical response of a footbridge due to crowd loading. 10.21427/D75R6M
3. Bachmann H (2004) Lebendige fugngerbrcken - eine herausforderung. Bautechnik 81(4):227–236. <https://doi.org/10.1002/bate.200490054>
4. Barela AMF, Duarte M (2008) Biomechanical characteristics of elderly individuals walking on land and in water. J Electromyography Kinesiology Official J Int Soc Electrophysiological Kinesiology 18(3):446–454. <https://doi.org/10.1016/j.jelekin.2006.10.008>
5. Brincker R, Zhang L, Andersen P (2001) Modal identification of output-only systems using frequency domain decomposition. Smart Mater Struct 10(3):441–445. <https://doi.org/10.1088/0964-1726/10/3/303>
6. Bungard V, Waldmann D, Maas S (2011) Condition assessment of concrete structures and bridges using vibration monitoring in comparison to changes in their static properties: Zugl: Luxembourg, Univ, Diss, 2010. Berichte aus dem Bauwesen, Shaker, Aachen
7. Bttner A (1992) Beitrag zur Beschreibung des Dmpfungsverhaltens von Stahlbetonbalken (Dissertation). HAB Weimar - Universitt
8. Caprani CC, Keogh J, Archbold P, Fanning P (2012) Enhancement factors for the vertical response of footbridges subjected to stochastic crowd loading. Comput Struct 102–103:87–96. <https://doi.org/10.1016/j.compstruc.2012.03.006>
9. Caprani CC, Ahmadi E (2016) Formulation of human-structure interaction system models for vertical vibration. J Sound Vibration 377:346–367. <https://doi.org/10.1016/j.jsv.2016.05.015>
10. da Silva IAR, da Silva JGS (2018) Experimental and numerical dynamic structural analysis of footbridges when subjected to pedestrians walking loads. J Civil Struct Health Monit 8(4):585–595. <https://doi.org/10.1007/s13349-018-0294-3>
11. Fitzpatrick T (2001) Linking London: the millennium bridge. Royal Academy of Engineering, London
12. Kilikeviius A, Bainskas D, Selech J, Matijoius J, Kilikeviien K, Vainorius D, Ulbrich D, Romek D (2020) The influence of different loads on the footbridge dynamic parameters. Symmetry 12(4):657. <https://doi.org/10.3390/sym12040657>
13. Kohm M, Stempniewski L (2019) Beam tests for a wireless modal-based bridge monitoring system. IABSE Congress New York City—The evolving Metropolis, New York City, USA
14. Kumar P, Kumar A (2013) Human induced vibration in structures. In: National conference on Recent Advances in Mechanical Engineering RAME
15. Leibniz University Hannover—Institute of Structural Analysis: STAB2D. <https://www.isd.uni-hannover.de/en/studies/software/>. Last accessed 06 08 2020
16. Maeck J (2003) Damage assessment of civil engineering structures by vibration monitoring. KU Leuven, Belgium
17. Matsumoto Y, Nishioka T, Shiojiri H, Matsuzaki K (1978) Dynamic design of footbridges. IABSE proceedings 2, Paper P-17/78, Zurich
18. Petersen C, Werkle H (2017) Dynamik der Baukonstruktionen. Springer Fachmedien Wiesbaden, Wiesbaden, 2. aufl 2017 edn. <http://dx.doi.org/10.1007/978-3-8348-2109-6>
19. Portier K, Tolson JK, Roberts SM (2007) Body weight distributions for risk assessment. Risk Anal: Official Publ Soc Risk Analysis 27(1):11–26. <https://doi.org/10.1111/j.1539-6924.2006.00856.x>

20. Retze U (2007) Beispielhafte Untersuchung zum Einsatz von Monitoringmethoden an einer Brücke: München, Univ der Bundeswehr, Diss, Neubiberg
21. SEMEX EngCon GmbH. <https://www.semex-engcon.com>. Last accessed 17 Apr 2020
22. Shahabpoor E, Pavic A, Racic V, Zivanovic S (2017) Effect of group walking traffic on dynamic properties of pedestrian structures. *J Sound Vibration* 387:207–225. <https://doi.org/10.1016/j.jsv.2016.10.017>
23. Shahabpoor E, Pavic A, Racic V (2013) Using msd model to simulate human-structure interaction during walking. *Conf Proc Soc Experimental Mech Ser* 39:357–364. https://doi.org/10.1007/978-1-4614-6555-3_39
24. Shahabpoor E, Pavic A, Racic V (2016) Interaction between walking humans and structures in vertical direction: a literature review. *Shock Vibration* 2016(1):1–22. <https://doi.org/10.1155/2016/3430285>
25. Solís M, Algaba M, Galvín P (2013) Continuous wavelet analysis of mode shapes differences for damage detection. *Mech Syst Signal Process* 40(2):645–666. <https://doi.org/10.1016/j.ymsp.2013.06.006>
26. Stewering U (2008) Schädigungsanalyse für Tragwerke anhand ihrer modalen Systemeigenschaften: Zugl: Bochum, Univ, Diss, Schriftenreihe des Instituts für Konstruktiven Ingenieurbau, Ruhr-Universität Bochum, vol 2008, 1. Shaker, Aachen

Advanced Monitoring of Structures and Infrastructures Through Smart Composite Sensors and Systems



Antonella D'Alessandro, Hasan Borke Birgin, and Filippo Ubertini

Abstract The monitoring of the performance conditions of structures and infrastructures during their service life and after critical events is an extremely timely topic. The potentialities of novel sensors and systems stay in their reliability and flexibility. Indeed, due to their peculiar characteristics which could possess localized features, structures should be instrumented by diffused sensing systems. Traditional sensors could generally be placed only in a limited number of locations by external applications: these occurrences weaken their durability and reliability. Boosted performance are coming from novel smart materials which can combine structural performance with enhanced properties, as sensing ones. In particular, the authors have made several research efforts on the preparation and the application of self-sensing structural materials, cement- and clay-based, doped with conductive fillers. This paper presents the investigation of sensing capabilities and the possible applications of cementitious materials with different carbon-based fillers. Such composites could be embedded or can constitute structural elements, thus generating a diffused smart monitoring system. Possible applications stay in the monitoring of all kinds of concrete structures and infrastructures, including dynamic monitoring, traffic monitoring, damage detection, analysis of the strain/stress field variations.

Keywords Smart sensors and systems · Carbon-based fillers · Cementitious materials · Structural health monitoring · Static and dynamic monitoring

1 Introduction

Recent advances of materials' science and sensing technology permitted the development of novel devices and systems for smart structures and infrastructures. In particular, the availability of novel particles and fillers for civil applications induced the production and the investigation of novel multifunctional composites with enhanced properties. Among the structural materials, concrete appears particularly suitable for

A. D'Alessandro (✉) · H. B. Birgin · F. Ubertini
Department of Civil and Environmental Engineering, University of Perugia, Via G. Duranti, 93,
06125 Perugia, PG, Italy
e-mail: antonella.dalessandro@unipg.it

© The Author(s), under exclusive license to Springer Nature Switzerland AG 2021
C. Rainieri et al. (eds.), *Civil Structural Health Monitoring*, Lecture Notes in Civil Engineering 156, https://doi.org/10.1007/978-3-030-74258-4_31

485

modifications through the addition of fillers, due to its composite nature. Conductive inclusions can confer electrical and electromechanical self-sensing capabilities to cementitious matrices, for applications in the monitoring of civil constructions, important topic of growing interest in the field of engineering. This paper is aimed at investigating the mechanical and electrical behavior of cementitious materials doped with various types of carbon-based nano- and micro- fillers, produced by using different types of preparation procedures, in order to compare their performances. In particular, electromechanical tests have been carried out applying cyclical compression loads. Results allowed to evaluate the load sensing capability of the different materials.

The paper is organized as follows: the rest of Sect. 1 describes the concept of self-sensing material which found the presented research, and reports the main works available in literature about the topic. Section 2 describes the materials of the samples investigated in the paper. Section 3 presents and comments the results, Sect. 4 concludes the paper.

1.1 Concept

The smart composite sensors investigated in this paper are self-sensing construction materials capable to monitor their state of strain or stress. They are made of a construction matrix doped with conductive fillers which enhance its electrical and piezoresistive behavior. They could be embedded within a structure or constitute elements of a construction itself (Fig. 1a).

The self-monitoring capability is obtained through the correlation between the variations of strains/stresses and the variations of electrical features, as resistance or resistivity. Such changes depend on the modification of internal diffusion of loads due for example to exceptional events, such as earthquake, typhoons and landslides, or to the degradation of the structure. For example, a decrease in load on a portion

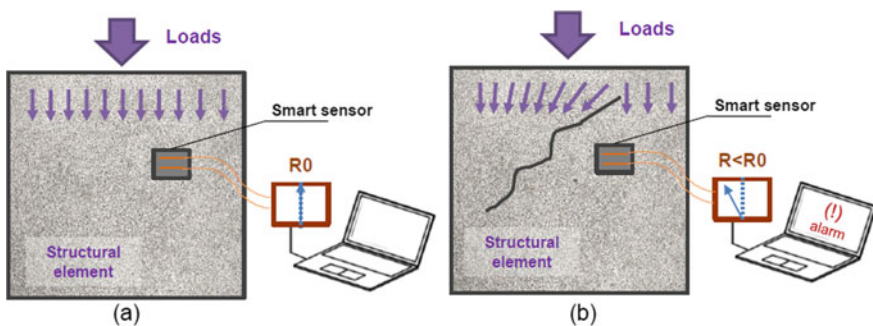


Fig. 1 Sketch of the concept of smart material. **(a)** Undamaged structural element monitored with an embedded smart sensor, **(b)** behavior of the structural element and of the smart sensors after loads' variation

of a structural element determines a reduction of electrical resistance, and vice versa (Fig. 1b).

This technology appears particularly useful for quick assessments of constructions after important environmental events, for the periodic control of structures' behavior during their service life, and for organizing effective maintenance and campaigns of intervention.

1.2 *State-of-Art*

Smart composites are materials with enhanced or novel capabilities [1]. Among all construction ones, cement-based materials are the most adopted in civil engineering. Due to their composite nature, they result particularly suitable for modification through the addition of filler and additives. A delicate task is the good dispersion of the inclusions into the matrix because it determines the homogenous behavior of the material, necessary for a reliable use of the modified composites [2, 3]. In literature, various types of dispersion methods are investigated: the main ones adopted for cementitious mixes are (i) sonication, by use of a tip or a bath, (ii) mechanical mixing, by use of a high-speed mixer, (iii) chemical approach, through the modification of the chemical connection of the structure of the components, (iv) functionalization of the fillers [4, 5]. The last two methods determine a substantial change of the chemical characteristics and behavior of the materials, thus affecting their enhancement in the composites they are dispersed in. The sonication appears the most effective method for nano-particles, especially for hydrophobic ones, but can be applied only for small quantities of material. Mechanical mixing, although usually less effective than sonication for nanosized fillers, results suitable for large scaled applications, as in constructions, and typically demonstrates a sufficient effectiveness for micrometrical fillers [6–8].

Fillers available in literature present various peculiarities, and in the last years they have greatly increased in number due to the progress of nanotechnology and of materials' science. Carbon-based ones demonstrate good applicability in the field of constructions because they can enhance both mechanical capabilities and electrical properties. Their addition in cement-matrix materials produces structural composites provided by piezoresistive and self-sensing abilities, suitable characteristics for monitoring applications [9–11]. Changes in external loads determine a variation of the electrical behavior of the fillers, of the matrix and of the contact surface among the internal components of the material. The monitoring action is carried out through the measurement of the variation in resistance, or other electrical features, of the material due to external load histories, as described in the previous section.

Various types of carbon-based fillers are suitable for monitoring purposes, both nano- and microsized: e.g. nano- or micro-fibers [12, 13], nanotubes [14, 15], carbon black [16, 17], graphene [18, 19] and graphite [20, 21]. Researches available in literature also demonstrate that a combination of different fillers could originate doped materials with enhanced properties [22, 23].

As asserted before, smart structural materials can be embedded within the structures, or constitute the construction materials of a whole structure with self-sensing capabilities. Compared to traditional monitoring systems, such smart sensors are less expensive, can be placed in an easier way and have less issues of maintenance. Moreover, unlike traditional ones, smart sensors are made of the same matrix of that one of the structures where they are applied, with the same durability and mechanical properties. By revealing changes in structural behavior, they could reveal losses in performance, damages and cracks, which are all signs of a possible incipient failure. This constitutes de facto a permanent Structural Health Monitoring system for constructions and infrastructures [24, 25]. Other possible applications are in traffic monitoring, management of roads, monitoring of bridges, control of strategic structures in smart cities [26–28] and more. As a matter of fact, the continuous monitoring of the structural conditions of buildings or infrastructures permits to warn the occupants and impending danger due to possible structural failure. The availability of a simple and economic sensors' system, as with smart sensors investigated in the present paper, allows its application on a great number of structures thus enhancing the safety of many users. In this scenario, the Authors developed a research campaign about the investigation of composite self-sensing materials doped with conductive fillers demonstrating their effectiveness in static and dynamic Structural Health Monitoring [29–31].

2 Samples

The electrical and electromechanical performance of the smart composites have been investigated on cubic samples with 51 mm of side, equipped with four embedded stainless-steel nets placed at mutual distances of 1, 2 and 1 cm, which constituted the electrodes of the smart sensors (Fig. 2). The cementitious matrix was cement paste, which has been doped with different types of carbon fillers, i.e. carbon nanotubes (CNT), carbon nanofibers (CNF), carbon black (CB), graphene nanoplatelets (GNP) and graphite (G), described in the next section.

2.1 Fillers

The fillers investigated in this paper were all carbon-based, but with different dimensions and aspect ratios. Figure 3 shows the images obtained on fragments of smart cementitious materials using a Scanning Electron Microscope (SEM) at the same magnification. In the picture are clearly visible the cementitious structures and the different inclusions, which can be divided in 2-dimensional (GNP, G), 1-dimensional (CNT, CNF) and 0-dimensional (CB). All the fillers appear intact after their mixing and the preparation of the composites.

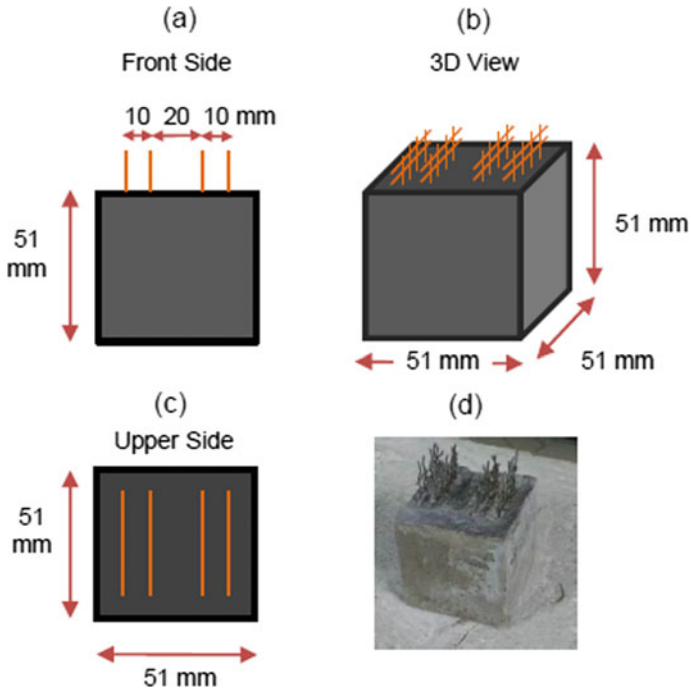


Fig. 2 Description of the samples. (a) Front side view; (b) Assonometric view; (c) Upper side view and (d) a picture of a sample

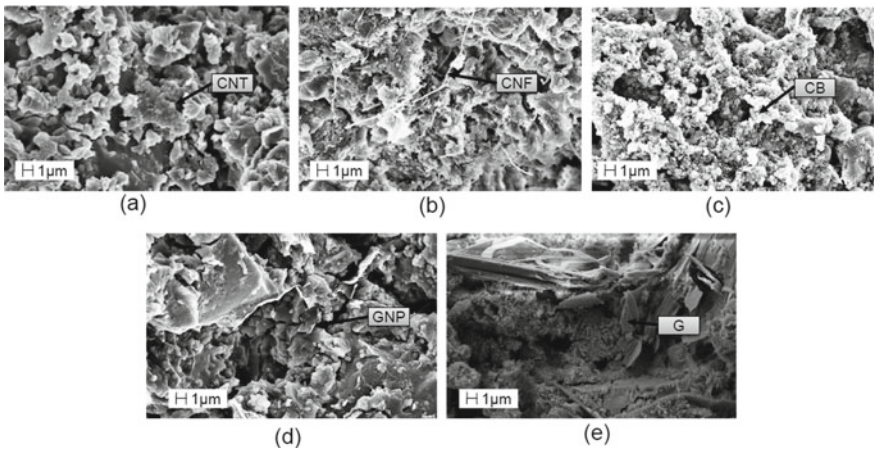


Fig. 3 SEM inspection of cement-matrix composite with (a) Carbon Nanotubes—CNT, (b) Carbon Nanofibers—CNF, (c) Carbon Black—CB, (d) Graphene Nanoplatelets—GNP, and (e) Graphite—G

Table 1 Main physical characteristics of fillers

Filler	Aspect ratio	Type of filler	Diameter	Density (g/cm ³)
CNTs	100	1Dimensional	10 nm	0.1
CNFs	650	1Dimensional	150 nm	1.0
CB	~1	0Dimensional	30 nm	1.8
GNP	200	2Dimensional	15 μm	1.8
G	12	2Dimensional	50 μm	1.2

Other physical properties of the fillers are reported in Table 1: particularly noticeable are the differences in aspect ratios.

Carbon nanotubes were Multi-Walled Graphistrength C-100 fillers provided by Arkema: they had an average diameter of 10–15 nm, length of 0.1–10 μm and specific surface area of about 100–250 m²/g. Carbon Nanofibers were Pyrograf-III Carbon Nanofiber PE-19-XT-LHT with diameter of 70–200 nm and length between 50 and 200 μm. Carbon Black fillers were type Printex XE-2B provided by Orion and consisted on spherical particles composed of pure elemental carbon with a diameter of about 30 nm. Graphene Nanoplatelets, from Cheap Tubes Inc., were small stacks of graphene with an average diameter of 15 μm and thickness of approximately 3–10 nm. Graphite was a fine powder, type silver, with particle size of about 50 μm, provided by Frigerio s.r.l. Graphite and Graphene Nanoplatelets had a macroscopic appearance of gray powder, while Carbon nanotubes, nanofibers and carbon black appeared as black powders.

2.2 Preparation

Cementitious samples were realized in two steps: firstly, the water suspension with fillers has been prepared, and secondly the cement has been mixed to obtain a homogeneous dough (Fig. 4). The cement pastes consisted of a mixture of Portland cement type 42.5 with a water/cement ratio of 0.45. The fillers were added in the amount of 1.5 or 2% by mass of cement. The addition of the different fillers to aqueous solution has been carried out through two different methods: sonication for CNT, CNF and GNP (Fig. 4b1), mechanical mixing for CNT, CB and G (Fig. 4b2). A commercial dispersant was used to improve the dispersion of the nanofillers in water. The fresh composite has been subsequently poured into cubic oiled molds and the nets have been embedded before the solidification of the materials (Fig. 4d). After 48 h the samples have been unmolded, and then got cured in laboratory conditions for 28 days (Fig. 4e).

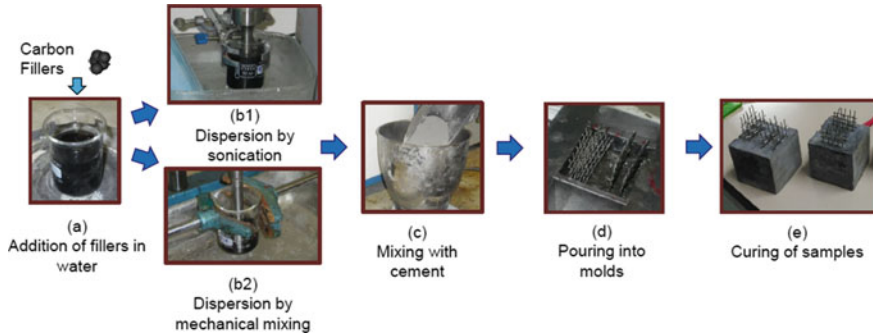


Fig. 4 Preparation procedure of smart cementitious composites. (a) addition of carbon fillers in deionized water, (b1) sonication of the aqueous suspension, (b2) alternative mechanical mixing of the water suspension, (c) addition of cement to the water suspension, (d) pouring of the mixture into oiled molds and placement of embedded electrodes, (e) curing of samples in laboratory conditions

2.3 Samples' Instrumentation

The steel net electrodes of the samples used in the experiments were the internal ones, at a mutual distance of 2 cm. The strain time history was recorded by 3 high-precision LVDT transducers, placed at 120° degrees in-plane. For the calibration of LVDT transducers, one sample has been instrumented with two 2-mm strain gauges. During the tests, the samples were connected to the electrical circuit by their electrodes. The electric circuit consisted on voltage supplier, sample, shunt resistor of 1 kΩ and two voltage readers, that recorded the voltage time histories through the sample and the shunt resistor. The test setup is presented in the Fig. 5a. Accordingly,

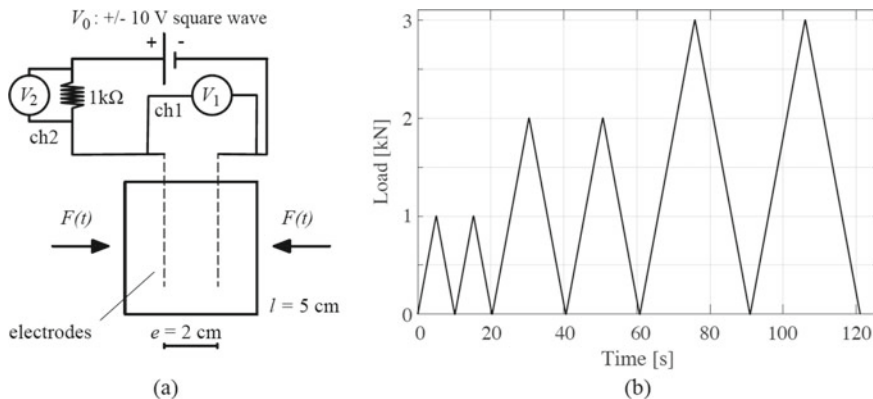


Fig. 5 Experimental setup for electrical and electromechanical tests. (a) Cubic sample geometry with side lengths l , placement of electrodes, electric circuit and voltage readings of interest, application of compression force $F(t)$; (b) the compression load time history in the electromechanical tests, $F(t)$

for the electrical measurements of the experimental setup, a DAQ model NI PXIe-1092 has been used. A biphasic square wave voltage input of 10 V was applied by a NI PXIe-4138 unit [32]. The use of biphasic square wave reduced the polarization drift caused by dielectric cement material matrix. Voltages were read through two different channels (ch1 and ch2 in Fig. 5a) in an Analog Input Module NIPXIe-4302 controlled by a NI PXIe-8840 unit. In the electromechanical tests, the compression load, $F(t)$, was applied using a testing machine model Advantest 50-C7600 by Controls. The loads were applied to the perpendicular direction with respect to the net electrodes and following cyclical time histories with increasing peak values, as depicted in Fig. 5b. The electrical resistance was obtained using Ohm's law:

$$R(t) = \frac{V}{I(t)} \quad (1)$$

where V was the applied constant voltage in the positive part of the square wave, equal to +10 V, I was the current intensity, and t represented the time of acquisition of the signal.

The next sections report the most significant results of the investigation of the sensing behavior of the smart composites doped with the filler types described in the previous sections. The percentages of the adopted carbon doping derived from previous studies which identified the percolation thresholds for the various materials and the ranges of enhanced sensitivity of the composites [6, 33, 34]. Composites obtained through sonication and mechanical mixing were compared and the effectiveness of various fillers added in the same amount has been investigated.

3 Electromechanical Characterization of Samples

The three important features investigated through electromechanical tests were (i) conductivity, (ii) gauge factor and (iii) linearity of the signal response of material. Conductivity of the material is strongly related to the filler amounts dispersed inside the material: it is a strong indicator of being in the optimal range of doping level for load sensing of the material. The conductivities of the smart composites were evaluated based on readings taken during the electromechanical tests. Figure 6a shows the conductivity versus type and amounts of fillers.

The investigated composites were (i) sonicated ones with 1.5% of fillers CNT [from 35], CNF and GNP (i.e., CNTS1,5p, CNFS1,5p, GNPS1,5p) and (ii) mechanically mixed ones with 1.5% of CNT and CB and 2% of CB and G (i.e., CNTM1,5p, CBM1,5p, CBM2,0p, GM2,0p).

The increase of conductivity of sample with CNTs was very significant with respect to that one of other samples with equal amounts of inclusions. The conductivity of the CB sample differed one order between 1.5% and 2.0% doped samples: this was related to being under- and over-percolated, respectively. If compared with

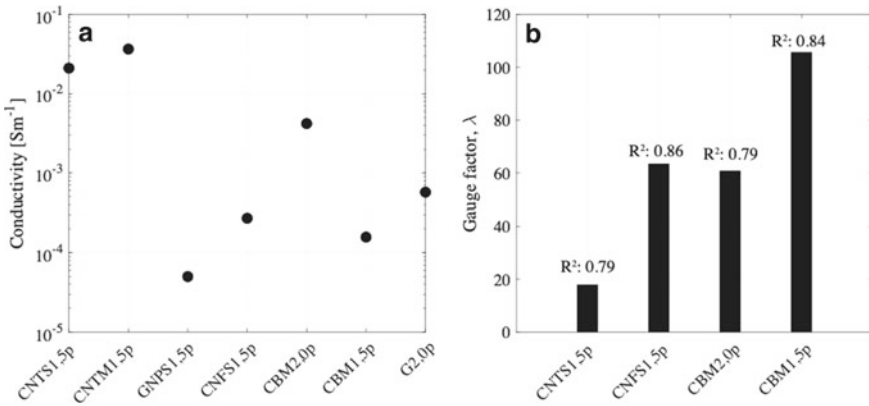


Fig. 6 Short summary of results. **a** Variation of conductivity according to samples, and **b** gauge factor and R² of linear fit of the sensing samples

2.0% G one, the sample of CB appeared more conductive because the percolation threshold of G should occur for higher amounts of particles.

The evaluation of linearity and gauge factor required the analysis of response of materials to the induced strain. To this purpose, electromechanical tests consisted on simultaneous application of compression cyclical loads (Fig. 5b) and voltage difference to the tested sample have been applied. During the tests, the variation of electrical resistance was achieved using Eq. (1). The aim of electromechanical tests was to obtain a reliable linear estimate of the relation between induced strain and the fractional variation of resistance. The slope of the best fit line, called gauge factor, λ, was obtained through the equation:

$$\lambda = - \frac{\Delta R / R_0}{\epsilon} \tag{2}$$

where ΔR was the incremental variation in electrical resistance of the composites, R₀ was the initial internal electrical resistance, and ε the axial strain, positive in compression. The reliability of the linear fit was indicated by its coefficient of determination, R². The gauge factors obtained through electromechanical tests are showed in Fig. 6b.

The samples' results were separated into two categories. First category indicated the samples that were sonicated during the mixing of the conductive filler; the second category included the mechanically mixed composites.

Figure 7 shows the recorded strain vs the fractional change of resistance of the samples. The outcome of the sample with GNPs was non-sensitive to the induced strain and included noise and chattering. On the other hand, the sample with CNFs was observed to have a good response to the evolution of strain. The results obtained through the linear model are presented in Fig. 8. As observed from the times histories,

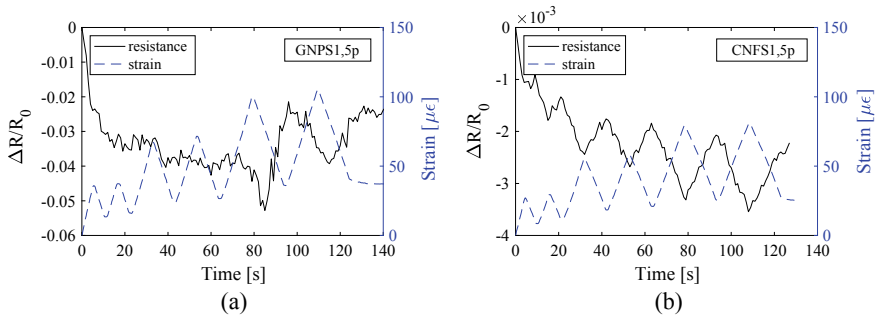


Fig. 7 The strain and fractional change of resistance of sonicated samples, recorded during electromechanical tests; **(a)** sample with GNPs; **(b)** sample with CNFs

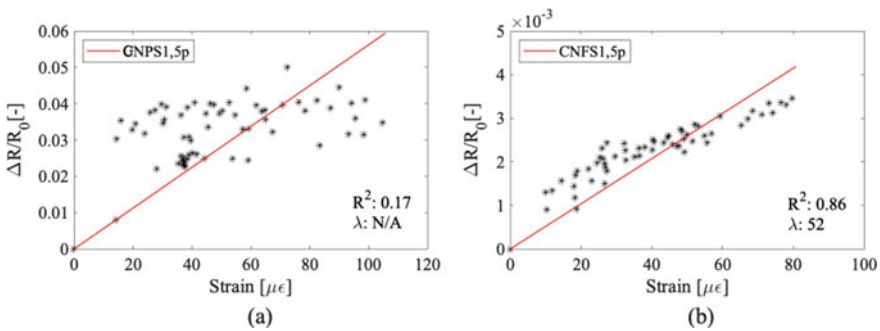


Fig. 8 The linear fit model of the discrete data points of strain vs fractional change of resistance time histories; **(a)** the sample with GNPs; **(b)** the sample with CNFs

the linear fit of the CNFs samples was very reliable. The gauge factor of the linear fit model was calculated as 52.

The signals attained from the electromechanical tests on samples mixed by mechanical process without sonication are presented in the Fig. 9.

Accordingly, all samples but 1.5% CB exhibited considerable polarization drifts. With mechanical mixing process, CNTs performance was not satisfactory. Graphite sample appeared under percolation, because polarization drift was observable. CB with 2.0% of doping level had also a polarization due to the increased dielectric behavior of over-percolated material matrix.

In accordance with conductivity chart presented in Fig. 6, the sample with 1.5% CB exhibited a good response to the external strain. The results obtained with the linear model for mechanically mixed samples are presented in Fig. 10. The data of CNTs are not reported since non clear sensing capability was observed.

According to the results, the sample with 1.5% CB exhibited a high linearity with 84% R^2 and a gauge factor of 118, showing the best performance. 2.0% CB showed

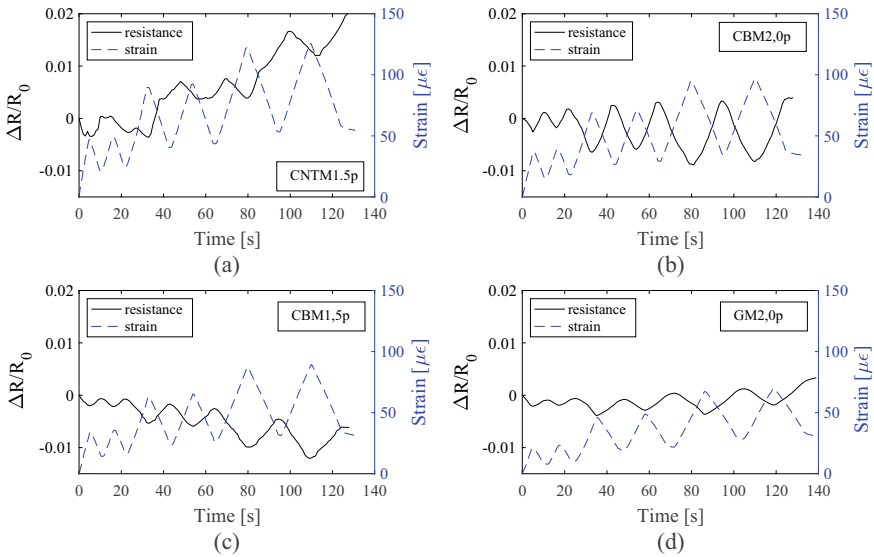


Fig. 9 The strain and fractional change of resistance of mechanically mixed samples, recorded during electromechanical tests; **(a)** sample with 1.5% CNTs; **(b)** sample with 2.0% CB; **(c)** sample with 1.5% CB; **(d)** sample with 2.0% G

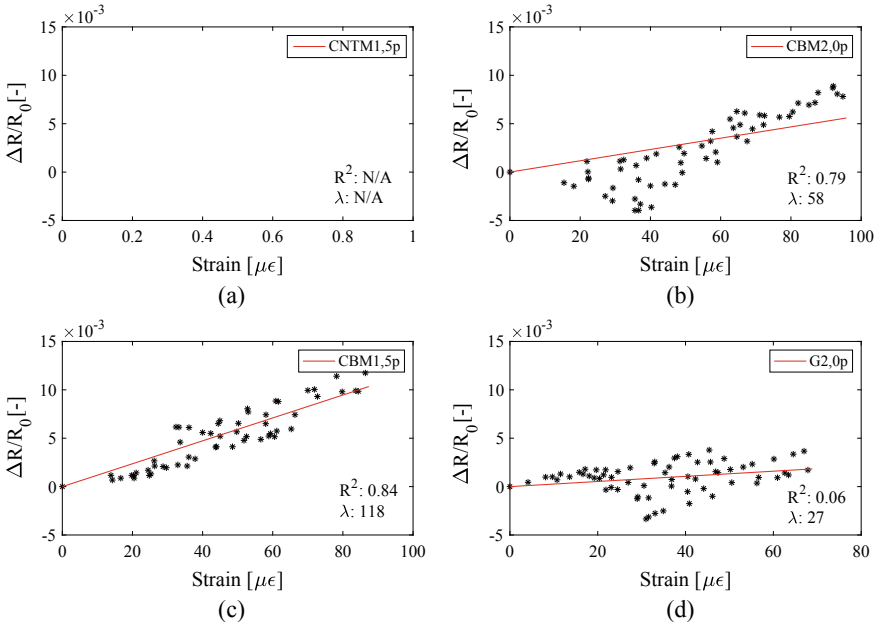


Fig. 10 The linear fit model of the discrete data points of strain vs fractional change of resistance time histories; **(a)** sample with 1.5% CNTs; **(b)** sample with 2.0% CB; **(c)** sample with 1.5% CB; **(d)** sample with 2.0% G

a sufficient linearity; however, it was affected by the polarization drift and the gauge factor was low. The results of 2.0% G sample were also found unreliable.

4 Conclusion

This paper reports the results of electrical and electromechanical tests carried out on smart cement-matrix composites doped with various types of carbon-based fillers (i.e., CNT, CNF, CB, GNP and G), dispersed through two different dispersion methods: sonication and mechanical mixing. Sonication appeared the most effective method for nano-sized particles, but not suitable for real scale applications. Mechanical method, applied in this research to some types of carbon fillers, demonstrated satisfactory results for civil engineering applications. The composite samples were investigated through electromechanical tests, applying cyclical compressive loads. In particular, conductivity, gauge factors and linearity of the signals have been evaluated and compared. Among the investigated sonicated fillers, CNF showed very good performances, with a gauge factor of 52 and a good linearity ($R^2 = 0.86$). Mechanical mixing was not effective for CNT, but was suitable for CB and G. In particular, the composite with 1.5% CB showed the best performance, with a gauge factor of 118 and a good linearity ($R^2 = 0.84$). The results of the experimental tests on sonicated and mechanically mixed samples, demonstrate that, if properly designed, self-sensing carbon-doped smart composites appear promising for their use in monitoring applications on buildings and infrastructures. They could be embedded as small sensors within the constructions (by use of sonication approach), or constitute bigger elements or structures (by use of mechanical mixing approach).

Acknowledgements The authors would like to thank the European Union's Horizon 2020 research and innovation programme (Grant Agreement N. 765057 - SAFERUP!).

References

1. Ali A, Andriyana A (2020) Properties of multifunctional composite materials based on nanomaterials: a review. *RSC Adv* 10:16390–16403
2. D'Alessandro A, Tiecco M, Meoni A, Ubertini F (2021) Improved strain sensing properties of cement-based sensors through enhanced carbon nanotube dispersion. *Cement Concrete Compos* 115:103842
3. D'Alessandro A, Rallini M, Ubertini F, Materazzi AL, Kenny JM (2016) Investigations on scalable fabrication procedures for self-sensing carbon nanotube cement-matrix composites for SHM applications. *Cem Concr Comp* 65:200–213
4. Hilding J, Grulke EA, Zhang ZG, Lockwood F (2003) Dispersion of carbon nanotubes in liquids. *J Dispers Sci Technol* 24:1–41
5. Han B, Yu X, Ou J (2011) Multifunctional and smart nanotube reinforced cement-based materials. In: Gopalakrishnan K, Birgisson B, Taylor P, Attouh-Okine N (eds) *Nanotechnology in civil infrastructure. A Paradigm shift*. Springer, Berlin, pp 1–48

6. Birgin HB, D'Alessandro A, Laflamme S, Ubertini F (2020) Smart graphite–cement composite for roadway-integrated weigh-in-motion sensing. *Sensors* 20(3)
7. Yoo D-Y, You I, Youn H, Lee S-J (2018) Electrical and piezoresistive properties of cement composites with carbon nanomaterials. *J Compos Mater* 52(24)
8. Han B, Yu X, Ou J (2014) Self-Sensing Concrete in *Smart Structures* 14:1–385
9. Tian Z, Li Y, Zheng J, Wang S (2019) A state-of-the-art on self-sensing concrete: mater fabrication properties. *Compos Part B: Eng* 177
10. Li H, Xiao H, Ou J (2003) A study on mechanical and pressure-sensitive properties of cement mortar with nanophase materials. *Cem Concr Res* 34:435–438
11. Metaxa ZS, Konsta-Gdoutos MS, Shah SP (2009) Carbon nanotubes reinforced concrete. *ACI Special Publication*, 267SP, 11–20
12. Wen S, Chung DDL (2007) Piezoresistivity-based strain sensing in carbon fiber-reinforced cement. *ACI Mater J* 104(2):171–179
13. Galao O, Baeza FJ, Zornoza E, Garcés P (2017) Carbon nanofiber cement sensors to detect strain and damage of concrete specimens under compression. *Nanomaterials* 7(12):413
14. Rainieri C, Song Y, Fabbrocino G, Markand JS, Shanov V (2013) CNT-cement based composites: Fabrication, self-sensing properties and prospective applications to Structural Health Monitoring. In: *Proceedings SPIE, Fourth International Conference on Smart Materials and Nanotechnology in Engineering* 8793, 10pp
15. Coppola L, Buoso A, Corazza F (2011) Electrical properties of carbon nanotubes cement composites for monitoring stress conditions in concrete structures. *Appl Mech Mater* 82: 118–123
16. Nalon GH, Ribeiro JCL, Araújo ENDD, Pedroti LG, Carvalho JMFD, Santos RF, Aparecido-Ferreira A (2020) Effects of different kinds of carbon black nanoparticles on the piezoresistive and mechanical properties of cement-based composites. *J Build Eng* 32: 101724
17. Zhang L, Ding S, Han B, Yu X, Ni YQ (2019) Effect of water content on the piezoresistive property of smart cement-based materials with carbon nanotube/nanocarbon black composite filler. *Compos A Appl Sci Manuf* 119:8–20
18. Tao J, Wang J, Zeng Q (2020) A comparative study on the influences of CNT and GNP on the piezoresistivity of cement composites. *Mater Lett* 15: 126858
19. Le JL, Du H, Pang SD (2014) Use of 2D Graphene Nanoplatelets (GNP) in cement composites for structural health evaluation. *Compos B Eng* 67:555–563
20. Fan X, Fang D, Sun M, Li Z (2011) Piezoresistivity of carbon fiber graphite cement-based composites with CCCW. *J Wuhan Univ Technol-Mater Sci Ed* 26: 339
21. Wang D, Wang Q, Huang Z (2019) Investigation on the poor fluidity of electrically conductive cement-graphite paste: experiment and simulation. *Mater Design* 169: 107679
22. Konsta-Gdoutos MS, Aza CA (2014) Self sensing carbon nanotube (CNT) and nanofiber (CNF) cementitious composites for real time damage assessment in smart structures. *Cem Conc Comp* 53:110–128
23. Azhari F, Banthia N (2012) Cement-based sensors with carbon fibers and carbon nanotubes for piezoresistive sensing. *Cem Concr Comp* 34:866–873
24. Wen S, Chung DDL (2000) Damage monitoring of cement paste by electrical resistance measurement. *Cem Concr Res* 30:1979–1982
25. Hou T-C, Lynch JP (2005) Conductivity-based strain monitoring and damage characterization of fiber reinforced cementitious structural components. In: *Proceedings of the smart structures and materials—sensors and smart structures technologies for civil, mechanical, and aerospace systems*, pp 419–429
26. Han B, Yu X, Kwon E (2009) A self-sensing carbon nanotube/cementcomposite for traffic monitoring. *Nanotechnology* 20: 5
27. Liu C, Gong Y, Laflamme S, Phares B, Sarkar S (2016) Bridge damage detection using spatiotemporal patterns extracted from dense sensor network. *Measurement Sci Technol* 28(1): 13
28. Han B, Ding S, Yu X (2015) Intrinsic self-sensing concrete and structures: a review. *Measurements* 59:110–128

29. Materazzi AL, Ubertini F, D'Alessandro A (2013) Carbon nanotube cement-based transducers for dynamic sensing of strain. *Cem Conc Comp* 37:2–11
30. D'Alessandro A, Ubertini F, García-Macías E, Castro-Triguero R, Downey A, Laflamme S, Meoni A, Materazzi AL (2017) Static and dynamic strain monitoring of reinforced concrete components through embedded carbon nanotube cement-based sensors. *Shock Vib* 2017
31. Birgin HB, Laflamme S, D'Alessandro A, Garcia-Macias E, Ubertini F (2020) A weigh-in-motion characterization algorithm for smart pavements based on conductive cementitious materials. *Sensors* 20:659
32. Downey A, D'Alessandro A, Ubertini F, Laflamme S, Geiger R (2017) Biphasic dc measurement approach for enhanced measurement stability and multi-channel sampling of self-sensing multi-functional structural materials doped with carbon-based additives. *Smart Mater Struct* 26
33. D'Alessandro A, Ubertini F, Materazzi AL, Laflamme S, Cancelli A, Micheli L (2016) Carbon cement-based sensors for dynamic monitoring of structures. In: *Proceedings of IEEE IC 2016—International Conference on Environment and Electrical Engineering* 29: 7555628
34. D'Alessandro A, Pisello AL, Sambuco S, Ubertini F, Asdrubali F, Materazzi AL, Cotana F (2016) Self-sensing and thermal energy experimental characterization of multifunctional cement-matrix composites with carbon nano-inclusions. In: *Proceedings of SPIE - The International Society for Optical Engineering*, vol 9800, Article number 98000Z
35. Meoni A, D'Alessandro A, Downey A, García-Macías E, Rallini M, Materazzi AL, Torre L, Laflamme S, Castro-Triguero R, Ubertini F (2018) An experimental study on static and dynamic strain sensitivity of embeddable smart concrete sensors doped with Carbon nanotubes for SHM of large structures. *Sensors* 18:831

Monitoring System of an Industrial Steel Tower Structure



João Zeferino , Eduardo Gonçalves, Paulo Carapito, and Filipe Santos

Abstract Structural Health Monitoring (SHM) systems of civil engineering structures aim to assess and ensure the safety of structures and people. This paper describes a real-world application of an SHM system in an industrial steel tower structure. This is a high steel structure, containing several mechanical equipment with different loads, which operate at various frequencies. The monitoring approach includes a computer modeling of the structure, primarily used to define the sensor network. The sensors were mounted at predetermined locations designed to continuously measure vibrations and deformations at critical points. The sensor network consists of an array of sensors and a gateway. The sensors include strain gauges and triaxial accelerometers, as well as other weather sensors. Data are acquired both from time series of values observed at regular intervals and from structurally relevant measured values, called events, where specific data are collected. Machine learning is used in the development of statistical models for feature discrimination. A visualization user interface is provided to access all data through a user friendly and accessible tool. The paper presents the main results obtained so far, with the primary assessment of the structural health conditions.

Keywords SHM · Sensor network · Machine learning · Real-world application

1 Introduction

Structural Health Monitoring (SHM) systems of civil engineering structures aim to assess and ensure the safety of structures and people. An SHM should detect possible damages as well as their locations and severity. Economic benefits are also expected if a predictive model can successfully forecast the remaining service life and need for maintenance interventions. Different types of SHM systems have been proposed and implemented in recent decades, such as vibration-based [1], guided wave-based [2], and computer vision-based [3].

J. Zeferino (✉) · E. Gonçalves · P. Carapito · F. Santos
VESAM Engenharia S.A, Cantanhede 3060-197, Portugal
e-mail: joao.zeferino@vesamgroup.com

Vibration-based techniques are a commonly researched area for global damage diagnosis. In the damage detection process, it is first necessary to determine the occurrence of damage according to the global change in structural integrity, by identifying differences in the vibration data before and after the damage occurs. The measured time domain can be converted into frequency domain or modal domain by transforming techniques [1]. Time domain approaches can be more straightforward and might eliminate the need for domain transformations. Data-driven time series methods use well-established statistical concepts. Along with data fusion, data-driven approaches are used to transform massive data obtained from monitoring into meaningful information [4]. To this end, Machine Learning (ML) has proven to be a powerful technique that can also contribute to determine the location and severity of damage [5].

This paper presents an SHM methodology applied to an industrial steel tower structure. In particular, the paper describes the application of an innovative ML approach to the continuous monitoring stage of the structure, which is able to distinguish influences on signals driven by operational, as well as changes in environmental conditions. This aspect is particularly relevant in such industrial structures, as they contain a large amount of mechanical equipment that operates at irregular schedules. A case study is used to validate the methodology, using vibration measurements to assess the integrity of the structure over time.

2 Methodology

The methodology applied in the present work to monitor industrial steel tower structures follows the flowchart presented in Fig. 1. The first steps relate to the installation procedure of the SHM system. Then, the system is implemented for long-term continuous monitoring.

In the installation process, a survey of structural and equipment elements is firstly conducted. This is based on the project documentation and outcomes of software for production control and management of structures, from which it is possible to obtain the real mechanical properties from laboratory test certificates of the raw material. Then, a computational modeling of the structural behavior is performed. After some in situ vibration measurements, the computer model is recalibrated. Finally, with complete knowledge of the structure, the sensor network is designed and installed.

The monitoring stage begins with the collection of data, made from two main sources: momentary long-term monitoring; and vibration events. The system is configured to automatically perform measurements on a fixed schedule, according to data triggers such as threshold exceedances. The sensors used are mainly composed of tri-axial accelerometers, inclinometers, strain gauges, as well as temperature, humidity, and other weather-related sensors. After the raw data is collected, it is processed, with data cleansing and computations. In addition, there is a signal

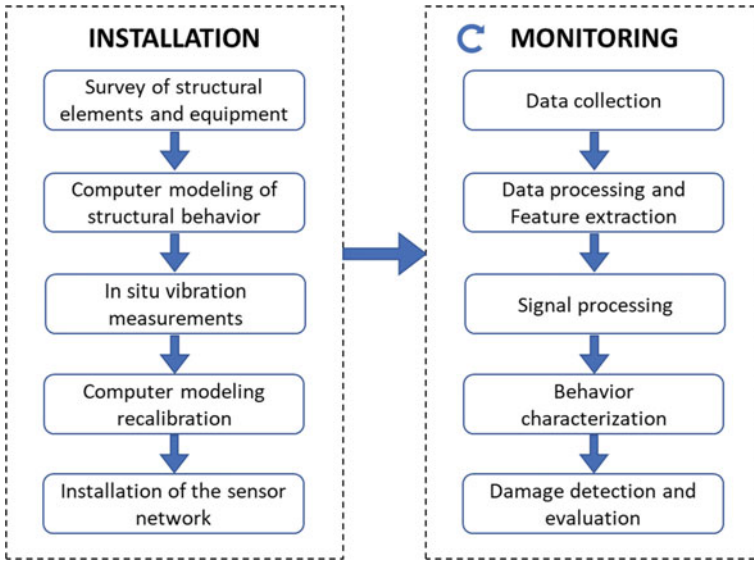


Fig. 1 Flowchart of the proposed methodology for SHM

processing procedure, where transformation of vibration signal to its equivalent frequency domain occurs, using the fast Fourier transform. This includes evaluating the frequency response, with natural frequencies determined through a peak picking procedure [6].

The subsequent step is to make a characterization of the structure behavior, using all the pertinent data. This is done through an ML algorithm, inspired by an unsupervised k-means clustering technique, followed by an assignment technique to appropriately allocate a classification label for the unlabeled data. The behavior characterization algorithm is executed regularly to classify the data and allow the update of the structural integrity evaluation. The variables used as input to the algorithm refer to all accelerations, strains and wind, for different sensor channels and for all vibration events. The algorithm can accurately classify each event registered by the monitoring system.

In the final step, the study is directed to a time-series analysis of the structural behavior in each type of event. In particular, the variability of eigenfrequencies when the structure is classified as stationary, without vibrations induced by operations, is compared with historical baseline values. When potential damage is identified, structural computer modeling from the installation stage can be used and updated to assist in the evaluation of the location and severity of the damage. Afterwards, repair and maintenance procedures can be planned and performed with confidence.

All the steps of the monitoring stage represented in Fig. 1 are made automatically. Data are transferred and contained in a secure cloud storage, and can be accessed by system administrators, while visualized in a web-based platform. To this end, a dashboard app is made available to the owners and defined users of the structure. This

web-app can be accessed through any browser, showing near real-time data about the structure, as well as its behavior characterization. In addition, an alert system sends direct warnings via SMS and email when severe actions on the structure are identified.

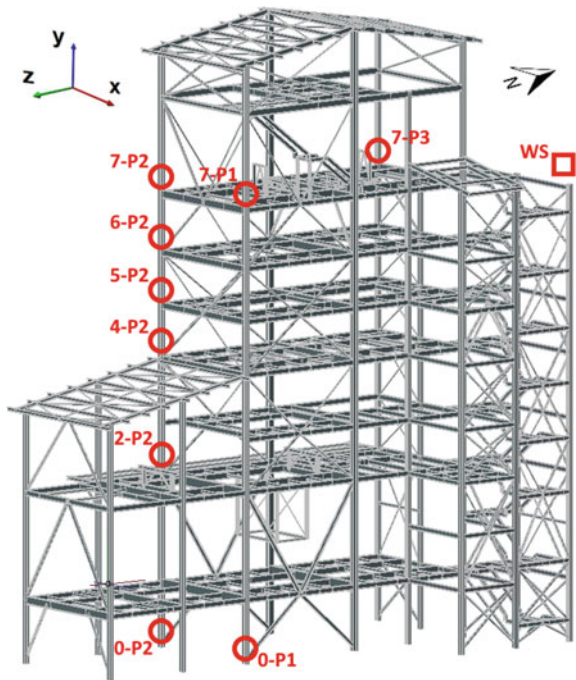
3 Case Study

The case study refers to a steel tower structure, 28 m high, located in the District of Coimbra, in Portugal (see Fig. 2). The steel structure is used for industrial purposes and includes several mechanical equipment operating at varying schedules. The vibration induced during its activity influences the structural behavior and might contribute to issues such as fatigue and loss of connection stiffness.

3.1 Installation

Structural Analysis. The preliminary stage was the analysis of the structure. After the first study and analysis of the structural documentation, and the consequent

Fig. 2 Industrial steel tower structure and sensor's main locations



development of a computer modeling of the structure and its structural behavior, a set of in situ vibrations measurements was carried out.

The measurements were performed with accelerometers, aimed at using the vibration signal obtained to determine the natural frequencies of the structure. To this end, tri-axial accelerometers were used, and piezoelectric accelerometers allowed to validate the quality of the solution. With the obtained data was also possible to analyze natural frequencies and the structural modes of vibration.

In situ measurements lead to a recalibration of the computer modeling of the structure. In this step, an additional external sound barrier wall made of sandwich panels was included, which had been inserted in one of the facades of the structure since the first computer modeling. The results showed similar vibration modes, with the natural frequencies differing less than 0.2 Hz. The computer modeling also allowed the knowledge of the structure and the locations with higher stress, assisting in the decision of the sensor network design.

Installation of the sensor network. The implemented SHM was optimized for the structure in order to provide meaningful and insightful data for the analysis of structural behavior.

The system consists of a wired network of 9 main locations, all including tri-axial accelerometers, temperature, and relative humidity sensors. The bottom 2 locations also include strain gauges. In addition, there is a weather station for environmental data, and a gateway to manage system data and send it through an LTE network. Figure 2 shows the industrial steel tower structure with the approximate location of the different sensors, gateway, and weather station.

3.2 Monitoring

Data collection is processed continuously on the administration servers. The transformed data is allocated on a specialized cloud server, including some statistical parameters and signal processing results. An ML algorithm based on k-means clustering runs regularly to classify the data and update the evaluation of structural integrity.

The output data can be visualized in a web-app. A concise report is delivered monthly to the client. When some thresholds exceed certain limits or the data is identified as dangerous events, the client receives alerts by SMS and email. Following are shown some examples of the outputs of this installation.

Long-term monitoring. This type of data is collected momentarily, at regular intervals of 5 min, with the aim of evaluating both actions and structural responses over time. In the steel structure of this case study, the data collected consists of weather data and strains (see Fig. 3).

Events. This mainly consists of vibration data collected at regular intervals of 30 min and in the case of threshold exceedances. The thresholds are updated dynamically,

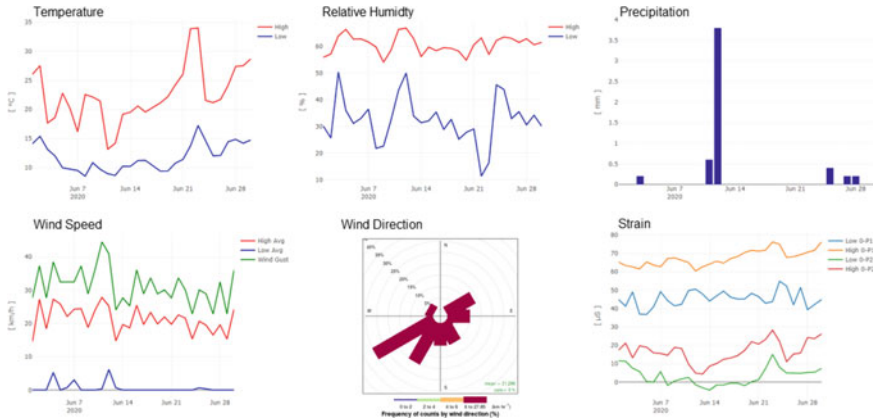


Fig. 3 Sample data from long-term monitoring of the structure under study

either increasing or decreasing to pre-set values automatically by the system, avoiding onerous and redundant measurements.

During the collection of vibration data, weather data and strain data are also collected, to evaluate actions on the structure and its structural response. The sampling frequency used in the vibration acquisitions is 100 Hz, with a duration of 20 s.

In Fig. 4 is shown an example of an event occurred after a threshold of strong wind. During this event, the wind speed was around 60 km/h, with a NE direction.

Frequencies analysis. The spectral analysis of the vibration signals is made for all vibration events through a peak picking procedure in the Fourier transform of the recorded signals. Together with the classification made through the ML algorithm, it is possible to analyze the natural frequencies of the structure, that is, when it is not affected by the operation of the industrial mechanical equipment. Figure 5a shows the Fourier transform of the x-axis direction in the sensors at the top of the structure. Natural frequencies have been analyzed since the beginning of the structural monitoring. A time series analysis has not shown any significant variability (see

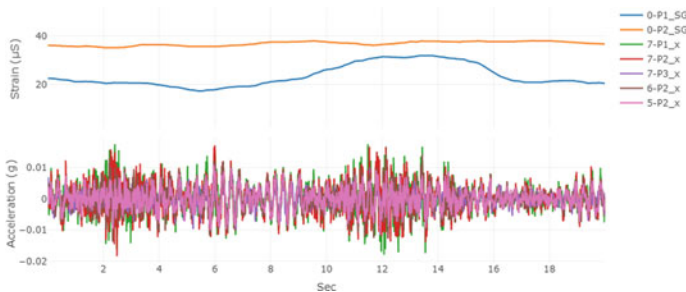


Fig. 4 Accelerations and strains during a vibration event of strong wind

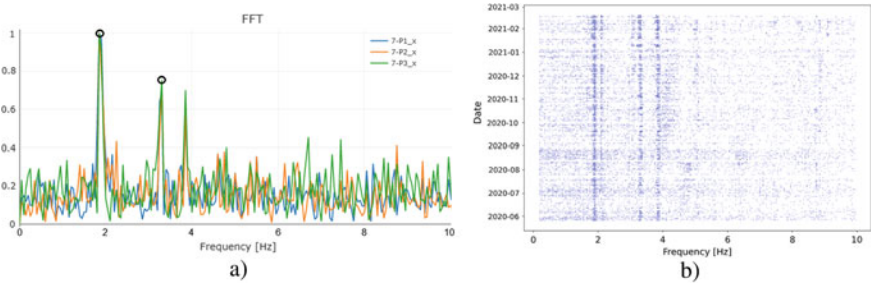


Fig. 5 Frequencies for 7-P1, 7-P2 and 7-P3 sensors, at x-axis direction **a** frequency spectrum during an event; **b** natural Frequencies observed during the monitoring period

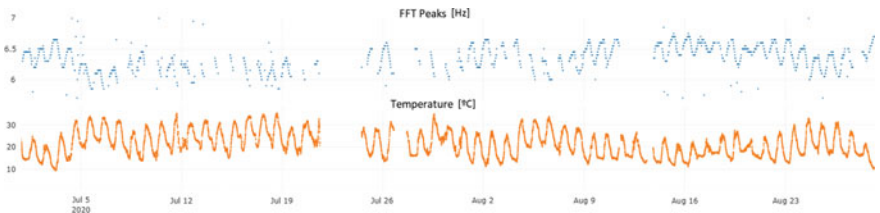


Fig. 6 Relation between frequency and temperature for 7-P1 sensor, at z-axis direction

Fig. 5b). The same approach was used in different positions and directions of the accelerometers. The results remain similar, except for the lowest floor, sensors 0-P1 and 0-P2, where the peaks couldn't be identified.

The temperature effect on structural vibration can be observed in some locations. Figure 6 shows the relation between a natural frequency of the structure and the temperature variation. As expected, the frequency increases for lower temperatures, and vice versa. This variation is observed with the daily oscillation, but also in the long-term.

4 Conclusion

This work presents a structural health monitoring methodology applied to an industrial steel tower structure. The approach was successfully implemented in the installation and monitoring system, showing the structural behavior in different situations, while classifying the events occurring in the structure.

The proposed approach is also able to provide a real-time feedback on structural integrity. As the ML algorithm used is applied for every new event and more historical data and information is known about the classification of events, potential damage to the structure is more securely identified. To this end, the effects of varying temperatures on structural vibration properties have been identified and should be further

explored. To improve the ML accuracy, including the ability to identify the type and severity of damage, further experiments will be conducted, including laboratorial simulations of damage in similar structures.

Acknowledgements The authors are grateful for the support received from the Portugal 2020, through the program “Projetos de I&D—Projetos Individuais” 34/SI/2018, co-financed by the European Fund FEDER.

References

1. Kong X, Cai CS, Hu J (2017) The state-of-the-art on framework of vibration-based structural damage identification for decision making. *Appl Sci* 7(5):497
2. Mitra M, Gopalakrishnan S (2016) Guided wave based structural health monitoring: a review. *Smart Mater Struct* 25(5):
3. Dong CZ, Catbas FN (2020) A review of computer vision-based structural health monitoring at local and global levels. *Struct Health Monit*, in press
4. Khoa NLD, Alamdari MM, Rakotoarivelo T, Anaissi A, Wang Y (2018) Structural health monitoring using machine learning techniques and domain knowledge based features. In: *Human and machine learning*. Springer, Cham, pp 409–435
5. Kurian B, Liyanapathirana R (2020) Machine learning techniques for structural health monitoring. In: *Proceedings of the 13th international conference on damage assessment of structures*. Springer, Singapore, pp 3–24
6. Bendat JS, Piersol AG (2011) *Random data: analysis and measurement procedures*, vol 729. Wiley

Two-Dimensional Deflection Maps by Using Fiber Bragg Grating Sensors



Pasquale Di Palma, Massimo Della Pietra, Vincenzo Canale,
Mariagrazia Alviggi, Agostino Iadicicco, and Stefania Campopiano

Abstract In this work, a novel technique to estimate the deflection of a bi-dimensional structure by means of fiber Bragg gratings (FBGs) is proposed. FBGs are embedded in monitored structure, avoiding the complex wiring typical of strain gauges, and provide local strain measurements. Then, by classical beam theory, from the strain maps measured by the FBGs, the two-dimensional deflection map of the monitored structure is numerically provided. The proposed method allows to overcome the difficulties existing in the direct measurement of the deflection: many types of structures (small and large) can be monitored in real-time thanks to this technique by using appropriate design parameters. In particular, this method can be useful in the structural monitoring of civil infrastructures and composite materials for aeronautics.

Keywords Deflection monitoring · Optical fibers · Optical sensors · Fiber bragg grating · Strain measurement · Structural monitoring

1 Introduction

Structural health monitoring of structures or objects have gained, in the last decades, huge interest in damage detection, real-time shape control and modification, for application fields ranging from robotics [1, 2] to civil infrastructures [3] and aerospace [4]. Shape monitoring, providing real-time information useful for diagnosing the structures, is very important both in the design and test phase and during the functioning of the objects.

One of the more important technology used in sensing solutions for the structural monitoring, as shows the scientific literature, is the fiber optic technology, in particular fiber Bragg gratings (FBGs), due to its unique advantages of lightweight, high

P. Di Palma · A. Iadicicco · S. Campopiano (✉)
Department of Engineering, University of Naples “Parthenope”, Centro Direzionale Isola C4,
80143 Naples, Italy
e-mail: stefania.campopiano@uniparthenope.it

M. D. Pietra · V. Canale · M. Alviggi
Physics Department, University of Naples, “Federico II” and I.N.F.N. Naples, Complesso
Universitario Monte S. Angelo, 80126 Naples, Italy

© The Author(s), under exclusive license to Springer Nature Switzerland AG 2021
C. Rainieri et al. (eds.), *Civil Structural Health Monitoring*, Lecture Notes in Civil
Engineering 156, https://doi.org/10.1007/978-3-030-74258-4_33

sensitivity, compactness, chemical stability, electromagnetic interference immunity, strong stability, wavelength division multiplexibility, wavelength encoded data, easy installation of the devices and so on [5, 6].

In the following sections we present an innovative process to embed bare FBGs giving protection to the fragile areas of the fiber optic sensors, and a method for the deflection estimation of a bi-dimensional structure, extending the one-dimensional approach based on the classical beam theory, previously demonstrated for a beam structure. Finally, the experimental results and the procedure validation by comparison with a reference instrument are described.

2 FBG in Strain Measurements

2.1 FBG Working Principle

A fiber Bragg grating is an intrinsic sensor consisting in a periodic refractive index modulation of the core of an optical fiber. This modulation induces the formation of a narrow peak in the reflected spectrum of the device, centered on a specific wavelength value called Bragg wavelength, with a bandwidth that decreases and reflectance that increases as the physical length of the grating increases. The Bragg wavelength λ_B depends on the effective refractive index of the fiber core n_{eff} and on the perturbation period Λ according to the following equation [7, 8]:

$$\lambda_B = 2n_{eff}\Lambda \quad (1)$$

Bragg wavelength changes when temperature T or/and strain ε change because both the effective refractive index n_{eff} and the perturbation period L are function of these two physical quantities. The dependence of the Bragg resonant peak on temperature and strain can be evaluated computing the differential of Eq. (1), according to the following equation:

$$\Delta\lambda_B = \frac{\partial\lambda_B}{\partial T}\Delta T + \frac{\partial\lambda_B}{\partial\varepsilon}\Delta\varepsilon \quad (2)$$

After some mathematical passage, and defining the photo-elastic coefficient as $p_e = \frac{1}{2}n_{eff}^2[p_{12} - \sigma(p_{11} + p_{12})]$, where p_{11} and p_{12} are the Pockels' coefficients and σ is the Poisson ratio, the thermo-optic coefficient $\xi = \frac{1}{n_{eff}}\frac{\partial n_{eff}}{\partial T}$ and the thermal expansion coefficient of the grating $\alpha = \frac{1}{\Lambda}\frac{\partial\Lambda}{\partial T}$ we obtain:

$$\frac{\Delta\lambda_B}{\lambda_B} = (\xi + \alpha)\Delta T + (1 - p_e)\Delta\varepsilon \quad (3)$$

where, introducing the temperature and strain sensitivity coefficients S_T and S_ϵ , it is possible to rewrite once again the Eq. (3) as follows:

$$\frac{\Delta\lambda_B}{\lambda_B} = S_T \Delta T + S_\epsilon \Delta\epsilon \tag{4}$$

with $S_T = \xi + \alpha$ and $S_\epsilon = 1 - p_e$.

2.2 Embedded FBGs

In many cases, especially when it is not possible to build in the FBGs in the monitored structure, it can be very useful to embed FBGs in plastic patches to protect the delicate region of the optical fiber without the coating and, consequently, increase the handling [9]. The plastic patch has the function of strengthening the FBG and the planar-like shape allows to increase the gluing surface improving the strain transfer from the monitored sample.

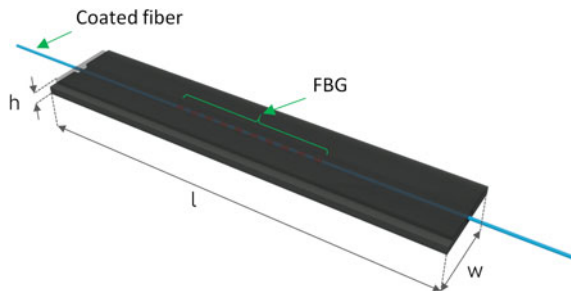
Thus, in this section some results, obtained on two different plastic patches embedding FBGs, are reported. The devices have been manufactured by a 3D printer in two different materials: polylactic acid (PLA), acrylonitrile butadiene styrene (ABS).

The selected patch size, showed in Fig. 1, is $l \times w \times h = 25 \text{ mm} \times 5 \text{ mm} \times 1 \text{ mm}$ to correctly incorporates a bare FBG 10 mm long.

The embedded FBGs were subjected to temperature and strain characterizations with the aim to investigate the thermal sensitivity and to verify the possibility to use efficiently these patches as strain and deformation sensors.

A linear behavior in temperature and a good reversibility were obtained in both embedded FBGs, as reported in Fig. 2a, b for the PLA and ABS patches respectively, while the temperature sensitivities of $107.6 \text{ pm}/^\circ\text{C}$ and $94.5 \text{ pm}/^\circ\text{C}$ are calculated for the two devices. These values are about ten time greater than the sensitivity of the bare FGB (about $10 \text{ pm}/^\circ\text{C}$) according to the thermal expansion coefficients of the plastic materials of which the patches are made (around $80 \text{ }\mu\text{m}/(\text{m}\cdot^\circ\text{C})$ for the PLA, around $70 \text{ }\mu\text{m}/(\text{m}\cdot^\circ\text{C})$ for the ABS and $6 \text{ }\mu\text{m}/(\text{m}\cdot^\circ\text{C})$ for the silica).

Fig. 1 Schematic view of the proposed device



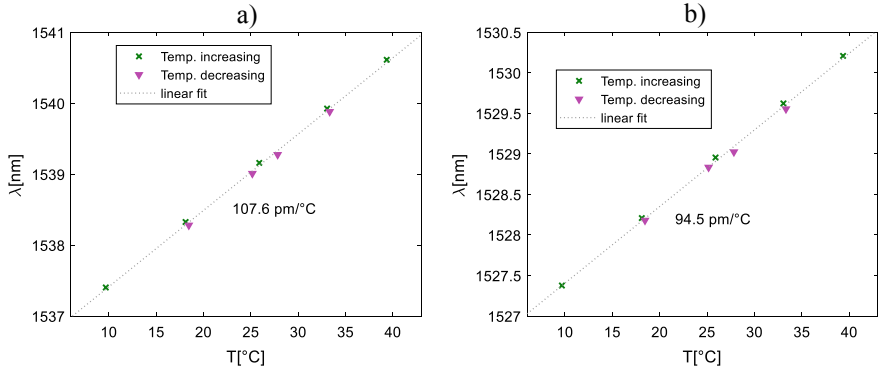


Fig. 2 Thermal characterization results for: **a** PLA patch and **b** ABS patch

To carry out the strain test, a metallic bar was placed onto two metallic supports and subjected to flexural load, as represented in Fig. 3a. Two bare FBGs, used as a reference, were bonded on the bar together with the two embedded ones by means of a cyanoacrylate adhesive at the same longitudinal coordinate and the sensorized structure was loaded. All the sensors are fixed on the same side excluding a bare FBG, named Bare 2 in the figure, used to determine the neutral axis position.

In Fig. 3b, according to their position, it is possible to observe the opposite trend of Bare 2 with respect to the others. In the first part of the test, the FBGs named PLA, ABS and Bare 1 are on the bottom of the bar, then measure an expansion, while Bare 2, on the upper side, correctly record a compression when the bare is loaded. In the second part of the test (time = 2090 s), the bar was rotated and, obviously, an inverted behavior was observed.

According to the beam theory, in a bent beam, the strain in the longitudinal axis is proportional to the distance of the sensor from the neutral axis, consequently, the strain values measured by the FBGs, the bare and the embedded ones, depend

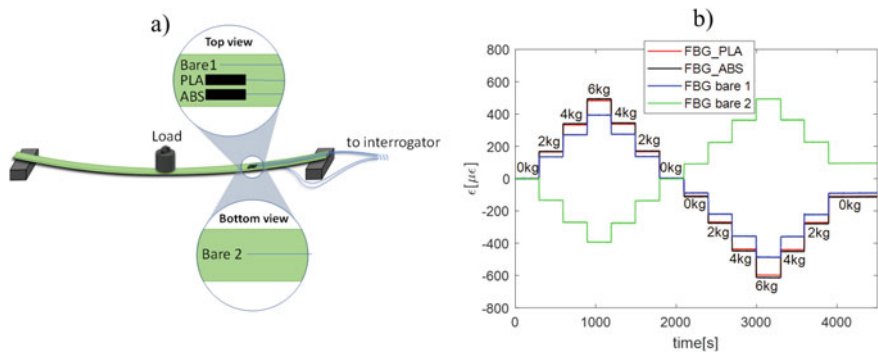


Fig. 3 **a** Schematic of the strain characterization setup with the FBG positions at the end of the test, **b** strain trends of the FBG sensors on the metallic bar

on their distance from the bar surface, and do not depend on the plastic materials used to embed the sensors, as demonstrated by the excellent overlap between the strain trends of the two embedded FBGs. Moreover, influencing the distance from the neutral axis, the plastic patch acts as gaining factor on the wavelength shift of the FBG sensor.

3 Bi-dimensional Deflection Map

To estimate the deflection of a structure from the measured strain, the classical beam theory with small deformation assumption is used. From the latter we know that there is a second derivative relationship between the displacement orthogonal to the surface and the strain component parallel to it. In the case of one-dimensional structure, the surface strain component along the longitudinal direction is linked to the vertical deflection $\omega(x)$ as follows

$$\varepsilon_x(x) = -d \frac{\partial^2 \omega(x)}{\partial x^2} \quad (5)$$

according to [10]. From Eq. (5), by integrating twice, the vertical deflection can be expressed according to the following equation:

$$\omega(x) = -\frac{1}{d} \iint \varepsilon_x(x) dx \quad (6)$$

where d represents the position of the neutral axis and is calculable by means of strain sensors on the opposite surface of the structure.

Using strain profiles along more than one line of the monitored structure, it is possible to extend the one-dimensional approach to a two-dimensional structure. With a polynomial expansion of the strain profiles we can achieve a continuous distribution [10, 11], and then, with a polynomial regression, the coefficients of a polynomial that fits the data, minimizing the differences between the measured strain values and the fitting function in the least-square sense, can be found. In this way, when the selected order for the polynomial is equal to $n-1$ (where n is the number of strain sensors along the line) the fitting function assumes, at the sensors coordinates, the same values recorded by the sensors. Then, the deflection functions along the different lines in the polynomial form are calculated directly from the strain polynomial coefficients [12]. By means of a final polynomial fitting in two variables, with effective boundary conditions, the bi-dimensional deflection map is computed.

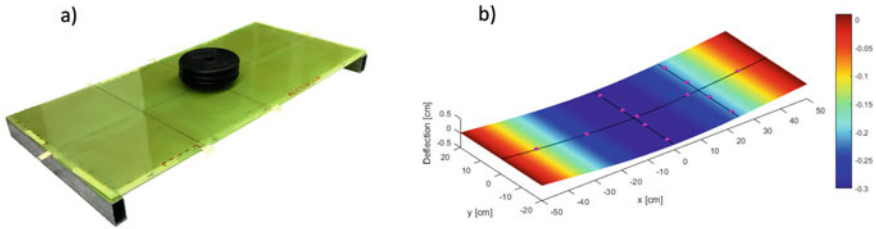


Fig. 4 **a** Photo of the loaded multilayer panel; **b** deflection map of the multilayer panel with a load of 6 kg

3.1 Experimental Results

This bi-dimensional deflection monitoring technique has been tested in a rectangular multilayer panel, showed in Fig. 4, with $100\text{ cm} \times 40\text{ cm} \times 0.95\text{ cm}$ in size, formed by aluminum honeycomb bonded between two epoxy glass layers. This panel has been sensorized with 13 commercial FBGs 10 mm long distributed along three straight lines on a side (two line parallel to y-axis, one along the x-axis), one on the other side useful for the neutral axis estimation and another strain free for the thermal compensation.

The structure has been subjected to bending load and the deflection maps has been obtained for the different loads applied. In Fig. 4b, the deflection map of the panel loaded with 6 kg (maximum applied load) is reported. The position of the FBGs strain sensors has been indicated with pink dots. As showed, the maximum deflection values of the panel is about -0.31 cm in the center, while the deflection values decrease toward the edges.

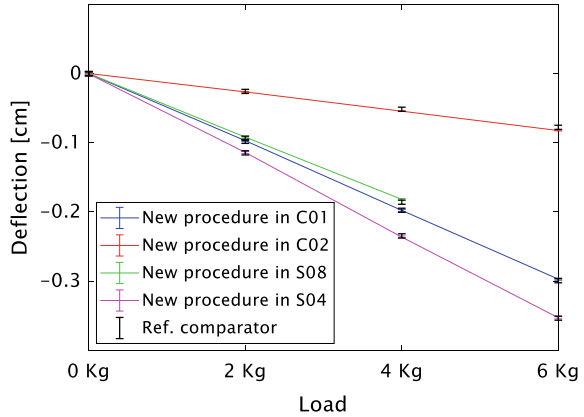
To validate our procedure, the deflection obtained indirectly with the FBGs have been compared with those provided by a mechanical comparator (Mitutoyo ID-C125XB) in four points: C01 [$x = -10\text{ cm}$, $y = 10\text{ cm}$], C02 [$x = -40\text{ cm}$, $y = 10\text{ cm}$], S08 [$x = -7.9\text{ cm}$, $y = 0\text{ cm}$] and S04 [$x = 0\text{ cm}$, $y = 16.4\text{ cm}$].

The result of this comparison is reported in Fig. 5, which shows a very good agreement between the two measurement methods and a resolution of few tens of microns was reached.

4 Conclusions

In this work we discussed on an innovative bi-dimensional deflection estimation method, extending a one-dimensional technique based on the classical beam theory. To perform the experiment test, a large multilayer panel has been equipped with an appropriate number of FBGs located along three straight lines, using only few optical fibers to avoid the complex wiring typical of electrical strain. Starting from the one-dimensional strain profiles, the deflection on the straight lines have been

Fig. 5 Deflection in four points of the tested structure in comparison with the one directly measured with a mechanical comparator with increasing load located in the center



evaluated with polynomial calculations and, by means of a bi-dimensional fitting, the deflection maps on the whole structure have been estimated.

To validate the method the deflection indirectly measured by the FBGs has been compared with that directly measured by a mechanical comparator. The results of the tests show a very good agreement between the two measurements, and a very good resolution (tens of microns) over a surface of about 1 m² has been reached.

In conclusion, we have demonstrated that the proposed technique allows an effective real-time indirect structural monitoring solving the existing difficulties in measuring the deflection directly. Moreover, although in this work the strain values have originated by bare FBGs incorporated in the multilayer panel during its manufacturing, the FBGs embedded in 3D printed patches can be also used efficiently for non-sensorized objects in production.

References

1. Kramer RK, Majidi C, Sahai R, Wood RJ (2011) Soft curvature sensors for joint angle proprioception. In 2011 IEEE/RSJ international conference on intelligent robots and systems. San Francisco, pp 1919–1926
2. Koivikko A, Raei ES, Mosallaei M, Mäntysalo M, Sariola V (2018) Screen-printed curvature sensors for soft robots. *IEEE Sens J* 18(1):223–230
3. Palumbo G et al (2019) Fiber bragg grating sensors for real time monitoring of early age curing and shrinkage of different metakaolin-based inorganic binders. *IEEE Sens J* 19(15):6173–6180
4. Derkevorkian A, Masri SF, Alvarenga J, Boussalis H, Bakalyar J, Richards WL (2013) Strain-based deformation shape-estimation algorithm for control and monitoring applications. *AIAA J* 51(9):2231–2240
5. Majumder M, Gangopadhyay TK, Chakraborty AK, Dasgupta K, Bhattacharya DK (2008) Fibre Bragg gratings in structural health monitoring—present status and applications. *Sens Actuators A Phys* 147(1):150–164
6. Li H-N, Li D-S, Song G-B (2004) Recent applications of fiber optic sensors to health monitoring in civil engineering. *Eng Struct* 26(11):1647–1657
7. Kashyap R (2010) Fiber Bragg gratings

8. Hill KO, Meltz G (1997) Fiber Bragg grating technology fundamentals and overview. *J Light Technol* 15(8):1263–1276
9. Palma PD, Iadicicco A, Campopiano S (2020) Study of Fiber Bragg gratings embedded in 3D-printed patches for deformation monitoring. *IEEE Sens J* 20(22):13379–13386
10. Di Palma P et al (2019) Deflection monitoring of bi-dimensional structures by fiber bragg gratings strain sensors. *IEEE Sens J* 19(11):4084–4092
11. Laflamme S et al (2013) Soft elastomeric capacitor network for strain sensing over large surfaces. *IEEE/ASME Trans Mechatron* 18(6):1647–1654
12. Di Palma P et al (2019) Fiber Bragg gratings strain sensors for deflection estimation of a two-dimensional structure. In: *Optical sensors 2019*. SPIE, Limassol, p 88

Bayesian Model Updating and Parameter Uncertainty Analysis of a Damaged Fortress Through Dynamic Experimental Data



Federico Ponsi , Elisa Bassoli , and Loris Vincenzi 

Abstract A probabilistic analysis for the uncertainty evaluation of model parameters is of great relevance when dealing with structural damage assessment. Indeed, the identification of the damage severity associated to its uncertainty can support the decision-maker to close a bridge or a building for safety reasons. In this paper the results of the model updating of an historical masonry fortress damaged by the seismic event that hits the town of San Felice sul Panaro and the surrounding localities in the Po Valley in the 2012 are presented. A standard and a Bayesian updating procedures are first applied to the calibration of the complex Finite Element (FE) model of the fortress with respect to experimental modal data. The uncertainty of the identified parameters of structural system is then obtained by using the Bayesian probabilistic approach. The most probable parameter vector is obtained by maximizing the posterior probability density function. The robustness and the efficiency of the procedure are evaluated through the comparison with the results obtained from the estimation of the Pareto-optimal solutions.

Keywords Aging structure · Bayesian model updating · Multi-objective optimization.

1 Introduction

Vibration-based structural monitoring methods have been widely used in recent years for the evaluation of the dynamic performance and damage assessment of a wide scenario of civil structures [1–4]. They represent powerful tools in the civil engineering field because they are able to provide real-time information on the structural

F. Ponsi (✉) · E. Bassoli · L. Vincenzi
University of Modena and Reggio Emilia, Modena, Italy
e-mail: federico.ponsi@unimore.it

E. Bassoli
e-mail: elisa.bassoli@unimore.it

L. Vincenzi
e-mail: loris.vincenzi@unimore.it

© The Author(s), under exclusive license to Springer Nature Switzerland AG 2021
C. Rainieri et al. (eds.), *Civil Structural Health Monitoring*, Lecture Notes in Civil Engineering 156, https://doi.org/10.1007/978-3-030-74258-4_34

health state during the structural life or after a catastrophic event (e.g. earthquake, hurricane). In particular, as regards damage identification purposes, these methods are well suited since damage induces a reduction of the stiffness of the structure and, consequently, a modification of its modal properties. Data-driven and model-based methods are different approaches to damage identification problem that have been largely studied and applied in literature. Data-driven methods are based on the extraction of damage-sensitive features from the experimental response recorded on the structure: the modification of these features is used to detect damage [5]. As concerns model-based methods, damage identification is performed by detecting the reduction of the value of some stiffness parameters among different states of a numerical model describing the structure [6]. Although model-based methods are computationally expensive compared to data-driven methods, they are preferred when localization and quantification of damage is further needed [7]. Every state of the model is calibrated on the basis of modal properties experimentally determined, in order to reproduce experimental data as well as possible. For this reason, model updating techniques have to be employed to determine the value of a set of structural parameters that reduces the discrepancy between model predictions and measured data [8].

Model updating methods based on several optimization techniques have been extensively applied in literature. A typical solution involves the use of evolutionary or genetic algorithms because they are designed for large-scale problems and to avoid local minima [9]. The main drawback of these kind of algorithms, namely the high number of evaluations needed to reach convergence, has been handled introducing a surrogate to approximate the objective function [10, 11]. Moreover, evolutionary algorithms are frequently employed for the identification of multiple alternatives in FE model updating solving a multi-objective optimization problem [12–14]. Objectives are usually defined as discrepancy functions with reference to natural frequencies and mode shapes. The set of optimal parameter vectors, represented in the space of the objectives, is called Pareto front.

It happens very frequently that modal properties derived by a long term monitoring exhibit significant variations. Main reasons of this behaviour are measurements noise, estimation errors or the modification of environmental condition that influences modal properties. Moreover, accuracy of deterministic model updating is affected by model errors and simplifications. Consequently, reliability of results can be highly compromised. Therefore, incorporating uncertainties in the updating process allows to handle the unavoidable variability of calibrated parameters caused by the previous factors.

In a probabilistic context, parameters of calibration and prediction errors are considered as random variables. Bayesian model updating enables to compute uncertainties of parameters combining information based on prior distributions and experimental data [15, 16]. Moreover, several data sets can be integrated in the process in order to reduce uncertainties related to measurement errors and noise. In this framework, damage detection can be carried out in a probabilistic way by evaluating the probability of exceeding a given damage threshold [17].

This paper presents a comparison between a deterministic model updating method that uses a surrogate-assisted evolutionary algorithm [18] to solve multi-objective optimization problem and a probabilistic method based on Bayes’ theorem. Discussion is first focused on a simple case study, namely a two floor frame. Three different prior distributions and two different likelihood functions are employed for the Bayesian model updating to study their influence on the results for a problem where enough data are available related to the complexity of the model. These solutions are then compared with the set that forms the Pareto front.

Finally, the same operation is performed on a more complex numerical model, representing the San Felice sul Panaro fortress. It is an historical masonry structure severely damaged by the seismic events occurred in 2012 in the Emilia-Romagna region (Italy). In this case, an uniform prior distribution and two different likelihood functions are used in Bayesian model updating. Focus is also addressed to standard deviation of calibrated parameters obtained with a single data set of measurements.

The paper is arranged as follows: in Sect. 2 bi-objective optimization for deterministic model updating is described and a criterion to select the preferred solution among the solutions of the Pareto front is presented; in Sect. 3 Bayesian model updating is described and the functions involved in the process are defined. Sections 4 and 5 present model updating results obtained with the different approaches for the simple case study and the finite element (FE) model of the San Felice sul Panaro fortress, respectively. Finally, conclusions are drawn in Sect. 6.

2 Bi-objective Optimization for Model Updating

FE model updating based on vibration measurements is performed simultaneously minimizing two objectives expressing the discrepancy between experimentally identified and numerically simulated modal properties:

$$\begin{cases} \min\{e_F(\mathbf{x}), e_M(\mathbf{x})\} \\ \mathbf{x} \in \mathbf{S} \end{cases} \tag{1}$$

where \mathbf{x} is the $n \times 1$ vector containing the calibration parameters and $\mathbf{S} \subset \mathbf{R}^n$ denotes the set of feasible solutions in the decision space. The objectives e_F and e_M , called frequency and mode shape residuals, respectively, are defined as:

$$e_F = \sum_{m=1}^M \left(\frac{f_{num,m} - f_{exp,m}}{f_{exp,m}} \right)^2 \tag{2}$$

$$e_M = \sum_{m=1}^M \left[\frac{1 - \text{MAC}(\boldsymbol{\phi}_{num,m}, \boldsymbol{\phi}_{exp,m})}{\text{MAC}(\boldsymbol{\phi}_{num,m}, \boldsymbol{\phi}_{exp,m})} \right]^2 \tag{3}$$

where M is the number of modes selected for the optimization, $f_{exp,m}$ and $\phi_{exp,m}$ are the experimental frequency and mode shape of the m -th mode, $f_{num,m}$ and $\phi_{num,m}$ are the numerical frequency and mode shape of the m -th mode and MAC is the Modal Assurance Criterion [19]. In Eqs. (2) and (3) dependence of the objectives e_F and e_M on \mathbf{x} is omitted.

Real multi-objective optimization problems have multiple optimal solutions due to modelling and measurement errors: the set of feasible non-dominated solutions is named Pareto front. A generic solution \mathbf{x}_A is said to dominate the solution \mathbf{x}_B if the following conditions are observed:

$$\begin{cases} e_F(\mathbf{x}_A) \leq e_F(\mathbf{x}_B) \\ e_M(\mathbf{x}_A) \leq e_M(\mathbf{x}_B) \\ e_F(\mathbf{x}_A) < e_F(\mathbf{x}_B) \vee e_M(\mathbf{x}_A) < e_M(\mathbf{x}_B) \end{cases} \quad (4)$$

The bi-objective optimization problem can be reduced to a single-objective optimization problem by defining the objective function H as the weighted sum of e_F and e_M [20]:

$$H(\mathbf{x}) = \alpha e_F(\mathbf{x}) + (1 - \alpha) e_M(\mathbf{x}) \quad (5)$$

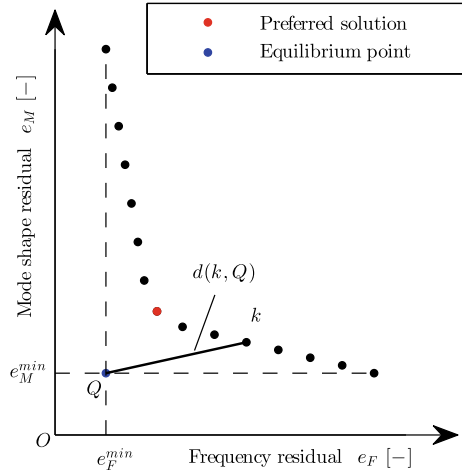
where $\alpha \in [0, 1]$ is the weighting factor that measures the relative importance between the objectives. The Pareto front can be generated by minimizing Eq. (5) using different values of α : depending on the value of the weighting factor the optimization procedure can lead to different results due to uncertainties that affect the measurements and the model. The minimization of the objective function H is carried out with a surrogate-assisted evolutionary algorithm proposed by one of the authors [18].

Once the Pareto front is computed, a preferred solution have to be selected among the set of non-dominated points of the front. This decision is based on additional and qualitative features, sometimes subjective or based on expertise of the operator. A selection criterion proposed by Dincer et al. [21] identifies the preferred solution as the closest one to the equilibrium point Q of the objective function space (see Fig. 1). This point is characterized by the minimum value of both objectives (e_F^{min} , e_M^{min}), so it does not belong to the Pareto front. Therefore, the point with the minimum distance from the equilibrium point ensures the best compromise between objectives e_F and e_M .

3 Bayesian Model Updating

The general principle of Bayesian model updating is to consider calibration parameters \mathbf{x} and prediction errors, that represent measurement and modelling uncertainties, as random variables. In particular, given a set of measured data \mathbf{d} , the prior prob-

Fig. 1 Criterion of minimum distance from the equilibrium point



ability distribution of the model parameters $p(\mathbf{x}|\mathcal{M})$ is updated into the posterior distribution $p(\mathbf{x}|\mathbf{d}, \mathcal{M})$ on the basis of the Bayes' theorem:

$$p(\mathbf{x}|\mathbf{d}, \mathcal{M}) = c^{-1} p(\mathbf{d}|\mathbf{x}, \mathcal{M}) p(\mathbf{x}|\mathcal{M}) \tag{6}$$

where c is the Bayesian evidence, a constant ensuring that the posterior distribution of parameters integrates to one, and it is computed as:

$$c = \int_{\mathbf{s}} p(\mathbf{d}|\mathbf{x}, \mathcal{M}) p(\mathbf{x}|\mathcal{M}) d\mathbf{x} \tag{7}$$

$p(\mathbf{d}|\mathbf{x}, \mathcal{M})$ is the likelihood function representing the probability that model \mathcal{M} parametrised by \mathbf{x} provides the measured data \mathbf{d} . It reflects the contribution of data in the determination of the updated posterior distribution of parameters. A very diffused choice to formulate the likelihood function is to define the error functions for a mode m as zero-mean Gaussian distributions [16, 22]:

$$e_{f_m} = f_{exp,m} - f_{num,m}(\mathbf{x}) \sim N(0, \sigma_{f_m}^2) \tag{8}$$

$$e_{\phi_m} = \phi_{exp,m} - l_m \phi_{num,m}(\mathbf{x}) \sim N(\mathbf{0}, \Sigma_{\phi_m}) \tag{9}$$

where l_m is a scaling factor computed as:

$$l_m = \frac{\phi_{exp,m}^T \phi_{num,m}(\mathbf{x})}{\|\phi_{exp,m}\| \|\phi_{num,m}(\mathbf{x})\|} \tag{10}$$

Under the assumption of statistical independence of identified modal properties, the likelihood function can be written as:

$$p(\mathbf{d}|\mathbf{x}, \mathcal{M}) = \prod_{m=1}^M N(f_{exp,m}, \sigma_{f_m}^2) N(\boldsymbol{\phi}_{exp,m}, \Sigma_{\boldsymbol{\phi}_m}) \quad (11)$$

where $N(f_{exp,m}, \sigma_{f_m}^2)$ is the Gaussian distribution with mean $f_{exp,m}$ and standard deviation σ_{f_m} and $N(\boldsymbol{\phi}_{exp,m}, \Sigma_{\boldsymbol{\phi}_m})$ is a multi-dimensional Gaussian distribution with mean vector $\boldsymbol{\phi}_{exp,m}$ and covariance matrix $\Sigma_{\boldsymbol{\phi}_m}$.

Qian and Zheng [23] employed another formulation for the likelihood function:

$$p(\mathbf{d}|\mathbf{x}, \mathcal{M}) = \frac{1}{(\sqrt{2\pi}\sigma)^{M(N_0+1)}} \exp\left(-\frac{J(\mathbf{x})}{2\sigma^2}\right) \quad (12)$$

where $J(\mathbf{x})$ is an overall discrepancy function, that combines frequency and mode shape residuals, σ is a shared standard deviation, that has to be calibrated in order to maximize posterior probability density of updated parameters, and N_0 is the number of measured mode shape components. Defining a normalizing factor β_m for mode shape m as:

$$\beta_m = \frac{\boldsymbol{\phi}_{exp,m}^T \boldsymbol{\phi}_{num,m}(\mathbf{x})}{\|\boldsymbol{\phi}_{num,m}(\mathbf{x})\|} \quad (13)$$

the discrepancy function can be expressed as:

$$J(\mathbf{x}) = \sum_{m=1}^M \left[\left(\frac{f_{num,m} - f_{exp,m}}{f_{exp,m}} \right)^2 + \frac{\|\beta_m \boldsymbol{\phi}_{num,m}(\mathbf{x}) - \boldsymbol{\phi}_{exp,m}\| N_0}{\|\boldsymbol{\phi}_{exp,m}\|^2} \right] \quad (14)$$

In practical applications, the computation of Bayesian evidence Eq.(7) and marginal posterior distributions, that requires multi-dimensional integration, is not usually a trivial task. For this reason, the updated distribution of parameters can be obtained analytically through asymptotic approximations [15] or numerically with a Markov Chain Monte Carlo (MCMC) algorithm [24, 25] or its derivatives [26, 27].

4 Case Study: Two Floor Frame

The first case study is a shear-type frame composed of two floors and one bay (Fig. 2). Axial deformation of all the elements is neglected, moreover beams are infinitely rigid in flexure. Distributed masses of the structure are represented as concentrated masses at the floor levels. In table 1, masses and stiffness, expressed as multiples of a reference stiffness $k_0=8000$ kN/m, of each floor are listed. The corresponding modal properties and the pseudo-experimental values, assumed as reference values in

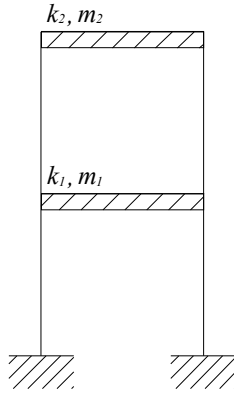


Fig. 2 Two floor frame: layout of the structure

Table 1 Two floor frame: mechanical parameters of the structure

Floor N.	1	2
Mass m [10^3 kg]	60.0	60.0
Stiffness multiplier r [-]	2.0	1.5
Stiffness k (kN/m)	16,000	12,000

the optimization process, are reported in Table 2. Pseudo-experimental properties are generated to account for errors that unavoidably affect real measurements. Parameters to identify are the factors that multiply the base stiffness k_0 to obtain the floor stiffness. They are denoted as r_1 and r_2 , where the subscript is related to the floor number. Both parameters are searched within the range [0.5;4].

4.1 Model Updating

This section presents results of model updating performed with the different approaches proposed in Sects. 2 and 3. In both cases the calibration is performed with reference to the pseudo-experimental modal properties listed in Table 2.

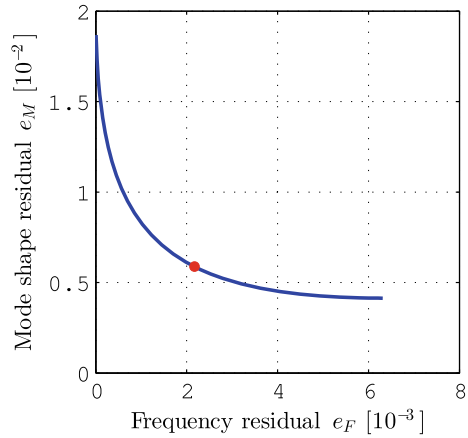
4.1.1 Deterministic Model Updating

The deterministic approach is based on the solution of a bi-objective optimization problem using the weighted-sum method, as described in Sect. 2. The Pareto front obtained is reported in Fig. 3 where the preferred solution, selected with the criterion of minimum distance from the equilibrium point, is shown in red. This solution

Table 2 Two floor frame: exact and pseudo-experimental modal properties. The first subscript of the mode shape component indicates the floor number while the second one is the mode number

Modal properties	Mode N.1			Mode N.2		
	f_1 (Hz)	ϕ_{11} [–]	ϕ_{21} [–]	f_2 (Hz)	ϕ_{12} [–]	ϕ_{22} [–]
Exact	1.535	0.535	1.000	3.812	1.000	–0.535
Pseudo-experimental	1.517	0.769	1.000	3.846	1.000	–0.633

Fig. 3 Two floor frame: Pareto front. Red dot: preferred solution



represents a compromise between objectives e_F and e_M , since it is located in the central part of the front. The weighting factor, calibration parameters and modal properties associated to the preferred solution are summed up in Table 3.

The variation of the updated parameter r_1 and r_2 with the weighting factor α is reported in Fig. 4a, b, respectively. Both parameters exhibit variations in the range [1.5;2], but associated to different trends: updated values of r_1 increase with α , while r_2 shows a decreasing trend.

Table 3 Two floor frame: weighting factor α , calibration parameters r_1, r_2 and modal properties of the preferred solution

α	r_1	r_2	Mode N.1			Mode N.2		
			f_1 (Hz)	ϕ_{11} [–]	ϕ_{21} [–]	f_2 (Hz)	ϕ_{12} [–]	ϕ_{22} [–]
[–]	[–]	[–]	1.465	0.657	1.000	3.969	–1.000	0.657

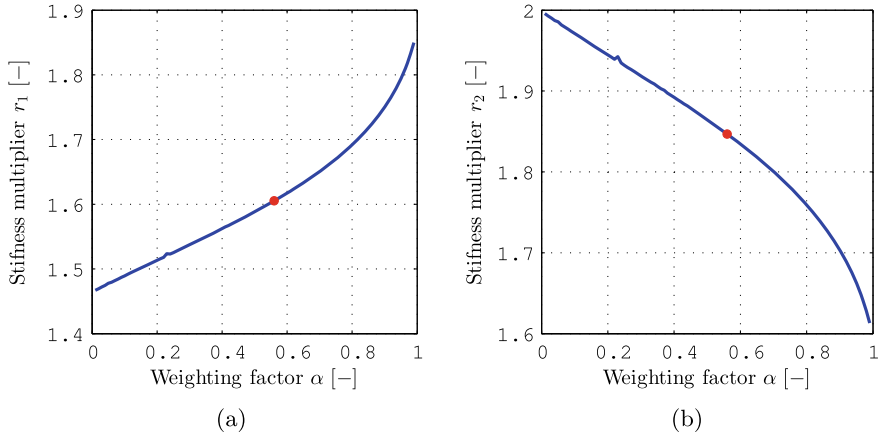


Fig. 4 Two floor frame: variation of the parameter, **a** r_1 and **b** r_2 with the weighting factor α . Red dot: value of the parameter for the preferred solution

4.1.2 Bayesian Model Updating

Bayesian model updating has been performed according to description made in Sect. 3. Six tests have been carried out using two different definitions of the likelihood function and three different prior distributions for parameters. Table 4 illustrates likelihood equation and parameters of the prior distribution used for each test. In the Table, a and b indicate the upper and lower bound of the uniform distribution, respectively, while μ and σ are the mean value and the standard deviation of the gaussian distribution. In all the tests, calibration parameters are considered as uncorrelated, hence the conjunct prior distribution can be expressed as the product of the marginal distributions. Due to the simplicity of the model and the limited number of the calibration parameters, Bayesian evidence Eq. (7) has been numerically evaluated on a very dense square grid (step size 0.005) built on the domain. Posterior distribution is then obtained according to Eq. (6).

Table 4 Two floor frame: description of the tests for Bayesian model updating

Test No.	Likelihood equation	Prior distribution	Parameters for r_1	Parameters for r_2
1	(11)	Uniform	$a=0.5 ; b=4.0$	$a=0.5 ; b=4.0$
2	(11)	Gaussian	$\mu=2.0 ; \sigma=0.4$	$\mu=1.5 ; \sigma=0.3$
3	(11)	Gaussian	$\mu=3.0 ; \sigma=0.6$	$\mu=1.0 ; \sigma=0.2$
4	(12)	Uniform	$a=0.5 ; b=4.0$	$a=0.5 ; b=4.0$
5	(12)	Gaussian	$\mu=2.0 ; \sigma=0.4$	$\mu=1.5 ; \sigma=0.3$
6	(12)	Gaussian	$\mu=3.0 ; \sigma=0.6$	$\mu=1.0 ; \sigma=0.2$

Table 5 Two floor frame: results of Bayesian model updating

Test N.	r_1		r_2	
	MAP	σ	MAP	σ
	[–]	[–]	[–]	[–]
1	1.825	0.069	1.635	0.060
2	1.835	0.068	1.625	0.059
3	1.885	0.078	1.570	0.061
4	1.920	0.075	1.555	0.061
5	1.920	0.109	1.555	0.088
6	1.865	0.107	1.480	0.081

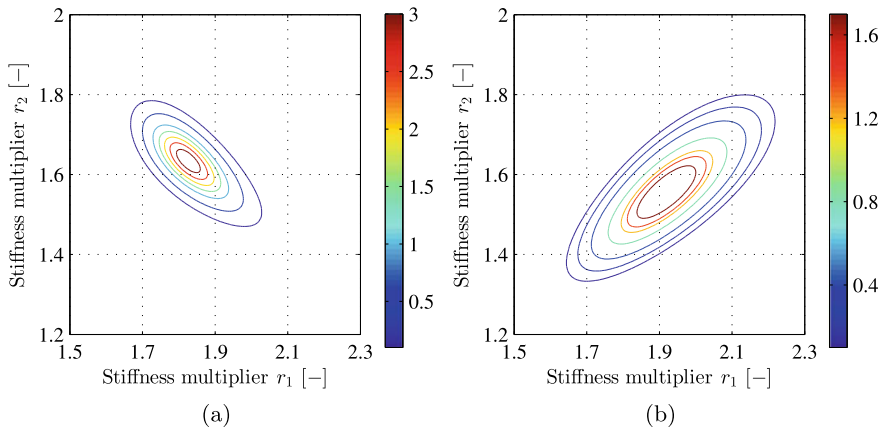


Fig. 5 Two floor frame: likelihood function employed for, **a** test N.1-N.2-N.3 scaled by a factor 10^{-4} and, **b** test N.4-N.5-N.6 scaled by a factor 10^{92}

Results of updating procedure are listed in Table 5. Maximum a posteriori (MAP) values obtained are very similar for all tests. This highlights how the prior information has a low importance for this simple problem: likelihood functions are very peaked and have a dominant numerical contribution in the updating process.

Standard deviations are very low for all tests, but if we compare tests characterized by the same prior distribution and different likelihood function, namely pairs N.1-N.4, N.2-N.5 and N.3-N.6, the lower uncertainty is obtained using Eq. (11). Indeed, the comparison between contour plot of the two likelihood functions used, performed in Fig. 5, shows how in the case of Eq. (11) the area of the domain with probability density different from zero is smaller than in the case of Eq. (12).

4.1.3 Comparison of Results

Table 6 presents results obtained by different approaches in terms of calibrated parameters, relative error ϵ for frequencies and MAC value for mode shapes. Relative error for the m -th frequency is computed as:

$$\epsilon = \frac{f_{num,m} - f_{exp,m}}{f_{exp,m}} \cdot 100 \tag{15}$$

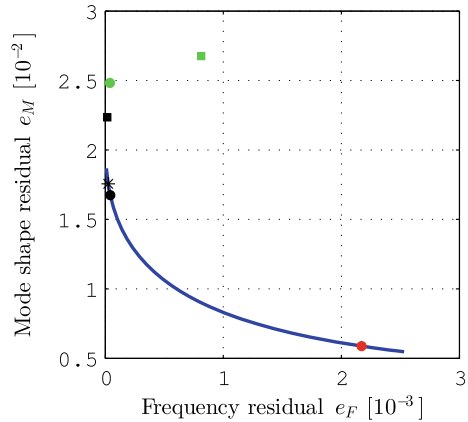
Results of Bayesian model updating for all tests described in Table 4 are characterized by smaller relative errors for frequencies compared to the preferred solution of the bi-objective optimization. On the contrary, a slightly higher correlation with the pseudo-experimental mode shapes is obtained with the deterministic updating rather than with the Bayesian model updating.

Figure 6 shows solutions obtained with Bayesian model updating in the objective space $e_F - e_M$, where objectives are defined by Eqs. (2) and (3): all the solutions are located in the part of the front characterized by values of α close to one. This highlights the predominant contribution of frequency residuals in the calibration procedure. In particular, solutions of test N.1 and N.2 are non-dominated by other solutions, hence they represent new points of the Pareto front that have not been obtained with the bi-objective optimization procedure described in Sect. 2. On the other hand, points corresponding to solutions of test N.3, N.4, N.5 and N.6 are dominated by points of the front. Note that the solutions of test N.4 and N.5 are the same as they present the same MAP value.

Table 6 Two floor frame: comparison among results of different methods

Method	r_1 [–]	r_2 [–]	Mode N.1		Mode N.2	
			ϵ (%)	MAC (%)	ϵ (%)	MAC (%)
Deterministic	1.605	1.847	–3.40	99.44	3.19	99.97
Bay. Test N.1	1.825	1.635	–0.46	98.46	0.46	99.89
Bay. Test N.2	1.835	1.625	–0.36	98.40	0.33	99.87
Bay. Test N.3	1.885	1.570	0.00	98.05	–0.41	99.76
Bay. Test N.4	1.920	1.555	0.46	97.87	–0.42	99.69
Bay. Test N.5	1.920	1.555	0.46	97.87	–0.42	99.69
Bay. Test N.6	1.865	1.480	–1.34	97.74	–2.52	99.64

Fig. 6 Two floor frame: solutions of Bayesian model updating in the objective space e_F - e_M . Red dot: preferred solution of bi-objective optimization. Black dot: solutions of test N.1. Black asterisk: solution of test N.2. Black square: solution of test N.3. Green dot: solution of test N.4 and N.5. Green square: solution of test N.6



5 The San Felice Sul Panaro Fortress

In this section, the FE model of the San Felice sul Panaro fortress (Modena, Italy) is updated according to the approaches described in Sects. 2 and 3. The fortress is an historical masonry structure whose configuration was subjected to several modifications during centuries. The main tower of the fortress is named “Mastio” due to its predominant dimension compared to the other four towers that are arranged in a quadrilateral plan (Fig. 7a). Several elements of the fortress has been damaged by the seismic sequence that affected the Emilia-Romagna region in May 2012: roofs of the minor towers collapsed and perimeter walls exhibited cracks of different extension. Relevant shear cracks arose also in the Mastio, moreover merlons and vaults of the main tower exhibited diffused damage. Due to these events, the municipality of San Felice sul Panaro planned the realization of some reinforcement operations in order to avoid further collapses. In particular, the diagonal cracks of the Mastio were filled with mortar and steel strands were introduced into the walls.

5.1 Ambient Vibration Test and FE Model of the Fortress

Dynamic behaviour of the Mastio has been characterized thanks to ambient vibration test performed in July 2016. The experimental tests and the identification of the modal properties are presented in Bassoli et al. [28]. The first three identified modes are described in the first column of Table 7, while the second column lists the corresponding frequencies.

A detailed FE model of the fortress, that is represented in Fig. 7b, has been developed by Castellazzi et al. [29, 30] adopting an innovative numerical modelling strategy (CLOUD2FEM). This strategy involves the laser scanner survey of the structure, that includes all the internal and external surfaces, obtaining a three-dimensional

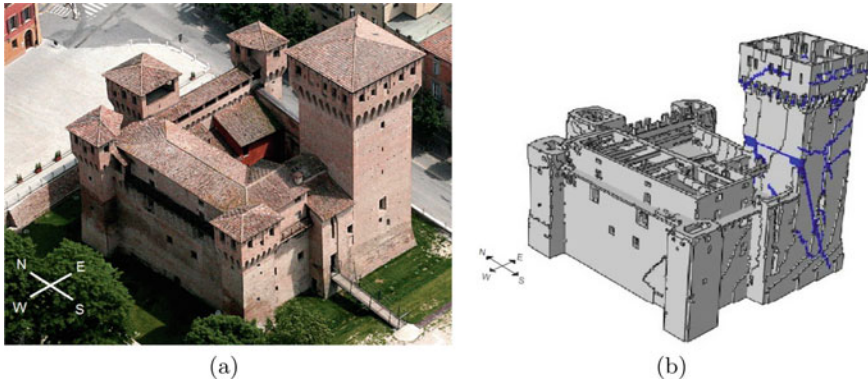


Fig. 7 San Felice sul Panaro fortress: **a** air view and, **b** FE model

Table 7 Fortress: Experimental and numerical modes—deterministic approach

Mode shape	Exp. Freq. (Hz)	Num. Freq. (Hz)	ϵ (%)	MAC (%)
1st Bending E-W	1.72	1.82	5.31	94.58
1st Bending N-S	1.75	1.66	-5.67	89.61
1st Torsional	3.55	3.53	-0.35	93.32

point cloud. The point cloud is then subjected to a semi-automatic transformation into a three-dimensional FE mesh. The survey has been performed after the 2012 earthquake, so the FE model represents the post-earthquake condition of the structure. For this reason, the effect of the complex crack pattern has to be taken into account for the accurate description of the Mastio behaviour. According to the results presented in [28], this is performed assigning a different elastic modulus to mesh elements corresponding to damaged masonry. In this way, it is possible to characterize the structural behaviour in operational conditions. Finally, the model parameters to be calibrated with respect to the experimental modal properties are the elastic moduli E_U and E_D of undamaged and damaged elements, respectively.

5.2 Model Updating

This section presents results of model updating performed with the different approaches proposed in Sect. 2 and 3. In both cases the calibration is performed on the basis of the first three experimentally identified modes.

Fig. 8 Fortress: Pareto front

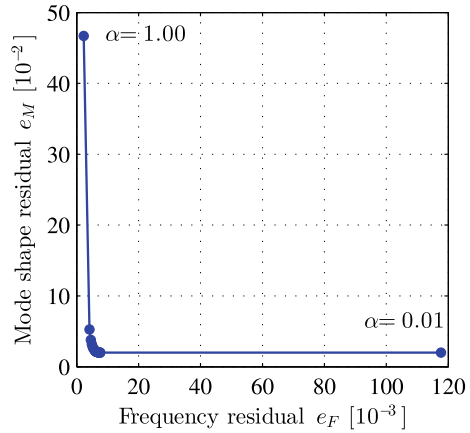


Table 8 Fortress: results of deterministic model updating

α [-]	e_F [10^{-3}]	e_M [10^{-2}]	E_D (MPa)	E_U (MPa)
0.62	6.0	2.2	342	983

5.2.1 Deterministic Model Updating

Deterministic model updating has been performed as described in Sect. 2. The Pareto front obtained is reported in Fig. 8. Note that extreme solutions, that correspond to values 0.01 and 1 of α , are very distant from other solutions of the front.

Table 8 denotes properties of the preferred solution in terms of weighting factor, calibrated parameters and objectives. Comparison between experimental and numerical modal properties, where the last are computed with reference to parameters of Table 8, is carried out in Table 7.

5.2.2 Bayesian Model Updating

Bayesian model updating has been performed considering an uniform distribution for the prior and two different expressions for the likelihood function defined by Eqs. (11) and (12). The corresponding contour plots, that have been realized on a regular grid with a step size of 25 MPa for both parameters, are reported in Fig. 9. The global identifiability of the problem is assured considering the first three mode experimentally identified. Indeed, both contour plots show that the likelihood functions have a single peak [31].

Once the MAP value has been identified through the Matlab function “fmin-search”, Bayesian evidence Eq. (7) has been numerically estimated on the grid previously described and the conjunct posterior distribution has been computed according

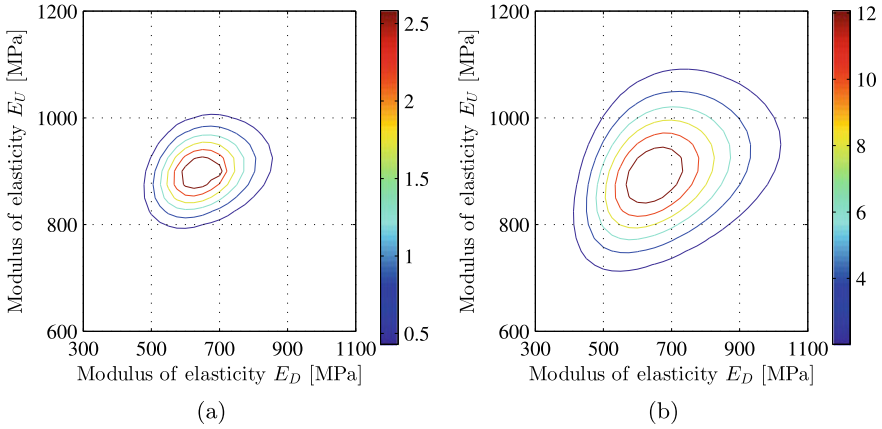


Fig. 9 Fortress: likelihood function defined by, **a** Eq. (11) scaled by a factor 10^{167} and, **b** Eq. (12) scaled by a factor 10^{195}

Table 9 Fortress: results of Bayesian model updating

Likelihood Eq.	E_D		E_U	
	MAP (MPa)	σ (MPa)	MAP (MPa)	σ (MPa)
(11)	637	100	897	53
(12)	655	165	906	95

to Eq.(6). In Table 9 the MAP values of E_D and E_U and the corresponding standard deviations, obtained using the different definitions of likelihood function, are summed up. Focusing on the standard deviation of parameters, the uncertainty computed in the second case is greater than in the first one. It depends on the definition of Eq.(12) for the likelihood function, where the use of dimensionless frequencies and a shared standard deviation carried to a more dispersed function: Fig. 10 enables the comparison between posterior distributions obtained.

Despite these differences, standard deviation of calibrated parameters is still high in both cases, especially for E_D . For this reason, the state of the structure defined on the basis of the modal property identified is uncertain. More data are needed to reduce dispersion: using Eq.(11) for the likelihood function less data will be presumably required to reach a lower uncertainty level than using Eq.(12).

Tables 10 and 11 present the comparison between numerical and experimental modal properties for both situations, where numerical properties are computed considering MAP values of Table 9.

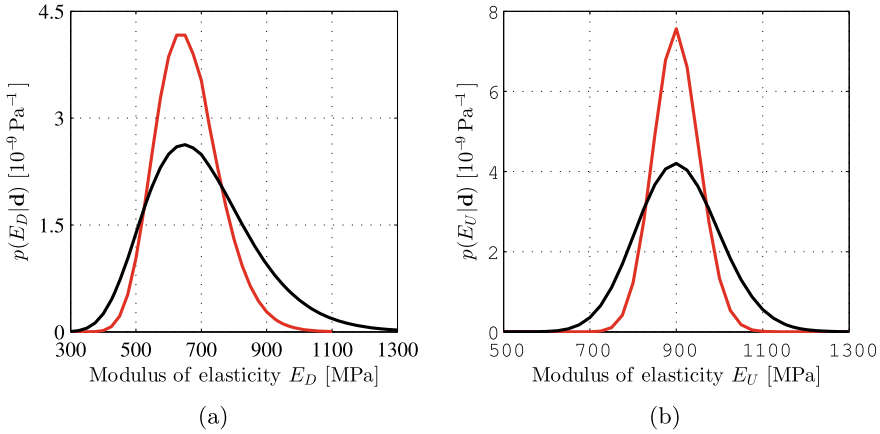


Fig. 10 Fortress: comparison between posterior probability distributions of, **a** parameter E_D and, **b** parameter E_U . Red curves: distributions related to likelihood function of Eq. (11); black curves: distributions related to likelihood function of Eq. (12)

Table 10 Fortress: experimental and numerical modes—Bayesian approach Eq. (11)

Mode shape	Exp. Freq. (Hz)	Num. Freq. (Hz)	ϵ (%)	MAC (%)
1 st Bending E-W	1.72	1.78	3.43	94.52
1 st Bending N-S	1.75	1.62	-7.78	90.12
1 st Torsional	3.55	3.61	1.84	93.58

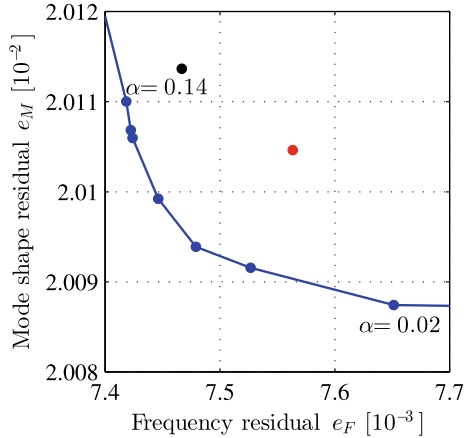
Table 11 Fortress: experimental and numerical modes—Bayesian approach Eq. (12)

Mode shape	Exp. Freq. (Hz)	Num. Freq. (Hz)	ϵ (%)	MAC (%)
1 st Bending E-W	1.72	1.79	4.02	94.52
1 st Bending N-S	1.75	1.63	-7.26	90.11
1 st Torsional	3.55	3.63	2.42	93.58

5.2.3 Comparison of Results

Tables 8 and 9 show that values of parameters updated by deterministic and Bayesian procedure are very different, in particular the value of E_D . Also the corresponding frequencies exhibit marked differences, while MAC values are similar for every mode. Figure 11 illustrates how solutions of Bayesian model updating represented in the objective space e_F - e_M , where objectives are defined by Eqs. (2) and (3), are not optimal solution in the sense of Eq. (4). This outcome is not surprising because different functions have been used to express discrepancy between experimental and

Fig. 11 Fortress: solutions of Bayesian model updating in the objective space $e_F - e_M$. Blue dots: solutions of the Pareto front. Red dot: solution obtained using likelihood function of Eq. (11). Black dot: solution obtained using likelihood function of Eq. (12)



numerical data. Solution of Bayesian model updating are located close to the part of the front generated using small values of α , highlighting how in this case the contribution of mode shape error is predominant in the calibration process.

6 Conclusions

In this paper, a comparison between deterministic and Bayesian model updating has been presented through the calibration of a simple case study and of the FE model of the San Felice sul Panaro fortress. Deterministic approach is based on the resolution of a bi-objective optimization problem using a surrogate-assisted evolutionary algorithm and on the subsequent choice of the preferred solution as the one characterized by the minimum distance from the equilibrium point of the Pareto front. In the context of Bayesian model updating, calibration parameters and prediction errors are modelled as random variables, enabling the estimation of the uncertainty of updated parameters. This is a central point especially when experimental modal properties exhibit significant variations from a measure to another. For both the two floor frame and the FE model of the fortress, two different definitions of the likelihood function have been employed and the lower standard deviation of updated parameters has been obtained considering the likelihood function defined as the product of normal distributions with mean equal to the experimental value of a modal property Eq. (11). As far as the fortress is concerned, both parameters of the structure defined through Bayesian model updating have large uncertainty. To reduce the uncertainty, a greater number of accelerometers is needed to improve the mode shape accuracy and to increase the number of experimental modes that can be used in the model updating. Representation of solutions of Bayesian model updating on the objective space $e_F - e_M$ revealed different situations for the two floor frame and the fortress: they are located in the extreme parts of the Pareto front. For the simple case study, these

solutions are in the part of the front characterized by large values of the weighting factor α , showing a predominant contribution of frequency error in the minimization process. On the contrary, for the fortress, solutions are in the opposite part, hence they have been obtained thanks to a predominant contribution of mode shape error.

Acknowledgements The authors would like to thank Giovanni Castellazzi and Antonio Maria D'Altri for the development of the FE model of the San Felice sul Panaro fortress.

References

1. Teughels A, De Roeck G (2004) Structural damage identification of the highway bridge Z24 by FE model updating. *J Sound Vib* 278(3):589–610. <https://doi.org/10.1016/j.jsv.2003.10.041>
2. Bassoli E, Vincenzi L, Bovo M, Mazzotti C (2015) Dynamic identification of an ancient masonry bell tower using a MEMS-based acquisition system. In: Proceedings of the (2015) IEEE workshop on environmental, energy and structural monitoring systems. Trento, Italy
3. Bursi OS, Zonta D, Debiasi E, Trapani D (2018) Structural health monitoring for seismic protection of structure and infrastructure systems. Springer, Cham, pp 339–358
4. Casapulla C, Ceroni F, Rainieri C, Argiento L, Arcamone P, Fabbrocino G (2019) Structural assessment of santa maria maddalena church in ischia island (italy) by experimental modal analysis under operational conditions. In: Proceedings of 7th international conference on computational methods in structural dynamics and earthquake engineering, COMPDYN 2019; Crete; Greece; 24–26 June 2019; vol 1, pp 1839–1852. <https://www.scopus.com/inward/record.uri?eid=2-s2.0-85079090240&partnerID=40&md5=e92b28099a2a36e7fdb699ff0429dca4>
5. Limongelli MP, Chatzi E, Döhler M, Lombaert G, Reynders, E (2016) Towards extraction of vibration-based damage indicators. In: 8th European workshop on structural health monitoring (EWSHM), 5–8 July 2016. Bilbao, Spain
6. Teughels A, Maeck J, De Roeck G (2002) Damage assessment by FE model updating using damage functions. *Comput Struct* 80(25):1869–1879. [https://doi.org/10.1016/S0045-7949\(02\)00217-1](https://doi.org/10.1016/S0045-7949(02)00217-1)
7. Friswell MI (2008) Damage identification using inverse methods. Springer, Vienna, pp 13–66
8. Mottershead J, Friswell M (1993) Model updating in structural dynamics: a survey. *J Sound Vib* 167(2):347–375. <https://doi.org/10.1006/jsvi.1993.1340>
9. Storn R, Price K (1997) Differential evolution—a simple and efficient heuristic for global optimization over continuous spaces. *J Glob Optimization* 11:341–359
10. Forrester AIJ, Sobester A, Keane AJ (2008) Engineering design via surrogate modelling: a practical guide. Wiley
11. Vincenzi L, Savoia M (2015) Coupling response surface and differential evolution for parameter identification problems. *Comput Aided Civil Infrastruct Eng* 30(5):376–393. <https://doi.org/10.1111/mice.12124>
12. Christodoulou K, Ntsios E, Papadimitriou C, Panetsos P (2008) Structural model updating and prediction variability using pareto optimal models. *Comput Methods Appl Mech Eng* 198(1):138–149. 10.1016/j.cma.2008.04.010, <http://www.sciencedirect.com/science/article/pii/S0045782508001680>
13. Perera R, Ruiz A (2008) A multistage FE updating procedure for damage identification in large-scale structures based on multiobjective evolutionary optimization. *Mech Syst Signal Process* 22(s4):970–991. 10.1016/j.ymsp.2007.10.004, <http://www.sciencedirect.com/science/article/pii/S0888327007002026>
14. Jin SS, Cho S, Jung HJ, Lee JJ, Yun CB (2014) A new multi-objective approach to finite element model updating. *J Sound Vib* 333(11):2323–2338. 10.1016/j.jsv.2014.01.015, <http://www.sciencedirect.com/science/article/pii/S0022460X14000595>

15. Beck JL, Katafygiotis LS (1998) Updating models and their uncertainties. i: Bayesian statistical framework. *J Eng Mech* 124:455–461
16. Beck JL (2010) Bayesian system identification based on probability logic. *Struct Control Health Monit* 17. <https://doi.org/10.1002/stc.424>
17. Beck JL, Au SK, Vanik M (1999) A bayesian probabilistic approach to structural health monitoring. In: *Proceedings of 1999 American control conference, San Diego, USA; 2–4 June 2019; vol 126, pp 1119–1123 vol 2*. <https://doi.org/10.1109/ACC.1999.783215>
18. Vincenzi L, Gambarelli P (2017) A proper infill sampling strategy for improving the speed performance of a surrogate-assisted evolutionary algorithm. *Comput Struct* 178:58–70. <https://doi.org/10.1016/j.compstruc.2016.10.004>
19. Allemang R, Brown D (1982) A correlation coefficient for modal vector analysis. In: *Proceedings of the 1st international modal analysis conference. Orlando, Florida, USA, pp 110–116*
20. Kim IY, de Weck OL (2005) Adaptive weighted-sum method for bi-objective optimization: Pareto front generation. *Struct Multi Optimization* 29(2):149–158. <https://doi.org/10.1007/s00158-004-0465-1>
21. Dincer I, Rosen M, Ahmadi P (2017) *Optimization of energy systems*. Wiley
22. Simoen E, De Roeck G, Lombaert G (2015) Dealing with uncertainty in model updating for damage assessment: a review. *Mech Syst Signal Process* 56–57:123–149. <https://doi.org/10.1016/j.ymsp.2014.11.001>
23. Qian F, Zheng W (2017) An evolutionary nested sampling algorithm for bayesian model updating and model selection using modal measurement. *Eng Struct* 140:298–307. <https://doi.org/10.1016/j.engstruct.2017.02.048>
24. Metropolis N, Rosenbluth A, Rosenbluth M, Teller A, Teller E (1952) Equation of state calculations by fast computing machines. *J Chem Phys* 21:1087–1092
25. Hastings WD (1970) Monte carlo sampling methods using markov chains and their applications. *Biometrika* 57:97–109
26. Beck JL, Au SK (2002) Bayesian updating of structural models and reliability using markov chain monte carlo simulation. *J Eng Mech* 128:380–391. [https://doi.org/10.1061/\(ASCE\)0733-9339](https://doi.org/10.1061/(ASCE)0733-9339)
27. Ching J, Chen YC (2007) Transitional markov chain monte carlo method for bayesian model updating, model class selection, and model averaging. *J Eng Mech ASCE* 133: [https://doi.org/10.1061/\(ASCE\)0733-9339\(2007\)133:7\(816\)](https://doi.org/10.1061/(ASCE)0733-9339(2007)133:7(816))
28. Bassoli E, Vincenzi L, D'Altri AM, de Miranda S, Forghieri M, Castellazzi G (2018) Ambient vibration-based finite element model updating of an earthquake-damaged masonry tower. *Struct Control Health Monit* 25(5). <https://doi.org/10.1002/stc.2150>
29. Castellazzi G, D'Altri AM, Bitelli G, Selvaggi I, Lambertini A (2015) From laser scanning to finite element analysis of complex buildings by using a semi-automatic procedure. *Sensors* 15(8):18360–18380 <https://doi.org/10.3390>
30. Castellazzi G, D'Altri AM, de Miranda S, Ubertini F (2017) An innovative numerical modeling strategy for the structural analysis of historical monumental buildings. *Eng Struct* 132:229–248. <https://doi.org/10.1016/j.engstruct.2016.11.032>
31. Yuen KV (2010) Bayesian methods for structural dynamics and civil engineering. <https://doi.org/10.1002/9780470824566>

Dynamic Identification and Model Updating of a Masonry Chimney



Valentino Santoro, Elisa Bassoli, and Loris Vincenzi

Abstract The paper presents the results of tests performed on a historical masonry chimney and its damage evaluation. The studied masonry chimney exhibits a clear and well visible crack pattern. To evaluate the safety condition and to design rehabilitation interventions, an extensive non-destructive test campaign is performed. The paper describes the dynamic tests, the identification of the structural modal properties, the calibration of a structural Finite Element (FE) model based on the experimental results and the evaluation of the effect of cracks on its dynamic properties. Modal identification is performed using the so called covariance-driven Stochastic Subspace Identification method (SSI-COV) to estimate natural frequencies, mode shapes and modal damping ratios. Then, the model updating is performed to localize the damage starting from the identified modal properties. Instead of adjusting the stiffness properties for all the elements, a stiffness distribution is determined by means of damage patterns. The results of two damage patterns are compared with those of the undamaged model and with the visual inspection carried out on the structure.

Keywords Dynamic identification · Model updating · Damage assessment

1 Introduction

Vibration-based structural monitoring is a widely used tool for the evaluation of the dynamic performance or for the damage assessment of historical towers and

V. Santoro (✉)

Giancarlo Maselli S.R.L. Diagnostica and Engineering, Nonantola, MO 41015, Italy
e-mail: info@giancarlomaselli.it

E. Bassoli · L. Vincenzi

Department of Engineering “Enzo Ferrari”, University of Modena and Reggio Emilia, Modena
41125, Italy
e-mail: elisa.bassoli@unimore.it

L. Vincenzi

e-mail: loris.vincenzi@unimore.it

chimneys [1–3]. These structures are generally tall and slender and they tend to be sensitive to dynamic loads [4]. Moreover, because of their size and flexibility, these kinds of structures can be highly vulnerable to the effects of dynamic actions of wind and earthquakes [5, 6].

The measured dynamic characteristics of a structure can be compared with the numerical ones to determine its health state [7–9]. In this context, the dynamic-based damage identification is the procedure of detecting and localizing damage from changes in modal parameters, especially natural frequencies, modes shapes and modal curvatures [10].

The paper presents the results of tests performed on a historical masonry chimney and its damage evaluation. The studied masonry chimney exhibits a clear and well visible crack pattern. To evaluate the safety condition and to design rehabilitation interventions, an extensive non-destructive test campaign is performed. The paper describes the dynamic tests, the identification of the structural modal properties, the calibration of a structural Finite Element model based on the experimental results and the evaluation of the effect of cracks on its dynamic properties.

The paper is organized as follows. In Sect. 2 the case study is presented and Sect. 3 describes the in situ tests performed to investigate the mechanical parameters of the chimney and its health state. In Sect. 4 the dynamic tests and the obtained results are presented. Finally, in Sect. 5 the results of the model updating and the damage localization are shown. The paper concludes with a critical comment on the effect of cracks on the chimney dynamic properties.

2 Description of the Masonry Chimney

The paper analyses the dynamic behaviour and the health state of an industrial chimney placed in the Pio Albergo Trivulzio complex. The Trivulzio is a public institution, based in Milan, which operates in health, social and educational fields. The chimney is located near the pavilions of the HCR—*health care residences*—and it was part of a thermal power plant (Fig. 1a). The structure, which has a typical truncated conical shape, was built in solid masonry brick with mortar joints arranged in regular horizontal rows (Fig. 1b). The dimensions of the trapezoidal bricks used for the construction are $15\text{ cm} \times 20\text{ cm} \times 12\text{ cm}$ with a thickness of 6.5 cm.

The structure is 34.94 m high and it is made up of two different parts: the upper chimney and the basement. The basement has the shape of an octagonal-based frustum pyramid and a variable section with a minimum width of 4.66 m.

The basement height is 4.56 m. The upper masonry part is composed of two coaxial cones. The external cone has a pipe cross-section that tapers upwards, with diameter decreasing from 3.53 m at the base to 2.25 m at the top. The coaxial inner pipe presents a 12 cm thick tapered shape (Fig. 2) that ensures the chimney effect for smoke circulation. The inner and the external cones are 5 cm apart. The chimney has 16 steel confining rings distributed along its height.



Fig. 1 **a** A general view of the structure with the temporary safety scaffolding and **b** a detail of the outer masonry layer

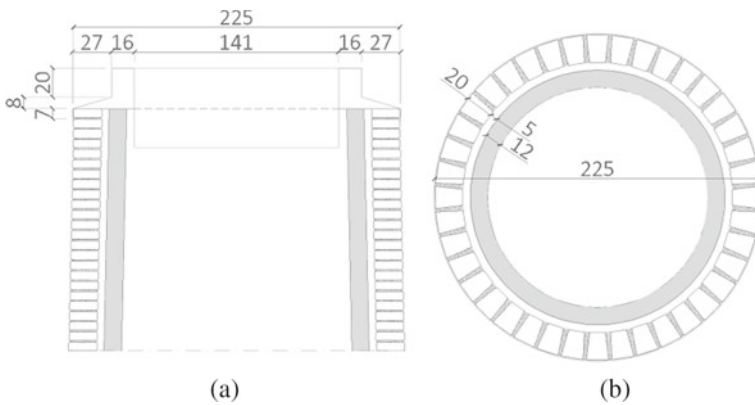


Fig. 2 **a** Vertical and **b** horizontal cross-section of external chimney and inner pipe—dimension in centimeters

3 Chimney Health State and Structural Surveys

The Pio Albergo Trivulzio Technical Service had already monitored the chimney in April 2019, when signs of damage and surface deterioration became obvious. According to the damage status, a multidirectional scaffolding was erected with the aim of ensuring HCR building safety.

Furthermore, to assess the structural state of the masonry chimney, adequate information was needed to obtain complete structural knowledge and diagnosis. The investigation covered several aspects:

- a. geometrical survey and accurate survey of crack pattern and deterioration distribution on the external wall;

- b. material characterization through destructive tests on cored samples and slightly destructive mechanical tests, like flat-jack and sonic pulse velocity tests;
- c. in situ material stress-strain behavior measurement;
- d. experimental modal analysis for evaluation of structural dynamic characteristics.

This work describes the detailed in situ survey, the structural and material assessment and the dynamic identification.

Chimney geometry was completely acquired in October 2019. The variation of the cross-section with respect to the height and the thickness of the wall were carefully documented, together with the position of main visible cracks.

As an essential step in the process of numerical evaluation of chimney health state, a visual inspection of the structure was performed, in order to identify the critical and damaged areas. With the help of the scaffolding, the chimney was surveyed along its height. In particular, the visual inspection detected the following deterioration phenomena, in order of importance:

- a. significant passing-through cracks, from 30 to 80 mm wide, with mutual disconnection between bricks;
- b. other oblique and widespread cracks, about 15–20 mm wide, that are slowly but continuously opening;
- c. washout of mortar joints, with removal of material up to a depth of 80 mm from the external wall surface, caused by the natural ageing and the lack of maintenance;
- d. biological growth, porosity and rising humidity in the bottom part of the chimney.

The crack pattern was mainly observed from the height of 19.00 m to the chimney top. Some of the confining steel rings were not properly closed and there were open cracks along the masonry crossing them. Different damages observed have been properly documented photographically as well as being supported by drawings. Major cracks are represented in Fig. 3. Since the cracks developed slowly, a likely hypothesis is that the crack growth is due to the combined effect of dead loads and wind dynamic actions. For this reason, a modal characterization of the chimney dynamic properties is needed.

Material characterization of masonry structures is a key issue when analyzing their behavior through numerical modelling. In this regard, after a visual inspection, flat-jack tests were carried out to estimate the failure stress and the masonry Young modulus. Each test was performed in a solid-unit masonry wall by inserting two flat-jacks in mortar joint cuts as shown in Fig. 4a. By gradually increasing the flat-jack pressure, the Young modulus and the compressive strength were obtained. In situ mechanical properties were acquired at two different height levels: between the 1st–2nd and the 3th–4th steel rings. Specifically, a Young's modulus of about 4100 MPa was obtained while the estimated failure strength ranged between 4.6 and 5.0 MPa (see Table 1).

Sonic tests were performed to map non-homogeneity of the materials used in the walls along the height of the chimney, such as the use of different kinds of bricks



Fig. 3 Damage identification: **a–b** typical passing-through crack and **b** washout of mortar joints on the top of chimney



Fig. 4 Material characterization of masonry structure: **a** flat-jack and **b** sonic test position

during the construction, and to detect the presence of voids and flaws (Fig. 4b). A mechanical pulse velocity equipment was used to acquire the velocity of the emitted elastic waves through the medium. The input signals were generated by an instrumented hammer and the transmitted pulses were received by an accelerometer positioned on the same masonry surface. The tests were carried out on some grids and repeated at different heights, to verify general morphology, state of damage and the variation in the materials of the walls. Measurements recorded at different levels suggest homogeneous sonic velocity between 1800 and 2000 m/s, that are typical values of compact and defect-free masonry. In the top part of the chimney, however, where the structure is seriously damaged, measured velocity decreases significantly with values of the order of 500–1000 m/s.

Finally, some laboratory tests on cored samples were performed to evaluate the physical and mechanical characteristics of the constituting materials, mainly the ultimate compressive strength of bricks (whose value ranges between 22 and 25 MPa) and the chemical–physical mortar composition.

Table 1 Summary of the surveys and the related results needed to obtain complete structural knowledge and diagnosis

Testing techniques	Targets	Results
Geometrical surveys	Analysis of global geometry and structural details	–
Local investigation	Analysis of crack pattern, specific detail failure and deterioration phenomena	From the height of 19.00 m to the chimney top, in order of importance: a. Passing-through cracks, 30–80 mm wide; b. Oblique and widespread cracks, 15–20 mm wide; c. Washout of mortar joints; d. Biological growth, porosity and rising humidity in the bottom part of the chimney
6 sonic tests in superficial transmission mode	Measurements recorded at different levels of the chimney, to map non-homogeneity of masonry along the height	Average wave velocities 1238 m/s (height 6.85 m) 1880 m/s (height 12.60 m) 2029 m/s (height 16.20 m) 1966 m/s (height 18.05 m) 806 m/s (height 33.75 m) 784 m/s (height 33.75 m)
2 flat jack tests	Evaluation of the mechanical parameters that characterize the compressive behavior of masonry	Failure stress value and Young's modulus 4.63–4131 MPa (height 6.85 m) 5.05–4147 MPa (height 10.60 m)
2 shove tests	Evaluation of the mechanical parameters that characterize the shear behavior of masonry	Sliding failure along mortar joints 0.543 MPa 0.635 MPa
3 non destructive tests on mortar joints	Evaluation of the failure stress of mortar	1.85 MPa 1.05 MPa 1.40 MPa
Laboratory tests on 3 samples	Evaluation of the failure stress of trapezoidal masonry bricks	22.40 MPa 24.90 MPa 22.60 MPa

4 Dynamic Tests

4.1 *In Situ Test Setup*

This section aims at analyzing the modal properties of the chimney starting from the ambient vibration response as well as the free vibration recorded after drop weight impact tests. To measure the dynamic response of the masonry structure and to

identify mode shapes, natural frequencies and damping coefficients, an output-only identification technique was used [11]. This method is generally well suited for the identification of dynamic properties of this kind of structures.

The chimney was instrumented using 10 uniaxial PCB 393B12 piezoelectric sensors (Fig. 5a) and a 12-channel data acquisition system (Fig. 5b). These sensors, that make it possible to record acceleration responses, are characterized by the following performances: voltage sensitivity of 10,000 mV/g, a resonance frequency greater than 10 kHz, measurement range of ± 0.5 g, frequency range of $(\pm 5\%) 0.15 \div 1000$ Hz.

Ambient vibration response, in terms of acceleration, was recorded in 4 different levels located along the height of the chimney. The accelerometers were placed along the two main horizontal directions x and y, orthogonal and tangential to the circular cross section, to identify bending and torsional modes. Four accelerometers (named A7-A10) were placed at the chimney top, in two diametrically opposed positions. To identify the bending mode shapes, 6 accelerometers were installed at height of $7/8$ H (30.57 m, sensors A5-A6), $3/4$ H (26.21 m, sensors A3-A4) and $H/2$ (17.47 m, sensors A1-A2). Figure 6 shows sensor positions along the height of the chimney, referred to the x-y reference system, together with the level of the instrumented cross-section. So as not to interfere with the vibration tests, the scaffolding for HCR



Fig. 5 Dynamic tests: **a** piezoelectric accelerometers on the top of chimney and **b** data acquisition system

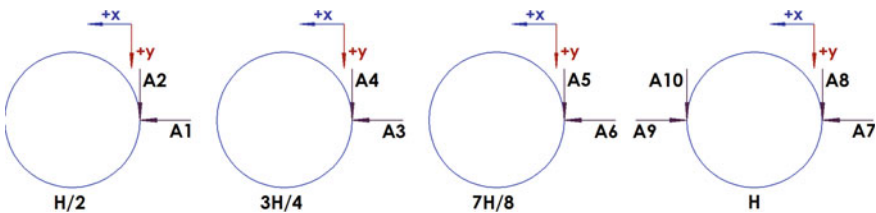


Fig. 6 Tests setup: measuring points



Fig. 7 **a** Drop weight input test and **b** masses of 25 kg

safety was duly detached from the chimney. According to the literature, in order to well characterize lower natural frequencies, the minimum acquisition time T should be evaluated as:

$$T \geq 1000/f_{\min} \quad (1)$$

where f_{\min} is the lower expected frequency to be identified. The response due to ambient excitation was acquired within a time frame of 90 min with a sampling frequency of 2048 Hz.

Being a small-size structure, a modal identification was also performed from the free vibrations caused by an impulsive input. Specifically, four drop weight impact tests were carried out, using masses of 25 or 50 kg. The weights lever arm was 15 m long and horizontal distance of the impact point from the chimney was 1.50 or 2.00 m, as shown in Fig. 7.

4.2 The Identification Algorithm

Modal identification was performed using the covariance-driven Stochastic Subspace Identification method (SSI-COV) [12, 13] to provide estimates of natural frequencies, mode shapes and modal damping ratios. The SSI-COV method addresses the so-called stochastic realization problem, that is the problem of identifying a stochastic state-space model from output-only data. The method is briefly described in the following.

For a n degree-of-freedom (DOF) linear vibratory system, the equation of motion can be expressed as

$$\mathbf{M}\ddot{\mathbf{q}}(t) + \mathbf{C}\dot{\mathbf{q}}(t) + \mathbf{K}\mathbf{q}(t) = \mathbf{F}(t) \quad (2)$$

where \mathbf{M} , \mathbf{C} and \mathbf{K} are the system mass, damping and stiffness matrices with dimension $n \times n$, $\mathbf{q}(t)$, $\dot{\mathbf{q}}(t)$ and $\ddot{\mathbf{q}}(t)$ are the vector of displacement, velocity and acceleration at the time t , respectively. The dot over a time function denotes the derivative with respect to time. $\mathbf{F}(t)$ is unmeasured excitation vector which is assumed to be a white noise process. The observation equation is given by:

$$\mathbf{y} = \mathbf{Z}\mathbf{q} \tag{3}$$

that correlates the output observation vector $\mathbf{y}(t)$ (with dimension $m \times 1$, being m the output number) with the vector of displacements by means of the matrix \mathbf{Z} . The latter is a $m \times n$ matrix that specifies which DOFs of the system are observed. By applying the model reduction, the Eq. (2) can be converted to the discrete-time stochastic state-space model:

$$\begin{aligned} \mathbf{x}_{k+1} &= \mathbf{A}\mathbf{x}_k + \mathbf{w}_k \\ \mathbf{y}_k &= \mathbf{C}\mathbf{x}_k + \mathbf{v}_k \end{aligned} \tag{4}$$

where \mathbf{x}_k and \mathbf{y}_k are respectively the state vector and the vector containing the output measurements, at the time instant k . \mathbf{w}_k and \mathbf{v}_k are vectors that represent the noise due to modelling inaccuracies and the noise content of the measurements. Their covariance matrices are defined as:

$$E[(\mathbf{w}_p \ \mathbf{v}_p), (\mathbf{w}_q^T \ \mathbf{v}_q^T)] = \begin{bmatrix} \mathbf{Q} & \mathbf{S} \\ \mathbf{S}^T & \mathbf{R} \end{bmatrix} \delta_{pq} \tag{5}$$

where E denotes mathematical expectation and δ_{pq} is the Kronecker operator. The matrix \mathbf{A} is the system matrix that describes the dynamic information of the system and it is related to the mass, damping and stiffness matrices; \mathbf{C} is the corresponding output matrix. The modal characteristics of the system, that is the natural frequencies f_j and the modal damping ratios ξ_j can be obtained by computing the eigenvalues $\bar{\lambda}_j$ of the matrix \mathbf{A} :

$$f_j = \frac{|\ln(\bar{\lambda}_j)|}{2\pi \Delta t}, \xi_j = -\frac{\text{Re}(\ln(\bar{\lambda}_j))}{|\ln(\bar{\lambda}_j)|} \tag{6}$$

The complex mode shapes stocked in matrix Ψ are extracted from the matrix \mathbf{L} formed with the eigenvectors of \mathbf{A} :

$$\Psi = \mathbf{C}\mathbf{L} \tag{7}$$

The aim of the SSI-COV method is to obtain modal estimates starting from the covariance matrices of the measured structural response time series. The output covariances Λ_i are defined as:

$$\Lambda_i = E[\mathbf{y}_{k+i}\mathbf{y}_k^T] \quad (8)$$

where i is the time leg. The output covariances are organized in a Hankel matrix of dimension $mi \times mi$:

$$\mathbf{H}_i = \begin{bmatrix} \Lambda_1 & \Lambda_2 & \dots & \Lambda_{i-1} & \Lambda_i \\ \Lambda_2 & \Lambda_3 & \dots & \Lambda_i & \Lambda_{i+1} \\ \dots & \dots & & \dots & \dots \\ \Lambda_{i-1} & \Lambda_i & \dots & \Lambda_{2i-3} & \Lambda_{2i-2} \\ \Lambda_i & \Lambda_{i+1} & \dots & \Lambda_{2i-2} & \Lambda_{2i-1} \end{bmatrix} \quad (9)$$

The value of i is chosen so that $mi \geq N$, where N is the model order. It can be shown that the output covariances are related to the system matrices by means of the following equations:

$$\Lambda_i = E[\mathbf{y}_{k+i}\mathbf{y}_k^T] = \begin{cases} \mathbf{C}\mathbf{A}^{i-1}\mathbf{G} & i > 0 \\ \Lambda_0 & i = 0 \\ \mathbf{G}^T(\mathbf{A}^{i-1})^T\mathbf{C}^T & i < 0 \end{cases} \quad (10)$$

where \mathbf{G} is defined as:

$$\mathbf{G} = E[\mathbf{x}_{k+1}\mathbf{y}_k^T] \quad (11)$$

From Eqs. (10) and (11), it is easy to verify that the Hankel matrix can be decomposed into the product of observability matrix Γ_i and controllability matrix Δ_i :

$$\mathbf{H}_i = \Gamma_i \Delta_i \quad (12)$$

where:

$$\Gamma_i = (\mathbf{C} \ \mathbf{C}\mathbf{A} \ \mathbf{C}\mathbf{A}^2 \ \dots \ \mathbf{C}\mathbf{A}^{i-1})^T \quad (13)$$

and

$$\Delta_i = (\mathbf{G} \ \mathbf{A}\mathbf{G} \ \dots \ \mathbf{A}^{i-2}\mathbf{G} \ \mathbf{A}^{i-1}\mathbf{G}) \quad (14)$$

The identification of the modal parameters is performed with a singular value decomposition (SVD) of the Hankel matrix:

$$\mathbf{H}_i = \mathbf{U}\mathbf{S}\mathbf{V}^T = [\mathbf{U}_1 \ \mathbf{U}_2] \begin{bmatrix} \mathbf{S}_1 & \mathbf{0} \\ \mathbf{0} & \mathbf{0} \end{bmatrix} \begin{bmatrix} \mathbf{V}_1 \\ \mathbf{V}_2 \end{bmatrix} = \mathbf{U}_1\mathbf{S}_1\mathbf{V}_1^T \quad (15)$$

where \mathbf{U} and \mathbf{V} are the orthogonal matrices and \mathbf{S} is the diagonal matrix with the singular values. The observability and controllability matrices are calculated from the SVD of the Hankel matrix:

$$\begin{aligned} \mathbf{\Gamma}_i &= \mathbf{U}_1 \mathbf{S}_1^{1/2} \\ \mathbf{\Delta}_i &= \mathbf{S}_1^{1/2} \mathbf{V}_1 \end{aligned} \tag{16}$$

The matrices \mathbf{A} and \mathbf{C} can be retrieved from the observability matrix. The matrix \mathbf{C} can be obtained as the first block rows of $\mathbf{\Gamma}_i$. Denoting with $\underline{\mathbf{\Gamma}}_i$ the matrix similar to $\mathbf{\Gamma}_i$ but without the last n rows and with $\overline{\mathbf{\Gamma}}_i$ that without the first n rows, the matrix \mathbf{A} can be estimated by the resolution of a least-square problem:

$$\mathbf{A} = (\underline{\mathbf{\Gamma}}_i^T \overline{\mathbf{\Gamma}}_i)^{-1} \underline{\mathbf{\Gamma}}_i^T \overline{\mathbf{\Gamma}}_i \tag{17}$$

Once the identification of the state space model is performed and the system matrices \mathbf{A} and \mathbf{C} are known, the modal parameters are easily extracted by means of Eqs. (6) and (7).

4.3 Test Results

In this section, results of the dynamic tests are described. Examples of acceleration time series recorded during the dynamic tests are reported in Fig. 8a, b for the ambient vibration test and for an impact test, respectively. The acceleration measured during the ambient vibration test (Fig. 8a), ranges between ± 0.5 mg, stating the low level

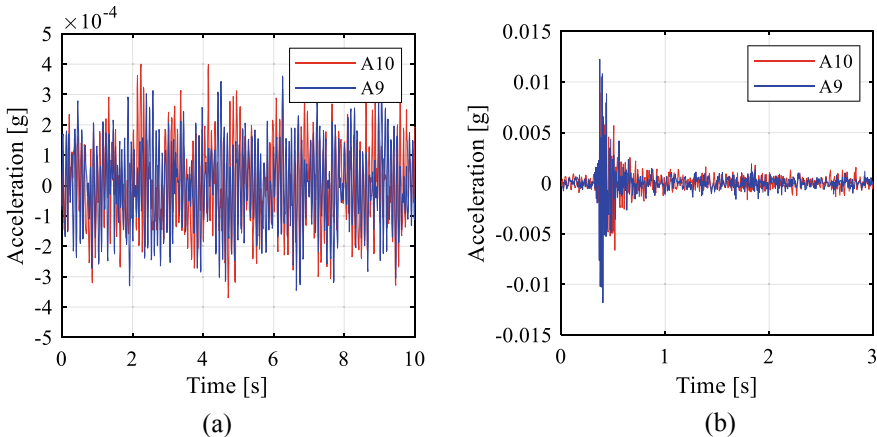


Fig. 8 Acceleration measured by sensors A9 and A10 during **a** the ambient vibration test and **b** the impact test

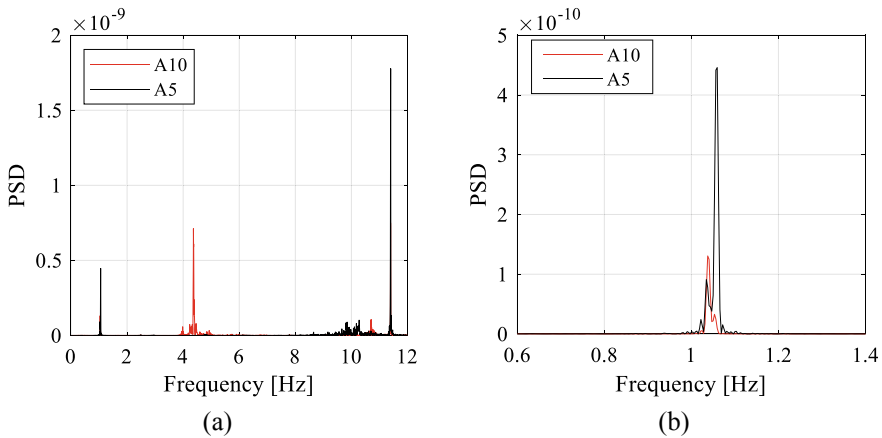


Fig. 9 PSD of acceleration: **a** ambient vibration test and **b** detail of the first two frequencies

of ambient excitation that existed during the tests. Moreover, examples of the Power Spectral Density (PSD) functions of the acquired accelerations are reported in Fig. 9. It is worth of note that several peaks appear at frequencies around 4.2 Hz. As shown in the following, this frequency corresponds to a second bending mode. However, the presence of several peaks around this frequency is probably due to the high non-linearity of the structure, caused by both the damage state and the nonlinear effects related to different levels of the dynamic force.

The procedure described in Sect. 4.2 is applied to the measured accelerations and the modal parameters of the chimney are identified. The identification procedure is implemented in MATLAB by the authors. Seven modes (six bending modes and a torsional mode) with frequencies in the range 1.026–12.50 Hz are clearly identified. Values of identified damping ratios are in the range 0.10–1.00%. The identified natural frequencies are reported in Table 2 while Fig. 10 shows the components of some of the most relevant identified mode shapes in plan and elevation, assuming the structure is fixed at the base. Regarding the elevation, the blue and the red color represent the mode shape components obtained in x and y direction, respectively.

Table 2 Identified modes

Mode	Mode shape type	Experimental frequency (HZ)
1	1st Bending mode	1.026 (1.026–1.036)
2	1st Bending mode	1.075 (1.045–1.075)
3	2nd Bending mode	4.229 (4.175–4.355)
4	2nd Bending mode	4.842 (4.804–4.948)
5	1st Torsional mode	10.69 (10.61–10.72)
6	3rd Bending mode	11.41 (11.40–11.42)
7	3rd Bending mode	12.50 (12.49–12.50)

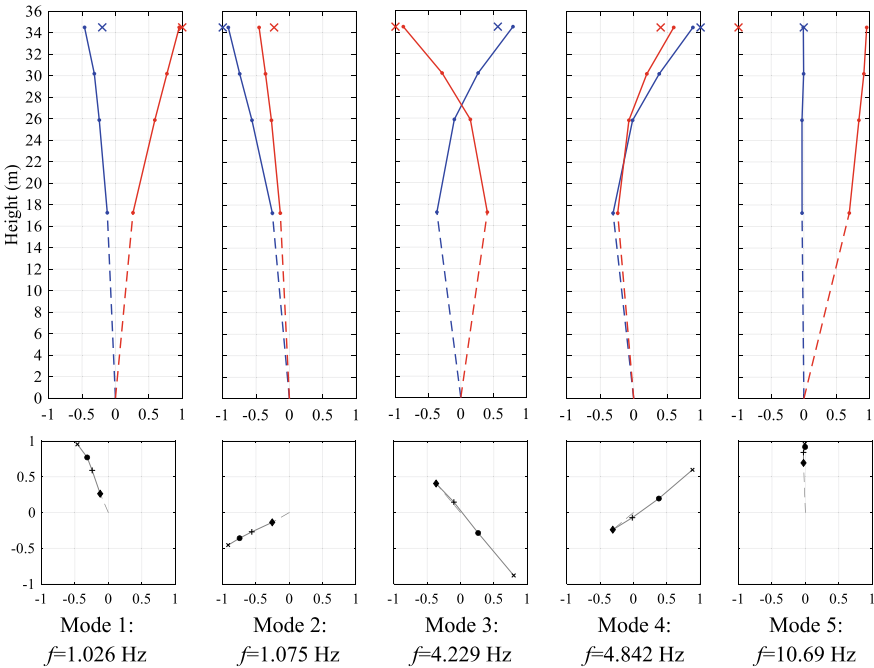


Fig. 10 Mode shape components of the first five modes—elevations and plans. Elevation view: mode shape components in x (blue) and y (red) direction. Plan view: displacement of the instrumented levels H/2 (♦ marker), H (+ marker), 7H/8 (● marker) and H (x marker)

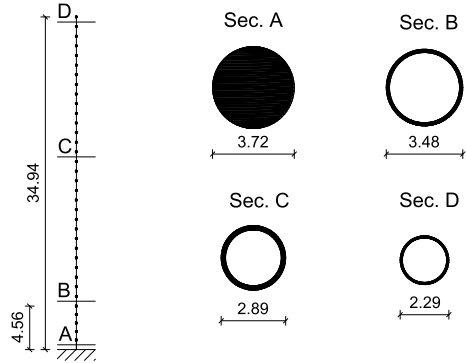
Moreover, the × marks indicate the mode shape components of accelerometers A9 and A10, which are placed at the top level in a diametrically opposed position with respect to accelerometers A7 and A8 (see Fig. 6). As far as the plan view is concerned, the displacement of each instrumented level (namely at H/2, 3H/4, 7H/8 and H) is obtained by combining the mode shape components in x and y direction. In this case, at the top level only the displacement obtained from the sensors A8 and A7 is plotted.

The identified modes agree with the typical expected mode shapes of a cantilever beam. Figure 10 shows that even if the structure has a circular cross section, the mode shapes are mainly found in two preferred directions, which are inclined by 116 and 26° with respect to the x direction. In the following, they are referred to as “principal directions” 1 and 2, respectively.

5 Numerical Modelling and Calibration

The model updating procedure allows to obtain a numerical model that can accurately simulate the dynamic behavior of a real structure. In the present case, the updating procedure aims to find the loss of stiffness at different levels due to the damage and/or

Fig. 11 Modeling scheme. Dimensions are in meters



to the inaccuracy of the numerical model to correctly represent the actual dynamic behavior of the chimney.

Instead of adjusting the stiffness properties for all the elements, a stiffness distribution is determined by means of damage patterns [14]. They are defined as function of the elastic modulus assuming that only the elastic modulus for each direction has to be corrected over the finite element. The unknown parameters to be calibrated are the amplitudes by which the damage function has to be multiplied. This approach reduces the total number of the updating parameters and ensures a more realistic and smooth pattern of the selected variables, without sharp changes of values due to numerical errors and approximations.

For this purpose, the chimney is modelled with a linearly tapered beam-like model composed of 35 Timoshenko beam elements. The structural model is represented in Fig. 11. The basement, which has an octagonal plan, is modeled through an equivalent circular cross section. Dimensions of the cross section are such as to obtain the same moment of inertia of the octagonal cross section in the two principal directions. The rest of the chimney is modeled with a hollow circular cross section with variable dimensions based on the geometrical survey. Only the external layer is modeled, and the mass of the inner layer is taken into account by increasing the mass of the external layer by a factor of 2.

The model updating is performed separately for the two principal direction. First, the mode shapes in the principal directions are computed by combining the modal components in x and y direction. The objective function H to be minimized is a measure of the difference between numerical (f_{num} , φ_{num}) and experimental (f_{sper} , φ_{sper}) natural frequencies and mode shapes. It is expressed in terms of frequency and mode shape residuals, respectively \mathbf{r}_f and \mathbf{r}_m , as follows [14]:

$$H(\mathbf{x}) = \|\mathbf{r}\|^2 = \left\| \begin{matrix} \mathbf{r}_f \\ \mathbf{r}_m \end{matrix} \right\|^2 \tag{17}$$

The vector \mathbf{x} represents the unknown multipliers that define the damage function. The components of the residual in term of frequencies \mathbf{r}_f for each mode i is computed

as:

$$r_{f,i} = \frac{f_{num,i}(\mathbf{x}) - f_{sper,i}}{f_{sper,i}} \quad (18)$$

while the i -th component of the mode shape residual is defined as:

$$r_{m,i} = \frac{\varphi_{num,i}(\mathbf{x})}{\bar{\varphi}_{num,i}(\mathbf{x})} - \frac{\varphi_{sper,i}}{\bar{\varphi}_{sper,i}} \quad (19)$$

Each mode shape component is divided by a reference component ($\bar{\varphi}_{num,i}(\mathbf{x}), \bar{\varphi}_{sper,i}$), since the numerical and experimental mode shapes are scaled differently. In this paper, the reference point is chosen at the top of the chimney, where all mode shapes exhibit the largest magnitude, which is equivalent to normalize each mode shape to one in its maximum displacement. The parameters that govern the damage function are calibrated by means of a surrogate assisted evolutionary algorithm described in the following section.

5.1 The Optimization Algorithm

The model calibration of the chimney is performed by means of a surrogate-assisted evolutionary algorithm called DE-S algorithm. The algorithm is originally proposed by Vincenzi and Savoia [15] and it combines a second-order surrogate with the differential evolution (DE) algorithm. Vincenzi and Gambarelli [16] introduces a proper infill sampling strategy to further reduce the number of objective function evaluations. Genetic and evolutionary algorithms are widely used to solve global optimization problems. Their architecture is designed for large-scale problems and allows avoiding local minima. The main drawback is that a large number of function evaluations is often required to reach the convergence. In order to reduce the computation time in expensive finite element model updating, a good choice is to use computationally inexpensive approximation models (i.e. the surrogate) which can replace the resolution of the FE model or decide the new candidate points for the next generation in the evolutionary algorithm.

In the DE-S algorithm, the candidate points are chosen trying to find a compromise between local and global search, that is, enhancing both the accuracy in the region of the optimum predicted by the surrogate (local exploitation) and the global exploration. The optimization process is based on the simultaneous adoption of NP vectors. Each vector has dimension D , being D the number of unknown structural parameters. First, the objective function values are evaluated for the initial population of vectors, randomly chosen in the search space. At each subsequent iteration, NP subsets of NS vectors are built, with $NS < NP$. Each subset is used to calibrate a second-order response surface as a local approximation of the objective function.

Depending on the shape of the approximating function, two possibilities occur. If the response surface is convex, the mutant vector of the evolutionary process is defined as the minimizer of the approximating function. Otherwise, the mutant vector is obtained from the classic Mutation operation of the Differential evolution algorithm.

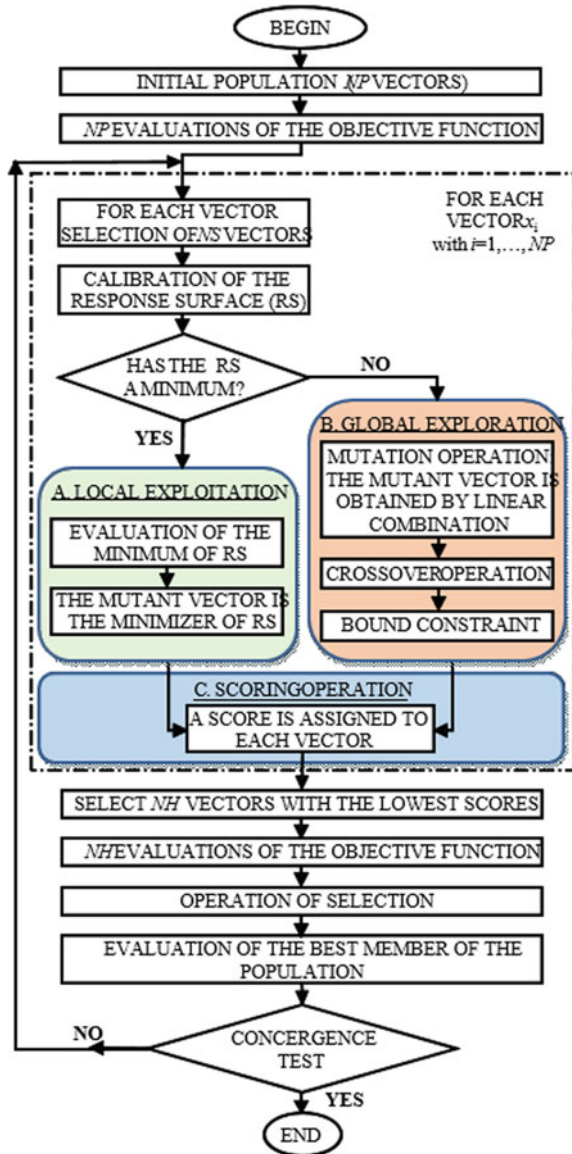
Each mutant vector represents a candidate for a new evaluation. To reduce the number of the objective function evaluations, a subset of NH candidates (with $NH < NP$) is selected. Candidates with the lowest score are preferred and only for this subset of points the objective function is evaluated. The score is defined as the weighted sum of two criteria. The first one depends on the objective function value predicted by the surrogate. The second criterion depends on the distances of the candidate from the points where the objective function has been already evaluated. A detailed flowchart summarizing the updating procedure can be found in Fig. 12. Finally, the reader can refer to [15, 16] for all details.

5.2 Results of the Updating Procedure

In this section, some preliminary results regarding the damage localization based on the modal parameters of the chimney are reported. Two different model calibrations are investigated, which are based on the adoption of two different damage functions. In the first case, a piecewise linear damage function is considered while the second case assumes a sixth degree polynomial damage function. In both cases, the optimization is performed separately in the principal directions 1 and 2 (identified in Sect. 4.3). For each direction, the natural frequencies and modes shapes of the first three bending modes are considered as input for the calibration procedure, namely modes 1, 3 and 6 for direction 1 and modes 2, 4 and 7 for direction 2. The calibration parameters are the damage coefficients of nine control sections along the height of the tower. The first and the ninth control sections are located at the base and the top of the chimney, respectively, while the other seven sections are equally spaced on the beam length. The damage coefficients are the coefficients that reduce the section stiffness in all the model elements. The section stiffness is evaluated as EI , being E the elastic modulus of the masonry and I the moment of inertia. According to the results of the structural survey, the initial value of the elastic modulus is assumed equal to 4100 MPa, while the moment of inertia is evaluated based on the cross section dimensions. The number of control sections is such as to ensure a well-conditioned optimization problem. In fact, the number of controlled sections equal to nine is the maximum number of identifiable parameters per direction. Starting from the general dynamic eigen-problem, it can be proved that the maximum number of identifiable parameters N_{\max} is:

$$N_{\max} = n \cdot (m + 1) - \sum_{i=1}^n i \quad (20)$$

Fig. 12 Flowchart of the DE-S algorithm



where n is the number of considered modes and m is number of the monitored degree-of-freedom. In this study, for each direction $n = 3$ and $m = 4$, leading to $N_{\max} = 9$. The reader can refer to [17] for the proof of Eq. (20).

The model calibration is performed adopting a MATLAB code developed by one of the authors [15] that implements the procedure described in Sect. 5.1 as mentioned

before, the calibration is performed adopting two different damage functions. In the first case, a piecewise linear function is assumed, implying that the damage coefficient of an element placed between two control sections is evaluated by linear interpolation. Table 3 shows a comparison between the experimental and numerical frequencies obtained with the piecewise linear function while Fig. 13 compares the

Table 3 Comparison between numerical and experimental natural frequencies—piecewise linear damage function

Mode	Mode shape type	Numerical frequency (HZ)	Experimental frequency (HZ)	Error (%)
1	1st Bending mode—direction 1	1.019	1.026	-0.68
3	2nd Bending mode—direction 1	4.198	4.229	-0.73
6	3rd Bending mode—direction 1	11.56	11.41	+1.31
2	1st Bending mode—direction 2	1.104	1.075	+2.70
4	2nd Bending mode—direction 2	4.685	4.842	-3.24
7	3rd Bending mode—direction 2	12.25	12.50	-1.97

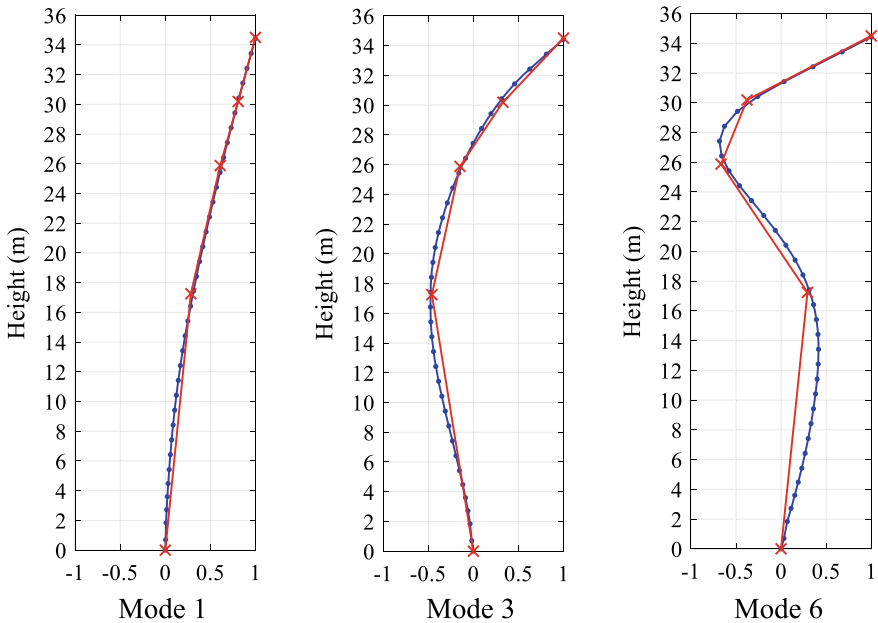


Fig. 13 Comparison between numerical (blue line) and experimental (red line) mode shape components of the first three identified modes—direction 1

experimental and numerical mode shapes for the direction 1. Similar results are obtained in the orthogonal direction. Generally, the correlation between numerical and experimental mode shapes is almost perfect and the numerical frequencies are in very good agreement with the experimental ones. Errors in terms of frequencies are lower than 2% for the selected modes in direction 1 and about 3% in the other direction.

The damage coefficients obtained from the piecewise linear damage function for each finite element are shown in Fig. 14a. It is observed that correction factors greater than one are obtained at about 10 m in both directions, indicating a stiffness greater than the initial value. On the contrary, in the upper part of the chimney a strong reduction of the model stiffness is needed to well fit the experimental mode shapes. It is worth of note that also at the base damage coefficients lower than one are obtained. In this case, this is probably due to inaccuracies of the structural model. In fact, the basement is modeled with a full cross section while a hollow cross section may actually be present. Moreover, the soil-structure interaction can produce a rotation of the basement that is interpreted in the model as a stiffness reduction (Table 4).

In the second case, a sixth degree polynomial damage function is assumed and the damage coefficients of each element are calculated by the polynomial damage function on the base of its height. Figure 14b shows a comparison between the correction factors obtained from the piecewise linear (PL) function (blue) and the

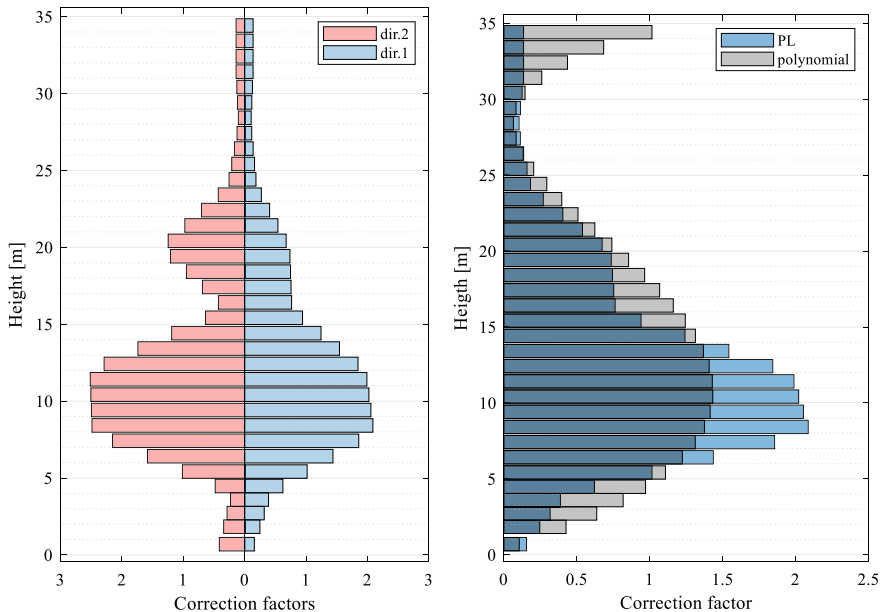


Fig. 14 **a** Correction factors for the two principal directions—piecewise linear damage function; **b** Comparison between correction factors for the direction 1—piecewise linear (PL) damage function (blue bars) versus polynomial function (grey bars)

Table 4 Comparison between numerical and experimental natural frequencies

Mode	Mode shape type	Numerical frequency (Hz)			Experimental frequency (HZ)
		PL damage function	Polynomial function	Uniform distribution	
1	1st Bending mode—direction 1	1.019	1.030	1.001	1.026
3	2nd Bending mode—direction 1	4.198	4.217	4.935	4.229
6	3rd Bending mode—direction 1	11.56	11.03	12.46	11.41

polynomial function (gray) in direction 1. The comparison confirms the global trend characterized by a strong stiffness reduction at the base and at about 25–30 m, while different values of the damage coefficients at both the height of 10 m and the top are obtained from the two different damage functions.

Finally, in Fig. 15, the mode shapes obtained with the piecewise linear damage function and the polynomial damage function are compared to those obtained imposing uniform values of elastic modulus along the chimney height (i.e. neglecting the contribution of the damage). It is shown that the mode shapes obtained by the

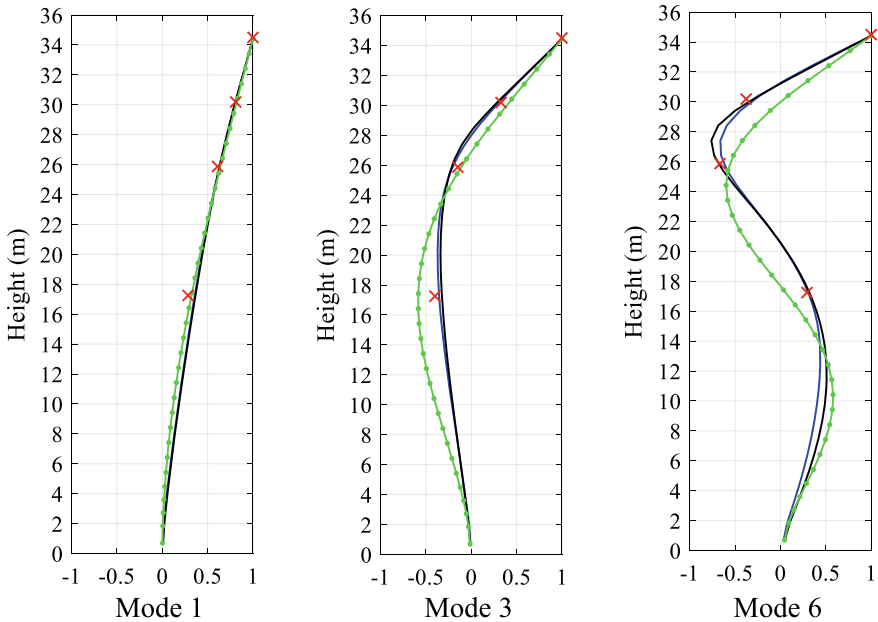


Fig. 15 Comparison among mode shapes obtained with the piecewise linear (PL) damage function (blue line), the polynomial damage function (black line) and the uniform elastic modulus (green line) with the experimental values (red marks)—direction 1

two calibrated models are almost the same; very small differences can be observed only for the third mode shape in between the monitored levels. On the contrary, large differences are found between the mode shapes with a uniform distribution of the elastic modulus and the experimental values, confirming that the variation of elastic modulus due to the damage is of great importance to have a good fit of experimental results.

6 Conclusion

The paper presents the results of tests performed on a historical masonry chimney and its damage evaluation. The studied masonry chimney exhibits a clear and well visible crack pattern. To evaluate the safety condition and to design rehabilitation interventions, an extensive non-destructive test campaign was performed. The test campaign involved a geometrical and crack pattern survey, material characterization, and ambient vibration testing. The measured accelerations allow for a clear identification of nine natural frequencies and the corresponding mode shapes. Based on the identified modes, a finite element model is calibrated to match as well as possible the experimental modal properties. The stiffness properties of the model elements are adjusted so that to represent the actual damaged state of the structure. Instead of a uniform modification of the stiffness, a variable stiffness distribution is determined by means of damage patterns. In the paper, the damage function are defined as functions of the section stiffness EI . To take into account the different damage pattern in the two principal directions, two different values of the elastic modulus are assumed, one for each direction, and adjusted separately. Moreover, two different damage functions are investigated: a piecewise linear damage pattern and a polynomial damage function.

Results show that the two considered damaged functions provide quite different elastic modulus distributions, and therefore different damage distributions. Nevertheless, the modal properties corresponding to the different stiffness distributions are very similar. Some differences in the mode shapes are observed in between the monitored positions. This implies that, even for a simple structure that mainly behaves as a cantilever beam, a higher number of measuring points along the height of the chimney is needed for damage localization purposes. Indeed, a high number of sensors and, consequently, of identified modes would make it possible to introduce several calibration parameters allowing for a more accurate damage localization. Moreover, the estimated damage distributions only partially match the observed crack pattern. In particular, cracks are mainly observed from the height of 19 m to the top, while numerical results obtained adopting the piecewise linear damage function and the polynomial damage function indicate that damage are mainly located in the range 25–35 m and 25–30 m, respectively. For both the considered damage functions, obtained values of the damage coefficients indicate possible inaccuracies in the structural model related to the lack of knowledge of the actual structural geometry. Indeed, damage coefficients are applied to the section stiffness EI and not only

to the elastic modulus. Hence, damage coefficients greater than one may indicate that the actual moment of inertia I of the cross section is greater than the modeled one. Similarly, the great reduction of the section stiffness obtained at the base may indicate that a hollow cross section is present rather than a full cross section.

Despite the low number of sensors, the comparison with the results obtained from a uniform distribution of stiffness confirms the importance of considering damage patterns to represent the actual structural behavior.

References

1. Ubertini F, Comanducci G, Cavalagli N (2016) Vibration-based structural health monitoring of a historic bell-tower using output-only measurements and multivariate statistical analysis. *Struct Health Monit* 15(4):438–457
2. Bassoli E, Vincenzi L, Bovo M, Mazzotti C (2015) Dynamic identification of an ancient masonry bell tower using a MEMS-based acquisition system. In: IEEE workshop on environmental, energy and structural monitoring systems EESMS 2015. Institute of Electrical and Electronics Engineering (IEEE), Trento, Italy, pp 226–231
3. Aoki T, Sabia D (2006) Structural characterization of a brick chimney by experimental tests and numerical model updating. *Masonry Int* 19:41–52
4. Górski P, Chmielewski T (2008) A comparative study of along and cross-wind responses of a tall chimney with and without flexibility of soil. *Wind Struct* 11(2):121–135
5. Minghini F, Milani G, Tralli A (2014) Seismic risk assessment of a 50 m high masonry chimney using advanced analysis techniques. *Eng Struct* 69:255–270
6. Pallares FJ, Ivorra S, Pallares L, Adam JM (2009) Seismic assessment of a CFRP-strengthened masonry chimney. *Struct Build* 162:291–299
7. Magalhães F, Cunha A, Caetano E (2012) Vibration based structural health monitoring of an arch bridge: from automated OMA to damage detection. *Mech Syst Sig Process* 28:212–228
8. Bursi OS, Kumar A, Abbiati G, Ceravolo R (2014) Identification, model updating, and validation of a steel twin deck curved cable-stayed footbridge. *Comput Aided Civil Infrastruct Eng* 29(9):703–722
9. Zonta D, Glisic B, Adriaenssens S (2014) Value of information: impact of monitoring on decision-making. *Struct Control Health Monit* 21(7):1043–1056
10. Fan W, Qiao P (2011) Vibration-based damage identification methods: a review and comparative study. *Struct Health Monit* 10:83–111
11. Van Overschee P, De Moor B (1996) Subspace identification for linear systems: theory- implementations-applications. Kluwer Academic Publishers, Dordrecht, Netherlands
12. Peeters B, De Roeck G (2001) Stochastic system identification for operational modal analysis: a review. *ASME J Dyn Syst Meas Control* 123:659–667
13. Reynders E (2012) System identification methods for (operational) modal analysis: review and comparison. *Arch Comput Methods Eng* 19(1):51–124
14. Teughels A, Maeck J, De Roeck G (2002) Damage assessment by FE model updating using damage functions. *Comput Struct* 80:1869–1879
15. Vincenzi L, Savoia M (2015) Coupling response surface and differential evolution for parameter identification problems. *Comput Aided Civil Infrastruct Eng* 30(5):376–393
16. Vincenzi L, Gambarelli P (2017) A proper infill sampling strategy for improving the speed performance of a surrogate-assisted evolutionary algorithm. *Comput Struct* 178:58–70
17. Tondi M (2018) Innovative model updating procedure for dynamic identification and damage assessment of structures. PhD Thesis, University of Bologna, Italy

Evolution of Modal Parameters of a Reinforced Concrete Building Subjected to Moderate Earthquakes



Davide Arezzo, Vanni Nicoletti, Sandro Carbonari, and Fabrizio Gara

Abstract Results of the dynamic monitoring carried out on a school building located in central Italy during the seismic sequence following the main shock of 2016 Central Italy earthquake are presented in this work. The building, located in the historical centre of Camerino (Marche Region), consists of a reinforced concrete frame structure with masonry infill walls. The school was built in the 1960s and was seismically retrofitted in 2013 through the construction of two dissipative towers, according to a recent patented system for the seismic protection of constructions. The system consists on steel truss towers built outside the building, pinned at their base and connected to the building through braces at the floor levels. Towers are equipped with dissipative devices that activate for the rocking of the tower triggered by the building displacements. In August 2016 a dynamic monitoring system was installed on the building, positioning accelerometers both at the last two floors of the structure and at the foundation level. The system allowed the recording of the building response to the aftershocks occurred during the monitoring period, and of the corresponding seismic input. Registrations are used to track of the modal parameters of the structure identified through input–output techniques (N4SID) in occurrence of seismic events, and through consolidated output-only techniques (SSI) in the periods between two subsequent events.

Keywords Structural health monitoring · Infilled RC frame building · Ambient vibrations · Seismic monitoring · Earthquake swarm · Dynamic system identification · Time-varying systems

D. Arezzo (✉) · V. Nicoletti · S. Carbonari · F. Gara
Department ICEA, Università Politecnica Delle Marche, Ancona, Italy
e-mail: d.arezzo@pm.univpm.it

V. Nicoletti
e-mail: v.nicoletti@pm.univpm.it

S. Carbonari
e-mail: s.carbonari@univpm.it

F. Gara
e-mail: f.gara@univpm.it

1 Introduction

Permanent monitoring systems in civil engineering structures are powerful tools to monitor the structure behavior and its changes during the time as well as to get useful information about the structure condition during and after a seismic event. Furthermore, a continuous dynamic monitoring allows the reduction of the seismic risk through the reduction of uncertainties related to the structural vulnerability, provided by information on the structural response subjected to inputs of different intensities occurring during the monitoring period.

With reference to high intensity earthquakes, the availability of simple and direct relationships between the variation of the modal parameters, with respect to the undamaged structure, and the expected damage level, are of the utmost importance for the practical utility of the data collected by monitoring systems [1]. These relationships depend on the structural typology and their calibration presents intrinsic problems related to the variability of the modal parameters of the structure both with respect to the intensity of the excitation and the environmental conditions [2–7]. The aforementioned aspects make the vibration-based damage identification a non-trivial problem. Different works can be found in the literature focusing on historic masonry buildings [8–10] while reinforced concrete structures are less investigated. With reference to frequency variations of reinforced concrete buildings during strong seismic events, an interesting state of the art of the problem can be found in the work by Calvi et al. [11]. More recently, the variation in modal parameters of civil structures subjected to seismic actions has been the subject of several studies [1, 12, 13]. However, the number of case studies analyzed and the scientific results available in literature are not enough to define a consolidate state of the art.

This work presents the dynamic response of a reinforced concrete school building in Camerino (Macerata, Italy) during the seismic swarm that followed the first main shock of the 2016 central Italy Earthquake. After a description of the case study and of the seismic retrofit carried out in 2013, a description of the measurement chain and the sensor configurations used for the dynamic measurements and for monitoring is reported. Finally, the results obtained from three days of continuous monitoring are addressed and discussed. During this period many shocks of medium–low intensity occurred but, although the building did not suffer appreciable damage, before the seismic event that occurred in October 2016, the modal parameters of the structure undergo significant variations with the level of the seismic input.

2 The Case Study

The building under study (Fig. 1) dates to the 1960s and was born from the choice to expand the old masonry building, which hosted the Liceo Ginnasio Napoleonico since 1833 and, before, the Convent of Santa Elisabetta. Part of the new building is founded on the rest of the Convent, while the other part is founded directly on the

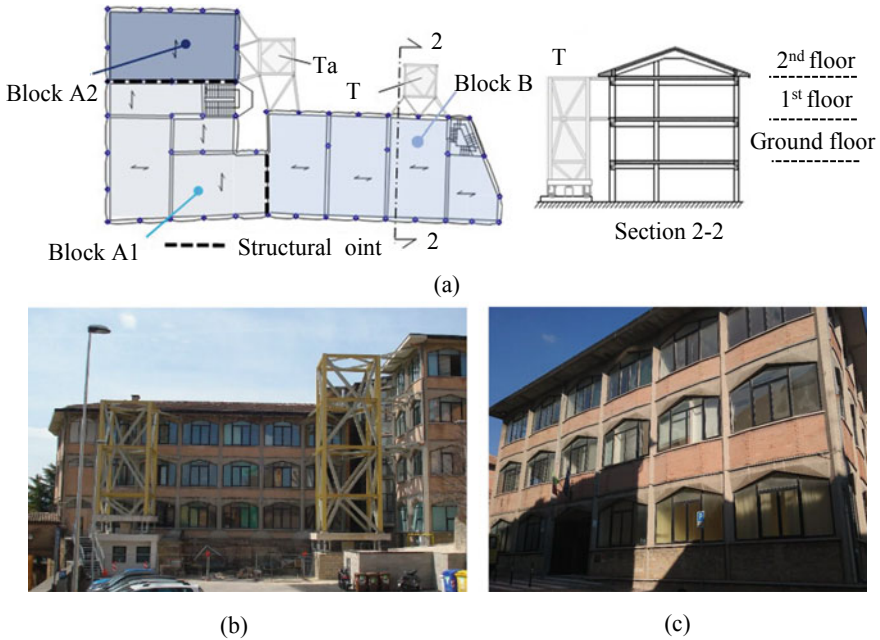


Fig. 1 The Costanza da Varano high school: **a** plan view and cross-section; **b** photo of the building with the Dissipative Towers; **c** photo of the facade of the building

ground. The building has an L-shaped plan consisting of two wings, indicated in Fig. 1a with “A” and “B”, with dimensions of approximately 12×19 m and 13×27 m, respectively. The two blocks are separated at all the levels of the building by a construction joint with a width of 2 cm. Wing “A” is divided into two rectangular areas, indicated in Fig. 1a with “A1” and “A2”, and separated by a second construction joint. Wing “A” rises for 4 floors, one of which is underground, while wing “B” rises for three floors coplanar to the first 3 floor of wing “A”. Overall, the total height at the roof is 20.40 m for block “A” and 14.05 m for block “B”. The two wings also differ in the type of foundations: block “B” is founded, through plinths, on the historic walls of the old convent which is in turn founded on sandstone rock; wing “A” is directly founded through plinths on sandstone rock. The structure consists of reinforced concrete frames; the beams have rectangular cross sections, except those along the perimeter, which are characterized by variable cross sections. Columns have square cross sections, rotated of 45° with respect to the direction of the frames for architectural reasons. All columns have 35×35 cm cross sections, excepting for two central columns of block “A” that have a 42×42 cm cross section. The floors are reinforced concrete and hollow tiles mixed floor with a thickness of $20 + 4$ cm while the infill panels are masonry walls. In 2013 a seismic retrofit was carried out through the construction of two Dissipative Towers [14], one connected to both block “A” and block “B” (Tower A), and the other one connected to the block “B” (Tower

B) (Fig. 1b). The Towers and the building interact at the floor levels through steel braces. Furthermore, the blocks were structurally connected each other with thick steel plates anchored to the RC elements in correspondence of the structural joints.

The Towers are located on a thick reinforced concrete plate that is connected through a central spherical hinge to a second plate founded on piles. The Towers have a twofold aim: (i) to linearize the deformation in order to obtain a constant floor drifts, and (ii) to increase dissipation during a seismic event, through viscous dampers located between the two concrete plates at the base. Dampers work for the relative vertical velocities between the two bases of the Tower, being the motion of the upper one triggered by the tower overall rotation induced by the building displacements. More details on the intervention can be found in Balducci et al. [15] and in Gara et al. [16].

3 Dynamic Tests and Monitoring

After the earthquake that struck central Italy on 24 August 2016, a dynamic monitoring system has been installed on the building. Before the monitoring installation, ambient vibration measurements have been carried out in order to perform a preliminary identification of the building dynamics and to provide a set of benchmark data through which future variation of the modal properties could be tracked.

Figure 2a and b, show the sensors arrangement on a typical floor plan. As for the preliminary identification, measurements have been pre-treated through signal processing techniques consisting in a first visual check, the elimination of spikes and spurious trends, a 51.2 Hz resampling to decrease the computational burden, and the application of a low pass filter at Nyquist frequency. The identification of the modal parameters has been carried out through the consolidated SSI-COV algorithm (Covariance Driven Stochastic Subspace Identification).

Figure 2c shows the first three identified modal shapes associated with the first three eigenfrequencies, while from the MAC matrix of Fig. 2d, it is possible to observe that the modal shapes are decoupled.

Finally, to interpret the results of the identification, a finite element model has been developed, and updated based on the results of the identification. Figure 2e shows the numerical modal shapes while Fig. 2f shows the MAC matrix obtained by comparing the numerical and experimental modal shapes. Finally, in Table 1, results of the preliminary identification are compared with results obtained from the calibrated model.

After the preliminary measurements, a continuous dynamic monitoring system has been installed on the structure placing sensors at the foundation level and on the top two floors of the building in order to measure both the seismic input and the structural response. The adopted sensors arrangement is the same of Fig. 2a and the data analyzed in this work are related to the first 3 days of monitoring.

Table 2 shows the main characteristics of the events for which the structure response has been recorded, sorted by decreasing intensity. The event of greater

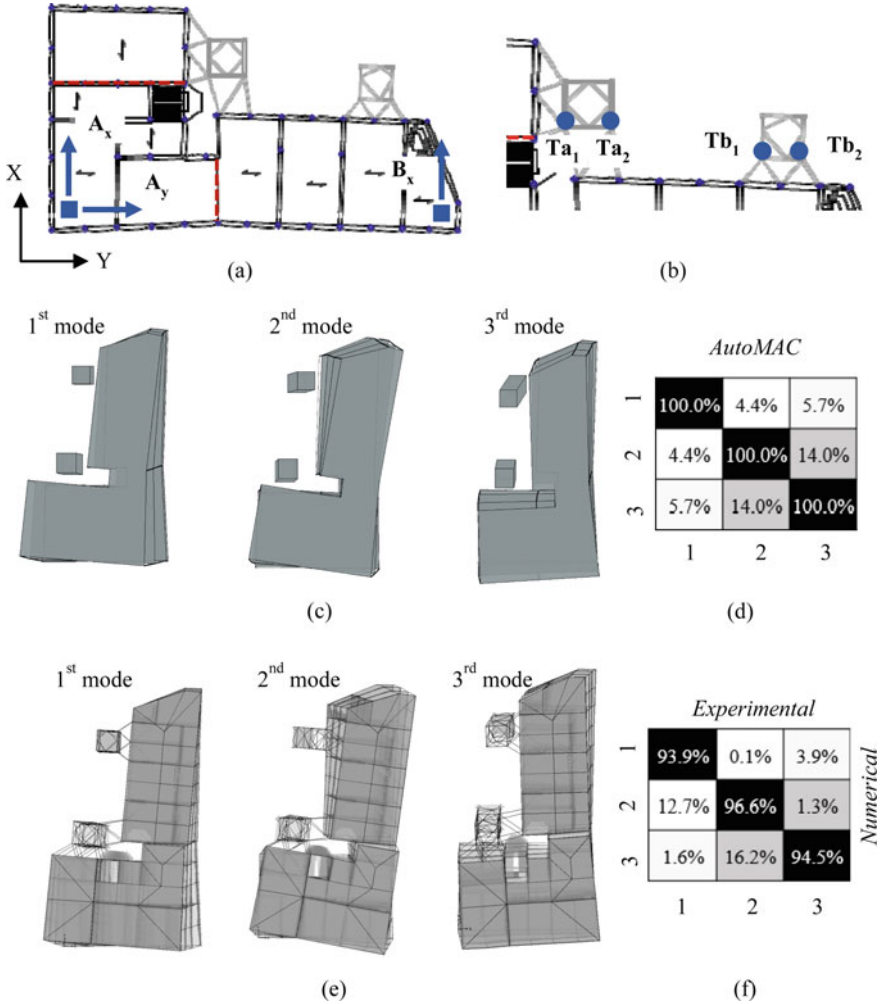


Fig. 2 Preliminary identification and modal updating: **a** sensors arrangement on the typical floor plan; **b** sensors at the base of the Dissipative Towers measuring in the vertical direction; **c, d** results of the preliminary identification; **e, f** results of the modal updating procedure

Table 1 Results of the preliminary identification and of the modal updating procedure

Mode	OMA			Updated FE	
	f [Hz]	ζ [%]	Complexity (MCF) [%]	f [Hz]	Err. [%]
1	3.49	1.62	1.65	3.50	0.29
2	3.63	1.20	0.64	3.81	4.72
3	4.05	1.42	0.63	4.14	2.17

Table 2 Seismic events occurred during the monitoring days

Event n	Intensity [ML]	Hypocentre [km]	Epicentre [km]	Date (2016)	Time
1	4.4	9	36.93	Aug. 28th	5:55 pm
2	3.8	9	35.40	Aug. 28th	6:42 pm
3	3.7	9	61.97	Aug. 28th	3:07 pm
4	3.6	10	43.47	Aug. 29th	8:20 am
5	3.6	12	40.30	Aug. 28th	5:37 pm
6	3.5	10	42.26	Aug. 29th	3:44 am
7	3.4	11	62.03	Aug. 27th	11:31 pm
8	3.4	11	46.88	Aug. 28th	8:37 am
9	3.2	8	59.20	Aug. 28th	11:18 am
10	3.1	8	45.02	Aug. 28th	10:22 pm
11	3.1	9	62.03	Aug. 28th	7:16 am
12	3.0	7	39.83	Aug. 28th	9:59 am
13	3.0	10	39.42	Aug. 28th	12:25 pm
14	2.9	8	59.75	Aug. 28th	8:13 am
15	2.9	10	60.11	Aug. 28th	1:53 am
16	2.8	11	46.83	Aug. 28th	6:25 pm
17	2.8	10	57.24	Aug. 27th	11:26 pm
18	2.8	10	37.31	Aug. 27th	7:50 pm
19	2.8	11	41.97	Aug. 28th	4:40 am
20	2.8	9	45.44	Aug. 29th	6:04 am
21	2.8	10	44.94	Aug. 28th	2:44 pm
22	2.7	9	61.41	Aug. 28th	10:00 pm
23	2.7	10	38.31	Aug. 28th	12:44 am
24	2.6	10	34.69	Aug. 27th	6:55 pm
25	2.6	10	39.20	Aug. 28th	5:34 pm

intensity, of magnitude 4.4, occurred on August 28, at about 37 km far from the building. During all the events, the structure has shown a non-linear response which made it difficult to identify its modal parameters from the seismic response. Figure 3 shows a time–frequency analysis, performed using the Short Time Fourier Transform (STFT), carried out on the measurement of the event of magnitude 4.4 for the sensor at the top floor (Ay position). From Fig. 3, it is possible to observe the non-stationarity of the structural response and this has led to the need of implementing a method to linearize the structural response.

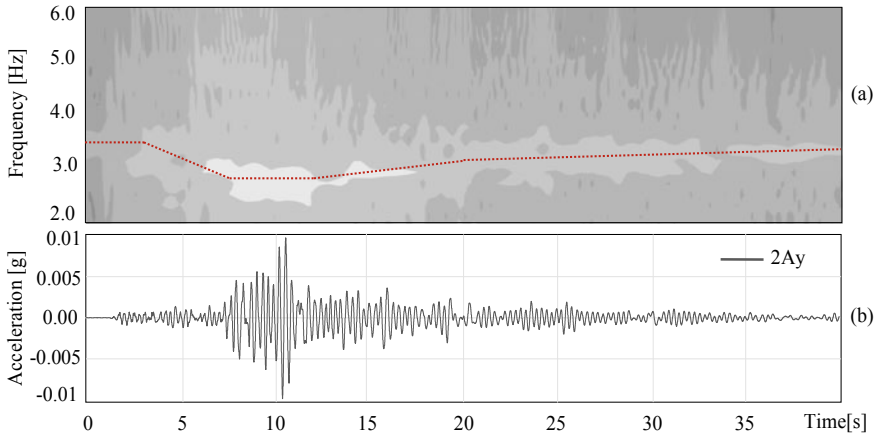


Fig. 3 Time–frequency analysis of the seismic response to the 4.4 ML event: **a** STFT of the time history registered in the measuring point Ay at the last floor, **b** time history registered in the measuring point Ay at the last floor

4 Identification Methodology and Monitoring Results

For the dynamic identification of complex multi-input multi-output systems (MIMO), subspace identification methods can be considered among the most robust and most used algorithms in the civil engineering field. In particular, two of the most commonly used algorithms for combined MIMO systems identification (deterministic and stochastic) are the Multivariable Output Error State Space (MOESP) [17] and the Numerical algorithm for Subspace State Space System Identification (N4SID) [18].

Many works can be found in the literature in which these algorithms have been successfully used for dynamic identification of full-scale case studies during seismic events [19–22].

The use of the subspace identification algorithms requires the description of the dynamic system in the state space, through the following set of equations, including a state equation (Eq. 1) and an output equation (Eq. 2):

$$\mathbf{x}_{k+1} = \mathbf{A}\mathbf{x}_k + \mathbf{B}\mathbf{u}_k + \mathbf{w}_k \tag{1}$$

$$\mathbf{y}_k = \mathbf{C}\mathbf{x}_k + \mathbf{D}\mathbf{u}_k + \mathbf{v}_k \tag{2}$$

where $\mathbf{u}_k \in \mathbb{R}^m$ and $\mathbf{y}_k \in \mathbb{R}^l$ denotes the input and output signals, respectively, at a certain time k , while $\mathbf{x}_k \in \mathbb{R}^n$ is the state vector. In addition, $\mathbf{A} \in \mathbb{R}^{n \times n}$ is the dynamical system matrix, $\mathbf{B} \in \mathbb{R}^{n \times m}$ is the input matrix that describes how the deterministic inputs influence the next state, $\mathbf{C} \in \mathbb{R}^{l \times n}$ is the output matrix that characterizes how the internal state influence the outputs and $\mathbf{D} \in \mathbb{R}^{l \times m}$ is the direct transition matrix. For a linear time-invariant system above matrices are constant.

Furthermore, $w_k \in \mathbb{R}^n$ and $v_k \in \mathbb{R}^l$ are unmeasurable vector signals, which are assumed to be normally distributed, zero mean, white noise signals.

As we observed in the previous paragraph, the structural response to the seismic events of the building at hand is clearly time variant and the state space system matrices change over the time k . Several works in the literature propose methods for identifying time-variant systems. In particular, some attractive algorithms are the MOESP-VAR [22], the N4SID-VAR [23], and the one proposed in Loh and Chen [24]; in the latter, an interesting application can also be found for a full-scale case study.

In this work, we propose an iterative procedure for the identification of the dynamic time-variant system, based on the optimization of the number of samples, and therefore the length of the signal windows, in which the system dynamics can be described as a linear time-invariant process. The length of the first window is selected from the results of the time–frequency analysis and varied until the identified dynamic model accurately reproduces the experimental response from the experimental input. The steps of the optimization procedure are summarized in the flow chart reported in Fig. 4; the identification within each window has been made through the “robust combined algorithm” proposed by Van Overschee and De Moor in [18]. The accuracy of the identified model in reproducing the response of the building is assessed using the comparison metrics proposed by Kavrakov et al. [25], which consider different signal properties, namely phase, peak, root mean square and also signal differences in the time–frequency plane through a wavelet transform based metric.

Figure 5 shows the results obtained by applying the proposed procedure on the seismic response of the building to the magnitude 4.4 event. In particular, Fig. 5a

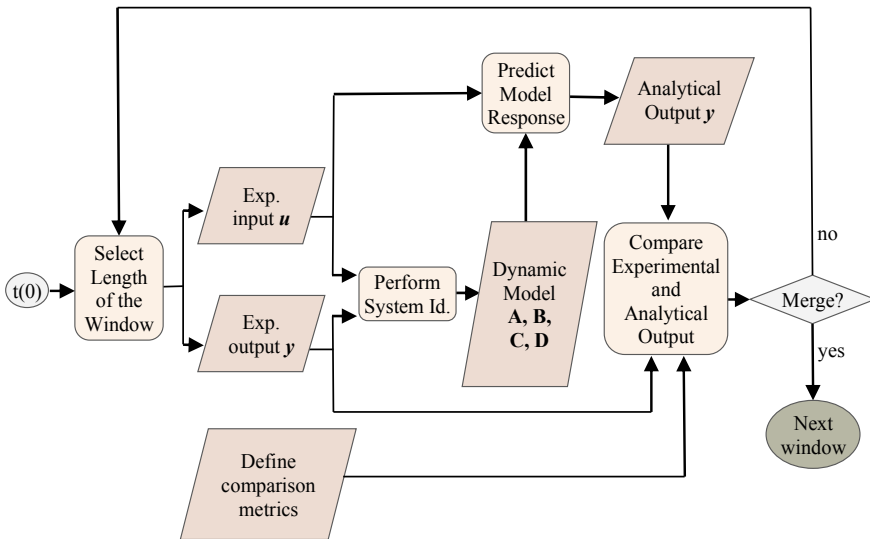


Fig. 4 Flow chart of the proposed methodology

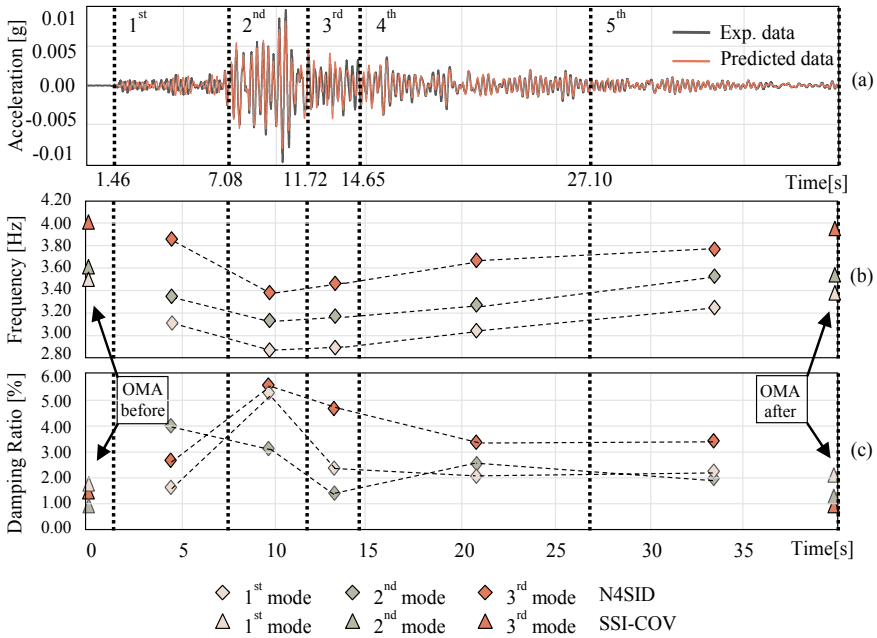


Fig. 5 Results of the identification carried out on the structural response to the 4.4 magnitude event

shows the comparison between the signal recorded at measurement point Ay at the top floor and the response estimated from the identified dynamic time-variant system.

Figure 5b and c show results in terms of modal parameters (resonance frequencies and damping ratios) and reveal how the first three frequencies of the structure decrease during the strong motion and then gradually return to the initial values at the end of the event; an opposite trend is observed for the damping ratios.

This procedure was carried out on the structural responses to all the earthquakes recorded during the three days of monitoring. By only considering the modal parameters identified in the strong motion window, Fig. 6 shows the correlations between the frequencies and the damping ratios with the PGA of the events. In both correlations data are interpolated with logarithmic functions and the relevant coefficient of determination are reported in the graph.

The decrease of vibration frequencies and the increase of damping ratios with the increase of accelerations are probably due to small non-linearities in the building and to the interaction between structural and non-structural components [3, 26]. It should be noted that this phenomenon is not associated with visible damage in the structure and the ambient vibration measurements carried out at the end of the monitoring period made it possible to identify the same dynamics measured at the beginning of the monitoring. Finally, seismic events induced overall low accelerations, velocities and displacements to the structure. In detail, the latter are of the order of 10^{-1} mm at

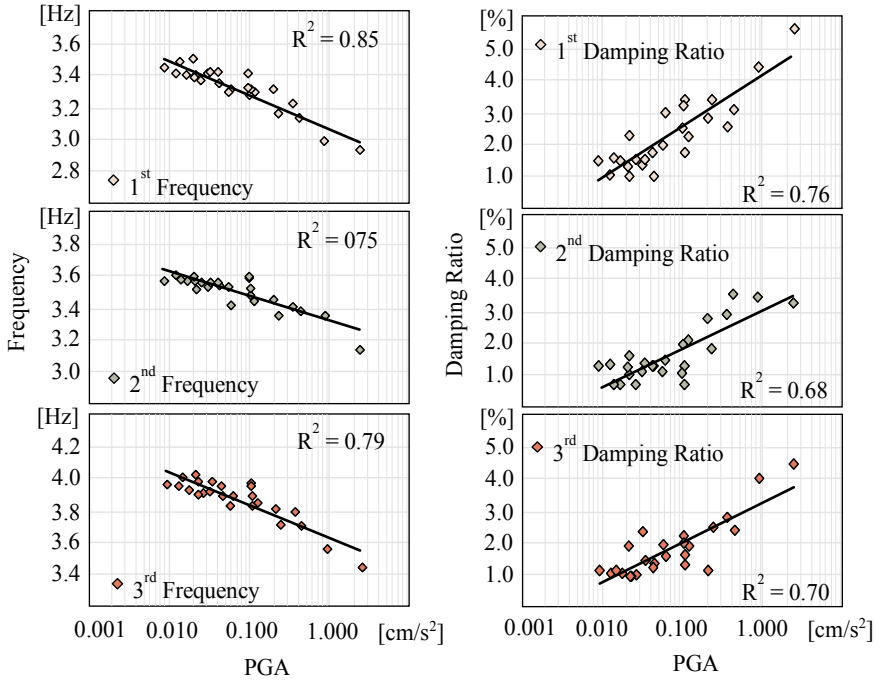


Fig. 6 Correlation between the modal parameters and the measured PGA

the second floor and of 10⁻² mm at the base of the dissipative towers, at the level of the viscous dampers, which were probably not activated during the events.

5 Conclusions

In this paper the “Varano” high school building seismic response during the seismic swarm that followed the Amatrice earthquake in central Italy on August 2016, has been analysed and a methodology to identify the building modal parameters starting from the input (seismic excitation) and output (building response) records has been proposed and validate. This methodology consists in an optimization procedure that allows to identify the structure dynamics within time windows in which the building dynamic behaviour can be considered linear time invariant. The procedure is applied to identify the building modal parameters during the twenty-five considered strong motions (with magnitude greater than 2.6). The identified dynamic system present frequency values that decrease with the increasing of the seismic intensity, expressed through the event (PGA), and damping ratios that increase with the increasing of PGA, despite the absence of damage. This work contributes, in terms of experimental

data, to enrich the state of the art of the dynamic based structural health monitoring topic.

References

1. Ceravolo R, Matta E, Quattrone A, Zanotti Fragonara L (2017) Amplitude dependence of equivalent modal parameters in monitored buildings during earthquake swarms: amplitude dependence of modal parameters in monitored structure. *Earthquake Eng Struct Dynam* 46(14):2399–2417. <https://doi.org/10.1002/eqe.2910>
2. Clinton JF, Bradford SC, Heaton HT, Favela J (2006) The observed wander of the natural frequencies in a structure. *Bull Seismol Soc Am* 96(1):237–257. <https://doi.org/10.1785/0120050052>
3. Regni M, Arezzo D, Carbonari S, Gara F, Zonta D (2018) Effect of environmental conditions on the modal response of a 10-story reinforced concrete tower. *Shock Vib* 1–16. <https://doi.org/10.1155/2018/9476146>
4. Rainieri C, Magalhaes F, Gargaro D, Fabbrocino G, Cunha A (2019) Predicting the variability of natural frequencies and its causes by second-order blind identification. *Struct Health Monit* 18(2):486–507. <https://doi.org/10.1177/1475921718758629>
5. Rainieri C, Gargaro D, Fabbrocino G (2019) Hardware and software solutions for seismic SHM of Hospitals. In: Pina Limongelli M, Çelebi M (ed) *Seismic structural health monitoring*, Springer Tracts in Civil Engineering. Cham, Springer International Publishing, pp 279–300. https://doi.org/10.1007/978-3-030-13976-6_12
6. Saisi A, Gentile C, Guidobaldi M (2015) Post-earthquake continuous dynamic monitoring of the Gabbia tower in Mantua, Italy. *Constr Build Mater* 81:101–112. <https://doi.org/10.1016/j.conbuildmat.2015.02.010>
7. Losanno D, Londono JM, Spizzuoco M (2013) Structural monitoring system for the management of emergency due to natural events. In: *IEEE Workshop on environmental, energy and structural monitoring systems, EESMS 2013—Proceedings*. <https://doi.org/10.1109/EESMS.2013.6661703>
8. Gentile C, Antonello R, Saisi A (2019) Continuous dynamic monitoring to enhance the knowledge of a historic bell-tower. *Int J Architect Heritage* 13(7):992–1004. <https://doi.org/10.1080/15583058.2019.1605552>
9. Cavalagli N, Comanducci G, Ubertini F (2018) Earthquake-induced damage detection in a monumental masonry bell-tower using long-term dynamic monitoring data. *J Earthquake Eng* 22(sup1):96–119. <https://doi.org/10.1080/13632469.2017.1323048>
10. Ubertini F, Cavalagli N, Kita A, Comanducci G (2018) Assessment of a monumental masonry bell-tower after 2016 central italy seismic sequence by long-term SHM. *Bull Earthq Eng* 16(2):775–801. <https://doi.org/10.1007/s10518-017-0222-7>
11. Calvi GM, Pinho R, Crowley H (2006) “State-of-the-knowledge on the period elongation of RC buildings during strong ground shaking. In: *ECEES First European conference on earthquake engineering and seismology*, Geneva, Switzerland, 3–8 September 2006, Paper n.1535
12. Ghahari SF, Abazarsa F, Ghannad MA, Taciroglu E (2013) Response-only modal identification of structures using strong motion data. *Earthquake Eng Struct Dynam* 42(8):1221–1242. <https://doi.org/10.1002/eqe.2268>
13. Hu R, Xu Y (2019) SHM-based seismic performance assessment of high-rise buildings under long-period ground motion. *J Struct Eng* 145(6):04019038. [https://doi.org/10.1061/\(ASCE\)ST.1943-541X.0002323](https://doi.org/10.1061/(ASCE)ST.1943-541X.0002323)
14. Balducci A (2005) “Dissipative Towers”. Application n. EP20100747238, PCT n. WO2010EP62748 20100831. International and European classification E04H9/02—Italian concession n° 0001395591

15. Balducci A, Castellano MG (2015) Adeguamento sismico del liceo Varano di Camerino mediante sistema a torri dissipative. *Progettazione Sismica* 01:69–91. <https://doi.org/10.7414/PS.6.1.69-91>
16. Gara F, Carbonari S, Roia D, Balducci A, Dezi L (2020) Seismic retrofit assessment of a school building through operational modal analysis and f.e. modelling. *J Struct Eng (ASCE)*. [https://doi.org/10.1061/\(ASCE\)ST.1943-541X.0002865](https://doi.org/10.1061/(ASCE)ST.1943-541X.0002865)
17. Verhaegen M (1994) Identification of the deterministic part of MIMO state space models given in innovations form from input-output data. *Automatica* 30(1):61–74. [https://doi.org/10.1016/0005-1098\(94\)90229-1](https://doi.org/10.1016/0005-1098(94)90229-1)
18. Van Overschee P, De Moor B (1996) *Subspace identification for linear systems*. Springer, US, Boston, MA. <https://doi.org/10.1007/978-1-4613-0465-4>
19. Skolnik D, Lei Y, Yu E, Wallace, J. W. (2006) Identification, model updating, and response prediction of an instrumented 15-story steel-frame building. *Earthq Spectra* 22(3):781–802. <https://doi.org/10.1193/1.2219487>
20. García-Illescas MÁ, Murià-Vila D, Alvarez-Icaza L (2019) Monitoring and identification of vibration frequencies on a portion of méxico city metro line 12. *Adv Civil Eng* 1–13. <https://doi.org/10.1155/2019/4128320>
21. Boroschek RL (2013) Structural health monitoring performance during the 2010 Gigantic Chile Earthquake. In: Garevski M (ed) *Earthquakes and health monitoring of civil structures*, Springer Environmental Science and Engineering. Dordrecht, Springer Netherlands, pp 197–216. https://doi.org/10.1007/978-94-007-5182-8_8
22. Tamariz ADR, Bottura CP, Barreto G (2005) Iterative MOESP type algorithm for discrete time variant system identification. In: *Proceedings of the 2005 IEEE international symposium on, Mediterrean conference on control and automation intelligent control*, Limassol, Cyprus, IEEE, pp 399–404. <https://doi.org/10.1109/2005.1467048>
23. Robles AE, Giesbrecht M (2018) N4SID-VAR method for multivariable discrete linear time-variant system identification. In: *Proceedings of the 15th international conference on informatics in control, automation and robotics*, Porto, Portugal, SCITEPRESS—Science and Technology Publications, pp 502–529. <https://doi.org/10.5220/0006907505020509>
24. Loh C, Chen J (2017) Tracking modal parameters from building seismic response data using recursive subspace identification algorithm: tracking modal parameters using recursive subspace identification. *Earthquake Eng Struct Dynam* 46(13):2163–2183. <https://doi.org/10.1002/eqe.2900>
25. Kavrakov I, Ahsan K, Morgenthal G (2020) Comparison metrics for time-histories: application to bridge aerodynamics. *J Eng Mech* 146(9):04020093. [https://doi.org/10.1061/\(ASCE\)EM.1943-7889.0001811](https://doi.org/10.1061/(ASCE)EM.1943-7889.0001811)
26. Nicoletti V, Arezzo D, Carbonari S, Gara F (2020) Expeditious methodology for the estimation of infill masonry wall stiffness through in-situ dynamic tests. *Constr Build Mat* 262:120807

Innovative Non-destructive Technique for the Structural Survey of Historical Structures



Alessio Cascardi, Andrea Armonico, Francesco Micelli,
and Maria Antonietta Aiello

Abstract Masonry heritage buildings are typically vulnerable under seismic forces, due to the original design based on gravity load and, at the same time, the long-term decay effects. Nowadays, the computation of the vulnerability index is crucial for seismic evaluation and conservation strategies. An accurate geometric survey is a keystone for the knowledge process, especially in geometry-governed structural elements (e.g. in vaults, members with variable cross-section, etc.). In the case of a huge building, scaffolding is commonly assessed in order to *touch* the structure for measuring or sensors installing (e.g. laser scanner). Minor damages are accepted when scaffoldings are fixed to the structure even in case of cultural heritage. In the present study, an innovative drone-based technique for the geometric survey, which aims to be fully non-destructive, is proposed. A drone is equipped with a high-resolution camera (3D rotating) and GPS-system for the spatial positioning. By reaching a sufficient number of photos, the whole surface of the building can be covered. The database is then processed in order to compute a points cloud. Consequently, the points are linked and the wireframe model is reached. Finally, surfaces are generated between the edges and the meshed model is made by a proper visual code. The procedure is intended to be reproduced over time for monitoring potential crack or local instability. In order to demonstrate the validity of the proposal, a *pilot building* was selected. It is a masonry church with a large dome on the top (about 15 m diameter) and the variable thickness of the walls (about 50%). The indoor and outdoor photos were acquired by drone. Finally, the solid model was met by means of a specific designed *Grasshopper-based code*. In addition, the solid model was imported in a finite elements environment.

A. Cascardi · M. A. Aiello

ITC—Construction Technology Institute, CNR—Italian National Research, Bari, Italy

A. Armonico (✉)

University of Lyon, University Lyon1, Laboratory of Composite Materials for Construction (LMC2), 82 bd Niels Bohr, 69622 Villeurbanne, France

e-mail: andrea.armonico@univ-lyon1.fr

F. Micelli · M. A. Aiello

Department of Innovation Engineering, University of Salento, Lecce, Italy

Keywords Masonry · Heritage · Seismic · Survey · Drone · Monitoring

1 Introduction

The history of construction is characterized by a large diffusion of huge and complex structures, whose geometry and state of conservation changed over the centuries. Many renowned cases of structures are significantly different from their initial conception (e.g. *Rome's Colosseum* or *Pisa's Tower*). It is worthy mentioned both the mechanical and geometrical parameters should be monitored over time.

During the last decade, the scientific community focused on assessing the material mechanical properties by means the development of several in-situ tests. While the full definition of a procedure for the full detection of their geometry is still a challenge.

For instance, thickness, curvature, and inclination are essential factors in case of curved structures where geometry-based equilibrium laws govern the stability. Likewise, often a regularized geometry is considered for structural analysis even if the outcomes could be inaccurate. Ancient buildings present local displacements and/or rotation that could change their behaviour (e.g. *Hagia Sofia's Basilica*), so the safety indexes respect to equilibrium limit often result strongly reduced. Arches, vaults and domes behaviour is strictly connected with geometry: curvature and variable thickness generally trigger mechanisms instead of materials limit strength, [1].

For these reasons, the paper is focused on a new methodology aimed to reduce geometric uncertainty. A non-destructive strategy was assessed by means of a commercial drone use. The procedure aims to obtain a digital model of buildings from a number of high-definition photos. A computer processing and the relative virtual mode are then performed by photogrammetry software (e.g. *Agisoft Metashape*) using *structure from motion* algorithm (SFM), [2]. First the point clouds and mesh are computed. In a second step, *Rhinoceros* (with *Grasshopper* plug-in) is used for a 3D modeling (see [3]) before FEM (Finite Elements Method) analysis.

St. Mary at the Gate's Church, in Lecce (Italy), is a particularly significant case study due to several features linked to geometry. In fact, irregularity in height, curvature and a huge dome make this structure strongly governed by equilibrium laws. In fact, the church has a series of empty spaces indoor (e.g. semi-domes, arches) and a 15 m diameter dome at the top as visible in Fig. 1. Thus, the paper reports first on the geometrical acquisition (issues and strategies for the survey); then post-processing, 3D modeling and finally a structural analysis performed with *Midas FEA*TM software [4] are illustrated.

2 Survey Strategies: The State of the Art

Commonly, the geometry is defined according to simplified models or by means of a few points' detection. In fact, physical meters or laser meters were largely adopted

Fig. 1 St. Mary at the Gate's dome



by practitioners from the late past. In the case of thickness investigations, holes were performed by an electrical drill; i.e. in a destructive way.

A historical building, located in India, was investigated to identify the cause of the manifest damage pattern, [5]. A lack of geometric information could lead to underestimate equilibrium-dominated problems. Generally, in curved masonry structures, local collapse due to loss of equilibrium, anticipates that due to overcoming the materials strength. Even if cracks were observed, the model was assumed un-damaged, for a faster modeling. Often, structural evaluation starts from un-damaged configuration while the load history identification is set as the target. Alternatively, undisturbed conditions are considered in a simplified approach, e.g. in [6].

In other cases, technical drawings are not available or are not sufficiently detailed. In such a way, engineer does not have a real knowledge of the thickness and the internal structure of the masonry wall. An example is described in [7] where a Turkish Mosque was modeled for a retrofitting design. The authors considered a complex geometry with the aim of reducing geometric uncertainties. The top dome was modelled by means of four different thickness shells. This modelling strategy generates geometrical discontinuity zones that produce issue in the generation of a FE model.

New technologies have been recently developed for acquiring geometry with improved accuracy. In such way, the *laser scanner* application results in a possible accurate solution; i.e. a source (laser) and a number of targets (sensors) make the measuring networks. Commonly, a huge number of points is acquired causing a severe computational cost.

Alternatively, photogrammetry tools represent a low-cost and, at the same time, full removable option. It delivers from topographic theory, whose application demonstrated appreciable results in the past. Nowadays, it finds interesting to use in the field of structural engineering. Examples are provided in [8–10], where valuable accuracy of the survey was met with null on-site risk. As for the laser scanner

method, photogrammetry allows obtaining a surface (usually outdoor). No expensive machines are required. This strategy exhibited good results that are time-saving with respect to the others; especially concerning constant thickness structure. Once detected the case study's geometry, it needed to use a tool for the Scan-to-FE step i.e. the transition from half-raw survey data (point clouds) to FE models. New trends are based on visual code, which allows the user to easily connect data arising from different sources while keeping a clear understanding of the relationships thanks to the flow chart representation [11]. These user-friendly digital tools are spreading great interest in the scientific community being also applied for the implementation of algorithms for the fast structural assessment of structures [12–14].

3 St. Mary at the Gate's Church: A Digital Acquisition for a Smart Monitoring

St. Mary at the Gate's Church in Lecce was built in 1855 with subsequent restoration in 1917. It is the building with the largest dome in the area (Fig. 2). At the top, a skylight diffuses light along with four semicircular windows. Vertical masonry presents empty spaces with arched openings and semi-domes, which make the identification of the building's resistant *skeleton* very uncertain, [15]. With one-axe symmetry, the building develops in 300 m² area. Currently, the structure does not manifest cracks or settlements.

Fig. 2 Bird's eye view of the building



3.1 Geometrical survey

In order to obtain a volume survey, a new strategy was used in this study. A number of high-definition photos were obtained by scheduled flights of a drone equipped with a digital camera. More details about this technique are provided in [16–20]. In particular, two stages were performed independently for the outdoor and the indoor survey, respectively taking a total of 272 high-definition photos. In order to achieve an accurate survey, photogrammetry software (i.e. *Agisoft Metashape*) requires ad photo overlapping factor. Likewise, a multiple low-altitude flights is needed, aimed to obtain a smaller *Ground Sample Distance* (GDS), allowing to define camera 3D-locations and a sparse cloud of points (see Figs. 3 and 4 respectively), [20]. Near points interpolation allow to create a dense cloud (Fig. 5). Their links provide a meshed model (Fig. 6). A further outcome is the textured model. In fact, every point has RGB (Red, Green, Blue) information, that allow to assign a colored texture at the mesh (Fig. 7). In this way, structural engineer may monitor humidity and macroscopic crack pattern too. In this study, a 30% photo overlapping factor was set. Satisfactory accuracy of the outcome did not suggest higher overlap level. The main goal of the proposed study is the full detection of the geometry. Therefore, after acquiring the two surfaces separately, it was necessary to align them. Eight matching points were defined on the windows’ surfaces and at the top of the dome, as illustrated in Figs. 8 and 9, respectively.

Fig. 3 Alignment of the drone photos

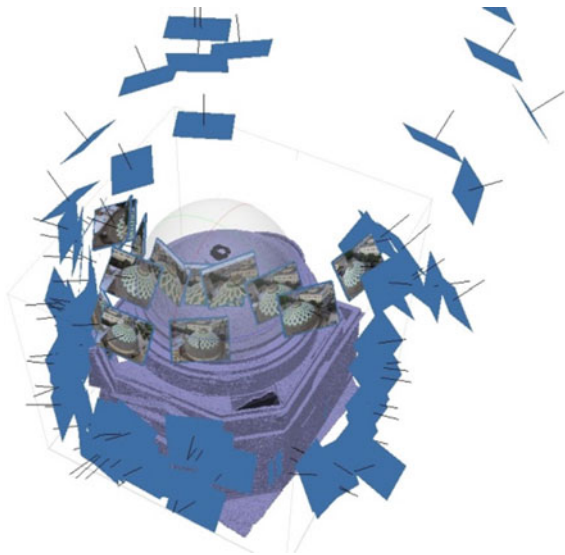


Fig. 4 Sparse cloud—146,005 points



Fig. 5 Dense cloud—84,494,750 points



3.2 Finite Element (FE) Model

Once the geometrical 3D model was completed, it was not yet suitable for a FE analysis. The Midas FEA™ code, used for the analysis, requires an *Initial Graphics Exchange Specification* file (IGES), not available in Metashape. In order to propose a solution, a general procedure for the model transformation is reported in the

Fig. 6 Meshing - 2,075,610 faces and 1,044,046 vertices



Fig. 7 Textured model



Fig. 8 Matching points

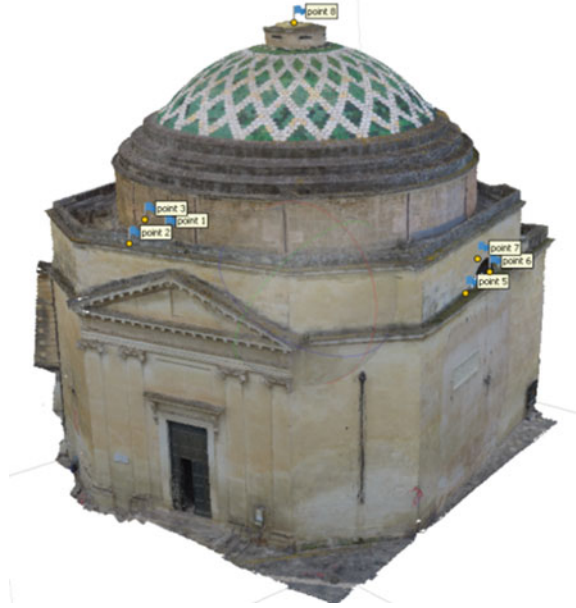


Fig. 9 Alignment of the inner and outer surfaces

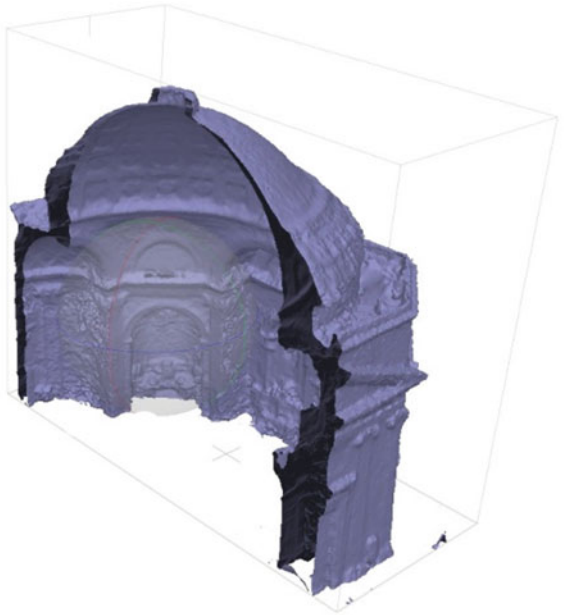
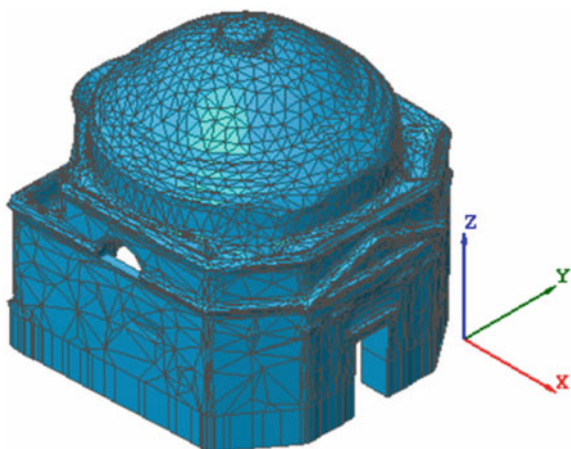


Fig. 10 Solid model imported in FE environment



following. The target is to assess a CAD (*Computer Aided Design*) model starting from the assemblage of the mesh faces generated by the joining of the cloud points. Main computational steps are:

- mesh decimation;
- assembling surfaces from mesh faces;
- generating a closed poly-surface which represent the real geometry of the structure;
- refining the geometry: introduction of the holed that represent doors and/or windows.

The workflow is all integrated into a computational tool implemented in the visual programming environment offered by *Grasshopper* 3D plug-in for *Rhino*, [21]. The so-obtained solid model is illustrated in Fig. 10., ie. Midas FEA™ habitat.

4 Analysis

Once the model was imported as a structural one, it has been discretized by means 273,497 tetrahedral elements with 300 mm length. The input data are reported in Table 1. The constitutive model was based on the total strain method with a smeared approach for the fracture energy as reported in [4]. A damage-plasticity material model for the masonry, already available in the standard software package was adopted. It allowed to reproduce a reliable non-linear behaviour with distinct damage parameters in tension and compression; i.e. [22] and [23] respectively.

Table 1 Mechanical properties of the masonry

Variable	Symbol	Unit	Value
Young's modulus	E	MPa	2500
Poisson ratio	ν	–	0.2
Weight density	γ	N/m ³	16,000
Compressive strength	f_c	MPa	6
Compressive fracture energy	G_c	N/mm	0.1
Tensile strength	f_t	MPa	0.3
Tensile fracture energy	G_f	N/mm	0.012

4.1 Modal

Masonry structures have not a consistent feedback from Eigen-frequency analysis, because of their behavior was strongly non-linear after the first seismic excitation. In this scenario, modal analysis was performed mainly to obtain coefficient necessary for non-linear static (*pushover*) procedure adopted in this study. When the participating mass of the fundamental mode is not less than 60%, the pushover analysis can be applied to masonry buildings as reported in Italian Technical Code (2018), [25]. The mathematical formulation utilized to calculate the natural frequencies is referred to an eigenvalue problem as reported in Eq. (2):

$$(K - \omega_i^2 M)\phi_i = 0 \tag{1}$$

where K is the stiffness matrix, ω_i is the i -th eigenvalue, M is the mass matrix and ϕ_i is the i -th eigenvector. Results are reported in Tables 2 and 3 in terms of modal period and mass participation factors of the first main modes. The results reflect the regular distribution of the structural shapes, due to the typical symmetry and regularity of such construction.

Table 2 Modal frequencies and periods

Mode #	Frequency (Hz)	Period (s)
1	5.57	0.180
2	5.62	0.178
3	8.27	0.121
4	8.32	0.120
5	9.01	0.111
6	12.55	0.080
7	12.79	0.078

Table 3 Modal participating masses

Mode #	Participating mass X-dir (%)	Participating mass X-dir (%)
1	0.01	80.33
2	78.29	0.01
3	0.00	0.07
4	0.26	0.00
5	0.00	0.05
6	0.00	0.00
7	0.00	0.00
8	0.02	0.00
9	3.26	0.00
10	0.00	3.41
Sum	81.84	83.87

4.2 Pushover

The Pushover analysis provides to evaluate buildings’ seismic capacity. In fact, a force field is defined under gravity loads and horizontal forces acting separately along with principal directions. As reported in Eurocode 8 (EC8) [24], every direction provides a constant-type and linear-type load pattern in order to evaluate separately a maximum base share and a maximum displacement of a control point (usually defined at the top).

A capacity curve set was obtained in the principal directions as reported in Figs. 11 and 12, in which base shear is reported on the vertical axis and control point displacement on the horizontal one. Each curve is referred to a *multi-degree of freedom system* (MDOF). EC8 gives a strategy for a seismic evaluation of the buildings by analyzing the displacement values. In order to make the capacity curves comparable, it is

Fig. 11 Capacity curves in X-direction

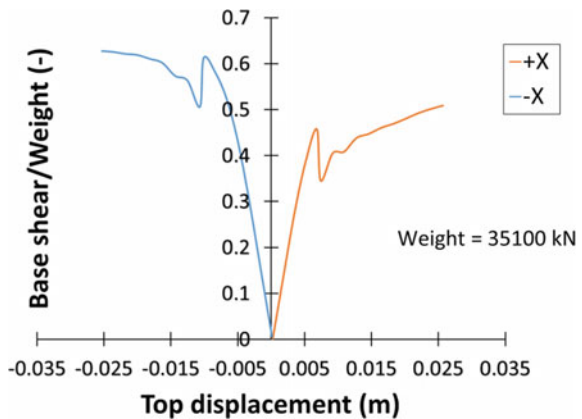
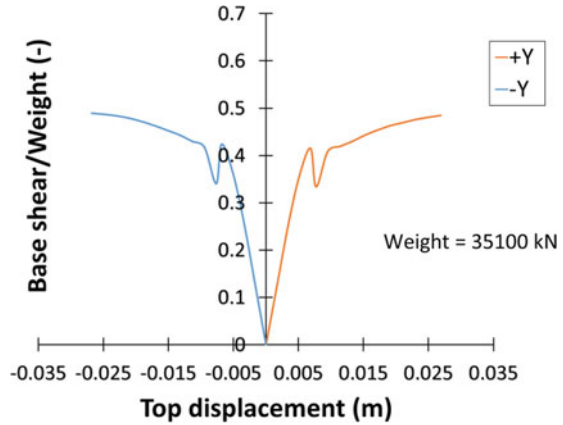


Fig. 12 Capacity curves in Y-direction



necessary to process them into an equivalent system with a *single degree of freedom* (SDOF) by means of the modal participation factor defined by the Eq. (2). In Figs. 11 and 12 the capacity curves are illustrated.

$$\Gamma = \frac{\sum m_i \phi_i}{\sum m_i \phi_i^2} \tag{2}$$

5 Results Discussion

Pushover analysis’ results provide a number of theoretical crack pattern. The Midas FEA code shows color maps in which red points represent full crack openings, while blue and violet points mean partially opened cracks as represented in Fig. 13 and 14.

For each direction, openings affect cracks propagation. In fact, as expressed by Heyman’s trust-line theory, above the openings, masonry is less almost un-load and so prone to damage. No critical issues are represented by the cracks along the meridians, also thanks to the contribution of the back-side wall. In any case, the crack pattern can be considered as a dissipative behaviour of the building for which geometry plays an important role. In this sense, an accurate geometrical survey proved to be a relevant tool for the analysis.

6 Conclusions

In this study, an innovative drone-based survey technology has been described, also by illustrating a case-study. The main objective was to provide a technique able to minimize the geometrical uncertainties. For this reason, a drone was used in

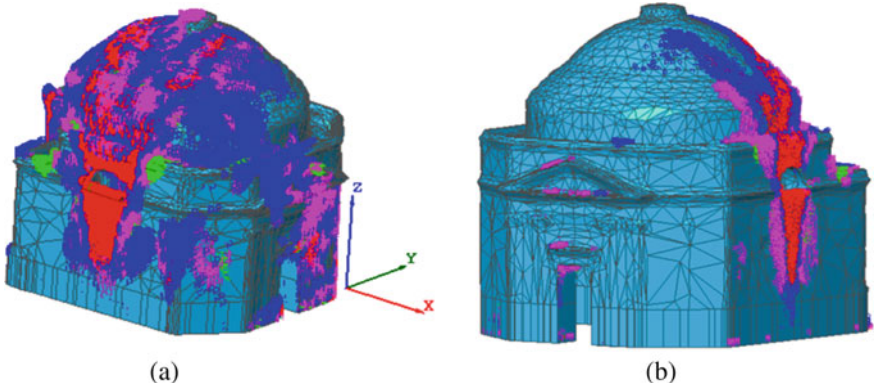


Fig. 13 Crack patterns: $-Y$ (a) and $+Y$ (b)

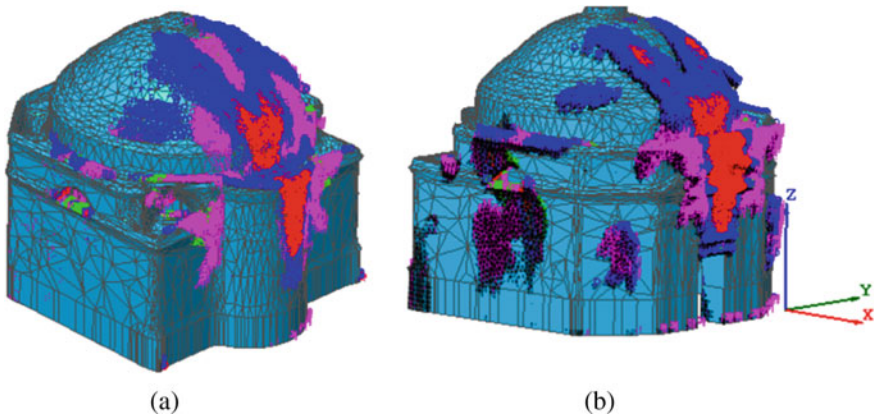


Fig. 14 Crack patterns: $-X$ (a) and $+X$ (b)

combination with the photogrammetric theory. Using a computer graphic software, a number of high-definition photos was processed in order to obtain a digital model of the building. Nevertheless, due to different working environments, some post-processing steps were necessary by means of 3D modeling software for a solid model creation. Then, in a finite element environment, structural analyses were run by means of linear dynamic and non-linear static (pushover) numerical techniques. The capacity curves in the main directions allowed to assess that the performance points of the building were found in the safety side.

The proposed procedure strongly reduces the processing time, allowing to repeat over time the survey in order to compare different life-steps of the buildings in terms of displacements and deterioration.

The proposed technique represents a fast, accurate, safe and no-destructive procedure, able to acquire complex geometry, providing a tool for monitoring and analysis, in which geometry can play an essential role in terms of balance and ductility.

References

1. Huerta S (2006) Galileo was wrong: the geometrical design of masonry arches. *Nexus Netw J* 8(2):25–52
2. Agisoft LLC, Manual AMU (2019) Professional Edition, Version 1.5; Agisoft LLC: St. Petersburg, Russia
3. Lagios K, Niemasz J, Reinhart CF (2010) Animated building performance simulation (ABPS)–linking Rhinoceros/Grasshopper with Radiance/Daysim. *Proc SimBuild* 4(1):321–327
4. Midas G (2017).MIDAS GEN-User Manual. ver 860. MIDAS IT inc.
5. Aranha CA, Menon A, Sengupta AK (2019) Analysis of the Dome of India’s presidential residence. In: *Structural analysis of historical constructions*. Springer, Cham, pp 957–965
6. Liberotti R, Cluni F, Gusella V (2020) Vulnerability and seismic improvement of architectural heritage: the case of Palazzo Murena. *Earthquakes Struct* 18(3):321–335
7. Aşıkoğlu A, Avşar Ö, Lourenço PB, Silva LC (2019) Effectiveness of seismic retrofitting of a historical masonry structure: Kütahta Kurşunlu Mosque, Turkey. *Bullet Earthquake Eng* 17(6):3365–3395
8. Marmo F, Demartino C, Candela G, Sulpizio C, Briseghella B, Spagnuolo R, Rosati L (2019) On the form of the Musmeci’s bridge over the Basento river. *Eng Struct* 191:658–673
9. Castellazzi G, D’Altri AM, de Miranda S, Ubertini F (2017) An innovative numerical modeling strategy for the structural analysis of historical monumental buildings. *Eng Struct* 132:229–248
10. Fortunato G, Funari MF, Lonetti P (2017) Survey and seismic vulnerability assessment of the Baptistery of San Giovanni in Tumba (Italy). *J Cult Herit* 26:64–78
11. Cascardi A, Micelli F, Aiello MA, Funari M (2020) Structural analysis of a masonry church with variable cross-section dome. In: *Brick and block masonry—from historical to sustainable masonry: proceedings of the 17th international Brick/Block Masonry conference (17thIB2MaC 2020)*, July 5–8, Kraków, Poland, CRC Press, pp 220
12. Funari MF, Mehrotra A, Lourenço PB (2021) A tool for the rapid seismic assessment of historic masonry structures based on limit analysis optimisation and rocking dynamics. *Appl Sci* 11(3):942. <https://doi.org/10.3390/app11030942>
13. Funari MF, Spadea S, Lonetti P, Fabbrocino F, Luciano R (2020) Visual programming for structural assessment of out-of-plane mechanisms in historic masonry structures. *J Build Eng* 31:101425
14. Turco C, Funari MF, Spadea S, Ciantia M, Lourenço PB (2020) A digital tool based on genetic algorithms and limit analysis for the seismic assessment of historic masonry buildings. *Procedia Struct Integrity* 28:1511–1519
15. Heyman J (1966) The stone skeleton. *Int J Solids Struct* 2(2):249–279
16. Micelli F, Cascardi A (2020) Structural assessment and seismic analysis of a 14th century masonry tower. *Eng Failure Anal* 107:104198
17. Trizio I, Savini F, Continenza R, Giannangeli A, Marchetti A, Redi F (2019) Photogrammetric survey and 3D GIS management of mesh in the integrated investigation of complex sites. The case study of the church of Santa Maria. In: Inglese C, Ippolito A (eds) *Conservation, restoration, and analysis of architectural and archaeological heritage*. Cesoni IGI Global, Hershey, pp 48–80
18. Parisi EI, Suma M, Güleç Korumaz A, Rosina E, Tucci G (2019) Aerial platforms (uav) surveys in the vis and tir range. applications on archaeology and agriculture. *Int Arch Photogramm Remote Sens Spatial Inf Sci XLII-2/W11*, pp 945–952. <https://doi.org/10.5194/isprs-archives-XLII-2-W11-945-2019>

19. Micelli F, Cascardi A, Aiello MA (2020) Seismic capacity estimation of a masonry bell-tower with verticality imperfection detected by a drone-assisted survey. *Infrastructures* 5(9):72
20. Khaloo A, Lattanzi D, Cunningham K, Dell'Andrea R, Riley M (2018) Unmanned aerial vehicle inspection of the placer river trail bridge through image-based 3D modelling. *Struct Infrastruct Eng* 14(1):124–136
21. McNeel RA (2010) “Rhinoceros Version 4.0, Service Release 8”
22. Reinhardt HW, Cornelissen HA, Hordijk DA (1986) Tensile tests and failure analysis of concrete. *J Struct Eng* 112(11):2462–2477
23. Thorenfeldt E, Tomaszewicz A, Jensen JJ (1987) Mechanical properties of high-strength concrete and applications in design. In: *Symposium proceedings, utilization of high-strength concrete*
24. Standard B (2005) Eurocode 8: Design of structures for earthquake resistance. Part 1, 1998-1
25. NTC LG (2018) *Norme tecniche per le costruzioni*. Italian technical norms for constructions

Structural Monitoring of a Railway Bridge in Southern Italy for Automatic Warning Strategy



Daniele Losanno, Nicola Caterino, Eugenio Chioccarelli, Carlo Rainieri, and Carolina Aiello

Abstract In the last few years, a growing interest towards structural safety of existing infrastructures has been paid. Due to very large number of structures, the scientific community is asked to provide innovative solutions that are both sustainable and reliable from the economical as well as technical point of view. This paper presents the case of Quarto bridge, selected as case study in an Italian research project for Risks and Safety Management of Infrastructures at Regional Scale (GRISIS). The structure is a railway viaduct on an urban train line, located in the Northern metropolitan area of Naples. It consists of 45 simply-supported prestressed girders sustained by reinforced concrete piers, for a total length of approximately one kilometer. According to the project, the viaduct was equipped with an on-site monitoring system for near-real-time mitigation of seismic risk. The system involves some innovative, low-cost, sensors developed and installed to be tested on the field. This paper describes the monitoring system and the implemented strategies for risk mitigation referring to a single beam-column system but its application can be potentially replicated and implemented for large scale mitigation strategies.

Keywords GRISIS project · FEM model · Innovative sensors · Monitoring system · Seismic alarm · Early warning

D. Losanno (✉)
University of Naples Federico II, 80125 Napoli, Italy
e-mail: daniele.losanno@unina.it

D. Losanno · N. Caterino · C. Rainieri · C. Aiello
Construction Technologies Institute, Secondary Branch of Naples, National Research Council of Italy (CNR), 80146 Naples, Italy

N. Caterino
University of Naples Parthenope, 80143 Napoli, Italy

E. Chioccarelli
Università Degli Studi Mediterranea Di Reggio Calabria, 89124 Reggio Calabria, Italy

1 Introduction

The GRISIS project—Risks and Safety Management of Infrastructures at Regional Scale—aims at developing methods, techniques and procedures for the risk assessment and the safety management of civil infrastructures at regional scale. The project is based on a multidisciplinary approach to achieve a holistic analysis of both natural and anthropic risks on civil infrastructures in the Campania region (Southern Italy). The main purpose of GRISIS is to develop a technological platform for overall risk management of infrastructures at regional scale.

With reference to seismic hazard, the project aims at defining active monitoring strategies that allow the implementation of real or near-real time strategies to mitigate the seismic risk. These systems belong to the broader family of so-called seismic “early warning” strategies which provide, precisely, the possibility of triggering an alarm in an “early” way and / or to implement—automatically—interventions to reduce the effects of a given earthquake on a specific component to be protected once a critical response has been recorded [1]. These strategies are based on a semi-probabilistic approach, where automatic decisions are implemented on both measured information and estimated parameters, the latter affected by uncertainties. The decision process must take into account these uncertainties and also the consequence that implementing (or not implementing) a specific intervention can produce on the community. In other words, the logic of the “early seismic alarm” cannot be separated from the optimization of decisions on a probabilistic basis, accounting for the likelihood of missed or false alarms. One of the aims of the project is also the development of low-cost technological solutions that can reasonably encourage their large-scale application for the real-time mitigation of an infrastructure network or a larger part of the territory.

Early attempts of integrating structural health monitoring and early warning systems can be found in the literature. The integration of structural monitoring and early warning systems applied to a number of bridges and public buildings in Canada is described in [2]. The issues related to sensor integration and redundancy of data acquisition and transmission systems are investigated in detail in [3]. The use of pre-trained surrogate models (or emulators) based on machine learning methods to make fast damage and loss predictions that are then used in a cost–benefit decision framework for activation of a mitigation measure is discussed in [4]. The development of low-cost multi-sensor strategies for the early warning of anomalous structural behaviors is illustrated in [5]. A novel integrated information system combining Internet of things, information management, early warning system, and cloud services is presented in [6], showing how an intelligent data box with enhanced connectivity and exchangeability for accessing and integrating the data obtained from distributed heterogeneous sensing devices can be developed. Three early warning levels were implemented according to rules based on the threshold value, which determined the specific safety personnel to be notified.

The above-mentioned references demonstrate that the effectiveness of early warning and structural health monitoring can take advantage of their integration

to enhance the reliability of results and support decision-making, in particular in earthquake prone regions.

In the framework of the GRISIS project, a case-study was selected for the application of an on-site automatic strategy for mitigation of seismic risk. A test field activity is currently ongoing for the installation of a monitoring system on a viaduct of the Circumvesuviana railway in Naples, namely Quarto bridge. Even if the monitoring system has not been activated to date, the development of an innovative system as well as the design of a control strategy for the mitigation of seismic risk are described in this work. In the first part of the paper, the case study (Sect. 2) and its finite element model (FEM) developed in SAP2000 (Sect. 4) are presented. Section 3 illustrates an innovative structural monitoring system developed through prototypal sensors with low-energy consumption acquisition and data processing systems. In Sect. 5 a mitigation strategy based on failure probability assessment is presented making a difference between directly measured and estimated response parameters.

2 Case Study

The case study is a railway-bridge (Quarto bridge) on the urban train line (Line 1) in the Northern metropolitan area of Naples. The viaduct (Fig. 1) is a 45-span simply supported bridge consisting of two end abutments (S5, S50) and forty-four intermediate piers (P6 to P49). Two metro stations are located along the bridge, i.e. “Quarto Centro” and “Quarto Stazione” in proximity of piers P9-P10 and P41-P42, respectively.

The viaduct is made of 45 simply-supported girders with equal span of 22,60 m and a pier center-to-center distance of 24,00 m for a total length of 1080 m. The viaduct has two railway tracks (#1, #2) on two separate decks (Fig. 2), i.e. one for each direction. A third railroad (#3) was built in the area of “Quarto Stazione” as an additional rail link passing back to the station (Fig. 3). Pedestrian platforms were built at the stations for the boarding of passengers.



Fig. 1 Plan view of the bridge with “Quarto centro” and “Quarto Stazione” stations



Fig. 4 View of the bridge near to Quarto Stazione (P29)



Fig. 5 View of Quarto Station from top of P39 on railway #2 (no installations)

3 Structural Monitoring System

A monitoring system was developed in order to implement an automatic warning strategy for mitigation of seismic risk and is currently being installed on the viaduct. After a seismic event, any damage scenario along the bridge involving either structural (e.g. piers, bearings, joints, etc.) or non-structural (e.g. installations, power grid, etc.) components should be predicted through a warning strategy. By also promoting innovative and low-cost sensors, the system has been designed to measure both accelerations, displacements and deformations at a certain number of points and installed by the company Tecno In Spa.

Two different sub-structures have been identified along the viaduct. The first is located near to Quarto Centro and is characterized by a single span (P8-P9), with an

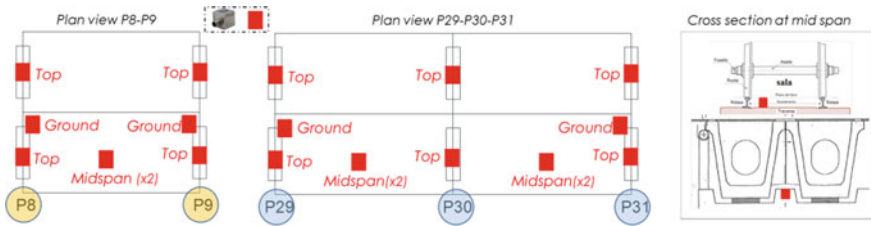


Fig. 6 Layout of accelerometers at piers P8-P9 and P29-P30-P31

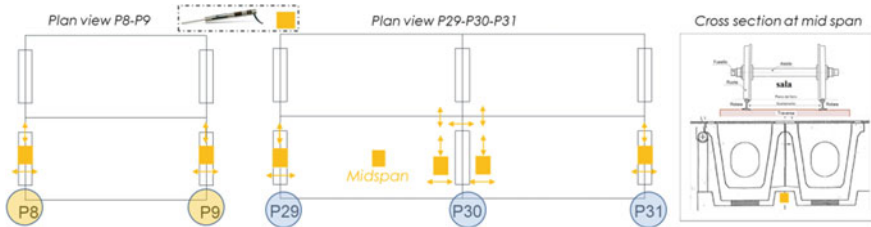


Fig. 7 Layout of displacement transducers at piers P8-P9 and P29-P30-P31

underpass road close to downtown. It was selected in order to implement a seismic strategy for risk mitigation in the urban area. The second sub-structure is located approximately at the mid-point between the two stations and is characterized by a couple of spans between piers P29 and P31. This system was deemed representative of a free-field installation, i.e. far enough from urban noise and breakaway forces.

A total of 20 triaxial accelerometers distributed along the pier (base and top) and the midspan of the deck (both at the intrados and the extrados) have been installed according to the layout in Fig. 6.

A total of 16 displacement transducers to measure the relative pier-to-deck and deck-to-deck movements were positioned as shown in Fig. 7.

At the base of piers P30 and P9, four strain-gauges on the main sides of the cross section are installed in order to detect any strain variation.

In addition to afore-mentioned system, two innovative prototype units were also provided by TME of T.R.E. consortium at the base of piers P29 and P31 to detect both accelerations and velocities.

3.1 Sensors and Acquisition System

Two types of triaxial-accelerometers were installed. The first sensor (TE) is a commercial accelerometer with a sensitivity of 1,000 mV/g and a frequency range from 0 to 200 Hz. The second sensor (MS) is an in-house, novel accelerometer,



Fig. 8 **a** Data acquisition units in the test room; **b** installation of LVDT across a deck transversal gap

based on the Analog Devices ADXL 335 chip which is a polysilicon surface-micromachined structure built on top of a silicon wafer. It has a sensitivity of 300 mV/g and a frequency range of 0–200 Hz. Both transducers belong to the family of Micro Electro-Mechanical Systems (MEMS) and have a voltage output.

MS is a novel low-cost transducer developed within the framework of the GRISIS project as an alternative to traditional accelerometers for a wide range of applications (Fig. 8a). From preliminary laboratory test, MS sensor would poorly perform in the case of very low amplitude ambient vibration measurements, but it might fit the needs of seismic response monitoring. The total cost of this sensor is about one-fifth of a commercial transducer. After a satisfactory preliminary calibration of MS sensors in laboratory environment, the layout of Fig. 6 was obtained by coupled installation of the two type of sensors at the top of the piers, thus obtaining a redundant measurement system [3] and permitting an in field-validation of the low-cost MS sensors.

The acquisition unit acquires data seamlessly and then saves and sends the event of interest when a predefined threshold is exceeded. When the threshold is exceeded, the software recovers data for both the 10 s before and the 50 s after the trigger instant. In practice, each event is characterized by a total of 60 s of data acquired at a sampling rate of 100 Hz.

Static monitoring is implemented using displacement transducers and strain-gauges. Displacement transducers are Linear Variable Differential Transformer (LVDT) type with ± 25 mm displacement (Fig. 8b). The LVDT is an analogue and contactless sensor with one primary and two secondary coils. An electrical signal is generated by the linear movement of the encoder rod. Attached to the sensor rod is the ferromagnetic core. The core induces a voltage in the secondary coils. A measurement amplifier or signal conditioner converts the induced voltage into a standard-compliant output signal, for example 0–10 V or 4–20 mA. The strain gauges are of the quarter-bridge type, each of which is connected to a bridge amplifier conditioner equipped with high-precision completion resistors and multilayer ceramic capacitors. They have a resistance of 120 ohms and a full scale of ± 1.500 microepsilon.

The system is completed by a digital temperature meter to correlate the variations of the monitored quantities with the seasonal temperature variations.

A different acquisition system is provided in terms of dynamic units for accelerations and static units for measures that evolve slowly over time (displacements and strains).

The distributed dynamic data system consists of a series of independent unit acquisition datalogger (UAD) each for a maximum of 9 channels corresponding to 3 accelerometers. Different units share information in real time about the occurrence of an event related to a possible hazard, once a threshold value has been set.

In order to reduce any latency, the motherboard has been designed to send a short text message (SMS) immediately, when a predefined threshold is exceeded, via a multi-manager telephone SIM. This action is associated with the activation, via digital output, of an audible or visual alarm. At the same time, the phenomenology both preceding the event (by means of the pre-trigger function) and inherent to the same event is acquired; everything is sent to the Cloud, in an FTP area, for subsequent viewing and post-processing.

Both static and dynamic UAD may stream periodically (with a given acquisition interval) as well as automatically when threshold values are exceeded (defined as hazard events). The file strings are characterized by different codes in order to be easily distinguished by the platform.

The system is modular, i.e. it is designed to be extended to measure dozens of transducers, even with high sampling rates. However, the electronics and management firmware is designed to absorb modest amounts of electrical current in the case, for example, of power supply from a solar panel in areas poorly exposed to the sun. The management software is fully configurable, so post-processing can be performed on board the microprocessor before sending the data to the Cloud. The units are designed to transmit data using various protocols, to be defined in the design phase, such as LoRa WAN, wi-fi, SIM 2G-3G-4G, LAN as well as satellite. All sensor acquisition and management parameters are fully configurable via FTP.

At piers P8-P9, three 9-channel dynamic units, interlaced, and one 16-channel static unit were installed, while five 9-channel dynamic units and one 16-channel static unit were installed at piers P29-P30-P31.

Given the availability of electricity, a 220 V power supply was provided, equipping the UADs with an internal UPS battery. Once the quality of the signal has been checked, data transmission is carried out by a mobile telephone operator.

A prototype unit of a stand-alone intelligent node-station was designed to be included in the monitoring system (Fig. 9). The unit was developed as an integrated sensor capable of providing a warning signal in case of seismic event. The monitoring system at the installation site can be affected by vibration phenomena due to the passage of trains. Each unit can record different accelerations and speeds on the 2 triaxial sensors which can be tuned to discriminate the different vibration source and filter out any phenomena not relevant for the seismic analysis.

The system can acquire 6 signals through 6 separate 32bit ADCs by combining two types of sensors, i.e. a velocimeter and an accelerometer.

Fig. 9 Picture of the prototype unit at the base of piers P29 and P31



The adopted velocimeter is a 4.5 Hz geophone while a low power consumption MEMS with a full-scale range of ± 2 g and a noise density of $50 \mu\text{g}/\sqrt{\text{Hz}}$ has been selected as accelerometer.

The system is equipped with an external GPS antenna which provides the TIMES-TAMP for the time sync, with the possibility to install the antenna several meters away from the sensor in order to improve the GPS signal reception if the installation should be lacking of the appropriate “sky view”.

The two sensors will have to be connected via LAN to a NUC mini-PC that will be responsible for data collection and analysis. For this purpose, an appropriate LAN has been designed and implemented on the installation site.

Given the distance from the Control-Room and the two monitoring points, the network system has been built up using optical fibers up to the top of pier P31 and, from this location, it has been developed through two LAN cables to reach the two seismic sensors placed at the base of P31 and P29.

The two detection nodes provide raw data in Seedlink format on port 18,000, while in the Control-Room side, located by the train station, the necessary hardware and software for the data stream analysis has been installed.

The data transmission delay between the acquisition system and the Control-Room is on average 0,2 s. This makes the system suitable and ready for Early Warning applications.

The Seedlink protocol has been implemented in the system for data transfer between the sensor and the remote host. The data streams required can be limited to specific networks, stations, locations and/or channels. All data packets are 512-byte Mini-SEED records. The system has been developed integrating a SoM (System on Module) processor in a Linux-based environment. This allows to integrate data sharing capabilities through an FTP server.

Furthermore, the station is completely manageable via WEB page (developed in PHP language) where the acquisition parameters can be configured, and data can be downloaded by entering the initial and final time frame. The system will process the data on board and prepare a.zip file with the requested data. Finally, the use of a Linux-based platform is suitable to create ad-hoc codes that can be run on the system.

4 Finite Element Model

With the aim to predict the seismic response of the bridge and properly design a control algorithm for the mitigation strategy, a three-dimensional (3D) model of the viaduct was implemented in SAP2000 [7] (Fig. 10). The pier (Fig. 11a) and the deck (Fig. 11b) were modeled by equivalent beam elements whose effective geometry was assigned in the “Section Designer” tool provided by the program.

Staircases and elevators were modeled through “shell” elements with a thickness of 0.15 m and 0.20 m, respectively. The piers were fixed at the base, i.e. no soil-structure interaction is considered at this stage. The effective height of each pier is spanning from the extrados of the beam foundation up to the bearing level. The pier cap was explicitly modeled only where transversally linking adjacent piers on the same alignment. In case of independent, i.e. single-pier substructure, it was only accounted in terms of additional concentrated mass at the top of the pier.

The beam section is defined for each deck including two box girders with the relative top slab. A horizontal frame link at the slab level is added where different railroads are connected. Two rigid links are also modeled to join the end-node of the pier with the bearing center (horizontal link) and this point to the mid-center of the deck (vertical link), respectively (Fig. 12). Internal flexural releases are applied at both ends of the deck, whereas at only one end an axial release is applied in order to model free longitudinal displacement for thermal variations. As a consequence of the statically determinate scheme of the deck, on each pier a couple of longitudinally-sliding bearing and fixed bearing are provided.



Fig. 10. 3D-view of the SAP2000 model

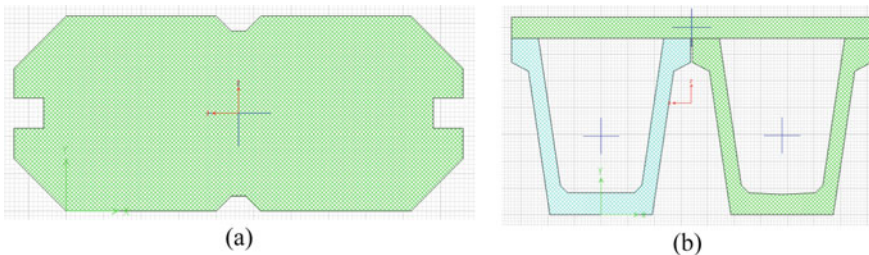


Fig. 11 SAP2000 model: pier **a** and deck **b** cross section

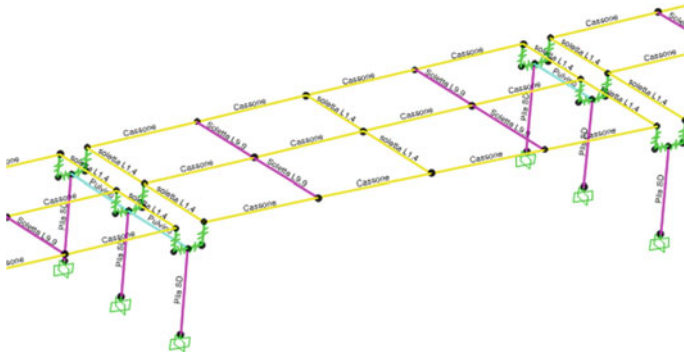


Fig. 12. 3D-view of a single span sub-structure in the model

Self-weight of the deck and the pier is properly accounted by the model through unit weight of material. Additional permanent loads (e.g. ballast) are assigned as distributed linear mass along the deck.

4.1 Preliminary Validation

In order to validate the dynamic behavior of the numerical model of the bridge, a preliminary assessment of the first vibration modes was attempted for a simple pier-deck sub-structure as shown in Fig. 12.

In the vertical direction, the first vibration period T_1^v can be estimated as for a simply-supported beam with uniform cross section and unit length mass properties by Eq. (1)

$$\omega_1 = \left(\frac{\pi}{L}\right)^2 \sqrt{\frac{EI_{deck}}{m_{deck}}} \rightarrow T_1^v = 2\pi/\omega_1 \tag{1}$$

where I_{deck} is the moment of inertia of the deck with respect to the horizontal axis, m_{deck} is the distributed linear mass of the deck including permanent loads, L is the span of the deck, E is the Young modulus of concrete.

A good matching is obtained between Eq. (1) and FEM model, i.e. $T_1^v = 0.22s$ for the railway #1 and $T_1^v = 0.17s$ for the railway #2.

In horizontal direction, the first mode of the pier-deck system is evaluated by lumping at the end-node of the pier the whole mass of the deck plus that of the pier-cap and one third of that of the pier by Eq. (2). Under the assumption of a SDOF oscillating system, the fundamental period T_1^h in case of separated decks is calculated as

$$k_{pier} = \frac{3EI_{pier}}{h_{pier}^3} \rightarrow T_1^h = 2\pi \sqrt{\frac{M_{pier}}{k_{pier}}} \quad (2)$$

where I_{pier} is the moment of inertia of the deck in either horizontal direction, M_{pier} is the total mass lumped at the top of the pier, h_{pier} is the total length from the base of the pier up to the center of mass of the deck, E is the Young modulus of concrete.

In the longitudinal direction, a value $T_1^l = 0.28s$ is obtained that is approximately 5% lower than the corresponding value from SAP model. In transverse direction, $T_1^t = 0.12s$ was found that is significantly lower than the value from SAP2000, i.e. $0.17s$. In this case, the scatter is due to a coupling effect between different sub-structures due to both (i) different height of adjacent piers and (ii) not-straight track of the viaduct.

The dynamic behavior of the bridge is affected by a number of features, including the variability of the deck and the piers geometry. In the numerical model, first horizontal vibration modes involve those piers close to the stations due to additional mass contribution from platforms.

The excitation of a total participating mass ratio equal to 85% along x and y directions corresponding to SAP model global axis, require a number of modes larger than two hundred and nine hundred, respectively.

In order to define an alarm strategy according to the procedure presented in Sect. 5, this model has to be run for seismic analysis in order to assess the failure probability. Operational modal analysis will be performed to properly calibrate the model on the basis of preliminary data under ambient-noise vibration and traffic passage thus reducing model uncertainties [8].

5 Failure Probability Assessment in Near-Real-Time

Hereafter it is assumed that a number of limit states are defined on the monitored structure and referring to a generic $i - th$ limit state, the latter can be identified by a threshold value of one engineering demand parameter (EDP), that is edp_i . Identifying three different levels of complexity, in each of the following section, the probability of exceeding edp_i , or the failure probability $P_{f,i}$, is computed. Based on such a probability, an alarm strategy can be implemented for the monitored structure.

While at level I, a simple control strategy could be applied to an EDP directly measured (to follow), in case of Level II and Level III, the mitigation strategy is developed in a stochastic framework to assess $P_{f,i}[edp_i^* > edp_i]$ and in case of any event the probability of false alarm should be taken into account prior to decision.

5.1 Level I

This section describes the simplest way in which information from the monitoring system can be used. At this level, a numerical model of the structure would not be required. Indeed, it is assumed that the considered limit state is defined by one of the recorded *EDPs*. Thus, assuming that the errors in recorded data are negligible (or corrected), $P_{f,i}$ is known comparing the recorded value, edp_i^* , with the threshold.

$$P_{f,i} = \begin{cases} 1 & \text{if } edp_i^* > edp_i \\ 0 & \text{if } edp_i^* < edp_i \end{cases} \quad (3)$$

In the case a limit state (either serviceability—SLS—or ultimate—ULS—limit state) is recorded, i.e. $P_{f,i}[edp_i^* > edp_i] = 1$, an alarm is sent without requiring additional judgment and the corresponding mitigation strategy applied.

To give an example, the case of relative displacements (x) at the sliding bearing level or between decks can be considered. Both SLS and ULS could be triggered upon the following criteria, respectively:

- Sliding of the bearing or relative movement between decks, $edp_i = 0mm$

$$|x| > 0mm \quad (4)$$

:

- Loss of support / collision between decks, $edp_i = 50mm$

$$|x| > 50mm \quad (5)$$

5.2 Level II

This section refers to limit states defined by *EDP* values that are not directly measured. In this case, the failure probability can be computed via a Bayesian approach that accounts for all the recorded information, that are, for example, ground motion intensity measure recorded at the base of the structure, IM , and a vector of observed structural responses, \underline{Q} .

First, a numerical model (nominal) of the monitored structure has to be built like the one presented in the previous section. To account for uncertainties in the structural analysis (i.e. model variability), some of the structural properties can be modelled as random variables. Those suggested in [9] to be considered are: modal damping, parameters describing the hysteric behavior of main structural components

and soil spring stiffnesses. Model variability could also include the static coefficient of friction of sliding bearings which is commonly addressed as a relevant source of uncertainty and has an influence on the dynamic response while it can be only indirectly evaluated through continuous modal based structural health monitoring [10, 11]. Once the probabilistic distribution of each parameter is defined (usually log-normal distributions are adopted assuming that each random variable is stochastically independent to the others), a Monte Carlo simulation can be implemented to generate S alternative realizations of the structural model. The (prior) probability of each of the S models is the same, i.e., indicating the generic model as m_s with $s = \{1, 2, \dots, S\}$, $P[m_s] = 1/S$.

Thus, nonlinear dynamic analyses can be performed for each model adopting a set of records in accordance with the recorded IM as input (i.e. record-to-record variability) and, the results of the analyses allow to compute the probability of the observed responses for each of the models, $P[Q|m_s]$. The posterior probability of each model, $P[m_s|Q]$, i.e. the weight of each model, w_s , that accounts for all the recorded information, can be computed as:

$$w_s = P[m_s|Q] = \frac{P[Q|m_s] \cdot P[m_s]}{\sum_{s=1}^S P[Q|m_s] \cdot P[m_s]} \quad (6)$$

With the computed weights, the probability that the structure has failed during the recorded earthquake can be computed via the following equation in which edp_s is the structural response provided by the numerical model m_s :

$$P_{f,i} = \sum_{s=1}^S P[edp_s > edp_i|im] \cdot w_s \quad (7)$$

Similarly, the failure probability can also be computed for future events if the marginal distribution of the IM , $f_{IM}(im)$, is known. This is represented by Eq. (8):

$$P_{f,i} = \sum_{s=1}^S P[edp_s > edp_i|im] \cdot w_s \cdot f_{IM}(im) \cdot dim \quad (8)$$

The latter equation can also be adopted to the case of the assessment of failure probability during an aftershock sequence from a mainshock of known magnitude and location as discussed in the following section.

This procedure can be applied to those limit states referring to internal stress which are not directly measured from the monitoring system, e.g, base shear and bending moment at the base of the pier. These $EDPs$ may either reflect a SLS or ULS at the pier level and a numerical prediction is required in order to assess the associated failure probability.

The weighting process of the different models is targeted on the vector \underline{Q} , i.e. the higher the number of measured *EDPs*, the more accurate prediction of $P_{f,i}$ is achieved.

In the case study, the vector of observed structural responses, \underline{Q} , include accelerations, displacements and strain variations at a discrete number of points. These *EDPs* were selected as closely related to the desired internal stress distribution.

In the case a non-zero value of the failure probability is associated to a limit state, i.e. $P_{f,i}[edp_i^* > edp_i] > 0$, the decision process would be based on the judgment of the decision maker and the consequent action must be evaluated on the basis of accepted risk. As a further development of the topic, a cost-based approach could be implemented in the decision making process thus considering both direct and indirect costs explicitly accounting for false or missed alarms. The cost assessment framework will aid the decision maker in the definition of the required actions to be undertaken, e.g. stop traffic circulation rather than make a visual inspection to railway installations or structural components before recovering the service.

5.3 Level III

The procedure described in this section refers to the case in which a mainshock of known magnitude and location occurred and, after completing the analyses associated to level II, one wants to estimate the structural failure probability given that an aftershock occurs. Indeed, in level II it was described how recorded information can be used to reduce the uncertainties on the structural side (see Eq. 6). On the other hand, the occurrence of a mainshock, also provide information on the hazard side that can be considered. More specifically, according to the aftershock probabilistic seismic hazard analysis (APSHA) described in [12], the *IM* distribution given the occurrence of an aftershock from a mainshock of known magnitude (m_m) and source-to-site distance (r_m), $f_{IM|A,m_m,r_m}(im)$, can be computed, by derivation, from the exceedance probability of the aftershock intensity measure IM_A given the aftershock occurrence after a mainshock of known characteristics, $P[IM_A > im|A, m_m, r_m]$, that is provided by the following equation:

$$\begin{aligned}
 & P[IM_A > im|m_m, r_m] \\
 &= \int_{r_{A,min}}^{r_{A,max}} \int_{m_l}^{m_m} P[IM > im|x, y] \cdot f_{M_A,R_A}(x, y|m_m, r_m) \cdot dx \cdot dy \quad (9)
 \end{aligned}$$

In the equation, $P[IM > im|x, y]$ is the conditional exceedance probability for an aftershock of known magnitude, x , and source-to-site distance, y . Such a probability is provided by a ground motion prediction equation (GMPE); $f_{M_A,R_A}(x, y)$ is the joint distribution of aftershock magnitude, M_A , and distance, R_A , that is defined for magnitude between a minimum value (m_l) and the mainshock magnitude and for

distances between a minimum and maximum value, $r_{A,min}$ and $r_{A,max}$ respectively, that depends on the mainshock magnitude and location (e.g., [13]).

Thus, the failure probability given the aftershock occurrence can be provided by Eq. (8) in which $f_{IM}(im)$ is substituted by $f_{IM|A,m_m,r_m}(im)$.

6 Conclusions

This paper has illustrated the complementary research activities developed with reference to a specific pilot application (a railway bridge) and aimed at integrating structural monitoring and early warning systems in a single platform. An innovative structural monitoring system was designed to implement an on-site real and near-real time warning strategy through low-cost equipment to promote wider application at a regional scale. The strategy is based on both measured (e.g. displacements) and predicted (eg. bending moment) values in order to define mitigation measures and interventions on the basis of predefined target values. Prediction of response parameters set the need for a numerical model of the bridge which is going to be calibrated based on the monitoring results. Even if the installation of the monitoring system is not complete yet, data processing solutions aimed at failure probability assessment at different scales depending on the type of response parameter (measured/not measured) and the occurrence of a seismic event (measured/predicted) have been developed. According to the estimated failure probability, an alarm can be triggered to automatically adopt interventions to reduce the effects of a given earthquake on a specific component to be protected. Given the stochastic approach of the procedure, the probability of occurrence of false as well as missed alarms should be properly accounted. In addition to this, a decision algorithm will be implemented in order to take into account both failure probability and related total (i.e. direct and indirect) costs including false or missed alarms. This further advancement will provide the management team a very useful tool in order to define a decision to be adopted for seismic risk mitigation.

Acknowledgements This work is supported by the GRISIS project (Cup: B63D18000280007, Surf:18033BP000000001, DD prot. 368 24/10/2018), implemented by STRESS scarl in the framework of FESR Campania 2014-2020. Additional acknowledgment is given to Ente Autonomo Volturmo (EAV) Srl for the collaboration offered to the realization of the demonstrator site. The authors are grateful to Tecno In Spa and TME of T.R.E. consortium for providing relevant information about the monitoring system.

References

1. Iervolino I (2011) Performance-based earthquake early warning. *Soil Dyn Earthq Eng* 31(2):209–222

2. Ventura CE, Kaya Y, Taale A (2019) BC earthquake early warning system, a program for seismic structural health monitoring of infrastructure. In Kasimzade A, Şafak E, Ventura C, Naeim F, Mukai Y (eds) *Seismic isolation, structural health monitoring, and performance based seismic design in earthquake engineering*. Springer, Cham
3. Rainieri C, Fabbrocino G, Cosenza E (2011) Integrated seismic early warning and structural health monitoring of critical civil infrastructures in seismically prone areas. *Struct Health Monitoring—An Int J* 10(3):291–308
4. Wu S, Beck JL (2012) Synergistic combination of systems for structural health monitoring and earthquake early warning for structural health prognosis and diagnosis. In: *Proceedings of SPIE 8348, health monitoring of structural and biological systems*
5. Andò B, Baglio S, Pistorio A (2014) A low cost multi-sensor strategy for early warning in structural monitoring exploiting a wavelet multiresolution paradigm. *Procedia Eng* 87:1282–1285
6. Wang J, Fu Y, Yang X (2017) An integrated system for building structural health monitoring and early warning based on an internet of things approach. *Int J Distrib Sens Netw* 13(1):1–14
7. Computers & Structures, Inc.(CSI) (2020) SAP2000-Integrated software for structural analysis and design. *Computers and Structures*.
8. Rainieri C, Notarangelo MA, Fabbrocino G (2020) Experiences of dynamic identification and monitoring of bridges in serviceability conditions and after hazardous events. *Infrastruct* 5(10). <https://doi.org/10.3390/infrastructures5100086>
9. Porter K, Mitrani-Reiser J, Beck JL (2006) Near-real-time loss estimation for instrumented buildings. *Struct Des Tall Spec Build* 15(1):3–20
10. Magalhães F, Cunha A, Caetano E (2012) Vibration based structural health monitoring of an arch bridge: from automated OMA to damage detection. *Mech Syst Signal Process* 28:212–228
11. Rainieri C, Magalhaes F, Gargaro D, Fabbrocino G, Cunha A (2019) Predicting the variability of natural frequencies and its causes by second-order blind Identification. *Struct Health Monit* 18(2):486–507
12. Yeo GL, Cornell CA (2009) A probabilistic framework for quantification of aftershock ground-motion hazard in California: methodology and parametric study. *Earthq Eng Struct Dyn* 38(1):45–60
13. Utsu T (1970) Aftershocks and earthquake statistics (1): Some parameters which characterize an aftershock sequence and their interrelations, *J Fac Sci Hokkaido Univ* 3(3):129–195

Dynamic Identification and Monitoring of a New Highway Bridge



Laura Marcheggiani , Francesco Clementi , and Antonio Formisano 

Abstract The structural behaviour of viaducts under traffic or seismic excitations can be evaluated using Structural Health Monitoring (SHM) methods, which can also be usefully employed to evaluate their health state under service conditions. These methods allow the calibration of suitable FEM models, based on accurate information on both material properties and structural elements, which are used to both design and evaluate the effectiveness of consolidation interventions, if needed. In the paper, static and dynamic testing procedures applied to a multi-span bridge, called Adda viaduct, along a new highway link inaugurated in 2014 in Northern Italy, are inspected. The structural performances of the investigated viaduct are evaluated based on both experimental static and dynamic loading test results. In particular, Operational and Experimental Modal Analyses are used, and their results are compared to each other. From the comparison it is shown that the dynamic load test can complement the static load one for the structural evaluation of new viaducts and can also be taken as an alternative for the monitoring of operational viaducts.

Keywords Structural health monitoring · Bridge · Load testing · dynamic testing · operational modal analysis · Experimental modal analysis

L. Marcheggiani

ENEA, Research Centre of Bologna and Research Laboratories of Faenza, Bologna, Italy
e-mail: laura.marcheggiani@enea.it

F. Clementi

Department of Civil and Building Engineering, and Architecture, Polytechnic University of Marche, Ancona, Italy
e-mail: francesco.clementi@univpm.it

A. Formisano (✉)

Department of Structures for Engineering and Architecture, University of Naples Federico II, Naples, Italy
e-mail: antoform@unina.it

1 Introduction

In the last two decades Structural Health Monitoring (SHM) methods received large attention from academics and designers. Nowadays, despite the available theoretical and practical developments, civil engineering is still hesitant to apply large scale SHM techniques. The reasons are [1]: (1) the strong variety of structural types in the construction industry; (2) differences in terms of economic interests, size and technical skills of the stakeholders involved in the civil engineering sector; (3) the difficulty in understanding of the potentiality of SHM methods.

Governments and professional groups all over the World published standard, guidelines and simple recommendations to protect the safety of crucial infrastructures [1]. Nevertheless, in Italy, apart §9.2 of the Italian law [2] and UNI 10,985:2002 standard [3], a lack of guidelines and procedures on SHM methods is noticed. However, the Morandi Bridge disaster in Genoa occurred on 2018 August 14th and a long series of previous failures of bridges demonstrated the need of both reviewing the regulations and planning monitoring actions at national level for new and existing road infrastructures. In particular, the Italian law gives the possibility to perform static tests and, if necessary, non-compulsory dynamic surveys.

Dynamic techniques play an important role in the SHM field. They allow to identify the main parameters governing the dynamic behaviour of a bridge, such as natural frequencies, mode shapes and damping factors, usually gained by Ambient Vibration Tests (AVTs) using operational identification methods. AVTs are generally less effective than Harmonically Forced Tests (HFTs), but their use does not require any additive equipment for test execution [4–7]. Contrary, measurements of a large number of points is possible even with a small number of available sensors [8–11]. However, dynamic data collected during experiments become more effective when used to improve FEM models of structures and bridges [12].

Based on the above premises, this paper shows the results of experimental environmental and forced dynamic testing procedure on the bridge crossing the Adda river along the new A35 BreBeMi motorway link between the cities of Brescia and Milan, in Northern Italy, before to be opened to traffic in July 2014.

2 The Viaduct Under Investigation

The investigated viaduct, crossing the Adda river, extends along the East–West axis of the A35 BreBeMi highway (Fig. 1). It is composed of two side-by-side decks, each of them made of 20 spans with different lengths: shore spans of 45 m, typological spans of 60 m, main spans of 90 m, across the riverbed of the Adda river and the spillway of the Muzza canal, and transition spans of 75 m between the last ones and the typological ones. The deck is supported by piers with RC circular cross-section having height ranging from 4.70–11.59 m. Along the longitudinal direction of the



Fig. 1 A photograph of the Adda viaduct

viaduct, the two carriageways have an offset of about 7 m in order to allow for the crossing of the river.

The plinths supporting the piers, based on a soil consolidated by jet-grouting technique, have a circular cross-section with diameter from 8.70 to 12.50 m and height between 2 and 2.5 m. The deck is joined to the side embankments by means of the abutments, having the same width of the deck (17.05 m) and height between 8.55 m (shoulder S2 South roadway) and 7.99 m (shoulder S1 North roadway). In the viaduct, there are four artifacts with differentiated carpentry both in the elevation of the ramp walls and in the shape of the gravel wall, but with identical foundations. The abutments on the same side are kept separated, despite the proximity of the artifacts, to decouple their behaviour in a seismic scenario (Fig. 2). The plinths supporting the abutments, founded on the consolidated ground, have rectangular cross-section of 18×14 m and height of 2 m.

The decks are continuous beams obtained by solidarizing individual “crutches” composed of prefabricated ashlar systems having symmetrical cantilevered advances

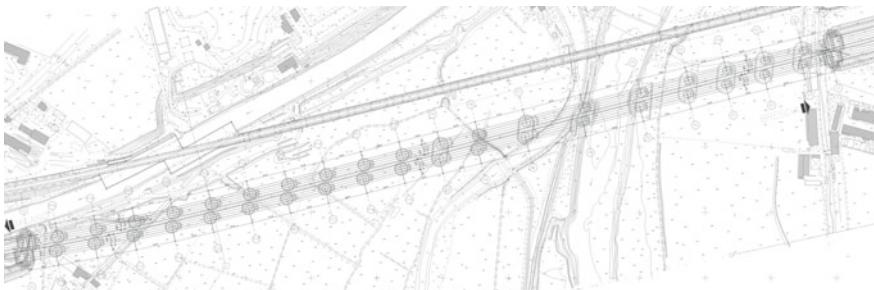


Fig. 2 A general plan view of the Adda viaduct

regarding the piers head. In particular, the continuous prefabricated box decks are assembled on site using the prestressed technique with internal sliding cables.

From the seismic point of view, the viaduct belongs to the category of continuous deck bridges with seismic isolation. The usual support structures of the deck are replaced by seismic isolators with the aim of containing the seismic energy transmitted by the substructure (piles and abutments) to the superstructure (deck). Sliding pendulum isolators are adopted, since they have good seismic dissipation capabilities with very small residual displacements at the end of a possible earthquake. These devices are characterized by a non-linear behaviour directly depending to the transmitted excitation. For modest excitations, they assume pseudo-elastic behaviour with stiffness features related to the extent of the applied actions.

3 Static Loading Tests

Loading and unloading tests with different configurations of trucks, each one having a total weight of 420 kN, were carried out on the viaduct to measure its deflections. To get the maximum bending stresses, the trucks were arranged with the loads transversely centred [13], as shown in Fig. 3a for the spans of 45 and 60 m and in Fig. 3b for the spans of 75 and 90 m. The displacement in the middle of the span was read through two optical sights placed between the second and third row of trucks in correspondence of lateral curbs.

To generate the design shear in a general pier, a loading train with 9 trucks arranged on 3 rows with a longitudinal centre distance of 9.5 m was used (Fig. 4a). Finally, aiming at having the maximum torque, 8 trucks, positioned in pairs close to the side overhang, were arranged (Fig. 4b).

The measurement was based on the precision spirit levelling technique with an accuracy of ± 0.01 mm. During the sessions, the deflections were measured at significant points identified as eleven benchmarks (see marker points in Figs. 3 and 4) fixed rigidly to the upper surface of the slab. Given the geometry of the deck, the

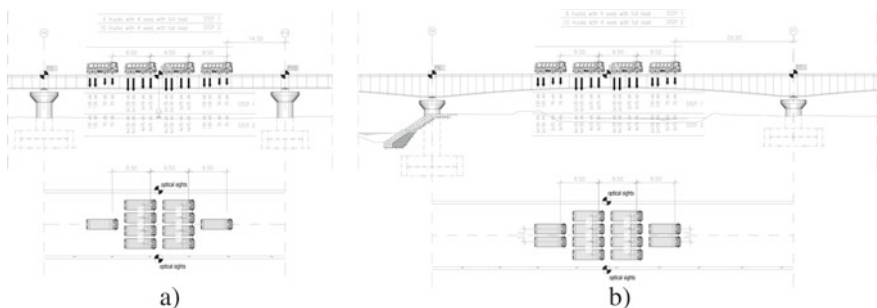


Fig. 3 General schemes of the trucks for maximising the bending moment in the span of the Adda Viaduct under static load tests

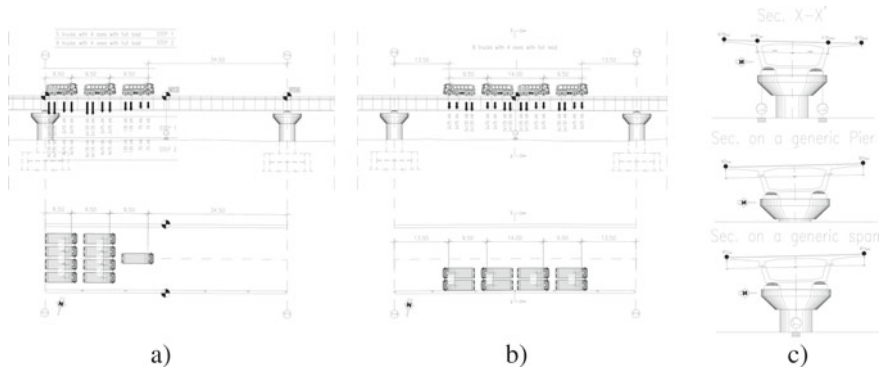


Fig. 4 A general scheme for the trucks during static load tests of the Adda Viaduct for the maximization of the shear in the piers and of the torsion in the deck

measurements were not limited to the central span only, but to catch all the possible displacements, the optical sights were positioned also in the external parts.

The measuring station consisted of a TRIMBLE 5603 robotic reflectorless total station, with 3'' of angular precision and reading accuracy at the levelling staff of 0.01 mm (Fig. 5a). Measurements were carried out for each test session by performing the readings on the staffs on the deck benchmarks and on an external benchmark positioned near the vertices of the station. In order to remove the deformation of the deck under the load induced by solar radiation, optical targets were positioned also in correspondence of the parallel discharged roadway. Strain gauge transducers TLDT50MM, with a high-resolution measure < 1 μ m and a standard output of 2 mV/V, were used to limit possible measurement errors (Fig. 5b and Table 1).

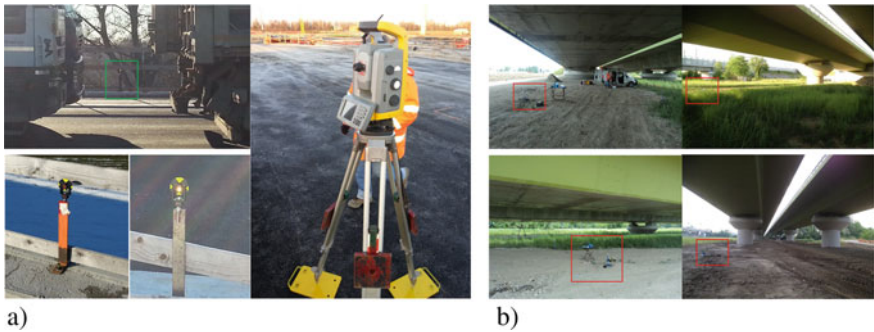


Fig. 5 The optical marker and the robotic reflectorless total station (a) and LVDTs (b) for static load tests

Table 1 Experimental results for the spans from P6 to P8 at different stages of the bending tests

Northern roadway												
	Marker	M4	P5	M5	P6	M6	P7	M7	P8	M8	LDTV	
Loading step 1 [55–60%]	Δ EXP [mm]	-2.8	0.05	8.36	-0.01	-21.62	-0.12	7.38	0.06	-1.45	7.4	
	Δ EXP* [mm]	-2.83	0	8.34	0	-21.56	0	7.41	0	-1.48	-	
	Δ EXP [mm]	-5.95	0.1	17.04	-0.26	-40.42	-0.17	12.73	-0.08	-3.11	11.33	
	Δ EXP* [mm]	-6	0	17.12	0	-40.21	0	12.85	0	-3.07	-	
Unloading step 1 [55–60%]	Δ EXP [mm]	-2.8	0.05	8.36	-0.01	-21.62	-0.12	7.38	0.06	-1.45	7.4	
	Δ EXP* [mm]	-2.83	0	8.34	0	-21.56	0	7.41	0	-1.48	-	
	Δ residual [mm]	-0.05	-0.15	0.06	-0.12	-0.3	-0.05	0.38	0.11	-0.1	1.04	
Southern roadway												
Loading step 1 [55–60%]	MARKER	M4	P5	M5	P6	M6	P7	M7	P8	M8	LDTV	
	Δ EXP [mm]	-3.26	0.05	8.87	-0.22	-20.65	0.01	6.43	-0.1	-1.33	6.1	
	Δ EXP* [mm]	-3.28	0	8.95	0	-20.55	0	6.47	0	-1.28	-	
Loading step 2 [100%]	Δ EXP [mm]	-5.34	-0.15	14.65	0.35	-43.21	0.19	14.32	0.04	-2.86	13.06	
	Δ EXP* [mm]	-5.27	0	14.55	0	-43.48	0	14.2	0	-2.88	-	
Unloading step 1 [55–60%]	Δ EXP [mm]	-3.36	0.05	8.8	0.2	-21.3	0.15	7.57	0.03	-1.75	6.84	
	Δ EXP* [mm]	3.38	0	8.68	0	-21.48	0	7.49	0	-1.76	-	
	Δ residual [mm]	-0.11	0.05	0.55	0.25	-0.91	0.14	0.31	0.14	0.1	0.47	

4 Dynamic Loading Tests

With the aim to assess the dynamic behaviour of the Adda Viaduct, AVTs and HFTs were carried out on spans P5-P6, P6-P7 and P7-P8 of the North carriageway (see Fig. 2) and on spans S1-P1, P1-P2 and P2-P3 at the lateral ends of the South carriageway [13].

Firstly, AVT was used to characterize the dynamic behaviour of the bridge under ambient vibration only. The Operational Modal Analysis (OMA) technique was then used to obtain the main frequencies, the associated modal shapes and the damping ratios. Then, the HFT was used with a known and controlled input, and the correlated induced vibrations were acquired, also providing a ratio between output and input.

The modal parameters thus obtained should allow a more reliable dynamic analysis of the structure with respect to the OMA. To provide excitation, imposed by inertia, a system for vertical forcing was used. Moreover, it was employed a hydraulic actuator loaded with appropriate masses. The choice was conditioned by the possibility of implementing the best control strategy in terms of both the amplitude of forcing and frequency.

4.1 Test Setup

The AVT response of the bridge with OMA was measured at different span (see Fig. 6a) and with different acquisitions. In particular, the AVT considers the spans between the piers P5 ÷ P8 for the North carriageway and between the abutment S1 and the piers P3 for the South carriageway. The accelerometers were fixed in direct contact with the structural elements (Fig. 6a) and parallel/perpendicular to the main directions of the span, in order to get both horizontal and vertical modes. The positions were chosen at $\frac{1}{2}L$, $\frac{1}{2}L$ and $\frac{2}{3}L$ of considered spans.

In general, two different types of highly sensitive accelerometers, measuring in two orthogonal directions, were placed (see Fig. 6a): the dots measure the vertical directions and the arrows the horizontal ones.

It was used a wired sensor network composed of two types of piezoelectric sensors (Integrated Electronic Piezoelectric-IEPE), namely 393B12-PCB and 393B31-PCB.

The digital recorder is composed of NI9234 modules with 24-bit A/D converter and integrated anti-aliasing filters. The data were acquired with a sampling frequency of 2048 Hz, pre-filtered and decimated 8 times, obtaining a final sampling frequency of 256 Hz.

For the Experimental Modal Analysis (EMA), the setup layout is essentially the same of OMA to facilitate the comparison of results between them. Nonetheless, in this case, the excitation is provided by an inertial exciter (see blue point in Fig. 6b) close to $\frac{1}{3}L$, being L the length of the central span of the three measured portions, in order to excite the greatest number of eigenmodes at low frequency.

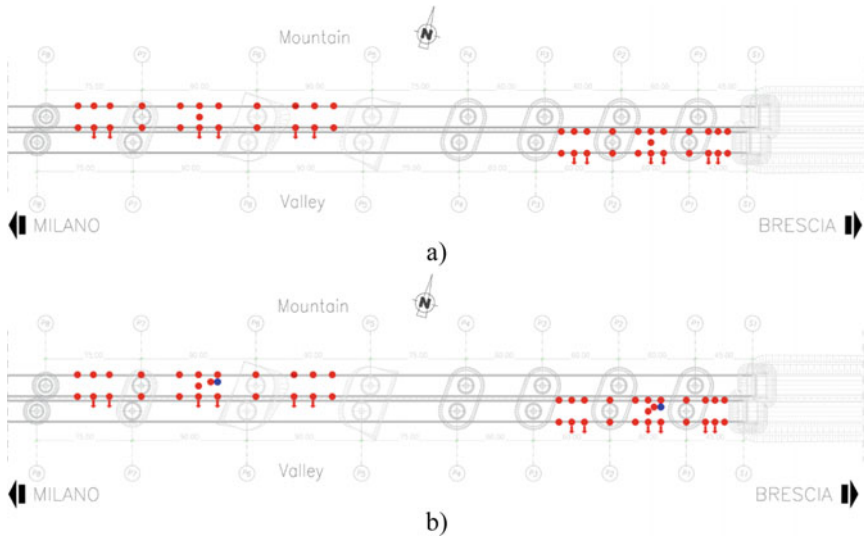


Fig. 6 Layout of the accelerometers at each span for operational modal analysis (a) and experimental modal analysis (b)

The hydraulic actuator (see Fig. 7) is placed in an asymmetrical position with reference to the centreline to force both vertical and torsional modes of the viaduct. It is powered by a portable pump with adequate characteristics. The actuator oscillates, at the desired frequency and amplitude, with its mass of 500 kg, which generates the desired forcing on the structure. The chosen test profile is a stepped sine. The frequency is increased with variable steps, cooled around the structural resonances, with a minimum step of 0.01 Hz.

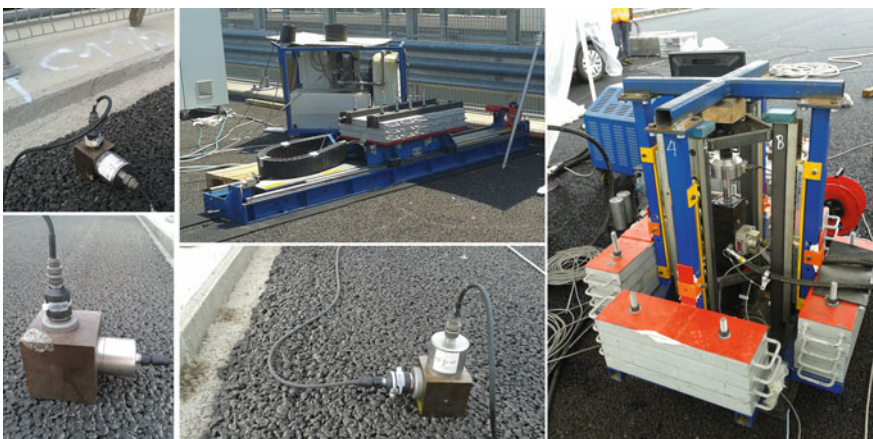


Fig. 7 Hydraulic actuator and accelerometers used in the experimental modal analysis

Table 3 Forces transmitted on the deck for experimental modal analysis for the two carriageways

Frequency [Hz]	North carriageway	South carriageway
	Force [N]	Force [N]
1–1.5	800	800
1.5–1.8	1500	1000
1.8–2	1800	1500
2–2.5	2500	3000

To estimate the force transmitted to the structure, the PCB 393A03 accelerometer, with a sensitivity of 1000 mV/g, was fixed to the basket that carried the mobile masses. The main values of the forces transmitted to the viaduct are reported in Table 3.

4.2 Operational Modal Analysis

Natural frequencies, vibrations modes and damping ratios were estimated for the lower modes of North and South girders. The Time-Histories (THs) are analysed by the Polyreference Least Square Frequency Domain [14].

Figure 8 shows the graph of the Power Spectral Density (PSD) of the accelerations detected during the 8 h of acquisition made on the North carriageway. Only three vibration modes were completely identified from the tests on North carriageway, as depicted in Fig. 9. The first and third modes involved a deformation of the bridge deck with a prevalence of vertical oscillations, i.e. transversal to the deck. Mode 1 (1.27 Hz, $\zeta = 0.67\%$) corresponded to a bending in-phase deformation of the deck, i.e. the out-of-plane deformation of the deck was the same with equal sign at the extremities, as happened for the Mode 3 (1.68 Hz, $\zeta = 0.48\%$).

The Mode 2 (1.59 Hz, $\zeta = 0.79\%$) vibrates both in out-of-plane and in-plane directions of the deck. Maximum amplitudes were recorded in the first span, if we consider the extremity near to the mountain, and in the middle of the central span, taking into account the extremity near to the valley.

A dynamic behaviour analogous to that of North carriageway was encountered in identifying the vibration modes of South carriageway, with some little differences. Herein, three frequencies and the associated mode shapes were identified. The most important differences are that all the modes still involved the deformation of the whole deck, with a prevalence of an in-phase oscillation of the two extremities of the deck in the vertical plane. These modes had very close natural frequency values, which were, respectively, 2.06 and 2.11 Hz for Mode 1 and Mode 2. The third mode corresponded to a natural frequency value equal to 2.21 Hz, having modal deformation with a greater contribution in anti-phase at the stack closest to Milan.

As a conclusion, it was noted that the test made on the North carriageway can identify with certainty the first three modes, while that on the South carriageway can identify only frequency modes higher than 2.06 Hz. In fact, in this latter case, the first three modes are local ones producing modal deformations too low to be

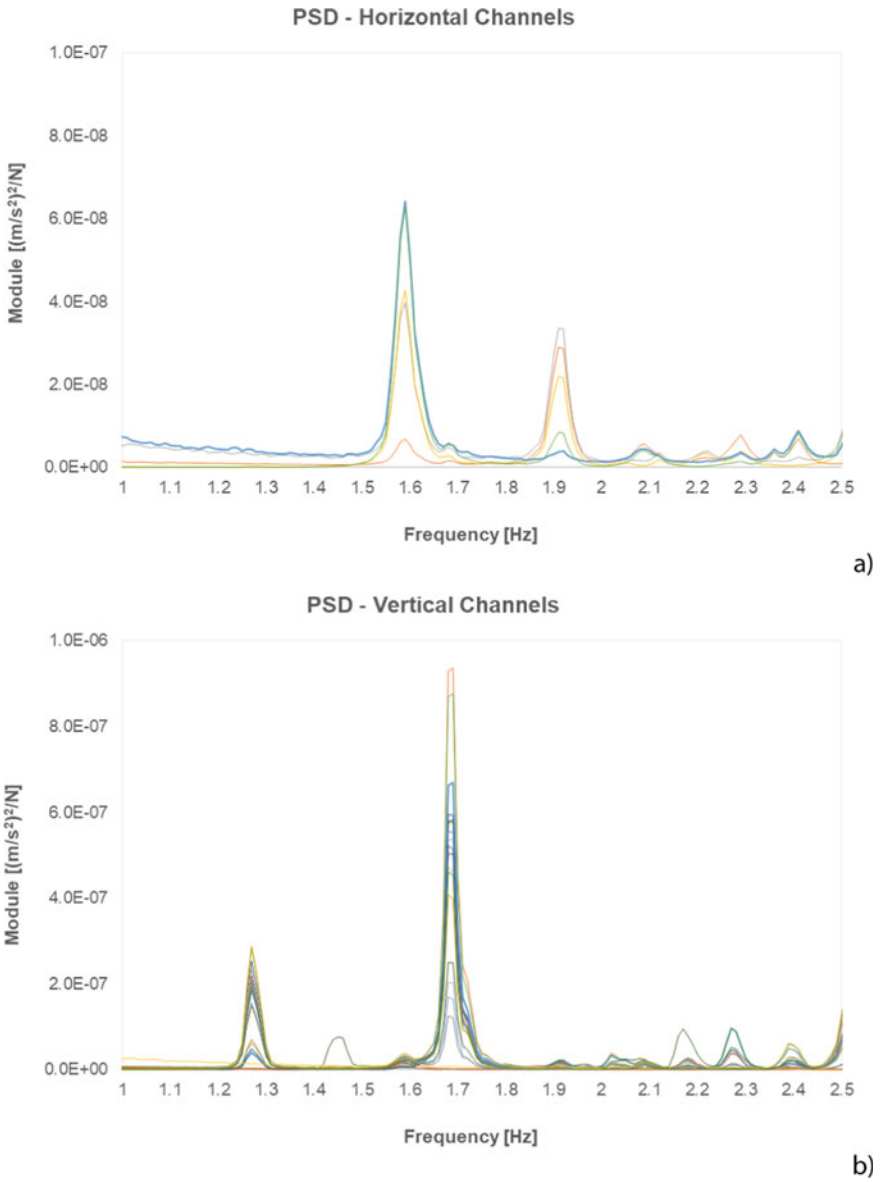


Fig. 8 PSD of horizontal (a) and vertical channels (b) for the OMA on the North carriageway

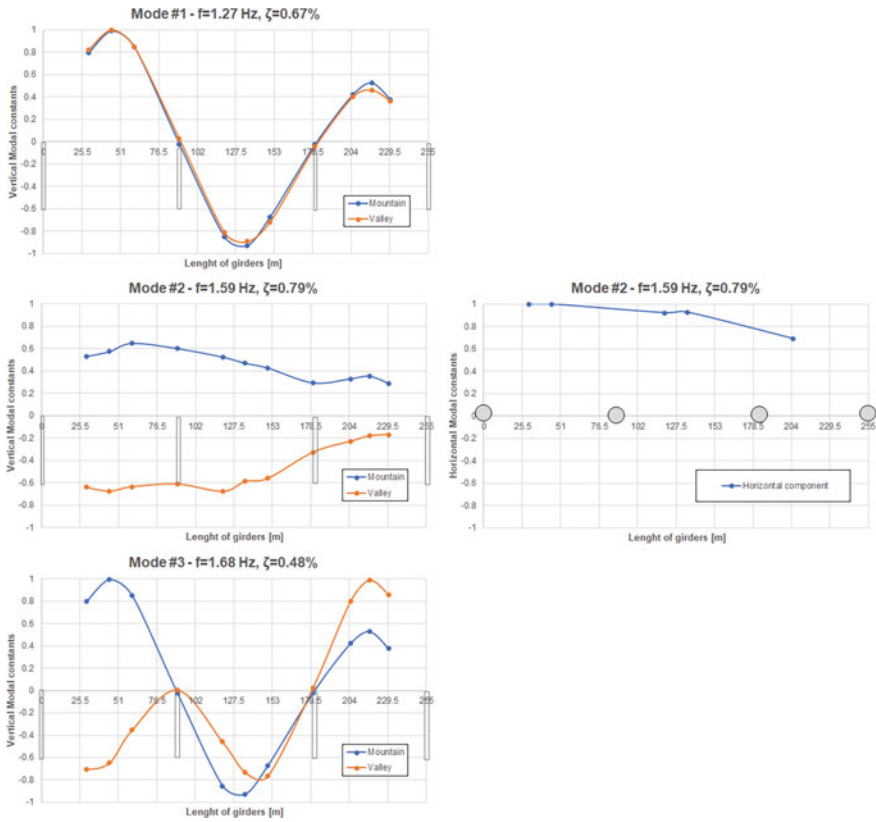


Fig. 9 Mode shapes of the three modes identified with OMA

appreciated in the OMA. The reason why is that in the North carriageway the spans with the greatest span were tested, while in the South carriageway, whose PSD and mode shapes were not depicted herein, only those starting from the bridge shoulder were examined.

4.3 Experimental Modal Analysis

On both carriageways, HFT tests were carried out with known dynamic excitation supplied by means of an oleodynamic exciter, according to the approach called EMA. All the available energy was applied on one frequency at a time, using a stepped sine forcing. The Time-Histories (THs) were analysed by the Polyreference Least Square Frequency Domain [14].

Figure 10 shows the Frequency Response Function (FRF) of the accelerations detected during acquisition on the North carriageway. The same first three vibration modes of OMA were completely identified, as seen in Fig. 11.

The first and third modes involved again a deformation of the bridge deck, with a prevalence of vertical oscillations, i.e. transversal to the deck. Mode 1 (1.26 Hz, $\zeta = 0.66\%$) corresponded to an out-of-plane deformation of the deck with the same sign in the extremities. It has a difference in terms of frequencies respect to OMA of about + 0.79%. The same happened with Mode 3 (1.69 Hz, $\zeta = 0.63\%$), where a difference in term of frequency of about -0.60% referred to OMA was detected.

Also with EMA, Mode 2 (1.57 Hz, $\zeta = 1.06\%$) involved both out-of-plane and in-plane directions of the deck. The difference in frequency with respect to OMA is about + 1.26%. Maximum amplitude was again recorded as in the previous analysis.

A dynamic behaviour analogous to that of North carriageway was encountered in identifying the vibration modes of South carriageway, with some little differences as observed for OMA. Three frequencies and the associated mode shapes were always

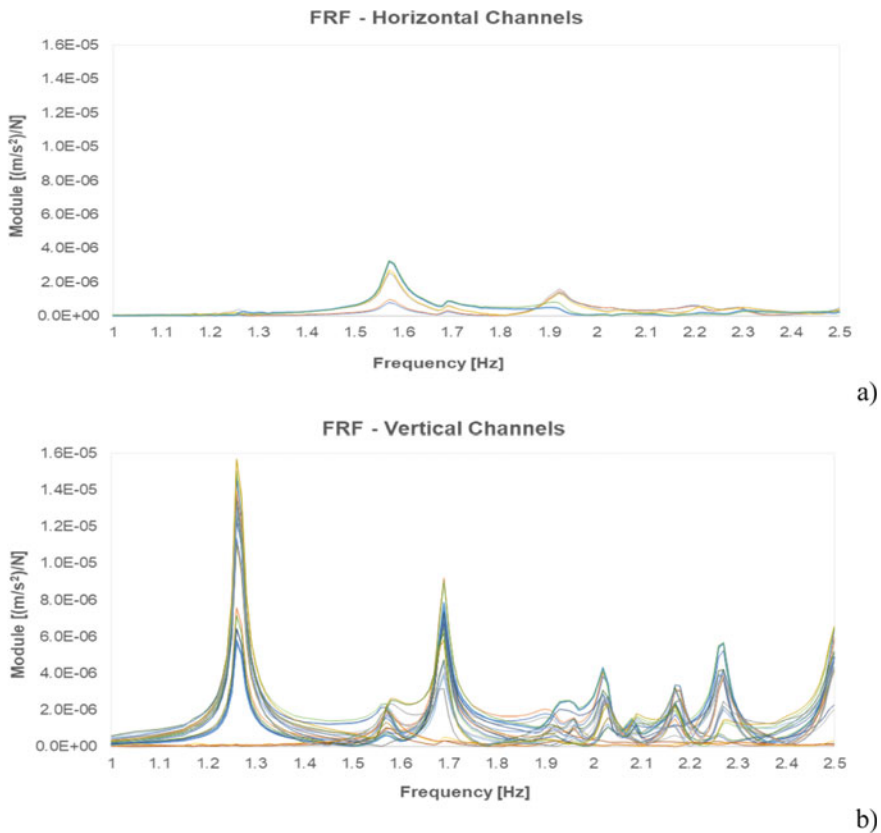


Fig. 10 FRF of horizontal (a) and vertical channels (b) for the EMA on the North carriageway

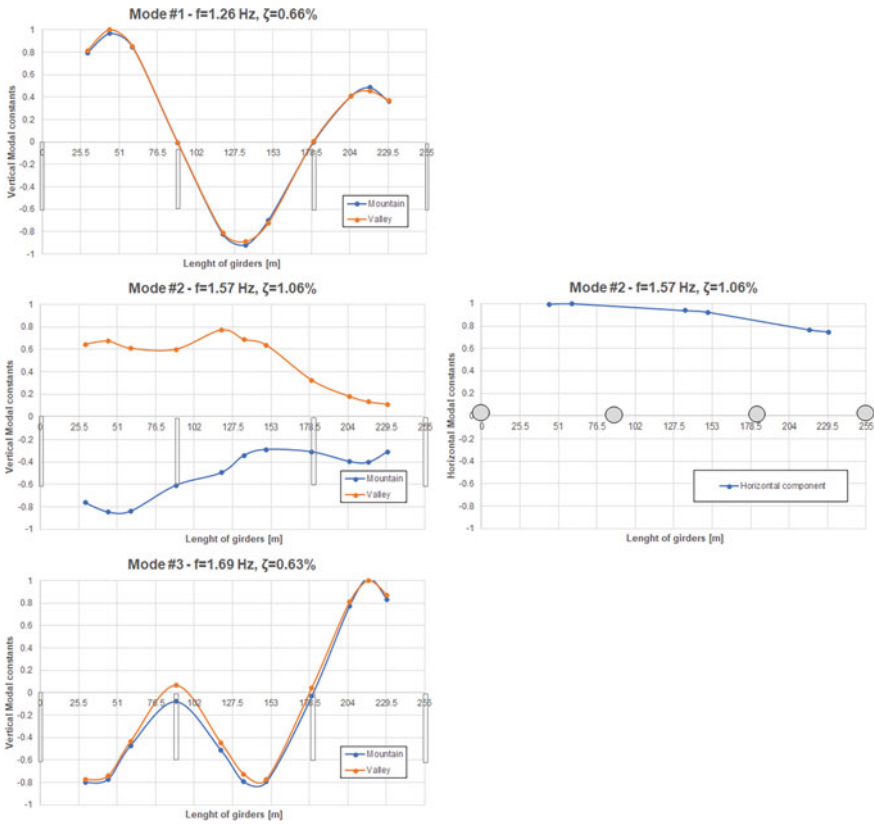


Fig.11 Mode shapes of the three modes identified with EMA

identified. The first two modes had natural frequency values very close to each other (2.05 and 2.11 Hz for Mode 1 and Mode 2, respectively), as observed in OMA. The third mode corresponds to the natural frequency value of 2.20 Hz and presents a modal shape with different signs near the piers P6 and P7 in the two extremities of mountain and valley.

The EMA on the North carriageway, in which the central spans were instrumented, allowed the identification of the first three modes, having high amplitude components on those spans and almost equal to zero on the shore spans. So, also with EMA tests, despite the greater input energy, appreciable modal amplitudes for the first three modes in the shoulder spans cannot be generated. The EMA tests on the South carriageway allowed the identification of higher modes, as also observed in OMA, whose contributions in terms of amplitude of vibration on the side bays were more significant. The damping derived from the processing of EMA were compatible with the real dissipative capacity of the structure in the field of small vibrations.

5 Concluding Remarks

The research paper herein presented dealt with an application of dynamic methods for structural identification of the viaduct inside the Northern Italy roadway between Milan and Brescia. The viaduct is composed of two side-by-side decks, each of them made of 20 spans with different lengths, supported by circular piers through elastomeric seismic isolators.

Before opening, the viaduct was subjected to static and dynamic tests, the latter with environmental and forced excitation of known value. The vertical deflections were measured by means of optical measurement and LVDT systems before, during, and after the trucks were positioned on the bridge deck on both the carriageways. All the deflections were lower than the design expected ones and they were almost completely reversible after complete unloading of the viaduct. The influence of solar radiation on the deformability of the deck was likewise investigated and clearly understood.

Natural frequencies, modes shapes and damping factors of the first modes of the viaduct were estimated on the basis of a series of AVTs and HFTs. In general, the two approaches, very different from each other due the unknown of the input in the AVTs, give the same results with very little differences, which are completely marginal from the engineering point of view. In particular, for the North carriageway, it was possible to identify the first three modes below 2 Hz because the monitored spans, located in the middle of the viaduct, allow recording even small environmental noises exciting the lower frequencies. Contrary, in the South carriageway, it was not possible to identify the first natural modes with both AVT and HFT due to the presence of the bridge abutments, which strongly conditioned the dynamic response.

In all the various identifications, the main modes were associated to modal shapes, that deformed the deck in the out-of-plane direction. The components of the modal shapes of the deck were always low, except for the second identified mode in both carriageways.

Finally, it is possible to affirm that the dynamic characterization of the examined viaduct can provide important advices to bridge constructors on the use of static and dynamic data to assess the quality of the techniques adopted for the realization of the viaducts. Furthermore, these experimental results permit a clear interpretation of future long-term monitoring data on the inspected viaduct, also addressing variations in seismic isolators [15].

Acknowledgements The Authors wish to gratefully acknowledge the “Società di Progetto Brebemi S.p.A.” for the permission to use the static and dynamic testing data of the Brebemi Viaducts.

References

1. Gatti M (2019) Structural health monitoring of an operational bridge: a case study. *Eng Struct* 195:200–209. <https://doi.org/10.1016/j.engstruct.2019.05.102>
2. Ministry of Infrastructures and Transportations: DM 17/01/2018 (2018) Upgrading of Technical Codes for Constructions” (in Italian). Rome, Italy
3. Italian National Body of Unification (UNI). UNI 10985 (2002) Vibrations on bridges and viaducts—guidelines for the execution of dynamic tests and surveys. Rome, Italy
4. Clementi F, Pierdicca A, Formisano A, Catinari F, Lenci S (2017) Numerical model upgrading of a historical masonry building damaged during the 2016 Italian earthquakes: the case study of the Podestà palace in Montelupone (Italy). *J Civ Struct Heal Monit* 7(5):703–717. <https://doi.org/10.1007/s13349-017-0253-4>
5. Formisano A, Krstevska L, Di Lorenzo G, Landolfo R, Tashkov L (2018) Experimental ambient vibration tests and numerical investigation on the Sidoni Palace in Castelnuovo of San Pio (L’Aquila, Italy). *Int J Masonry Res Innov* 3(3):269–294. <https://doi.org/10.1504/IJMRI.2018.093487>
6. Di Lorenzo G, Formisano A, Krstevska L, Landolfo R (2019) Ambient vibration test and numerical investigation on the St. Giuliano church in Poggio Picenze (L’Aquila, Italy). *J. Civil Struct Health Monit* 9(4):477–490. <https://doi.org/10.1007/s13349-019-00346-7>
7. Krstevska L, Tashkov L, Naumovski N, Florio G, Formisano A, Fornaro A, Landolfo R (2010) In-situ experimental testing of four historical buildings damaged during the 2009 L’Aquila earthquake. In: COST ACTION C26: urban habitat constructions under catastrophic events—proceedings of the final conference. Taylor & Francis, London, pp 427–432
8. Benedettini F, Dilena M, Morassi A (2015) Vibration analysis and structural identification of a curved multi-span viaduct. *Mech Syst Signal Process* 54–55:84–107. <https://doi.org/10.1016/j.ymssp.2014.08.008>
9. Lamonaca F, Scuro C, Grimaldi D et al (2019) A layered IoT-based architecture for a distributed structural health monitoring system. *ACTA IMEKO* 8(2):45–52. https://doi.org/10.21014/acta_imeko.v8i2.640
10. Lamonaca F, Sciammarella PF, Scuro C et al. (2018) Internet of things for structural health monitoring. In: 2018 Workshop on metrology for industry 4.0 and IoT. IEEE, pp 95–100
11. Lamonaca F, Sciammarella PF, Scuro C et al (2018) Synchronization of IoT layers for structural health monitoring. In: 2018 Workshop on metrology for industry 4.0 and IoT. IEEE, pp 89–94
12. Formisano A, Di Lorenzo G, Krstevska L, Landolfo R (2020) Fem model calibration of experimental environmental vibration tests on two churches hit by L’Aquila earthquake. *Int J Archit Heritage*. <https://doi.org/10.1080/15583058.2020.1719233>
13. Consorzio BBM (2014) Motorway connection between the cities of Brescia and Milano. CUP E3 1 B05000390007. Execution of works. Motorway body. Major artworks. Lot 7–VI003. Adda viaduct—Km 43+220,95–44+487,92. Report on the static loading test (in Italian).
14. Peeters B, Van der Auweraer H, Guillaume P, Leuridan J (2004) The PolyMAX frequency-domain method: a new standard for modal parameter estimation? *Shock Vib* 11:395–409. <https://doi.org/10.1155/2004/523692>
15. Bedon C, Morassi A (2014) Dynamic testing and parameter identification of a base-isolated bridge. *Eng Struct* 60:85–99. <https://doi.org/10.1016/j.engstruct.2013.12.017>

SS#1 Investigation in Structural Performances of High-Power Horizontal Axis Wind Turbines by OMA-Based SHM



Luca Sbaraglia

Abstract A monitoring campaign of the tower mast vibrations of four identical high-power Horizontal Axis Wind Turbine Generator (HAWTG) was conducted by Rina Consulting S.p.A. The scope of the work was to find the reasons of different performances between the investigated wind turbines. The monitoring was conducted by using real time chains of seismic accelerometers and the data analysis was completed by the OMA, operational modal analysis technique. The results made it possible to highlight the differences in dynamic behavior between the investigated WTs. Starting from OMA results and using the design characteristics of the turbines, a set of dynamic indicators like unitary mass normalized modal shapes, flexibility matrix and modal shape curvature were calculated. The differences in the calculated indicators made it possible to provide an explanation of differences in WT performances and to suggest a series of interventions to mitigate the consequences of the sub-optimal performances.

Keywords Operational modal analysis · Wind turbine · Scaled mode shape · Flexibility matrix · Mode shape curvature · Short time fourier transform · Rotational stiffness · Lateral stiffness

1 Introduction

This manuscript is based on an industrial project that Rina carried out on behalf of a *Wind Turbine* (WT) manufacturer. The aim of the project was to identify the causes of the unsatisfactory behaviour of some turbines in an onshore wind farm. The problematic behaviour of the WT consisted in the fact that the characteristic frequency of the first oscillation mode, measured by the vibrating sensors installed in the nacelle, was close to the lower limit of 1P, the period of rotation of the blades. This entailed the entry of the structure into a regime of dynamic behaviour close to the resonance which was averted with the shutdown of the generator or the downgrade

L. Sbaraglia (✉)
Rina Consulting S.p.A, Viale Cesare Pavese, 305-00144 Rome, Italy
e-mail: luca.sbaraglia@rina.org

of the operating regimes. Therefore, this was the cause of economic damage due to the lack of production. A dynamic investigation was therefore conducted on four turbines, indicated in this work by terms WT #1, #2, #3 and #4, of which only the #2 presented satisfactory behaviour. The WT #1, #2 and #4 were investigated also by a continuous and contemporary monitoring campaign with the aim to determinate the experimental rotational stiffness (K_r).

As is known, [1, 2] the dependence of the vibration frequency of the first mode is strongly influenced, in this type of structures, by the value of rotational stiffness (K_r). It therefore seemed natural to first check the value of this parameter for each of the selected turbines. The Rina Consulting Geoscience team conducted a review of the geotechnical study of the foundation soil and the review of the foundations design [3]. In parallel, the Smart Monitoring group of Rina Consulting S.p.A. implemented continuous structural monitoring of the K_r and a campaign of Operational Modal Analysis (OMA) [4]. In particular, the monitoring was conducted on WT #1, #2 and #4, it lasted for about three months during which both the rotation of the pedestal head and the strain on the internal wall of the tower, close the base, were measured. Overall, the design review and the experimental determination of the K_r showed low values of rotational stiffness, compared to the design requirements, only in the case of WT #1.

Therefore, the dynamic monitoring campaigns object of this paper had the purpose of evaluating the possible presence of structural problems on the *Wind Turbine Tower Mast* (WTTM) that are part of the WT.

In operating conditions, wind turbines are time-variant systems, since [5] changes in wind intensity, in rotor speed, in blade pitch cause the dynamic response to change significantly, modifying both stiffness and damping properties.

On the other hand, OMA is based on the hypothesis that the behaviour of the structure under investigation is on the contrary *Linear and Time-Invariant* (LTI) and this is a cause of difficulty in obtaining reliable results by applying OMA techniques tout court, without particular precautions to this type of structures [6]. There are two possible ways to remedy this incompatibility between the OMA requirements and the time variant nature of the TW. The first is to [7] reduce the response data sets of a wind turbine in operating conditions to a time-invariant data set, for example through the *Multi Blade Coordinate* (MBC). The second is to eliminate harmonic components from post processing data due to mass rotations (blades and alternators) [5]. However, for the purpose of the project, which was to identify the dynamic characteristics of the tower and make a comparison between the turbines examined, it was preferred to analyse the dynamic behaviour of the generators in parked conditions, i.e. with the rotor stopped, electrical equipment deactivated, and low wind speeds. In fact [5–7] in parked condition it is possible to consider turbines as time invariant structures and excited by a set of sources which together constitute a white spectrum excitation. Under these conditions it is therefore possible to perform an extraction of the modal parameters of the structure by means of the OMA analysis.

A *Finite element Model* (FEM) of the WTTM was created to compare the modal parameters provided by the OMA with those of a numerical model corresponding to the structure of the tower in terms of geometry and materials. The model was

created using structural design software used in the civil sector (ProSap—2Si srl) and the dynamic analysis were carried out in the linear field. The FEM model was created in two variants. In the first the nacelle and the rotor were schematized as a weight placed at the head of the tower, in the second variant the nacelle and the rotor were modelled as a structure rigidly connected to tower's top with shape, position and weights tuned on the mass and stiffness characteristics of the nacelle + rotor assembly.

1.1 Proposed Investigation Approach

On the basis of the framework described above, the following methodology, based on OMA and WT design data, has been implemented to identify structural problems on the respective WTTMs in parked conditions. The proposed methodology consists of the following steps:

- (1) OMA analysis and modal parameters estimation, for all WTs investigated.
- (2) Realisation of FEM and its updating according to the results provided by the OMA for the reference WT.
- (3) Calculation of the mass matrix from WTTM design data
- (4) Calculation of UMM, for all WTTMs investigated.
- (5) Calculation of damage indicators, flexibility matrix and curvature, for all WTTMs investigated.
- (6) Calculation of STFT on data used for OMA analysis, for all WTTMs investigated.
- (7) Comparison of results obtained in (5) and (6) to identify measuring nodes where damage indicators suggest the presence of structural problems.

The pre-requisite to apply this methodology is that the analysed Wts must be identical for construction and type and that at least one must be considered a reference, as considered the WT with the best performance and a WT without structural problems.

2 Structure Description

The wind generators discussed in this experience are HAWTG with power exceeding 2 MW. The height of the hub from the ground is approximately 118 m. The tower structure is made of precast reinforced concrete keystones assembled on site to form six tower sections or rings, of variable thickness with height. The keystones and the tower's rings are jointed by means of pre-stressed connections and filling grout. The foundations are gravity base type, constituted by a concrete ring slab and a cylindrical hollow pedestal both realized by cast in situ reinforced concrete. The union between the foundation head and the base of the tower is composed by means of pre-stressed

connections and filling grout. The constraint tension is achieved through post tension cables. In fact, the tower is a post-tensioned structure thanks to the presence, inside the tower, of 5 unbonded tendons. The total tension load due to the tendons is equal to about 1/2 of the tower's own weight. The lower end of the tendons is fixed to the base of the foundation while the upper end is fixed to the top of the tower. Due to the demand for higher and more powerful WT, this type of tower construction has been developed in recent years [8]. The 1P frequency is between 0.15 and 0.25 Hz

The wind farm is made up of no. 25 HAWTG identical in construction, design and environmental conditions. The characterization of the foundation soil was carried out and the foundations were designed for each WT tower.

2.1 *Kr Investigation*

As mentioned in the introduction, a continuous monitoring of the rotational stiffness K_r for WT #1, #2 and #4 was carried out for more than a month. Although it is not the subject of this paper, for completeness, the obtained results are briefly described. K_r was obtained from the simultaneous measurement of both the strain on the inner wall of the towers, in four points uniformly distributed on the inner circumference, and both of the rotation the foundation top along two horizontal and orthogonal axes.

Table 1 contains the averaged values K_r for each WTTM, referred to the entire set of data acquired during the monitoring period s . These values are obtained by the formula:

$$K_r = M/\alpha, \quad (1)$$

where M is the bending moment measured at the base of the tower by means of the strain sensors installed into the internal surface of the tower, and α is the rotational angle of the tower, measured by means of a biaxial dynamic inclinometer installed on the top of foundation.

Table 1 K_r mean values—whole data set

Kr [G Nm/rad]				
WTTM	#1	#2	#3	#4
Kr	102	220	Not measured	297

3 Measuring System Description

The WTTM’s accelerations of four WT were continuously monitored in ten days one at once by using a cabled, synchronous, dynamic measuring system. For each monitored WTTM the continuous monitoring campaign lasted about 36 h with a sampling frequency of 200 Hz (200 samples/second) for all measuring channels. The same measurement setup was used for each turbine. The position of measuring points is sketched in the picture below, while the table reports the height of the installed measuring points with respect to the base of the tower. The data were achieved by signals recorded by 14 accelerometers. These ones were installed internally on the tower, on seven measuring points along a vertical alignment close to the elevator area. The measuring points were settled in bi-axial configuration, by means of two piezoelectric accelerometers orthogonally positioned in a horizontal plan along the X and Y directions (Fig. 1).

No sensors were installed on the blades or in the nacelle. The monitoring campaigns, as mentioned before, were therefore not performed simultaneously on the four turbines, but on one turbine at a time, in ten days. A data acquisition system were employed to collect acceleration data. The sensors were connected to the acquisition system by 14 separate RG174 coaxial cables. The measuring chain is composed by:

- a dynamic acquisition unit (Dewesoft SIRIUSe-HD-16xSTGS);
- a fan less& rugged PC;
- 14 Coaxial sensor cables, from 30 to 130 meters length;
- Fourteen seismic accelerometers PCB 393B04 (Sensitivity 1 V/g, Range +/- 5 g, Frequency Range 0.06–450 Hz, Broadband Res.3E-6 g RMS, Non Linearity 1%);
- A PT100 (Temp Range 0–100 °C, total precision 1%, Resolution 0.1 °C) (Fig. 2).

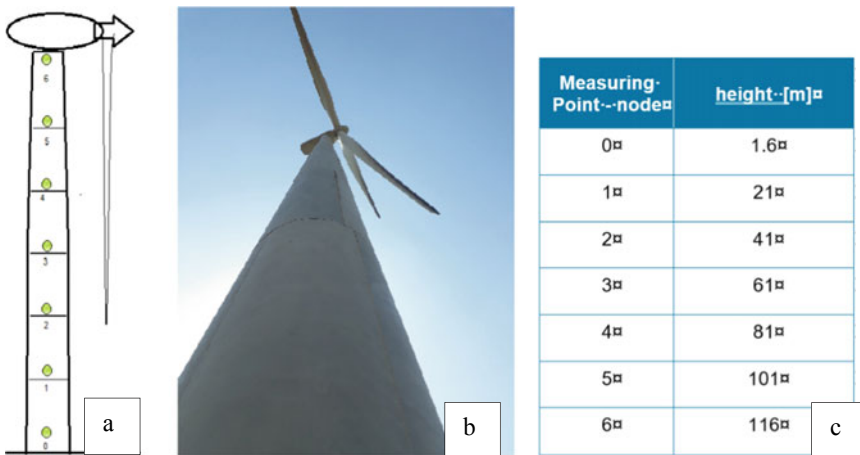


Fig. 1 a Measuring point schema b WT’s picture and c measuring point coordinates

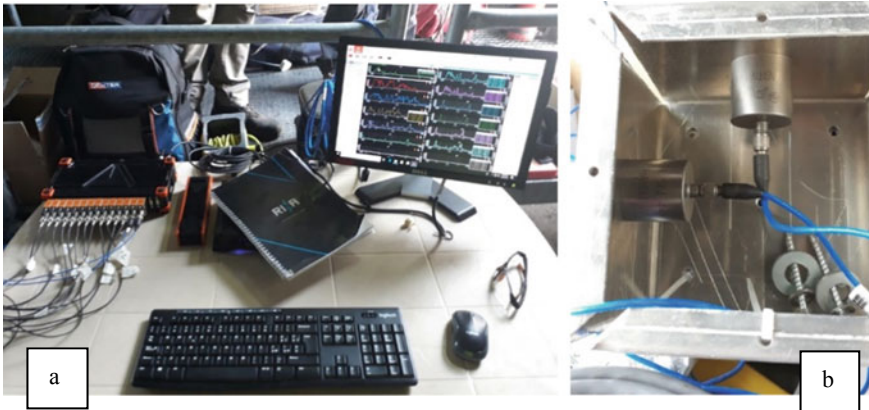


Fig. 2 a Data acquisition unit, b mono-axial sensors arranged in bi-axial setup

The temperature sensor was placed inside the tower in contact with the surface of the concrete. The variation of the measured temperature appeared limited in the time intervals to which the data used for the OMA analysis belong. The effect of temperature on vibration frequencies over the entire monitoring period was not assessed, as the effects of turbine operation on the variation of natural vibration frequencies were not removed.

In Fig. 3 the whole time histories of all measuring channels are reported for the WT #1 measuring campaign. The measures were recorded in many batches of one hour long, separated each by a time period of about 7 min. During the recording period, the four WTs experienced different working conditions at different rates of

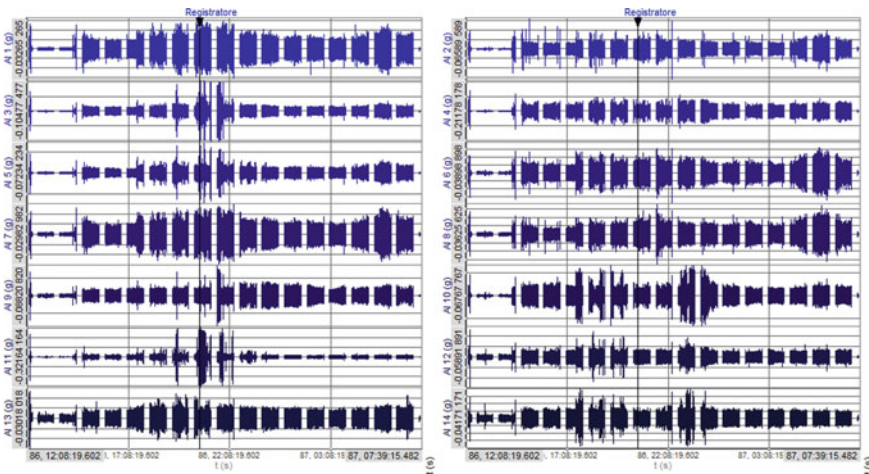


Fig. 3 Whole recorded data time series—WT #1

energy production and phases in parked condition. For the OMA analysis only the data referring to parked condition were used.

For the OMA analysis, as mentioned before, only data batches referring to parked condition was selected, choosing from those where the WT was in no-operating conditions. The total time series length chose for the OMA analysis was between 45 and 60 min, so more than proposed in [9] for expected values of ζ , and f_{min} equal to 0.02 and 0.3 Hz respectively. In Fig. 4 the time histories used in WT #3's OMA analysis (acceleration, blue and temperature, red) are showed.

Table 2 shows the temperature variation observed for all monitored WTTM during each time period considered for OMA.

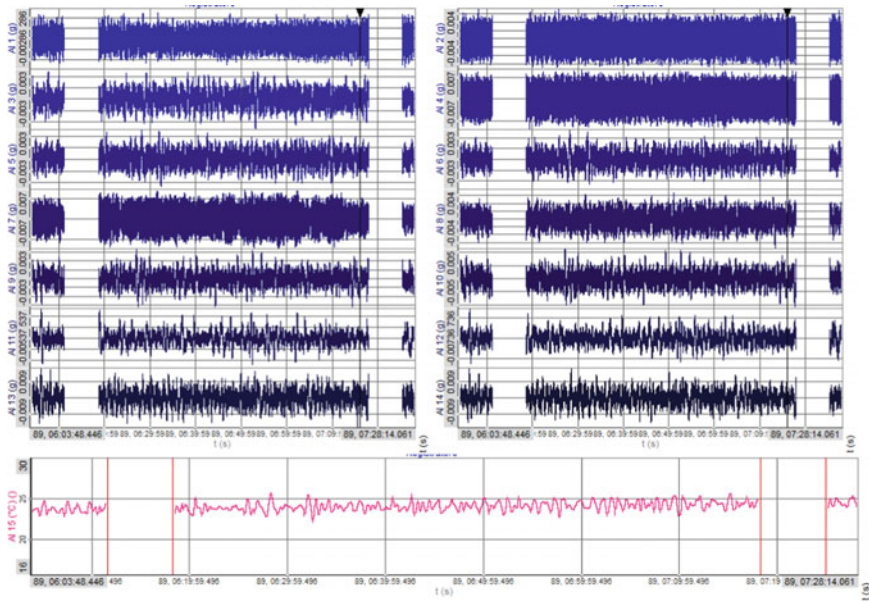


Fig. 4 Acceleration (blue) time series used in OMA analysis and temperature (red), WT #3

Table 2 Temperature observed range, OMA considered time period

Temperature variation	
WTTM	°C
#1	26–28
#2	23–24
#3	24–25
#4	24–23

4 Modal Parameter Estimation in Parked Condition

From the time histories of the sensors, those in which the turbines were in parked condition were isolated. The modal parameters of the tower were identified by means of operational modal analysis using the Artemis Modal Pro[®] software and the *Enhanced Frequency Domain Decomposition* (EFDD) technique. The EFDD [21], an extension of the *Frequency Domain Decomposition* (FDD) technique, was used because it allows you to easily view the parts of the spectrum in which there is structural information from those in which the noise is predominant. Being the WT noise sources for the signals sensor (electrical generation and transformation apparatus) and presenting the WT towers a structural behaviour biased by physical phenomena of various nature (aerodynamic turbulence, gyroscopic effects, etc.), the choice of the EFDD seemed the most suitable. However, the main limitation of this technique lies in the fact that it is based on the approximate decomposition of the spectral density matrix (SD matrix) built with the sensor data [9]. Because of this approximation, therefore, the FDD unlike other techniques (like Poly reference) necessarily introduces a bias in the results. This is especially true in the definition of modal deformations if their degree of complexity is high.

This method was introduced by Brincker et al. [10] in 2000. “*FDD is an improvement to the classical approach in EMA to pick resonance peaks from frequency response plots. Modal frequencies are directly obtained from the peaks of the Auto Spectral Density (ASD) or Power Spectral Density (PSD) calculated on acquired data. the SD matrix of the measured response channels can be expressed as*

$$G_y(j\omega) = \sum_{r=1}^{n^*} \left(\frac{d_r \psi_r \psi_r^T}{j\omega - \lambda_r} + \frac{d_r \psi_r \psi_r^T}{j\omega - \lambda_r} \right) \quad (2)$$

where n^* denotes that only dominant modes at a certain frequency ω are relevant d_r is a scalar constant depending on the modal participation factor and the unknown volume of the input noise. d_r is inversely proportional to natural frequency, damping and modal mass.”

Since mode shapes, ψ_r , in a modal model are generally unscaled, d_r is not of further interest in pure OMA. With Eq. (2), a direct link between the measurement data G_y and the modal parameters ψ_r and λ_r is established. λ_r is a complex value, which contains the natural frequency and the damping ratio.

The FDD technique estimates modes from spectral density matrices by applying a Singular Value Decomposition. It involves singular value decomposition of power spectra matrix G_y at each frequency into left and right singular vectors (U , V) and singular values $S(\omega)$:

$$G_{yy}(j\omega) = USV^H \cong \sum_{r=1}^N 2d_r^2 \text{Re} \left(\frac{\psi_r \psi_r^T}{j\omega - \lambda_r} \right) \quad (3)$$

The singular values composing the diagonal matrix S should be interpreted as the auto spectral densities of the modal coordinates and the singular vectors U and V^H as the mode shapes [9]. Singular vectors near the resonance are good estimate of the mode shapes and the frequency corresponding to the peak in the singular value curve is an estimate of the modal frequency. Actually, under a series of assumptions (lightly damped structure, well separated modes, imaginary part of modes negligible) the mentioned Eqs. (2) and (3) can be used to derive frequencies and modal shapes.

The EFDD is a further development of the FDD. In addition to modal frequencies and shapes, the EFDD can estimate modal damping. For this, singular value data are transferred to time-domain by an inverse Fourier transformation. Modal damping can then be estimated from the free decay. In this work the aspects due to damping have not been studied in depth. For further information on this technique please refer to the mentioned literature. The *Singular Value Decomposition* SVD lines calculated for the WT #4 in parked condition is shown in the Fig. 5.

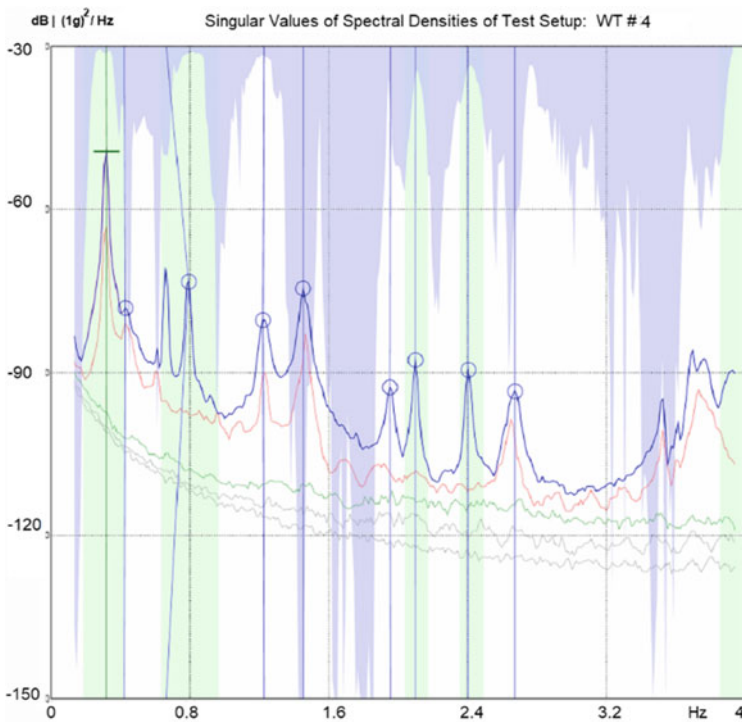


Fig. 5 SVD lines of PSD matrix—parked condition WT #4

5 Modal Parameters Extraction and Further Indicators

Starting by PSD calculated on recorded data with the help of numerical calculation, the FDD and EFDD algorithms (implemented in Artemis Modal Pro) have provided the modal parameters Frequencies ω_r , Damping factors (expressed as percentage of value of critical damping) ζ_r and Modal shapes $\{\psi_r\}$, being the r the indicator of r th mode. The characteristic frequencies and the modal shapes can be viewed also as the eigenvalues and the eigenvectors of the characteristic equation of the (undamped) system respectively:

$$\text{Det}([K] - \omega^2[M]) = 0 \tag{4}$$

where $[K]$ and $[M]$ are the stiffness and masses matrix.

For each of the WT, the estimated modal parameters frequency and damping factors of the first three bending modes are showed in Table 3. In the case of WTTMs, the modal damping factor is very susceptible to external excitation conditions and is not recognized as a complete indicator of damage. Therefore, the values obtained with the EFDD are reported for completeness. In the last row frequency results provided by FEM are also reported, while the damping factor was settled to the 5% value. In the same Table 3, the values of K_r measured are also reported for each WT. This to permit a direct comparison between first oscillating frequency and the K_r value.

In this manuscript the terms mode shapes and eigenvectors are used to indicate the same parameters $\{\psi_r\}$. The modal shapes of the first mode, provided by analysis carried out by Artemis Modal Pro, are showed in Fig. 6 for each WTTM.

The same modal shapes showed above are reported in Fig. 7 and Fig. 8 by using graph of MS Excel™ and by using the eigenvector values supplied by OMA, $\{\psi_r\}$.

Table 3 Bending mode— ω_r , frequency (eigenvalues) and ζ_r , damping factors

WT	K_r (GNm/rad)	I Mode. X ω_r and ζ_r (Hz) (%)	I Mode. Y ω_r and ζ_r (Hz) (%)	II Mode. X ω_r and ζ_r (Hz) (%)	II Mode. Y ω_r and ζ_r (Hz) (%)	III Mode X ω_r and ζ_r (Hz) (%)	III Mode Y ω_r and ζ_r (Hz) (%)
#1	102	0.31	0.32	1.43	1.44	3.68	3.73
		0.99	0.92	2.1	2.25	0.33	0.74
#2	220	0.35	0.36	1.54	1.55	3.61	3.88
		1.5	0.85	0.29	0.38	0.09	0.16
#3	Not measured	0.32	0.31	1.45	1.45	3.68	3.9
		2.3	3.5	0.75	0.81	0.24	0.46
#4	297	0.34	0.33	1.47	1.49	3.92	3.75
		1.1	0.99	0.47	0.51	0.75	0.8
FEM	Clamped	0.31	0.32	1.37	1.39	3.31	3.36
		5	5	5	5	5	5

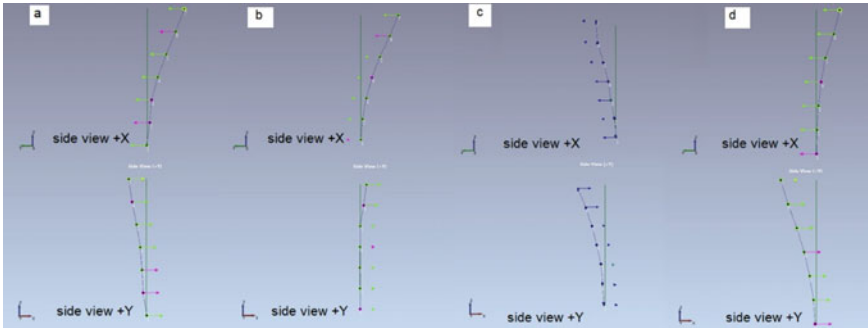


Fig. 6 I bending mode, modal shape of WTTM #1, #2, #3 and #4, (a), (b), (c) and (d)

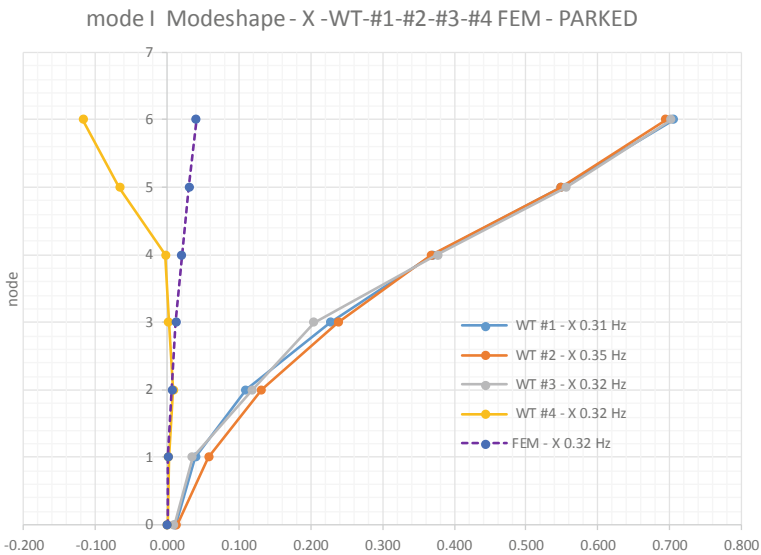


Fig. 7 Mode I, X components for all WTTMs plus FEM

5.1 Indicators Derived from the Modal Parameters

The modal parameters allow to achieve indications on the dynamic behaviour of the towers, but they are not very sensitive to local changes in stiffness as they are essentially governed by the mass distribution which in the event of damage does not change. In addition, some indicators, [11], derived from the modal parameters, are very useful for having clues about the possible onset of damage on the structures. In this work, however, these indicators are used to identify differences in stiffness by the four WTTM studied. Due to the fact that measuring sensor was installed close the junctions of the tower’s sections, the investigation object of this study is limited to

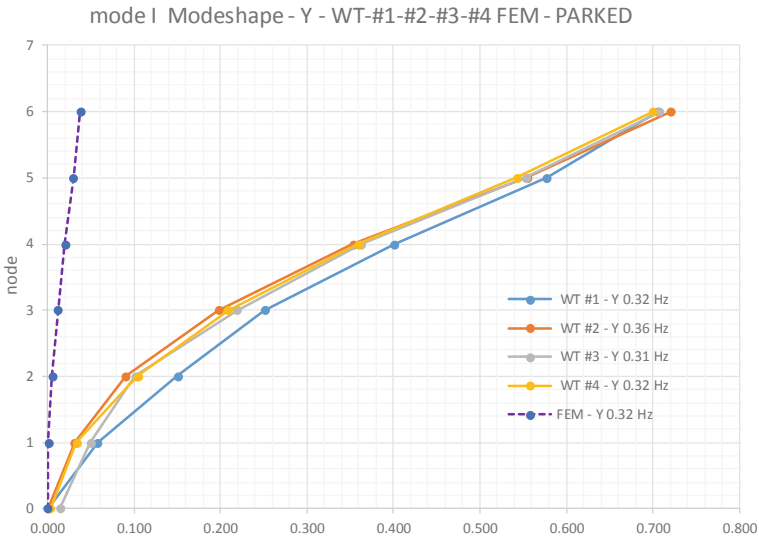


Fig. 8 Mode I, Y components for all WTTMs plus FEM

the tower, with special attention to the joint’s efficiency. Therefore, the influence of generator, gearbox, blades and tendons cannot be directly observed with the available data and are not the object of direct study of this work.

By the simple visual inspection of mode shape, it is not easy to detect signals of structural differences on WTTMs. In this case, for example, the WT #4 shows the X component of first mode shape that is different by others WTTMs: the total displacement is lower than other WTTM and it’s close the displacement of the FEM’s mode shape. Without considering the change in shape on node no. 4, the WTTM #4 appears to be much stiffer than other WTTMs in X direction. For this reason, we have tried in this experience to calculate a series of indicators based on the modal parameters obtained with the OMA analysis, with the aim of obtaining more detailed information on the mechanical properties of the WT towers. Starting from the modal parameters identified for the four turbines, the following indicators have been calculated:

- UMM (Unitary Modal Mass normalized mode shapes)*
- Flexibility Matrix*
- Curvature of modal shapes.*

And, starting from dataset, the *STFT, Short Time Fourier Transform* was calculated with the aim of identifying differences in the behaviour of the turbines in non-linear response conditions [12].

5.2 UMM Normalized Mode Shapes

In general, the modal deformations of the modes represent a discrete source of clues about a possible damage of the structures in the linear field. A change over time of the shape of these modes or a shift in the frequencies is taken into consideration as the first signal of the onset of big changes in the rigidity of the structure. However [13] the modal shapes $\{\psi_r\}$ obtained with the OMA technique, unlike the eigenvectors obtained by means of classic techniques with measured excitation (EMA), are not directly usable for this purpose or to perform direct comparisons with the modal deformations provided by a FEM analysis. This is because the elements of each mode in the modal matrix $[\psi]$ are only known within an *indeterminate scaling factor*, d_r , which as explained above, reminds us that in OMA the value of excitation and the mass associated at each mode are not known. Therefore, the assumption was made that the excitation sources that invested our WT's during the acquisition of data in parked condition was uniform throughout the structure and was of the same (averaged) intensity for all four WT's. The aim is to compare the modal deformations of the four WT analysed with each other and also to compare these modal deformations with those provided by the FEM. To do this, the eigenvectors provided by the OMA analysis and those provided by the FEM have been scaled compared to the *modal masses*, m_r .

The m_r are the masses associated with the r -th mode of vibration of the structure but the OMA technique does not provide this value. So let's take advantage of a fact: the WT are identical and their towers are made up of prefabricated panels whose mass and geometry are known. Therefore, referring to Eq. (4), in our case it's possible to compose the matrix of the masses $[M]$ of the tower, thanks to the project data and thanks to the uniform construction (precast panels in situ assembled) of the tower composing the four studied WTTM. In [9] various methods for scaling the modal shapes obtained with the OMA are described: mass change method, mass-stiffness change method, and the use of FEM mass matrix. Instead of the FEM mass matrix, a reduced mass matrix $[M_-]$ was created, imagining that the mass of the six sections of the tower was concentrated at the nodal positions. The normalized vectors are defined as UMM (Unitary Modal Mass) normalized mode shapes, $\{\phi_r\}$. The m_r , then, are calculated starting from the eigenvectors, ψ , identified with the OMA technique by using:

$$m_r = \psi_r^T [M_-] \psi_r \quad (5)$$

where $[M_-]$ is a reduced mass matrix, it is diagonal, and it is associated to a simple model of the tower composed by 7 nodes and where the masses of the six tower's section and nacelle + rotor are concentrated in the measuring point (nodes) (Table 4).

Finally, the UMMs normalized mode shapes as [13, 14] are:

$$\{\phi_r\} = \gamma_r \{\psi_r\} \quad (6)$$

Table 4 Reduced mass matrix diagonal elements used

Reduced Mass Matrix [M_]—values are in ton						
M ₁₁	M ₂₂	M ₃₃	M ₄₄	M ₅₅	M ₆₆	M ₇₇
128	242.5	219.5	197.5	165	128	239.5

where γ_r is defined as:

$$\gamma_r = \frac{1}{\sqrt{\psi_r^T [M_-] \psi_r}} = \frac{1}{\sqrt{m_r}} \tag{7}$$

that is, by subdividing the X and Y directions of each r-mode:

$$\gamma_{rX} = \frac{1}{\sqrt{\psi_{rX}^T [M_-] \psi_{rX}}}, \gamma_{rY} = \frac{1}{\sqrt{\psi_{rY}^T [M_-] \psi_{rY}}} \tag{8}$$

The $\{\phi_r\}$ will be useful for the calculation of other indicators and to identify differences in the modal deformations of the modes in the four WT object of this work.

The pictures from Figs. 9, 10 and 11 show the (ϕ) UMM eigenvector calculated as described above for the four WT in parked condition and for the FEM, associated to the first two modes.

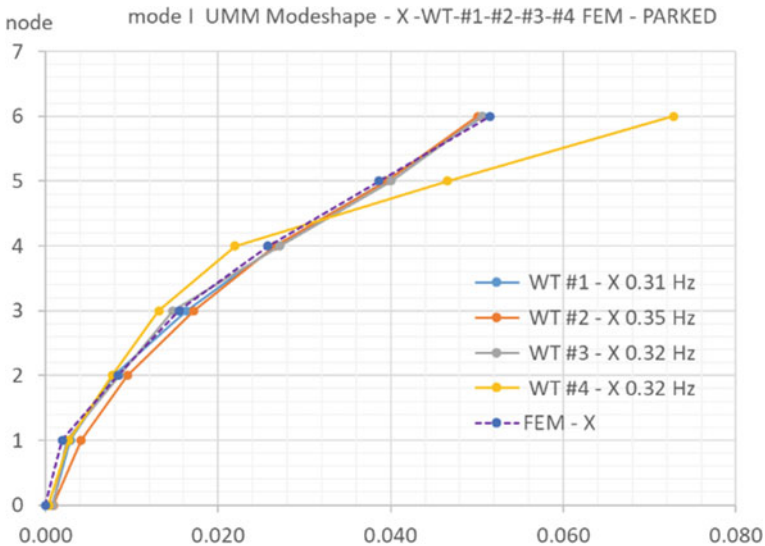


Fig. 9 UMM normalized I mode shape, X components

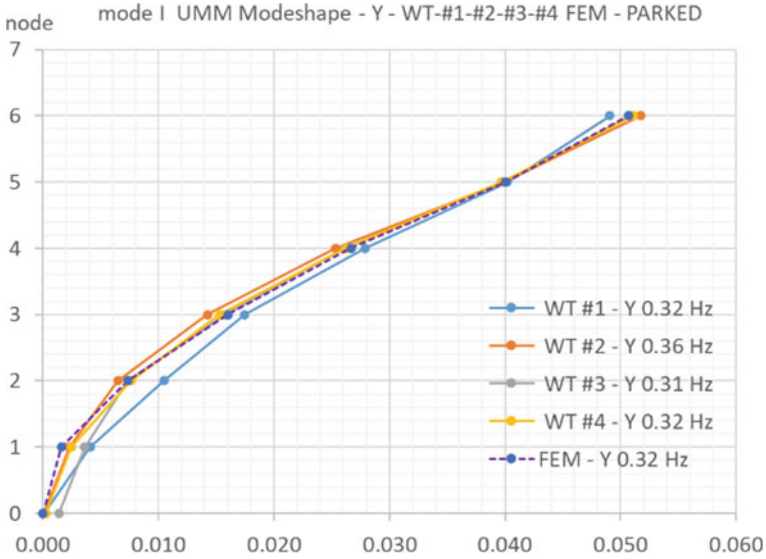


Fig. 10 UMM normalized I mode shape, Y components

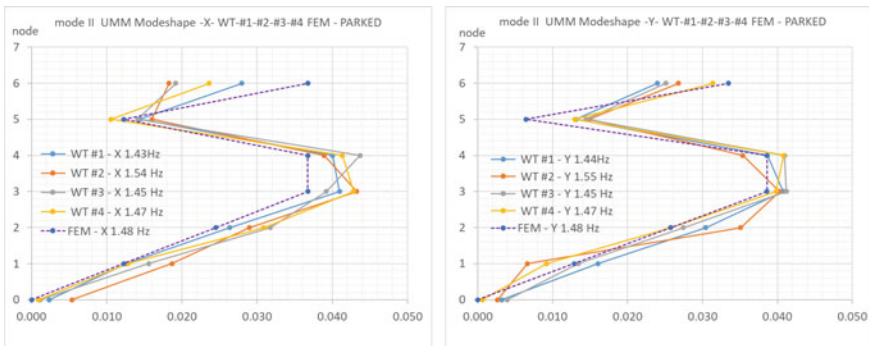


Fig. 11 UMM normalized II mode shape, X and Y components

5.3 Flexibility Matrix

The flexibility matrix $[F]$ is defined as [13, 15]:

$$[F] = [\Phi][\Omega]^{-1}[\Phi]^T = \sum_{r=1}^n \{\phi_r\} \frac{1}{\omega_r^2} \{\phi_r\}^T \tag{9}$$

where ϕ_r are the UMM normalized vectors mentioned above, $[\Omega] = \text{diag}(\omega_r^2)$ is the eigenmatrix and ω_r is the r-th modal frequency (refer to Table 1 for whole ω_r values).

The diagonal components of $[F]$ can be considered as static displacement in point I for a unitary force applied in i one, so the flexibility matrix of a structure can be regarded as the inverse of the structural stiffness matrix. Differences in these values are indicative of the structure's condition.

[15] The flexibility matrix is affected by the mode shapes and the natural frequencies. The localized damage reduces the stiffness and increases the flexibility of the structure. The modal contribution to the flexibility matrix decreases as the frequency increases, so the flexibility matrix converges rapidly with lower modes.

The damages result in stiffness reduction and the flexibility increment in the corresponding elements near the damages. Increase in the flexibility can be used to detect and locate damages or more in general loss in stiffness, into the structures. As stated above, $[F]$ is synthesized by using the mode shapes. In our case, the WT modes were obtained both through OMA analysis and from a FEM model. The use of $[F]$ to obtain information about the WTTM condition is done here by comparing the $[F]$ synthesized by the OMA analysis with that synthesized by the FEM modal parameters.

In Fig. 13 for each of four studied WT tower, the diagonal values of the flexibility matrix will be illustrated in graphic form showing the values of the diagonal elements along the measurement points. In the same Fig. 12 is also showed the diagonal elements of the flexibility matrix calculated on FEM's modal shapes.

Table 5 shows the mean value of the diagonal's elements of $[F]$. The mean value can be indicative of differences in the condition between identical structures. In fact, WT #2 is the one with the lowest value and the one with the best structural behaviour, on the contrary WT #4 is the one with the highest value and the one with a not satisfactory structural behaviour, despite the best value of K_r . Another use of $[F]$ can be to consider the following relation to indicate the change in flexibility [16]:

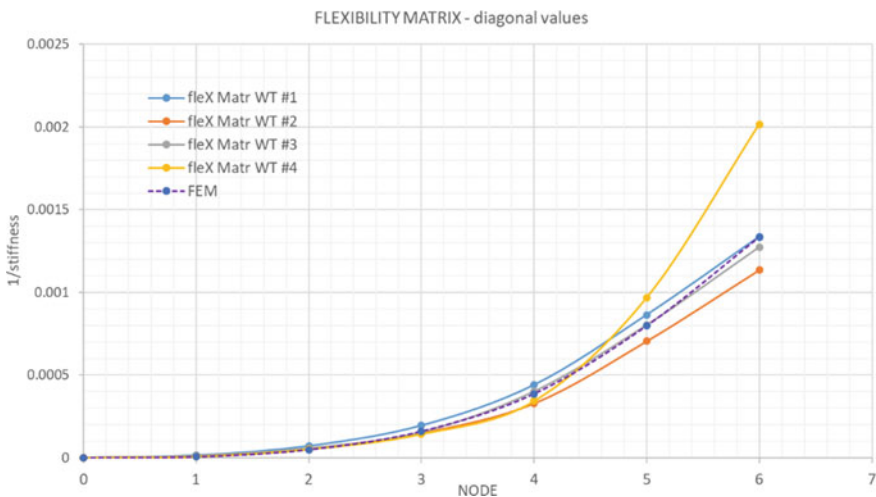


Fig. 12 Flexibility matrix diagonal elements calculated for WT #1, 2, 3, 4 and FEM

Table 5 Averaged values diagonal elements of Flexibility matrix

Averaged values Flexibility matrix—diagonal elements	
WTTM	
#1	418×10^{-6}
#2	341×10^{-6}
#3	386×10^{-6}
#4	505×10^{-6}
FEM	391×10^{-6}

$$[\Delta F] = [F_{WT}] - [F_{FEM}] \tag{10}$$

Equation (10) represents the calculated difference between the corresponding elements of the diagonals of the matrix [F] associated with a WTTM and that calculated for the FEM model. In this case the FEM model represents an ideal structure of WT. The results of (10) are shown in graphical form in Fig. 13.

The distribution along the nodes of the value of [F] and $[\Delta F]$ in the two previous figures follows the shape of the first mode, so that as the distance from the foot of the WT (node 0) increases, the values of [F] and $[\Delta F]$ increase. However, WT #4 shows in node 5 an important deviation from the expected values while for WT #2 the values of [F] are lower than those calculated for the FEM model.

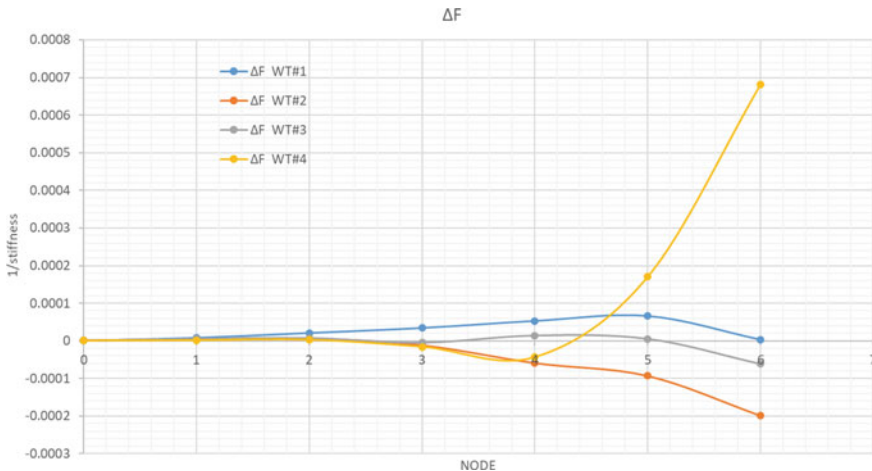


Fig. 13 Change in flexibility matrix ΔF , calculated for WT #1, 2, 3, 4 respect to FEM

5.4 Modal Shapes Curvature

Starting by undamaged condition of a structure, a reduction of stiffness will lead to an increase in curvature. This parameter can therefore be useful for determining over time the onset of stiffness reductions, associated with specific damage or more general loosening of the structure (in our case the tendons or the efficiency of the joints between the tower’s sections). Starting from the available data, this work will compare the curvature of the modal deformations of each turbine with respect the turbines themselves, these being identical in design and construction. This parameter is also compared whit a curvatures outputs calculated on FEM’s UMM modal shape.

Curvature is defined, in this work, by using the central difference approximation [15, 17, 18]:

$$k_{i,r} = \frac{\phi_{(i+1)r} - 2\phi_{ir} + \phi_{(i-1)r}}{l^2} \tag{11}$$

With r being mode shape number, i the node number, ϕ_{ir} is the modal displacement (mass normalized mode shape) of the coordinate i at mode r , l is the distance between the nodes (equal to 19.5 m in our case).

The curvatures calculated for the four WTTM starting from the modal shapes identified by the OMA, and normalized with respect to the modal masses, are presented from Figs. 14, 15 and 16.

Table 6 shows, for each mode and for each WTTM, the averaged value of the curvature values calculated at nodes by using the (11).

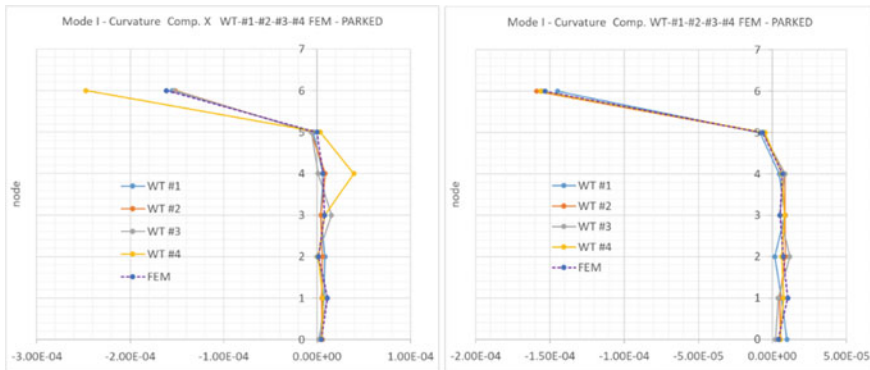


Fig. 14 Curvature of UMM normalized I mode shape, parked condition, X and Y measuring directions

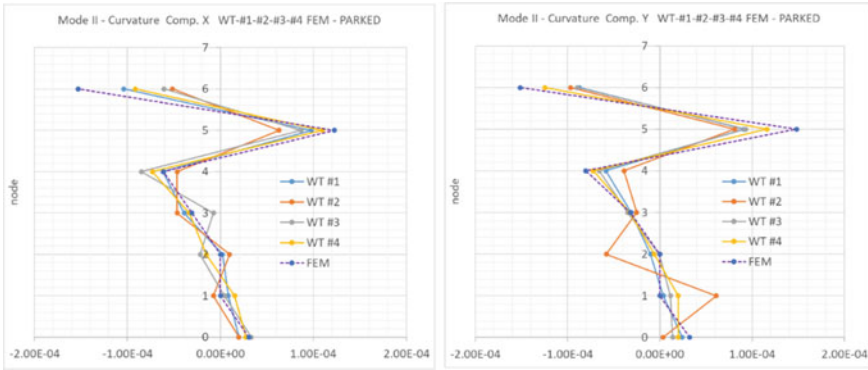


Fig. 15 Curvature of UMM normalized II mode shape, parked condition, X and Y measuring directions

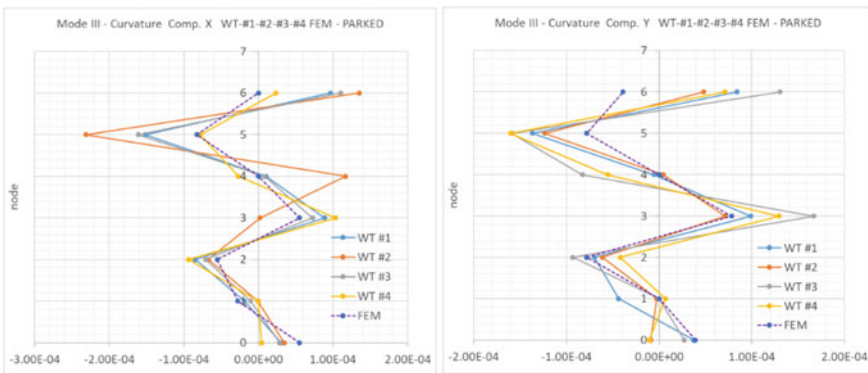


Fig. 16 Curvature of UMM normalized III mode shape, parked condition, X and Y measuring directions

5.5 Short Time Fourier Transform

[19] “Short-time Fourier Transform (STFT) is a sequence of Fourier transforms of a windowed signal. STFT provides the time-localized frequency information for situations in which frequency components of a signal vary over time, whereas the standard Fourier transform provides the frequency information averaged over the entire signal time interval.

The STFT pair is given by

$$\begin{cases} X_{STFT}[m, n] = \sum_{k=0}^{L-1} x[k]g[k - m]e^{-j2\pi nk/L} \\ x[k] = \sum_m \sum_n X_{STFT}[m, n]g[k - m]e^{j2\pi nk/L} \end{cases} \quad (12)$$

Table 6 Averaged values of curvature calculated at nodes

Mode		I		II		III	
		X	Y	X	Y	X	Y
#1		-1.839E-05	-1.755E-05	-1.082E-05	-9.709E-06	-4.185E-06	-5.156E-06
#2		-1.822E-05	-1.849E-05	-8.443E-06	-1.052E-05	-1.445E-06	-1.042E-05
#3		-1.837E-05	-1.868E-05	-7.254E-06	-1.038E-05	-3.172E-06	-1.492E-06
#4		-2.611E-05	-1.832E-05	-8.771E-06	-1.144E-05	-9.687E-06	-8.776E-06
FEM		-1.840E-05	-1.809E-05	-1.312E-05	-1.195E-05	-7.875E-06	-1.117E-05

where $x[k]$ denotes a signal and $g[k]$ denotes an L -point window function. From previous formulation the STFT of $x[k]$ can be interpreted as the Fourier transform of the product $x[k]g[k-m]$.” The time-variation of the dynamic response of a structure, for example during a transient excitation forcing, can be an indication of the change in structure’s characteristics or also the of a nonlinear behaviour [12]. In this paper the modifications of the frequency values associated to the modes indicated in Table 2 have been considered as change in dynamic response. The STFT has been used to observe in detail the response of the nodes and therefore in order to identify differences in the various measuring points of the four towers during transitory modifications of the input excitation. The transitory modification of input can be represented for example by of gusts of wind that generate sudden stresses capable to mobilize the tower structure or generate sudden increases in the bending moment.

STFTs were calculated using the Dewesoft X3 SP6 software, [20]. The STFTs were calculated for the four turbines investigated and the 0.2–2 Hz frequency range was analyzed where the first and second modes of vibration reside. The STFTs were calculated with the following parameters:

- Block size*—defines the number of real data samples to be taken for the calculating FFT = 2048 samples
- FFT size*—defines the number of resulting lines and with that the ratio between real and zero padded lines = 8096
- Window type*—describes the FFT window to be used = Blackman
- Overlap*—defines how much will two FFT shots overlap between each other: 50%.

In Table 7 are reported all the results obtained. These are expressed as percentage of the frequency value associated to the first mode ($\omega_{r=1}$, see Table 3).

In Figs. 17 and 18 are reported some significant result regarding the calculation of the STFT conducted on the same data set used for OMA. All obtained results are referred to the first bending mode.

Table 7 Changing in frequencies detected by STFT calculation—percent values of frequencies reported in Table 3

Node	Component	WT	Frq. Var (%)
4	X	#1	6.5
6	X	#1	6.5
5	X	#3	9.4
5	Y	#3	6.7
6	Y	#3	9.7
5	X	#4	8.8

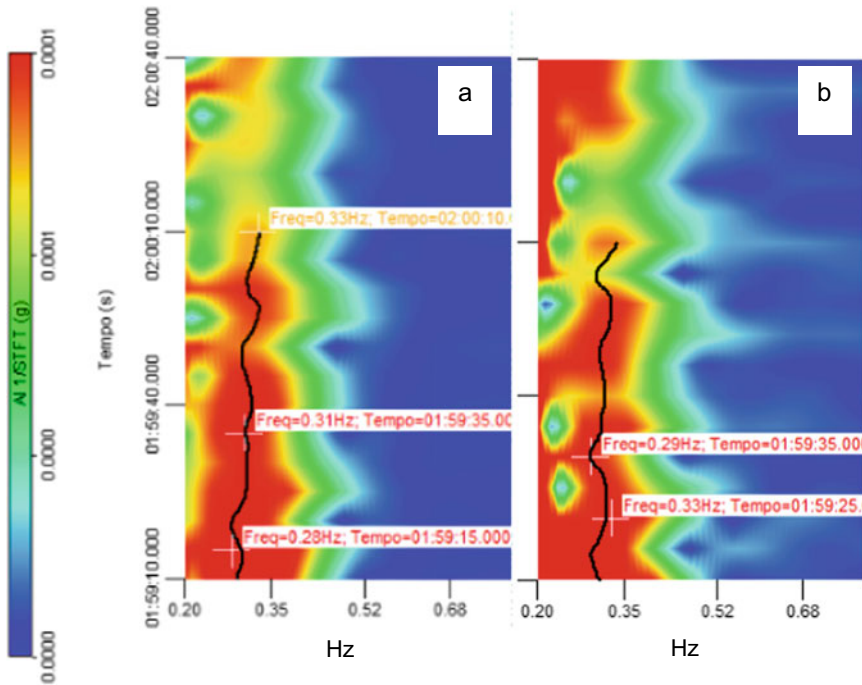


Fig. 17 STFT calculated for measuring point 6 (a) and point 4 (b) X component—WT #1

6 FEM Analysis

The following Fig. 19 shows the modal shapes provided by a simple FEM model, by means of a seismic dynamic analysis in the linear field. In the FEM the damping coefficient is set at 5%, a default value imposed in the national regulations. The frequency values are shown in Table 1 above. The model consists of 2043 nodes and 1200 shell elements. The material used is concrete (isotropic and elastic) with Young modulus of 41,000 MPa, density equal to 2500 kg/m³ and Poisson’s coefficient of 0.2. The action of the tendons was modelled as a load at the head of the tower and the nacelle + rotor set was modelled as a structure that follows their position and mass distribution. The boundary condition at the tower base is clamped, while on site the tower is resting on the pedestal and held in place by the tensioning force of the tendons.

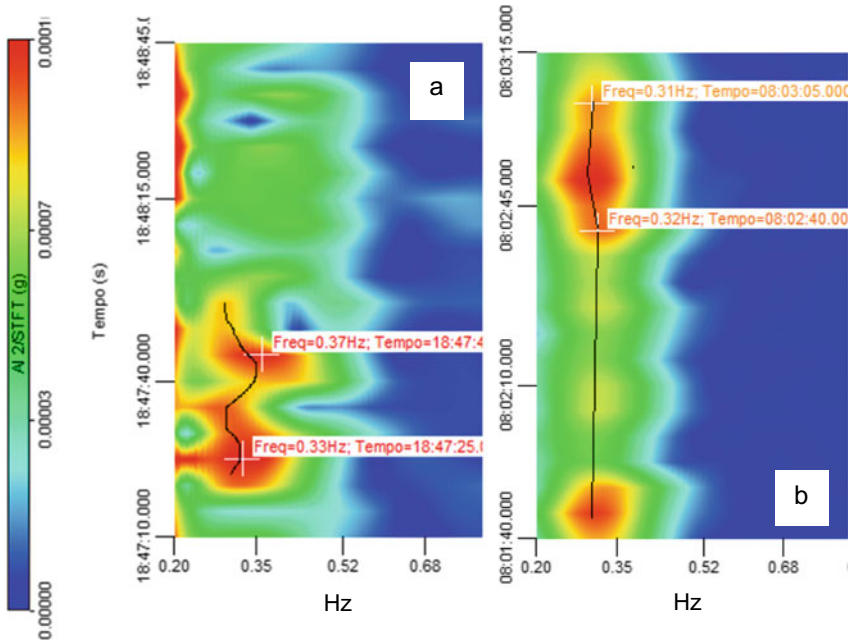


Fig. 18 STFT calculated for node 6, Y component, WT #3 (a) and node 5, X component, WT #4 (b)

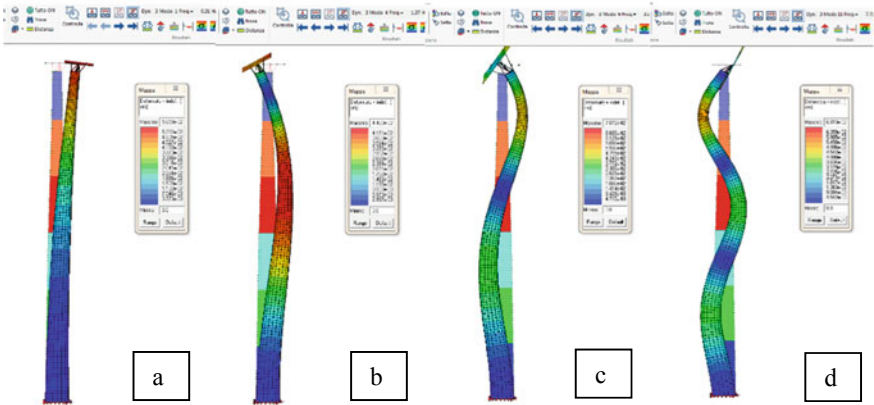


Fig. 19 Modal Shapes by FEM analysis I, II, III, IV from (a) to (d) respectively

7 Comparison of the WTTMs Results

The **UMMs** show that the WT #4 is the one that has great amplitudes in the modal deformation of the first mode, while the others WTTM present shapes almost superimposable to those of the FEM. This is less true for the superior modes. For all WTTMs the values of the modal displacement calculated at the node 0, close the base of tower, show important differences between FEM and WTTM. Probably the differences are a measure of the lateral stiffness, K_l . This parameter concerns the resistance to lateral loads performed by connection between tower base and foundation and K_l . Here it's important note that the first vibration frequency is influenced by K_l [1, 2] like the rotational stiffness K_r . This aspect will be treated in subsequent work.

The **Flexibility Matrix** shows that WT #2 is the one that has the highest overall stiffness in the tower. WT #4, instead, has greater flexibility value (see Table 5). In particular, the flexibility for WT #4 increases in nodes 4 and 5 (see graph on Figs. 13 and 14).

The **Curvature** shows, in modes higher than the first, values greater than those calculated on the FEM modes for all WTs. WT #2 is the one that in the first mode has the least curvature values compared to the other WT. Instead the WT #4 shows the highest value of this parameter (see Table 6).

The **STFT** shows significant variations in the frequency of the first mode at nodes 6 and 5 of WT #1 and #3. The frequency ranges variation are respectively [0.28–0.35 Hz] and [0.29–0.37 Hz] for WT #1 and WT #3.

The **WT #1** is the one that during the working operations has periods of oscillation so close to 1P that it must often be turned off. The damage indicators do not show particular problems from a structural point of view, but its K_r value was found to be lower than the design values.

The **WT #2** is the one with the best performances of its WTT, not presenting resonance problems with 1P during the different operating conditions. The damage indicators do not show particular problems from the structural point of view and the K_r value is in line with the project performance.

Regarding **WT #3** the analysis carried out on the dynamic data did not indicate particular problems related to the tower, even if the STFT indicates in points 6 (118 m elevation) and 5 (100 m elevation) of the frequency variations of the first mode concentrated in short periods of time, the order of 20–30 s. For WT #3 can be speculated local inefficiencies of the joints in particular wind conditions. During working operations, the period of oscillation related the first mode results to be dependent by the thrusts and to avoid frequency alarms, it is normally set to work at a power levels production lower than the design ones.

The **WT #4** presents the highest K_r values and a period of the first mode quite far from the 1P level but strongly dependent by thrust conditions and often the frequency of the first mode brings down. For WT #4 results an excessive flexibility of the tower, probably concentrated around the junction between 4 and 5 tower rings, around 80 m elevation above ground level.

8 Conclusion

In this manuscript was described an experimental experience born from an industrial project in which Rina Consulting S.p.A. was charged with identifying the causes of unsatisfactory structural behavior of some WTs. Four WTs were instrumented with acceleration, temperature, strain and tilt sensors and continuously monitored for a period of 2 days (acceleration and temperature) and a month (strain, inclination and temperature). The experience described in this work refers to the analyses carried out on the data provided by the acceleration sensors. In this paper, Sect. 1.1 a procedure for investigating the structural problems of WTTM based on OMA and project data has been proposed.

The results of the proposed procedure demonstrate that it provides a coherent framework between the values of the damage indicators adopted in it and the actual structural problems identified on the structures.

As no inspection of the WTTM was carried out, it was not possible to verify the presence of defects in the points indicated by the damage indicators. The results of the proposed procedure show, however, that the matrix variables of flexibility, curvature and STFT can provide an explanation for unsatisfactory structural behavior on WTs, as well as providing guidance on where to conduct in-depth investigations and inspections. The experience reported in this paper also seems to suggest that for homogeneous and symmetrical structures the usefulness of these functions exists even in the presence of a low density of measuring points.

References

1. Adhikari S, Bhattacharya S (2012) Dynamic analysis of wind turbine towers on flexible foundations 2010. *Shock Vib* 19:37–56. <https://doi.org/10.3233/sav-2012-0615>
2. Wang S, Huang Y, Li L, Liu C, Zhang D (2017) Dynamic analysis of wind turbines including nacelle–tower–foundation interaction for condition of incomplete structural parameters. *Adv Mech Eng* 9(3):1–17. <https://doi.org/10.1177/1687814017692940journals.sagepub.com/home/ade>
3. Rina Consulting Report P0008750-1 March 2018, POO13733-1-H1 Rev March 2019
4. Rina Consulting report P0008750-5-1-01 H4 Rev. 1 September 2019
5. Manzato S, White JR, LeBlanc B, Peeters B, Janssens K Advanced identification techniques for operational wind turbine data Advanced identification techniques. LMS International, Interleuvenlaan 68, B-3001 Leuven, Belgium, Sandia National Laboratories, Wind Energy Technologies, Albuquerque, NM, USA
6. Ozbek M, Meng F, Rixen DJ (2013) Challenges in testing and monitoring the in-operation vibration characteristics of wind turbines. Elsevier Ltd. <http://dx.doi.org/10.1016/j.ymsp.2013.07.023>
7. Di Lorenzo E, Manzato S, Peeters B, Marulo F (2013) Modal parameter estimation for operational wind turbines. LMS, A Siemens Business, RTD Test Division, Interleuvenlaan 68, 3001 Leuven, Belgium. University of Naples «Federico II», Department of Industrial Engineering, Via Claudio 21, 80125 Naples, Italy
8. Von der Haar C, Marx S (2015) Design aspects of concrete towers for wind turbines. *J South African Inst Civil Eng* 57(4):30–37. Paper 1228

9. Brincker R, Ventura C (2015) Introduction to operational modal analysis. Wiley. ISBN 978-1-119-96315-8
10. Brincker R, Zhang L, Andersen P (2000) Modal identification from ambient responses using frequency domain decomposition. In: Proceedings of the 18th international modal analysis conference (IMAC), San Antonio, Texas, pp 625–630
11. Ciang CC, Lee J-R, Bang H-J (2008) Structural health monitoring for a wind turbine system: a review of damage detection methods. *Meas Sci Technol* 19122001 (20 pp). <https://doi.org/10.1088/0957-0233/19/12/122001>
12. Ditommaso R, Mucciarelli M, Ponzio FC (2012) Analysis of non stationary structural systems by using a and b variable filter. *Bull Earthquake Eng.* <https://doi.org/10.1007/s10518-012-9338-y>. DiSGG, University of Basilicata, Potenza, Italy
13. Bungard V (2011) Condition assessment of concrete structures and bridges using vibration monitoring in comparison to changes in their static proprieties. Shaker Verlag. ISBN 978-3-8440-0077-1
14. Viola E (2001) Fondamenti di dinamica e vibrazione delle strutture. ISBN 88-371-1138-X. Pitagora Ed. Bologna
15. Dawari VB, Vesmawala GR (2012) Modal curvature and modal flexibility methods for honeycomb damage identification in reinforced concrete beams. In: NUICONE 2012. Elsevier. <https://doi.org/10.1016/j.proeng.2013.01.018>
16. Andersen JT (2012) Studies in damage detection using flexibility method. Master iKonstruksjonero gmaterialerSpesialisering: Offshore konstruksjoner. Universiteteti Stavanger
17. Cao MS, Xu W, Ren WX, Ostachowicz W, Sha G-G, Pan L-X (2016) A concept of complex-wavelet modal curvature for detecting multiple cracks in beams under noisy conditions. <http://dx.doi.org/10.1016/j.ymsp.2016.01.0120888-3270/&>. Elsevier Ltd
18. Mosti F, Quaranta G, Lacarbonara W (2014) Numerical and experimental assessment of the modal curvature method for damage detection in plate structures. In: MATEC web of conferences. <https://doi.org/10.1051/mateconf/20141602007>
19. Kehtarnavaz N (2008) Frequency domain processing in digital signal processing system design, 2nd ed. Academic Press University of Texas at Dallas. <https://doi.org/10.1016/B978-0-12-374490-6.00007-6>
20. Dewesoft User Manual—rel. 2019. support@dewesoft.com
21. Greiner B (2009) Operational modal analysis and its application for SOFIA telescope assembly vibration measurements. InstitutfürRaumfahrtssysteme, Universität Stuttgart

Digital Tools for the Knowledge and Safeguard of Historical Heritage



Adriana Marra , Ilaria Trizio , and Giovanni Fabbrocino 

Abstract In last years, the Italian historical heritage revealed its high fragility due to relevant events caused both by natural phenomena and by lack of maintenance. The suffered damages highlighted the need to act to prevent and/or control degradation and mitigate the effects of endogenous and external hazards. The increased need of safeguarding the historical heritage and the advances in digital technologies applied to cultural heritage pushed towards novel conservation and risk mitigation procedures, such as proactive conservation plans. These plans may take advantage of novel digital tools for the survey, diagnosis, conservation and monitoring associated to a digital twin of the construction and of its relevant structural and non-structural components. These tools are able to manage and deploy a digital knowledge of the buildings conditions, both conservative and structural, and thus drive maintenance and restoration process with the aim of increasing the resilience of historical heritage. In the paper, a prototypal digital model of historical architectural and artistic assets is illustrated to discuss the maturity of the approach and the aspects still open. The testing covers both structural and artistic components from a conservation and

Author Contributions The research presented is the result of authors' collective work, of continuous comparison and of a common discussion. Adriana Marra wrote Sect. 3, she defined the parameters for the SeVAMH protocol and modeled the family created. Ilaria Trizio wrote Sect. 2; she also supervised the modelling phase and paper. Giovanni Fabbrocino conceived and supervised the research, he validated the tools for the artworks survey for seismic Artistic Limit State assessment in SeVAMH protocol and the parameters for the sensor modeled. All authors wrote Sects. 1 and 4.

The students of the "Rilievo e modellazione digitale dell'architettura" course at University of L'Aquila, with the coordination of the Professor Ilaria Trizio, realized the parametric model of the building and mathematical and numerical models of the artistic asset of the Church of San Menna.

A. Marra (✉) · I. Trizio · G. Fabbrocino

ITC-CNR, Construction Technologies Institute-National Research Council, 67100 L'Aquila, Italy
e-mail: marra@itc.cnr.it

I. Trizio

e-mail: trizio@itc.cnr.it

G. Fabbrocino

e-mail: fabbrocino@itc.cnr.it; giovanni.fabbrocino@unimol.it

G. Fabbrocino

Department of Biosciences and Territory, University of Molise, 86100 Campobasso, Italy

seismic viewpoint. A cost-benefit analysis is proposed in order to point out perspectives of the novel technologies and the opportunities of integration between static data coming from the geometry, history (construction sequences and technology) and dynamic data resulting from monitoring systems envisaged as an additional support to operators having in charge the conservation and safety of historical constructions.

Keywords Historical heritage · Digital tools · Architectural survey · Conservation · Structural monitoring

1 Introduction

The cultural heritage is a valuable evidence of our past and culture. It consists of all artefacts having cultural interest and exceptional features since they are “unique and irreplaceable property, to whatever people it may belong” [1] and, therefore, they must be protected and valorized. However, the real concretization of these ideal objectives is particularly difficult to achieve due to the peculiarities of heritage and due to the structural, natural and man-made hazards to which the assets are exposed, so that the value of reliable and accurate analyses combined with effective decision-making processes is clearly pointed out.

Specific recommendations, agreed at International level [2, 3], identified strategies and methodologies to address these issues and ensure the safeguard of tangible and intangible cultural values of historical and architectural heritage, as well as of artistic and valuable assets [4, 5]. They clearly highlight two attributes of any methodology to be applied to cultural heritage: (i) multidisciplinary and (ii) preventive.

It is deemed, indeed, mandatory an in-depth cross-sectional knowledge of the artefacts, in its current state and in the different periods of the past, in its details and in its totality, and to define the analyses to be implemented both to assess the current conditions and to develop proper interventions for its safety and conservation.

Then, it is recognized that damage and degradation must be prevented, rather than repaired once observed. Consequently, it is recommended to plan the actions aimed at preventing the development of degradation or damage phenomena avoiding invasive restoration practices [6, 7]. Several experiences carried out at National and International level, for example the Great Pompeii project [8], Monumentenwacht [9], Monumentendienst [10], Maintain our Heritage [11], provided a wide range of contributions and explanatory cases to the topic of preventive and programmed conservation of historical-architectural heritage. They also emphasized that knowledge, monitoring and constant maintenance can ensure the safeguard of asset and the preservation of its authenticity.

However, the drafting of conservation and maintenance plans often fails due to high costs related both to the implementation of interventions and to the control phase, which involves the use of diagnostic and monitoring systems.

The long-term benefits about the implementation of such plans are immeasurable and digital technologies can provide a useful support for their drafting. In

this perspective, the multidisciplinary research group suggested the development of proactive conservation plans [12] and some results are described in the following pages.

The proposed plans can be defined as planned conservation plans [13] that use the most advanced technologies of architecture, structural engineering and of information and communication (ICT) by exploiting the Internet of Things (IoT) technologies.

The implementation of proactive conservation plans is a challenging task since their feasibility is connected to the available technologies, in particular in the field of architecture and structural engineering, and it is affected by the level of knowledge about built heritage and its single elements.

It is worth noting that, the proactive conservation plans can be implemented from the Informative Virtual Tour (IVT), such as the tool described in Trizio et al. [14] and presented in this volume, since these plans take advantage of all technologies and tools available in several areas concerning the cultural heritage. The IVT, conceived as hub able to record and manage different information, is a first possible step towards the development of parametric model and Historic Digital Twin of historical heritage.

Starting from these assumptions, the paper provides the results of the analyses carried out on the Church of San Menna in Lucoli, a municipality of Abruzzi region near L'Aquila city in central Italy, which led to the development of a prototype of an integrated informative system, whose functionality has been checked and validated in view of the development of an Historic Digital Twin based proactive conservation plan.

In particular, Sect. 2 provides an overview of the digital twin concept and deals with the approach to a Historic Digital Twin (HDT) capable of driving the maintenance and management of built heritage. Section 3 deals with the workflow and the tools used to setup the informative system via the reference to a real case; it also reports a description of history and main features of the selected asset, a church. In the same, the advantages and disadvantages of this system in the perspective of future development of HDT and proactive conservation plans are evaluated. Finally, Sect. 4 provides some considerations on results obtained with the aim of facilitating the development of more complex digital model for the conservation and management of cultural heritage.

2 Towards a Historic Digital Twin

Over the last twenty years, the scientific literature has demonstrated how digital technologies aimed at three-dimensional representation and modelling of multi-scale models are suitable for the gathering of heterogeneous data topologically related to the digital replicas of historical built heritage. The different research teams that have dealt with the issue have explored the potential of GIS3D [15–17] and of semantic digital models [18–20] before the possibility of applying parametric modelling to

the historical built environment was outlined with the coding of procedures known as HBIM [21–23].

As a consequence, the architectural heritage is correlated to models with different level of details and oriented towards the performance monitoring of historical building, the recognition of their condition and to the predictive evaluation of their residual life. The natural evolution of this process provides a support for decision-making and management processes as well as a guide for all activities aimed at maintenance and restoration works of heritage itself.

The concept of Digital Twin (DT), as digital replica of real artefacts and paradigm of the Industry of Construction 4.0 [24], derives from this cultural and research background. The DT enables the acquisition and interpretation of data in real time from the original in order to perform simulation and analyses of possible response on digital replicas. The implementation of DT, in particular when it concerns the historical built heritage [25, 26], requires an integrated multidisciplinary approach. The first step of this approach is the design of ontologies that are useful for the indexing of the acquired data, for the following management processes of the same data that will represent the preliminary phase for the implementation of DT [27, 28] and for its correct development and evolution [29].

The data input in the DT development process consists of static and dynamic data. The first category, derived from active and passive sensors used in the process and from data available on semantic databases properly developed, is used for the creation of digital parametric model as copy of the real. In this 3D informative model, all data linked to geometric and spatial entities converge, as well as the standards used for the classification of risks, material consistency, damage state and interventions carried out [26]. On the other hand, the dynamic data refer to the ways in which real-time operational information collected in situ by the sensors network interacts with digital models, as well as the way in which data aimed at monitoring of environmental parameters and specific risks are analyzed [26].

The use of open standards for the identification of risks, damage and possible interventions and the need to facilitate the interrelation and interoperability between the DT and informative systems of several organizations and institutions represent an open challenge, together with the information modelling, in the implementation of DT. The use of open source formats should be improved for this purpose, in order to have a unique format and to facilitate the sharing of information collected in the model. However, further efforts are necessary to achieve this challenge and to ensure the interoperability and the standardization of DTs and their data format, as well as the involvement of several stakeholders engaged in the management and protection of infrastructures heritage. The research team, which is approaching to the topic of DT, aims to make efforts in this direction and to face the challenge related to the issues of use, also for the future, of data concerning infrastructure artefacts.

The preservation of data on infrastructure assets must be guaranteed for the period necessary to deal with analysis, monitoring and intervention throughout all the life cycle of the assets. This goal must necessarily be faced with the rapid obsolescence of hardware and software that makes current data formats highly unlikely to be readily usable in software developed in the future. Therefore, issues related to the use of

more stable, standardized and universal data formats that can be easily accessed and adopted in a future perspective will also be addressed.

3 A Workflow for HDT Implementation

This section, according to the outline provided in the introduction, covers some aspects related to the definition of an effective workflow for the HDT implementation. The discussion of this relevant topic is made with reference to a real historical construction. The choice fell on a church located in the village of Lucoli, near L'Aquila in the Abruzzi region, Central Italy. It represents an interesting example of minor historical building located in the Inner Areas of the Apennines, being its dimensions and features characterized by a low-to-moderate complexity. This circumstance makes the building really effective as an illustrative case and a good base for the interpretation of the outcomes of the analysis concerning the Strengths, Weaknesses, Opportunities and Threats (SWOT analysis) of the proposed informative system and reported in the last sub-section.

3.1 *The Church of San Menna in Lucoli (Aq)*

The church of San Menna (Fig. 1) is located in the municipality of Lucoli in an area that today seems neglected while in the past was a place of important commercial and economic interchanges due to its intermediate position between Lazio and Umbria.

The building is modest in size but has a high cultural value for the presence of valuable artistic elements and for the use of traditional materials and construction techniques, which should be preserved since they are a significant evidence of local knowledge and culture.

These features made the church an interesting case to implement an integrated informative system aimed at the Historic Digital Twin. The previous research carried



Fig. 1 Panoramic views of the church

out on the building, namely the multidisciplinary study [30], the integrated instrumental survey and the creation of a detailed digital model [31], represent the starting point for this scope, as proved by the SWOT analysis.

The age of the structure is uncertain, but it is cited in a document of 1215 by Pope Innocent III. The church has a double nave; the lateral one dates back to a later period than its construction and was built during the several interventions and renovations that affected the ancient building [32, 33]. The traces of past interventions can be found on the main façade of the church where, in addition to the decentered access, are visible differences in masonry textures and are recognizable elements of previous perimeter of the church, such as the corner wall to the left of the entrance portal (Fig. 1).

The interventions that modified the original layout of the church would be occurred before the fifteenth century, as the church interiors is enriched by decorations of Abruzzi Renaissance [34]. Further interventions were carried out during the seventeenth century, when was built an altar at the end of the nave hiding a fresco attributed to the Abruzzi painter Pompeo Cesura (Fig. 2), and after in eighteenth century, when the portal that frames the ancient access was realized.

At the end of the twentieth century and beginning of twenty-first century several restoration works were carried out. The first were made to renovate the church after it was closed to worship [33], the second were carried out to make the church safe after the earthquake that struck the region in 2009.

Fig. 2 View of church interior. In the background, the fresco attributed to Pompeo Cesura



3.2 HDT Methodology

The analyses previously performed on the Church of San Menna have provided heterogeneous data, 3D model and digital applications that are particularly useful in the protection and valorization processes of cultural heritage [30, 31]. At the same time, the data acquired within proper databases and the solutions developed currently represent the starting point for implementing an integrated informative system in the perspective of drawing up proactive conservation plans [12]. Therefore, an effort to correlate all the information collected and to develop elements to support structural and environmental monitoring analyses has been performed after the achievement of these first results.

The approach adopted in this phase has been multidisciplinary and systemic, a procedure that provided a comprehensive and integrated view of the assets analyzed and able to support the design of the prototype of integrated informative system (Fig. 3).

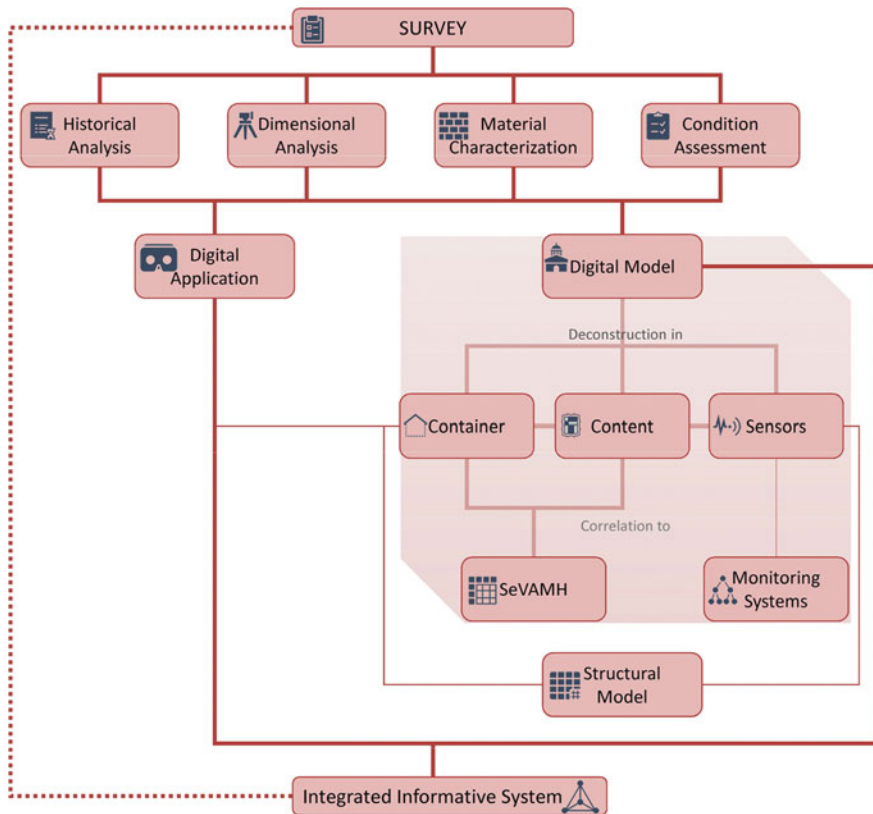


Fig. 3 Workflow for the development of integrated informative system

In a first phase of the research, on the base of the multidisciplinary study previously carried out [30], the single elements that characterize the asset have been identified in relation to specific issues of different fields of application. This led to critically deconstruct the asset in “container”, namely the building in its several structural parts, and “content”, which includes all the artistic and valuable assets located in the building and that interact more or less directly with the container. In a second phase, the information of construction features of container and content assets has been collected in the Seismic Vulnerability Assessment of Movable Heritage—SeVAMH—form [35].

This tool enables the collection of heterogeneous information, the knowledge and the qualitative assessment of conservation state of artistic assets, as well as the identification of seismic response and damage mechanisms for each category of art objects detected. The correlation between qualitative and quantitative information of the container and content assets, collected in the form, provides an adequate level of knowledge for the development of diagnostic investigation and the planning of structural monitoring.

These surveys can be implemented in analogy with other critical structures, like the hospitals [36] and taking advantage of advanced survey and analysis methods for valuable assets, like statues [37]. The digital model obtained from integration of parametric model with the mathematical and numerical ones [31], although realized in a different moment, fits the requirements of a reliable management of historical assets based on a rational decomposition of the elements.

However, additional parameters have been defined to link the digital model to the SeVAMH form, in order to integrate all the available information in a single, organic and comprehensive system. At the same time, the conservation state, and the location of the church in an area exposed to relevant risks highlighted the need to develop elements that could link the model to the data acquired through experimental investigations.

The opportunity offered by the integration of information associated to the sensors used for the experimental characterization can cover the needs of an effective and accurate technological and mechanical characterization of the main structural elements in the line with the recommendations provided by relevant National and International guidelines [38]. The same perspective applies to the integration of short-term and long-term monitoring of physical and mechanical parameters associated to given structural performance of the construction.

This is the case of vibration-based identification systems [39], which work under operational conditions do not need any excitation of the structure [40]. To this end, a family associated to dynamic sensors commonly used in structural monitoring has been parametrically modelled, identifying the properties and features of the sensors as well as the parameters able to link the model with the data acquired during the monitoring phases [41].

The digital applications for virtual/augmented reality, such as the digital models, are useful as a tool for implementing the Integrated Informative System. The virtual tour environment of San Menna church, as described in Trizio et al. [30], is designed to manage and support multidisciplinary data acquisition making them available to a wider community. Diverse and inhomogeneous data can be combined and easily

accessed remotely by using also mobile devices even not characterized by high performance. As a consequence, the digital preservation processes, as well as the valorization ones, can be facilitated since the cultural heritage and all data acquired for its knowledge are more accessible. The digital models, indeed, are available within the virtual tour through a links to existing online platforms that allow the interaction with the three-dimensional contents (i.e. Sketchfab platform [42]). At the same time, links to database and external platforms, from which among other things can be made available monitoring data, are accessible through the virtual tour (i.e. HBIM Portal [43] allows the data management, visualization and analysis of 3D contents). A more detailed description of main features and potential of Informative Virtual Tours in the development of Integrated Informative System, as well as of HDT, is provided in Trizio et al. [14].

The Integrated Informative System (IIS) created represents the first step towards the implementation of HDT. The IIS collects all the information achieved during the knowledge process and correlated them with the data acquired by active monitoring sensors. These data are the ‘static’ part of the DT and can be updated, at this time, manually by an operator.

Therefore, the HDT can achieve its full development by means of Internet of Things (IoT) technologies and the implementation of complex algorithms, based on Machine or Deep Learning; in such way, the ‘dynamic’ part of the system is defined. The development of dynamic part will enable the definition of the cultural heritage processes, from conservation and maintenance to management and valorization, in predictive manner.

The HDT will be able to manage the big-data collected, to analyze and visualize them in an automated manner and, by the interaction of possible courses of action, to provide support to decision makers—i.e. the authorities in charge of protection and enhancement of cultural heritage—prescribing optimal interventions in real time. Finally, it should be noted, as mentioned in Sect. 2, that it is necessary to define data standards more open and interoperable, possible web-based, in the passage between the static part and dynamic one of Digital Twin. In such way, the information collected will not be lost and the right ones will be available during the processing phase for the identification of actions to be implemented [29].

3.3 *SWOT Analysis*

The knowledge acquired about the Church of San Menna during the previous research and the proposed methodological approach represent an opportunity to carry out a SWOT analysis (Strengths, Weaknesses, Opportunities and Threats) and to test the feasibility and disadvantages of the suggested informative system [44, 45].

The SWOT matrix (Table 1) reports particularly the:

- Strengths, i.e. the positive elements and the success factors of the developed solutions;

- Weaknesses, which are the negative factors that must be overcome because they reduce the opportunities or increase the threats;
- Opportunities, i.e. the objectives that can be achieved through the value conditions implemented and from which it is possible to define future benefits;
- Threats, which are the risk factors that can affect the expected results in the short or long term.

Table 1 SWOT matrix

Strengths	Weaknesses
<ul style="list-style-type: none"> • Extensive knowledge of history and morphological-dimensional features of artefact • Availability of complex digital applications and models • Ability to correlate tools and heterogeneous information • Active collaboration between experts from different fields 	<ul style="list-style-type: none"> • Lack of environmental and structural monitoring data • Non-automated information update processes • Subjectivity in the interpretations of data and results
Opportunities	Threats
<ul style="list-style-type: none"> • Protection of cultural heritage • Promotion of new forms of knowledge and dissemination • Support to conservation and management processes of cultural heritage • Availability of real-time structural and environmental monitoring of hazardous areas • Availability of integrated non-destructive diagnostic techniques • Rationalization of activities related to heritage conservation, management and valorization • Increased awareness of the resources of the territory and its values 	<ul style="list-style-type: none"> • Lack of knowledge about the advantages of digital technologies • Management of mega-data and information extrapolation • Unavailability of high-performance technological tools • Lack of resources to promote and develop novel solution and new management and conservation processes • Management difficulties caused by the lack of coordination between organization responsible of historical and architectural heritage

The information currently available on the Church of San Menna in Lucoli [30, 31] defines a well-established knowledge framework on history, morphological-dimensional features and conservation state of structural elements and artistic heritage.

All this information has been digitalized and computerized into digital models and databases. However, the lack of some significant quantitative data for the assessment of the current condition and the need to interact manually in the developed solutions represent a weakness in the drawing up of proactive conservation plans and in the development of integrated informative system.

Although there is a lack of a widespread knowledge of digital technologies by the authorities in charge of protection and valorization of historical heritage, as well as of high-performance hardware tools, the implemented solutions and the proposed

approach prove that the management and fruition phases of cultural heritage can be properly supported. The digital correlation between the data contributes to the correct prioritization of the interventions and it helps in the optimization of interventions time. As a consequence, the cultural heritage can be adequately valorized and protected from possible threats related to natural and anthropic hazards.

3.4 Explanatory Results of the Workflow Pilot Application

The research integrates and develops previous experiences, and its main scope is the topological correlation between the detailed digital model and the information collected in other databases, in order to guarantee the preservation of the asset and to provide a proper support in the planning process of maintenance interventions. The parametric model of the religious building has been enriched with specific parameters useful to evaluate the state of conservation of the artefact and to link the model to the fields of the SeVAMH form concerning the container and content. The shared parameter “ID-masonry” has been created to achieve this purpose; it is a unique code defined by the location and asset identification and by a progressive number (Fig. 4).

The introduction of the parameter within the schedules, which the software generates automatically, enables the correlation between the data collect in the model with the two modules—concerning the location and characterization of the work—of the SeVAMH form. The first module provides information about building details (geolocation, name, etc.), also in relation to its position in hazardous areas and to the history of the building (construction period, renovation period and bibliographic sources).

The second module includes the metric data, dimensional information, and identification of the elements of the resistant structure, from a material and constructive point of view, focusing in particular on construction techniques, construction details and connection modalities of the masonry elements, in order to highlight the presence of possible critical issues. An additional univocal code (ID-Artwork) has been defined as shared parameter to link the artistic and valuable assets located in the building with the building itself, to connect the content and container by the location and characterization modules of the SeVAMH form (Fig. 5).

This second parameter is defined by a code for each asset categories and a progressive number, in addition to the location and artwork code (Fig. 6). In this way, the typological, dimensional and material features of the artistic heritage—although specific parameters have been created for these aspects—can be understand but, above all, the state of conservation can be known and the response in case of earthquake can be assess according to the mechanical behavior [46]. In perspective of possible further diagnostic investigations to be performed on the church, a new family able to digitally represent the accelerometers commonly used in dynamic monitoring has been modelled. The 3D model simulates a standard force balance accelerometer in its morphology. Three different sets of shared parameters have been created in the modelling phase: (i) Specification, a parameter which reports the characteristics



Fig. 4 Correlation between the parametric model and the building module of the SeVAMH form

of the sensor; (ii) Geometric data, which defines family type parameters representative of the geometric characteristics of the sensor; (iii) Sensor out-put data, which reports the identification parameters of the sensor, namely ID-Node, and the relevant recorded data.

As an example, the main features of a dynamic sensor family, which can be interfaced with records of measured data, are reported in Fig. 7. The parameters within the last group correlate the digital model to the data acquired by the single sensors and, consequently, to the monitoring system and to the records of the measurement. Although the parameters defined refer to a force-balance accelerometer, the model and the parameters can be adapted to different sensors and other monitoring systems.

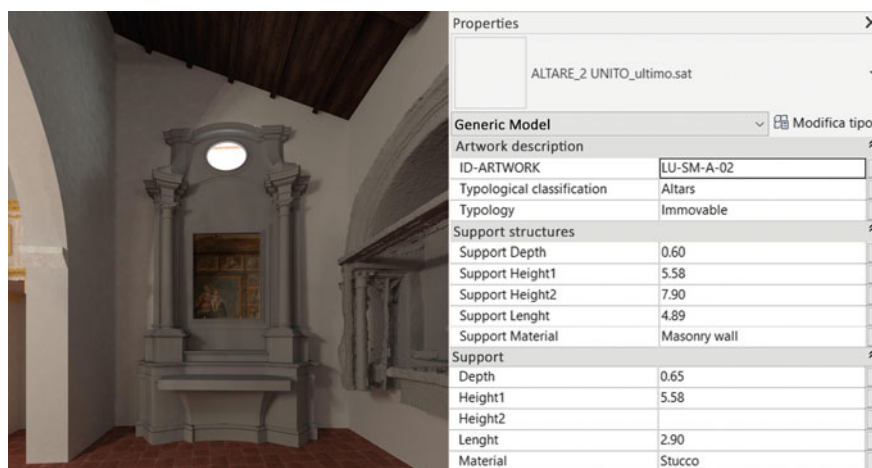


Fig. 5 Creation of shared parameters for artistic assets


The correlations created between the digital model and other databases through shared parameters prove the real interoperability of the created models and represent the first step towards the development of the integrated informative system.

Further processing and testing are required both to relate the created model with analysis models or other monitoring systems (environmental and structural) and to automate the integration of data already available on databases into the 3D model. The resolution of these issues will lead to the development of the Historic Digital Twin. It is conceived as a digital replica of main historical, geometrical, mechanical and structural features of a physical object that, thanks to the mutual relation with other data acquisition and management systems, has the potential to change the preservation, management, maintenance and valorization of historical and built heritage.

4 Final Remarks

The protection and valorization of architectural and artistic heritage are a complex challenge due to the several skills involved and the lack of unique tools able to support these processes. The recent technological developments in the cultural heritage field prove that innovative solutions can be developed to support proper actions for risks' mitigation, as well as for the safety and safeguard of historical structures. However, further efforts are required both to link the large number of data concerning the architectural and artistic heritage and to identify a single and open standard able to improve the interoperability with existing databases and solutions.

The present paper deals with this topic and it aims to provide a contribution in the development of technological and procedural solutions that can ensure a reliable and



Artworks X

<Artworks>

A	B	C	D	E	F	G	H	I
ID-ARTWORK	Typology	Typological classif.	Material	Height1	Leight	Depth	Height2	Support Material
LU-SM-P-02	Movable	Movable painting	Tempera painting	1.90	1.42			Canvas
LU-SM-F-01	Immovable	Frescoes	Plaster	2.60	3.00			Masonry wall
LU-SM-F-02	Immovable	Frescoes	Plaster	1.64	1.28		2.10	Masonry wall

Artwork No. LU-SM-F-01

Object Fresco Subject Crucifixion Author Saturnino Gatti

Cultural context Abruzzese Renaissance Year 1486 Century XV

Main biblio refere Lico, M. (2001).

Previous restorati Interventions documented Note First works 1998/2000

Renovation-Additi Note

Location Church Specific Location Wall (I)

Typology Immovable Other Typological classification Frescoes

Support structures

Material Plaster/Masonry Type of Support Fixed Auxiliary Structures Masonry base

Measures
H: 7.9 De: 0.6 L: 4.89 Di: H2

State of conservatio Good

Degradation form Moisture stain

Support

Integral to the support or part of it Material Paint

Rigidly constrained Auxiliary Structure Masonry base

Measures
H: 2.6 D: 3 Di: H2

State of conservation Good


Degradation form Salt effloresce Moisture stain

Finishing

Preparatory layers Plaster Paint fill Tempera painting

State of conservatio Good

Degradation form Moisture stain Salt effloresce Colour loss



Dynamic and damages response of artistic assets

Typological categories T6-Others

T1 Support/restraint; T2 Support/restraint; T3 Support/restraint;

T4 Support/restraint; T5 Support/restraint; T6 Support/restraint

D-Other

A Dynamic and damage mode; B Dynamic and damage mode;

C Dynamic and damage mode; D Dynamic and damage mode

R1-Stick motion Excessive stress

Fig. 6 Correlation between the artistic heritage and the artwork module of the SeVAMH form

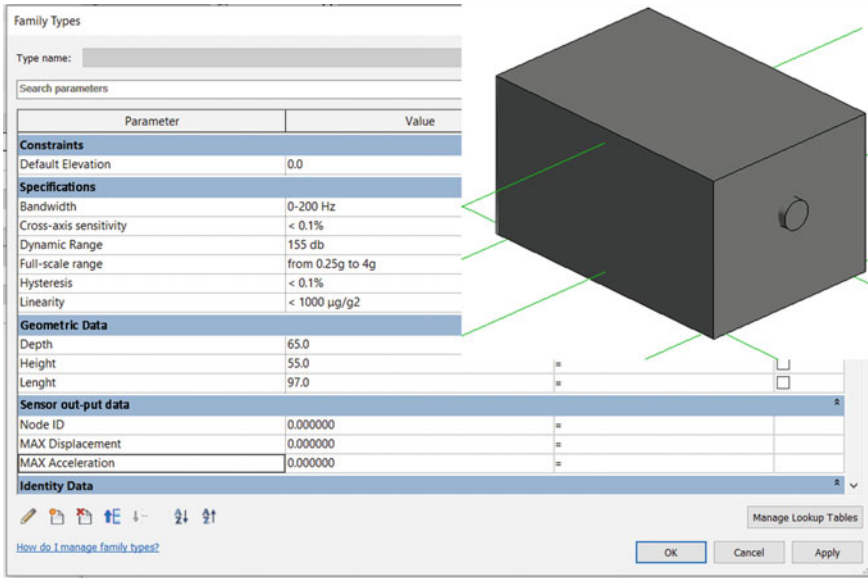


Fig. 7 Shared parameters and 3D model of the sensor

continuous conservation of cultural heritage. A SWOT analysis has been carried out with reference to a real case study, the church of San Menna in Lucoli, to provide a rational approach to this issue and to have an objective view of the operational scenarios concerning the impacts of tools and procedure proposed in the context of protection and valorization of architectural and artistic heritage.

The experimentation described represent a first application for the integration of an historical building’s parametric digital model with a sensors system and, therefore, it is the first step toward what is proposed as Historic Digital Twin. The HBIM model of the church of San Menna has been conceived in line with the expectations of parametric digital model; it is a hub to foster the collaboration between all operators involved in the process of restoration, management, and maintenance. However, its evolution towards a Historic Digital Twin is expected in the future. This challenge, to be achieved through the bidirectional flow of data within the “Virtual-Real” system, finds in the innovations offered by these technologies the effective possibility of protecting and preserving cultural assets in their whole, as well as the artistic heritage associated with them, even when they are located in remote territories and are considered minor assets.

References

1. UNESCO (1972) Convention concerning the protection of the world cultural and natural heritage. <http://whc.unesco.org/en/conventioncontext/>. Last accessed 2020/11/30
2. ICOMOS (2003) Principles for the analysis, conservation and structural restoration of architectural heritage. <https://www.icomos.org/en/resources/charters-and-texts>. Last accessed 2020/11/30
3. UNESCO (2019) Operational guidelines for the implementation of the World Heritage Convention. <http://whc.unesco.org/en/guidelines/>. Last accessed 2020/11/30
4. ICOMOS (1994) The Nara document on authenticity. <https://www.icomos.org/en/resources/charters-and-texts>. Last accessed 2020/11/30
5. ICOMOS (2003) Principles for the preservation and conservation-restoration of wall paintings. <https://www.icomos.org/en/resources/charters-and-texts>. Last accessed 2020/11/30
6. Van Balen K (2015) Preventive conservation of historic buildings. *Restor Build Monuments* 21(2–3):99–104. <https://doi.org/10.1515/rbm-2015-0008>
7. Kerr JS (2013) The conservation plan. Australia ICOMOS, Sydney
8. Pompeii (2021) The Great Pompeii Project. <http://pompeisites.org/grande-progetto-pompei/>. Last accessed 2021/01/08
9. Monumentenwacht (2021) <https://www.monumentenwacht.be/>. Last accessed 2021/01/08
10. Monumentendienst. <https://www.monumentendienst.de/>. Last accessed 2021/01/08
11. Maintain our Heritage. <https://www.maintainourheritage.co.uk/>. Last accessed 2021/01/08
12. Marra A, Sabino A, Bartolomucci C, Trizio I, Mannella A, Fabbrocino G (2021) On a rational and interdisciplinary framework for the safety and conservation of historical centres in Abruzzo Region. *Int J Arch Heritage* 15(4):608–626. <https://doi.org/10.1080/15583058.2019.1637478>
13. Della Torre S (ed) (2014) La strategia della conservazione programmata: dalla progettazione delle attività alla valutazione degli impatti. In: *Proceedings of the international conference preventive and planned conservation Monza, Mantova, 5–9 May 2014*. Nardini, Firenze
14. Trizio I, Savini F, Ruggieri A, Fabbrocino G (2021) Digital environment for remote visual inspection and condition assessment of architectural heritage. In: Rainieri C. et al. (eds.) *Civil Structural Health Monitoring, Lecture Notes in Civil Engineering* 156. https://doi.org/10.1007/978-3-030-74258-4_55
15. Centofanti M, Continenza R, Brusaporci S, Trizio I (2011) The architectural information system SIARCH3D-Univaq for analysis and preservation of architectural heritage. *Int Arch Photogramm Remote Sens Spatial Inf Sci XXXVIII-5/W16:9–14*. <https://doi.org/10.5194/isprsarchives-XXXVIII-5-W16-9-2011>
16. Campanaro DM, Landeschi G, Dell’Unto N, Leander Touati AM (2015) 3D GIS for cultural heritage restoration: a “White Box” workflow. *J Cult Herit* 18:321–332. <https://doi.org/10.1016/j.culher.2015.09.006>
17. Trizio I, Savini F, Continenza R, Giannangeli A, Marchetti A, Redi F (2019) Photogrammetric survey and 3D GIS management of mesh in the integrated investigation of complex sites. The case study of the church of Santa Maria in Cesoni. In: Inglese C, Ippolito A (eds.) *Conservation, restoration and analysis of architectural and archaeological heritage*. IGI Global, Hershey, PA, pp 48–80. <https://doi.org/10.4018/978-1-5225-7555-9.ch003>
18. Apollonio FI, Gaiani M, Sun Z (2013) 3D modelling and data enrichment in digital reconstruction of architectural heritage. *Int Arch Photogramm Remote Sens Spatial Inf Sci XL-5/W2:43–48*. <https://doi.org/10.5194/isprsarchives-XL-5-W2-43-2013>
19. Remondino F, Campana S (eds.) (2014) 3D recording and modelling in archeology and cultural heritage, theory and best practices. *BAR Int Ser* 2598
20. Maietti F, Di Giulio R, Medici M, Ferrari F, Ziri AE, Turillazzi B, Bonsma P (2020) Documentation, processing, and representation of architectural heritage through 3D semantic modelling: the INCEPTION project. In: Bolognesi CM, Santagati C (eds.) *Impact of Industry 4.0 on architecture and cultural heritage*. IGI Global, Hershey, PA, pp 202–238. <https://doi.org/10.4018/978-1-7998-1234-0.ch009>

21. Murphy M, McGovern E, Pavia S (2009) Historic building information modelling (HBIM). *Struct Surv* 27(4):311–327. <https://doi.org/10.1108/02630800910985108>
22. Dore C, Murphy M (2015) Historic building information modelling (HBIM). In: Brusaporci S (ed.) *Handbook of research on emerging digital tools for architectural surveying, modeling, and representation*. IGI Global, Hershey, PA, pp 233–273. <https://doi.org/10.4018/978-1-4666-8379-2.ch007>
23. Oreni D, Brumana R, Della Torre S, Banfi F, Barazzetti L, Previtali M (2014) Survey turned into HBIM: the restoration and the work involved concerning the Basilica di Collemaggio after the earthquake (L'Aquila). *ISPRS Ann Photogramm Remote Sens Spatial Inf Sci* II-5:267–273. <https://doi.org/10.5194/isprsannals-II-5-267-2014>
24. Bolognesi CM, Santagati C (ed.) (2020) *Impact of Industry 4.0 on architecture and cultural heritage*. IGI Global, Hershey, PA. <https://doi.org/10.4018/978-1-7998-1234-0>
25. Jouan P, Hallot P (2019) Digital twin: a HBIM-based methodology to support preventive conservation of historic assets through heritage significance awareness. *Int Arch Photogramm Remote Sens Spatial Inf Sci* XLII-2/W15:609–615. <https://doi.org/10.5194/isprs-archives-XLII-2-W15-609-2019>
26. Jouan P, Hallot P (2020) Digital twin: research framework to support preventive conservation policies. *ISPRS Int J Geo-Inf* 9:228. <https://doi.org/10.3390/ijgi9040228>
27. Acierno M, Cursi S, Simeone D, Fiorani D (2017) Architectural heritage knowledge modelling: an ontology based framework for conservation process. *J Cult Herit* 24:124–133. <https://doi.org/10.1016/j.culher.2016.09.010>
28. Brumana R, Ioannides M, Previtali M (2019) Holistic Heritage Building Information Modelling (HHBIM): from nodes to hub networking, vocabularies and repositories. *Int Arch Photogramm Remote Sens Spatial Inf Sci* XLII-2/W11:309–316. <https://doi.org/10.5194/isprs-archives-XLII-2-W11-309-2019>
29. Boje C, Guerriero A, Kubicki S, Rezgui B (2020) Towards a semantic construction digital twin: directions for future research. *Autom Constr* 114. <https://doi.org/10.1016/j.autcon.2020.103179>
30. Trizio I, Savini F, Giannangeli A, Fiore S, Marra A, Fabbrocino G, Ruggieri A (2019) Versatil tools: digital survey and virtual reality for documentation, analysis and fruition of cultural heritage in seismic areas. *Int Arch Photogramm Remote Sens Spatial Inf Sci* XLII-2/W17:377–384. <https://doi.org/10.5194/isprs-archives-XLII-2-W17-377-2019>
31. Trizio I, Brusaporci S, Tata A, Ruggieri A (in Press) Advanced digital technologies for built heritage survey and historical analysis. In: *Proceedings of XV international conference on graphic expression applied to building—APEGA 2021. Redrawing the Future*
32. Placidi V (1986) *Strutture urbane e tipologie architettoniche: i centri minori dell'alta e media Valle dell'Aterno*. Marcello Ferri Editore, L'Aquila
33. Lico M (2001) *San Menna di Lucoli. Cenni storici ed agiografici sulla Chiesa e sul Santo*. Tipolito 95, L'Aquila
34. Arbace L (2012) *Saturnino Gatti: i volti dell'anima. Vita e opere di un artista del Rinascimento*. De Siena, Pescara
35. Fabbrocino G, Marra A (2018) Strumenti di rilievo caratterizzazione dei beni museali e artistici. In: Fabbrocino G, Savorra M (eds.) *La Certosa di Trisulti*. Silvana Editoriale, Milano, pp 200–219
36. Rainieri C, Gargaro D, Fabbrocino G (2019) Hardware and software solutions for seismic SHM of hospitals. In: Limongelli MP, Çelebi M (eds.) *Seismic structural health monitoring—from theory to successful applications*. Springer, Cham, pp 279–300. https://doi.org/10.1007/978-3-030-13976-6_12
37. Marra A, Gerbino S, Fabbrocino G (2020) High performance laser survey and 3D stress analysis for maintenance and preservation of artistic assets. In: *IMEKO international conference on metrology for archaeology and cultural heritage, MetroArchaeo 2020*. Athena SRL, pp 214–219
38. Rainieri C, Fabbrocino G (2011) Operational modal analysis for the characterization of heritage structures. *Geofizika* 28(1):109–126

39. Rainieri C, Marra A, Fabbrocino G (2014) On the estimation of the fundamental modal properties of Italian historical masonry towers. *Ingegneria Sismica* 31(3)
40. Rainieri C, Marra A, Rainieri GM, Gargaro D, Pepe M, Fabbrocino G (2015) Integrated non-destructive assessment of relevant structural elements of an Italian heritage site: the Carthusian monastery of Trisulti. *J Phys Conf Ser* 628. <https://doi.org/10.1088/1742-6596/628/1/01201>
41. Mora R, Sánchez-Aparicio LJ, Maté-González MÁ, García-Álvarez J, Sánchez-Aparicio M, González-Aguilera D (2021) An historical building information modelling approach for the preventive conservation of historical constructions: application to the historical library of Salamanca. *Autom Constr* 121. <https://doi.org/10.1016/j.autcon.2020.103449>
42. Sketchfab. <https://sketchfab.com/>. Last accessed 2021/02/03
43. HBIM PORTAL. <http://www.hbim.org/web-portal/>. Last accessed 2021/02/03
44. Carrión-Mero PC, Morante-Carballo FE, Herrera-Franco GA, Maldonado-Zamora A, Paz-Salas N (2020) The context of Ecuador's world heritage, for sustainable development strategies. *Int J Des Nat Ecodyn* 15(1):39–46. <https://doi.org/10.18280/ijdne.150106>
45. Doratli N, Hoskara SÖ, Vehbi BO, Fasli M (2007) Revitalizing a declining historic urban quarter—the walled city of Famagusta, North Cyprus. *J Arch Planning Res* 24(1):65–88
46. Ciampoli M, Augusti G (2000) Vulnerabilità sismica degli oggetti esibiti nei musei: interventi per la sua riduzione. In: Liberatore D (ed.) *Vulnerabilità dei beni archeologici e degli oggetti esibiti nei musei*. CNR-Gruppo Nazionale per la Difesa dai Terremoti, Roma

A Technological Platform for Multi-risk Management and Mitigation in Campania Region, Italy



I. Nuzzo, N. Caterino, A. Novellino, M. Esposito, A. Occhiuzzi,
and E. Rubino

Abstract Urban areas and relative built heritage may be exposed to different types of risk, according to their specific features. Safety management of civil infrastructures should be oriented towards a multidisciplinary approach to achieve a holistic analysis of risks (both natural and human made). In this perspective, the GRISIS research project (Risks and Safety Management of Infrastructures at Regional Scale) aims at developing a multi-risk technological platform for Campania region, in South Italy. It allows to gather and store different types of data concerning the area of interest, thus providing essential information in order to conceive methods and tools for management and mitigation of multiple risks to infrastructures and building networks. This paper focuses on the proposal of methods and tools for the management and mitigation of seismic risk on infrastructures and building networks, developed within GRISIS project framework. Tolerable seismic risk levels for an existing building are a balance between the reduction of risk and the cost of rehabilitation. This study attempts to develop a decision-making procedure to figure out how to distribute the available budget in order to get the maximum possible portfolio risk reduction, identifying how to intervene on each single building. The proposed seismic risk mitigation strategy is uploaded in the GRISIS multi-risk technological platform, creating an interactive user-friendly tool, available online, that provides the best economic resources allocation after selecting the available budget for a specific portfolio of buildings.

Keywords Risk management · Multi-risk analysis · Regional scale risk · Seismic risk mitigation · Optimal budget allocation

I. Nuzzo (✉) · N. Caterino · A. Occhiuzzi

Institute of Technologies for Construction, Italian National Research Council (CNR), Naples, Italy
e-mail: nuzzo@itc.cnr.it

N. Caterino

Department of Engineering, University of Naples “Parthenope”, Naples, Italy

A. Novellino

ETT S.p.A, Genova, Italy

M. Esposito · E. Rubino

STRESS S.c.ar.l., Naples, Italy

1 Introduction

The GRISIS project—Risks and Safety Management of Infrastructures at Regional Scale—aims at developing methods, techniques and procedures for the risks assessment and the safety management of civil infrastructures at regional scale. The project is based on a multidisciplinary approach to achieve a holistic analysis of both natural and anthropic risks on civil infrastructures on the Campania region, in south Italy. In detail, the aim of GRISIS is not only to develop techniques and tools for the mitigation and the management of risks, but also to define safety measures for civil infrastructures.

GRISIS is structured into four work packages (OR), dealing with the above mentioned topics respectively with concern to (i) seismic risk, (ii) hydrogeological risk, (iii) management of waste caused by hazardous, (iv) vulnerabilities of ICT infrastructures and data centres to natural and human-made hazardous events. In parallel, demonstrators are made to validate some of the methodologies.

The main purpose is to create a technological platform for overall risk management of infrastructures at regional scale. The platform is still under development. The idea is to manage different natural risk scenarios (mainly seismic and hydrogeological) in a single framework, providing to different infrastructure managers a complete view of the regional territory, which is essential for implementing effective risk mitigation measures.

There is the interesting possibility of implementing not only vulnerability studies, but also prototypes of monitoring systems deriving from real field applications installed within the research project activities. In fact, a test field activity is currently ongoing for the automatic and continuous hydrogeological monitoring along a slope close to the NA-SA motorway, connecting the cities of Naples and Salerno (south Italy), aimed at predicting the possible onset of slope subsidence phenomena. A real-time monitoring system is going to be installed on a viaduct of the Circumvesuviana railway, in Naples, aimed at providing a forecasting tool for seismic alert. Finally, a health monitoring system for communication infrastructures will be implemented into the platform too. The idea is certainly very ambitious, but it represents a point of arrival for the development of a tool that is more and more necessary.

This paper presents the main results concerning the first work package of GRISIS project, i.e. management and mitigation of seismic risk at regional scale. A decision-making tool is proposed to optimize the selection strategy of determined alternatives among the class which satisfies the financial constraint given by the available budget. Basically, the decision process is divided into two sections: (1) seismic risk assessment to calculate the risk of having failure at each building of class and then (2) decision-making for any intervention for all included buildings which might or might not be subjected to the seismic retrofit, based on the defined strategy to reduce the expected future loss. The procedure is then applied to the case study of a school buildings stock, investigating not only the vulnerability [7, 11], but also retrofitting of risky buildings is concerned. The case study is implemented in the GRISIS project platform, specifically providing an interactive section concerning the analysis of the

seismic risk and its evolution according to the definition of a certain available budget intended to the risk mitigation.

The project is implemented by STRESS scarl, in the framework of FESR Campania 2014–2020. It will end on 12/31/2021, and is currently still underway, although many of the activities are in the process of being completed.

2 Management of Large-Scale Seismic Risk for a Class of Buildings

Seismic risk assessment is an essential first step to study the structural safety for large inventories. The challenging part of structural analysis of existing building is inaccessibility to the architectural and constructional database, causing uncertainty of the structural characteristics, i.e. geometry, material and detailing. The geometrical parameters could be collected simply by survey, thus they are considered as deterministic data, as listed below:

- Number of storeys
- Interstorey height of building
- Effective width of frame
- Number of frame bays
- Bay length of frame.

Differently, the knowledge about material and detailing is not accessible without making destruction tests on structural members. For this reason, in this large-scale seismic risk analysis, the latter are considered as random variables (RV):

- Shear rebar diameter of stirrups in column section
- Shear spacing of stirrups in column section
- Column section width
- Column section height
- Number of column longitudinal rebars
- Diameter of column longitudinal rebars
- Beam section height
- Number of beam longitudinal rebars in beam section
- Diameter of beam longitudinal rebars
- Concrete compressive strength
- Yield strength of steel rebar.

Consequently, several possible realizations of each building have to be considered in the process, as a combination of deterministic variables and RVs.

The vulnerability assessment is done in the sense to find out whether building has enough capacity to tolerate the demand or not, stochastically. The probability of failure is calculated for SLV damage limit state [15] since risk evaluation is being done for school buildings (class III of CNR-DT 212 2013 [13]). The simplified SP-BELA

method [6] is employed due to the advantage of limiting calculations, consequently saving the time of process, which is very crucial in large-size problems. On the other hand, horizontal elastic response spectrum for 9 return periods [15] is used to account for the dynamic seismic demand on the building portfolio. The Capacity-Spectrum Methods [10] found consistent with the suit of this study to observe any of possible failure and safe domain.

The probability of exceedance of k th damage limit state at j th intensity level of earthquake motion for i th building in portfolio is calculated by counting number of system failure (capacity < demand) weighted by the probability of occurrence of each realization of random variables:

$$PF_{pre-int}^i(ds_k > DS_k | s_j) = \sum_{m=1}^n JPDM \times (ISL)_m \tag{1}$$

In the above equation JPDM is the joint probability density function of n number of realizations made for set of random variables ($\sum JPDM = 1.0$) and ISL is the number of structural system failure which is equal to 1 when it fails and 0 when it does not.

The seismic risk for i th building at k th damage limit state would be calculated by:

$$SR_{pre-int}^{ik} = E[L_i | DS_k] \cdot \lambda_{pre-int}^{ik} = E[L_i | DS_k] \cdot \sum_{j=1}^9 \Delta \bar{\lambda}^j(s_j) \cdot PF_{pre-int}^{ik}(s_j) \tag{2}$$

where $E[L^i | DS_k]$ is the expected loss that the i th building suffers exceeding k th damage state, while $\lambda_{pre-int}^{ik}$ is the mean annual frequency of the i th building of exceeding k th damage limit state. The latter is calculated for 9 points standing for different return periods of earthquake scenario, considering that $PF_{pre-int}^{ik}(s_j)$ is the probability of exceeding k th damage limit state conditioned to ground motion intensity s where the i th building is located and $\bar{\lambda}$ is the mean annual frequency of exceeding j th intensity level of ground motion intensity of a site under consideration. The physical damage cost to a building which may suffer from significant rate of structural loss is calculated by 0.75 of SLC limit state, thus, the economic loss at significant state is calculated as 75% of replacement value of building. According to some regional previous studies in Italy, the replacement value is assumed to be equal to 1500 €/m² [1].

To make decision about how to intervene for upgrading the building system structurally, the vulnerability index of i th building when it may suffer at k th level of damage before making any intervention is introduced:

$$\chi_{pre-int}^{ik} = \frac{\lambda_{SL}}{\lambda_{pre-int}^{ik}} \tag{3}$$

Table 1 Decision solutions according to the initial vulnerability index

Zone 1:	$\chi_i \leq 0.2$	(1) Demolition and reconstruction
Zone 2:	$0.2 < \chi_i < 0.7$	(1) No intervention (2) Partial retrofitting and (3) Full retrofitting
Zone 3:	$0.7 \leq \chi_i < 0.8$	(1) No intervention and (2) Full retrofitting
Zone 4:	$\chi_i \geq 0.8$	(1) No intervention

where $\lambda_{SL} = 0.0032$ is the allowable reliability level for class III buildings analyzed with respect to the SLV damage limit state (CNR-DT 212 2013 [13]).

According to the obtained value of vulnerability indices, decision measure has to be made for all the possible conditions according to Table 1.

Among four decision options, when “No intervention” is the case evidently no cost has to be paid, while for the case of “Demolition/reconstruction” the cost to rebuild a new building with the same area of construction is imagined. For the two other mitigation options (i.e. partial and full retrofitting) cost is estimated as a partial of reconstruction cost, adopting specific cost models [14] as a function of the vulnerability index (the more vulnerable a building is, the larger the amount of money that needs to be paid to repair) and year of construction [4].

A simplified method is proposed to estimate the post-intervention fragility curves, based on the use of a suitable scale factor defined by engineering judgment. The seismic risk of *i*th building when any intervention plan is made can be calculated by:

$$SR_{post}^{ik} = E[L^i | DS_k] \cdot \sum_{j=1}^9 \Delta \bar{\lambda}^i(s_j) \cdot PF_{post}^{ik}(s_j) = E[L]_{post}^{ik} \quad (4)$$

where PF_{post}^{ik} is the probability of exceeding *k*th damage state of *i*th building when it is decided to be repaired, either partially or fully, determined from the pre-intervention probability of failure multiplied by the scale factor [4].

The total cost due to seismic risk mitigation of the portfolio corresponds to the summation of single intervention for each building. The cost-risk relation in portfolio risk management project has a constant downward trend, as the one shown in Fig. 1. The initial seismic risk is the highest point of the curve, as it corresponds to the pre-intervention condition. As the investment spent for retrofitting increases, the seismic risk is reduced. Knowing the available investment, it is possible to identify the affordable solution providing the higher seismic risk reduction.

3 Technological Platform for Multi-risk Monitoring, Management and Mitigation in Campania Region, Italy

The GRISIS web-platform is the operational demonstrator for the assessment and management of natural and anthropic risks at regional scale and organizes the risks

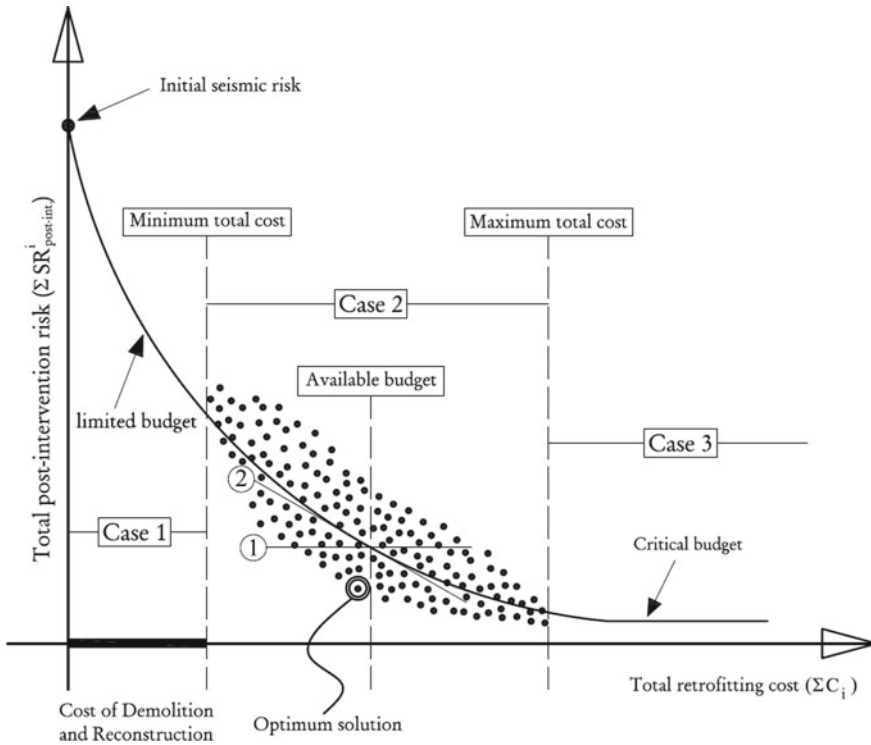


Fig. 1 Total retrofitting cost versus total post-intervention seismic risk [2]

per themes, namely: seismic, hydrogeological, infrastructures, monitoring on demonstrative cases as described in the previous sections. The web-platform is available online <http://151.1.25.86/GrisisWeb/GrisisPortal/> and studies Campania region data to offer a demonstrator of the Disaster Risk Reduction system and products. The GRISIS backend data management infrastructure (developed by ETT—www.ettolutions.com) is combining technologies and features to integrate and make available IoT, geo-referred data, reprocessed data and products. The backend is integrating up to date data services and catalogue such as GeoServer, THREDDS Data Server, ERDDAP that also implement system layer for machine-to-machine interoperability according OGC standards. On top of this backend private-cloud infrastructure a webGIS portal is providing a gateway to data, metadata and data products. It provides digital maps, with panning, zooming, and selecting features allowing users to view and interact with data products, with full metadata including links to retrieve further documentation and references. These features are designed to help users and providers understanding the density of measurements, the typology of measurements, where there are data gaps etc. The portal front end is developed in Angular, using

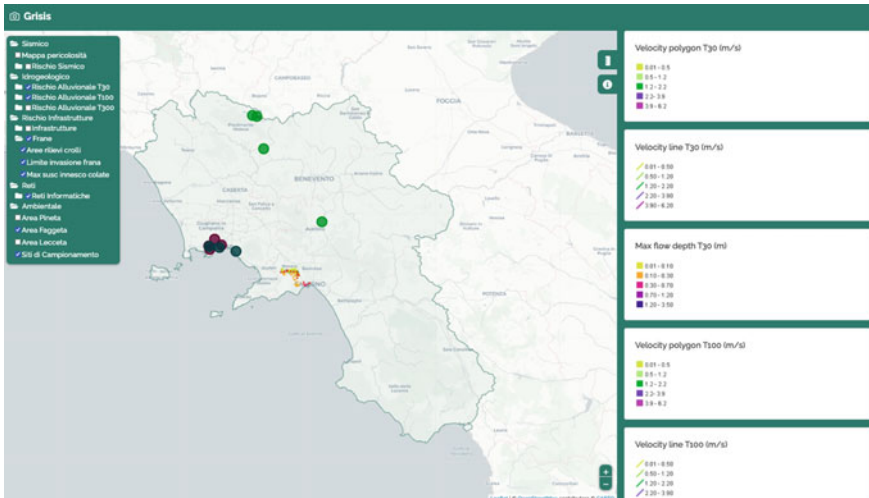


Fig. 2 GRISIS interactive mapviewer. On the left: the risk assessment and management menu, on the body the interactive map presenting the selected layers and data, on the right the layer and data legend

Leaflet libraries, and it is compliant to the Web Content Accessibility Guidelines 2.0 of the World Wide Web Consortium (W3C).¹

The dynamic map has three control/filters areas and each item (dots, lines, shape) is interactive (Fig. 2).

The multi-risk platform presents a specific section implementing the decision-making tool for the management and mitigation of regional seismic risk of a portfolio of buildings. It collects geo-referenced information and data about buildings belonging to a specific portfolio, which can be consulted by users on practical maps. On the basis of such data, that can be considered the result of a visual inspection, the seismic risk of the buildings portfolio can be determined through the framework previously illustrated. In addition, seismic hazard gridded map is available in the platform (Fig. 3), presenting the peak ground acceleration (PGA) in false-colors with a grid resolution of 4 km by 4 km. Clicking on an indicator opens the data panel and shows the PGA value for the selected grid-cell.

The seismic risk thematic section presents three layers, namely the current status of the seismic risk of the building, the retrofit strategy and the reduction of seismic risk for given buildings. By selecting the pre-intervention seismic risk layer, a regional map shows the distribution of seismic risk on the territory (Fig. 4). Then, by interacting with the control tool on the right of the panel it is possible to select an available budget and simulate its allocation for retrofit strategy. In particular, according to the given budget the system elaborates and presents the location and type of suggested

¹ http://ec.europa.eu/ipg/standards/accessibility/index_en.htm; <http://www.w3.org/WAI>.

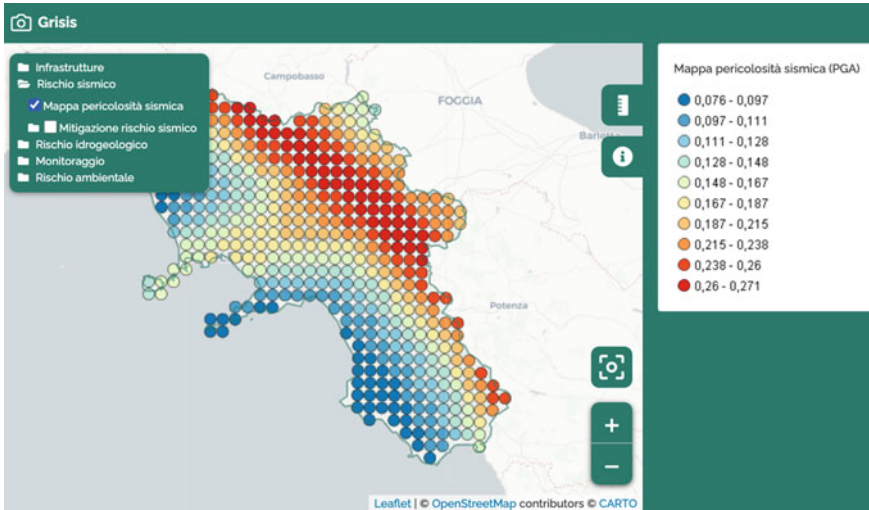


Fig. 3 Seismic risk map. The PGA false color scale is presented on the right side of the page

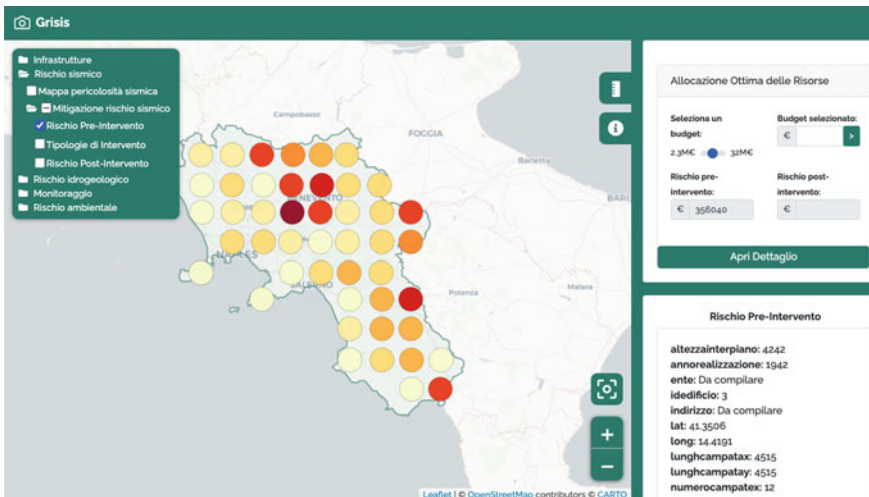


Fig. 4 Pre-intervention seismic risk map—the risk is presented in false color scale from light yellow (minimum risk): 1.5 M€ to dark red (maximum risk): 45 M€

intervention strategies (Fig. 5). Finally, the impact of suggested intervention is shown by the platform on a further map providing the post-intervention seismic risk (Fig. 6).

The user can also see the impact of the seismic mitigation measure by selecting the three layers at once (Fig. 7).

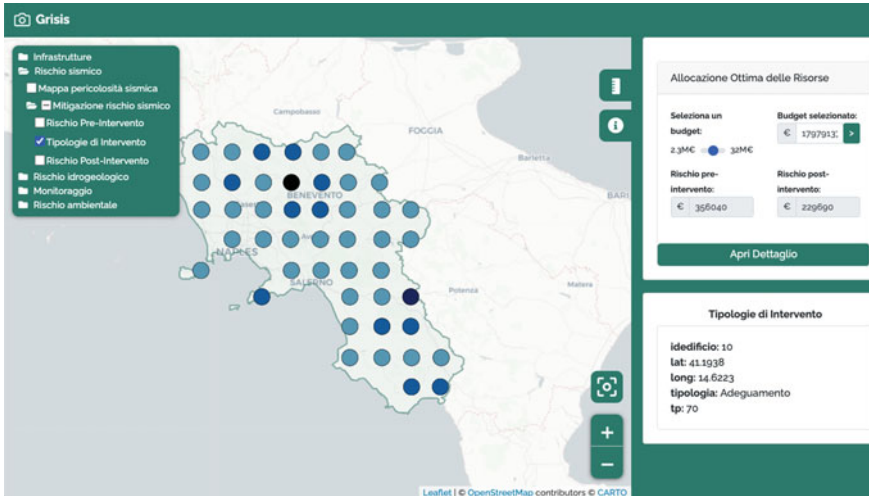


Fig. 5 Intervention strategy map to mitigate the seismic risk given the allocated budget of 17.979.137,00 €. The mitigation intervention is presented in false color: black item indicates where to apply a demolition and reconstruction strategy, dark blue item indicates where to apply building adaptation strategy, blue item indicates where to apply a building improvement strategy, and light blue item indicates where not to apply any intervention

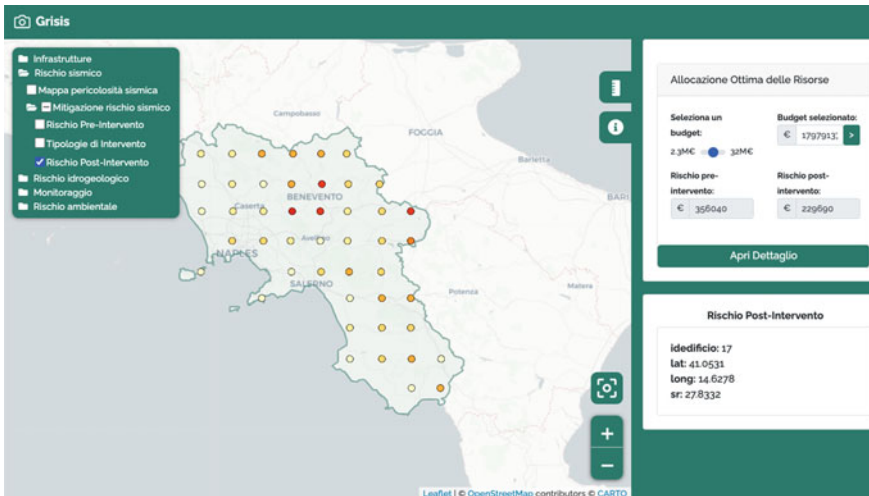


Fig. 6 Post-intervention seismic risk map—the risk is presented in false color scale from light yellow (minimum risk): 1.5 M€ to dark red (maximum risk): 45 M€

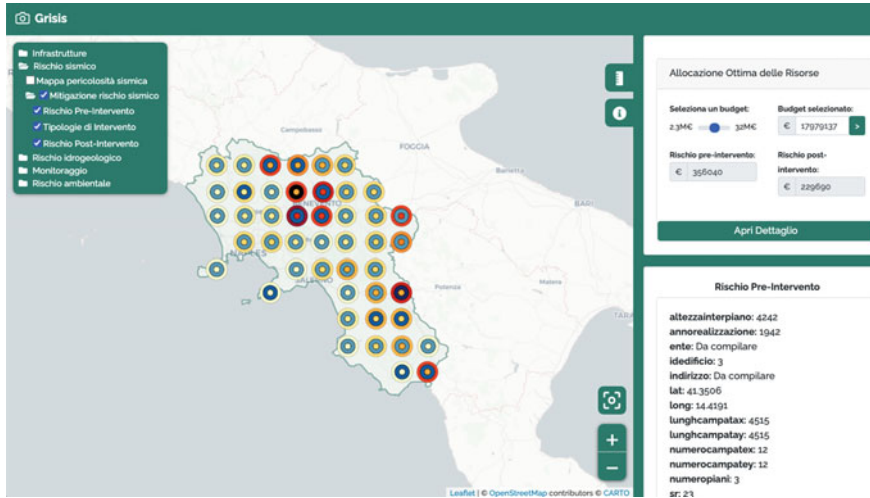


Fig. 7 Pre and post-intervention seismic risk and intervention strategy map. The webmap presents the pre-intervention risk (outer rings) together with the post-intervention risk (inner circles) and the proposed intervention strategy (middle rings). Pre and post intervention risks are presented in false color—from light yellow (minimum risk): 1.5 M€ to dark red (maximum risk): 45 M€. For the mitigation intervention black items indicate where to apply a demolition and reconstruction strategy, dark blue items indicate where to apply adaptation, blue items indicate where to apply a building improvement, and light blue items indicate where not to apply any intervention

To investigate in the risk-cost curve the user can access a second more detailed level of information page (Fig. 8). It provides the pre-intervention risk vs the post intervention risk (top left), the typology of retrofit and the cost–benefit curve (bottom left) and details of retrofit-strategy and impact on buildings (right).

The effectiveness of the platform is validated implementing the results of the case-study of 46 RC school buildings uniformly distributed on the territory of the Campania region, in southern Italy. It consists in a simulated building stock defined by means of deterministic and random structural parameters, analysed in [4] through the seismic risk assessment. The deterministic parameters should be basically collected by conducting survey of existing buildings. However, in the simulated case study the Latin Hypercube sampling method (LHS) is used to randomly select predefined values from the set of deterministic variables assumed in Table 2.

The variability of random parameters concerning structural details and material are introduced at this step of the framework, assuming specific values from relevant literature or by expert judgment. In particular, probability distributions defined by mean and standard deviation are set for each random variable distinguishing two different classes of buildings according to their year of construction [4]. The building sampling is introduced by combining the structural parameters required for the structural analysis to obtain the building capacity. The Design of Experiments (DoE) of sampling in this study is made by picking three values of mean and mean \pm standard deviation of each probability distribution of random variable when they are



Fig. 8 Seismic risk detailed information page

Table 2 Assumed interval for adopted parameters of building geometry

Parameters	Minimum value	Steps	Maximum value
Number of stories (n_h)	2	1	8
Interstorey height of frame (h)	3.0 m	0.5 m	4.5 m
Effective width of frame (w)	4.0 m	2.0 m	10 m
Number of bays in length of frame (n_l)	2	1	12
Bay length of frame (l)	2.0 m	0.5 m	6.0 m
Year of construction	1920	1	2013

distributed continuously. For the discrete distribution, the predefined values have been determined above. Thus, a total of 3^f possible alternatives for each building is identified, where f is the total number of random variables, and the vulnerability analysis is performed in correspondence of each of them through simplified methodologies previously detailed.

The results of the case-study have been uploaded into the proposed web platform system, thus providing the final report of optimal budget allocation in a more direct and graphical supported approach, thanks to the interactive user-friendly interface. Assuming the available budget equal to 2.5×10^7 €, the suggested retrofit intervention for each building, maximizing the seismic risk mitigation, is provided in Fig. 9. The seismic risk distribution on the area of interest allows to have a prompt and clear summary of the most vulnerable buildings in the pre-intervention condition (up left-sided map) and the achievable mitigation (up right-sided map) thanks to the suggested retrofit interventions (down left-sided map). In addition, moving the cursor on the pie-charts in the down-right side of the platform provides a picture of the distribution

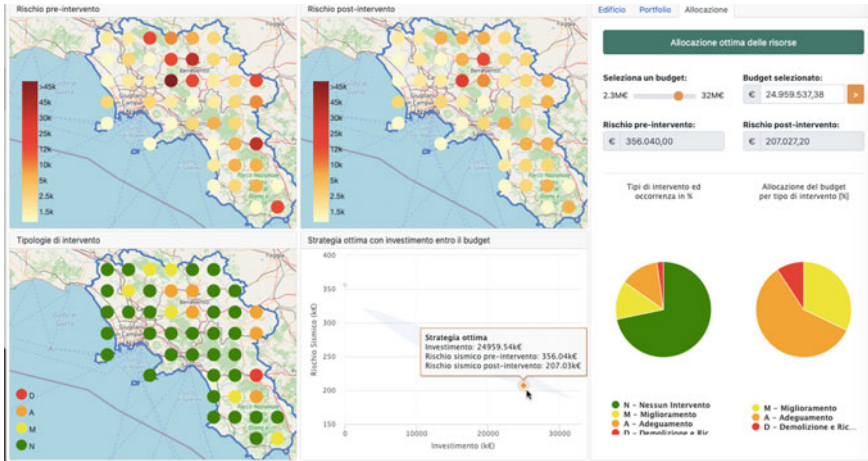


Fig. 9 Optimal budget allocation for an investment of 2.5×10^7 €

of interventions and corresponding budget allocation. This strategy allows to achieve a total seismic risk reduction of 41.8%, decreasing the initial seismic risk ($SR_{pre-int} = 356.04$ k€) to the final value of $SR_{post-int} = 207.03$ k€, as provided on the cost-risk curve of the platform.

4 Conclusions

In Italy the allocation of budget has been made unsystematic since no solid principle had been established. In this regard, decision-makers face a challenge given that there is a large number of vulnerable buildings. The project inspired the idea from the aforementioned missing point in seismic risk management of building portfolio. It attempts to develop a decision-making procedure to figure out how to distribute the budget not casual but wisely with cogent reason.

The study has been built on the platform of seismic risk analysis of buildings to know how to manage the budget to lessen the future risk. The seismic risk is calculated in dimension of monetary loss by combining the data of hazard, vulnerability and exposure. Four intervention strategies have been assumed to intervene each building; demolition/reconstruction, no intervention, partial retrofitting and full retrofitting. The best choice of intervention has been defined as the one which both meets all the needs and limits of the clients. From all the combinations of interventions for all the buildings the total cost and total seismic risk of post-intervention can be calculated. The optimum selection of intervention is the one which is less than the budget limit and yields the minimum seismic risk in post-intervention. At the end, it is figured out how to intervene each building and how much should have been spent for each building to get the perceived minimum seismic risk.

A web platform system has been developed with the collaboration of ETT industrial partner within the framework of the GRISIS research project. The platform is able to provide a practical map of the seismic risk of a certain stock of RC buildings in the pre-intervention conditions, particularly indicating the contribution of each building to the overall seismic risk of the portfolio. In a different section, geo-referenced data concerning buildings identity and geometry are stored. Then, according to the available budget, selectable by the user, the optimal combination of retrofit solutions in correspondence of the whole stock is provided as the one maximizing the seismic risk reduction within the available economic limit. The optimal post-intervention seismic risk map is given, indicating again which is the seismic risk associated to each building belonging to the portfolio. Moreover, the map of the type of intervention for each building is provided as well, finally indicating, through useful pie charts, the percentage of the adopted type of intervention and relative cost for the analysed portfolio in correspondence of the optimal solution.

Acknowledgements This work is supported by the GRISIS project (Cup: B63D18000280007, Surf: 18033BP000000001, DD prot. 368 24/10/2018), implemented by STRESS scarl in the framework of FESR Campania 2014–2020.

References

1. Asprone D, Jalayer F, Simonelli S, Acconcia A, Prota A, Manfredi G (2013) Seismic insurance model for the Italian residential building stock. *Struct Saf* 44:70–79
2. Azmoodeh BM (2015) Optimum budget allocation to mitigate seismic risk for portfolio of RC buildings, Tesi di dottorato. Università degli studi di Napoli Parthenope
3. Caterino N. (2006), Analisi Decisionale Multicriterio per l' Adeguamento Sismico di Edifici in c.a., Tesi di dottorato, Università degli studi di Napoli Federico II
4. Caterino N, Azmoodeh BM, Manfredi G (2018) Seismic risk mitigation for a portfolio of reinforced concrete frame buildings through optimal allocation of a limited budget. *Adv Civil Eng* 18
5. Bal IE, Crowley H, Pinho R, Gulay FG (2007) Structural characteristics of Turkish RC buildings stock in Northern Marmara region for loss assessment applications. In: European School for Advanced Studies in Reduction of Seismic Risk, Research report No. ROSE-2007/03
6. Borzi B, Pinho R, Crowley H (2008) Simplified pushover-based vulnerability analysis for large-scale assessment of RC buildings. *Eng Struct* 30(3):804–820
7. Borzi B, Ceresa P, Faravelli M, Fiorini E, Onida M (2011) Definition of a prioritization procedure for structural retrofitting of Italian school buildings, III ECCOMAS Thematic Conference on Computational Methods in Structural Dynamics and Earthquake Engineering (COMPdyn 2011), Corfu, Greece
8. D.M. LL.PP. 30/4/72 (1972) Norme tecniche alle quali devono uniformarsi le costruzioni in conglomerato cementizio, normale e precompresso ed a struttura metallica (in Italian)
9. Eurocode 2 (2004) Design of concrete structures-Part 1–1: General, rules and rules for buildings, European Committee for Standardization
10. Fajfar P (1999) Capacity spectrum method based on inelastic demand spectra. *Earthquake Eng Struct Dynam* 28(9):979–993
11. Grant DN, Bommer JJ, Pinho R, Calvi GM, Goretti A, Meroni F (2007) A prioritization scheme for seismic intervention in school buildings in Italy. *Earthq Spectra* 23(2):291–314

12. Iervolino I, Petruzzelli F (2011) NODE v.1.0 beta: attempting to prioritize large-scale seismic risk of engineering structures on the basis of nominal deficit, atti di XIV Convegno Nazionale “L’Ingegneria Sismica in Italia”, Bari, settembre 2011, paper no 975
13. Istruzioni per la Valutazione Affidabilistica della Sicurezza Sismica di Edifici Esistenti (2013) Commissione di Studio per la predisposizione e l’analisi delle norme tecniche per le Costruzioni (CNR-DT 212 2013), Consiglio Nazionale delle Ricerche
14. Masi A, Santarsiero G, Chiauzzi L (2014) Development of a seismic risk mitigation methodology for public buildings applied to the hospitals of Basilicata region (Southern Italy). *Soil Dyn Earthq Eng* 65:30–42
15. NTC08, 2008. D.M. 14 gennaio, Norme tecniche per le costruzioni. Ministero delle Infrastrutture (in Italian)
16. Petruzzelli F (2013) Scale-dependent procedures for seismic risk assessment and management of industrial building portfolios. Università degli studi di Napoli Federico II, Tesi di dottorato
17. Ricci P, De Risi MT, Verderame GM, Manfredi G (2013) Influence of infill distribution and design typology on seismic performance of low- and mid-rise RC buildings. *Bull Earthq Eng* 11(5):1585–1616

Machine Learning Approach for Damage Detection of Railway Bridges: Preliminary Application



A. Bilotta, G. Testa, C. Capuano, and E. Chioccarelli

Abstract In the framework of structural health monitoring, a ‘model-free’ approach has been gaining increasing attention to describe the structural behavior without building a numerical model but adopting the so-called artificial neural networks (ANNs) that must be trained on data (e.g., accelerations) recorded on the existing structure. However, the lack of complete ‘real-life’ applications is the biggest current shortcoming to the use of ANNs. Indeed, the application of ANNs is often limited to medium-scale structures. The few applications on full scale structures are rarely run for a time interval sufficient to recognize structural deterioration due to material degradation and/or damage due to external loads. Moreover, the formulation of a methodology to design the sensor network serving a neural network is necessary.

In the context of a regional research project for Risks and Safety Management of Infrastructures at Regional Scale (GRISIS), ANNs are used by authors to develop a methodology for damage detection of railway bridges where the repetitive load condition, due to the passage of trains, is particularly favorable to the purpose. The potential damage detection is investigated referring to the structural accelerations recorded at a limited number of points of the structure. At this stage of the project, recorded data are not yet available, so an auxiliary numerical model of the structure is considered.

Keywords Data driven methods · Bridge maintenance · Machine learning · Artificial neural network

A. Bilotta (✉) · G. Testa · C. Capuano

Department of Structures for Engineering and Architecture, University of Naples Federico II, Naples, Italy

e-mail: antonio.bilotta@unina.it

E. Chioccarelli

Department of Civil Energy, Environmental and Materials Engineering, Mediterranean University of Reggio Calabria, Reggio Calabria, Italy

1 Structural Health Monitoring

In last decades, the structural health monitoring (SHM) gained an important role for preserving existing structures, both to avoid their collapse and to guarantee their operating conditions. Establishing the needed interventions is essential to reduce the maintenance costs and to ensure compliance with either operating or ultimate limit state. Hence, the structural monitoring controls the structural behaviour during the life cycle of a structure with the aim of identifying presence, extent, location, and type of damages. Moreover, SHM can provide a support for managing maintenance strategies, making predictions on the remaining life of the monitored structure, and highlighting any need for interventions. A challenge for SHM is enhancing classic monitoring systems with automated investigation in operational conditions.

In the last years, the implementation of artificial intelligence (AI) methodologies has strongly grown in SHM [9, 17]. The AI techniques for the SHM are frequently based on the application of feed-forward artificial neural network (ANN), inspired by the structure of the human neural network. ANN architecture can be simple—with single hidden layer [4, 15] or more hidden layers [16] and variable number of neurons based on the input numerosity—or complex (Lee et al. 2019).

The study of existing literature shows that:

- the traditional techniques of dynamic identification, used for damage detection, may require a large number of sensors, depending on the structural typology and complexity [1, 3],
- techniques based on ANNs, being in recent development, are mainly assessed on laboratory tests (Sahin and Shenoj 2003; [10, 14, 15]) and/or numerical simulations (Jeyasehar and Sumangala 2006; [4, 12, 13]; Lee et al. 2020);
- the current research aims to improve the performance of the network adopting optimization algorithms both for the network architecture and for weights' update associated to the neuron connections [15] or studying the architecture of the network with best performance in term of damage identification (Sahin and Shenoj 2003; Lee et al. 2020; [10]).

The paper is focused on the application of ANN to railway bridges, where homogeneous traffic conditions may be favourable to the use of an automated damage detection system based on a machine learning approach. Although the results are obtained by numerical simulation, the authors want to emphasize the importance of considering the criticalities that may occur during the ANN use (e.g., unexpected variation in load conditions). The discussion of some issues that affect data acquisition in SHM applications (e.g., effects of seasonal temperature variations) are mentioned but not yet addressed.

With the aim to assess the ANN prediction capabilities for detecting structural damage on railway's bridges, we referred to one case study, in the hypothesis of having a limited number of accelerometers (i.e., nine acceleration time histories recorded by three triaxial sensors) and using a multilayer perceptron ANN.

2 Methodology

The methodology proposed is based on a machine learning approach and foresees the application of ANNs. The method uses the accelerations recorded on the structure during the passage of a train as damage sensitive features. The effects of different acceleration components are analysed in this paper to provide useful suggestions for the design of the sensors' network, whereas the study of alternative structures of the ANN is postponed to future applications on real data. Indeed, the focus of this paper is the definition of the methodology for the application of ANN for bridges' structural health monitoring, highlighting the role of parameters which affect the structural behaviour, such as acceleration components, load position and load direction.

In this application, we adopt a multilayer perceptron ANN, with input layer, output layer and hidden layers. Each layer is constituted by neurons that interact with neurons of the other layers through weighed connections. The computational model can be summarized by Eq. (1):

$$a_i^{(k)} = f \left(\sum_j w_{ji}^k \cdot a_j^{(k-1)} + b^{(k)} \right). \tag{1}$$

In the equation, $a_i^{(k)}$ is the output of i -th neuron belonging to the layer k , $a_j^{(k-1)}$ is the output of j -th neuron belonging to layer $k - 1$, $w_{ji}^{(k)}$ is the weight associated with the connection between the neurons i and j of layer k , $b^{(k)}$ is the bias, namely a translation constant of the activation threshold, and f is the activation function.

The methodology for the damage detection is divided in the following steps (see Fig. 1). *Step 0* is the preliminary choice of sensors location and ANN hyper-parameters: this step is often influenced by practical issues, not discussed here, such as the possibility of accessing to each part of the structure and the limitation on the

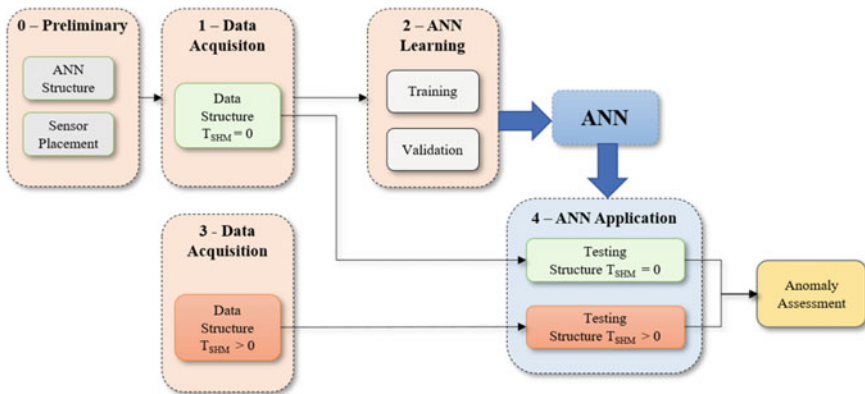


Fig. 1 Flow chart of the methodology

number and the quality of the sensors. *Step 1* is the acquisition of monitoring data (e.g., accelerations) for the structure at a time in which the structural behaviour is assumed as a benchmark to which compare the structural behaviour at the subsequent time: this time is referred to as time zero with respect to the monitored life of the structure, i.e., $T_{SHM} = 0$. Data processing and ANN learning identify *step 2*, with training and validation phases that refer to data recorded at $T_{SHM} = 0$. Once *step 2* is completed, the ANN is defined and ready to be used for damage detection.

At generic time, $T_{SHM} > 0$, monitoring data are again recorded (*step 3*). Hence, at *step 4*, the ANN (representative of the structural behaviour at time zero) is used for predicting the structural behaviour and quantifying the differences (errors) between predicted behaviour and actual recorded data. Comparing errors computed at $T_{SHM} = 0$ and $T_{SHM} > 0$, the ANN can identify a change in the structural behaviour, that is a potential damage.

Although the methodology is conceived to be used on sensors measurement, a feasibility study of this methodology to protect railway bridges is under development. For this reason, before applying the sensors on an existing structure, a numerical finite element (FE) model of the structure was built to simulate the real bridge behaviour during operational conditions (e.g., train passages) and to study the main issues in using ANN for damage detection. Hence, the data required for the training and validation of the ANN, at *step 2*, and the testing of the ANN at *step 4* are derived by the numerical model, as if they were recorded by real sensors. Doing that, one damage scenario was introduced. More details concerning the monitoring system (i.e., position and typology of sensors), the ANN structure (i.e., number of neurons, layers, duration of analysis, performance, etc.), the training and the validation of the ANN are given in the next sections.

3 Analyzed Structure

The bridge structure is one of the most common bridge structures—with concrete piers and prestressed concrete beams with “U” shaped section—belonging to the Circumflegrea railway viaduct that connects the stations of “Quarto Centre” and “Quarto Station” of the Montesanto—Quarto line in Naples, Italy. The viaduct consists of forty-five simply supported spans. We considered the twenty-four meters long span (22.60 m clear span), connecting the piers 15 and 16 (see Figs. 2 and 3). The tracks are independent structures, with separate reinforced concrete (C25/30) five meters long piers, each supporting two pre-stressed reinforced concrete (C45/55) U-shape girders, 1.65 m height (1.42 t/m), connected to a slab of precast reinforced concrete (C35/45) 20 cm thick and 4.90 m wide (2.00 t/m). Above the slab, there are the 50 cm thick ballast (3.37 t/m) and the finishes (1.98 t/m). The equivalent mass for each girder beam is 265 ton.

The structure has been modelled in a FE software [18] (see Fig. 4). The deck (i.e., the pair of U-shaped girders with the slab) has been modelled by one-dimensional elements, each beam was discretized into 24 elements to approximate the actual mass

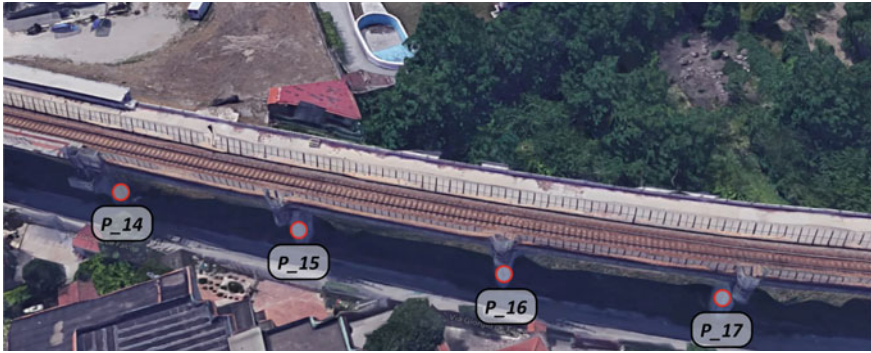


Fig. 2 3D view of the bridge



Fig. 3 Picture of a single span of the bridge from below

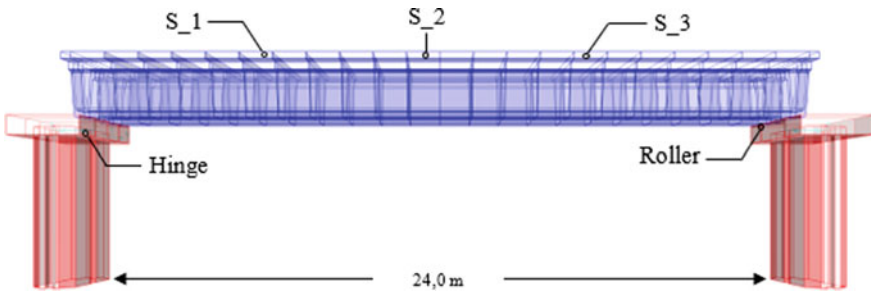


Fig. 4 Concrete FE model; lateral view with sensors placement

distribution along the deck. The material has been assumed elastic with Young's modulus calculated according to Eurocode 2 [5]. With the static scheme hinge-roller, the beam longitudinal deformation was free.

Three triaxial sensors, S1, S2 and S3, were located on the extrados of the beam at 6 m, 12 m, and 18 m from the support, respectively (see Fig. 4).

4 ANN Prediction Capabilities

The objective of the ANN is to describe the dynamic behaviour of the structure during operational conditions, that is during the passage of the trains. More specifically, known in s time steps the accelerations of the points where the sensors are located, the ANN should predict the accelerations of the same points in the subsequent time step, $s + 1$. These predictions can be compared with the observed accelerations, that are the *target* of prediction. The predictions can be iteratively repeated for the whole acceleration record (excluding the $s - 1$ time steps at the beginning of the record) so that, predicted acceleration time-histories can be compared with the observed (i.e., target) acceleration time-histories.

In this application, three independent ANNs were created, one for each sensor. To clarify this issue, Fig. 5 graphically shows the way in which the network works for a single point of the structure: referring to a generic time of the acceleration time-history, and assuming s equal to five (according to the following application), the red dots in the plot identify the five input acceleration values. From these values, the ANN provides a sixth acceleration that is the prediction of the acceleration in the subsequent step. Thus, the prediction must be compared with the blue dot that is a target value. It should be noted that the ANNs could also account for other data. In the following, apart from five accelerations, a_s , the train velocity (assumed constant for each train passage), v_6 , is also provided as an input parameter to the ANN.

Starting from Eq. (1), the predicted acceleration a_1^o is defined by Eq. (2):

$$a_1^o = f \left(\sum_{s=1}^5 w_{s,1}^o \cdot a_s^h + w_{6,1}^o \cdot v_6^h + b^o \right) \tag{2}$$

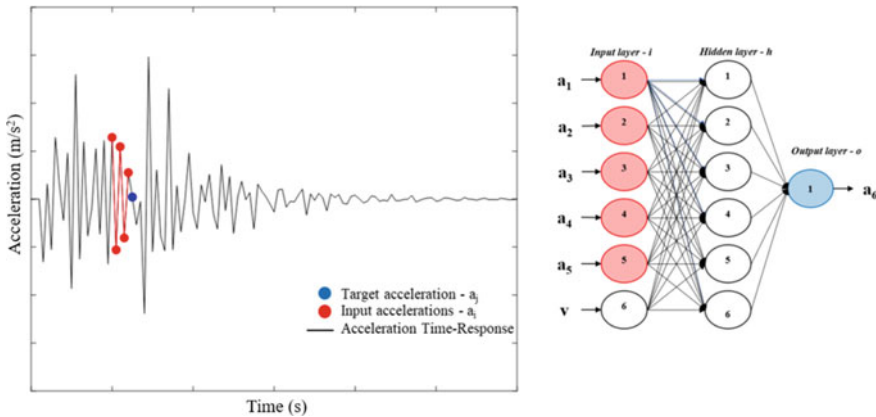


Fig. 5 Artificial neural network prediction

where the apex “*o*” indicates the output layer consisting in one neuron and the apex “*h*” indicates the hidden layer.

A prediction error, P_E , can be defined according to Eq. (3) in which N is the number of accelerations for each record, n is the generic time step ranging between 6 and N (i.e., predicted accelerations), P_n is the predicted value at time n and A_n is the corresponding observed value.

$$P_E = \sqrt{\frac{\sum_{n=6}^N (P_n - A_n)^2}{(N - 5)}} \tag{3}$$

Thus, the lower is the value of P_E the higher is the capacity of the ANN to predict the structural response.

4.1 ANN Learning

In the previous section we defined the architecture of the ANN, i.e. both the network type and the number of layers and neurons [2]. An iterative network’s learning process has been performed (see Fig. 6) that consists in defining the weights of each connection and the bias for each neuron. For such a learning process, a supervised approach has been used adopting labelled dataset [11].

To calibrate the network, one hundred train passages in one direction were simulated via linear time history analyses. For this preliminary application, the train is modelled as a single vertical force representative of three values of the train weight (i.e., 190, 220 and 250 kN); during each passage, the train maintain a constant velocity that ranges, among different passages, between 70 and 80 km/h with a step of 0.1 km/h.

For each dynamic analysis, the accelerations of the points in which the three sensors will be located are recorded. Thus, 100 three-components accelerations time-histories at $T_{SHM} = 0$ are available for network’s learning. These data are divided in two subsets, named 80% in Set 1 and 20% in Set 2. The first is used for the training phase and the second for the validation phase.

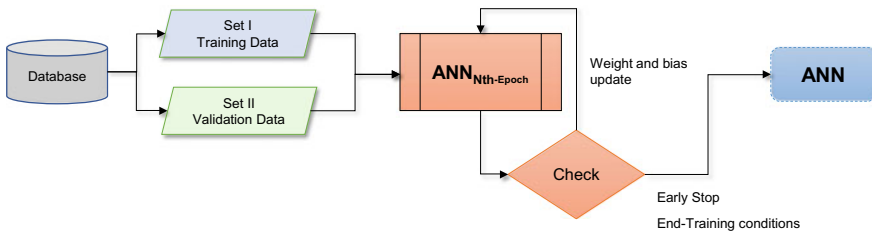


Fig. 6 Artificial neural network learning

At each iteration, called epoch, there is the learning of the network. The performance of the network is assessed through the evaluation of P_E . Then, the validation evaluates the predictive capacity of the network using different data with respect to those used in the training. Through an error function gradient descent algorithm [7] it is possible to improve the predictive capacity of the network (by updating weights and bias) until either end-training condition (i.e., sufficient accuracy) or the early stop (i.e., overfitting [6]) are reached. At the end of the learning, the network can be used at full capacity (testing).

5 ANN Application for Damage Detection

In the framework adopted in this paper, the ANN, trained at $T_{SHM} = 0$, is adopted to identify any modifications on the dynamic behaviour of the structure. With this aim, accelerations time-histories recorded at time $T_{SHM} > 0$ are analysed by the ANN. Thus, the values of P_E associated to data recorded at $T_{SHM} = 0$ and $T_{SHM} > 0$ are compared. Significant differences in the P_E values are considered as a proxy of structural damage: the values of P_E computed for the damaged structure are expected higher than those computed for the healthy structure (i.e., a threshold of P_E associated to damage is not established).

To quantify the values of P_E that can be representative of structural damage, a damage scenario is artificially introduced in the FE model via the modification of the constraint conditions (i.e., restrained longitudinal displacements at both supports), which could occur due to (i) hammering effects between adjacent beams or (ii) damage to the support, with a consequent increase in frictional forces.

First, the vertical accelerations of the studied monitored points of the structure are considered. Figure 7 shows the values of P_E computed on the original model, named as *Healthy* because representative of the undamaged structure, and those computed on the modified model, representative of the damaged structures, named as *Damaged*.

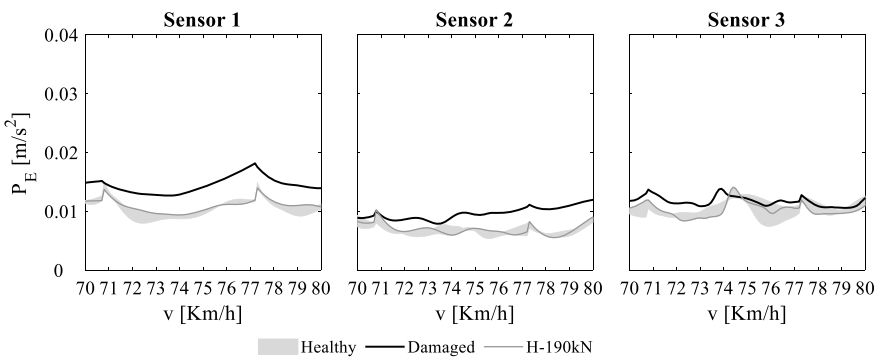


Fig. 7 Prediction errors using vertical acceleration

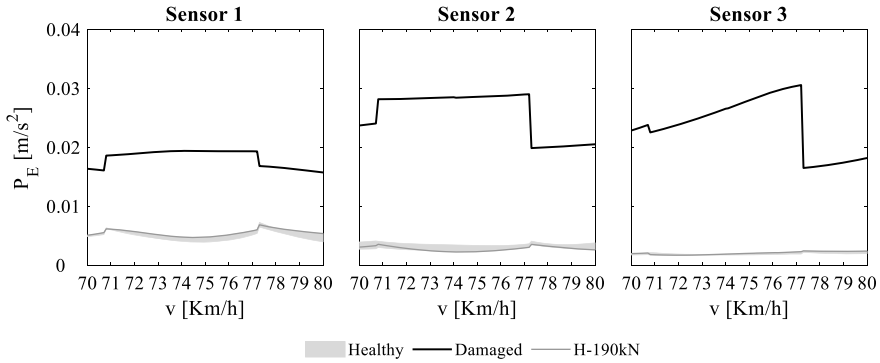


Fig. 8 Prediction errors using horizontal acceleration

The values of P_E are obtained considering one direction of train passage and they are plotted as a function of the train velocity. Moreover, imagining that more data are available at $T_{SHM} = 0$, results for three different values of the train weight (i.e. 190, 220, 250 kN) are considered and the envelope of computed P_E is represented via the grey band. On the other hand, data from the damaged structure are computed for a single value of weight equal to 190 kN and represented by the black line (the grey line represents the corresponding weight, namely 190 kN, for the undamaged structure).

The comparison of predicted errors shown in the figure suggests that two of the three sensors allow to detect an anomaly, with negligible intersection between the errors computed for the damaged and healthy structure, whereas the sensor closer to the damage, S3, provides unclear results.

Figure 8 shows the same comparison referring to longitudinal accelerations, i.e., parallel to the direction of the kinematism that is modified by the anomaly. The ANN shows greater damage detection capabilities for all sensors. Thus, in this case, it is more useful to monitor acceleration in the direction in which the anomaly strongly changes the response of the structure than acceleration in the direction of the applied load. Therefore, when designing the sensor network, foreseeing the use of tri-axial sensors seems useful to record data that will identify the different damage scenarios that may occur.

6 Limitations

The previous section showed some promising results. The aim of this section is to understand if introducing some differences between the load conditions during learning and those observed during the structural life may reduce the capabilities of the network. The differences refer to the load distribution (i.e., number of traveling forces) and the direction of the traveling force.

6.1 Load Distribution

While the learning of the ANN was performed modeling a single travelling force, the recorded data are here computed considering that the travelling parallel forces are two spaced 1.0 m or four spaced 0.5 m; in both cases, the forces result in the same total load adopted for learning (i.e. 190 kN). This variation may represent the introduction of new trains that are characterized by the same total mass but different mass distribution.

Figure 9 shows the results of the ANN trained on the single force load configuration, when a single force is travelling: gray dashed lines refer to the undamaged structure at $T_{SHM} = 0$ while black dashed lines is for the damaged structure at $T_{SHM} > 0$. The same panel shows results computed when two forces (blue lines) or four forces (red lines) are travelling; note that in the last two cases, no damages are introduced in the model (i.e., *Healthy* in the legend). In accordance with Fig. 7, the values of P_E are plotted against the train’s velocity. As shown, the values of P_E calculated in the case of two forces and four forces are often higher than the values of P_E calculated for one force, even if the latter refers to the case of damaged structure. In other words, according to the proposed framework, the ANN would detect a “false” damage on the structure, because the structure is undamaged and the dynamic of the structure is anomalous since load conditions are changed with respect to the phase of training of

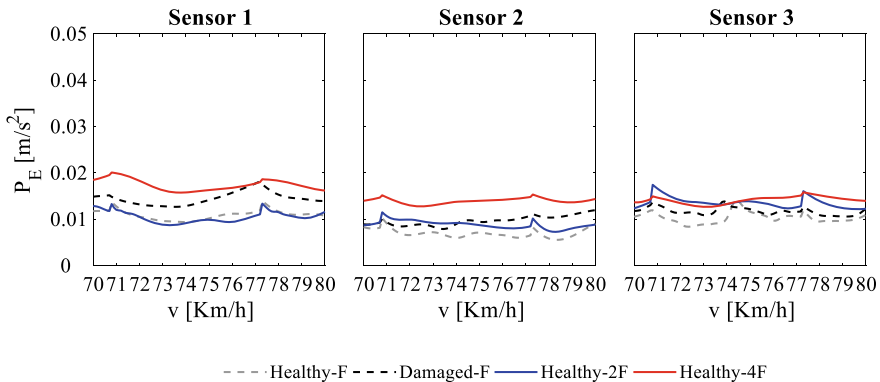


Fig. 9 ANN results for different load configuration

Table 1 Prediction errors (average on three sensors) for different load configuration on healthy and damaged structure

Load	Structural condition	P_E (m/s ²)
F	Undamaged	0.009
F	Damaged	0.012
2F	Undamaged	0.011
4F	Undamaged	0.015

the ANN. To summarize the results of Fig. 9, Table 1 lists the values of P_E , averaged over the different trains' velocity and different sensors.

6.2 Traveling Direction

So far, all the considered travelling loads moved in the same direction (left-to-right) in both learning and testing phases. This section shows the effect of considering both load travelling directions during the ANN learning, to evaluate the prediction capability of the network once the data recorded by the passage of the train in the opposite direction is used.

Therefore, the structure was considered without damage for both the learning and the testing. The analysis was conducted only for the load $F = 190$ kN, with moving directions left-to-right and right-to-left, named LR and RL, respectively.

Four scenarios were considered:

- (1a) both learning and testing performed with data obtained with load moving in LR direction, i.e. benchmark;
- (1b) learning performed with data obtained with load moving in LR direction, and testing performed with data obtained with load moving in RL direction;
- (2a) learning performed with 66% of data obtained in LR direction and 34% of data obtained in RL direction, and testing performed with data obtained in LR direction;
- (2b) learning was performed as for the scenario 2a, while data obtained in RL direction were used for testing.

Table 2 shows average values of P_E for each scenario. In scenario 1b, the value of P_E is about doubles with respect to the scenario 1a and, hence, the ANN prediction capability is affected by the load moving direction. When data for both directions are considered for learning (scenarios 2), the ANN has best performance (i.e., lower P_E) when data for testing are in accordance with the highest percentage of load moving in the same direction (i.e., scenario 2a). This result, although intuitive, is useful to underline the importance of resizing the prediction error for the definition of the warning threshold.

Table 2 Prediction error (average on three sensors) on healthy structure varying the load moving direction in learning and testing phases

Scenario	Moving direction during learning	Moving direction during testing	P_E (m/s ²)
1a	100% LR	LR	0.0102
1b		RL	0.0228
2a	66% LR	LR	0.0114
2b	34% RL	RL	0.0136

7 Conclusion

The proposed methodology for structural health monitoring is based on a machine learning approach, belonging to the class of ‘data driven’ methods. Hence, the approach is model-free, i.e. it can be applied without creating a model of the structure, since it is based on the data recorded by sensors.

The procedure has been preliminary applied to an ideal case with data simulated as if recorded on real structure. The results are promising but also highlight some limitations. The method is valid even if the operational loads are unknown, provided that their values are included in the variability considered during the learning, while variations in the load configuration could be incorrectly recognised as anomaly by the ANN. Also, the direction of the load path is significant during the learning, and homogeneous data set is preferable. Since different acceleration component can be used for damage detection, it is important to highlight that, for structural applications, the most effective direction of the acceleration could be completely different (e.g., orthogonal) to the direction of the action applied on the structure.

The methodological application to the case study will be assessed on actual data recorded on a similar full-scale bridge in the framework of the GRISIS research project.

Exogenous environmental factors—and their effects—such as temperature, wind, humidity, etc., that can alter measurements and generate false positives, should also be contemplated in the learning algorithm to improve the forecast robustness.

Acknowledgements This work was partially developed within the ReLUIS-DPC 2019-2021 program, funded by the Presidenza del Consiglio dei Ministri—Dipartimento della Protezione Civile (DPC) and partially supported by the GRISIS project (Cup: B63D18000280007, Surf:18033BP00000001, DD prot. 368 24/10/2018), implemented by STRESS scarl in the framework of FESR Campania 2014–2020. Additional acknowledgment is given to Ente Autonomo Volturino Srl for the collaboration offered to the realization of the demonstrator site. The opinions and conclusions presented do not necessarily reflect those of the funding entities.

References

1. Alamdari MM, Anaissi A, Khoa NLD, Mustapha S (2018) Frequency domain decomposition based multisensor data fusion for assessment of progressive damage in structures. *Struct Control Health Monit* 26. <https://doi.org/10.1002/stc.2299>
2. Apicella A, Isgro F, Prevete R (2019) A simple and efficient architecture for trainable activation functions. *Neurocomputing* 370:1–15
3. Brincker R, Zhang L, Andersen P (2000) Modal identification from ambient responses using frequency domain decomposition. In: *Proceedings of the 18^o international modal analysis conference (IMAC), San Antonio, Texas*
4. Chalouhi EK, Gonzalez I, Gentile C, Karoumi R (2017) Damage detection in railway bridges using machine learning: application to a historic structure. *Procedia Eng* 199:1931–1936. <https://doi.org/10.1016/j.proeng.2017.09.287>

5. EN 1992-2-2006 Eurocode 2: design of concrete structures—Part 2: concrete bridges. Design and detailing
6. Haykin S (1994) *Neural networks a comprehensive foundation*. Macmillan
7. Hecht-Nielsen R (1992) Theory of the backpropagation neural network for perception computation. *Learn Archit* 65–93. <https://doi.org/10.1016/B978-0-12-741252-8.50010-8>
8. Hsieh KH, Halling MW, Barr PJ (2006) Overview of vibrational structural health monitoring with representative case studies. *J Bridge Eng* 11(6):707–715. [https://doi.org/10.1061/\(asce\)1084-0702\(2006\)11:6\(707\)](https://doi.org/10.1061/(asce)1084-0702(2006)11:6(707))
9. Sun L, Shang Z, Xia Y, Bhowmick S, Nagarajaiah S (2020) Review of bridge structural health monitoring aided by big data and artificial intelligence: from condition assessment to damage detection. *J Struct Eng*. [https://doi.org/10.1061/\(ASCE\)ST.1943-541X.0002535](https://doi.org/10.1061/(ASCE)ST.1943-541X.0002535)
10. Krishna BM, Reddy VGP, Shafee M, Tadepalli T (2020) Condition assessment of RC beams using artificial neural networks. *Structures* 23. <https://doi.org/10.1016/j.istruc.2019.09.014>
11. Montalto A, Stramaglia S, Faes L, Tessitore G, Prevete R, Marinazzo D (2015) Neural networks with non-uniform embedding and explicit validation phase to assess Granger causality. *Neural Netw* 71:159–171
12. Neves AC, Gonzalez I, Karoumi R, Leander J (2020) The influence of frequency content on the performance of artificial neural network-based damage detection systems tested on numerical and experimental bridge data. *Struct Health Monit*. <https://doi.org/10.1177/1475921720924320>
13. Neves AC, Gonzalez I, Leander J, Karoumi R (2017) Structural health monitoring of bridges: a model-free ANN-based approach to damage detection. *J Civil Struct Health Monit*. <https://doi.org/10.1007/s13349-017-0252-5>
14. Ruffels A, Gonzalez I, Karoumi R (2020) Model-free damage detection of a laboratory bridge using artificial neural networks. *J Civil Struct Health Monit*. <https://doi.org/10.1007/s13349-019-00375-2>
15. Tran-Ngoc H, Khatir S, De Roeck G, Bui-Tien T, Abdel Wahab M (2019) An efficient artificial neural network for damage detection in bridges and beam-like structures by improving training parameters using cuckoo search algorithm. *Eng Struct* 199. <https://doi.org/10.1016/j.engstruct.2019.109637>
16. Weinstein JC, Sanayei M, Brenner BR (2018) Bridge damage identification using artificial neural networks. *J Bridge Eng* 23(11):04018084. [https://doi.org/10.1061/\(asce\)be.1943-5592.0001302](https://doi.org/10.1061/(asce)be.1943-5592.0001302)
17. Yuan FG, Zargar SA, Chen Q, Wang S (2020) Machine learning for structural health monitoring: challenges and opportunities. In: SPIE 11379, sensors and smart structures technologies for civil, mechanical, and aerospace systems. <https://doi.org/10.1117/12.2561610>
18. Computers & Structures, inc. (CSI) Structural and earthquake engineering software. SAP2000 v 21

Assessment of the Applicability of DInSAR Techniques for Structural Monitoring of Cultural Heritage and Archaeological Sites



Luisa Berto, Andrea Doria, Anna Saetta, Alberto Stella, and Diego Talledo

Abstract Structural health monitoring (SHM) practices have become increasingly important in the field of vulnerability assessment and risk mitigation of cultural heritage, especially after the past strong seismic events. The monitoring practice of monumental buildings and archaeological sites could be really expensive using traditional on-site techniques. In recent years, many steps towards have been taken in the development of Differential Synthetic Aperture Radar Interferometry (DInSAR) techniques, which allow monitoring huge areas both in ordinary maintenance situations and post-emergency conditions. This work aims to analyse the applicability of recent DInSAR techniques for the structural monitoring of buildings belonging to cultural heritage and archaeological sites. After a literature review highlighting the most relevant applications in this field, two case studies from the built cultural heritage are examined to evaluate the major issues occurring in the use of DInSAR data and their reliability for monitoring the health status of these structures. COSMO-SkyMed data relative to the urban area of Rome in the period 2011–2019 are used for the analyses. The small baseline subset (SBAS) processing technique was employed to obtain interferometric displacement measures.

Keywords Archaeological sites · Heritage buildings · Remote sensing · DInSAR

L. Berto · A. Doria · A. Saetta · A. Stella (✉) · D. Talledo
DCP, Università IUAV di Venezia, Dorsoduro 2206, 30123 Venice, Italy
e-mail: astella@iuav.it

L. Berto
e-mail: lberto@iuav.it

A. Doria
e-mail: adoria@iuav.it

A. Saetta
e-mail: saetta@iuav.it

D. Talledo
e-mail: dtalledo@iuav.it

1 Introduction

Recent collapses and damages of socially relevant structures had once more highlighted the need for monitoring and maintenance practices in order to avoid massive social and economic losses. Damages on buildings and infrastructures can be caused by several phenomena. Among these, ground rotations or differential settlements of few millimetres per year at structure basements can induce cracks, local damages and collapses of portions of the structures. A particularly relevant class of vulnerable structures is represented by buildings belonging to cultural heritage and archaeological sites. These objects are present in several European and Mediterranean countries, and many of them are subjected to ageing, low maintenance issues, ground settlements and structural damages. Although established structural health monitoring (SHM) techniques [1] have been widely employed for the monitoring of the built cultural heritage, the huge costs for their application on complex buildings and wide archaeological sites still represent one of their major limitations. Satellite remote sensing performed using Differential Synthetic Aperture Radar Interferometry (DInSAR) [2] could be an effective tool to improve the structural monitoring of archaeological sites and monumental buildings. By using this technique, it is possible to monitor wide areas over a relatively long period in order to detect anomalous trends or unexpected movements. However, even though this approach has been successfully employed to measure land subsidence, few attempts have been made in using DInSAR data to monitor buildings or parts of them, e.g. [3, 4]. Nowadays, X-band satellites provide a high-resolution sampling of the Earth's surface, which allows monitoring wide areas with a high detail level [5]. Although, satellite data still need to be validated and integrated with in situ measurements. This paper illustrates some preliminary results of a study whose aim is to analyse the effective applicability of recent DInSAR techniques for the structural monitoring of cultural heritage buildings and archaeological sites. First, a literature review of relevant past applications is presented. Then, a brief description of DInSAR data used in this study is provided. Two case study objects belonging to the cultural heritage of the city of Rome are studied, namely, the San Michele building at Ripa Grande and the Aqua Claudia (Claudian Aqueduct). Some preliminary results and observations are presented.

2 Overview of Past Applications of DInSAR for the Monitoring of Cultural Heritage Buildings and Archaeological Sites

During the last decade, some studies have been devoted to the application of DInSAR techniques for the structural monitoring of archaeological sites and buildings belonging to the cultural heritage. The pioneering works of Tapete et al. [6–8] explored the capabilities of DInSAR monitoring applied to this kind of objects, considering case studies located in Tuscany and in the centre of Rome, in areas

subjected to landslides or where previous instabilities have been recorded. Satellite and on-ground radar interferometry were employed to study deformation processes at site scale and at the single monument scale, respectively. Using satellite data from ERS-1/2, RADARSAT-1/2 and ENVISAT, some past collapses have been recognized, and early-stage warning procedures have been developed. Other relevant applications have been reported by Tang et al. [9], Alberti et al. [10] and Bonano et al. [11], who analysed deformations and instabilities in the cultural heritage sites of the Summer Palace, Petra, and Pompei, respectively.

For its unique cultural and conservation history, the city of Rome includes several world-recognized archaeological sites and cultural heritage buildings nowadays. A detailed study on the deformation of the historic centre of Rome has been performed by Cigna et al. [12] using COSMO-SkyMed data. The study showed the innovative possibility to detect motions at a single-building scale.

3 DInSAR Data Used for the Analyses

The present study is developed using COSMO-SkyMed StripMap HIMAGE data relative to the period 2011–2019, processed by the National Research Council of Italy (CNR-IREA) using the small baseline subset (SBAS-DInSAR) technique [13]. The SRTM 1 arc-sec [14] digital elevation model (DEM) is used to remove the topographic phase component [13]. For a set of measurement points, traditionally called persistent scatterers (PSs), time-series of displacement along the satellite line of sight (LOS) are provided, along with LOS mean deformation velocity values obtained from linear regression of displacement histories. A positive LOS velocity value indicates that the PS is moving towards the satellite. PSs are referenced with respect to both a geographic coordinate system (GCS) and a vertical coordinate system (VCS), so their location is fully determined. This way, PSs can be easily compared with other geometric features such as buildings, infrastructures or the terrain. The adopted processing technique allows obtaining spatially dense distributions of PSs. Data obtained from both ascending (ASC) and descending (DES) satellite orbits are provided.

4 Case Studies

The first case study examined to assess the information provided by DInSAR data is the San Michele monumental building located near the banks of the Tiber in Trastevere (Rome, Italy). A simplified representation of the building geometry is obtained using data available in the Carta Tecnica Regionale Numerica (CTRN) 2014 [15]. The SRTM 1 arc-sec DEM [14] is used to describe the ground topography, and Bing Aerial Maps [16] are employed over the DEM to represent features on

the ground. Heights of PSs, buildings and ground points are referred to EGM96-geoid VCS. Good correspondence of the spatial position of descending orbit PSs with ground topography is observed, while a significant difference along the vertical direction is noticed between ASC and DES points. In order to compare PSs from the two orbits, a rigid vertical translation of -5 m is applied to the ASC points. Geometry and location of building volumes obtained from CTRN show some discrepancy with the DEM, so the lower part of some construction appears to be underground. Figure 1 shows top and 3D views of PSs distribution and LOS velocity, for PSs with a coherence value greater than 0.5, after the correction of the vertical coordinates for ASC data. Although the number of PSs is in this case substantially the same for both orbits, the areas where both ASC and DES PSs are available are very limited. This fact critically affects the possibility to combine information from the two orbits. Both ASC and DES LOS velocity maps shown in Fig. 1 evidence a different behaviour between the N-E and the S-W portions of the San Michele building. In detail, it can be observed that the S-W portion seems to move faster than the N-E one. Before drawing some conclusion concerning this tendency, an in-situ survey should be performed.

The second case study is represented by Aqua Claudia (Claudian Aqueduct), an ancient Roman aqueduct built during the first century and restored several times. It is located in the South-Eastern rural area of Rome, Italy. As for many other elements belonging to the cultural heritage, geometric data available in the CTRN do not allow to build a complete geometric representation of the aqueduct. Figure 2 shows LOS

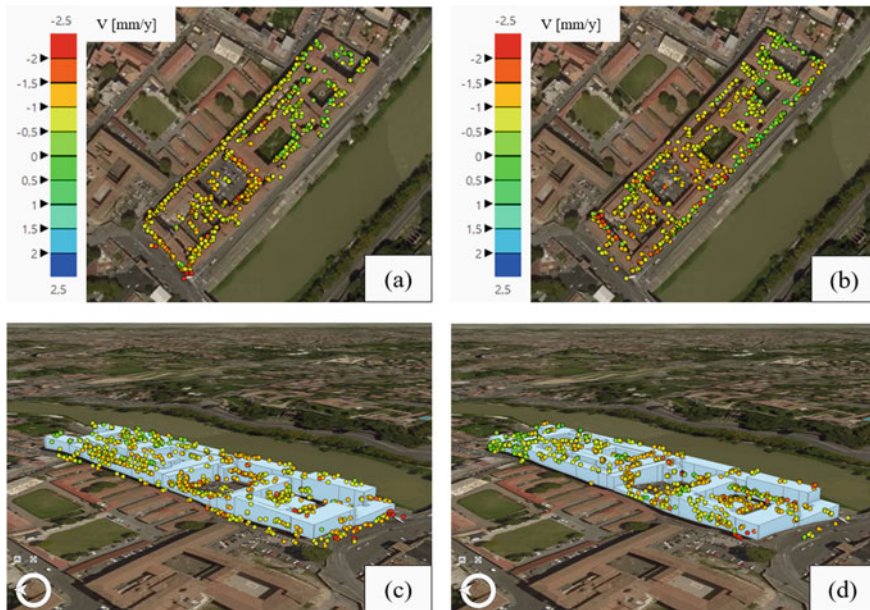


Fig. 1 Mean LOS velocity for San Michele building PSs having coherence greater than 0.5 **a** Top view ASC, **b** Top view DES, **c** 3D view ASC, **d** 3D view DES

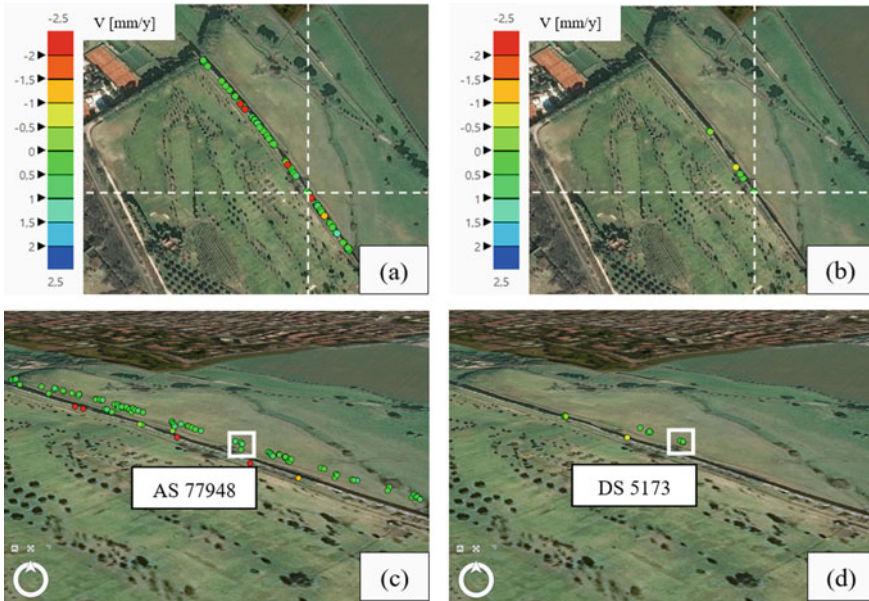


Fig. 2 Mean LOS velocity for Aqua Claudia PSs having coherence greater than 0.5 **a** Top view ASC, **b** Top view DES, **c** 3D view ASC, **d** 3D view DES

velocity of aqueduct PSs having a coherence greater than 0.5. In this case, the number of DES PSs is very limited, implying a greater difficulty in the combination of data from the two orbits in several parts of the structure. Figure 2c shows that PSs located at ground level show higher LOS velocity values. This result was previously recorded by Tapete et al. [17], and further in situ controls had already been suggested. An estimation of the East–West (E-W) and vertical (U) velocity components is developed for a zone near the top of the structure indicated in Fig. 2, where data from both ASC and DES orbits are available. In calculating velocity components, an approximation is adopted; namely, it is assumed that the plain which nearly contains the ASC and DES LOS directions is orthogonal to the North–South direction. PSs positions, LOS velocities and resulting velocity components are presented in Table 1. A slightly

Table 1 Calculation of velocity components along with East-West (E-W) and vertical (U) directions

ID	Lat [°]	Lon [°]	Height [m]	Coherence [–]	V _{LOS} [mm/y]	V _{E-w} [mm/y]	V _U [mm/y]
ASC 77948	41.84379	12.56385	77.88 ^a	0.56	+0.58	–0.42	+0.43
DES 5173	41.84378	12.56386	77.84	0.50	+0.19		

^a After rigid vertical translation

upward motion is detected, together with a horizontal component in the West direction. However, since this measure is obtained from a single couple of PSs, further investigations are needed in order to validate it.

5 Conclusions

This work presents some preliminary results on the assessment of DInSAR monitoring capabilities applied to cultural heritage buildings and archaeological sites. Case studies show that despite the number of available PSs, their location and presence in both ASC and DES orbital data can affect the possibility of correctly understand the structural deformation process. Further studies are currently ongoing.

Acknowledgements This work is part of the DPC-ReLUIIS project 2019-2021—WP6—“Monitoraggio e dati satellitari”, sponsored by the Italian Civil Protection Department. The authors are grateful to Dr Renato Gibin for useful discussions and suggestions.

References

1. Balageas D, Fritzen C-P, Gemes A (eds) (2006) In: Structural health monitoring. ISTE, London, UK
2. Bürgmann R, Rosen PA, Fielding EJ (2000) Synthetic aperture radar interferometry to measure earth's surface topography and its deformation. *Annu Rev Earth Planet Sci* 28:169–209
3. Peduto D, Nicodemo G, Maccabiani J, Ferlisi S (2017) Multi-scale analysis of settlement-induced building damage using damage surveys and DInSAR data: a case study in the Netherlands. *Eng Geol* 218:117–133
4. Zhu M, Wan X, Fei B, Qiao Z, Ge C, Minati F, Vecchioli F, Li J, Costantini M (2018) Detection of building and infrastructure instabilities by automatic spatiotemporal analysis of satellite SAR interferometry measurements. *Remote Sens* 10
5. Bonano M, Manunta M, Pepe A, Paglia L, Lanari R (2013) From previous C-band to new X-band SAR systems: aAssessment of the DInSAR mapping improvement for deformation time-series retrieval in urban areas. *IEEE Trans Geosci Remote Sens* 51:1973–1984
6. Tapete D, Fanti R, Cecchi R, Petrangeli P, Casagli N (2012) Satellite radar interferometry for monitoring and early-stage warning of structural instability in archaeological sites. *J Geophys Eng* 9
7. Tapete D, Cigna F (2012) Rapid mapping and deformation analysis over cultural heritage and rural sites based on persistent scatterer interferometry. *Int J Geophys*
8. Tapete D, Casagli N, Fanti R (2013) Radar interferometry for early stage warning on monuments at risk. In: *Landslide science and practice*. Springer, pp 619–625
9. Tang P, Chen F, Zhu X, Zhou W (2016) Monitoring cultural heritage sites with advanced multi-temporal InSAR technique: the case study of the summer palace. *Remote Sens* 8
10. Alberti S, Ferretti A, Leoni G, Margottini C, Spizzichino D (2017) Surface deformation data in the archaeological site of Petra from medium-resolution satellite radar images and SqueeSAR™ algorithm. *J Cult Herit* 25:10–20
11. Bonano M, Manzo M, Casu F, Manunta M, Lanari R (2017) DInSAR for the monitoring of cultural heritage sites. In: *Sensing the past*. Springer

12. Cigna F, Lasaponara R, Masini N, Milillo P, Tapete D (2014) Persistent scatterer interferometry processing of COSMO-skymed stripmap HIMAGE time series to depict deformation of the historic centre of Rome, Italy. *Remote Sens* 6
13. Berardino P, Fornaro G, Lanari R, Sansosti E (2002) A new algorithm for surface deformation monitoring based on small baseline differential SAR interferograms. *IEEE Trans Geosci Remote Sens* 40:2375–2383
14. USGS (2021) Digital Elevation—Shuttle Radar Topography Mission 1 Arc-Second Global
15. Regione Lazio (2014) CTRN 2014 scala 1:5.000—Prov. di Roma
16. Bing Maps Portal (2020) <https://www.bingmapsportal.com/>. Last Accessed 30 Mar 2020
17. Tapete D, Morelli S, Fanti R, Casagli N (2015) Localising deformation along the elevation of linear structures: An experiment with space-borne InSAR and RTK GPS on the Roman Aqueducts in Rome Italy. *Appl Geogr* 58:65–83

On the Dynamic Performance of the Santa Maria Maddalena Church, Ischia Island (Italy): Numerical and Experimental Comparative Analysis



Claudia Casapulla , Thomas Celano , Carlo Rainieri ,
Giovanni Fabbrocino , and Francesca Ceroni 

Abstract After the seismic event of August 21st, 2017 that hit the Ischia Island (Italy), in-situ surveys were carried out on several masonry churches located in the island in order to assess the damage induced by the earthquake. Among the inspected churches, a very interesting case study is represented by the Santa Maria Maddalena Church, located on the hill of Casamicciola Terme, close to the epicentre. The church was built in 1896 with a ‘mixed’ structure, made of yellow tuff masonry walls strengthened by iron profiles in its main body and by wooden elements in its back part. After the seismic event, in addition to a detailed survey of the church, thermography imaging and in-situ dynamic tests under operational conditions were carried out. The paper describes the experimental procedures adopted during the tests and the results in terms of experimentally identified fundamental modal parameters. An attempt of correlating the experimental results with those obtained from a finite element numerical model of the only church façade is carried out. The comparison evidences some discrepancies between the dynamic features of the single façade and

C. Casapulla

Department of Structures for Engineering and Architecture, University of Naples “Federico II”,
Via Forno Vecchio, 80134 Naples, Italy
e-mail: casacla@unina.it

T. Celano · F. Ceroni

Department of Engineering, Centro Direzionale Is. C4, University of Naples “Parthenope”, 80143
Naples, Italy
e-mail: thomas.celano@uniparthenope.it

F. Ceroni

e-mail: francesca.ceroni@uniparthenope.it

C. Rainieri (✉) · G. Fabbrocino

ITC-CNR. Construction Technologies Institute, National Research Council of Italy (CNR),
L’Aquila & Naples Branch, Naples, Italy
e-mail: rainieri@itc.cnr.it

G. Fabbrocino

e-mail: giovanni.fabbrocino@unimol.it; giovanni.fabbrocino@itc.cnr.it

G. Fabbrocino

Department of Biosciences and Territory, StreGa Lab, Via F. De Sanctis, University of Molise,
86100 Campobasso, Italy

the whole church. This confirms that the church is characterized by a ‘box behaviour’, most likely favoured by the presence of the iron frames, and, thus, the behaviour of the single façade cannot be considered independent of that of the whole church.

1 Introduction

The identification of the dynamic behaviour of an existing structure is a crucial topic for the assessment of its seismic vulnerability and is more and more important for heritage masonry structures, especially if they are characterized by complex architectural layouts, as in the case of historical churches. Several in-situ surveys carried out after earthquakes have in fact evidenced how churches are sensitive to horizontal actions [1–5], confirming the necessity of further investigation for complex cases, e.g. by means of in-situ dynamic tests.

In the literature there are several research works focused on the updating of the finite element models of historical masonry structures by means of operational modal analysis (OMA) [6–11]. Based on these works, Pellegrini et al. [12] carried out a numerical approach to match the linear perturbation and the modal analysis of such structures. The validation of the approach was firstly based on a masonry arch and then, on a historical masonry structure.

More in general, the use of the OMA seems a reliable technique to update a finite element model used to set realistic and reliable elastic numerical models of masonry structures [13]. Moreover, the dynamic modal analysis is an important tool to assess the integrity of such structures, even if subjected to limitations of the laws on artistic and cultural heritage [14]. In fact, this technique is based on non-destructive analysis of the dynamic behaviour of the structure and requires small invasive interventions due to the insertion of different recording sensors.

It is worth noting that, although in the literature there are many research works on the modal analysis of masonry buildings, so far there is a lack of clear and established guidelines on their interpretation and use for the analysis of simple walls or single parts of a structure [15]. Recent proposal appeared in the technical literature based on novel use of parameters aimed to check the correlation between modal shapes and to distinguish between local and global modes [16].

The assessment of the dynamic behaviour of masonry structures may become more and more complicated in the case of masonry reinforced by means of frames and/or braces made of different materials, such as the Italian so-called ‘baraccato’ constructive technique. Examples of timber reinforced masonry (herein ‘timber baraccato’ systems) exist worldwide: from the Asian ‘Dhajji Dewari’ in Central Asia [17], to the Turkish ‘Himis’ system [15], and the Portuguese ‘Pombalino’ [18]. Due to its diffusion, several research studies are available on the behaviour of ‘timber baraccato’ systems [19–21]. A detailed description of the static and dynamic behaviour of these ‘mixed structures’ is also reported in [22].

A very particular typology of ‘baraccato’ constructive system is present in the Ischia Island (Italy) and has been examined by Casapulla et al. [23] with reference

to the Santa Maria Maddalena Church. Such a mixed constructive system, herein identified as ‘iron baraccato’ system, is represented by masonry walls encaged in frames made of iron elements and was used in the Ischia Island after the seismic event of 1883.

The paper firstly presents the results of in-situ surveys carried out on the Santa Maria Maddalena Church in Ischia after the seismic event of August 2017. Attention is mainly focussed on thermography imaging and in-situ dynamic tests realized under environmental operational conditions. Then, the dynamic response of the main façade of the church is examined by means of a finite element model. The study of the façade is, indeed, preliminary for the future study of the whole church in order to assess the role of the iron elements on the façade behaviour and their interaction with masonry. Parametric analyses are presented to highlight the sensitivity of modal shapes and eigenfrequencies to the Young’s modulus and the unit weight of masonry and to the restraint conditions of the façade to the church.

2 The Santa Maria Maddalena Church (Ischia)

2.1 Description of the Church

After the catastrophic seismic event that hit the Ischia Island (Napoli, Italy) in 1883, part of the city of Casamicciola Terme was destroyed and then rebuilt. In particular, the most characteristic masonry building there rebuilt was the Church of Santa Maria Maddalena, whose main façade is shown in Fig. 1a.

In agreement with the post-seismic recommendations provided by the municipality after 1883, the building was designed using one of the most advanced

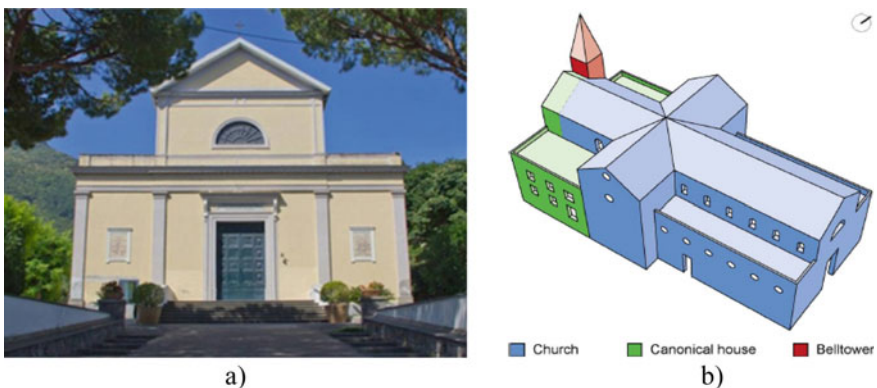


Fig. 1 Santa Maria Maddalena Church (Ischia): **a** photo of the main façade of the church, **b** volumetric description with different construction typologies

earthquake-resisting systems at the time, the so-called ‘baraccato’ construction technique. A proof of the effectiveness of such a system was recently demonstrated by the limited damage suffered by the church after the 2017 Ischia earthquake [23].

As shown in Fig. 1b, the building can be divided into three functional parts:

- the main body of the church with a Latin-cross shape (in blue);
- the back part of the church with two storeys (in green), where there is the canonical house, the sacristy and the library;
- the bell tower (in red), that can be assumed as a structure independent of the other parts of the church.

It is worth noting that the division of the church in three functional parts is also related to the different construction systems used for each of them. In fact, the main body of the church was realized with a rare ‘iron baraccato’ system, made of yellow tuff masonry strengthened with external thin iron frames (Fig. 2a), while the back part was made using the more classical ‘timber baraccato’ system (Fig. 2b), characterized by timber frames crossing the masonry walls.

Finally, it is worth noting that the bell tower was totally made of iron frames and, since weak connections with the other parts of church were observed, it can be considered as a light and independent structure.

The ‘timber baraccato’ system was made of timber elements with a square cross section of 150–200 mm for the vertical, horizontal, and diagonal elements. As shown in Fig. 2b, the typical Saint Andrew’s cross configuration for the diagonal elements is present, in which the masonry has only a filling function within the spaces left by the frame elements. For this constructive typology, the masonry material is characterized by a less regular texture if compared with that present in the ‘iron baraccato’ system. On the other hand, the presence of a regular pattern of diagonal elements is an important issue since the configuration of timber elements surely influences stiffness, capacity and ductility of the in-plane response of the walls realized with the ‘timber baraccato’ technique.

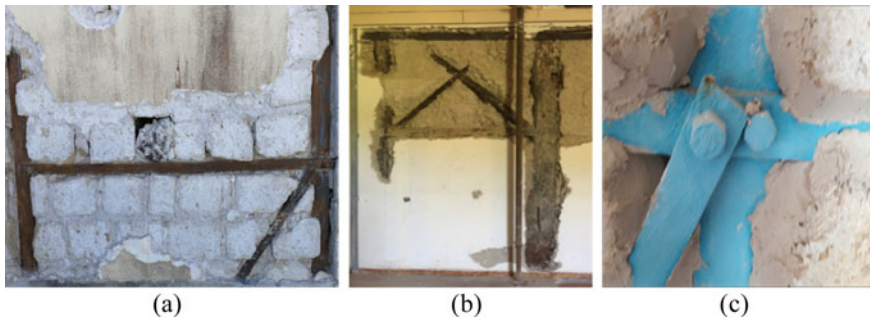


Fig. 2 Details of constructive technique used in the Santa Maria Maddalena Church: **a** ‘iron baraccato’ system, **b** ‘timber baraccato’ system, **c** bolted connection between iron profiles

Conversely, in the 'iron baraccato' system, the masonry material appears to be continuous since the external frames are arranged in special grooves realized on the surface of the tuff blocks (Fig. 2a). In this case, more regular and repetitive yellow tuff stones, with dimensions of $0.27\text{ m} \times 0.23\text{ m} \times 0.15\text{ m}$, are bonded with lime-based mortar joints and arranged according to the 'rubble masonry' building technique (i.e. the commonly called '*sacco*' technique). Such a building technique was commonly adopted for this type of masonry and consists of two external layers of blocks, with different or equal thickness, and an inner core filled with a mix of waste material and mortar. In the 'iron baraccato' part of the church, the vertical iron elements are T-shaped profiles, with dimensions of $100\text{ mm} \times 70\text{ mm} \times 10\text{ mm}$, while the horizontal and diagonal elements are simple flat plates with dimensions of $50\text{ mm} \times 20\text{ mm}$.

The connections of iron elements are mostly made of bolts (Fig. 2c), which represents a very rare and innovative connecting system for that time. The external iron frames are also constrained to each other through a number of transversal flat plates, arranged inside the walls with a vertical spacing of 1 m and aimed to realize an iron cage where the masonry is constrained inside. The iron cage has the purpose of avoiding local out-of-plane mechanisms and ensure a global behaviour of the masonry building, according to the so-called 'box behaviour'.

2.2 *In-Situ Survey After the 2017 Earthquake*

The earthquake that hit the Ischia Island on August 21st, 2017 [24] represents the first significant event in the area since 1883 in terms of magnitude and severity of the ground shaking. Due to the shallow hypocentre depth and the subsoil properties, the observed magnitude of the ground accelerations was relatively high in the order of the 0.27 g (g equal to 9.81 m/s^2) at the IOCA station in Casamicciola. Despite such high intensity actions, the church behaved in a positive manner since no relevant structural damages were observed. Post-event surveys made possible the identification of the primary effects of the ground motion and particularly demonstrated the absence of typical damage patterns exhibited by churches with similar geometrical configurations in case of earthquakes [4]. In particular, no mechanisms of the façade or of the lateral walls were activated, indeed, during the event and only extensive shallow cracks in the plaster were detected (Fig. 3a), as well as large portions of plaster detached from the ceiling (Fig. 3b).

Moreover, where the masonry walls are confined by the iron cages, a detachment of the plastering from the iron elements was observed (Fig. 4a). The cracks were evidently caused by different values of stiffness between the tuff blocks and the iron elements and by the lack of connection between plaster and iron. The in-situ surveys also evidenced spread corrosion phenomena in the external wrought iron frames (Fig. 4b).



Fig. 3 **a** Distribution of spread shallow cracks along the longitudinal walls of the main part of the church, **b** particular of the ceiling detachment

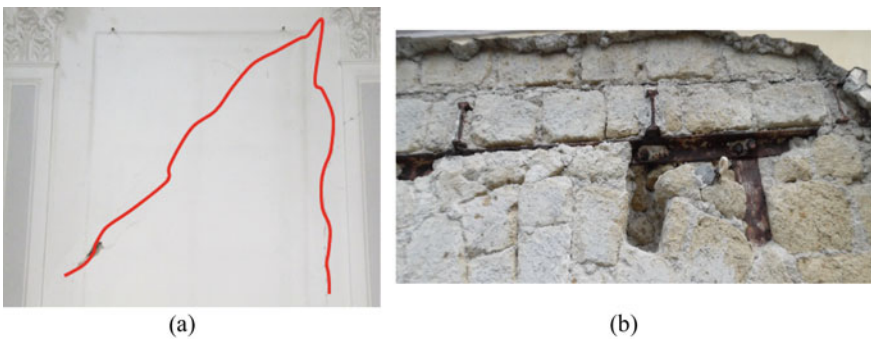


Fig. 4 **a** Cracks in the plaster along the iron profiles, **c** corrosion phenomena on the iron elements [23]

2.3 *Thermographic Non-Destructive Diagnostics of the Masonry*

As a part of survey aimed to assess technological and structural features of the church, the in-situ inspections took advantage of the infrared thermography [25, 26]. A number of pictures was taken by means of a thermal imaging camera and the distribution of the surface temperature in structural and non-structural components was measured. This is a very effective and reliable way of improving the material characterization in heritage construction, being the measures taken without any invasive contact between the component of interest and the sensors. The temperature distribution on the surface of interest is reported for example in Figs. 5 and 6 by means of colour maps, based on the correlation between the magnitude of the radiated infrared rays and its temperature.

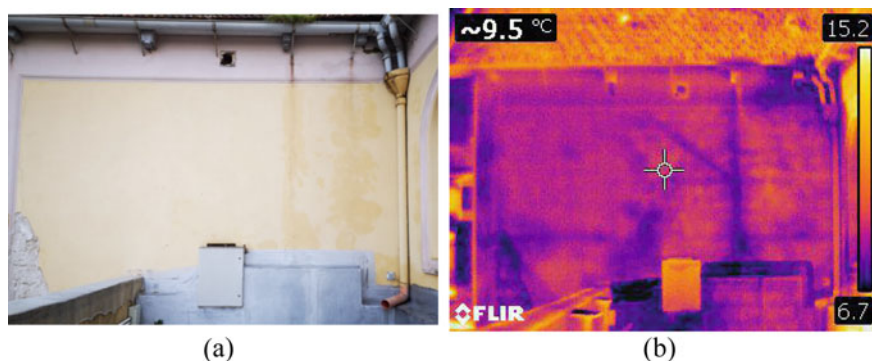


Fig. 5 Thermographic survey of the transept from the roof of the naves



Fig. 6 Thermographic survey of the transept from the ground floor

Depending on the environmental conditions (outdoor, indoor) and the test objectives, passive thermography was performed. Passive tests took advantage of the effect of the daily temperature variations. The main features of the thermal imaging camera used for tests are: 320×240 pixels IR image resolution, $7.5\text{--}13 \mu\text{m}$ spectral range, thermal sensitivity $<0.045 \text{ }^\circ\text{C}$, 60 Hz frame rate.

The infrared thermography has provided a systematic support for the validation of the data coming from the historical research. Despite the harsh environmental conditions, it can be observed that passive thermography is able to guide in a reliable way prospective the experimental insights of the masonry reinforced system. This circumstance is confirmed by the pictures of the southern transept, whose technological properties are detected both from a closer (Fig. 5) and a faraway (Fig. 6) view. Clearly, some criticisms arise from the thickness of the masonry cover, guiding the expert operator to recommend the use of active thermography whenever the masonry is not affected by evident cracking.

2.4 Operational Modal Analysis of the Church

2.4.1 Overall Modal Analysis of the Church

The overall dynamic response of the church has been experimentally evaluated by means of an operational modal analysis (OMA); vibrations of the structure under the operational conditions have been recorded and processed in order to estimate relevant modal parameters, that are natural frequencies and modal shapes. The OMA test has been carried on the structure affected by the cracking pattern due to the seismic event of 2017 and described above. Sensor positions have been selected in order to balance two different needs: (i) the observability of the modes of interest; (ii) the accessibility of the sensor location. This led to design a two-stage modal analysis in order to increase the total number of observed degrees of freedom and so doing to provide a better description of the vibrational modes. In other words, two different sensor layouts, characterised by a proper number of devices maintained at the same location, were designed.

Figure 7 offers the view of the selected sensor locations; in particular, the first layout was characterized by 23 sensors, while the second one consisted of 25 sensors. Since 12 sensors were kept at the same location in both layouts, vibrations were taken in a total number of 36 degrees of freedom. This delivered a good observability of the most relevant modes, being the recorded degrees of freedom associated with both to in-plane and out-of-plane vibrations.

The sensors installed on the church have the following characteristics: 0.5 g full scale range and 10 V/g sensitivity. Vibration data were acquired by a customized 24-bit data acquisition system based on two synchronised programmable hardware acquisition devices. 3600 s long records of the structural response under ambient vibrations were acquired at a sampling frequency of 100 Hz for each of the two sensor configurations.

The modal parameters of the church were estimated by means of well-established operational modal analysis (OMA) procedures, such as the frequency domain decomposition (FDD) and the covariance driven stochastic subspace identification (Cov-SSI). The measurement chain was able to resolve, as expected, the structural response under ambient vibrations, so that additional excitations were avoided. An accurate inspection and validation of the recorded data was carried out in agreement with well-established procedures for random data analysis. Data processing was carried out in the frequency domain by using the Hanning windowing with a 66% overlap in the spectrum computation. Cross-validation checks of the results obtained from different OMA techniques ensured their reliability. Table 1 reports the natural frequencies and damping ratio values corresponding to the first three modes, whose identification according to the FDD method is shown in Fig. 8, where the singular value decomposition is reported with reference to each designed layout. Accurate merging techniques were finally used [27] in order to identify the overall modal shape of the church according to the total number of 36 degrees of freedom mentioned above.

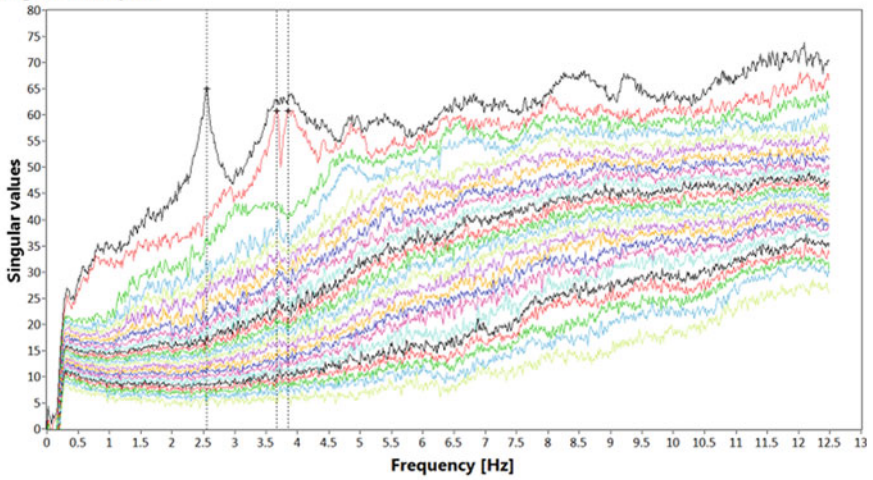


Fig. 7 Layout of the installed sensors. Red colour identifies the sensors common to the two configurations identified by the green and blue roving sensors. The position of the sensor in terms of height measured from the church floor is identified as H_i , being the subscript 'i' the channel identifying number. The geometry of the church is sketched at a height of 7.35 m

Table 1 Summary of the results of the overall modal analysis

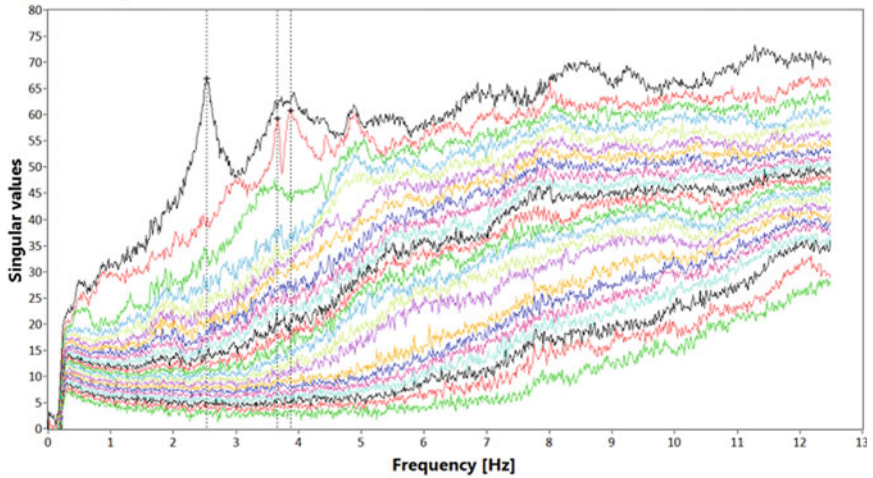
Mode	Frequency (Hz)	ξ (%)
I	2.54	1.8
II	3.74	6.0
III	3.89	2.7

Singular value plots



(a)

Singular value plots



(b)

Fig. 8 Singular value decomposition plots for: **a** first layout; **b** second layout

Figure 9 summarizes the results obtained in terms of overall modal shapes and confirms, as expected, a certain level of complexity of the dynamic response of the structure. This is mainly associated with the lack of connections at the top of each wall and to the reduced values of flexural and shear stiffness of the wooden panelled ceiling, which is actually effective only in the transverse direction (see Mode I in Fig. 9) thanks to the action of the roof trusses. The damping ratio estimates exhibit a magnitude that is not so usual for tests carried out under environmental conditions. However, they have been extensively checked and validated according to the state-of-the-art methods of analysis. Anyway, it can be observed that these results refer to a post-earthquake condition of the structure and, thus, to a widespread cracking of the masonry panels generated by the dynamic interaction with the iron frames. It is also worth noting that the estimated damping ratio is higher in the second mode (6%), being this specific mode characterised by the deformation of the perimeter walls. Such walls are the masonry elements affected by higher and more spread damage due to the local stresses exchanged between the steel trusses and the surrounding masonry. The reliability of the obtained results was also confirmed by cross-checks in terms of estimates of both natural frequencies and modal shapes. Indeed, consistent results have been obtained. Moreover, the computation of the AutoMAC matrix [28] provided a matrix with the main diagonal characterized by values basically equal to the unity and the rest of the elements equal to zero.

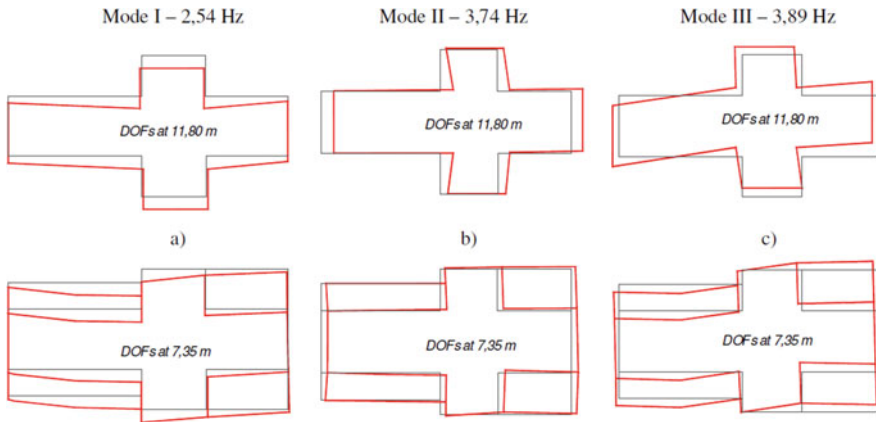


Fig. 9 Plan view of the first three vibration modes of the church

3 An Experimental and Numerical Insight on the Modal Response of the Main Façade of the Santa Maria Maddalena Church

Based on the structural characterization of the church, a numerical analysis has been designed to study in detail the response of ‘iron baraccato’ masonry structures under seismic actions. A gradual approach to the modelling of the entire structure has been outlined with the aim of defining reliable tools and releasing recommendations and guidelines on the structural analysis of similar buildings. Attention has been paid first to the main façade of the church and detailed numerical analyses aimed at defining its role in the development of the dynamic response of the church were carried out and presented in the following.

3.1 Description of the Main Façade

The masonry façade of the Santa Maria Maddalena Church presents a symmetrical geometry with a total length of 16.9 m, height of 15.9 m and a thickness of 0.58 m, as displayed in Fig. 10a. Along the height, there is an in-plane tapering of the length mainly due to the presence of the two side roof terraces. The gable starts from an altitude of 13.1 m, where the top floor of the church is located, up to the highest point of 15.9 m, corresponding to the longitudinal timber beam that connects the floor timber trusses. The façade presents two openings: one related to the main door and one to the rose window. The openings are an important issue in the numerical modelling since the distribution of the masses is surely influenced by empty spaces, as well as by the lateral reduction of the façade length.

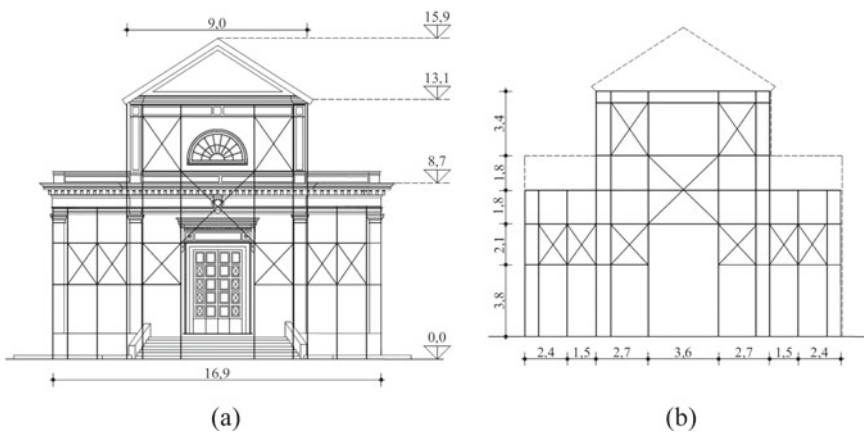


Fig. 10 Geometrical description of: a main façade, b iron frame configuration

Table 2 Summary of the results of OMA for the only façade

Mode	Frequency (Hz)
I	2.53
II	3.66
III	3.72
IV	3.93

Figure 10b shows the configuration of the iron elements on the façade. A regular distribution of Saint Andrew's crosses is observed on both sides of the façade, starting from the heights of 3.8 m and 9.5 m. Two diagonal elements are located between the two openings in order to provide a shear resistance of the resultant spandrel.

3.2 *An Insight of the Results of OMA Tests for the Main Façade*

The selected layout of the accelerometers combined with the merging of two different sensor configurations provided the overall response of the structure. Obviously, the sensors deployed on the main façade describe the response of this specific component in relation with the other components. However, based on the perspective of the study described above, it appeared useful to pay specific attention to a single component of the structure. This is the reason why an operational modal analysis of the data recorded by means of the only sensors installed on the main façade has been carried out. This type of analysis was based on the data processing of the nine degrees of freedom allocated in the area of the main façade. Table 2 reports the results of the OMA circumscribed to the degrees of freedom related to the façade. It can be observed that the values of the frequencies identified for the first three modes are basically the same as the ones identified in the context of the overall analysis. Furthermore, a fourth frequency with the associated modal shape has been identified.

Moreover, the data collected in Table 3 summarize the main features of the identified mode shapes and particularly show that they are characterized by a negligible imaginary part, confirming, thus, the significance of the results. This means that there is consistency between local and global analyses.

3.3 *The Finite Element Model of the Façade*

The dynamic behaviour of the isolated façade can be different from the one related to the same façade but obtained from the global behaviour of the entire church. In the latter case, indeed, the real distribution of the global masses and the restraint conditions of the façade are implicitly considered, while in the model of the isolated façade some assumptions have to be introduced, even if not exactly corresponding

Table 3 Summary of the identified modal shapes

ID	DoF1	DoF2	DoF3	DoF4	DoF5	DoF6	DoF7	DoF8	DoF9
I	Re	1	0.1257	0.5568	-0.183	-0.8361	-0.0265	-0.7076	-0.1731
	Im	0	0.0171	-0.0021	-0.0189	-0.007	0.0065	-0.0286	0.0076
II	Re	1	-0.057	0.6787	-0.0381	-0.8678	-0.1345	-0.7882	-0.0407
	Im	0	0.1484	0.0074	-0.0969	-0.0097	0.1031	-0.0258	0.0642
III	Re	1	0.8098	0.093	-0.547	-0.0837	0.5243	-0.0806	0.371
	Im	0	-0.004	0.0228	0.0031	-0.0353	0.0046	-0.0298	-0.023
IV	Re	1	0.803	-0.3631	-0.4558	0.5134	0.5329	0.4668	0.3375
	Im	0	-0.0035	0.1001	0.0035	-0.1123	0.0025	-0.094	-0.0145

to the real behaviour. The experimental results obtained thanks to OMA for both the whole church and the façade will represent a benchmark for assessing the possibility of studying the façade as a single macro-element.

A refined finite element (FE) model of the church's façade has been realized in the DIANA FEA software [29] in order to carry out linear modal analysis for both the unreinforced masonry (URM) and the reinforced masonry (RM) façades. The main objective is to numerically estimate the effectiveness of the iron reinforcement into improving the in-plane dynamic behaviour of the wall. It is worth noting that the numerical modelling of the 'iron baraccato' system is dependent on the choice of an appropriate modelling strategy of the iron profiles and on the type of their interaction with masonry.

The modelling approach used for masonry is based on the common 'total strain crack model'; it assumes masonry as an isotropic, homogenous and continuum material, characterized by a non-linear response both in tension and compression, according to a parabolic and an exponential law, respectively. Clearly, the strengths and the non-linear parameters of the materials are not required in the modal analysis of the façade, but were only fixed for developing non-linear analysis at a later stage.

The refined mesh model of the masonry wall is a twenty-node iso-parametric solid brick element, CHX60, based on quadratic interpolation and Gauss integration. The mesh size, resulted by an optimization analysis, is assumed equal to 0.20 m.

Iron is modelled assuming an isotropic material, independently of the type of interaction with masonry, and an elastic-perfectly plastic model both in tension and compression. A continuous interaction between masonry and iron profiles is taken into account for the vertical and horizontal iron elements, which are modelled as 'beam elements', while all the other iron elements are modelled as 'truss', i.e. connected to the masonry blocks only at the nodes [30].

For the iron profiles, the Young's modulus is assumed 153,000 MPa, as suggested in [31] and the unit weight is assumed 78.6 kN/m³. Conversely, for the tuff masonry, several values of the Young's modulus and unit weight have been used in order to implement a sensitivity analysis and calibrate them based on the comparison between experimental and numerical results, in terms of both modal shapes and eigenfrequencies. At the first stage, the Young's modulus and the unit weight of tuff masonry were assumed equal to 880 MPa and 14 kN/m³, respectively, based on previous analyses carried out by Di Napoli [32].

3.3.1 Effect of Restraint Conditions

Firstly, a very simple configuration has been considered for the façade: this is supposed fixed at the base ($u_x = u_y = u_z = 0$, where u is the generic displacement), in order to simulate the good interaction with the foundations, and simply pinned ($u_y = 0$) on both lateral vertical edges in order to take into account the interaction with the transversal walls of the church, as well as for the top point of the gable (Fig. 11). Moreover, the self-weight of the façade is assumed as the only loading condition.

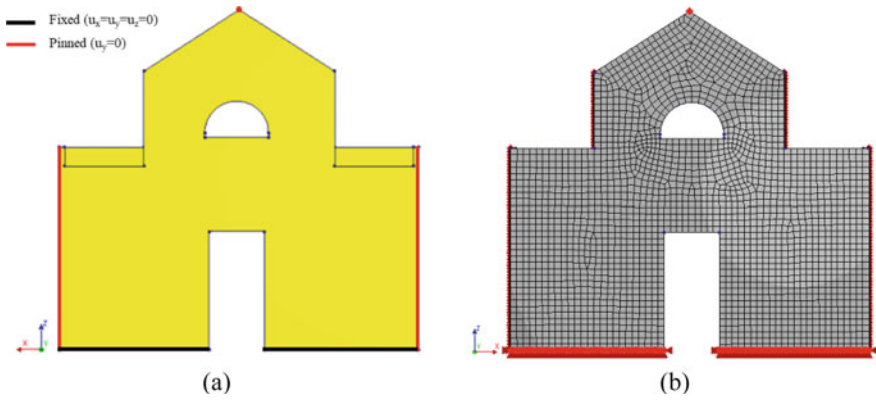


Fig. 11 Initial restraint configuration for the façade: **a** geometrical model (back view), **b** finite element model (front view)

The first result of the modal analysis has evidenced that such a configuration of the restraints does not provide the same order as the experimental vibration modes, since the out-of-plane modes result predominant with respect to the in-plane one (Fig. 12). The first modes in both façade configurations are, indeed, related to local out-of-plane displacements of the central part of the wall (Fig. 12a and Fig. 13a). Conversely, the first vibration mode in the in-plane direction is represented by the fourth (Fig. 12b) and the third one (Fig. 13b) for the URM and RM façades, respectively. Finally, the second, the third and the sixth modes for the URM façade and the second, the fourth and the sixth modes for the RM facade present a negligible modal mass because they are mainly related to a torsion of the façade’s piers. Under these assumptions, the numerical values of the frequencies associated to the first in-plane modes are 6.74 and 7.95 Hz for the URM and RM façades, respectively, while for the out-of-planes modes the frequencies are 3.59 and 4.78 Hz. These values evidence, thus, that also in terms of eigenvalues there is no agreement with the experimental results. Table 4 shows the results of the first modal analyses performed on the URM and RM façades.

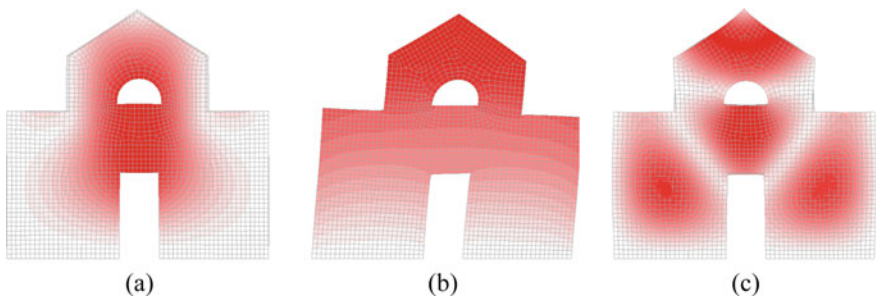


Fig. 12 Modal shapes for the unreinforced (URM) façade: **a** 1st mode (Y direction), **b** 4th mode (X direction), **c** 5th mode (Y direction)

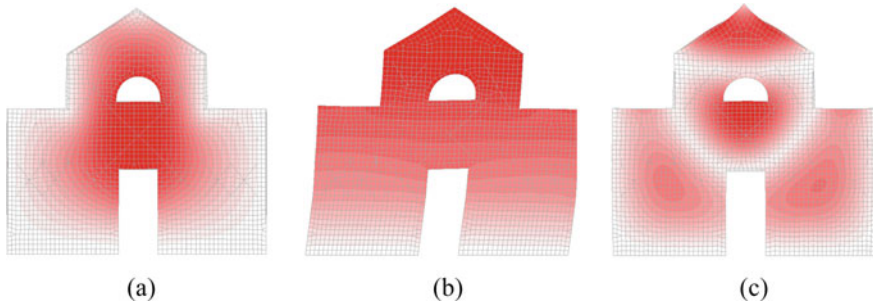


Fig. 13 Modal shapes for the reinforced (RM) façade: **a** 1st mode (Y direction), **b** 3rd mode (X direction); **c** 5th mode (Y direction)

Table 4 Results of the first numerical modal analyses

	MODE	1	2	3	4	5	6
URM	<i>f</i> (Hz)	3.59	5.10	6.29	6.74	8.25	9.85
	<i>Part. Mass X</i> (%)	0.0	0.0	0.1	69.7	0.0	0.0
	<i>Part. Mass Y</i> (%)	51.3	2.0	0.0	0.0	17.3	0.0
RM	<i>f</i> (Hz)	4.78	6.82	7.95	8.22	11.28	13.44
	<i>Part. Mass X</i> (%)	0.0	0.0	74.5	0.0	0.0	0.0
	<i>Part. Mass Y</i> (%)	57.5	0.6	0.0	0.0	15.3	2.4

However, before proceeding with a sensitivity analysis on the Young’s modulus and the unit weight of masonry, a more accurate analysis of the restraining and loading conditions of the façade has been carried out assuming other restraints against the out-of-plane behaviour of the façade ($u_y = 0$), aimed at achieving results better matched to the experimental modal shapes.

In particular, horizontal restraints at the level of the scale, of the roof terraces, of the internal chorus and of the rooftop have been added and vertical restraints to account for the effects of the columns have been considered too.

Regarding the loading condition, the analyses have been performed adding to the self-weight of the main façade the distributed masses of the rooftop ($Q1 = 2.89$ kN/m), the terraces ($Q2 = 1.79$ kN/m), and the choir over the main entrance ($Q3 = 3.36$ kN/m). The values of the masses have been obtained according to the analysis of the related diaphragms. Figure 14 shows the geometrical model of the URM (Fig. 14a) and RM (Fig. 14b) façades evidencing the new restraining and loading conditions assumed.

The results of the numerical modal analyses on the URM and RM façades, with total weights of 1473 kN and 1593 kN, respectively, and considering $E_m = 880$ MPa and $\gamma_m = 14$ kN/m³, are listed in Table 5 for the first 6 modes in terms of frequencies and participation masses, considering the translation along the three directions X, Y and Z.

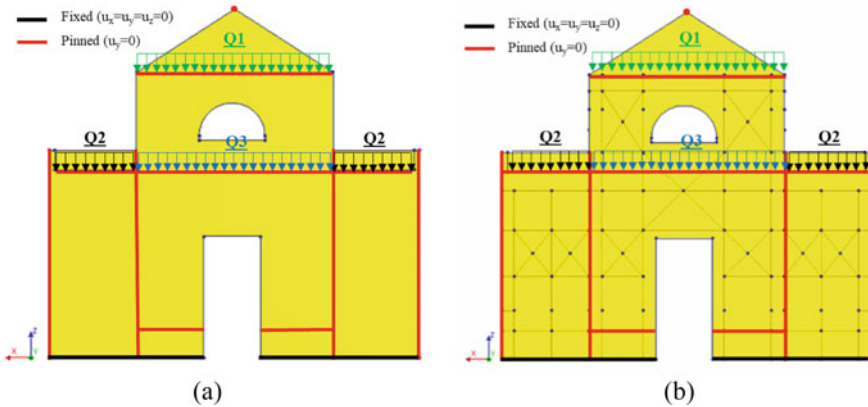


Fig. 14 Geometrical model of the façade (back view): **a** URM configuration; **b** iron RM configuration

Table 5 Results of the numerical modal analyses

	MODE	1	2	3	4	5	6
URM	<i>f</i> (Hz)	6.68	9.17	10.14	12.02	13.56	15.08
	<i>Part. Mass X</i> (%)	66.15	0.00	0.05	6.90	0.34	0.00
	<i>Part. Mass Y</i> (%)	0.00	10.20	0.46	0.00	0.33	1.30
	<i>Part. Mass Z</i> (%)	0.00	2.10	50.90	0.01	0.00	1.02
RM	<i>f</i> (Hz)	7.92	10.62	16.34	17.29	17.67	20.82
	<i>Part. Mass X</i> (%)	74.33	0.00	8.57	0.01	0.00	0.01
	<i>Part. Mass Y</i> (%)	0.00	12.66	0.00	0.00	0.13	0.00
	<i>Part. Mass Z</i> (%)	0.00	0.00	0.07	0.02	0.00	54.43

It can be noted that, in this new configuration, the first in-plane vibration mode (X direction) is the first one for both the URM and the RM facades, while the second mode is always related to an out-of-plane behaviour (Y direction) of the central part of the façade. These numerical results are now in agreement with the experimental ones obtained by OMA.

It can be observed that the iron reinforcement increases the frequency of the first in-plane vibration mode by 19% and the participation mass by 12%.

The second mode of the RM façade evidences an increase of frequency by about 16% in comparison with the URM one. Regarding the participation mass along the Y direction, the iron cage increases the portion of the wall involved in the local out-of-plane failure by about 24%.

The other vibration modes have a negligible participation mass in the in-plane direction, since they are mainly related to local out-of-plane failures involving smaller portions of the façade. The first vibration mode in the vertical direction is represented by the third and the sixth mode for the URM and RM façades, respectively, with a

negligible difference in the participation mass (51% for the URM façade and 54% for the RM façade) and a significant difference in terms of frequency (10.14 Hz and 20.82 Hz for the URM and the RM façades, respectively).

Figures 15 and 16 show three main vibration modes of the URM and RM façades, respectively. It is clear that the first modes in both façade configurations are related to a global in-plane behaviour (Figs. 15a and 16a), while the second modes are associated to local out-of-plane displacements of the central part of the façade, with zero inflection point of the modal shape (Figs. 15b and 16b).

Figures 15c and 16c show the first vertical vibration modes for the URM (third mode) and the RM (sixth mode) façades, respectively.

Thus, under the initial assumption of $E_m = 880 \text{ MPa}$ and $\gamma_m = 14 \text{ kN/m}^3$, the values of the frequencies associated to the first in-plane modes are 6.68 Hz and 7.92 Hz for the URM and RM façades, respectively, and 9.17 Hz and 10.62 Hz for the out-of-plane modes. These results evidence that in terms of eigenvalues there is still no good agreement with the experimental values and, thus, some sensitivity analyses have been carried out, as reported in the following.

The results of the numerical analyses have, indeed, evidenced that the restraint conditions mainly influence the order of the vibration modes and the modal shapes, especially with reference to the out-of-plane behaviour of the façade. Conversely,

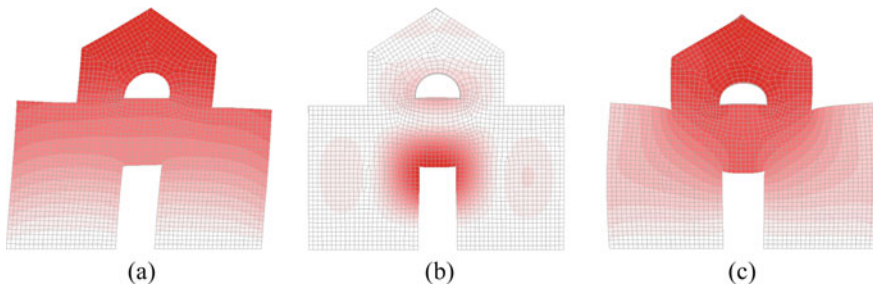


Fig. 15 Modal shapes for the unreinforced (URM) façade: **a** 1st mode (X direction), **b** 2nd mode (Y direction), **c** 3rd mode (Z direction)

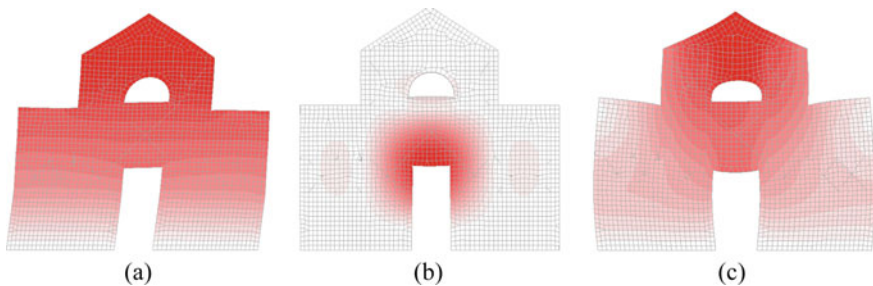


Fig. 16 Modal shapes for the reinforced (RM) façade: **a** 1st mode (X direction), **b** 2nd mode (Y direction); **c** 6th mode (Z direction)

a slight effect of the restraint conditions can be observed on the eigenfrequencies and the participation masses of the in-plane mode: they are, indeed, very similar to the values provided in the first configuration. Also, the additional distributed masses used in the new configuration slightly reduce the frequencies and the participation masses associated to the first in-plane vibration mode, since they are significantly lower in comparison with the total mass of the façade. With reference to the out-of-plane modes, the additional restraints increase by double the corresponding eigenfrequencies and reduce, clearly, the masses participant to these modes.

3.3.2 Effect of Young's Modulus and Unit Weight

Since the numerical analyses are strongly dependent on the mechanical properties used to model the materials behaviour, a sensitivity analysis is required as a reliable way to identify a range of possible results for the modal parameters of the main church façade, with reference to the URM and RM conditions. To this aim, the Young's modulus, E_m , and the specific weight, γ_m , are assumed as the main parameters for masonry, while no variation in the stiffness of the iron profiles is considered, since it slightly influences the frequencies and the mass participation of the RM façade. With respect to the initial values $E_m = 880$ MPa and $\gamma_m = 14$ kN/m³, the following ranges of variability are considered: 370–1540 MPa and 14–22 kN/m³, respectively. For these analyses, the second configuration of the restraints is assumed since it provides an order of the vibration modes that better reproduces the experimental one.

Table 6 reports the results of the parametric analysis, in terms of frequencies f and participant masses M , on both the first in-plane (1) and out-of-plane (2) vibration modes of the URM and RM façades. In all cases, the variations of the Young's modulus and unit weight do not change the type of modes detected in the previous analyses.

For both façades, the increase of the Young's modulus provides an increase of the frequency since it affects the whole stiffness of the masonry façade. Moreover, there is no variation in the participation mass of the URM façade, while a slight reduction is observed for the RM façade, where the modal mass decreases from 77.5% to 72.8% and from 13.4% to 12.4% for the first (in plane) and second (out-of-plane) vibration mode, respectively, for a Young's modulus varying from 370 to 1540 MPa.

On the other hand, the increase of the unit weight leads to a reduction of the frequencies for both façades and a slight effect on the participant mass, as expected. In particular, for the URM façade the frequencies reduce from 6.68 Hz to 5.35 Hz and from 9.17 Hz to 7.36 Hz for the first mode and second mode, respectively, when the unit weight increases from 14 kN/m³ to 22 kN/m³. For the RM façade there is a reduction of the frequencies from 7.92 Hz to 6.36 Hz and from 10.62 Hz to 8.52 Hz for the first mode and second mode, respectively.

These variations are plotted for the URM and RM façades in Fig. 17. Figure 17a shows the sensitivity of both the first in-plane and out-of-plane vibration mode's frequency with the Young's modulus of masonry. It can be noted that the range of frequencies for the RM façade is always greater than the one for the URM, but a very

Table 6 Results of the parametric analysis

Case	E_m (MPa)	E_s (MPa)	γ_m (kN/m ³)	Self-Weight (kN)	f (1) (Hz)	M (1) (%)	f (2) (Hz)	M (2) (%)
URM-1	370	–	14	1473	4.33	66.1	6.55	10.2
URM-2	880	–			6.68		9.17	
URM-3	1100	–			7.47		10.26	
URM-4	1320	–			8.18		11.24	
URM-5	1540	–			8.84		12.14	
URM-6	880	–	14	1473	6.68	66.2	9.17	10.2
URM-7		–	16	1683	6.26	69.2	8.60	10.8
URM-8		–	18	1894	5.91	71.8	8.12	11.3
URM-9		–	20	2104	5.61	73.9	7.71	11.6
URM-10		–	22	2315	5.35	75.8	7.36	12.0
RM-1	370	153,000	14	1593	5.67	77.5	8.10	13.4
RM-2	880				7.92	74.3	10.62	12.7
RM-3	1100				8.66	73.7	11.43	12.5
RM-4	1320				9.32	73.2	12.16	12.4
RM-5	1540				9.93	72.8	12.83	12.4
RM-6	880	153,000	14	1593	7.92	74.3	10.62	12.7
RM-7			16	1821	7.43	74.3	9.95	
RM-8			18	2049	7.01	74.4	9.40	
RM-9			20	2276	6.66	74.4	8.92	
RM-10			22	2504	6.36	74.4	8.52	

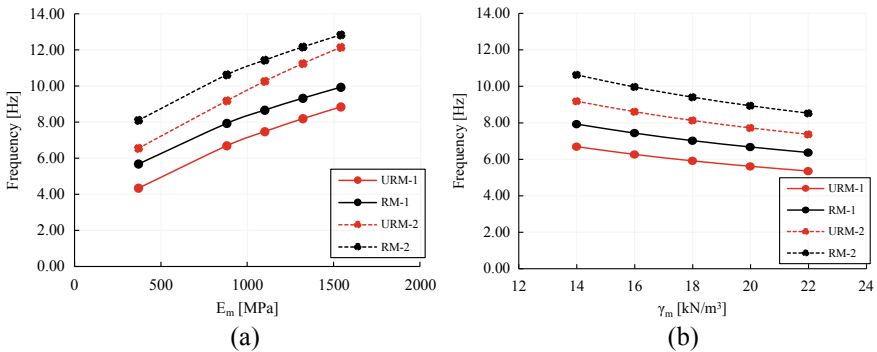


Fig. 17 Comparison among frequencies of URM and RM façades for the first in-plane (1) and out-of-plane (2) modes versus: **a** E_m and **b** γ_m

similar trend is evident. Figure 17b shows the sensitivity analysis of the frequencies with the unit weight; a reduction of the frequencies is observed with the increase of the unit weight. As evidenced, the two considered parameters have same effects on the frequencies of both the in-plane and out-of-plane vibration modes.

Results listed in Table 6 show that the minimum values of the numerical frequencies for the URM and the RM facades are higher than the experimental ones for both the in-plane and the out-plane modes. Moreover, even if the minimum value of E_m and the maximum value of γ_m considered in the ranges (i.e. 370 MPa and 22 kN/m³) were assumed in the analyses, in order to make the numerical frequencies closer to the experimental ones, they would be quite unrealistic material properties for the tuff masonry of the church.

Finally, the analysis of the dynamic behaviour of the isolated façade by means of a finite element model has evidenced some differences from the experimental one, especially in terms of frequencies of the in-plane mode. Such differences can be ascribable to the strong global box-behaviour of the church, probably further improved by the diffuse presence of the iron frames. Thus, despite considering different restraint conditions to simulate the connections of the façade wall with the rest of the church, the modelling of the isolated wall is not able to catch the real dynamic behaviour of the façade. Basically, this can be explained by considering that its actual vibration when connected with the church does involve mass and stiffness percentages that are not accounted in the modelling of the sole façade.

4 Conclusions

The paper deals with the study of the dynamic behaviour of a masonry church located in the Ischia Island (Italy) and built with a very particular typology of ‘baraccato’ constructive system. The Santa Maria Maddalena Church was, indeed, realized according to an ‘iron baraccato’ system made of masonry walls engaged in thin iron frames. Such a constructive system was used in some new constructions in the Ischia Island after the catastrophic seismic event of 1883.

The paper firstly presents the results of in-situ surveys carried out on the church after the seismic event that hit the Ischia Island in August 2017, focussing mainly on geometrical and damage inspections, thermography imaging, and in-situ dynamic tests under environmental operational conditions. The latter allowed to reliably identify the main modal parameters of the churches. The first three modal shapes of the church were reliably identified and a certain level of complexity of the dynamic was highlighted, mainly associated with the lack of connections at the top of each wall and with the reduced values of flexural and shear stiffness of the wooden panelled ceiling.

The estimation of the damping ratios evidenced unusual values for this kind of tests under environmental conditions, that could be justified by the post-earthquake conditions of the structure and, thus, to a widespread cracking of the masonry walls.

Then, the paper focusses on the study of the dynamic response of the main façade of the church by both applying OMA to the only sensors located on the façade and carrying out numerical modal analysis by means of a finite element model.

OMA evidenced that the values of the frequencies identified for the first three modes are basically the same as the ones identified in the analysis of the overall church. In particular, the main modal shape of the façade is in its plane. This is a confirmation that the church behaves as a 'box' and there is no trend to activate local mechanisms, as observed in the in-situ survey after the seismic event of August 2017.

A refined finite element model of the façade was realized in the DIANA FEA software aimed to carry out linear modal analysis for both the unreinforced masonry (URM) and the reinforced masonry (RM) façades in order to evidence the contribute of the iron frames. Parametric analyses were developed to highlight the sensitivity of modal shapes and frequencies to the Young's modulus and the unit weight of masonry, to the restraint conditions of the façade with the church, and to the presence of iron frames.

The numerical analyses evidenced that the restraint conditions mainly influence the order of the vibration modes and the modal shapes, especially with reference to the out-of-plane behaviour of the façade. Conversely, a slight effect of the restraint conditions can be observed on the frequencies and the participation masses of the in-plane mode. A reliable choice of the restraint conditions of the façade allowed, indeed, to obtain the same sequence of modal shapes as the experimentally ones provided by OMA.

With respect to the initial values of 880 MPa and 14 kN/m³ of the Young's modulus and the unit weight of masonry, respectively, the parametric analyses were performed considering the following ranges: 370–1540 MPa and 14–22 kN/m³. For both RM and URM facades, the increase of the Young's modulus provides an increase of the frequency, while there is no variation in the participation mass of the URM façade and a slight reduction is observed for the RM façade. On the other hand, the increase of the unit weight leads to a reduction of the frequency for both façades and a slight effect on the participant mass. As expected, the RM façade is characterized by higher frequencies in comparison with the URM one, i.e. +10–30% according to the values of Young's modulus and unit weight, but the trend of variation with these two parameters is substantially the same as the modal shapes.

It was found that the minimum values of the numerical frequencies for the URM and the RM facades are higher than the experimental ones for both the in-plane and the out-plane modes. However, the values of Young's modulus and unit weight, which make the numerical frequencies closer to the experimental ones, are quite unrealistic for the tuff masonry of the church.

Therefore, the conclusion is that the dynamic analysis of the single façade cannot properly represent the actual behaviour of the same wall as a part of a whole, although the connections can be simulated with several restraint conditions. This is because the modelling of the single façade is not able to catch the mass and stiffness contributions activated during the vibrations of the whole church.

These results are preparatory to the further modelling of the church, which should account for a global ‘box’ behaviour. This behaviour reflects also the good performance of the iron frames and, thus, the effectiveness of the ‘iron baraccato’ system under seismic actions, preventing those local mechanisms that other churches with similar geometries often undergo.

References

1. Cescatti E, Salzano P, Casapulla C, Ceroni F, da Porto F, Prota A (2020) Damages to masonry churches after 2016–2017 Central Italy seismic sequence and definition of fragility curves. *Bull Earthq Eng* 18:297–329. <https://doi.org/10.1007/s10518-019-00729-7>
2. Salzano P, Casapulla C, Ceroni F, Prota A (2020) Seismic vulnerability and simplified safety assessments of masonry churches in the Ischia Island (Italy) after the 2017 earthquake. *Int J Archit Heritage* 1–27. <https://doi.org/10.1080/15583058.2020.1759732>
3. Lagomarsino S (2012) Damage assessment of churches after L’Aquila earthquake (2009). *Bull Earthq Eng* 10:73–92. <https://doi.org/10.1007/s10518-011-9307-x>
4. De Matteis G, Criber E, Brando G (2016) Damage probability matrices for three-nave masonry churches in Abruzzi after the 2009 L’Aquila earthquake. *Int J Archit Heritage* 10:120–145. <https://doi.org/10.1080/15583058.2015.1113340>
5. Canuti C, Carbonari S, Dall’Asta A, Dezi L, Gara F, Leoni G (2019) Post-earthquake damage and vulnerability assessment of churches in the Marche Region struck by the 2016 Central Italy seismic sequence. *Int J Archit Heritage* 1–22. <https://doi.org/10.1080/15583058.2019.1653403>
6. Torres W, Almazán JL, Sandoval C, Boroschek R (2017) Operational modal analysis and FE model updating of the Metropolitan Cathedral of Santiago, Chile. *Eng Struct* 143:169–188. <https://doi.org/10.1016/j.engstruct.2017.04.008>
7. Bassoli E, Vincenzi L, D’Altri AM, de Miranda S, Forghieri M, Castellazzi G (2018) Ambient vibration-based finite element model updating of an earthquake-damaged masonry tower. *Struct Control Health Monit* 25(5). <https://doi.org/10.1002/stc.2150>
8. Bayraktar A, Altunışık AC, Sevim B, Türker T (2011) Seismic response of a historical masonry minaret using a finite element model updated with operational modal testing. *JVC/J Vibration Control* 17(1):129–149. <https://doi.org/10.1177/1077546309353288>
9. Türker T, Bayraktar A (2014) Structural safety assessment of bowstring type RC arch bridges using ambient vibration testing and finite element model calibration. *Measurement* 58:33–45. <https://doi.org/10.1016/j.measurement.2014.08.002>
10. Ceroni F, Pecce M, Manfredi G (2009) Seismic assessment of the bell tower of Santa Maria del Carmine: problems and solutions. *J Earthquake Eng* 14:30–56. <https://doi.org/10.1080/13632460902988968>
11. Ceroni F, Sica S, Garofano A, Pecce M (2014) SSI on the dynamic behaviour of a historical masonry building: Experimental versus numerical results. *Buildings* 4:978–1000. <https://doi.org/10.3390/buildings4040978>
12. Pellegrini D, Girardi M, Lourenço PB, Masciotta MG, Mendes N, Padovani C, Ramos LF (2018) Modal analysis of historical masonry structures: linear perturbation and software benchmarking. *Constr Build Mater* 189:1232–1250. <https://doi.org/10.1016/j.conbuildmat.2018.09.034>
13. Rainieri C, Fabbrocino G (2011) Operational modal analysis for the characterization of heritage structures. *Geofizika* 28(1):109–126
14. Russo S (2014) Using experimental dynamic modal analysis in assessing structural integrity in historic buildings. *Open Constr Build Technol J* 8:357–368. <https://doi.org/10.2174/1874836801408010357>

15. Aloisio A, Alaggio R, Fragiaco M (2019) Dynamic identification of a masonry façade from seismic response data based on an elementary Ordinary Least Squares approach. *Eng Struct* 197:0141–0296. <https://doi.org/10.1016/j.engstruct.2019.109415>
16. Rainieri C, Fabbrocino G, Brigante D (2020) Differentiating local and global vibration modes of heritage masonry buildings through the spatial correlation of modal displacements. *Int J Archit Heritage*. <https://doi.org/10.1080/15583058.2020.1825876>
17. Hicyilmaz KMO, Wilcock T, Izatt C, da Silva J, Langenbach R (2012) Seismic performance of Dhajji Dewari. In: 15th World Conference on Earthquake Engineering, Lisbon, Portugal
18. Mendes N, Lourenco PB (2009) Seismic assessment of masonry Gaioleiro buildings in Lisbon, Portugal. *J Earthquake Eng* 14:80–101. <https://doi.org/10.1080/13632460902977474>
19. Salerno G, Geremia F, Pagano E, Zampilli M, Ruggieri N, Stellacci S (2015) The masonry timber framed load bearing structure of ‘baraccato’ system: a numerical model. In: Cruz H, Saporiti Machado J, Campos Costa A, Candeias XP, Ruggieri N, Catarino MJ (eds) *Historical earthquake-resistant timber framing in the Mediterranean Area*. Springer, Netherlands, pp 205–213
20. Ruggieri N (2017) The Borbone “Istruzioni per Gli Ingegneri”: a historical code for earthquake-resistant constructions. *Int J Archit Heritage*. <https://doi.org/10.1080/15583058.2016.1212128>
21. Ruggieri N, Tampone G, Zinno R (eds) (2015) *Historical earthquake-resistant timber frames in the Mediterranean area*. Springer, Netherlands
22. Stellacci S, Ruggieri N, Rato V (2016) Gaiola vs. Borbone system: a comparison between 18th century anti-seismic case studies. *Int J Archit Heritage* 10(6): 817–828. <https://doi.org/10.1080/15583058.2015.1086840>
23. Casapulla C, Ceroni F, Ranieri C, Argiento LU, Arcamone P, Fabbrocino G (2019) Structural assessment of Santa Maria Maddalena Church in Ischia (Italy) by experimental modal analysis under operational conditions. In: Papadrakakis M, Fragiadakis M (eds) *Computational Methods in Structural Dynamics and Earthquake Engineering (COMPDYN 2019)*, Crete, Greece
24. Gruppo di Lavoro INGV (2017, September 6) Rapporto di sintesi preliminare sul Terremoto dell’isola d’Ischia (Casamicciola) M4.0 del 21 agosto 2017 (6 settembre 2017). Zenodo. <https://doi.org/10.5281/zenodo.886045>
25. Avdelidis NP, Moropoulou A (2004) Applications of infrared thermography for the investigation of historic structures. *J Cult Herit* 5:119–127
26. Maione A, Argiento LU, Casapulla C, Prota A (2018) Management of multi-source information to identify the typology of the horizontal structures in historical masonry buildings: the case study of the Museum of Capodimonte in Naples (Italy). *Frattura ed Integrità Strutturale* 46:240–251. <https://doi.org/10.3221/IGF-ESIS.46.22>
27. Reynders E, Magalhaes F, De Roeck G, Cunha A (2009) Merging strategies for multi-setup operational modal analysis: application to the Luiz I steel arch bridge. In: *Conference Proceedings of the Society for Experimental Mechanics Series*
28. Allemang RJ, Brown DL (1982) A correlation coefficient for modal vector analysis. *Proceedings of the 1st international modal analysis conference, Orlando, FL, USA*, pp 110–116
29. DIANA FEA BV (2019) *Diana user’s manual, Release 10.3*, DIANA FEA BV. <https://doi.org/10.1080/15421400600788682>
30. Argiento LU, Celano T, Ceroni F, Casapulla C (2020) Modelling strategies for the in-plane behaviour of iron-framed masonry structures: parametric analysis on simple panels and a church façade. *Int J Archit Heritage*, 1–26. <https://doi.org/10.1080/15583058.2020.1858369>
31. Brussel MN (1998) *Appraisal of existing iron and steel structures*. The Steel Construction Institute, Ascot-Berkshire
32. Di Napoli B (2019) *Modelling and safety assessment of the Santa Maria Maddalena Church, Ischia, Italy*. Msc Thesis, Universidade do Minho, Portugal

Monitoring of Bridges by Using Static and Dynamic Data from MEMS Accelerometers



Mathieu Desbazeille, Nathalie Saguin Sprynski, Viviane Cattin, Malvina Billères, Laurent Jouanet, and Audrey Vidal

Abstract Structural Health Monitoring methods may be divided into two major categories depending on the type of data used during the damage identification: static or dynamic. In this paper, it is shown that both analyses can be performed with the same instrumentation composed only of Micro Electro Mechanical System (MEMS) accelerometers. The latter has the capability to measure static and dynamic data. In very low frequency, accelerometers are used as inclination sensors to estimate static deflection. In higher frequency, accelerometers are used as vibration sensors to perform modal analysis. Both analyses are illustrated in the case of a real foot-bridge. Static deflections and modal flexibility-based deflections are compared in operational conditions, including pedestrian loads and temperature changes, and in artificially-introduced damage conditions. Very good agreements are obtained showing the relevance of the two approaches. Static and dynamic analyses could be used in a complementary way and provide additional information in order to reinforce the confidence and the accuracy of the damage identification.

Keywords Structural health monitoring · Damage identification · Static and dynamic data · Deflection · Modal flexibility matrix · Modal flexibility-based deflection

1 Introduction

Structural Health Monitoring (SHM) aims at decreasing the maintenance cost and increasing the safety level of structure. It consists in identifying abnormal state of a structure due to damage by measuring its responses from an array of sensors.

Damage is usually defined as a stiffness decrease or flexibility increase of the structure caused by normal aging or by accidental events. The damage identification is decomposed into four levels [16]:

M. Desbazeille (✉) · N. S. Sprynski · V. Cattin · M. Billères · L. Jouanet · A. Vidal
CEA Centre de Grenoble, 17, avenue des Martyrs, 38054 Grenoble, France

1. detection of the occurrence of damage,
2. localization of damage,
3. quantification of the severity of damage,
4. and prediction of remaining service life of the structure.

Existing methods may be divided into two major categories depending on the type of data used during the identification: static (deflection) or dynamic (vibration). These two types of data may be processed to obtain damage-sensitive indicators with or without the need of a Finite Element (FE) model of the structure. A FE model of the structure gives a deep knowledge of the system behavior. However, a lot of effort may be required to fit the model to the healthy or damaged state of the structure.

Static methods are based on deflection measurements. Loading tests show a long tradition in civil engineering and are usually performed to validate design of new bridges or to verify integrity of old bridges. Deflection of a bridge is directly related to its stiffness. Analysis of deflections obtained from periodically loading tests or continuous monitoring can enable to detect and localize damage [8, 11]. However, measurement of deflection is still a challenging task. Deflection are often obtained from Linear Variable Differential Transformers (LVDT) which require a fixed reference. This reference may be unavailable especially in the case of high bridges. Indirect measurement of displacement from accelerometers seems to be attractive. However, double integration of acceleration signals suffers from integration errors especially in low frequency and when the observation time is long [19]. Alternative methods based on GPS [21], strain or inclination [6] data are still investigated.

Dynamic methods based on vibration measurements have been extensively developed in the literature due to the simplicity of instrumentation. The dynamical characteristics of a structure can be represented by its structural parameters (mass, stiffness or flexibility and damping matrices) or its modal parameters (frequencies, mode shapes and damping factors). Many researchers have used changes in modal parameters to detect damage. Modal frequencies have drawn a lot of attention from decades because these can be measured very accurately with a limited number of sensors. However, localization of damage is rarely possible when using only changes in modal frequencies. The flexibility matrix, corresponding to the inverse of the stiffness matrix, has attracted a lot of researchers since the pioneer work of [12]. Contrary to the stiffness matrix, the flexibility matrix can be accurately estimated by considering only the first modal frequencies and the corresponding mode shapes providing spatial information of the structure. Analysis of flexibility-based deflections obtained by applying special load vectors (uniform or non-uniform) to the estimated flexibility matrix can enable to detect and localize damage [2, 7].

It can be seen that there exists a strong relation between some of the static and dynamic methods. Both approaches may attempt to detect and localize stiffness reduction by estimating directly or indirectly deflections. In addition, similar features or indicators can be extracted from these deflections as maximum deflection or curvatures for the most known.

The aim of this paper is to show that both analyses, static and dynamic, can be performed with Variable Capacitive (VC) Micro Electro Mechanical System (MEMS)

accelerometers. Actually, these accelerometers, which are easy to install, inexpensive and compact, have the capability to measure static (gravity) and dynamic (vibration) data. In very low frequency, the accelerometer is used as inclination sensor or tilt sensor to estimate static deflection. In higher frequency, the accelerometer is used in its normal usage as vibration sensor to perform modal analysis and to estimate modal flexibility-based deflection. It is believed that static and dynamic analyses could be used in a complementary way and provide additional information. This dual analyses is illustrated on a real application in the case of a footbridge located on CEA site in Grenoble (France).

The main contribution of this paper concerns the use of accelerometers as tilt sensors in the estimation of deflections for SHM applications in civil engineering. The use of tilt sensors in the estimation of bridge deflection has already been suggested in previous works [6, 10]. The former, only developed in a theoretical point of view, requires the knowledge of analytical mode shape functions which may be a limitation in the case of real structures. The latter approximates the deflection curve with a polynomial function. Estimation results may be affected by the choice of the polynomial order in some applications. The proposed method, inspired by previous works of CEA in shape reconstruction [18] and monitoring of flexible risers in the oil and gas industry [17], is based on spatial integration and does not require any *a priori* information of the structure.

This paper is organized as follows. The first part is devoted to the theoretical background. The estimation of deflections from inclination data and the estimation of modal flexibility-based deflections from vibration data are presented. The second part presents the results of the experimental application. Sensitivity of both approaches to an artificially introduced damage and natural thermal effect are analyzed.

2 Theoretical Background

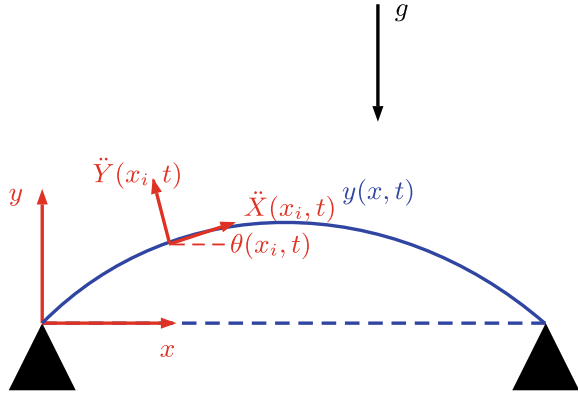
2.1 Deflection Estimation from Static Acceleration Data

Deflection estimation from static acceleration data is mainly composed of two steps:

- Estimation of inclination angles
- Estimation of deflection

For a sake of clarity, the proposed method is illustrated in the case of a simply supported beam of length L under Euler-Bernoulli theory as shown in Fig. 1. This simple model has been extensively used in the monitoring of civil buildings such as bridges. It gives a first good estimate of the dynamical behavior of many structures. Tri-axial accelerometers are regularly placed along its main axis. g is the gravity of earth. $y(x, t)$ and $\theta(x, t)$ are respectively the vertical deflection and the rotation of the beam function of position x and time t . $\ddot{X}(x_i, t)$ and $\ddot{Y}(x_i, t)$ are respectively the longitudinal and the vertical components of accelerometer i located at position x_i .

Fig. 1 Simply supported beam



The lateral component $\ddot{Z}(x_i, t)$ is not of interest and is deliberately omitted. In the case of small deflections, the following approximations are valid:

$$\begin{aligned} \cos(\theta) &= 1 \\ \sin(\theta) &= \theta \\ \frac{\partial y(x, t)}{\partial x} &= \theta(x, t) \end{aligned} \tag{1}$$

Estimation of inclination angles In static or quasi-static situation, the longitudinal and vertical components of accelerometer i have the following expressions:

$$\begin{cases} \ddot{X}_i(t) = -g\theta_i(t) \\ \ddot{Y}_i(t) = -g \end{cases} \tag{2}$$

The inclination angles is directly obtained from the longitudinal component:

$$\theta_i(t) = -\frac{\ddot{X}_i(t)}{g} \tag{3}$$

In static and dynamic situation (general case), additional terms caused by the vertical and angular acceleration of the beam are superimposed to Eq.2. The estimation of inclination angles by using Eq.3 is only possible after removing the additional terms by applying a low-pass filter to the acceleration data. The estimation of inclination angles is restricted to the low frequency. Therefore, only static or quasi-static deflections can be estimated. The choice of the cut-off frequency f_c is a complicated task strongly depending on the application. Its choice is a compromise between signal and noise reduction.

Estimation of deflection At each time step t_n , the deflection of the beam can be estimated by spatial integration of the inclination angles from 0 to x or from L to x with similar results in noise-free condition:

$$y^+(x, t_n) = \int_0^x \theta(u, t) du \tag{4}$$

$$y^-(L - x, t_n) = \int_L^x \theta(u, t) du \tag{5}$$

These integrals are approximated by simple numerical integration schemes such as the trapezoidal rule. Inclination angles are only known at a limited number of points. Interpolation with spline functions as a preliminary step is strongly recommended in order to reduce numerical integration errors.

Estimation of errors Accelerometer outputs are contaminated by additive random noise. Errors are mainly caused by the process of integrating this noise. Errors due to interpolation and integration approximation are considered as secondary sources of errors for the followings reasons: First, spatial sampling of the beam is assumed to be sufficient. Secondly, static or quasi-static deflections of beams are correctly approximated by smooth functions such as splines.

Noise in MEMS accelerometers comes from many sources and can be modelled by a combination of random processes [14]. In this work, it is only considered the Gaussian white noise process whose integration leads to random walk process. It is worthwhile to say that this simple random process does not model for the bias drift of MEMS accelerometers.

At each time step t_n , the estimated deflection can be considered as the sum of two contributions:

$$\hat{y}(x, t_n) = y(x, t_n) + b(x, t_n) \tag{6}$$

$y(x, t_n)$ is the true deflection. $b(x, t_n)$ is the error term corresponding to the spatial integration of a low-pass filtered white noise. Its variance is given by the following expressions:

$$\sigma_b^2(x) = \begin{cases} psd^2 2 f_c \frac{L}{(N - 1)} x \text{ int. } 0 \rightarrow x \\ psd^2 2 f_c \frac{L}{(N - 1)} (L - x) \text{ int. } L \rightarrow x \end{cases} \tag{7}$$

psd is the power spectral density of the noise expressed in g/\sqrt{Hz} that is usually given in datasheets of accelerometers. N is the number of accelerometers regularly placed along the main axis of the beam. Variances increase with the spatial position x .

In the special case of a simply supported beam (zero deflection at the two ends), the best estimator in the maximum likelihood sense is given by:

$$\hat{y}(x, t_n) = \frac{(L - x) \hat{y}^+(x, t_n) + x \hat{y}^-(L - x, t_n)}{L} \quad (8)$$

with variance

$$\sigma_b^2(x) = psd^2 2f_c \frac{L}{(N - 1)} \frac{x(L - x)}{L} \quad (9)$$

More confidence is given to y^+ from $x = 0$ to $x = L/2$ because its variance is lower. Reciprocally, more confidence is given to y^- from $x = L/2$ to $x = L$ because its variance is lower.

2.2 Flexibility-Based Deflection Estimation from Dynamic Data

Operational modal analysis Operational Modal Analysis (OMA) consists in identifying modal parameters of a structure by only analyzing its responses under natural excitations such as wind and traffic. This is made possible by assuming that unknown forces are random and uncorrelated. OMA offers advantages compared to the traditional Experimental Modal Analysis (EMA). Among these, OMA is well appropriate in the monitoring of structures. It may be performed continuously without immobilizing the structure as EMA usually requires during dynamical tests. On the other hand, OMA suffers from a few limitations. First, the number of identifiable modes is often low because of the low-frequency contents of the natural excitations. Moreover, estimation accuracy of the modal parameters decreases with increasing mode order. Secondly, the modal identification is incomplete. Only unscaled mode shapes can be identified. However, mass normalized mode shapes are needed in many SHM applications. Solutions have been proposed in the literature such as the mass change method [13] but the latter is often not applicable in the case of large structures. In this work, mode shapes will be scaled by using the mass matrix of a finite element modeling of the structure as suggested by [1]. The technique is based on the assumption that the differences between the experimental and the finite element mass matrices are small.

Many modal identification algorithms have been developed in the literature. These are usually classified as time and frequency methods but also as non-parametric and parametric methods. An excellent review of most common existing methods in civil engineering is available in [9]. The Frequency Domain Decomposition (FDD) is a very attractive and user-friendly method that was first presented in [5]. This non-parametric frequency domain method overcomes the limitations of the Peak-Picking (PP) method in the case of closely spaced modes and noisy data. It is based on

successive singular value decompositions (SVD) of spectral matrices function of frequency. Modal frequencies are estimated by identifying peaks on the first singular value spectrum. The latter concentrates all the information from the spectral densities. Mode shapes are estimated by taking the corresponding singular vectors. Original FDD algorithm does not permit the estimation of modal damping, the Enhanced FDD (EFDD) was latter developed to fill this need [4]. The EFDD does not only give the modal damping but also a better estimate of the modal frequencies.

Automation of the modal analysis Given the amount of data to be post processed in the application of a continuous monitoring system, identification algorithms, which always require a user interaction, have to be automated. In the case of the EFDD algorithm, this mainly concerns the process of identifying peaks on a spectrum [3] that is easier to automate than parametric identification algorithms which have to deal with stabilization diagrams [15]. Automation must also be able to discriminate noise peaks from physical peaks. This can be accomplished by computing modal validation criteria. Structures in civil engineering are lightly damped. Damping ratio are close to zero and mode shapes are real values. Modes that do not exhibit this behavior may be considered as spurious modes.

Flexibility-based deflection estimation The flexibility matrix $[\mathbf{F}]_{N \times N}$ is computed using the following expression:

$$[\mathbf{F}] = \sum_{i=1}^R \frac{1}{\omega_i^2} \{\Phi_i\} \{\Phi_i\}^T \quad (10)$$

where $\{\Phi_i\}_{N \times 1}$ and ω_i are respectively the mass-normalized mode shape and the angular frequency of mode i . N is the number of nodes. R is the number of modes included in the computation. Contribution of the modes to the flexibility matrix decreases as frequency increases. The flexibility matrix rapidly converges by considering only the first modes.

Damage identification could be done by directly detecting changes in the flexibility matrix. However, it is often more complicated to deal with matrix than vector. This is the motivation of the flexibility-based deflection method.

Flexibility-based deflection $\{y\}_{N \times 1}$ is computed by applying the load vector $\{u\}_{N \times 1}$:

$$\{y\} = [\mathbf{F}] \{u\} \quad (11)$$

The load vector may be a distributed load (a vector only composed of non-zero terms) or a concentrated load (a vector composed of zero terms except at one location). The first choice presents the advantage of considering all the elements of the flexibility matrix.

3 Experimental Application

Experimental tests were conducted on a footbridge located on CEA site in Grenoble (France) in order to implement the above static and dynamic analyses on a real structure. The experimental campaign started the 10th of July, 2018 (day 0) and lasted more than one year with a few interruptions. Only post processing of data at selected periods are presented in the present paper.

3.1 Presentation of the Footbridge

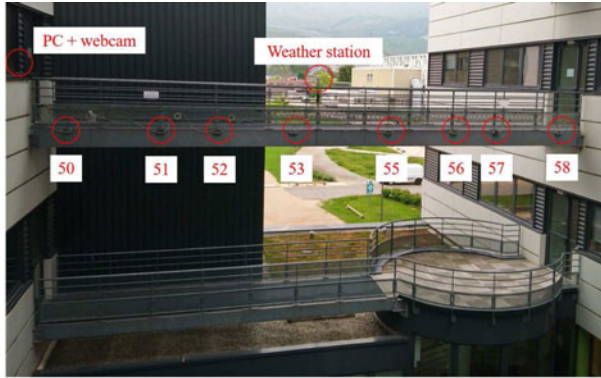
The footbridge is a steel frame structure composed of two U-shaped longitudinal beams of length 12.7 m, twelve I-shaped lateral beams of length 1.7 m and a guardrail (see Fig. 2). A monitoring system has been installed on the structure including nine MEMS accelerometers ADXL 355 (Analog Device), a weather station and a PC equipped with a webcam. Accelerometers are numbered from 50 to 58. The choice of the locations is a compromise between static and dynamic constraints. Static analysis requires to install sensors at maximum inclination angles while dynamic analysis requires to install sensors at maximum deflection. When looking at the two first modes of a simply supported beam, it is clear that these requirements are in opposition. It was decided to fix all the sensors on the same beam except one (54) on the other one to discriminate torsion modes from flexion modes. Calibration (including thermal calibration) and characterization (in terms of noise) of the accelerometers were conducted in laboratory before installation. The *psd* of the sensor is $10 \mu\text{g}/\sqrt{\text{Hz}}$ as mentioned in the datasheet of the manufacturer. Responses of the footbridge are recorded every hours during 300 s at a sampling rate of 200 Hz.

A Finite Element (FE) model of the structure composed of beam elements was constructed (see Fig. 3). Its total mass is 2530 kg. The static deflection of the footbridge under a pedestrian load (700 N) at midspan is approximately -0.3 mm. The six first modes are shown in Fig. 4. As expected, these modes are very similar to those of a simply supported beam. The first mode is the first lateral flexion of the structure located at 3.1 Hz. Many modes in the frequency range [20, 21] Hz corresponding to the modes of the guardrail were disregarded as this work focuses on the main structure.

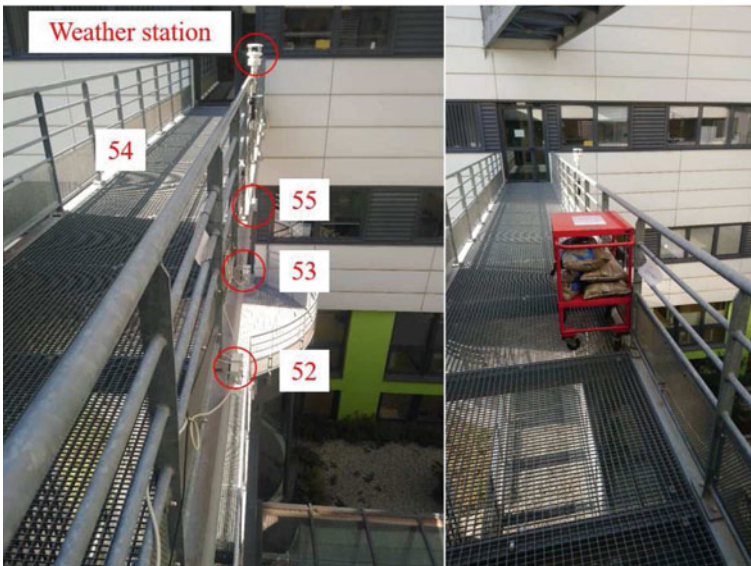
For safety reasons, it was not permitted to modify the stiffness of the structure. Artificial damages were introduced by adding some mass. Sandbags were added at midspan next to the guardrail (see Fig. 2) as follows:

- 100 kg (4 % of the total mass of the structure) from 2018/09/25 17h30 (day 77) to 2018/09/28 8h30 (day 80),
- and 50 kg (2 % of the total mass of the structure) from 2018/09/28 8h30 (day 80) to 2018/10/01 09h30 (day 83).

Increasing the mass instead of decreasing the stiffness has a quite similar impact on the structure behavior.



(a) Location of the sensors



(b) Location of the sensors

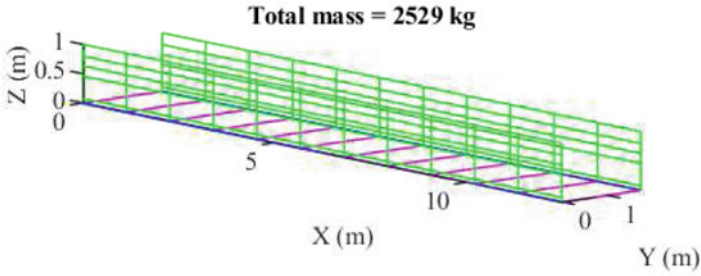
(c) Addition of mass

Fig. 2 Footbridge

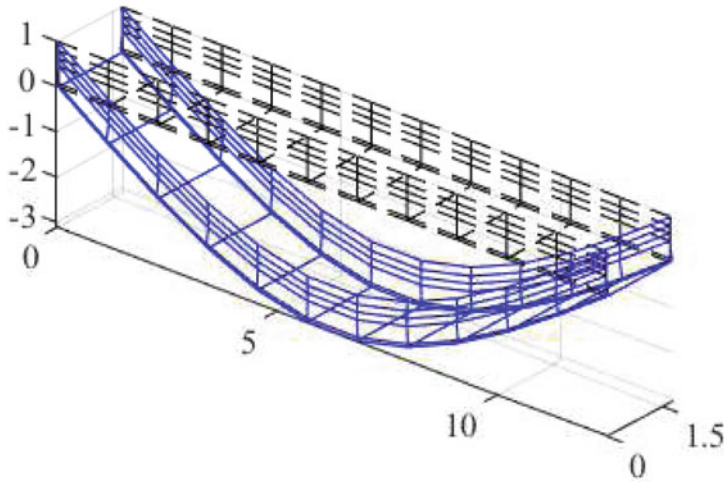
3.2 Deflection Analysis

Alignment of the sensor frames with the structure frame is almost impossible during installation. Only relative deflections and not absolute deflections can be estimated. This requires the choice of an arbitrary zero-deflection reference.

Deflection under pedestrian load Fig. 5 shows the quasi-static deflection obtained on one complete recording. Inclination angles were obtained by low-pass filtering the longitudinal acceleration data with a cutoff frequency equal to 0.125 Hz. The crossing



(a) Model composed of beam elements



(b) Static deflection of the footbridge under a load of 700 N at midspan ($\times 10^4$)

Fig. 3 Finite element modeling of the footbridge

time of a pedestrian is approximately 8 s ($1/8 = 0.125$). A lower cutoff frequency may lead to serious signal information loss. The first seconds of measurement were used as zero-deflection reference. According to Eq. 9, the accuracy is approximately $\pm 30 \mu m$ ($\pm 3\sigma_b$). Four events happened during the 300 s of recording. 6, 5, 3 and 2 pedestrians successively crossed the bridge. As expected, deflections increase with the number of pedestrians. Maximum deflections up to 1 mm are recorded. These values are in the same order of magnitude than those given by the FE model. It is observed that the structure does not come back to its rest position after each loading

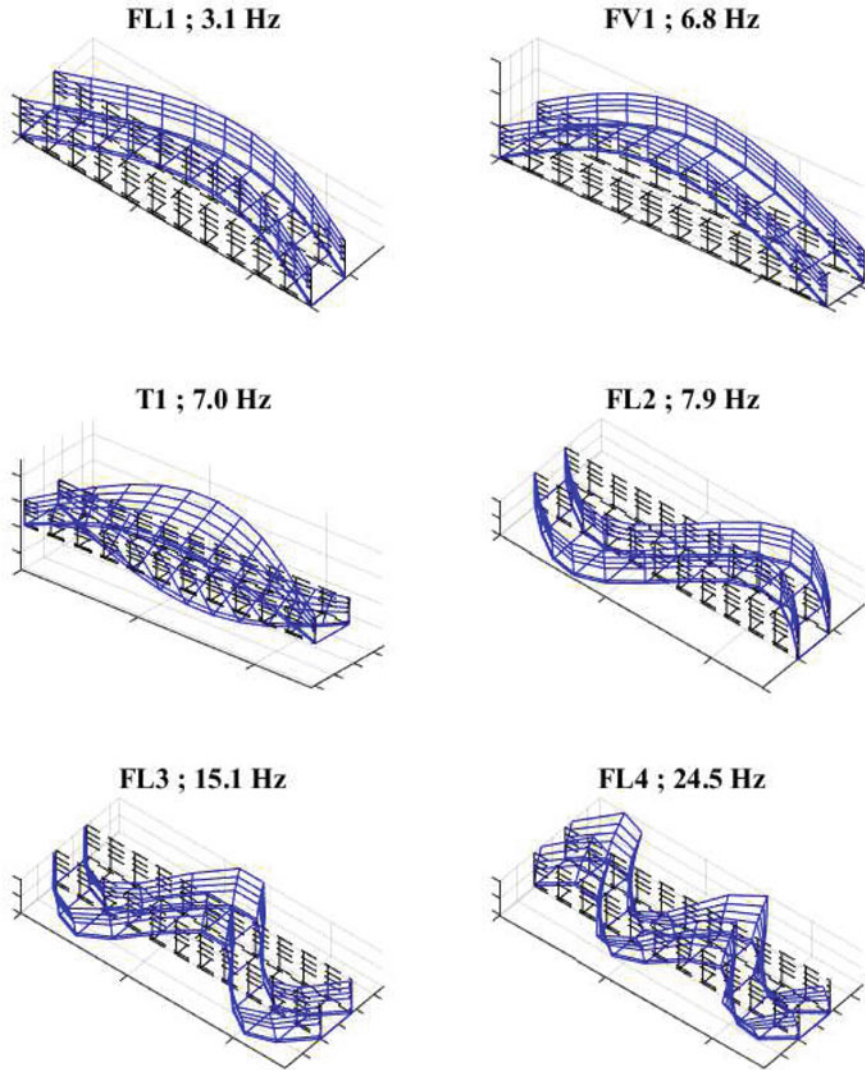
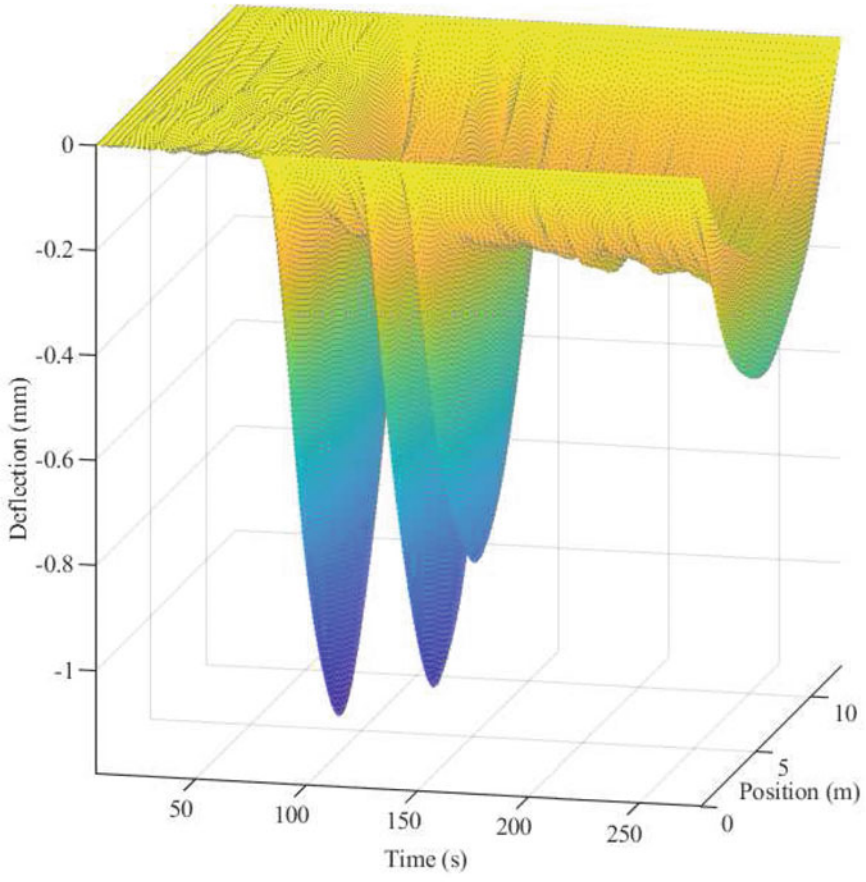


Fig. 4 First modes of the footbridge model; LF: lateral flexion, VF: vertical flexion, T: torsion

during the observation time. This behavior that could be caused by clearances in the structure still have to be investigated.

Figure 6 shows the monitoring of the maximum deflection of the footbridge under pedestrian load during five days from day 251 to day 255. Points with plus markers correspond to measurements during which at least one pedestrian crossed the bridge. Points with cross markers correspond to noise measurement. As expected, these points are very close to the $\pm 30 \mu\text{m}$ margins represented in dashed lines.



(a)



(b)

Fig. 5 Quasi-static deflection of the footbridge under pedestrian load

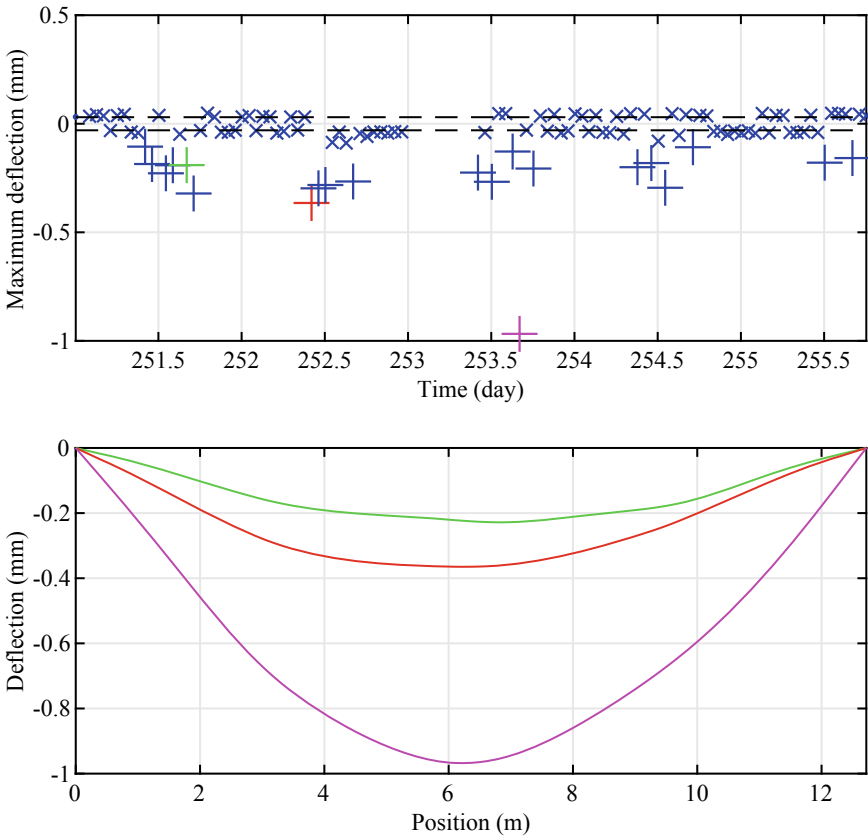


Fig. 6 Monitoring of the maximum deflection of the footbridge under pedestrian load from 2019/03/18 (day 251) to 2019/03/22 (day 255). Points with plus markers correspond to measurements during which at least one pedestrian crossed the bridge. Points with cross markers correspond to noise measurement. The corresponding deflection curves of three points (green, red and mauve) are shown.

Deflection under temperature change Fig. 7 shows the evolution of the static deflection of the footbridge during one week from day 426 to day 432. Inclination angles were obtained by averaging the longitudinal acceleration data on the 300 s of each recording. The first measurement (2019/09/09 00h00mn) was used as zero-deflection reference. Temperatures measured by the weather station are also shown on the same period. It can be observed that the footbridge is strongly sensitive to temperature change. Maximum deflections up to 2 mm are recorded. These values are higher than those obtained under pedestrian load. The structure tends to lift up when the temperature increases, especially in mid-afternoon when it is exposed to solar radiation (the footbridge is exposed south-west). This could be caused by thermal expansions of the different parts of the structure that induce bending known as thermal bowing or buckling [20]. In SHM applications, these variations, which may mask the changes

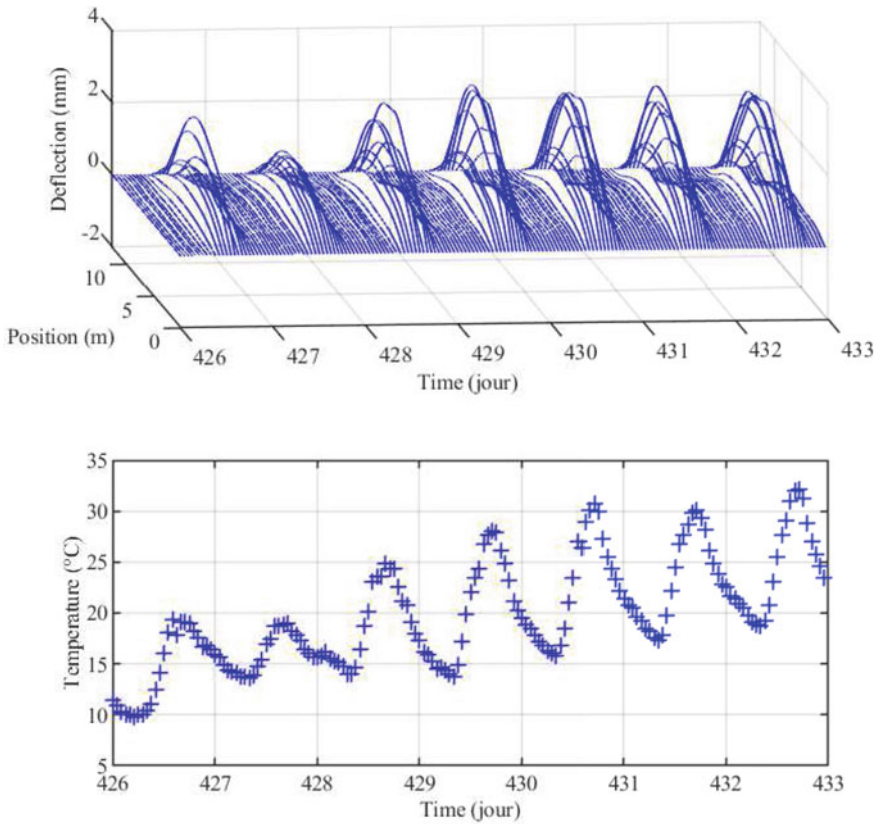


Fig. 7 Static deflection of the footbridge under temperature change from 2019/09/09 (day 426) to 2019/09/15 (day 432)

caused by structural damages, are not desirable however a direct correlation between deflections and ambient temperatures is not straightforward. The ambient temperature seems not to be the only meteorological input parameters responsible of this behavior.

Deflection in damage condition Fig. 8 shows the static deflections of the footbridge during one week from day 77 to day 83. As previously, inclination angles were obtained by averaging the longitudinal acceleration data on the 300 s of each recording. The first measurement (2018/09/25 00h00mn) was used as zero-deflection reference. Only deflections from 00h00mn to 06h00mn (color crosses and color lines) are represented because meteorological conditions are more appropriate in the nighttime: temperature more stable and no radiation from the sun. It can be observed three clusters of deflections corresponding to the normal condition and the two artificially introduced damage conditions. High variations are observed in each condition that

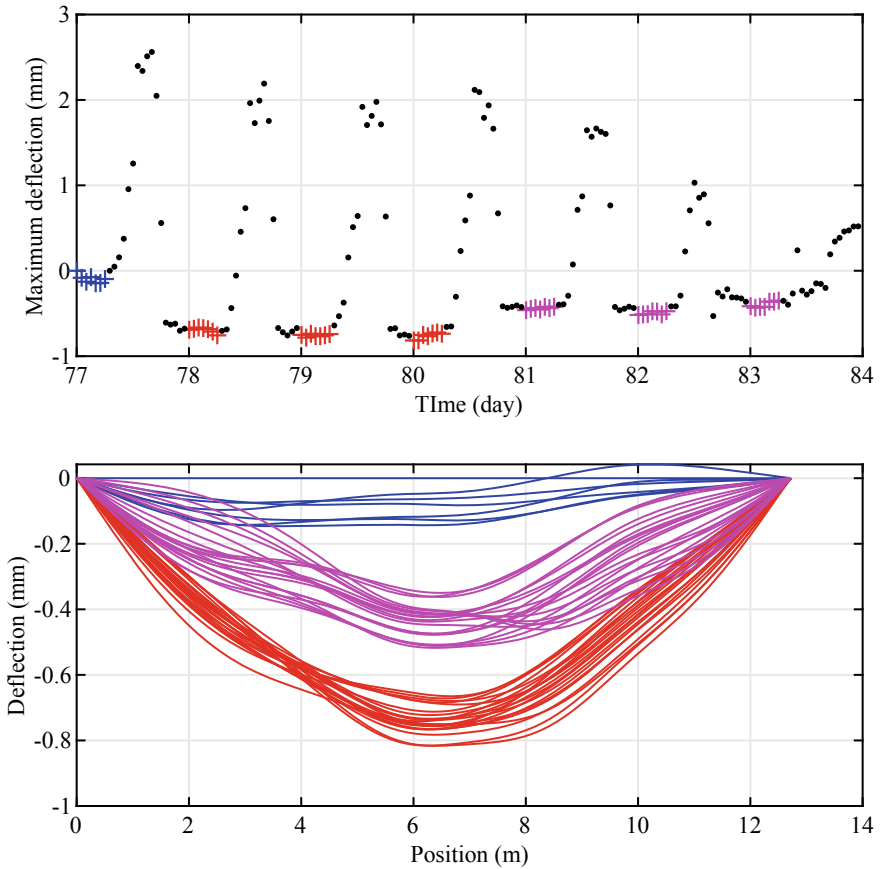
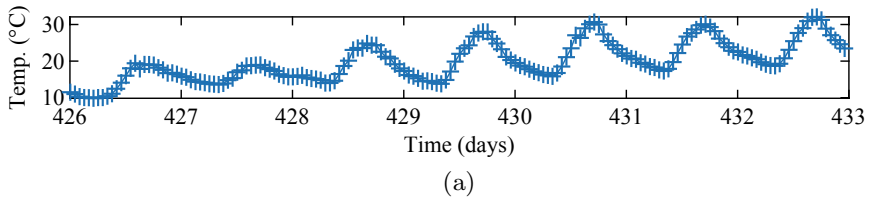
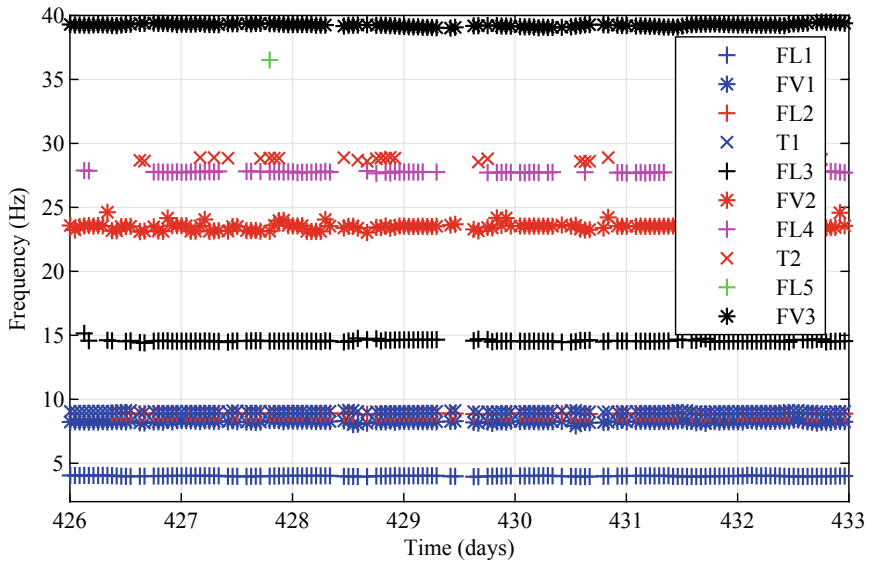


Fig. 8 Static deflection of the footbridge in damage condition from 2018/09/25 (day 77) to 2018/10/01 (day 83). Only deflections between 00h00mn and 06h00mn (color crosses and color lines) are represented with 50 kg added mass in mauve, 100 kg added mass in red at midspan and no added mass (reference) in blue

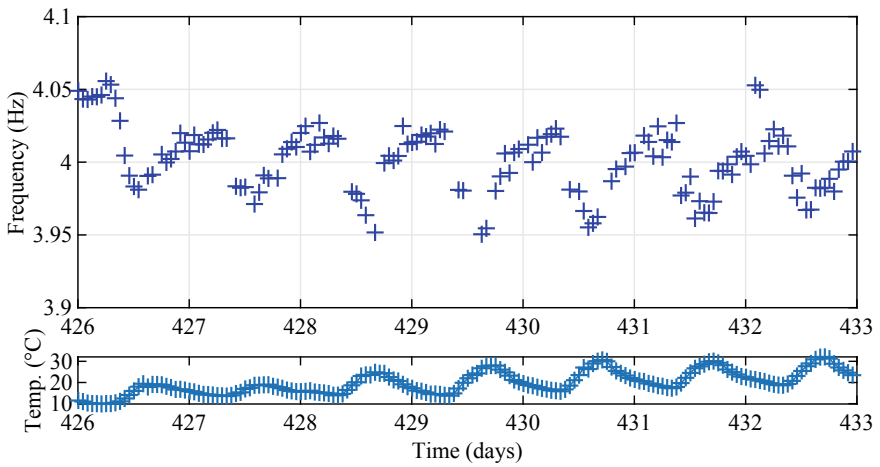
may be attributed to noise and temperature changes. Nevertheless, damage detection can be performed very simply by monitoring the maximum deflection.

3.3 Flexibility-Based Deflection Analysis

OMA Fig.9 shows the monitoring of the ten first natural frequencies from day 426 to day 432 by using the automated modal identification algorithm described in Sect. 2.2. OMA was not performed during pedestrian crossing. Additional harmonic response caused by pedestrian excitation may disturb the identification process. Ref-



(a)



(b) zoom

Fig. 9 Monitoring of the first natural frequencies from 2019/09/09 (day 426) to 2019/09/15 (day 432)

Table 1 Comparison between estimated and observed natural frequencies

	Estimated (Hz)	Observed (Hz)	Error (Hz)	Error (%)
FL1	3.1	4.0	-0.9	-22.5
FV1	6.8	8.2	-1.4	-17.0
T1	7.0	9.0	-2.0	-22.2
FL2	7.9	8.8	-0.9	-10.2
FL3	15.1	14.6	0.5	3.4
FL4	24.5	27.9	-3.4	-12.2
T2	26.2	28.9	-2.7	-9.3
FV2	26.9	23.4	3.5	14.9
FL5	45.8	37.0	8.8	23.8

erence modes were previously defined with an arbitrary set of measurements. Missing points in the figure are due to either an inopportune shutdown of the PC or a non-identification of the corresponding modes. It can be observed that the first mode FL1 is strongly correlated to the ambient temperature. This correlation is less evident for modes in higher frequency because of more estimation inaccuracies. Table 1 shows a comparison between simulated and observed natural frequencies. Although differences in natural frequencies are quite significant, it is expected that the FE model gives a reasonable estimate of the mass matrix of the real structure.

Flexibility-based deflection in damage condition Fig. 10 shows the flexibility-based deflections of the footbridge during one week from day 77 to day 83. The three first vertical modes of the structure (FV1, FV2 and FV3) were considered in the computation of the flexibility matrix. Modes in higher frequency have very low contribution. Mode shapes were first scaled by using a lumped mass matrix approximation of the FE model. Deflections of the footbridge were obtained by applying a uniform load equivalent to its own weight and were smoothed by using cubic spline interpolation. The first measurement (2018/09/25 00h00mn) was used as zero-deflection reference. Only deflections from 00h00mn to 06h00mn are represented. Figures 10 and 8 show very similar deflections in terms of shapes and magnitudes with a good separation between the normal and the damage conditions.

3.4 Comparison

Figures 8 and 10 show that very similar information related to the structure condition can be extracted from static data (via static deflections) and dynamic data (via modal flexibility-based deflections). A comparison is now presented between both approaches.

Static deflections enable to estimate true deflections relative to a reference condition without any knowledge of the structure. On the contrary, modal flexibility-based

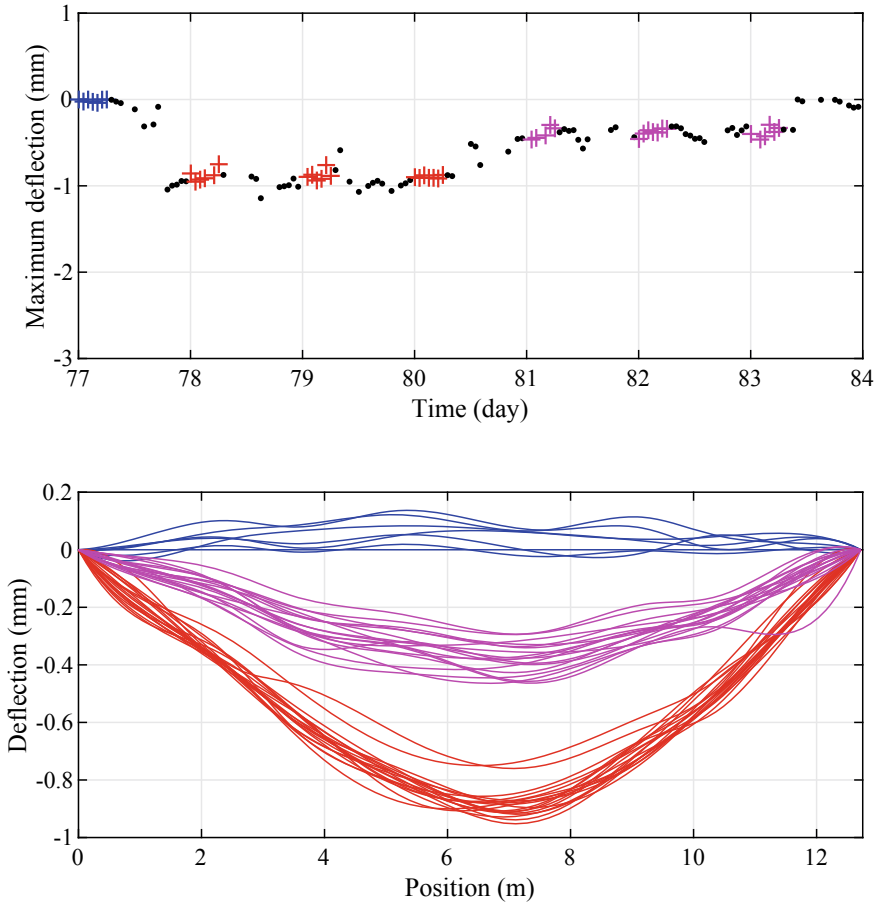


Fig. 10 Flexibility-based deflection of the footbridge in damage condition from 2018/09/25 (day 77) to 2018/10/01 (day 83). Only deflections between 00h00mn and 06h00mn are represented with 50 kg added mass in mauve, 100 kg added mass in red at midspan and no added mass (reference) in blue

deflections enables to predict deflections only if the mass distribution of the structure is known to scale the mode shapes and the load vector.

Static deflections are more sensitive to thermal effects. Actually, these correspond to the measured responses of the structure to thermal and mechanical loads whereas flexibility-based deflections correspond to the simulated responses of the structure to only mechanical load. In the first case, both the excitation and the structure are temperature dependent. In SHM applications, sensitivity to thermal effects is often not desirable because this may lead to false damage detections. On the other hand, the response of the structure under thermal effects may be desirable in some applications.

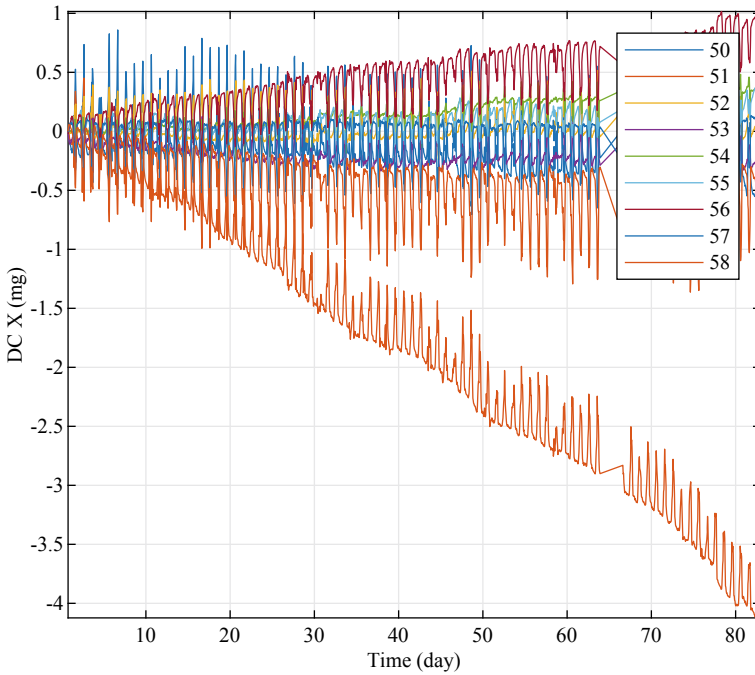


Fig. 11 Monitoring of the mean values on 80 days of recording

Estimation of static deflections is less accurate in long-term applications. MEMS accelerometers are affected by random bias instability. This very low-frequency noise that is negligible during short period of time (several days) becomes more significant when the observation time is longer (several weeks). In the case of this application, high drifts, up to ± 0.05 mg per day, were observed on few sensors leading to non-physical deflections (see Fig. 11). Stability over time is a very important parameter especially in the case of SHM applications where long periods of observation are considered.

4 Conclusions

In this paper, it was shown that static and dynamic analyses can be performed with the same instrumentation composed only of VC MEMS accelerometers. It is believed that both analyses provide additional information and could be used in a complementary way in SHM applications. Accelerometers may be used either as inclinometer sensors for the estimation of static deflections or traditional vibration sensors for the estimation of modal parameters. A strong relation exists between some of the damage identification methods using static and dynamic data. These are based on

direct or indirect estimation of deflections. This dual analyses was illustrated in the case of the monitoring of a footbridge. Calculated deflections using static data and predicted deflections using dynamic data were compared in artificially-introduced damage conditions with well agreement. Both approaches enable to identify the damage conditions reinforcing the confidence in the damage detection. In the case of this application, it was shown that flexibility-based deflections are less sensitive to thermal effects. Using accelerometers as inclinometers enables to estimate true deflections relative to a reference condition without any knowledge of the structure but still faces some issues. These sensors are strongly affected by random bias instability, which may lead to inaccurate deflection estimation in long-term applications.

References

1. Aenlle M, Brincker R (2013) Modal scaling in operational modal analysis using a finite element model. *Int J Mech Sci* 76:86–101
2. Bernagozzi G, Mukhopadhyay S, Betti R, Landi L, Diotallevi PP (2018) Output-only damage detection in buildings using proportional modal flexibility-based deflections in unknown mass scenarios. *Eng Struct* 167:549–566
3. Brincker R, Andersen P, Jacobsen NJ (2007) Automated frequency domain decomposition for operational modal analysis. In: *Proceedings of the IMAC 25, international modal analysis conference*. Orlando, FL, USA
4. Brincker R, Ventura C, Andersen P (2001) Damping estimation by frequency domain decomposition. In: *Proceedings of the IMAC 19, international modal analysis conference*. Kissimmee, FL, USA
5. Brincker R, Zhang L, Andersen P (2000) Modal identification from ambient responses using frequency domain decomposition. In: *Proceedings of the IMAC 18, international modal analysis conference*. San Antonio, USA
6. Helmi K, Taylor T, Zarafshan A, Ansari F (2015) Reference free method for real time monitoring of bridge deflections. *Eng Struct* 103:116–124
7. Koo KY, Lee JJ, Yun CB, Bownjohn JM (2009) Damage detection in beam-like structures using deflections obtained by modal flexibility matrices. In: *Proceedings of the IMAC 27, international modal analysis conference*. Orlando, FL, USA
8. Le N, Thambiratnam D, Nguyen A, Chan T (2019) A new method for locating and quantifying damage in beams from static deflection changes. *Eng Struct* 180:779–792
9. Magalhães F, Cunha A (2011) Explaining operational modal analysis with data from an arch bridge. *Mech Syst Signal Process* 25:1431–1450
10. Nagayama T, Zhang C (2017) A numerical study on bridge deflection estimation using multi-channel acceleration measurement. *J Struct Eng* 63A
11. Nguyen VH, Schommer S, Maas S, Zürbes A (2016) Static load testing with temperature compensation for structural health monitoring of bridges. *Eng Struct* 127:700–718
12. Pandey A, Biswas M (1994) Damage detection in structures using changes in flexibility. *J Sound Vib* 169(1):3–17
13. Parloo E, Verboven P, Guillaume P, Overmeire MV (2002) Sensitivity-based operational mode shape normalisation. *Mech Syst Signal Process* 16(5):757–767
14. Quinchia AG, Falco G, Falletti E, Dovis F, Ferrer C (2013) A comparison between different error modeling of mems applied to gps/ins integrated systems. *Sensors* 13:9549–9588
15. Reynders E, Houbrechts J, Guido DR (2012) Fully automated (operation) modal analysis. *Mech Syst Signal Process* 29:228–250

16. Rytter A (1993) Vibration based inspection of civil engineering structures. Ph.D. thesis, Aalborg University, Denmark
17. Saguin-Sprynski, Carmona M, Jouanet L, Delcroix O (2016) New generation of flexible risers equipped with motion capture- morphopipe system. In: Proceedings of the EWSHM 8, European workshop on structural health monitoring. Bilbao, Spain
18. Sprynski N, Lacolle B, Biard L, David D (2006) Curves and surfaces reconstruction via tangential informations. In: Proceedings of the ICSD 6, international conference on curve and surface design. Avignon, France
19. Thong Y, Woolfson M, Crowe J, Hayes-Gill B, Jones D (2004) Numerical double integration of acceleration measurements in noise. *Measurement* 36:73–92
20. Usmani A, Rotter J, Lamont S, Sanad A, Gillie M (2001) Fundamental principles of structural behaviour under thermal effects. *Fire Saf J* 36:721–744
21. Xu Y, Brownjohn J, Hester D, Koo K (2017) Long-span bridges: enhanced data fusion of gps displacement and deck accelerations. *Eng Struct* 147:639–651

Realization and Testing of Textile Reinforced Concrete Panels Sensorized with Distributed Fiber Optic Sensors



Paolo Corvaglia, Eriselda Lirza, Michael Brancato, Marco Nucci,
and Vincent Lanticq

Abstract The paper presents the realization and testing of Textile Reinforced Concrete (TRC) panels sensorized with distributed Fiber Optic Sensors (FOS). Proper procedures for fastening the sensor to the textile before its insertion as panel reinforcement, as well as for protecting the sensor during and after concrete casting were investigated. Two samples were then realized, one reinforced with traditional steel mesh, one reinforced with sensorized textile mesh. FOS and reference electrical strain gages were applied to both. The panels were tested in flexure up to failure, in order to investigate the effect of mesh substitution and of strain monitoring by means of the embedded distributed FOS, interrogated with Brillouin technique with enhanced spatial resolution. The paper discusses the samples preparation and the test results, which confirm the feasibility of the proposed set-up, though evidencing the need of few enhancements to the sensor embedding technique.

Keywords Textile reinforced concrete (TRC) · Fiber optic sensors (FOS) · Strain · Monitoring · Brillouin

1 Introduction

Textile Reinforced Concrete (TRC) has emerged in recent years as a new and valuable construction material [1]. It can be categorized as a strain-hardening cement composite, made by a continuous textile fabric incorporated into a cementitious matrix consisting of a cement binder and small-size aggregates.

TRC technology is particularly promising for realizing durable and slender concrete structures, thanks to several factors:

P. Corvaglia (✉) · E. Lirza · M. Brancato
Rina Consulting SpA, Genoa, Italy
e-mail: paolo.corvaglia@rina.org

M. Nucci
Nuova Tesi System Srl, Casale sul Sile (TV), Italy

V. Lanticq
Febus Optics, Pau, France

- High corrosion resistance of the non-metallic fibres;
- Enhanced crack control, characterized by multiple cracking upon loading;
- Fibres corrosion resistance, allowing thin-walled lightweight structures;
- Possibility to align the yarns in the direction of expected tensile stresses, enhancing effectiveness in load-carrying capacity;
- Textile formability, allowing complex freeform geometries.

On the other hand, monitoring of structural behavior can detect anomalies in due time, thus enhancing safety level and enabling maintenance and repair actions to be implemented more efficiently, directly impacting on the reduction of operating costs.

In the present work the TRC technology is implemented and further enhanced by studying textile sensorization, so potentially providing structural self-monitoring capability to the components, enabling its in-service integrity monitoring from the interior.

Fiber Optic Sensors (FOS), serving as both sensor and data conduit, are particularly interesting for the long-term health monitoring of civil structures [2]. Fiber Optic sensing can be implemented with two types of approach in terms of spatial distribution of measures, namely discrete and distributed measurement. While discrete measurement approach is usually preferable in terms of accuracy, resolution and dynamic behavior, distributed measurement is the cheapest and winning strategy when one does not know in advance where critical conditions can take place. Nevertheless, in distributed sensing the main challenge is to achieve an acceptable spatial resolution on sufficiently long distances [3]. The solution investigated in the present work is a truly-distributed sensing based on Brillouin scattering, which allow monitoring on several kilometers length, and on the application of a post-processing algorithm for the enhancement of spatial resolution.

Proper procedures for fastening the sensor to the textile before its insertion as panel reinforcement, as well as for protecting the sensor during and after concrete casting were preliminarily investigated. Two samples were then realized, one reinforced with traditional steel mesh, one reinforced with sensorized textile mesh. FOS and reference electrical strain gages were applied to both samples.

The panels were tested in flexure up to failure, investigating the effect of mesh substitution and of strain monitoring by means of the embedded distributed FOS.

The obtained results confirm the feasibility of the proposed set-up, though evidencing the need of few enhancements to the sensor embedding technique.

2 Textile, Sensor and Integration Procedure Definition

The first stage of the work led to the definition of the most suitable textile material and FOS and of a suitable procedure for integrating these two components.

Based on TRC literature analysis, specific requirements were set for the choice of the fiber material (in terms of alkali resistance) and the textile structure (in terms of tensile strength, fabric structure, mesh stability and size, yarn straightness, degree

of orthotropy, finishing). A set of suitable commercial textile products were then selected and compared on the basis of the trade-off they can offer on such set of requirements (Table 1). This process eventually led to select the AR 640 TEXTILE produced by Kast, made of AR-glass fibers, sewed with a leno weave structure and coated with SBR finishing. The textile presented a tensile strength of 58×65 (kN/m) \times (kN/m) and a mesh size of 3.45×3.45 cm \times cm (the two figures refer to longitudinal and transverse directions).

With reference to the sensor cables, the choice was made on the basis of their robustness (to survive concrete casting) and capability to provide adequate shear strain transfer from concrete. On this basis, distributed sensors produced by Solifos AG (hereinafter referred to as SOL sensors) and by Smartec SA (hereinafter referred to as SMA sensor) were selected, based on single-mode fiber and allowing two different temperature compensation strategies. More in detail, the SOL system consists of two different cables, a strain-sensitive one (trade name BRUsens DSS 3.2 mm V9 grip) and a strain insensitive one (trade name BRUsens DTS STL PA),

Table 1 Compared textile products

	Kast	FTS	Alpe Adria textil	Alpe Adria textil	Extreme materials	Kerakoll
Trade name	-AR 640 -AR 720	370 GM2	Arter [®] GTS G 50-50	Multitexco A-type and B-type geogrid	N.A.	ARV 100
Fabric structure	Leno weave	Plain wave (plus steel fibers)	Weft insertion warp-knitted	Weft insertion warp-knitted	Leno weave	Leno weave
Fibre material	AR-glass	Basalt	E-glass	E-Glass	PP or glass	AR-glass plus aramid
Finishing	SBR	Thermo-fixing + coating	EVA/AC coating	EVA/AC coating	To be defined	Alkali-resistant coating
Aerial weight (g/m ²)	-340 -450	370	194	300	300 for PP	250
Tensile strength (kN/m) \times (kN/m)	58*65 94*89	N.A.	50*50	N.A.	N.A.	49*60
Mesh size (cm \times cm)	3.45*3.45 3.26*3.47	1*1	3*3	3*3	1*1	1.5*1.8
Notes	High stability	Steel fibers not suitable	Low crimp degree	Low crimp degree	No basalt or AR-glass options	Low stability



Fig. 1 Tested solutions for sensor-textile integration: gluing (left), stitching (center), weaving (right)

while the SMA systems is a single multi-fiber cable containing both strain insensitive and strain sensitive fibers (trade name SMARTProfile). The SOL sensors have round-shaped cross-section with radius of 3.2 and 3.8 mm, respectively, while the SMA sensor cross-section is rectangular, with dimensions 8×4 mm. In terms of external surface, all the sensors present a polymeric sheath, which is roughened in the case of the SOL strain sensor in order to guarantee a more effective strain transfer.

Different solutions (see Fig. 1) for integrating the sensor inside the textile were evaluated and tested, including gluing, stitching and weaving (i.e. embedding during the textile production). Stitching was successfully implemented but eventually discarded because, in order to properly house the cable onto the textile warp, it was necessary to insert a ribbon between the sensor and the textile, which could, in principle, induce some bonding defects to the concrete-textile-sensor chain. On the other hand, proper weaving resulted unfeasible due to thickness and stiffness of the selected sensor cables. Continuous gluing by means of hot melt EVA was tested to quantify the shear adhesion strength between the sensors and a 15 cm portion of a single textile warp. An average adhesion strength of 2.1 and 3.1 kg/cm was found, respectively with SMA and strain-sensitive SOL sensor, which eventually led to select such solution for integrating the sensor.

3 Samples Design and Preparation

Two middle-scale sensorized concrete samples were designed and produced, both in panel form with overall dimensions $250 \times 90 \times 10$ cm and equipped with lateral curbs made of steel bars: Sample A (reinforced with traditional welded steel mesh), used as reference, and Sensor B (reinforced with textile mesh). The reinforcing meshes

were placed on the lower (tensile) edge. The two panels were designed in order to have the same flexural stiffness, applying the semi-competitive method to the Limit States in compliance with the current Standards and in agreement with the current Italian guidelines [4]. Both the samples were equipped with FOS and different types of reference electrical strain gages, as shown in Fig. 2.

Sensors were glued to the textile and their egress points from concrete were protected by including them in corrugated plastic ducts (Fig. 3). Textile reinforcement straightness during casting was guaranteed by clamping it on a perimetral steel rebar, serving also to fasten four steel hooks for panel demolding and handling. It's worth mentioning that sample B showed a crack already before testing, likely due to an impact during handling.

After sensors installation and concrete casting, a bracket with standard optical connectors was applied to both ends of each cable, followed by connection and cable integrity testing by means of light source and power meter. Testing showed that all the FOS sensors survived both the processes of sensor fastening to the net and of concrete panel production, with acceptable optical losses.

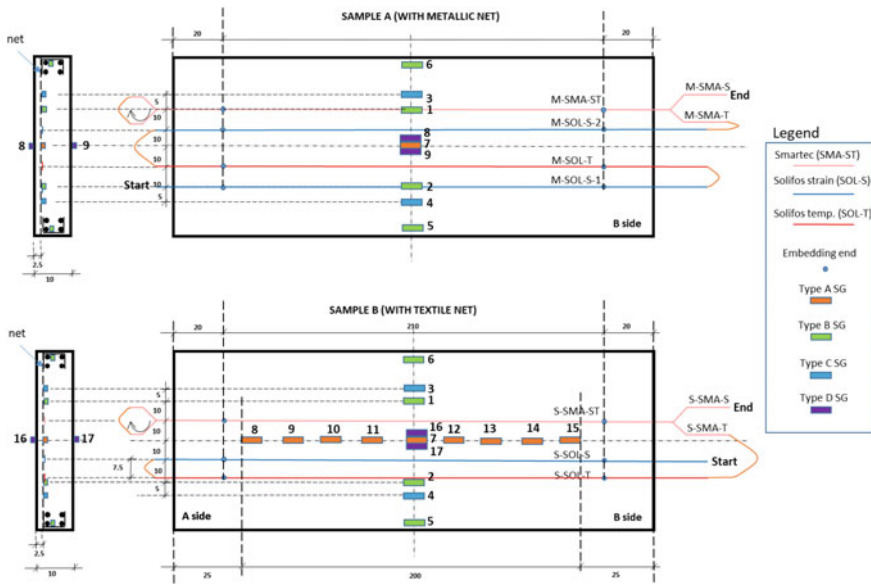


Fig. 2 Overview of the FOS and electrical strain gages and of their relative positions (drawing not to scale)



Fig. 3 Some steps of samples preparation

4 Mechanical Testing

4.1 Test Set-up

The loading scheme is that of a simply supported beam loaded to flexure in one point, implemented as shown in Fig. 4.

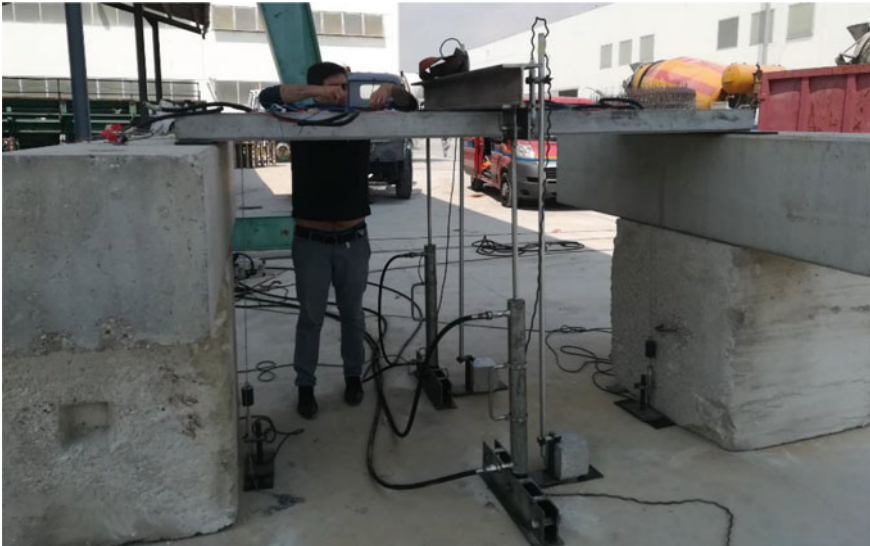


Fig. 4 Experimental set-up

Neoprene pads were interposed between the panel and the supporting structures, in order to allow free rotation without stress concentration. Load was applied quasi-statically by means of two hydraulic jacks, anchored to ground and pulling down an IPE steel beam, able to evenly distribute load along the panel width. The jacks were controlled in parallel by a hydraulic pump.

The goal of the mechanical tests was two-fold, namely (a) Check reliability of the strain-measuring system by means of FOS and (b) Assess the structural performances of the textile reinforcement.

The used Data Acquisition Unit (FEBUS G1-R) implements, for the determination of the Brillouin Frequency shift, the so called “parabolic fitting” algorithm. Such algorithm is generally the fastest and most accurate way to determine the Brillouin shift but it can lead to poor results in zones of very high strain gradient, due to the lack of spatial resolution (1 m). Therefore, Febus provides an alternative algorithm for it, namely the “Spatial Resolution Enhancement” one, which allows obtaining an enhanced spatial resolution value of 25 cm.

4.2 Results

4.2.1 Assessment of the Measuring Behavior

General considerations

Figures 5 and 6 report the strain curves for Samples A and B, respectively, measured by the FOS, at increasing load. It’s worth recalling that the sensors are all connected in a row along the same channel. Though all the sensors were able to read data up to

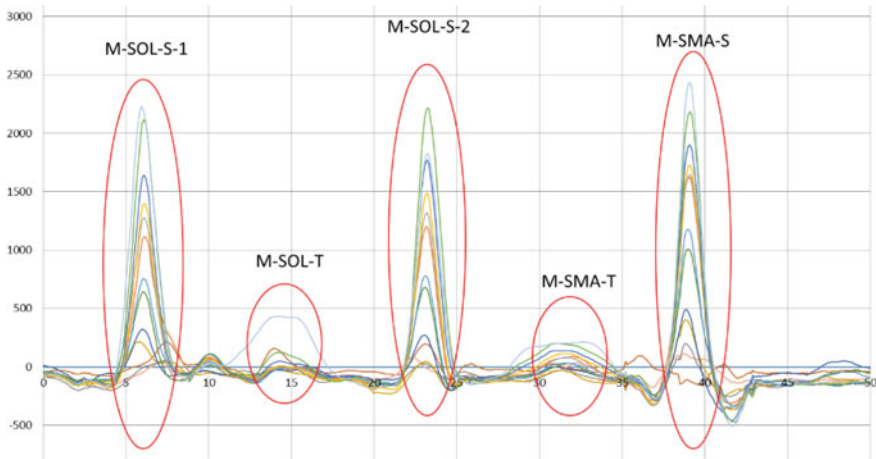


Fig. 5 Data obtained along the single FOS channel—Sample A

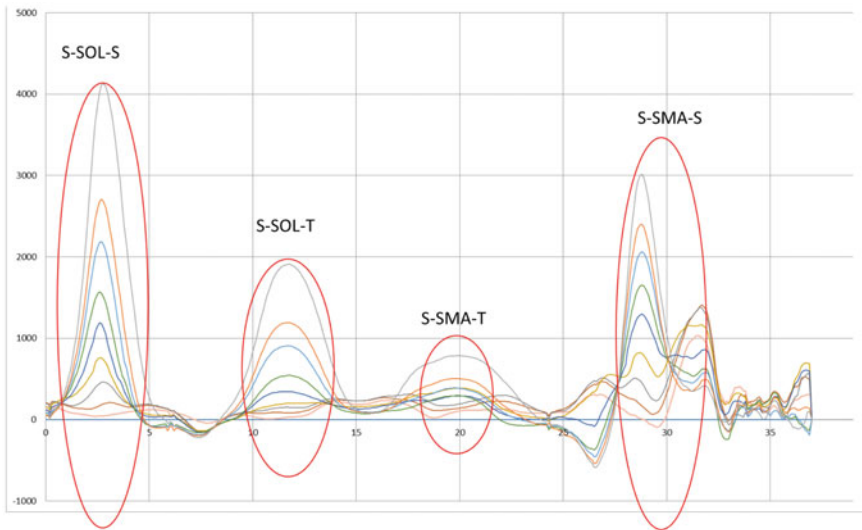


Fig. 6 Data obtained along the single FOS channel—Sample B

samples failure, the SMA sensors presented more irregularity at higher loads, likely due to sliding of the cable inside concrete due to its smooth surface.

Moreover, the strain-insensitive sensors, at higher loads, show strain values which are too high for being due to only thermal effects. This is likely due to fusion splicing, which provokes some small tension on the fibre and which, on the relatively small length of the tested sample, does not vanish. Hence, thermal compensation is unreliable in such situation; for this reason, taking also into account that temperature is nearly constant in a short time test and uniform along the panel, no thermal compensation was carried out in the present data analysis. It's worth stressing, however, that, in real applications, where much higher lengths are monitored, the possible small tension due to splicing should vanish along the length, so that thermal compensation can be correctly implemented.

Strain profile from FOS at increasing loads

Data from sensors M-SOL-S1 (for Sample A) and S-SOL-S (for Sample B) are reported in Figs. 7 and 8, respectively. It can be noted that the curves at low load are quite irregular, showing also unphysical negative values, which probably means that the sensor system is still settling, with the sensors recovering some initial compression state. This finding leads to the suggestion to apply a slight pre-tension to the FOS. On the other hand, at the highest load values the strain pattern is again irregular, likely due to cracking.

Strain comparison between FOS and electrical strain gages

M-SOL-S-1 and S-SOL-S are considered, respectively for Sample A and Sample B. As these sensors were bonded, respectively, to steel bar and to longitudinal textile thread, the corresponding strain gages considered for benchmark are the E2 ones,

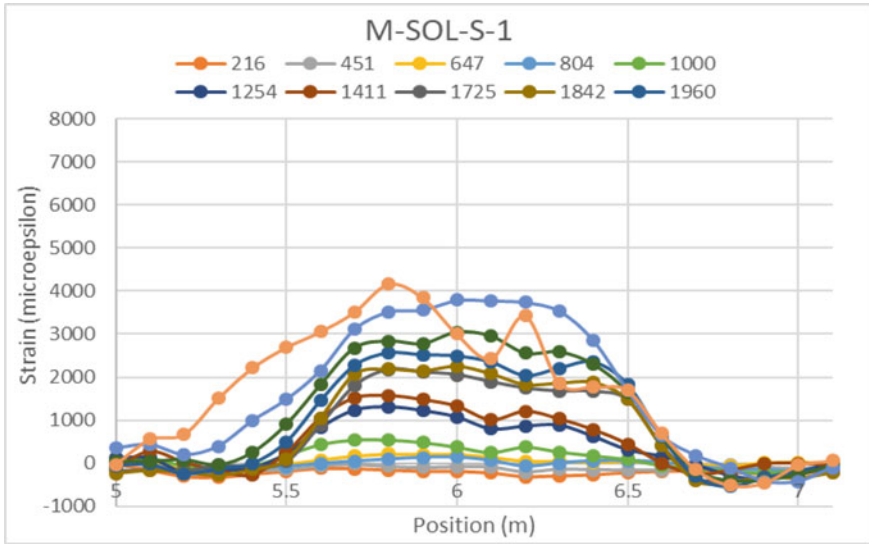


Fig. 7 Strain profile from M-SOL-S-1 at different load values (in kg)—Sample A

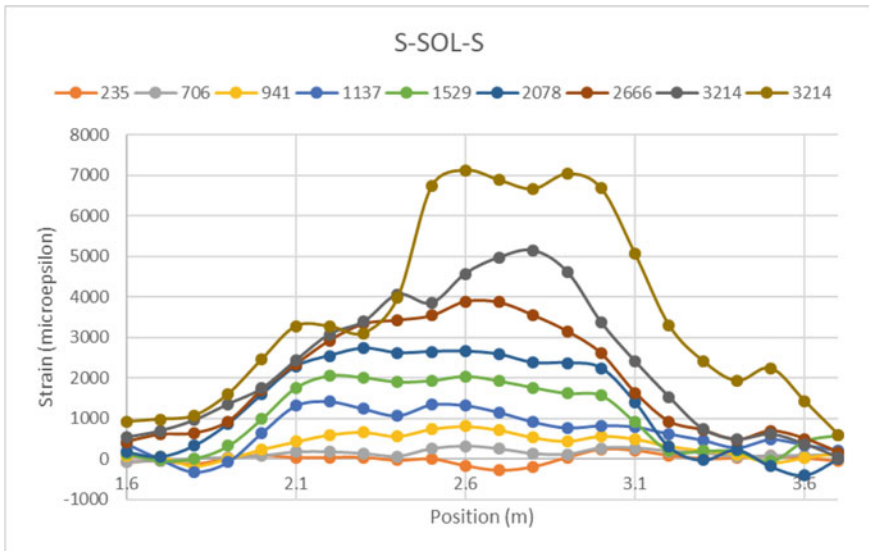


Fig. 8 Strain profile from S-SOL-S at different load values (in kg)—Sample B

Table 2 Strain comparison between FOS and electrical Strain Gages (SG)

Sample	Load (kg)	Strain ($\mu\text{m/m}$)		
		FOS	SG	FOS/SG ratio (%)
A	647	215	1404	15
	1000	545	1828	30
	1960	2556	4070	63
B	706	317	411	77
	941	810	1986	41
	1529	2059	1887	109
	2078	2735	2055	133
	2666	3870	1982	195

which are bonded onto the same elements. Results are shown in Table 2, where strain values at low load levels are not reported due to their unreliability, as explained in previous section.

The above results confirm that FOS and strain gages provide strain values which are comparable, as order of magnitude. Nevertheless, a not negligible results scattering is observable. This finding must be interpreted taking into account, first of all, that the two sensors have very different gage length: about 1 cm for the strain gages, 25 cm for the FOS (spatial resolution). This means that the two values are not fully comparable, in principle. Moreover, at high loads concrete is cracked, then tension (hence strain) is released in the cracked concrete, while it is increased in the reinforcement, so assuming a very localized behavior. As a consequence, local values measured by strain gages are already scattered on their own. In this framework, it was hard to expect much closer results than observed.

4.3 Assessment of the Structural Behavior

Figure 9 reports the load-deflection curves obtained in the flexure tests, which allows us taking some conclusions in terms of global stiffness, ductility and ultimate load of the two systems.

In terms of stiffness, two different regions can be identified:

- Region I: Different initial stiffness, likely due to the pre-existing crack in Sample B, which makes it less stiff than Sample A;
- Region II: Same stiffness, according to design, where both panels are in post-cracking stage.

After Region II the stiffness is still comparable but not perfectly superimposable, due to diffused cracking.

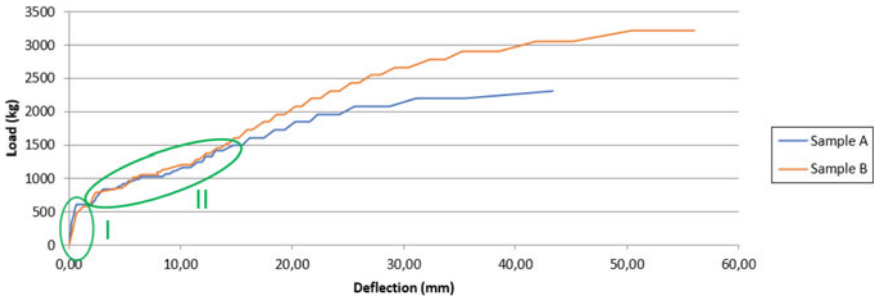


Fig. 9 Load-deflection curves

Table 3 Ultimate loads of the tested samples

	Sample A (kg)	Sample B (kg)
Theoretical value	2200	2780
Experimental value	2300	3200

In terms of ductility, Sample B shows a significant enhancement (ultimate deflection 56 mm vs. 43 mm of the Sample A).

Table 3 reports the ultimate load of the two specimens, in terms of design and experimental values.

It can be observed that Sample B attains a significantly higher (39% experimental, 25% theoretical) ultimate load with respect to Sample A, when the panels are designed for the same stiffness. In terms of difference between theoretical and experimental values, a slight increase is obtained for both samples, as expectable taking into account that design models are precautionary.

Finally, cracks appear more diffused in Sample B (Fig. 10), though it is hard to discriminate whether this is due to the different reinforcing materials (glass instead of steel) or to the different spatial arrangement of the reinforcing nets (more closely spaced in textile).

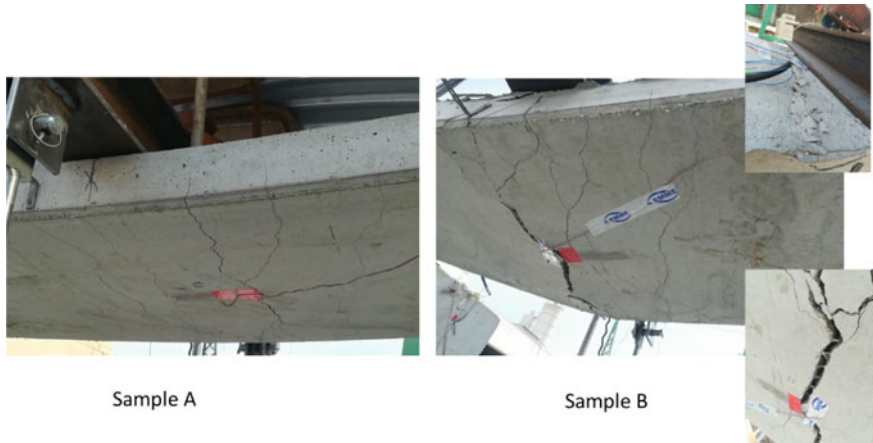


Fig. 10 Crack patterns of the tested samples (details on the right are referred to top and bottom of Sample B)

5 Conclusions and Acknowledgements

A study on design, implementation and testing of TRC panels sensorized with two different types of distributed FOS is presented in this paper. The potential of such a solution relies in the easiness of realizing a structural health monitoring system on site, namely by simply connecting each component to the adjacent one by means of fiber optic patch cords and by plugging the last one to the data acquisition unit. Moreover, this solution can enable in-service integrity monitoring from the interior of the component.

Two samples, one of which reinforced with traditional steel mesh, used as reference, were realized and tested in flexure, investigating the FOS performances in strain monitoring and the structural performances of TRC.

The main conclusions drawn from the research are reported in the following.

Regarding the FOS measuring capability:

- All the FOS sensors survived both sensor fastening to the net and concrete panel production;
- The sensors were able to read data up to advanced cracking stage;
- The SMA tested sensors evidenced some sliding at higher loads, unlike SOL strain sensors;
- Fusion splicing introduces a slight tension on the optical fibre, which makes unreliable thermal compensation at higher load level in short-length tests;
- It is important to apply a slight pre-tension to the FOS at installation stage;
- At high load levels FOS and strain gages provided comparable strain values, in the limits of the inherent differences between the two sensor types.

Regarding the load-carrying capability:

- The two samples exhibited the same stiffness in the post-cracked phase, according to the design;
- The TRC sample showed a more diffused crack pattern and enhanced ductility and ultimate load with respect to the steel-reinforced panel designed for the same stiffness.

The work was carried out in the framework of the Research Project EnDur-Crete, (New Environmental friendly and Durable conCrete, integrating industrial by-products and hybrid systems, for civil, industrial and offshore applications) funded by the EU's H2020 Framework Programme, under G.A. n. 760639. The Project is still ongoing and currently in the field demonstration phase.

References

1. Peled A, Bentur A, Mobasher B (2017) Textile reinforced concrete. CRC Press
2. Glišić B, Inaudi D (2007) Fibre optic methods for structural health monitoring. Wiley
3. Samiec D (2012) Distributed fibre-optic temperature and strain measurement with extremely high spatial resolution. *Photonik Int* 1:10–13
4. EN 1992-1-1 (2004) Eurocode 2: design of concrete structures

Increasing the Resilience of European Transport Infrastructure



Kostas Bouklas, Angelos Amditis, Rafael Weilharter, Visvanathan Ramesh, Miguel Ángel Trujillo Soto, Guillermo Heredia, Luca Belsito, Stephanos Camarinopoulos, and Friedrich Fraundorfer

Abstract Extreme weather conditions, climate change, damages to the infrastructure (caused by natural and man-made hazards) and traffic impediments negatively impact the reliability of mobility solutions. Risk analysis, adaptation measures and strategies that enable minimizing the impact of both natural and man-made extreme events on seamless transport operation, protect the users of the transport network in case of extreme conditions, as well as provide optimal information to operators and users of the transport infrastructure, need to be developed. Road transport is vulnerable to extreme weather events, while bridges and tunnels are among the most critical land transport structures. A large number of bridges and tunnels have been in operation for more than 50 years and there are widespread signs of deterioration. They need inspection, vulnerability assessment and, when needed, appropriate interventions. Inspection, though, in inaccessible areas, or structures with high volumes of traffic, is expensive, time-consuming, and potentially dangerous. At the same time, structural/vulnerability assessment is also a lengthy process which is especially painful after extreme events. The overall goal of RESIST (RESilient transport InfraStructure to extreme events) a RIA H2020 project funded by the EU commission with grant number 769,066 is to increase the resilience of seamless transport

K. Bouklas (✉) · A. Amditis
Institute of Communication and Computer Systems, Athens, Greece
e-mail: kostas.bouklas@iccs.gr

R. Weilharter · F. Fraundorfer
Technische Universitaet Graz, Graz, Austria

V. Ramesh
Johann Wolfgang Goetheuniversitatfrankfurt Am Main, Frankfurt, Germany

M. Á. T. Soto
Fundacion Andaluza Para El Desarrollo Aeroespacial, Seville, Spain

G. Heredia
Universidad de Sevilla, Seville, Spain

L. Belsito
Consiglio Nazionale Delle Ricerche, Bologna, Italy

S. Camarinopoulos
Risa Sicherheitsanalysen GMBH, Berlin, Germany

operation to natural and man-made extreme events, protect the users of the European transport infrastructure and provide optimal information to the operators and users of the transport infrastructure. In the context of RESIST, robotics for visual and contact inspection of structures, structural vulnerability assessment, infrastructure risk management as well as mobility continuity applications considering stress levels of the drivers are being developed towards a high level of resilience of the transport infrastructure.

Keywords Extreme events · Risk management · Resilience · Prevention · Response · Mitigation · Seamless mobility · Bridges · Tunnels

1 Introduction

1.1 *The RESIST EC Project*

The overall goal of RESIST is to increase the resilience of seamless transport operation to natural and man-made extreme events, protect the users of the European transport infrastructure and provide optimal information to the operators and users of the transport infrastructure. The project will address extreme events on critical structures, implemented in the case of bridges and tunnels attacked by all types of extreme physical, natural and man-made incidents, and cyber-attacks. The RESIST technology will be deployed and validated at 2 pilots in real conditions and infrastructures.

1.2 *Challenge and Requirements*

Road transport is the most vulnerable mode to extreme weather events while bridges and tunnels are among the most critical land transport structures. A large number of bridges and tunnels have been in operation for more than half a century and there are widespread signs of deterioration. They need inspection, vulnerability assessment and, when needed, appropriate interventions. Inspection, though, in inaccessible bridge/tunnel areas, or structures with high volumes of traffic, is expensive, time consuming, potentially dangerous and frequently traffic interrupting, while structural/vulnerability assessment is also a lengthy process which is especially painful after extreme events.

The private and public expenditure directed every year at inspecting and assessing the vulnerability of transport structures to extreme events are highly inadequate.

Aerial robotics can revolutionize inspection and physical vulnerability assessment for critical structures in all transport modes because they can dramatically reduce the required cost and time, increase the safety of workers and limit disruptions avoiding bottlenecks. Their impact can be even more dramatic after a damaging incidence

when the decrease in required time to assess damage and structural safety can save lives.

2 Robotic Actors

The RESIST robotic actors will be aerial robots carrying the sensors needed for the inspection of the bridges and tunnels, which will be presented in Sect. 3. There will be two types of aerial robotic actors in RESIST, the visual inspection robot and the contact inspection robot.

2.1 Visual Inspection Robots

The main purpose of the visual inspection robot (see Fig. 1) is to autonomously take pictures of the bridge and tunnel in order to find and classify visual defects. The main capabilities this robot will have are:

- Autonomous navigation in GNSS denied environments where the satellite signal is poor or inexistent. Avoiding the use of a total station is possible for at least the bridge use case, minimizing in this way the cost of the system for a possible future exploitation.
- Localization of the camera during the whole flight with respect to a global common coordinate system defined by a total station.



Fig. 1 Visual inspection aerial robot

- Robust and precise localization fusing the pictures localization with photogrammetry software. The software processing commands have been automated.
- Integration of the camera system developed by TUG.

This visual inspection robot has been the result of the hardware and electric integration of commercial components, such as the LIDAR, computers, and professional stabilization system. Furthermore, additional designs to cover the electronics and to protect the propellers during the flight are in process to be tested.

2.2 *Contact Inspection Robots*

The contact inspection robots are responsible for all the measurements that need physical contact of the sensor with the surface of the bridge or tunnel, including the ultrasonic sensors and the radiometric sensor. The contact inspection robots will also be in charge of installing the permanent vibration sensor modules on the surface of the bridges and tunnels. After studying the very different working and environmental conditions when flying inside a tunnel and around a bridge, two designs have been decided, each one adapted to the special conditions of tunnels and bridges.

A bridge contact inspection aerial robot has been developed. This aerial robot is coming from the FADA-CATEC technological base of aerial robots with contact capabilities. This new robot (see Fig. 2) changes vastly the previous version with the objective to increase its Technology Readiness Level (TRL). The main changes are:

- Weight and size reduction of a 40%.



Fig. 2 Bridge contact inspection aerial robot

- Change in the flying configuration to a standard widely used one (Octo-quad).
- The use of commercial autopilot with more robustness and reliability.
- Multiple changes on the contact design allows robust contact with relative control of the orientation of the robot for even curved surfaces, much easier operation, etc.

The main objective of this aerial robot is to be able to push against the bridge the sensors that need to be in contact as, for example, the ultrasonic sensors, which need to be held against the concrete with a certain force, and the vibration module, that has to be hold pushing while the glue curates.

The tunnel contact inspection robot has been developed considering that it has to be smaller and more compact to be able to operate inside the confined space of a tunnel. It adapts the concept of operation of the bridge contact inspection robot (Fig. 2) with the experience of the tests performed during the initial steps of the project with a first prototype developed in RESIST, the FAIR aerial robot [3] (see Fig. 3-left), and the design of the ARBI robot [4], developed in the AEROBI project (see Fig. 3-right). In this way, the design exploits the benefits of establishing a full contact condition with the bridge similar to how ARBI did, using an articulated docking system which also acts as a landing gear mounted on the top of the aerial platform and helps to establish the contact between the tunnel and the aerial robot. It is also able to inspect horizontal, vertical and tilted surfaces using a mechanism inspired in the bridge constant inspection robot. The aerial robot will also have a Cartesian manipulator embedded in the docking device which mounts the radiometric sensor and also allows repositioning the sensor and taking measurements of several points of the workspace.

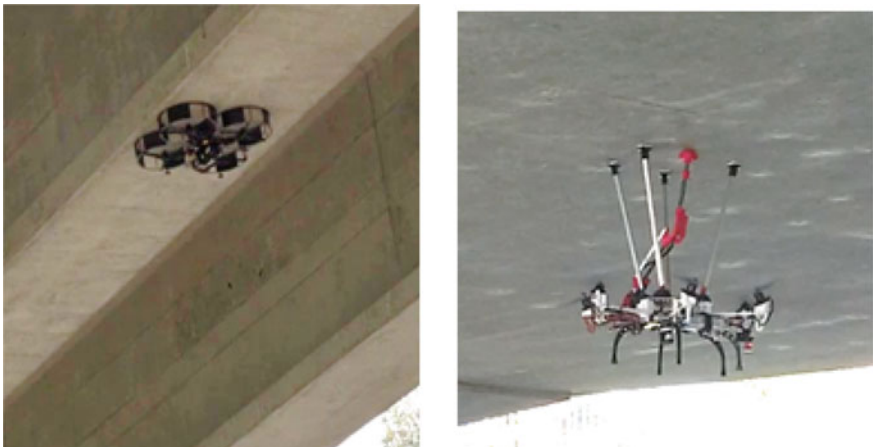


Fig. 3 (left) ARBI (aerial robot for bridge inspection) developed in the AEROBI project; (right) FAIR (fully-actuated inspection robot) first proof of concept for RESIST con-tact inspection

2.3 Ground Control Station

The development of the Ground Control Station (GCS) is reaching its end and after that, the final integration with the modular aerial robotics system will be performed

The GCS has been developed considering the following characteristics:

- It can be executed in multiple devices as a standard laptop
- As it can be installed in a laptop, its transportation is really easy.
- It can be deployed in very short time due to its programming and short use of computer requirements.
- The user interface is adapted to the different roles of people operating it providing a complex interface for an engineering role, a friendly interface for a not experienced user focused on the sensors, and a simple but powerful interface for the pilot.

The GCS is providing the exact and right information to each type of operator. So, two different and complementary ground control stations have been developed, one for the pilot, and the other for the sensors and mission management. At the same time, this last GCS could be divided in two in case that the mission and the sensor is not managed by the same operator.

For the pilot GCS, we developed an interface to allow the pilot flying close to the structures even without looking directly to the aerial robot. For that reason, essential information as, the distances to obstacles, the drone control references, a frontal camera image and the photographic camera, plus some other important information as the battery and signal are detailed. As it is shown in Fig. 4, the information is presented in a visual form so it is perceived in a fast way, being this critical for this type of operation.

Finally, the mission interface (see Fig. 5), allow the operator to generate inspection missions in a friendly way. At the same time, it provides numerous detailed information. This information is not needed to be easy and fast to read, as the role

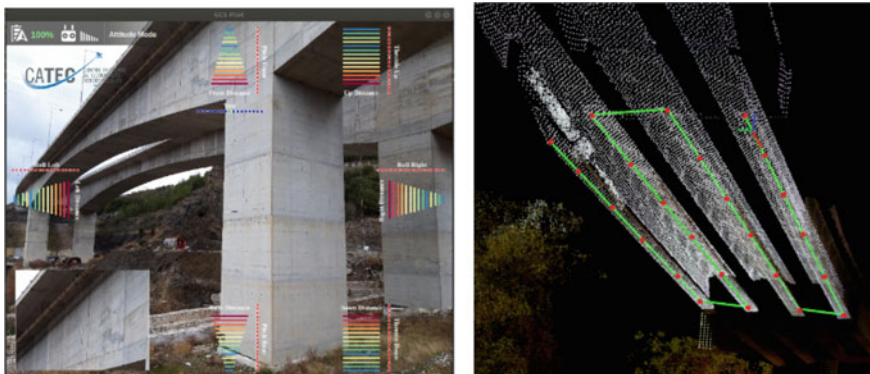


Fig. 4 Pilot GCS on the left figure. Detail of the mission GCS at the right

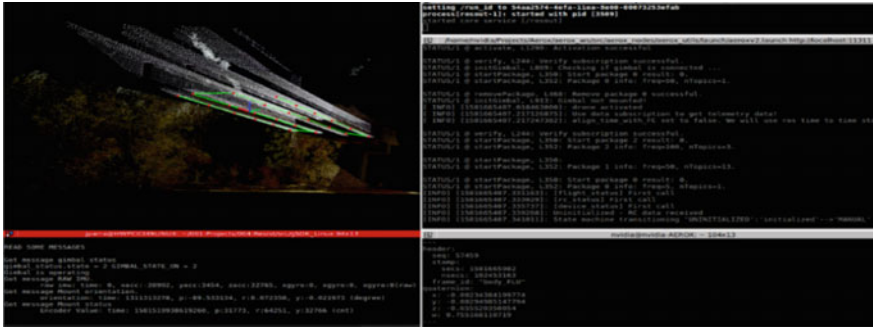


Fig. 5 Mission interface of the ground control station

of this user is to have as much information as possible of the status of the complete system.

3 Contact and Visual Inspection Sensors

3.1 Vision Inspection

As a means for visual inspection, the RESIST system deploys a high-resolution stereo camera sensor. The sensor is a custom fit for the RESIST requirements utilizing two 12 Megapixel sensors with an 11 cm baseline and lenses with a focal length of 8–12 mm. This setup allows for an estimated depth uncertainty as low as 0.5 cm at an expected working distance of 2 m.

Captured images are stored directly on the drone mounted sensor but are transferred to a separate laptop in the field for the next step. An external Graphics Processing Unit (GPU) enables the use of Convolutional Neural Network (CNN) techniques for depth estimation which could not directly be run on the drone. The reason for the utilization of CNNs is two-fold: (1) latest CNN algorithms show exceptional accuracy on well-known benchmarks [1, 2]. (2) Through massive parallel processing on the GPU a depth image can be calculated within a second, whereas classical methods might take up to several minutes per image [3, 4]. The latter is especially valuable for the RESIST application where time can be of utmost importance.

The software pipeline, which is running on the laptop, takes as input the stereo image pairs and their respective camera positions and outputs a detailed depth map for each pair as well as an overview point cloud of the observed structure. For the detailed inspection an adapted version of the Hierarchical Stereo Matching CNN (HSM) [5] is used, while for the overview point cloud generation a newly developed multi-view stereo (MVS) CNN is deployed. The MVS network exploits multiple images for better consistency and a more appealing 3d model with a wider depth range through

the use of a larger, variable baseline. Furthermore, a 3d model generated by a MVS CNN tends to be much better in terms of completeness [6].

In tests, the newly developed software is able to calculate a depth image from a high-resolution image within 0.5 s while also keeping the GPU memory requirements quite low (i.e. < 5 GB). It is one of the first networks that is able to process 12 Megapixel images in such an efficient way.

3.2 Cognitive Computer Vision System

Our cognitive vision system design builds upon model-based and data-driven strategies to address both small-data and big-data scenarios. It focuses on transparency, explainability of design, ability to work with small amounts of data based on models, ability to leverage generative models in simulation, and exploit modern deep learning (data-driven) techniques for classification.

Our architecture is inspired by human-like cognition, which uses parallel hypotheses-generation threads for defect detection in the field:

- **Topology based analysis (TPE):** the essence of TPE is the design of a multi-scale nonlinear filter that checks whether anomalies with respect to appearance and geometry exist. For instance, in the case of cracks, this is a connected fractal like geometry with pit-like structure on the texture level in only few directions, and flat intensity in the remaining homogenous areas.
- **Geometric (3D) data analysis on point clouds:** we leverage transformed depth information given by the stereo camera. In defect-free areas, we cannot assume a uniformly distributed, but locally planar, depth structure of the surface. Therefore, we denoise the depth structure locally through a robust transformation. By assuming cracks and sharp discontinuities are outliers, the transformed output should separate cracks from background.
- **Data driven deep learning methods:** training of data driven feature extraction with deep neural networks is used as a complementary approach to above expert designed models. The aim is to capture difficult to model defect categories with extensive expected variability in appearance. Specifically employed training methods build upon prior state-of-the-art work on meta-learning of neural networks for defect classification [12] and leverage auxiliary virtual training data, generated with our custom generative model to render images with defects using computer graphics simulation tools. The former is additionally extended with means to assess neural network prediction uncertainty for detection of unknown data. For the latter, we make use of the automatically obtainable ground-truth information from simulation to learn a multi-modal neural network, which we have coined Multi-Unet. As an extension to the popular neural Unet architecture, this allows for simultaneous learning of semantic crack segmentation, with joint prediction of depth and surface normal.

This three-fold parallel processing allows to capture diverse application contexts. The parallel hypotheses with subsequent voting allow for robustness and false alarm reduction, while maintaining high sensitivity/detection rates. The hypotheses are finally fused to detect defects and mensuration is performed on these defects. Results can be finetuned further by controlling high-level module parameters. By using system uncertainty assumptions determined by the RESIST hardware setting, the mensuration pipeline can additionally estimate defect property uncertainties for robustness improvements.

The computer vision analysis runs together with the vision inspection analysis software on the same hardware. GPU-supported hardware is used to reduce computational time of our analysis. To address environment of low transmission capacity, annotated images which are generated during our analysis are compressed before sending to the RESIST platform.

3.3 Contact Inspection

The deployment of UAV platforms equipped with contact sensors for monitoring operation could provide the technological basis for a revolutionary way to implement inspection tasks of difficult-to-access structures' areas. In order to perform depth and width measurements of emerging cracks in concrete and steel structures, two independent ultrasonic systems have been designed to be easily integrated on the Resist platform and performance measurements with high resolution and accuracy. By exploiting a custom high voltage electronic readout, the crack depth measurement is realized by using simultaneously an ultrasound emitter and a detector placed in contact with the concrete or steel structure under examination at a known distance d from a crack and by measuring the ultrasound time of flight between the ultrasound generation and detection, Fig. 6 (left).

In fact, once generated by the emitter, the ultrasound waves propagate through the material, reach deepest point of the crack and they are scattered by its tip toward the surface before being detected from the receiver. The crack depth is then derived by the propagation time once the velocity of sound is measured as well [1]. By using a time to digital converter with high resolution and accuracy in the custom electronic

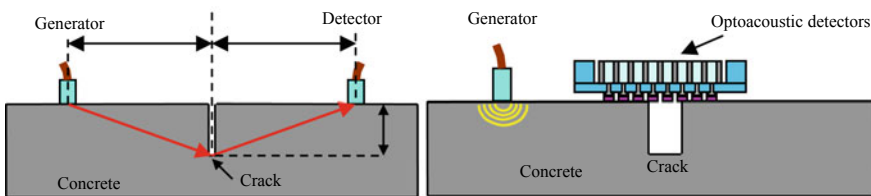


Fig. 6 Crack depth (left) and width (right) measurements

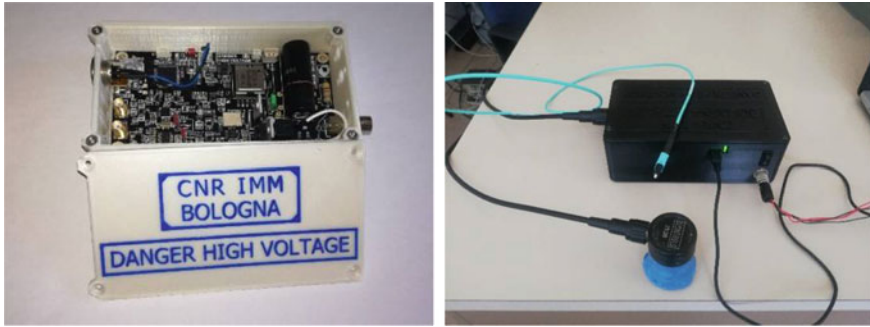


Fig. 7 Pulsar/receiver unit for the crack depth measurements (left) and crack width measurement

readout developed for the measurement, the Time of Flight (ToF), and then the crack depth, can be measured with really high precision. The crack width measurement (Fig. 6 right) is instead performed by using an opto-acoustic MOMS (Micro Opto Mechanical Systems) sensor array mounted on a fan-out connector and put in contact with the surface of the concrete or steel specimen across the surface opening of the crack, with the sensor array oriented transversally with respect to it [2]. In this way, some of the opto-acoustic sensor pixels are in contact with concrete or steel (those outside the crack surface opening) and some other are not in contact with it (those inside the crack surface opening). The crack width measurements technique is based on the difference between the ultrasonic signals detected by the sensor pixels in these two situations. In order to generate the signal, a traditional 54 kHz piezoelectric transducer is utilized on one side of the crack and the measurement resolution is obviously dependent on the pixel pitch space.

The prototype of the two measurement systems to be integrated on the Resist platform are finally shown in Fig. 7.

The pulser/receiver unit used in the crack depth measurement has overall weight of 90 g and size of $12 \times 5 \times 5 \text{ cm}^3$, also including the package. It assures frequency and amplitude tunability of the emitter pulse voltage, allowing driving transducers with different resonance frequencies and powerful. The width measurement system, which is constituted by several components (it requires the use of a tunable laser source, an optical switch, an optical circulator, a photodiode and, finally, the electronics needed for the ultrasonic wave generation), is instead $17 \times 10 \times 6 \text{ cm}^3$ in volume, with a weight of approximately 700 g.

By exploiting the end effector degrees of freedom of the Resist platform, the contact sensors can be displaced in every point of interest located on the beam's and piles' surface under monitoring, both in vertical and horizontal directions, reaching precisely the emerging crack and performing the contact ultrasonic measurements (Fig. 8).

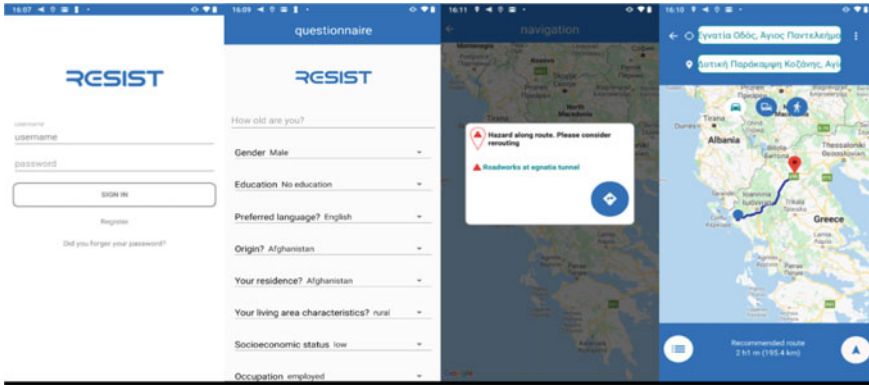


Fig. 8 RESIST mobile application

4 Structural Vulnerability and Risk Management

Exclusively based on robotic measurements RESIST can assess the probability of structural failure and damage for the transport structure of interest under extreme loading that includes, severe earthquakes, explosions, fire, landslides, high winds and scouring in tandem with adverse climatic conditions that accelerate material deterioration. Then, based on damage, impacts are being assessed, including casualties, environmental loss and direct and indirect economic impacts, with and without protection measures and the risk is being determined. Finally, a protection measure is selected that minimizes the risk and is cost effective (the cost of the protection measure is less than risk reduction it produces).

The work has been implemented in three case studies involving bridges and tunnels. Table 1 shows some of the results from the case study involving bridge T9 on the Egnatia Highway network in Northern Greece, however, they are representative of the other case studies as well.

From the above it is clear that the duration of the reinstatement dramatically affects costs and that indirect costs are a multiple of direct costs.

Inspecting the damaged bridge is difficult, dangerous and slow. It has been assumed that this inspection is performed by the RESIST RPAS that will provide all the required measurements for structural assessment and that this will save 20 days in the pre-construction process. Table 2 shows the monetary implications of the above.

5 Mobility Continuity

The mobility continuity module takes into consideration the highway users (i.e. drivers) needs and the overall interaction between drivers and infrastructure managers. With that in mind, a mobility continuity module has been developed that

Table 1 Monetarised consequences of damage due to a severe earthquake without protection measures

Type of cost	Cost if average no. of vehicles are on the bridge at the time of the incident (€)	Cost if max. no. of vehicles are on the bridge at the time of the incident (€)
Reconstruction	2,100,000	2,100,000
Local traffic safety measures	66,000 (12 months × 5500 €/month)	66,000 (12 months × 5500 €/month)
Loss of revenue because the bridge is out of service	10,399,489	10,399,489
Total direct cost	12,565,489	12,565,489
Fatalities/injuries (3 of the severely injured people died)		19,110,000
Fatalities/injuries (2 of the severely injured people died)	9,213,750	
Damaged vehicles	85,000	185,000
Travel delay cost to road users due to detours	2,241,145,260 (6,140,124€/day × 365 days)	2,241,145,260 (6,140,124€/day × 365 days)
Total indirect cost	2,250,444,010	2,260,440,260
Total cost	2,263,009,499	2,273,005,749

Table 2 Monetarised consequences of damage due to a severe earthquake without protection measures and with the RESIST RPAS performing the inspection of the damaged bridge

Type of cost	Cost if average No. of vehicles on the bridge at the time of the incident (€)	Cost if Max. No. of vehicles on the bridge at the time of the incident (€)
Reconstruction	2,100,000	2,100,000
Local traffic safety measures	62,333 ((11 months + 1/3 Month) × 5500€/month)	62,333 ((11 months + 1/3Month) × 5500€/month)
Loss of revenue because the bridge is out of service	9,829,654	9,829,654
Total direct cost	11,991,987	11,991,987
Fatalities/injuries (2 of the severely injured people died)		17,290,000
Fatalities/injuries (1 of the severely injured people died)	7,393,750	
Damaged vehicles	85,000	185,000
Travel delay cost to road users due to detours	2,118,342,780 (6,140,124€/day x345days)	2,118,342,780 6,140,124€/day x345days)
Total indirect cost	2,125,821,530	2,135,817,780
Total cost	2,137,813,517	2,147,809,767

includes a mobile application, a road operator user interface and a road traffic simulation environment. The mobile application will assist the highway driver to select a route as well as provide alternative routes in case of an event leading to closure or road capacity reduction. The same mobile application will also be the means of dissemination of personalized messages via behavioral analysis based on data provided by the user during the registration process and sentiment analysis through a social media interface. The road operator user interface will be accessed via the RESIST platform and will be coupled by a simulation environment where the road operator will be able to run scenarios based on specific parameters and forecast the traffic flow and effect of an event.

6 Conclusions

RESIST project is right now in the phases of integration and testing producing very exciting results and innovations. It will provide a holistic approach to the increase of resilience in the transportation sector with the use of robotics and ICT tools allowing for a closer connection between the infrastructure managers/owners and the actual users of the infrastructure (i.e. the drivers). The actual integrated system will be field tested in 2 pilots taking place in real, operational infrastructure namely the T9-T11 bridge in Greece (Metsovo area) and the St Petronilla tunnel and Millaures Viaduct in Italy. The 1st pilot (Metsovo area) will see the testing of the whole system in a landslide scenario in the T9-T11 bridge. The aerial robots will take measurements, both visual and contact, which will be transmitted to the vulnerability and risk assessment modules for analysis. On the same time the ability of the mobility continuity module will be tested on live conditions to see the ability to reroute traffic and properly disseminate information to users of the road. In the second pilot, the GPS denied capabilities of the drones will be testing by operating them within the tunnel and the vision system will be tested in damage detection of steel sections.

References

1. Pinto R, Medeiros A, Padaratz I, Andrade B (2010) Use of ultrasound to estimate depth of surface opening cracks in concrete structures. <http://www.ndt.net/?id=9954>
2. Marini D et al (2019) Acoustic micro-opto-mechanical transducers for crack width measurement on concrete structures from aerial robots. In: 2019 TRANSDUCERS Germany, pp 893–896
3. Menze M, Geiger A (2015) Object scene flow for autonomous vehicles. In: Proceedings of the IEEE conference on computer vision and pattern recognition, pp 3061–3070
4. Scharstein D, Szeliski R (2002) A taxonomy and evaluation of dense two-frame stereo correspondence algorithms. *Int J Comput Vis* 47(1–3):7–42
5. <https://colmap.github.io/>
6. <https://www.pix4d.com/>

7. Yang G, Manela J, Happold M, Ramanan D (2019) Hierarchical deep stereo matching on high-resolution images. In: Proceedings of the IEEE conference on computer vision and pattern recognition, pp 5515–5524
8. Yao Y, Luo Z, Li S, Fang T, Quan L (2018) Mvsnet: depth inference for unstructured multi-view stereo. In: Proceedings of the European conference on computer vision (ECCV), pp 767–783
9. Martin M, Sagnik M, Sreenivas M, Panagiotis P, Ramesh V (2019) Meta-learning convolutional neural architectures for multi-target concrete defect classification with the concrete defect bridge image dataset. In: Proceedings of the IEEE computer society conference on computer vision and pattern recognition (CVPR)
10. Martin M, Iuliia P, Sagnik M, Ramesh V (2019) Open set recognition through deep neural network uncertainty: does out-of-distribution detection require generative classifiers? In: Proceedings of the IEEE computer society international conference on computer vision (ICCV), 1st workshop on statistical deep learning for computer vision (SDL-CV)
11. Gal Y, Ghahramani Z (2015) Dropout as a Bayesian approximation: representing model uncertainty in deep learning. In: Int Conf Mach Learn (ICML) 48
12. Olaf R, Fischer P, Brox T (2015) U-net: convolutional networks for biomedical image segmentation. MICCAI 9351:234–241

Possibilities of Composite Distributed Fibre Optic 3DSensor on the Example of Footing Pulled Out from the Ground: A Case Study



Rafał Sienko , Łukasz Bednarski , Tomasz Howiacki ,
Katarzyna Zuziak , and Sławomir Labocha 

Abstract Distributed fibre optic sensing (DFOS) provides breakthrough possibilities in the field of structural health monitoring (SHM) in comparison to conventional spot measurements. It allows the measurements to be registered over the entire measuring length, not only in one point of the structure. That is why this technology is becoming more and more attractive for geotechnics and civil engineering applications, providing both technical and economic benefits. However, to utilize all advantages of distributed sensing it is necessary to apply appropriate sensors, which will be able to accurately reflect the real structural behaviour. This paper discusses in situ application of unique (patented) composite DFOS displacements sensors (3DSensors), which were embedded into the ground layers and compacted around the footing. The research was conducted to observe the potential slip plane generated during the vertical pulling of the footing out of the ground. Distributed measurements were performed to obtain vertical displacement profiles around the footing within the selected ground layers with a spatial resolution of 1 cm. Finally, special visualization of ground deformation in 3D space was performed to analyze in detail the physical changes between the footing and the surrounding ground. No other techniques are currently able to obtain such information, as their application inside the ground layers would disturb its behaviour. The operational rules of displacement DFOS sensor, way of installation, course of the study as well as the exemplary results are discussed hereafter.

R. Sienko (✉) · T. Howiacki
Cracow University of Technology, Warszawska 24, 31-155 Kraków, Poland
e-mail: rafal.sienko@pk.edu.pl

T. Howiacki
URL: <https://www.shmsystem.pl>

E. Bednarski
AGH University of Science and Technology, Mickiewicza 30, 30-059 Kraków, Poland

T. Howiacki · K. Zuziak
SHM System, Jana Pawła II 82A Libertów, 30-444 Kraków, Poland
URL: <https://www.shmsystem.pl>

S. Labocha
University of Technology, Katowice, Rolna 43, 40-555 Katowice, Poland

Keywords Shape sensors · Strain · Displacement · Optical fibres · DFOS · Composites · Footing · Geotechnics

1 Introduction

1.1 Structural Health Monitoring (SHM)

Nowadays, Structural Health Monitoring (SHM) Systems are an essential and indispensable tool for obtaining information on the operational behaviour of engineering [1] and geotechnical structures [2]. Such systems are usually operated on the basis of automatic sensors installed in real in situ conditions.

The knowledge acquired this way is very important for optimal decision making [3, 4] and improving the safety of critical infrastructure while generating financial savings. These savings should be considered in the context of the entire lifecycle of the structure [5]. Additional in situ measurement information should be used for optimization the designing procedures and standards, calibration of numerical models, verification of theoretical assumptions, controlling the structural behaviour during long-term operation with changing external conditions and finally managing the maintenance of the structure (including renovation strategies)—see the scheme in Fig. 1.

The need for performing in situ measurements results from many factors, including the construction law and standard requirements [6, 7], but the most important are the physical ones related to uncertainties arising from:

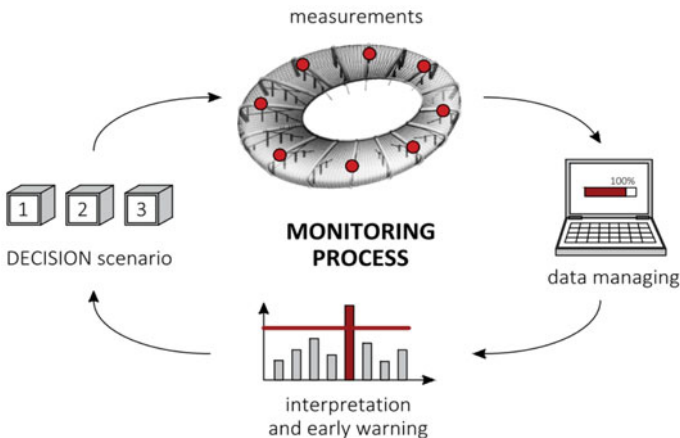


Fig. 1 The simplified scheme of the structural health monitoring process

- material's heterogeneity and associated random variations in its physical and mechanical parameters (e.g. strength, elasticity modulus, coefficients of thermal expansion, etc.),
- geometrical imperfections and tolerances (deviations from design, idealized assumptions),
- random actions and loads (there is always a probability of occurring over-standard values),
- time-dependent effects (e.g. creeping, shrinkage, fatigue), which are very difficult to predict with required certainty,
- cyclic loads and changing external conditions (e.g. temperature, ground humidity, barometric pressure, etc.),
- assumed theoretical simplifications and idealized models applied during designing stage,
- the pressure of time and money that usually accompanies the investments and increases the risk of human error at every stage of the process (design, construction, exploitation and maintenance).

It is worth to underline that the number of the above factors are particularly important for geotechnical structures, where uncertainties regarding the ground parameters are much higher than in standard (cubature, overground) civil engineering applications. The ground parameters may differ significantly depending on their location and what is more, they are changing over time with the changing external conditions (e.g. the humidity).

1.2 Distributed Fibre Optic Sensing (DFOS)

Due to the increasing number of applications in the field of structural health monitoring systems and taking into account the complexity of this problem resulting from the above-mentioned factors, the new measurement solutions are constantly being sought. The main goal is to provide comprehensive and reliable structural information while keeping the system cost-effective. The newly-designed solutions should focus on early detection of local damages or defects [8], which could bring measurable financial savings and improve safety.

Nowadays, one of the most promising technologies in this context is distributed fibre optic sensing (DFOS) [9], which, in contrast to spot measurements, allows to perform measurements in geometrically-continuous way along the entire length of the optical fibre (see Fig. 2). When using conventional spot sensors, there is always a high uncertainty about what is happening between them and even advanced mathematical models are not able to compensate for this uncertainty. On the other hand, the use of multiple spot sensors at the same time (quasi-distributed measurements) is usually economically and technically not justified. Thus, distributed sensing over distances from several millimeters [10] to even hundreds of kilometers [11], can be considered as a completely breakthrough solution.

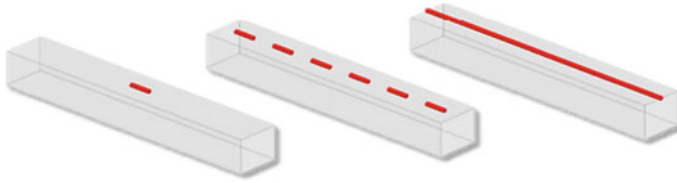


Fig. 2 The scheme of the measurements: spot (left), quasi-distributed and distributed (right)

The optical sensor, in which measuring element is the optical fibre, can replace thousands of conventional spot sensors, depending on the applied spatial resolution and measuring distance (usually from 100 to 5 measuring points per one meter of the sensor). This creates completely new possibilities for the assessment of technical condition of different types of engineering and geotechnical structures.

Performing measurements of selected physical quantities (usually strains or temperature) in a distributed way is possible thanks to utilizing different optical phenomena, like Rayleigh [12], Brillouin [13] and Raman [14] scattering. Each approach is characterized by its own advantages and disadvantages and should be chosen individually depending on the requirements of a given installation. For example, Rayleigh scattering, due to its high spatial resolution, is adequate for precise measurements with localized events over the length of tens of meters, while Brillouin scattering is usually applied for km-range measuring distances, but with worse spatial resolution.

Another important aspect is the appropriate construction of the sensor itself, which should allow to utilize all benefits of the DFOS technology. Applying the sensor which is susceptible to plasticity effects or which is constructed with layers (analogously like cables) causing the debonding or slippage effects, may invalidate the correct measurements and lead to wrong decisions.

The concept and implementation of the monolithic, composite DFOS sensor (the 3DSensor) dedicated for measuring displacements (changes in shape) is presented and discussed hereafter. The article describes the practical application of this solution within the geotechnical field research, where the footing foundations were pulled-out from the ground.

1.3 Research Problem

Research work was carried out within the framework of the project realized by ENPROM Sp. z o.o. [15], NCBIR No. POIR.01.01.01-00-0789/17, entitled “*Elaboration of the new series of types of transmission towers 400 kV and suitable for them foundations, in this of foundations to the use on grounds about particularly disadvantageous geotechnical parameters*”. This project used 400 kV transmission towers and varying shallow foundations with increased pull-off capacity. During

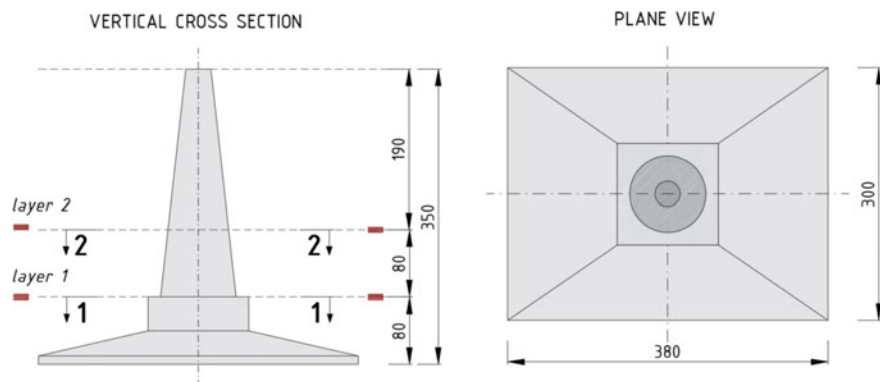


Fig. 3 The cross section and plan view of the exemplary footing investigated during research

the realization of the project, different types of footing foundations were investigated (see example in Fig. 3), including prefabricated special overlay plates, hybrid monolithic-prefabricated special footings strengthened with anchoring micropiles. The uniqueness and usability of the performed research results from the fact that tests were carried out on a full-scale (1:1) objects, in relation to foundations currently used within 400 kV lines.

The project was led in cooperation with the Institute of Roads and Bridges, the Faculty of the Civil Engineering of the Warsaw University of Technology. The structural solutions used in the project were patented and implemented during construction of new important 400 kV transmission lines in Poland, including the lines of the relation Mikułowa-Czarna and Piła-Plewiska-Krzewina.

Another innovative aspect implemented during research was the application of distributed fibre optic sensing for advanced analysis of the cooperation between the footing and the surrounding ground. One of the aims was to observe the ground deformations generated during the vertical pulling the footing out of the ground. Thanks to the application of dedicated 3DSensors, it was possible to determine vertical displacement profiles around the footing within the selected ground layers with a spatial resolution of 1 cm. No other techniques are able to obtain such detailed information, as the presence of traditional sensors inside the ground layers would disturb its behavior and invalidate the results. The operational guidelines of the displacement DFOS sensor, manner of installation, course of the study as well as exemplary results are discussed hereafter.

2 DFOS Measuring System

2.1 Construction of 3DSensor

The basic physical quantity measured with distributed sensing approach is axial strain ($\mu\epsilon$) in the optical fibre. There are number of solutions available on the market (e.g. sensing fibres, cables or DFOS strain sensors) which are dedicated for this purpose. However, in many engineering and geotechnical applications, it would be very favorable to obtain the knowledge about displacements (mm) in the planes perpendicular to the sensor's axis. These displacements represent the change in shape of the monitored structure.

The possibility of converting the measured axial strains into the three-dimensional displacements with practical and reasonable accuracy was investigated in some publications [16–18]; however, their commercial application is very limited. In the research described within this article, the patented (US and PL patents) solution was applied in the form of the composite displacement sensor called 3DSensor. This unique measuring tool was elaborated by SHM SYSTEM company [19] during realization of the research project entitled “*Development of the new fibre optic sensor allowing for the determination of the vertical and horizontal displacements of the studied objects at the distances of up to 120 km*”. This project was funded by the grant won at the National Centre for Research and Development within the framework of Intelligent Development Operational Program 2014–2020 (POIR.01.01.01-00-0550/15).

During the design stage, the inventors of the 3DSensor were able to avoid the main limitations and disadvantages of the widely applied DFOS sensing solutions (usually based on the cable production technology). First of all, they did not use plastic and steel to protect the optical fibre, due to their very limited elastic range and plasticity effects, which disrupts the ability to take correct measurements. In the 3DSensor's core a special composite was applied, which allows for the use of the fibre in a wide elastic range without fear of damage. Furthermore, there are no intermediate layers inside the sensor, which usually would cause debonding and slippage effects, not allowing for the appropriate strain transfer. Within the 3DSensor, optical fibres, in their primary coatings, are fully integrated with the composite core during production (pultrusion) stage, creating a monolithic cross-section. Exemplary view of the laboratory and in situ version of 3DSensor are presented in Fig. 4a, b respectively.

The main idea of the 3DSensor solution is to determine the displacement profile based on axial strain measurements. For this purpose, there is a need to apply more than one optical fibre and employ a special algorithm for data conversion (see also Sect. 2.3).



Fig. 4 Composite DFOS fibre optic 3DSensor for displacement (shape’s changes) monitoring: **a** laboratory version; **b** in situ version

2.2 Optical Datalogger

Today’s market offers a wide range of DFOS devices for strain measurements, characterized by many important factors such as: accuracy, resolution, distance range, spatial resolution, frequency of measurement, price and many others. All of these factors have to be carefully taken into account when testing innovative measurement technologies such as the 3DSensor. In the research discussed in this paper, optical backscatter reflectometer OBR4600 from Luna [20] was applied (Fig. 5a) to read the 3DSensors. Because a large number of optical sensors had to be read simultaneously during tests, also optical switch operating with 15 channels was used (see Fig. 5b).

The optical backscatter reflectometer OBR is based on the Rayleigh scattering phenomenon [21–23], which occur in every cross-section of the fibre due to the partial structure of the matter and resulting fluctuations of the refractive index. These imperfections cause the light to scatter in all directions, as well as backwards into the optical device. Finally, the reflectometer determines the positions of all imperfections and calculates their changes caused by both mechanical and thermal strains. The positions of all local imperfections are random but constant for a given fibre and can

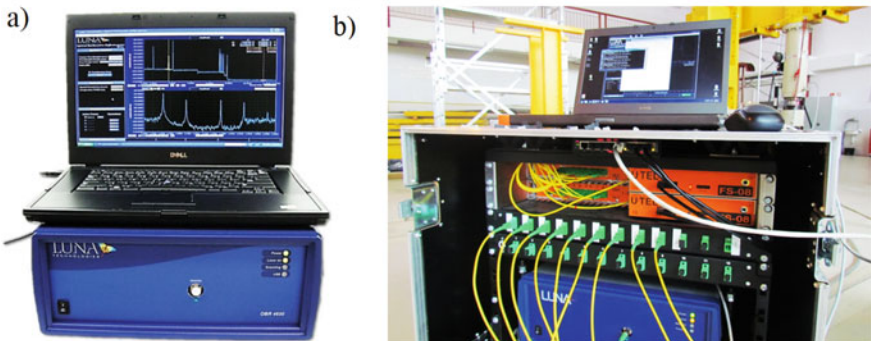


Fig. 5 a The view of optical backscatter reflectometer OBR4600 with the software; **b** the view of the reflectometer with optical switch applied during measurements

be compared to a unique fingerprint. By comparing the two patterns (e.g. before and after loading), it is possible to determine strain or temperature changes, which could be expressed by the following equation:

$$-\Delta v/v = K_T \cdot \Delta T + K_\varepsilon \cdot \Delta\varepsilon \quad (1)$$

v mean optical frequency (Hz),
 K_T temperature calibration constant ($^{\circ}\text{C}^{-1}$),
 K_ε strain calibration constant (-),
 ΔT temperature change ($^{\circ}\text{C}$),
 $\Delta\varepsilon$ strain change ($\mu\varepsilon$).

v mean optical frequency (Hz),
 K_T temperature calibration constant ($^{\circ}\text{C}^{-1}$),
 K_ε strain calibration constant (-),
 ΔT temperature change ($^{\circ}\text{C}$),
 $\Delta\varepsilon$ strain change ($\mu\varepsilon$).

It should be underlined that the final result of the measurement is a linear combination of mechanical and thermal effects. In the research described hereafter, sensors were embedded inside the ground and measurements were performed in short-term, thus there was no need to provide any thermal compensation. The temperature effect could be neglected. It is also worth noting, that the temperature changes are very important during long-term measurements of axial strains. However, the algorithm for displacements calculation is capable of self-compensation due to temperature changes, so even during long-term monitoring there is no need to install additional temperature sensors.

The applied reflectometer software also allows for some measuring parameters to be chosen during post-processing. Optical fibre can be graphically represented by the chain of the individual spot gages as shown in Fig. 6. During data analysis, gauge length (base of averaging the strains) as well as spatial resolution (gauges spacing) should be defined.

Table 1 summarizes selected measuring specifications of the applied backscatter reflectometer and shows the values of parameters chosen for further analysis.



Fig. 6 Graphical interpretation of selected parameters defined during data post-processing

Table 1 Specifications of applied optical reflectometer and post-processing parameters

Heading level	Value	Unit
Distance range (normal mode)	up to 70	m
Strain measurement resolution	± 1	$\mu\epsilon$
Individual gauge length (base)	10	mm
Spatial resolution (gauges spacing)	10	mm

2.3 Algorithm for Data Conversion

The construction of the 3DSensor, as stated before, needs to consist of more than one optical fibre. For analyzing displacements in one plane, at least two fibres are required and for full 3D calculations, at least three fibres. Usually, four fibres are applied to increase accuracy and to minimize the risk of losing data through accidental breakage of the fibre.

Let's consider the simplest situation, were the 3DSensor is used only for measuring vertical displacements, which is the most important factor for many geotechnical and engineering applications (e.g. settlement of embankments, bridge span deflections). The key feature enabling the precise calculation is the very accurate arrangement of the fibres around the neutral axis of the composite core.

The 3DSensor could be represented analogously by the chain of individual gauges (see Fig. 7); however, each individual gauge is now represented by the geometry of trapezoid. This trapezoid is defined by the distance between the optical fibres (approximately equal to the height of the composite core), the spatial resolution and

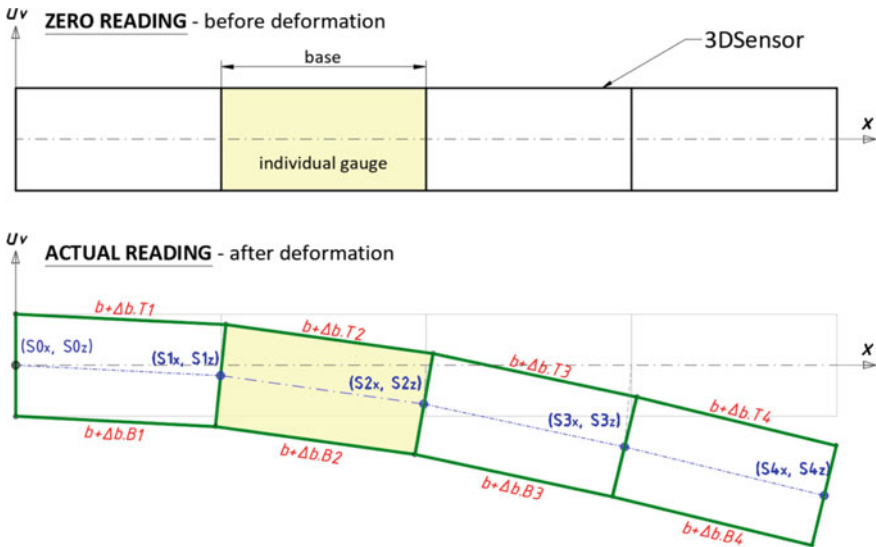


Fig. 7 Graphical representation of the 3DSensor divided into individual trapezoidal gauges

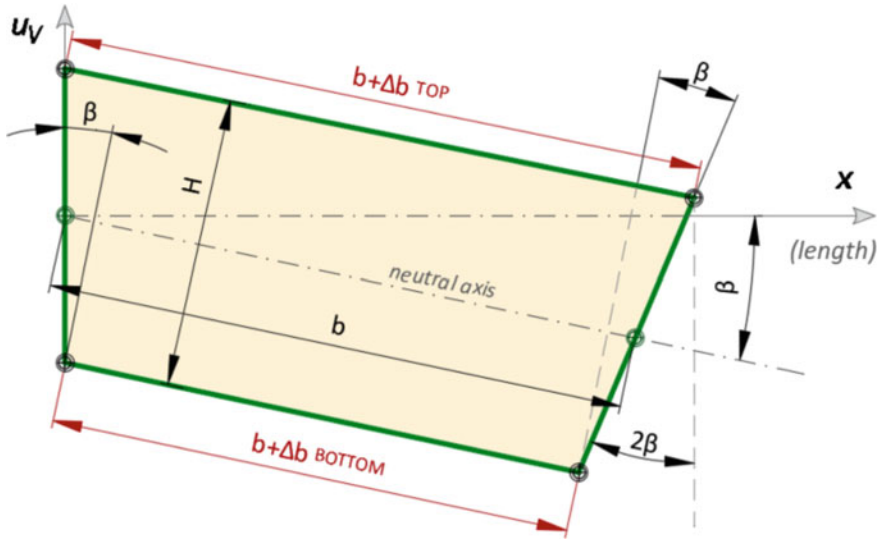


Fig. 8 Trapezoidal geometry of the individual gauge within the 3DSenor

measured strain profiles, causing the elongations and shortenings of the trapezoid bases—see Fig. 8. It is worth noting, that the proposed approach excludes from the analysis all axial effects causing the same changes of the lengths of trapezoid bases. This means that for shape calculations only bending effects are important. Mechanical axial force as well as temperature changes are compensated for by the algorithm.

Finally, the calculated vertical displacement profile depends on the measured strain profiles at the bottom and top surfaces of the composite core, the distance between the fibres (height of the composite core), spatial resolution of applied reflectometer and assumed boundary conditions (“Eq. 2”).

$$u_v(x) = f(\varepsilon_B(x), \varepsilon_T(x), H, r, bc) \tag{2}$$

$u_v(x)$ vertical displacement profile (mm) over length,
 $\varepsilon_B(x)$ strain profile ($\mu\varepsilon$) over the bottom surface of the sensor,
 $\varepsilon_T(x)$ strain profile ($\mu\varepsilon$) over the top surface of the sensor,
 H distance between the bottom and top optical fibre (mm),
 r spatial resolution (mm) (base length and spacing of individual gauges),
 bc boundary conditions.

$u_v(x)$ vertical displacement profile (mm) over length,
 $\varepsilon_B(x)$ strain profile ($\mu\varepsilon$) over the bottom surface of the sensor,
 $\varepsilon_T(x)$ strain profile ($\mu\varepsilon$) over the top surface of the sensor,
 H distance between the bottom and top optical fibre (mm),
 r spatial resolution (mm) (base length and spacing of individual gauges),

bc boundary conditions.

The boundary conditions should be defined depending on the way of installation. For a free-supported beam, displacements within the supports are assumed to be equal to zero. For the cantilever scheme the displacements and rotation at the first node are equal to zero. In practice, usually the knowledge about displacements in any two points along the sensor is required, which could be obtained from geodetic surveys or through installation the sensor in the areas free from any deformations.

3 Installation and Location of the 3DSensors

The installation process of 3DSensors in ground layers around the analyzed footing is quite fast and comfortable due to their lightweight and easy operation rules. The sensors must be simply placed in the designed positions and covered with the earth, which is further compacted according to standard procedures. There is no need to provide a perfect bonding between the sensor and the surrounding ground—this is one of the main differences between the DFOS strain and displacement sensors. The slippage between the sensor and surrounding medium will significantly disturb strain measurements, but still the shape of the sensor will reflect correctly the shape of the medium. In other words, there is no need to provide bonding between the sensor and the ground for correct displacement measurements.

During research, two measuring layers (planes) were arranged (see spatial visualization in Fig. 9, compare also Fig. 3). The sensors were placed parallel to the footing's edges at 80 cm and 160 cm from the footing's base. The photo from the installation stage, showing the arrangement of the sensors within the second measuring layer, is presented in Fig. 10. The sensors pigtailed were protected with the special tubes and led to the mobile measuring station.

4 Experimental Research

4.1 Course of the Study

Altogether, three tests for different types of footings were investigated and this article presents exemplary results in order to discuss the measuring possibilities. However, all the tests had a similar course. The footing was pulled out from the ground through specially designed stand (Fig. 11). The optical measurements were performed step by step with the increasing force (with its fixed values).

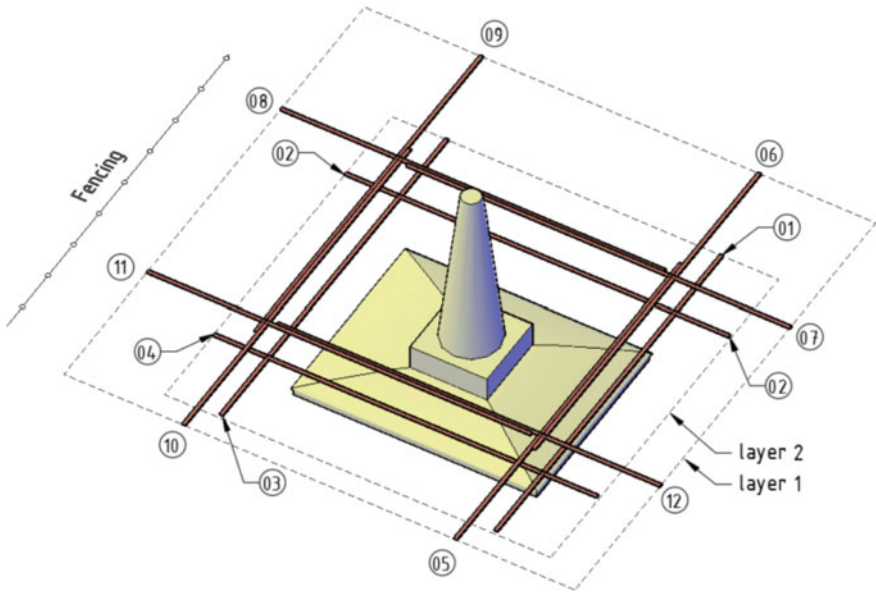


Fig. 9 The spatial visualization of the 3DSensor’s arrangement within the ground layers around the analysed footing



Fig. 10 The view of the 3DSensor’s arrangement within the second layer: installation stage

4.2 Measured Strain Profiles

In each measuring step, strain profiles at the bottom (lower) and top (upper) surface of the composite core of the sensor were measured with the resolution of $\pm 1 \mu\epsilon$. The spatial resolution was set to 10 mm and it means that there were 100 measuring



Fig. 11 The view of the stand for pulling the footing out from the ground

points defined over one meter of sensor. Including all sensors, one can state that during one measurement session almost 10,000 individual gauges were analyzed.

Exemplary raw strain data from the 3DSensor no. S03 are presented in Fig. 12 both for the lower and upper surface. The shape of these plots indicates that both the axial and bending effects influenced the sensor’s behaviour. Axial tension was caused in this case by the force generated due to the sensor’s restraint (friction) caused by the surrounding ground during bending. In the long-term structural monitoring, axial effects are also caused by temperature changes. However, for the shape’s change analysis, only bending effects are important, while axial effects can be simply neglected (see Fig. 13).

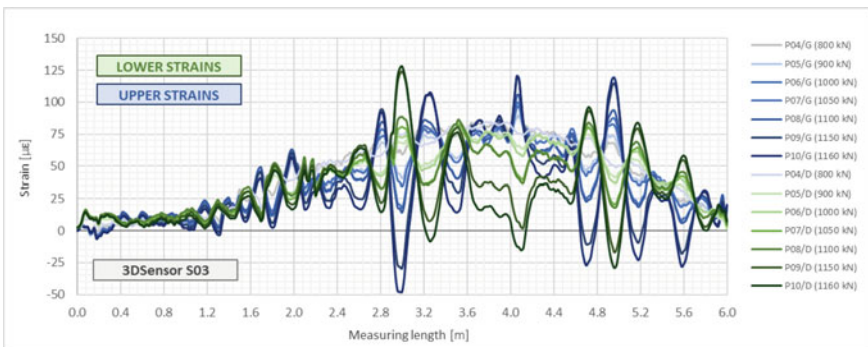


Fig. 12 Exemplary raw strain data from the lower and upper surface of 3DSensor no. S03 coming from both bending and axial effects

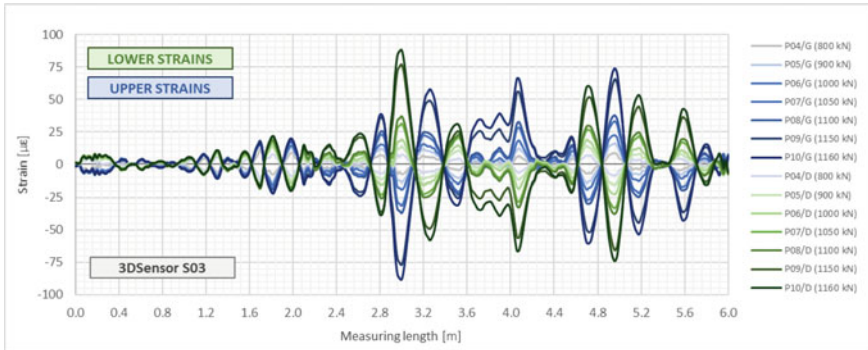


Fig. 13 Exemplary strain data from the lower and upper surface of 3DSensor no. S03 coming from bending effects (with the axial effects excluded)

4.3 Calculated Displacement Profiles

The strain profiles at the lower and upper surface are the input data for the displacement algorithm described in Sect. 2.3. The assumption about boundary conditions was that the vertical displacements at the beginning and at the end of the measuring length are equal to 0. Results are expressed directly in millimeters. Vertical displacements profiles from exemplary measuring stage (at fixed values of pull-out force) are presented in Fig. 13 (top view, plots projected onto the measuring plane) and in Fig. 14 (spatial visualization).

It should be noted that no other reference techniques were applied due to their infeasibility or economical limitations. The presence of massive spot sensors or other methods could significantly disturb the ground behaviour, while flexible composite 3DSensors do not disturb (reinforce) the ground in any way.

Despite the lack of a reference technique, the accuracy of the proposed solution was verified during a number of laboratory tests and other in situ installations (these will be the subjects of the authors' upcoming publications). For example, the reference horizontal inclinometer system, installed together with the 3DSensor along the road embankment, indicated that the mean difference between these two independent techniques was less than 0.5 mm over a distance of 50 m. The results of the tests performed under laboratory conditions are even better.

5 Discussion and Conclusions

The article presents and discusses the new measurement solution based on DFOS technology and the unique and patented 3DSensor. This solution allows to determine displacement profiles based on the measured strain profiles and is directly dedicated for geotechnical and engineering applications. It could be successfully applied for

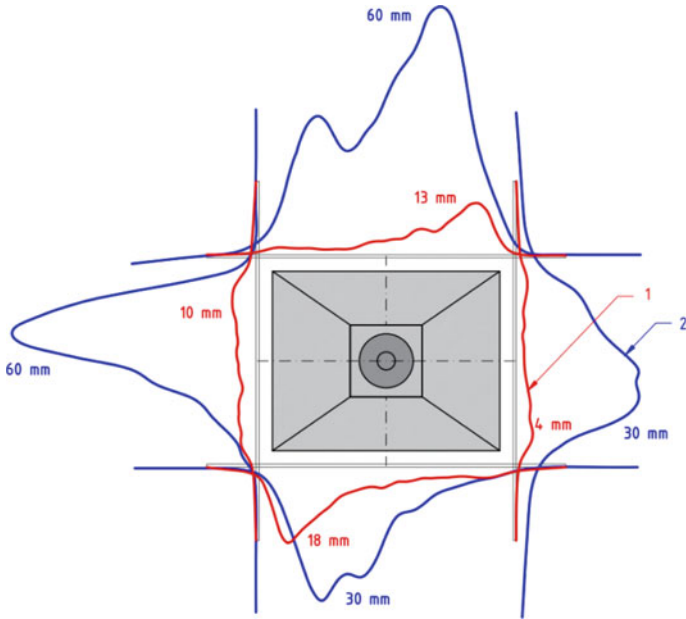


Fig. 14 The view of the exemplary vertical displacement profiles in both layers projected onto the measuring plane: top view

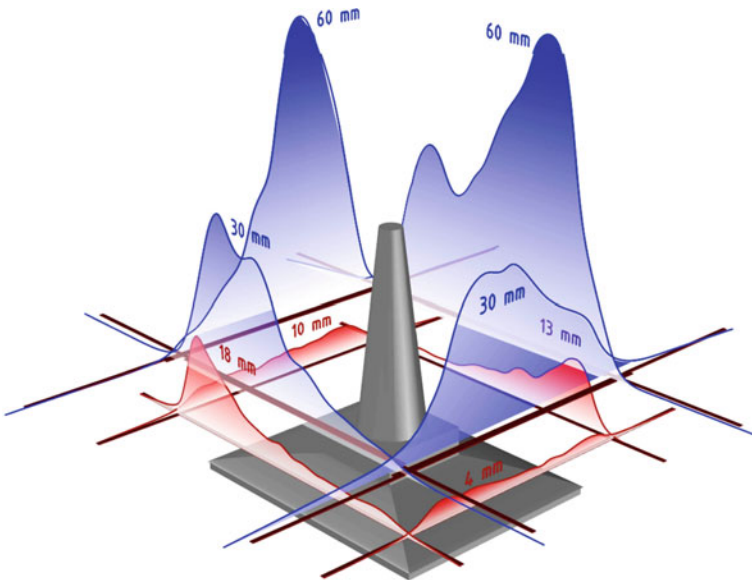


Fig. 15 The view of the exemplary vertical displacement profiles: spatial visualization

bridges, dams, embankments, slurry and retaining walls, roads, highways, pipelines, landslide areas and many others structures. The proposed solution is also suitable for experimental researches, both in the laboratory and in situ conditions.

This relatively simple approach to displacement calculation is based on the challenging production technology of the sensor itself, where the optical fibres are fully integrated into the composite core at the production stage. The key to the innovative technology is the precise position of the fibres in reference to the neutral axis of the composite core. Excessive deviations in position, could cause that the final accuracy of the method to be negatively affected in practical applications. The accuracy of the 3DSensor is guaranteed by an appropriate production regime and quality control.

It is worth noting, that the parameters of the sensor are adjustable depending on the requirements of a given project. For example, the core material and its mechanical properties such as elasticity modulus can be modified (the lower the modulus, the lower the impact of the sensor on the structural behaviour of the monitored specimen or structural member). Another example could be the geometry of the composite core: the higher the sensor's cross-section, the more sensitive the sensor to small vertical displacements.

In this article, world's first unique research was described, showing the proposed measurement solution successfully being applied in a structural test setting. The full-scale footings applied as foundations of 400 kV transmission towers were prepared in a special research field and placed under physical stress. Effects on the surrounding ground layers were studied using the patented 3DSensor technology. One of the aims of the research was to propose an optimal structural solution, which will provide appropriate level of safety and economical benefits at the same time. Distributed fibre optic displacement measurements significantly contributed to this challenging task.

The development of DFOS techniques and measuring tools have resulted in a clear increase in applications in this field in recent years. DFOS displacement monitoring systems were installed in Poland e.g. within:

- industrial, reinforced concrete tower,
- steel and composite bridges,
- innovative smart bridge deck panels,
- road embankments,
- road (asphalt) layers,
- gas pipelines,
- slurry walls and concrete piles (as an alternative for conventional inclinometer system),
- prestressed-concrete slabs and girders,
- composite collectors, and
- other structures.

It should be noted, that the number of the installed displacements monitoring systems is still much lower than the number of systems dedicated for strain measurements. Despite the successfully implemented examples, there are still some challenges that need to be addressed, e.g.: remote and automated measurements within structural health monitoring, clear and useful software for data processing, data acquisition, final accuracy for longer distances and poor spatial resolution (for Brillouin-based systems), long-term stability including the resistance to environmental factors. However, the potential benefits coming from DFOS displacement measurements clearly indicate that this technology will continue to be dynamically developed in the near future.

References

1. Balageas D, Fritzen CP, Güemes A (2006) Structural health monitoring. Wiley-ISTE
2. Dunncliff J (1993) Geotechnical instrumentation for monitoring field performance. Wiley-Interscience
3. Benjamin JR, Cornell CA (1970) Probability. Statistics and decision for civil engineers. McGraw-Hill, New York
4. Faber MH (2012) Statistics and probability theory in pursuit of engineering decision support. Springer, Berlin
5. Furuta H, Frangopol DM, Akiyama M (2015) Life-cycle of structural systems: design, assessment, maintenance and management. Taylor & Francis Group, London
6. EN 1990: Eurocode—basis of structural design
7. EN 1997-1: Eurocode 7: Geotechnical design—Part 1: general rules
8. Farrar CR, Worden K (2007) An introduction to structural health monitoring. *Philos Trans R Soc A* 365:303–315
9. Glišić B, Inaudi D (2007) Fibre optic methods for structural health monitoring. Wiley, Hoboken
10. Samiec D (2012) Distributed fibre-optic temperature and strain measurement with extremely high spatial resolution. *Photonic International*
11. Inaudi D, Glišić B (2010) Long-range pipeline monitoring by distributed fiber optic sensing. *J Pressure Vessel Technol* 132(1)
12. Pamileri L, Schenato L (2013) Distributed optical fiber sensing based on rayleigh scattering. *Open Opt J* 7(Suppl-1, M7):104–127
13. Feng Ch, Kadum JE, Schneider T (2019) The state-of-the-art of Brillouin distributed fiber sensing. *IntechOpen*. In: Liaw SK (ed) Fiber optic sensing—principle, measurement and applications
14. Wang W, Chang J, Lv G, Wang Z, Liu Z, Luo S, Jiang S, Liu X, Liu X, Liu Y (2013) Wavelength dispersion analysis on fiber-optic raman distributed temperature sensor system. *Photon Sens* 3(3):256–261
15. ENPROM Homepage. <https://www.enprom.pl/en/>. Last accessed 02 Nov 2020
16. Wu H, Zhu HH, Zhang Ch-Ch, Zhou G-Y, Zhu B, Zhang W, Azarafza M (2020) Strain integration-based soil shear displacement measurement using high-resolution strain sensing technology. *Measurement* 166:108210
17. Amanzadeh M, Aminossadati SM, Kizil MS, Rakić AD (2018) Recent developments in fibre optic shape sensing. *Measurement* 128:119–137
18. Zeni L, Picarelli L, Avolio B, Coscetta A, Papa R, Zeni G, Maio CD, Vassakki R, Minardo A (2015) Brillouin optical time-domain analysis for geotechnical monitoring. *J Rock Mech Geotech Eng* 7:458–462
19. SHM SYSTEM Homepage. <http://www.shmsystem.pl/?lang=en>. Last accessed 02 Nov 2020

20. LUNA Homepage. <https://lunainc.com/product/obr-4600>. Last accessed 02 Nov 2020
21. Güemes A, Fernández-López A, Soller B (2010) Optical fiber distributed sensing—physical principles and applications. *Struct Health Monit Int J* 9(3):233–245
22. Gifford D, Soller B, Wolfe M, Froggatt ME (2005) Distributed fiber-optic sensing using Rayleigh backscatter. In: European Conference on Optical Communications (ECOC) Technical Digest, Glasgow, Scotland
23. Kishida K, Guzik A (2014) Study of optical fibers strain-temperature sensitivities using hybrid Brillouin-Rayleigh system. *Photon Sens* (2014)

Multidisciplinary Investigations of a Steel–Concrete Composite Bridge



**Lorenzo Benedetti, Paolo Borlenghi, Manuel D'Angelo,
Alessandro Menghini, Giacomo Zonno, Francesco Ballio, Marco Belloli,
and Carmelo Gentile**

Abstract The paper presents the results from the multidisciplinary investigations performed on Baghetto Bridge. The structure, built in 1966, crosses the Adda river between the Municipalities of Castello dell'Acqua and Chiuro. It consists of three steel–concrete composite girders of different lengths supported by stone-masonry piers. The research program involved several investigations: (i) documentary research, (ii) ambient vibration testing, (iii) hydraulic study, and (iv) FE modelling and updating. After a concise review of the bridge history and a brief description of the structure, the hydraulic study based on existing topographic surveys is presented. This latter analyses allowed the estimation of hydraulic actions as well as the evaluation of possible hydro-geomorphologic scenarios. Subsequently, the complete results of the experimental tests are described and discussed. The modal

L. Benedetti (✉) · M. Belloli

Department of Mechanical Engineering (MECC), Politecnico di Milano, Milan, Italy
e-mail: lorenzo.benedetti@polimi.it

M. Belloli

e-mail: marco.belloli@polimi.it

P. Borlenghi · A. Menghini · G. Zonno · C. Gentile

Department of Architecture, Built Environment and Construction Engineering (DABC),
Politecnico di Milano, Milan, Italy
e-mail: paolo.borlenghi@polimi.it

A. Menghini

e-mail: alessandro.menghini@polimi.it

G. Zonno

e-mail: giacomo.zonno@polimi.it

C. Gentile

e-mail: carmelo.gentile@polimi.it

M. D'Angelo · F. Ballio

Department of Civil and Environmental Engineering (DICA), Politecnico di Milano, Milan, Italy
e-mail: manuel.dangelo@polimi.it

F. Ballio

e-mail: francesco.ballio@polimi.it

parameters identified from the dynamic survey allowed validation of the numerical model, together with a more in-depth interpretation of the actual behaviour of the bridge. Moreover, the overall investigation allows to sound the presented multidisciplinary approach for the structural assessment of existing bridges.

Keywords Bridge monitoring · Operational modal analysis · Model updating · River bridge · Scouring

1 Introduction

Bridges and infrastructure networks play an essential role in the development and economic growth of a country. In Italy, numerous bridges were designed before the 70s according to codes and regulations that today are considered outdated, making their structural assessment of increasing interest. Furthermore, these structures are exposed to several causes of damage: ageing of materials, increase of traffic loads and vibrations, and natural hazards. Particularly, river bridges are threatened by floods; different statistics [1–3] indicate that the most frequent causes of bridge failures are attributed to floods. As a consequence, the integration of the investigations focused on the structure and on the hydraulic aspects, in a multidisciplinary context, is crucial to perform a complete safety evaluation for river bridges.

Within a recent collaboration between Politecnico di Milano and Regione Lombardia, several bridges in the north of Italy were studied. The main objective of the project was the definition of criteria and guidelines for the maintenance and management of roadway infrastructures. Firstly, a risk-based prioritization methodology at a regional scale was adopted, and, subsequently, recommendations for the implementations of Structural Health Monitoring (SHM) systems were provided. In addition, nine bridges were selected for the validation and the practical application of the proposed approach.

The paper describes the multidisciplinary investigation performed on one of the selected structures: the Baghetto bridge (Fig. 1). The Baghetto bridge was built in 1966 over the Adda river, and it still represents today a node for the local vehicular



Fig. 1 The Baghetto bridge: view from the upstream (a) and downstream (b) side

traffic. It has a steel–concrete composite deck with stone masonry piers, a total length of about 50 m and three spans of different lengths. The selected SHM strategy for this structure was the periodic ambient vibration testing (AVTs). As known from the scientific literature [4–9], vibration-based techniques are particularly suitable for existing bridges allowing the estimation of the modal parameters of the structure in operational conditions. According to the recent Italian Guidelines for the Management and Monitoring of Bridges [10], the AVTs will be repeated every four months.

The paper is structured as follows: Sect. 2 presents the documentary research and the detailed description of the bridge; Sect. 3 focuses on the hydraulic study; Sect. 4 describes the first dynamic survey performed in July 2020; Sect. 5 presents the FE modelling and the results of the updating procedure. Conclusions are then proposed in Sect. 6.

2 The Baghetto Bridge: Description and Documentary Research

The Baghetto Bridge (Fig. 1) is a three-span steel–concrete composite bridge built in 1966 over the Adda river. It carries the route SP23 between the municipalities of Chiuro and Castello dell'Acqua, about 10 km from the city of Sondrio, in the north part of Lombardy (Italy).

The structure is approximately 50 m long, and it is composed of three simply supported girders. The steel–concrete composite girders have different lengths, equal to 19.06, 17.22 and 13.40 m, and have a free span (i.e. the distances between the supports) respectively equal to 18.76, 16.62 and 13.10 m. The carriageway has a width equal to 4.5 m providing an alternating one-lane. The piers and one abutment are in roughly cut stone masonry with a concrete strengthening in the upper part, while the other abutment is in reinforced concrete. Regarding the geometry, piers and abutments have a height—starting from the foundation level—of about 7 m. The piers have an approximately rectangular section (2.30 m × 5.50 m) with rounded edges. The longitudinal and plan views of the bridge are shown in Fig. 2a.

The metallic part of the cross-section consists of three identical steel I-girders spaced of 1.5 m, connected by intermediate cross-bracings (double channel sections) and diagonals (angular sections). The upper part of the cross-section consists of a reinforced concrete slab with a height of 0.18 m. The detailed dimensions of the cross-section are shown in Fig. 2b. According to [11], the collaboration between the concrete slab and the steel beam is obtained by welded stud connectors (Fig. 2b). Regarding the layout of the metallic bearing supports, they restrain transverse and longitudinal displacements on one side of each span, while allowing longitudinal translations on the opposite side (flat-sided roller bearing typology).

The documentary research revealed the presence of the original design documents in the archives of the Local Authority responsible for the route maintenance. As stated

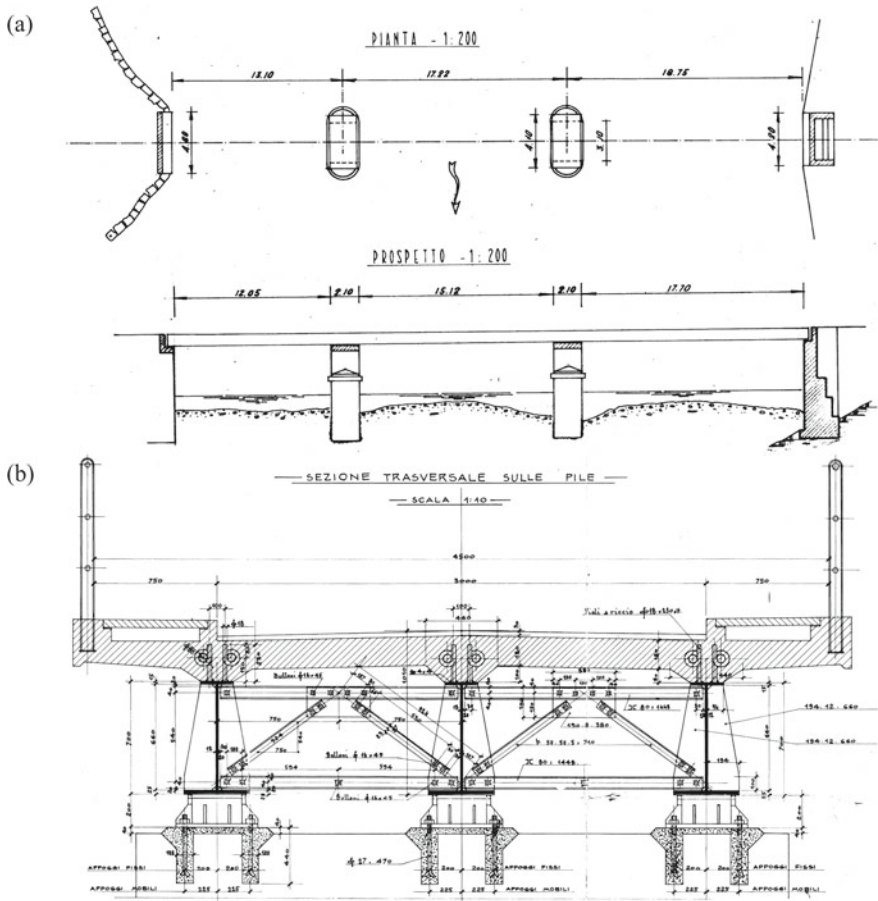


Fig. 2 Original blueprints of Baghetto bridge: **a** plan and longitudinal section; **b** detail of the steel-concrete composite deck



Fig. 3 **a** View of the right embankment to access the bridge; **b** detail of rust signals

in the design report [11], the investigated bridge was built in 1966 in substitution of an older timber structure. The older bridge was designed in 1877 by Francesco Polatti and built by the “Stabilimento Nazionale di Costruzioni in ferro Pietro Bizzarini” [11]. The project of the newer bridge involved the substitution of the deck with the aforementioned steel–concrete composite structure, the construction of a new abutment in reinforced concrete and the strengthening of the existing piers and abutment, involving mainly the use of inclined and vertical micro-piles for the foundations.

In summary, the bridge underwent different phases of maintenance and reconstruction works that are herein listed:

- 1877—Construction of the original timber bridge;
- 1966—I-girders bridge construction (actual structure) and strengthening of stone masonry piers and abutment;
- 2016—Maintenance of the steel girders with sandblasting and powder coating.

Nowadays, the structure exhibits a fairly good state of preservation with only a few signs of rust expansion, generating the deformation of some diagonal members of the girder (Fig. 3).

3 Hydraulic Investigations

Hydraulic processes on a bridge can develop at different spatial and temporal scales. For this reason, a hydraulic study on a bridge considers processes at the local scale of the bridge up to the river basin scale.

In general, for hydraulic actions on bridges three main categories are usually considered: (i) the hydraulic force on the structure, intended as the lateral load on the piers and the deck; (ii) the erosion of the riverbed at the base of the piers (foundations) that can provoke changes in the structural behaviour of the bridge or even lead to a structural failure; (iii) erosion of the abutment and asportation of the access road embankment due to lateral migration of the river.

3.1 Definition of the Hydraulic Scenario

Hydraulic modelling based on the existing topographic surveys of the river and the basin was performed to evaluate the hydraulic actions (i) and (ii) on the Baghetto bridge.

Figure 4 shows the flow field in the area around the bridge in case of a 200-year flood (the reference event in the Italian code). Adda river runs with a subcritical current and very variable speed depending on the topographic conditions (up to 3.7 m/s). On the left the flow is bounded by the steep valley side, while it can freely expand on the right side, which is not protected by levees or embankments, to occupy part of the agricultural and natural floodplain with water depths up to 2.0 m and low

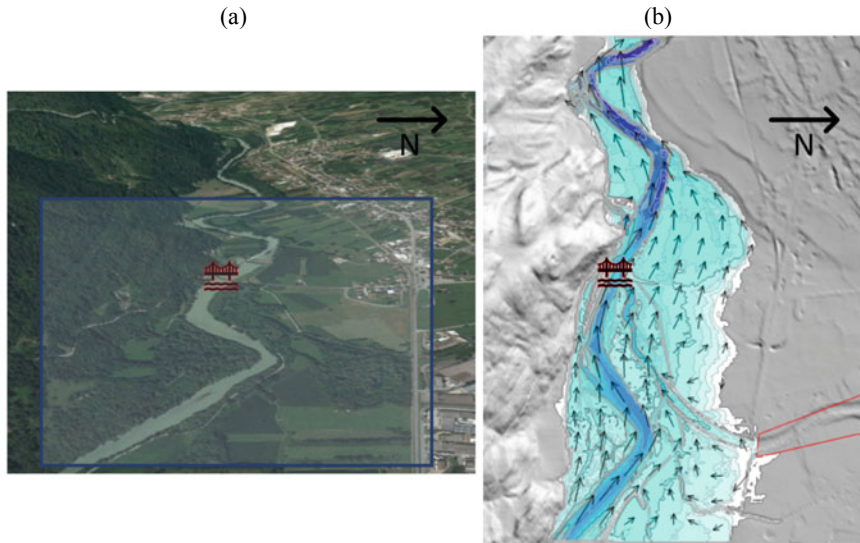


Fig. 4 a View from upstream of Adda river crossed by the bridge. The blue rectangle highlights the 2D model domain of figure (b). The arrows indicate the direction and the intensity of the current velocity up to 3.7 m/s for the event $T = 200$ years. Note the expansion of the river in the right floodplain

speeds (<1.0 m/s). Therefore, the right access road to the bridge, that crosses the floodplain perpendicularly is submerged: embankment is covered in stonemasonry, so that it appears little vulnerable to direct erosion by the flow, at least in a first-level evaluation. A further threat for the right embankment (and shoulder) may come from lateral shift of the riverbed (action (iii)); however, by observing historical aerial and satellite images since 1954, no evident signs of bank erosion—that induces the lateral migration of the river—were noted; lateral erosion may be, therefore, considered as little probable.

The presence of a weir, 150 m downstream of the bridge, used for the exploitation of a hydroelectric power plant, influences the morphology and the hydraulic regime of the river upstream. The main result from the simulation is that the bridge is hit by the current at the level of the deck with a water depth equal to 5.6 m (with respect to the lowest point of the riverbed at the bridge) and a depth-averaged-flow velocity equal to 2.63 m/s. Therefore, the bridge results to be inadequate with respect to the Italian code, which states that the distance between the water surface and the deck must be not lower than 1 m. Moreover, in case of debris transport (trees' logs, shrubs, etc.), the vegetation would increase the hydrodynamic force on the structure by hitting the deck or occluding one or more spans. The observation of historical series of satellite images and the visual inspection carried out at the bridge did not show evidence of frequent debris accumulation at the bridge. However, the same may not be valid in case of extreme events.

3.2 Hydraulic Actions on the Bridge

In this section hydraulic actions on the structure are estimated from a quantitative point of view.

Loads on deck and piers. Both hydrostatic and hydrodynamic force act on the bridge, due to the difference of water depths between upstream and downstream of the structure. The hydraulic force is calculated singularly for each structural element (the piers and the deck).

The two piers have equivalent hydraulic conditions. Assuming a drag coefficient equal to 1.33 [12] on each pier, the total hydraulic force along the river current direction is equal to 93 kN (45 and 48 kN for the hydrostatic and hydrodynamic component, respectively), as shown in Fig. 5a. Note that the static component weighs about half

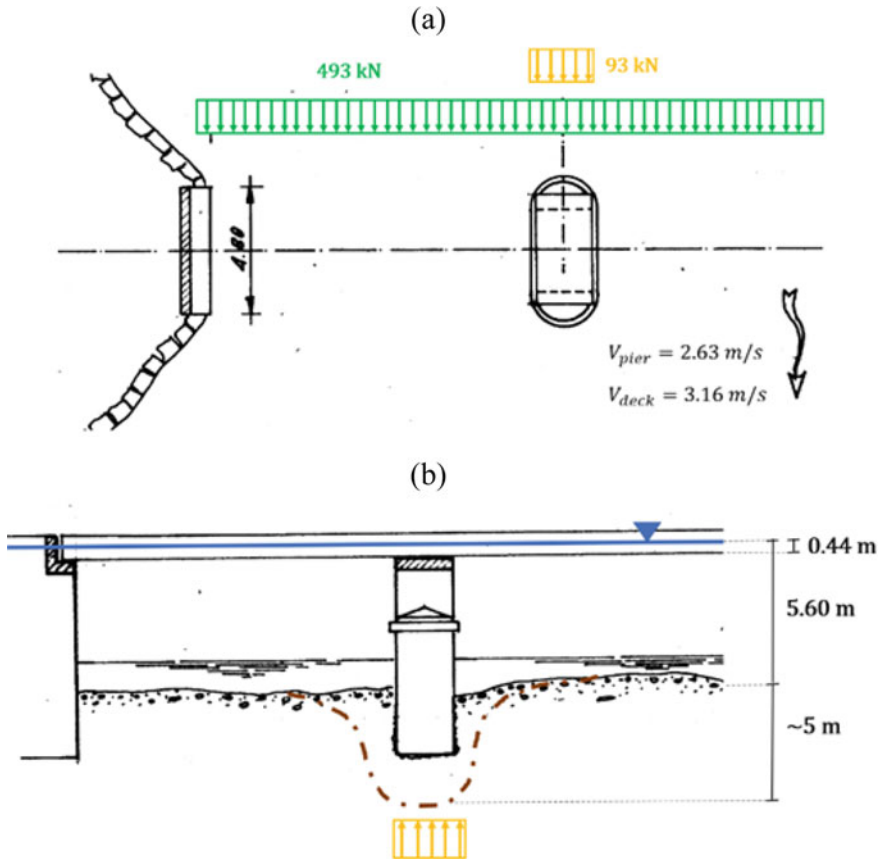


Fig. 5 Hydraulic actions on the bridge for a 200-year event: **a** plan view of the total lateral force acting on one pier (yellow) and on the deck (green); **b** longitudinal view of the buoyancy force acting on one pier and of the maximum estimated scour depth

of the total. Considering that the static component is approximately proportional to the difference in water level between upstream and downstream, there is a considerable uncertainty in the calculation of this value. In fact, the water level difference is approximately equal to the energy losses at the bridge, in turn governed by the concentrated loss coefficients. These coefficients represent an element of significant arbitrariness in the hydraulic calculation. For example, a variation from the standard values for a bridge ($m_1 = 0.3$; $m_2 = 0.5$) to the typical values of the most abrupt transitions ($m_1 = 0.5$; $m_2 = 0.8$), produces an increase of 29% to the total force calculated for the 200-year event.

For the calculation of the lift component, only the buoyancy force has to be considered. The up-thrust corresponds to a reduction of 10 kN/m^3 of the specific weight of the submerged part of the structure.

For the calculation of the hydraulic force on the deck, it was assumed a surface of impact $A = 22.31 \text{ m}^2$ ($L = 50.70 \text{ m}$; $h = 0.44 \text{ m}$) and a current velocity $V = 3.16 \text{ m/s}$, increased of the 20% with respect to the depth-averaged velocity, according to the typical vertical velocity profile. The total force along the river current direction is equal to 493 kN (123 and 370 kN for the static and dynamic component, respectively).

Drag coefficient is chosen according to Parola et al. [13], indicating the value $C_d = 1.9$ as the upper envelope of the coefficient for a rectangular prismatic obstacle.

For what concerns the vertical component of the force, the static component depends on the submerged volume of the deck. In the most extreme condition, when the air is entrapped between the beams, the buoyancy force can reach 1000 kN. Few experiments exist for the evaluation of the lift dynamic coefficient of a submerged deck. Relying on Malavasi and Guadagnini [14], it was calculated a negative lift force (downward direction) of the same order of magnitude of the buoyancy force.

To have better perception of the lateral hydraulic loads, it is possible to compare it to the lateral wind load acting on the deck, although it was not considered in the design loads of the bridge. For a column of trucks that occupies the bridge in length and 3 m in height (to be added to the thickness of the deck, equal to 1 m) and wind speed equal to 25 m/s, the resulting force is equal to 155 kN.

Erosion processes on foundations. The erosion of the riverbed, reducing the level of the ground around the foundations of the piers and abutments, can affect the stability of the entire structure.

Erosion is a cyclic process that can develop at different spatial and temporal scales. Whereas the processes are characterized by very distinct spatial scales, their effects remain separate and can simply be added. The general degradation of the river bed at the largest scales (both spatial and temporal) can be excluded due to the presence of the weir, which stabilizes the topographic longitudinal profile of the riverbed. At smaller scales, local and contraction erosions around the piers may arise during an extreme event. Local erosion is due to the presence of the pier which creates vortices at their base. On the other hand, contraction scour is caused by the increase of velocity generated by the constriction of the cross-section area of the riverbed at the bridge.

In the literature there are several models that estimate the maximum scour depth that may develop at pier foundations in case of flood. The local scour was calculated

through CSU equation [15] and Melville model [16]. Both approaches estimate a maximum scour depth of approximately 5 m. Contraction scour, calculated through Larsen model, is equal to 2 m. In this case study, local and contraction scour processes act at similar spatial scale. Thus, it seems more appropriate to consider only the most severe of the contributes, and not the sum of the two (Fig. 5 b). However, a post-event survey of the riverbed should verify the likelihood of this estimate, which is mainly based on laboratory tests.

The evaluation of the resultant bearing capacity of the foundation in case of extreme event was not assessed in this paper. According to the original blueprints, a pile cap with a group of piles support the piers 7 m below the ground. A 5 m lowering of the riverbed elevation could therefore threat the stability of the structure.

4 Ambient Vibration Testing and Modal Identification

In order to evaluate the dynamic characteristics of the bridge in operational conditions, an ambient vibration test (AVT) was performed on July 20th, 2020. During the test, the vertical and transverse structural response was measured: three cross-sections for each span were instrumented for a total of eighteen measuring positions. 24-bit resolution DAQs and high sensitivity (10 V/g) piezo-electric accelerometers and servo accelerometers were used during the tests. The structural responses to ambient and operational excitation were recorded at a sampling frequency of 200 Hz and datasets of 3600 s were collected.

The modal identification was carried out applying the Frequency Domain Decomposition (FDD) technique [17].

Only the vertical dynamic characteristics are herein discussed. Figure 6 shows the results of the data processing in terms of the largest singular value (SV) lines for each span in the range of 0–26 Hz. Four vibration modes are identified by the local maxima of the first SV line for the longest spans S1 and S2 (Fig. 6a, b), whereas two vibration modes are identified for the shortest span S3 (Fig. 6c). The corresponding mode shapes are reported in Fig. 7: the mode shapes follow the expected sequence of bending (B) and torsion (T) modes of first and second order.

5 FE Modelling and Updating

The 3D numerical model of the bridge (Fig. 8) was developed with MIDAS software. In particular, the three main girders, as well as the diagonals and transverse trusses, are simulated by frame elements with appropriate cross-sections. The concrete deck is modelled through 4-noded rectangular shell elements and the connection between the shell elements and the main girders is performed with rigid links with the rotation along the vertical direction released. The connection between the bracings and the chords was assumed as an ideal hinge.

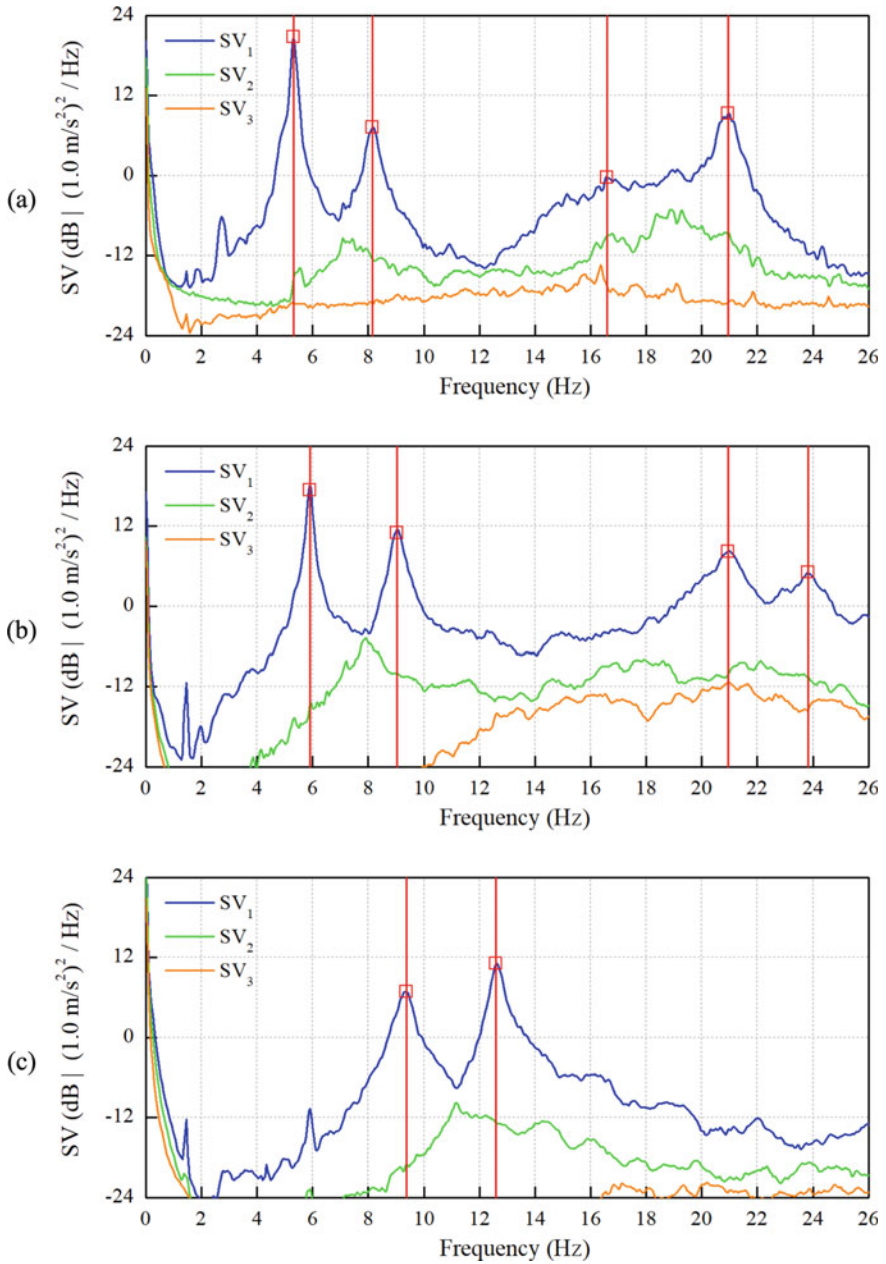


Fig. 6 Largest singular value (SV) lines and identification of natural frequencies (FDD): **a** Span S1, **b** Span S2 and **c** Span S3

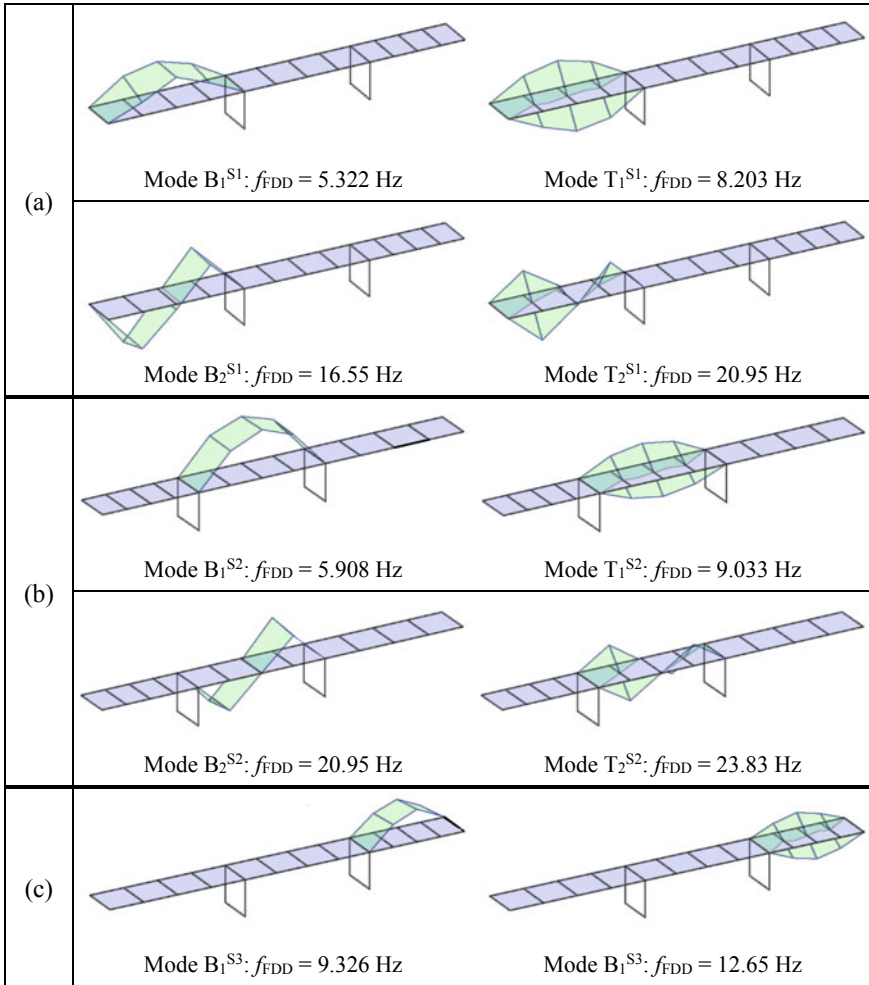


Fig. 7 Vibration modes identified from AVT: **a** Span S1, **b** Span S2 and **c** Span S3

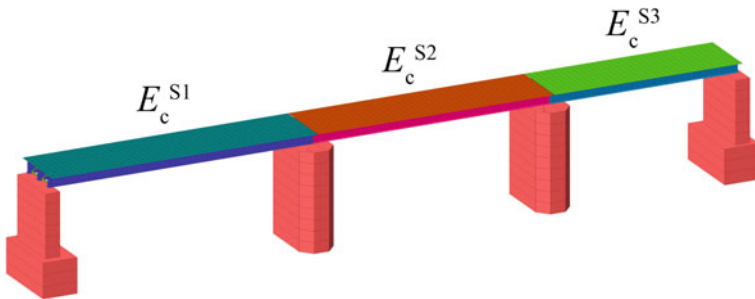


Fig. 8 FE model of the Baghetto bridge with the indication of the calibrated parameters

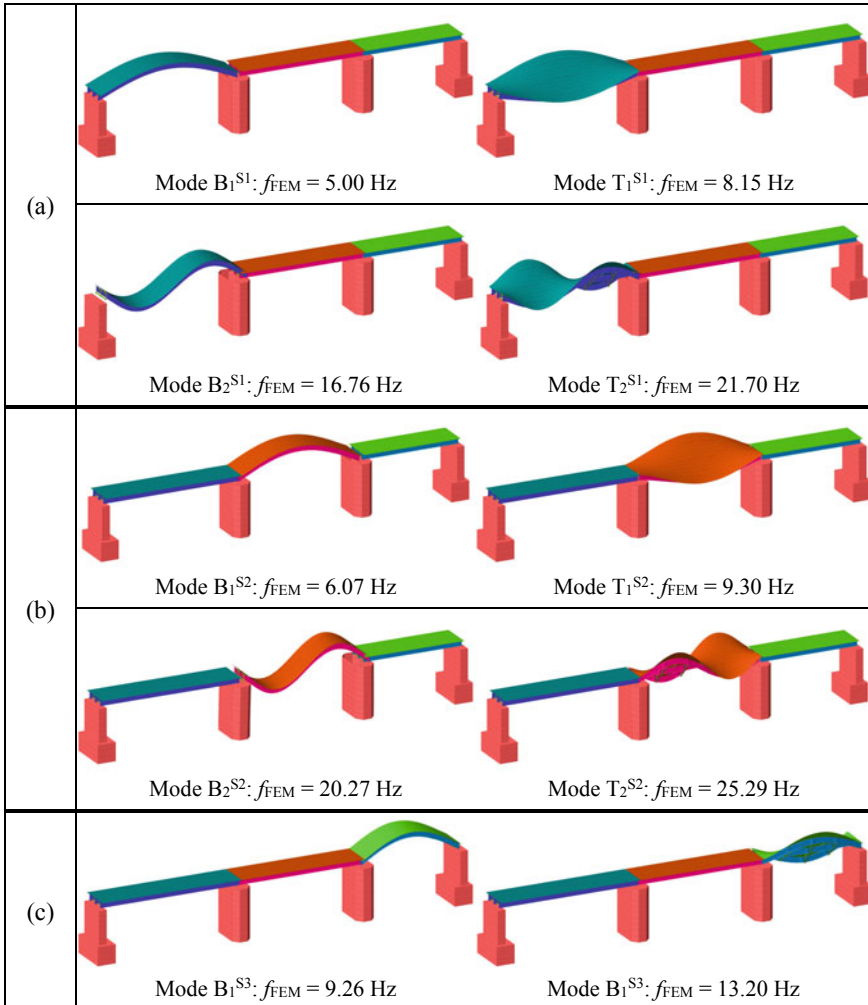


Fig. 9 Vibration modes of the updated model: **a** Span S1, **b** Span S2 and **c** Span S3

In total, a relatively large number of elements were employed to obtain a regular distribution of masses, a good description of geometrical details and to avoid frequency sensitivity to mesh size. Overall, the numerical model consists of 816 elements, 6441 nodes and an average mesh size of 0.7 m (Fig. 8).

Once the geometry of the numerical model is established, the selection of the structural parameters to be updated is the next key issue. Broadly speaking, the following aspects should be always considered to prevent the ill-conditioning of the inverse problem and to improve the robustness of the updated parameter estimates: (i) consider a smaller number of updating variables than experimental parameters used as targets; (ii) update only the uncertain structural parameters; (iii) check the

Table 1 Comparison between experimental and numerical frequencies

Mode Id	Exp	Base model		Manual tuning	
	f_{FDD} (Hz)	f_{FEM} (Hz)	DF (%)	f_{FEM} (Hz)	DF (%)
B_1^{S1}	5.32	4.94	-7.11	5.00	-6.08
T_1^{S1}	8.15	7.91	-2.89	8.15	0.02
B_2^{S1}	16.55	16.59	0.26	16.76	1.25
T_2^{S1}	20.95	21.24	1.36	21.70	3.58
B_1^{S2}	5.90	6.10	3.35	6.07	2.79
T_1^{S2}	9.03	9.40	4.08	9.30	3.03
B_2^{S2}	20.95	20.34	-2.90	20.27	-3.23
T_2^{S2}	23.83	25.48	6.91	25.29	6.13
B_1^{S3}	9.33	9.30	-0.36	9.26	-0.69
T_1^{S3}	12.70	13.33	4.92	13.20	3.93
$DF_{ave}(\%)$			3.42		3.07
$DF_{max}(\%)$			7.11		6.13

sensitivity of natural frequencies to the selected parameters and avoid low-sensitivity structural parameters. In addition to the latter considerations, the following assumption were adopted for the Baghetto bridge: (a) the effect of soil-structure interaction was neglected, (b) all the materials were considered isotropic with constant mass density ($\gamma_s = 7850 \text{ kg/m}^3$; $\gamma_c = 2400 \text{ kg/m}^3$) and Poisson’s ratio ($\nu_s = 0.3$; $\nu_c = 0.2$), (c) the concrete deck was assumed 0.18 m thick based on the original blueprints, (d) a mass per unit area of 200 kg/m^2 was applied on the concrete slab to account for the non-structural masses (i.e. asphalt and curbs).

An initial FE model (Base model) was developed to check the similarity between experimental and numerical modal parameters. The initially adopted elastic modulus of steel and concrete was set equal to 205 GPa and 32 GPa, respectively. The results in term of natural frequencies are shown in Table 1: the sequence of vibration modes corresponds to the observed one while the frequency discrepancy ($DF = f_{FEM}/f_{FDD} - 1$) between experimental (f_{FDD}) and numerical values (f_{FEM}) exhibits an acceptable correspondence, with the major difference being equal to 7% for the first bending mode of the first span.

In order to improve the quality of the match between numerical and experimental frequencies, a manual tuning procedure was performed considering the structural parameter that is mostly affected by uncertainty, namely the elastic modulus of the concrete deck (E_c). As shown in Fig. 8, the parameter E_c was considered separately for each span.

The manual tuning procedure involved the variation of the selected parameter in a constrained range until a minimum in the average discrepancy function (DF_{ave}) was found. For the first span (S1) the best solution was obtained with E_c being equal to 35 GPa, while for the other two spans (S2 and S3) the minimum was obtained with E_c being equal to 31 GPa. As shown in Table 1, the correlation with the experimental

natural frequencies have been increased, achieving a preliminary validation of the numerical model with a discrete accuracy (Fig. 9).

6 Conclusions

The paper focuses on the multidisciplinary investigations performed on the Baghetto bridge (Sondrio Province, Italy), within a recent collaboration between Politecnico di Milano and Regione Lombardia, aimed at the definition of criteria and guidelines for the maintenance and management of roadway infrastructures.

The investigations on the Baghetto bridge included documentary research, hydraulic study, ambient vibration testing, FE modelling and updating. From the attained results, the following conclusions can be drawn:

- (1) The hydraulic load on the bridge and the maximum scour depth in case of flood event were estimated, with some uncertainties, through the hydraulic study;
- (2) During the AVT, performed with the bridge fully open to traffic, 10 vertical vibration modes (4 modes for spans 1–2 and 2 for span 3) were identified in the frequency range of 0–26 Hz;
- (3) The identified natural frequencies allowed the manual tuning of the elastic modulus of the concrete deck—the structural parameter affected by the higher uncertainties—obtaining a preliminary calibration of the model ($DF_{ave} = 3.07\%$, $DF_{max} = 6.13\%$).

The adopted SHM strategy for Baghetto bridge, namely periodic dynamic testing, involves the execution of other AVTs in the next months, also including the analysis of the lateral modal behaviour. In addition, to conclude the structural evaluation of the bridge, the estimated hydraulic loads and the scour depth, and the updated FE model will be used to predict the expected variations in the modal parameters of the structure.

Acknowledgements The support of Regione Lombardia is gratefully acknowledged. Sincere thanks are due to G. Cazzulani, PhD (MECC, Politecnico di Milano) who assisted the authors in conducting the field tests.

References

1. Wardhana K, Hadipriono FC (2003) Analysis of recent bridge failures in the United States. *J Perform Construct Facil* 17(3):144–150
2. Imhof D (2004) Risk assessment of existing bridge structures. PhD Thesis, University of Cambridge, UK
3. Ballio F, Bianchi A, Franzetti S, De Falco F, Mancini M (1998) Vulnerabilità idraulica dei ponti fluviali. *XXVI Convegno Nazionale di Idraulica e Costruzioni Idrauliche* 3:69–80

4. Salawu OS, Williams C (1995) Review of full-scale dynamic testing of bridge structures. *Eng Struct* 17(2):113–121
5. Gentile C, Martinez y Cabrera F (1997) Dynamic investigation of a repaired cable-stayed bridge. *Earthq Eng Struct D* 26(1):41–59
6. Carden EP, Fanning P (2004) Vibration based condition monitoring: a review. *Struct Health Monit* 3(4):355–377
7. Brownjohn JMW, Magalhaes F, Caetano E, Cunha A (2010) Ambient vibration re-testing and operational modal analysis of the Humber Bridge. *Eng Struct* 32(8):2003–2018
8. Brownjohn JMW, de Stefano A, Xu Y-L, Wenzel H, Aktan AE (2011) Vibration-based monitoring of civil infrastructure: Challenges and successes. *J Civil Struct Health Monit* 1(3–4):79–95
9. Fan W, Qiao P (2011) Vibration-based damage identification methods: a review and comparative study. *Struct Health Monit* 10(1):83–111
10. Ministero delle Infrastrutture e dei Trasporti–Consiglio Superiore dei Lavori Pubblici: Linee guida per la classificazione e gestione del rischio, la valutazione della sicurezza ed il monitoraggio dei ponti esistenti
11. Ufficio Tecnico Provinciale di Sondrio (1966) Progetto per la ricostruzione del ponte del Baghetto sull’Adda della strada provinciale da Castello dell’Acqua alla Stazione F.A.V. di Chiuro – Relazione
12. Lindsey WF (1938) Drag of cylinders of simple shapes. National Advisory Committee for Aeronautics (NACA) Technical Report 619
13. Parola AC, Apelt CJ, Jempson MA (2000) Debris forces on highway bridges. *Transp Res Board*
14. Malavasi S, Guadagnini A (2007) Interactions between a rectangular cylinder and a free-surface flow. *J Fluids Struct* 23:1137–1148
15. U.S Department of Transportation (2012) Federal highway administration: hydraulic engineering circular n. 18. Evaluation Scour at Bridges. Publication n. FHWA-HIF-12-003
16. Melville BW, Coleman SE (2000) Bridge scour. Water Resources Publication LLC
17. Brincker R, Zhang LM, Andersen P (2001) Modal identification of output-only systems using frequency domain decomposition. *Smart Mater Struct* 10(3):441–445

Data Management in Structural Health Monitoring



Elia Favarelli , Enrico Testi , and Andrea Giorgetti 

Abstract With the advent of 5G and the future 6G communication systems, the number of devices interconnected to the network will increase exponentially, offering unprecedented monitoring capability. The autonomous structural health monitoring (SHM) of many structures and bridges represents an important application that can exploit such capability; however, generating a considerable amount of data that must be elaborated and managed. In such a scenario, this paper proposes a set of machine learning (ML) tools to detect anomalies in a bridge from vibrational data. The proposed framework starts from the first two fundamental frequencies extracted through operational modal analysis (OMA) and clustering, followed by a density-based time-domain tracking algorithm. The fundamental frequencies extracted are then fed to one-class classification (OCC) algorithms that perform anomaly detection. Then, the effect of reducing the number of sensors used to monitor the network, the number of bits used to quantize the accelerometric measurements, and the observation time is reported, with the purpose to reduce the amount of data stored without degrading the damage detection capability of the system. As a case study, the Z-24 bridge is considered because of the extensive database of accelerometric measurements in both standard and damaged conditions. In numerical results a widely comparison of OCC algorithms is reported; more in detail, principal component analysis (PCA), kernel principal component analysis (KPCA), Gaussian mixture model (GMM) and one-class classifier neural network (OCCNN)² are tested and their robustness is evaluated. In many cases, OCCNN² algorithm increases the performance with respect to classical anomaly detection techniques in terms of accuracy. Moreover, it is observed that only three sensors are sufficient to accomplish the anomaly detection task and that the number of bits and the observation time can be reduced considerably without affecting the algorithms performance.

E. Favarelli (✉) · E. Testi · A. Giorgetti
Department of Electrical, Electronic, and Information Engineering Guglielmo Marconi,
University of Bologna, 40136 Bologna, Italy
e-mail: elia.favarelli@unibo.it

E. Testi
e-mail: enrico.testi@unibo.it

A. Giorgetti
e-mail: andrea.giorgetti@unibo.it

Keywords Anomaly detection · Dimensionality reduction · Modal analysis · Neural network · Structural health monitoring · Vibration measurement.

1 Introduction

Nowadays, structural health monitoring (SHM) represents a fundamental research field in a society where historical and modern infrastructures coexist harmoniously. In this scenario, despite replacing the existing infrastructures, buildings, and bridges with functionally and economically costly solutions, it is preferred to maintain and protect the existing structures [1]. This preservation can be achieved through appropriate monitoring.

As far as bridges are concerned, some statistics highlight the relevance of the problem. For example, currently, in Italy there are almost 2,000 bridges that require special monitoring; in France, 4,000 bridges need to be restored, and 840 are considered in critical conditions; in Germany, 800 bridges are reputed critic; in the United States of America, among the 600,000 bridges, according to a conservative estimate, at least 1% of them is considered deficient. In this sense, SHM offers numerous solutions for anomaly detection [2–4].

In literature, numerous damage detection and localization strategies have been presented and tested [5, 6]. Part of them focuses on the extraction of the most significant damage-sensitive features of the structure under analysis. Such techniques can be divided into model-free and model-based: in the former, information is gathered by measurements (e.g., acceleration, temperature, position), while in the latter, data comes from measurements and prior knowledge of a model of the structure [7].

Since the whole procedure results complex and requires a specific fine-tuning of several parameters that depend on the structure under analysis, the adoption of machine learning (ML) techniques to detect changes in the damage sensitive features received increasing interest recently [8–12].

In this work, we attempt to investigate strategies to detect anomalies in bridges and structures with a reduced number of sensors, samples, and resolution bits, to find low-cost solutions and reducing the data storage requirements, with the aim to extend this strategy to an extensive set of infrastructures. The proposed framework starts from the fundamental frequencies extraction from the accelerometer measurements through stochastic subspace identification (SSI), cleaning, and clustering [7, 8, 14–18] and then performs modal frequencies tracking in the time domain [11]. The first two fundamental frequencies are then considered as a feature space used to train one-class classifiers to perform damage detection. In particular, the main contributions are the following:

- We compare several ML algorithms performance for the anomaly detection task.
- We propose strategies to reduce the amount of data stored to detect anomalies in structures.
- We investigate the effect of sensor failure on algorithm performance.

- We evaluate the effects of reducing the number of samples on the classification accuracy.
- We consider the effect of resolution bits to account for low-cost sensors unavoidable in large-scale monitoring.

The performance of the proposed solution is investigated on a real dataset using the accelerometric data available for the Z-24 bridge [19, 20]. The proposed anomaly detection algorithms principal component analysis (PCA), kernel principal component analysis (KPCA), Gaussian mixture model (GMM), and one-class classifier neural network (OCCNN)² are compared in terms of accuracy.

Throughout the paper, capital boldface letters denote matrices and tensors, lowercase bold letters denote vectors, $(\cdot)^T$ stands for transposition, $\|\cdot\|$ is the ℓ_2 -norm of a vector, and $\mathbb{1}\{a, b\}$ is the indicator function equal to 1 when $a = b$, and zero otherwise.

The paper is organized as follows. In Sect. 2, a brief overview of the acquisition system, the accelerometers setup, and the monitoring scenario is presented. The fundamental frequencies extraction technique adopted is rapidly revised in Sect. 3. A survey of anomaly detection techniques is reported in Sect. 4. The traffic generated by the acquisition system and some possible strategies to reduce it are presented in Sect. 5. Numerical results are given in Sect. 6. Conclusions are drawn in Sect. 7.

2 System Configuration

The Z-24 bridge was located in the Switzerland canton Bern. The bridge was a part of the road connection between Koppigen and Utzenstorf, overpassing the A1 highway between Bern and Zurich. It was a classical post-tensioned concrete two-cell box girder bridge with a main span of 30 m and two side spans of 14 m. The bridge was built as a freestanding frame with the approaches backfilled later. Both abutments consisted of triple concrete columns connected with concrete hinges to the girder. Both intermediate supports were concrete piers clamped into the girder. An extension of the bridge girder at the approaches provided a sliding slab. All supports were rotated with respect to the longitudinal axis that yielded a skew bridge. The bridge was demolished at the end of 1998 [19]. During the year before its demolition, the bridge was subjected to long-term continuous monitoring to quantify the bridge dynamics' environmental variability. Moreover, progressive damage tests took place over a month, shortly before the complete demolition of the bridge, alternated with short-term monitoring tests while the continuous monitoring system was still running. The tests proved experimentally that realistic damage has a measurable influence on bridge dynamics.

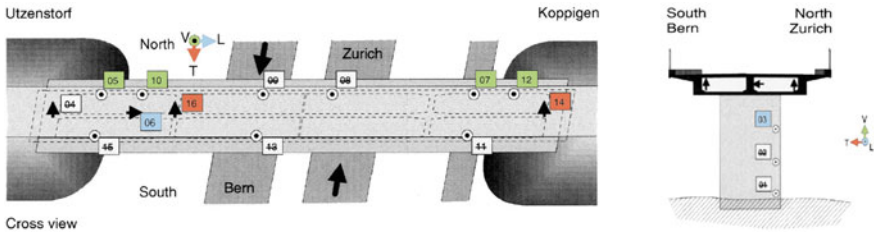


Fig. 1 Data acquisition setup along the Z-24 bridge: the selected accelerometers, their positions, and the measured acceleration direction [13].

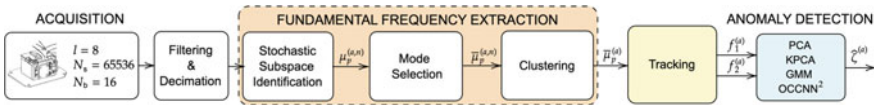


Fig. 2 Block diagram for signal acquisition, processing, feature extraction, tracking, and anomaly detection

2.1 Data Collection

The accelerometer’s position and their measurement axis are shown in Fig. 1. In this work, we considered $l = 8$ accelerometers, identified as 03, 05, 06, 07, 10, 12, 14, and 16, which are present in both long-term continuous monitoring phase and in the progressive damage one.¹ The accelerometer orientation is highlighted in Fig. 1 with different colors, red, green, and blue, staying respectively for transversal, vertical, and longitudinal orientation. Every hour $N_s = 65, 536$ samples are acquired from each sensor with sampling frequency $f_{\text{samp}} = 100$ Hz which corresponds to an acquisition time $T_a = 655.36$ s. Since the measurements are not always available, there are $N_a = 4, 107$ acquisitions collected in a period of 44 weeks.

2.2 Data Pre-processing

The block diagram depicted in Fig. 2 represents the sequence of tasks performed for the fully automatic anomaly detection approach presented in this work.

Some pre-processing steps have been applied to the data to reduce disturbs, the computational cost, and the memory occupation of the subsequent elaborations. First, a decimation by a factor of 2 is applied to each acquisition; hence the sampling frequency is scaled to $f_{\text{samp}} = 50$ Hz. Such sampling frequency is considered sufficient because the Z-24 fundamental frequencies fall in the [2.5, 20] Hz frequency range

¹ Some accelerometers that experienced failures during the long-term monitoring have been avoided.

[19]. After decimation, data are processed with a finite impulse response (FIR) band-pass filter of order 30 with band [2.5, 20] Hz, to remove disturbances outside the band of interest.

At the end of the decimation step, the amount of samples for each acquisition N_{dec} is already halved ($N_{dec} = N_s/2 = 32,768$) and that represent a first important step in the data management process.

3 Frequency Extraction and Data Partitioning

The fundamental frequencies extraction chain is depicted in Fig. 2; from the vibrational data the fundamental modes $\mu_p^{(a,n)}$ are extracted through the widely known SSI algorithm [7], where p represent the p th mode, a stays for the acquisition index, and n represent the model order varied in the range $n \in [2, 160]$ (with step 2) [11]. The resulting modes can be cleaned up by the spurious ones through classical mode selection methods (i.e., modal assurance criterion (MAC), mean phase deviation (MPD), complex conjugate poles check, and damping ratios check) [15, 17, 18, 21] and clustered with the K -means algorithm [8, 14]. The residual modes after selection are represented with $\tilde{\mu}_p^{(a,n)}$, and the modes after clustering with $\bar{\mu}_p^{(a)}$. The results of this approach applied for all the acquisitions are the blue points depicted in Fig. 3. After that, a density-based mode tracking algorithm is proposed to track the fundamental frequencies; firstly the algorithm is initialized evaluating 200 acquisition to detect the number of tracks s and their starting position, after that through a Gaussian kernel evaluation their position is update step-by-step for each acquisition [11]. At the end of the tracking algorithm the first two fundamental frequency tracks $\mathbf{f}_s = \{f_s^{(a)}\}_{a=1}^{N_a}$ with $s \in \{1, 2\}$ are extracted and stored in the following matrix (see also Fig. 3b)

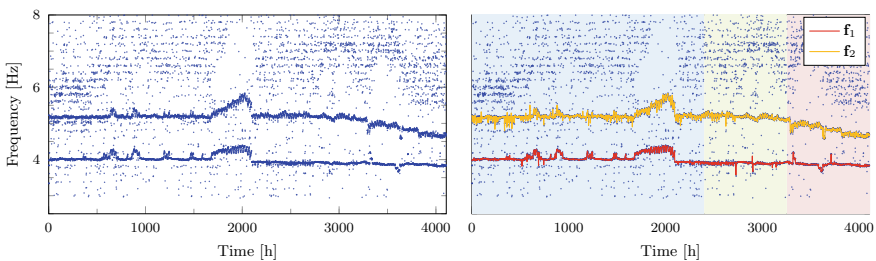


Fig. 3 On the left, fundamental frequencies extracted through SSI for each measurement on the right first two natural frequencies estimation after the density-based tracking algorithm. Blue and green backgrounds highlight the acquisitions made during the bridge’s normal condition, used respectively as training and test sets, while the red background stands for damaged condition acquisitions used in the test phase

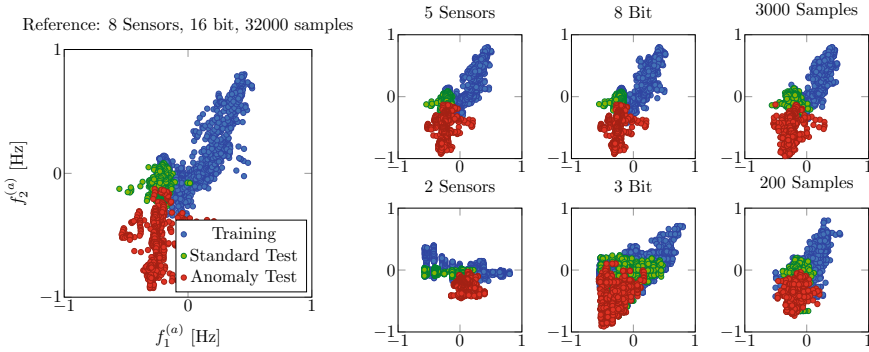


Fig. 4 Examples of feature transformation due to the effect of a low number of sensors, a low number of bits, and a low number of samples with respect to the standard measurement condition reported on the left

$$\mathbf{F} = \begin{bmatrix} \mathbf{f}_1 \\ \mathbf{f}_2 \end{bmatrix}^T = \begin{bmatrix} f_1^{(1)} & f_1^{(2)} & \dots & f_1^{(N_a)} \\ f_2^{(1)} & f_2^{(2)} & \dots & f_2^{(N_a)} \end{bmatrix}^T.$$

At this point, the fundamental frequencies extracted must be divided into training, test in standard condition, and test in damaged conditions sets. As described in [19], the damage is introduced at the acquisition $a = N_d = 3, 253$, corresponding to the installation of a lowering system. Therefore, from now on, the matrix $\bar{\mathbf{X}} = \mathbf{F}_{1:2N_d-N_a-1,:}$ contains the training points (blue background in Fig. 3b), $\bar{\mathbf{Y}} = \mathbf{F}_{2N_d-N_a:N_d-1,:}$ contains the test points in standard condition (green background in Fig. 3b), and $\bar{\mathbf{U}} = \mathbf{F}_{N_d:N_a,:}$ contains the test points in damaged condition (red background in Fig. 3b). The three subsets of acquisitions that correspond to training, standard test, and damaged test points are, respectively, $\mathcal{I}_x = \{1, \dots, 2N_d - N_a - 1\}$, $\mathcal{I}_y = \{2N_d - N_a, \dots, N_d - 1\}$, and $\mathcal{I}_u = \{N_d, \dots, N_a\}$.

Let us define the offset $\hat{\mathbf{x}}$ as the column vector containing the row-wise mean of the matrix $\bar{\mathbf{X}}$, and the rescaling factor $x_m = \max_{a,s} |\bar{x}_{a,s} - \hat{x}_a|$. Before proceeding with the anomaly detection, the matrices $\bar{\mathbf{X}}$, $\bar{\mathbf{Y}}$ and $\bar{\mathbf{U}}$ are centered and normalized subtracting the offset $\hat{\mathbf{x}}$ row-wise and dividing each entry by the rescaling factor x_m . The resulting data matrices are \mathbf{X} , \mathbf{Y} and \mathbf{U} , of size $N_x \times D$, $N_y \times D$, and $N_u \times D$, respectively, with $D = 2$ features. The result of this procedure is depicted on the left of Fig. 4.

4 Survey of Anomaly Detection Techniques

In this section we briefly review PCA, KPCA, GMM which are often adopted for one-class classification (OCC) and introduce OCCNN², a neural network based approach recently presented [22–26].

4.1 Principal Component Analysis

This technique remaps the training data from the feature space \mathbb{R}^D in a subspace \mathbb{R}^P (where $P < D$ is the number of components selected) that minimizes the Euclidean distance between the data in the feature space and their projection into the chosen subspace [27]. To find the best subspace to project the training data, the evaluation of the $D \times D$ sample covariance matrix

$$\Sigma_x = \frac{\mathbf{X}^T \mathbf{X}}{N_x - 1} \quad (1)$$

is needed. The sample covariance matrix Σ_x can be factorized by eigenvalue decomposition as $\Sigma_x = \mathbf{V}_x \Lambda_x \mathbf{V}_x^T$, where \mathbf{V}_x is an orthonormal matrix whose columns are the eigenvectors, while Λ_x is a diagonal matrix that contains the D eigenvalues. The eigenvalues magnitude represents the importance of the direction pointed by the relative eigenvector. In our setting we select the largest component, hence $P = 1$, therefore the best linear subspace of dimension one is \mathbf{v}_P , which coincides with the eigenvector related to the largest eigenvalue of Σ_x . The projection into the subspace is obtained multiplying the data by \mathbf{v}_P , i.e., $\mathbf{x}_P = \mathbf{X} \mathbf{v}_P$, $\mathbf{y}_P = \mathbf{Y} \mathbf{v}_P$, and $\mathbf{u}_P = \mathbf{U} \mathbf{v}_P$.

The error is evaluated reconstructing the data in the original feature space, i.e., $\tilde{\mathbf{X}} = \mathbf{x}_P \mathbf{v}_P^T$, $\tilde{\mathbf{Y}} = \mathbf{y}_P \mathbf{v}_P^T$, and $\tilde{\mathbf{U}} = \mathbf{u}_P \mathbf{v}_P^T$. After the reconstruction, it is possible to calculate the error as the Euclidean distance between the original and reconstructed data.

Unfortunately, PCA is usually ineffective with a low number of monitored modes; moreover, the variability of the frequencies estimated due to environmental effects can affect the PCA performance [28]. This is because PCA can find only linear boundaries in the original feature space; hence it is recommended when the problem dimensionality of the problem is high and the boundaries between the classes can be considered linear.

4.2 Kernel Principal Component Analysis

Due to the inability of PCA of finding non-linear boundaries, here we propose KPCA as an alternative [29]. KPCA firstly maps the data with a non-linear function, named kernel, then applies the standard PCA to find a linear boundary in the new feature space. The kernel function, applied to the linear boundary, makes it non-linear in the original feature space. A delicate point in the development of KPCA algorithm is the kernel function choice. In [30], where the data distribution is unknown, the radial basis function (RBF) kernel is proposed as the right candidate. Given a generic point \mathbf{z} that correspond to a $1 \times D$ vector, we can apply the RBF as

$$K_n^{(\mathbf{z})} = e^{-\gamma \|\mathbf{z} - \mathbf{x}_n\|^2}, \quad \text{with } n = 1, 2, \dots, N_x \quad (2)$$

where γ is a kernel parameter (which controls the width of the Gaussian function) that must be set properly, \mathbf{x}_n is the n th row of \mathbf{X} , and $K_n^{(\mathbf{z})}$ is the n th component of the point \mathbf{z} in the kernel space. Overall, the vector \mathbf{z} is mapped in the vector $\mathbf{k}^{(\mathbf{z})} = [K_1^{(\mathbf{z})}, K_2^{(\mathbf{z})}, \dots, K_{N_x}^{(\mathbf{z})}]$. Remapping all the data in the kernel space, we obtain the subsequent matrices \mathbf{K}_x of size $N_x \times N_x$ for training, \mathbf{K}_y of size $N_y \times N_x$ for validation, and \mathbf{K}_u of size $N_u \times N_x$ for test, respectively.

Applying now the PCA to the new dataset, it is possible to find non-linear boundaries in the original feature space.

4.3 Gaussian Mixture Model

Another well-known data analysis tool, named GMM, has been used to solve OCC problems in literature [31]. This approach assumes that data can be represented by a mixture of \mathcal{M} multivariate Gaussian distributions. The outputs of the algorithm are the covariance matrices, Σ_m , and the mean values, μ_m , of the Gaussian functions, with $m = 1, 2, \dots, \mathcal{M}$. The GMM algorithm finds the set of parameters Σ_m and μ_m of a Gaussian mixture that better fit the data distribution through iterative algorithms like stochastic gradient descent or Newton-Raphson [8, 9].

4.4 One-Class Classifier Neural Network²

This algorithm exploits the flexibility of the standard feed-forward neural network (NN) in an anomaly detection problem. It is based on the OCCNN paradigm [24] that provide to generate artificially anomalous points with a spatial density proportional to the one inferred by the Pollard's estimator [32]. Such anomalous points will be used during the training to estimate the class boundaries. This procedure is repeated several times to refine the edges step-by-step. Unfortunately, Pollard's estimator may exhibit accuracy degradation when the dataset points distribution deviates from Poisson. Based on these considerations, the OCCNN² share the same strategy of OCCNN but the first boundary estimation is made by an autoassociative neural network (ANN) that provide good boundaries estimation also with non-Poisson data distributions [11].

5 Data Management

This section analyzes the amount of data that must be stored to perform anomaly detection on the vibrational waveforms and some strategies that can be implemented to reduce such volume of data. Considering a network of $l = 8$ synchronized sensors interconnected to a coordinator that stores the accelerometric measurements, it is

easy to observe that if each sensor collects $N_s = 65,536$ samples each acquisition with $N_b = 16$ resolution bits, the total amount of data stored by the coordinator is $M_t = N_s N_b N_a l \simeq 32 \text{ Gbit} = 4 \text{ GB}$ for $N_a = 4,107$ acquisitions. This considerable amount of data has been stored in an year of non continuous measurements, where the actual acquisition time is $T_t = T_a N_a \simeq 44,860 \text{ m} \simeq 448 \text{ h}$. The volume of data in a continuous measurement system in a year would be around 47 GB. To reduce the mass of data the first step is decimation. Considering that in this application the fundamental frequencies of the bridge fall in the interval $[0, 20] \text{ Hz}$, to comply with the sampling theorem with a guard band of 5 Hz a sampling frequency $f_{\text{samp}} = 50 \text{ Hz}$ is enough to capture the bridge oscillations. Since the measurements are acquired by accelerometers with $f_{\text{samp}} = 100 \text{ Hz}$, a decimation by factor 2 can be adopted so that data volume is halved: $M_d = M_t/2 \simeq 2 \text{ GB}$. Starting from the decimated waveforms, three other tunable parameters can be modified to reduce the volume of data without deteriorating the performance of the OCC algorithms significantly:

- The number of sensors l ; this also reduces the network costs.
- The number of samples N_s or equivalently the acquisition time T_a ; this has benefits also on the energy consumption and network lifetime in battery-powered sensors [33, 34].
- The number of bits N_b ; this also reduces the accelerometer cost.

All these possibilities will be analyzed and widely discussed in the next section. In Fig. 4 some working points of the system are reported and compared with the reference working condition after decimation ($l = 8, N_d = 32,768, N_b = 16$).

6 Numerical Results

In this section, the proposed algorithms are applied to the Z-24 bridge dataset to detect anomaly based on the fundamental frequencies estimation [7, 35, 36], and a reduced number of features. The performance is evaluated through the accuracy, considering only the test set:

$$\text{Accuracy} = \frac{T_P + T_N}{T_P + T_N + F_P + F_N} \quad (3)$$

where T_P , T_N , F_P , and F_N , represent respectively true positive, true negative, false positive, and false negative predictions. Such indicators are obtained comparing the actual labels $[\zeta^{(1)}, \dots, \zeta^{(N_a)}]$, with those predicted by the OCC $[\widehat{\zeta}^{(1)}, \dots, \widehat{\zeta}^{(N_a)}]$. In this application, labels are 0 for normal condition and 1 for anomaly condition, respectively. Therefore,

$$T_P = \sum_{a \in \mathcal{L}_u} \mathbb{1}\{\zeta^{(a)}, \widehat{\zeta}^{(a)}\} \quad \text{and} \quad T_N = \sum_{a \in \mathcal{L}_y} \mathbb{1}\{\zeta^{(a)}, \widehat{\zeta}^{(a)}\}$$

with $F_N = N_u - T_N$, and $F_P = N_y - T_P$. In the case of unbalanced classes in the test set, the F_1 (function 1) score represents a more reliable metric to evaluate the performance regarding accuracy: it is the harmonic mean of precision and recall; a perfect model has an F_1 score equal to 1.

The feature space has dimension $D = 2$, and the three dataset used for training, test in normal condition, and damaged condition, have cardinality $N_x = 2, 399$, $N_y = 854$, and $N_u = 854$, respectively. For PCA, the number of components selected is $P = 1$. For KPCA, after several tests the values of P and γ that ensure the minimum reconstruction error are $P = 3$ and $\gamma = 8$. For GMM the order of the model that maximize performance is $\mathcal{M} = 10$. Regarding the OCCNN² the first step boundary estimation is made by a fully connected ANN with 7 layers of, respectively, 50, 20, 10, 1, 10, 20 and 50 neurons, with ReLU activation functions, and a fully connected NN with 2 hidden layers with $L = 50$ neurons each one for the second step. All the NNs are trained for a number of epochs $N_e = 5, 000$ with a learning rate $\rho = 0.05$. The error adopted to evaluate the points displacement in the feature space from the original position due to the different configurations is the root mean square error (RMSE), defined as

$$\mathcal{E}_f = \frac{1}{\sqrt{N_a N_s}} \sqrt{\sum_{s=1}^{N_s} \sum_{n=1}^{N_a} (f_s^{(n)} - \tilde{f}_s^{(n)})^2} \quad (4)$$

where N_s is the number of features ($N_s = 2$), $f_s^{(n)}$ is the s th feature of the n th acquisition in the initial configuration, and $\tilde{f}_s^{(n)}$ is the relative data point in the modified configuration.

6.1 Sensors Relevance

Before evaluating the effect of reducing the number of sensors, it is informative to evaluate each one's importance in the modal frequencies estimation. It is widely known in the literature that the sensor position strongly affects the mode estimation [7]. To verify the sensors' relevance, we removed sensors one-by-one and evaluated the error resulting in the feature space points with respect to the standard condition. The error is calculated as the RMSE defined previously. As can be seen in Fig. 5, sensor S_{10} generates the most significant error in the fundamental frequencies extraction when removed. With this technique it is possible to sort the sensors from the most relevant to the less one as follows: S_{10} , S_{03} , S_{16} , S_{14} , S_{05} , S_{12} , S_{06} , S_{07} . To evaluate the performance with respect to the number of sensors used to extract fundamental frequencies, the sensors will be removed in the same order, to consider always the worst condition with the given number of sensors.

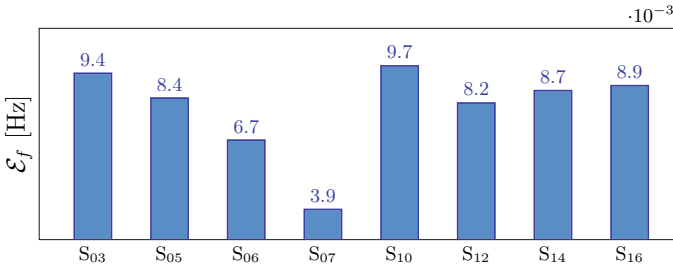
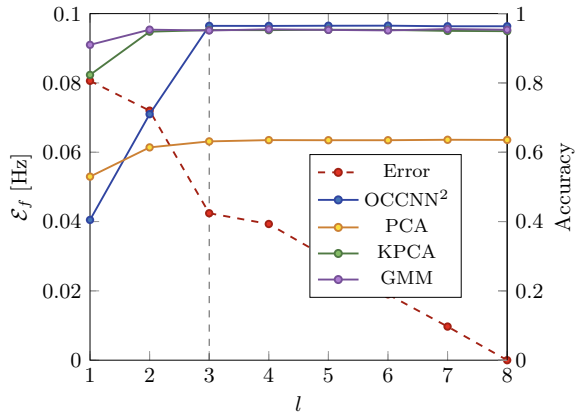


Fig. 5 Error produced removing the selected sensor

Fig. 6 Error varying the number of sensors available



6.2 Number of Sensors

Now that the sensor relevance is defined, we are able to verify the performance by varying the number of sensors used on the structure to derive the fundamental frequencies with low error. As we can see in Fig. 6 the accuracy of the algorithms remains almost the same as long as the number of sensors available is greater than 2, as the error present a significant increase in correspondence of the gap between 2 and 3 sensors. Thus we can deduce that the minimum number of sensors that must be used to monitor the Z-24 bridge is equal to 3. In this configuration it is easy to notice that the amount of data stored is reduced to $M_{sen} = N_s N_b N_a 3 \simeq 0.8$ GB.

6.3 Number of Samples

To evaluate the effect of the acquisition time on the anomaly detection performance, we progressively reduced the number of samples used to extract the structure’s fundamental frequencies. As we can see in Fig. 7 the performance of the algorithms

Fig. 7 Error varying the number of samples

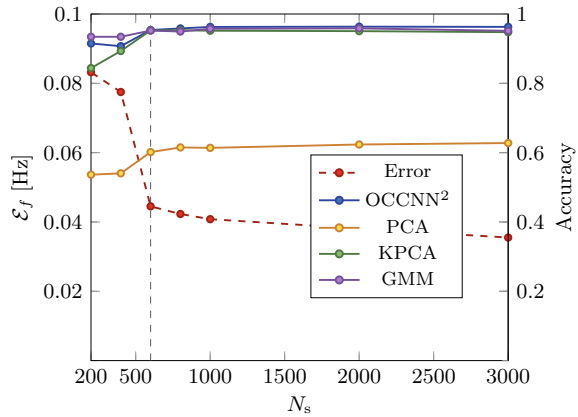
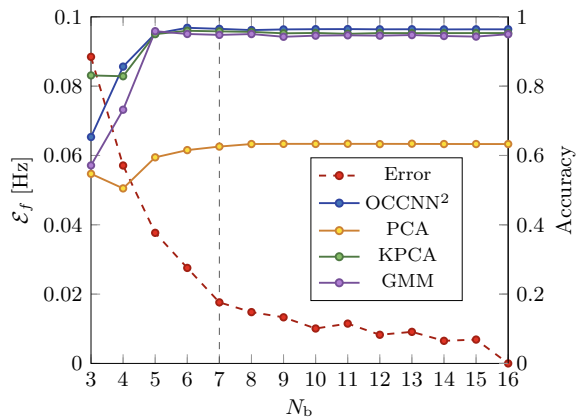


Fig. 8 Error varying the number of bits



remain almost constant as long as the number of samples N_s is greater than 600, that corresponds to an acquisition time of 12 s with a sampling frequency $f_{\text{sam}} = 50$ Hz. Reducing drastically the acquisition time, we achieve a significant reduction of the data occupation, that in this configuration is $M_{\text{sam}} = 600N_bN_a l \simeq 0.04$ GB, without performance degradation.

6.4 Number of Bits

he number of bits can also be dropped to reduce the volume of data stored and the accelerometer cost. To test their impact on the performance, we progressively reduced the number of bits used to encode the waveforms extracted from the accelerometers as reported in Fig. 8. As we can see, the error remains contained as far as the number of bits used to encode the samples is greater than 6; likewise, the accuracy of the

algorithms remain high as long as the error remains contained. Several low-cost accelerometers are available on the market with a resolution $N_b = 8$, and these results show that this type of sensor could accomplish the anomaly detection task. In this case, the data occupation is $M_{\text{bit}} = 8N_s N_a l \simeq 1 \text{ GB}$. This relevant reduction of the number of resolution bits is possible because of the anomaly detector capability to cope with the error introduced in the modal frequencies estimation (depicted in red in Fig. 8) caused by quantization.

7 Conclusion

In this paper, we presented a SHM system that aims to extract damage-sensitive features with the minimum amount of resources necessary for anomaly detection with high accuracy. An overview of some widely used anomaly detection algorithms is provided. Three different approaches are proposed to reduce the volume of data stored and limit sensors and network infrastructure costs. When the goal is to reduce the amount of data stored, it is good practice to reduce the observation time and use several high-resolution sensors; when the target is to minimize the sensor cost, a good practice is to adopt several low-resolution sensors combined with long observation time; when the objective is to contain the network infrastructure cost, few high-resolution sensors and long observation time can be considered. To evaluate the error introduced by these strategies and the performance of the algorithms, the RMSE and the accuracy are used as metrics, respectively. The results show that these strategies, when properly designed, can be adopted without significant loss of performance; in fact, all the algorithms except the PCA, ensure an accuracy greater than 94% in all of the proposed configurations, with the maximum performance reached by OCCNN² whose accuracy never goes down below 95%.

References

1. Ferrari R, Froio D, Chatzi E, Pioldi F, Rizzi E (2015) Experimental and numerical investigations for the structural characterization of a historic RC arch bridge. In: Proceedings of the international conference on computational methods in structural dynamics and earthquake engineering, vol 1, Athens, Greece, pp 2337–2353
2. Benedetti A, Tarozzi M, Pignagnoli G, Martinelli C (2019) Dynamic investigation and short-monitoring of an historic multi-span masonry arch bridge. Proceedings on international conference on Arch Bridges, vol 11. Porto, Portugal, pp 831–839
3. Benedetti A, Pignagnoli G, Tarozzi M (2018) Damage identification of cracked reinforced concrete beams through frequency shift. *Mater Struct* 51:1–15
4. Benedetti A, Colla C, Pignagnoli G, Tarozzi M (2019) Static and dynamic investigation of the Taro masonry bridge in Parma, Italy. In: Proceedings on international conference on structural analysis of historical constructions, vol 18. Cusco, Peru, pp 2264–2272
5. Roeck GD (2003) The state-of-the-art of damage detection by vibration monitoring: the SIMCES experience. *J Struct Control* 10(2):127–134

6. Worden K, Farrar C, Haywood J, Todd M (2008) A review of nonlinear dynamics applications to structural health monitoring. *Struct Control Health Monit* 15(4):540–567
7. Fabbrocino G, Rainieri C (2014) *Operational modal analysis of civil engineering structures*. Springer, New York
8. Bishop CM (2006) *Pattern recognition and machine learning*. Springer, New York
9. Watt J, Borhani R, Katsaggelos AK (2016) *Machine learning refined*. Cambridge University Press, Cambridge
10. Goodfellow I, Bengio Y, Courville A (2016) *Deep learning*. MIT Press
11. Favarelli E, Giorgetti A (2021) Machine learning for automatic processing of modal analysis in damage detection of bridges. *IEEE Trans Instrum Meas* 70:1–13
12. Pucci L, Testi E, Favarelli E, Giorgetti A (2020) Human activities classification using biaxial seismic sensors. *IEEE Sens Lett* 4(10):1–4
13. Z-24 bridge data. (Online). Available: <https://bwk.kuleuven.be/bwm/z24>
14. Carden EP, Brownjohn JMW (2008) Fuzzy clustering of stability diagrams for vibration-based structural health monitoring. *Comput Aided Civil Infrastruct Eng* 23(5):360–372
15. Wu C, Liu H, Qin X, Wang J (2017) Stabilization diagrams to distinguish physical modes and spurious modes for structural parameter identification. *J Vib* 19(4):2777–2794
16. Rainieri C, Fabbrocino G (2015) Development and validation of an automated operational modal analysis algorithm for vibration-based monitoring and tensile load estimation. *Mech Syst Signal Process* 60–61:512–534
17. Cabboi A, Magalhães F, Gentile C, Cunha Á (2017) Automated modal identification and tracking: Application to an iron arch bridge. *Struct Control Health Monit* 24(1)
18. Pastor M, Binda M, Harčarik T (2012) Modal assurance criterion. *Procedia Eng* 48:543–548
19. Reynders E, Roeck GD (2009) Continuous vibration monitoring and progressive damage testing on the z 24 bridge. *Encyclopedia Struct Health Monit* 10:127–134
20. Reynders E, Houbrechts J, Roeck GD (2012) Fully automated (operational) modal analysis. *Mech Syst Signal Process* 29:228–250
21. Brigante D, Rainieri C, Fabbrocino G (2017) The role of the modal assurance criterion in the interpretation and validation of models for seismic analysis of architectural complexes. In: *Proceedings on international conference on structural dynamics (Eurodin)*, vol 199. Italy, Rome, pp 3404–3409
22. Santos A, Silva M, Sales C, Costa J, Figueiredo E (2015) Applicability of linear and nonlinear principal component analysis for damage detection. In: *Proceedings on IEEE international instrumentation and measurement technology conference (I2MTC)*. Pisa, Italy, May, pp 869–874
23. Favarelli E, Testi E, Pucci L, Giorgetti A (2019) Anomaly detection using wifi signal of opportunity. In: *Proceedings on IEEE international conference on signal processing and communication systems (ICSPCS)*. Surfers Paradise, Gold Coast, Australia, pp 1–7
24. Favarelli E, Testi E, Giorgetti A (2019) One class classifier neural network for anomaly detection in low dimensional feature spaces. In: *Proceedings on IEEE international conference on signal processing and communication systems (ICSPCS)*. Surfers Paradise, Gold Coast, Australia, pp 1–7
25. Perera P, Patel VM (2019) Learning deep features for one-class classification. *IEEE Trans Image Process* 28(11):5450–5463
26. Chalapathy R, Menon AK, Chawla S (2018) Anomaly detection using one-class neural networks. *CoRR*, vol abs/1802.06360
27. Abdi H, Williams LJ (2010) *Principal component analysis*. Wiley Interd Rev Comp Stat 2(4):433–459
28. Rainieri C, Magalhaes F, Gargaro D, Fabbrocino G, Cunha A (2019) Predicting the variability of natural frequencies and its causes by second-order blind identification. *Struct Health Monit* 18(2):486–507
29. Schölkopf B, Smola A, Müller K-R (1997) Kernel principal component analysis. In: *Proceedings on international conferences on artificial neural networks*, vol 1327, no 6. Springer, Lausanne, Switzerland, pp 583–588

30. Schölkopf B, Smola A, Smola E, Müller K-R (1998) Nonlinear component analysis as a kernel eigenvalue problem. *Neural Comp* 10:1299–1319
31. Santos A, Figueiredo E, Silva M, Santos R, Sales C, Costa JCWA (2017) Genetic-based EM algorithm to improve the robustness of gaussian mixture models for damage detection in bridges. *Struct Control Health Monit* 24(3)
32. Pollard JH (1971) On distance estimators of density in randomly distributed forests. *Biometrics* 27(4):991–1002
33. Chiani M, Elzanaty A (2019) On the LoRa modulation for IoT: waveform properties and spectral analysis. *IEEE Internet of Things J*: 1–8
34. Elzanaty A, Giorgetti A, Chiani M (2019) Lossy compression of noisy sparse sources based on syndrome encoding. *IEEE Trans Comm* 67(10):7073–7087
35. Silva M, Santos A, Figueiredo E, Santos R, Sales C, Costa J (2016) A novel unsupervised approach based on a genetic algorithm for structural damage detection in bridges. *Eng Appl Artif Intell* 52:168–180
36. Silva M, Santos A, Santos R, Figueiredo E, Sales C, Costa JC (2017) Agglomerative concentric hypersphere clustering applied to structural damage detection. *Mech Syst Signal Process* 92:196–212

Distributed Fibre Optic Sensing for Long-Term Monitoring of Tunnel Inner Linings in Anhydrite



Fabian Buchmayer, Christoph M. Monsberger, and Werner Lienhart

Abstract Tunnels are civil engineering structures with a very long design lifetime of 100 years or more. In order to assess their long-term integrity monitoring systems with high robustness, long-term stability and high accuracy are required. Furthermore, monitoring should not disturb the operation of the traffic since tunnel closures are costly. This article discusses the design, installation and first results of a distributed fibre optic monitoring system installed in the inner lining of a railway tunnel. Five individual cross sections in an anhydrite area were equipped with the fibre optic monitoring system. Anhydrite regions can cause problems over a long time as water ingress causes anhydrite material to swell, which increases loads acting on the tunnel lining. All instrumented cross sections are connected to the central communication network of the tunnel and measurements can be conducted without interfering with the tunnel traffic. The developed approach focuses on long-term monitoring, which comprises special challenges regarding hardware, data processing and independent verification measurements to evaluate the long-term stability of the measurements. Additionally, issues such as cable bites by animals or forced changes of computer operating systems must be considered to guarantee the suitability of the monitoring system over decades.

Keywords Distributed fibre optic sensing · Long-term tunnel monitoring · Strain distribution · Anhydrite area

1 Introduction

Nowadays civil engineering structures like railway tunnels are designed with a lifetime of more than a century. To ensure such long lifetimes, monitoring is important not only during, but also after the construction phase. Sufficient and well-developed

F. Buchmayer (✉) · C. M. Monsberger · W. Lienhart
Institute of Engineering Geodesy and Measurement Systems, Graz University of Technology,
Graz, Austria
e-mail: fabian.buchmayer@tugraz.at

monitoring approaches increase safety and provide the basis for predictive maintenance. However, it must be considered that monitoring results have to be delivered also at times when limited or no access to the tunnel is possible.

Furthermore, the number of tunnels which have to be maintained and monitored is constantly increasing. In Austria alone, three long tunnels (Semmering Base Tunnel, Koralm Tunnel and Brenner Base Tunnel) with a total length of about 115 km are currently under construction (see Fig. 1). In total, 440 railway tunnels with a total length of 548 km exist in Austria [1]. These numbers show the potential and the need for reliable monitoring systems in the future.

After the construction of a tunnel, the main monitoring program is finished and only limited monitoring operations take place from time to time (e.g. every five years). Possible are conventional methods like total station measurements, which are commonly used also during construction to measure displacements of geodetic targets mounted on the tunnel surface [3]. In geotechnical fault sections, different geotechnical sensors are used to measure displacements, strain, and pressure [4]. Examples for such sensors are vibrating wire sensors (VWS), extensometers, inclinometers or pressure cells. These sensors give information about a specific location and usually utilize one cable per sensor. Hence, the number of installed sensors in one cross section is limited and the deformation behaviour of the structure must be well known before the installation to select the right sensor positions. If the estimated deformations are different and strains occur at locations where no sensors are placed, important structural deficiencies may remain undetected. Many common geodetic

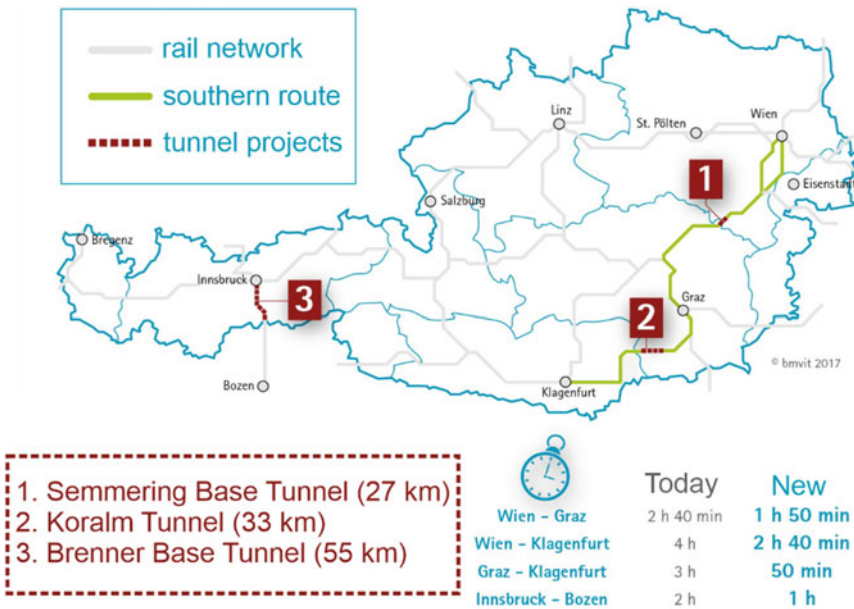


Fig. 1 Overview of three biggest tunnels currently under construction in Austria (after: [2])

and geotechnical sensors additionally require a person to access the tunnel every time a monitoring takes place. Since railway tunnels, especially in alpine regions like Austria, are often bottlenecks, closures must be reduced to a minimum. Therefore, new monitoring technologies are required, which reduce the need to access the tunnel on the one hand, but also raise the number of the observed regions. The present study intends to fill this gap, with a monitoring system based on distributed fibre optic sensing (DFOS).

DFOS enables strain and temperature measurements along an installed sensing cable. Hence, only one single cable is needed to collect measurements every 0.5 m or 1 m up to a total cable length of 50 km or even 100 km. With DFOS, it is possible to realise hundreds of measurement points inside one tunnel cross section. By connecting several cross sections to one measurement chain, an analogy to the neural system of a human body can be drawn. One measurement instrument together with an appropriate software (the “brain”) can observe thousands of points directly within the object, without any direct access to the monitoring section itself. Since the instrument can be outside, e.g. in the service building, the tunnel can be monitored and used for transportation at the same time.

This paper gives an overview of the practical realisation of a long-term monitoring system of tunnel inner linings based on DFOS. Since the monitored area is within an anhydrite geological fault section, the geotechnical model predicts that the deformation process will not be finalised in a few years after the construction is completed. Rather, the section will continue to deform for 40, 50 years or even longer. Therefore, all parts of the monitoring system must be selected with a focus on long durability. In the following, the used measurement system (chap. 2), the geological background of the monitored section and the installation process (chap. 3) are introduced. Finally, first results (chap. 4) are presented and challenges of long-term monitoring are discussed (chap. 5).

2 DFOS Measurement System

Fibre optic sensors become more and more popular in recent years in different applications, e.g. oil industry, military, medicine, automobile industry, air- and space industries and many more. They can be basically divided into three different sensor types: single point sensors (usually interferometric sensors like Fabry-Pérot and SOFO (Surveillance d’Ouvrages par Fibres Optiques)), quasi distributed sensors (Fibre Bragg Gratings—FBG), and distributed sensors (Rayleigh, Raman and Brillouin). All of them are advantageous compared to conventional electrical sensing techniques, since large distances between the reading unit and the sensors can be realised using optical signals only. Due to the designed lifespan of more than 100 years, this is a real benefit, since no power supply and, therefore, no electrical components are required directly at the monitoring locations.

Moreover, distributed fibre optic sensing provides the advantage that the sensing cable can be directly embedded into structures (e.g. concrete) and the deformation

behaviour can be obtained without a direct line-of-sight between the sensor and the measurement unit.

In general, distributed sensing uses natural backscattering, which occurs when light is injected into glass fibres. Depending on the method, intensity (Raman and Rayleigh) or frequencies (Brillouin) are measured. This backscattering light is affected by temperature and strain changes acting on the glass fibre and, hence, it is possible to capture these physical quantities. The different measurement techniques enable either only temperature (Raman) or a combination of temperature and strain measurements (Rayleigh and Brillouin).

2.1 Sensing Principle

The presented DFOS installation is based on the Brillouin Optical Frequency Domain Analysis (BOFDA), which requires an injection of the light on both sides of the fibre for an improved signal to noise ratio. The achievable measurement precision ranges from 2 to 10 $\mu\text{m/m}$ (see e.g. [5]) for long distances of up to several ten kilometres. BOFDA uses the so-called Stimulated Brillouin Scattering (SBS). On one side of the cable, an amplitude modulated pump light is injected into the fibre (see Fig. 2). At the same time, a continuous wave (CW, probe light) is injected into the other

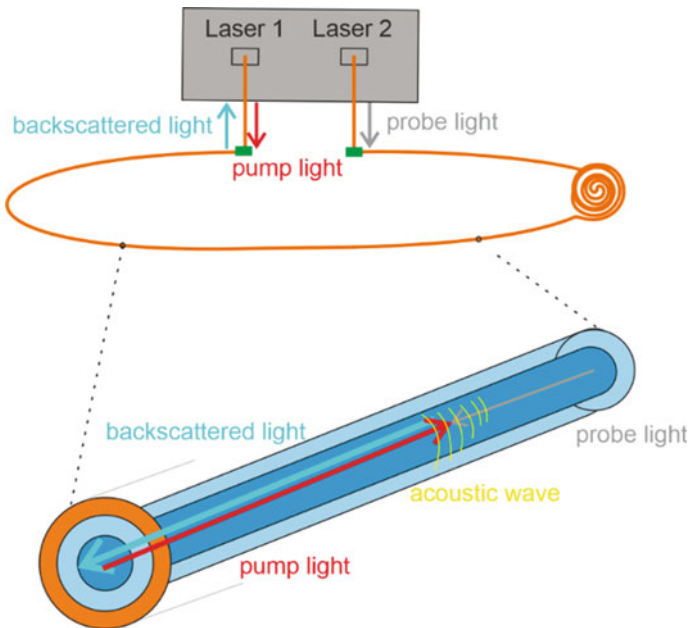


Fig. 2 BOFDA principal (after [6])

side of the fibre. At the location, where these light waves meet inside the fibre, the intensity increases and the glass begins to tremble. This generates an Acoustic Wave (AW), which travels through the fibre with high frequency. The AW itself disturbs the propagation of the light and, hence, also backscattering.

The backscattered light meets the incoming light, which increases the AW even further. This self-amplifying effect increases the backscattering. The condition, which must be fulfilled to generate this effect is, that the frequency of the two injected light waves is not equal. Instead, the frequencies have to have a certain offset, which is equal to the speed of sound in the glass fibre. In order to determine the right Brillouin Frequency Shift (BFS), the instrument tunes the offset until the maximum backscattering is found. Since temperature and strain are directly proportional to the acoustic speed, it is possible to measure these quantities [6]. The distance information, where temperature or strain changes occur, is calculated from the run time of the light.

The two-sided measurement principle implies that measurements are no longer possible, if the fibre breaks somewhere along the line. In that case, an instrument based on the Brillouin Optical Frequency Domain Reflectometer (BOFDR) can be used, where the light pulse is injected into the fibre at one side of the cable only (see [7] and [8]). Since the natural backscattering is low, the signal to noise ratio is decreased. Nowadays, commercially available instruments provide measurements in both BOFDA and BOFDR mode. Therefore, it is not only possible to measure with higher precision in loop configuration, but also to continue the monitoring with lower precision if the fibre breaks along the sensing path.

The Brillouin frequency shift $\Delta\nu$ at every position along the fibre can be calculated with the formula

$$\Delta\nu = \pm \frac{2n\nu_a}{\lambda_p} \quad (1)$$

where n is the refractive index, ν_a the acoustic speed and λ_p the wavelength of the pump light. The BFS is the frequency difference between the peak of the Brillouin Gain Spectrum (probe light) and the pump light [9]. Usually the BFS is between 10 and 13 GHz [10]. If the BFS changes between two measurement epochs, this implies a change in temperature and/or strain.

2.2 Sensing Cables

As already discussed, Brillouin sensing units are sensitive to strain and temperature. Therefore, when deriving strain values, temperature effects must be considered. In practice, this is realised by installing two sensing cables next to each other.

The strain cable (blue cable in Fig. 3) used in the presented application is manufactured by SOLIFOS AG (see [11] for datasheet). This BRUsens V9 with a diameter

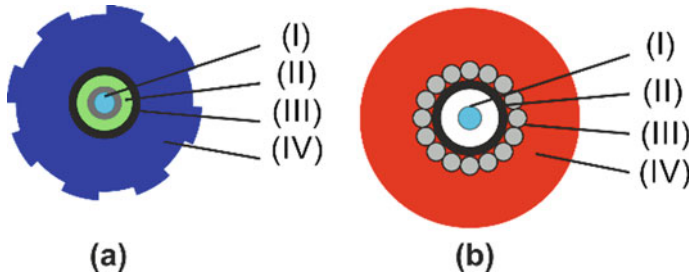


Fig. 3 Used fibre optic sensing cables: (a) strain cable BRUsens V9 and, (b) temperature cable BRUsens TEMP

of 3.2 mm, where the outside is made of polyamide coating (IV) with a structured surface, which enables a solid connection with the surrounding concrete. The next two layers are a special metal tube (III) and an interlocking multi-layer (II). The inmost part of the cable is the fibre (I) itself. All protection layers and the fibre itself are properly connected with each other, hence, the strain is transferred from the outside to the sensitive fibre.

The temperature sensing cable BRUsens Temp (red cable in Fig. 3), as well from SOLIFOS AG (see [12] for datasheet), consists of several outer protection layers. The cable is 3.8 mm thick and provides a special wired stainless-steel armoring (III) for protection, which is surrounded by a polyamide outer sheath (IV). Inside, a stainless-steel loose tube (II) filled with gel ensures that no strain is transferred to the fibre (I) itself.

The measured BFS $\Delta\nu$ consists of temperature changes (ΔT) and strain changes (ϵ)

$$\frac{\Delta\nu}{\nu} = C_{\epsilon} \epsilon + C_T \Delta T \quad (2)$$

where C_{ϵ} and C_T are the sensitivity coefficients and ν is the central frequency of the measurement. Typical values of the linear sensitivity coefficients are around 500 MHz/1% for strain and 1 MHz/1 °C for temperature readings. Although cable manufacturers often list default literature values for these coefficients, it is recommendable to reliably determine these calibration parameters to avoid errors of up to some percent [13–15].

The coefficients vary depending on different cable structures, or even on the individual manufacturing process of each cable batch. Furthermore, slight variations might occur between different Brillouin sensing units. Therefore, we developed our own calibration facility at the Institute of Engineering Geodesy and Measurement Systems—IGMS to perform fully automatic calibrations of strain transducers with lengths of up to 30 m. The reference length is measured by a high-resolution laser interferometer system. Detailed information on the calibration facility can be found in [16].

3 Geological Background and Installation

The installation of the fibre optic sensing cable took place in the years 2018 and 2019 in the tunnel “Langer Berg” in Austria. Together with one other tunnel and an open construction part, the tunnel will have a total length of 6.1 km and is one part of the so-called “Koralm Bahn”. The “Koralm Bahn” is a combination of newly built railway tunnels and existing railway routes to shorten the travel time between the cities Klagenfurt and Graz from more than 3 h to 50 min.

3.1 Geological Background

The section where the monitoring system is installed is challenging from a geological point of view. The area is crossed by a 90 m long anhydrite section [17], which makes it necessary to implement extensive construction methods to increase the stability and durability of the tunnel. Anhydrite is a swelling mineral, comparable with plaster, and swells when it encounters water.

Usually in areas without anhydrite, the forces acting on the tunnel are be around 200–300 KN/m². This is about 20–30 tons, equivalent to 20–30 small cars. If there is anhydrite in the soil, these forces increase to around 2000–5000 KN/m², thus, up to 500 tons, which is comparable to an airplane. This is why enormous reinforcement constructions are necessary when tunnels are built in anhydrite areas. Hence the stability of the tunnel must be strengthened with enormous reinforcement to be able to withstand these forces [18].

3.2 Installation Process

In order to reliably detect strain changes at an early stage, five cross sections in this anhydrite area were equipped with the fibre optic sensing system. The construction of the inner tunnel lining was carried out in two steps: First, the tunnel invert, and a few months later, the tunnel vault was constructed. In each measurement cross section, the sensing cables were installed in two layers. The first layer is closer to the mountain and the second one is next to the tunnel cavity. A detailed overview of the cable routing in the first construction step can be seen in Fig. 4. The temperature sensing cable (red) was mounted at one side of the reinforcement, the strain sensing cable (blue) next to it on the other side (see Fig. 4 in left upper corner) and hence, reliable temperature compensation of the measured strain values can be guaranteed.

Since the sensing systems always requires a loop configuration for highly precise measurements, the fibre optic installation also had to be separated into two parts. Therefore, a temporary box was mounted in the invert (on the left side in Fig. 4), which protected the remaining cables between the two installation stages. The cable

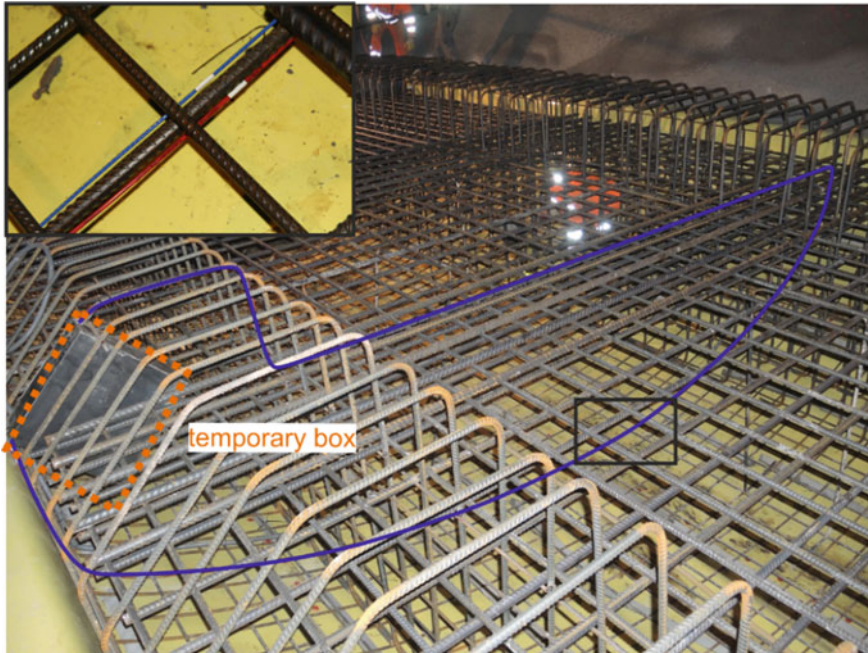


Fig. 4 Installed fibre optic sensing cable in invert section

itself was guided along the reinforcement of the inner lining and fixed with cable ties to be at the desired position during the concreting.

To assign coordinates to strain and temperature changes measured along the installed sensing cables, selected position along the cables are measured with a total station. The resulting 3D coordinates are used to transfer the cable routing to the 3D tunnel coordinate system.

In addition to the spatial allocation of the fibre optic sensing signal, laser scans of the instrumented cross-sections were performed to enable further analysis of the potential deformations. Figure 5 depicts a laser scan of a cross section. The sensing cables are shown in blue. Furthermore, the box with the connectors on the right side can be seen. The red dotted line separates the two construction steps.

After the cables were installed in the vault, the second construction step was cast in place using a moving formwork platform, Fig. 6.

Since the presented DFOS approach was designed for the long-term monitoring over decades from the beginning, all individual cross sections were equipped with a connection box. Starting from these connection boxes, the individual sensing lines were connected to one total sensing line to form a fibre optic sensing network (see Fig. 7).

At the current construction status, epoch-wise measurements of all cross section are performed at the first connection box. Later, monitoring will be carried from outside the tunnel without interrupting the tunnel traffic, which, however, requires

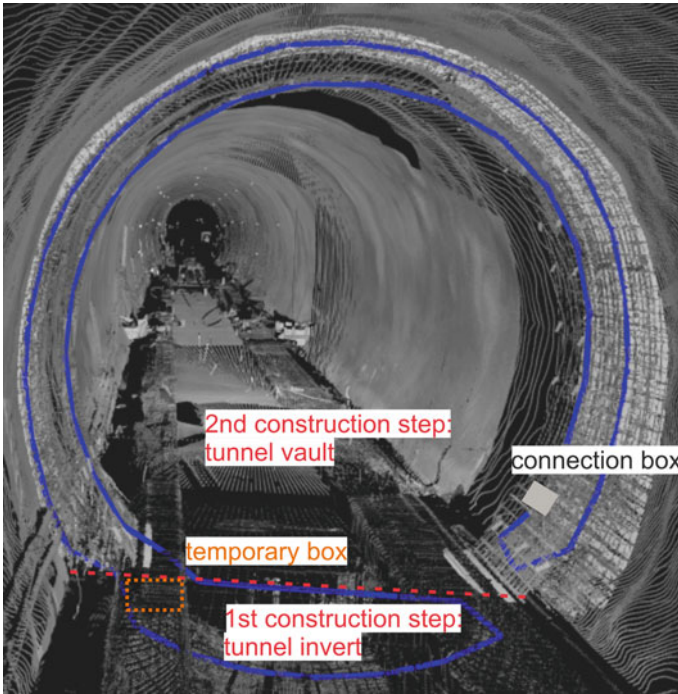


Fig. 5 Laserscan of one measurement cross section with sensing cable (blue line)

further installation steps. As soon as the service building at the tunnel portal is constructed, fibre optic supply fibres will be introduced in an already prepared empty conduit. The connection cable with a length of about 1000 m can be used to link the sensing cables to the measurement unit, but also to measure potential temperature changes along its entire length. If the fibre optic instrument were installed permanently at the service building, it would be possible to use it as a detector for e.g. water penetration, since the temperature around the connection cable would change in such cases.

4 First Results

The fibre optic sensing network is designed for long-term monitoring, where first significant deformations will only arise after years, or even decades. Therefore epoch-wise measurements are performed on a quarterly basis at the beginning. Later, they are carried out once to twice per year.

Figure 8 depicts temperature-corrected strain profiles of one selected measurement cross section. The strain changes are relative to the zero measurement, which was made on February 20th, 2019 immediately after the vault section was concreted. The



Fig. 6 Formwork platform made of steel for the construction of the concrete inner lining

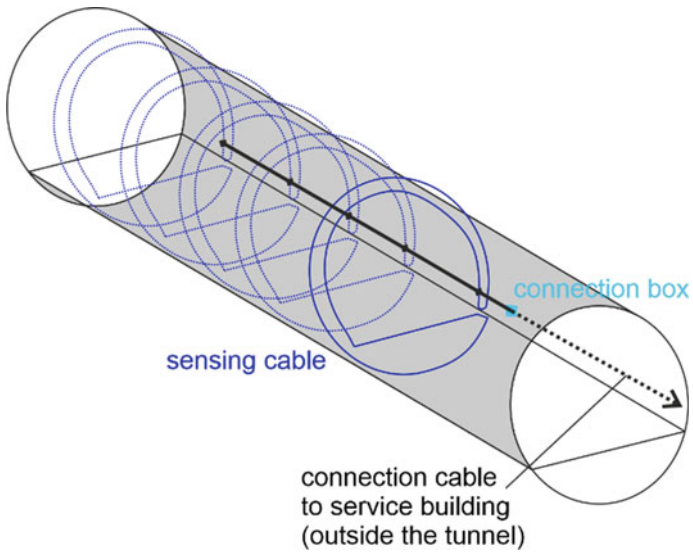
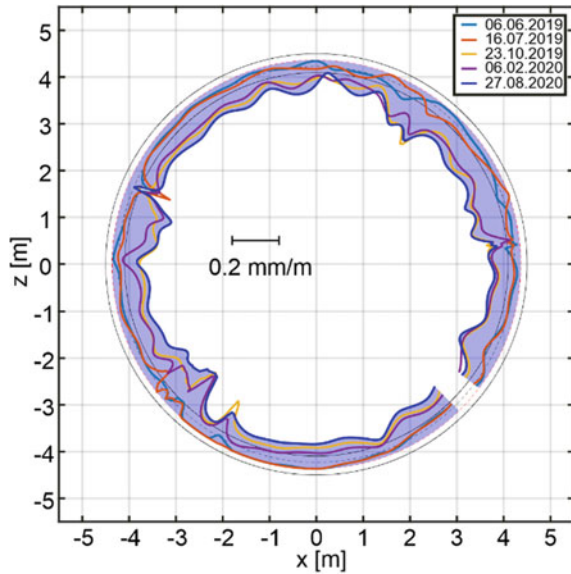


Fig. 7 Schematic overview of DFOS network

Fig. 8 Temperature corrected strain results of measurement cross section



strain changes of the first two measurement epochs are up to around $-50 \mu\text{m}/\text{m}$. Between these two measurements and the following three epochs there was just minor changes. The total strain changes are up to $-180 \mu\text{m}/\text{m}$ and homogenously distributed along the entire lining. This indicates that the structural integrity of the anhydrite is not affected at the current state.

5 Challenges and Outlook

Although such projects are planned and organized before the installation in detail, unexpected incidents can never be ruled out completely. One incident happened during one of the first measurement epochs after the installation. All cables had been protected after the installation either through their embodiment inside the concrete or inside empty conduits without any gaps. Nevertheless, the cables were found at this epoch as depicted in Fig. 9a. A mouse or some other rodent had walked 1000 m inside the empty conduit, which was already gaplessly installed from the outside of the tunnel to the connection box. The connection box became the new “home” for this little animal. Luckily, the mouse only destroyed one cable, which could be repaired. To make all boxes inside the measurement cross sections and the connection box safer, every entry inside the boxes was additionally sealed with a metal grid (see Fig. 9b).

Another challenge are the hardware and software components of such a long-term monitoring system. Nowadays, new operating systems come onto the market every few years, and new security breaches are detected. The implemented monitoring

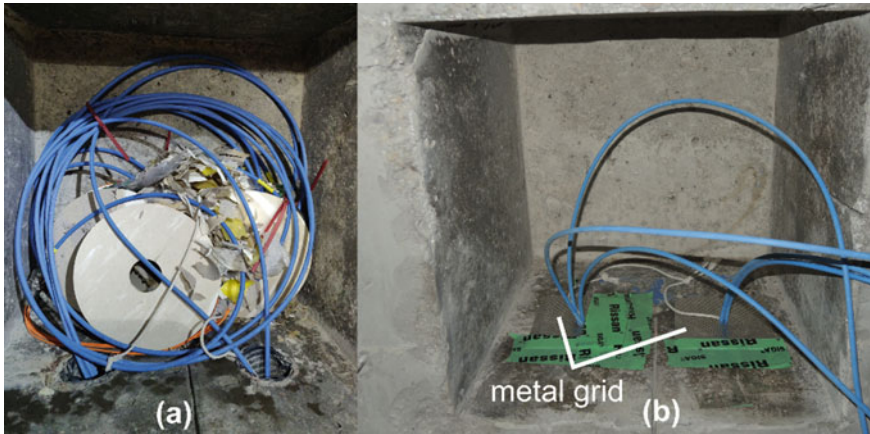


Fig. 9 Connection box after mouse incident (a), and after protection (b)

system should be able to detect strain changes over decades, which means that every step must be considered also from a temporal point of view. Some parts are already designed in a special way to be prepared for a long durability. For example, the file formats are transferable and no specific software is required, which might not exist anymore in a few years. Hardware components, e.g. the fibre optic laser or the entire measurement unit, might also be exchanged after decades, but can be reliably calibrated in the IGMS laboratory.

Although all these upcoming challenges, the introduced DFOS installation represents an innovative monitoring concept for big infrastructure projects. Distributed measurements can be performed without any access to the tunnel over decades, which will hopefully lead to a better understanding of the structural behaviour and a strengthening of predictive maintenance steps.

References

1. Brill L Statistik der Eisenbahn-Tunnel in Österreich. (in German Language). <https://www.eisenbahntunnel.at/inhalt/statistik.html>. Last accessed 21 Dec 2020
2. Tunnelblick Die größten Bahnprojekte. (in German language) BMK. <https://infothek.bmk.gv.at/investitionen-bahn-tunnel-suedstrecke>. Last accessed 21 Dec 2020
3. Austrian Society for Geomechanics (2014) Handbook - geotechnical monitoring in conventional tunnelling. 1st edn. Salzburg
4. Dunicliff J (1993) Geotechnical instrumentation for monitoring field performance, 1st edn. Wiley-Interscience publication, New York
5. fibrisTerre Systems GmbH (2018) Fiber-optic sensing system fTB 2505. Datasheet 2018. https://www.fibristerre.de/files/fibrisTerre_flyer.pdf. Last accessed 21 Dec 2020
6. fibrisTerre Systems GmbH (2018) Distributed fiber-optic Brillouin sensing. Technical note: understanding BOFDA. https://www.fibristerre.de/files/BOFDA_distributed_fiber-optic_sensing.pdf. Last accessed 21 Dec 2020

7. Measures RM (2001) Structural monitoring with fiber optic technology. 1st edn. Elsevier professional
8. Engelbrecht R (2014) Nichtlineare Faseroptik, 1st edn. Springer, Berlin Heidelberg
9. Tur M, Motil A, Sovran I, Bergman A (2014) Recent progress in distributed Brillouin scattering fiber sensors. In: Arregui FJ (ed) 13th IEEE Sensors Conference, Valencian Spain, pp 138–141
10. Nikles M, Thevenaz L, Robert PA (1996) Simple distributed fiber sensor based on Brillouin gain spectrum analysis. *Opt Lett* 21(10):758
11. Solifos AG (2020) BRUsens V9. Datasheet 2020. https://solifos.com/app/uploads/2020/01/Solifos_3-50-2-005_en.pdf. Last accessed 21 Dec 2020
12. Solifos AG (2020) BRUsens temperature. Datasheet 2020. https://solifos.com/app/uploads/2020/01/Solifos_3-50-1-001_en.pdf. Last accessed 21 Dec 2020
13. Buchmayer F, Monsberger CM, Lienhart W (2020) Advantages of tunnel monitoring using distributed fibre optic sensing. *J Appl Geodesy* 15(1):1–12
14. Monsberger CM, Woschitz H, Lienhart W, Racansky V, Hayden M (2017) Performance assessment of geotechnical structural elements using distributed fiber optic sensing. In: Sensors and smart structures technologies for civil, mechanical, and aerospace systems. vol 10168. SPIE, Portland, Oregon, USA, pp 101680Z-1–12
15. Moser F, Lienhart W, Woschitz H, Schuller H (2016) Long-term monitoring of reinforced earth structures using distributed fiber optic sensing. *J Civ Struct Heal Monit* 6(3):321–327
16. Woschitz H, Klug F, Lienhart W (2015) Design and calibration of a fiber-optic monitoring system for the determination of segment joint movements inside a hydro power dam. *J Lightwave Technol* 33(12):2652–2657
17. Gschwandner GG, Kahn U, Kohlböck B, Moritz B, Wagner S (2017) Granitztal tunnel chain - experience from the construction of the langer berg tunnel and challenges in the anhydrite zone. *Geomech und Tunneling* 10(6):730–739
18. FH Münster: Stuttgart 21 wird teurer (2018) Experte erklärt, warum Anhydrit zum Problem wird. (in German language) 2018. <https://www.fh-muenster.de/hochschule/aktuelles/news/index.php?newsId=595>. Last accessed 21 Dec 2020

Long-Term Monitoring Using GNSS: Lessons Learned and Experiences from 20 years of Operation



Caroline Schönberger and Werner Lienhart

Abstract Global Navigation Satellite Systems (GNSS) like GPS, Galileo, GLONASS and Beidou are used for monitoring of civil structures and natural phenomena since the 1980s. However, most of the implementations were either short term or realized in a very controlled environment. In this article we report about the experiences of more than 20 years of GNSS based monitoring of a large-scale object. In 1999 the GNSS monitoring system was developed and installed at a deep-seated gravitational mass movement in Austria and it is still operating. The system gradually evolved during the years of operation to maintain a reliable operation and to take new developments of information and communication technology (ICT) into account. This included the change from radio communication to UTMS and continuous maintenance of the hardware (revision of GNSS stations, revision of solar collectors, exchange of batteries) as well as software maintenance (Firmware updates of GNSS receivers, software updates, change to new operating systems). Especially the constant changes in the used software system results in maintenance time, which is often underestimated. From these experiences we derive lessons learned which can be a guideline for other long-term GNSS based monitoring systems.

Keywords GNSS monitoring system · ICT · Landslides · Long-term monitoring · Mass movement · Early warning system

1 Introduction

Since the 1980s Global Navigation Satellite Systems (GNSS) are used for the monitoring of civil structures and natural phenomena. The advantages of GNSS to other geodetic techniques are independency of weather, the determination of deformations in 3D and its economic efficiency due to the automated operation.

C. Schönberger (✉) · W. Lienhart
Institute of Engineering Geodesy and Measurement Systems, Graz University of Technology,
Graz, Austria
e-mail: c.schoenberger@tugraz.at

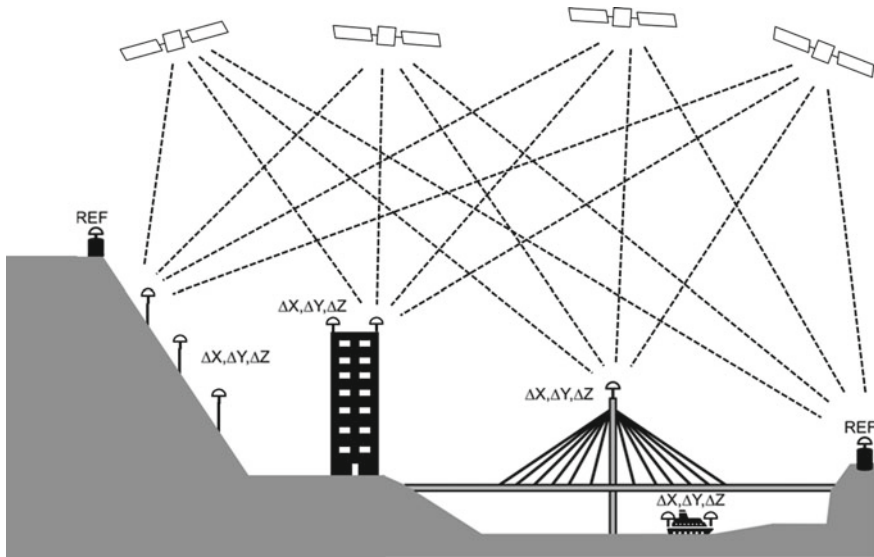


Fig. 1 GNSS Monitoring using one or more static reference stations (REF) and several rovers on moving objects (based on Lienhart and Ehrhart [5]). Note: exemplarily the required measurements to at least 4 satellites are shown for one reference station and 3 rovers

Therefore, GNSS was used in monitoring projects in different fields: suspension bridges [1], super-tall buildings [2], ships [3], landslides [4] and many more. Figure 1 shows the versatility of GNSS monitoring.

In 1999 a global GNSS measurement system was developed for the deformation monitoring of a deep-seated gravitational mass movement in Austria. Previously, traverse measurements, were carried out after a catastrophe in 1965/1966 [4]. The improvement with the GNSS monitoring system was seen in a continuous observation all year long, with minimum yearly maintenance work. This concludes to a better time resolution of the monitoring object with less working hours.

Chapter 2 gives an overview of the monitoring object and the aim of the monitoring system. Its development, from manual measurements to the current system with a 24/7 operation with online presentation and early warning, is described in Chap. 3. Chapter 4 takes a closer look to the current system and to challenges that are faced in the long-term operation on the engineering side, where Chap. 5 focuses on additional challenges.

2 Mass Movement Gradenbach

The mass movement Gradenbach is located in the south of Austria. Over the last 20 years, the behavior of the movement was observed via GNSS monitoring. The

GNSS monitoring system consist of 2 reference sites on stable ground. One is located on the mountain ridge (R1) and the other one on an opposite hill (R2). With a large height distance of about 800 m, correct handling of atmospheric influence is crucial to achieve high accuracy of the position of the monitoring points. Gassner et al. [6] demonstrated a point precision of around 7 mm can be achieved with specially developed algorithms for the tropospheric modelling. An overview of the location is shown in Fig. 2.

As seen in Fig. 2 there are 5 monitoring sites in the deformation area. Since 2012, the sites MA and MC are monitored continuously. Those two sites were chosen, because they are easy to reach, show large deformations and are at different heights. The other monitoring sites are observed epoch wise.

The time series of the of the slope movement recorded by the monitoring stations is shown in Fig. 3. It can be seen, that there are years with steady low movement (~0.4 cm/month) and years with accelerated movements (up to 2 cm/day), where accelerating phases start in spring, during the snow melting season, and stop in the end of summer. However, additional acceleration phases can also occur [7]. Especially 2018 was a year with a lot of movement (more than 40 cm for MC), which shows the importance of the still ongoing monitoring in this area. With the distribution of GNSS sites, the behavior of the slope can be observed and an early warning system for the

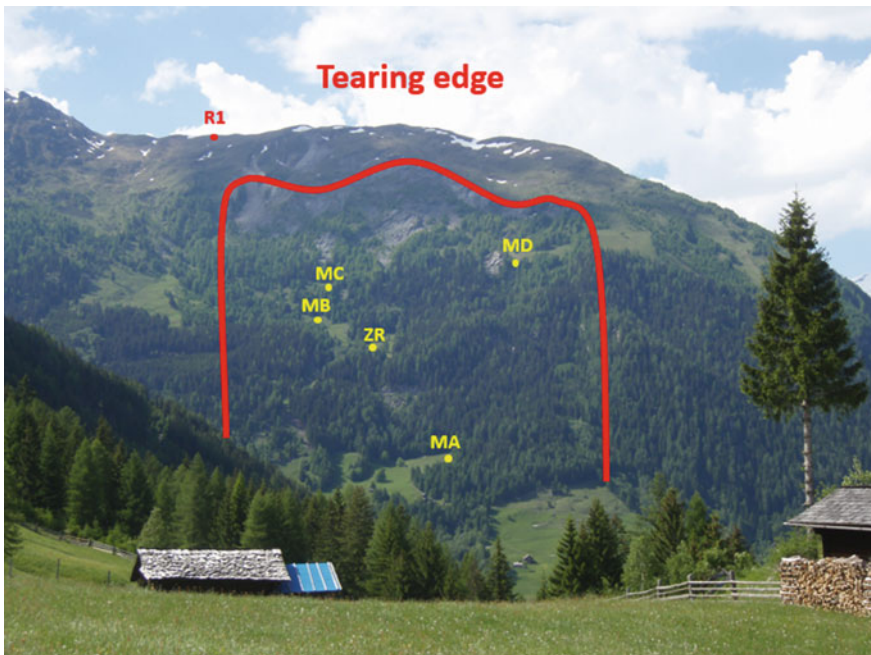


Fig. 2 Monitoring object: mass movement Gradenbach. Image taken from location of reference site R2

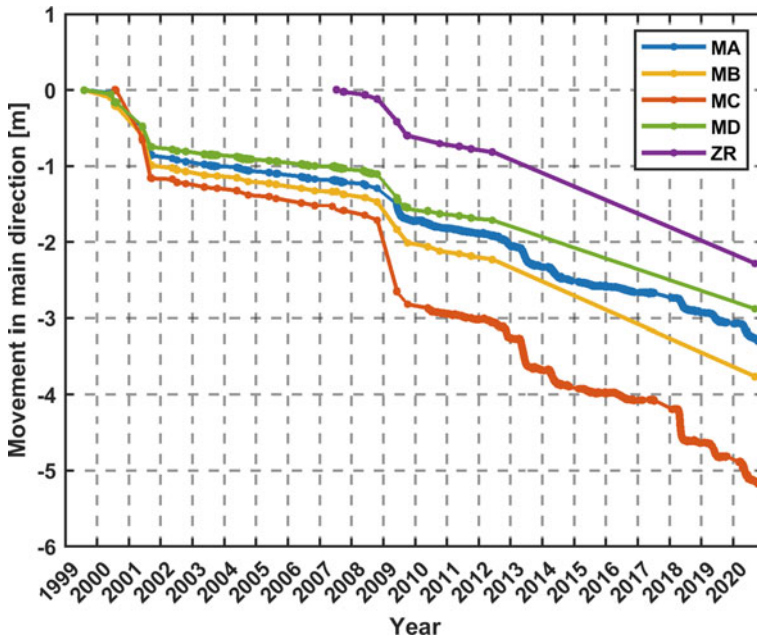


Fig. 3 Time series of the monitoring stations in the main direction of slope movement

local community, based on empirical data, is provided. Furthermore, the impact of counter measures like an additional drainage system can be assessed.

3 System Development

The system development can be divided into three main stages, starting from manual measurements to a continuous monitoring system over the summer to the current system of a continuous operation with online presentation. Table 1, shows an overview of the used hardware and software over the years. Remarkably, the GNSS Antennas are still working after more than 20 years and the receiver hardware has only been upgraded once. However, a significant amount of labor went into the constant upgrade to the latest operating systems which was necessary due to IT-security reasons and drivers for peripheral devices like modems.

Table 1 Timeline of the system development

		Hardware			Software		
		Antenna	Receiver	Data transfer	Analysis Software	Windows Systems*	Online Presentation
Manual Measurements	1999	Choke-Ring Antenna		Local Internal Storage	GRAZIA	NT	
	2000					2000	
	2001					XP	
	2002						
Continuous Measurements	2003		Ashtec	Radio Link	KFrUn	Vista	
	2004						
	2005						
	2006			7			
	2007						
	2008						
Yearlong Measurements	2009	Novatel	UMTS	Bernese with IGMS Routines	8	gbonline	
	2010						
	2011						
	2012						
	2013						
	2014		10				
	2015						
	2016						
	2017						
	2018						
2019	Canary						
2020							
2021							

* Not all Versions were used

3.1 Manual Measurements

From 1999 to 2002 measurements were carried out for 72 h, two times a year, one in spring and one in autumn. The whole equipment had to be carried by foot to the measurement locations and the data was stored on the laptop and on the internal memory of the receivers, Fig. 4. Calculations were carried out manually after the measurement with GRAZA, a software from GPSofT developed at the University of Calgary. This first era was also used to develop and implement algorithms for an improved multi-path elimination and height dependent tropospheric corrections [6].

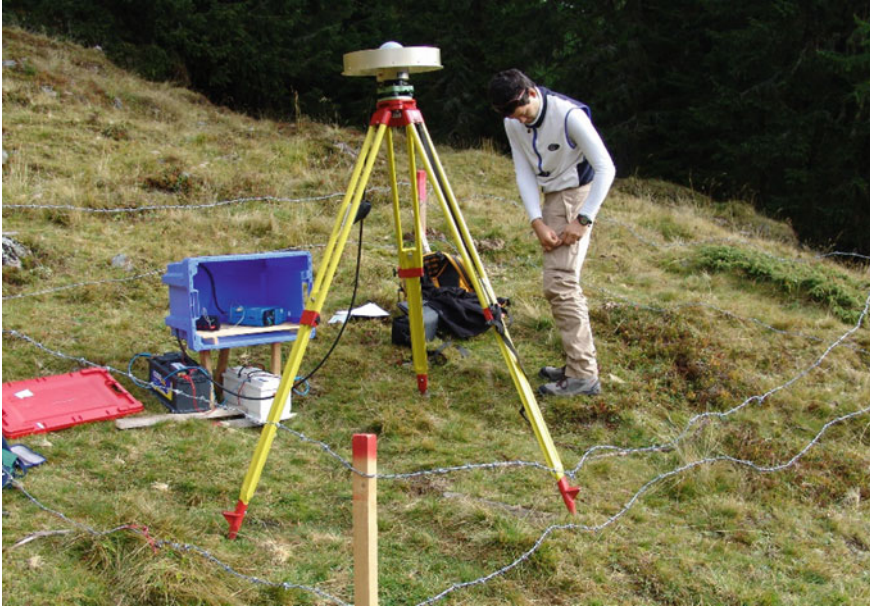


Fig. 4 First manual measurements

3.2 *Continuous Measurements*

In the second phase, data was collected during the whole summer and the data collection changed to a real time transfer over radio link to a calculation center in the valley, where coordinates were calculated with KRun, a program developed at the Institute of Engineering Geodesy and Measurement Systems (IGMS) of TU Graz., see Fig. 5. Those improvements could be established with the use of solar panels which continuously charge back-up batteries for an uninterrupted power supply to the instruments. Furthermore, this era laid the foundation for the current system. First, tests with different receivers and antennas lead to usage of the current hardware. Second, license agreements with the land owners for operating the sites a whole year were contracted [8].

3.3 *Yearlong Measurements*

In the current state of the system the stations are not dismantled anymore, Fig. 6. Once a year in spring, maintenance work is done at all sites. Especially the snow in the winter damages the stations, or moves their center point away from the marker point. This maintenance work is therefore essential. The data transfer was changed to a Universal Mobile Telecommunications System (UTMS) connection, so the data



Fig. 5 Continuous measurements with data transfer over radio link, left: radio antenna at a site, right: radio antenna at the calculation center



Fig. 6 Current system with data transfer over UTMS

is sent directly to Graz, where it is processed automatically and then added to an online presentation tool [9]. This system is explained in more detail in Chap. 4.

4 Current System

As mentioned in Chap. 2, the monitoring system consists of the data collection at the monitoring sites and the data processing, which is carried out at IGMS, in Graz.

Figure 7 shows the systems at both places. The left side shows a photo of the reference site R1, with its equipment, on the top of the hill in around 2100 m. The right side is a drawing of the data processing computer in Graz. The data transfer is done via Universal Mobile Telecommunications System UMTS.

4.1 Monitoring Site

For a better understanding of the setup at a site Fig. 8 shows a photo of a site and 3 colors are used to distinguish between the Parts: Data Acquisition (blue), Communication (green) and Infrastructure (red).

Infrastructure. The infrastructure part, consisting of a tripod, solar panel, batterie, fence and a box for lightning protection, is very important for operating functional.

The fence is needed to keep cows and sheep away from the station without harming them. It is made out of wood and barbed wire, which both suffer under the weather conditions during winter. This is why it is very important to repair it every spring before the animals come back to the slope, since a broken or not properly tensioned fence may harm animals. Besides animal suffering, an incident may also have an impact on the relation to the land owner resulting in a termination of the land-use license agreement. Fortunately, vandalism has not been a problem so far.



Fig. 7 Current system, left: Photo of a site, right: Data processing in Graz, Data Transfer via UMTS

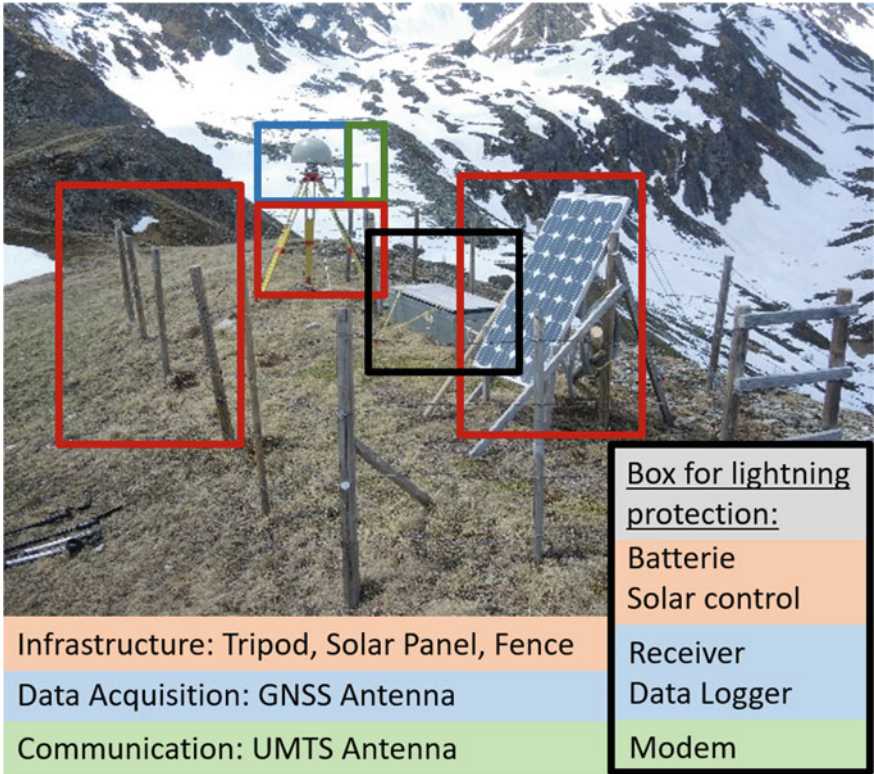


Fig. 8 Equipment at a site

Also, the tripod, made out of wood, needs to be checked for functionality during maintenance work and, in case of malfunction, replaced.

The electricity circle containing the solar panel, the solar control and the battery are checked every year. Batteries should be changed every 5–10 years for environmental reasons.

Data Acquisition For GNSS data acquisition every site is equipped with a GNSS antenna, a receiver, a data logger and the needed cable connections. Currently the GNSS antennas used at the sites are choke ring antennas with radons and used since the beginning of the GNSS measurements. They work totally fine, and no problems have been detected so far. There was one change of GNSS receivers in 2009 to upgrade to receivers with lower power consumption and more satellite channels. Since then, the receiver needed one firmware update, because of an early Global Positioning System (GPS) week roll over in 2017. Because the system is supposed to run without permanent intervention, the missing firmware update was not recognized immediately leading to a loss of data for a few months. Because of End of Life (EOL) notifications for our receivers, no more updates will be available, and in case of a severe error, new receivers need to be purchased [10].

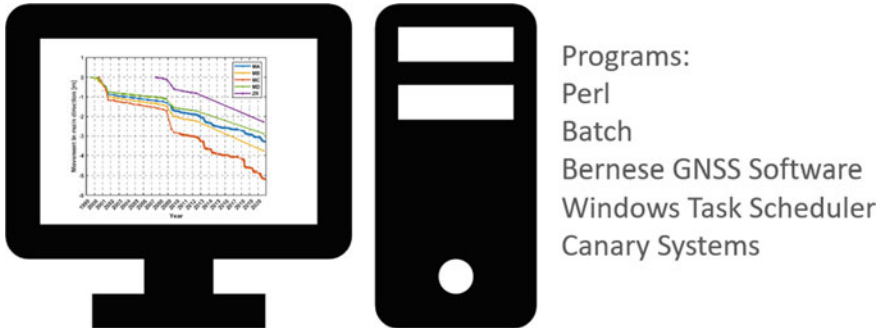


Fig. 9 Data processing in Graz with its main tasks and programs

Communication For the communication part, a modem with a SIM card and a UMTS antenna is needed. So far, the modems work properly, but there are no digital drivers available to access them. For accessing the modem, a Windows XP notebook is used. Furthermore, there is also an EOL notification, which will lead to a replacement, in case of severe errors. The UMTS antenna is exposed to all weather conditions, which are very harsh in this area. Therefore, it has to be changed every now and then.

4.2 Data Processing in Graz

Figure 9 covers the data processing in Graz. It uses the programs: Perl, Batch, Bernese GNSS Software [11], with built in tropospheric modelling algorithms by IGMS, Windows Task Scheduler and Canary Systems (ML Web v.2019.1.0.46, [12]) to cover the whole data processing part from importing data to an online presentation of the coordinates.

Hardware and Operating System The computer is a Windows Computer with a high-end server mainboard from 2011. Until the end of 2019 Windows 7 was used as an operating system, but with the end of the support for Windows 7 in the early 2020, the system needed to be upgraded. Some programs could not run with Windows 10 anymore. Another disadvantage with Windows 10 is the constantly installed updates and reboots of the computer. Those updates could result in compatibility problems with the monitoring system. All in all, it is not a high-end computer anymore, and because of the constant data writing and access to the hard disk, it suffers in speed and capacity.

Software Focusing on the software of the computer, the data process contains different software packages accessed by various programming languages and coordination tools to get all necessary additional data (orbit correction data, ionospheric data) and to calculate coordinates. This system is therefore dependent on the IT-infrastructure of institutions that provide the data and updates in their IT-environment

- **Change of the FTP address:**
 The URL of our FTP server has changed from `ftp://ftp.unibe.ch/aiub` to `ftp://ftp.aiub.unibe.ch`. The old URL is no longer active. **Please adapt your scripts if needed.** If you do not use FTP to download our products you can still use <http://www.aiub.unibe.ch/download>

Fig. 10 Notification for FTP server address change on the website: <http://www.bernese.unibe.ch/>

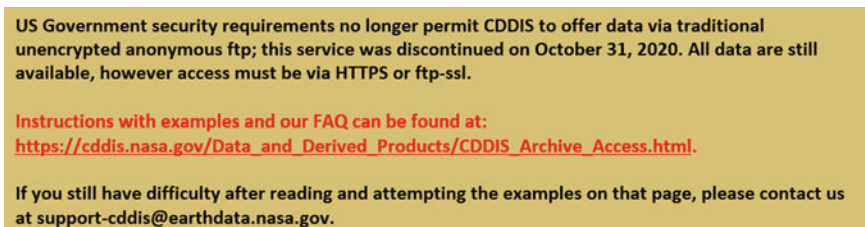


Fig. 11 Notification for FTP access change on the website: <https://cddis.nasa.gov/>

result in updating the data processing scripts. Adaptation can be e.g. the change of domain names from servers (Fig. 10) or change of the way of accessing servers, e.g. FTP to FTP-SSL (Fig. 11) and are mainly caused by enhanced security standards. Additionally, some files for Bernese GNSS Software expired in 2020 and had to be created again (planetary ephemeris).

Online Presentation The system need only little supervision and changes like those mentioned before can be left unseen for some time, which results in manually reprocessing old data. With the current Online Presentation Platform, those changes are detected earlier and it is possible to react timely.

For the online presentation we use the program Canary System, where limits can be set and automatic e-mail notification is sent. (Screenshot in Fig. 12), in case of exceeding limits or if no data is available to import. It also includes a security

Alarm Notification

The following alarms have been triggered:

Alarm Name	Alarm Source	Alarm Status	Alarm Type	Date Triggered	Previous Alarm	Alarm Threshold	Current Value	Notes
GBGPS	MC#3D VERSCHIEBUNG 1MONAT	ON	Three Level - High Low	5/2/2020 10:00:00 PM	N/A	0.05	0.05	
GBGPS	MC#3D VERSCHIEBUNG 1MONAT	ON	Three Level - High Low	5/3/2020 2:00:00 PM	5/2/2020 10:00:00 PM	0.05	0.06	
GBGPS	MC#3D VERSCHIEBUNG 1MONAT	ON	Three Level - High Low	5/4/2020 6:00:00 AM	5/3/2020 2:00:00 PM	0.05	0.05	
GBGPS	MC#3D VERSCHIEBUNG 1MONAT	ON	Three Level - High Low	5/4/2020 6:00:00 PM	5/4/2020 6:00:00 AM	0.05	0.05	

Fig. 12 Screenshot of an automatic E-Mail Notification after reaching a set limit

protection. Our previous self-programmed Version in PHP & HTML was online from 2012 to 2016, but then hacked and spam mails were sent from this server. This should not happen with our current online presentation tool.

Communication Furthermore, our mobile operator changed the IP addresses of the modems to private IP addresses, which resulted in the impossibility to access them. This problem has already been solved from our mobile provider by resetting to a public IP address.

5 Additional Challenges

The engineering part of a monitoring system is challenging, but especially in a long-term project other challenges occur.

One of those problems is that the people who accepted license agreements of monitoring systems leave and their successors are not interested anymore. This constant change over time also occurred at our institute, which highlights the importance of an excellent documentation.

In Chap. 3, harsh winters are mentioned. Those tones of snow results in trees bursting, danger of avalanches and closed roads during the winter. After the winter, the road must be cleared from the fallen trees and the road is often not accessible until early summer. This phenomenon of massive snowfall happened both in November 2019 and in December 2020 (Fig. 13).



Fig. 13 Massive snow, closed roads and fallen trees during winter

6 Summary

For over 20 years now a GNSS monitoring system was developed, improved and maintained on a mass movement in the Austrian alps. The system evolved from manual epoch measurements to a full-automatic monitoring system with a data transport over UMTS and an online presentation.

In those 20 years the IT-infrastructure of the system changed and needed to be modified to keep operational. Security reasons were the major part of those adaptations. Nevertheless, those changes need to be detected and a very important tool to spot them is the online presentation of the data. If no data is updated, there is something wrong with the system.

Modifications in the engineering hardware are rarer, but there won't be a support of aging hardware anymore. Especially in the rural area with a lot of snow, maintenance work has to be done every spring, to keep the system operative.

Never forget a good documentation, especially on long-term projects.

7 Conclusion and Outlook

A long-term monitoring system will run through a lot of changes, that need to be faced. Those can occur in various fields. Obviously, a steady development takes place in hardware and software and in the way of communication, but also changes in responsibilities or extreme weather will occur. These variations need to be addressed so supervision and maintenance time is always required.

On the other hand, with a data series of more than 20 years conclusions on the long-term behavior of the mass movement can be made, which are very important for an early warning system and the impact of counter measures like additional drainage systems can be assessed.

This article focuses on the long-term monitoring using GNSS. However, satellite measurements are only one part of the deformation measurements at the Gradenbach mass movement. Additionally, terrestrial total station measurements are available since 1968, fiber optic strain measurements are performed since 2007 and wire extensometer data is available since 1999. Furthermore, the measurement program is constantly upgraded, taking new technology developments into account. Recently, corner cube reflectors for satellite based interferometric synthetic aperture radar (InSAR) were installed to complement the GNSS measurements.

References

1. Roberts GW, Brown CJ, Ogunidipe O (2011) Monitoring the severn suspension bridge by GNSS. In: Proceedings on TS01E-deformation monitoring 4934, FIG Working Week 2011

2. van Cranenbroeck J (2010) Controlling vertical towers. Reporter 63: The Global Magazine of Leica Geosystems, pp 29–31
3. Roberts GW, Hancock CM, Lienhart W, Klug F, Zuzek N, de Ligt H (2020) Displacement and frequency response measurements of a ship using GPS and fibre optic-based sensors. Appl Geomat. <https://doi.org/10.1007/s12518-020-00338-z>
4. Brückl E, Brunner FK, Lang E, Mertl S, Müller M, Sary U (2013) The Gradenbach observatory—monitoring deep-seated gravitational slope deformation by geodetic, hydrological, and seismological methods. Landslides 10(6):815–829
5. Lienhart W, Ehrhart M (2015) State of the art of geodetic bridge monitoring. In: Proceedings of international workshop on structural health monitoring (IWSHM), Stanford, USA, pp 449–456. <https://doi.org/10.12783/SHM2015/58>
6. Gassner G, Wieser A, Brunner FK (2002) GPS software development for monitoring of landslides. In Proceedings of the 2002 FIG 22 international congress. Washington, DC USA, April, pp 19–26
7. Lienhart W, Brunner F (2013) Geodätische Überwachung von gravitativen Massenbewegungen am Beispiel des Gradenbach-Observatoriums. ZfV 138:64–74
8. Brunner F, Gander D, Klostius R (2008) Gefahrenbewertung von tiefreichenden Massenbewegungen: Projektteil TUG–Monitoring der Verformungen.
9. Brunner FK, Lienhart W, Müller M, Wöllner J (2014) Acceleration and deceleration of large landslides: TUG. doi: <https://doi.org/10.1553/ISDR-23s1>
10. Schönberger C, Lienhart W, Lang E, Sary U (2020) Erfahrungen aus 20 Jahre GPS Monitoring der Massenbewegung Gradenbach
11. Dach R, Hugentobler U, Fridez P, Meindl M (2007) Bernese GPS software version 5.0. Astronomical Institute, University of Bern
12. Canary Systems (2020). Retrieved from <https://canarysystems.com/>

Assessment of Similar Reinforced Concrete Arch Bridges by Operational Modal Analysis and Model Updating



Giacomo Zonno and Carmelo Gentile

Abstract Results of the multidisciplinary activities carried out on the different spans of a historic RC arch bridge are presented in the paper. The bridge, completed in May 1917, crosses the Adda river between the small towns of Brivio and Cisano Bergamasco (about 50 km North-East of Milan) and represents a crucial node for the regional vehicular traffic. The investigation program included: (i) documentary research in the archives of Brivio town hall and National Roadway Authority (ANAS), (ii) visual inspection and geometric survey of the arches intrados, (iii) ambient vibration tests, (iv) mechanical characterization of the concrete materials, (v) finite element modeling of each span and vibration-based model tuning. The present paper, after a concise summary of the multidisciplinary investigation carried out on the different spans of the bridge, is mainly focused on structural modeling and vibration-based model updating. In order to take advantage of the similarity of the different tied arches, a simple system identification technique was used to update the models. The application of this technique provided optimal models that accurately fit the identified modal parameters of each span; in addition, the identified structural parameters are in good agreement with the available characterization of the materials.

Keywords Arch Bridge · FE Modeling and Updating · Non-Destructive Testing · Operational Modal Analysis · Reinforced Concrete

1 Introduction

The ageing of existing Italian bridges and viaducts, often dating back to the fifties and the sixties, as well as the almost constant increase in the service loads have

G. Zonno · C. Gentile (✉)

Department of Architecture, Built Environment and Construction Engineering (DABC)
Politecnico Di Milano, Piazza Leonardo da Vinci 32, 20133 Milan, Italy
e-mail: carmelo.gentile@polimi.it

G. Zonno

e-mail: giacomo.zonno@polimi.it

highlighted the need to prioritize the maintenance of bridges in the national agenda and to assess their state of preservation [1].

Within this context, a joint research between Lombardy Region and Politecnico di Milano is ongoing to define guidelines for the assessment and maintenance of regional key infrastructures and the historic Brivio bridge [2] was selected for a comprehensive investigation and the installation of a monitoring system. The bridge, built between June 1913 and May 1917 [2], crosses the Adda river between the municipalities of Brivio and Cisano Bergamasco (about 50 km North-East of Milan) and still represents a crucial node for the regional vehicular traffic. The bridge consists of three tied arch spans, which are in principle perfectly equal.

The paper summarizes the main results of the dynamic-based assessment of the bridge spans. The investigation includes documentary research in the archives of Brivio town hall and National Roadway Authority (ANAS), visual inspection and geometric survey of the arches intrados, physical tests on few cored samples carried out to evaluate the Young's modulus and the strength of the concrete in arches and hangers, ambient vibration tests, FE modeling of each span and model updating.

In the theoretical part of the study, a base FE model was firstly developed and the distribution of the Young's modulus over each arch span was updated [3]. In order to limit the number of parameters in the structural identification procedure and to solve a well-conditioned inverse problem, each bridge was divided in 4 regions, with the concrete Young's modulus being assumed as constant within each zone.

In order to take advantage of the similarity of the structures, the simple technique proposed in [4] was used to update the models. According to this approach, the approximate dependence of each modal parameter of the model on the updating parameters is firstly approximately determined; afterwards, the same set of approximating functions was compared to its experimental counterpart of each arch span in a minimization algorithm to provide the optimal estimate of the structural parameters. The application of [4] provided optimal models accurately fitting the identified modal parameters of each arch; in addition, the identified parameters turn out to be in good agreement with the available characterization of the materials.

The paper is structured as follows: (a) Sect. 2 describes the main characteristics of the bridge; (b) Sect. 3 describes the experimental tests; (c) Sect. 4 describes the implemented FE models and model updating of each span and (d) Sect. 5 concludes the paper.

2 Description of the Bridge

The Brivio bridge (Figs. 1 and 2), crossing the Adda river about 50 km North-East of Milan, is 132.0 m long and consists of three reinforced concrete (RC) tied arches spanning about 44.0 m each. Each span is in principle symmetric with respect to its middle longitudinal and transverse planes.

The three spans are supported by two piers, whose foundations are built in the riverbed, and two end abutments. The tapered concrete piers present a maximum

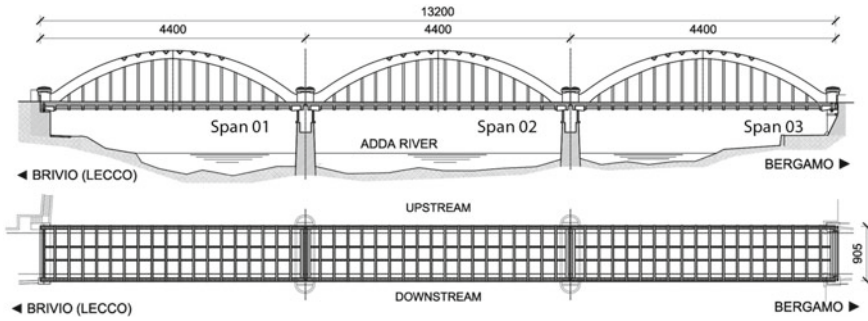


Fig. 1 General arrangement of the Brivio bridge (dimensions in cm)



Fig. 2 Construction phases of the Brivio bridge

dimension at the base of 12.8 m (transverse direction) and 3.8 m (longitudinal direction). The piers rest on RC piles driven into the riverbed for a depth ranging between 13 and 16 m.

The deck of each arch bridge is about 9.05 m wide (Fig. 1), for two traffic lanes and two pedestrian walkways, and consists of a cast in place RC slab supported by: (a) two main longitudinal girders (0.45 m × 1.26 m, with 22φ44 steel bars of reinforcement); (b) two minor longitudinal girders (0.20 m × 0.40 m) and (c) 16 transverse floor beams. The deck suspension is performed by 16 RC hangers (0.31 m × 0.65 m), per each side of each span.

It should be mentioned that the bridge underwent several maintenance and strengthening interventions during its lifetime, so that its current geometrical configuration exhibits some remarkable differences with respect to the original drawings [2]. The most significant variations involve: (a) the height of the arches cross-section, that was originally (Fig. 3) varying between 1.25 m (crown) and 1.50 m (springers) and is nowadays ranging between 1.32 m (crown) and 1.65 m (springers); (b) the width of the arches cross-section, that was increased from 0.60 to 0.65 m; (c) the height of the hangers (Fig. 4) that is slightly reduced due to the increase in the vertical dimensions of both arches and deck slab; (d) the deck slab, now including one layer (14 cm) of concrete (conceivably dating back to the original construction, Fig. 3) and a further layer (about 26 cm thick) of lightweight concrete.

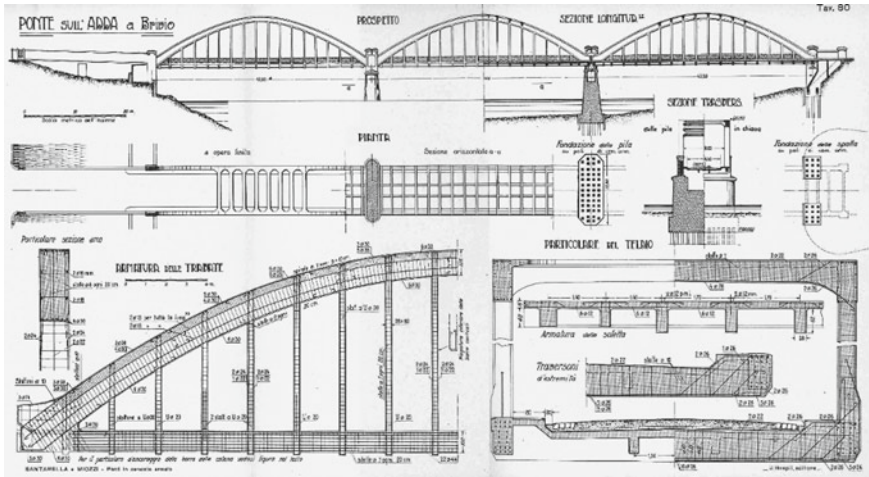


Fig. 3 Original design drawings of the Brivio bridge [2]

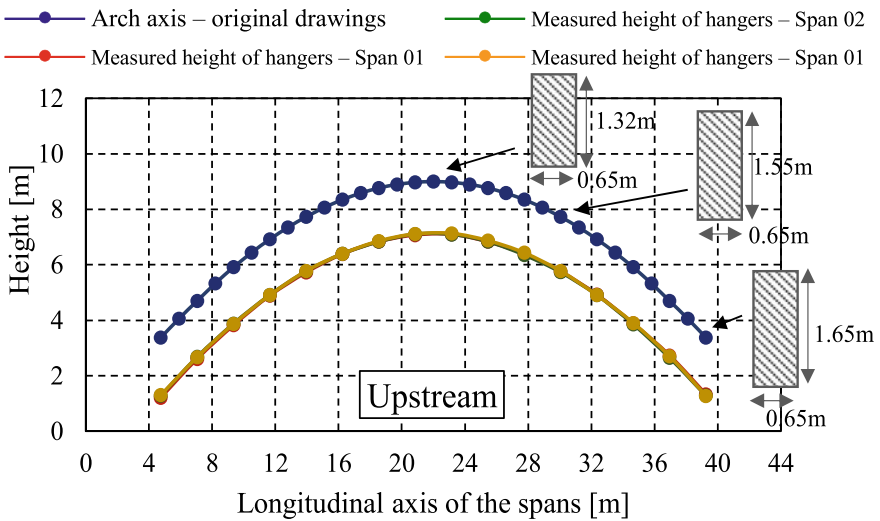


Fig. 4 On site survey of the heights of the hangers on upstream side (i.e. of the arches intrados) and arch axis according to the original drawings [2]

According to the documents and the geometric survey available in the archives of ANAS [5], it seems that the previously described variations date back to a strengthening intervention performed in the '80 s; further maintenance were carried out at the end of the '90 s (substitution of the bearings) and in 2014 (strengthening of one pier).

An upstream view of the bridge is shown in Fig. 1. The Brivio (Lecco) side is on left bank, whereas the Cisano Bergamasco (Bergamo) side is on the right bank. In this paper, the Lecco-side span is identified as Span 01, whereas the central span and the Bergamo-side span is denoted to as Span 02 and Span 03, respectively.

3 Documentary Research, Geometric Survey and On-Site Testing

After the strengthening of the pier supporting spans 2 and 3 (Fig. 1), performed in 2014, documentary research in the archives of Brivio and a first series of ambient vibration tests was carried out [6]; furthermore, the FE model of one span was developed [6] by assuming that the geometry of the model corresponded to the original drawings.

More recently (March 2020), several other activities took place: documentary research in the ANAS archives, on-site measurement of the dimensions of all hangers and of some cross-section of the arches to verify the information collected in the more recent geometric survey of the structure [5], mechanical sampling of materials and a second series of dynamic tests.

3.1 Documentary Research and Geometric Survey

As previously stated, the bridge was built between the end of 1913 and May 1917, and was designed by the Italian engineer Giuseppe Banfi [2]. Almost complete information on the bridge design was found during the documentary research in the archives of Brivio town hall, including original drawings, static calculation of the arches, structural details of reinforcement and foundation system, construction materials and code regulation adopted in the bridge design.

On the other hand, the bridge underwent several maintenance works during its lifetime and the documentary research recently performed in the ANAS archives revealed that the current geometrical configuration of the bridge exhibits some differences [5] with the original drawings. The subsequent (March 2020) on-site geometric survey of the arches intrados and of the dimensions of hangers confirmed a substantial reliability of the variations observed in the last available geometric survey [5], in terms of dimensions of the hangers (Fig. 4) and cross sections of the arches.

3.2 Mechanical Characterization of the Concrete Materials

The mechanical characterization of the concrete materials was performed by coring arches, hangers and deck in 24 different positions (Figs. 5 and 6). As shown in Fig. 5, the samples were homogeneously distributed along the structure to obtain an approximate representation of the mechanical properties of the different structural elements of each span. In particular, 10 samples (from H01 to H10 in Fig. 5) were drilled into the hangers, 11 samples into the arches (from A01 to A11 in Fig. 5) and 3 samples on the deck (D01, D02 and D03 in Fig. 5).

The 3 samples obtained from the deck (Figs. 5 and 6) were mainly aimed at verifying the current height and stratification of the concrete slab.

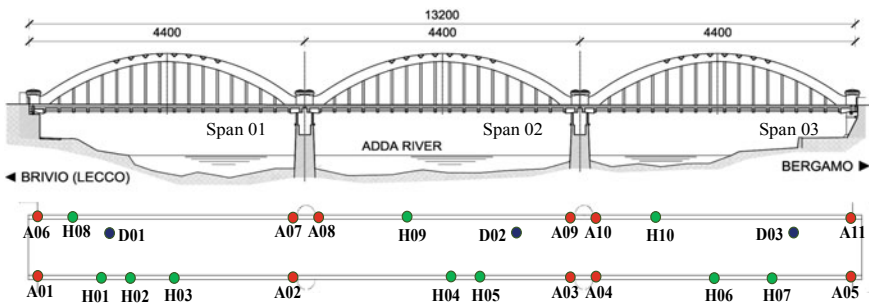


Fig. 5 Samples location for the mechanical characterization of the concrete materials



Fig. 6 Coring samples from arches, hangers and deck

The samples extracted from arches and hangers (Figs. 5 and 6) were subjected to ultrasonic investigations and compression tests aimed at estimating the compressive strength and the elastic modulus. Table 1 summarizes the dimension of each specimen, the mass density, the ultrasonic pulse velocity and the compressive strength.

In more details, 27 cylindrical specimens were obtained from the 21 cored samples from arches and hangers and—after the cutting, grinding, weighing and measurement

Table 1 Results of the mechanical characterization

	SpecimenId	Diameter	Height	Mass density	Ultrasonic pulse velocity	Compressive strength
		(mm)	(mm)	(kg/m ³)	(m/s)	(N/mm ²)
Span01	A01	99	95	2446	4481	59.24
	A02a	99	196	2336	4424	31.44
	A02b	99	100	2353	4354	48.33
	A06	99	196	2246	4475	32.22
	A07a	99	198	2361	4377	32.74
	A07b	99	104	2345	4177	41.05
Span02	A03a	75	155	2405	4220	39.61
	A03b	75	152	2390	4364	44.59
	A08	99	207	2421	4759	49.89
	A09	99	99	2437	4576	58.20
Span03	A04	99	196	2429	4663	35.34
	A05a	99	208	2410	4538	49.11
	A05b	99	104	2452	4483	57.55
	A10a	99	103	2268	3941	29.75
	A10b	99	203	2227	4079	28.71
	A11a	99	197	2348	4298	35.21
	A11b	99	177	2311	4407	39.62
Span01	H01	75	150	2277	3903	19.69
	H02	75	151	2184	3946	18.33
	H03	75	153	2382	4211	23.99
	H08	99	201	2344	4382	28.58
Span02	H04	75	153	2411	4791	28.75
	H05	75	156	2327	4112	15.39
	H09	99	200	2365	4471	29.88
Span03	H06	75	140	2352	4074	25.35
	H07	75	152	2334	4149	28.07
	H10	99	201	2378	4238	20.92

Specimens **a**, **b** are extracted from the same core drilling

operations—the ultrasonic pulse velocity was firstly evaluated in accordance with the EN 12,504–4: 2004 standard [7]. Three measurements were carried out for each specimen and the average results are listed in Table 1. The ultrasonic pulse velocity values, ranging between 3903 and 4791 m/s, suggest a relatively good degree of homogeneity of the concrete materials.

Subsequently, all the specimens underwent compression test according with the EN 12,390–3: 2019 standard [8] and 6 specimens were subjected to controlled loading ramps to determine the modulus of elasticity, as established by the EN 12,390–13 standard [9]. The values of the compressive strength are summarized in Table 1, whereas the following average values were obtained for the Young' modulus:

Span 01	Arches	$E_A = 34.77$ GPa
	Hangers	$E_H = 28.09$ GPa
Span 02	Arches	$E_A = 33.34$ GPa
	Hangers	$E_H = 36.00$ GPa
Span 01	Arches	$E_A = 36.46$ GPa
	Hangers	$E_H = 25.07$ GPa

3.3 Ambient Vibration Tests

Two series of ambient vibration tests (AVTs) were carried out to study the dynamic behaviour of the bridge.

As previously pointed out [6], the first series of tests was performed on June 2014 (Span 01 and Span 02) and September 2015 (Span 03), with the air temperature ranging between 30 and 35 °C. In this AVT, the structural response to ambient and operational excitation was collected in 16 vertical measuring positions, according to the sensors layout shown in Fig. 7a. In particular, data were acquired in two set-ups, considering two sensors as reference transducers (the blue arrows in Fig. 7a). For each set-up, 10 piezoelectric accelerometers (WR 731A, 10 V/g sensitivity and ± 0.50 g measuring range, Fig. 7b) and a multi-channel acquisition—with NI 9234 data acquisition modules (24-bit resolution, 102 dB dynamic range and anti-aliasing filters)—were used. The acceleration time-histories were recorded for about 7200 s at a sampling frequency of 200 Hz.

The second series of AVT was carried out more recently, on March 3–4 2020, by adopting the same experimental procedures of the previous test (in terms of number and position of instrumented points, number of set-ups, sampling frequency and length of the collected time windows) but different sensors. In particular, the dynamic sensing system was based on tri-axial SARA SS45 seismometers (electro-dynamic velocity transducers).

It should be noticed that the electro-dynamic transducers exhibit technical characteristics—such as high sensitivity (78 V/m/s^{-1}), no need for powering and very

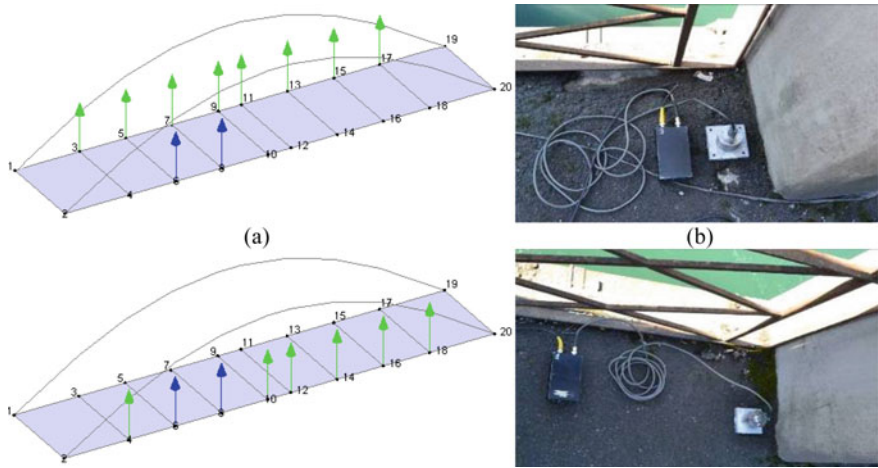


Fig. 7 Ambient vibration tests: **a** Sensors layout; **b** Views of the devices used in the first test (WR731A accelerometers and WRP31 amplifiers)

good performance in the low frequency range ($f \leq 100$ Hz)—making those sensors very attractive for the application in vibration testing [10] or monitoring of civil engineering [11] structures.

During the test of March 2020, the air temperature was lower than in previous tests and approximately varying between 12 and 15 °C.

Before the application of the modal identification tools, the collected data (accelerations and velocities) were low-pass filtered—using a classic 7th order Butterworth filter with cut-off frequency of 20 Hz—and decimated 5 times, reducing the sampling frequency from 200 to 40 Hz.

The modal identification was carried out applying the Frequency Domain Decomposition (FDD) technique [12]. For example, the first four singular value (SV)

Lines obtained by applying the FDD to the data collected on Span 03 in the first test are shown in Fig. 8: 7 vibration modes are generally identified for each span and for each AVT in the frequency range 0–20 Hz. The dynamic characteristics of the various spans identified in the different tests are summarized in Table 2.

The results presented in Table 2 suggest the following comments:

- 7 vibration modes were identified from ambient vibration tests in the frequency range 0–20 Hz for each span and the dynamic characteristics of the 3 spans are very similar;
- 4 bending modes ($B_i, i = 1, \dots, 4$) and 3 torsion modes ($T_i, i = 1, \dots, 3$) clearly characterize the dynamic behavior of each tied arch span;
- The results of the two tests, performed in different temperature conditions, suggest that natural frequencies tend to increase with decreased temperature. It is further

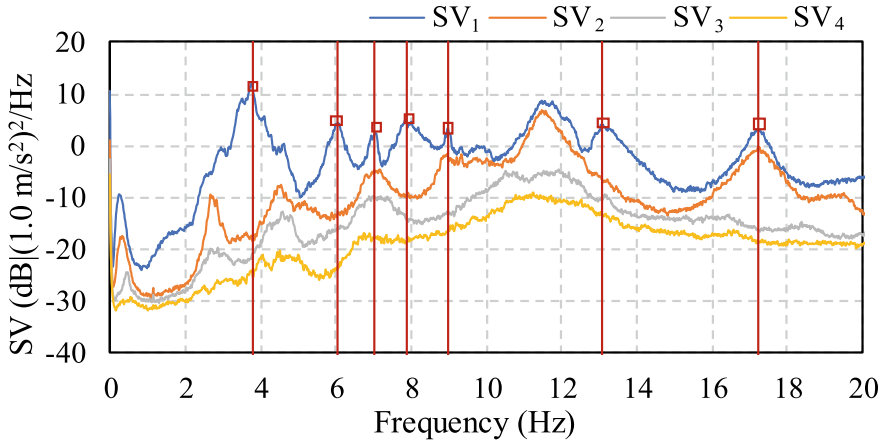


Fig. 8 Span 03: singular value lines (SV) and identification (FDD) of resonant frequencies (accelerometer data collected on September 2015)

noticed that just two tests were performed, so that no more information can be extracted on the environmental effects on natural frequencies;

- No remarkable difference in terms of mode shapes are detected between the two tests.

It is worth mentioning that the use of tri-axial seismometers in the second series of AVTs confirmed that the transverse modes are not excited by operational and ambient excitation.

4 Structural Modeling and Vibration-Based Model Updating

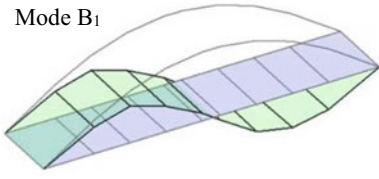
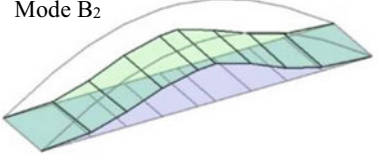
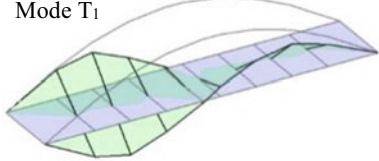
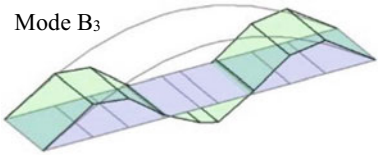
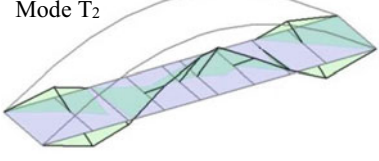
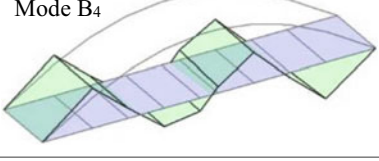
In order to assess the health state of the structure, a numerical 3D model of the Brivio bridge was developed (Fig. 9).

Due to the geometric arrangement of the bridge and the similarity of the investigated spans, a unique model was established for the three spans. The model includes: (a) 1980 beam elements to represent the longitudinal girders and the transverse beams of deck, arches and vertical hangers and (b) 1184 shells to simulate the concrete slab.

Concerning the boundary conditions, the model was considered as ideally supported in the transversal direction, whereas vertical springs were added at both ends of each span to simulate the vertical deformability due to presence of piers and abutments. In addition, longitudinal springs were added on one end to account for the possible interaction between contiguous spans.

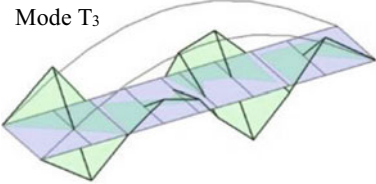
The model was formulated using the following assumptions: (i) the weight per unit volume and the Poisson's ratio of the reinforced concrete was assumed equal to

Table 2 Vibration modes identified from AVT (FDD) for the 3 spans of Brivio bridge

Mode Id	Span 01		Span 02		Span 03	
	f_{2014} (Hz)	f_{2020} (Hz)	f_{2014} (Hz)	f_{2020} (Hz)	f_{2015} (Hz)	f_{2020} (Hz)
Mode B ₁ 	3.821	3.821	4.126	4.138	3.772	3.796
Mode B ₂ 	6.018	6.018	6.055	6.189	6.030	6.152
Mode T ₁ 	7.178	7.324	7.471	7.581	7.019	7.275
Mode B ₃ 	7.666	7.766	7.813	8.057	7.874	8.032
Mode T ₂ 	9.009	9.143	9.399	9.558	8.972	9.204
Mode B ₄ 	13.06	13.28	13.55	13.82	13.10	13.42

(continued)

Table 2 (continued)

Mode Id	Span 01		Span 02		Span 03	
	f_{2014} (Hz)	f_{2020} (Hz)	f_{2014} (Hz)	f_{2020} (Hz)	f_{2015} (Hz)	f_{2020} (Hz)
Mode T_3 	17.02	17.33	17.61	18.05	17.21	17.54

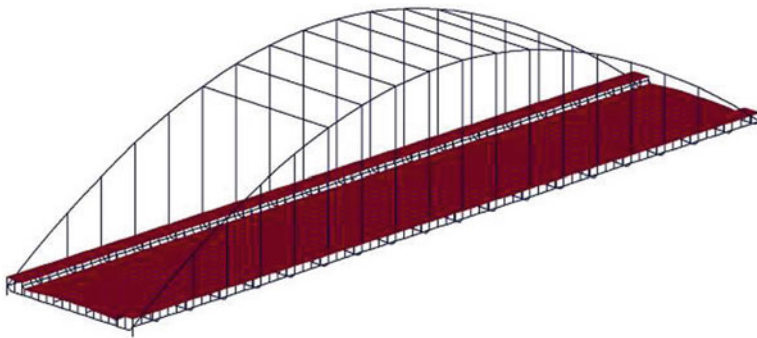


Fig. 9 3D FE model of the spans of Brivio bridge

25 kN/m³ and 0.20, respectively; (ii) the stiffness of vertical springs was assumed equal 0.85×10^6 kN/m.

Assuming that the geometry of the structures is well described and represented, a sensitivity analysis confirms that the dynamic characteristics of each span significantly depend on the elastic properties of the concrete and to the stiffness of longitudinal springs. Hence, the distribution of the Young’s modulus was updated. In order to limit the number of parameters in the structural identification procedure and to have a well-conditioned updating problem, the set of uncertain parameters involve:

- The Young’s modulus of arches (E_A) and hangers (E_H);
- The Young’s modulus of the deck lattice grid (E_{DG}) and deck slab (E_{DS});
- The stiffness k_L of the longitudinal springs.

In order to take advantage of the similarity of the investigated structures, the structural parameters of each model were determined, by minimizing the difference between theoretical and experimental natural frequencies, through the procedure proposed in [4]. According to [4], each natural frequency of the model is approximated by a simple polynomial expression $f_i^*(X)$, depending on the uncertain parameters collected in the vector X . After a few FE runs needed to evaluate the polynomials

Table 3 Optimal values of the updating parameters and comparison with the available mechanical characterization

Updating parameter	Span 01	Span 02	Span 03
E_A (GPa)	34.00 ⁽¹⁾	37.00 ⁽³⁾	35.12 ⁽⁵⁾
E_H (GPa)	31.97 ⁽²⁾	32.00 ⁽⁴⁾	28.48 ⁽⁶⁾
E_{DG} (GPa)	28.51	27.26	29.77
E_{DS} (GPa)	25.07	29.50	26.83
k_L (kN/m)	1.70×10^6	1.25×10^6	1.26×10^6
From tests on cored samples		⁽¹⁾ $E_A = 34.77$ GPa	⁽²⁾ $E_H = 28.09$ GPa
		⁽³⁾ $E_A = 33.34$ GPa	⁽⁴⁾ $E_H = 36.00$ GPa
		⁽⁵⁾ $E_A = 36.46$ GPa	⁽⁶⁾ $E_H = 25.07$ GPa

$f_i^*(\mathbf{X})$, the updating parameters are computed by minimizing the following objective function:

$$J(\mathbf{X}) = \sum_{i=1}^M w_i [f_i^{\text{EXP}} - f_i^*(\mathbf{X})]^2 \tag{1}$$

where w_i ($i = 1, 2, \dots, M$) are weighting constant (which were set equal to 1 in the present case) and f_i^{EXP} represents the i -th experimentally identified frequency. It is further noticed that the natural frequencies f_i^{EXP} adopted in the structural identification (1) refer to the first AVT, as those values were identified at larger air temperature and are generally lower (Table 2) than those identified in the second AVT.

Table 3 summarizes the optimal values of the updating parameters for each span, and the comparison with the available mechanical characterization of the materials. It should be noticed that the optimal estimates of the Young’s modulus generally suggest a satisfactory quality of the concrete and an acceptable state of preservation of the bridges. Furthermore, the estimated values of the elastic modulus are generally in close agreement with the available characterization of the materials, as indicated in Table 3.

The stability of the results was checked either by repeating the optimization with different starting points or by using different base values to evaluate the approximating functions $f_i^*(\mathbf{X})$.

However, the optimal models turned out to fit accurately the experimental modal parameters (natural frequencies and mode shapes). The theoretical frequencies are compared with the experimental ones in Table 4, for all the investigated systems; it can be observed that the maximum relative error between natural frequencies is less than 4.0, 6.9 and 2.0% for the 3 different spans, respectively. As a further demonstration, the mode shapes of the updated model of Span 03, corresponding to the experimental ones (Table 2), are shown in Fig. 10.

Table 4 Correlation between experimental (f^{EXP}) and numerical (f^{FEM} , optimal model) frequencies

Span 01			Span 02			Span 03		
f^{EXP} (Hz)	f^{FEM} (Hz)	Δf (%)	f^{EXP} (Hz)	f^{FEM} (Hz)	Δf (%)	f^{EXP} (Hz)	f^{FEM} (Hz)	Δf (%)
3.82	3.78	1.19	4.13	3.85	6.82	3.77	3.77	—
6.02	6.00	0.34	6.06	6.06	—	6.03	5.98	0.92
7.18	7.14	0.60	7.47	7.27	2.75	7.02	7.02	—
7.67	7.97	— 3.94	7.81	8.13	— 4.10	7.87	8.02	— 1.79
9.01	9.37	— 4.00	9.40	9.51	— 1.14	8.97	9.11	— 1.48
13.06	13.36	— 2.33	13.55	13.57	— 0.11	13.10	13.36	— 1.98
17.02	17.02	—	17.61	17.41	1.11	17.21	17.15	0.37
$\Delta f = 100 \times (f^{EXP} - f^{FEM}) / f^{EXP} $								

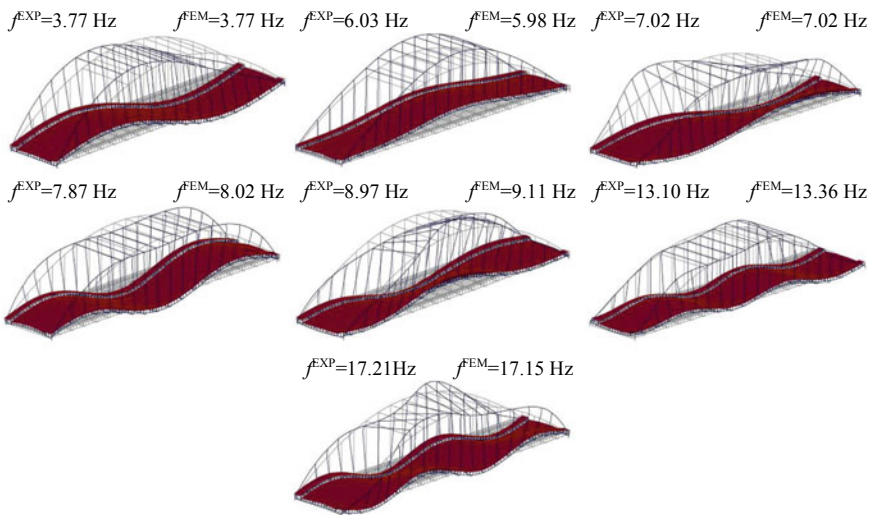


Fig. 10 Vertical and torsion vibration modes of the updated model of Span 03

5 Conclusions

The paper focuses on the multidisciplinary activities carried out on the different spans of the Brivio bridge, with these activities being performed in a joint research between Lombardy Region and Politecnico di Milano to define guidelines for the assessment and maintenance of regional key infrastructures.

Extensive investigation was carried out, including documentary research, visual inspection, geometric survey of the arches intrados, ambient vibration tests, mechanical characterization of the concrete materials and FE modeling. Based on the results presented in the paper, the following conclusions can be drawn:

- The mixed approach between documentary research (historic investigation of the structures evolution along the time), visual inspection and the on-site geometric survey have provided valuable information on structural details and on changes occurred to the structure during its lifetime. Those information allowed the development and validation of 3D FE models for each span, taking advantage of the similarity of the different tied arches;
- 7 vibration modes were identified from ambient vibration tests in the frequency range 0–20 Hz for each span and the similarity of the 3 spans was confirmed in terms of modal parameters, as well;
- The results of two dynamic tests in operational conditions, performed in different temperature conditions, suggest that natural frequencies of the bridges tend to increase with decreased temperature. No remarkable difference in terms of mode shapes are detected between the two tests;
- The application of a simple structural identification method to the investigated bridges provided, with a very limited computational effort, stable estimates of the updating parameters, which are also in good agreement with the available characterization of the materials. In addition, the resulting optimal models accurately fit the actual modal parameters of each bridge.

Acknowledgements The support of Lombardy Region is gratefully acknowledged. The authors would like to thank A. Cocco, M. Cucchi and the technical staff of the LPM Laboratory of Politecnico di Milano for the assistance in conducting the field tests.

References

1. Ministero delle Infrastrutture e dei Trasporti / Consiglio Superiore dei Lavori Pubblici: Linee Guida per la Classificazione e Gestione del Rischio (2020) la Valutazione della Sicurezza ed il Monitoraggio dei Ponti Esistenti. Roma, Italy
2. Santarella L, Miozzi E (1924) Italian bridges in reinforced concrete (in Italian). Hoepli, Milan
3. Gentile C (2006) Modal and structural identification of a RC arch bridge. *Struct Eng Mech* 22(1):53–70
4. Douglas BM, Reid WH (1982) Dynamic tests and system identification of bridges. *ASCE J. Struct. Eng.* 108(10):2295–2312
5. Rocca C (1992) Ponte sul fiume Adda km 21+000—Rilievi geometrici. ANAS S.p.A.
6. Ferrari R, Froio D, Rizzi E, Gentile C, Chatzi EN (2019) Model updating of a historic concrete bridge by sensitivity-and global optimization-based Latin Hypercube Sampling. *Eng Struct* 179:139–160
7. EN 12504–4 (2004) Testing concrete. Part 4: Determination of ultrasonic pulse velocity
8. EN 12390–3 (2019) Testing hardened concrete. Part 3: Compressive strength of test specimens
9. EN 12390–13 ((2013)) Testing hardened concrete. Determination of secant modulus of elasticity in compression
10. Roselli I, Malena M, Mongelli M, Cavalagli N, Giofrè M, De Canio G, de Felice G (2018) Health assessment and ambient vibration testing of the “Ponte delle Torri” of Spoleto during the 2016–017 central Italy seismic sequence. *J Civ Struct Health Monit* 8(2):199–216

11. Azzara RM, De Roeck G, Girardi M, Padovani C, Pellegrini D, Reynders E (2018) The influence of environmental parameters on the dynamic behaviour of the San Frediano bell tower in Lucca. *Eng Struct* 156:175–187
12. Brincker R, Zhang LM, Andersen P (2001) Modal identification of output-only systems using frequency domain decomposition. *Smart Mater Struct* 10(3):441–445

Digital Environment for Remote Visual Inspection and Condition Assessment of Architectural Heritage



Ilaria Trizio , Francesca Savini , Andrea Ruggieri ,
and Giovanni Fabbrocino 

Abstract The methods and the tools aimed to documenting and analysing the historical built heritage often follow different paths according to several disciplines involved in the knowledge process. Being aware about the importance that the scientific community confers to 3D digital representation of the buildings, this tool can play a role of a hub able to relate different data and languages. Therefore, the 3D digital model represents the privileged tool to ensure effective management of data derived from geometric, formal, architectural, diagnostic, archaeological and structural features, all aimed to subsequent restoration interventions. Despite the certain advantages associated to the use of this tool, the time to produce 3D models often conflicts with the need to document assets in emergency situations. In order to overcome this issue, the testing of a tool, the virtual tour of the artefacts, has been carried out; the tour is placed in a time phase between the survey and the construction of the digital model, representing a rapid way to geolocalize, view and record data by remote visual inspection. The virtual tour, obtained from the 360° photos deriving from the survey campaigns with the laser scanner, properly processed, allows you to remotely record the detected data on them, for example the damage analysis. The virtual tour, suitably enriched with contents, therefore turns into a connecting hub, and represents a versatile way of collaboration between various professionals, also lending itself to visualizing and recording information that can be implemented over time and which, if organized according to a logical and functional architecture,

I. Trizio (✉) · F. Savini · G. Fabbrocino
ITC-CNR, Institute for Construction Technologies, Italian National Research Council, L'Aquila
67100, Italy
e-mail: ilaria.trizio@itc.cnr.it

F. Savini
e-mail: francesca.savini@itc.cnr.it

G. Fabbrocino
e-mail: giovanni.fabbrocino@unimol.it; Fabbrocino@itc.cnr.it

A. Ruggieri · G. Fabbrocino
Department of Biosciences and Territory, University of Molise, Campobasso 86100, Italy
e-mail: a.ruggieri3@studenti.unimol.it

they provide a real opportunity for tracing the temporal evolution of the degradation phenomena on the wall surfaces.

Keywords Digital survey · Image editing · Informative virtual tour · Visual inspection · Damage detection

1 Digital Procedures for Data Management and Sharing for Architectural Heritage Condition Assessment and Monitoring

Most of the architectural heritage located on the Italian country is characterised by a constructive complexity resulting from the long evolutionary history of the sites. The historical building, like a real archive, returns this data in the form of traces of its past. In-depth knowledge of these aspects that characterise cultural heritage is fundamental for both material (of structures, sculptural works, decorative apparatus, etc.) and intangible preservation (of construction techniques, empirical knowledge, representative cultural value, etc.).

In order to achieve this goal, it is important to implement a multidisciplinary strategy with the aim of producing useful preliminary data for the design of possible conservation interventions for the safety and protection of the built heritage. In this perspective, the partnership between the different expertise involved becomes crucial, as there are many disciplines that analyse artefacts as a main and direct source of knowledge. The architectural historian, the archaeologist, the architect-restorer and the engineer, by recognising the stratigraphic sequences, the structural behaviour and the type of degradation on the artefact, are able to process the data that are indispensable for the knowledge of the historic built heritage. The common aim is to reconstruct the evolutionary history of architectural complexes by analysing the construction stages, life phases and post-depositional transformations. This approach is aimed at protecting and preserving the historical heritage, therefore it is essential to start with an understanding of the state of the artefacts. To this purpose, monitoring techniques ranging from diagnostics to the use of several sensors are used to assess the behaviour of the artefact and observe its response to external factors of both anthropic and natural.

The research team, composed of scholars from different fields (structural engineering, design, architecture, restoration, archaeology), has for years been asking questions about the methods and procedures for the acquisition, recording and analysis of such data, structuring the process in steps (Fig. 1), with a view to correct knowledge aimed at the conservation, management, use and enhancement of the historical and archaeological built heritage.

It is clear the difficulty of integrating different data acquired in different ways and the need to standardise formats and work with a view to constant exchange and sharing, especially when it comes to a multidisciplinary team, but it is also worth facing a challenge of a coral approach to the research in order to empower its impact

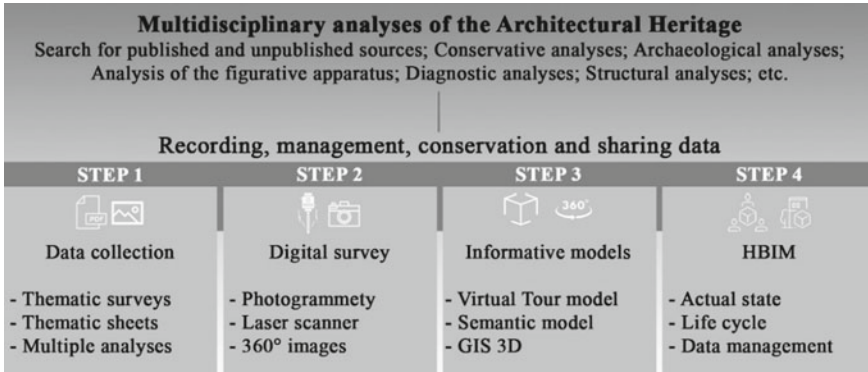


Fig. 1 Methods of documenting the historical built heritage

in practical applications. This circumstance obviously requires a joint effort not only in identifying the objectives to be achieved, but also in defining common lexicon.

3D digital models resulting from integrated survey and parametric modelling (HBIM) are privileged tools for answering these needs as they are useful for multidisciplinary data management and exchange. Furthermore, the monitoring data linked to the parametric model is directing our research towards the definition of a Historic Digital Twin (HDT), as well illustrated in a further paper that the team presents at this same volume [1]. Awareness of the unquestionable efficiency of 3D digital models is, however, combined with becoming conscious of the complexity of creating them. Indeed, their execution is subordinate not only to the needs of the project and the skills of the team, but also to the processing time, which is generally related to the level of detail and reliability to be achieved by the model.

Furthermore, in order to create digital replicas of the built heritage, which reflect the real artefact, it is important to have previously acquired and organised datasets to carry out an appropriate semantization. It is therefore essential to find intermediate solutions that meet these requirements. A system that is able to integrate the documentation of several professionals, topologically linking data to physical entities, becomes indispensable; a system that is performing with respect to a constant exchange of information with a view to a real multidisciplinary approach and not only final consultation.

In this context, therefore, a digital procedure for recording and exchanging data is presented, this has been developed from the equirectangular images taken by the laser scanner for each station point, appropriately edited with the results of conservation status and archaeological analyses. These image post-processing operations have been effective for recording damage and degradation in order to assess the structural health of the historic built heritage increasing the monitoring system through the possibility of visual inspections. The images, specially adjusted and included in an Informative Virtual Tour, proved capable of conveying information. The Virtual Tour has demonstrated many potentials starting from the archiving and consultation of multiple data—structured in a multi-level mode and with different languages, to be

used by both experts and a wider user— to the possibility of remote visual inspections by professionals, thus facilitating the monitoring of the built heritage.

The paper shows, after a brief overview of similar studies for the digitisation of data through digital procedures (Sect. 2), the potential of the Virtual Tour applied to cultural heritage with particular reference to the monitoring of architectural heritage (Sect. 3). Through the description of a case study (Sect. 4) the procedure for the elaboration of the Informative Virtual Tour is illustrated (Sect. 5). Finally, the discussion of the data (Sect. 6) underlines the results achieved and the validity of the proposed tool for the documentation and management of the historical built heritage, especially in respect to the multidisciplinary analyses carried out by the team.

2 Digitisation of Heritage Related Data, an Overview

In most of cases the innovative methods for registering and documenting the state of conservation of the historic buildings are entrusted to methods—now widely codified [2]—mainly contemplating the use of procedures linked to a three-dimensional visualization of the artifact. Digital 3D models also allow exchanging inhomogeneous information provided by the different specialists involved in the analysis as in the preservation processes.

These procedures range from the mapping of numeric models derived from Terrestrial Laser Scanning (TLS) [3] or digital photogrammetry [4], as well as the registration of many kind of data accessible in GIS 3D [5] environment or directly by generating parametric models (HBIM) suitably prepared [6]. Each of these approaches is clearly unique and undoubtedly useful for registering and sharing the amount of heterogeneous data required by the activities of the heritage conservation.

Nevertheless, the choice of the method to use is often strongly influenced by the work context and, in particular, by the time and the available budget. The generation of 3D parametric or mathematic models, as well as the mapping of digital numerical models, often requires a remarkable effort in terms of time and so of financial resources.

To overcome those issues there are intermediate procedures of interchange, registration and visualization of the 3D data, using the Virtual Tour generated from the equirectangular images, often borrowed from experiences linked to the use of the Cultural Heritage [7]. Such procedures, whose workflow has been accurately developed by a research team of the University of Princeton [8] allow to make the Informative Models usable for a series of demands such as, for instance, the ones regarding the registration of the damage state directly on the 360° images.

This approach, allowing to the user the visualization of the data overlaid on the equirectangular images, has been tested by the Authors in two different occasions: for visualizing and analysing the state of conservation of valuable frescoes on an historic masonry in one case [9], and for mapping on the 360° images the surface degradation and archaeological analyses in the other [10].

For what concerns the case study described in these pages, they report the main outcomes Virtual Tour for the analysis of the structural damage and the registration of the crack pattern, by overlaying the images of the artifact with those edited on the base of the results of the research study, evaluating the potential in the field of the visual inspection.

The Informative Model derived enables the overlapping of more data, with the aim of understanding the behaviour assumed by the artifact investigated during the 2009 earthquake on the basis of some results of the archaeological analysis.

The image editing with the results of the research study allowed us to reason about the cracks, about their position in the architectural complex and their morphology. This operation turned out to be useful for the definition of the cracks—that are collected in a database—as well as for the realization of a photographic dataset aimed to the automatic crack detection.

In the field of civil engineering, almost every study about digital images processing is directed to analyse the procedures and methods integrating the image acquisition with the computer vision techniques that, combined with the Artificial Intelligence—using a proper algorithm—allow the automatic detection of damage and deterioration on the structures, especially concrete ones. In this regard, has been made recently an accurate review of the scientific literature in the field of the crack detection on the concrete structures and the road pavements analysing about fifty scientific papers about this topic [11].

Regarding instead the historic built heritage, for which the damage analysis is usually directed to the consequent planning of restoration interventions, the crack detection is still an underused procedure, although in literature there are first examples related to this kind of approach [12].

3 Virtual Tour as Support to Architectural Heritage Monitoring

The team has for some time been carrying out research studies aimed at identifying common lexicons and ways of exchanging data between the different branch of knowledge involved in documenting and analysing of the historical built heritage, with the aim of conserving it through restoration and planned conservation, starting with the implementation of monitoring techniques. The research carried out by the team are outlining digital procedures that combine different methodologies and tools, from integrated survey to multi-data topological linking on the 3D models. In this respect, an important example is the already defined integrated digital system for the analysis and monitoring of historical infrastructures, in particular masonry bridges [13]. Furthermore, more experiments are aimed at creating 3D parametric models, now uncontested and increasingly oriented towards of Digital Twins [14, 15], to define procedures and workflows to develop of this HDT [1]. At the same time, the following are being tested Virtual Reality systems applied to the management and

access of data are being tested [16, 17] aware of the massive potentials of these tools for virtual technical visits. As well as its undoubted capacity for communication and enhancement, Virtual Reality has potential for documenting the historical built heritage and for managing heterogeneous data in several formats (from 2D to 3D data, from alphanumeric data to images, from text to audio files, etc.). This is due to the ability of Game Engine platforms to use different models ranging from photogrammetric mesh [16] to parametric models (HBIM) [18] and to link a lot of information to these that the user can freely use. System capabilities are also useful for structural analysis and risk management [19].

Another type of Virtual Reality, not based on polygons, is the Virtual Tour generated from images. This is a different kind of Virtual Reality with dissimilar functions, which is widely used in the field of cultural heritage, from archaeological sites to museums, and which has become more widespread with the Sars-Cov-2 pandemic [20–26]. In addition, Virtual Tours can implement more complex virtual networks [27] that allow the enjoyment of a wide range of heritage from intangible heritage [28] to inaccessible contexts such as underwater sites [29].

The Virtual Tour, however, also has capabilities in the more technical field of data recording and exchange since, if suitably designed, it becomes a hub capable to store a multitude of information, also those relating to the state of conservation of the artefact and the assessment of the damage [8, 9, 30–32]. The opportunity to create a multilevel structure can meet the needs of different professionals, but also of operators and administrators who are involved in the management process of the historical built heritage in various ways.

The features of the Informative System, together with the possibility of structuring it by levels, from the general one useful for the fruition of a wide public, to the specialised one for experts, transforms the Virtual Tour into a useful digital tool for monitoring the architectural heritage. This tool, by internal and external links, allows the use of different types of data in a single environment: from sheets to processed images with the results derived from multidisciplinary studies and diagnostic analyses, such as thermographic images. In addition, the possibility of annotating, directly in the virtual environment, the observations resulting from the analysis of the images at the time of acquisition and the several data linked to them, such as sheets, historical images, catalogues and tables with the diagnostic results, makes the Virtual Tour useful for remote visual inspection.

The main goal of the Virtual Tour, which is part of the broader field of Virtual Reality, is to reduce the time between the detection of the pathology or damage and the identification of the needed intervention to limit the effects of degradation with the subsequent decrease in the related costs. Visualisation within a virtual environment, as well as being aimed at the virtual fruition of the digital replica, is an interesting way of analysing the degree of knowledge of the artefact and the way in which the data, particularly dynamic data, is managed within the model.

The most effective benefit of virtual reality as an information system for data visualisation is the opportunity to provide information at decision makers and project managers. These can be organised, according to the type of target, in a short space of time, while also providing a range of possible scenarios and solutions. Stakeholders

involved in this phase do not always have the necessary knowledge to analyse and interpret the results and make the appropriate decision.

4 San Giovanni Complex, Damage and Degradation Assessment

The Abbey of San Giovanni Battista (Fig. 2) is located in Lucoli, a small municipality formed by 16 hamlets far about 15 km from the city of L'Aquila. Its quite wide territory lies just beyond the northern boundaries of the Sirente-Velino Natural Park and can be divided into an inhabited sub-mountain area and an uninhabited mountain one. Nowadays, the municipality presents itself as an aggregate of small hamlets separated by the orography of the area.

Each of these has, in its small way, very interesting historic-religious monuments: among them, the most important is for sure the Abbey of San Giovanni Battista, with its thousand-year history and its grandeur. Local people even today look at the Abbey as a community symbol, just like this sense of identity had never extinguished. Despite of the partial inaccessibility of the building, the citizens go there to pray as to enjoy the pleasant tranquillity of the place.

The abbey—dated to 1077 [33]—was founded *ex novo* by Odorisio, Count of Marsi in a typical scheme of expansion of the rural seignories [34], and has played its part in the new foundation of L'Aquila city during the Angevin time, carried out by all the Castles spread throughout the territory (the current hamlets in the province of L'Aquila), to which was granted a space called *locale* in the area enclosed by the city's defensive walls. Thus, the church in the Lucolan's *locale* was entitled to San Giovanni, as the abbey in Lucoli hamlet, that also named the entire *quarto* (quarter), one of the four parts in which the city is still nowadays divided.

The complex maintained its importance during the medieval times, enriched by interventions between the XIII and the XIV century [35] and decorative works in modern times [36]. At the end of the XX century, the abbatial church was restored [37] as well as following the 2009 earthquake. A detailed review of the published material produced during the restoration phase in the 90 s [36, 37], in the context of a Ph.D. project about light archaeological drafted in 2007 [34, 35, 38, 39] and finally a degree thesis [40] in 2020 have been accomplished as an informed approach to the multidisciplinary survey carried out onsite [10].

The case study has been subjected of a laser scanner survey employing the phase difference scanner Faro Focus S70, equipped with an integrated camera. The survey has been carried out in three different campaigns, reaching a total of 77 scans. The scanning parameters (point density, quality, HDR) were ranged depending on the circumstances respect the dimensions of the spaces surveyed, their complexity and the lighting conditions. Subsequent to the procedure of data acquisition, the post-processing of the point cloud has been carried out into the software SCENE 2018



Fig. 2 The abbey of san giovanni battista in Lucoli (AQ)



Fig. 3 View of the point cloud

(version 2018.0.0.648) [41], finally obtaining a cloud formed by 1.833.460.115 points (Fig. 3).

The deterioration analysis of the building has been recorded by image processing on the spherical panoramas starting from the damage analysis made in situ on the orthomosaic plans. The correct detecting of the degradation phenomena requires experience in recognizing the different forms such as a critical attitude evaluating them. In this direction, acts as reference the “Raccomandazioni NorMal—1/88. Alterazioni macroscopiche dei materiali lapidei: lessico” [42].

The document reports and describes the different forms of degradation and alteration, along with the causes and photographic reproductions, also with a normalized graphic symbology (not adopted in this case, being not well suitable with the image processing procedure). The unhealthier prospects are the ones facing the road (North-East and South-East): have been detected encrustations, biological colonies and stains on the stonework; detachment, exfoliation, erosion, stains and swelling on the plasterwork. About the anthropic interference there’s no presence of acts of vandalism, nevertheless, were detected the signs of inappropriate workings.

Furthermore, has been implemented a damage analysis on the cracks mainly caused by the 2009 earthquake—that seriously affected the entire territory of L’Aquila—as the followings, not excluding the 2016 central-Italy one. The reference in this field is the regulation about the Central Italy 2016 earthquake, specifically the ordinances of the Special Commissioner for the Reconstruction [43–45]. In the present case the crack pattern does not appear so severe, but specifically in the images here presented - regarding the inner court - there are some breakage of structural elements (stone columns as wooden beams) as different types of cracking typical in a post-earthquake scenario: vertical cracks at the corners pointing walls disconnection, such as diagonal cracks as signs of shear breakage; also, damaged floors and vaults provisionally supported by wood and steel props.

5 Informative Virtual Tour of St. Giovanni’s Abbey: Design and Structure of a Digital Medium

The experimentation presented in this paper is specifically aimed at testing the validity of the Virtual Tour for recording structural damage and the state of conservation of surfaces, in order to assess its effectiveness for SHM, the analysis of the state of artefacts and visual inspection, as already demonstrated by similar works in this field [8, 9, 30–32]. The Informative Virtual Tour has been developed with a proprietary software 3DVista Virtual Tour Pro (release 2020.4.0). The Virtual Tour has been designed on several levels, selectable from a drop-down menu available in the tour home page. The first part contains general information about the Abbey and its history, written in a popular key for a wide public, but with bibliographical details for technicians and experts. Thanks to the structure of the project, it is possible to view the parts of the Abbey and to access additional content such as texts and photos using interactive buttons (Fig. 4).

From the main menu it is also possible to start the guided tour structured by themes, from a simple tour of the complex to a tour with scientific data. The Virtual Tour of the Abbey has been created from the images obtained for each point of the laser scanner station during cloud acquisition. The images after being edited in their original size using 2D graphics software to achieve the equirectangular format, they have been imported into the software 3DVista to generate spherical panoramas. The different spherical panoramas were then linked together within the same software, creating a guided tour of the Abbey.

It is possible to switch from one panorama to another thanks to special hotspots that function as teleporters or by selecting the appropriate icon on the map (Fig. 5).

Using the same system, thematic tours have been created from the previously processed equirectangular images with the results of the research study in 2D image



Fig. 4 Multilevel structure of the virtual tour with general information and specific reference

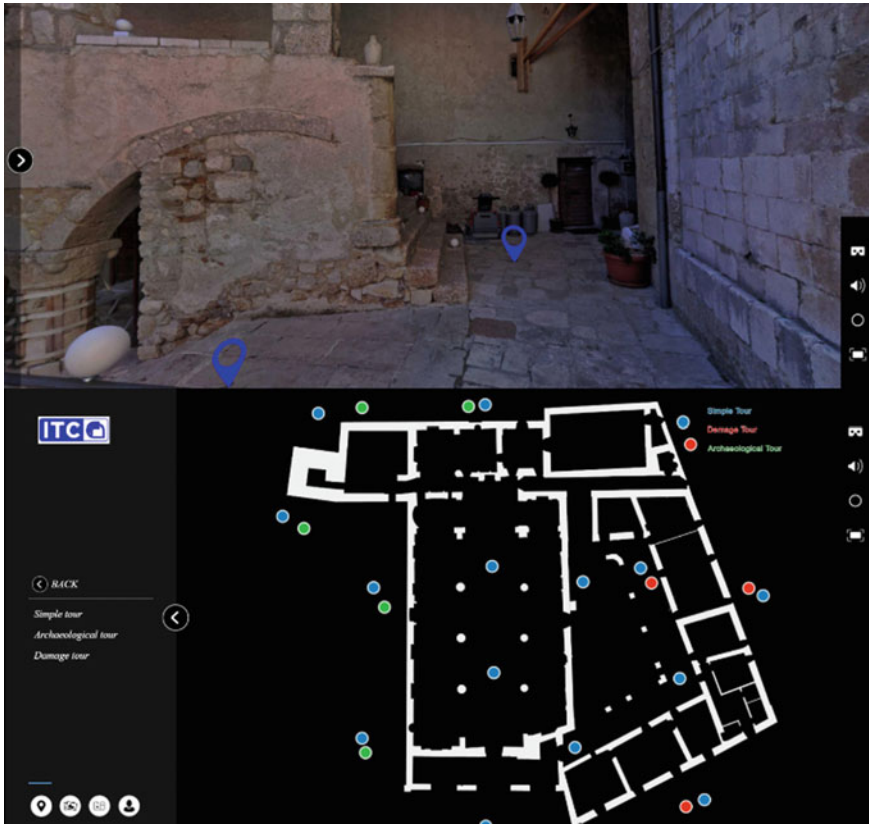


Fig. 5 Transporter system ensuring movement between points for the virtual visit

editing environments. For the thematic tours, it has been decided to use a black-and-white base on which the data have been colour-coded, each having a meaning encoded in the legend (Fig. 6). The Virtual System has been designed to allow the user to move freely between the thematic itineraries; through specific hotspots, it is possible to switch from one path to another, as well as simultaneously displaying data from the research studies.

In the damage tour it is possible to display the data in different colours, which are then shown in the legend, which can also be activated with a button. In addition, it is possible to query the system to obtain information on the state of conservation of the selected area and at the same time make notes for visual inspection, thanks to a special button that links to an online shared sheet (Fig. 7).

Linking external applications allows the Virtual Tour to include references to specific cataloguing systems, such as the SURvey and CoNDition AssessmEnt (SUNDAE catalogue) developed by the team. The ability to connect to this database, which is enriched with data from web mapping and social media platforms, exploiting



Fig. 6 Virtual tour of the damage path with information hotspots and damage survey legend

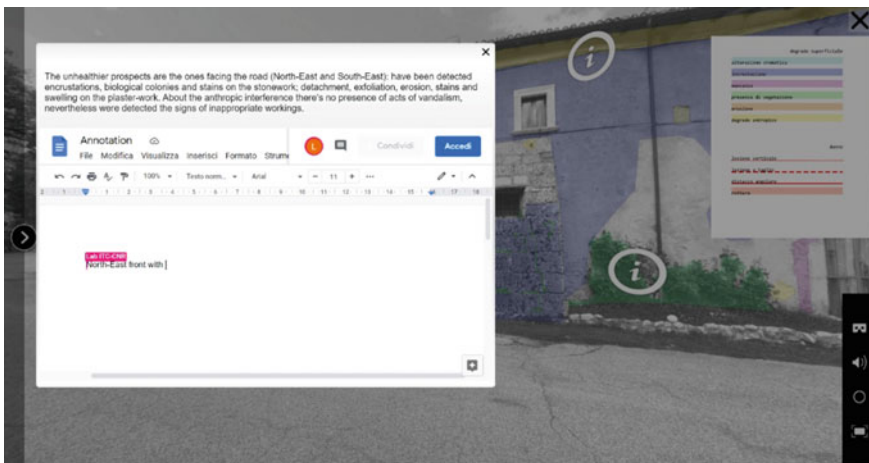


Fig. 7 Annotation tool in the virtual environment

the resources offered by new technologies and crowdsensing tools, allows the Virtual Tour to be implemented. So, this last is transformed into a complex informative system that is useful for assessing the state of conservation of the cultural heritage and for developing proactive programming plans based on a holistic view of the artefact [46, 47].

In addition, through the main menu, it is possible to view the technical reports resulting from the research and from a recently written dissertation [40]—fundamental for a correct analysis—and, using the dedicated buttons, download these technical datasheets. In addition, the possibility of adding hotspots, as well as the

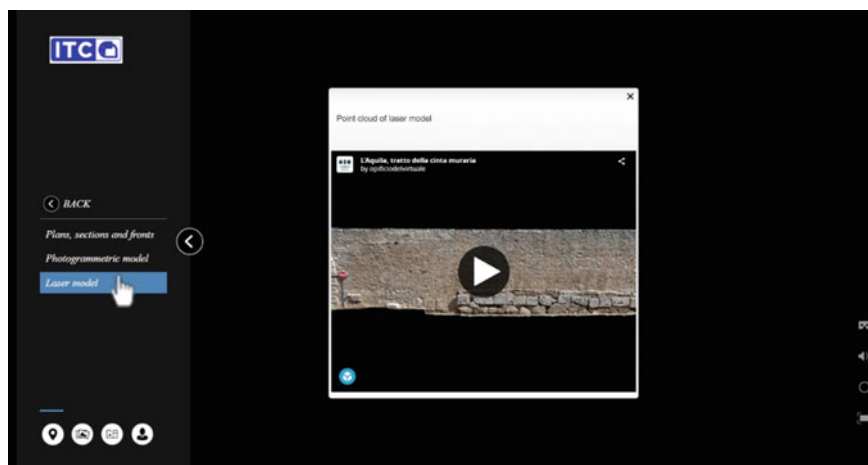


Fig. 8 Link to technical documents and the Sketchfab online viewer for visualising part of the digital models (photogrammetry and laser) of the Abbey

aforementioned references to external applications (drives, databases, videos, etc.), allows the use of 3D objects (point cloud or mesh) in the same environment, thanks to pop-up windows that connect with online viewers (Fig. 8).

The potential of the Virtual Tour augmented with multidisciplinary data, thus structured as an information model, or rather as a hub capable of storing multilevel information, is manifold. It is an effective tool for managing the documentation of historical architectural heritage in emergency contexts and the exchange of data between professionals. In addition, it has a key role in the subsequent stages of heritage documentation involving the creation of 3D data and the linking of data to this (informative photogrammetric models, 3D GIS, HBIM, Informative Virtual Reality System), as already tested by the team [1]. The dialogue between several professionals and research fields is facilitated by the system's ability to overlay different thematic readings in a single digital environment. In addition, the system allows: the opportunity to simulate the third dimension, linking several images that allow a complete view of the artefact; the possibility to link data and use them in the Virtual Tour and the relative ease of creating the tour (with limited costs and time).

Finally, the possibility of access to technical documents produced with the multidisciplinary analyses, easily and in a way, that is overlaid on the representation of reality, makes it a useful tool also for heritage administrators who are called upon to protect historic buildings.

6 Discussion and Final Remarks

The Informative Virtual Tour presented in this conference does not claim to replace the classic survey tools (thematic survey, sheets, diagnostics, etc.) and does not want to underestimate the effectiveness of 3D models for the analysis and management of the historical built heritage. The main goal is to present a versatile tool for recording multiple data related to the representation of the artefact useful for monitoring the current condition of the asset, as well as to define the workflow developed for its implementation (Fig. 9). Although it is a 2D representation, the ability to simulate the third dimension offered by the spherical projection created around the user also allows us to consider the spatiality of the artefacts under investigation.

With the experimentation, the potential of the Informative Virtual Tour has been outlined, confirming its effectiveness for the digital documentation of the built heritage, already positively evaluated by the team for the management of data on the conservation of the decorative elements [9] and further highlighting its validity for the recording of damage and deterioration. This tool becomes also useful for visual inspection, which also allows observations and notes to be made during the tour directly in the virtual environment, thanks to the support of several professionals who are able to interact in this environment, reporting any critical issues in remote mode.

The Virtual Tour also has great potentials for monitoring the state of conservation of the asset, since it is possible to capture images several times to update the project and analyse the state of preservation over time. A Virtual Tour based on the equirectangular images obtained from the laser survey of the architectural complex was presented at this conference. This is not the only way of capture images, as it is possible to obtain spherical panoramas by processing photos taken with a digital camera placed on a tripod with a rotating head or with a special Cam360°. This reduces acquisition time and costs and demonstrates the effective potentials of the presented system for monitoring the historic built heritage.

The exercise achieved unexpected results in the exchange of data within the multidisciplinary team and directed the work towards an integration of knowledge. This was made possible by the processing of the images, which in turn facilitated the interpretation of the data in a truly multidisciplinary way. The strength of the tool, as well as the short processing time, is its ability to collect data and make it available in a single environment. Through the images elaborated from the scientific data, it is possible to follow thematic paths (archaeological tour or damage tour).

The analysis of the Abbey of San Giovanni Battista in Lucoli (AQ), chosen as a case study for defining the operational procedure, made it possible to think about some significant aspects, integrating the data from the damage survey and stratigraphic analysis of the masonry with image editing techniques to combine several thematic readings in a single environment. The use of heterogeneous data in an interactive virtual environment confirmed the effectiveness of the multidisciplinary approach and the common lexicon for a correct knowledge of the built heritage.

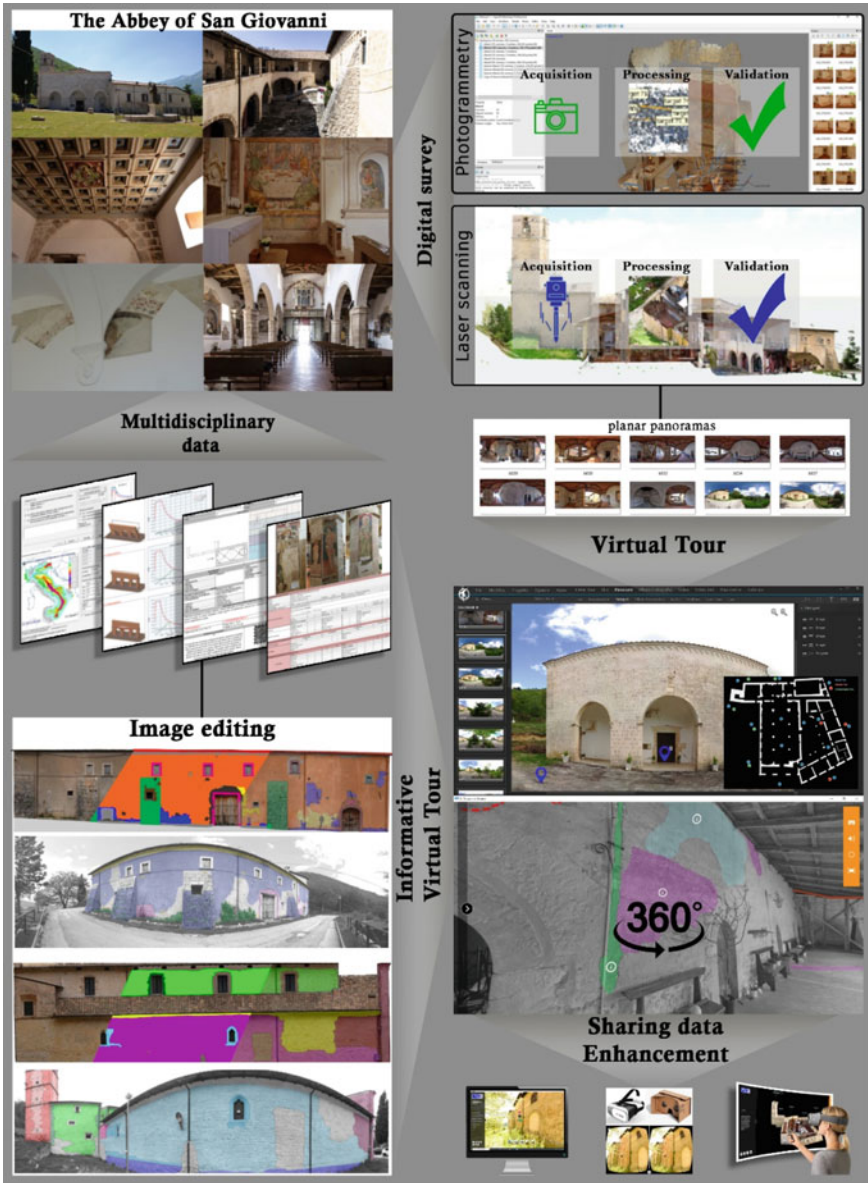


Fig. 9 Operational procedure for the implementation of the informative virtual tour

Although the aim of the paper is not to present data from multidisciplinary analyses [10], which have already been discussed in other contexts, in order to better clarify the potential of the tool, some examples are given below which confirm the effectiveness of the simultaneous visualisation of the different thematic readings.

Indeed, the simultaneous availability of the data from the archaeological analysis and the one from the study of the state of conservation has contributed to identifying stratigraphic relationships that were not visible between the various parts of the architectonic complex. This is especially so in cases where the layers of covering (historical plaster or modern cement), by edging the masonry, have obliterated the stratigraphic relationships making it difficult to reconstruct the evolutionary history of the complex. For example, there is an injury in the southern corner of the first floor of the inner court, which is the result of a corner fracture; this confirms the presence of two historical walls from different periods, built on top of each other, as hypothesised by archaeological analysis based on the relationships between the architectural elements of two portals placed side by side (Fig. 10).

Furthermore, it has been possible to observe how some injuries present on the masonry, consequent to the 2009 earthquake, partially follow the interfaces of the Stratigraphic Units of Masonries (SUM), i.e. the various parts that make up the building and that are the result of historical construction and destructive actions. This confirms the effectiveness of the archaeological analysis of masonry in identifying potential ‘weak points’ caused by historical interventions such as the rebuilding of a wall following a collapse, the addition of a building to support older structures or the opening of doors and windows not originally planned. The possibility of accessing highly scientific, technical and popular information in different formats (text, video and audio) makes this a very versatile tool. Indeed, the Informative Virtual Tour structured with the layering of different topics and different levels of consultation, as well as fulfilling technical documentation needs and being a useful tool for remote



Fig. 10 Virtual tour with overlapping thematic readings

visual inspection by professionals, becomes a useful tool for the stakeholder, both in terms of heritage conservation and for its enhancement and use.

The implemented Virtual Tour system not only provides access to information by increasing the knowledge of the cultural heritage, but also improves the accessibility of the heritage to a wide public through the possibility of a virtual, interactive and innovative visit. The opportunity to navigate the digital space, in desktop or immersive mode with pc, cardboard or VR box, places the user at the centre of the scene, allowing him or her to enjoy the asset from both a technical and cultural point of view, while at the same time increasing the area's tourist offer.

In addition to the above-mentioned results, other aims have been achieved with the experimentation, which the team is further investigating with further research. Specifically, the Informative Virtual Tour has proved to be a useful tool for the creation of 3D digital copies of artefacts such as informative photogrammetric models, 3D GIS, HBIM and HDT [1].

Based on the assumption that 3D models, which are undisputed in the management of data and its exchange, are effective if elaborated from the results of a research study and its interpretation, it is possible to use the Virtual Tour with the data linked topologically to the physical entities, in the phase of realisation of the replicas. Finally, one of the potential developments of the tool, in the broadest terms of a collection hub, is the connection to monitoring systems for the built heritage; it is possible to virtually place sensors in the Virtual Tour and use the monitoring data in this environment thanks to links to external databases, confirming the enormous potential of virtual reality for the condition assessment of historical built heritage.

Author Contributions The research presented is the result of authors' collective work, of continuous comparison and of a common discussion. Ilaria Trizio wrote Sect. 2; she also supervised the survey phase and paper. Francesca Savini wrote Sects. 3 and 5; she also defined the Informative Virtual Tour. Andrea Ruggieri wrote Sect. 4; he also realized the laser survey. Giovanni Fabbrocino conceived and supervised the research. All authors wrote Sects. 1 and 6.

References

1. Marra A, Trizio I, Fabbrocino G, Digital tools for the knowledge and safeguard of historical heritage. In: Rainieri C et al (eds) *Civil Structural Health Monitoring, Lecture Notes in Civil Engineering* 156. https://doi.org/10.1007/978-3-030-74258-4_41
2. Tucci G, Conti A, Fiorini L (2018) Geomatics for structural assessment and surface diagnostic of CH. *Procedia Struct Int* 11:2–11
3. Bitelli G, Castellazzi G, D'Altri AM, de Miranda S, Lambertini A, Selvaggi I (2018) On the generation of numerical models from point clouds for the analysis of damaged Cultural Heritage. In: *IOP conferences. Series: materials science and engineering*, p 364
4. Marchetti A, Redi F, Savini F, Trizio I, Giannangeli A (2017) La chiesa di San Cipriano a Castelvecchio Calvisio (AQ) nella Baronìa di Carapelle: documentazione speditiva e analisi stratigrafica 3D del manufatto (In Italian). *Archeologia dell'Architettura*, XXII, 239–253
5. Continenza R, Trizio I, Rasetta A (2013) Digital integrated models for the restoration and monitoring of the cultural heritage: the 3D architectural information system of the church of

- santa maria del carmine in Penne (Pescara, Italy). In: Di Giamberardino P, Iacoviello D, Natal Jorge AM, Tavares JMRS (eds) *Computational modelling of objects represented in images: fundamentals, methods and applications III*. Taylor & Francis Group, London, pp 439–443
6. Oreni D, Brumana, Della Torre S, Banfi F (2017) Survey, HBIM and conservation plan of a monumental building damaged by earthquake. *Int Arch Photogramm Remote Sens Spatial Inf Sci XLII-5/W1*
 7. Maiellaro N, Varasano A, Capotorto S (2019) Digital data, virtual tours, and 3D models integration using an open-source platform. In: Duguleană M et al (eds), *VRTCH 2018, CCIS 904*, pp 148–164. https://doi.org/10.1007/978-3-030-05819-7_12
 8. Napolitano RK, Scherer G, Glisic B (2018) Virtual tours and informational modeling for conservation of cultural heritage sites. *J Cult Heritage* 29:123–129
 9. Trizio I, Savini F, Giannangeli A, Fiore S, Marra A, Fabbrocino G, Ruggieri A (2019) Versatil tools: digital survey and virtual reality for documentation, analysis and fruition of cultural heritage in seismic areas. *Int Arch Photogramm Remote Sens Spatial Inf Sci XLII-2/W17:377–384*
 10. Trizio I, Savini F, Ruggieri A (2020) Archeologia dell'architettura e rappresentazione digitale: procedure e strumenti tra connessioni e intersezioni/Archaeology of the Architecture and Digital Representation: Procedures and Instruments between Connections and Intersections. In: Arena A, Arena M, Brandolino RG, Colistra D, Ginex G, Mediati D, Nucifora S, Raffa P (eds) *Connettere. Un disegno per annodare e tessere/Connecting. Drawing for weaving relationships*, pp 2821–2842, FrancoAngeli, Milano
 11. Mohan A, Poobal S (2017) Crack detection using image processing: a critical review and analysis. *Alexandria Eng J* 57(2):787–798
 12. Galantucci RA, Fatiguso F (2019) Advanced damage detection techniques in historical buildings using digital photogrammetry and 3D surface analysis. *J Cult Heritage* 36:51–62
 13. Savini F, Rainieri C, Fabbrocino G, Trizio I (2021) Applications of stratigraphic analysis to enhance the inspection and structural characterization of historic bridges. *Infrastructures* 6:7
 14. Jouan P, Hallot P (2019) Digital twin: a HBIM-based methodology to support preventive conservation of historic assets through heritage significance awareness. *Int Arch Photogramm Remote Sens Spatial Inf Sci XLII-2/W15*
 15. Jouan P, Hallot P (2020) Digital twin: research framework to support preventive conservation policies. *ISPRS Int J Geo-Inf* 9:228
 16. Trizio I, Savini F, De Gasperis G, Cordisco A (2018) Siti perduti e inaccessibili: l'interpretazione del patrimonio attraverso applicazioni di realtà virtuale (In Italian). In: Salerno R (eds). *Rappresentazione materiale/immateriale. Drawingas (in) tangible representation*, pp 831–836, Gangemi Editore, Roma
 17. Trizio I, Savini F, De Gasperis G, Cordisco A, Fiore S (2019) La navigazione VR di un'opera d'arte per la narrazione di una fabbrica storica/ VR navigation of a work of art for the tale of a historical building. In: Belardi P (eds) *Riflessioni. L'arte del disegno/Il disegno dell'arte. Reflections. The art of drawing/ The drawing of art*, pp 1767–1774, Gangemi Editore, Roma
 18. Banfi F (2020) HBIM, 3D drawing and virtual reality for archaeological sites and ancient ruins. *Virt Archaeol Rev* 1
 19. Lee J, Kim J, Ahn J, Woo W (2019) Context-aware risk management for architectural heritage using historic building information modeling and virtual reality. *J Cult Heritage* 38:242–252
 20. Neovesky A, Peinelt J (2015) A virtual tour to the inscriptions of the UNESCO World Heritage Site St. Michael in Hildesheim. *Electron Visualisation Arts*. 285–290
 21. Moysiadis AK (2018) Photogrammetry and interactive 3D virtual tour to the out-reach of cultural heritage. The case study of the Church of Panagia Episkepsi, Trikala, Greece. In: ICOMOS 19th general assembly and scientific symposium “heritage and democracy”, 13–14th Dec 2017, New Delhi, India
 22. Kersten TP (2018) 3D Models and virtual tours for a museum exhibition of viet-namese cultural heritage exhibits and sites. In: Ioannides M et al (eds) *Digital heritage. progress in cultural heritage: documentation, preservation, and Protection*. EuroMed 2018. Lecture Notes in Computer Science, vol 11196. Springer, Cham

23. Wallgrün JO, Huang J, Zhao J, Ebert C, Roddy P, Awe J, Murtha T, Klippel A (2018) Immersive technologies and experiences for archaeological site exploration and analysis. In: Fogliaroni P, Ballatore A, Clementini E (eds) Proceedings of workshops and posters at the 13th international conference on spatial information theory (COSIT 2017). COSIT 2017. Lecture Notes in Geoinformation and Cartography, pp 307–314, Springer, Cham
24. Wolf K, Reinhardt J, Funk M (2018) Virtual exhibitions: what do we win and what do we lose? In: Proceedings of the conference on electronic visualisation and the arts (EVA '18), pp 79–86, BCS Learning & Development Ltd., Swindon, GBR
25. Maach I, Azough A, Meknassi M (2018) Development of a use case for virtual reality to visit a historical monument. In: 2018 International conference on intelligent systems and computer vision (ISCV), pp 1–4
26. De Luca V, Conati Barbaro C, La Marca C, Savino ML, Rosati P (2019) L'open source per i musei: il tour virtuale del Museo delle Origini (Sapienza Università di Roma) [In Italian]. *Archeologia e Calcolatori* 30:479–482
27. De Fino M, Ceppi C, Fatiguso F (2020) Virtual Tours and Informational Models for improving territorial attractiveness and the smart management of architectural heritage: the 3D-IMP-ACT project. *Int Arch Photogramm Remote Sens Spatial Inf Sci XLIV-M-1-2020*:473–480
28. Mah OBP, Yan Y, Tan JSY, Tan Y-X, Tay GQY, Chiam DJ, Wang Y-C, Dean K, Feng C-C (2019) Generating a virtual tour for the preservation of the (in)tangible cultural heritage of Tampines Chinese Temple in Singapore. *J Cult Heritage* 39:202–211
29. Bruno F, Lagudi A, Barbieri L, Muzzupappa M, Mangeruga M, Pupo F, Cozza M, Cozza A, Ritacco G, Peluso R, Tusa S (2017) Virtual diving in the underwater archaeological site of Cala Minnola. *Int Arch Photogramm Remote Sens Spatial Inf Sci XLII-2/W3*:121–126
30. Napolitano R, Blyth A, Glisic B (2018) Virtual environments for visualizing structural health monitoring sensor networks, data, and metadata. *Sensors* 18:243
31. Blyth A, Napolitano R, Glisic B (2019) Documentation, structural health monitoring, and numerical modeling for damage assessment of the Morris Island Lighthouse under environmental loading. *Philos Trans R Soc*
32. De Fino M, Galantucci RA, Fatiguso F (2019) Remote diagnosis and control of Heritage Architecture by photorealistic digital environments and models. *Scires-it* 9(2):1–16
33. Muratori AL (1741) *Antiquitates Italicae Medii Aevii*, vol. V, ex Typographia Societatis Palatinae in Regia Curia, Roma
34. Marcotulli C (2008) Il conte e l'abate. Incastellamento comitale e trasferimento dei poteri sui monti di Lucoli (AQ) da un'indagine di archeologia 'leggera' (In Italian). *Temporis Signa. Rivista di archeologia della tarda antichità e del medioevo III*, 117–139
35. Marcotulli C, Lo viscovo e lo abbate, ... ambo con le mitre, stavano cantu lato (2019) San Giovanni Battista di Collimonto di Lucoli dentro e fuori le mura dell'Aquila: luoghi del potere e maestranze (In Italian). In: Volpe G, Favia P (eds) V Congresso Nazionale di Archeologia Medievale, pp 767–772, Insegna del Giglio, Firenze
36. Pasqua M (1996) La chiesa di San Giovanni Battista a Collimonto di Lucoli (In Italian). *Opus. Quaderno di Architettura e Restauro* 5:25–56
37. Mancini R (2001) San Giovanni Battista di Lucoli. Storia, cronologia, restauro (In Italian). Japadre, L'Aquila
38. Marcotulli C (2010) De ecclesiis construendis: maestranze e committenti. La "rifondazione angioina" dell'Aquila e la costruzione di un'identità cittadina nella prima metà del XIV secolo (In Italian). *Archeologia Medievale XXXVII*:467–484
39. Marcotulli C (2011) Chiese, castelli e strategie 'baronali'. Le trasformazioni del paesaggio medievale abruzzese fra feudalità signorile e città fondata alla luce della ricerca archeologica: un caso di studio (In Italian). *Ricerche Storiche XLI* (1):181–208
40. D'Angelo A (2019) *Rilievo e mitigazione della vulnerabilità sismica dell'Abbazia di San Giovanni Battista di Lucoli* (In Italian). (Unpublished Master Degree thesis). Università degli Studi dell'Aquila
41. FARO Technologies Inc. SCENE (Computer Software) (2018). Retrieved from https://knowledge.faro.com/Software/FARO_SCENE/SCENE. Accessed on 16 Feb 2021

42. CNR-ICR: Raccomandazioni NorMaL-1/88 (1990) Alterazioni macroscopiche dei materiali lapidei: lessico (In Italian). Roma
43. Presidenza del Consiglio dei Ministri: Misure per il ripristino con miglioramento sismico e la ricostruzione di immobili ad uso abitativo gravemente danneggiati o distrutti dagli eventi sismici verificatisi a far data dal 24 agosto 2016 (In Italian). Ord. 19 07/04/2017. <https://sisma2016.gov.it/2017/04/11/ordinanza-n-19-registrata-il-07042017-al-numero-761/>. Accessed on 14 Jan 2021
44. Presidenza del Consiglio dei Ministri: Misure per il ripristino con miglioramento sismico e la ricostruzione di immobili ad uso abitativo gravemente danneggiati o distrutti dagli eventi sismici verificatisi a far data dal 24 agosto 2016 (In Italian). Ord. 28 09/06/2017. <https://dev.sisma2016data.it/wp-content/uploads/2017/06/Ordinanza-n.-28-del-giugno-2017.pdf>. Accessed on 14 Jan 2021
45. Presidenza del Consiglio dei Ministri: Modifiche alle ordinanze n. 4 del 17 novembre 2016, n. 8 del 14 dicembre 2016, n. 9 del 14 dicembre 2016, n. 13 del 9 gennaio 2017, n. 19 del 7 aprile 2017, n. 32 del 21 giugno 2017, n. 33 dell'11 luglio 2017, n. 37 dell'8 settembre 2017, n. 38 dell'8 settembre 2017 e n. 39 dell'8 settembre 2017 (In Italian). Ord.46 11/01/2018. <https://sisma2016.gov.it/wp-content/uploads/2017/12/Ordinanza-n.-46-del-10.01.2018-1.pdf>. Accessed on 14 Jan 2021
46. Marra A, Fabbrocino G (2020) Open-access web mapping as a virtual survey tool for cultural heritage: an application to the Armenian religious architecture documented by Paolo Cuneo. *DisegnareCon*, 13(25)
47. Marra A, Fabbrocino G (2021) Crowd-based tools for indirect condition assessment and conservation of cultural heritage. In: Ioannides M, Fink E, Cantoni L, Champion E (eds) *Digital Heritage. Progress in Cultural Heritage: Documentation, Preservation, and Protection*. EuroMed 2020. Lecture Notes in Computer Science 12642, pp 38-50, Springer, Cham

Stange Overpass: Finite Element Model Updating of an Unconventional Railway Bridge



Emrah Erduran, Kltigin Demirlioglu, Albert Lau, Kameran Aziz, Ian Willoughby, Endre Hyldmo, Tomislav Arsenovic, and Enzo Martinelli

Abstract Stange Overpass is a three-span railway reinforced concrete bridge on the Dovre line that connects the cities of Oslo and Trondheim in Norway. It was built in 2002 and has been extended by 1,5 m in each direction in 2004. During the extension operation, the part of the deck that has been extended from the abutments had not been placed on a foundation but, instead, had directly been constructed over the soil mass. Within the context of the Intercity project that has recently been undertaken by the Norwegian Railway Authority (BaneNOR), passenger trains that cross Stange Overpass will be upgraded to high-speed trains. For this, the existing bridge needs to be evaluated for the new train type. This requires a finite element model that correctly and reliably models the dynamic behavior of the bridge under various environmental and loading conditions. Preliminary analysis results show that the most significant

E. Erduran (✉) · K. Demirlioglu
Department of Civil Eng. and Energy Tech., Oslo Metropolitan University, Oslo, Norway
e-mail: emrah.erduran@oslomet.no

K. Demirlioglu
e-mail: kultigin@oslomet.no

A. Lau
Department of Civil and Environmental Engineering, Norwegian University of Science and Technology, Trondheim, Norway
e-mail: albert.lau@ntnu.no

K. Aziz · I. Willoughby · E. Hyldmo · T. Arsenovic
Bane NOR, Oslo, Norway
e-mail: kameran.aziz@banenor.no

I. Willoughby
e-mail: ian.willoughby@banenor.no

E. Hyldmo
e-mail: endre.hyldmo@banenor.no

T. Arsenovic
e-mail: tomislav.arsenovic@banenor.no

E. Martinelli
Department of Civil Engineering, University of Salerno, Fisciano, Italy
e-mail: e.martinelli@unisa.it

© The Author(s), under exclusive license to Springer Nature Switzerland AG 2021
C. Rainieri et al. (eds.), *Civil Structural Health Monitoring*, Lecture Notes in Civil Engineering 156, https://doi.org/10.1007/978-3-030-74258-4_56

parameter that governs the dynamic behavior of the bridge is the load-deformation behavior of the soil that directly supports the ends of the deck that extends outwards from the abutments. The load-deformation behavior of the soil can be expected to be highly sensitive to the environmental conditions and the changes in these conditions from summer to Nordic winter. To provide a reliable estimate of the load-deformation behavior of soil as well as a reliable finite element model, an instrumentation setup will be installed in the bridge by Oslo Metropolitan University in collaboration with BaneNOR. A new finite element model updating algorithm will be developed that can not only estimate the traditional linear parameters but also the non-linear force-deformation relationship of the soil mass that supports the bridge deck. This article provides a summary of the project together with initial results that include sensitivity analysis that has been conducted to quantify the effects of the soil model on the dynamic behavior of the bridge.

Keywords Acceleration measurements · Finite element model updating · Railway bridge

1 Introduction

The existing railway bridge infrastructure in Norway and Europe is aging rapidly. As of 2017, more than 35% of half a million railway bridges in Europe are over 100 years old with many more on the wrong side of their 50-year design life [1]. In addition, the bridge infrastructure is subject to ever-increasing speeds and heavier axle loads due to the rapid advances in train technology.

Bane NOR is responsible for monitoring, maintenance and control of over 3000 railway bridges in Norway. With an increase in the design velocity and design axle load of the trains that will be used on a specific line, Bane NOR is required to ensure that all the bridges on that line is capable of carrying the new design loads safely and without hindering the comfort of the passengers. This often requires detailed finite element (FE) analysis of the bridges under generic or specific train loads [2]. The accuracy of verification of a bridge under the changing train loads and the entailing decision with regards to the future of the bridge depends solely on the accuracy of the finite element model. As such, an accurate FE model that is capable of simulating the actual behavior of the bridge is indispensable for the verification of existing bridges under changing loads. However, FE models are generally created based on design drawings and material specifications. The results obtained from these models do not usually match the field measurements [3]. The differences are generally related to material properties and uncertainties in boundary conditions. Therefore, calibration of finite element models to accurately replicate the behavior of the bridge to be evaluated is crucial. This is especially true for bridges that have unique structural systems which potentially have significantly different behavior compared to regular bridges.

Stange Overpass is a bridge with such a unique structural system. It is located near the Stange Station and spans over the Fv222 road. The bridge, which was designed in 1999 and constructed in 2002, is part of the Dovre line (*Dovrebanen*) project. The Intercity project aims to build a double-track train line between Oslo and Lillehammer and is part of the Intercity development. As part of this project, Stange Overpass, which was originally designed for speeds up to 200 km/h, needs to be verified for train speeds up to 250 km/h. Stange Overpass, which is a set of twin bridges that house one track each, has a unique structural system as the extensions of the bridge from the abutments were designed as cantilevers without any contact between the bridge deck and the abutment. The field observations show that one of the two twin bridges indeed has such a structural system. However, the deck of the second bridge sits on a concrete slab that covers the top of the abutment, which, in turn, is seated on the soil mass that is filled in the u-shaped abutment.

Recently, an assessment of the bridge using sophisticated finite element models for HSLM-A train load for speeds ranging from 30 km/h to 300 km/h. As a result of this assessment, which is based on a FE model created using design drawings, it was concluded that the bridge is far from satisfying neither the safety nor the comfort criteria set forth by current standards. For the comfort criteria, EN 1991-2 [2] requires that maximum accelerations should not exceed 3.5 m/s^2 . However, the analysis results show that the maximum accelerations reach up to 35 m/s^2 . The computed accelerations exceeded the limit by three folds even for train speeds of 30 km/h. These excessive vibration levels should have led to significant displacement in the ballast, which in turn could have led to track misalignment and derailment. Furthermore, the acceleration levels exceeding the gravity of acceleration should have led to between the wheel and the rail [4]. Despite the extremely high acceleration levels computed using finite element models based on the design drawings, the trains continue to cross the bridge several times each day without any problems or any reported passenger discomfort. These observations suggest that the finite element model based on the design drawings is far from providing reliable estimates of the acceleration levels occurring on the bridge due to train traffic.

Within this context, Bane NOR and Oslo Metropolitan University (OsloMet) has commenced on a collaborative research project (*NEAR: Next Generation Finite Element Calibration Method for Railway Bridges*) that aims to develop a finite element model updating method for railway bridges that can reliably estimate the acceleration demands under various boundary and environmental conditions and train loads. This article summarizes the outline of the project as well as the initial results.

2 Stange Overpass

Stange Overpass is a 48 m long, three-span railway bridge situated on the Dovre line (*Dovrebanen*) which connects the cities of Oslo and Trondheim in Norway. The bridge is situated right by the Stange station and is heavily trafficked by both passenger and freight trains. The bridge is constructed as twin bridges; each one

housing one set of tracks. The bridges were constructed in 2002 and originally both were 9.0 m shorter than their current length. The original bridges were seated at elastomeric bearings at each end that are mounted at the top of U-shaped abutments. In 2004, the bridges were extended 4.5 m in each direction from both abutments. During the extension operation, the newly constructed bridge deck have not been seated on the wings of the U-shaped abutments but have been left as cantilevering at both sides. The decks were then connected to the rest of the tracks with the help of transfer plates that are seated at the edge of the deck at each end of the bridge. The bridge is supported by two reinforced concrete circular piers. Figure 1 shows the location and overhead view of the bridge (a), a 3D rendering of the bridge with focus on one of the abutments (b) as well as the view from the east side of the bridge (c).

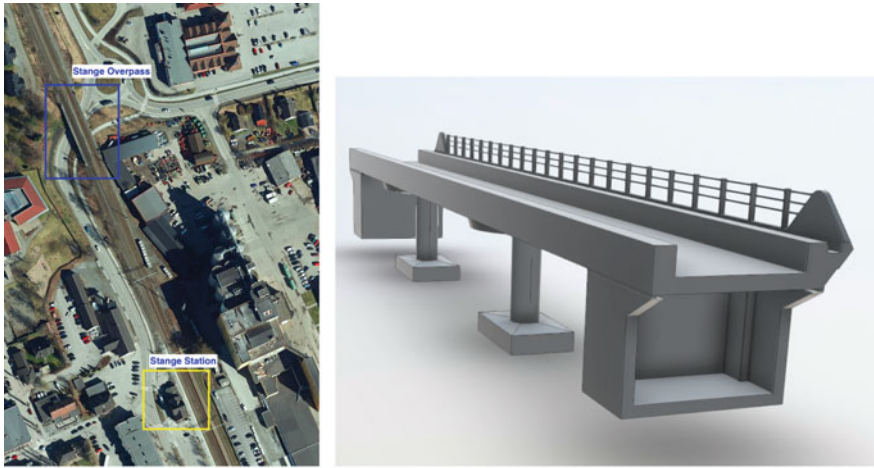
The site inspection conducted by the authors revealed that the twin bridges have significantly different boundary conditions at the ends of the bridge decks. The first bridge is constructed as shown in the design drawings with the extended parts of the deck cantilevering from the elastomeric bearings at each end with a clear separation between the deck and the wings of the abutment. On the other hand, the other bridge, which has the exact same structural configuration has been seated on concrete slabs that are placed on the backfill material that fills the abutments (see Fig. 1c). Therefore, the two bridges can be expected to have a significantly different behavior. In addition, the temperature difference between summer and winter, which has previously been documented to impact the stiffness and damping of ballast and track [5], can be expected to have an even more significant impact on the dynamic behavior of Stange Overpass due to the unconventional boundary conditions.

Figure 2 depicts the plan and the elevation views of the Stange Overpass where the overall dimensions of the bridge along with the placement of the elastomeric bearings are shown.

3 State of the Art, Knowledge Needs and Preliminary Results

Calibration of finite element models, also known as FE model updating, is a procedure to determine the uncertain physical properties in the FE model based on experimental results to achieve a FE model that can represent the observed behavior of the structure accurately. As the need for accurately assessing the existing structures under varying conditions continue to increase, so does the need for accurate finite element models. As such, calibration of FE models of engineering infrastructure has been gaining attention in the last decade. Among the different type of field experiments, use of vibration data from traffic loading remains the most useful and popular approach as this data is readily available to harvest and process.

FE model calibration methods can be divided into two based on their approach to the problem: (i) Direct methods and (ii) Indirect methods [3]. The first approach directly updates the mass and stiffness matrices of the structure but it is very difficult



(c)

Fig. 1 Overview of the stange overpass

to apply to large structures with very large matrices. It can also lead to ill-conditioned problems for very complicated models [6, 7]. The iterative methods, on the other hand, rely on updating the physical properties behind the FE model such as material and geometric properties. As a result, they are more flexible and efficient for large scale structures [3].

Almost all available methods that leverage vibrations due to regular traffic on bridges aim to accurately match either the vibration frequencies, mode shapes or a combination of these two parameters [8]. These vibration parameters are popular

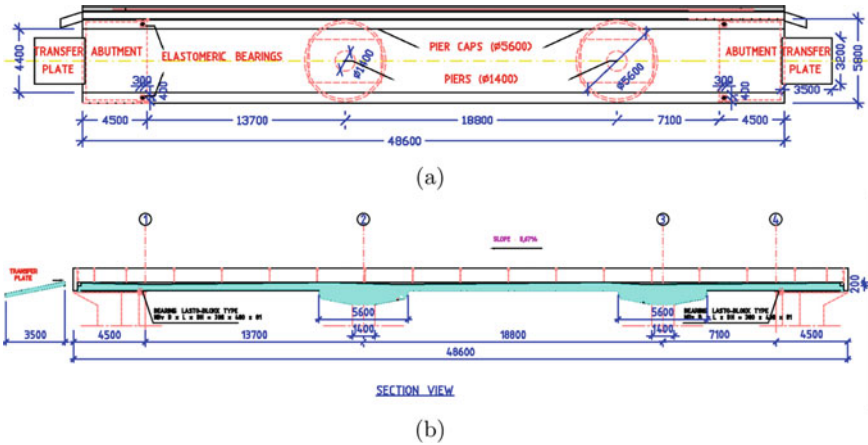


Fig. 2 a Plan and b elevation view of the stange overpass

because they depend solely on the material and geometric properties of the structure, i.e. independent of the loading. On the other hand, the evaluation of bridges is based on the maximum accelerations and forces occurring on the bridge under different train loads. So far, to the best of our knowledge, no available method tackled the challenge of calibrating FE models to provide accurate estimates of observed accelerations under different loads. Furthermore, all the available methods in literature [8] have been developed and validated for bridges that are supported by conventional foundations at both ends. Stange Overpass provides an important challenge as each of the twin bridges has very unconventional boundary conditions: In one of the bridges, the deck is cantilevering 4.5 m from the bearing in each direction, while in the other bridge this portion rests on a concrete slab of unknown thickness, which, in turn, sits on backfill material with unknown properties. Here, it should be noted that, even though the first bridge has been described as cantilevering from the bearings, the bridge is connected to the rest of the track by a 20 mm thick concrete transfer plate at each end. However, this transfer plate had not been designed to transfer any loads and it has been placed on a seating on the deck that is 200 mm deep and 4400 mm wide; Fig. 3. On the other hand, despite the lack of a stiff connection, the transfer plate can be assumed to be held in place by the weight of the ballast and track impeding the deck from behaving as a cantilever. In short, both bridges have challenging boundary conditions that are highly likely to impact their dynamic behavior and the maximum accelerations occurring on the bridge due to various train loads.

In order to evaluate the impact of the boundary conditions on the dynamic behavior of the bridge, a series of preliminary analysis was conducted. For this, a detailed 3-D model of the bridge was developed in the finite element program SAP2000. The deck and the columns of the bridge were modeled using 8-node solid elements while the elastomeric bearings have been modeled using elastic springs in three orthogonal direction. An overview of the preliminary analysis model is shown in Fig. 4. This

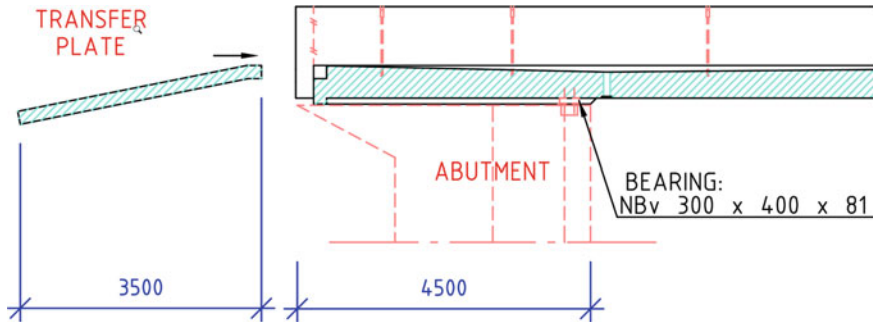


Fig. 3 Detail of the connection between the bridge deck, abutment and the transfer plate

Table 1 Modeling parameters used in the preliminary analysis

Parameter	Value	Spring stiffness
Modulus of elasticity (E), Concrete	38,000 MPa	–
Modulus of elasticity (E), Elastomeric bearing	550 MPa	815,000 kN/m
Shear modulus GE), Elastomeric bearing	0.90 MPa	1500 kN/m
Soil stiffness—Soft soil	16,000 kN/m ³	–
Soil stiffness—Stiff soil	64,000 kN/m ³	–

model, where the last 4.5 m of the bridge deck (i.e. from the elastomeric bearings to the edge of the deck) is working as a cantilever, was used as the baseline model. The effect of the concrete slab seated on soil mass is then modeled using surface springs acting at the bottom of the bridge. Since the soil properties are unknown, a range of spring stiffnesses, that were taken from [9], has been applied to simulate various soil conditions from soft to stiff soil. It should be noted that, the values given in Table 1 for soft soil stiffness can represent both loose sand and clayey soil with a tip resistance lower than 200 kPa while the stiff soil can represent both dense sand and clayey soil with a tip resistance higher than 800 kPa. Thus, the preliminary analysis covers both sandy and clayey soils as the soil type is unknown. Table 1 summarizes the properties of concrete, the elastomeric bearing and the stiffness of the surface spring that simulates the behavior of soft and stiff soil. The stiffness of the point springs that simulate the elastomeric bearings computed using the mechanical and geometric properties of bearings are also given in Table 1.

Modal analysis have been conducted to evaluate the impact of the boundary conditions on the vibration frequencies and mode shapes of the bridge. Table 2 summarize the frequencies and the modal mass participations of the first three modes in the vertical direction for different boundary conditions. The corresponding mode shapes are depicted in Fig. 5. Both the values summarized in Table 2 and the mode shapes

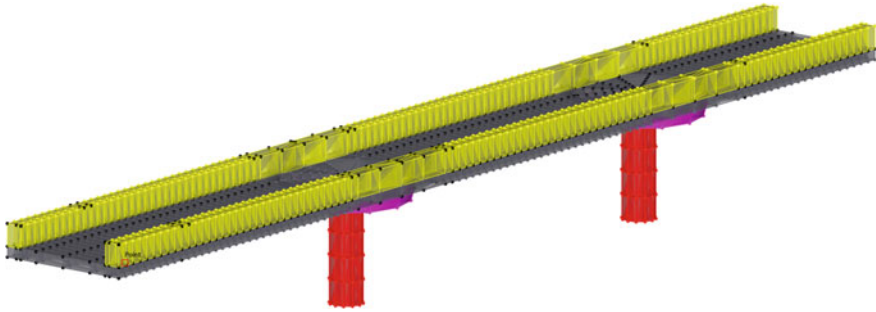


Fig. 4 Overview of the preliminary analysis model

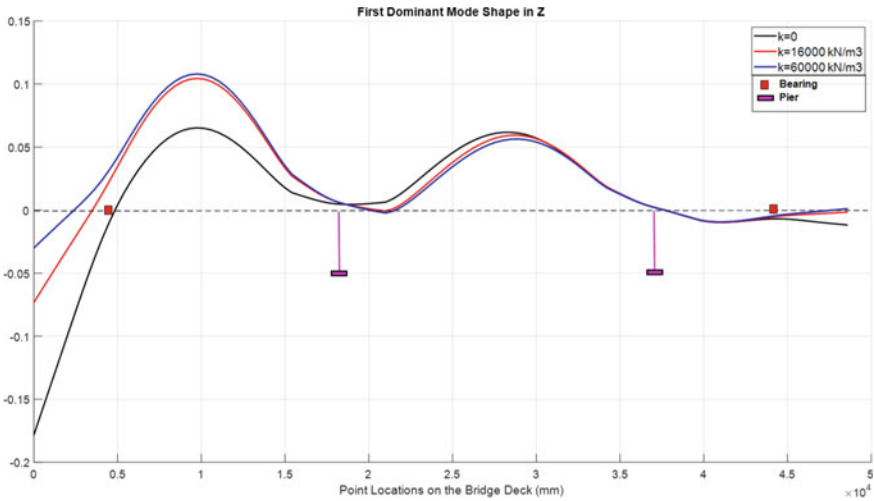
Table 2 Frequencies and modal mass contributions of the first three modes in the vertical direction

Parameter	Cantilever	Soft soil ($k = 16,000 \text{ kN/m}^3$)	Stiff soil ($k = 64,000 \text{ kN/m}^3$)
First mode frequency (Hz)	14.75	16.05	16.35
First mode mass part (%)	7.0	29.1	36.2
Second mode frequency (Hz)	17.50	20.93	30.42
First mode mass part (%)	37.0	20.3	7.0
Third mode frequency (Hz)	33.72	33.90	38.69
Third mode mass part (%)	14.1	13.2	3.1

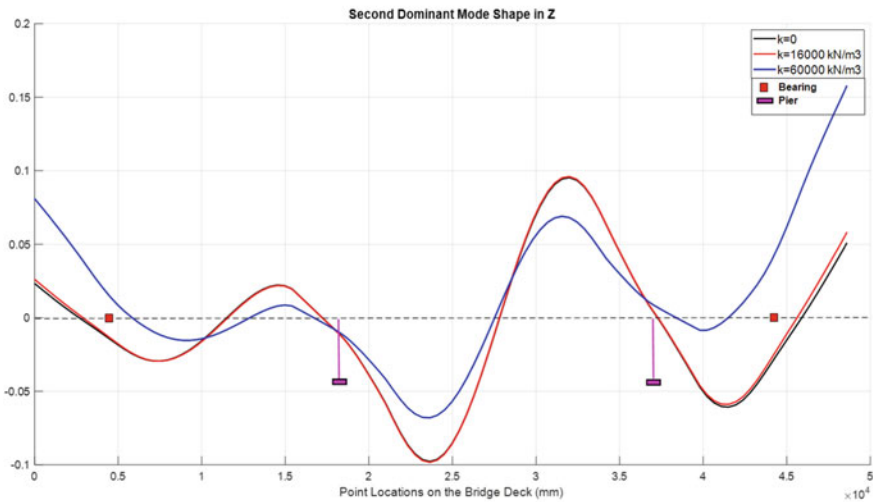
shown in Fig. 5 show that the dynamic behavior of the Stange Overpass is significantly influenced by the boundary conditions. It should be noted that, the modal contributions of the three first vertical modes of the bridge is relatively low. This can be attributed to the high stiffness in the vertical direction with potentially six support points, i.e. two piers, two elastomeric bearings and two parts supported by a slab resting on elastic foundations (Fig. 2) within a total span length of 50m. This would lead to a higher number of modes contributing significantly in the vertical direction and, hence, lower mass participation ratios for the individual modes. Apart from the effect on the modal shape values at the ends of the bridge, which can be stated to be expected, the modal mass contributions of different modes are also significantly influenced by the boundary conditions. More specifically, the predominant mode shape in the vertical direction in terms of modal mass contribution shifts from the second mode to the first mode with increasing soil stiffness at the bridge ends.

The preliminary numerical analysis presented above indicate that, the boundary conditions at the ends of the bridge is by far the most important parameter as far as the vibrations on the bridge is concerned. Hence, accurate estimation of the boundary conditions is of paramount importance for the calibration of the finite element model. As the behavior of soil varies significantly with the load it is exposed to as well as the environmental conditions, the boundary conditions of the bridge can be expected to be dependent on the weight and the speed of the train crossing the bridge. As such,

conventional finite element models updating methods that are based on estimating the modal frequencies and the mode shapes of the structure, which considers only the linear behavior of the structure, cannot be expected to be sufficient for the calibration of the finite element model of the Stange Overpass.



(a)



(b)

Fig. 5 Effect of soil stiffness on the first three dominant mode shapes in the vertical direction

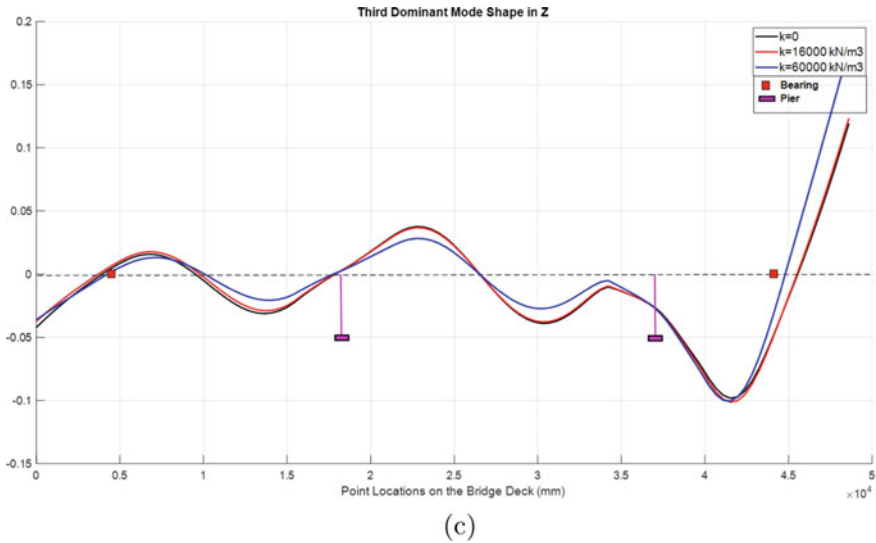


Fig. 5 (continued)

4 Open Challenges and Proposed Methodology

The conventional finite element calibration procedures rely mainly on predicting the mode shapes identified from acceleration measurements. By their nature, modal analysis and modal parameters are based on linear structural behaviour. However, for the structures where soil structure interaction is expected to be significant, these methods may not be sufficient as the behavior of soil can become nonlinear even at relatively small strains. For structures, where nonlinear behaviour of soil is expected to play a significant role, an improved finite element calibration method that provides reliable estimation of the nonlinear force-deformation relationship of the soil and its interaction with the structure is required.

The NEAR project will develop a two-step iterative procedure to overcome this shortcoming. For this, Stange Overpass will be used as the testbed as its behavior is expected to be significantly impacted by soil-structure-interaction. Figure 6 provides an overview of the proposed methodology.

The first step of the proposed methodology will utilize the free-vibration measurements and the response parameters such as the vibration frequency and the mode shapes to calibrate the physical parameters of the finite element model. The physical parameters to be calibrated will be selected from a large set of parameters based on the sensitivity study carried out on the initial FE model out of a larger set. This set will include but not be limited to Young's modulus of the deck, Young's Modulus of the piers, mass of the sleepers and ballast, mass density of the bridge deck, stiffness of the bearings between the abutments and the deck, stiffness of the support springs at the two ends of the deck. The preliminary numerical analysis show that

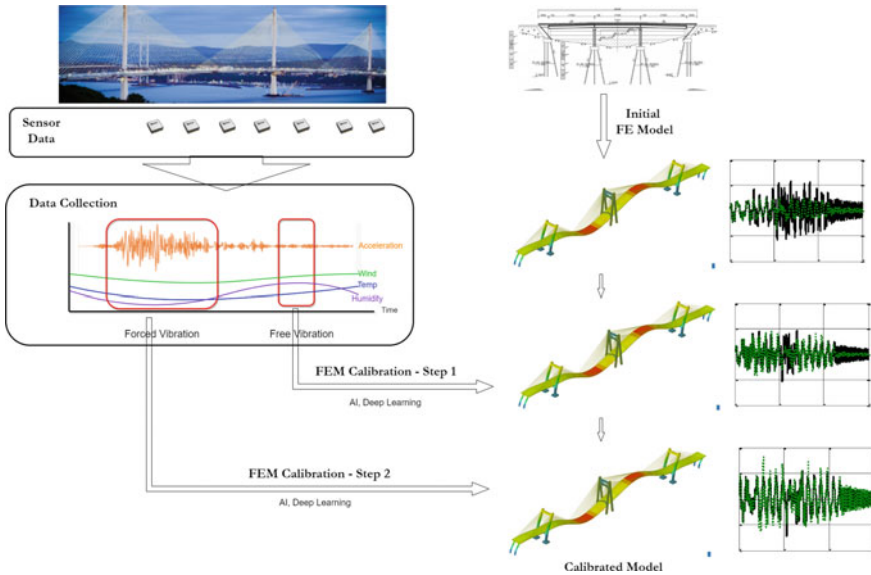


Fig. 6 Methodology of the NEAR project

the stiffness of the support springs at the ends of the bridge, which simulate the behavior of the bridge deck sitting directly on soil, is arguably the most important parameter that affects the vibrations on the bridge. Considering this unique behavior, the methodology will have special focus on estimating this parameter accurately and reliably by sensor clustering at the ends of the bridge, i.e., by deploying an array of accelerometers and displacement sensors near and at the ends of the bridge. The data from the sensor clusters will be evaluated and analyzed using various methods including machine learning and artificial intelligence to provide an accurate estimate of the boundary conditions under varying environmental conditions using the free vibration data. Due to the nature of modal analysis and modal parameters, the estimated structural parameters at this stage will be limited to equivalent linear values. Therefore, one short coming of the finite element model calibrated using free vibration data in this stage will be its inability to capture the potential nonlinearity in the soil behavior that would lead to a change in behaviour for various train loads and speeds as well as the environmental conditions.

In order to capture the nonlinear soil behaviour, the finite element model will be further calibrated using the recorded forced vibration data, i.e., vibrations induced by train crossings. The linear parameters computed from the first step will be used as the starting point of the second step in order to obtain a more reliable, accurate and effective machine learning algorithm. The second step will focus solely on the calibration of the nonlinear force-deformation relationship of soil that directly supports the deck at both ends of the bridge. More specifically, the structural parameters that are expected to remain elastic such as Young’s modulus of concrete, mass of the

sleepers and ballast, mass density of the deck will be taken directly from the first step and will be kept constant in the second step. The linear springs that are used in the first step will be replaced by nonlinear springs that can capture the effects of the loading on the spring stiffness.

For the analysis of the FE model under the train load, first the train load including the number of axles, the weight of each axle and the speed of the train will be determined using the strain gauges placed on the rail tracks. This data will then be combined with the information recorded at the accelerometer and displacement sensors and strain gauges to calibrate the weight at each axle. The train loading data will then be used as input to the finite element model and several numerical analysis with various nonlinear force-deformations for the soil springs will be conducted in order to create the training data for the machine learning algorithms. These numerical analysis will be repeated under various train types and speeds. The trained machine learning algorithm will provide the best estimates of the nonlinear-force deformation relationship that will emulate the behavior of the soil on which the ends of the bridge deck rests. This second step, where the objective is to calibrate the nonlinear force-deformation relationship for the soil springs based on the estimations of the maximum accelerations recorded under external loads, is a novel approach to finite element model calibration as current state-of-the art methods consider only the first step, i.e., free vibration, which is limited to linear models.

The novel two-step calibration procedure will be repeated several times during the project duration for different types of trains and various environmental conditions in order to fine-tune the finite element model and to ensure that the model can capture the effects of variations in the environmental conditions on the dynamic behavior of the bridge.

5 Summary and Conclusion

This article summarizes the background of a collaboration project undertaken by the Norwegian Railway Authority and the Oslo Metropolitan University. The project aims to develop a two-step finite element model calibration methodology that can be used to reliably and estimate the accelerations on railway bridges whose behavior is significantly influenced by non-linear soil-structure-interaction. The methodology will be developed based on long term monitoring of vibrations on the Stange Overpass. Numerical analysis conducted on initial model of the Stange Overpass reveals that the dynamic behavior of the bridge is dominated by the boundary conditions at each end of the bridge where the bridge deck had been extended 4.5 m from the elastomeric bearings. Through long term monitoring of the accelerations, extensive numerical analysis and machine learning algorithms, the finite element model of the bridge will be calibrated with particular attention to the nonlinear soil structure interaction at the bridge ends.

The proposed method aims first to use classical finite element model calibration methods in order to calibrate the linear structural parameters using the free vibration

data. As the next step, the nonlinear force-deformation relationship of the springs that represent the soil behavior will be calibrated by training machine learning algorithms so that the acceleration estimates from the numerical models will match the forced vibration data for various train loads and speeds.

References

1. Casas JR, Moughty JJ (2017) Bridge damage detection based on vibration data: past and new developments. *Front Built Environ* 3:4
2. EN: EN 1991-2 Eurocode 1 (2003) Actions on structures—part 2: Traffic loads on Bridges. CEN, Brussels
3. Chen X, Omenzetter P, Beskhyroun S (2014) Calibration of the finite element model of a twelve-span prestressed concrete bridge using ambient vibration data. In: 7th European workshop on structural health monitoring
4. Zacher M, Baeßler S (2009) Dynamic behaviour of ballast on railway bridges. In: *Dynamics of high-speed railway bridges*. pp 99–112. Taylor & Francis
5. Gsemyr H, Aziz K (2019) Dynamic modelling regarding stresses on existing bridges in heavy haul operation considering track irregularities on ofotbanen. In: *International heavy haul conference*
6. Friswell M, Mottershead J, Ahmadian H (2001) Finite element model updating using experimental test data: Parametization and regularization. *Philos Trans Roy Soc Lond Ser Math Phys Eng Sci* 359:169–186
7. Wang H, Li A, Li J (2010) Progressive finite element model calibration of a long-span suspension bridge based on ambient vibration and static measurements. *Eng Struct* 32:2456–2556
8. Moravej H, Jamali S, Chan T, Nguyen A (2017) Finite element model updating of civil engineering infrastructures: a review literature. In: 8th International conference on structural health monitoring of intelligent infrastructure
9. Bowles J (1996) *Foundation analysis and design*. McGraw-Hill Company, New York

OMA: From Research to Engineering Applications



Salvatore Russotto, Alberto Di Matteo, Chiara Masnata,
and Antonina Pirrotta

Abstract Ambient vibration modal identification, also known as Operational Modal Analysis (OMA), aims to identify the modal properties of a structure based on vibration data collected when the structure is under its operating conditions, i.e., when there is no initial excitation or known artificial excitation. This method for testing and/or monitoring historical buildings and civil structures, is particularly attractive for civil engineers concerned with the safety of complex historical structures. However, in practice, not only records of external force are missing, but uncertainties are involved to a significant extent. Hence, stochastic mechanics approaches are needed in combination with the identification methods to solve the problem. In this context, this paper's contribution is to introduce an innovative ambient identification method based on the Hilbert Transform to obtain the analytical representation of the system response in terms of the correlation function. This approach opens the pathway for a monitoring system that is user friendly and can be used by people who have little to no knowledge of signal processing and stochastic analysis such as those who are responsible for the maintenance of a city's historical buildings. In particular, this method operates in time domain only. Specifically, firstly the correlation functions matrix $\mathbf{R}_X(\tau)$ is determined based on the recorded time domain data. Next, performing a Singular Value Decomposition (SVD) on $\mathbf{R}_X(\tau)$ for $\tau = 0$ leads to an estimate of the modal matrix Φ containing all the modal shapes. In this manner, once Φ is known, the entire correlation functions matrix in modal space $\mathbf{R}_Y(\tau)$ is recovered. Further, the analytical signals of the auto-correlation functions in modal space are determined performing the sum of each auto-correlation function with its Hilbert transform. Moreover, since the analytical signal can be expressed in terms of amplitude and phase, then frequencies and damping ratios estimation is possible. Finally, in order to prove the reliability of the method several numerical examples and an experimental test are reported.

Keywords Operational modal analysis · Structural identification · Correlation function · Hilbert transform · Analytical signal

S. Russotto (✉) · A. Di Matteo · C. Masnata · A. Pirrotta
Dipartimento di Ingegneria, Università degli Studi di Palermo, Viale delle Scienze Ed.8, Palermo, Italy
e-mail: salvatore.russotto01@unipa.it

1 Introduction

A fundamental step for the *Structural Health Monitoring* (SHM) is the structural identification that, from a dynamic point of view, coalesces with the identification of natural frequencies, damping ratios and modal shapes.

In literature there are a lot of dynamic identification methods that can be subdivided into two main classes: *Experimental Modal Analysis* methods (EMA) and *Operational Modal Analysis* methods (OMA) [1]. The first one can identify the non-linear behavior of a structure but requires the knowledge of the structural input. This aspect is penalizing because the artificial generation of the structural input is complicated and very expensive in the in situ tests. On the other hand, the set-up of the OMA methods is very cheap and simple because these methods don't require the knowledge, and thus the artificial generation of the structural input. Furthermore, since the structural input in the OMA method is an ambient noise due to traffic, wind, ground vibrations, use of the structure and so on, it is possible to identify the dynamic properties in the real operative conditions and the structural input is moldable as a white noise. For these advantages, in the last decades, the researchers focused their attention on the OMA methods.

Another classification of the identification methods can be done considering the domain in which they are developed, in fact OMA methods are subdivided in: time domain methods, frequency domain methods and hybrid domain methods [2]. Frequency domain methods in OMA, like *Peak Picking and Half Power Bandwidth Method* (PP+HP) [3] and *Frequency Domain Decomposition* (FDD) [4, 5], are usually based on the *Power Spectral Density* (PSD) estimation that can be performed by using the Welch's method [6, 7]. The estimation of the PSD with the Welch's method allows to have different advantages due to the decomposition of the structural output in sub-signals to which is possible to apply time windows (Tukey, Hamming, Hanning) and to assign an overlap length. However, the use of this method is difficult for a non-expert user and the choice of the sub-signals length, the kind of window to apply to every sub-signal and the overlap length can influence the results especially in terms of damping ratios estimation. Furthermore, if the modes are very close the identification of the dynamic properties might not be very accurate [3]. There are several time domain methods in literature, such as: *Natural Excitation Technique* (NExT) [8] that, when the excitation is an ambient vibration, it requires that the analytical form of free-vibration and the analytical form of the structural output are the same; *Stochastic Subspace Identification* methods (SSI) [2] divided into *covariance-driven* models (SSI-COV) and *data-driven* models (SSI-DATA); *Auto Regressive Moving Average* models (ARMA) [9] that are articulated into *Auto Regressive* (AR) step and *Moving Average* (MA) step. Hybrid domain methods can be developed in time-frequency domain, like methods based on the Wavelet transform [10], or they can be divided into different steps some in the time domain, others in the frequency domain. An example of the latter is the *Analytical Signal Method* (ASM) [11] that profits by the advantages due to the use of the analytical signal i.e. a high sensitivity to the

minimum variations of the natural frequency. Due to the aforementioned advantages the analytical signal is also used for the identification of structural damage [12, 13].

In this paper, a new OMA method founded upon stochastic mechanic's principles is proposed. It uses a *Singular Value Decomposition* (SVD) [14] to reproduce the relationship between the correlation functions matrix in the nodal space and correlation functions matrix in the modal space. The proposed method, called *Time Domain Analytical Signal Method* (TD-ASM) for the similarity with the hybrid method ASM, does not involve the difficulties due to the use of Welch's method, in fact it is developed only in time domain. Furthermore, the analytical signals of the correlation functions are used in order to have a high precision in the frequencies identification.

2 Proposed Method: *Time Domain Analytical Signal Method* (TD-ASM)

2.1 *Identification Algorithm for SDOF Systems*

In this section, a novel OMA method is proposed. This method allows to identify natural frequency and damping coefficient of the SDOF structures enforced by ambient vibration. After the acquisition of the output process $X(t)$, its correlation function $R_X(\tau)$ is calculated. The analytical signal of the correlation function can be estimated by summing the correlation function to its Hilbert transform multiplied by the imaginary unit; in fact, the analytical signal is a complex signal in which the real part is the original function and the imaginary part is its Hilbert transform. Finally, the dynamic properties of the structural system can be estimated from the properties of the analytical signal: amplitude $A(\tau)$ and phase $\theta(\tau)$. The different steps of the proposed method for SDOF structures can be resumed in:

- (1) Acquisition of the structural output process $X(t)$;
- (2) Estimation of the correlation function $R_X(\tau)$;
- (3) Reconstruction of the analytical signal $z_X(\tau)$;
- (4) Identification of the dynamic properties.

For SDOF structures the proposed method is very similar to the ASM but it is simpler than the latter because the estimation of the PSD with the Welch's method is removed. In particular, the direct estimation of the correlation function allows to overcome the difficulties introduced by the use of the Welch's method for the evaluation of power spectral density; in fact, the choice of the time windows applied to the sub-signals and the overlap length between two successive sub-signals can influence the results, furthermore the use of the Welch's method requires high specialized skills.

In order to introduce the proposed method in details, a linear SDOF shear-type frame with mass m , stiffness k and damping c is used. The dynamic properties to

identify are: the natural frequencies of the structure $f = \sqrt{k/m}/(2\pi)$ and the damping ratio $\zeta = c / (4\pi mf)$.

When the signal of the input force is not acquired and the excitation source is due to ambient vibrations, the key hypothesis of OMA is that the structure can be considered as excited by a white noise process, defined as in [15–18], and, consequently, the stochastic differential equation governing the structural motion is

$$\ddot{X}(t) + 2\zeta\omega_0\dot{X}(t) + \omega_0^2X(t) = W(t) \tag{1}$$

where ω_0 is the circular frequency that is equal to $2\pi f$. Adding the initial condition to the Eq. (1), the structural response process $X(t)$ can be obtained.

The correlation function $R_X(\tau)$ of the output response process $X(t)$ can be estimated as

$$R_X(\tau) = E[X(t)X(t + \tau)] - \mu_X^2 \tag{2}$$

where μ_X is the mean of the process $X(t)$. Since $X(t)$ is a zero-mean process the Eq. (2) coalesces with

$$R_X(\tau) = E[X(t)X(t + \tau)]. \tag{3}$$

The Hilbert transform $\hat{R}_X(\tau)$ of the correlation function $R_X(\tau)$ is, for definition, the convolution of $R_X(\tau)$ with the signal $1/(\pi \tau)$, i.e. it is the response to $R_X(\tau)$ of a linear time-invariant filter having impulse response $1/(\pi \tau)$. Therefore $\hat{R}_X(\tau)$ can be calculated as

$$\hat{R}_X(\tau) = \frac{1}{\pi} \wp \int_{-\infty}^{\infty} \frac{R_X(\tilde{\tau})}{\tau - \tilde{\tau}} d\tilde{\tau} \tag{4}$$

where \wp is the principal value.

The analytical signal is calculated as

$$z_X(\tau) = R_X(\tau) + i\hat{R}_X(\tau) \tag{5}$$

and, can be written in polar form as

$$z_X(\tau) = A(\tau)e^{i\theta(\tau)} \tag{6}$$

where $A(\tau)$ is the amplitude

$$A(\tau) = \sqrt{R_X^2(\tau) + \hat{R}_X^2(\tau)} \tag{7}$$

and $\theta(\tau)$ is the phase

$$\theta(\tau) = \arctan\left[\frac{\text{Im}[z_X(\tau)]}{\text{Re}[z_X(\tau)]}\right] = \arctan\left[\frac{\hat{R}_X(\tau)}{R_X(\tau)}\right]. \quad (8)$$

Taking into account the Euler's formula, the analytical signal in Eq. (6) can be expressed in the form

$$z_X(\tau) = A(\tau) \cos(\theta(\tau)) + i A(\tau) \sin(\theta(\tau)). \quad (9)$$

The correlation function of a SDOF structure enforced by a white noise can be approximated, for $\tau > 0$, as

$$R_X(\tau) = Qe^{-2\pi f\zeta\tau} \cos(2\pi \bar{f}\tau) \quad (10)$$

and thus its Hilbert transform can be expressed as

$$\hat{R}_X(\tau) = Qe^{-2\pi f\zeta\tau} \sin(2\pi \bar{f}\tau) \quad (11)$$

where $\bar{f} = f\sqrt{1 - \zeta^2}$ is the damped frequency and Q is a constant equal to the variance of the structural response.

Replacing Eqs. (10) and (11) in the Eq. (5) it leads to

$$z_X(\tau) = Qe^{-2\pi f\zeta\tau} \cos(2\pi \bar{f}\tau) + i Qe^{-2\pi f\zeta\tau} \sin(2\pi \bar{f}\tau) \quad (12)$$

and thus, using Eqs. (12) and (9) is clear that

$$A(\tau) = Qe^{-2\pi f\zeta\tau} \quad (13)$$

and

$$\theta(\tau) = 2\pi \bar{f}\tau. \quad (14)$$

The instantaneous damped frequency can be calculated performing the first derivative of the phase and dividing by 2π , i.e.

$$\bar{f}(\tau) = \frac{1}{2\pi} \frac{d}{d\tau}[\theta(\tau)]. \quad (15)$$

By performing the average of the instantaneous damped frequency it is possible to obtain the damped frequency of the structure like

$$\bar{f} = E[\bar{f}(\tau)]. \quad (16)$$

The damping ratio can be obtained from the logarithm of the amplitude that has a linear form as it can be seen from the following equation

$$\ln[A(\tau)] = \ln[Q] - 2\pi f \zeta \tau = c_2 + c_1 \tau. \tag{17}$$

From the linear form of the Eq. (17) it is clear that the angular coefficient of the amplitude’s logarithm is related to the structural damping ratio; in particular, the damping ratio is obtained as

$$\zeta = -\frac{c_1}{2\pi f}. \tag{18}$$

Since only the damped frequency is identified, we need to take into account that $f = \bar{f} / \sqrt{1 - \zeta^2}$, and thus the Eq. (18) reverts to

$$\zeta = \sqrt{\frac{\bar{c}_1^2}{1 + \bar{c}_1^2}} \tag{19}$$

with $\bar{c}_1 = c_1 / (2\pi \bar{f})$.

2.2 Identification Algorithm for MDOF Systems

The proposed method, introduced in the previous section, requires another step if applied to the MDOF systems. As a matter of fact, the components of the correlation functions matrix are “multi-component” functions and then they have a not well-behaved Hilbert transform. Therefore, it needs a “mono-component” correlation function, such as the modal correlation function, to restore the efficiency of the Hilbert transform. In light of the above, the identification method for MDOF systems can be resumed as:

- (1) Output processes $\mathbf{X}(t)$ acquisition;
- (2) Correlation functions matrix $\mathbf{R}_X(\tau)$ estimation;
- (3) Singular Value Decomposition of $\mathbf{R}_X(0)$ and modal shapes identification;
- (4) Calculation of the correlation functions matrix in the modal space $\mathbf{R}_Y(\tau)$;
- (5) Reconstruction of the analytical signals of the auto-correlation functions in the modal space;
- (6) Frequencies and damping ratios estimation.

In order to extend the proposed method to a MDOF system, a shear-type MDOF frame with mass matrix \mathbf{M} , stiffness matrix \mathbf{K} and damping matrix \mathbf{C} is used. The dynamic properties to be identified are: the modal matrix Φ , the natural frequencies f_i and the damping ratios ζ_i where $i = 1, 2, \dots, N$ and N is the number of degree of freedom of the system. In this case the differential equations system that governs

the structural motion is

$$\mathbf{M}\ddot{\mathbf{X}}(t) + \mathbf{C}\dot{\mathbf{X}}(t) + \mathbf{K}\mathbf{X}(t) = -\mathbf{M}\mathbf{V}W(t) \quad (20)$$

where \mathbf{V} is the influence vector. The correlation functions contained into the correlation functions matrix are estimated as

$$R_{X_i X_j}(\tau) = E[X_i(t)X_j(t + \tau)] - \mu_{X_i}\mu_{X_j} \quad (21)$$

where μ_{X_i} and μ_{X_j} are respectively the averages of the i-th and j-th response process.

As it is well known, the differential equation system in Eq. (20) can be expressed in the modal space pre-multiplying for the modal matrix Φ and taking into account the modal transformation

$$\mathbf{X}(t) = \Phi\mathbf{Y}(t) \quad (22)$$

where $\mathbf{X}(t)$ is the response process in the nodal space and $\mathbf{Y}(t)$ is the response process in the modal space. The Eq. (20) expressed in the modal space thus becomes

$$\ddot{\mathbf{Y}}(t) + \mathbf{\Lambda}\dot{\mathbf{Y}}(t) + \mathbf{\Omega}\mathbf{Y}(t) = -\Phi^T\mathbf{M}\mathbf{V}W(t) \quad (23)$$

in which $\mathbf{\Omega} = \Phi^T\mathbf{K}\Phi$ is a diagonal matrix containing the squares of the circular frequencies of the system and $\mathbf{\Lambda} = \Phi^T\mathbf{C}\Phi$ is, for classically damped system, a diagonal matrix that have the i-th term on the diagonal equal to $2\zeta_i\omega_i$.

The auto-correlation functions contained into the diagonal of the correlation functions matrix expressed in the modal space are

$$R_{Y_i Y_i}(\tau) = E[Y_i(t)Y_i(t + \tau)] - \mu_{Y_i}^2 \quad (24)$$

where μ_{Y_i} is the average of the i-th response process in the modal space.

Since the modal matrix Φ is unknown, the proposed method takes into account the relationship between the correlation functions matrix expressed in the nodal space $\mathbf{R}_X(\tau)$ and the correlation function matrix expressed in the modal space $\mathbf{R}_Y(\tau)$ [14], i.e.

$$\mathbf{R}_X(\tau) = \Phi\mathbf{R}_Y(\tau)\Phi^T. \quad (25)$$

In order to decompose $\mathbf{R}_X(0)$ in the product of three matrices is possible to use a SVD as it is reported in the following equation

$$\mathbf{R}_X(0) = \mathbf{U}\mathbf{S}\mathbf{V}^H. \quad (26)$$

In Eq. (26) \mathbf{S} is a diagonal matrix that contains the singular values of $\mathbf{R}_X(0)$, \mathbf{U} and \mathbf{V} are unitary matrices that contain respectively the left singular vectors and the

right singular vectors of $\mathbf{R}_X(0)$; and the apex H denote the conjugated transpose. If $\mathbf{R}_X(0)$ is a normal matrix, i.e. if it is square and $(\mathbf{R}_X(0))^H \mathbf{R}_X(0) = \mathbf{R}_X(0)(\mathbf{R}_X(0))^H$, then $\mathbf{U} = \mathbf{V}$. Since $\mathbf{R}_X(0)$ is a normal and real matrix, Eq. (26) becomes

$$\mathbf{R}_X(0) = \mathbf{U}\mathbf{S}\mathbf{U}^T. \tag{27}$$

If the frequencies are well separated, then $\mathbf{R}_Y(0)$ is almost a diagonal matrix and thus $\mathbf{S} \approx \mathbf{R}_Y(0)$ and $\mathbf{U} \approx \Phi$. In light of the above, the modal matrix Φ is estimated performing a SVD of $\mathbf{R}_X(0)$ and the correlation functions matrix in the nodal space can be calculated with the inverse formula of Eq. (25), i.e.

$$\mathbf{R}_Y(\tau) = \Phi^T \mathbf{R}_X(\tau) \Phi \tag{28}$$

The analytical signals $z_i(\tau)$ of the auto-correlation functions in the modal space are calculated as

$$z_i(\tau) = R_{Y_i Y_i}(\tau) + i \hat{R}_{Y_i Y_i}(\tau) \tag{29}$$

where $\hat{R}_{Y_i Y_i}(\tau)$ is the Hilbert transform of $R_{Y_i Y_i}(\tau)$.

For each degree of freedom of the system, the frequencies and the damping ratios can be estimated with the same procedure proposed for SDOF system. In particular, applying Eqs. (7) and (8) is possible to calculate respectively the amplitudes $A_i(\tau)$ and the phases $\theta_i(\tau)$ of the analytical signals, by using Eqs. (15) and (16) the damped frequencies \tilde{f}_i can be estimated and, finally, Eqs. (17–19) can be used to estimate the damping ratios ζ_i of the system.

3 OMA: From Research to Engineering Applications

As regards, the paper’s contribution is to provide a user friendly method, that can be used by people who have little to no knowledge of signal processing and stochastic analysis such as those who are responsible for the maintenance of a city’s historical buildings. To aim at this, all the aforementioned steps have been implemented into an algorithm in MatLab environment reported in the Appendix.

Specifically, this algorithm only requires as input the time vector and the recorded structural outputs, then automatically returns all steps necessary to provide the dynamic properties of the structure. In sequential order the aforementioned algorithm estimate: the correlation functions matrix in the nodal space, the modal shapes, the correlation functions matrix in the modal space, the analytical signals of the auto-correlation functions in the modal space, the amplitudes, the phases, the damped frequencies and the damping ratios. To assess the reliability of the method and the algorithm, several numerical simulations and an experimental test are reported as it follows.

3.1 Validation of the Proposed Algorithm Through a SDOF System

In order to prove the reliability of the identification algorithm for SDOF system, a numerical simulation on a linear SDOF shear-type frame was performed for different values of the damping coefficient ζ . In particular, the SDOF structure has a natural frequency $f = 30$ Hz and the damping ratio is variable between 0.01 and 0.10 with a step equal to 0.01. The structural input $W(t)$ has been generated with the Shinozuka’s formula [19] and the number of the generated samples is equal to 1000. Every sample has a duration of 100 s with sampling frequency 1000 Hz. The instantaneous damped frequency $\bar{f}(\tau)$ and the logarithm of the amplitude $A(\tau)$ are depicted respectively in Figs. 1 and 2 for $\zeta = 0.02$.

The results obtained by using the proposed method and PP + HP are reported, with the relative discrepancies $\varepsilon\%$, in Tables 1 and 2. These results suggest that both methods are reliable for the estimation of the natural frequency and damping ratio in a SDOF system. However, the proposed method has less discrepancy than PP + HP, both in terms of damped frequency estimation and in terms of damping ratio estimation. In this section the proposed method is compared only with PP + HP because other automated algorithm in MatLab environment, like FDD.m [20] and SSICOV.m [21], can be used only for MDOF systems.

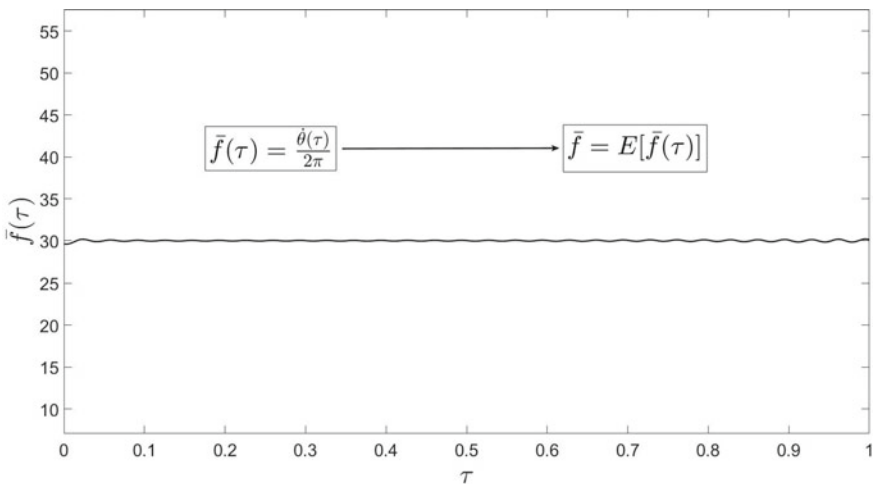


Fig. 1 Instantaneous damped frequency for $f = 30$ Hz and $\zeta = 0.02$

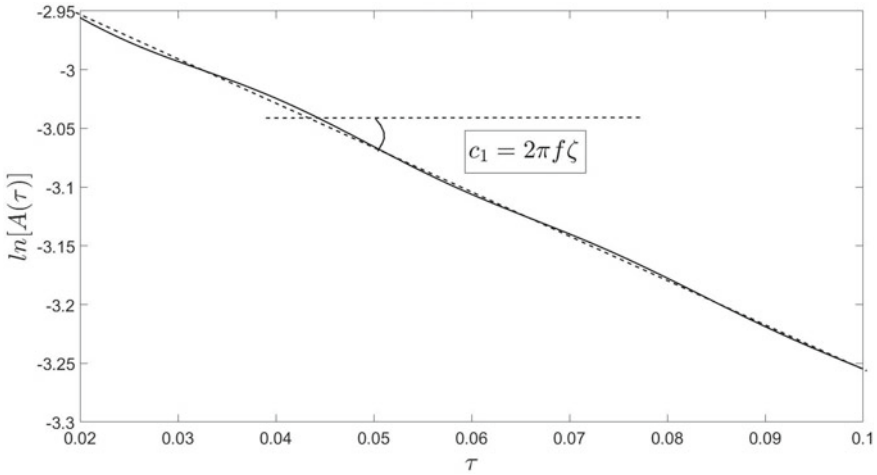


Fig. 2 Amplitude’s logarithm for $f = 30$ Hz and $\zeta = 0.02$

Table 1 Comparison among the exact damped frequency and the estimated damped frequency

Damping ratio	Exact frequency	TD-ASM frequency	Discrepancy $\varepsilon\%$	PP + HP frequency	Discrepancy $\varepsilon\%$
0.0100	29.9985	29.9999	0.0046	29.9900	0.0283
0.0200	29.9940	29.9967	0.0090	29.9700	0.0800
0.0300	29.9865	29.9901	0.0121	29.9500	0.1217
0.0400	29.9760	29.9798	0.0125	29.9500	0.0867
0.0500	29.9625	29.9647	0.0074	29.9500	0.0416
0.0600	29.9460	29.9434	0.0087	29.9500	0.0135
0.0700	29.9264	29.9130	0.0447	29.9400	0.0454
0.0800	29.9038	29.8694	0.1152	29.9400	0.1209
0.0900	29.8783	29.8064	0.2405	29.9400	0.2067
0.1000	29.8496	29.7173	0.4433	29.5600	0.9703

3.2 Validation of the Proposed Algorithm Through a MDOF System

In order to prove the reliability of the identification algorithm for MDOF systems, a numerical simulation on a linear 3DOF shear-type system was performed at various values of the damping coefficient ζ_1 . In particular, the range of variation of the first damping ratio is $\zeta_1 = 0.05 \div 0.10$ with a step equal to 0.01. ζ_2 and ζ_3 are calculated considering a Rayleigh damping. The shear-type 3DOF frame used for the numerical simulations has mass $m_j = 794$ kg for $j = 1, 2, 3$ and

Table 2 Comparison between the exact damping ratio and the estimated ramping ratio

Exact damping ratio	TD-ASM damping ratio	Discrepancy $\epsilon\%$	PP + HP damping ratio	Discrepancy $\epsilon\%$
0.0100	0.0100	0.3102	0.0104	3.6540
0.0200	0.0200	0.0063	0.0202	1.1639
0.0300	0.0300	0.0623	0.0299	0.4492
0.0400	0.0400	0.0485	0.0394	1.4300
0.0500	0.0500	0.0157	0.0492	1.5617
0.0600	0.0599	0.1252	0.0595	0.7978
0.0700	0.0698	0.2866	0.0703	0.4566
0.0800	0.0796	0.5158	0.0795	0.6002
0.0900	0.0908	0.8370	0.0886	1.5493
0.1000	0.1013	1.2787	0.1022	2.2490

stiffness $k_j = 6.18 \times 10^6 \text{N/m}$ for $j = 1, 2, 3$ and thus the natural frequencies are $f_1 = 6.2489 \text{ Hz}$, $f_2 = 17.5091 \text{ Hz}$, $f_3 = 25.3014 \text{ Hz}$, and the modal shapes are $\phi_1 = [0.328 \ 0.591 \ 0.737]^T$, $\phi_2 = [0.737 \ 0.328 \ -0.591]^T$, $\phi_3 = [0.591 \ -0.737 \ 0.328]^T$. The results in terms of damped frequencies (for each value of $\zeta_1 = 0.05 \div 0.01$) evaluated by using the proposed method are compared with those obtained by SSI-COV [21] and FDD [20], as reported in Table 3.

From these results it is apparent that all methods are performing very well, in particular the SSI-COV results have the least discrepancy, but SSI-COV is not direct as the proposed method TD-ASM, since it requires the knowledge of a parameter related to the first frequency, that is a priori unknown. This means that it needs at least a Fourier Transform of the signal to get this value, while the proposed method does not require any preliminary information of the unknown characteristics. Further, results in terms of damping ratios are compared with SSI-COV only, since the algorithm FDD.m does not allow the damping ratios' evaluation. Also in this case the proposed method gets satisfactory results as shown in Table 4 (for each value of $\zeta_1 = 0.05 \div 0.01$).

As regards the modal shapes, Fig. 3 reports the discrepancies of results obtained with the proposed method, FDD and SSI-COV with respect the exact ones at different values of damping ratios. Also in this case, the proposed method and SSICOV (both developed in the time domain and based on the correlation function) are more precise than FDD (developed in the frequency domain and based on the PSD) especially for the first modal shape that gives the major contribution to the total structural motion.

Table 3 Comparison between the exact damped frequencies and the estimated damped frequencies

ζ_1	Mode	Exact	TD-ASM	$\epsilon\%$	FDD	$\epsilon\%$	SSI	$\epsilon\%$
0.05	1	6.2411	6.2363	0.0770	6.1646	1.2261	6.2433	0.0356
	2	17.4872	17.4529	0.1961	17.8833	2.2650	17.4595	0.1584
	3	25.2522	25.0554	0.7794	25.3296	0.3065	25.2753	0.0916
0.06	1	6.2376	6.2262	0.1823	6.1646	1.1713	6.2426	0.0802
	2	17.4776	17.4344	0.2472	17.8833	2.3213	17.4334	0.2529
	3	25.2305	24.9680	1.0405	25.3296	0.3926	25.2255	0.0201
0.07	1	6.2335	6.2255	0.1290	6.1646	1.1065	6.2381	0.0734
	2	17.4662	17.4128	0.3060	17.8833	2.3880	17.4147	0.2950
	3	25.2049	24.7680	1.7334	25.3296	0.4947	25.1682	0.1455
0.08	1	6.2288	6.2223	0.1042	6.1646	1.0315	6.2353	0.1036
	2	17.4531	17.3857	0.3858	17.8833	2.4652	17.4209	0.1844
	3	25.1753	24.3554	3.2568	25.3296	0.6129	25.0907	0.3362
0.09	1	6.2234	6.2133	0.1625	6.1035	1.9271	6.2361	0.2033
	2	17.4381	17.3575	0.4626	17.8833	2.5528	17.3813	0.3257
	3	25.1417	24.2051	3.7254	25.3296	0.7473	25.1235	0.0723
0.10	1	6.2175	6.2222	0.0761	6.1035	1.8326	6.2377	0.3251
	2	17.4215	17.3323	0.5117	17.8833	2.6510	17.3420	0.4562
	3	25.1041	24.1537	3.7860	25.3296	0.8982	25.1216	0.0698

3.3 Validation of the Proposed Algorithm Through Experimental Test

In order to prove the reliability of the proposed method on real structures, an experimental test was performed on a three-story frame. The set-up of the experimental test is reported in Fig. 4. In particular, the structure was excited by a broad-band noise from 0.01 to 80 Hz through an electro-magnetic shaker APS-ELECTRO-SAIS. The input and the output signals were recorded using piezo-electric accelerometers Brüel&Kjaer 4507 002 connected to the acquisition unit NI PXIe 1082. Some tests of 240 s with sampling frequency equal to 1000 Hz were performed and the proposed algorithm was used to obtain the modal shapes, the frequencies and the damping ratios of the structure. Since the tests are performed on a real system that has unknown dynamic properties, is impossible to report a discrepancy between the exact properties and the identified properties. However, the results obtained by the used methods are reported in Tables 5 and 6.

From these results, it is clear that all the used algorithms well identify the same frequencies and that the differences between the damping ratios identified with the proposed algorithm and SSICOV.m are very low.

Table 4 Comparison between the exact damping ratios and the estimated damping ratios

ζ_1	Mode	Exact	TD-ASM	$\epsilon\%$	SSI	$\epsilon\%$
0.05	1	0.0501	0.0519	3.6703	0.0481	3.9291
	2	0.0500	0.0493	1.2739	0.0521	4.2302
	3	0.0623	0.0623	0.0697	0.0646	3.6640
0.06	1	0.0601	0.0607	0.9509	0.0582	3.2513
	2	0.0600	0.0597	0.3966	0.0629	4.8558
	3	0.0748	0.0746	0.2821	0.0739	1.1238
0.07	1	0.0702	0.0727	3.6792	0.0666	5.0789
	2	0.0699	0.0699	0.1102	0.0726	3.8543
	3	0.0872	0.0824	5.5115	0.0858	1.6690
0.08	1	0.0802	0.0838	4.5188	0.0757	5.5309
	2	0.0799	0.0793	0.7807	0.0850	6.3065
	3	0.0997	0.0915	8.2092	0.1034	3.6762
0.09	1	0.0902	0.0953	5.6554	0.0848	6.0208
	2	0.0899	0.0894	0.5921	0.0926	2.9736
	3	0.1122	0.1038	7.4214	0.1106	1.4040
0.10	1	0.1002	0.1046	4.3784	0.0935	6.7502
	2	0.0999	0.1004	0.4290	0.1015	1.6203
	3	0.1246	0.1081	13.2609	0.1215	2.5302

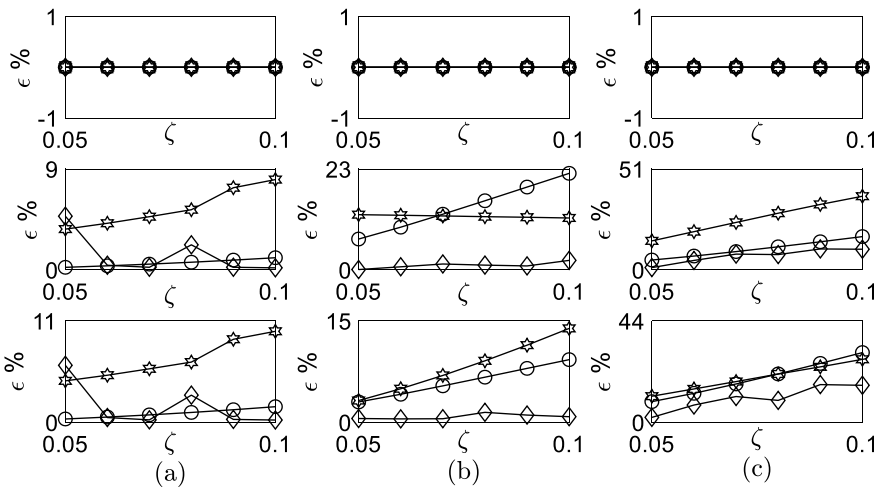


Fig. 3 Discrepancy of results obtained with the proposed method TD-ASM (circular marker), FDD (hexagram marker) and SSICOV (diamond marker) with respect the exact ones at different values of damping ratios: first mode **a**, second mode **b**, third mode **c**

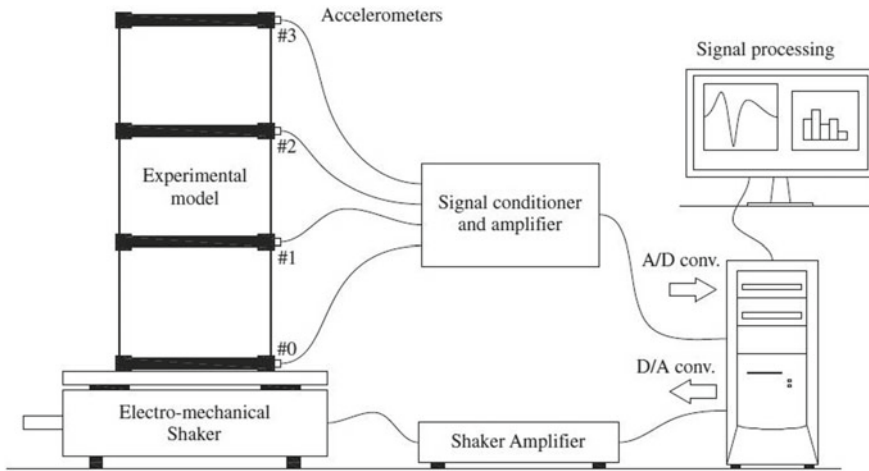


Fig. 4 Experimental set-up

Table 5 Comparison between TD_ASM.m, SSICOV.m and FDD.m in terms of damped frequencies and damping ratios

Mode	Frequencies			Damping ratios		
	TD-ASM	FDD	SSICOV	TD-ASM	FDD	SSICOV
1	2.1438	2.2125	2.1511	0.0853	–	0.0717
2	6.0719	6.0730	6.0868	0.0075	–	0.0080
3	8.7321	8.7280	8.7285	0.0013	–	0.0016

Table 6 Comparison between TD_ASM.m, SSICOV.m and FDD.m in terms of modal shapes

TD-ASM			FDD			SSICOV		
ϕ_1	ϕ_2	ϕ_3	ϕ_1	ϕ_2	ϕ_3	ϕ_1	ϕ_2	ϕ_3
1.0000	1.0000	1.0000	1.0000	1.0000	1.0000	1.0000	1.0000	1.0000
1.7306	0.3794	-1.2784	2.0377	0.3328	-1.4188	1.9186	0.7549	-1.4351
1.9751	-0.8388	0.6139	2.5393	-0.7784	0.7477	2.3581	-0.8516	0.7672

4 Conclusions

This paper introduces an innovative ambient identification method based on the Hilbert Transform to obtain the analytical representation of the system response in terms of the correlation function. It leads to identify the modal shapes performing a SVD of the correlation function matrix in $\tau = 0$, the frequencies by the phase of each analytical signal of the auto-correlation functions in the modal space and the damping ratios by the amplitude of each analytical signal of the auto-correlation functions in

the modal space. The numerical simulations prove that for SDOF structures the proposed method can identify the dynamic properties better than the PP+HP and for MDOF structures the proposed method TD-ASM can identify very well the dynamic properties of the structural systems, especially in terms of the damping ratios. The performed experimental tests prove that the dynamic properties identified with the proposed method are similar to the properties identified by other automated algorithm and that the proposed algorithm have some advantages compared to the others. However, the greatest advantage of TD-ASM is that it is user friendly, in fact the developed MatLab function requires only the time vector and the recorded outputs and can be used also by a not-expert user. As a concluding remark, the authors wish that this approach could open the pathway for a monitoring system that is user friendly and can be used by people who have little to no knowledge of signal processing and stochastic analysis such as those who are responsible for the maintenance of a city's historical buildings.

Acknowledgements S. Russotto, A. Di Matteo, C. Masnata and A. Pirrotta gratefully acknowledge the support received from the Italian Ministry of University and Research, through the PRIN 2017 funding scheme (project 2017J4EAYB 002 - Multiscale Innovative Materials and Structures "MIMS").

Appendix

The proposed algorithm, entirely reported in this appendix, requires as input only the output signals (X) and the time vector (time). It calculates automatically the frequencies (fid), the damping ratios (Z_ID_LOG) and the modal shapes both normalized with respect to the first component of each mode (PHI_IDNN) and not-normalized (PHI_ID). The entire developed MatLab function, called TD_ASM.m, is shown below.

```

function [PHI_ID,PHI_IDNN,fid,Z_ID_LOG] = TD_ASM(X,time)
% number of performed tests
n_cam=size(X,2);
% number of degree of freedom
ndof=size(X,3);
% tau vector
tau=[-fliplr(time(2:end)) time];
% length of time vector
N=length(time);
% time sampling
dt=time(2)-time(1);
% Correlation functions matrix estimation (nodal space)
for j=1:n_cam
for jj=1:ndof
for ii=1:ndof
Rx(j,ii,jj,:)=xcorr(squeeze(X(:,j,ii)),squeeze(X(:,j,jj)),'biased');
end
end
end
Rx_m=squeeze(mean(Rx,1));
% SVD and modal shapes estimation
[PHI_ID RY0 U]=svd(Rx_m(:, :, N));
for ii=1:ndof
PHI_ID_N(:,ii)= PHI_ID(:,ii)/PHI_ID(1,ii);
End
% Correlation functions matrix estimation (modal space)
for tt=1:length(tau)
Ry(:, :, tt)= PHI_ID'*Rx_m(:, :, tt)*PHI_ID;
End
% Calculus of: analytical signals, instantaneous frequencies and
% amplitudes
for ii=1:ndof
Zy(ii,:)=hilbert(squeeze(Ry(ii,ii,:)));
fist(ii,:)=gradient(unwrap(angle(squeeze(Zy(ii,:)))),dt)/(2*pi);
A(ii,:)=abs(squeeze(Zy(ii,:)));
End
% Damped frequencies estimation
for ii=1:ndof
[NPi NPf]=TimeStopSelection(fist(ii,:));
f_id(ii)=mean(fist(ii,N+NPi:N+NPf));
end
% Damping ratios estimation
for ii=1:ndof
[NPi NPf]=TimeStopSelection(A(ii,:));
y=log(A(ii,N+NPi:N+NPf));
x=tau(N+NPi:N+NPf);
C_coef(1:2)=polyfit(x,y,1);
cl_bar=-C_coef(1)/(2*pi*f_id(ii));
zid_log(ii)=sqrt(cl_bar^2/(1+cl_bar^2));
end
% Dynamic properties sorting
[fid ind]=sort(f_id);
for ii=1:ndof
PHI_ID(:,ii)=PHI_ID(:,ind(ii));
PHI_IDNN(:,ii)=PHI_ID_N(:,ind(ii));
Z_ID_LOG(ii)=zid_log(ind(ii));
end
end

```

In this code only two kind of interactions with the user are requested. The first one is the organization of the input data i.e. the time vector that is a row vector and

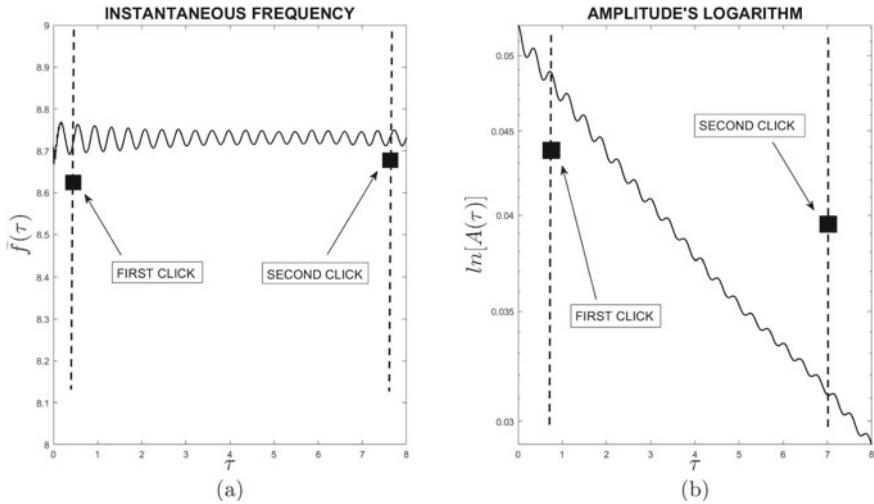


Fig. 5 Interactive graphic interface of TimeStopSelection.m: for frequency estimation **a**, for damping ratio estimation **b**

the structural output process that is a three-dimensional array. The second one is a step of the function TimeStopSelection.m that is contained into TD_ASM.m and that requires the choice of the time interval to be used to perform the average in Eq. (16) and to identify the coefficient c_1 in Eq. (17). In order to simplify this step, TimeStopSelection.m has an interactive graphic interface that allows to choose, with few clicks, the aforementioned time intervals as reported in Fig. 5a, b respectively for frequency identification and damping ratios identification.

References

1. Brinker R, Zhang L, Andersen P (2005) An overview of operational modal analysis: major development and issues. In: Proceedings of the 1st international operational modal analysis conference. Aalborg Universitet, Copenhagen, pp 179–190
2. Shokravi H, Shokravi H, Bakhary N, Rahimian Kolor SS, Peetrû M (2020) Health monitoring of civil infrastructures by subspace system identification method: an overview. Appl Sci 10(8):2786–2814
3. Bendat JS, Piersol AG (2010) Random data: analysis and measurement procedures, 4th edn. Wiley, Hoboken
4. Brincker R, Zhang L, Andersen P (2000) Modal identification from ambient responses using frequency domain decomposition. In: Proceedings of the international modal analysis conference (IMAC). Aalborg Universitet, San Antonio, pp 625–630
5. Brincker R, Zhang L, Andersen P (2000) Output-only modal analysis by frequency domain decomposition. In: Proceedings of ISMA25. Aalborg Universitet, Leuven, pp 717–723
6. Welch PD (1967) The use of fast Fourier transform for the estimation of power spectra: a method based on time averaging over short, modified periodograms. IEEE Trans Audio Electroacoust 15(2):70–73

7. Barbé K, Pintelon R, Schoukens J (2010) Welch method revisited: nonparametric power spectrum estimation via circular overlap. *IEEE Trans Signal Process* 58(2):553–565
8. Siringoringo DM, Fujino Y (2008) System identification of suspension bridge from ambient vibration response. *Eng Struct* 30(2):462–477
9. Lardies J (2010) Modal parameter identification based on ARMAV and state-space approaches. *Arch Appl Mech* 80:335–352
10. Perez-Ramirez CA, Amezcua-Sanchez JP, Adeli H, Valtierra-Rodriguez M, Camarena-Martinez D, Romero-Troncoso RJ (2016) New methodology for modal parameters identification of smart civil structures using ambient vibrations and synchrosqueezed wavelet transform. *Eng Appl Artif Intell* 48:1–12
11. Matteo AD, Masnata C, Russotto S, Bilello C, Pirrotta A (2020) A novel identification procedure from ambient vibration data. *Meccanica*. <https://doi.org/10.1007/s11012-020-01273-4>
12. Cottone G, Pirrotta A, Salamone S (2008) Incipient damage identification through characteristics of the analytical signal response. *Struct Control Health Monit* 15(8):1122–1142
13. Lo Iacono F, Navarra G, Pirrotta A (2012) A damage identification procedure based on hilbert transform: experimental validation. *Struct Control Health Monit* 19(1):146–160
14. Brincker R, Ventura C (2015) *Introduction to operational modal analysis*. Wiley, Chichester
15. Di Paola M, Falsone G, Pirrotta A (1992) Stochastic response analysis of nonlinear systems under gaussian inputs. *Probab Eng Mech* 7(1):15–21
16. Pirrotta A (2005) Non-linear systems under parametric white noise input: digital simulation and response. *Int J Non-Linear Mech* 40(8):1088–1101
17. Bilello C, Di Paola M, Pirrotta A (2002) Time delay induced effects on control of non-linear systems under random excitation. *Meccanica* 37:207–220
18. Di Paola M, Pirrotta A (1999) Non-linear systems under impulsive parametric input. *Int J Non-Linear Mech* 34(5):843–851
19. Shinozuka M (1971) Simulation of multivariate and multidimensional random processes. *J Acoust Soc Am* 49(1B):357–368
20. MatLab File Exchange. <https://it.mathworks.com/matlabcentral/fileexchange/69030-operational-modal-analysis-with-automated-ssi-cov-algorithm>
21. MatLab File Exchange. <https://it.mathworks.com/matlabcentral/fileexchange/50988-frequency-domain-decomposition-fdd>

Time-Domain Damage Detection of Structures with Complex Modes Under Variable Environmental Conditions Using Bayesian Virtual Sensors



Jyrki Kullaa

Abstract A time-domain algorithm for damage detection is introduced. It is based on hardware redundancy in which the number of sensors is greater than the number of excited modes plus the number of environmental variables. Therefore, for a structure with complex modes, the minimum number of sensors is expected to be higher than that of the same structure with real modes. A two-step detection algorithm is proposed. First, the accuracy of each sensor is increased by Bayesian virtual sensing. Second, the signal of each sensor is estimated using the remaining sensors utilizing a correlation model of the training data under different environmental conditions. The residual is used to detect damage. The algorithm was studied in a numerical experiment of a frame structure having a discrete damper element, which resulted in complex mode shapes. A comparison was made with the same structure having real modes due to proportional damping. The performance of damage detection was higher with real modes and virtual sensors outperformed the raw measurements. Damage localization was also relatively successful revealing the region close to the actual damage.

Keywords Complex modes · Virtual sensing · Environmental effects · Damage detection · Hardware redundancy · Time-domain structural health monitoring

1 Introduction

Structural health monitoring (SHM) utilizes sensor data to get an early warning of structural failure. Vibration-based SHM is a non-destructive technique, in which damage can be detected remotely from the sensors. Damage detection can be approached using time-domain or feature-domain techniques. In this paper, time-domain data analysis is studied. It is assumed that a sensor network is installed on the structure. Training data are needed from an undamaged structure under different environmental or operational conditions. With the proposed approach it is possible

J. Kullaa (✉)

Metropolia University of Applied Sciences, P.O. Box 4071, 00079 Metropolia, Finland
e-mail: jyrki.kullaa@metropolia.fi

to take into account the influences of the environmental or operational variability [1]. The excitation or the environmental or operational variables are not measured.

In the data analysis for damage detection, each sensor reading is estimated using the data from the remaining sensors. Therefore, the sensor network has to be redundant. The required number of sensors in the network depends on the number of active modes as well as the number of environmental or operational variables. Generally, the mode shapes are complex due to viscous damping. Only in a special case of proportional damping the modes are real.

For under-critical damping, at each natural frequency there exist two complex conjugate modes. The response can be expressed using mode superposition. This means that the response, which is a real number, is expressed with twice the number of terms compared to the case with real modes.

A two-step algorithm is proposed for damage detection [2]. First, noise reduction is performed applying Bayesian virtual sensing to the measurement data. This is an important step, because according to detection theory, the probability of detection depends on the signal-to-noise ratio (SNR) [3]. The result of the first step is virtual sensors that are more accurate than the corresponding physical sensors. Second, applying a correlation model of the training data, each (virtual) sensor is estimated using the remaining (virtual) sensors in the network resulting in a residual vector. The residual is the difference between the (virtual) sensor reading and the corresponding estimate and its increase beyond a threshold is an indication of damage.

This paper is organized as follows. Complex modes are introduced in Sect. 2. Bayesian virtual sensors are derived in Sect. 3. The proposed algorithm for damage detection is presented in Sect. 4. A numerical experiment comparing damage detection with real or complex modes using either physical or virtual sensors is studied in Sect. 5. Finally, concluding remarks are given in Sect. 6.

2 Complex Modes

Complex modes occur if damping is non-proportional. Then, the real modal matrix cannot diagonalize the damping matrix and the equations of motion remain coupled. Highly complex modes can occur for example, if there exist discrete damper elements.

Starting with the second order equation of motion

$$\mathbf{m}\ddot{\mathbf{u}} + \mathbf{c}\dot{\mathbf{u}} + \mathbf{k}\mathbf{u} = \mathbf{f}(t) \tag{1}$$

where \mathbf{m} , \mathbf{c} , and \mathbf{k} are respectively the mass, damping, and stiffness matrix of the structure, $\mathbf{u} = \mathbf{u}(t)$ is the displacement vector, $\mathbf{f}(t)$ is the load vector, and t is time. Equation (1) can be written in a state space form, resulting in a first-order differential equation

$$\begin{bmatrix} -\mathbf{k} & \mathbf{0} \\ \mathbf{0} & \mathbf{m} \end{bmatrix} \begin{Bmatrix} \dot{\mathbf{u}} \\ \ddot{\mathbf{u}} \end{Bmatrix} + \begin{bmatrix} \mathbf{0} & \mathbf{k} \\ \mathbf{k} & \mathbf{c} \end{bmatrix} \begin{Bmatrix} \mathbf{u} \\ \dot{\mathbf{u}} \end{Bmatrix} = \begin{Bmatrix} \mathbf{0} \\ \mathbf{f}(t) \end{Bmatrix} \tag{2}$$

or

$$\mathbf{M}\dot{\mathbf{x}} + \mathbf{K}\mathbf{x} = \mathbf{F}(t) \tag{3}$$

where $\mathbf{x}(t) = [\mathbf{u} \ \dot{\mathbf{u}}]^T$ is the state vector and \mathbf{M} , \mathbf{K} , and $\mathbf{F}(t)$ are defined by the above equations. The objective is to derive a truncated mode superposition solution to Eq. (3) and study the vector space of the response. The eigenvalue analysis of Eq. (3) is first performed resulting in eigenvalues λ_r that are complex for underdamped modes, and negative real numbers for overdamped modes. Also the mode shapes are complex for underdamped modes, and real for overdamped modes. The complex eigenvalues and mode shapes exist in conjugate pairs, because the response $\mathbf{x}(t)$ must be real. Therefore, for each natural frequency, there exist two modes. The eigenvalues are related to the natural frequencies ω_r and modal damping ζ_r by

$$\lambda_r = -\omega_r \zeta_r \pm i \omega_r \sqrt{1 - \zeta_r^2} \tag{4}$$

Equations (3) can be made independent with the transformation

$$\mathbf{x}(t) = \sum_{s=1}^{2N} \phi_s q_s(t) \approx \sum_{s=1}^{2n} \phi_s q_s(t) \tag{5}$$

where N is the number of degrees-of-freedom (DOF) in the finite element model, $n \ll N$ is the number of active modes, ϕ_s is the mode shape vector, and $q_s(t)$ the modal, or generalized, coordinate of mode s .

Substituting Eq. (5) into Eq. (3), multiplying with ϕ_r^T from the left, and taking into account the orthogonality of the eigenvectors [4], results in

$$\phi_r^T \mathbf{M} \phi_r \dot{q}_r(t) + \phi_r^T \mathbf{K} \phi_r q_r(t) = \phi_r^T \mathbf{F}(t) \tag{6}$$

or

$$m_r \dot{q}_r(t) + k_r q_r(t) = \phi_r^T \mathbf{F}(t) \tag{7}$$

which is the equation of motion for mode r , where $m_r = \phi_r^T \mathbf{M} \phi_r$ is the modal mass and $k_r = \phi_r^T \mathbf{K} \phi_r$ is the modal stiffness, which are generally complex. There are $2N$ such single-degree-of-freedom equations, one for each mode. In the truncated model, it is assumed that only the $2n$ lowest modes correspond significantly to the response. The solution $q_r(t)$ for Eq. (7) can be found analytically or numerically.

Let us assume that solution $q_r(t)$ is available. It depends on the loading and the initial conditions. In the underdamped case, the solutions exist in complex conjugate

pairs, for example for the first two modes:

$$\begin{aligned} q_1(t) &= q_{1R}(t) + q_{1I}(t)i \\ q_2(t) &= \bar{q}_1(t) = q_{1R}(t) - q_{1I}(t)i \end{aligned} \tag{8}$$

Their contribution to the physical response according to Eq. (5) is

$$\begin{aligned} \mathbf{x}(t) &= \phi_1 q_1(t) + \phi_2 q_2(t) \\ &= \phi_1 q_1(t) + \bar{\phi}_1 \bar{q}_1(t) \\ &= \phi_1 [q_{1R}(t) + q_{1I}(t)i] + \bar{\phi}_1 [q_{1R}(t) - q_{1I}(t)i] \\ &= (\phi_1 + \bar{\phi}_1)q_{1R}(t) + (\phi_1 - \bar{\phi}_1)q_{1I}(t)i \\ &= 2\text{Re}\phi_1 q_{1R}(t) - 2\text{Im}\phi_1 q_{1I}(t) \end{aligned} \tag{9}$$

which shows that the solution $\mathbf{x}(t)$ lies in a space spanned by vectors $\text{Re}\phi_1$ and $\text{Im}\phi_1$. Therefore, the dimension of the vector space is two. In other words, two basis vectors are needed to describe the physical response if the active mode is complex.

On the other hand, if damping is zero, the eigenvalues and modes are purely imaginary, resulting in response

$$\mathbf{x}(t) = -2\text{Im}\phi_1 q_{1I}(t) \tag{10}$$

In this case the solution $\mathbf{x}(t)$ lies in a space spanned by vector $\text{Im}\phi_1$ only. The dimension of the vector space is one.

With overdamped modes, the eigenvalues and modes are real, and the response is

$$\mathbf{x}(t) = \phi_1 q_{1R}(t) \tag{11}$$

In this case the solution $\mathbf{x}(t)$ lies in a space spanned by vector ϕ_1 only. The dimension of the vector space is one.

3 Bayesian Virtual Sensing

Virtual sensing (VS) gives an estimate of a quantity of interest using the available measurements. The objective of this study is to design virtual sensors that are more accurate than the hardware [1]. Empirical virtual sensing is applied, and no mathematical model of the structure is needed. In addition, the excitation is not measured or estimated. Hardware redundancy is assumed with a sufficiently large number of sensors measuring the response of the structure.

Consider a sensor network measuring p simultaneously sampled responses $\mathbf{y} = \mathbf{y}(t)$ at time instant t . The measurement \mathbf{y} includes a measurement error $\mathbf{w} = \mathbf{w}(t)$:

$$\mathbf{y} = \mathbf{x} + \mathbf{w} \quad (12)$$

where $\mathbf{x} = \mathbf{x}(t)$ are the true values of the measured degrees of freedom. The objective is to find an estimate of the true values \mathbf{x} utilizing the noisy measurements \mathbf{y} from the sensor network. Equation (12) can be written in the following form at each time instant t [5].

$$\begin{Bmatrix} \mathbf{x} \\ \mathbf{y} \end{Bmatrix} = \begin{bmatrix} \mathbf{I} & \mathbf{0} \\ \mathbf{I} & \mathbf{I} \end{bmatrix} \begin{Bmatrix} \mathbf{x} \\ \mathbf{w} \end{Bmatrix} \quad (13)$$

For simplicity but without loss of generality, assume zero-mean variables \mathbf{x} and \mathbf{y} . The partitioned covariance matrix is:

$$\begin{aligned} \Sigma &= E\left(\begin{Bmatrix} \mathbf{x} \\ \mathbf{y} \end{Bmatrix} \begin{bmatrix} \mathbf{x}^T & \mathbf{y}^T \end{bmatrix}\right) = \begin{bmatrix} \Sigma_{xx} & \Sigma_{xy} \\ \Sigma_{yx} & \Sigma_{yy} \end{bmatrix} \\ &= \begin{bmatrix} \mathbf{I} & \mathbf{0} \\ \mathbf{I} & \mathbf{I} \end{bmatrix} E\left(\begin{Bmatrix} \mathbf{x} \\ \mathbf{w} \end{Bmatrix} \begin{bmatrix} \mathbf{x}^T & \mathbf{w}^T \end{bmatrix}\right) \begin{bmatrix} \mathbf{I} & \mathbf{0} \\ \mathbf{I} & \mathbf{I} \end{bmatrix}^T \\ &= \begin{bmatrix} \mathbf{I} & \mathbf{0} \\ \mathbf{I} & \mathbf{I} \end{bmatrix} \begin{bmatrix} \Sigma_{xx} & \mathbf{0} \\ \mathbf{0} & \Sigma_{ww} \end{bmatrix} \begin{bmatrix} \mathbf{I} & \mathbf{I} \\ \mathbf{0} & \mathbf{I} \end{bmatrix} \\ &= \begin{bmatrix} \Sigma_{xx} & \Sigma_{xx} \\ \Sigma_{xx} & \Sigma_{xx} + \Sigma_{ww} \end{bmatrix} \end{aligned} \quad (14)$$

where $E(\cdot)$ denotes the expectation operator and the measurement error \mathbf{w} is assumed to be zero mean Gaussian, independent of \mathbf{x} , with a (known) covariance matrix Σ_{ww} . The covariance matrix Σ_{xx} is not known, but Σ_{yy} can be estimated from the measurement data, and if the noise covariance matrix can be approximated, then the following estimate applies: $\Sigma_{xx} = \Sigma_{yy} - \Sigma_{ww}$. In this study, the measurement errors are assumed uncorrelated between sensors resulting in a diagonal noise covariance matrix. In addition, because Σ_{xx} must be positive definite, an upper bound of the noise level in each sensor can be derived [1].

A linear minimum mean square error (MMSE) estimate for $\mathbf{x}|\mathbf{y}$ (\mathbf{x} given \mathbf{y}) is obtained by minimizing the mean-square error (MSE) [5]. The expected value, or the conditional mean, of the predicted variable is:

$$\hat{\mathbf{x}} = E(\mathbf{x}|\mathbf{y}) = \Sigma_{xx}(\Sigma_{xx} + \Sigma_{ww})^{-1}\mathbf{y} = \Sigma_{xx}\Sigma_{yy}^{-1}\mathbf{y} \quad (15)$$

and the estimation error is

$$\text{cov}(\mathbf{x}|\mathbf{y}) = \Sigma_{xx} - \Sigma_{xx}(\Sigma_{xx} + \Sigma_{ww})^{-1}\Sigma_{xx} = \Sigma_{xx} - \Sigma_{xx}\Sigma_{yy}^{-1}\Sigma_{xx} \quad (16)$$

4 Damage Detection

Residual generation is an integral part of damage detection. The residual can be defined as a difference between the actual and estimated data:

$$\mathbf{r} = \mathbf{y} - \hat{\mathbf{y}} \tag{17}$$

where \mathbf{y} represents either the physical or virtual sensors, $\hat{\mathbf{y}}$ is the estimate of the sensor reading obtained as follows.

Each sensor in turn is estimated using the remaining sensors in the network by applying the MMSE estimation [2]. The measured response \mathbf{y} is partitioned into observed variables \mathbf{v} and estimated variables \mathbf{u} (typically a single sensor u):

$$\mathbf{y} = \begin{Bmatrix} \mathbf{y}_u \\ \mathbf{y}_v \end{Bmatrix} \tag{18}$$

For simplicity but without loss of generality, assume zero-mean variables \mathbf{y} . The data covariance matrix Σ_y is estimated using the training data consisting of several measurements under different environmental or operational conditions.

$$\Sigma_y = E(\mathbf{y}\mathbf{y}^T) = \begin{bmatrix} \Sigma_{y,uu} & \Sigma_{y,uv} \\ \Sigma_{y,vu} & \Sigma_{y,vv} \end{bmatrix} \tag{19}$$

Similarly to the previous section, a linear minimum mean square error (MMSE) estimate for the conditional mean of $\mathbf{y}_u | \mathbf{y}_v$ is obtained by minimizing the mean-square error (MSE):

$$\hat{\mathbf{y}}_u = E(\mathbf{y}_u | \mathbf{y}_v) = \Sigma_{y,uv} \Sigma_{y,vv}^{-1} \mathbf{y}_v \tag{20}$$

and the MSE is

$$\text{cov}(\mathbf{y}_u | \mathbf{y}_v) = \Sigma_{y,uu} - \Sigma_{y,uv} \Sigma_{y,vv}^{-1} \Sigma_{y,vu} \tag{21}$$

The residual for the sensor u is then generated:

$$\mathbf{r}_u = \mathbf{y}_u - E(\mathbf{y}_u | \mathbf{y}_v) \tag{22}$$

Once damage occurs, the correlation structure does not fit the experimental data producing a larger residual, which will then trigger an alarm.

Residuals are standardized according to the training data. Principal component analysis (PCA) is applied to all data, and the first principal component (PC) is only retained indicating the direction with the largest change in the data space. The one-dimensional PC score vector of the residuals is then subjected to statistical analysis.

The PC scores are divided into batches of d data points. Extreme value distributions are estimated both for the block minima and block maxima of the training data [6, 7]. The extreme values are plotted on a control chart [8] with corresponding control limits. The control limits are computed for a specified probability of exceedance. In the present study, the subgroup size of $d = 100$ and the probability of exceedance of 0.001 were used. If the plotted data points exceed the control limits, an alarm is triggered indicating possible damage.

5 Numerical Experiment

A numerical experiment was performed to investigate damage detection of a structure having real or complex modes.

The structure was a two-dimensional steel frame (Fig. 1) with a height of 4.0 m and a width of 3.0 m. Both columns were fixed at the bottom. The frame was also supported with a horizontal spring and a discrete viscous damper at an elevation of 2.75 m with a spring constant of $k = 2.0$ MN/m and viscous damping coefficient of $c = 11$ kNs/m. For the structure with real modes, the discrete damper was absent. The frame was modelled with 44 simple beam elements with equal lengths of 250 mm and a square hollow section of 100 mm \times 100 mm \times 5 mm.

The lowest natural frequencies and the corresponding damping ratios of the undamaged structure with real or complex modes under nominal environmental condition were computed using Eq. (4) and are listed in Table 1. Notice that all modes were underdamped and in the case of complex modes there were two complex modes for each natural frequency. Modal damping was the only source of damping for real

Fig. 1 Steel frame

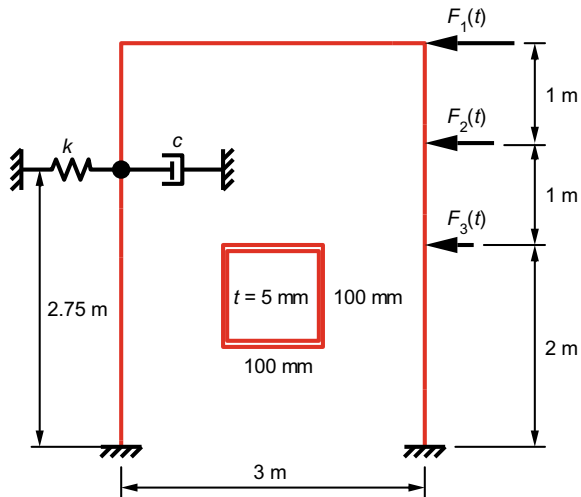


Table 1 Seven lowest natural frequencies and damping ratios of the two structures

Mode number	Real modes		Complex modes	
	f_n (Hz)	ζ	f_n (Hz)	ζ
1	13.9257	0.0100	14.2361	0.0828
2	37.3384	0.0100	39.0230	0.0453
3	50.2279	0.0150	54.3517	0.3515
4	59.8129	0.0200	58.6689	0.0322
5	112.6560	0.0200	110.0559	0.2782
6	120.1176	0.0200	113.0101	0.0209
7	167.8757	0.0200	166.2691	0.0317

modes, whereas for the complex modes damping was composed both of the discrete damper and modal damping.

Horizontal random loading was applied to the right column at elevations of 4 m, 3 m, and 2 m (Fig. 1). The loads $F_1(t)$, $F_2(t)$, and $F_3(t)$ were mutually independent. The maximum frequency of the excitation was 50 Hz.

Steady state analysis with modal superposition was applied to compute the response of the structure. Periodic pseudorandom excitations in the frequency range between 0 and 50 Hz with random amplitudes and phases were generated [9], and the analysis was performed in the frequency domain [4]. Seven lowest modes were included in the analysis.

The analysis period was 4.096 s with a time increment of 4 ms resulting in 1024 data points. Transverse accelerations were measured with 43 sensors located at the nodes of the FE model. Gaussian noise was added to each sensor. The average SNR was 30 dB and noise standard deviations were equal in all sensors. For validation and comparison, exact transverse accelerations were also recorded.

A relatively complex environmental model was applied. The temperature of the left corner, T_{17} varied randomly between -25°C and $+40^\circ\text{C}$. The subscript 17 indicates the node number. The temperature of the other end points varied randomly: $T_{29} = T_{17} \pm 5^\circ\text{C}$; $T_1 = T_{17} \pm 3^\circ\text{C}$; and $T_{45} = T_{29} \pm 3^\circ\text{C}$. Temperature variation between the aforementioned points was linear. The relationship between temperature and the Young’s modulus, E , was stepwise linear as shown in Fig. 2a. Sample distributions of the Young’s modulus in the elements are plotted in Fig. 2b. Within each short measurement, the distribution did not change.

Due to the temperature effect, the natural frequencies varied between measurements. Figure 3a shows the frequency variation for the structure having real modes, while Fig. 3b shows the frequency variation for the structure having complex modes. The data points to the right of the dashed vertical lines are from the damaged structure. Visually, it is difficult to detect damage from the frequency changes due to the strong environmental effect.

Damage was removal of material inside a beam element due to corrosion. The damaged element was located at the bottom of the left leg. Five different damage

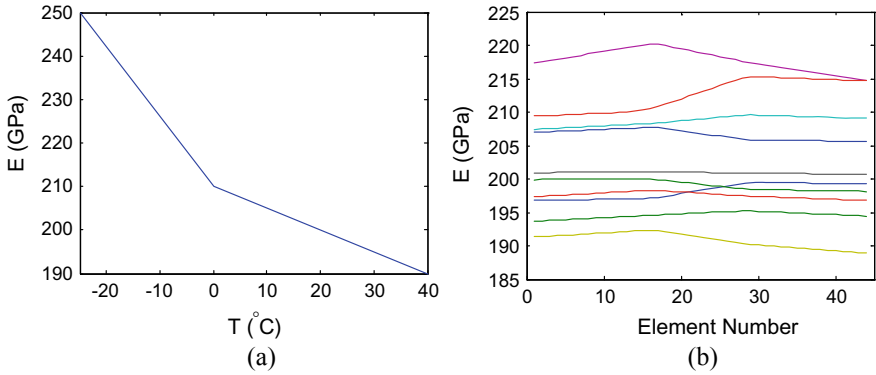


Fig. 2 **a** Young's modulus versus temperature, **b** sample distributions of the Young's modulus

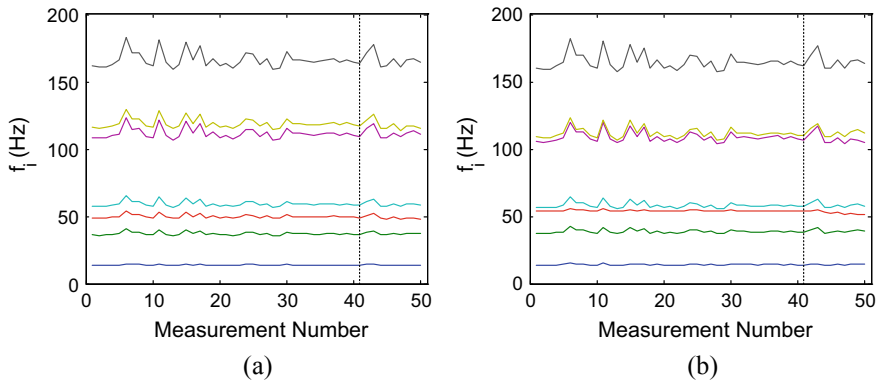


Fig. 3 Variation of the seven lowest natural frequencies due to temperature and damage for the structure with **a** real modes and **b** complex modes

levels were considered with the wall thicknesses of 4.5, 4.0, 3.5, 3.0, and 2.5 mm. Notice that as the material was removed, both the stiffness and mass were decreased.

The first 40 measurements were taken from the undamaged structure and each damage level was monitored with two measurements. Training data were the first 20 measurements. The extreme value statistics (EVS) control charts were designed using the same training data.

5.1 Dimensions of the Data Space

Studying first the noiseless response in a single measurement with constant environment, the data matrix consisted 1024 data points from 43 accelerometers. The rank of the data matrix was 7 if the modes were real, and 14 if the modes were complex.

These observations support the discussion in Sect. 2. When noise was present and several measurements were included with different environmental conditions, full rank data matrices resulted with either model. Even in a noiseless case, the data matrix had a full rank, because the complex relationship between temperature and Young’s modulus could not be completely eliminated using linear MMSE.

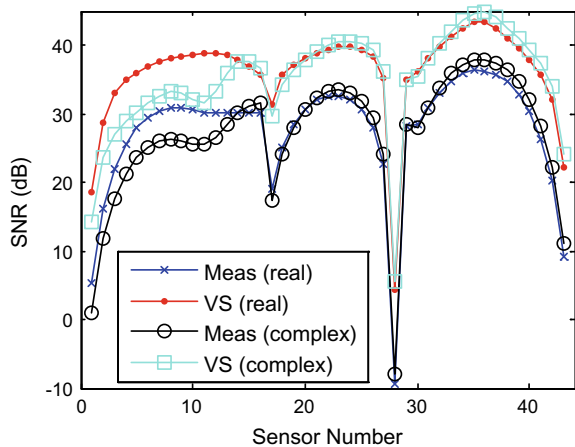
5.2 Damage Detection

Figure 4 shows the SNR of each physical sensor and the corresponding virtual sensor for both models. It can be seen that the SNRs of the virtual sensors were always larger than those of the hardware. Due to different acceleration levels at different regions of the structure, the SNRs varied considerably. In particular, damage was located in a region with a low SNR (closest to sensor 1).

The residuals were first subjected to principal component analysis. The first PC scores were only retained, and the PC scores of the training data were used to identify the probability density functions (PDF) of the extreme values. Separate PDFs for the minima and maxima (or negative maxima) were identified using a subgroup size of 100. The histograms of the minima and negative maxima for the complex mode case are plotted in Fig. 5 together with the fitted PDFs. It can be seen that the theoretical PDFs closely agree with the data. Similar results were obtained for the real mode case.

EVS control charts for the first PC scores of the residual with a subgroup size of 100 are shown in Fig. 6 for real modes and in Fig. 7 for complex modes. Control charts were plotted both for the actual measurement data (left) and virtual sensor data (right). The leftmost vertical line corresponds to the end of training data, and the other vertical lines indicate the five damage levels. It can be seen that the virtual

Fig. 4 SNR of raw data and the corresponding virtual sensors from the structure with real modes or complex modes



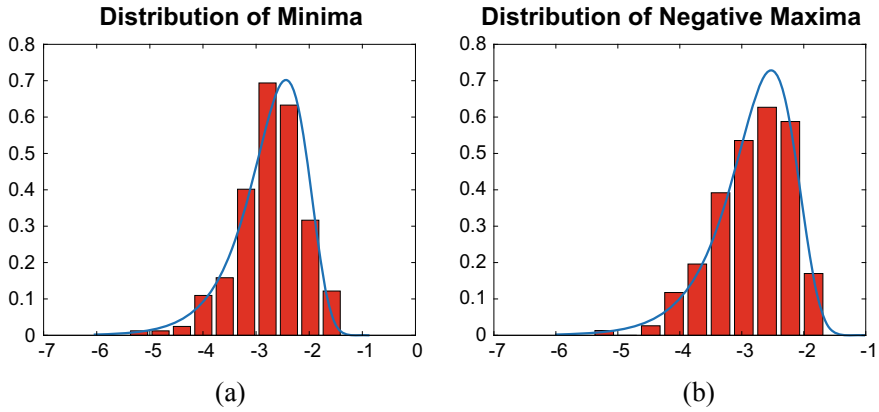


Fig. 5 Identified EVS distributions and histograms for the first PC scores of the residual of the training data: **a** minima, **b** negative maxima. The data were from the structure with complex modes

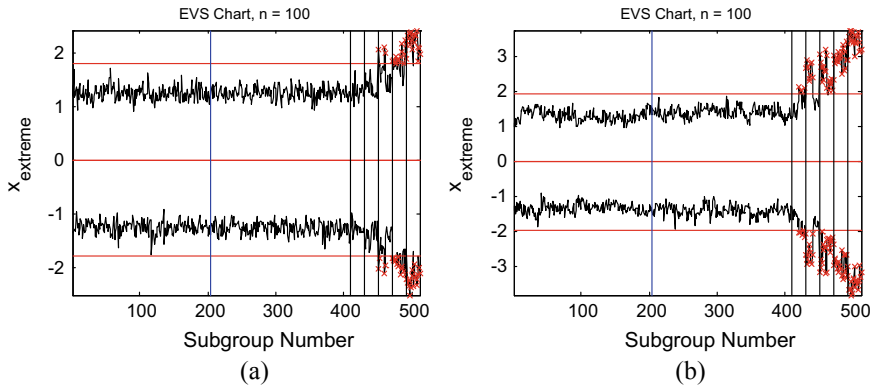


Fig. 6 Damage detection for the structure with real modes: **a** raw data, **b** virtual sensors

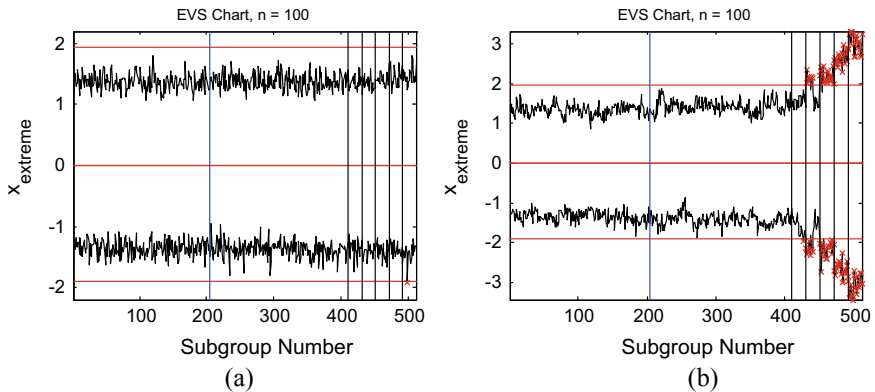


Fig. 7 Damage detection for the structure with complex modes: **a** raw data, **b** virtual sensors

sensors were capable of detecting smaller damage than the physical sensors in both models. This is because virtual sensors had a larger SNR than the physical sensors.

For the structure with real modes, three largest damage levels were detected using the physical measurements, whereas with virtual sensors, all five damage levels could be detected. For a structure with complex modes, damage detection missed all damage levels if physical measurements were used, whereas with virtual sensors, the four largest damage levels could be detected. Damage detection with complex modes was therefore more difficult than with real modes in this particular case. Similar results were obtained if damage was located at the bottom of the right leg. Quite surprisingly, the results were similar also in the case with no environmental effects. The noise effect was probably more significant compared to the remaining environmental influences that could not be eliminated.

5.3 Damage Localization

Damage was assumed to locate in the vicinity of the sensor with the largest Mahalanobis distance (MD) [10] of the residual, Eq. (22). The MDs of the residuals for each sensor are plotted both for the structure with real modes (Fig. 8a) and complex modes (Fig. 8b). In both cases, damage was localized to sensor 3 that was relatively close to the actual damage location. The closest sensor was sensor 1. The inaccuracy in damage localization was probably due to the low SNR of sensors 1 and 2, which were closer to damage than sensor 3.

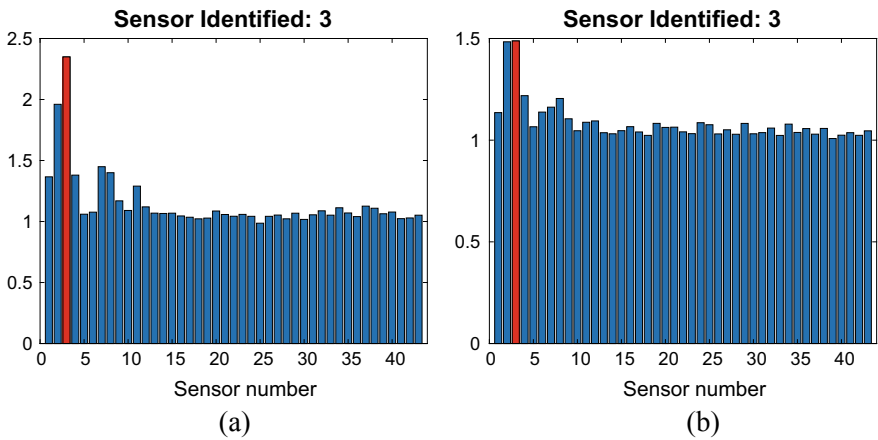


Fig. 8 Damage localization using virtual sensors: **a** real modes, **b** complex modes. The actual location of damage was close to sensor 1

6 Conclusion

Damage detection of structures having complex modes was studied. Data analysis was made directly in the time domain. A redundant sensor network with a large number of sensors was assumed. Detection performance was compared using physical or virtual sensors. In addition, the same structure with real modes was analyzed. It was shown that virtual sensors outperformed the corresponding hardware, because the SNR of the virtual sensors was higher than that of the physical sensors. Damage detection was easier for a structure with real modes than for a similar structure with complex modes. The main conclusion is that for the same detection performance in the time domain, a structure with complex modes must be equipped with a larger number of sensors than the same structure having real modes. Damage localization performance was similar in both cases revealing the region where inspection could be concentrated. The localization did not, however, result in the closest sensor to damage. An experimental study is still needed to verify the findings made in this paper.

Acknowledgements This work was supported by Metropolia University of Applied Sciences.

References

1. Kullaa J (2018) Bayesian virtual sensing in structural dynamics. *Mech Syst Signal Process* 115(2019):497–513
2. Kullaa J (2019) Robust damage detection using Bayesian virtual sensors. *Mech Syst Signal Process* 135(2020):
3. Kay SM (1998) Fundamentals of statistical signal processing. Detection theory. Prentice-Hall, Upper Saddle River, NJ
4. Clough RW, Penzien J (1993) Dynamics of structures, 2nd edn. McGraw-Hill, New York
5. Scharf LL (1991) Statistical signal processing: detection, estimation, and time series analysis. Addison-Wesley, Reading, MA
6. Coles S (2001) An introduction to statistical modeling of extreme values. Springer, Bristol
7. Worden K, Allen D, Sohn H, Farrar CR (2002) Damage detection in mechanical structures using extreme value statistics. In: SPIE proceedings, 9th annual international symposium on smart structures and materials, San Diego, CA, vol 4693, pp 289–299
8. Montgomery DC (1997) Introduction to statistical quality control, 3rd edn. Wiley, New York
9. Brandt A (2011) Noise and vibration analysis: signal analysis and experimental procedures. Wiley, Chichester; Hoboken, N.J
10. Bishop CM (2006) Pattern recognition and machine learning. Springer, New York

Use of Sar Satellite Data in Bridge Monitoring with Application to Urban Areas



Luca Sartorelli, Mattia Previtali , Pier Francesco Giordano ,
Maria Pina Limongelli , Francesco Ballio , and Andrea Uttini

Abstract In the last 20 years, SAR sensors installed on satellites have been increasingly used to monitor large scale phenomena such as subsidence, uplifting, or landslides. Recently several research groups started to investigate the use of remote sensing for damage detection in civil infrastructures. This technique presents in principle several advantages, not least the possibility to monitor a network of structures using the same sensor. However, its implementation for civil engineering projects is still at its infancy and a limited number of applications can be found in literature. The goal of this paper is to investigate the feasibility of using InSAR data for structural health monitoring of bridges with reference to a number of case studies. Data measured by radar satellites with different spatial and temporal resolutions and different frequency bands are processed to extract bridge displacement data and analyzed to identify possible structural damages. The SqueeSAR technique is used to extract displacement time histories from SAR images acquired by radar sensors with different spatial and temporal resolution (TerraSAR-X and RADARSAT 1–2). Displacements are then processed to identify anomalies possibly related to damage. Results show that high-resolution radar data enable the detection of very small structural displacements due to environmental changes, such as temperature variation.

Keywords Satellite SAR remote sensing · Bridge health monitoring · Data processing · SqueeSAR

L. Sartorelli
Politecnico di Milano, Milan, Italy

M. Previtali (✉) · P. F. Giordano · M. P. Limongelli
Department of Architecture, Built Environment and Construction Engineering, Politecnico di Milano, Milan, Italy
e-mail: mattia.previtali@polimi.it

F. Ballio
Department of Civil and Environmental Engineering, Politecnico di Milano, Milan, Italy

A. Uttini
Tre Altamira, Milan, Italy

1 Introduction

Bridges, which are critical elements of transportation networks, are subjected to several degradation phenomena, such as aging, fatigue, and chemical attacks. Insufficient maintenance interventions, joined with increased traffic loads with respect to the design values as well as effects connected with climate change, often accelerate materials deterioration. Over the last decades, global warming has led to a growth in intensity, frequency, and duration of extreme natural events that exacerbate the effect of deterioration, often leading to conditions not accounted for in the original design standard [1]. Currently, a large percentage of road and railway bridges in Europe needs urgent rehabilitation due to structural damages. A considerable number of Italian infrastructures were designed and constructed over 50 years ago and they need maintenance to avoid serious and dramatic consequences. It has been estimated [2] that tens of billions of euro are needed to preserve the Italian bridges' health.

Visual inspections are traditionally used to collect information about the bridge conditions and to support maintenance planning. These operations are time-consuming, strongly subjective, and above all, they do not provide real time information able to support prompt decisions for maintenance management. To fill this gap, in the last two decades, Structural Health Monitoring (SHM) techniques, based on the extraction of information through the processing of data collected by sensors, have been developed [3–6]. Traditional sensors are installed on the monitored structure to record its response. However, the acquisition and processing of data can lead to high costs that network owners may not be available to or cannot sustain.

In the last 20 years, due to technological advances in radar sensing and data processing, Synthetic Aperture Radar (SAR) satellite data have been increasingly used for monitor purposes in earth sciences. In particular, Interferometry Synthetic Aperture Radar (InSAR) is a remote sensing technique that allows to detect displacements with sub-centimetric accuracy over large areas. The InSAR feasibility to measure displacements related to large-scale events such as landslides or subsidence has been assessed for the past two decades. Recently, with the increase of radar spatial resolution, the use of this technique to monitor displacements of civil structures, such as bridges, has become feasible.

The goal of this paper is to report some preliminary results of an investigation aimed to assess the possibility to use SAR data to monitor the evolution of the structural health of bridges. In particular, a procedure to extract information from satellite radar data is presented with reference to several case studies in the Milan urban area. Interferometric data acquired by high and low spatial resolution sensing devices—namely TerraSAR-X and RadarSAT-1/2—are used to extract displacement and to verify the capabilities of the two types of sensors. InSAR data are processed using the multi-interferogram SqueeSAR[®] technique [7].

The paper is structured as follows. Section 2 contains a short literature review analysis on the application of InSAR monitoring to bridges. Section 3 briefly presents the SqueeSAR technique and the features of two sensing systems and of the data used in the paper. Section 4 describes the methodology implemented to extract preliminary

information about the bridge condition from displacement time series. The case studies and the discussion of results are described in Sect. 5 and Sect. 7 concludes the paper.

2 Related Work on the Use of InSAR for Bridges

In the last decades, the InSAR technique has been increasingly used to monitor large scale phenomena such as subsidence, uplifting, or landslides [8–11]. Recently, thanks to the improved spatial resolution of radar satellites, its use to monitor civil structures has been developing, leading to several applications. One of the main advantages of remote sensing is that it can offer a look back in time over the study area. In several papers, it is highlighted how the analysis of InSAR displacements could have provided useful information about impending structural failures months before the collapses. Sousa and Bastos [12] showed that the use of multi-temporal InSAR techniques might have foreseen the collapse of the Hintze Ribeiro centennial bridge in Portugal. Based on this observation the authors propose an early warning system triggered by the exceedance of a displacement alarm threshold. Selvakumaran et al. [13] showed that the partial collapse of the Tadcaster Bridge due to scour could have been predicted within one month by an automatic outliers identification method. Recently, Milillo et al. [14] studied the evolution of the configuration of the Morandi bridge over a period of about 15 years before the failure, although their results have been questioned by other authors [15].

SAR satellites have a constant revisiting time ranging from weeks to months thereby they can be used to follow the evolution of the structural condition during all life phases of a bridge, from the design to the construction and operational phases. Pigorini et al. [16] showed as Persistent Scatters InSAR (PSInSAR) could have been applied in the preliminary design of the new Venice-Trieste railway to study the behavior of the study area. In Pigorini et al. [16] and Koudogbo et al. [17], InSAR is used as a monitoring survey during the construction and operational phases of the Scianina-Tracoccia tunnel and Grand Paris Express metro network respectively.

Several authors highlighted that the effect of environmental factors in InSAR displacements monitoring must be properly taken into account to avoid false or missing indications when these data are used to assess the structural health. Besides, InSAR data can be used to study the effect of environmental factors (such as temperature and water action) on a specific infrastructure.

In literature, the correlation between temperature and displacements measured by SAR data at different radar bands (C and X) has been extensively investigated. Both Fornaro et al. [18] and Lazecky et al. [19] demonstrated the high level of correlation between temperature and displacement acquired by X-band, while Huang et al. [20] studied the correlation between displacement from C-band scenes and temperature for the metal Nanjing Dashengguan Yangtze River bridge. Other authors studied the correlation between InSAR displacements and other environmental conditions. In References [12, 13], the authors highlighted that SAR can detect changes correlated

to water actions, such as scour and changes in flow rates during flooding, in riverine bridges. Zhang et al. [21] used SAR to study the performance of the Donghai bridge, which is located in a very rough sea environment, and suggested that the InSAR displacements could be correlated to seasonal winds and tide. Another phenomenon that might be studied using SAR data is bridge settlements due to soil consolidation, as presented by Del Soldato et al. [22].

The effect of environmental factors on bridge displacements may hinder the correct identification of damage if not properly accounted for. In this respect, Huang et al. [23] developed a damaged detection method based on the removal of the thermal effect from the detected displacements.

The comparison between information provided by satellite images and in-situ data is an important factor to prove the InSAR capability in structural damage detection. Despite a large number of civil structures such as dams [24–26], buildings [27], and historical monuments [28] monitored using InSAR techniques, the validation of results using data collected directly on bridges is seldom performed, as highlighted by Cusson et al. [29].

3 Extraction of Bridge Displacements from InSAR Images

In this section, a brief description of the interferometric technology is presented to make the paper self-contained.

SAR is a radar satellite measurement system that provides images stored as matrices of complex numbers that represent amplitude and phase values of the reflected radar signal. Interferometry is the technique that is used to derive displacement time series from the radar data by detecting phase differences through time [17]. Differential interferometric SAR (DInSAR) relies on the processing of two SAR images acquired over the same area at different times, using the same acquisition geometry, and measures possible phase variations induced by surface displacements [27]. The main drawback of DInSAR is that phase differences may not only be induced by displacements. Indeed, temporal and geometric decorrelation phenomena, as well as atmospheric effects may have an impact on the signal phase, thereby reducing the quality of DInSAR results. In the late nineties, new, multi-interferometric, techniques were developed, aiming at identifying individual pixels exhibiting stable radar returns (now referred to as Persistent or Permanent Scatterers—PS). Multi-image algorithms can improve significantly any DInSAR analysis, allowing one to increase the sensitivity and the quality of the results. InSAR requires the processing of long time series to remove the atmospheric component which varies slowly in space and is not correlated in time. Persistent Scatterer InSAR (PSInSAR) was the first multi-temporal technique exploiting pointwise PS [30]. About ten years later, to overcome the limits of PSInSAR, mainly related to the low PS density in non-urban areas, a new multi-interferogram InSAR algorithm was developed [7]. This new technique allows one to identify Measurement Points (MP) belonging to two groups: i.e. Persistent Scatterers (PS) and Distributed Scatterers

(DS). The PS are discrete point-wise radar targets characterized by high signal-to-noise values and stable radar signature (i.e. high reflectivity and coherent phase values) in time. PS are slightly affected by temporal and geometric decorrelation as is the case of points lying on buildings, poles, rocky outcrops and man-made structures. The DSs are patches of ground exhibiting lower but homogenous and consistent radar returns. DSs can be exploited only if they form sufficiently large homogeneous groups of pixels sharing the same scattering mechanism: In these conditions statistical analysis can be used to reduce noise effects.

SqueeSAR needs a dataset of at least 15–20 SAR images, acquired over the same area with the same acquisition mode and geometry, to identify MPs on the Earth surface. For each MP, this technique provides the ground target's position (in WGS84 coordinates), the ellipsoidal elevation (referred to the ellipsoid WGS84), the annual average displacement rate along the Line-of-Sight (LOS) and its standard deviation (expressed in mm/year), displacement time series (in mm) measured along the LOS, and other MP features, such as coherence and average seasonal components. The precision of SqueeSAR displacement measurements mainly depends on the quality of the processed dataset and of the estimation of the atmospheric contributions. The former relies on: the number of processed SAR images, the length of the period time analysed, temporal continuity of acquisition and correctness of phase unwrapping. The atmospheric noise intensity depends on the tropospheric conditions at the time of the acquisitions, the acquisition geometry and the distance from a reference point (REF) used for calibration [25]. Overall, SqueeSAR has an accuracy of about 1 mm/year and a precision for the single measurement around 5 mm, for a MP located less than 1 km away from the REF and considering a dataset of at least 30 SAR images covering 2-year period [7].

The data used for the investigation reported in this paper are acquired by RadarSAT-1/2 (RSAT) and TerraSAR-X (TSX) and processed through SqueeSAR. The features of the dataset are reported in Table 1.

For both datasets, the displacement time series and annual displacement rate are measured along the LOS of the descending orbit trajectory. Since one satellite geometry is used in this paper (namely the descending one), it has not been possible to retrieve the displacement components in vertical and horizontal (East–West) directions [31]. Hence, a negative displacement corresponds to MP movement away from the satellite, while a positive one is directed towards the satellite.

4 Analyses of Displacement Data

This section describes the procedure adopted to process the LOS displacements provided by the SqueeSAR technique and to extract preliminary information about the bridge health. The workflow represented in Fig. 1 was followed.

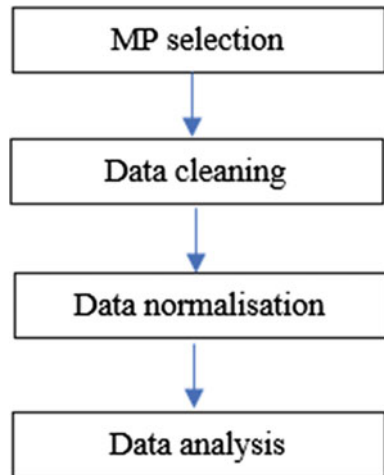
Firstly, MP selection is carried out by using the software QGIS Desktop 3.10.6 [32] that allows one to superimpose the MPs to the orthophoto of the study area, downloaded by Geoportale Regione Lombardia [33]. The MPs located on the bridge

Table 1 Comparison between two datasets: TerraSAR-X and RadarSAT-1/2

	TerraSAR-X	RadarSAT-1/2
Space agency	DLR (Germany)	CSA (Canada)
Radar band	X	C
Wavelength λ (cm)	3.11	5.66 (RSAT1)–5.55 (RSAT2)
Spatial resolution (m ²)	3 × 3	20 × 5
Elevation precision ^a (m)	±1.5	±1.5
Revisiting time (day)	11	24
Acquisition period	31/08/2009–23/02/2020	13/10/2003–23/10/2017
N° images	267	198
Satellite geometry	Descending	Descending
Sensor Mode	SM010 (StripMap)	S3 (Standard)

^aTypical precision value of MP, located less than 1 km from the REF and a dataset of at least 30 SAR images, associated with the UTM coordinate of MP at mid-latitudes

Fig. 1 Analysis of displacement data workflow



deck are selected and furtherly processed to infer bridge displacements and preliminary information about the bridge’s health. The remaining MPs are used to investigate the displacements affecting the area near the bridge.

The second step consists in data cleaning which is applied to each bridge dataset to identify possible outliers and remove them from the datasets used for further processing. Two types of outliers are considered, namely: MPs erroneously located on the bridge deck due to inaccuracies in the overlap of the SqueeSAR outcomes to the orthophoto, and MPs exhibiting anomalous values of the annual displacement rate. The first type of MPs is identified by comparing their elevation with the elevation of the bridge deck and accounting for the positioning accuracy of the two satellites (Table 1). For example, the limits shown in Fig. 2, which are related to the Via

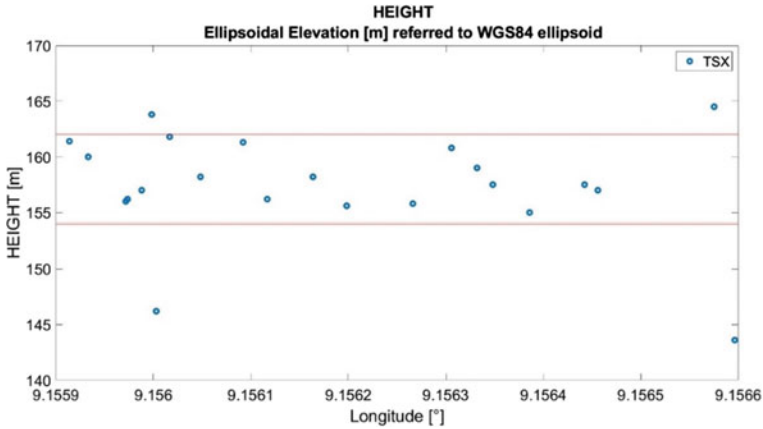


Fig. 2 An example of detection of the first type outlier for Via Lodovico il Moro bridge 2. Red lines are the bridge elevation limits, so the dots out of the red lines are considered outliers

Lodovico il Moro bridge 2 (see Sect. 5.2), correspond to the lower and upper elevation of the bridge deck above the WGS84 ellipsoid (between 154 and 162 m) considering the precision of satellite radar. The second type of outliers are those with values of the displacement rate outside the confidence interval of two standard deviations relevant to the dataset including the annual displacement rate of all the MP_s located on the bridge. Under the assumption that the MP displacements are normally distributed, this assumption corresponds to a probability of 5% to wrongly discard an MP that is actually located on the bridge.

In the following data normalization phase, the two datasets are normalized to allow comparison. Indeed, the two datasets, TSX and RSAT, have different acquisition times (see Table 1). To allow the comparison of datasets, an overlapping period is selected (RSAT-1/2: 18/08/2009—23/10/2017 and TSX: 31/08/2009—18/10/2017), and the mean of the displacements measured during the first two-years is subtracted to the displacement time series of each MP. Moreover, a moving average over 4 months of the displacement time series is applied to filter some oscillations due to noise.

Finally, data analysis is carried out to detect trends and patterns that may provide preliminary information about bridge health. This analysis entails several operations on the displacement dataset, as follows:

- a. Identification of regions of the bridge deck that may be assumed to behave as rigid bodies and relevant clustering of the dataset. These regions can be identified based on the analysis of the geometry of the bridge such as, for example, influence zones of the piers or regions separated by expansion joints. More details will be given in the case study sections.
- b. Identification of a Representative Displacement (RD) for each cluster of data. In the analysis reported in this paper, the mean displacement computed for each epoch over the cluster MP displacements is assumed as RD.

- c. Comparison of the RD of each cluster with the displacements of the area surrounding the bridge. This is aimed to discard in the damage detection analysis large scale displacements that affect the entire region surrounding the bridge, thereby causing only rigid body motions of the entire structure.
- d. Analysis of the correlation between RDs and environmental changes (i.e. temperature). This is performed through the analysis in the frequency domain of the displacement time history and the computation of the Pearson correlation coefficient between the displacement and the temperature time histories.
- e. Validation of the trends identified in the previous step through information collected on-site or through documents and reports relevant to maintenance interventions performed on the bridge.

5 Case Studies: Railway and Road Bridges in Milan

The procedure outlined in the previous section was applied to several bridges in the Milan urban area crossed by a wide transportation network of roads, highways, and railway. One of the aims of the analysis was to compare interferometric data acquired by sensors with different spatial resolution. Data acquired by TerraSAR-X (high resolution) and RadarSAT-1/2 (low resolution) were available for slightly different portions of the Milan urban area, thereby the analysis was carried out only for bridges located in the overlapping region between the tiles relevant to the two satellites. Bridges spanning more than 20 m were selected since the RSAT spatial resolution is limited to about $20 \times 5 \text{ m}^2$. So, bridges with a span smaller than 20 may result in having a MPs density insufficient for a fair and meaningful comparison with TerraSAR-X. In this paper, the results obtained for four bridges, detailed in Table 2 and Fig. 3, are reported and discussed.

5.1 Large Scale Analysis of the Milan Urban Area

The large-scale analysis of the study area highlighted a peculiar trend of the LOS displacements measured along the railway infrastructure. These displacements are all

Table 2 Studied bridges

Bridge	Long. (°)	Lat. (°)	Length (m)	Type	MP/m ² (TSX)
Via Farini	9.182400	45.487175	150	Vehicular + Tramvia	0.03
Viale Monza 101	9.219933	45.497004	26	Railway	0.06
Viale Monza 119	9.220472	45.498395	28	Railway	0.07
Via Lodovico il Moro 2	9.1566659	45.447836	45	Railway	0.05

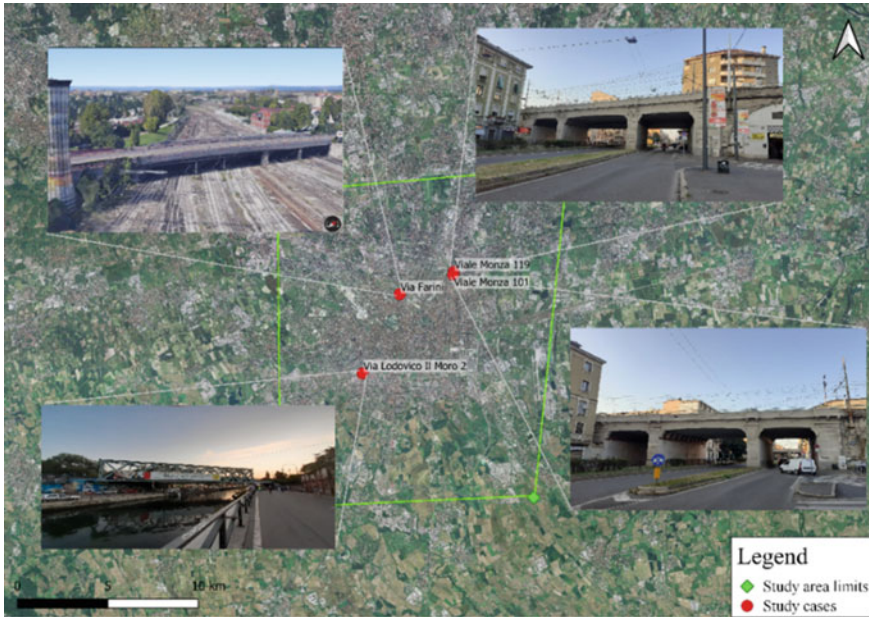


Fig. 3 Location of the case studies

directed away from the satellite highlighting a global settlement of this infrastructure. This is very clearly shown by Fig. 4, where the annual displacement rates along the LOS are reported for the considered area: The location of the MPs with higher velocity follows exactly the path of the railway tracks. These displacements are attributed

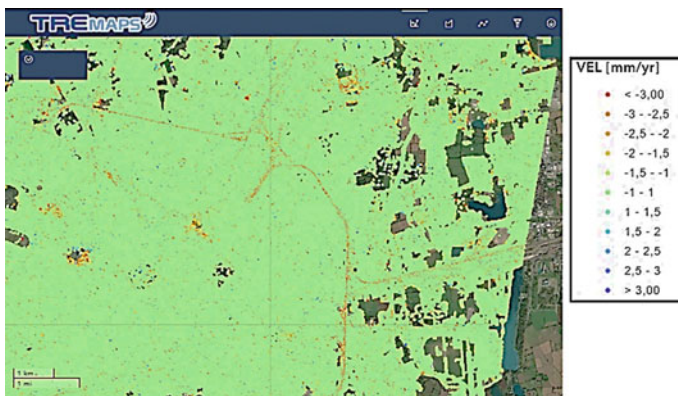


Fig. 4 Annual displacement rate along LOS (descending trajectory). Long red lines, made by MPs, are observable. They correspond to railway tracks

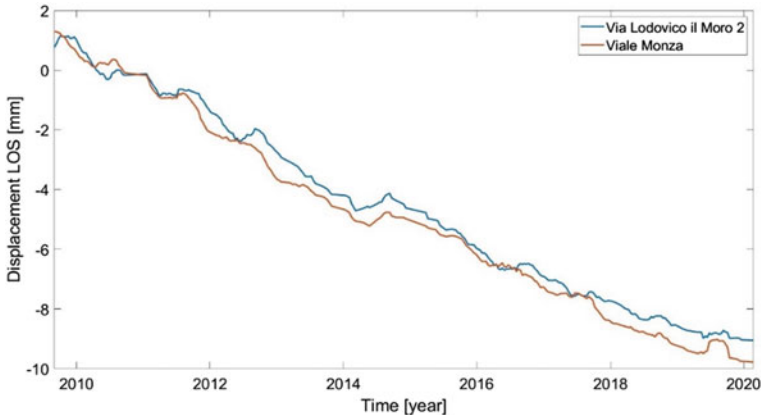


Fig. 5 The mean displacement between MPs belonging to the railway areas in proximity of Via Lodovico il Moro 2 and the two Viale Monza bridges

to gradual settlement of railway ballast due to repeated loading cycles during the usage.

Figure 5 displays the average displacement of the MPs located on the railway in proximity of the Lodovico il Moro 2 and the two Viale Monza bridges. Indeed, in it is evident that railway areas are subject to a decreasing trend in the displacement time series. During the analysis of InSAR data, these displacements might be wrongly interpreted as structural displacements and therefore must be carefully accounted for. Herein, in order to remove this possible source of errors in the study of the bridge condition, the MPs located in proximity of the railway are not considered in the analysis.

5.2 Via Lodovico Il Moro 2 Bridge

Via Lodovico il Moro 2 bridge crosses the Channel Alzaia Naviglio Grande and is one of the longest metal railway bridges in the study area. It is a steel truss bridge that lays on two lateral concrete piers.

The analysis of bridge displacements was carried out using the two available datasets, RSAT and TSX. The MPs detected on the bridge by the two satellites are visible in Fig. 6. In this case, all the MPs were supposed to be part of the same cluster and the average displacement was considered as the reference displacement for the bridge.

Figure 7 reports the RDs retrieved from TSX and RSAT data. Both time series oscillate around the zero displacement and show a certain periodicity.

The correlation coefficient between RSAT and TSX displacements is equal to 0.43 which indicates a low but not negligible correlation between the two displacement



Fig. 6 Via Lodovico il Moro 2: MPs on the bridge acquired by TSX and RSAT

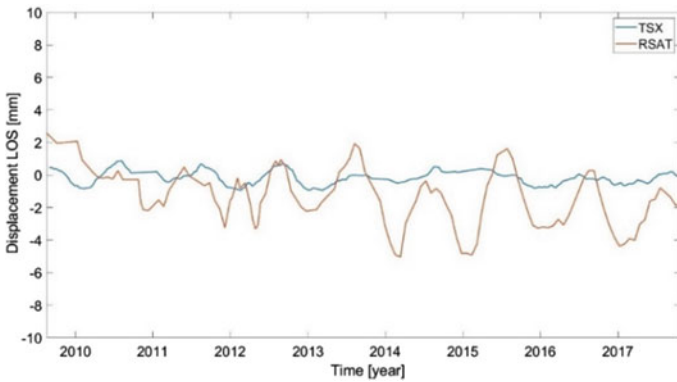


Fig. 7 Via Lodovico il Moro 2 bridge: Comparison between RDs time series provided by TSX and RSAT

datasets. However, the magnitude of the displacements of the two datasets are quite different. This difference is likely due to the different acquisition geometries (both the incidence and the azimuth angles are not identical), as well as the sensor parameters of the two radar systems, which in turn identify two distinct families of radar targets. The ratio between the mean values of the displacement measured by the two satellites is (on average) equal to 2, a value close to the ratio (1.8) of the two radar wavelengths. However, there is no reason that should be the case. Again, the PS from the two datasets correspond to different sections of the bridge and different objects on ground, which can have different thermal dilation effects along the satellite line of sight.,

For all the case studies considered, the correlation between the displacement and the minimum daily temperature [34] is investigated. The minimum value is considered for the daily temperature because both satellites pass over the study area at around 05:30 AM, when temperature values are at their minimum.

Figure 8 reports the time histories of the temperature and of the displacement extracted from the two datasets. The Pearson correlation coefficient [35] between

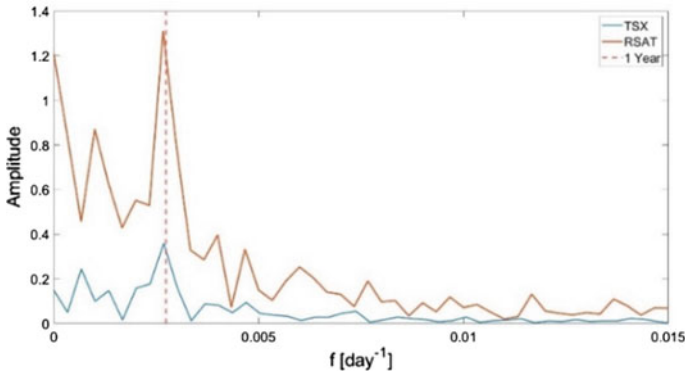


Fig. 8 Via Lodovico il Moro 2 bridge: Representative Displacement (blue) and temperature (red) time series for TSX (above) and RSAT (below) datasets

the two time series is respectively 0.68 and 0.60 for TSX and RSAT. This trend highlights the strong correlation between the two series indicating that for this bridge the structural displacements are mainly due to thermal variations. A further indication is given by the displacement Fourier spectra (see Fig. 9) which presents a sharp peak at the yearly frequency of the temperature cycle.

The comparison between the displacements of the bridge and those of the surrounding area show that there are not significant relative displacements between the two. The bridge displacements are mainly due to thermal variations thereby structural damages do not seem to have occurred in the observation period.

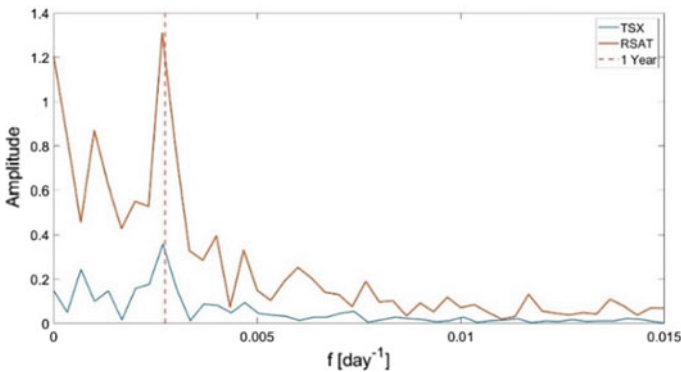


Fig. 9 Via Lodovico il Moro 2 bridge: Fourier spectra of displacement time series

5.3 Via Farini Bridge

Via Farini bridge spans around 200 m with a hyperbolic profile. The southern span is simply supported on the piers whereas the northern spans form a continuous beam on three supports. The MPs provided by both the TSX and the RSAT are all located on the eastern and western sides of the deck thereby ten MPs clusters were identified on the regions delimited by four transversal and the longitudinal central joints (see Fig. 10a). Since the RSAT dataset contains a lower number of MPs with respect to the TSX dataset (as should be expected), their comparison was possible only on the six clusters represented in Fig. 10b by the hatched areas. For this case study, the data retrieved by the two different satellites are not comparable in terms of displacement magnitude, as highlighted in Fig. 11.

The Pearson correlation coefficients between the temperature and the RDs extracted from the TSX dataset are shown in Fig. 12 for each of the 10 clusters. The dataset is relevant to the period between September 2009 and February 2020 when maintenance works were initiated on the bridge. For the blocks showing higher coefficients ρ , also the linear regression line is displayed.

The analysis of these datasets shows (see Fig. 12) that the displacements of the central blocks (indicated as B1E, B2E, B3E, B2W, and B3W in Fig. 10b) are linearly correlated with the temperature, while very low values of correlation is shown by the displacements of the clusters close to the abutments (B0E, B0W, B4W and B4E, and B1W). The RDs of the central-eastern blocks (1E, 2E, 3E) have a positive correlation with the temperature, while the central-western blocks have a negative correlation. This displacement pattern, with displacements of central-eastern blocks specular

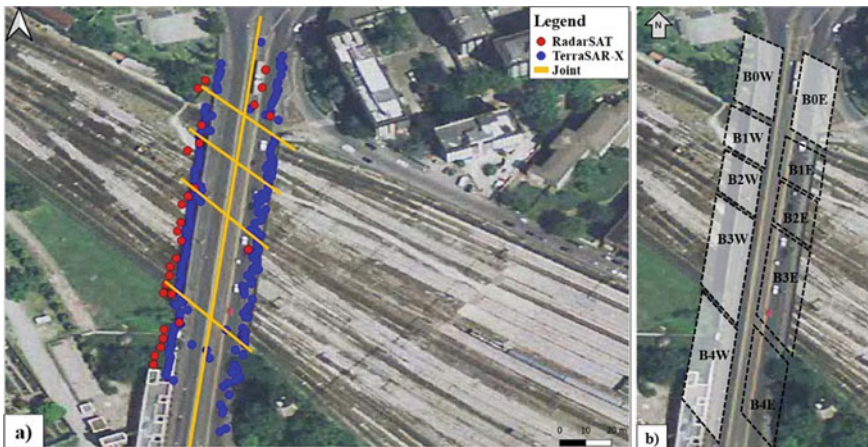


Fig. 10 Via Farini bridge: **a** MPs detected (before the data cleaning) by TerraSAR-X in blue and RadarSAT in red, separated by the joints in yellow; **b** MP clusters: Hatched areas where both TerraSAR-X and RadarSAT MPs are detected

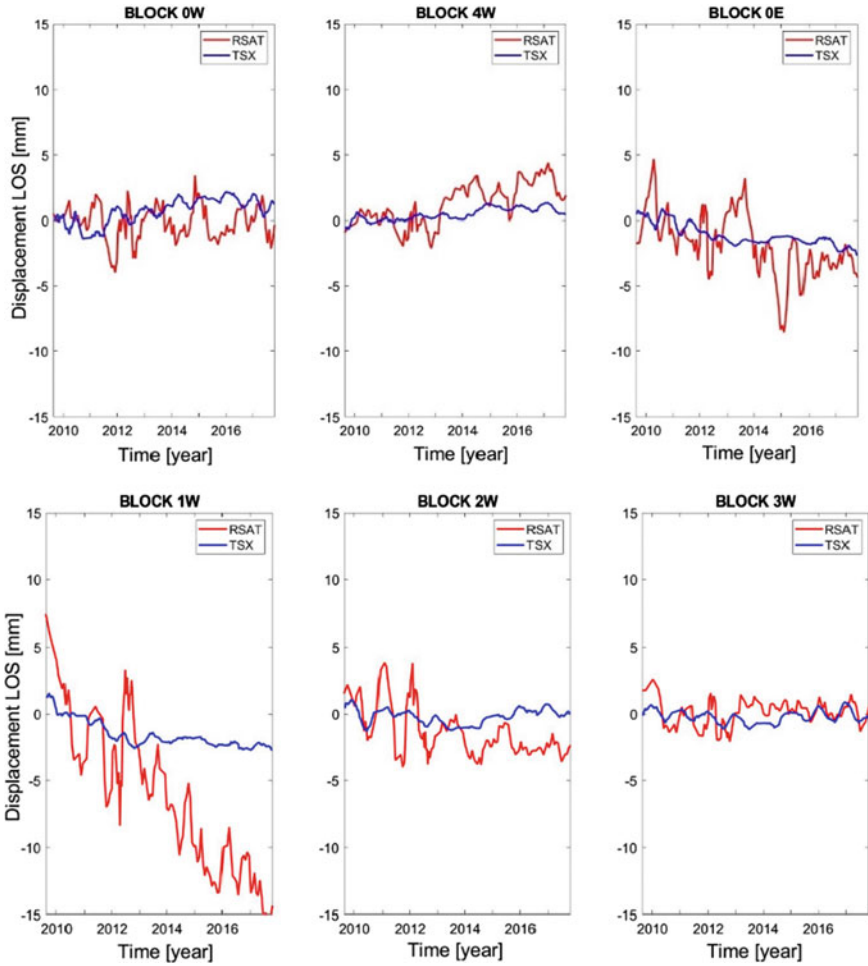


Fig. 11 Comparison between RD of TSX and RSAT datasets for the 10 clusters

with respect to those of the central-western side, is consistent with the longitudinal expansion and shrinking at the longitudinal central joint, induced by thermal variations.

The eastern and western sides of the three blocks B0, B1 and B3 move in opposite directions in time (Fig. 13). Furthermore, from the maintenance reports, it is noticed that these blocks were recently impacted by important maintenance works such as enlargement of the loading piers, reinforcement of the abutment, and strengthening of the supporting structures. The anomalous behaviour of the blocks and the fact that maintenance works have been carried out leads to suppose that the displacement trends were due to damage.

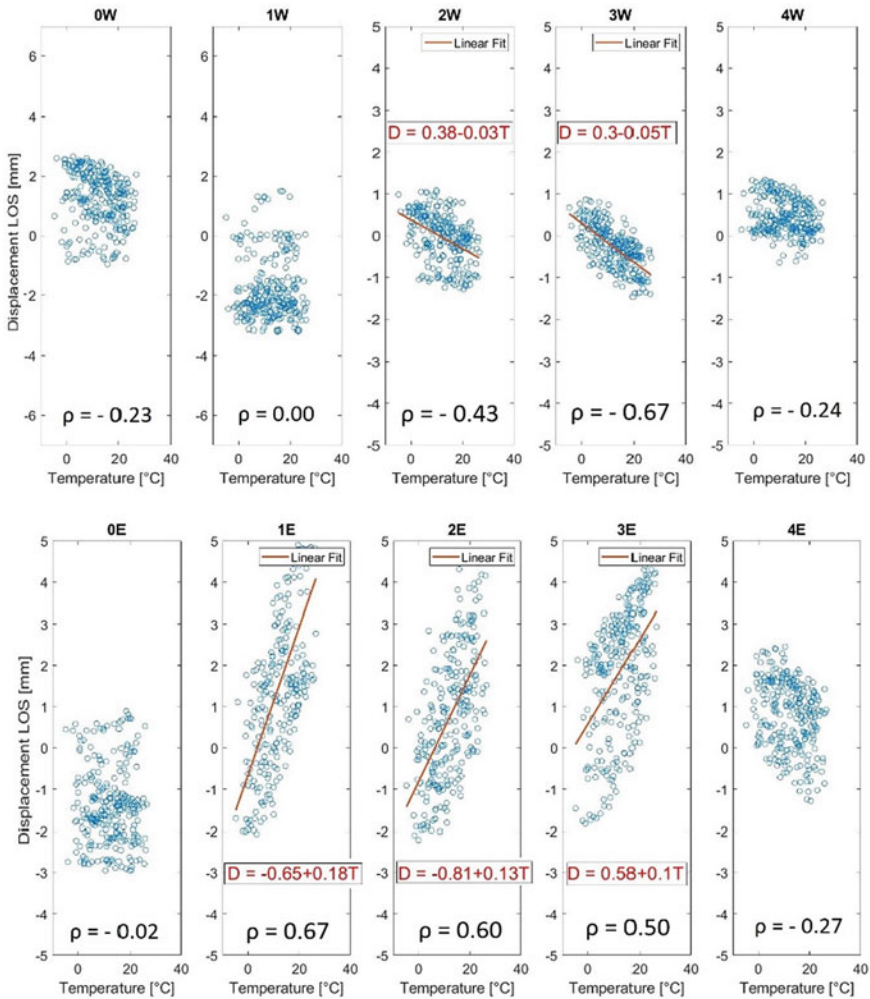


Fig. 12 Via Farini bridge: TRX displacements versus minimum daily temperature plots and Pearson correlation coefficients (ρ) for all TSX blocks. For the blocks showing higher coefficients ρ , the linear regression line $D(T)$ is displayed

5.4 Viale Monza 101 and 119 Bridges

Viale Monza 101 bridge is a 26 m long railway bridge that crosses a road (Viale Monza). The deck is supported by two high concrete columns. The nearby Viale Monza 119 bridge is a 28 m long railway bridge that crosses the same road (Viale Monza) 150 m further North (see Fig. 14). The double-deck structure rests on two long concrete columns. Both bridges are surrounded by buildings of similar height over the ground level. This condition makes the selection of the MPs located on the

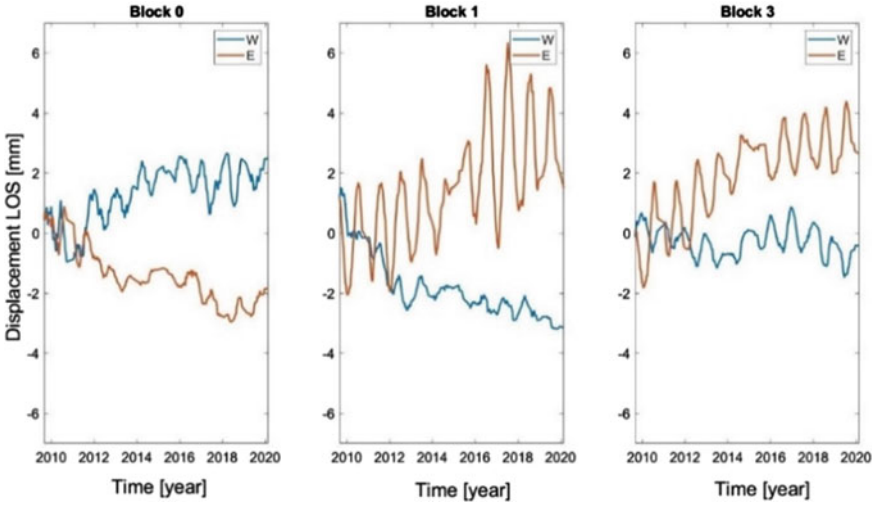


Fig. 13 Via Farini bridge: TRX displacement time histories at the West (W) and East (E) of the deck for possibly damaged blocks

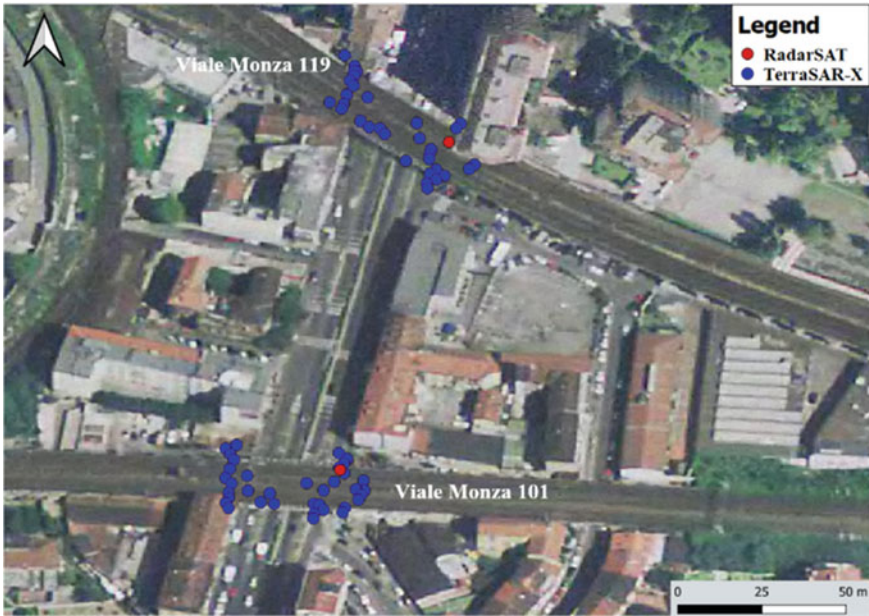


Fig. 14 Viale Monza 101 and 119 bridges: A view from above with MPs detected by RSAT and TSX datasets

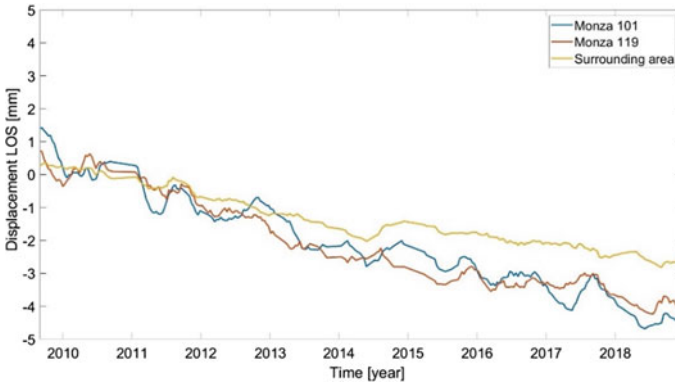


Fig. 15 Viale Monza 101 and 119 bridges: Displacement time series of bridges' RP and the surrounding area

bridge more challenging. Moreover, due to the short length of the bridges' span, the RSAT dataset contains a very limited number of MPs after the preprocessing of data. For this reason, the comparison between the high and low spatial resolution datasets was not possible. The analysis of the InSAR data is carried out using only the TSX dataset available for the period between September 2010 and the beginning of January 2019 when maintenance interventions were carried out on both bridges.

In this case, all the MPs were supposed to be part of the same cluster and the average displacement was considered as the reference displacement for the bridge.

The mean LOS displacement of the area surrounding the two bridges has been calculated considering the MPs in a range of 200 m around the bridge. Over the observation period (about 10 years), a total displacement of about 3 mm was measured.

The RDs of the two bridges are compared in Fig. 15 with the mean displacement of the surrounding area. The relevant Pearson correlation coefficients are equal to 0.97 (Viale Monza 101) and 0.98 (Viale Monza 119) for the two bridges which lead to attribute the displacements of the two bridges to a slow settlement of the soil.

For these two case studies, as expected for reinforced concrete bridges, the correlation between LOS displacements and temperature is negligible.

5.5 Discussion of Results

The analysis of InSAR data carried out according to the procedure outlined in Sect. 4 allowed to investigate the correlation of bridge displacements with thermal variations, with settlements of the area surrounding the bridge, and to highlight anomalies possibly related to structural changes.

The comparison of the results that can be obtained using high- or low- spatial resolution datasets shows that the use of the former enables not only to measure displacements with a higher resolution but, more importantly, to apply the InSAR technique to acquire information about short bridges that are prevalent in urban areas.

In the case studies considered, the comparison between low and high spatial resolution satellites was not always possible due to the lower number of MPs obtained with low resolution satellites. For the cases where the comparison was possible, results were not always consistent. As an example, for the bridge in Via Lodovico il Moro 2, the low and the high-resolution radars detect a similar seasonal pattern of displacement, but with a significant difference in the magnitude of the deformation. This is likely due to the fact that the two families of measurement points identified by the two radar systems are not identical and correspond to different objects on ground.

The use of InSAR in urban areas is also challenged by the presence of constructions around the bridge that might not only impede the radar beam to reach the bridge surface thereby reducing the number of MPs over the bridge deck, but can also prevent to distinguish the MPs located on the bridge deck from those located on the surrounding constructions. High spatial resolution and X-band satellites suite better for the monitoring of urban bridges since they ease and provide higher accuracy in MPs detection and positioning on the bridge. Furthermore, the presence of obstacles (such as buildings) and inhomogeneous distribution of natural reflectors might determine the presence of a smaller number of MPs in some portions of the bridge with respect to others. Concerning the impact of such inhomogeneous distribution on the analysis we can observe that Viale Monza 101/119 and Via Lodovico il Moro 2 bridges can be considered as single blocks from the structural point of view, as confirmed by the high correlation between the displacements of the MPs. In this situation, the discretization of the bridge with a single element (a single cluster of MPs) is justified. On the contrary, in case of a low correlation, a more in-depth analysis should be carried out. This entails the discretization of the bridge in a higher number of clusters as for the case of Via Farini bridge.

The availability of high-resolution data also provides information about the influence of thermal variations on displacements and to study the relevant movements of the bridge when these are not negligible with respect to the accuracy of the sensor on the satellite and the InSAR technique. The results obtained for the case studies confirm a higher sensitivity of the X-band radar to temperature variation. However, for the case of Via Lodovico il Moro 2, also C-band enables to catch the displacements of the steel bridge induced to temperature variation.

6 Conclusion

This paper reports the outcomes of a study aimed to investigate the potentiality of the InSAR technology to detect anomalies in urban bridges. A procedure to process displacement data provided by this technique is proposed and applied to four bridges

located in the Milan urban area using both high and low-spatial resolution radar data. Results show that high-resolution data enable to identify displacements correlated to thermal variations and trends in displacement time histories correlated with the settlement of the soil at a large scale or to anomalies in specific portions of the same bridge. This outcome provides interesting information to run possible screening procedures over large areas, aiming to select bridges requiring more in-depth investigations. It should be noted that the dataset available in this study contained only data acquired along “descending orbits”. In general, the availability of both acquisition geometries (corresponding to ascending and descending acquisition modes) allows the computation of the displacements in the vertical and horizontal planes thus enabling a clearer interpretation of the structural behavior.

Further analysis will investigate how the integration of information from InSAR data with information from other sources, such as contact sensors, visual inspections, and design plans can improve the assessment of the structural condition and possibly allow the definition of displacement thresholds to use for the setup of an alarm procedure at large scale triggered by the InSAR data.

An interesting finding of this study is that MPs located in proximity of the railway show large negative displacements, which are attributed to movements of the railway ballast. These MPs should be carefully considered during the analysis since they might be wrongly associated to structural displacements.

The results reported in this paper show that the selection of MPs on the bridge is a crucial operation. The availability of a Dense Digital Surface Model (DDSM) that enables an accurate 3D spatial description of the sensed object could help to improve the assignment of the MPs to the monitored structure.

As a general comment, the use of the InSAR technology with high spatial resolution data can provide information useful to perform a large-scale survey on a large number of bridges, that may enable to detect anomalies. This information enables to trigger more refined investigations, carried out for example through visual inspections or non-destructive tests, on selected bridges for which an alert is provided by the InSAR data. It is worth recalling that the resolution and the temporal frequency of acquisition of satellite data is increasing steadily and sub-meter radar imagery, so far used for intelligence and security applications only, has now become available for commercial projects and civilian applications.

References

1. Schrotten A et al (2019) Overview of transport infrastructure expenditures and costs. Publications Office of the European Union. doi: <https://doi.org/10.2832/853267>
2. Occhiuzzi A, Consiglio Nazionale delle Ricerche. <https://www.cnr.it/it/nota-stampa/n-8247/direttore-cnr-itc-sul-viadotto-morandi-di-genova>
3. Limongelli MP, Chatzi E, Döhler M, Lombaert G, Reynders E (2016) Towards extraction of vibration-based damage indicators. In: 8th European workshop on structural health monitoring (EWSHM 2016)

4. Giordano PF, Limongelli MP (2020) Response-based time-invariant methods for damage localization on a concrete bridge. *Struct Concr* 21(4):1254–1271. <https://doi.org/10.1002/suco.202000013>
5. Giordano PF, Ubertaini F, Cavalagli N, Kita A, Masciotta MG (2020) Four years of structural health monitoring of the San Pietro bell tower in Perugia, Italy: two years before the earthquake versus two years after. *Int J Mason Res Innov* 5(4):445. <https://doi.org/10.1504/IJMRI.2020.111797>
6. Domaneschi M, Limongelli MP, Martinelli L (2012) Damage detection in a suspension bridge model using the interpolation damage detection method, bridge maintenance, safety, management, resilience and sustainability. In: *Proceedings of the 6th international conference on bridge maintenance, safety and management*, pp 2975–2980. <https://doi.org/10.1201/b12352-452>
7. Ferretti A, Fumagalli A, Novali F, Prati C, Rocca F, Rucci A (2011) A new algorithm for processing interferometric data-stacks: SqueeSAR. <https://doi.org/10.1109/TGRS.2011.2124465>
8. Hooper A, Segall P, Zebker H (2007) Persistent scatterer interferometric synthetic aperture radar for crustal deformation analysis, with application to Volcán Alcedo, Galápagos. *J Geophys Res Solid Earth* 112(7):1–21. <https://doi.org/10.1029/2006JB004763>
9. Barla G, Tamburini A, Del Conte S, Giannico C (2016) InSAR monitoring of tunnel induced ground movements. *Geomech Tunn* 9(1):15–22. <https://doi.org/10.1002/geot.201500052>
10. Bischoff CA, Ferretti A, Novali F, Uttini A, Giannico C, Meloni F (2020) Nationwide deformation monitoring with SqueeSAR[®] using sentinel-1 data. *Proc Int Assoc Hydrol Sci* 382:31–37. <https://doi.org/10.5194/piahs-382-31-2020>
11. Hoppe EJ et al (2019) Deformation monitoring of posttensioned bridges using high-resolution satellite remote sensing. *J Bridg Eng*. [https://doi.org/10.1061/\(asce\)be.1943-5592.0001479](https://doi.org/10.1061/(asce)be.1943-5592.0001479)
12. Sousa JJ, Bastos L (2013) Multi-temporal SAR interferometry reveals acceleration of bridge sinking before collapse. *Nat Hazards Earth Syst Sci* 13(3):659–667. <https://doi.org/10.5194/nhess-13-659-2013>
13. Selvakumaran S, Plank S, Geiß C, Rossi C, Middleton C (2018) Remote monitoring to predict bridge scour failure using Interferometric Synthetic Aperture Radar (InSAR) stacking techniques. *Int J Appl Earth Obs Geoinf* 73:463–470. <https://doi.org/10.1016/j.jag.2018.07.004>
14. Milillo P, Giardina G, Perissin D, Milillo G, Coletta A, Terranova C (2019) Pre-collapse space geodetic observations of critical infrastructure: the Morandi Bridge, Genoa, Italy. *Remote Sens* 11(12):1403. <https://doi.org/10.3390/rs11121403>
15. Lanari R et al (2020) Comment on ‘pre-collapse space geodetic observations of critical infrastructure: the Morandi Bridge, Genoa, Italy’ by Milillo et al (2019). *Remote Sens*. <https://doi.org/10.3390/rs12244011>
16. Pigorini A, Ricci M, Sciotti A (2010) La tecnica PSInSAR TM di telerilevamento satellitare applicata al progetto ed alla realizzazione delle infrastrutture ferroviarie Satellite remote-sensing PSInSAR TM technique applied to design and construction of railway infrastructures 2:729–757
17. Koudogbo F, Urdiroz A, Robles JG, Chapron G (2019) Radar interferometry as an innovative solution for monitoring the construction of the Grand Paris Express metro network—first results. *Insa Pap Altamira*
18. Fornaro G, Reale D, Verde S (2013) Bridge thermal dilation monitoring with millimeter sensitivity via multidimensional SAR imaging. *IEEE Geosci Remote Sens Lett* 10(4):677–681. <https://doi.org/10.1109/LGRS.2012.2218214>
19. Lazecky M, Hlavacova I, Bakon M, Sousa JJ, Perissin D, Patricio G (2017) Bridge displacements monitoring using space-borne X-band SAR interferometry. *IEEE J Sel Top Appl Earth Obs Remote Sens* 10(1):205–210. <https://doi.org/10.1109/JSTARS.2016.2587778>
20. Huang Q, Crosetto M, Monserrat O, Crippa B (2017) Displacement monitoring and modelling of a high-speed railway bridge using C-band Sentinel-1 data. *ISPRS J Photogramm Remote Sens* 128:204–211. <https://doi.org/10.1016/j.isprsjprs.2017.03.016>
21. Zhang L, Sun Q, Hu J (2018) Potential of TCPIInSAR in monitoring linear infrastructure with a small dataset of SAR images: application of the Donghai Bridge, China. *Appl Sci* 8(3). <https://doi.org/10.3390/app8030425>

22. Del Soldato M, Tomás R, Pont J, Herrera G, Lopez-Davalillos JCG, Mora O (2016) A multi-sensor approach for monitoring a road bridge in the Valencia harbor (SE Spain) by SAR interferometry (InSAR). *Rend Online Soc Geol Ital* 41:235–238. <https://doi.org/10.3301/ROL.2016.137>
23. Huang Q et al (2018) Displacement monitoring and health evaluation of two bridges using sentinel-1 SAR images. *Remote Sens* 10(11):1714. <https://doi.org/10.3390/rs10111714>
24. Tomás R et al (2013) Monitoring an earthfill dam using differential SAR interferometry: La Pedrera dam, Alicante, Spain. *Eng Geol* 157:21–32. <https://doi.org/10.1016/j.enggeo.2013.01.022>
25. Zhou W, Li S, Zhou Z, Chang X (2016) Remote Sensing of deformation of a high concrete-faced Rockfill Dam using InSAR: a study of the Shuibuya Dam, China. *Remote Sens* 8(3):255. <https://doi.org/10.3390/rs8030255>
26. Di Martire D et al (2014) Comparison between Differential SAR interferometry and ground measurements data in the displacement monitoring of the earth-dam of Conza della Campania (Italy). *Remote Sens Environ*. <https://doi.org/10.1016/j.rse.2014.03.014>
27. Arangio S, Calò F, Di Mauro M, Bonano M, Marsella M, Manunta M (2014) An application of the SBAS-DInSAR technique for the assessment of structural damage in the city of Rome. *Struct Infrastruct Eng* 10(11):1469–1483. <https://doi.org/10.1080/15732479.2013.833949>
28. Cavalagli N, Kita A, Falco S, Trillo F, Costantini M, Ubertini F (2019) Satellite radar interferometry and in-situ measurements for static monitoring of historical monuments: the case of Gubbio, Italy. *Remote Sens Environ* 235:111453. <https://doi.org/10.1016/j.rse.2019.111453>
29. Cusson D, Trischuk K, Hébert D, Hewus G, Gara M, Ghuman P (2018) Satellite-based InSAR monitoring of highway bridges: validation case study on the north channel bridge in ontario, Canada. *Transp Res Rec J Transp Res Board* 2672(45):76–86. <https://doi.org/10.1177/0361198118795013>
30. Ferretti A, Prati C, Rocca F (2001) Permanent scatterers in SAR interferometry. *IEEE Trans Geosci Remote Sens*. <https://doi.org/10.1109/36.898661>
31. Blasco JMD, Fomelis M, Stewart C, Hooper A (2019) Measuring urban subsidence in the Rome metropolitan area (Italy) with sentinel-1 SNAP-StaMPS persistent scatterer interferometry. *Remote Sens*. <https://doi.org/10.3390/rs11020129>
32. QGIS (2020). <https://www.qgis.org/it/site/>
33. Geoportale Regione Lombardia. <http://www.geoportale.regione.lombardia.it/>
34. ARPA Lombardia. https://www.arpalombardia.it/Pages/ARPA_Home_Page.aspx
35. Pearson K (1895) VII. Note on regression and inheritance in the case of two parents. *Proc R Soc Lond* 58(347–352):240–242. <https://doi.org/10.1098/rspl.1895.0041>

Expeditious Dynamic Tests for the Estimation of Infill Masonry Wall Stiffness



Vanni Nicoletti, Davide Arezzo, Sandro Carbonari, and Fabrizio Gara

Abstract The importance of assessing the overall behaviour of buildings considering the contribution of non-structural infills has been nowadays widely recognised. Indeed, infills can trigger fragile mechanisms of structural members preventing the evolution of dissipative mechanisms and can play an important role in the verifications at damageability limit states, especially in the case of strategic structures for which often high performance levels are required, including the full operativity (i.e. absence of damage to both structural and non-structural members) after severe earthquakes, in order to guarantee the building occupancy during the emergency management. With reference to a case study, the paper presents a simplified approach for estimating the stiffness of masonry infill walls through expeditious dynamic impact tests on infills. The case study is constituted by a laboratory real-scale mock-up for which a complete dynamic identification is carried out before and after the realization of infill masonry walls. The adopted procedure is then validated through results from a refined finite element model of the mock-up in which infills are modelled adopting stiffnesses obtained from the proposed approach.

Keywords Impact load tests · Ambient vibration tests · Experimental modal analysis · Operational modal analysis · Infill masonry wall stiffness · Model updating

V. Nicoletti (✉) · D. Arezzo · S. Carbonari · F. Gara
Department ICEA, Università Politecnica Delle Marche, Ancona, Italy
e-mail: v.nicoletti@pm.univpm.it

D. Arezzo
e-mail: d.arezzo@pm.univpm.it

S. Carbonari
e-mail: s.carbonari@univpm.it

F. Gara
e-mail: f.gara@univpm.it

1 Introduction

The role of infill masonry walls in characterizing the dynamic behavior of buildings is nowadays widely recognized by the overall scientific and technical communities. Indeed, both the stiffness and strength of infill non-structural elements may significantly affect the global behavior of buildings and must be considered in numerical models for the design or assessment of infilled frame structures, especially in earthquake prone areas [1–4]. Furthermore, when results of dynamic tests have to be interpreted, it becomes crucial to reproduce the real behavior of buildings through refined numerical models and this requires infills to be included in the modelling. Such refined models can also be useful to design and develop Structural Health Monitoring (SHM) systems that can be used as important support to control the status of the building during its life, with particular interest after seismic events [5–8].

Many researchers studied the in-plane and out-of-plane behavior of infills subjected to static and cyclic loads with the target of providing drift capacity models but only few works focused on the investigation of the infill dynamic properties [9, 10].

In this paper, a procedure based on experimental dynamic tests and finite element modelling is adopted to estimate an equivalent elastic modulus for the infill masonry walls of a real-scale laboratory mock-up. The combined experimental and numerical procedure requires the execution of Impact Load Tests (ILTs) on the wall that has to be investigated, and through which the infill out-of-plane modal parameters are identified, and the wall finite element modelling for the elastic modulus calibration. The reliability of the adopted procedure is assessed through the comparison between numerical and experimental modal parameters of the whole structure, which is derived from dynamic tests on the whole structure.

2 The Laboratory Mock-up

The laboratory mock-up displayed in Fig. 1 is a steel-concrete composite structure composed by a one-storey two-bay moment-resisting frame with height of 3.00 m and span length of 4.20 m. The composite deck is obtained with 0.12 m thick r.c. slab casted on a collaborating steel sheet, connected to beams by means of Nelson studs. To simulate the presence of non-structural and imposed loads, 9 concrete blocks are added over the slab. Two light infill masonry walls (IMW1 and IMW2) with thickness of 6 cm are built filling only one bay for each longitudinal frame. The hollow clay bricks adopted have dimensions of 0.25 x 0.25 x 0.06 m. More details about the case study and the infill properties can be found in [11].

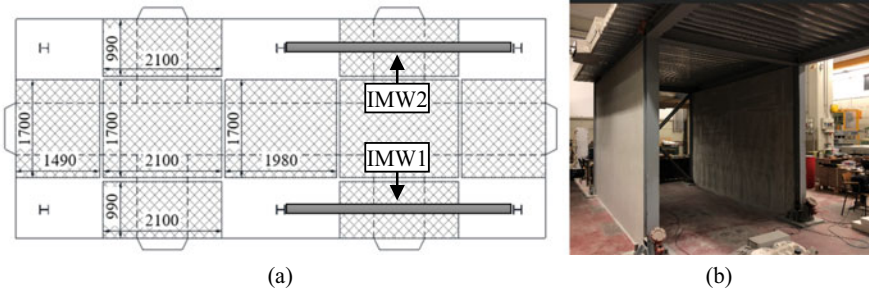


Fig. 1 Laboratory mock-up: **a** plan scheme with added masses and infills, **b** picture after infill construction

3 The Experimentation

Two types of dynamic tests are performed in order to identify both the infill out-of-plane and the mock-up modal parameters. Tests are carried out in three crucial stages of the mock-up construction: (i) bare frame, (ii) mock-up with infills before the plaster and (iii) after the plaster realization.

For the infill dynamic investigation, ILTs are performed on the two mock-up walls; tests consist in exciting the panels with hammer blows applied in the direction orthogonal to the wall plane, and in recording the time histories of the impulses and those of the accelerations produced in the same direction. Impulses are provided in a set of points on the panel; spatial resolution of the points depends on the desired accuracy in reproducing the infill mode shapes. For this reason, the masonry panels are divided with grids of 25 points (Fig. 2a) and 2 uniaxial shear piezoelectric accelerometers (S1 and S2) for each panel are placed in different grid points. Two sensors in different positions are employed instead of one in order to identify with redundancy a significant number of modes, and, moreover, to allow the identification of also those modes that have null value of the modal displacement in proximity of one of the two sensors. Hence, preliminary tests were performed to evaluate the best sensor

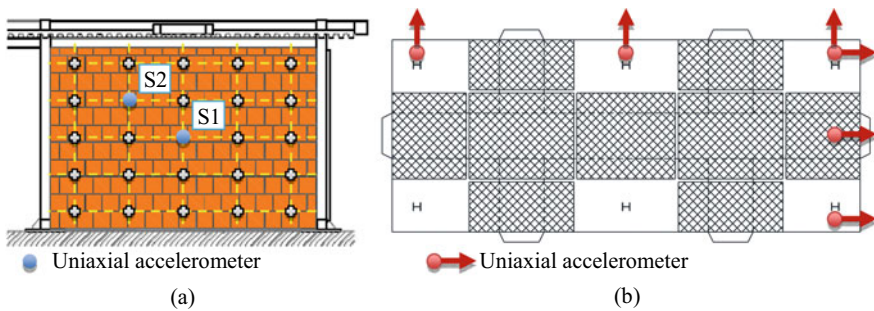


Fig. 2 Dynamic test layouts: **a** ILTs, **b** AVTs

Table 1 Identified natural frequencies for both tested infills without and with plaster

Mode name	Frequency values [Hz]			
	IMW1		IMW2	
	No plaster	Yes plaster	No plaster	Yes plaster
1,1	16.80	17.30	17.90	18.10
2,1	27.47	31.60	29.53	32.15
1,2	40.10	49.00	48.00	49.97
3,1	46.55	49.40	45.35	50.50
2,2	57.54	63.88	59.20	64.50
4,1	63.07	66.50	66.85	68.10
5,1	76.85	120.71	78.93	119.90
3,2	79.79	85.98	76.10	82.67
2,3	/	105.30	/	107.13
4,2	104.98	113.75	104.40	127.30
3,3	117.77	131.19	119.40	133.20
5,2	132.28	143.93	139.10	155.90
5,3	177.60	198.85	175.24	212.50

placement to better capture the first modes of the infills. All the tests were carried out at a nearly constant temperature so that no influence of it on the results is expected [12].

The out-of-plane modal parameters of the walls (natural frequencies and relevant mode shapes) are identified through the “Line-Fit” algorithm [13], which is a S-dof methodology working in the frequency domain. In Table 1 the identified resonant frequency values for both walls without and with plaster, are listed. Each vibration mode is named with a couple of number (n,m) which represent the number of semi-waves present in the mode shape along the horizontal and vertical directions, respectively. The mode 2,3 is not found for non-plastered walls. By comparing frequency values obtained without and with the plaster, a general increase emerges in the range between 2 and 22% (with a mean value of about 14%), excepting for mode 5,1, for which an increase of about 60% is observed. In Fig. 3 the mode shapes inherent to all the identified vibration modes of IMW1 with plaster are shown; those relevant to IMW2 are qualitatively the same and are not reported for the sake of brevity.

Together with ILTs on infills, also ILTs and Ambient Vibration Tests (AVTs) on the mock-up are carried out to identify the global dynamic behavior of the structure. Six uniaxial piezoelectric accelerometers are deployed over the composite slab, three measuring in transverse and other three in longitudinal direction (Fig. 2b). This high number of sensors allows the identification of the overall dynamic behavior of the frame, including possible in-plane floor deflections due to the aspect ratio of the floor (characterized by a slender rectangular shape).

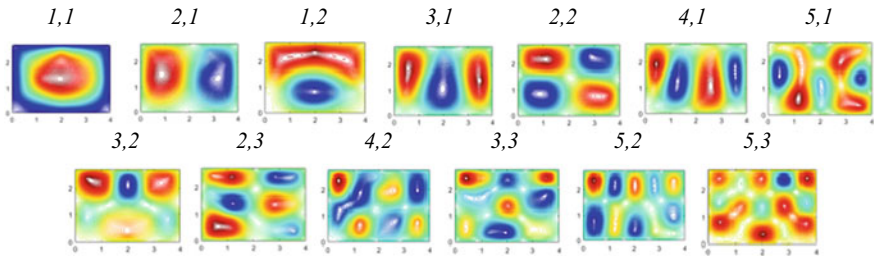


Fig. 3 Identified mode shapes after plastering for IMW1

For the ILTs, the input is given through hammer blows provided in a corner of the composite slab (to excite both translational and torsional modes), while for AVTs the input is provided by the surrounding environment (ambient vibration). To identify the structure modal parameters, the Numerical algorithm for Subspace State Space System Identification (N4SID) [14] input-output technique and the Covariance-driven Stochastic Subspace Identification (SSI-COV) [15] output-only technique are adopted, starting from impact and ambient vibration measurements, respectively. The identified natural frequencies for all the considered construction stages are reported in Table 2, while the relevant mode shapes are shown in Fig. 4. It can be observed that the transverse vibration mode of the mock-up remains almost the same after the infill

Table 2 Mock-up experimental natural frequencies at different construction stages

Mode	Mode type	Frequency values [Hz]					
		Bare frame		Frame+infill (no plaster)		Frame+infill (with plaster)	
		SSI	N4SID	SSI	N4SID	SSI	N4SID
1	Longitudinal	2.95	2.95	16.32	16.38	17.69	17.63
2	Transverse	8.42	8.42	8.40	8.41	8.37	8.38
3	Rotational	11.62	11.60	12.72	12.77	13.39	13.38

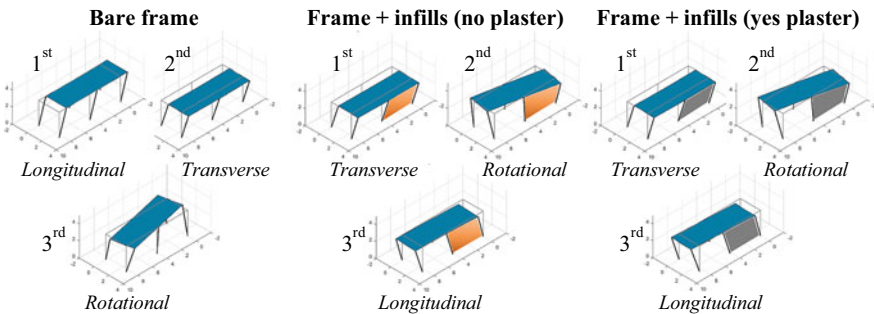


Fig. 4 Mock-up mode shapes during the construction

construction and after plastering, both in terms of frequency and mode shape since, as expected, the infill stiffness contribution in the transverse direction is negligible. Moreover, it can be noted a decreasing trend in the frequency values after the infills construction, probably due to the mass increase. On the contrary, resonant frequency values of the longitudinal and rotational modes sensibly increase.

4 Infill Elastic Moduli Estimation

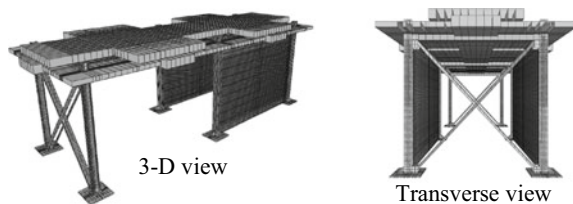
Starting from results of above tests the following issue is considered: determining the infill stiffness to be used in the finite element modelling of the mock-up able to provide the modal experimental parameters of the whole infilled structure.

Despite masonry infills are generally characterized by an orthotropic behavior, the adopted strategy stems from the idea that the dynamic behavior of infills subjected to low input excitations can be well captured through homogenous isotropic elastic thin plates. The term equivalent incorporates the aforementioned simplified assumptions, as well as a geometric issue relevant to numerical modelling practices; indeed, the estimated moduli define the material of the elements that are used to fill-in the bare structure, neglecting thicknesses of structural elements. This aspect is better addressed in [11] with reference to a real infilled building application.

The procedure starts modelling the infills within a refined mock-up finite element model (Fig. 5) preliminarily calibrated on the basis of the AVTs and ILTs results on the bare frame. The mock-up finite element model is developed with a commercial software [16] where shell elements are used for all the structural members. The shear connection between the steel beams and the composite slab is modelled with elastic links of suitable stiffness. The infills are modelled with shell elements with their real thickness and assuming as mass density an estimation based on the adopted construction materials. The Poisson's coefficient is assumed to be constant and equal to 0.25 [17]. Whereupon, a tentative elastic modulus E_0 for the masonry panel is estimated through the closed-form expression (1) [18] for clamped rectangular plates based on the fundamental frequency of the wall $f_{1,exp}$, the plate mass per unit area ρ , the plate thickness t , the Poisson's coefficient ν and the plate geometric dimensions (a and b).

The terms m and n are the numbers of $\frac{1}{2}$ waves in the mode shapes in the two principal directions, while Δm and Δn are the so-called "edge effect factors" that

Fig. 5 Mock-up refined finite element model



can be expressed as a function of the mode number and the plate dimensions; details are available in [11].

$$E_0 = \frac{48(1 - \nu^2)}{\pi^2 t^2} f_{1,exp}^2 \left[\left(\frac{m + \Delta m}{a} \right)^2 + \left(\frac{n + \Delta n}{b} \right)^2 \right]^{-2} \tag{1}$$

Then, resonant frequencies and mode shapes that characterize the out-of-plane response of the investigated infills are determined numerically through eigenvalue analyses and the equivalent elastic modulus E of the infills is iteratively adjusted in order to minimize differences between the experimental and numerical modal parameters of the infills. Focusing on both frequency values and mode shapes, the following convergence criteria are considered:

$$\frac{\sum_{i=1}^N \frac{1}{i} \left| \frac{f_{i,exp} - f_{i,num}}{f_{i,exp}} \right|}{\sum_{i=1}^N 1/i} \leq \delta_f \tag{2a}$$

$$1 - \frac{\sum_{i=1}^N \frac{MAC_i}{i}}{\sum_{i=1}^N 1/i} \leq \delta_s \tag{2b}$$

where $f_{i,exp}$ and $f_{i,num}$ are the experimental and numerical values of the i -th frequency and MAC_i is the Modal Assurance Criterion index [19]; N is the number of vibration modes on which the calibration is based while δ_f and δ_s are the admissible percentage errors in the comparisons of frequencies (f) and mode shapes (s); in this work, $\delta_f = 5\%$ and $\delta_s = 25\%$ are assumed. The latter is deemed to be good to capture the correct mode shape, considering local differences between numerical and experimental data at the measuring points due to the intrinsic inhomogeneity of the real wall. The iterative procedure stops when both convergence criteria (Eq. (2a) and (2b)) are satisfied. An automated approach is adopted in this work.

The procedure is performed twice considering the wall without and with plaster and the relevant estimated elastic moduli E for each panel are reported in Table 3. The four elastic modulus values are around 5000 MPa, which is a reasonable value for this infill typology, as reported in [20], where values from 2500 to 10,000 MPa are found.

To verify the reliability of the wall stiffness estimation and the modelling effectiveness on the overall structural dynamic response, the numerical modal parameters of the whole structure are compared with the experimental ones. Here, for brevity,

Table 3 Estimated elastic moduli E for both walls IMW1 and IMW2

Wall	Elastic modulus [MPa]	
	No plaster	Yes plaster
IMW1	4700	4900
IMW2	5340	5360

Table 4 Comparison between experimental and numerical mock-up natural frequencies

Mode	Mode typology	Frequency values [Hz]					
		Bare frame		Frame+infill without plaster		Frame+infill with plaster	
		OMA	NUM	OMA	NUM	OMA	NUM
1	Longitudinal	2.95	2.96	16.32	16.38	17.69	17.71
2	Transverse	8.42	8.40	8.40	8.40	8.37	8.38
3	Rotational	11.62	11.67	12.72	12.94	13.39	13.08

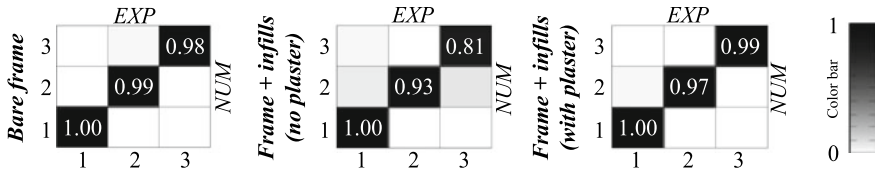


Fig. 6 MAC indexes between experimental and numerical mock-up mode shapes

only the AVTs results are considered, since those relevant to ILTs are almost the same.

The comparison in terms of frequency values is reported in Table 4, while those relevant to the mode shapes, in terms of MAC indexes, are displayed in Fig. 6.

A very good agreement between experimental and numerical results is observed for both frequencies and mode shapes, proving that the infill stiffness estimation is realistic, and the proposed procedure is reliable.

5 Conclusions

Starting from a wide set of data of experimental dynamic tests on a laboratory real-scale infilled mock-up, an approach to estimate the infill masonry wall stiffness has been presented in this paper. The adopted approach furnishes a practical and expeditious tool which can be suitably used to reduce uncertainties in the finite element modelling of framed buildings when infills must be included. This is fundamental when the results of ambient vibration measurements have to be interpreted with a refined finite element model of the structure and when these models are used as a support for the structural health monitoring development or for the design of seismic retrofitting systems and devices. The adopted procedure has the advantage of requiring fast and non-invasive dynamic tests on infills; thus, it can be executed in new or existing buildings. The procedure revealed effective for estimating the stiffness of infills for the investigated case study and led to the development of a numerical model able to predict resonance frequencies and mode shapes with good accuracy.

References

1. Di Trapani F, Shing PB, Cavaleri L (2018) Macroelement model for in-plane and out-of-plane responses of masonry infills in frame structures. *J Struct Eng* 144(2):1–13
2. Gioiella L, Tubaldi E, Gara F, Dezi L, Dall'Asta A (2018) Modal properties and seismic behaviour of buildings equipped with external dissipative pinned rocking braced frames. *Eng Struct* 172:807–819
3. Astroza R, Ebrahimian H, Conte JP, Restrepo JI, Hutchinson TC (2016) Influence of the construction process and nonstructural components on the modal properties of a five-story building. *Earthquake Eng Struct Dyn* 45(7):1063–1084
4. Penna A, Morandi P, Rota M, Manzini C, Porto F, Magenes G (2014) Performance of masonry buildings during the Emilia 2012 earthquake. *Bull Earthquake Eng* 12(5):2255–2273
5. Gara F, Carbonari S, Roia D, Balducci A, Dezi L (2021) Seismic retrofit assessment of a school building through operational modal analysis and f.e. modeling. *J Struct Eng* 147(1):04020302
6. Garcia-Macias E, Ubertini F (2020) MOVA/MOSS: two integrated software solutions for comprehensive structural health monitoring of structures. *Mech Syst Sign Proc* 143
7. Erazo K, Moaveni B, Nagarajaiah S (2019) Bayesian seismic strong-motion response and damage estimation with application to a full-scale seven story shear wall structure. *Eng Struct* 186:146–160
8. Rainieri C, Magalhaes F, Ubertini F (2019) Automated operational modal analysis and its applications in structural health monitoring. *Shock and Vibration* 2019
9. Furtado A, Rodrigues H, Arede A, Varum H (2017) Modal identification of infill masonry walls with different characteristics. *Eng Struct* 145:118–134
10. De Angelis A, Pecce MR (2018) Out-of-plane structural identification of a masonry infill wall inside beam-column RC frame. *Eng Struct* 173:546–558
11. Nicoletti V, Arezzo D, Carbonari S, Gara F (2020) Expeditious methodology for the estimation of infill masonry wall stiffness through in-situ dynamic tests. *Constr Build Mater* 262:
12. Regni M, Arezzo D, Carbonari S, Gara F, Zonta D (2018) Effect of environmental conditions on the modal response of a 10-Story reinforced concrete tower. *Shock. Vib.* 9476146
13. Kouroussis G, Ben Fekih L, Conti C, Verlinden O (2012) EasyMode: a MatLab/SciLab toolbox for teaching modal analysis. In: *Proceedings of the 19th international congress on sound and vibration*, Vilnius, Lithuania
14. Juang J (1994) *Applied system identification*. Prentice-Hall Englewood Cliffs, New Jersey, USA
15. Van Overschee P, De Moor B (1996) *Subspace identification for linear systems: theory–implementation–applications*. Kluwer Academic Publishers, Dordrecht, The Netherlands
16. SAP2000 advanced (v20.2) (2018) *Static and dynamic finite element analysis of structures*, Berkeley, CSI Computer & Structures, Inc.
17. EN1996-2 (2006) *Eurocode 6: design of masonry structures—Part 2: design consideration, selection of materials and execution of masonry*. European Community for Standardization, Brussels
18. Mitchell AK, Hazell CR (1986) A simple frequency formula for clamped rectangular plates. *J Sound Vibr* 118(2):271–281
19. Allemang RJ, Brown DL (1982) A correlation coefficient for modal vector analysis. In: *Proceedings of the 1st international modal analysis conferences* Bethel, CT, USA, pp 110–15
20. Frumento S, Magenes G, Morandi P, Calvi GM (2009) Interpretation of experimental shear tests on clay brick masonry walls and evaluation of q-factors for seismic design. *Research report EUCENTRE 2009/02*, EUCENTRE and University of Pavia, Pavia

Field Evaluation of Sensing Sheet Prototype Exposed to Cracking



Vivek Kumar , Levent E. Aygun, Matthew Gerber, Campbell Weaver, Sigurd Wagner, Naveen Verma, James C. Sturm, and Branko Glisic

Abstract Reliable crack detection and characterization is challenging. Sparsely spaced discrete strain sensors are insensitive to cracks if placed at even modest distances from damage. Improving spatial density of sensors significantly improves reliability in crack detection and characterization, but also significantly increases the costs associated with hardware, sensor installation, and data analysis and management. In the case of very large structures, one-dimensional distributed fiber optic sensors can be applied with reasonable costs, and while they significantly improve reliability in crack detection and characterization, they still cover only one dimension of a structure. In order to address the above challenges, two-dimensional sensor, called sensing sheet, have been developed. It consists of dense array of discrete sensors patterned over thin-film substrate, with integrated computational and power management circuits. The aim of this paper is to present field test performed on the sensing part of sensing sheet and evaluate its performance in crack detection and characterization in real-life settings. Two prototypes of sensing sheet were manufactured and tested. Each of them consisted of eight discrete full-bridge resistive strain sensors. One prototype was installed on the underside of the superstructure of a deck stiffened arch and the other over existing shrinkage cracks on the foundation of Streicker Bridge. The behavior of the sensors was observed under daily temperature change. The test confirmed applicability of sensing sheet in real-life settings and its excellent performance in crack detection and characterization.

Keywords Crack monitoring · Sensing sheet · 2D Quasi-distributed sensor · Full-bridge strain sensor · Prestressed concrete bridge

1 Introduction

The aging infrastructure of United States is in dire need of improvement interventions. The ASCE in its 2017 report card grades the current infrastructure at D+ with an

V. Kumar (✉) · L. E. Aygun · M. Gerber · C. Weaver · S. Wagner · N. Verma · J. C. Sturm · B. Glisic

Princeton University, Princeton, NJ 08544, USA

e-mail: vivekk@princeton.edu

© The Author(s), under exclusive license to Springer Nature Switzerland AG 2021
C. Rainieri et al. (eds.), *Civil Structural Health Monitoring*, Lecture Notes in Civil Engineering 156, https://doi.org/10.1007/978-3-030-74258-4_62

967

expected requirement of \$4.6 trillion in repairs and maintenance [1]. The bridges though graded slightly better at C+ are still in critical condition. According to the same report, around 188 million trips are made on structurally deficient bridges. Structural Health Monitoring (SHM) provides a cost-effective option for extending the useful life of structures through real-time information about the structure's performance [2, 3]. This information can be used for condition monitoring of the structure and timely intervention. Condition monitoring reduces the life-cycle cost of the structure, making it possible to redirect the resources to more critical projects [4–6].

Damage to the structure results in the changes in local and global parameters such as strain, acceleration and natural frequency, just to name a few. An SHM system monitors these parameters and detects changes. These changes are used as indicators for identifying damage [7] through data analysis. However, the capability of a sensing system to identify these changes depend on the density of the sensors on the structure. Changes in environmental conditions such as temperature and humidity could result in large variation of these parameters over days and months, and these effects need to be removed while identifying damage. In the case of strain sensing, it has been shown that sparsely placed sensors cannot detect damage more than a meter away from the sensor locations due to low signal-to-noise ratio (SNR) [8]. Even though one-dimensional distributed fiber-optic sensors have been installed at reasonable cost to identify damage over civil structures, they still cover only one-dimension of these structures. In the last ten-fifteen years there has been an increased focus on design and development of two-dimensional sensors for improved spatial coverage to obtain two-dimensional information about the structure. A variety of sensors such as carbon-nanotube based [9, 10], piezoelectric based [11], and soft-elastomeric capacitance based [12, 13], have shown promise for such applications. Researchers at Princeton University have developed a novel thin-film dense array of resistive strain sensors for damage detection and localization [14] called "Sensing Sheet". These sensing sheets are based on the principles of large area electronics (LAE) and enable sensor-to-sensor communication through CMOS ICS. Previous works have demonstrated capabilities of (i) Communication [15], (ii) AI-enabled intelligent spaces [16, 17], (iii) Static and dynamic strain measurements [18, 19] and (iv) fatigue measurement [20]. The Sensing Sheet has the potential to be low cost (~\$100 per m²) solution for two-dimensional monitoring of the structure. All the above works show promise for damage detection but have yet to be characterized for the same. This work addresses the question of performance of these upcoming technologies for real-life applications to civil structures and characterization of two-dimensional sensors exposed to cracking.

In a recent published work [21], the authors demonstrated the capability of the sensing sheet to (i) measure the strain changes on a real-life bridge (ii) measure the crack opening and closing in a pre-existing shrinkage crack due to diurnal thermal changes. The work addresses the issue of scalability of the sensing systems to the size of civil structures. In this paper, we present those results of real-life application of two-dimensional sensors.

2 Methodology

To demonstrate the damage detection and localization potential of sensing sheet two real-life tests were conducted. In this section, a brief detail of the working of the sensing sheet prototype is presented. This is followed by the description of the two-field experiments conducted to establish the strain measurement, and damage detection and localization capability of the sensing sheet.

2.1 Sensing Sheet Prototype

Sensing Sheet prototype consists of a flexible substrate on which 8 sensing elements are fabricated. The 2D prototype used in the experiments measures $19.6\text{ cm} \times 7.8\text{ cm}$ and were manufactured by a commercial PCB manufacturer [22]. The prototype and the three layers comprising Sensing Sheet are shown in Fig. 1.

Each sensing element is a full-bridge resistive strain gauge, i.e., it consists of four resistors forming Wheatstone bridge, as shown in Fig. 2.

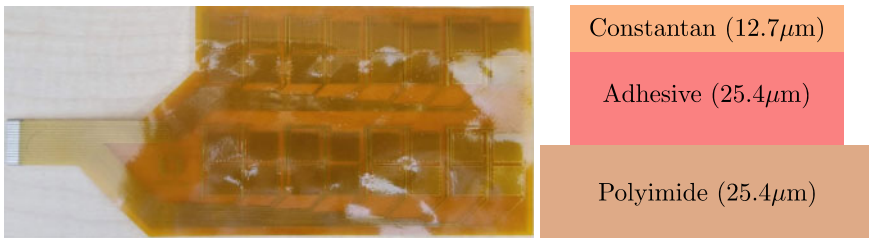


Fig. 1 Left: the sensing sheet prototype; right: the three layers of the sensing sheet with dimensions

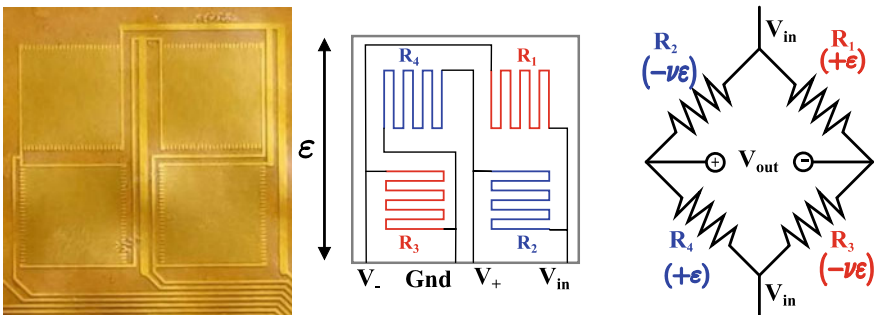


Fig. 2 A view to single sensing element and its schematic (left and middle) and general schematic of Wheatstone bridge (right)

Electrical resistance of metal changes under mechanical strain and for a given gauge factor (GF) [11], the sensitivity to strain of a single resistor is given as:

$$GF = \frac{\Delta R/R}{\Delta L/L} = \frac{\Delta R/R}{\varepsilon} \quad (1)$$

where R is the initial resistance (before strain is applied), L is the initial length of the resistor, ΔR is the change in resistance due to strain ε and ΔL is the change in length of resistor. Wheatstone bridge transforms the strain induced resistance change to a voltage difference which can be measured. The ratio of the output to input voltage, called voltage ratio V_r is given by Eq. 2.

$$V_r = \frac{V_{out}}{V_{in}} = \frac{R_4}{R_4 + R_2} - \frac{R_3}{R_3 + R_1} \quad (2)$$

The sensing system measures this change in voltage ratio to determine in the uniaxial strain using the relation given in Eq. 2, which is derived taking into account that two resistors are oriented in one direction and two others in perpendicular direction (refer [11] for derivations).

$$\varepsilon = \frac{2V_r}{GF[(1 + \nu) - (1 - \nu)V_r]} \quad (3)$$

where ν is Poisson's ration of the metallic traces used in the resistor. It is important to note that a full Wheatstone bridge design was chosen as it automatically provides temperature compensation. In case of a temperature change each of the resistor experiences the same change in resistance and hence V_r is equal to $0V$ (as $\Delta R_1 = \Delta R_2 = \Delta R_3 = \Delta R_4$). This temperature sensitivity was studied in detail by previous work [11]. Further, the orientation of the crack with respect to the resistors can affect the sensitivity of the change in resistance, and bi-directional orientation of resistors in the full-bridge sensing element helps improve the sensitivity to damage [7].

2.2 Real-Life Testing

For the field test of sensing sheet, the pedestrian bridge on Princeton University campus was chosen. Streicker Bridge is located over the Washington Road connecting the east and west side of the campus. The bridge consists of a deck-stiffened arch and y-shaped columns. The testing of the sensing sheet was per-formed at two locations using two different prototypes. The first prototype was glued on the underside of the deck at location P12 as shown in Fig. 3. The strain measured using the sensing sheet was compared with that measured with the embedded fiber-optic sensors (see Fig. 3)

The second prototype was glued over a pre-existing shrinkage crack on the foundation of the bridge. The foundation has two beam elements connected to it, one

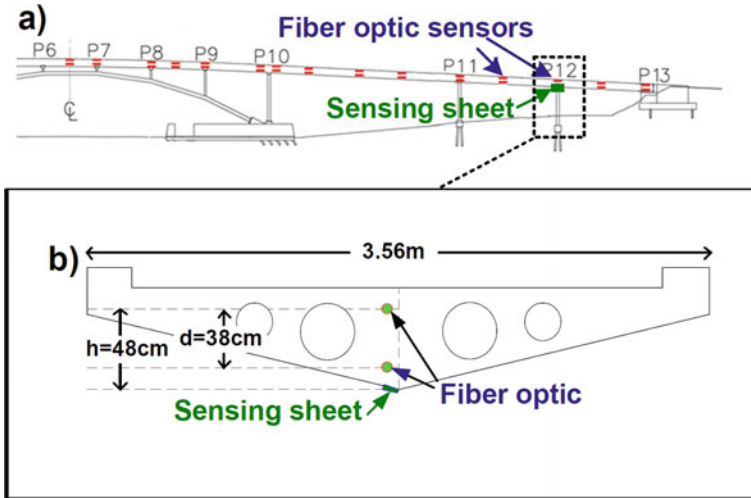


Fig. 3 a View to part of Streicker Bridge equipped with fiber-optic strain sensors and location of sensing sheet prototype for the first field test; b view to cross-section P12 and location of fiber-optic sensors and sensing sheet; adapted from [22]

vertical and one at an angle. The initial crack opening was less than 1 mm (least count of the ruler used), The sensing sheet was glued over the crack in a way that sensors numbered 1–4 do not overlap over the crack and only sensors 5–8 cover the crack (see Fig. 4). The sensors 1–4 hence acted as control group experiencing the same temperature change. Since the size of the cracks could only be influenced by the temperature of the concrete, it was important to have a control group to differentiate the effect of crack opening from the thermal effects.

3 Results

The real-life measurements shown in Figs. 5 and 6 (modified from [22]). Figure 5 shows that extrapolated values of the fiber-optic strain measurements to the surface of the deck compare well with the measurements of the sensing sheet over the five-hour period. Because of a problem in connectors between the sensing sheet and readout circuitry, only six out of eight of the sensors were recorded. Figure 6 shows the results of the crack opening and closing test performed on the pre-existing shrinkage crack. The strain measurements correlate well with the air-temperature after accounting for the lag due to delayed heating or cooling of concrete. The thermal expansion of the concrete resulted in differential movement in the parts of foundation left and right from the crack. The negative sign indicates that the crack was closing with increase of temperature due to thermal expansion of two sides. Based on the previous works [11], the maximum crack closure can be computed as 24 μm . It is interesting to note



Fig. 4 The pre-existing shrinkage crack on the foundation (left), the sensing sheet glued to the crack (center), the setup of field experiment (right)

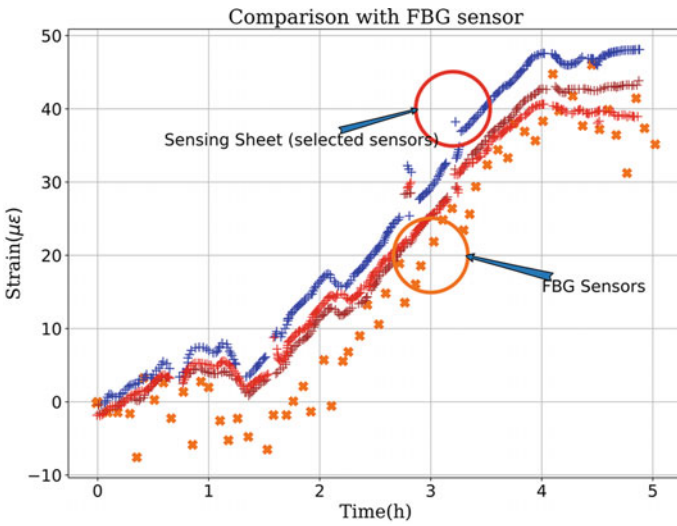


Fig. 5 Comparison of strain measurement using sensing sheet and fiber-optic sensors in the first field test. Adapted from [22]

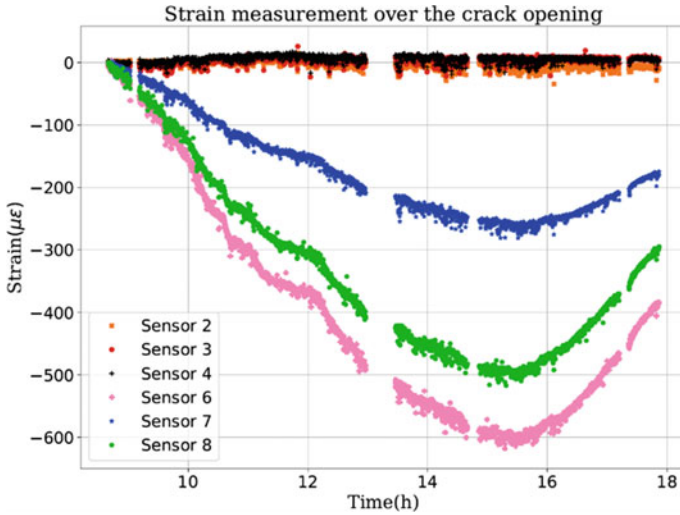


Fig. 6 Strain measurement of 6 sensors over the shrinkage crack in second field test. Adapted from [22]

the difference in strain measured by the sensors 6, 7 and 8. The lower value of strain measured by sensor 7 is attributed to minimal contact of the resistors with the crack. Sensor 8 measures lower value of the strain as it is further down from the top surface. The wedge like crack opening means that the lower locations would measure smaller strain values. This can be intuitively thought of measuring zero opening where the foundation meets the ground and maximum at the top surface. As the temperature decreases in the evening the strain measurements return to their original baseline values. The experiment was ended at the evening due to safety concerns.

4 Conclusion

This paper presented field-tests to evaluate the performance of the sensing sheet exposed to cracking. These tests demonstrate that the crack initiation and growth (referring to crack opening here) can be reliably captured. The dense array of sensors further allows to localize the damage as the sensors away from the crack do not register significant change in strain measurements. The field measurements further validate the sensing sheet capabilities in real-life setting including the automatic temperature compensation. The sensing sheets hence provide a real solution as a two-dimensional sensing system capable of monitoring civil engineering sized structures.

Acknowledgements The authors would like to acknowledge the help of Dr. John Reilly in fiber-optic data acquisition and Gabbie Acot in the field measurements.

Funding

This research was supported in part by Princeton University and in part by the USDOT OST-R UTC Program, grant no. 69A3551847102, enabled through the Center for Advanced Infrastructure and Transportation (CAIT) at Rutgers University (subcontract agreement # 0615).

References

1. ASCE (2017) Infrastructure report card. ASCE Reston, VA
2. Cao W, Liu W, Koh CG, Smith IF (2019) Exploring potential benefits of bridge condition assessment in highway operations. In: IABSE congress 2019 (2019). <http://infoscience.epfl.ch/record/273255>
3. Farrar CR, Worden K (2007) An introduction to structural health monitoring. *Philos Trans Royal Soc A Math Phys Eng Sci* 365(1851):303–315
4. Fu G, Devaraj D (2014) Bridge management using pontis and improved concepts. In: *Bridge engineering handbook*, 2nd edn. CRC Press, pp 233–246. <https://doi.org/10.1201/b16467-10>, <http://www.crcnetbase.com/doi/abs/10.1201/b16467-10>
5. Kim J, Ahn Y, Yeo H (2016) A comparative study of time-based maintenance and condition-based maintenance for optimal choice of maintenance policy. *Struct Infrastruct Eng* 12(12):1525–1536
6. Ni Y, Wong K (2012) Integrating bridge structural health monitoring and condition-based maintenance management. In: 4th International workshop on civil structural health monitoring, pp 6–8
7. Yao Y, Glisic B (2012) Reliable damage detection and localization using direct strain sensing. *Bridge Maintenance, Safety, Management, Resilience and Sustainability* pp, pp 714–721
8. Yao Y, Tung STE, Glisic B (2014) Crack detection and characterization techniques-an overview. *Struct Control Health Monit* 21(12):1387–1413
9. Loh KJ, Hou TC, Lynch JP, Kotov NA (2009) Carbon nanotube sensing skins for spatial strain and impact damage identification. *J Nondestruct Eval* 28(1):9–25. <https://doi.org/10.1007/s10921-009-0043-y>, <https://doi.org/10.1007/s10921-009-0043-y>
10. Loh KJ, Kim J, Lynch JP, Kam NWS, Kotov NA (2007) Multifunctional layer-by-layer carbon nanotube–polyelectrolyte thin films for strain and corrosion sensing. *Smart Mater Struct* 16(2):429
11. Schulz MJ, Sundaresan MJ (2006) Smart sensor system for structural condition monitoring of wind turbines: May 30 2002–April 30 2006. *Nat Renew Energy Lab*
12. Laflamme S, Saleem HS, Vasan BK, Geiger RL, Chen D, Kessler MR, Rajan K (2013) Soft elastomeric capacitor network for strain sensing over large surfaces *IEEE/ASME Trans Mechatron* 18(6):1647–1654
13. Laflamme S, Ubertaini F, Saleem H, D’Alessandro A, Downey A, Ceylan H, Materazzi AL (2014) Dynamic characterization of a soft elastomeric capacitor for structural health monitoring. *J Struct Eng* 141(8):04014186
14. Glisic B, Yao Y, Tung STE, Wagner S, Sturm JC, Verma N (2016) Strain sensing sheets for structural health monitoring based on large-area electronics and integrated circuits. *Proc IEEE* 104(8):1513–1528
15. Sturm J, Mehlman Y, Aygun LE, Wu C, Zheng Z, Kumar P, Wagner S, Verma N (2019) (keynote) machine learning and high-speed circuitry in thin film transistors for sensor interfacing in hybrid large-area electronic systems. *ECS Trans* 92(4):121

16. Ozatay M, Aygun L, Jia H, Kumar P, Mehlman Y, Wu C, Wagner S, Sturm JC, Verma N (2018) Artificial intelligence meets large-scale sensing: using large-area electronics (lae) to enable intelligent spaces. In: 2018 IEEE Custom integrated circuits conference (CICC). IEEE, pp 1–8
17. Verma N, Hu Y, Huang L, Rieutort-Louis WS, Robinson JS, Moy T, Glisic B, Wagner S, Sturm JC (2015) Enabling scalable hybrid systems: Architectures for exploiting large-area electronics in applications. *Proc IEEE* 103(4):690–712
18. Kumar V, Aygun LE, Verma N, Sturm JC, Glisic B (2019) Sensing sheets based on large area electronics for structural health monitoring of bridges. In: *Sensors and smart structures technologies for civil, mechanical, and aerospace systems*, vol 10970. International Society for Optics and Photonics, p 109702G
19. Kumar V, Aygun LE, Verma N, Sturm JC, Glisic B (2019) Static and dynamic strain measurements using sensing sheets for damage detection. In: 20th IABSE congress, New York City 2019: the evolving metropolis. International Association for Bridge and Structural Engineering (IABSE), pp 390–396
20. Yao Y, Glisic B (2015) Detection of steel fatigue cracks with strain sensing sheets based on large area electronics. *Sensors (Basel, Switzerland)* 15(4):8088–8108. <https://doi.org/10.3390/s150408088>
21. Aygun LE, Kumar V, Weaver C, Gerber M, Wagner S, Verma N, Glisic B, Sturm JC (2020) Large-area resistive strain sensing sheet for structural health monitoring. *Sensors* 20(5):1386
22. Q-flex inc. <https://www.qflexinc.com/>. Accessed 21 Dec 2020

Long-Term Vibration Monitoring of the Sultan Ahmet Mosque in Istanbul



Eser Çaktı and Kökcan Dönmez

Abstract The 400-year-old Sultan Ahmet Mosque, aka the Blue Mosque, is one of Istanbul's most prominent historical structures. The primary structural system of the mosque consists of the main dome, four main arches and four semi-domes supporting the main dome; four pendentives, four main pillars and the secondary arches and piers that support the semi-domes. The structural health monitoring system in the Sultan Ahmet Mosque was installed in 2012. It consists of ten three-component accelerometers deployed at four different levels within the structure. Istanbul is in a seismically active region of Turkey. Istanbul shores are at about 20 km to the north of the segments of the North Anatolian Fault within the Marmara Sea. The mosque was damaged during the two M7+ earthquakes in 1766 and also in the M7.0 1894 earthquake. Since the deployment of the structural health monitoring system in October 2012, more than 200 earthquakes with local magnitudes varying from 2.1 to 6.6 have been recorded by the sensors in the structure. This paper is about the time-domain and frequency-domain analyses of this data set with the aim of identifying dynamic response characteristics of the structure, its modal frequencies and their dependence on time, earthquake magnitude and ground motion amplitude.

Keywords Structural health monitoring · Modal analysis · Historical structures · Sultan ahmet mosque

1 Introduction

The Sultan Ahmet Mosque is one of Istanbul's most prominent historical structures (Fig. 1). It is included in the World Heritage List of UNESCO as part of '*Historical*

E. Çaktı (✉) · K. Dönmez
Department of Earthquake Engineering, Kandilli Observatory and Earthquake Research Institute,
Boğaziçi University, Istanbul, Türkiye
e-mail: eser.cakti@boun.edu.tr

K. Dönmez
e-mail: kokcan.donmez@boun.edu.tr



Fig. 1 The general view of the Sultan Ahmet Mosque, June 2006 (Wikimedia Commons)

Areas of Istanbul'. Sultan Ahmet Mosque was constructed between 1609 and 1617 and is the last example of the classical period of Ottoman architecture.

The primary structural system of the mosque is crowned by the main dome, which reaches a height of 43 m and is 23.5 m in diameter. Four main arches, four semi-domes and four pendentives symmetrically support the main dome. Further down, four main pillars, six buttresses, eleven exedra domes, secondary arches and colonnade systems provide support to the upper structure (Fig. 2). The main pillars have a diameter of 5 m each and are surmounted by octagonal and hollow weight towers. The prayer hall's interior can be defined as a nearly square area inside the sidewalls with dimensions of 53.50 m by 49.47 m. In terms of structural materials, all domes are of brick masonry, while the main pillars and arches were built of cut stone [1]. Individual columns are of Marmara marble.

Istanbul is in a seismically active region of Turkey. Its shores are at about 20 km to the north of the segments of the North Anatolian Fault in the Marmara Sea. The mosque, located in Istanbul's historical peninsula, experienced many earthquakes in its history. Among them, three earthquakes are of particular importance: the May 22nd and August 5th earthquakes in 1766 and the July 10th, 1894 earthquake. It is reported that there were several slight cracks in the main dome as a result of two M7+ earthquakes in 1766. The semi-domes, exedra domes, corner domes and the main arches were also damaged. It is impossible to differentiate the damages sustained during these events. Yet it appears that the damages that occurred in the first event were enhanced during the second earthquake [2]. Some parts of the mosque were damaged heavily in the earthquake of 1894. Whereabouts of damages are not detailed

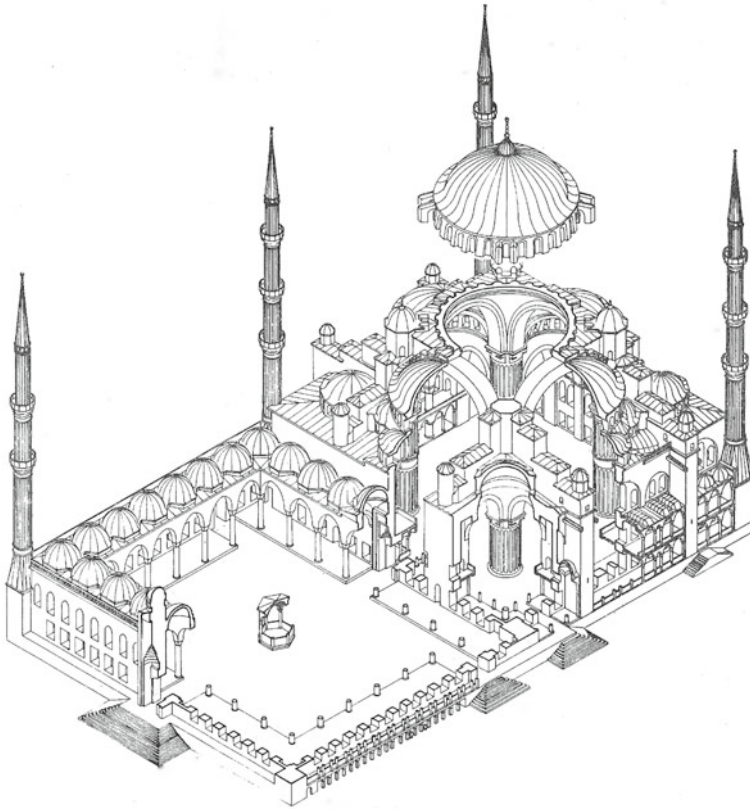


Fig. 2 Axonometric view of the Sultan Ahmet Mosque [1]

but indicated as the prayer hall and the minarets [3]. The last major earthquake in the Marmara region occurred in 1999. There were no reported damages to the mosque related to the M_w 7.4, 1999 Kocaeli event.

The structural health monitoring (SHM) system in the Sultan Ahmet Mosque was installed in October 2012. It collects vibration data continuously and transmits it in real-time to the SHM Laboratory at the Department of Earthquake Engineering of Bogazici University’s Kandilli Observatory and Earthquake Research Institute. The SHM system consists of ten three-component (horizontal: X and Y, vertical: Z) accelerometers (type: Güralp CMG-5TD) deployed at four different levels within the structure (Fig. 3a, b). Starting from the top, there are four sensors at the dome base level (KUB 1/2/3/4). Four others are installed on the catwalk adjacent to the main pillars at their top level (GAL 1/2/3/4). There is one sensor placed at the ground level within the prayer hall near one of the main pillars (MUMA). The last sensor is at the basement that extends along the qibla side of the mosque as can be seen in Fig. 3a (HAMU). The instrument layout was designed to optimally capture the modal shapes and general earthquake response characteristics. The sampling rate was 100 Hz until

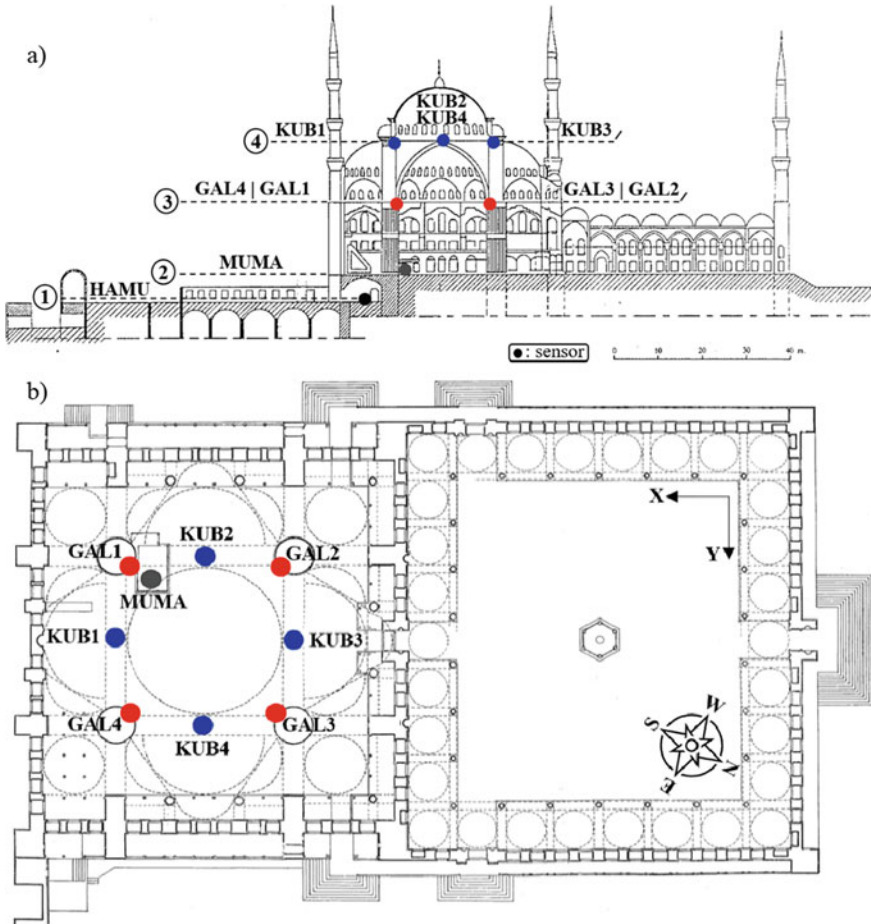


Fig. 3 The sensor layout; a eastern section and b plan view (modified from [1] and [4], respectively)

2014. Since then, it is set at 200 Hz. Since the deployment of the system, more than 200 earthquakes with local magnitudes varying from 2.1 to 6.6 have been recorded. In addition to earthquakes, the system registered three explosions that took place at various locations in Istanbul during the terrorist attacks in 2016.

In this paper, our aim is to provide a uniform analysis of existing data and to present preliminary interpretations of findings. Time-domain and frequency-domain analyses of recordings from earthquakes of the last eight years are conducted. Dynamic response characteristics of the structure, its modal frequencies and their dependence on time, earthquake magnitude and ground motion amplitude are identified and discussed.

2 The Data Set and Data Processing

There are 209 earthquakes recorded by the Sultan Ahmet SHM system from October 2012 to March 2020. All recordings were carefully checked for completeness (i.e., each earthquake in the data set should be recorded by all stations at dome and gallery levels) and for signal-to-noise ratio (5 minimum). The records that did not comply with these criteria were eliminated. There are two earthquakes that occurred in late 2020, which we found important because of their magnitudes and the response levels they have induced in the mosque. The final data set consists of recordings from 103 earthquakes and includes the two events of late 2020.

The map in Fig. 4 shows the location and magnitudes of earthquakes included in our data set. 9% of events are in the magnitude range of 2.0–2.9. The majority of recorded earthquakes are in the magnitude range of 3.0–4.9 (79%), while earthquakes having magnitudes between 5.0 and 5.9 constitute 9% of the data set. The presence of M_L6+ earthquakes is about 4%. From Fig. 4, it is evident that while earthquakes with magnitudes <2.9 are limited to the Marmara Sea, earthquakes <3.9 cover a large elliptical area around it. Furthermore, the majority of earthquakes (67%) took place to the south-west of the structure’s location, meaning they are aligned more or less with its Y-axis (Fig. 3b). About 30% of events originated from the south-east, aligning with the X-axis of the structure.

The records were uniformly baseline corrected to remove the mean and band-pass filtered by fourth-order Butterworth type filters. The low-pass frequency limit was selected as 25 Hz. The high-pass filter limit was record-specific. It was decided by changing the filter limit and visually checking the displacement time histories

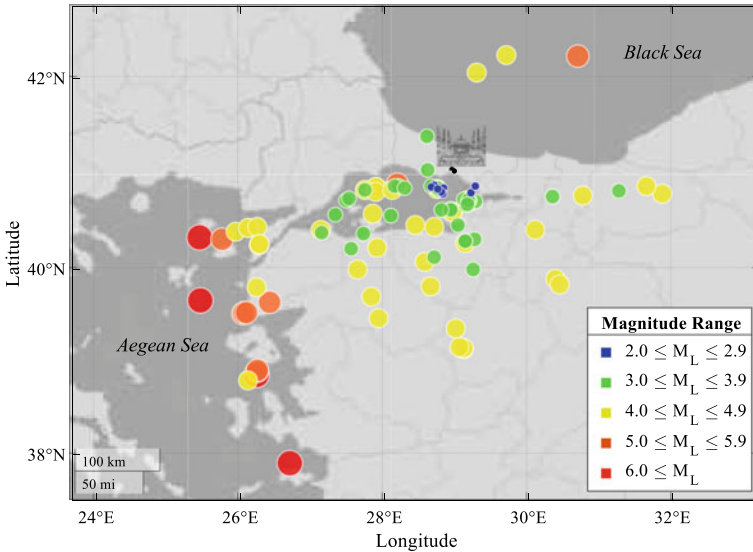


Fig. 4 Locations of earthquakes in the data set

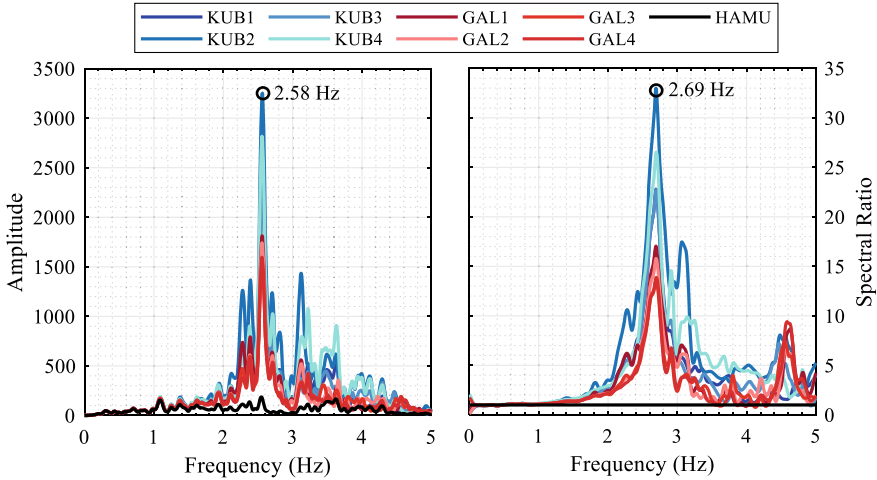


Fig. 5 FAS (left) and TF with respect to station HAMU (right) associated with the M_L 6.2 Aegean Sea earthquake in 2013 (direction: Y; signal duration: 108 s; band-pass filter: 0.1–25 Hz; smoothing window length: 13 (FAS) and 25 (TF))

until there is no residual displacement (it is known that there are no damages to the structure as a result of earthquakes in our data set). The high-pass filter limit varied between 0.1 and 0.5 Hz. Corrected records were analysed in the time domain to obtain maximum absolute acceleration, velocity and displacement values. In the frequency domain, modal frequencies were identified with the help of Fourier amplitude spectra (FAS) and transfer functions (TF) [5]. To ease interpretation, both FAS and TF were smoothed as proposed by Safak [6]. FAS and TF of records from the stations of the system associated with one of the significant earthquakes in our catalogue (M_L 6.2 Aegean Sea event in 08.01.2013) are shown in Fig. 5.

3 Dynamic Response Characteristics

This section presents time-domain and frequency-domain analyses to identify dynamic response characteristics of the structure, location and earthquake specific variations of amplitudes and earthquake and time specific variations of modal frequencies.

3.1 Analyses in Time Domain

We examined acceleration, velocity and displacement time histories belonging to 103 earthquakes and identified the peak values in three components at each sensor location.

In Fig. 6, we plot peak accelerations at all sensor locations distributed over four levels within the structure in three components: X, Y and vertical. Ten earthquakes stand out as they led to the largest responses. They are indicated in the legend. The variation in the level of peak accelerations across the earthquake recordings studied, as well as among the four structural levels can be clearly observed in Fig. 6. Stations coded by KUB are at the dome base, while stations coded by GAL are at the level where the main arches spring from the top of the main pillars. The Sultan Ahmet Mosque is a symmetrical structure (Fig. 2). Therefore, it should be natural to expect a certain general regularity in structural response levels. At the dome level, for instance, the in-plane vibration levels (i.e., axis Y at KUB1, KUB3 and axis X at KUB2 and KUB4) should be smaller than the out-of-plane vibrations at the same station (note that the plane in this context is the plane of a main arch). The order of out-of-plane vibrations should be more or less similar to each other (i.e., KUB1 and KUB3 in axis-X and KUB2 and KUB4 in axis-Y). It can be hypothesized that any significant deviation among the peak values at a specific level and direction should be associated with structural interventions, repairs and/or earthquake characteristics. The general character described is observed at the sensor and component specific peak accelerations shown in Fig. 6. However, there are some variations among the peak values, which tend to change from earthquake to earthquake.

The pillars, with which GAL1 and GAL4 are associated, extend until the basement. The other two pillars also continue below the ground level, but their extension is less. The peak accelerations at GAL1 and GAL4 are consistently larger than those at GAL2 and GAL3, which is probably related to this. The vertical amplitudes at KUB3 are particularly high. It is known that the main arches have similar geometry and material properties. In the vertical direction, the vibration levels at their crowns should be similar to each other and smaller than their horizontal counterparts. This was indeed the general observation in previous earthquakes. In the 26 September 2019 event, though, the vertical acceleration level was comparable to the accelerations in the Y-direction.

Geometric means of two horizontal components were used to check on any dependency between the earthquake magnitude and peak amplitudes. The log-linear relationship between the two variables indicates significant scatter in peak accelerations and displacements as a function of earthquake magnitude (Figs. 7 and 8). Despite this, a trend between the two is still evident. The fact that the scatter in the peak amplitudes at stations HAMU and MAMU, which are the ground-level stations, is very similar to the scatter at the upper levels suggests that a second look at the data set is worthwhile; this time with respect to ground level amplitudes.

In Fig. 9, we plot peak accelerations at KUB and GAL stations with respect to peak accelerations at stations HAMU and MUMA. Station HAMU is at the basement

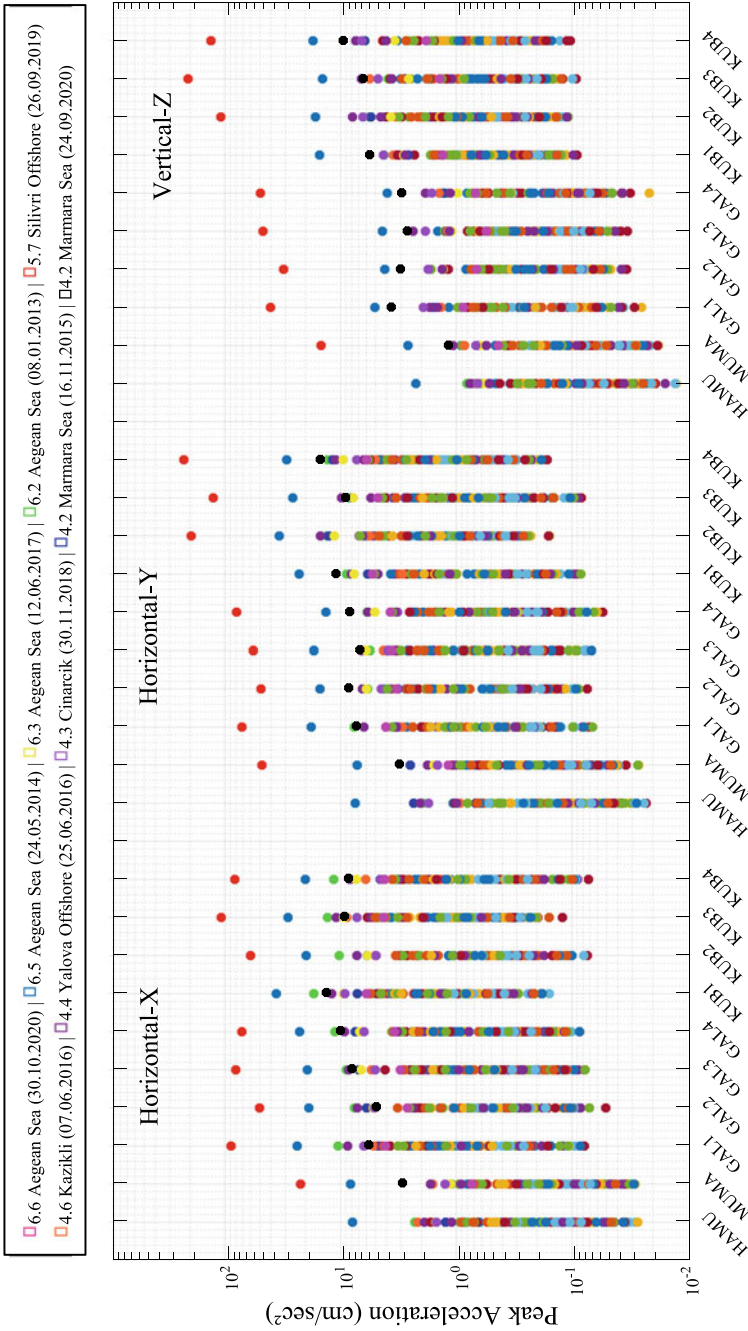


Fig. 6 Peak accelerations in X, Y and Z

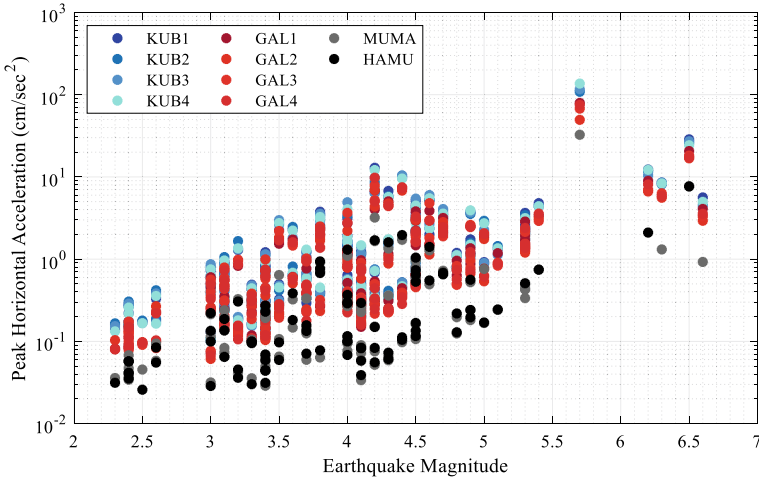


Fig. 7 The variation of peak accelerations as a function of earthquake magnitude

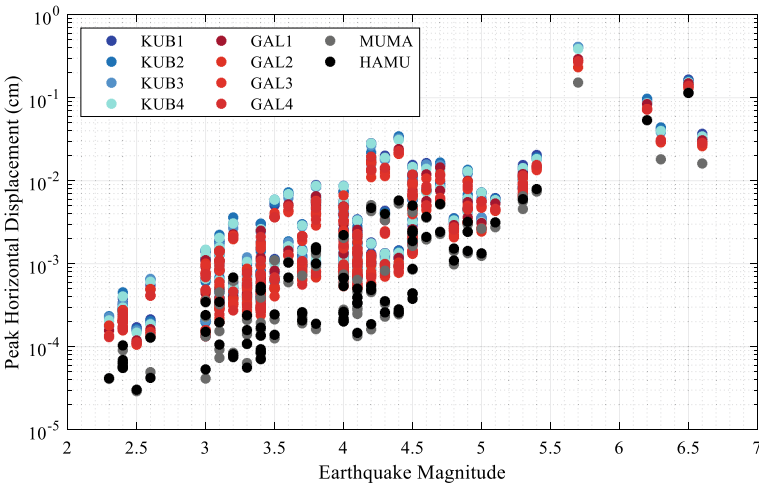


Fig. 8 The variation of peak displacements as a function of earthquake magnitude

which extends along one side of the mosque and is below the ground level at which station MUMA is located. In some important earthquakes in our data set, either HAMU or MUMA functioned. As these were events that produced large-amplitude ground motions, we decided to analyse our data set with respect to both stations. The log-log plot indicates a linear relationship between HAMU and MUMA that closely follows the 45-degree line. It further indicates a linear relationship between the ground level accelerations (HAMU or MAMU) and the accelerations at the upper levels. This observation is naturally valid for the available response level

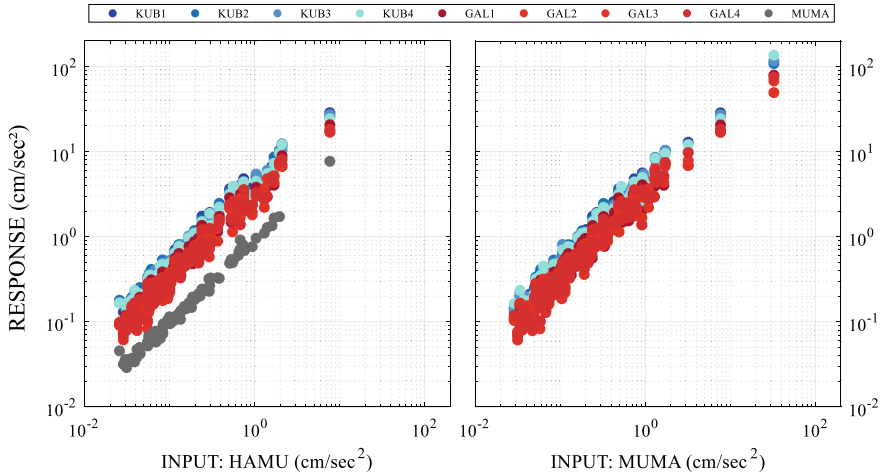


Fig. 9 The relationship between the ground level accelerations (HAMU (left) and MUMA (right)) and accelerations at the gallery and dome levels

range. However, it strongly suggests that the upper-level amplitudes can be predicted if the ground-level motions are known, provided that a representative data set is available that covers a sufficiently wide range of ground motion amplitudes, i.e., larger magnitude earthquakes over a much longer observation period.

3.2 Analyses in Frequency Domain

The first (along axis X) and the second (along axis Y) modal frequencies were estimated using FAS and TF by peak-picking and are shown in Figs. 10 and 11. The most significant earthquake in our catalogue is the 26.09.2019 M_L5.7 Silivri event. It resulted in a maximum acceleration of 226.6 cm/s² at KUB4 along the Y-axis. At MUMA, maximum accelerations in this event were 22.1 cm/s² and 47.8 cm/s² along X and Y axes, respectively. A substantial frequency drop was detected in both directions, which necessitated a closer look to understand whether the frequency drop has recovered or not in the period following the event. For this purpose, eleven additional earthquakes that occurred after the 26.09.2019 event were used. Station MUMA was the reference station in transfer functions instead of HAMU because station HAMU malfunctioned during the earthquakes after the 26.09.2019 event. In Figs. 10 and 11, we demonstrate that there is no permanent impact of this frequency drop on the structure. The figures show the identified first modal frequencies in two orthogonal directions over the observation period. In the period following September 2019, the frequencies seem to recover their previous levels.

We know that a tension ring was installed at the base of the main dome in August 2018. The time is marked in Figs. 10 and 11. The intervention does not seem to have

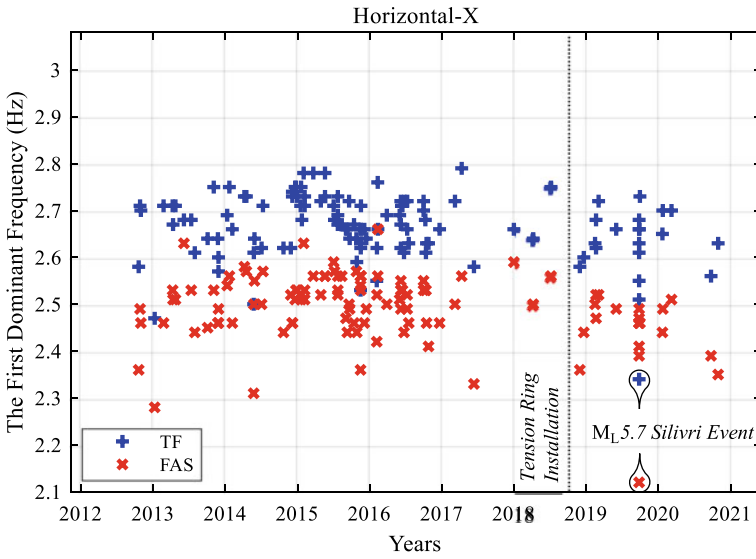


Fig. 10 Time-variation of the first dominant frequency in the X-direction (the date of application of the tension ring is indicated with a dashed line)

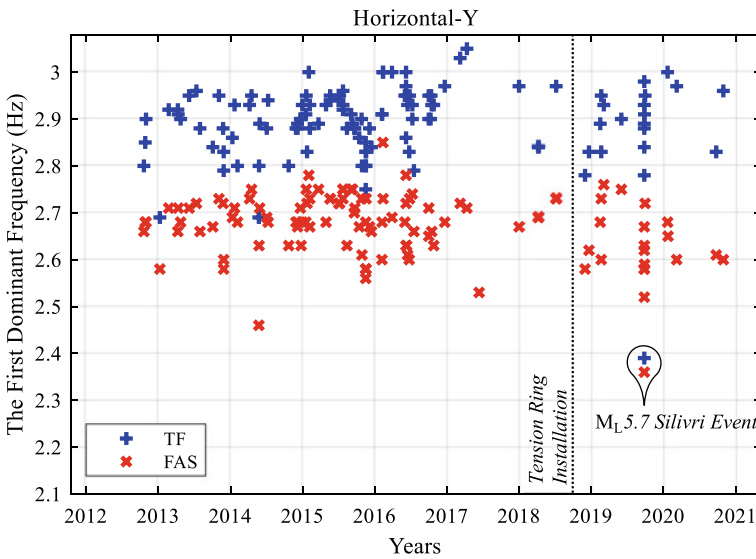


Fig. 11 Time-variation of the first dominant frequency in the Y-direction (the date of application of the tension ring is indicated with a dashed line)

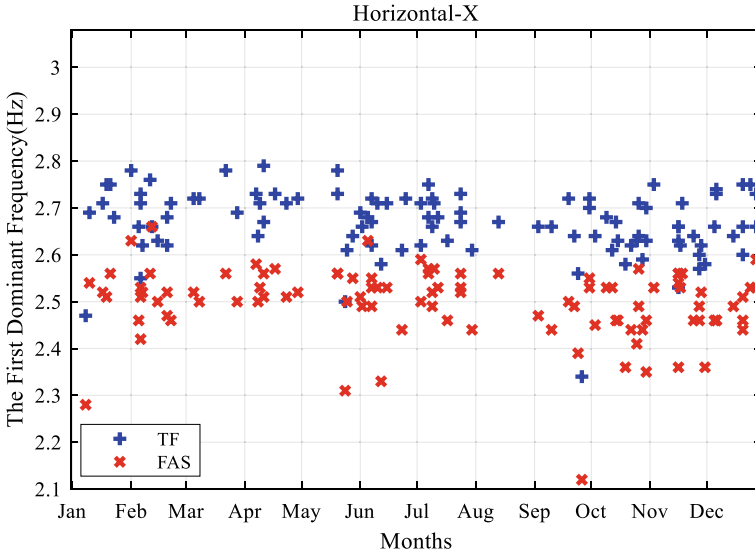


Fig. 12 The annual/seasonal change of the first dominant frequency in the X-direction

any impact as no clear change in identified frequencies could be detected looking at recordings of late 2018, 2019 and 2020. This could also be related to the design of the tension ring. Displacement and acceleration levels experienced were probably lower than those assumed as the design criteria. Analysis of modal shapes and particle motions could provide further clues about this point.

In Fig. 12, the first modal frequencies identified from recordings of an eight-year period are plotted against the day and month of the earthquake they are associated with whereby ignoring the year. The figure suggests no seasonal variation of frequencies. Therefore, no clear correlation between temperature and modal frequencies seems to exist.

The variation of modal frequencies of a structure is affected by the ground motion levels and the duration of strong shaking, the increase of which results in a drop of natural frequencies of vibration. When we plot identified frequencies in two directions as a function of ground-level acceleration (Fig. 13), the order and character of the drop become clearer. In the majority of recorded events, the ground-level accelerations were below 1 cm/s^2 . Events producing larger ground accelerations in the mosque are relatively rare, and if this is the case, there is a tendency in frequencies to drop sharply. From Fig. 13, two regions become evident. The first region (accelerations less than 1 cm/s^2) is identified by a slight linear drop in frequencies. In the second region, the drop becomes distinctly sharper.

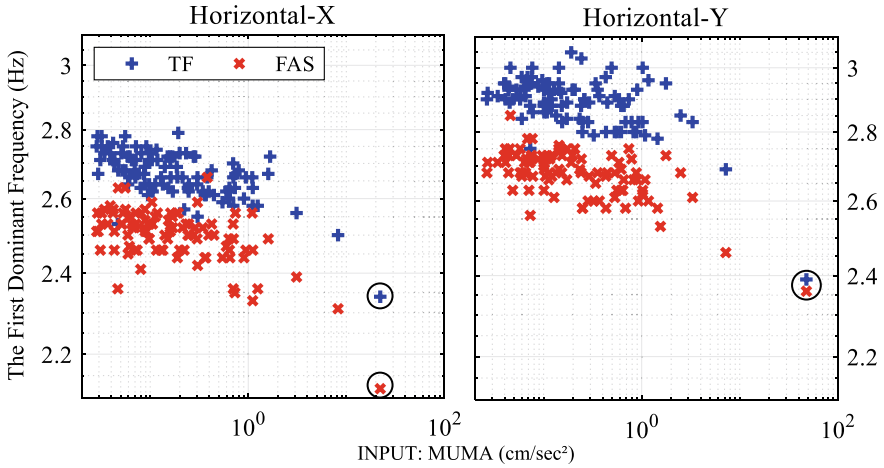


Fig. 13 The change of the first dominant frequencies with mean accelerations of MUMA ($M_{L5.7}$ Silivri event is indicated within circles)

4 Conclusions

This paper collates our first observations on the dynamic response characteristics of the Sultan Ahmet Mosque in Istanbul, which are made using a catalogue consisting of earthquakes collected by an SHM system installed on the structure.

The Sultan Ahmet Mosque has a symmetrical architectural and structural layout. There are differences between the structural response levels along X and Y axes, which need to be analysed further and explained in more detail. The observations we can cite here are related to the main pillars on the qibla side of the structure and the excessive vertical response of the main arches, particularly during the 26.09.2019 Silivri earthquake.

Taking advantage of the extensive data set compiled, we showed that a significant correlation between the ground level accelerations and accelerations at upper levels exist, which suggests that the structural response can be predicted when observations over extended periods of time and of larger magnitude earthquakes are made. Within the limitations of the present data set (i.e., recordings from earthquakes ≤ 6.6 and ground-level peak accelerations less than about 48 cm/s^2), we observed that the response at upper-level stations is almost linearly proportional to the excitation at the ground and/or basement levels. The data vaguely hint a slight reduction in response amplitudes at relatively higher excitation levels, which is an expected finding and could be attributed to non-linearity. Further modelling (data modelling and structural analysis) and more importantly recordings of larger earthquakes are needed for the confirmation of this observation.

We identified the first two modal frequencies of the structure by FAS and TF. We showed that the decrease of modal frequencies was related to the increase in

excitation amplitudes. We were able to identify two zones in which two different mechanisms of non-linearity might be effective.

No convincing evidence was found to show that the mosque is affected by seasonal temperature variations.

We also investigated the impact of the tension ring that had been implemented at the dome base in 2018 and could not detect any significant difference in structural response before and after its installation. A closer look at the effect of this intervention in the time domain, in particular, is needed, and we intend to further our research in this regard.

References

1. Nayir Z (1975) Osmanlı Mimarlığında Sultan Ahmet Külliyesi ve Sonrası (1609–1690). Ph.D. dissertation (in Turkish), Istanbul Technical University
2. Mazlum D (2011) 1766 İstanbul Depremi Belgeler Işığında Yapı Onarımları (in Turkish), 1st edn. İstanbul Araştırmaları Enstitüsü Yayınları, İstanbul
3. Finkel CF, Ambraseys NN (1997) The marmara sea earthquake of 10 july 1894 and its effects on historic buildings. *Yeni Anadolu*, Tome 7:49–58
4. Sayin GP (1999) Structural identification of the Sultan Ahmet Mosque through dynamic Response Studies. M.Sc. thesis, Bogazici University
5. Safak E, Caktı E (2014) Simple techniques to analyze vibration records from buildings. In: EWSHM—7th european workshop on structural health monitoring. IFFSTTAR, Inria, Universite de Nantes, Nantes, France
6. Safak E (2006) On estimation of site amplification from ambient ground noise. In: Proceedings of 1st european conference on earthquake engineering and seismology, Geneva, Switzerland

Experimental Evidence for Structural Damage During the 30.10.2020 Samos-Sığacık Earthquake by Laser Vibrometry



Eser Çaktı and Sefer Ömercan Ertürk

Abstract The Mw 6.9 earthquake of 30.10.2020 that took place to the immediate north of the island of Samos in the Aegean Sea was an important event. It was widely felt in the surrounding areas of both Turkey and Greece. It was an almost pure normal earthquake and recorded by a significant number of strong motion stations deployed in the region. The event caused a small-scale tsunami that led to some damage in the shores of Sığacık, a neighbourhood of the Izmir province to the north of the earthquake source zone. Regional distribution of structural damage was parallel to the ground motion levels. However, the city of Izmir, the third largest city of Turkey and about 60 to 70 km to the north of the epicentral area was severely affected. 117 lives were lost and more than 500 buildings either collapsed or received heavy damage. The majority of collapses and casualties were in the Bayraklı district of İzmir, known for its poor site conditions. This paper reports on a survey that we carried out soon after the earthquake in central Izmir. It relies on laser vibrometry, which was used to measure the dominant frequencies of a series of buildings in low, moderate and heavy damage state. Measurements were carried out remotely in 38 buildings. General structural characteristics of the buildings, such as number of stories, height, structural system and earthquake damage state were visually assessed. The dominant frequencies of vibration were estimated through analysis of vibration data. The fact that the majority of the buildings were more or less similar provided a unique opportunity for comparing their measured natural frequencies of vibration under different levels of damage.

Keywords Laser vibrometry · Ambient vibrations · Modal frequency · Earthquake-induced damage

E. Çaktı (✉) · S. Ö. Ertürk
Department of Earthquake Engineering, Kandilli Observatory and Earthquake Research Institute,
Boğaziçi University, Istanbul, Türkiye
e-mail: eser.cakti@boun.edu.tr

1 Introduction

An earthquake of Mw 6.9 took place on 30.10.2020 off shore between the Greek island of Samos and the Izmir province of Turkey. It was felt widely in western provinces of Turkey and on nearby Greek islands. İzmir is the third largest city of Turkey and the regional economic hub. As a result of the earthquake, 117 lives were lost and 6136 buildings received damages of varying degrees. More than 500 buildings either collapsed or received heavy damage (<https://hasartespit.csb.gov.tr>). Regional effects of the earthquake were actually not severe, except in some neighborhoods of central Izmir, which is at about 60-70 km to the epicentral area. In central Izmir the earthquake devastated particularly the Bayraklı district. The majority of collapses and casualties were in Bayraklı, well known for its poor site conditions. It was notable that most of the buildings that collapsed had been built before the year 2000. Example images of damaged buildings are shown in Fig. 1.

This paper outlines an experimental study carried out very soon after the earthquake in central Izmir. Taking advantage of the laser vibrometer, which is a recent addition to the infrastructure of the non-destructive testing laboratory of the Department of Earthquake Engineering (<https://eqe.boun.edu.tr/en/non-destructive-testing-laboratory>), we wanted to measure the dominant frequencies of a series of buildings in low, moderate and heavy damage states with the aim of testing the performance of this remote measurement technique in completely unfavourable conditions such as those posed by a real earthquake and to provide estimates of modal frequencies of buildings in different states of damage.



Fig. 1 Images of buildings in different damage states. *Photo credit* Sefer Ömercan Ertürk

2 The Survey

Laser vibrometer is a non-contact vibration-measuring device based on the Doppler effect, which occurs when the laser light is back scattered from a vibrating surface. The scanning devices developed using this principle are widely used across many disciplines, particularly in those that require research and development, non-contact condition assessments using vibrations and imaging of vibrations. Its use in civil/structural/earthquake engineering and architecture is particularly interesting due to the fact that in certain structures the access to install standard vibration measurement devices is very difficult or impossible such as earthquake damaged buildings.

In the survey we made use of Polytec RSV-150 type laser vibrometer. The plan was to select a group of buildings that were in different damage states ranging from no to heavy damage. To do this, we made use of information on the website <https://hasartespit.csb.gov.tr>, that belongs to the Ministry of Urbanization and Environment to publicly disclose the damage level estimates made by trained engineers following earthquakes. We selected buildings in Bayraklı and Karşıyaka districts. Measurements were carried out remotely in 38 buildings. 26 of them were in Bayraklı. 12 buildings were in the Karşıyaka district. Their locations are shown in Fig. 2.

The heights of the buildings were measured on site with the help of a laser distance-meter. They ranged between 16 and 51 m. Except two buildings that were 16 m high and two which had a height of 51 m, the heights of the remaining 34 buildings varied between 19 and 32 m. The buildings were predominantly 8 or 9 stories high and all were reinforced-concrete. The breakdown with respect to damage state was as follows: 14 buildings were heavily damaged, 10 were moderately damaged and 8 were slightly damaged. In 6 buildings, there was no damage.



Fig. 2 Locations of buildings in the survey



Fig. 3 Selected images from the experimental survey. *Photo credit* Sefer Ömercan Ertürk

In each building ambient vibrations were recorded for about four minutes. Two sets of measurements along the two orthogonal axes were taken in each case. We spent about an hour in each building. The survey took four days to complete. The dominant frequencies were estimated from the Fourier amplitude spectra. Figure 3 shows selected images taken during the survey.

3 Results and Discussion

Figure 4 shows estimated frequencies with respect to the building height. The states of damage, the buildings were in, are also indicated in Fig. 4 using different colors. The frequencies that we measured correspond to the first modal frequency. The decrease in modal frequency with increasing building height can immediately be captured and is particularly evident from data that represent undamaged buildings. Furthermore, the differences between measured frequencies of buildings in different damage states are clearly demonstrated. Structural damage is essentially degradation of stiffness. Therefore, modal frequencies tend to drop with increasing levels of damage, as indicated by data presented in Fig. 4. The difference between the frequency levels of undamaged and slightly damaged buildings is easily distinguishable. However, the separation between the estimates made on moderately and heavily damaged buildings is not that clear, as they are very close. This is in fact an expected outcome. At higher levels of structural damage or under conditions of strong non-linearity, assumptions made for modal analysis are not valid anymore. Therefore, interpretations for relating the measured frequencies to higher damage states can be misleading.

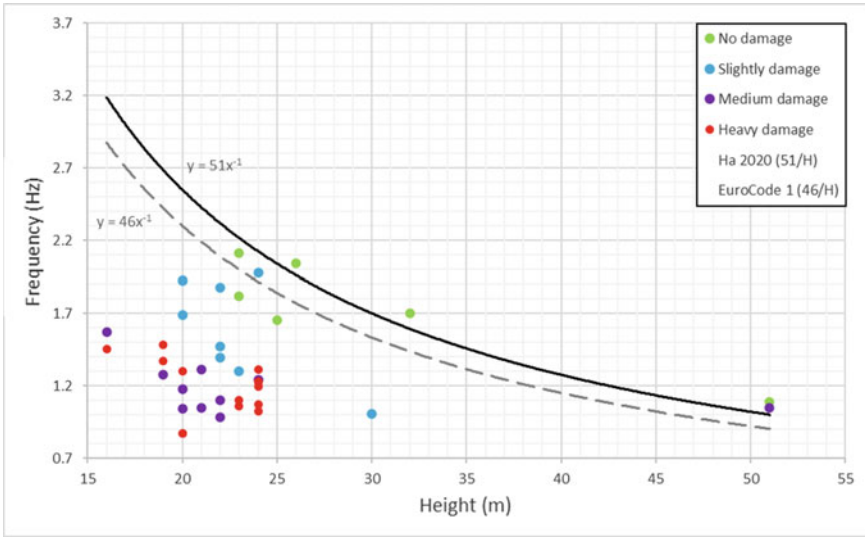


Fig. 4 Experimentally identified first modal frequencies versus building height. The damage states individual buildings are in are indicated by different colors

Relationships between the first modal frequency and the height of a building (or the number of stories) can be found in several codes and studies [1–8]. Existing relationships are for buildings in undamaged state. There are, however, considerable differences between them regarding the level of frequency estimates. Among the equations that we investigated two were more aligned with our findings. They are expressed as $f = 51/H$ [6] and $f = 46/H$ [7] and plotted in Fig. 4. In both equations H is the building height in m.

The drop in modal frequency can be related to many factors; structural damage being one and the most important of them. There is not a consensus among researchers if it can be used as an indicator of damage on its own. Its co-use with other structural indicators is probably a more rational path to take. Our findings show the frequencies may become inseparable at damage states medium and higher. They also indicate that it is definitely a good parameter for warning the onset of slight damages and the potential for higher level of damage. In support of this discussion, we calculated average frequencies of buildings in each damage state despite the differences in the building heights which we acknowledge but decide to keep except two buildings which were 51 m high. (Table 1).

Table 1 Average frequencies of buildings with similar heights

Damage level	Heavy	Medium	Slight	Undamaged
Average frequency (Hz)	1.18	1.20	1.58	1.86

Based on information presented in Table 1 it can be estimated that with respect to undamaged state the drop in measured average frequencies are 0.37, 0.35 and 0.15 for heavy, medium and slight damage states respectively. The scatter in data for moderately and heavily damaged buildings was considerable and the frequencies were not separable (Fig. 4). As a consequence, average frequencies are very close to each other. However, a drop in the order of 15% can be meaningful for identification or onset of slight damages. Needless to say, this observation is simply a first order approximation and needs further verification by independent field measurements. Our findings also suggest damage levels medium and higher are associated with about 35% frequency drop.

Acknowledgements The field measurements were possible through the financial support provided by Boğaziçi University under project BAP - Remote Structural Monitoring Via Laser Vibrometry (project no. 11717, project code 18TS2) and by technical and logistical support of Mr Ahmet Korkmaz and Mr Nafiz Kafadar. All contributions are gratefully acknowledged.

References

1. Yoon SW, Joo YK (2003) Natural periods of reinforced concrete apartments for serviceability design. *J Archit Inst Korea* 19:3–10
2. ASCE (American Society of Civil Engineers) (2011) ASCE/SEI 7-10. Minimum design loads for buildings and other structures; ASCE (American Society of Civil Engineers): Reston, VA, USA
3. Lagomarsino S (1993) Forecast models for damping and vibration periods of buildings. *Wind Eng Ind Aerod* 48:221–239
4. Satake N, Suda KI, Arakawa T, Sasaki A, Tamura Y (2003) Damping evaluation using full-scale data of buildings in Japan. *J Struct Eng* 129:470–477
5. Architectural Institute of Korea (2009) Korean building code—structural. Seoul, Korea, Ministry of Construction and Transportation of Korea
6. Ha Taehyu (2020) Damping and natural period evaluation of tall RC buildings using Full-Scale data in Korea. *Applied Sci* 10(5):1568
7. EN 1991-1-4 (2005) Eurocode 1: actions on structures—Part 1–4: general actions—wind actions. CEN, European committee for standardization, Brussels, Belgium
8. Fritz WP, Jones NP, Igusa T (2009) Predictive models for the median and variability of building period and damping. *J Struct Eng* 135(5):576–586

Structural Monitoring and Dynamic Characterization of the Main Fire Station Building in Naples



M. Spizzuoco, D. Losanno, I. Nuzzo, V. Schiavone, and G. Serino

Abstract The main Firemen Station of Naples is a steel–concrete composite building structure, that is peculiar due to its suspended configuration and to the seismic devices installed at the time of construction. The latter represents one of the first Italian applications of vibration control systems and the assessment of seismic performance according to current codes is strongly needed. The installation of a static and dynamic monitoring system of the structure and the performing of a rising test of one seismic bearing could allow to better understand the structural behaviour and to determine the best choice of seismic retrofit intervention of the building. A simplified structural model is developed to be used for predicting and evaluating the experimental results of dynamic shaking tests with vibrodine.

Keywords Structural monitoring system · Suspended structure · Seismic control system · Strategic structure

1 Introduction

The main Fire Station in Naples (Italy), designed in 1979, consists of eight buildings. The headquarter structure is a suspended structure, which allows to satisfy the need to have a large space at the ground level, free of columns in order to allocate a wide garage and allow the easy motion of big vehicles. After the Irpinia seismic event in November 1980, a higher seismic risk had to be considered for new construction in Naples. Therefore, the executive project, completed in 1983, had to adapt the suspended configuration of the main building to the new seismic requirements: a complex dissipation system was installed, able to exploit the devices' hysteretic behaviour to dissipate energy [1–4]. After more than 30 years from the original

M. Spizzuoco (✉) · D. Losanno · V. Schiavone · G. Serino
Department of Structures for Engineering and Architecture, University of Napoli Federico II,
Naples, Italy
e-mail: spizzuoc@unina.it

I. Nuzzo
Construction Technologies Institute, National Research Council of Italy, Napoli, NA, Italy

construction, the seismic and fire assessment of the pioneering structure has been deeply analyzed [5]. The present work discusses the interventions suggested for the investigation and control of the real mechanical and dynamic behaviour of the logistic building, as required by the wide Urban Regeneration Project of East Naples.

Therefore, the case-study building structure is a 4-storey steel–concrete composite suspended structure, supported by means of R.C. towers, that represent vertical connections for stairs and elevators too. Its plan (Fig. 1) is composed by five independent rectangular sub-structures (of dimensions 26 m × 18 m) and one trapezoidal sub-structure (26 m × 18 m to 32 m).

The longitudinal and transversal sections (Fig. 2) just show the composite floor slabs hanging from the reticular girders at the top, by means of steel tie-rods. The top reticular girders are supported by R.C. towers, through the interposition of a total number of 24 devices (Fig. 3a), that enable thermal excursions in service conditions by preventing states of coaction in structural elements, and dissipate seismic energy when horizontal and vertical earthquakes occur. On each R.C. tower, a different type of support is mounted (hinge, uni-directional or bi-directional rollers), in order that

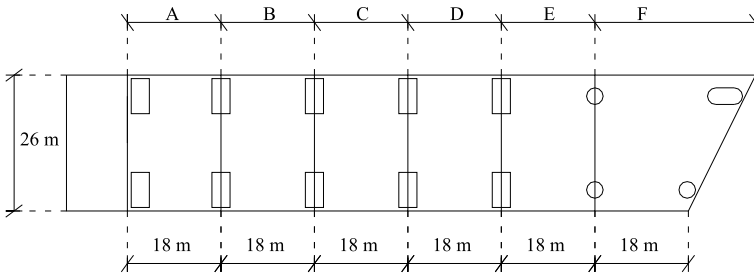


Fig. 1 Simplified plan view and labelling of the substructures

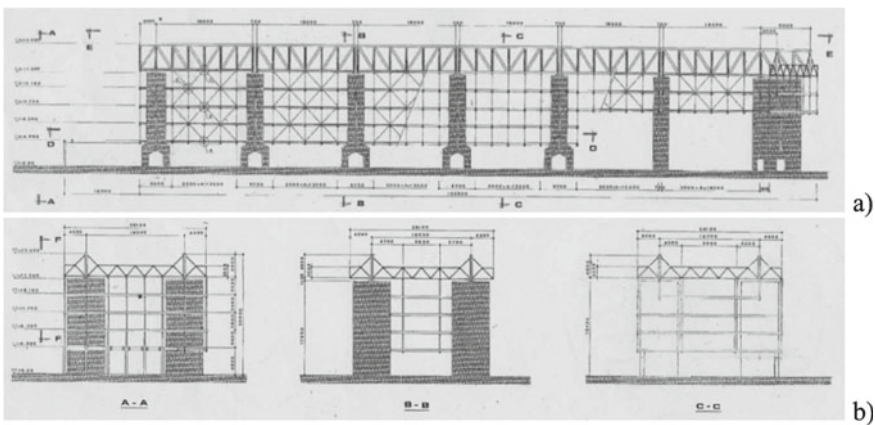


Fig. 2 Original charts of: a longitudinal (along x) section, and b transversal (along y) sections

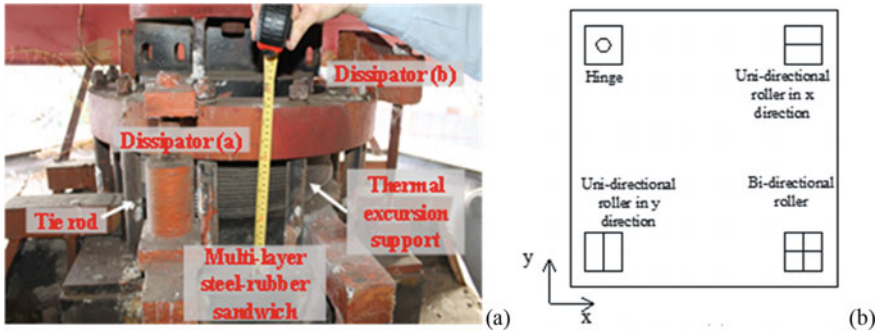


Fig. 3 a Thermal/seismic device between each R.C. tower and the upper structure; b distribution of supports in a general substructure

their configuration provides the substructure’s movements under thermal variations (Fig. 3b). The hinge is obtained with the contact of two steel surfaces, while the interposition of teflon sheets between them provides a bi-directional roller, and the introduction of a rail parallel to the direction of free translation determines a uni-directional roller.

The bottom part of each support consists in a multi-layer steel-rubber isolator, able to resist to vertical loads, but having a low horizontal stiffness, so that, when a significant horizontal action occurs, it deforms and the steel rods devices (a) in Fig. 3a yield in bending and shear. Figure 4a shows that the isolator doesn’t deform when a seismic force has the direction of free thermal movements, but it is loaded after the gap between the upper part of the support and the outer part of the system is closed. On the other hand, the isolator deforms horizontally along the restrained direction of thermal motion, but it hits the rigid connection due to a very small gap (Fig. 4b) and loads the external dampers.

As a consequence, the isolator never works in the horizontal direction. Besides, in case of a vertical seismic action, the isolator is always compressed because of the presence of the tie rods connecting its upper face with a bottom steel plate fixed to the R.C. tower. Dissipation of energy is provided by dampers of type (b), which

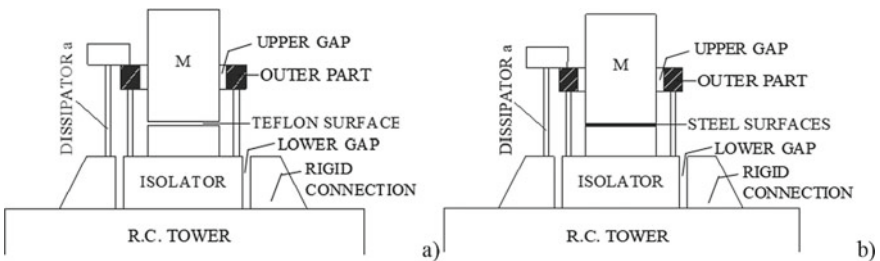


Fig. 4 Schematic working of the special device, a along the free thermal movement direction, b along the restricted thermal movement direction

yield under axial deformations (see Fig. 3a), while neoprene bumpers are mounted between the beams of the suspended floors and the R.C. tower walls, in order to prevent damaging due to pounding effects caused by the horizontal oscillations of the suspended decks. Four kinds of bearings have the properties listed in Table 1. The stiffness and the yielding force of the bumpers are equal, respectively, to $k_b = 340$ kN/mm and 30 kN.

In the framework of the above mentioned Urban Regeneration Project of East Naples, a static and dynamic structural monitoring system, a rising test of one supporting bearing and dynamic tests using vibrodine, have been designed in order to get a better understanding of the whole mechanical and dynamic behavior of the suspended building, even due to a complex system of devices. The outcomes of the monitoring system are useful also to improve the structural numerical models and to single out a proper seismic retrofit intervention.

2 Structural Assessment

2.1 Numerical 3D Model

A 3D model of one sub-structure (module named D) has been developed by using SAP2000 software. Steel (Fe 360 C) and R.C. ($R_{bk} = 200$ kg/cm²) members have been modelled as frame elements (Fig. 5a). For example, vertical towers are four elements having a total height of 17.5 m and a hollow rectangular cross section, with thickness 40 cm and external dimensions 6.7 m \times 3.5 m. Steel elements represent a wide number of section's geometries, thus they aren't mentioned for sake of shortness. The steel tie-rods sustaining the floor slabs have a rectangular section of dimensions 40 mm \times 80 mm, 40 mm \times 120 mm and 40 mm \times 250 mm. The braces by the perimetric longitudinal sections have circular section with diameter $\Phi 39$.

The floor slabs are considered infinitely rigid by applying body constraints, and their mass is assumed lumped at the center of mass, according to Table 2. These masses comprise that one of the other steel elements, but they don't include the mass of the cores, which is assigned to each R.C. members.

As regards the steel roof truss model, the lateral flexibility of the rubber bearing gives a negligible contribution in the horizontal direction, as explained in the above section. Even the lateral stiffness of the steel dampers [(a) in Fig. 3a] is negligible due to high flexibility of the steel rods and their small section. Based on these considerations, under the action of a seismic load, two fixed points are modelled in longitudinal and transversal direction. In vertical direction, a linear spring (of stiffness 6210 kN/mm) and a dashpot (of damping coefficient 4.45 kN s/mm), connected in parallel, are considered to represent rubber behaviour, while rubber bumpers at each floor have been simulated in both horizontal directions by linear elements having a stiffness of 6.25 kN/mm and a damping coefficient of about 0.081 kN s/m.

Table 1 Different types of bearings

Capacity	G	E = 3G	Φ	Φ'	t_l	n_s rubber	A_c	A'_c	T_r	S	k_v	M	ξ	c_v	k_h	c_h
t	Mpa	Mpa	mm	mm	mm	-	mm ²	mm ²	mm	-	kN/mm	t	-	kNs/mm	kN/mm	kNs/mm
420	0.9	2.7	680	670	7.2	15	363,168.1	352,565.2	108	23.26	6210.18	1274	0.05	4.45	3.03	0.14
240	0.9	2.7	620	610	7.2	15	301,907.1	292,246.7	108	21.18	4268.27	1274	0.05	3.69	2.52	0.13
540	0.9	2.7	850	840	7.2	15	567,450.2	554,176.9	108	29.17	15,335.50	1274	0.05	6.99	4.73	0.17
300	0.9	2.7	650	640	7.2	15	331,830.7	321,699.1	108	22.22	5171.11	1274	0.05	4.06	2.77	0.13

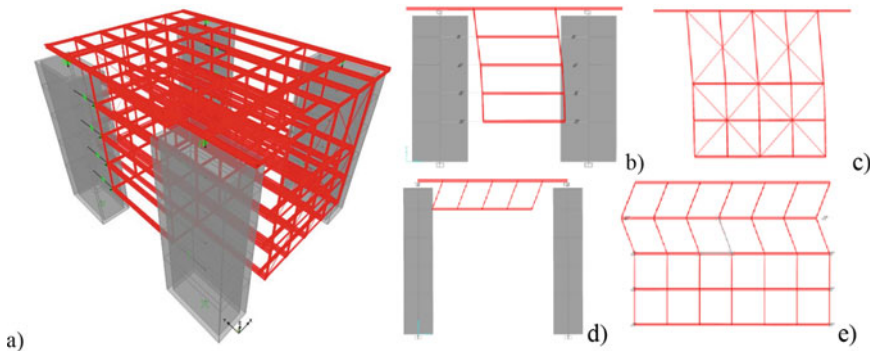


Fig. 5 a 3D structural model; b 1st mode in y direction— $T_1 = 0.59$ s; c, d 1st mode in x direction— $T_2 = 0.56$ s; e 2nd mode in x direction— $T_2 = 0.47$ s

Table 2 Translational and rotational mass distribution

Floor	Area (m ²)	Transl. mass (t) $M_x = M_y = M_z$	Rot. mass (tm ²) M_{xx}	Rot. mass (tm ²) M_{yy}	Rot. mass (tm ²) M_{zz}
Roof	488	285	11,550	8295	19,846
4°	313	211	5270	5480	10,750
3°	415	280	13,168	6803	19,971
2°	415	249	11,705	6047	17,752
1°	415	249	11,705	6047	7752
Total	2046	1274			

The fundamental mode of vibration is along y direction (Fig. 5b), that corresponds to a higher flexibility with respect to x direction, due to the absence of external braces. The second mode of vibration coincides in the first translational mode along x direction (Fig. 5c with the braces, and Fig. 5d with the towers). The second mode along x direction is relative to the internal sections (Fig. 5e). The first and second periods of vibration, 0.59 s and 0.56 s respectively, have participating mass ratios of 39 and 18%, mainly accounting for the contribution of the suspended structure. The mass of R.C. towers is excited by higher modes (10th and 13th modes, respectively in x and y directions). The first vibration mode in vertical direction (15th mode) corresponds to a period of 0.1 s.

2.2 Simplified Model

A simplified model of the considered sub-structure (module D) has been developed, with the aim of using the numerical results to design the dynamic tests with vibrodine.

The modelling of module D has been performed in both the transversal direction, where the braces are absent, and the longitudinal direction including the bracing system.

The structure has been considered as an inverted shear-type frame and the following simplifying hypotheses have been assumed (Fig. 6) to derive the 5×5 mass and stiffness matrices of two numerical systems simulating the structural behaviour in transversal and longitudinal direction, respectively: (i) the mass of each

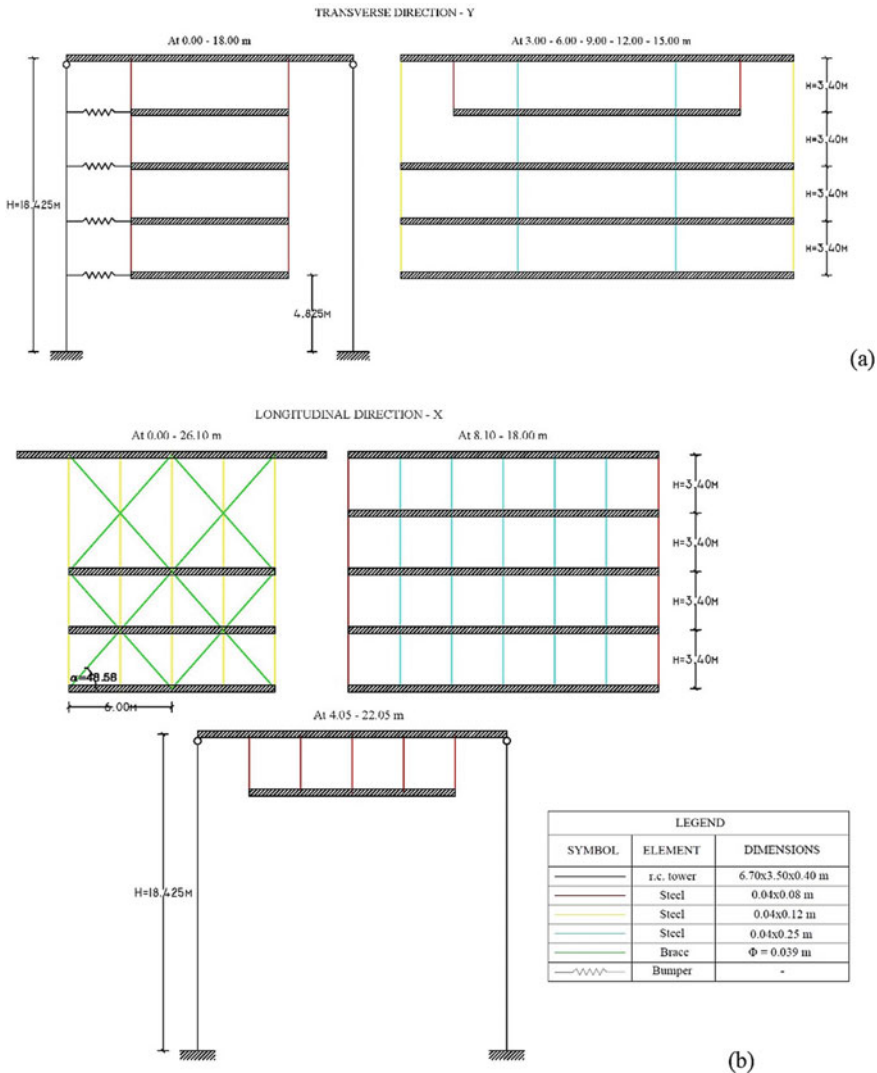


Fig. 6 Scheme of the frame's structural elements needed to define the simplified model in **a** transversal direction, and **b** longitudinal direction

deck, thought as infinitely rigid, is lumped at its center of mass; (ii) the third part of every R.C. core’s mass is assumed concentrated in the covering deck; (iii) the tie-rods supporting the decks are assumed axially rigid but featuring flexural deformability; (iv) the masses of tie-rods and transversal elements are neglected; (v) the bumpers are modelled as linear elastic elements and their stiffness is included in the main diagonal of the stiffness matrix obtained in transversal direction; (vi) the bracing elements connecting the floor levels along longitudinal direction are assumed clamped by the decks and contribute to the stiffness matrix, derived in longitudinal direction, through their axial stiffness.

The mass matrix is shown in Eq. (1), while the stiffness matrices computed in transversal and longitudinal direction are written in Eqs. (2) and (3), respectively:

$$\mathbf{M} = \begin{bmatrix} m_{11} & m_{12} & m_{13} & m_{14} & m_{15} \\ m_{21} & m_{22} & m_{23} & m_{24} & m_{25} \\ m_{31} & m_{32} & m_{33} & m_{34} & m_{35} \\ m_{41} & m_{42} & m_{43} & m_{44} & m_{45} \\ m_{51} & m_{52} & m_{53} & m_{54} & m_{55} \end{bmatrix} = 10^5 \begin{bmatrix} 2.49 & 0 & 0 & 0 & 0 \\ & 2.49 & 0 & 0 & 0 \\ & & 0 & 2.80 & 0 \\ & & & 0 & 2.11 \\ & & & & 0 \\ & & & & & 0 & 0 & 0 & 3.30 \end{bmatrix} \quad [\text{N}] \quad (1)$$

$$\mathbf{K}_T = \begin{bmatrix} k_{11}^t & k_{12}^t & k_{13}^t & k_{14}^t & k_{15}^t \\ k_{21}^t & k_{22}^t & k_{23}^t & k_{24}^t & k_{25}^t \\ k_{31}^t & k_{32}^t & k_{33}^t & k_{34}^t & k_{35}^t \\ k_{41}^t & k_{42}^t & k_{43}^t & k_{44}^t & k_{45}^t \\ k_{51}^t & k_{52}^t & k_{53}^t & k_{54}^t & k_{55}^t \end{bmatrix} = 10^8 \begin{bmatrix} 3.81 & -3.75 & 0 & 0 & 0 \\ -3.75 & 7.57 & -3.75 & 0 & 0 \\ 0 & -3.75 & 7.24 & -3.38 & -0.0462 \\ 0 & 0 & -3.38 & 6.94 & -3.49 \\ 0 & 0 & -0.0462 & -3.49 & 270 \end{bmatrix} \quad [\text{N/m}] \quad (2)$$

$$\mathbf{K}_L = \begin{bmatrix} k_{11}^l & k_{12}^l & k_{13}^l & k_{14}^l & k_{15}^l \\ k_{21}^l & k_{22}^l & k_{23}^l & k_{24}^l & k_{25}^l \\ k_{31}^l & k_{32}^l & k_{33}^l & k_{34}^l & k_{35}^l \\ k_{41}^l & k_{42}^l & k_{43}^l & k_{44}^l & k_{45}^l \\ k_{51}^l & k_{52}^l & k_{53}^l & k_{54}^l & k_{55}^l \end{bmatrix} = 10^8 \begin{bmatrix} 9.82 & -0.137 & -9.69 & 0 & 0 \\ -0.137 & 0.275 & -0.137 & 0 & 0 \\ -9.69 & -0.137 & 19.6 & -0.0964 & -9.73 \\ 0 & 0 & -0.0964 & 0.22 & -0.124 \\ 0 & 0 & -9.73 & -0.124 & 101 \end{bmatrix} \quad [\text{N/m}] \quad (3)$$

For example, the element k'_{11} of the stiffness matrix derived in transversal direction is computed in Eq. (4) by adding the contributions of the flexurally deformable tie rods and that one of the bumper installed at first level.

On the other hand, the element k'_{11} of the stiffness matrix obtained in longitudinal direction is calculated in Eq. (5) by adding the contributions of the tie rods and that one of the braces involving the first floor.

In both transversal and longitudinal directions, the problem of eigenvalues and eigenvectors (Eq. 6) has been solved by using Matlab software (Fig. 7).

$$k'_{11} = 2 \cdot 2 \left(\frac{12EI_y}{h^3} \right) + 2 \cdot 5 \left(\frac{12EI_y}{h^3} \right) + 2 \cdot 5 \left(\frac{12EI_y}{h^3} \right) + k_{bumper} \quad (4)$$

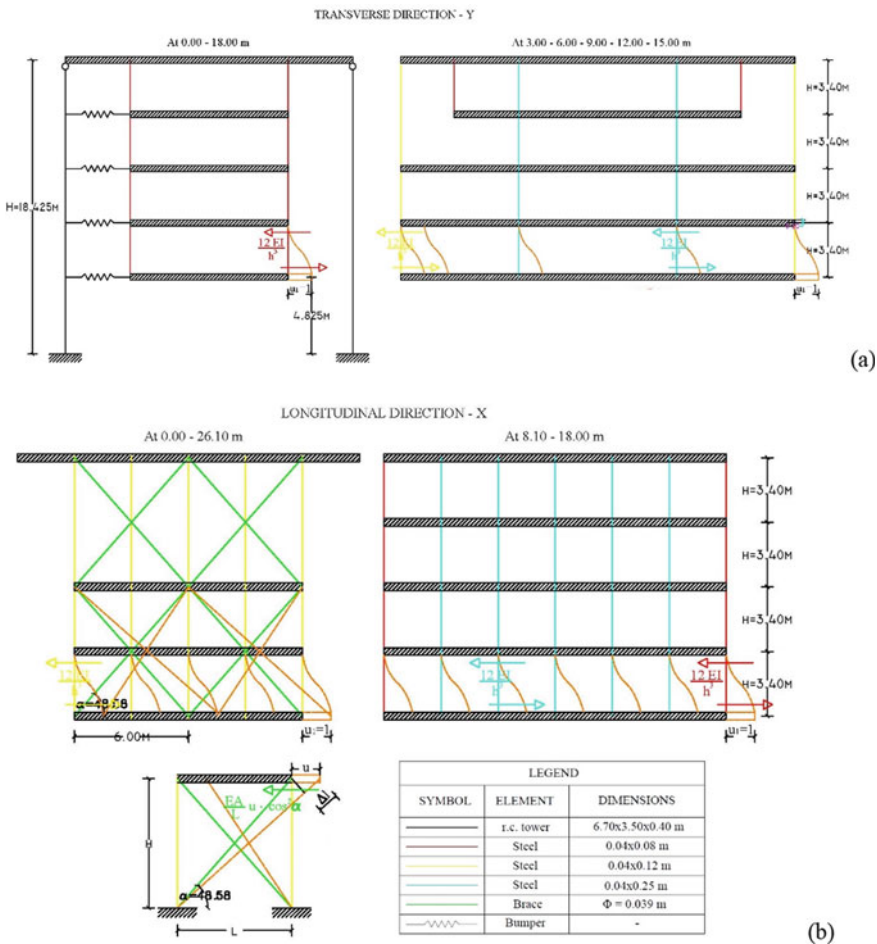


Fig. 7 Computation of the element k'_{11} of the stiffness matrix in **a** transversal direction, and **b** longitudinal direction

$$k_{11}^l = 2 \cdot 5 \left(\frac{12EI_x}{h^3} \right) + 2 \cdot 2 \left(\frac{12EI_x}{h^3} \right) + 2 \cdot 5 \left(\frac{12EI_x}{h^3} \right) + 2 \cdot 4 \left(\frac{EA}{l} \cos^2 \alpha \right) \quad (5)$$

$$\mathbf{M} \cdot \ddot{\mathbf{u}} + \mathbf{K} \cdot \mathbf{u} = \mathbf{0} \quad \Rightarrow \quad \det(\mathbf{K} - \omega_n^2 \cdot \mathbf{M}) = 0, \quad (\mathbf{K} - \omega_n^2 \cdot \mathbf{M}) \cdot \boldsymbol{\Psi} = \mathbf{0} \quad (6)$$

The first periods of vibration, along transversal (y) and longitudinal (x) directions, are equal to 0.44 s and 0.62 s, respectively. Due to the simplifying hypotheses made to develop the equations of motion of the models shown in this section, the vibration periods do not satisfactorily match those obtained through the numerical 3D model. However, the simplified models are essential to depict preliminary considerations on the design of the dynamic tests with vibrodine. Both numerical and analytical models of the unit will be properly calibrated through preliminary measurements provided by the monitoring system presented in the next section.

3 Structural Monitoring System

An integrated static and dynamic monitoring system [6] has been designed for evaluating the amount of damage and the reliability level of the investigated structure, either when natural inputs and human activities (i.e., passage of light and heavy vehicles, workers' training, thermal excursions, etc.) excite the building, or under the action of earthquakes. It also has the objective to check the behaviour of the seismic devices installed. The acquired data could be shared with the Department of Civil Protection at both local and national levels. The proposed monitoring system can manage static, dynamic and environmental channels, by using independent units. The acquired data are stored according to their category, and can be transferred by a remote access to FTP areas and e-mail addresses.

The static acquisition system includes no. 40 displacement sensors with a stroke of 100 mm or 200 mm, no. 3 temperature transducers, no. 1 humidity sensor, and a digital acquisition system for 48 channels. The displacement transducers having a measurement interval of ± 50 mm (total stroke of 100 mm) have been assumed for the intermediate decks where 4 cm joints are placed between successive modules, while the displacement sensors having a measurement range of ± 100 mm (total stroke of 200 mm) have been thought by the seismic bearings.

The dynamic acquisition system consists in no. 10 tri-axial accelerometers, no. 5 uni-axial accelerometers, no. 20 displacement sensors having a stroke of 100 mm or 200 mm located in structural module D, no. 1 tachy-anemometer, no. 1 gonio-anemometer, and a dynamic digital acquisition system for 64 channels. The presence of a sensor mounted at top of the building to measure wind's velocity and direction, is important to correlate such data to the vibrations of the suspended structure under horizontal ordinary excitations like the wind action.

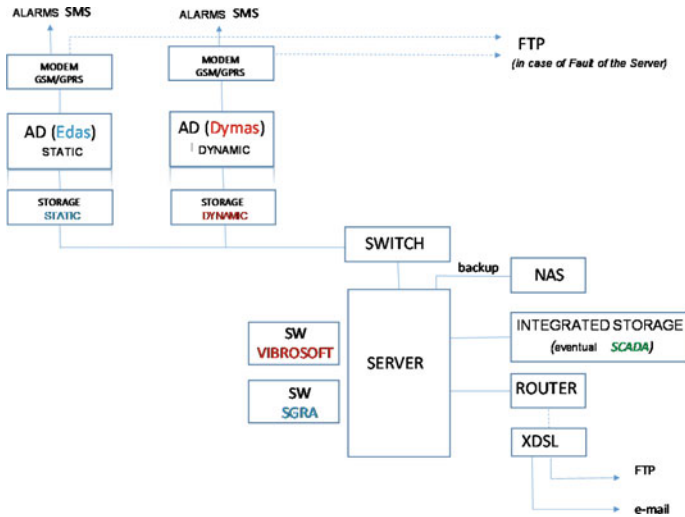


Fig. 8 Architecture of the monitoring system

Figure 8 shows the five sub-systems of the defined monitoring system: the automatic static acquisition system, the automatic dynamic acquisition system, the data management, storage and processing system, the remote management system, and the power supply system. The data acquisition systems are 2 independent units, which acquire according to a defined sampling frequency; each of them has both power supply and acquisition features. The system for management, storage and processing of the data includes a static/dynamic system for the data logging of recorded data, a Network Attached Storage (NAS) unit for back-up of data, and a dedicated integrated software. Besides the advanced management of all the data, the software in cloud “SPIDERNET” of the dynamic system is able to implement a system for remote maintenance of the equipment; it also doesn’t need any installation because its interface is available by browser, with the potentiality of Internet network which provides an AA (always and anywhere) service. This sophisticated monitoring software just represents the next generation of platforms Big Data e Fast Data. The remote management system allows the automatic transfer of the data and of alarms via e-mail to dedicated FTP areas. Finally, the power supply system has a Uninterruptible Power System (UPS) with an autonomy of at least 30 min. On the other hand, both the data acquisition systems include a battery for the back-up in case of energy lacking: the guaranteed autonomy time is at least 36 h.

The Monitoring Room, located at fourth floor of structural module D, houses the Control Hub of the monitoring system, that consists in the acquisition and powering systems.

The static sensors are (Figs. 9a, 10a, and 11a): no. 2 displacement transducers by every bearing at top of the R.C. cores, installed along two orthogonal horizontal directions of the restraints (no. 8 of them, relative to module D, are acquired by

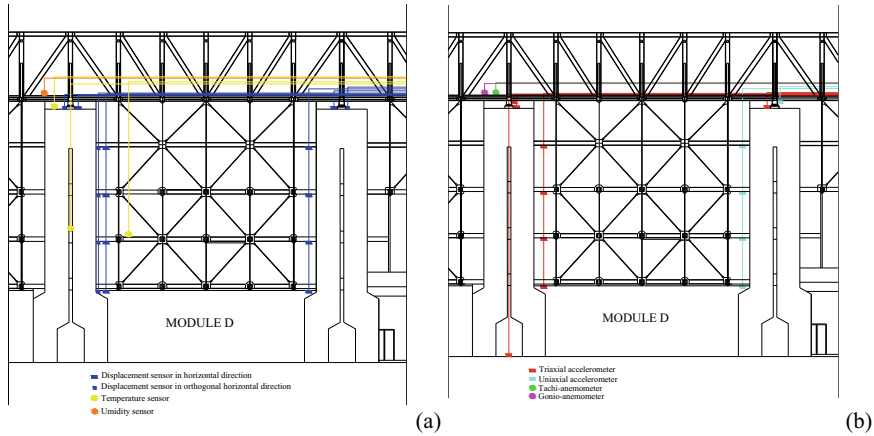


Fig. 9 a Displacement transducers, temperature and humidity sensors; b accelerometers at the longitudinal cross-section of the structural module D

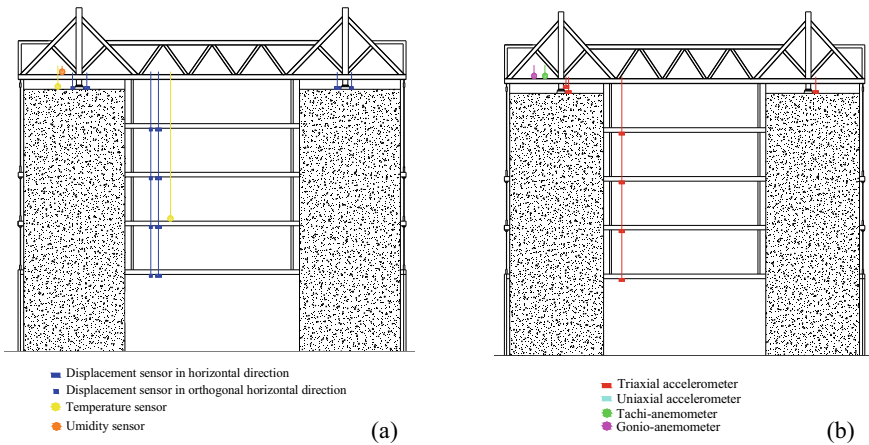


Fig. 10 a Displacement transducers, temperature and humidity sensors; b accelerometers at the transversal cross-section of the structural module D

the dynamic system, so that only no. 40 displacement transducers are statically recorded); no. 3 temperature sensors, the first one mounted towards outside by one antiseismic bearing of module D, the second one installed inside module D at II floor in intermediate position with respect to structural elevation, and the third one placed inside a core of module D in correspondence of II floor; no. 1 igrometer by the covering deck of module D.

The dynamic sensors are installed in structural module D of the logistic building (Figs. 9b, 10b, 11b): no. 5 tri-axial accelerometers by the decks of module D, including the covering; no. 5 uni-axial accelerometers, one by each deck of module

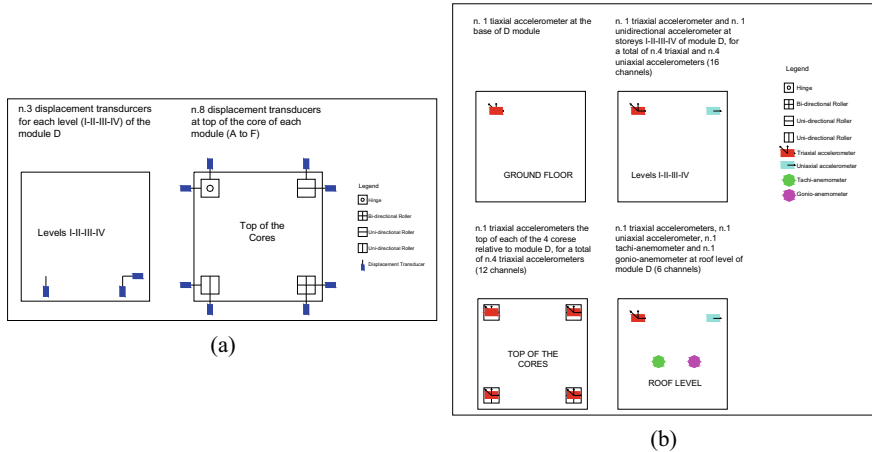


Fig. 11 Schematic distribution of **a** the displacement sensors, and **b** the acceleration sensors and tachy-gonio-anemometer in the structural module D

D; no. 4 tri-axial accelerometers on the top of the cores of module D; no. 1 tri-axial accelerometer at the base of module D to investigate the ground accelerations; no. 2 displacement transducers by every bearing at top of the R.C. cores relative to module D, installed along two orthogonal horizontal directions of the restraints (i.e., no. 8 sensors with a stroke of 200 mm); no. 3 displacement transducers at each intermediate deck (I-II-III-IV deck) of module D, two of them mounted along horizontal parallel directions, and the third one perpendicular to the latter (i.e., no. 12 sensors with a stroke of 100 mm); no. 1 tachy-anemometer by the covering deck of module D; no. 1 gonio-anemometer on the covering. The tri-axial accelerometers allow to record along three directions (two horizontal and one vertical) the possible accelerations induced by human activities, natural causes and seismic events. Therefore, the installation of a tri-axial accelerometer at the base of module D fixed to the ground, enables to measure the intensity of occurring earthquakes. In correspondence of each deck, the monitoring system involves the mounting of a tri-axial sensor together with a uni-axial accelerometer oriented along a horizontal direction parallel to one of the horizontal accelerations measured by the first triaxial sensor: this arrangement lets obtain the signal amplification with respect to those acquired at the base and by the other decks, and provides an evaluation of the rotational acceleration of the deck. The installation of the acceleration sensors by the intermediate decks (I, II, III and IV floor) is planned at the intrados of the bottom flange of the main beams. On the other hand, the uni-axial and tri-axial accelerometers (two sensors) of the covering deck, have to be placed on the top of the antiseismic bearings, i.e. above the device's part which absorbs the movements due to thermal excursions. Finally, the last four tri-axial accelerometers have to be put by the seismic bearings of module D, each at the bottom of one device, i.e. fixed to core's top.

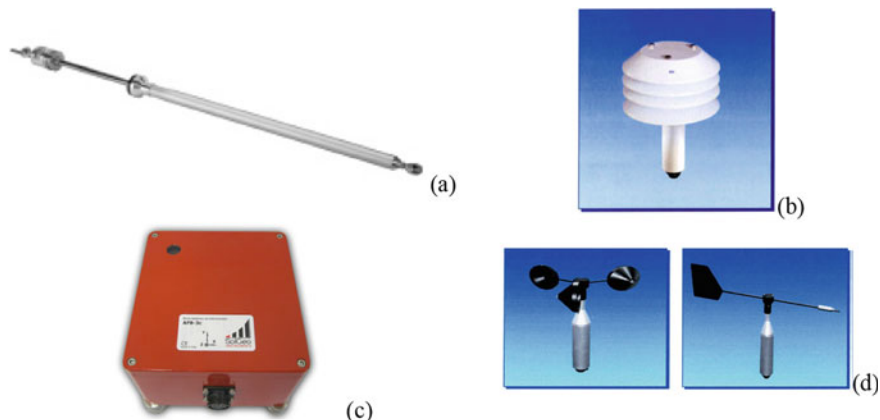


Fig. 12 Displacement transducer (a), temperature and humidity sensors (b), acceleration transducer (c), the displacement sensors, and tachy-gonio-anemometer (d)

The magnetostrictive linear position transducers (Fig. 12a), type GEFTRAN RK XL0319 (<https://www.gefran.com/en>), have a measurement range of ± 50 mm or ± 100 mm, and the ability to react to maximum accelerations of 100 m/s^2 . Their installation by the supports in both the horizontal directions, has to be carried out by means of a rigid bar between that upper part of the seismic bearing able to move under thermal variations, and the core's top representing the fix reference.

The uni-axial and tri-axial accelerometers (Fig. 12c) are “Force-balance” (type AFB—http://www.solgeo.it/media/strumento/SOLGEO_AFB_r.pdf) and have overall dimensions $14 \text{ cm} \times 15.5 \text{ cm} \times 8.5 \text{ cm}$. They are characterized by high sensitivity and low noise, and they are able to measure in each direction accelerations in the range $\pm 2.0 \text{ g}$ with sensitivity 2.5 V/g and acquisition frequency in the range $0\text{--}200 \text{ Hz}$.

The temperature transducers (Fig. 12b), in compliance with the WMO (World Meteorological Organization) standards, operate with natural ventilation and are able to measure temperatures in the range -40 to $+60 \text{ }^\circ\text{C}$ with a resolution of $0.01 \text{ }^\circ\text{C}$. They are made of a platinum Pt100 thermo-resistance sensitive to the changes of temperature.

The humidity sensor (Fig. 12c) contains a thin film that changes the capacity in linear mode with the air humidity; their measurement range is from 0% up to 100% , with a resolution of 0.05% .

The tachy-gonio-anemometer (Fig. 12d) consists in a sensor measuring the wind velocity (tachy-anemometer) in the range $0\text{--}50 \text{ m/s}$ by means of a toroidal magnet and a Hall effect probe, while a special high accuracy potentiometer is used to measure the wind direction (gonio-anemometer).

The above data acquisition systems are configured to provide data according to three acquisition strategies, each storing files in pre-defined directories:

- ‘*Threshold*’ acquisition strategy, connected to the dynamic sensors previously listed, is programmed to continuously record when a seismic event occurs that exceeds a fixed threshold value, the latter being modifiable by the software; therefore, data from the displacement transducers are recorded at the same sampling frequency of accelerations. Besides, it is possible to modify the acquisition frequency, the pre-trigger and post-trigger time values. Therefore, the ‘*Threshold*’ acquisition strategy is activated when a seismic event occurs, causing that, for example, the horizontal accelerations at building’s covering exceed a threshold value of 0.004 g. Thanks to the setting of a trigger, the dynamic monitoring system records the accelerations in all the measurement points, thus permitting to define or quantify the damaging produced by strong earthquakes to the structure and the antiseismic bearings.
- ‘*Periodical*’ acquisition strategy, programmed to store every 6 h the signals provided by the displacement transducers, the temperature transducers, as well as the igrometer. The ‘*Periodical*’ acquisition strategy allows to verify the proper operation of the whole constraint scheme of each module. Only in module D, the relative displacements with respect to the R.C. towers are measured at all the floors, in order to obtain a complete overview of the structural response to thermal variations and of the bumpers’ action.
- ‘*Continuous time*’ acquisition strategy, programmed to record, over a 10 min period, the mean value of the signal produced by the tachy-gonio-anemometer, as well as minimum and maximum values of wind velocity and direction. The ‘*Continuous time*’ acquisition strategy makes it possible to obtain a large amount of data regarding wind intensity and direction, that can be exploited to apply operational dynamic identification techniques with environmental input. The suspended configuration of the structure makes deeply interesting the correlations between the wind phenomena and the structural vibrations.

4 Up-Lifting Test of a Seismic Bearing and Dynamic Tests with Vibrodine

In order to validate the results of numerical analyses performed on the structure, it is useful to obtain an experimental reliable measure of the vertical stiffness of the supporting devices, by means of an intervention of local lifting at the roof level at one of the special seismic bearings. This would also permit to assess the integrity of the device and its rubber core. Two hydraulic jacks, symmetrically installed with respect to the bearing along transversal direction (Fig. 13), are required to rise the top steel girder by the seismic device, up to the unloading of the latter from the gravitational force: by knowing the measured vertical displacement upwards corresponding to the relaxation of the device and the force applied from the jacks to contrast the covering’s weight and produce the uplift, a measure of the device’s vertical stiffness can be computed.

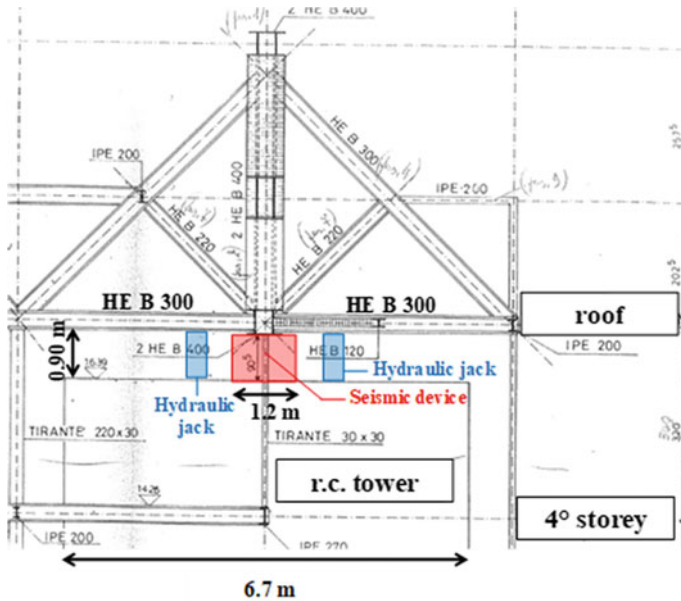


Fig. 13 Layout of the up-lifting test of the seismic device

It has been planned to unload a uni-directional or bi-directional bearing of module D. The available space where to work and install the hydraulic jacks is around 0.90 m, while the expected required force to be applied is in the range of 320–420 ton. The two actuators (each having a maximum force of 2500 kN) and the displacement sensors (with 50 mm stroke) have to be mounted between the extrados of the top floor of the R.C. core and the intrados of the transversal steel girder, in the available space of approximately 90 cm.

Further dynamic tests, using a vibrodine, have been designed to the aim of evaluating the dynamic behaviour of the structure once the monitoring system will be installed. A linear oleodynamic vibrodine, having piston's stroke of ± 125 mm, minimum and maximum moving masses of 75 and 475 kg respectively, and 12kN instability loading, is able to ensure high performance at low testing frequencies. During the experimental tests, carried out at different force levels, the response of the structure is acquired by the sensors of the monitoring system installed on the building, and by additional six accelerometers. The vibrodine will be placed by the first deck of module D to shake the whole structure.

5 Conclusions

Starting from the requirement of an effective seismic retrofit intervention of the headquarter suspended structure of the main Fire Station in Naples, the proposed work discusses the design of some interventions defined in the Urban Regeneration Project of East Naples: a static and dynamic monitoring system of the very peculiar investigated building structure, a rising test of one supporting bearing, and some dynamic tests using vibrodine. Their objective is: (i) to get a complete understanding of the whole mechanical and dynamic behavior, even influenced by an articulated system of devices, (ii) to improve the structural numerical models of the structure, and (iii) to single out a proper seismic retrofit intervention.

The integrated static and dynamic monitoring system is very important for the evaluation of the damage and the reliability level of the investigated structure, subjected to both environmental inputs and rare events like earthquakes. The lifting intervention on one seismic bearing will consist in the unloading of one bearing through the simultaneous operation of two hydraulic jacks thus providing a measure of its effective vertical stiffness. Then, as further contribution to the assessment of the structural dynamic behaviour, some dynamic tests with a vibrodine have to be performed. All the obtained results are useful to better calibrate both the complex FEM model and the simplified model, and then to more accurately predict the response of the structure under the effect of different dynamic inputs.

References

1. Mazzolani FM (1986a) Le strutture sismo-resistenti della nuova caserma VV.FF. di Napoli. *Costruzioni Metalliche* 38(6):343–362 (in Italian)
2. Mazzolani FM (1986b) L'applicazione del 'base isolation system' a strutture sismo-resistenti in acciaio. *Acciaio* n°4 (in Italian)
3. Mazzolani FM (1990) Le strutture sismo-resistenti del fabbricato A della nuova Caserma VV.FF. di Napoli. *L'ingegnere* n°12 (in Italian)
4. Mazzolani FM, Serino G (1997) Top isolation of suspended steel structures: modelling, analysis and application. In: 2nd international conference on behaviour of steel structures in Seismic areas. Kyoto, Japan
5. De Silva D, Nuzzo I, Bilotta A, Losanno D, Nigro E, Serino G (2017) Fire and seismic assessment of an existing steel-concrete composite structure. In: 8th European conference on steel and composite structures. September 13–15, Copenhagen, DK
6. Losanno D, Londono JM, Spizzuoco M (2013) Structural monitoring system for the management of emergency due to natural events. In: 2013 IEEE workshop on environmental, energy and structural monitoring systems—Proceedings 6661703

A Structural Engineering Perspective on the Use of Remote Sensing Measurements for Civil SHM



Giovanni Fabbrocino , Emanuele Petracca, and Carlo Rainieri 

Abstract The last decades offered to the civil engineering scientific and technical community the opportunity to improve their diagnostic and assessment capability due to a significant sensing technology development. Many non-destructive testing techniques have been developed in a way that no-contact measurement can be taken, even in harsh environments. At the same time, dynamic testing and vibration-based monitoring are becoming very attractive for the health assessment of structures, also thanks to the increasing availability of powerful and compact devices able to perform complex calculations with low or moderate power demand. On the other hand, remote sensing techniques, which are currently well established for earth observation and therefore adopted in the assessment of large-scale geological phenomena, are increasing their resolution and capabilities of detailed description of changes in the configuration of the surface based on data collected by the satellite constellations. Because of the enhanced observation capacity, their use for detailed monitoring of structures and infrastructures, not necessarily distributed in nature, has been largely debated by the technical and scientific community in recent years. Starting from these technological advances in the field of satellite measurements, the present paper reports some insights made by the research group on the use of remote sensing data for health monitoring of civil structures. Attention is focused on the approach to data analysis. The applicative perspectives of remote sensing in the field of civil Structural Health Monitoring are finally discussed with reference to some explanatory case studies.

G. Fabbrocino (✉)

ITC-CNR, Institute for Construction Technologies, Italian National Research Council, L'Aquila 67100, Italy

e-mail: giovanni.fabbrocino@unimol.it

G. Fabbrocino · E. Petracca

Department of Biosciences and Territory, University of Molise, Campobasso 86100, Italy

e-mail: emanuele.petracca@studenti.unimol.it

C. Rainieri

ITC-CNR, Institute for Construction Technologies, Italian National Research Council, Napoli 80146, Italy

e-mail: rainieri@itc.cnr.it

Keywords DinSAR · Remote sensing · Bridge monitoring · Data processing

1 Introduction

The last decades offered to the civil engineering scientific and technical community the opportunity to improve their diagnostic and assessment capability due to the dramatic development of the technology [1, 2]. Many non-destructive testing techniques have been developed in a way that no-contact measurement can be taken, even in harsh environments [3–5]. Dynamic testing and vibration-based monitoring is becoming at the same time a very attractive solution for the health assessment of structures in near-real-time thanks to the availability of reliable and robust analysis tools supported by the diffusion of powerful and compact devices able to perform complex calculations with moderate to low energy demand [6–8].

On the other hand, remote sensing techniques, which are well established for the observation of the earth and therefore adopted in the assessment of large-scale geological phenomena, are increasing their resolution and capabilities of detailed description of changes in the configuration of the surface based on data collected by the satellite constellations [9]. Because of the increased observation capacity, their use for detailed monitoring of structures and infrastructures, not necessarily distributed in nature, is being more and more debated by the technical and scientific community.

The present paper reports some experiences from the activities carried out by the authors in the context of a National research project on the use of remote sensing data for health monitoring of civil structures. Attention is herein focused on the approach to data analysis and the applicative perspectives of remote sensing for civil structural health monitoring (SHM). Some considerations made from the perspective of structural engineering are proposed along with some explanatory case studies.

2 The Measurement Technique

Remote sensing is the set of techniques used to obtain qualitative and quantitative information of objects placed at a distance from the acquisition sensor, consisting in a properly designed structure—the antenna—for transmitting and receiving radiated energy that interacts with the investigated body. The support platforms for the acquisition equipment can vary between planes, drones, satellites, and space probes.

The main function of the antenna is to concentrate a radiated microwave energy into a beam of a given shape (pattern) for transmitting in a selected direction (look direction) and receive the energy reflected by the object and/or surface of interest.

Microwaves are characterized by wavelengths ranging from a few centimeters to tens of centimeters and are very effective due their capacity of penetrating the atmosphere independently from the presence of clouds, fog, or pollution. For remote

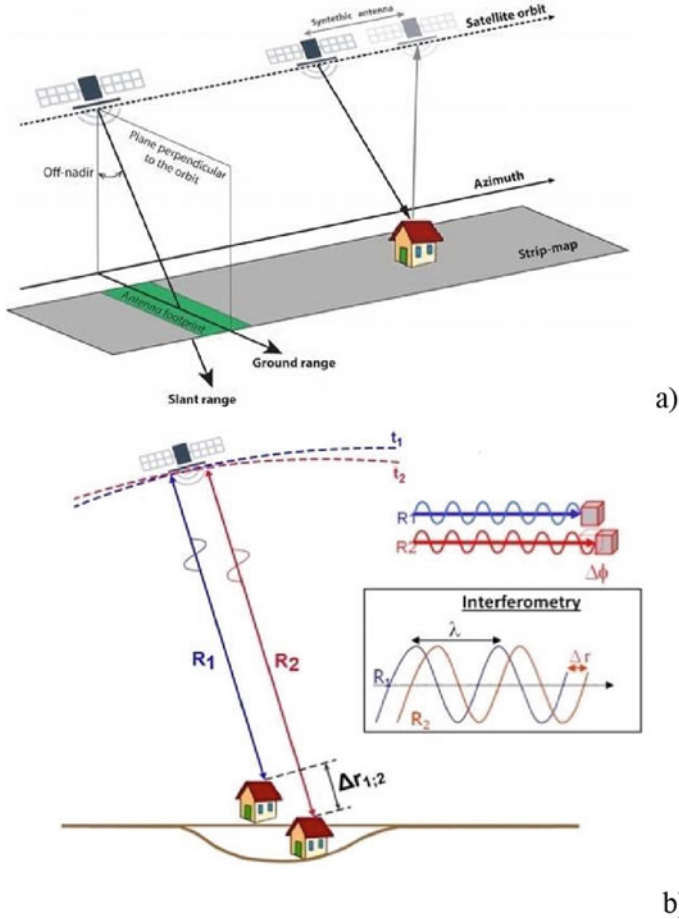


Fig. 1 Schematic view of SAR measurement configuration and basic nomenclature **a** principle, where λ is the microwave wavelength and $\Delta\phi$ is the measured phase of the returned signal **b** adapted from [12, 13]

sensing applications, the use of a coherent radar system able to provide high-resolution imagery is commonly called SAR (Synthetic Aperture Radar) [10, 11]. It is based on a travelling radar sensor and the processing of the signals taken over successive pulses, so that an image can be created, and the length of the antenna is artificially increased.

The portion of the earth’s surface illuminated by the satellite is called the footprint, while the direction joining the antenna to the target is usually indicated with LOS (line of sight) or with slant range (inclination range), the angle formed between this direction and the vertical is the angle of incidence (off-nadir) [10, 11].

Figure 1 offers a schematic view of the geometry of the measurement system and identifies the parameters, wavelength, and phase of the returned signal, associated with the displacements of the ground surface or of the object of interest [12].

The sketches in Fig. 1 also show that any displacement of the target system is detected by the radar in the form of its projection on the LOS direction identified by blue and red lines. Consequently, the problem of the definition of the real displacement of the target is not well conditioned and characterized by a unique solution. The combination of the data coming from two different orbits (ascending and descending along the meridians) can partially solve this issue.

Figure 2, indeed, reports a geometrical representation of the displacements along the LOS direction along with the perpendicular flat surfaces that identify all the movements that cannot be seen by the radar system; the intersection of the two surfaces associated to the ascending and the descending orbit, approximately identifies the N-S direction, highlighted by a dashed line.

In summary, use of the remote sensing data for structures point out the following aspects to be assessed for an accurate and reliable data processing: (i) measures suffer a time distribution that is not dense and regular; (ii) the data associated to a single orbit suffer of an incomplete description of the motion; (iii) the combination of the orbits can improve the description of the motion; (iv) the measures along the LOS coming from different orbits are not simultaneous; (v) fast changes of the

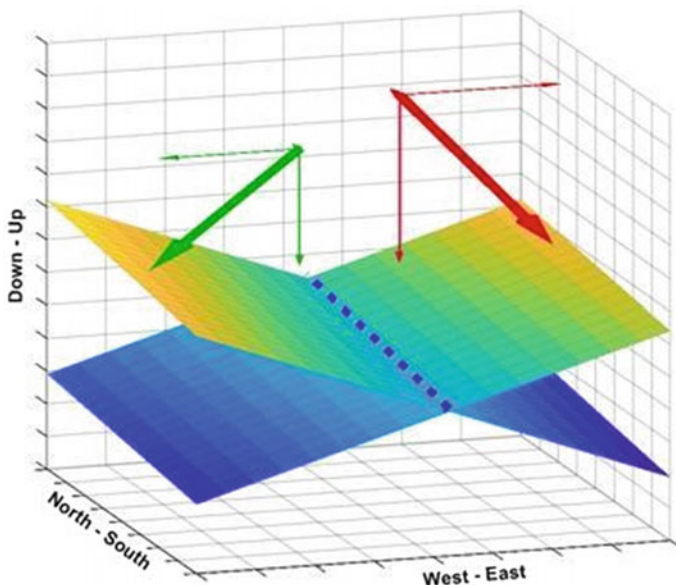


Fig. 2 Visualization of the velocity vectors along with the loci of the missing data: flat surfaces perpendicular to the LOS and approximately the N-S direction, which is the direction of the satellite motion

environment due to sudden phenomena associated to high magnitude displacements can be reconstructed [14, 15].

3 Remote Sensing for Structural Monitoring: The Radar Specialist's Perspective

The potentialities of the technology are well described in Fig. 1 and they are very attractive and relevant for large-scale monitoring, i.e. monitoring of regions affected by geological and geotechnical phenomena [16]. Another interesting field of application of the remote sensing techniques relies with the coseismic effects associated with earthquakes in the form of single events or in terms of sequences of events [14, 15].

It is worth noting that the results provided in the recalled technical literature may be demanding in terms of methodology refinement and associated computational effort, but they are not constrained in terms of compatibility of the kinematics of the observed items. This is not the case of the civil engineering structures, which in general may be monolithic (rigid) or suffer internal deformation depending on the type of the imposed load. In the present section, the perspective of the radar specialists is described according to the results of an investigation focused on the Polcevera bridge in Genoa [17], whose service ended with a collapse in summer 2018 [18]. Staying apart from the discussion of the data processing issues [19, 20], attention is here paid on the outcomes of the study and the claims by the authors—radar domain specialists—based on a complex and rigorous, but demanding from the computational standpoint, processing of the data collected from different satellites constellations during the three years before the collapse of the so-called balanced system (pillar) #9 of the viaduct.

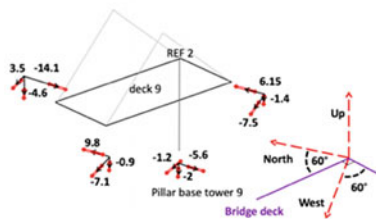
Figure 3 shows the satellite view of the well-known bridge and its orientation with respect to the North direction. With reference to the collapsed balanced system, it summarizes the main results of the radar specialist's analysis; the sketches and the data are adapted from the original data, expressed in terms of trends - velocities - identified by the direction and the orientation of the vector.

According to the outcomes of the analysis, a trend is shown by the measures; in particular, they sustain that a downward motion affects some parts of the balanced system #9 and that the magnitude of the displacement is affected by a stable trend.

An insight of the results is provided in Fig. 4, where the deformed shape of the deck computed according to the trends computed by Milillo et al. [17] are given. The deformation of the deck is computed by a quadrangular mesh computed to fit the provided data. The calculated displacements show transverse deformations in the deck that reach values of about 0.31% at the Northern end, while the vertical translations, which would be expected to be predominant in a cable-stayed structure subject to collapse, remain extremely limited.



a)



	Trends [mm/yr]			Accuracy [mm/yr]		
	E	N	U	EE	EN	EU
NW	-3.5	-14.1	-4.6	2.1	7.5	1.1
SW	-7.1	9.8	-0.9	2	6.1	1
SE	-7.5	6.15	-1.4	3.5	6	1.1
B	-1.2	-5.6	-2	2	5.3	1.5

b)

Fig. 3 View of the Polcevera Viaduct, **a)** source Google Maps; results of the remote sensing data for the balanced system (pile) #9, **b)** adapted from [17]; B stands for ‘Bottom’, ‘Base’

However, regardless of the magnitude of the deck strain, some issues exist in the presentation of the data and their setting. The displacement velocity, indeed, refers to a point positioned at the North-East end for each deck and does not account for the intermediate support of the deck placed at the two sides of the tower.

This circumstance points out the relevance of a proper interpretation of the main features of the structure under investigation, which must interact and guide the processing of the data collected by the remote sensors.

4 Data Processing from DinSAR Technique from the Perspective of the Structural Engineer

The present section is devoted to report preliminary considerations by the authors in relation to the direct management and interpretation of remote sensing data. They are generated by the research group from the IREA-CNR coordinated by

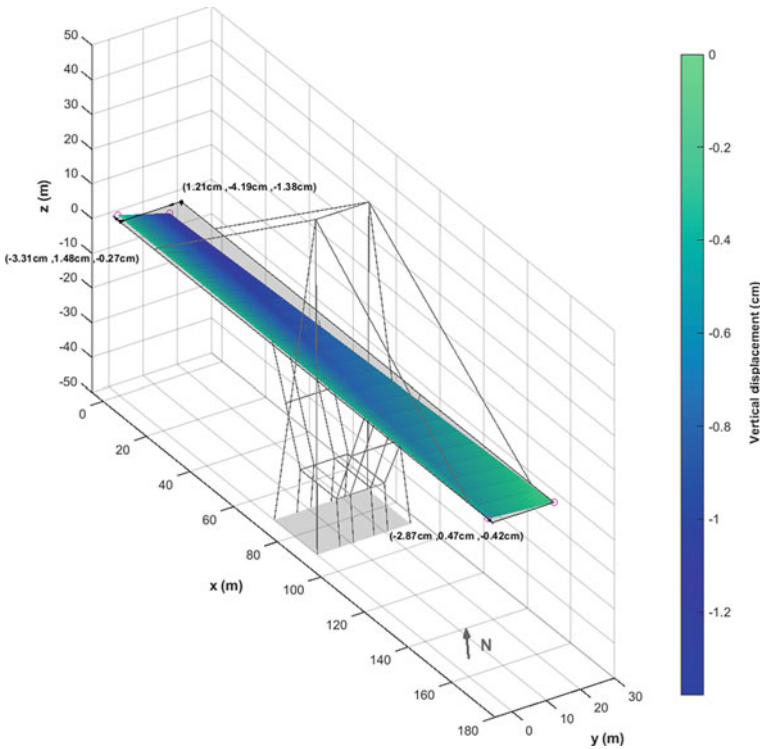


Fig. 4 Schematic view of the balanced system #9 of the Polcevera Viaduct; deformation of the deck is based on the data in Table 1, adapted from [17]

Riccardo Lanari. The data refer to the metropolitan area of Rome and cover a period between 2011 and 2019; measurements are processed by using the COSMO-SkyMed Stripmap HIMAGE according to the small baseline subset (SBAS) algorithm [21].

The radar measurements taken during the ascending and descending orbital trajectories of the satellites have been processed to make available to the community involved in the WP6 ‘Monitoring and remote sensing’ issued by Reluis Consortium under coordination of the DPC (Department of the Civil Protection) a relatively dense array (about 41 million points, resolution 3 m by 3 m) of displacements in the LOS direction along with the average velocity of the point of interest.

One of the most relevant features of the methodology chosen by IREA-CNR is the number of points per surface unit and the potential extension in time of the measurements due to the long-lasting operation time of the satellite constellation. Due to the specialistic nature of the topic and need of brevity associated with the present contribution, the interested reader can refer to the background literature for details [22, 23].

Following the outcomes of the critical review of previous experiences on critical infrastructures, an effort is made to focus the attention on the problem from the

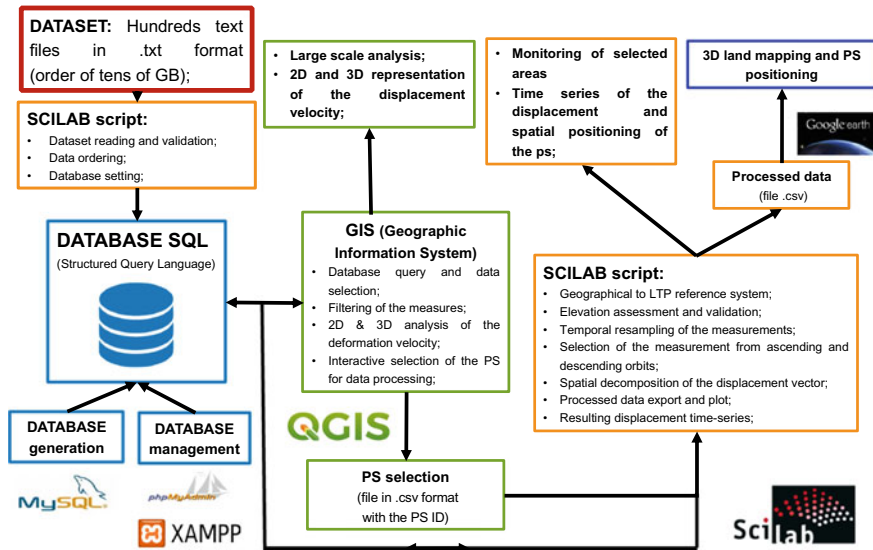


Fig. 5 Workflow for the data processing of the DinSAR data

perspective of the SHM operator, whose primary skills and technical knowledge fall in the area of civil engineering and physical measurement processing.

The availability of a large amount of data, like those provided by IREA-CNR, represented an attractive opportunity to establish a methodology able to exploit the potential of remote measures for detecting response anomalies and damage to civil engineering structures.

Data provided by IREA-CNR are given in the geographical coordinate system, therefore a change of the reference system is needed to place in the Local Tangent Plane (LTP) coordinates system and make the data useful for structural evaluations.

Figure 5 represents the workflow designed for the data processing. It enables a full management of the measurement datasets in compliance with the available computational resources. On this point, it is worth noting that the operational framework has been designed so that an area associated with a number of urban blocks or with extended architectural complexes or infrastructures can be assessed.

4.1 What Does the Radar See?

It is known that the data provided by the radar sensors are differential, so that all the deformation data provide a displacement from a reference configuration of the observed space that can be computed in a LTP coordinate system, as previously mentioned.

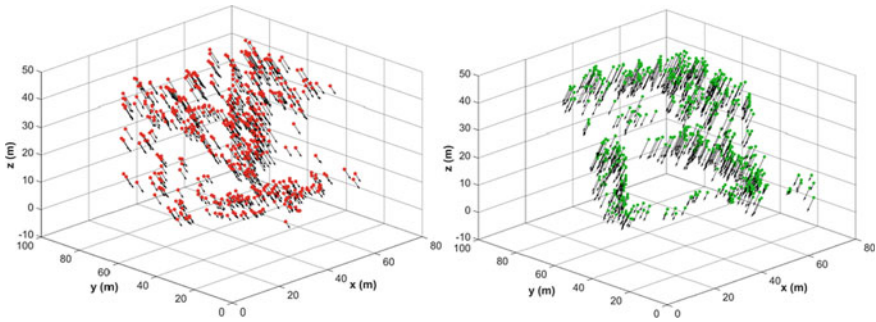


Fig. 6 Displacements in the LTP reference system; red is the ascending orbit; green is the descending orbit

The processed radar measures provide a cloud of points associated to each satellite passage, which can be reported in a 3D reference system, like those reported in Fig. 6 for both the ascending and descending orbit. The two plots describe the geometry that can be associated to the initial position of the Persistent Scatterers (PS) and provide a view of the measured displacements along the radar LOS direction at a given time of observation. The point clouds clearly describe a volume, whose shape reports to a building framed from different standpoints [25].

This circumstance is clearly explained by the graphical material collected in Fig. 7. It reports the views of a building located in metropolitan area of Rome taken from the Google Earth platform along with the representation of the point clouds associated to the ascending and descending orbits; on this subject, it is worth mentioning the need of validation of the reference elevation of the points, which in general is affected by an offset; its magnitude must be assessed in each cloud and removed from the data. The procedure is not complex, but it is a key step for the geometrical identification of the point clouds. Figure 7a reports the view of the building from the radar sensor location associated with the ascending orbit; Fig. 7b reports the view from the location of the descending orbit radar antenna.

It is worth noting that point clouds are different and in a certain way complementary, since they define the geometry of the target building integrating the two different points of view.

An attempt to sketch the overall shape of the building is reported in Figs. 7c, d, that show a triangular mesh based on the combination of the two-point clouds, the first one associated to the view available from the ascending orbit, the latter based on the view from the descending orbit.

The result of data processing is basically coarse, and the definition of the building shape is not effective, even though the computed mesh seems to be useful for operators in another relevant phase of data interpretation consisting in the matching between remote sensing data and tools for the realistic 3D representation of urban environment. It is worth noting that the comments reported above indeed apply to the data processed by means of the DinSar technique and that different procedures can provide a more refined definition of the building volumes [26–28] in the case

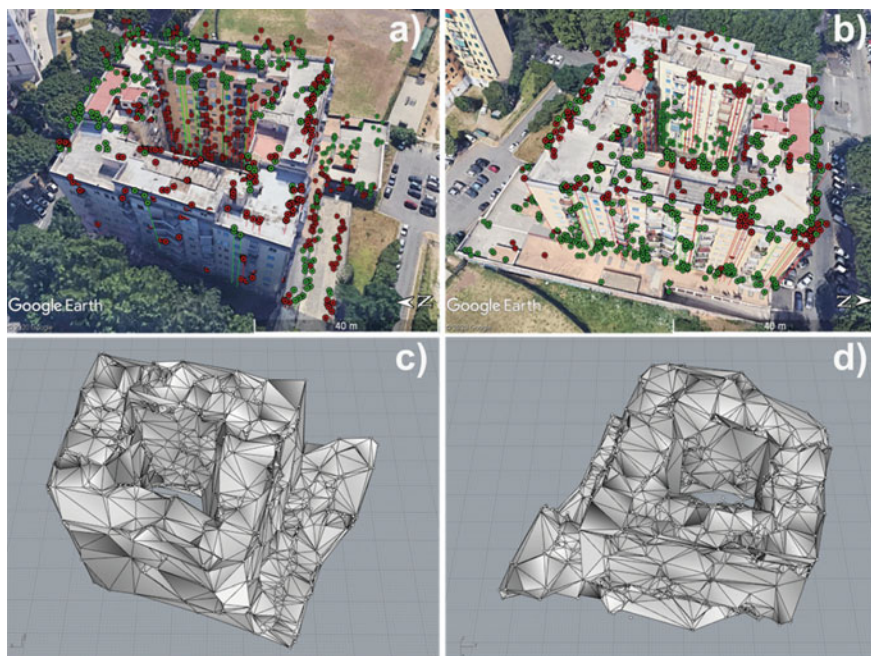


Fig. 7 Point clouds allocated in Google Earth [24] 3D view of the selected building, **a**) & **b**) (red is the ascending orbit, green is the descending orbit); 3D mesh of the point clouds associated to each satellite orbit **c**) & **d**)

of dimensions larger than the common structures located outside densely inhabited areas.

4.2 Time and Space Lags of the Measurements

The dispersion of the data in time and space represents a key problem of the remote sensing data and clearly introduces uncertainties and bias in the measurements. It is well known that measuring means to ascertain the size, amount, or degree of (something) by using an instrument or device marked in standard units. This action actually corresponds to the way the sensor works in the LOS direction, but more complicated is the knowledge in the area of civil engineering, since the data are required in the LTP coordinates and are affected by a blind sensor in a single direction in the favourable case of combination between ascending and descending orbit.

This is the reason why, the first problem to be solved is the time synchronization of data. Figure 8 (top) shows the displacements measured along the LOS direction of one of the points shown in the previous plots—the two time series are identified by green triangles and red circle, given that the color identifies the orbit of interest.

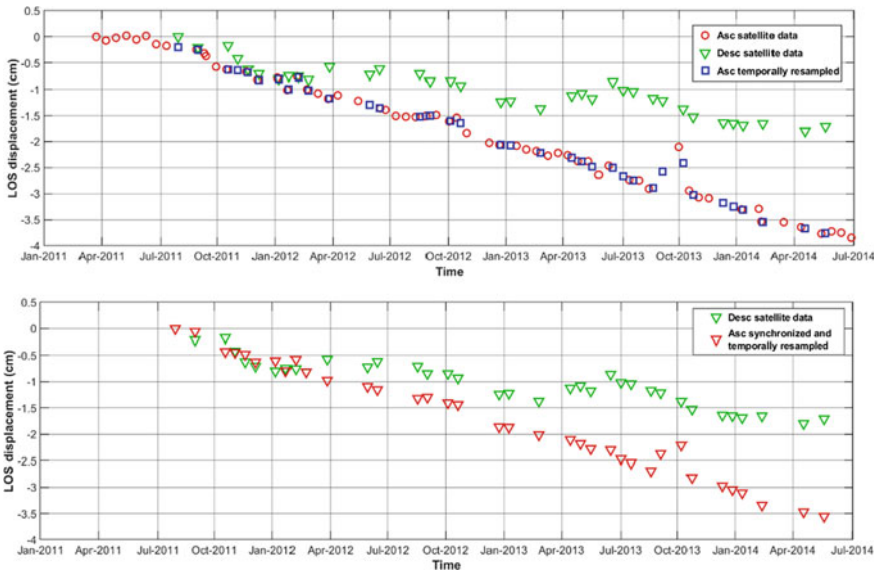


Fig. 8 Time distribution of the measures (points identified by circles) and resampling of the data associated to the ascending orbit (points identified by squares), top; displacements of the two orbits realigned in time (points identified by triangles), bottom

It is easy to recognize that the starting time of the data associated with the two orbits is affected by a lag, which makes the combination of the data associated to the two orbits complex. As civil engineering structures are concerned, this can be an issue that threatens the quality of the measures and their interpretation. Among the others, a rational approach to the treatment of the data and to reduce the uncertainty associated with the time lag is sketched in the same plot. Indeed, it shows that one of the arrays of measures is maintained unaltered, preserving in this way the data; the second one, particularly the one that starts first, is resampled in time, so that a reconstruction of the curve is achieved.

The time series identified by blue squares—Fig. 8 (top)—is the result of the resampling process carried out by the Modified Akima cubic Hermite interpolation [29], in a way that estimates at the time of the other orbit are synchronous. This leads to identify a time distribution of the synchronized displacements associated with the two orbits given in Fig. 8 (bottom), which are ready for further analyses. Interpolation techniques aimed at providing the resampling in time of the measures need careful consideration and validation in order to reduce undesired effects on the significance of the data; however they are not discussed here for sake of brevity, being such an aspect out of the scope of the present paper. Obviously, the workflow in Fig. 2 is scalable, modular, and flexible, so that insights on the resulting measures can be easily carried out.

The representation of the combination between ascending and descending orbit data is given in Fig. 9 along with the equation that provides the relation between the

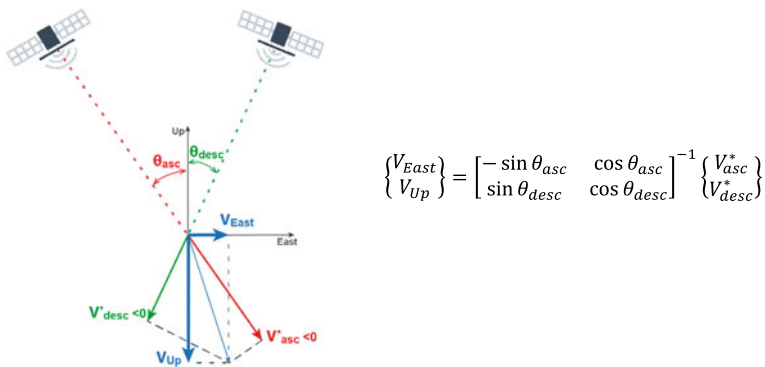


Fig. 9 Combination of the LOS measurements, sketch of the vector combination in the East West EW-UD Up Down plane (left); calculation associated with the vector combination, right

two LOS displacements and the estimated ones under the assumption of displacement equal to zero in the N-S (North-South) direction. It is worth noting that measures made available by radar specialists provide to the technical community the three direction cosines. A component of the measure along the North direction - depending on the real satellite trajectory and on its height - exists, even though very small and commonly neglected. This is not the case reported in Fig. 9, since the sketch reported on the left-hand side identifies the projection of the LOS displacement associated to each orbit on the vertical flat surface identified by the E-W (East-West) and U-D (Up-Down) directions.

The space lag between the points is commonly addressed in the literature, but there are not well-established processing procedures to select the points of interest. Depending on the radar data processing technique and the associated density of the PSs a certain level of judgement of the operator is leveraged. As usual in the case of diagnostics and interpretation of experimental data, the skill and the capacity of the operator is certainly relevant, but it may also represent a drawback in the case of large amount of data and structures of interest. This is the motivation of the selected approach to the processing of the measures described below. Automation, scalability, and flexibility are the main characteristics of the code section devoted to the extraction of displacements associated to a target building.

Figure 9, unfortunately, illustrates an ideal condition, whose probability of occurrence in practice is low, ideally zero. In other words, the two estimates in terms of displacement of the reflecting area on the structure or on the ground may exist, but they cannot be associated to a single point. This circumstance may be clear if Fig. 7 is carefully analyzed, but it is better illustrated in the plots of Fig. 10.

The plots show the geometrical representation of the automated clustering procedure implemented to combine the time synchronized data associated to the ascending (red) and descending (green) orbits. They refer to the same collection of points shown in Fig. 7 and clearly confirm the statement reported above. It is unusual in a

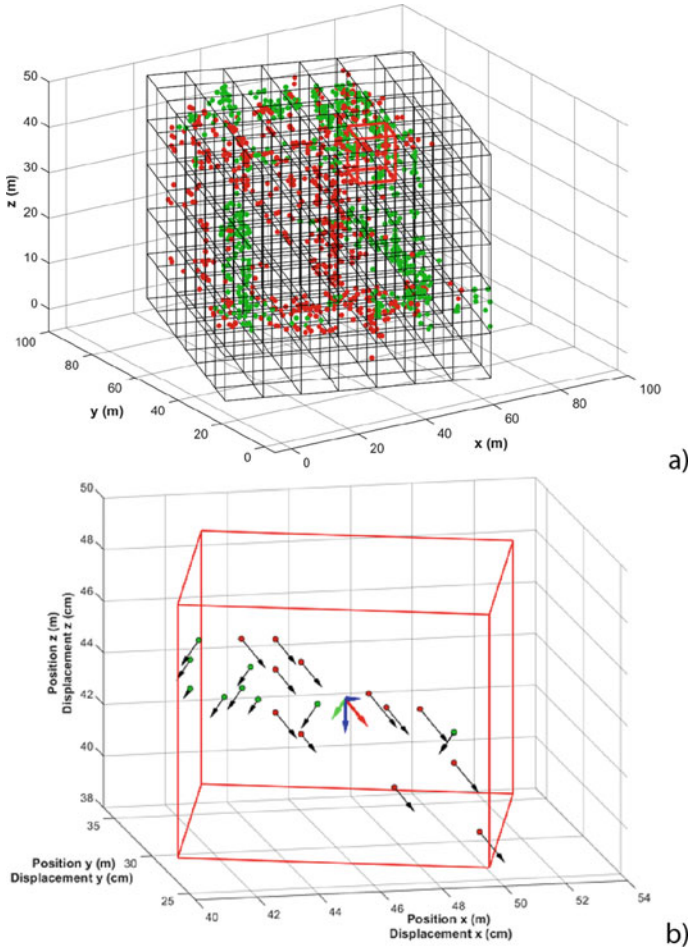


Fig. 10 Geometrical clustering of the data; view of the 3D grid for point selection in the LTP coordinates, **a)**; local cluster of measures and averaged measures, **b)**

real database that the combination of data can be performed according to the sketch reported in Fig. 9.

Conversely, an intermediate passage through a clustering of the points and the computation of average values of the displacement/velocity magnitudes is required.

This is what the two plots illustrate; particularly Fig. 10b shows the extraction of the 3D points allocated in the generic reference cubic volume identified in Fig. 10a in red, predetermined by the definition of the side length. The automated extraction of the points and of the associated displacements makes possible the computation of an average displacement vector that can be tracked in time and assumed as a reference for diagnostic purposes.

Despite the specifications of the measurements in the radar coordinate plane (slant range image), the geometrical reconstruction of the observed environment offered by the DinSAR technique is affected by an irregular distribution of points, so that in the case of radar illuminated surfaces, an inhomogeneous distribution of the points in the elementary volumes is expected, even determining the presence of void cubes. This leads to recognize that the combination of the orbits can be affected by an intrinsic bias depending on the time shift between the two orbits, and on the position in the space of the reflecting surfaces [28]. A detailed assessment of the mentioned uncertainties is out of the scope of the present paper; however, the issue of the combination of different orbits or even different satellites constellations is relevant and requires a careful consideration in the measurement validation and interpretation. The latter are certainly critical phases of the process, that should be as much as objective and automated as possible, as the concept of measure requires.

In summary, Fig. 10 shows that an automated clustering of the measurement points can support the combination of the information gathered by the two orbits and the interpretation of the measurements in view of physical and built environment monitoring. On this specific aspect, it is worth noting that this approach is basically novel compared to all the GIS based approaches, whose utilization is in the technical area of geological and geotechnical problems.

4.3 Some Effects of the Synchronization Procedure

As mentioned before, an extensive validation of the remote sensing data processing is out of the scope of the present paper; nevertheless, it is deemed to offer to the reader some considerations on the main characteristics of the measurements before and after the synchronization process. This objective is here pursued by means of the analyses of two sets of data: (i) the first one is represented by the PS selected on the building of Fig. 7, which is located in one of the sites of the investigated area where major displacement velocities are found; (ii) the second is a bridge on the Tevere river, the S. Angelo Bridge—Fig. 11, which is one of the most attractive Rome attractions. The latter has been selected because of its different typology - it is an historical bridge - and the average displacement velocity - see Fig. 7a - is low.

The 3D PSs reported in Fig. 7c are processed and collected in the reference volumes represented in Fig. 8, which reports on the analogy with the process described before the clustering technique. On this subject, it is worth noting that the procedure can be applied without any problem to structures different from buildings; this leads only to count a larger number of void volumes, being the shape of the bridge marked by the distance between the piers and the deck placed at a given elevation.

Another aspect worth of attention is the orientation of the structure with respect to the North direction. This leads to a concentration of the points of each orbit on the surface illuminated by the radar; this means that the two-point clouds are fully separated, but the combination of the LOS displacements is more complex (Fig. 12).

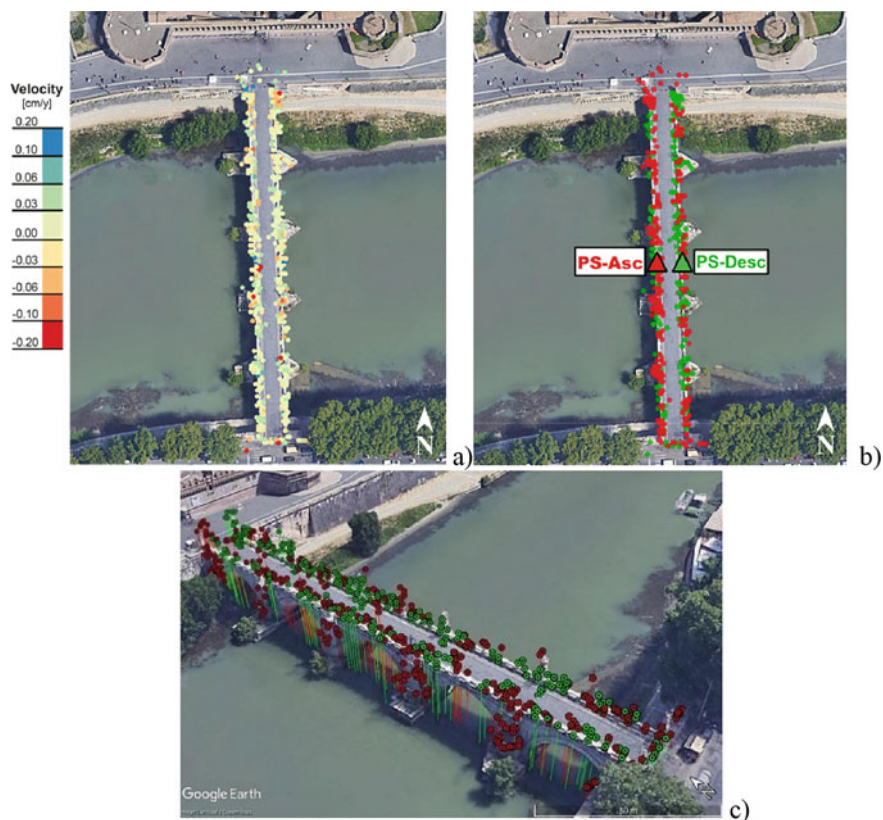


Fig. 11 S. Angelo Bridge. View of the LOS velocity distribution, by means of QGIS a); Selected points of interest on the two orbits, b); 3D PS view in Google Earth, c)

Figure 13 reports the results of the synchronization carried out for the two points of interest identified in Fig. 11b, which have been selected without the reference to a specific criterion. This is done to perform a sample check of the potential interference of the synchronization procedure with the basic features of the measurements.

The idea behind the assessment consists of a statistical characterization of the measures before and after the synchronization; this task is simplified by the availability of the descending orbit measurements that have been maintained unaltered and that therefore represent the term of comparison.

Table 2 collects the results of the comparative analysis of the data; they cover both cases in which geological and geotechnical features of the soil generated relevant deformation of building, plot of Fig. 8 (bottom), and stable cases like those represented in Fig. 13, the S. Angelo Bridge.

The statistical assessment has been performed on the data according to the following treatment sequence: i) the time series has been analyzed in order to remove linear trends, or in other terms a linear regression has been performed in order to

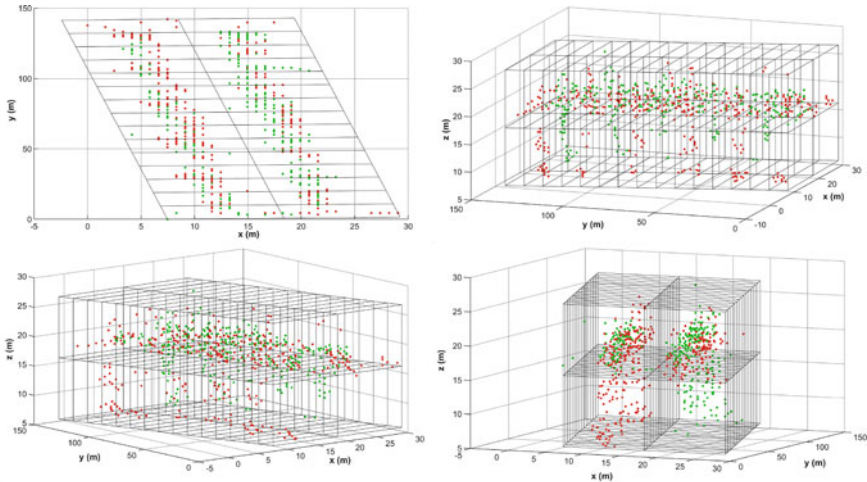


Fig. 12 Diverse views of the S. Angelo Bridge point clustering process

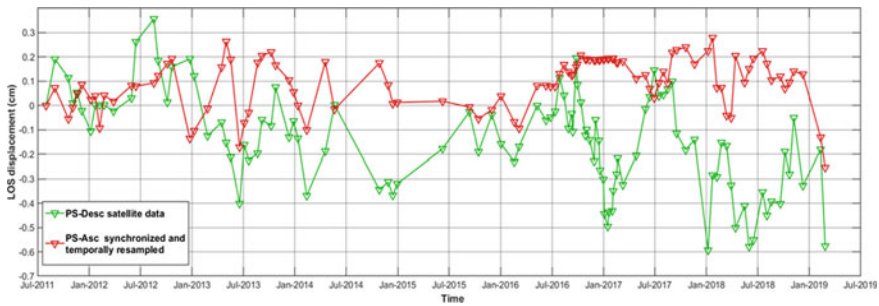


Fig. 13 S. Angelo Bridge; synchronized displacements of the POIs after Fig. 11

Table 1 Conversion of the trends in displacements; the time span is assumed as long as the observation period, adapted from [17]

Reference vertex	X-displacement [cm]	Y-displacement [cm]	Z-displacement (cm)
North-West	1.21	-4.19	-1.38
South-West	-3.31	1.48	-0.27
South-East	-2.87	0.47	-0.42

Axis identification is provided in Fig. 4

define a reference model of the data; the residues computed as the scatter between estimated and the real measures have been computed; residues have been characterized from a statistical point of view, computing the mean, μ , and the standard deviation, σ .

Table 2 Statistical assessment of the measures available for PSs available for the S

(1) (-)	(2) (-)	(3) [°]	(4) (°)	(5) (m)	(6) (-)	(7) (cm/y)	(8) (-)	(9) (-)	(10) (cm)	(11) (cm)
A. Asc*	113,806	41,90193	12.46640	26.58	0.81	0.020	0.013	0.038	0.000	0.101
Desc	96,661	41,90192	12.46651	20.96	0.62	-0.009	-0.044	0.046	0.000	0.172
B. Asc*	11,4414	41,85566	12.48513	48.28	0.87	-1.140	-1.128	-0.186	0.000	0.106
Desc	40,457	41,85520	12.48488	45.29	0.79	-0.540	-0.534	-0.271	0.000	0.184

Table title keys:

(1) Orbit	(2) Point ID	(3) Latitude	(4) Longitude
(5) Elevation	(6) Coherence	(7) LOS velocity	(8) Regression slope
(9) Regression intercept	(10) Residue μ	(11) Residue σ	

Angelo Bridge—Fig. 13—(A.) and Giustiniano Imperatore building—Fig. 8, bottom—(B.). The asterisk identifies the synchronized orbit

The analysis of the data, including the computed parameters of the linear regression slope and intercept, show that the basic features of those associated with the descending orbit are similar to the synchronized data coming from the ascending orbit. In addition, it is worth noting that the statistical parameters, at least for the selected points, are not influenced by the magnitude of the displacements.

The result seems to be positive, but it cannot be offered as consolidated, being generated for a single case. Further and more comprehensive assessments are needed to mark this observation as generally applicable.

5 Concluding Remarks

The present paper dealt with the opportunities and potentialities offered by remote sensing techniques in providing useful data on the deformation of large areas, including structures and infrastructures. In the field of geology and geotechnics, a consolidated knowledge and experience deliver to the technical and scientific community reliable data, even in the case of natural events, like earthquakes.

However, two concurrent forces are empowering the capacity of radar-based sensing techniques in the field of the condition assessment of single civil engineering structures: the first one is the increased accessibility to high performance satellite networks, the second one is the spreading of high-performance computational capacity.

Consequently, it is the time of supporting from the point of view of the civil engineer the specialists in data processing, so that optimized and standardized approaches to the data interpretation can be defined. In such a context, the considerations reported above along with some basic aspects related to the measurement manipulation for an effective condition assessment of structures are aimed to point out the points of strength as well as the drawbacks of the technique, which in principle should provide interpretation of data independently upon the experience and the skill of the operator.

It is a complex problem that must be analyzed and tackled, so that potentialities and limits are well defined, and false alarms and missed alarms can be managed in a reliable way.

Acknowledgements The research carried out by the research unit UniMol belongs to the WP6 Project ‘Monitoring and Remote sensing data’ issued in the context of the ReLuis-DPC Executive Project 2019–2021, coordinated by Prof. F.C. Ponzo & Prof. M. Savoia. The Authors are grateful the colleagues Riccardo Lanari and Manuela Bonano from IREA-CNR for their openness to the debate and to a continuous exchange of opinions that opened the door towards an attractive and challenging technical and scientific field.

References

1. Chen H, Yi-Qing N (2020) Sensors and sensing technology for structural monitoring. *Structural health monitoring of large civil engineering structures*, Wiley 2018, pp 15–49
2. Zhang L et al (2018) Application of internet of things technology and convolutional neural network model in bridge crack detection. *IEEE Access* 6:39442–39451. Institute of Electrical and Electronics Engineers Inc.
3. Xu Y, Brownjohn JMW (2018) Review of machine-vision based methodologies for displacement measurement in civil structures. *J Civil Struct Health Monit* 8(1):91–110
4. Agdas D et al (2016) Comparison of visual inspection and structural-health monitoring as bridge condition assessment methods. *J Perform Constructed Facil* 30(3):909–916
5. Yi T et al (2010) Full-Scale measurements of dynamic response of suspension bridge subjected to environmental loads using GPS technology. *Sci China Technol Sci* 53(2):469–79
6. Rainieri C et al (2019) Hardware and software solutions for seismic SHM of hospitals. *Springer Tracts in Civil Engineering*, Springer, pp 279–300
7. Rainieri C, Fabbrocino G (2014) Operational modal analysis of civil engineering structures: an introduction and guide for applications. Springer, New York, USA
8. Rainieri C, Fabbrocino G (2015) Development and validation of an automated operational modal analysis algorithm for vibration-based monitoring and tensile load estimation. *Mech Syst Signal Process* 60–61:512–534
9. Bürgmann R, Rosen PA, Fielding EJ (2000) Synthetic aperture radar interferometry to measure earth's surface topography and its deformation. *Annu Rev Earth Planet Sci* 28:169–209
10. Moreira A, Prats-Iraola P, Younis M, Krieger G, Hajnsek I, Papatthanassiou K (2013) A tutorial on synthetic aperture radar. *IEEE Geosci Remote Sens Mag (GRSM)*. 1:6–43. <https://doi.org/10.1109/mgrs.2013.2248301>
11. VV. AA. (2009) Ministero dell' Ambiente e della Tutela del Territorio e del Mare, Direzione Generale per la Difesa del Suolo. Linee guida per l'analisi di dati interferometrici satellitari in aree soggette a dissesti idrogeologici. (in Italian)
12. Ferretti A, Monti-Guarnieri A, Prati C, Rocca F, Massonnet D (2007) InSAR principles: guidelines for SAR interferometry processing and interpretation. ESA Publications, TM-19. ISBN 92-9092-233-8
13. Mari R, Bottai L, Gozzini B, Bianchini S, Del Soldato M, Montalti R, Raspini F, Solari L, Casagli N, Pellegrineschi V, Bigiarini M, Massini G (2019) Monitoraggio radar satellitare delle deformazioni del terreno della Regione Toscana. Il sistema informativo e la rappresentazione dei dati. *Atti ASITA*
14. Solaro G, De Novellis V, Castaldo R, De Luca C, Lanari R; Manunta M, Casu F (2016) Coseismic fault model of Mw 8.3 Illapel Earthquake (Chile) retrieved from multi-orbit sentinel1-A DInSAR measurements. *Remote Sens* 8:323
15. Lanari R, Berardino P, Bonano M, Casu F, Manconi A, Manunta M, Manzo M, Pepe A, Pepe S, Sansosti E, Solaro G, Tizzani P, Zeni G (2010) Surface displacements associated with the L'Aquila 2009 Mw 6.3 earthquake (central Italy): New evidence from SBAS-DInSAR time series analysis. *Geophys Res Lett* 37:L20309
16. Fabbrocino S, Lanari R, Celico P, Termolini G, Zeni G (2007) Groundwater pumping and land subsidence in the sarno river plain (Campania). In *Mem. Descr. Carta Geol. d'It. LXXXVI*, pp 163–174
17. Milillo P, Giardina G, Perissin D, Milillo G, Coletta A, Terranova C (2019) Pre-Collapse space geodetic observations of critical infrastructure: the Morandi bridge, Genoa, Italy. *Remote Sens* 11:1403
18. Calvi GM, Moratti M, O'Reilly GJ, Scattarreggia N, Monteiro R, Malomo D, Martino Calvi P, Pinho R (2018) Once upon a time in Italy: the tale of the Morandi bridge. *Struct Eng Int* 29(2):198–217
19. Lanari R, Reale D, Bonano M, Verde S, Muhammad Y, Fornaro G, Casu F, Manunta M (2020) Comment on “pre-collapse space geodetic observations of critical infrastructure: the morandi bridge, Genoa, Italy” by Milillo et al. (2019). *Remote Sens* 12:4011

20. Milillo P, Giardina G, Perissin D, Milillo G, Coletta A, Terranova C, Lanari R et al (2020) Comment on “pre-collapse space geodetic observations of critical infrastructure: the morandi bridge, Genoa, Italy” by Milillo et al. (2019). *Remote Sens* 12:4016
21. Berardino P, Fornaro G, Lanari R, Sansosti E (2002) A new algorithm for surface deformation monitoring based on small baseline differential SAR interferograms. *IEEE Trans Geosci Remote Sens* 40:2375–2383
22. Bonano M, Manunta M, Marsella M, Lanari R (2012) Long-term ERS/ENVISAT deformation time-series generation at full spatial resolution via the extended SBAS technique. *Int J Remote Sens* 33(15):4756–4783
23. Bonano M, Manunta M, Pepe A, Paglia L, Lanari R (2013) From previous C-band to new X-band SAR systems: assessment of the DInSAR mapping improvement for deformation time-series retrieval in urban areas. *IEEE Trans Geosci Remote Sens* 51:1973–1984
24. Gorelick N, Hancher M, Dixon M, Ilyushchenko S, Thau D, Moore R (2017) Google Earth Engine: planetary-scale geospatial analysis for everyone. *Remote Sens Environ* 202:18–27
25. Yang K, Yan L, Huang G, Chen C, Wu Z (2016) Monitoring building deformation with InSAR: experiments and validation. *Sensors* 16:2182
26. Peng X, Wang C, Li X, Du Y, Fu H, Yang Z, Xie Q (2018) Three-Dimensional structure inversion of buildings with nonparametric iterative adaptive approach using SAR Tomography. *Remote Sens* 10:1004
27. Liu H, Pang L, Li F, Guo Z (2019) Hough transform and clustering for a 3-D building reconstruction with tomographic SAR point clouds. *Sensors* 19:5378
28. Dănișor C, Fornaro G, Pauciullo A, Reale D, Datcu M (2018) Super-resolution multi-look detection in SAR tomography. *Remote Sens* 10:1894
29. Akima H (1970) A new method of interpolation and smooth curve fitting based on local procedures. *J Assoc Comput Machinery* 17(4):589–602

Author Index

A

Aiello, Carolina, 585
Aiello, Maria Antonietta, 569
Alaggio, Rocco, 339
Aloisio, Angelo, 339
Altabey, Wael A., 431
Alviggi, Mariagrazia, 507
Amditis, Angelos, 761
Anastasopoulos, Dimitrios, 289
Anaya, Miguel, 271
Angelis De, Alessandra, 219
Arab, Zakwan, 115
Arezzo, Davide, 557, 957
Armonico, Andrea, 569
Arsenovic, Tomislav, 889
Ascari, Gianluca, 389
Auletta, Gianluca, 373
Aygun, Levent E., 967
Aziz, Kameran, 889

B

Ballio, Francesco, 793, 935
Basso, P., 151
Bassoli, Elisa, 515, 535
Bednarski, Lukasz, 775
Belloli, Marco, 793
Belsito, Luca, 761
Benedetti, Lorenzo, 793
Bernagozzi, Giacomo, 97
Berto, Luisa, 691
Billères, Malvina, 725
Bilotta, A., 677
Birgin, Hasan Borke, 485
Bolognani, Denise, 129
Bonano, Manuela, 373

Borlenghi, Paolo, 793
Bouklas, Kostas, 761
Brancato, Michael, 747
Buchmayer, Fabian, 825
Budillon, Alessandra, 257

C

Cademartori, M., 151, 159
Caetano, Elsa, 15
Çakti, Eser, 977, 991
Camarinopoulos, Stephanos, 761
Campopiano, Stefania, 507
Canale, Vincenzo, 507
Capuano, C., 677
Carapito, Paulo, 499
Carbonari, Sandro, 557, 957
Carrión, Francisco J., 271
Casapulla, Claudia, 699
Cascardi, Alessio, 569
Castelli, Paolo, 233
Caterino, Nicola, 585, 663
Cattin, Viviane, 725
Cavalagli, Nicola, 415
Celano, Thomas, 699
Ceroni, Francesca, 699
Chioccarelli, Eugenio, 585, 677
Cirella, Riccardo, 339
Clemente, Paolo, 311
Clementi, Francesco, 603
Corvaglia, Paolo, 747
Cunha, Álvaro, 15
Cuomo, Vincenzo, 373

© The Editor(s) (if applicable) and The Author(s), under exclusive license to Springer Nature Switzerland AG 2021

C. Rainieri et al. (eds.), *Civil Structural Health Monitoring*, Lecture Notes in Civil Engineering 156, <https://doi.org/10.1007/978-3-030-74258-4>

D

D' Alessandro, Antonella, [485](#)
 D' Angelo, Manuel, [793](#)
 De Angelis, Alessandra, [205](#)
 Del Zoppo, Marta, [177](#)
 Demirlioglu, Kltigin, [889](#)
 Deng, Baichuan, [197](#)
 Desbazeille, Mathieu, [725](#)
 Di Cicco, Antonio, [311](#)
 Di Giacinto, D., [403](#)
 Di Ludovico, Marco, [177](#)
 Diotallevi, Pier Paolo, [97](#)
 Ditommaso, Rocco, [373](#)
 Dönmez, Kökcan, [977](#)
 Doria, Andrea, [691](#)

E

Early, Juliana, [367](#)
 Erduran, Emrah, [889](#)
 Ertürk, Sefer Ömercan, [991](#)
 Esposito, M., [663](#)

F

Fabbrocino, Giovanni, [645](#), [699](#), [869](#), [1015](#)
 Facchini, Massimo, [167](#)
 Falco De, Melania, [359](#)
 Favarelli, Elia, [809](#)
 Federici, F., [151](#)
 Ferraioli, Giampaolo, [257](#)
 Formisano, Antonio, [603](#)
 Forte, Giovanni, [359](#)
 Fragiaco, Massimo, [339](#)
 Fraundorfer, Friedrich, [761](#)

G

Gara, Fabrizio, [557](#), [957](#)
 García-Macías, Enrique, [415](#)
 Gasca, Héctor M., [271](#)
 Gennaro Di, F., [151](#)
 Gentile, Carmelo, [793](#), [853](#)
 Gerber, Matthew, [967](#)
 Ghiasi, Ramin, [431](#)
 Giordano, Pier Francesco, [935](#)
 Giorgetti, Andrea, [809](#)
 Glisic, Branko, [967](#)
 Gonçalves, Eduardo, [499](#)
 Grassia, L., [403](#)
 Grosso Del, A., [151](#), [159](#)
 Guzmán, Germán M., [271](#)

H

He, Jia, [197](#)
 Heredia, Guillermo, [761](#)
 Hernández, Jorge A., [271](#)
 Howiacki, Tomasz, [775](#)
 Hyldmo, Endre, [889](#)

I

Iacovino, Chiara, [373](#)
 Iadicicco, Agostino, [507](#)
 IanWilloughby, [889](#)
 Ierimonti, Laura, [415](#)

J

Johnsy, Angel Caroline, [257](#)
 Jouanet, Laurent, [725](#)

K

Kanellopoulos, Georgios, [69](#)
 Kohm, Mareike, [457](#)
 Koutsomarkos, Vasileios, [69](#)
 Kromanis, Rolands, [83](#), [115](#)
 Kullaa, Jyrki, [921](#)
 Kumar, Vivek, [967](#)

L

Labocha, Sławomir, [775](#)
 Landi, Luca, [97](#)
 Lanticq, Vincent, [747](#)
 Lau, Albert, [889](#)
 Laudante, G., [403](#)
 Law, Angus, [69](#)
 Lienhart, Werner, [825](#), [839](#)
 Limongelli, Maria Pina, [935](#)
 Lirza, Eriselda, [747](#)
 Losanno, Daniele, [585](#), [997](#)
 Lubrano Lobianco, Alessandro, [177](#)
 Luchetta, Michele, [389](#)
 Lydon, Darragh, [367](#)
 Lydon, Myra, [367](#)

M

Machorro, José M., [271](#)
 Magalhães, Filipe, [15](#)
 Manfredi, Vincenzo, [205](#)
 Marcheggiani, Laura, [603](#)
 Marchiondelli, Alessandra, [389](#)
 Marra, Adriana, [645](#)
 Martinelli, Enzo, [889](#)

Martínez, Luis A., 271
Masi, Angelo, 205
Masnata, Chiara, 903
Matteo Di, Alberto, 903
McGetrick, Patrick, 243
Menghini, Alessandro, 793
Micelli, Francesco, 569
Migliorino, Placido, 389
Mohammad, Fouad, 115
Monsberger, Christoph M., 825
Moutinho, Carlos, 15
Musone, V., 403

N

Nicoletti, Vanni, 557, 957
Noori, Mohammad, 431
Nöther, Nils, 167
Novellino, A., 663
Nucci, Marco, 747
Nuzzo, I., 663, 997

O

Obiechefu, Chidiebere B., 115
Occhiuzzi, A., 663
Osmani, S., 151, 159

P

Palma Di, Pasquale, 507
Pascazio, Vito, 257
Pastorelli, D., 159
Pecce, Marisa, 205, 219
Pereira, Sérgio, 15
Petraça, Emanuele, 1015
Pietra, Massimo Della, 507
Pirone, Marianna, 359
Pirrota, Antonina, 903
Polydorou, Efstathios, 243
Ponsi, Federico, 515
Ponzo, Felice Carlo, 373
Previtali, Mattia, 935

Q

Quigley, John, 129
Quintana, Juan A., 271
Quqa, Said, 97

R

Rainieri, Carlo, 585, 699, 1015
Ramesh, Visvanathan, 761

Reynders, Edwin, 289
Reynolds, Thomas P. S., 57, 69
Rizzo, Michele, 233
Robinson, Des, 243
Roeck, Guido De, 289
Rossi, Francesco, 389
Rubino, E., 663
Ruggieri, Andrea, 869
Ruocco, E., 403
Russotto, Salvatore, 903

S

Saetta, Anna, 691
Salvatori, Antonello, 311
Santamato, Francesco, 205, 219
Santarsiero, Giuseppe, 205
Santo, Antonio, 359
Santoro, Valentino, 535
Santos, Filipe, 499
Sartorelli, Luca, 935
Savini, Francesca, 869
Sbaraglia, Luca, 619
Schönberger, Caroline, 839
Schiavone, V., 997
Schirinzi, Gilda, 257
Selleri, Alberto, 389
Serino, G., 997
Shi, Bin, 1
Sieńko, Rafał, 775
Silik, Ahmed, 431
Soldovieri, Francesco, 373
Soto, Miguel Ángel Trujillo, 761
Spadaccini, Ostilio, 233
Spizzuoco, M., 997
Sprynski, Nathalie Saguin, 725
Stella, Alberto, 691
Stempniewski, Lothar, 457
Stratford, Tim, 57, 69
Sturm, James C., 967

T

Talledo, Diego, 691
Taylor, Su, 243, 367
Testa, G., 677
Testi, Enrico, 809
Tonelli, Daniel, 389
Trizio, Ilaria, 645, 869

U

Ubertini, Filippo, 415, 485
Urciuoli, Gianfranco, 359

Uttini, Andrea, [935](#)

V

Valeri, Enrico, [389](#)

Venanzi, Ilaria, [415](#)

Verma, Naveen, [967](#)

Verzobio, Andrea, [129](#)

Vidal, Audrey, [725](#)

Vincenzi, Loris, [515](#), [535](#)

W

Wagner, Sigurd, [967](#)

Weaver, Campbell, [967](#)

Weilharter, Rafael, [761](#)

Wu, Zhishen, [431](#)

Wynne, Zachariah, [57](#), [69](#)

X

Xu, Bin, [197](#)

Y

Ye, Xiao, [1](#)

Z

Zeferino, João, [499](#)

Zhang, Lei, [1](#)

Zhao, Ye, [197](#)

Zhu, Hong-Hu, [1](#)

Zonno, Giacomo, [793](#), [853](#)

Zonta, Daniele, [129](#), [389](#)

Zuziak, Katarzyna, [775](#)